nagra.

TECHNICAL REPORT 24-17

Geosynthesis of Northern Switzerland

November 2024

Nagra | National Cooperative for the Disposal of Radioactive Waste
Hardstrasse 73 | 5430 Wettingen | Switzerland
T. +41 56 437 11 11 | info@nagra.ch | nagra.ch

nagra.

TECHNICAL REPORT 24-17

Geosynthesis of Northern Switzerland

November 2024

Nagra | **National Cooperative for the Disposal of Radioactive Waste**
Hardstrasse 73 | 5430 Wettingen | Switzerland
T. +41 56 437 11 11 | info@nagra.ch | nagra.ch

The report *"Geosynthesis of Northern Switzerland"* has been elaborated by a core team consisting of Michael Schnellmann, Gaudenz Deplazes, Silvio Giger, Angela Landgraf, Fabian Maier, Raphael Schneeberger and Daniel Traber with text contributions by Lukas Aschwanden, Jens Becker, Eleonora Crisci, Urs Fischer, Thomas Gimmi, Andreas Jenni, Mirjam Kiczka, Nathan Looser, Andreas Ludwig, Martin Mazurek, Nicolas Roy, Daniel Rufer, Christoph Wanner, Paul Wersin and Carmen Zwahlen.

Many additional people contributed their expertise to this report: Ramon Arrowsmith, Misha Baldachin, Wolfgang Betz, Andrea Bianchin, Jens Birkholzer, Petra Blaser, Evelina Bros, Marius Büchi, Patrick Burgert, Denis Cohen, Jean Desroches, Alessio Ferrari, Quentin Fisher, Reto Flückiger, Andreas Gautschi, Lukasz Gregorczyk, Barbara Habermacher, Oliver Heidbach, Susanne Incorvaia, Peter Jordan, Lukas Keller, Jean-Marc Lavanchy, Jin Ma, Stefano Mazzoli, Fiona McEvoy, Linda McKinley, Jon Mosar, Richard Ott, Armin Pechstein, Arnaud Ruchat, Michael Ruff, Frank Scherbaum, David Schofield, Wolfgang Schwanghart, Richard Shaw, Manfred Strecker, Miryam Unger, Tim Vietor, Kristin Vogel, Anne Voigtländer, Niklaus Waber, Stephan Wohlwend, Valentina Zampetti, Géraldine Zimmerli and Marco Zuber.

This report has benefited from numerous technical discussions and reviews by various people inside and outside Nagra. We would like to thank these people and all others who have contributed to this report.

ISSN 1015-2636

Copyright © 2024 by Nagra, Wettingen (Switzerland) / All rights reserved. All parts of this work are protected by copyright. Any utilisation outwith the remit of the copyright law is unlawful and liable to prosecution. This applies in particular to translations, storage and processing in electronic systems and programs, microfilms, reproductions, etc.

Summary

In accordance with the regulatory requirements, the geological investigation and integration work carried out during the third and final stage of the site selection process substantiates the safety-relevant knowledge and understanding of the geological barrier. The chosen approach combines a broad spectrum of methods and multiple independent lines of evidence to ensure robust conclusions for site selection and the demonstration of long-term safety. The studies confirm and emphasise the excellent barrier function of the Opalinus Clay, as documented previously by extensive research in Northern Switzerland and at the Mont Terri rock laboratory over a 30-year period. The results are compatible with worldwide findings from applied studies and research projects including international radioactive waste disposal programmes, hydrocarbon industry, carbon capture and storage, and tunnelling.

The ~ 100 to 120 m thick Opalinus Clay is the host rock and primary geological barrier in the three investigated siting regions Jura Ost (JO), Nördlich Lägern (NL) and Zürich Nordost (ZNO). It is characterised by a low lithological variability, a high clay-mineral content (typically around 60 wt.-%), a very low hydraulic conductivity, and favourable geochemical conditions for radionuclide retention (high sorption capacity, reducing conditions). Low-permeability confining units above and below the host rock provide an additional contribution to the geological barrier. Independent evidence for slow transport in the high-clay low-conductivity sequence of the host rock and its confining units is provided by profiles of natural tracer in porewater. These profiles indicate diffusion-dominated transport over hundreds of thousands to millions of years in the geological past.

Potential disturbance of the barrier function by natural processes is minimised by placing the repository in an area with subhorizontal to gently dipping strata at sufficient depth and taking into account faults mappable in the 3D seismic reflection surveys. Subseismic faults in the Opalinus Clay are small and self-sealing processes ensure low fault transmissivity over safety-relevant timescales. New larger faults are not expected to develop in the disposal area during the time period under consideration, because deformation rates in Northern Switzerland are low and future deformation will preferentially take place along inherited large-scale structures, as observed in the geological history of the area.

The systematic assessment of future fluvial and glacial erosion is based on a detailed reconstruction of the past landscape evolution. The overburden of the Opalinus Clay remains sufficiently large over the entire time period under consideration preventing relevant changes in porosity and hydraulic conductivity and ensuring robust self-sealing. The changes in diffusion coefficients will be very limited. Regarding the long-term stability of the engineered barriers, geochemical conditions in the host rock will remain reducing with a neutral pH because of the high buffering capacity of the host rock minerals.

The three investigated siting regions provide a high-quality geological barrier, with the Opalinus Clay comprising comparable properties, located at a suitable depth range and with areas devoid of seismically mappable faults. However, some distinct differences between the siting regions exist. They relate to the thickness of the confining units, the hydrogeological and tectonic situation and resilience regarding future erosion. The low-permeability sequence of host rock and confining units is thickest in NL and thinnest in JO. The porewater composition in the Opalinus Clay in NL is characterised by a larger fraction of old porewater and a smaller overprint by meteoric water compared to the other siting regions, indicating a particularly efficient isolation of the host rock from surface waters. The NL siting region also has the largest area devoid of seismically mappable faults and is most robust to future erosion, mainly because of the greatest emplacement depth.

Key Outcomes for the demonstration of long-term safety and site comparison

The following section highlights the main characteristics of the geological barrier with regard to long-term safety and the key differences between the siting regions Jura Ost (JO), Nördlich Lägern (NL) and Zürich Nordost (ZNO)[1]. The latter are marked in blue.

- **The large-scale geological setting is favourable:**

  In the Swiss context, the siting regions are characterised by low seismic activity and uplift rates. The three siting regions are located away from large-scale tectonic zones of increased geological complexity (Alps, Internal Jura, Upper Rhine Graben, Hegau – Bodensee Graben). In all three siting regions, the host rock Opalinus Clay has overall thicknesses of more than 100 m and occurs at depths that are suitable for repository construction and long-term safety. ► *Section 1.4*

- **The host rock provides an efficient and robust transport barrier:**

  The Opalinus Clay host rock represents the core of the geological barrier. It exhibits excellent and comparable barrier properties in all three siting regions. These are:

  – Very low hydraulic conductivity and, consequently, diffusion-dominated mass transport. ► *Sections 5.6, 5.9*

  – Host rock thicknesses of ~ 100 to 120 m. ► *Section 4.2.6*

  – Low variability of the host-rock properties including a consistently high clay-mineral content. ► *Sections 4.2.6, 5.2.3*

  – Lack of significant preferential flow paths:

    · Fracture frequencies are lower compared to mechanically more competent units. Deformation in the Opalinus Clay is accommodated in a more distributed and discontinuous manner with soft-linked fault segmentation. ► *Sections 4.3.4, 5.5.4*

    · Efficient self-sealing in the Opalinus Clay is ensured by the high clay-mineral content (low stiffness and high swelling capacity) and sufficient effective stress (overburden thickness). ► *Sections 5.5.2, 5.7*

  – High sorption capacity (favouring radionuclide retention) due to the mineral composition (high clay-mineral content) and the corresponding high external surface area. ► *Section 5.3.4*

  – Stable and favourable geochemical conditions with regard to the stability of the engineered barriers (porewater pH near neutral, reducing conditions, moderate salinity, buffering by mineralogical composition). ► *Section 5.4*

[1] Note that the systematic site comparison according to the criteria defined in the Sectoral Plan for Deep Geological Repositories (SFOE 2008) is not part of this report. It is treated in Nagra (2025a) and takes into account the geological information contained in this report.

- **Low-permeability units above and below the host rock complement the transport barrier, resulting in a thick low-permeability zone with diffusion-dominated transport:**
  - The low permeability of the units above and below the Opalinus Clay is demonstrated by hydraulic tests. ► *Section 4.5.3*
  - Compared to the host rock, the confining units are more heterogeneous and include sections with intermediate to low clay-mineral contents with thicknesses of up to a few metres ("hard beds"). In the upper confining units these are less frequent in NL compared to JO and ZNO. Particularly in the eastern part of NL, the units directly overlying the Opalinus Clay have a high clay-mineral content (► *Section 4.2.7*). Evidence such as the observed low hydraulic conductivities (► *Sections 4.5.3, 5.6.3.2*), absence of relevant excursions in the tracer profiles (► *Section 4.6*) and their restricted thicknesses (► *Sections 4.2.7.2, 4.5.3.5, 5.6.3.2*) suggest that these "hard beds" do not represent significant flow paths.
  - The 40 m thick, clay-mineral-poor «Herrenwis Unit» in eastern NL is regarded as part of the low-permeability upper confining units, because the observed hydraulic conductivities are low, and the unit is embedded in clay-mineral-rich units. Also, the observed low hydraulic heads indicate that the unit is hydraulically isolated from the regional flow systems. ► *Sections 4.2.7.2, 4.5.3.7*
  - The distance between the centre of the host rock and the next overlying aquifer is largest in NL and smallest in JO. In NL and ZNO, the upper confining units are bounded by the Malm aquifer, in JO by the Hauptrogenstein aquifer. ► *Sections 4.5.3, 4.9*
  - The distance between the centre of the host rock and the closest underlying aquifer (Keuper aquifer) delimiting the lower confining units is similar in all the siting regions. However, the Keuper aquifer shows a different appearance in the three siting regions. In ZNO, and also JO, a continuous aquifer seems to be present across the region (Seebi Member and Gansingen Member, respectively). In contrast, in NL, permeable zones are limited to locally occurring sandstone channels in a stratigraphically lower level compared to the Seebi and Gansingen Members. Consequently, in NL, units down to the Muschelkalk aquifer could contribute to the barrier function. ► *Sections 4.2.3, 4.2.4, 4.5.3, 4.9*

- **Independent evidence demonstrates the barrier efficiency of the geological system over very long timescales**
  - In all the siting regions, the barrier efficiency is demonstrated by the profiles of natural tracers in porewater, which are best explained by molecular diffusion between the aquifers as the dominant transport mechanism. ► *Section 4.6*
  - In NL, the isotopic composition of the Opalinus Clay porewater indicates a larger fraction of old porewater and a smaller overprint by meteoric water compared to the other siting regions. ► *Sections 4.6.2, 4.9*
  - The Malm aquifer bounding the low-permeability units in NL and ZNO represents a quasi-stagnant flow system with old waters, more strongly so in NL. The Hauptrogenstein aquifer, which constitutes the bounding aquifer above the host rock and confining units in JO, represents a slightly more active flow system. The Keuper aquifer is less active in NL compared to the other siting regions. ► *Sections 4.5.6, 4.6*

- **Areas devoid of seismically mappable faults and with limited tectonic deformation occur in all the siting regions**
  - All three siting regions show areas devoid of seismically mappable faults providing flexibility for repository placement and design. Also, along the deep boreholes drilled in the siting regions, long intervals devoid of any fractures were observed within the Opalinus Clay. There is no indication that the Opalinus Clay acted as a décollement horizon within the siting regions. ► *Sections 4.3.4, 4.3.7*
  - In NL, the area free of seismically mappable faults is largest and thus the flexibility regarding repository layout is greatest. ► *Sections 4.3.4, 4.3.7*
- **The key properties of the host rock are not negatively affected by climatic and geological processes in a relevant way and remain stable over the time period under consideration**
  - Recent tectonic deformation rates in Northern Switzerland are small, with a slight north-south shortening (~ 1 – 2.8 m/Myr/km). This pattern is anticipated to continue. Future deformation is expected to result in the reactivation of inherited faults, primarily the regional fault zones. These are taken into account when planning the locations of the disposal areas. If new faults were to develop in the host rock in the future, they are expected to be segmented and short in length and offset. ► *Sections 6.2.3, 6.2.4*
  - Future erosion (glacial and non-glacial) is expected to be comparable to that observed in the Quaternary, but probably at lower rates (no major drainage reorganisation, smaller glaciers, delay in glacial inception, protection of host rock and confining units by overlying hard-to-erode rocks). ► *Section 6.4.3*
  - A residual host rock overburden thickness of a minimum of 200 m is considered reliable for efficient self-sealing. The expected evolution of future erosion indicates that this criterion can be safely met for the time period under consideration in NL and ZNO at the position of the provisional disposal area. However, JO is sensitive to less likely scenarios with changing river courses. These may result in overburden thickness < 200 m towards the end of the time period under consideration at the position of the provisional disposal area. ► *Sections 6.4.4, 6.4.5*
  - The probability of a repository excavation by erosive processes within the next one million years can be considered extremely low in the provisional disposal areas of all siting regions but are about an order of magnitude lower in NL. NL is best protected against future erosion because of the greatest emplacement depth and enhanced resilience to the main erosive processes. ► *Sections 6.4.4, 6.4.5*
  - Climate change, glaciations, permafrost, erosion and tectonic movements can affect aquifer dynamics, including a shortening of the transport paths along aquifers or increased flow rates. Glacial loading may temporarily lead to overpressures in the host rock and to an increased hydraulic gradient from the host rock towards the aquifers. The effect can be constrained and shown to be not relevant for overall tracer transport. Geochemical conditions will remain reducing and pH neutral because of the buffering capacity of the host rock minerals. ► *Section 6.5*
  - No relevant dissolution of rock and related development of preferred transport pathways are expected in the host rock because the low hydraulic conductivities are maintained, and because a limited amount of soluble (e.g. carbonate) minerals is disseminated within the clay-mineral-rich rock (► *Section 6.5.2.3)*. Dissolution processes below the host rock are also unlikely to affect the long-term stability because of small driving forces, slow processes and effective self-sealing processes in the host rock. ► *Section 6.5.5*

Zusammenfassung

Die gemäss den behördlichen Anforderungen für die dritte und letzte Etappe des Standortwahlverfahrens durchgeführten geologischen Arbeiten substantiieren das Wissen zum Aufbau und zur Funktionsweise der geologischen Barriere eines Tiefenlagers. Die für die Standortwahl und den Langzeitsicherheitsnachweis relevanten Aussagen stützen sich auf mehrere unabhängige Argumentationslinien und auf eine umfangreiche Datenbasis ab, die unabhängige Mess- und Auswertungsmethoden kombiniert. Die Studien bestätigen und unterstreichen die hervorragende Barrierenfunktion des Opalinustons, und untermauern die umfangreichen Erkenntnisse, die in den letzten 30 Jahren in der Nordschweiz und durch Forschungsprojekte im Felslabor Mont Terri gewonnen wurden. Die Ergebnisse sind kompatibel mit weltweiten Erkenntnissen aus diversen Forschungsprojekten und angewandten Projekten (internationale Programme zur Entsorgung radioaktiver Abfälle, Kohlenwasserstoffindustrie, CO_2-Sequestrierung, Tunnelbau).

In den drei untersuchten Standortgebieten Jura Ost (JO), Nördlich Lägern (NL) und Zürich Nordost (ZNO) bildet das ca. 100 – 120 m mächtige Wirtgestein Opalinuston die primäre geologische Barriere. Sie zeichnet sich durch eine geringe laterale und vertikale Variabilität, einen hohen Tonmineralgehalt (typische Werte ca. 60 Gew.-%), eine sehr geringe hydraulische Leitfähigkeit und günstige geochemische Bedingungen (hohe Sorptionsfähigkeit, reduzierende Bedingungen) aus. Direkt angrenzende gering durchlässige Rahmengesteine tragen zusätzlich zur Barrierenfunktion bei. Ein unabhängiger Nachweis für die Barrierenwirkung von Wirt- und Rahmengesteinen ergibt sich aus den Profilen der natürlichen Tracer im Porenwasser. Sie zeigen einen sehr langsamen, diffusionsdominierten Stofftransport über Hunderttausende bis Millionen Jahre auf.

Die Beeinträchtigung der Barrierenfunktion durch natürliche Prozesse wird minimiert durch die Platzierung des Tiefenlagers in einer Zone mit subhorizontalen bis leicht geneigten Schichten in genügend grosser Tiefe unter Berücksichtigung der Lage von seismisch kartierbaren tektonischen Störungen. Subseismische Störungen im Opalinuston sind klein und Selbstabdichtungsprozesse sorgen für eine geringe Transmissivität dieser Störungen über sicherheitsrelevante Zeiträume. Die Bildung von neuen, grösseren Störungen wird im Betrachtungszeitraum nicht erwartet, da die Deformationsraten in der Nordschweiz gering sind und zukünftige Deformation, wie in der Vergangenheit, bevorzugt im Bereich der ererbten Grossstrukturen lokalisieren wird.

Die systematische Beurteilung der zukünftigen fluviatilen und glazialen Erosion basiert auf einer detaillierten Rekonstruktion der vergangenen Landschaftsentwicklung. Die Überlagerung des Opalinustons bleibt über den gesamten Betrachtungszeitraum genügend gross, um relevante Veränderungen von Porosität und hydraulischer Durchlässigkeit zu verhindern und eine effektive Selbstabdichtung des Opalinustons sicherzustellen. Die Änderungen der Diffusionskoeffizienten werden sehr begrenzt sein. Wegen der hohen Pufferkapazität der Wirtgesteinsminerale werden die geochemischen Bedingungen im Wirtgestein über den Betrachtungszeitraum reduzierend und pH-neutral bleiben und so zur Langzeitstabilität der technischen Barrieren beitragen.

Alle drei Standortgebiete verfügen über eine hochwertige geologische Barriere. Die Opalinuston-Eigenschaften sind vergleichbar, und es gibt überall geeignete Tiefenbereiche ohne seismisch kartierbare Störungen. Deutliche Unterschiede zwischen den Gebieten betreffen die Mächtigkeit der Rahmengesteine, die hydrogeologische und tektonische Situation sowie die Widerstandsfähigkeit gegenüber zukünftiger Erosion. Die gering durchlässige Abfolge (Wirtgestein und Rahmengesteine) ist in NL am mächtigsten und in JO am dünnsten. Die Porenwasserzusammensetzung im Opalinuston ist in NL durch einen grösseren Anteil an altem Porenwasser und eine geringere Überprägung durch meteorische Wässer gekennzeichnet, was auf eine besonders effiziente Isolation des Wirtgesteins von Oberflächenwässern hinweist. Das Standortgebiet NL weist zudem die grösste Fläche ohne seismisch kartierbare Störungen auf und ist vor allem wegen der grössten Lagertiefe am besten gegen zukünftige Erosion geschützt.

Schlüsselergebnisse für Langzeitsicherheit und Standortvergleich

Im Folgenden werden die wichtigsten Eigenschaften der geologischen Barriere in Bezug auf die Langzeitsicherheit dargestellt und die wesentlichen Unterschiede zwischen den Standortgebieten Jura Ost (JO), Nördlich Lägern (NL) und Zürich Nordost (ZNO) hervorgehoben[2]. Letztere sind blau markiert.

- **Die grossräumigen geologischen Verhältnisse sind insgesamt günstig:**

  Im Schweizer Kontext sind die drei Standortgebiete durch eine geringe seismische Aktivität und Hebungsrate gekennzeichnet. Sie befinden sich abseits grossräumiger tektonischer Zonen mit erhöhter geologischer Komplexität (Alpen, Interner Jura, Oberrheingraben, Hegau – Bodensee-Graben). In allen drei Standortgebieten weist das Wirtgestein Opalinuston Mächtigkeiten von mehr als 100 m auf und kommt in Tiefen vor, die für den Bau des Tiefenlagers und die Langzeitsicherheit geeignet sind. ► *Kap. 1.5*

- **Das Wirtgestein stellt eine effiziente und robuste Transportbarriere dar:**

  Das Wirtgestein Opalinuston bildet den Kern der geologischen Barriere. Es weist in allen drei Standortgebieten hervorragende und vergleichbare Barriereneigenschaften auf. Diese sind:

  – Sehr geringe hydraulische Leitfähigkeit und damit diffusionsdominierter Stofftransport. ► *Kap. 5.6, 5.9*

  – Wirtgesteinsmächtigkeiten von ~ 100 bis 120 m. ► *Kap. 4.2.6*

  – Eine geringe Variabilität der Wirtgesteinseigenschaften mit einem durchgehend hohen Tonmineralgehalt. ► *Kap. 4.2.6, 5.2.3*

  – Das Fehlen signifikanter präferenzieller Fliesswege

    · Die Störungsfrequenz ist im Vergleich zu mechanisch kompetenteren Einheiten geringer. Deformation wird im Opalinuston eher verteilt aufgenommen in Form von segmentierten, häufig diskontinuierlichen Bruchflächen. ► *Kap. 4.3.4, 5.5.4*

    · Eine effiziente Selbstabdichtung im Opalinuston wird durch den hohen Tonmineralgehalt (geringe Steifigkeit, hohe Quellfähigkeit) und eine ausreichende effektive Spannung (Überlagerungsmächtigkeit) gewährleistet. ► *Kap. 5.5.2, 5.7*

  – Eine für die Radionuklidrückhaltung günstige, hohe Sorptionskapazität aufgrund der mineralogischen Zusammensetzung mit hohem Tonmineralgehalt und der damit verbundenen grossen äusseren Oberfläche. ► *Kap. 5.3.4*

  – Stabile und günstige geochemische Bedingungen im Hinblick auf die Stabilität der technischen Barrieren (Porenwasser pH-Wert nahe neutral, reduzierende Redoxbedingungen, moderate Salinität, Pufferung durch Mineralogie). ► *Kap. 5.4*

[2] Der systematische Standortvergleich gemäss den im Sachplan geologische Tiefenlager (BFE 2008) definierten Kriterien ist nicht Teil dieses Berichts. Er wird in Nagra (2025a) behandelt und berücksichtigt die in diesem Bericht enthaltenen geologischen Informationen.

- **Gering durchlässige Einheiten über und unter dem Wirtgestein ergänzen die Transportbarriere und resultieren in einer mächtigen, gering durchlässigen Zone mit diffusionsdominiertem Stofftransport:**
  - Die geringe Durchlässigkeit der Einheiten oberhalb und unterhalb des Opalinustons wird durch hydraulische Tests aufgezeigt. ► *Kap. 4.5.3*
  - Die Rahmengesteine sind im Vergleich zum Wirtgestein heterogener und enthalten Abschnitte mit mittleren bis geringen Tonmineralgehalten, die Mächtigkeiten bis zu einigen Metern erreichen («harte Bänke»). In den oberen Rahmengesteinen treten diese in JO und ZNO häufiger auf als in NL, wo insbesondere im Ostteil die Einheiten direkt über dem Opalinuston sehr tonmineralreich sind (► *Kap. 4.2.7*. Die beobachteten geringen hydraulischen Durchlässigkeiten (► *Kap. 4.5.3, 5.6.3.2*), das Fehlen relevanter Anomalien in den Tracerprofilen (► *Kap. 4.6*) und ihre begrenzten Mächtigkeiten (► *Kap. 4.2.7.2, 4.5.3.5, 5.6.3.2*) weisen darauf hin, dass diese «harten Bänke» keine signifikanten Fliesswege darstellen.
  - Die 40 m mächtige, tonmineralarme «Herrenwis-Einheit» im Osten von NL wird zu den gering durchlässigen oberen Rahmengesteinen gezählt, weil die beobachteten hydraulischen Leitfähigkeiten niedrig sind und die Einheit in tonmineralreiche Einheiten eingebettet ist. Ausserdem deuten die beobachteten geringen hydraulischen Druckhöhen darauf hin, dass die Einheit hydraulisch von den regionalen Fliesssystemen isoliert ist. ► *Kap. 4.2.7.2, 4.5.3.7*
  - Der Abstand zwischen dem Zentrum des Wirtgesteins und dem nächsten darüber liegenden Aquifer ist in NL am grössten und in JO am kleinsten. In NL und ZNO werden die oberen Rahmengesteine durch den Malm-Aquifer, in JO durch den Hauptrogenstein-Aquifer begrenzt. ► *Kap. 4.5.3, 4.9*
  - Der Abstand zwischen dem Zentrum des Wirtgesteins und dem nächstgelegenen Aquifer (Keuper-Aquifer), der die unteren Rahmengesteine begrenzt, ist in allen Standortgebieten ähnlich. Der Keuper-Aquifer zeigt jedoch in den drei Standortgebieten ein unterschiedliches Erscheinungsbild. In ZNO und auch in JO scheint ein durchgehender Aquifer in der gesamten Region vorhanden zu sein (Seebi-Member in ZNO und Gansingen-Member in JO). Im Gegensatz dazu beschränken sich in NL die durchlässigen Zonen auf lokal vorkommende Sandsteinrinnen in einem stratigraphisch tieferen Niveau als das Seebi und das Gansingen-Member. Folglich könnten in NL auch Einheiten bis hinunter zum Muschelkalk-Aquifer zur Barrierenfunktion beitragen. ► *Kap. 4.2.3, 4.2.4, 4.5.3, 4.9*
- **Unabhängige Evidenzen belegen die Barrierenwirkung des geologischen Systems über sehr lange Zeitskalen**
  - In allen Standortgebieten wird die Barrierenwirksamkeit durch die Profile natürlicher Tracer im Porenwasser nachgewiesen, die sich am besten durch molekulare Diffusion als dominierenden Transportmechanismus erklären lassen. ► *Kap. 4.6*
  - Die Isotopenzusammensetzung des Opalinuston-Porenwassers weist in NL auf einen grösseren Anteil von altem Porenwasser und eine geringere Überprägung durch meteorische Wässer hin als in den anderen Standortgebieten. ► *Kap. 4.6.2, 4.9*
  - Der Malm-Aquifer, der die gering durchlässigen Einheiten in NL und ZNO begrenzt, stellt ein quasi-stagnierendes Fliesssystem mit alten Wässern dar, in NL noch ausgeprägter. Der Hauptrogenstein-Aquifer, der den begrenzenden Aquifer über dem Wirtgestein und den Rahmengesteinen in JO darstellt, ist ein etwas aktiveres Fliesssystem. Der Keuper-Aquifer ist in NL im Vergleich zu den anderen Standortgebieten weniger aktiv. ► Kap. 4.5.6, 4.6

- **In allen Standortgebieten gibt es Bereiche ohne seismisch kartierbare Störungen und mit geringer tektonischer Deformation**
  - Alle drei Standortgebieten enthalten Bereiche ohne seismisch kartierbare Störungen, was Flexibilität für die Platzierung und Ausgestaltung des Lagers ergibt. Auch in den Tiefbohrungen wurden im Opalinuston lange Intervalle ohne Störungen beobachtet. Es gibt keine Hinweise darauf, dass der Opalinuston in den Standortgebieten als Abscherungshorizont fungiert. ► *Kap. 4.3.4, 4.3.7*
  - In NL ist das Gebiet frei von seismisch kartierbaren Störungen am grössten und damit auch die Flexibilität bezüglich Anordnung des Tiefenlagers. ► *Kap. 4.3.4, 4.3.7*
- **Die Schlüsseleigenschaften des Wirtgesteins werden durch klimatische und geologische Prozesse nicht in relevanter Art und Weise negativ beeinflusst und bleiben über den Betrachtungszeitraum stabil**
  - Die rezenten tektonischen Deformationsraten in der Nordschweiz sind gering, mit einer leichten Nord-Süd-Verkürzung (~ 1 – 2.8 m/Myr/km). Es wird erwartet, dass sie langfristig in einem ähnlichen Bereich bleibt und dass zukünftige Deformation in erster Linie zur Reaktivierung ererbter Störungen, vor allem der regionalen Störungszonen, führen wird. Deren Lage wird bei der Platzierung der Lagerstollen berücksichtigt. Sollten sich in Zukunft neue Störungen im Wirtgestein entwickeln, so werden diese voraussichtlich segmentiert sein, mit limitierter Ausdehnung und limitiertem Versatz. ► *Kap. 6.2.3, 6.2.4*
  - Die künftige (glaziale und nicht-glaziale) Erosion dürfte mit der im Quartär beobachteten vergleichbar sein, allerdings wahrscheinlich mit geringeren Raten (keine grössere Umgestaltung des Drainagesystems, kleinere Gletscher, Verzögerung des Beginns der Vergletscherungen und Schutz der Wirt- und Rahmengesteine durch darüberliegende schlecht erodierbare Einheiten). ► *Kap. 6.4.3*
  - Eine Überdeckung des Wirtgesteins von mindestens 200 m Mächtigkeit wird als zuverlässig für eine effiziente Selbstabdichtung angesehen. Die erwartete Entwicklung der zukünftigen Erosion zeigt, dass dieses Kriterium für den betrachteten Zeitraum in NL und ZNO sicher erfüllt werden kann. JO ist vergleichsweise empfindlich gegenüber weniger wahrscheinlichen Szenarien mit veränderten Flussläufen. Diese können gegen Ende des Betrachtungszeitraums beim exemplarischen Lagerfeld zu einer Gesteinsüberdeckung von weniger als 200 m führen. ► *Kap. 6.4.4, 6.4.5*
  - Die Wahrscheinlichkeit einer Freilegung des Lagers durch erosive Prozesse innerhalb der nächsten Million Jahre ist im Bereich der exemplarischen Lagerfelder in allen Standortgebieten als äusserst gering einzuschätzen, in NL jedoch um eine Grössenordnung geringer. NL ist aufgrund der grössten Einlagerungstiefe und der erhöhten Widerstandsfähigkeit gegenüber den wichtigsten Erosionsprozessen am besten gegen zukünftige Erosion geschützt. ► *Kap. 6.4.4, 6.4.5*
  - Klimawandel, Vergletscherung, Permafrost, Erosion und tektonische Bewegungen können sich auf die Dynamik der Tiefenaquifere auswirken einschliesslich einer Verkürzung der Transportwege zu den Exfiltrationsgebieten und/oder erhöhter Fliessgeschwindigkeiten. Gletscherbelastungen können vorübergehend zu Überdrücken im Wirtgestein und dadurch zu einem vorübergehend erhöhten hydraulischen Gradienten in Richtung der Aquifere führen. Diese können eingegrenzt werden und sind für den Tracertransport nicht relevant. Die geochemischen Bedingungen bleiben aufgrund der Pufferkapazität der Wirtgesteinsminerale reduzierend und pH-neutral. ► *Kap. 6.5*

- Es wird keine relevante Gesteinslösung und damit verbundene Entwicklung bevorzugter Transportwege im Wirtgestein erwartet, da die niedrigen hydraulischen Leitfähigkeiten beibehalten werden und die begrenzte Menge löslicher (z. B. karbonatischer) Minerale innerhalb des tonmineralreichen Gesteins verteilt ist (► *Kap. 6.5.2.3*). Auch Lösungsprozesse unterhalb des Wirtgesteins werden die Langzeitstabilität nicht beeinträchtigen, da die treibenden Kräfte gering sind, die Prozesse langsam ablaufen und das Wirtgestein eine hohes Selbstabdichtungsvermögen aufweist. ► *Kap. 6.5.5*

Table of Contents

Summary I

Key Outcomes for the demonstration of long-term safety and site comparison II

Zusammenfassung V

Schlüsselergebnisse für Langzeitsicherheit und Standortvergleich VI

Table of Contents XI

List of Tables XVIII

List of Figures XVIII

List of Acronyms XXXI

1 Introduction 1
1.1 Context 1
1.2 Purpose and scope of the present report 4
1.3 Structure of the report and ways to read it 4
1.4 Geological barrier: Function and required geological input for site selection and demonstration of long-term safety 5
1.4.1 Safety concept 5
1.4.2 Site selection 6
1.4.3 Characteristics of the geological barrier as input for site selection and demonstration of long-term safety 8
1.5 Why the Opalinus Clay in Northern Switzerland? 9

2 Overview of geological investigations with relevance for siting and demonstration of post-closure safety 11
2.1 Overview 11
2.2 Reflection seismic data 13
2.3 Deep boreholes 14
2.4 Investigation programme related to Quaternary deposits 18
2.5 Long-term monitoring systems 18
2.6 Investigations in the Mont Terri rock laboratory 19
2.7 International experience with clay-rich rocks 19

3 Geological evolution of Northern Switzerland 21
3.1 Overview 22
3.2 Paleozoic 26
3.3 Mesozoic 27
3.3.1 Triassic 27
3.3.2 Jurassic 31
3.3.2.1 Early Jurassic 31
3.3.2.2 Middle Jurassic 32
3.3.2.3 Late Jurassic 34
3.3.3 Cretaceous 36

3.4 Paleogene and Neogene ... 36
3.4.1 Paleocene ... 36
3.4.2 Eocene ... 36
3.4.3 Oligocene ... 37
3.4.4 Miocene ... 37
3.4.5 Pliocene ... 39
3.5 Quaternary ... 42
3.6 Present-day geodynamic situation ... 44

4 Detailed geological framework ... 47
4.1 Introduction ... 47
4.2 Sedimentology and stratigraphy ... 49
4.2.1 Overview ... 49
4.2.2 Schinznach Formation ... 55
4.2.2.1 Introduction ... 55
4.2.2.2 Facies and lithostratigraphy ... 55
4.2.2.3 Variability ... 56
4.2.2.4 Chronology ... 56
4.2.2.5 Depositional evolution ... 56
4.2.3 Bänkerjoch Formation ... 59
4.2.3.1 Introduction ... 59
4.2.3.2 Facies and lithostratigraphy ... 60
4.2.3.3 Variability ... 61
4.2.3.4 Chronology ... 61
4.2.3.5 Depositional evolution ... 61
4.2.4 Klettgau Formation ... 64
4.2.4.1 Introduction ... 64
4.2.4.2 Facies and lithostratigraphy ... 65
4.2.4.3 Variability ... 67
4.2.4.4 Chronology ... 67
4.2.4.5 Depositional evolution ... 72
4.2.5 Staffelegg Formation ... 74
4.2.5.1 Introduction ... 74
4.2.5.2 Facies and lithostratigraphy ... 75
4.2.5.3 Variability ... 78
4.2.5.4 Chronology ... 78
4.2.5.5 Depositional evolution ... 78
4.2.6 The Opalinus Clay ... 80
4.2.6.1 Introduction ... 80
4.2.6.2 Facies and lithostratigraphy ... 81
4.2.6.3 Variability ... 83
4.2.6.4 Depositional evolution ... 86
4.2.7 Dogger Group above Opalinus Clay ... 89
4.2.7.1 Introduction ... 89
4.2.7.2 Facies and lithostratigraphy ... 91

4.2.7.3 Variability ... 102
4.2.7.4 Chronology ... 102
4.2.7.5 Depositional evolution ... 102
4.2.8 Wildegg Formation ... 110
4.2.8.1 Introduction ... 110
4.2.8.2 Facies and lithostratigraphy ... 111
4.2.8.3 Variability ... 111
4.2.8.4 Chronology ... 111
4.2.8.5 Depositional evolution ... 112
4.2.9 Malm Group above Wildegg Formation ... 115
4.2.9.1 Introduction ... 115
4.2.9.2 Facies and lithostratigraphy ... 116
4.2.9.3 Variability ... 117
4.2.9.4 Chronology ... 117
4.2.9.5 Depositional evolution ... 117
4.2.10 Conclusions ... 120
4.3 Tectonic setting ... 121
4.3.1 Overview ... 121
4.3.2 Terminology of structures ... 121
4.3.3 Tectonic situation of Northern Switzerland ... 125
4.3.4 Structural inventory in the siting regions ... 132
4.3.5 Detailed tectonic and burial temperature evolution since the Early Jurassic ... 151
4.3.6 Deformational style and tectonic domains ... 158
4.3.7 Conclusions ... 162
4.4 Current stress field ... 163
4.4.1 Overview ... 163
4.4.2 Stress orientations ... 164
4.4.3 Stress magnitudes and stress regime ... 165
4.4.4 3D geomechanical-numerical models of the siting regions ... 170
4.4.5 Conclusions ... 173
4.5 Hydrogeology and hydrogeochemistry ... 174
4.5.1 Overview ... 174
4.5.2 Regional hydrogeological situation ... 175
4.5.3 Hydrostratigraphy ... 177
4.5.3.1 Introduction ... 177
4.5.3.2 Overview ... 178
4.5.3.3 Malm aquifer ... 180
4.5.3.4 Wildegg Formation ... 183
4.5.3.5 Clay-mineral-rich aquitard units above the Opalinus Clay (Dogger Group) ... 184
4.5.3.6 Hauptrogenstein aquifer ... 186
4.5.3.7 «Herrenwis Unit» ... 186
4.5.3.8 Opalinus Clay ... 189
4.5.3.9 Lias Group and uppermost Keuper ... 190
4.5.3.10 Keuper aquifer ... 191
4.5.3.11 Bänkerjoch Formation ... 194

4.5.3.12 Muschelkalk aquifer 194
4.5.4 Analysis of the flow system based on the regional hydrodynamic model 196
4.5.4.1 Model description 196
4.5.4.2 Malm aquifer 198
4.5.4.3 Hauptrogenstein aquifer 201
4.5.4.4 Keuper aquifer 202
4.5.4.5 Muschelkalk aquifer 204
4.5.4.6 Differences in hydraulic heads between the aquifers 206
4.5.5 Hydrogeochemistry of deep groundwaters 207
4.5.5.1 Introduction 207
4.5.5.2 Malm aquifer 208
4.5.5.3 Hauptrogenstein aquifer including Birmenstorf Member 216
4.5.5.4 Keuper aquifer 219
4.5.5.5 Muschelkalk aquifer 224
4.5.5.6 Cross-formation flow 232
4.5.6 Concluding summary hydrogeology 234
4.6 Solute transport in the host rock and confining units demonstrated by the profiles of natural tracers 237
4.6.1 Overview 237
4.6.2 Profiles of stable isotopes of water 240
4.6.3 Chloride profiles and Br/Cl ion ratios 249
4.6.4 Profiles of helium in porewater 253
4.6.5 Concluding summary of natural tracer profiles 257
4.7 Palaeo-fluid flow reconstructed by geochemical investigations of secondary mineralisations 259
4.7.1 Overview 259
4.7.2 Approach, methodology and limitations 260
4.7.3 Investigated structures and inventory of mineralisations 260
4.7.4 Results of geochemical investigations of vein calcite 263
4.7.5 Results of geochemical investigations of vein celestite 269
4.7.6 Implications for palaeo-transport processes and distances 271
4.8 Current temperature conditions 272
4.9 Detailed geological framework: Summary 275

5 Key characteristics of the host rock and clay-mineral-rich confining units as geological barriers 281
5.1 Introduction 281
5.2 Lithology and mineralogy 284
5.2.1 Overview 284
5.2.2 Lithology and structure of the Opalinus Clay from microscopic to formation scale 284
5.2.3 Whole-rock mineralogy 286
5.2.4 Composition of the clay-mineral fraction 289
5.2.5 Trace and diagenetic minerals 290
5.2.6 Conclusions 292

5.3 Porosity ... 293
5.3.1 Overview ... 293
5.3.2 Porosity profile ... 293
5.3.3 Correlation of porosity with other rock properties ... 296
5.3.4 Pore-size distribution and external surface area ... 301
5.3.5 Conclusions ... 303
5.4 Porewater chemistry (geochemical conditions) ... 304
5.4.1 Overview ... 304
5.4.2 Solute distribution in the pore space ... 305
5.4.3 Porewater composition in the Opalinus Clay and the confining units ... 308
5.4.4 Reference porewaters for the Opalinus Clay ... 309
5.4.5 Extrapolating from standard conditions to in-situ temperature and pressure ... 310
5.4.6 Geochemical stability and buffering capacity of the Opalinus Clay ... 312
5.4.7 Conclusions ... 312
5.5 Geomechanical behaviour and tectonic overprint ... 313
5.5.1 Overview ... 313
5.5.2 Volumetric deformation behaviour ... 314
5.5.3 Shear deformation behaviour ... 318
5.5.4 Tectonic deformation and fault architecture in the Opalinus Clay ... 326
5.5.5 Conclusions ... 334
5.6 Hydraulic properties and hydraulic heads ... 335
5.6.1 Overview ... 335
5.6.2 Small-scale properties from lab tests ... 335
5.6.3 Rock mass scale properties from in-situ hydraulic tests ... 337
5.6.3.1 Opalinus Clay ... 337
5.6.3.2 Confining units ... 342
5.6.4 Observations in tunnels ... 344
5.6.5 Profiles of formation hydraulic heads ... 345
5.6.6 Conclusions ... 348
5.7 Self-sealing of fractures ... 348
5.7.1 Overview ... 348
5.7.2 Empirical evidence ... 349
5.7.3 Relevant processes and mechanisms ... 352
5.7.4 Importance of effective stress for robust self-sealing ... 354
5.7.5 Influence of other factors on the self-sealing potential ... 357
5.7.6 Relevance of veins for self-sealing potential ... 358
5.7.7 Conclusions ... 360
5.8 Diffusion properties ... 361
5.8.1 Overview ... 361
5.8.2 Diffusion properties at the laboratory scale (HTO and chloride) ... 361
5.8.3 Diffusion at the underground rock laboratory scale ... 368
5.8.4 Relevance at formation scale ... 370
5.8.5 Comparison with data from other clay-rich rocks ... 371
5.8.6 Conclusions regarding diffusion ... 372

5.9 Dominant transport mechanisms in the Opalinus Clay ... 373
5.10 Overall conclusions on key characteristics of the host rock and confining units ... 375

6 Long-term geological evolution ... 379
6.1 Introduction ... 379
6.1.1 Aim and content of this chapter ... 379
6.1.2 Overview of the principal geological processes potentially affecting the geological barrier ... 381
6.2 Geodynamic evolution ... 386
6.2.1 Large-scale geodynamic framework ... 387
6.2.2 Uplift and subsidence domains along the route of the Rhine River ... 389
6.2.3 Present-day horizontal crustal movements in Northern Switzerland ... 396
6.2.4 Proposed tectonic evolution with respect to faulting ... 401
6.2.5 Conclusions ... 402
6.3 Climate evolution ... 403
6.3.1 Climate during the Quaternary ... 404
6.3.1.1 Global Quaternary climate ... 404
6.3.1.2 Past climate conditions in Northern Switzerland ... 405
6.3.2 Glacier development and erosion potential in Northern Switzerland ... 409
6.3.3 Future climate evolution ... 413
6.3.3.1 Timing of future glaciations ... 413
6.3.3.2 Future climate characteristics during interglacials ... 415
6.3.4 Conclusions ... 416
6.4 Erosion ... 417
6.4.1 Key erosion processes and resulting landscape characteristics of Northern Switzerland ... 418
6.4.1.1 Erosion processes and landscape compartmentalisation ... 418
6.4.1.2 Fluvial incision ... 420
6.4.1.3 Evolution of local topography ... 427
6.4.1.4 Deep glacial erosion ... 432
6.4.2 From past to future erosion ... 438
6.4.2.1 Interpretation of present landscape characteristics in the siting regions ... 438
6.4.2.2 Site-specific constraints with respect to future erosion assessment ... 440
6.4.2.3 Approach to assessing future erosion ... 442
6.4.3 Future erosion processes and rates ... 446
6.4.3.1 Future fluvial incision ... 447
6.4.3.2 Future evolution of local topography ... 453
6.4.3.3 Future deep glacial erosion ... 461
6.4.4 Remaining overburden thickness and potential for repository excavation ... 468
6.4.5 Conclusions ... 471
6.5 Long-term hydrogeological and hydrogeochemical evolution ... 473
6.5.1 Changes in deep aquifer flow systems ... 474
6.5.1.1 Variations in groundwater recharge as a result of climate change ... 474
6.5.1.2 Changes due to erosion and changing morphology ... 474

6.5.1.3 Changes related to glaciations and permafrost 475
6.5.1.4 Changes in deep aquifer flow systems due to neotectonic activity 476
6.5.2 Changes regarding the hydraulic barrier efficiency of the Opalinus Clay and confining units 477
6.5.2.1 Change of porewater pressure and hydraulic gradient 477
6.5.2.2 Change in hydraulic conductivity due to reduction of overburden thickness 478
6.5.2.3 Changes of hydraulic conductivity due to dissolution processes in host rock and confining units 479
6.5.3 Change in diffusion properties of the host rock due to reduction of the overburden 480
6.5.4 Alteration of porewater composition by diffusive exchange with aquifers and effects on radionuclide mobility 481
6.5.5 Dissolution processes below the host rock 481
6.5.6 Alteration of host rock mineralogy 482
6.5.7 Conclusions on long-term hydrogeological and hydrogeochemical evolution 483
6.6 Long-term geological evolution: Summary 483
6.6.1 General conclusions regarding the long-term geological evolution 483
6.6.2 Storyboard for the expected long-term geological evolution in Nördlich Lägern 486

7 Conclusions 493
7.1 Developments of the knowledge base and key learnings compared to previous investigation phases 493
7.2 Overall conclusions regarding site comparison and demonstration of post-closure safety 498

8 References 503

List of Tables

Tab. 2-1: List of Nagra's 9 deep boreholes drilled 2019 – 2022 and other important deep boreholes (shown in italics), including references to data reports 15

Tab. 2-2: List of Nagra's 11 Quaternary boreholes drilled 2018 – 2020 including references to data reports 18

Tab. 4-1: Summary of the structural terminology for faults across the observation scales 122

Tab. 4-2: Evolution times derived from the modelling of the $\delta^{2}H$ and $\delta^{18}O$ profiles 247

Tab. 5-1: Constraints on major component concentrations used for modelling of reference porewaters (Mäder & Wersin 2023) 310

Tab. 5-2: Empirical findings and key experiments on self-sealing in the Opalinus Clay 350

Tab. 5-3: Modelled diffusion data for the Opalinus Clay (parallel to bedding) for HTO, I^- and Br^- of in-situ diffusion experiments at the Mont Terri rock laboratory and comparison with data (parallel to bedding) from small-scale lab experiments with Mont Terri samples 369

Tab. 6-1: Inferred future rock uplift rates 448

List of Figures

Fig. 1-1: Positioning of this report, NTB 24-17 ("Geosynthesis"), in relation to key reports for site selection and demonstration of post-closure safety and to supplementary geological reports 3

Fig. 1-2: Criteria to be used for site selection (SFOE 2008) 7

Fig. 1-3: Key aspects used for selecting the location of the Jura Ost (JO), Nördlich Lägern (NL) and Zürich Nordost (ZNO) siting regions in Northern Switzerland 10

Fig. 2-1: Schematic overview of important sources of information for the characterisation of the geological barrier 12

Fig. 2-2: Important geophysical datasets and boreholes in Northern Switzerland 13

Fig. 2-3: Increase in size of the database for key parameters during the 2019 – 2022 deep drilling campaign 17

Fig. 3-1: Visualisation of the structure of the chapter 21

Fig. 3-2: Simplified tectono-geological map of Northern Switzerland with a profile between the Aar Massif and the Black Forest Massif 23

Fig. 3-3: Stratigraphic column, geological map and profile of Northern Switzerland 24

Fig. 3-4: Timeline focusing on the geological evolution of Northern Switzerland 25

Fig. 3-5: Palaeogeographic reconstruction showing Switzerland in the larger context 29

Fig. 3-6: Geological evolution of the study area demonstrated on a schematic NNW-SSE cross-section 30

Fig. 3-7: Palaeogeographic situation of Western to Central Europe in the Norian during the sedimentation of the Klettgau Formation (Seebi Member) and its time equivalents 31

Fig. 3-8: Palaeogeographic situation of Western to Central Europe in the Aalenian during the sedimentation of the Opalinus Clay and its time equivalents 33

Fig. 3-9: Palaeogeographic situation of Western to Central Europe in the Bajocian during the sedimentation of the Hauptrogenstein and «Parkinsoni-Württembergica-Schichten» and their time equivalents 34

Fig. 3-10: Palaeogeographic situation of Western to Central Europe in the Kimmeridgian during the sedimentation of the Burghorn Formation, «Felsenkalke» and «Massenkalk» and their time equivalents 35

Fig. 3-11: Main landscape-forming events in Northern Switzerland during the past 5 Myr 41

Fig. 3-12: Present-day geodetic movements relative to Eurasia 45

Fig. 4-1: Schematic overview of the content and structure of the chapter 48

Fig. 4-2: Lithological overview correlation with the focus on Mesozoic sedimentary rocks of the three siting regions 50

Fig. 4-3: Schematic representation of depositional environments of Mesozoic sedimentary rocks in Northern Switzerland 51

Fig. 4-4: Schematic lithostratigraphic column for JO with depositional environments, schematic sedimentation rates and estimated location relative to sea level 52

Fig. 4-5: Schematic lithostratigraphic column for NL with depositional environments, schematic sedimentation rates and estimated location relative to sea level 53

Fig. 4-6: Schematic lithostratigraphic column for ZNO with depositional environments, schematic sedimentation rates and estimated location relative to sea level 54

Fig. 4-7: Map of depositional environments during the Middle Triassic (Anisian – Ladinian) preserved in the Schinznach Formation 55

Fig. 4-8: Stratigraphic borehole correlation of the Schinznach Formation 57

Fig. 4-9: Selected core photos of the Schinznach Formation 58

Fig. 4-10: Map of depositional environments during the Middle Triassic (Late Ladinian – Early Carnian) preserved in the Bänkerjoch Formation 59

Fig. 4-11: Stratigraphic borehole correlation of the Bänkerjoch Formation 60

Fig. 4-12: Selected core photos of the Bänkerjoch Formation 63

Fig. 4-13: Map of depositional environments during the Late Triassic (Carnian to Rhaetian) preserved in the Klettgau Formation 64

Fig. 4-14: Schematic synoptic section of the Klettgau Formation with its different members 65

Fig. 4-15: Stratigraphic borehole correlation of the Klettgau Formation 66

Fig. 4-16: Selected core photos of the Klettgau Formation 68

Fig. 4-17: Map of depositional environments during the Late Triassic (Middle Carnian) preserved in the Ergolz Member of the Klettgau Formation 69

Fig. 4-18: Microfacies of porous dolostone and sandstone with argillaceous matrix and open pores 70

Fig. 4-19: «Channel facies» intercalated with «floodplain facies» in the Ergolz Member at Steigrabe in Hemmiken 70

Fig. 4-20: Map of depositional environments during the Late Triassic (Late Carnian) preserved in the Gansingen and Berlingen Members of the Klettgau Formation..... 71

Fig. 4-21: Map of depositional environments during the Late Triassic (Norian) preserved in the Seebi Member of the Klettgau Formation and its western equivalent (part of the Gruhalde Member of the Klettgau Formation)..... 73

Fig. 4-22: Map of depositional environments during the Early Jurassic (Hettangian to Toarcian) preserved in the Staffelegg Formation 74

Fig. 4-23: Stratigraphic borehole correlation of the Staffelegg Formation 76

Fig. 4-24: Selected core photos of the Staffelegg Formation (slabbed cores)..... 77

Fig. 4-25: Outcrop of the Staffelegg Formation in the Frick Gruhalde clay pit..... 78

Fig. 4-26: Map of depositional environments during the Hettangian to Sinemurian preserved in the Beggingen and Weissenstein Members and part of the Herdern Member..... 80

Fig. 4-27: Map of depositional environment during the Middle Jurassic (mainly Early Aalenian) preserved in the Opalinus Clay 81

Fig. 4-28: Stratigraphic borehole correlation of the Opalinus Clay 82

Fig. 4-29: Selected core photos of the Opalinus Clay (slabbed cores)..... 84

Fig. 4-30: Subfacies classification and lithologies of the Opalinus Clay and adjacent formations in boreholes of Northern Switzerland..... 85

Fig. 4-31: Block diagrams showing depositional models of the Opalinus Clay in Northern Switzerland..... 88

Fig. 4-32: Map of depositional environments during the Middle Jurassic (Middle Aalenian to Early Oxfordian) preserved in the Dogger Group above Opalinus Clay..... 89

Fig. 4-33: Stratigraphic borehole correlation of the units of the Dogger Group above Opalinus Clay 90

Fig. 4-34: Stratigraphy of the Middle Jurassic of Northern Switzerland and the correlation with neighbouring Southern Germany 92

Fig. 4-35: Biostratigraphy and lithostratigraphy of the Middle Jurassic (Aalenian to Bathonian) of Northern Switzerland with sequence stratigraphic correlation..... 93

Fig. 4-36: Selected core photos of the Dogger Group above Opalinus Clay (slabbed cores)..... 94

Fig. 4-37: Detailed correlation of the sedimentary succession directly above the Opalinus Clay in boreholes of JO..... 96

Fig. 4-38: Detailed correlation of the sedimentary succession directly above the Opalinus Clay in boreholes of NL 99

Fig. 4-39: Detailed correlation of the sedimentary succession directly above the Opalinus Clay in boreholes of ZNO 100
Fig. 4-40: Subcrop map (top reflection of the «Herrenwis Unit») of the geophysical survey area acquired in NL with seismically derived extent of the isolated carbonate platform and of the periplatform wedge 101
Fig. 4-41: E-W-oriented seismic profile across the western edge of the «Herrenwis Unit» and conceptual sketch of the extent of the «Herrenwis Unit» and adjacent units 101
Fig. 4-42: Map of depositional environments during Middle Aalenian 104
Fig. 4-43: Map of depositional environments during late Middle Aalenian to Early Bajocian 105
Fig. 4-44: Map of depositional environments during the Early Bajocian 107
Fig. 4-45: Bioherms at two levels (Calcaire à polypiers inférieur et supérieur) shown as a time-equivalent analogue for the bioherms of the «Herrenwis Unit» 108
Fig. 4-46: Map of depositional environments during Late Bajocian to Early Oxfordian 109
Fig. 4-47: Map of depositional environment during the Late Jurassic (Middle to Late Oxfordian) preserved in the Wildegg Formation 110
Fig. 4-48: Stratigraphic borehole correlation of the Wildegg Formation 113
Fig. 4-49: Selected core photos of the Wildegg Formation 114
Fig. 4-50: Map of depositional environments during the Late Jurassic (Late Oxfordian to Early Tithonian) preserved in the Malm Group above Wildegg Formation 115
Fig. 4-51: Stratigraphic borehole correlation of the Malm Group above Wildegg Formation 118
Fig. 4-52: Selected core photos of the Malm Group above Wildegg Formation 119
Fig. 4-53: Conceptual block diagram showing fault terminology across the observation scales 124
Fig. 4-54: Geological map of Northern Switzerland with the siting regions and major faults 125
Fig. 4-55: Conceptual tectonic map at top basement showing the main faults and the extent of the Konstanz – Frick Trough 127
Fig. 4-56: Large-scale geological cross-section through Jura Ost 128
Fig. 4-57: Large-scale geological cross-section through Nördlich Lägern 128
Fig. 4-58: NNW-SSE large-scale geological cross-section through Zürich Nordost 129
Fig. 4-59: WSW-ENE large-scale geological cross-section through Zürich Nordost 129
Fig. 4-60: Tectonic map of Northern Switzerland showing regional fault zones and regional tectonic domains 132
Fig. 4-61: Fault map for JO (shown on three stratigraphic levels) and fracture frequencies in the recent deep boreholes 134
Fig. 4-62: NW-SE cross-section in time domain extracted from 3D seismic reflection data through Jura Ost 135

Fig. 4-63: Cross-section extracted from 3D seismic reflection data showing the Effingen Fault 137
Fig. 4-64: 3D view showing the less deformed block in NL between the regional fault zones 138
Fig. 4-65: Fault maps for NL (shown on three stratigraphic levels) and fracture frequencies in the recent deep boreholes 139
Fig. 4-66: N-S cross-section in time domain through the 3D seismic reflection data across NL 141
Fig. 4-67: Focused view in time domain showing interpreted fault geometries in the Baden – Irchel – Herdern Lineament 142
Fig. 4-68: Focused view in time domain showing the relationship of thrusting in the Siglistorf Anticline and the underlying faults in the Paleozoic strata 144
Fig. 4-69: Fault map for ZNO (shown on three stratigraphic levels) and fracture frequencies in the recent deep boreholes 147
Fig. 4-70: 2D seismic reflection line extracted from 3D seismic reflection data across major structures in ZNO 148
Fig. 4-71: 2D seismic reflection showing high-angle faults in the "Strukturzone von Niderholz" 149
Fig. 4-72: Rheinau Fault in a 2D seismic reflection line oriented parallel to the borehole path 150
Fig. 4-73: Evolution of burial temperature and oxygen isotope composition of pore fluids ($\delta^{18}O_{fluid}$) since the Early Jurassic 154
Fig. 4-74: Simplified tectonic map of Northern Switzerland showing absolute ages obtained from veins sampled in outcrops and drill cores and shortening estimates 156
Fig. 4-75: Tectonic map of Northern Switzerland showing the influence of the neighbouring tectonic domains 161
Fig. 4-76: Orientation of maximum horizontal stress S_{Hmax} in the siting regions 165
Fig. 4-77: Stress magnitudes and comparison to clay-mineral content (proxy for layer stiffness) 166
Fig. 4-78: Control of mechanical layering on stress magnitude data 168
Fig. 4-79: Conceptual sketch of the evolution of the horizontal stress magnitude S_h in a mechanically layered limestone – claystone sequence 169
Fig. 4-80: Compilation of stress magnitude data in the Opalinus Clay across siting regions 170
Fig. 4-81: Stress magnitude data from MHF/SR tests and modelled stress bandwidth 171
Fig. 4-82: Comparison of stress regimes within the rock formations across the different siting regions 172
Fig. 4-83: Aquifer outcrops, river network, regional fault zones and potential recharge and discharge areas relevant for the siting regions 176
Fig. 4-84: Hydrostratigraphic units of Northern Switzerland 177

Fig. 4-85: Hydrogeological correlation of key boreholes with summarised results of hydraulic packer tests and location of regional and local deep aquifers 179
Fig. 4-86: Histogram of the transmissivities measured in the aquifers 180
Fig. 4-87: Drill core pictures from the hydraulic test interval in the «Felsenkalke» and «Massenkalk» of the BUL1 borehole 181
Fig. 4-88: Hydraulic conductivities from in-situ hydraulic tests in the Malm aquifer in Northern Switzerland and Southern Germany 182
Fig. 4-89: Profile of the Wedelsandstein Formation in the TRU1 borehole: mineralogical composition, porosity, structural inventory and hydraulic conductivity 185
Fig. 4-90: «Herrenwis Unit» of the BUL1 borehole: CT-scan-based visualisation of mainly calcareous and clay-mineral-rich zones and macropores 187
Fig. 4-91: Hydraulic heads in the «Herrenwis Unit» observed by packer testing and comparison with data from the long-term monitoring system (LTM) in STA3 ... 188
Fig. 4-92: Hydraulic conductivity from in-situ hydraulic packer tests in the «Herrenwis Unit» 189
Fig. 4-93: Results of in-situ hydraulic packer tests in the Staffelegg Formation and comparison to values from laboratory tests on drill cores 190
Fig. 4-94: Results of the hydraulic packer testing and hydrogeochemical investigations in the Klettgau Formation 192
Fig. 4-95: Hydrogeological synopsis of the Keuper aquifer indicating the permeable lithofacies of the Klettgau Formation in the different siting regions 193
Fig. 4-96: Hydraulic conductivities from in-situ hydraulic tests in the Muschelkalk aquifer in Northern Switzerland and Southern Germany 195
Fig. 4-97: 3D view of the northeastern part of the hydrogeological model, with respective cross-sections showing the main regional aquifers, together with the Opalinus Clay 197
Fig. 4-98: Simulated hydraulic heads and the particle paths identifying recharge and discharge areas in the Malm aquifer 199
Fig. 4-99: Head difference map between the Malm aquifer and the Lower Freshwater Molasse Group (USM) 200
Fig. 4-100: Simulated hydraulic heads and particle paths identifying recharge and discharge areas in the Hauptrogenstein aquifer 201
Fig. 4-101: Simulated hydraulic heads and particle tracking in the Keuper aquifer identifying recharge and discharge areas for the base case (upper figure) and alternative homogeneous isotropic case (lower figure) 203
Fig. 4-102: Simulated hydraulic heads and particle tracking identifying recharge and discharge areas in the Muschelkalk aquifer 205
Fig. 4-103: Difference in hydraulic heads between aquifers above and below the Opalinus Clay 207
Fig. 4-104: Cross-plots illustrating the behaviour of key hydrogeochemical parameters in groundwaters collected from the Malm (closed symbols) and Molasse aquifers (open symbols) in Northern Switzerland and Southern Germany 210

Fig. 4-105: Map showing the spatial distribution of $\delta^{18}O$ values in groundwaters collected from the Malm aquifer as an indication for the origin of the different water types 211

Fig. 4-106: Correlations between values of stable isotopes of water and Cl concentrations as well as ^{81}Kr model ages of Na-Cl type Malm groundwaters collected in the ZNO and NL siting regions 214

Fig. 4-107: Map showing the spatial distribution of the $\delta^{18}O$ values of the Malm groundwaters as an indication for dilution of the modified seawater component with meteoric water..... 215

Fig. 4-108: Map showing the spatial distribution of $\delta^{18}O$ values in groundwaters collected from the Hauptrogenstein aquifer and the overlying Birmenstorf Member in Northern Switzerland..... 217

Fig. 4-109: Cross-plots illustrating the behaviour of key hydrogeochemical parameters in groundwaters collected from the Hauptrogenstein aquifer in Northern Switzerland 218

Fig. 4-110: Cross-plots illustrating the behaviour of key hydrogeochemical parameters in groundwaters collected from the Keuper aquifer in Northern Switzerland..... 220

Fig. 4-111: Map showing the spatial distribution of $\delta^{18}O$ values in groundwaters collected from the Keuper aquifer as indication of the recharge conditions of the different water types 221

Fig. 4-112: Cross-plots illustrating the behaviour of key hydrogeochemical parameters in groundwaters collected from the Muschelkalk aquifer in Northern Switzerland and Southern Germany 225

Fig. 4-113: Map showing the spatial distribution of $\delta^{18}O$ values in groundwaters collected from the Muschelkalk aquifer as indication of the recharge conditions of the different water types 226

Fig. 4-114: Correlations between $\delta^{18}O$ values and selected other parameters of Muschelkalk groundwaters collected in the siting regions as well as comparison to a potential endmember of the mixing trend (WEI, crystalline)..... 229

Fig. 4-115: Sketch illustrating the upwelling of groundwater from the crystalline basement into the Muschelkalk aquifer along regional fault zones some 8 – 13 Myr ago..... 230

Fig. 4-116: Map showing the distribution of the $\delta^{18}O$ values in groundwaters of the Muschelkalk aquifer as manifestation of the regional groundwater flow system in the ZNO and NL siting regions 231

Fig. 4-117: Chloride concentrations and ^{81}Kr model ages in groundwater collected from boreholes in the three siting regions 233

Fig. 4-118: Illustration of possible evolution of tracer profiles across an aquitard sequence driven by concentration changes in two or more bounding aquifers 240

Fig. 4-119: Profiles of $\delta^{2}H$ (top row) and $\delta^{18}O$ (bottom row) in porewater (pw) and groundwater (gw) in the different siting regions 242

Fig. 4-120: Comparison of profiles of $\delta^{2}H$ (a) and $\delta^{18}O$ (b) in porewater (pw) and groundwater (gw) of the different geological siting regions 244

Fig. 4-121: Signatures of stable water isotopes for BOZ2, STA2 and TRU1 (all influenced by Keuper groundwater) as well as for STA3 (no Keuper groundwater) ... 245

Fig. 4-122: Signatures of stable isotopes in porewater of the Opalinus Clay in the different siting regions ... 246

Fig. 4-123: Comparison of measured and simulated profiles of stable water isotopes in BOZ2, STA2, STA3 and TRU1 ... 248

Fig. 4-124: Profiles of chloride (top row) and Br/Cl ratios (bottom row; grey vertical lines indicate seawater ratio) in porewater of the different boreholes ... 250

Fig. 4-125: Comparison of measured and simulated profiles of chloride (top row) and of the Br/Cl ratio (bottom row; grey vertical lines indicate seawater ratio) at BOZ2, STA2, STA3 and TRU1 ... 252

Fig. 4-126: Profiles of ^{4}He concentrations and $^{3}He/^{4}He$ ratios in porewater (pw) and groundwater (gw) for the BOZ2 and BOZ1 (JO), STA3 and BUL1 (NL) and MAR1 and TRU1 (ZNO) boreholes ... 256

Fig. 4-127: Examples of veins from the TBO boreholes ... 261

Fig. 4-128: Mineralised structures in the Opalinus Clay and other Mesozoic units ... 262

Fig. 4-129: Evolution of $\delta^{18}O$ of calcite-forming fluids over the last 70 Ma as obtained from coupled clumped isotope thermometry and U-Pb and U-Th dating of calcite cements ... 264

Fig. 4-130: Depth profiles of the oxygen isotope composition of calcite-forming fluids derived from clumped isotope thermometry for different time periods ... 266

Fig. 4-131: Temperature and $\delta^{18}O$ values of calcite-forming fluids from clumped isotope thermometry ... 267

Fig. 4-132: Depth profiles of the carbon isotope composition of vein calcite and matrix carbonate ... 268

Fig. 4-133: Depth profiles of strontium isotope ratios of vein calcite, vein celestite and present-day porewater ... 269

Fig. 4-134: $\delta^{18}O$ and $\delta^{34}S$ values for vein celestite observed in boreholes in Northern Switzerland ... 270

Fig. 4-135: Temperature profiles and lithology-dependent temperature gradients ... 273

Fig. 4-136: Cross-plots of temperature (°C) vs. depth below surface (m) for the Malm aquifer, Opalinus Clay and Muschelkalk aquifer ... 274

Fig. 4-137: Key observations between Muschelkalk and Hauptrogenstein aquifers in JO ... 275

Fig. 4-138: Key observations between Muschelkalk and Malm aquifers in NL ... 276

Fig. 4-139: Key observations between Muschelkalk and Malm aquifers in ZNO ... 277

Fig. 4-140: Extent of host rock and low-permeability confining units and location of neighbouring aquifers for the JO, NL and ZNO siting regions ... 279

Fig. 5-1: Coupling between structure, deformation behaviour and transport properties in the Opalinus Clay ... 283

Fig. 5-2: Conceptual representation of the structure of the Opalinus Clay over a length scale range of 13 orders of magnitude ... 285

Fig. 5-3: Mineralogical composition of formations in boreholes of the siting regions 287
Fig. 5-4: Clay-mineral content of the Opalinus Clay in boreholes of the siting regions, based on laboratory data 288
Fig. 5-5: Mineralogical composition of the Opalinus Clay based on laboratory data from X-ray diffraction 289
Fig. 5-6: Composition of the clay-mineral fraction in the TBO boreholes in profile view 290
Fig. 5-7: Diagenetic minerals and their relative temporal sequence of precipitation in the Opalinus Clay and its confining units in Northern Switzerland 291
Fig. 5-8: Porosity profiles from selected boreholes in the siting regions 294
Fig. 5-9: Water-loss porosity of the Opalinus Clay 295
Fig. 5-10: Water-loss porosity of the Opalinus Clay in different boreholes as a function of current depth 296
Fig. 5-11: Relationship between clay-mineral content and porosity in the Jurassic section 298
Fig. 5-12: Conceptual view of the porosity types (white) in clay-carbonate mixtures 298
Fig. 5-13: Key rock data for Jurassic samples from TBO boreholes shown in the Füchtbauer triangle 299
Fig. 5-14: Water-loss porosity of the Opalinus Clay as a function of clay-mineral content and comparison to other clay-rich rocks 300
Fig. 5-15: Mineral surface areas and pore-size distributions in the Jurassic profile 302
Fig. 5-16: Correlation between external surface area and cation-exchange capacity based on Cs consumption 303
Fig. 5-17: Conceptual model of anion-accessible porosity (white), anion-depleted porosity (blue), cations, anions, neutral species (+, -, 0, in dark blue) and the negative charge on clay mineral surfaces (red) 305
Fig. 5-18: Chloride-accessible porosity fraction (f_{Cl}) 307
Fig. 5-19: Schoeller plots visualising the chemical composition of porewater in the Opalinus Clay and in the adjacent confining units in the three siting regions 308
Fig. 5-20: Modelled concentrations of main porewater components (upper panel) as well as log(pCO_2) (bar) and pH (lower panel) as a function of temperature using an alternative porewater model including clay mineral phases (curves) 311
Fig. 5-21: Comparison of oedometric curves of the Opalinus Clay from Mont Terri and BUL1 315
Fig. 5-22: Swelling index (C_s) as a function of the clay-mineral content 316
Fig. 5-23: Axial swelling strain in the Opalinus Clay constrained by different methods 317
Fig. 5-24: Schematic of the mechanical response of the Opalinus Clay for different stress paths 318
Fig. 5-25: Different mechanical response of Mesozoic sedimentary rocks with contrasting clay-mineral contents 320
Fig. 5-26: Shear strength of the Opalinus Clay from the siting regions 321

Fig. 5-27: Peak and post-peak strength of the Opalinus Clay in the siting regions in comparison to Mont Terri 322
Fig. 5-28: Comparison of mechanical behaviour in numerical (bold lines) and laboratory test results (dashed lines) 323
Fig. 5-29: Typical fault microstructure of the Opalinus Clay obtained in triaxial testing 325
Fig. 5-30: Unconfined compressive strength (UCS) as a function of the clay-mineral content 326
Fig. 5-31: Examples of tectonic deformation accommodated in the Opalinus Clay from the recent deep boreholes 327
Fig. 5-32: Distribution of small-scale fault and micro fault frequency in the Opalinus Clay from new boreholes and overall fracture frequency 329
Fig. 5-33: Outcrop examples of fault structures in the Opalinus Clay 330
Fig. 5-34: Example of the "Main Fault" in the Opalinus Clay at the Mont Terri rock laboratory 331
Fig. 5-35: Fault architecture of a seismically mappable fault (Wildensbuch Flexure in ZNO) 332
Fig. 5-36: Synthesis of trench mapping exposing fault propagation across mechanical layering 333
Fig. 5-37: Matrix hydraulic conductivity of the Opalinus Clay and clay-mineral-rich confining units as a function of mineral composition and porosity 336
Fig. 5-38: Hydraulic conductivities of the Opalinus Clay as a function of depth 338
Fig. 5-39: In-situ test best estimate transmissivities of the Opalinus Clay derived from hydraulic packer tests as a function of the length of the test intervals 339
Fig. 5-40: Distribution of the logarithm of the best estimate of the in-situ hydraulic packer test transmissivities in the Opalinus Clay 340
Fig. 5-41: Comparison of the horizontal hydraulic conductivity of the Opalinus Clay with examples of clay-rich rocks worldwide 341
Fig. 5-42: Hydraulic conductivity of the in-situ hydraulic packer tests as a function of the clay-mineral content of the test interval 342
Fig. 5-43: Transmissivity as a function of the total thickness of a layer with clay-mineral content < 20 wt.-% 344
Fig. 5-44: Hydraulic head profiles based on hydrogeological long-term monitoring and in-situ hydraulic packer test data in the BOZ1, STA3, MAR1 and BEN boreholes 347
Fig. 5-45: Experimental evidence of self-sealing in laboratory experiments 351
Fig. 5-46: Concept of self-sealing sequence in the Opalinus Clay 353
Fig. 5-47: Dependence of fracture transmissivity on the effective normal stress 354
Fig. 5-48: Relationship of fault-related flow and effective stress in the Opalinus Clay at the RHE1 borehole at approximately 580 m depth below ground 356
Fig. 5-49: Relationship between porosity and hydraulic conductivity in crushed and recompacted ("remoulded") Opalinus Clay 358

Fig. 5-50: Measured effective diffusion coefficients De for chloride and HTO of the investigated formations in the three siting regions 363

Fig. 5-51: Box plots illustrating the range of effective diffusion coefficients De for HTO (left column) and for Cl (right column), grouped by siting regions 364

Fig. 5-52: Box plots illustrating the range of accessible porosities ε for HTO and for Cl, grouped according to the siting regions 366

Fig. 5-53: Correlation of geometric factor G with clay-mineral content for HTO (a) and Cl (b) as a basis for estimating De of HTO and Cl for the Dogger Group above Opalinus Clay, the Opalinus Clay and the Lias Group 367

Fig. 5-54: Comparison of effective HTO and anion diffusion coefficients De for the Opalinus Clay obtained in Mont Terri field and laboratory experiments 370

Fig. 5-55: Comparison of Opalinus Clay diffusion coefficients with data from other clay-rich rocks worldwide 371

Fig. 5-56: Dominant transport mechanisms in the Opalinus Clay based on the Peclet number illustrated for chloride 374

Fig. 5-57: Link of texture and clay-mineral content with key hydromechanical properties in Jurassic sediments of the siting regions (lower confining units to upper aquifers) 377

Fig. 6-1: Schematic visualisation of the principal geological processes potentially affecting the geological barrier and corresponding structure of the chapter 381

Fig. 6-2: Geological processes acting at different timescales compared with the time period relevant for repository safety 382

Fig. 6-3: Velocity fields, seismicity and stress vectors in Europe 388

Fig. 6-4: Present-day Rhine catchment in a morphotectonic and geodynamic context for fluvial incision and sediment accumulation 390

Fig. 6-5: Sketch of the Rhine River course with domains of Quaternary vertical motion 392

Fig. 6-6: Patterns and rates of surface uplift and incision proxies on different timescales 394

Fig. 6-7: Geodetic precise levelling data with measurement uncertainties 395

Fig. 6-8: Present-day horizontal motion of permanent GNSS stations in Northern Switzerland 397

Fig. 6-9: Horizontal velocity components deduced from repeated GNSS measurements 398

Fig. 6-10: Distribution of earthquakes and selected focal mechanisms 400

Fig. 6-11: Comparison of climate proxies for the northern hemisphere during the last million years 405

Fig. 6-12: Key glacials in Northern Switzerland 406

Fig. 6-13: Temperature, precipitation and climate classification for pre-industrial and LGM climates 408

Fig. 6-14: Modelled maximum ice thickness and extent of the Alpine Ice Field during MIS 2 409

Fig. 6-15: Boxplots of modelled ice characteristics during the LGM 410
Fig. 6-16: The Rhine Glacier system and erosion potential at the LGM..... 412
Fig. 6-17: Future climate simulations based on orbital configurations and different Anthropogenic CO_2 scenarios 414
Fig. 6-18: Maps showing the main landscape compartments around the siting regions 419
Fig. 6-19: Catchment competition between the Rhine and Danube watersheds and drainage reorganisation..... 423
Fig. 6-20: Morphostratigraphic units in Northern Switzerland with selected age information 424
Fig. 6-21: Unconfined compressive strength and abrasion mill erosion rates as quantitative indicators of bedrock erodibility 427
Fig. 6-22: Conceptual figures of local landscape evolution by (a) local baselevel fall of a main river, and (b) the formation of a breakthrough channel in an ice-marginal setting 428
Fig. 6-23: Comparison of a geomorphically quiet (JO) with a highly active landscape (Wutach) 431
Fig. 6-24: Overview map showing the glacial overdeepenings and the underlying rock units 434
Fig. 6-25: Longitudinal profile through the Gebenstorf – Stilli Trough close to Brugg 435
Fig. 6-26: Cross-sections characterising the Quaternary deposits in the lower Aare Valley, the Glatt Valley and the Thur Valley 437
Fig. 6-27: Cross-section through the siting regions with the morphological and geological conditions that are key to assessing future erosion processes 439
Fig. 6-28: Site-specific constraints of the landscape compartments within the siting regions 441
Fig. 6-29: Simplified flowchart for calculating the remaining overburden thickness and probability of excavation at time T_x..... 445
Fig. 6-30: Inferred future rock uplift rates in the three siting regions over the next 100'000 and one million years 448
Fig. 6-31: Total assumed probabilities for baselevel drop downstream of Basel..... 450
Fig. 6-32: Results of fluvial incision modelling using the Stream Power Incision Model (SPIM)..... 452
Fig. 6-33: Histogram and statistical measures of slope gradients within the hillslope domain of JO and surrounding area: two examples..... 454
Fig. 6-34: The siting regions with present-day and alternative main drainage network scenarios 454
Fig. 6-35: Results of modelling the evolution of local topography at one million years using the present-day drainage network 456
Fig. 6-36: Outcrop maps representing the evolution of local topography at one million years using the present-day drainage network..... 457
Fig. 6-37: Results of modelling the evolution of local topography at one million years using alternative drainage networks for JO..... 458

Fig. 6-38: Outcrop maps representing the evolution of local topography at one million years using alternative drainage networks for JO 459

Fig. 6-39: Distributions of remaining overburden thickness after one million years including local topography for JO 460

Fig. 6-40: Total assumed probabilities for reference overdeepening depth per key-size glaciation 463

Fig. 6-41: Total assumed probabilities of erodibility scaling with respect to the Molasse of Northern Switzerland 464

Fig. 6-42: Step-wise illustration of procedure to evaluate the probabilities of fluvial and deep glacial erosion at a certain point 465

Fig. 6-43: Scenarios for spatial occurrence of future overdeepenings within the siting regions, one million years 467

Fig. 6-44: Estimated probabilities of remaining overburden thickness above the provisional disposal area in the three siting regions 471

Fig. 6-45: Schematic representation showing Pleistocene subglacial meltwater recharge into the Malm aquifer in the Bodensee area 476

Fig. 6-46: Rock properties of the Opalinus Clay in the shallow decompaction zone: Synopsis of the observations in the Lausen case study 479

Fig. 6-47: Synthesis profiles for visualising future non-glacial erosion in the three siting regions 485

Fig. 6-48: Schematic diagram summarising the long-term geological evolution of the NL site 491

List of Acronyms

a	Year (age)
Aal	Aalenian
AD	Advective displacement
AGNES	Automated GNSS Network for Switzerland
a.s.l.	Above sea level
BAC1	Bachs-1-1 borehole (TBO campaign)
Baj	Bajocian
BEN	Benken borehole (Nagra)
BEZ	Beznau borehole
BOZ1	Bözberg-1-1 borehole (TBO campaign)
BOZ2	Bözberg-2-1 borehole (TBO campaign)
BUL1	Bülach-1-1 borehole (TBO campaign)
BUL1B	Bülach-1-1 borehole side track (TBO campaign)
b.g.l.	Below ground level
Car	Carnian
CDF	Cumulative Distribution Function
CRZ	Containment-providing Rock Zone
C_s	Swelling index
$\delta^{18}O$, $\delta^{2}H$	Composition of stable isotopes of the water molecule in the delta notation. The delta symbol is a way to express the relative difference of isotope ratios between sample and the standard VSMOW (Vienna Standard Mean Ocean Water)
DEM	Digital Elevation Model
D_e	Effective diffusion coefficient
D_p	Pore diffusion coefficient
D_w	Diffusion coefficient in bulk water
E	Young's Modulus
ε	Water-filled accessible porosity
ε_a	Axial strain
EC	Erodibility classes (grouping of similar rock units, used for the assessment of future erosion)
ECRIS	European Cenozoic Rift System
EDZ	Excavation damage zone

Eh	Redox potential
ENSI	Swiss Federal Nuclear Safety Inspectorate
ERCS	Erosion rate from the concentration of solids (a procedure for measuring erosion rates with abrasion mill experiments, as a quantitative indicator of bedrock erodibility)
f_a	Anion-accessible porosity fraction
f_{Cl}	Chloride-accessible porosity fraction
Fm.	Formation
FMI	Formation Microresistivity Imaging
FMT	Mont Terri rock laboratory
FOP	Fracture opening pressure
G	Geometric factor (Tortuosity)
g	Gravitational acceleration constant
GIA	Glacial isostatic adjustment
GMWL	Global Meteoric Water Line
GNSS	Global navigation satellite system
GR	Gamma Ray
GTS	Grimsel Test Site
HDS	Höhere Deckenschotter
Het	Hettangian
HI	Constant head injection test
HLW	High-level waste (spent fuel assemblies and high-level waste from reprocessing)
HT	Hochterrasse
HTO	Tritiated water
HW	Constant pressure withdrawal test/phase
HWS	HW test with subsequent pressure recovery phase
IPCC	Intergovernmental Panel on Climate Change
IQR	Interquartile range
JO	Jura Ost siting region
K	Erodibility coefficient
K	Hydraulic conductivity
K_h	Horizontal hydraulic conductivity
K_v	Vertical hydraulic conductivity

ka	Thousand years (age)
Kim	Kimmeridgian
kyr	Thousand years (duration)
l	Characteristic length of the porous medium
L/ILW	Low- and intermediate-level waste
Lad	Ladinian
LAU	Lausen borehole
LEB	Local erosion base
LGM	Last Glacial Maximum
LR04 stack	An average of 57 globally distributed benthic $\delta^{18}O$ records (which measure global ice volume and deep ocean temperature) collected from the scientific literature
LTM	Long-term monitoring system
Ma	Million years (age)
MAR1	Marthalen-1-1 borehole (TBO campaign)
Mb.	Member
MHF	Microhydraulic Fracturing
MIS	Marine Isotope Stages
M_L	Local magnitude (scale)
MPT	Mid-Pleistocene Transition
MuddPILE	Parsimonious Integrated Landscape Evolution model
M_W	Moment magnitude (scale)
Myr	Million years (duration)
n	Number of data points
NAB	Nagra Work Report ('Nagra Arbeitsbericht')
NaGNet	Nagra's permanent GNSS Network
NEA	Nuclear Energy Agency
NL	Nördlich Lägern siting region
NMR	Nuclear Magnetic Resonance
Nor	Norian
NPB	Nagra Project Report ('Nagra Projektbericht')
NT	Niederterrasse
NTB	Nagra Technical Report ('Nagra Technischer Bericht')
OD	Overdeepening

OFT	Oftringen borehole
OPA	Opalinus Clay
OMM	Obere Meeresmolasse (Upper Marine Molasse Group)
OSM	Obere Süsswassermolasse (Upper Freshwater Molasse Group)
Oxf	Oxfordian
p'	Mean effective stress
P32 value	Fracture area per unit volume
pCO_2	CO_2 partial pressure
PDF	Probability density function
Pe	Peclet number
PEGASOS	Probabilistic seismic hazard analysis for Swiss nuclear power plant sites
PMT	Pressure meter test
PgC	Petagrams of carbon (1 PgC is equal to 1 Gigatonne of carbon)
proj.	Projected
PRP	PEGASOS Refinement Project
q	Deviator stress
$\|q\|$	Module of Darcy flux
QoI	Quantities of interest
ρ	Rock bulk density
R, r	Pearson correlation coefficient
R^2	Coefficient of determination. Number between 0 and 1 that measures how well a statistical model predicts an outcome
Rha	Rhaetian
RHE1	Rheinau-1-1 borehole (TBO campaign)
RIN	Riniken borehole (Nagra)
RIO	Rational Impartial Observer (part of SHELF elicitation protocol)
RSR	Regime Stress Ratio
σ'_n	Normal effective stress
SED	Schweizerischer Erdbebendienst (Swiss Seismological Service)
SEM	Scanning Electron Microscopy
SFOE	Swiss Federal Office of Energy
SGT	Sectoral Plan for Deep Geological Repositories
S_{Hmax}	Maximum horizontal stress magnitude

S_{hmin}	Minimum horizontal stress magnitude
SHA	Schafisheim borehole (Nagra)
SHELF	Sheffield Elicitation Framework
Sin	Sinemurian
SLA	Schlattingen borehole
SPIM	Stream Power Incision Model
SQ	High-pressure squeezing
SR	(Dry) Sleeve reopening test
SRTM	Shuttle Radar Topographic Mission (of NASA)
STA2	Stadel-2-1 borehole (TBO campaign)
STA3	Stadel-3-1 borehole (TBO campaign)
STP	Standard temperature and pressure
S_v	Vertical stress magnitude
T	Transmissivity
TBO	Nagra's deep drilling campaign (9 deep boreholes drilled between 2019 and 2022 in the three siting regions of JO, NL, ZNO)
TDS	Tiefere Deckenschotter or Total Dissolved Solids
Toa	Toarcian
TRU1	Trüllikon-1-1 borehole (TBO campaign)
TEM	Transmission Electron Microscopy
TVD	True Vertical Depth
TWT	Two-Way Travel time
U	Rock uplift
UCS	Unconfined Compressive Strength
UMM	Untere Meeresmolasse (Lower Marine Molasse Group)
USM	Untere Süsswassermolasse (Lower Freshwater Molasse Group)
vol.-%	Volume percent
WEI	Weiach borehole (Nagra)
wrt.	With respect to
wt.-%	Weight percent
yr	Year(s) (duration)
z	Depth
ZNO	Zürich Nordost siting region

1 Introduction

Key points:

- The present report synthesises the geological information for repository site selection and for the demonstration of post-closure safety.
- Repository safety is ensured by a multi-barrier system including engineered and geological barriers. The geological barrier isolates the waste from humans and the environment, ensures immobilisation, retention and slow release of radionuclides and contributes to the long-term stability of the repository system.
- The site selection process in Switzerland considers 13 criteria addressing long-term safety and construction feasibility. The final stage of the site selection process evaluates three remaining siting regions, all located in Northern Switzerland, an area with an overall low geodynamic activity and tectonic complexity and containing the host rock Opalinus Clay at a suitable depth and tectonic configuration.
- Key geological information provided for the general licence application includes (1) a detailed characterisation of the host rock and low-permeability confining units, (2) independent evidence for the barrier function over long timescales, (3) a detailed tectonic characterisation and (4) an assessment of the future geological evolution (geodynamics, climate, erosion) and its effects on the geological barrier.

1.1 Context

In Switzerland, legal regulations (Nuclear Energy Act, KEG 2003 and Nuclear Energy Ordinance, KEV 2004) and guidelines are in place for the management of radioactive waste. The Nuclear Energy Ordinance (KEV) classifies Switzerland's radioactive waste into low- and intermediate-level waste (L/ILW), alpha-toxic waste[3] and high-level waste (HLW), the latter comprising spent fuel and vitrified HLW from reprocessing. The Nuclear Energy Act (KEG) requires the disposal of all these types of radioactive waste in deep geological repositories. The feasibility of this disposal solution has been demonstrated for L/ILW in Nagra (1985) and for HLW (including long-lived intermediate-level waste) in Nagra (2002).

The Sectoral Plan for Deep Geological Repositories (SGT) regulates the search for suitable siting regions for deep geological repositories in Switzerland. This site selection process is conducted in three stages (SFOE 2008). SGT Stages 1 and 2 have been completed and Stage 3 is currently ongoing. Clarifications of the safety-related specifications for this stage are provided in ENSI 33/649 (ENSI 2018), while ENSI Guideline G03 (ENSI 2023) and the corresponding explanatory report (ENSI 2020) specify the protection objective, protection criteria and design principles for the deep geological repositories.

In SGT Stage 3, three siting regions in Northern Switzerland have been investigated – Jura Ost (JO), Nördlich Lägern (NL) and Zürich Nordost (ZNO) – with the objective of selecting one siting region for a HLW repository, one for a L/ILW repository, or one for a combined repository for all waste types. Following a comparison of these siting regions, Nagra concluded that NL is the safest and most flexible siting region and is therefore applying for a general licence for a combined repository for both HLW and L/ILW at the Haberstal site within the region (Nagra 2022).

[3] According to Nagra (2024d), alpha-toxic waste can coexist with L/ILW within the same emplacement caverns. As a result, for the sake of simplicity, the term L/ILW encompasses ATW without explicit mention.

The justification for selection of a site, as well as the demonstration of post-closure safety at the site, are key components of the general licence application (RBG[4]). Fig. 1-1 shows the post-closure safety and site selection reports that provide the underpinning evidence and assessment for the general licence application. From the top level downwards, they comprise:

- The overarching safety report NTB 24-01 *("Sicherheitsbericht"*; Nagra 2025b) which summarises the safety-related argumentation, including post-closure and operational safety shown at the top of Fig. 1-1).
- The upper left side of Fig. 1-1 shows the reports supporting Nagra's site comparison. The available options are compared with respect to safety and engineering feasibility and the results are synthesised in NTB 24-03 ("*Bericht zur Begründung der Standortwahl*"; Nagra 2025a).
- The upper right side of Fig. 1-1 shows the reports documenting the post-closure safety case for the combined repository at the site, including its synthesis in NTB 24-10 (*"Post-Closure Safety Report"*; Nagra 2024r).
- The central part of Fig. 1-1 shows a report presenting the safety and repository concept, including the provisional design.

The lower part of Fig. 1-1 shows a selection of geological reports providing the scientific basis for the relevant aspects of the geological barrier and its future evolution. The present report, NTB 24-17 ("Geosynthesis") essentially synthesises the geological information presented in the lower-level geological reports.

[4] From the German *Rahmenbewilligungsgesuch*.

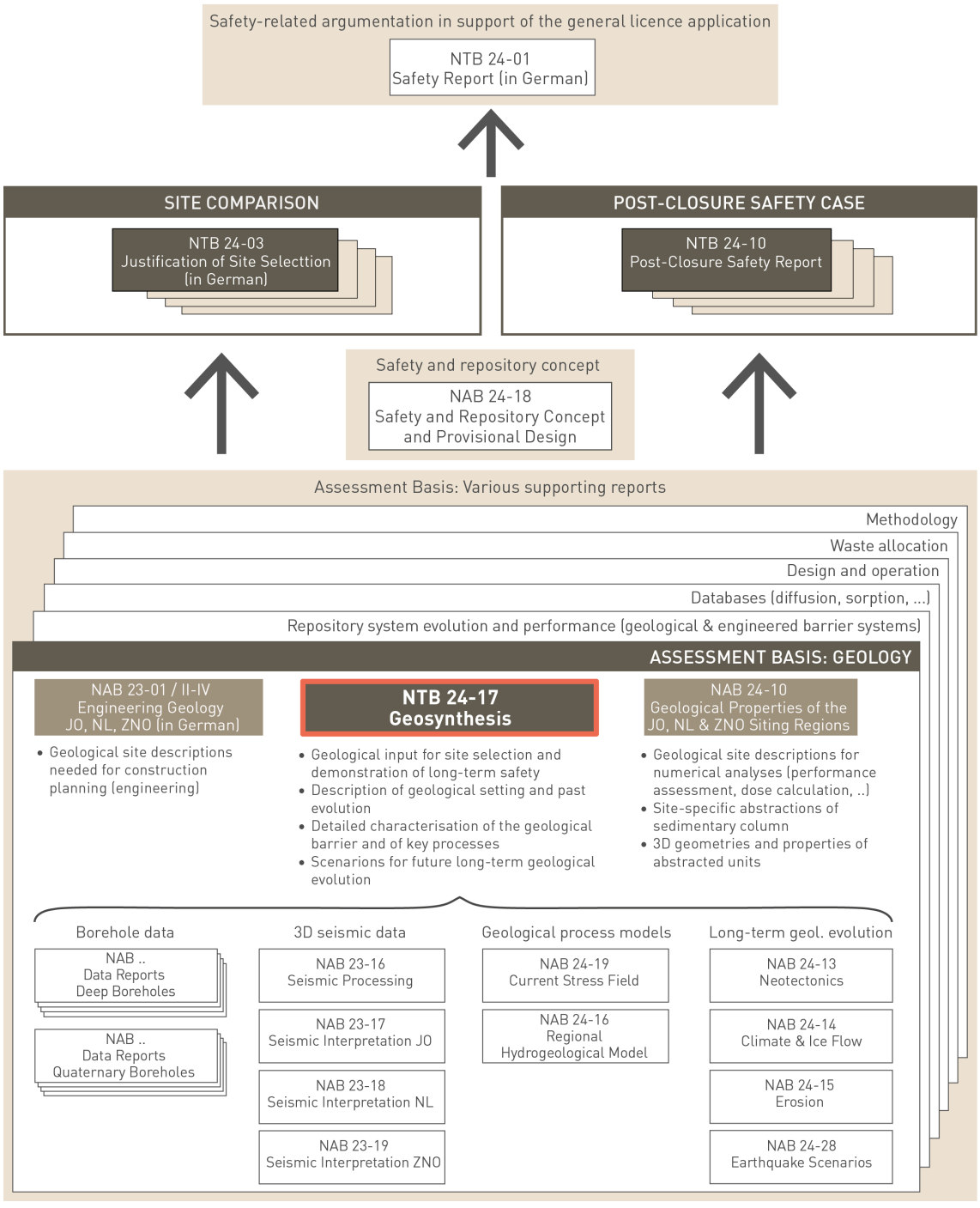


Fig. 1-1: Positioning of this report, NTB 24-17 ("Geosynthesis"), in relation to key reports for site selection and demonstration of post-closure safety and to supplementary geological reports

1.2 Purpose and scope of the present report

This geosynthesis provides the geological basis for comparing the three siting regions JO, NL and ZNO, selected for further evaluation as a repository site in SGT Stage 3 based on a defined set of safety-based criteria (Nagra 2025a and references therein; Fig. 1-2). The report sets out the geological basis for demonstrating post-closure safety for the proposed site (Nagra 2024r) and references therein). Specifically, the report describes the current geological situation in Northern Switzerland and its past evolution with an emphasis on the rock formations that form the geological barrier of the planned repository. Particular emphasis is placed on the geological properties and processes relevant for the long-term stability of the barrier. As well as describing the current geological situation, the report presents scenarios of the natural processes that could affect the barrier or modify its geological environment over the next one million years, that is the time period under consideration for the high-level waste repository (HLW; Nagra 2024r). The scenarios are based on a detailed reconstruction of geological history and related processes. To ensure a robust geological argumentation, key findings relevant to site selection and safety draw on multiple lines of arguments and different, independent methodologies.

This geosynthesis is the central document integrating the geological knowledge base for site comparison and demonstration of long-term safety. It is complemented by two further reports addressing specific user groups (Fig. 1-1):

- NAB 24-10 (Nagra 2024m) provides quantitative geological descriptions of the three sites in relation to repository performance assessment (Nagra 2024v) and dose calculations (Nagra 2024u). It documents how the sedimentary column is divided into geological units with similar properties, presents the 3D geometry of these units in the relevant area of the siting regions and suggests unit-specific parameter ranges for key properties.
- NAB 23-01 / Volumes 2 – 4 (Nagra 2023a, Nagra 2023b, Nagra 2023c) contains the engineering geological characterisation of the three siting regions with regard to construction planning and construction risk analyses.

In contrast to earlier geosynthesis reports (e.g. Nagra 2002), this report only addresses the relevant natural processes and their effect on the geological barrier. The interactions between waste inventory, engineered barriers and the near-repository geological barrier (repository-induced effects) are treated in the performance assessment reports (Nagra 2024v and references therein), including the parametrisation of the excavation damaged zone and gas transport through the geological barrier.

The reports and scientific papers forming the underpinning knowledge base upon which this geosynthesis is predicated are cited in the present document. A selection of Nagra reports detailing the geological findings of the investigations undertaken in SGT Stage 3 is shown in Fig. 1-1.

1.3 Structure of the report and ways to read it

The report is organised as follows:

- **Chapter 1** introduces the function and key characteristics of the geological barrier with regard to long-term safety and site selection. It also summarises why the final stage of site selection focuses on three regions in Northern Switzerland.
- **Chapter 2** gives an overview of the geological knowledge base supporting this report, with a special focus on the detailed site investigations carried out in the third and final phase of the site selection process (SGT Stage 3).

- **Chapter 3** summarises the regional geological evolution and natural tectonic and climatic processes in the past with a view to understanding the geological barrier as it exists today, as well as its future evolution.
- In **Chapter 4** the present-day geological situation in the siting regions is described in detail, with emphasis on the similarities and differences between the regions.
- **Chapter 5** focuses on the host rock and the adjacent low-permeability confining units, with a focus on barrier properties and processes ensuring their long-term stability.
- In **Chapter 6** scenarios for future geological evolution are developed. These focus on the next one million years and include climate, tectonic and erosion scenarios. Their effects on the geological barrier are discussed.
- **Chapter 7** summarises the most important geological findings with regard to site comparison and long-term safety.

Depending on background and interests, the reader may choose different ways to read the report. Besides the classical way of reading a report from front to back or studying specific chapters based on the table of contents, the report structure offers two alternative approaches:

- **Track the scientific basis supporting the key geological outcomes for the demonstration of long-term safety and site comparison:** Start with the 3-page text summarising the 'Key outcomes for the demonstration of long-term safety and site comparison' at the very beginning of the report (English and German versions available). For each statement you will be guided directly to chapters and sections of the report containing the background information necessary to understand and trace the arguments.
- **Track the evolution of the database and the key findings in SGT Stage 3 compared to earlier reference studies:** Readers who are familiar with past investigation phases and the corresponding geological documentation may start reading with Section 7.1. This section summarises the evolution of the geological database and the related key findings since the demonstration of disposal feasibility for HLW (*Entsorgungsnachweis;* Nagra 2002) and since the submission of the documentation for Stage 2 of the Sectoral Plan (Nagra 2014h). For each listed bullet point, links to the sections setting out the current state of knowledge are given.

The report describes geological features and processes in varying levels of detail. This is intentional and, for the most part, reflects their importance for safety-relevant aspects or its scientific complexity. Where concepts are not described in the report, to keep the report as succinct as possible, the reader is referred to where further information describing the concept can be accessed.

1.4 Geological barrier: Function and required geological input for site selection and demonstration of long-term safety

1.4.1 Safety concept

In line with the Swiss legal and regulatory framework as well as national and international principles and practices, the deep geological repository provides safety by means of multiple geological and engineered barriers, i.e. a multi-barrier system (Nagra 2024r).

Regarding post-closure safety, the geological barrier has to provide the following functions (Nagra 2024r):

- Isolation of radioactive waste from humans and the environment
- Immobilisation, retention and slow release of radionuclides
- Contribution to the stability of the repository system with regard to long-term geological and climate evolution

Furthermore, the geological and the engineered barriers must be compatible. This means that the conditions in the host rock should not influence the long-term stability of the engineered barriers in a critical way and the engineered barrier system should not adversely affect the natural barrier afforded by the host rock.

For the three siting regions, the Opalinus Clay host rock provides the primary geological barrier characterised by excellent barrier properties mainly attributed to its high clay-mineral content. The repository will be constructed in this roughly 100 m thick unit. Directly above and below the Opalinus Clay, low-permeability confining units with a partially lower and more heterogeneous clay-mineral content, further contribute to the retardation and slow transport of radionuclides.

The Opalinus Clay host rock and adjacent overlying and underlying low-permeability confining units comprise the containment-providing rock zone (CRZ)[5]. The safety concept requires the CRZ to be located at sufficient depth over the period under consideration to limit any detrimental impact of surface processes, such as erosion, on the safety-related properties of the Opalinus Clay itself and its confining units.

1.4.2 Site selection

In Switzerland, a formal site selection process was put in place by the federal government to identify the most suitable geological situation for the deep geological repository (SFOE 2008). The Sectoral Plan for Deep Geological Repositories (SGT) defines 13 site selection criteria addressing long-term safety and engineering suitability (Fig. 1-2), grouped as follows:

- **Group 1** criteria mainly consider the geometry and safety-relevant properties of the CRZ including the geochemical conditions in the host rock relevant for the stability of the engineered barriers. The assessment of the hydrogeological situation at the sites considers independent evidence for slow transport (e.g. porewater composition, hydraulic heads, groundwater residence times in neighbouring aquifers).
- **Group 2** is concerned with the evolution of the CRZ during the period under consideration (up to 100'000 years for L/ILW and up to one million years for HLW), specifically to consider the effects of geodynamic, climatic and erosional long-term processes, repository-induced effects and human actions.
- **Group 3** addresses uncertainties originating from limitations on the level to which it is possible to characterise the geological barrier and extrapolate understanding as well as to predict its long-term evolution.
- **Group 4** criteria assess the constructability of the repository in the host rock and the access infrastructure through the overlying strata at each site.

[5] Note that 'CRZ' is an established term that is used for safety assessment and site comparison. In Chapters 2 – 7 of this report, instead of 'CRZ' we generally use the corresponding, but more geological description 'host rock and low-permeability confining units'. See Fig. 4-140 for site-specific delimitations of the confining units.

The SGT (SFOE 2008) requires site selection in Switzerland to be staged, based on a safety-based site comparison. The first of the three stages comprised a nationwide screening process for suitable host rocks and siting regions, resulting in the identification of six siting regions and three potential host rocks. Further investigations in Stage 2 selected the Opalinus Clay as the only host rock to be further investigated. This stage also selected three of the six siting regions to be taken forward for detailed investigations in Stage 3, the final stage. These three siting regions, JO, NL and ZNO, are located in Northern Switzerland. Section 1.5 presents the main arguments favouring these regions.

Criteria group	Criteria
1. Properties of the host rock and the effective containment zone	1.1 Spatial extent 1.2 Hydraulic barrier effect 1.3 Geochemical conditions 1.4 Release pathways
2. Long-term stability	2.1 Stability of the site and rock properties 2.2 Erosion 2.3 Repository-induced influences 2.4 Conflicts of use
3. Reliability of geological findings	3.1 Ease of characterisation of the rock 3.2 Explorability of spatial conditions 3.3 Predictability of long-term changes
4. Engineering suitability	4.1 Rock mechanical properties and conditions 4.2 Underground access and drainage

Fig. 1-2: Criteria to be used for site selection (SFOE 2008)

The site comparison process in SGT Stage 3 includes the following key steps (see Nagra 2025a for a full description with links to the regulatory guidelines):

- Definition of the potential disposal zone and delineation of the CRZ with spatial reserves:

  All three siting regions have potential disposal zones in the Opalinus Clay with large lateral extents that far exceed the spatial requirements according to the current repository design. Key factors determining the lateral extent of the potential disposal zone are (1) the avoidance of regional tectonic elements and larger tectonic faults and (2) the choice of an overall suitable minimum depth of the host rock with respect to future erosion.

  For the site comparison, CRZs were defined with lateral dimensions considerably smaller compared to the potential disposal zone. These fulfil a standardised lateral spatial requirement (2 km^2 and 1.2 km^2 for HLW and L/ILW, respectively). CRZs with spatial reserves include a multiple of this (6 km^2 and 3.6 km^2 for HLW and L/ILW, respectively). Vertically, the CRZ includes the host rock and the surrounding low-permeability confining units. The delineation of the CRZ and spatial reserves requires a detailed geological and hydrogeological characterisation of the geological units above and below the host rock and a well-known host rock geometry and local fault pattern in the area of the potential disposal zone.

- Definition of provisional site-specific repository designs as the basis for quantitative safety analyses and qualitative evaluation:

  The delineation of these elements considers the local geological conditions (particularly the host rock geometry and the location of local faults) and further construction and operation requirements.

- Quantitative safety analyses for site comparison:

  Each site-specific safety analysis evaluates radionuclide release rates to the surface environment as a function of time for a defined set of safety scenarios. The dose calculations consider the site-specific geological description and the parametrisation of the CRZ, with particular emphasis on the thickness of subunits with similar characteristics, their transport properties and the hydraulic gradients[6].

- Qualitative evaluation of the CRZ according to the 13 criteria for safety and engineering feasibility defined in the SGT (Fig. 1-2):

  This evaluation requires a detailed geological description of the host rock and the confining units, including independent evidence documenting the efficiency of the CRZ as a transport barrier over the relevant timescales. Furthermore, a description of the local fault pattern in the context of the regional tectonic situation is required. The evaluation of the long-term stability of the geological barrier requires scenarios for the geodynamic, climatic and erosional evolution of the sites and their effects on the geological barrier. The descriptions should address the uncertainties regarding the current state of the geological barrier and its future evolution. Finally, the engineering geological basis for the construction risk evaluation of the underground repository and the access infrastructure needs to be provided[7].

- Overall comparative safety evaluation:

  The overall comparative safety evaluation and site selection combines the steps introduced above. For further information and final outcomes, see Nagra (2025a).

1.4.3 Characteristics of the geological barrier as input for site selection and demonstration of long-term safety

According to ENSI (2018), the geological investigations in SGT Stage 3 must provide the level of site-specific knowledge required to evaluate the 13 safety criteria, undertake a comparative safety analysis for the siting regions, and develop a safety case for the proposed site with robust and well evidenced arguments. Based on the considerations summarised in Sections 1.4.1 and 1.4.2, the geological investigations should therefore provide the underpinning evidence and argumentation base to support the demonstration of the following required characteristics:

- The **host rock provides** the primary geological containment function and is a particularly efficient and robust transport barrier. This requires a sufficiently thick host rock, limited llithological and mineralogical variability, very low hydraulic conductivities, low hydraulic gradients, a lack of distinct transport paths and thus diffusion-dominated transport conditions. Furthermore, the mineralogical composition and the related pore structure should favour the sorption of radionuclides and the geochemical conditions needed to promote the stability of the engineered barriers.
- **Low-permeability confining units** above and below the host rock contribute to the barrier effect. Compared to the host rock, the properties of the confining units may show a higher variability (e.g. concerning the clay-mineral content), but, as a whole, the CRZ should be characterised by low hydraulic conductivities, and transport should be diffusion-dominated.
- The efficiency of the geological barrier over long timescales is **independently evidenced.**

---

[6] The site-specific geological parametrisation for the dose calculations is not included in the geosynthesis but in Nagra (2024m) (see Fig. 1-1).

[7] The engineering geological description and parametrisation is not included in the geosynthesis, but in Nagra (2023a; 2023b; 2023c) (see Fig. 1-1).

- The host rock occurs in a **simple, subhorizontal to slightly inclined bedding configuration** wherby areas **devoid of seismically mappable faults** should be as large as posible, providing flexibility for repository placement and design.
- **The key properties of the host rock remain stable over the period under consideration with regard to long-term geological evolution.** This requires that porewater composition, hydraulic conductivity, self-sealing capacity and diffusion coefficients in the CRZ do not change in a detrimental way in response to natural processes that may be active during the next 100'000 to 1 million years. This includes climate change, glacial loading and unloading, erosion, geodynamic activity or rock dissolution phenomena. The depth of the host rock and the lateral distance to regional tectonic fault systems are pivotal considerations for long-term stability.

The points above address the geological barrier and its contribution to post-closure safety. In addition, geological investigations will provide the basis for the construction risk engineering analyses in the three siting regions as well as for planning the provisional engineering design of the repository at the proposed site[8].

The investigation campaign described in Chapter 2 focused on the provision of the data and information to support assessment of the required characteristics in line with the regulatory requirements (ENSI 2018).

1.5 Why the Opalinus Clay in Northern Switzerland?

The emphasis on Northern Switzerland as the preferred area for the location of a deep geological repository is the result of a systematic approach followed during SGT Stages 1 and 2 consisting of a stepwise narrowing-down process, starting from an investigation of all of Switzerland (SFOE 2008, Nagra 2008a, 2014i).

Northern Switzerland possessed the following positive attributes for siting a deep geological repository (Fig. 1-3):

- **Low geological complexity:** The siting regions are located outside large-scale tectonically complex zones, namely the Alps and the internal Jura, as well as the European Cenozoic Rift System (Upper Rhine Graben and its eastern border zone) and the related conjugated smaller Bonndorf – Hegau – Bodensee Graben system.
- **Low recent tectonic activity:** The siting regions are located away from areas with enhanced historically or instrumentally documented seismic activity, namely the Valais, Graubünden, the Prealps and the Basel areas.
- **Low uplift rates:** The siting regions are situated in the external Alpine Foreland characterised by low uplift rates compared to areas further south (Alps and internal Alpine Foreland).
- **Host rock with favourable properties at suitable depth and tectonic configuration:** Based on a systematic screening of potential host rocks throughout the country (Nagra 2008b), the Opalinus Clay proved to be best suited on the basis of its extremely low permeability and high lateral continuity. In Northern Switzerland, the Opalinus Clay is around 100 m thick and occurs in a depth window between 400 m and 1'000 m, suitable with regard to both long-term stability (protection against future erosion) and repository construction.

[8] Note that the engineering geological characterisation for construction-related issues is given in separate reports (Nagra 2023a; 2023b; 2023c).

In the JO, NL and ZNO siting regions, the Opalinus Clay occurs in subhorizontal to slightly inclined bedding configurations distal to regional fault zones.

Other candidate host rocks and regions were systematically evaluated earlier in the siting process but were excluded from further consideration because they were deemed less suitable for hosting a deep geological repository (e.g. unfavourable host-rock properties, insufficient thickness or lateral extent; see Nagra 2008b and 2014h for details).

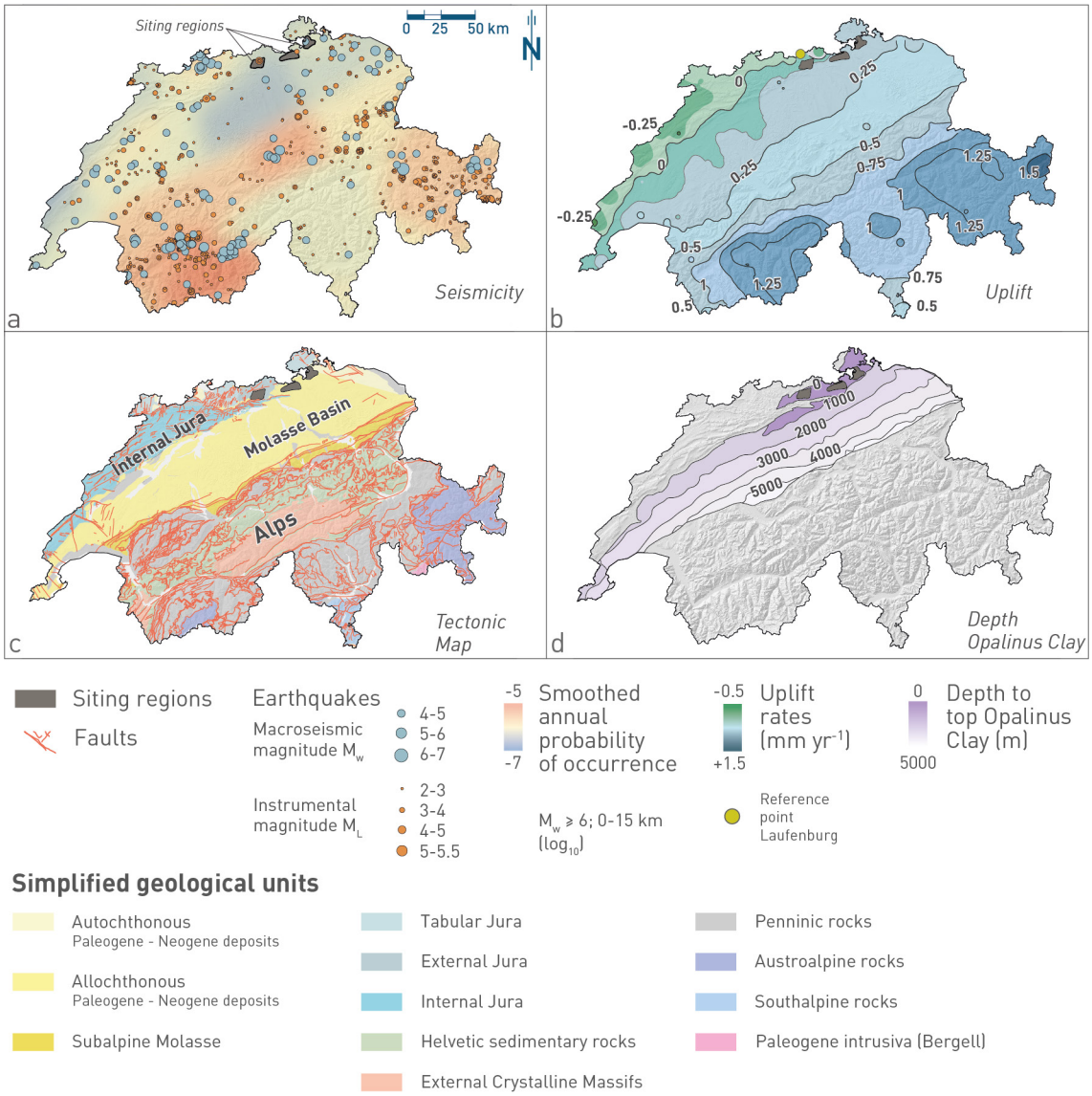


Fig. 1-3: Key aspects used for selecting the location of the Jura Ost (JO), Nördlich Lägern (NL) and Zürich Nordost (ZNO) siting regions in Northern Switzerland

(a) Earthquake catalogue of Switzerland (Fäh et al. 2011, update 30.09.2023) and probability map for earthquakes with magnitude $M_w \geq 6$ at 0 – 15 km depth in an area of 0.05° longitude × 0.05° latitude (~ 21 km^2) based on expert elicitation (swissnuclear 2013). (b) Uplift rates derived from high-precision levelling data (based on Schlatter 2014). The movements are shown relative to a reference point located in Laufenburg. (c) Tectonic map of Switzerland (Swisstopo 2005 modified). (d) Depth of Top Opalinus Clay in the Swiss Molasse Basin and adjacent areas (based on the Nagra regional geological model and GeoMol; Allenbach et al. 2017).

2 Overview of geological investigations with relevance for siting and demonstration of post-closure safety

Key points:

- A comprehensive scientific field investigation programme was carried out to characterise the safety-relevant geological properties and processes in the three siting regions.
- 3D seismic datasets provide detailed information for determining the depth and thickness of the relevant geological units, the location of faults and lateral facies changes.
- Investigations in 9 deep boreholes included detailed core descriptions, petrophysical logging and an extensive in-situ hydrogeological and geomechanical test programme. Host rock, low-permeability confining units and bounding aquifers were almost continuously cored. A large range of laboratory tests allowed a detailed characterisation of the relevant rock properties.
- A dedicated field investigation programme focused on Quaternary deposits improved the understanding of the erosion history over the past 1 – 2 million years and provided input for the estimation of future erosion to assess the long-term stability of the repository.
- Data integration included knowledge and concepts derived from academic research, industry projects (hydrocarbon exploration, carbon capture and storage, geothermal energy) and from work carried out by other radioactive waste management organisations. The latter include investigations in underground rock laboratories.

2.1 Overview

This chapter provides an overview of the geological knowledge base of Northern Switzerland (Fig. 2-1) with a special focus on the detailed site investigations carried out in the third and final stage of the site selection process (SGT Stage 3).

The geology of Northern Switzerland was intensively investigated prior to the start of the Sectoral Plan for Deep Geological Repositories (SGT) process in 2008, providing a well-established understanding of the subsurface and its geological evolution. The stratigraphic, tectonic and hydrogeological framework has been analysed since the middle of the 19th century through applied projects and academic research (e.g. Mösch 1867, Mühlberg 1901, Frei 1912, Amsler 1915, Buxtorf 1916, Heim & Hartmann 1919, Hartmann 1925, Schmassmann 1945, Laubscher 1961, Büchi et al. 1965, Hantke 1967). The intensive exploration campaigns carried out by Nagra in the 1980s (summarised in Thury et al. 1994) and in the 1990s (summarised in Nagra 2002), together with related scientific work (e.g. Matter & Peters 1987, Mazurek et al. 2006, Gimmi et al. 2007), significantly enhanced subsurface understanding of Northern Switzerland. Geophysical field work, together with participation in third-party drilling projects undertaken in the first two stages of the siting process (SGT Stage 1 and 2), further extended the knowledge base, and the integration of this new information improved process understanding (summarised in Nagra 2008b, 2014b). Swisstopo's 1:25'000 scale geological maps and corresponding detailed explanatory notes (accessible via map.geo.admin.ch), and regional 3D models of key geological horizons and faults developed within the framework of the GeoMol project (Allenbach et al. 2017), supplement this understanding.

The site investigations conducted for the third stage of the siting process (SGT Stage 3) took place between 2015 and 2022. The aim was the characterisation of the key attributes for site selection and the demonstration of the long-term safety for the proposed site (see Section 1.4.3), as well as the demonstration of engineering feasibility. The initial planning of the investigations was summarised in site-specific exploration concepts (Nagra 2014a, 2016). The exploration plan was refined and adapted during the investigations, incorporating learnings as new data were acquired and experience gained. It was also ensured that the regulatory requirements for the geological site investigations (ENSI 2018) were met.

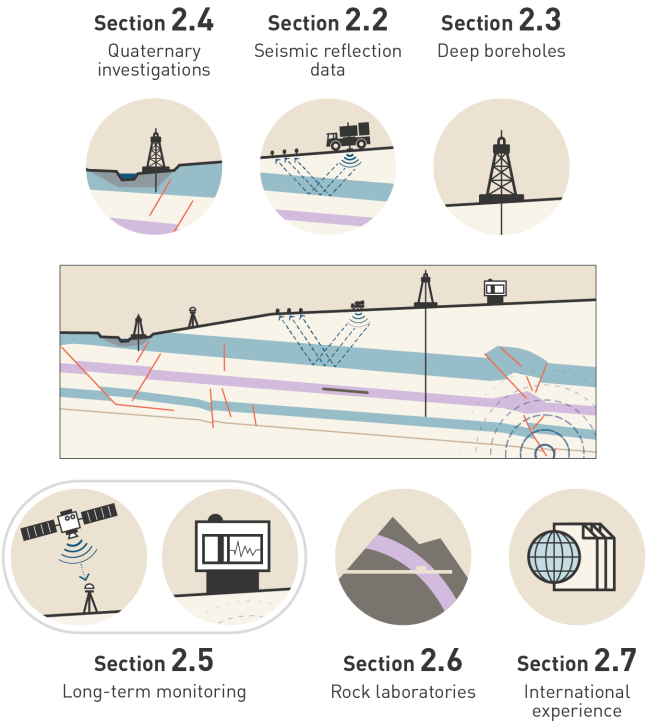


Fig. 2-1: Schematic overview of important sources of information for the characterisation of the geological barrier

Note that the project also benefited from selected geological outcrop studies (not shown in the figure).

An overview of the most important data sources used to characterise the geological barrier and to evaluate its past and future evolution is provided below and illustrated in Fig. 2-1. They include data arising from Nagra and third-party field investigations (seismic surveys, boreholes) as well as from decades of research in the Mont Terri rock laboratory. Seismic investigations (Section 2.2) provide 2D or 3D information on the geometry of the geological units and tectonic faults. This information is fundamental for siting a deep geological repository in a subhorizontal to slightly inclined host rock configuration with low deformation. Deep boreholes allow characterisation of the rocks and their properties and the calibration of seismic data (Section 2.3). A shallow investigation programme (shallow geophysics, shallow boreholes, outcrop analyses; Section 2.4) quantifying the processes and rates of the Quaternary geodynamic and erosional evolution provides the understanding necessary to assess the evolution of the geological barrier during the next one million years. Further input regarding future geological evolution is provided by long-term monitoring systems delivering, for example, information on recent seismicity and movements of the Earth's surface (Section 2.5). Experiments in the Mont Terri rock laboratory

hosted in the Opalinus Clay give further insights into key processes in the host rock (Section 2.6). Lastly, the project benefits from the general understanding of the behaviour of clay-rich rocks built up by applied and academic research (Section 2.7).

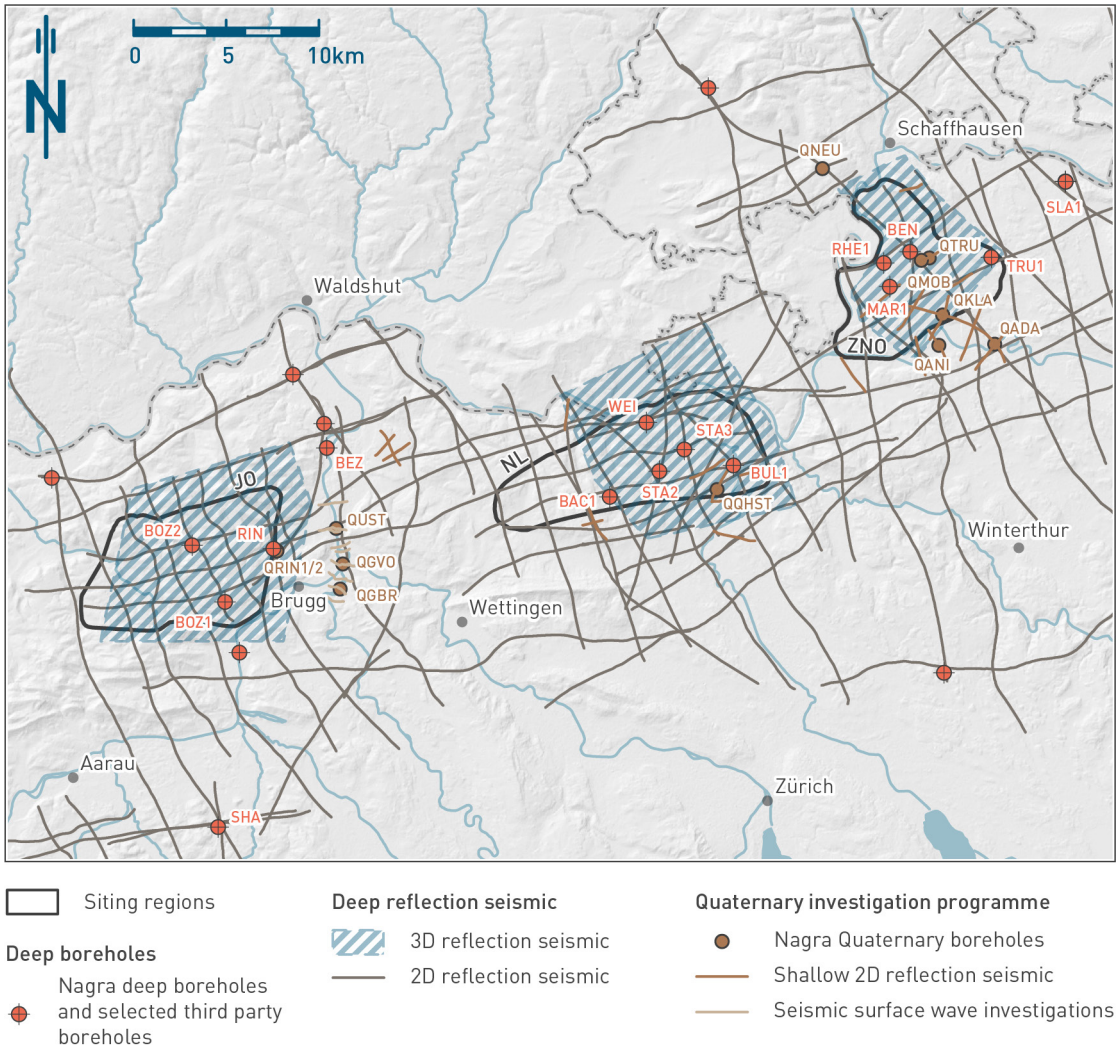


Fig. 2-2: Important geophysical datasets and boreholes in Northern Switzerland

Boreholes discussed in this report are labelled. See Tab. 2-1 (deep boreholes) and Tab. 2-2 (Quaternary boreholes) for further information and references to data reports.

2.2 Reflection seismic data

Northern Switzerland is covered by a dense grid of 2D seismic lines (Fig. 2-2) acquired over several exploration campaigns from the early 1980s by Nagra and third parties (mainly the hydrocarbon exploration industry). In SGT Stage 2 the existing seismic data were reprocessed in a consistent way, and further complementary 2D seismic data were acquired to fill gaps in and around the siting regions. These lines of data, with a typical line spacing of 1 – 3 km, provided a robust understanding of the regional tectonic framework and elements as well as the depth and geometry of key Mesozoic units including the Opalinus Clay (Madritsch et al. 2013, Nagra 2014a, 2014b, Meier et al. 2014).

In conjunction with SGT Stage 3, Nagra acquired 3D seismic surveys in all three siting regions between 2015 and 2017 to provide a continuous and more comprehensive image of the subsurface necessary for site-scale geological characterisation. Part of the Zürich Nordost (ZNO) siting region had previously been covered by a 3D survey, acquired by Nagra in 1997 in connection with the demonstration of disposal feasibility for a HLW repository (Nagra 2001). To include areas with shallower Opalinus Clay potentially suited for a L/ILW repository, the existing survey in ZNO was extended to the north. The processing of the seismic data included data from both the original and the new acquisition, resulting in a merged continuous 3D dataset. The area covered by 3D seismic data in the three siting regions amounts to a total of 240 km^2. The seismic processing is documented in Nagra (2024s) and the final interpretation in Nagra (2024a) for Jura Ost (JO), Nagra (2024b) for Nördlich Lägern (NL) and Nagra (2024c) for Zürich Nordost (ZNO).

The aims of the new surveys were 3D mapping of key geological horizons to provide detailed information on depth, thickness and inclination of relevant geological units, the distribution and geometry of faults, the identification of lateral facies changes and the reconstruction of the tectonic history. The survey design was informed by existing geological knowledge from Stage 2 of the Sectoral Plan, primarily 2D seismic data, outcrop information and a few deep boreholes (Madritsch et al. 2013, Nagra 2014b). The surveys primarily targeted the host rock and the confining units in the central areas with flat-lying little disturbed strata, but also provided information on the larger-scale tectonic elements in the surrounding regions. The processing of the seismic field data was optimised to support the comparison of the three siting regions for the purpose of the site selection (Nagra 2024s). The seismic imaging in the potential disposal zones in all the siting regions is of high quality, achieving the survey aims and providing the data necessary for site selection and the demonstration of post-closure safety. This, together with the systematic interpretation approach applying rigorous criteria (Nagra 2024a, 2024b, 2024c) ensures a high comparability of the interpretation results between the regions despite some differences in topography, geological setting and acquisition method.

2.3 Deep boreholes

A total of 9 new deep boreholes were drilled between 2019 and 2022. Together with the existing deep boreholes Riniken (RIN; JO), Weiach (WEI; NL) and Benken (BEN; ZNO), each of the three siting regions has between 3 and 5 deep boreholes, which were used for calibration and depth conversion of the 3D seismic data (Fig. 2-2).

The main aims of the most recent drilling programme were the calibration of the 3D seismic data and the geological characterisation of the host rock and the adjacent low-permeability confining units (e.g. mineralogy, porosity, transport properties, geomechanical properties, hydraulic state, stress conditions; see Chapters 4 and 5). A further aim was to characterise the deep aquifers above and below the host rock and its low-permeability confining units as they define the boundary conditions for transport in the aquitard sequence and represent the most important hydraulic connection to the biosphere. The investigations of the deep aquifers included an assessment of hydraulic conductivities, hydraulic heads and the characterisation of the groundwater geochemistry and residence times.

In most of the boreholes, the bulk of the Mesozoic rock sequence and the uppermost part of the underlying Paleozoic rock was cored, providing information on the host rock, confining units, neighbouring aquifers and on the underlying evaporitic series, known to be relevant for tectonic evolution. One of the boreholes, RHE1 (ZNO), was deviated to investigate the structural and hydrogeological characteristics of the Opalinus Clay in the area of a steeply dipping fault.

A comprehensive programme of investigations was undertaken downhole and on rock cores, and fluid samples were obtained from the boreholes. Downhole investigations included petrophysical logging, groundwater sampling and in-situ testing (fluid logging, hydraulic packer tests, micro-

hydraulic fracturing tests). Following detailed core logging, a comprehensive characterisation programme of laboratory measurements was performed, including mineralogy, porosity, hydraulic conductivity, porewater and groundwater chemistry, groundwater dating, as well as a suite of geomechanical properties with customised on-site sampling and sample conditioning procedures (Rufer & Stockhecke 2019) and laboratory measurement protocols (e.g. Minardi et al. 2021, Waber 2020).

A generic work programme including a short description of the exploration tools can be found in Nagra (2019a). The results of field investigations and laboratory measurements are documented in comprehensive borehole-specific data reports (Tab. 2-1).

Tab. 2-1: List of Nagra's 9 deep boreholes drilled 2019 – 2022 and other important deep boreholes (shown in italics), including references to data reports

MD: Measured depth below ground level. [1] ≈ 498.51 m true vertical depth (TVD), [2] ≈ 745.33 m TVD, [3] only middle and lower sections of Opalinus Clay (OPA) encountered. Borehole locations are shown in Fig. 2-2.

Siting region	**Borehole name**	**Abbreviation used in report**	**Data reports**	**Nagra Report No.**	**Depth Top OPA** [m MD]	**Final depth** [m MD]
JO	Bözberg-1-1	BOZ1	Nagra (ed.) 2022a	NAB 21-21	530.28	1'037.39
JO	Bözberg-2-1	BOZ2	Nagra (ed.) 2022b	NAB 21-22	451.54	829.11
JO	*Riniken*	*RIN*	*Nagra 1990*	*NTB 88-09*	*450.93*	*1'800.50*
JO	*Beznau*	*BEZ*	*Nagra 1984*	*NTB 84-34*	*(20.3)* [3]	*321.8*
NL	Bülach-1-1	BUL1	Nagra (ed.) 2021a	NAB 20-08	891.70	1'370.19
NL	Stadel-3-1	STA3	Nagra (ed.) 2022d	NAB 22-01	779.26	1'280.88
NL	Stadel-2-1	STA2	Nagra (ed.) 2022c	NAB 22-02	799.67	1'288.12
NL	Bachs-1-1	BAC1	Nagra (ed.) 2023b	NAB 22-04	808.34	1'306.26
NL	*Weiach*	*WEI*	*Nagra 1989*	*NTB 88-08*	*665.67*	*2'482.20*
ZNO	Trüllikon-1-1	TRU1	Nagra (ed.) 2021c	NAB 20-09	816.42	1'310.0
ZNO	Marthalen-1-1	MAR1	Nagra (ed.) 2021b	NAB 21-20	590.35	1'099.25
ZNO	Rheinau-1-1	RHE1	Nagra (ed.) 2023a	NAB 22-03	524.61 [1]	827.99 [2]
ZNO	*Benken*	*BEN*	*Nagra 2001*	*NTB 00-01*	*652.04*	*1'007.00*
–	*Schafisheim*	*SHA*	*Nagra 1992*	*NTB 88-11*	*1'079.95*	*2'006.50*
–	*Schlattingen-1*	*SLA1*	*Albert et al. 2012*	*NPB 12-16*	*949.70*	*1'508.00*

The deep drilling programme substantially expanded the database for characterising and quantifying radionuclide transport in the geological barrier. Fig. 2-3 shows the marked increase in the available data for some key measurements relating to safety:

- The large number of additional hydraulic packer tests increases confidence in the hydraulic characterisation of the host rock, adjacent low-permeability confining units and neighbouring aquifers (Sections 4.5.3 and 5.6).
- A large number of diffusion measurements from various lithologies across the host rock and confining units allows the diffusion properties to be quantitatively linked to the clay-mineral content (Section 5.8). This increases the representativity and robustness of the diffusion properties used for transport modelling.
- Closely spaced porewater chemistry determinations along all boreholes (profiles of natural tracers in the porewater; see Section 4.6), in combination with groundwater geochemistry measurements and ^{81}Kr groundwater residence times from the aquifers (see Section 4.5.5), provide key information on transport over the past 10^4 to 10^7 years. Furthermore, the porewater chemistry measurements in the Opalinus Clay allow the characterisation of the geochemical conditions in the host rock to understand the stability of the engineered barriers (Section 5.4).
- A detailed programme of mineralogical characterisation of the host rock and confining units (Section 5.2) allows the relationship to other key parameter measurements (e.g. geomechanical properties, diffusion coefficients and hydraulic conductivity) to be quantified (Sections 5.5, 5.6 and 5.8). This is important in assessing long-term stability, because the clay-mineral content is a key factor controlling the self-sealing behaviour of faults (Section 5.7).
- A thorough understanding of the stress state in the host rock is important for engineering design and long-term stability (repository-induced effects, self-sealing of faults). The dataset gained from microhydraulic fracturing in the new campaign is exceptional both in terms of methods applied and data frequency and allows a robust characterisation of the stress magnitudes (Section 4.4).

A more detailed discussion of the evolution of the database and the related progress in site characterisation and process understanding is given in Section 7.1.

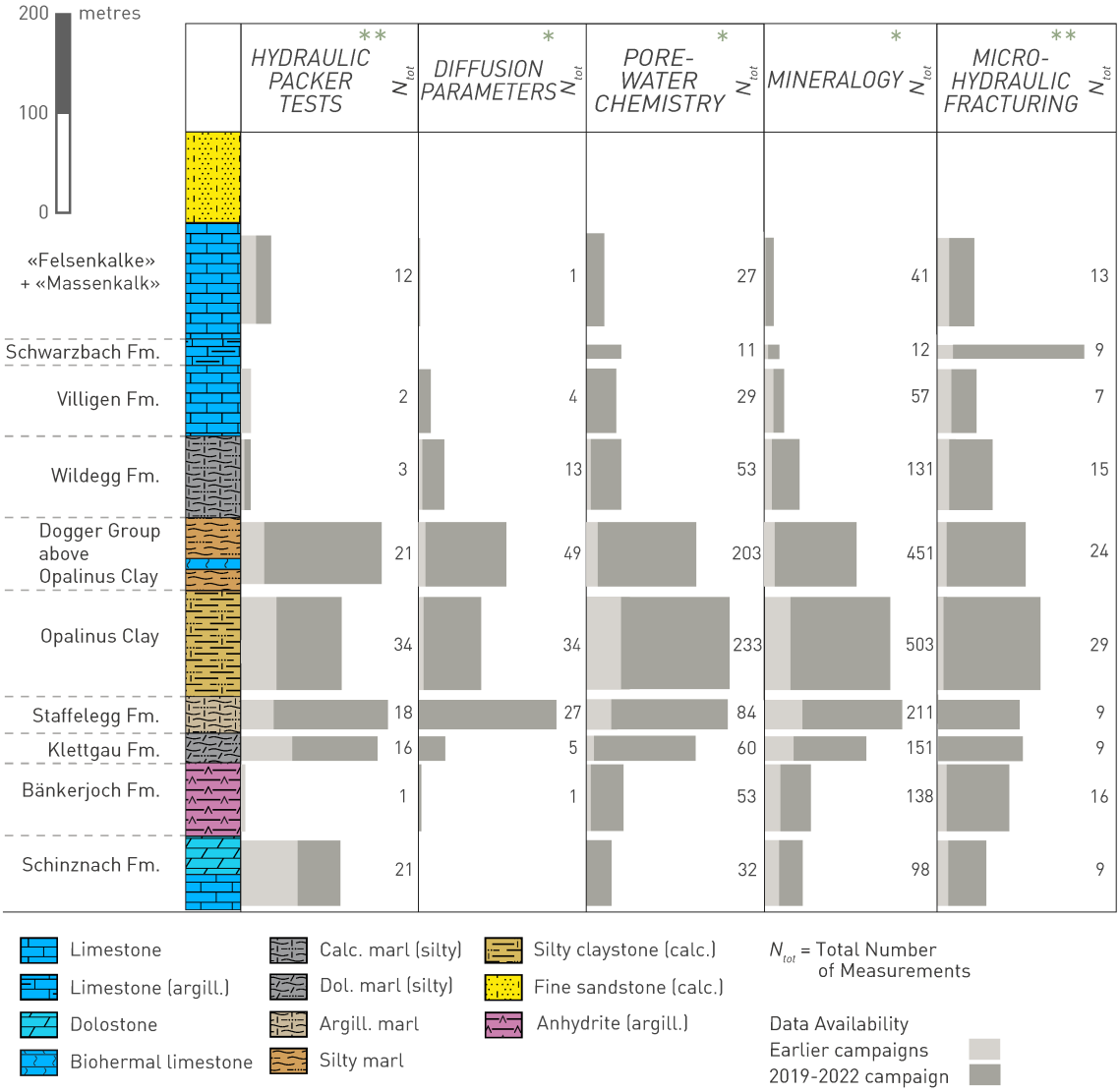


Fig. 2-3: Increase in size of the database for key parameters during the 2019 – 2022 deep drilling campaign

The above overview includes the 9 new boreholes as well as the BEN, RIN, WEI, SLA1, BEZ and SHA boreholes. Data are projected onto the lithostratigraphic column for the STA2 borehole, which is shown as a reference on the left. For an introduction to the lithostratigraphic column see Section 3.1. N_{tot} indicates the total number of measurements per formation. The length of the horizontal bars represents the number of measurements normalised by the thickness of the formation. Longer bars thus indicate higher densities of data points in the corresponding formation. Parameters with one asterisk indicate laboratory experiments on drill cores, while parameters with two asterisks represent in-situ measurements in the boreholes.

The figure shows the substantial increase in the database resulting from the new drilling campaign and reflects the investigation focus on the host rock and the surrounding confining units.

2.4 Investigation programme related to Quaternary deposits

A dedicated field investigation programme was undertaken to reconstruct the erosion history of the siting regions over the past 1 – 2 million years as a basis for establishing future erosion scenarios (Section 6.4). In addition to characterising the depth, shape and age of glacially over-deepened troughs, the investigations sought to constrain the age of the Early to Middle Pleistocene gravel deposits for reconstructing past fluvial incision history.

The investigations involved the acquisition of high-resolution 2D reflection seismic data (Nagra 2018), data for seismic surface wave investigations (Nagra 2021) and 11 Quaternary boreholes with ~ 50 to 300 m length (Fig. 2-2, Tab. 2-2). The boreholes were fully cored and numerous laboratory investigations were carried out, including sediment age determinations (e.g. Mueller et al. 2024, Tomonaga et al. 2024). Surface outcrops were also studied and sampled to determine relative and absolute ages of the deposits (e.g. Grischott et al. 2020, Scheidt et al. 2023, Thew et al. 2024). Understanding of the past landscape evolution has significantly improved as a result of these investigations (e.g. Gegg et al. 2023, Buechi et al. 2024; see Sections 3.5 and 6.4.1).

Tab. 2-2: List of Nagra's 11 Quaternary boreholes drilled 2018 – 2020 including references to data reports

MD: Measured depth below ground level. Borehole locations are shown in Fig. 2-2.

Siting region	Borehole name	Abbrevi-ation	Data reports	Nagra NAB No.	Depth Base Quaternary [m MD]	Final depth [m MD]
JO	Riniken-1 Riniken-2	QRIN1 QRIN2	Gegg et al. 2018	NAB 18-40	41.2	52.7 41.2
JO	Untersiggenthal	QUST	Gegg et al. 2019c	NAB 19-01	76.0	86.4
JO	Gebenstorf-Brüel	QGBR	Gegg et al. 2019b	NAB 19-02	111.5	123.5
JO	Gebenstorf-Vogelsang	QGVO	Gegg et al. 2019a	NAB 19-03	65.0	77.0
NL	Hochfelden-Strassberg	QHST	Amschwand et al. 2020	NAB 20-02	267.2	278.0
ZNO	Marthalen-Oobist	QMOB	Kuster et al. 2019	NAB 19-04	24.5	48.0
ZNO	Neuhausen	QNEU	Buechi et al. 2019	NAB 19-05	127.1	137.2
ZNO	Trüllikon-Rudolfingen	QTRU	Huber et al. 2020	NAB 20-01	88.0	99.0
ZNO	Kleinandelfingen-Laubhau	QKLA	Schuster et al. 2020	NAB 20-03	253.6	263.4
ZNO	Andelfingen-Niederfeld	QANI	Reichenwallner et al. 2021	NAB 20-04	313.7	324.0
ZNO	Adlikon-Dätwil	QADA	Buechi et al. 2022	NAB 22-14	303.0	313.2

2.5 Long-term monitoring systems

The seismic monitoring network in Northern Switzerland has been considerably densified over the last 15 years (Plenkers 2014). The Nagra network operated by the Swiss Seismological Service (SED) currently includes 24 measurement stations, including three in shallow boreholes and one deep borehole station (Diehl et al. 2023, Spillmann et al. 2022). Using this system, all (micro)-seismic events with magnitude $M_w > 1$ can be detected and located reliably. Nagra also runs a permanent network of 11 Global Navigation Satellite System (GNSS) stations in and around the siting regions (Studer & Zanini 2013). The horizontal and vertical position of these stations is

determined with high accuracy and temporal resolution, providing robust information on recent uplift and deformation. The seismic and geodetic monitoring systems substantially improved the understanding of the seismotectonic situation, providing input for the assessment of future tectonic movements (Section 6.2) and erosion (Section 6.4). In the three boreholes MAR1, STA3 and BOZ1, Nagra installed hydrogeological monitoring systems, adding to the pre-existing monitoring system in the BEN borehole (Longridge et al. 2024). This instrumentation aims to derive robust hydraulic heads in the Opalinus Clay, which cannot be deduced from hydraulic packer testing because of short-term drilling-induced effects and the short duration of the packer tests (see Section 5.6.5).

2.6 Investigations in the Mont Terri rock laboratory

The Mont Terri project is an international research project with currently 22 partner organisations from 10 different countries (https://www.mont-terri.ch). The rock laboratory is located approximately 75 km to the west of the JO siting region in an anticline of the Jura Fold-and-Thrust Belt. It includes a network of underground galleries and niches in the Opalinus Clay designed for various underground experiments. More than 25 years of intensive scientific investigations have significantly increased the understanding of safety- and construction-relevant properties and processes in this rock (see Bossart et al. 2017 and references therein for an overview). The laboratory plays an important role in the development and testing of methodologies (e.g. geomechanical testing, porewater investigations; Minardi et al. 2021, Wersin et al. 2020). It also allows for in-situ testing at larger scales and over longer durations compared to deep borehole experiments (see Section 5.8.3). This report frequently refers to knowledge gained at the Mont Terri rock laboratory, taking into account the differences in the geological history and depth of the laboratory compared to the Opalinus Clay in Northern Switzerland.

2.7 International experience with clay-rich rocks

Clay-rich rocks are being investigated as host rocks for radioactive waste disposal in various countries (e.g. Belgium, Canada, France, Germany, Hungary, UK). The rock types range from soft, plastic and poorly indurated clays or claystones to brittle, hard mudstones and shales, i.e. very weak to very strong rocks according to the ISRM (1981) classification. The most recent compilation of characteristics of such argillaceous rocks was published by the Clay Club of the OECD Nuclear Energy Agency (OECD/NEA 2022). Comparisons of the properties of the different clay-rich rocks are discussed e.g. by Mazurek et al. (2003; features, events and processes), Mazurek et al. (2009; natural tracer profiles) and Bock et al. (2010; self-sealing properties). Figures comparing the mineralogy, porosity, hydraulic conductivity and diffusion coefficients of the Opalinus Clay with other clay-rich rocks are included in Chapter 5.

The clay-rich rocks with the closest similarities to the Opalinus Clay are two formations under investigation in France:

1. The Callovo-Oxfordian clay host rocks for the planned Cigéo (acronym for *Centre Industriel de stockage géologique*), a repository for high- and intermediate-level radioactive waste in the eastern Paris basin. Detailed multidisciplinary site investigations of the Callovo-Oxfordian rocks have been conducted nearby in the Meuse/Haute Marne Underground Rock Laboratory (Delay et al. 2007, Leverd 2023).
2. Toarcian – Domerian clay-rich rocks are investigated by a multi-disciplinary research programme in an abandoned railway tunnel in the Causses Basin (see Annex III of OECD/NEA 2022).

Clay-rich rocks much weaker than the Opalinus Clay are investigated in the HADES underground research facility in the Oligocene Boom Clay in Mol (Belgium). The research programme was launched already in the 1970s and included a detailed host rock characterisation programme (see e.g. De Craen et al. 2023 as an example for geochemical aspects). Besides the Boom Clay, the Eocene Ypresian Clay (also a very weak clay formation) is considered as an alternative host rock in the Belgian programme.

Clay-rich rocks much stronger than the Opalinus Clay also play an important role as a radionuclide transport barrier. In the Canadian programme, the potential sedimentary host rock[9] for the spent fuel repository is a 30 m thick very low-permeability argillaceous limestone (the Ordovician Cobourg Formation). This formation is sandwiched between more than 200 m of strong clay-rich rocks (shales) above and more than 150 m of argillaceous limestones below (NWMO 2011, 2023), all in all an excellent geological barrier system.

The host rock for the German repository project Konrad for low- and intermediate-level radioactive waste is an Oxfordian oolithic limestone succession. The geological barrier is formed by overlying Lower Cretaceous claystones and marls. Below the host rock low-permeability clay-rich rocks of the Lower Dogger and Lias Groups form a geological barrier (e.g. Rübel et al. 2019). Moreover, a variety of clay-rich formations is currently investigated as potential host rocks for the German repository for high-level radioactive waste (BGE 2020). Among them is also the Opalinus Clay in Southern Germany.

The Permian Boda Claystone Formation – an albitic clay-rich formation deposited in a saline playa lake – is being investigated in Hungary with respect to host-rock properties (see Annex III of OECD/NEA 2022, with detailed references and illustrations). The formation is highly overconsolidated due to a maximum burial of 3.5 to 4.5 km. The hydraulic characteristics of the Boda Claystone Formation partly resemble those of crystalline rocks (large difference in hydraulic conductivities between intact rock matrix and fractured rock).

In the UK programme, two mudstone successions are at early stages of investigation to assess their potential to host higher activity radioactive waste. In the inshore adjacent to the East Coast of England, the focus is on the Ancholme Group, a Middle to Upper Jurassic aged, mudstone-dominated succession. In this area, the Ancholme Group comprises a ca. 180 to 450 m thick succession dominated by clay-rich units, gently inclined towards the offshore within which areas largely unaffected by significant faults are anticipated. In the inshore adjacent to the northwest of England, a mixed succession dominated by Triassic mudrocks and evaporites of the Mercia Mudstone Group is under investigation. Here the group comprises a ca. 200 to 1'600 m thick succession preserved in an extensional sub-basin, part of the East Irish Sea Basin, at depths between ca. 50 m and > 1'600 m.

Clay-rich rocks have a known ability to act as a barrier to fluid flow in the subsurface and have therefore been investigated extensively by the hydrocarbon industry and, in recent years, for carbon capture and storage, as a common caprock and seal hindering upward migration of fluid. Data and understanding from such studies (e.g. Fisher et al. 2023) provide independent evidence for the effectiveness of the clay-rich rocks as a transport barrier (Section 5.7).

[9] In the Canadian programme also crystalline host rocks are investigated.

3 Geological evolution of Northern Switzerland

Key points:

- The Paleozoic basement of Northern Switzerland is characterised by ENE-WSW-trending Permo-Carboniferous troughs and NW-SE- and NNE-SSW-trending faults. These structures acted as zones of weakness localising subsequent strain.
- During the Mesozoic, Northern Switzerland was located in the subsiding Central European Basin where sedimentary deposition mostly took place in shallow marine epicontinental environments. The Opalinus Clay was deposited at around 174 Ma during a phase of rapid subsidence and high clay-mineral input probably in combination with ocean currents favouring rapid sediment accumulation.
- Miocene times in Northern Switzerland saw the northwest-ward propagation of the Alpine deformation front and the formation of the Jura Fold-and-Thrust Belt.
- During the Pliocene and Quaternary, uplift and drainage reorganisation resulted in river incision. Quaternary foreland glaciations led to the erosion and infill of overdeepened valleys and the deposition of thick fluvioglacial deposits.

This chapter provides an overview of the geological evolution of Northern Switzerland (Fig. 3-1). It links the larger scale with the local conditions and processes that gave rise to the deposition, diagenesis and deformation of the rocks occurring in the study area. It aims to contextualise subsequent chapters, which will provide further details on the topics relevant for the characterisation of the geological barrier and its long-term evolution.

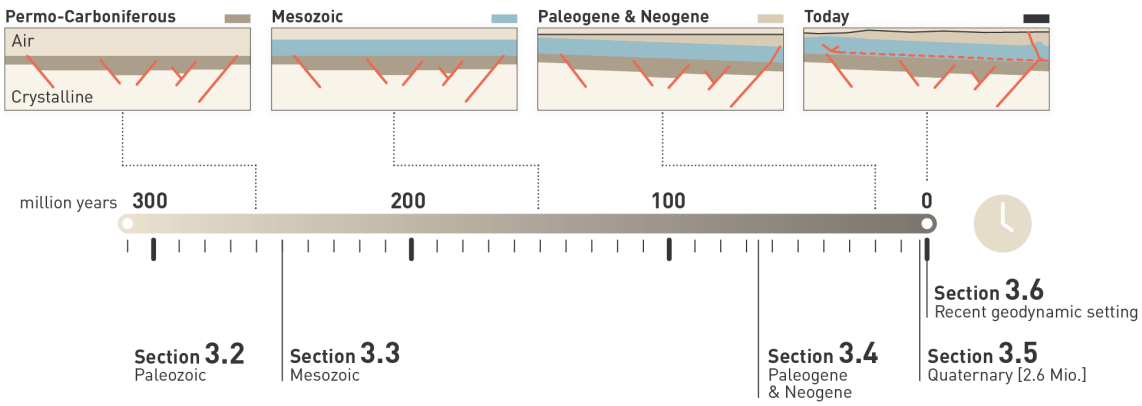


Fig. 3-1: Visualisation of the structure of the chapter

3.1 Overview

Regional geological research over more than 100 years, complemented by site investigations (Chapter 2), provide a basis for reconstructing the geological evolution of Northern Switzerland and adjacent areas. The area considered in the present report is termed Northern Switzerland. It is bordered by the Black Forest Massif and the Tabular Jura in the north, the Hegau – Bodensee Graben in the northeast, the Upper Rhine Graben in the west, and the northern Swiss Molasse Basin in the south (Fig. 3-2, Fig. 3-3). In Northern Switzerland, the Mesozoic strata considered autochthonous are referred to as the Tabular Jura. The Jura Fold-and-Thrust Belt comprises External Jura and Internal Jura, where the Internal Jura is defined as the more strongly deformed part. A summary of the geological evolution of Northern Switzerland is presented in Fig. 3-4.

The Black Forest Massif is composed mainly of crystalline rocks and is considered to be autochthonous. The Variscan orogeny, however, strongly deformed the crystalline basement of the Black Forest and adjacent Northern Switzerland, resulting in crustal-scale shear zones. Post-Variscan orogenic collapse and transtension resulted in the formation of the Konstanz – Frick Trough, which is a Permo-Carboniferous ENE-WSW-trending graben crossing Northern Switzerland. During the Permo-Carboniferous, coarse- to fine-grained siliciclastic sediments were deposited on alluvial plains under humid to arid conditions.

Towards the end of the Permian, the landscape was generally eroded to form a peneplain. In conjunction with renewed subsidence in the Triassic, Northern Switzerland lay within the southern part of the Central European Basin. Deposition during the Middle and Late Triassic was controlled by two major phases of transgression and regression preserved in the Muschelkalk and Keuper Groups respectively. Siliciclastic, evaporitic and carbonate sediments were deposited in terrestrial, coastal to marine depositional environments under subtropical to arid conditions.

During the Early and Middle Jurassic, mostly argillaceous and calcareous sediments (Lias and Dogger Groups) were deposited in a shallow epicontinental sea that formed during the opening of the Piemont – Liguria Ocean, part of the Neotethys. At this time, accommodation space was created by subsidence resulting from stretching and/or cooling of the lithosphere. During the Late Jurassic, mostly calcareous and marly sediments (Malm Group) were deposited in a shallow marine environment. The Mesozoic sequence outcrops in the Jura Fold-and-Thrust Belt. The Subalpine Molasse, the Swiss Molasse Basin and the Jura Fold-and-Thrust Belt together form the North Alpine Foreland. The Molasse Basin formed as flexural foreland basin. It comprises Paleogene and Neogene sedimentary rocks.

From the latest Mesozoic to the Oligocene, terrestrial conditions again prevailed in the region. Exhumation and a tropical climate led to intense weathering and erosion resulting in the top of the Malm Group being heavily karstified. Residual sediments (Siderolithic Group) of Eocene age can be found in palaeokarst depressions and infills.

North Alpine Foreland subsidence resulted in the Late Eocene in the deposition of the Lower Marine Molasse Group (UMM). In Northern Switzerland, terrestrial sedimentation resumed during the Late Oligocene with deposition of medium- to fine-grained siliciclastic sediments on large debris fan systems (Lower Freshwater Molasse Group, USM). Note that the classical German abbreviations for the Molasse deposits are used (Fig. 3-4; Matter 1980). During late Early Miocene times, the latest transgression to affect Northern Switzerland led to deposition of sandstone and marl in shallow marine and coastal environments (Upper Marine Molasse Group, OMM).

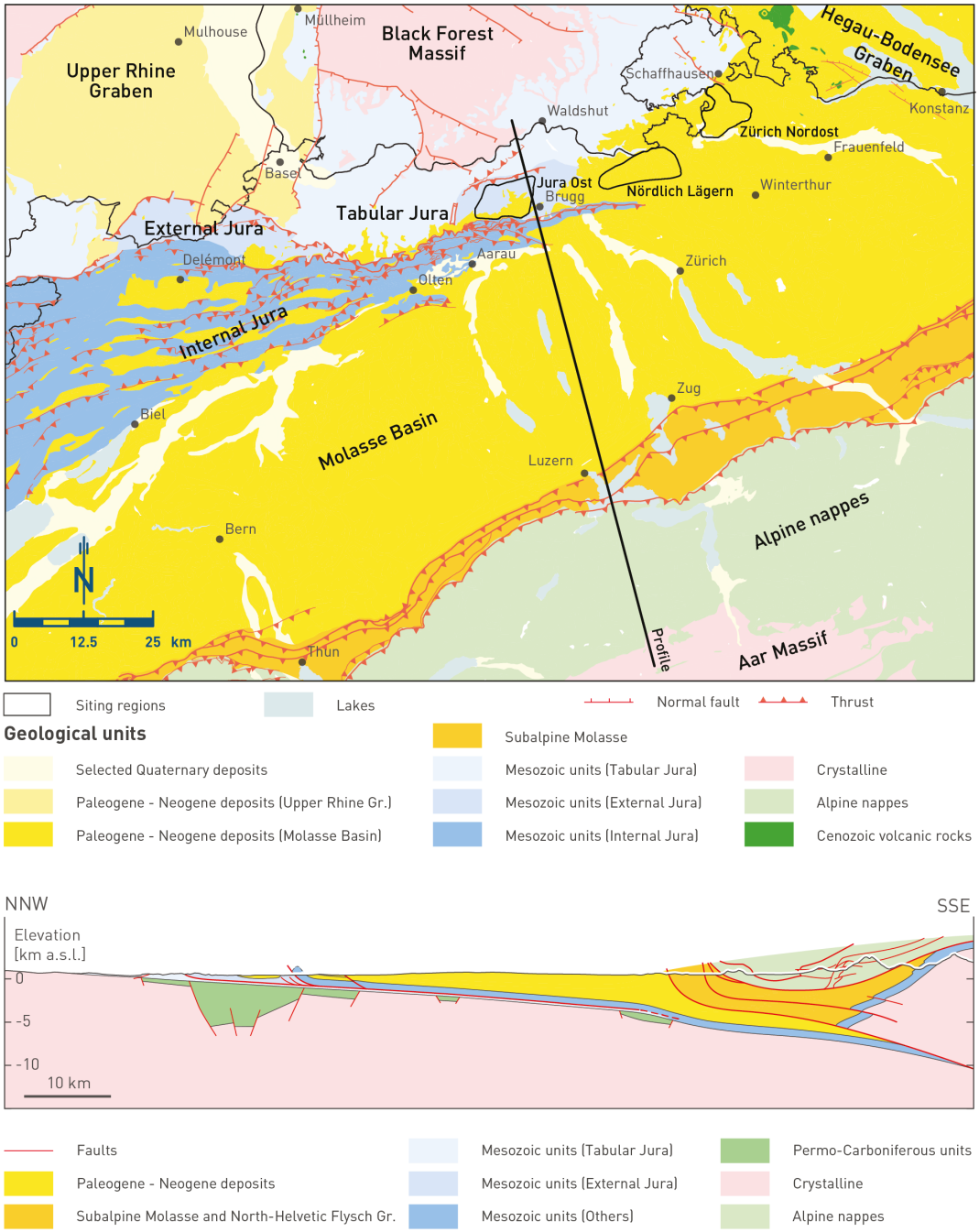


Fig. 3-2: Simplified tectono-geological map of Northern Switzerland with a profile between the Aar Massif and the Black Forest Massif

Modified after Nagra (2014b). Geological map 1:500'000 was simplified (©swisstopo), i.e. no faults are shown within the Alps. Gr.: Graben (map above) or Group (cross-section below).

The Middle Miocene saw the opening of the Hegau – Bodensee Graben coeval with the deposition of medium- to fine-grained siliciclastic sediments on large debris fan systems (Upper Freshwater Molasse Group, OSM). The main deformation in the Jura Fold-and-Thrust Belt occurred within the Middle to Late Miocene to Pliocene, but it remains active until today.

During the Pliocene, the river drainage evolved from eastward-directed (Aare-Danube draining towards the Black Sea) to a westward- (Aare-Doubs draining towards the Mediterranean) and finally to a northward-directed system (Aare-Rhine draining towards the North Sea). During the Quaternary, glaciers advanced and retreated in the Alpine Foreland driven by glacial/ interglacial climate cycles. Together, these climate cycles, tectonic uplift and the progressive eastward migration of the Rhine River catchment resulted in fluvial and glacial incision. In the forefield of the glaciers, vast gravel plains were deposited. Glaciers also incised overdeepened troughs, which were filled by lacustrine sand and silt. With the disappearance of the glaciers in the North Alpine Foreland, fluvial and hillslope processes dominated the pre-sculptured landscape.

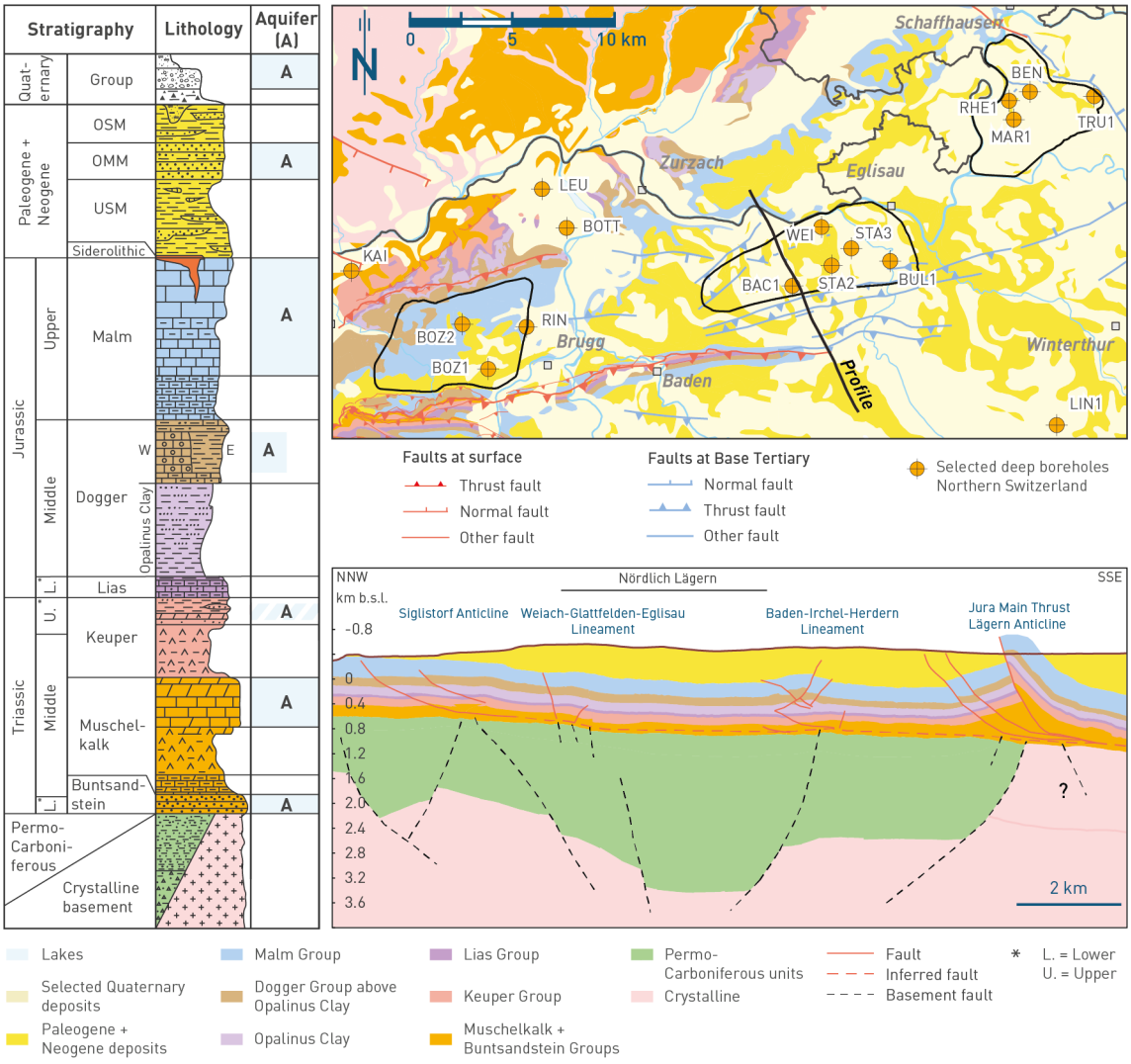


Fig. 3-3: Stratigraphic column, geological map and profile of Northern Switzerland

Geological map modified after 1:500'000 geological map of Switzerland (©swisstopo). Cross-section modified after Meier et al. (2014) with the recent results from the 3D seismic interpretation.

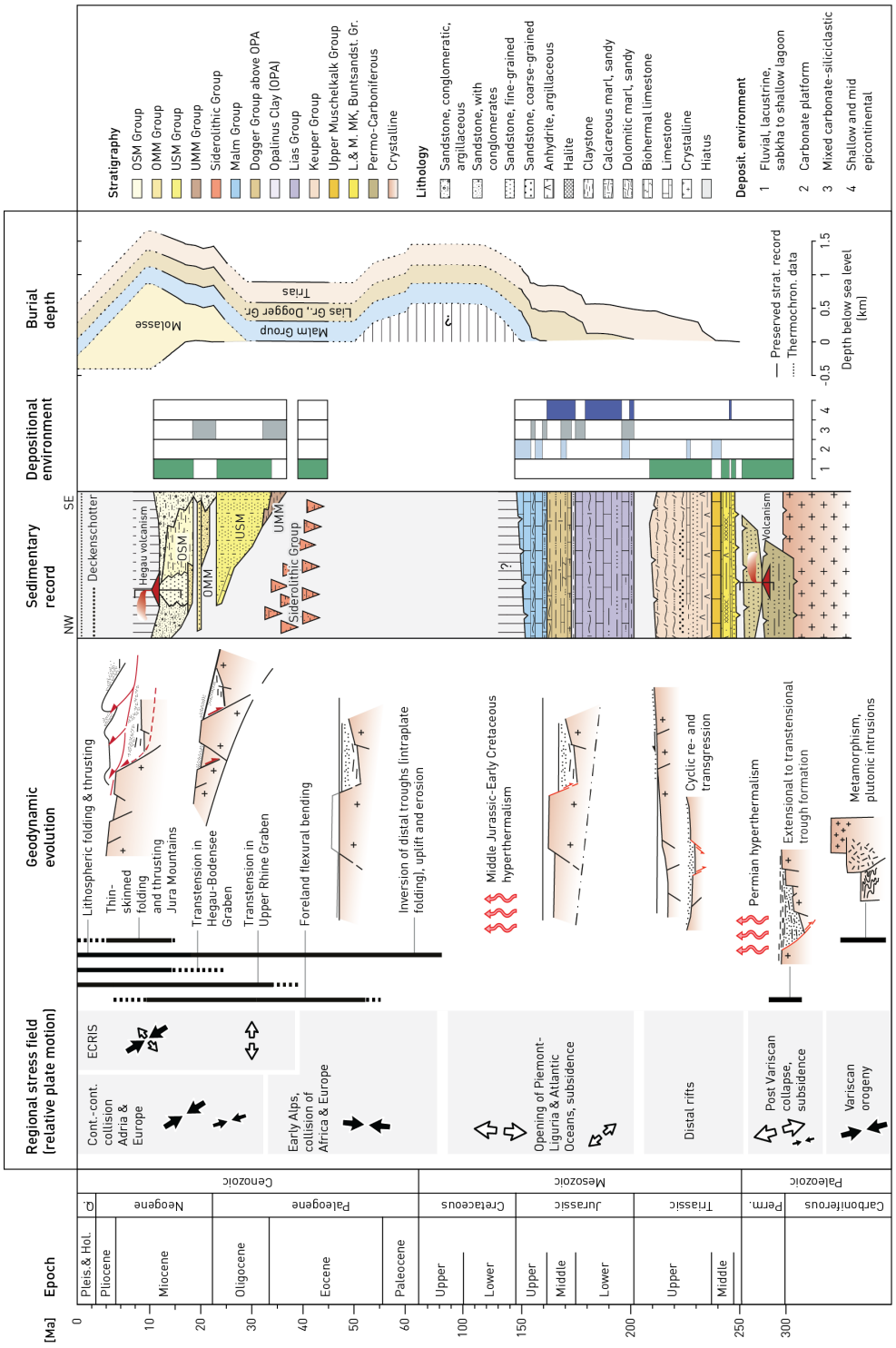


Fig. 3-4: Timeline focusing on the geological evolution of Northern Switzerland

Modified after Müller et al. (2002). Large-scale stress field characteristics and tectonic events after Schori (2021), burial evolution after Mazurek et al. (2006). White arrows indicate tension-dominated stress field. Black arrows indicate compression-dominated stress field. Pleis.: Pleistocene, Hol.: Holocene, Q.: Quaternary, Perm.: Permian, Cont.: Continent, ECRIS: European Cenozoic Rift System, OSM: Upper Freshwater Molasse, OMM: Upper Marine Molasse, USM: Lower Freshwater Molasse, UMM: Lower Marine Molasse, Gr.: Group.

3.2 Paleozoic

The geological framework of Northern Switzerland is largely controlled by the Pre-Mesozoic basement and the Variscan orogeny. The Pre-Mesozoic basement is composed of crystalline basement and overlying Permo-Carboniferous sedimentary troughs (Fig. 3-3).

The crystalline basement is composed of polymetamorphosed, pre-Variscan sedimentary rocks and intrusive granites preserved as orthogneisses (Thury et al. 1994). Variscan metamorphism was accompanied by anatexis and intrusion of granite bodies and numerous dykes. Crystalline rocks from the Black Forest outcrops as well as from boreholes in Northern Switzerland show evidence for substantial post-metamorphic deformation and polycyclic hydrothermal alteration (Mazurek & Peters 1992).

The Variscan orogeny overprints the crystalline basement and was the result of the Late Paleozoic collision of Gondwana in the south and Laurussia in the north (Lorenz & Nicholls 1984, Stampfli & Borel 2002, Raumer et al. 2009). The main shortening phase of the Variscan orogeny occurred during the Carboniferous by strike-slip-dominated deformation, which produced NNE-SSW-trending faults (Rhenish orientation; Thury et al. 1994, Schori 2021). In addition, NW-SE-trending dextral shear zones formed (Hercynian orientation; e.g. Schori 2021 and references therein). Inherited NW-SE-trending faults also acted as zones of weakness during the later (i.e. Middle Miocene) subsidence of the Hegau – Bodensee Graben (e.g. Egli et al. 2017).

During into two phases. An initial strike-slip-dominated phase occurred after the Late Carboniferous and Early Permian, post-Variscan orogenic collapse gave rise to wrench tectonics and the formation of the Permo-Carboniferous Konstanz – Frick Trough in Northern Switzerland (Fig. 3-4, Fig. 3-6a; Diebold et al. 1991, Marchant et al. 2005, Naef & Madritsch 2014, Schori 2021). The kinematic evolution of the trough can be subdivided 334 Ma, recorded for instance by the offset of the Albtal granite (Madritsch et al. 2018). This was followed by a main subsidence phase with normal faulting localised along inherited structures (e.g. Vorwald Fault). With the formation of ENE-WSW-trending faults (i.e. Erzgebirgian trend) related to the graben formation, three fault orientations occur within the Paleozoic basement of Northern Switzerland and acted as zones of weakness localising future deformation (NW-SE-trending Hercynian, ENE-WSW-trending Erzgebirgian, NNW-SSE-trending Rhenish).

The central Konstanz – Frick Trough preserves a sedimentary succession reaching up to several km in thickness (Fig. 3-2; Naef & Madritsch 2014, Madritsch et al. 2018), but significantly thinner on its shoulders. Based on boreholes drilled between the Upper Rhine Graben and the Bodensee area, a multiphase depositional history can be outlined. However, the detailed sedimentary succession remains poorly defined and is laterally variable. Volcanic activity also occurred during Permo-Carboniferous times, resulting in deposition of tuffites (Matter et al. 1988). Based mainly on the findings in the Weiach (WEI) borehole, three depositional phases were differentiated in the sedimentary succession (Matter et al. 1987, 1988, Diebold 1988, Madritsch et al. 2013):

- Late Carboniferous times saw varying humid tropical conditions and deposition from anastomosing fluvial systems on externally drained fan complexes in the Konstanz – Frick Trough («Pre-Weitenau Formation deposits»). Fine- to coarse-grained sediments were deposited in fluvial channels, overbanks and floodplains. Organic-rich sediments were deposited in mires or shallow bog lakes on floodplains (later transformed into a few coal beds).
- Late Carboniferous to Early Permian deposition («Pre-Weitenau Formation deposits») was characterised by anastomosing fluvial and lacustrine systems in a varying humid climate. Towards the end of this period, the relief surrounding the Konstanz – Frick Trough was generally flattened, leading to reduced sediment input.

- During the Early to Middle Permian (Weitenau Formation; Fig. 3-5a), the relief and erosion at the margin of the Konstanz – Frick Trough increased (Fig. 3-6a) and vast alluvial plains developed with the deposition of locally reddish siltstone, fine- to coarse-grained sandstone and fanglomeratic breccias in an arid climate. Towards the end of the Permian, the landscape was generally flattened, forming a peneplain.

3.3 Mesozoic

3.3.1 Triassic

At the beginning of the Triassic Period, the relief formed during the Variscan orogeny was mostly eroded to form a peneplain. At that time, Northern Switzerland was part of the Central European Basin, separated from the Neotethys by the Vindelician – Bohemian Massif and the Alemannic Land (Fig. 3-5b). Possible synsedimentary tectonics related to rifting are inferred to have given rise to variations in sediment thickness, observed along the bounding faults of the Konstanz – Frick Trough (Birkhäuser et al. 2001, Diebold et al. 1991, Pietsch et al. 2023).

During the Early to Middle Triassic, terrestrial and subordinately coastal sediments were deposited in an extensive intracontinental basin (Buntsandstein Group, Dinkelberg Formation). Fluvial systems sourced mostly from the west deposited a succession of fine- to coarse-grained sandstone and some clay-mineral-rich beds (Wurster 1968). Several phases of fluvial accumulation were followed by phases of pedogenesis.

The overlying Middle Triassic succession (Muschelkalk Group) preserves 3 depositional phases:

- The first phase (Lower Muschelkalk Group, Kaiseraugst Formation) was deposited during a period of marine transgression. At this time, a succession of silt- and sandstone with wave ripples, crossbedding and bioclastic calcareous beds were deposited in sublittoral and beach settings, passing up into a shallow marine environment. These are overlain by silty claystone and argillaceous marl with silty to fine sandy and bioclastic beds which were deposited during a period of intermittent sea-level rise. These are, in turn, overlain by dolomitic marl, evaporitic beds and some sandy and calcareous beds which were deposited in an intertidal to lagoonal environment recording a subsequent regression.
- These are overlain by a second depositional phase (Middle Muschelkalk Group, Zeglingen Formation) recording a period of significant regression and emergence (Dronkert et al. 1990, Pietsch et al. 2023). Deposition took place in lagoons, ephemeral ponds, salina and intertidal to supratidal areas attesting to arid conditions and records a number of shallowing-upward sedimentary cycles (Pietsch et al. 2023). These cycles comprise successions of dolostone, marl, claystone, anhydrite and partly halite. Some of the halite was subsequently dissolved syn- to mesogenetically during the Middle Triassic, leading to the formation of dissolution breccias.
- The third phase of Middle Triassic deposition (Upper Muschelkalk Group, Schinznach Formation) records two subsequent marine transgressions and regressions (Pietsch et al. 2016, Adams & Diamond 2019). At this time, a temporarily open marine seaway was established, connecting the Central European Basin with the Neotethys. Deposition of micrite with scattered, locally oolitic, bioclastic beds took place in a shallow marine environment during a transgression and regression. During later diagenesis, the sediments were partially or completely dolomitised and, in bioclastic or oolitic beds, some open porosity developed (Stamberg Member). This phase ends with the deposition of fossiliferous claystone and dolostone in a littoral, deltaic to brackish environment during a subsequent transgression and start of a regression.

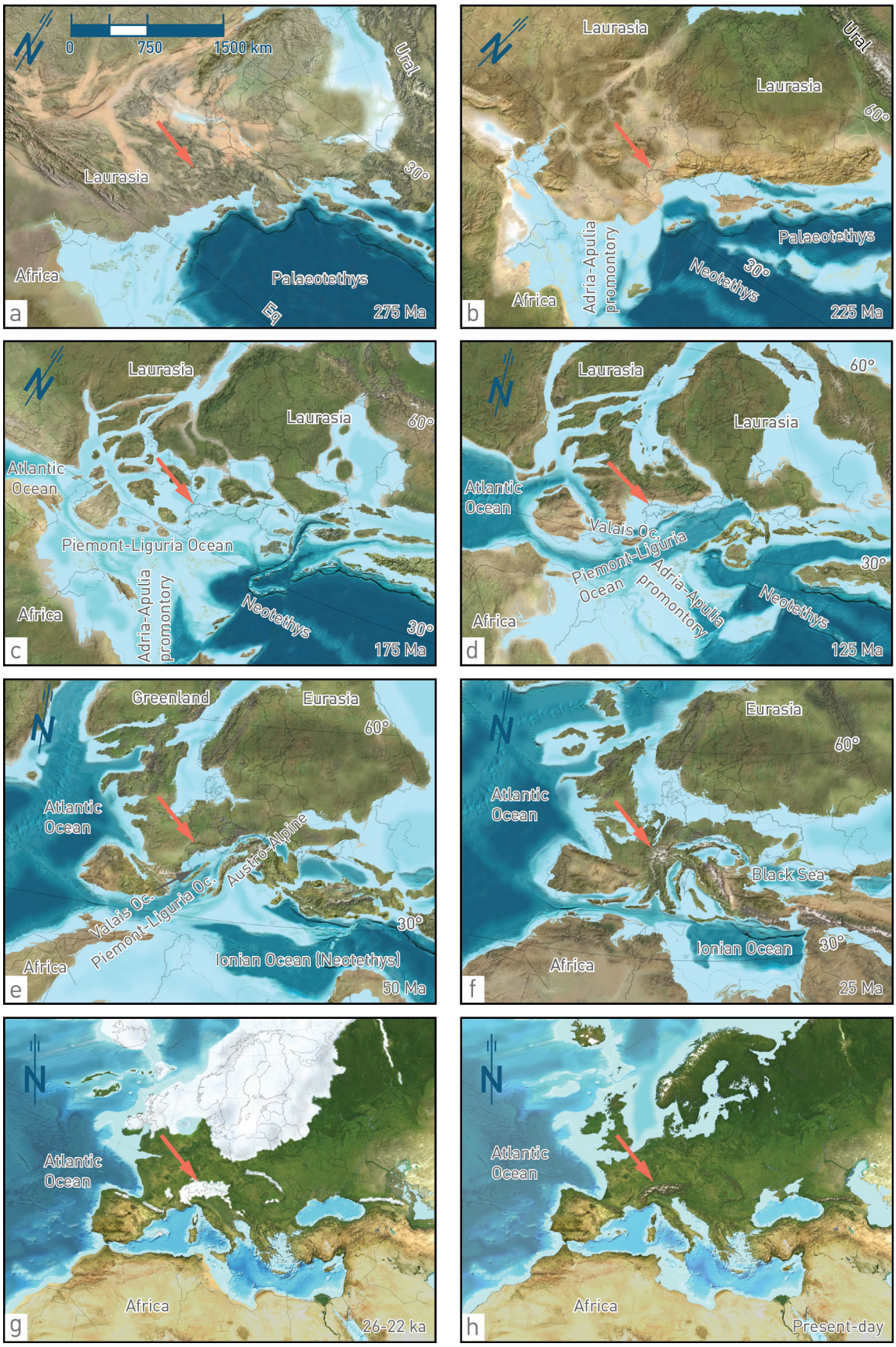

0
750
1500 km
Ural
Laurasia
30°
Africa
Palaeotethys
Eq
275 Ma
a
Laurasia
Ural
Laurasia
60°
Palaeotethys
Adria-Apulia promontory
30°
Neotethys
Africa
225 Ma
b
Laurasia
Laurasia
60°
Atlantic Ocean
Piemont-Liguria Ocean
Adria-Apulia promontory
Africa
Neotethys
30°
175 Ma
c
Laurasia
Laurasia
60°
Atlantic Ocean
Valais Oc.
Piemont-Liguria Ocean
Adria-Apulia promontory
30°
Africa
Neotethys
125 Ma
d
Greenland
Eurasia
60°
Atlantic Ocean
Austro-Alpine
Valais Oc.
Piemont-Liguria Oc.
30°
Africa
Ionian Ocean (Neotethys)
50 Ma
e
Eurasia
60°
Atlantic Ocean
Black Sea
Ionian Ocean
30°
Africa
25 Ma
f
Atlantic Ocean
Africa
26-22 ka
g
Atlantic Ocean
Africa
Present-day
h

Fig. 3-5: Palaeogeographic reconstruction showing Switzerland in the larger context

Modified after Palaeogeography of Europe ©2012 Colorado Plateau Geosystems Inc. The sediments of the following lithostratigraphic units were deposited during the presented time periods in Northern Switzerland: (a) Weitenau Formation, (b) Klettgau Formation, (c) Staffelegg Formation, (d) no sedimentary rocks preserved, (e) Siderolithic Group, (f) Lower Freshwater Molasse Group (USM), (g) Niederterrasse and (h) recent sediments.

Red arrows indicate the approximate location of Northern Switzerland. Eq: Equator; Oc.: Ocean.

Deposition at the southern extension of the Central European Basin during the Middle to Late Triassic (Keuper Group, Bänkerjoch Formation) took place during continued regression. At this time, terrestrial sediments were deposited in sabkha plains and comprised partly cyclic successions of chicken-wire anhydrite overlain by dolomitic claystone with thin anhydritic layers, in turn succeeded by claystone (Dronkert et al. 1990). The basin was influenced by sporadic marine incursions and deposition of dolomitic and sandy interlayers.

The Late Triassic succession (Keuper Group, Klettgau Formation; Fig. 3-5b) was deposited in a largely terrestrial environment. As a result, sedimentary facies and thicknesses are highly variable, which is reflected in the heterogeneous Keuper aquifer in the three siting regions (Fig. 3-3). Siliciclastic sediments were transported by rivers from the southern Norwegian Caledonides (Paul et al. 2008) and later from the Vindelician – Bohemian Massif and deposited on a continental playa under (semi)arid conditions (Fig. 3-7; Jordan et al. 2016b). Deposits include sandstone-dominated fluvial channels and dolomitic marl-dominated floodplains, sometimes with pedogenic overprint. In the area of today's Zürich Nordost (ZNO) siting region, porous dolomitic breccias were also deposited on the continental playa. Additionally, an intermediate marine transgression, from the southwest (Burgundy Gate) resulted in deposition of partly porous and bioclastic dolostone in the Jura Ost (JO) and Nördlich Lägern (NL) siting regions, and anhydrite in a shallow marine to coastal environment in ZNO. The youngest Triassic succession was also affected by two major erosional events, the Old Cimmerian and the Base Jurassic unconformities. As a result of the latter, Rhaetian sediments are completely absent over large areas.

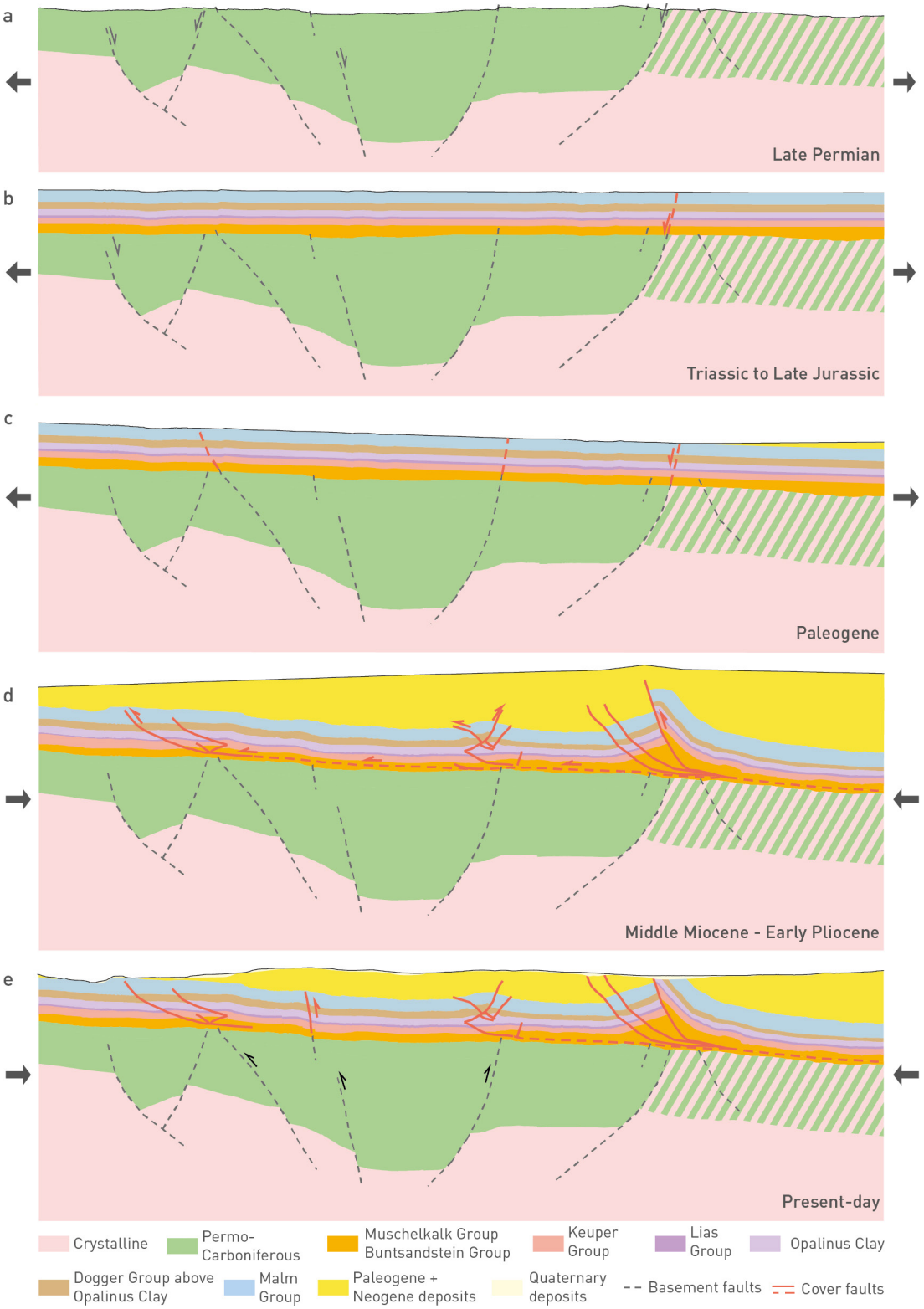


Fig. 3-6: Geological evolution of the study area demonstrated on a schematic NNW-SSE cross-section

Black arrows are tentative indications for whether the time step was extension- or contraction-dominated. Green hatched zone reflects zone with Permo-Carboniferous or crystalline rocks.

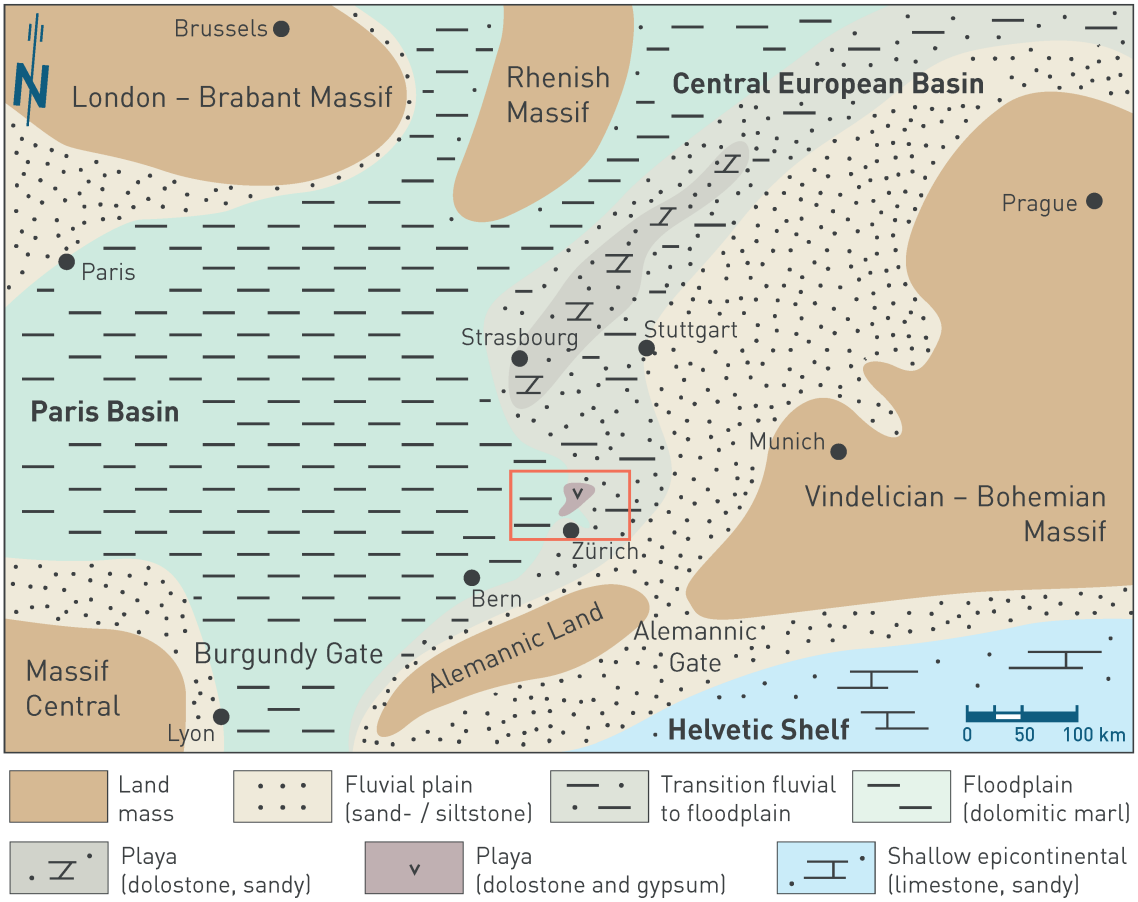


Fig. 3-7: Palaeogeographic situation of Western to Central Europe in the Norian during the sedimentation of the Klettgau Formation (Seebi Member) and its time equivalents

The red rectangle shows the extent of the detailed palaeoenvironment maps (Section 4.2). Maps based on Geyer et al. (2023), Hagdorn & Nitsch (2009) and Pozsgai et al. (2017). The north arrow refers to present-day geographic north. The approximate locations of the cities are shown to simplify orientation.

3.3.2 Jurassic

3.3.2.1 Early Jurassic

The Jurassic Period was affected by the opening of the Atlantic Ocean and the associated development of the Piemont – Liguria Ocean (Schmid et al. 1996, Handy et al. 2010, Winkler 2024; Fig. 3-5c). Associated extension gave rise to multiple pulses of increased heat flow that affected the burial history in Northern Switzerland (e.g. Mazurek et al. 2006). Peak Early Cretaceous burial temperatures are recorded in the Early Jurassic units.

During the Early Jurassic, Northern Switzerland continued to be in a shallow, subtropical to tropical epicontinental sea. It was bordered to the east and south by the Vindelician Land and its promontory, the Alemannic Land, in the area of the present-day External Crystalline Massifs. The Early Jurassic succession (Lias Group, Staffelegg Formation) is characterised by a condensed succession of calcareous hardgrounds with phosphatic and reworked nodules, and iron-oolites,

with common reworking and multiple hiatuses (Reisdorf et al. 2011). In addition, there are phases with expanded deposition recorded by units of siltstone and partly organic-rich claystone. In Northern Switzerland, the different stratigraphic intervals can be well correlated.

3.3.2.2 Middle Jurassic

During the Middle Jurassic, Europe was characterised by continued N-S-directed extension during the continued opening of the Piemont – Liguria Ocean. This was accompanied by development of a number of sedimentary basins preserving siliciclastic infill from surrounding landmasses and calcareous sediments from carbonate platforms (Dogger Group). Bottom currents played an important role in both transport and accumulation of these sediments.

The lower division of the Middle Jurassic succession comprises the Opalinus Clay. This was deposited in the shallow epicontinental sea located between the Vindelician – Bohemian Massif in the east, the Alemannic Land to the south and the very shallow area in Burgundy to the west (Fig. 3-8). Within the shallow epicontinental sea deeper areas are referred as "shallow mid epicontinental". The accommodation space needed to deposit the compacted ca. 100 m thick unit of Opalinus Clay in relatively shallow water – especially considering uncompacted sediment thicknesses – was provided by regional subsidence (Wetzel & Allia 2003). High siliciclastic input from the Alemannic Land, the Vindelician – Bohemian Massif or landmasses even further to the northeast led to deposition of mostly claystone with varying contents of silt and fine sand over the entire Northern Switzerland (Lauper et al. 2021b, Zimmerli et al. 2024). This environment resulted in the deposition of the relatively homogeneous facies of the Opalinus Clay with little lateral variability compared with other Mesozoic formations of Northern Switzerland. Within the Opalinus Clay, a shallowing-upward trend, with increased silt and fine sand contents towards the top, is thought to reflect an overall regression (Zimmerli et al. 2024). Towards the top of the formation, reduced sedimentation is recorded by calcareous, partly iron-rich beds intercalated in claystone, which can be correlated on a local to regional scale (Wohlwend et al. 2024).

The overlying succession, Dogger Group above Opalinus Clay, preserves more lateral variability and complexity. A first phase of deposition largely comprises siltstone, claystone and argillaceous marl (Passwang Formation and its time equivalents in the east). However, local metre-scale beds or bedded intervals of sandy, bioclastic and biomicritic limestone were also deposited. Additionally, during episodes of reduced deposition, iron-rich, decimetre- to metre-scale beds, including iron-oolites were deposited. These sediments locally preserve cycles of claystone overlain by sandy and/or bioclastic marl, limestone and, finally, iron-oolitic beds. These cycles may represent shallowing-upward trends related to sea-level variations (Burkhalter 1996) and/or climate variability. The preservation of cycles is laterally highly variable, thought to be in response to local variations in bathymetry with local swells and depressions in combination with sediment transport by bottom currents. Such bottom currents may have locally (i.e. at the present location of NL) deposited a several-km-scale, clay-mineral-rich sediment drift. On top of this positive relief, an isolated carbonate platform consisting of mostly coral and bioclastic limestone developed («Herrenwis Unit»; Ruchat et al. 2024).

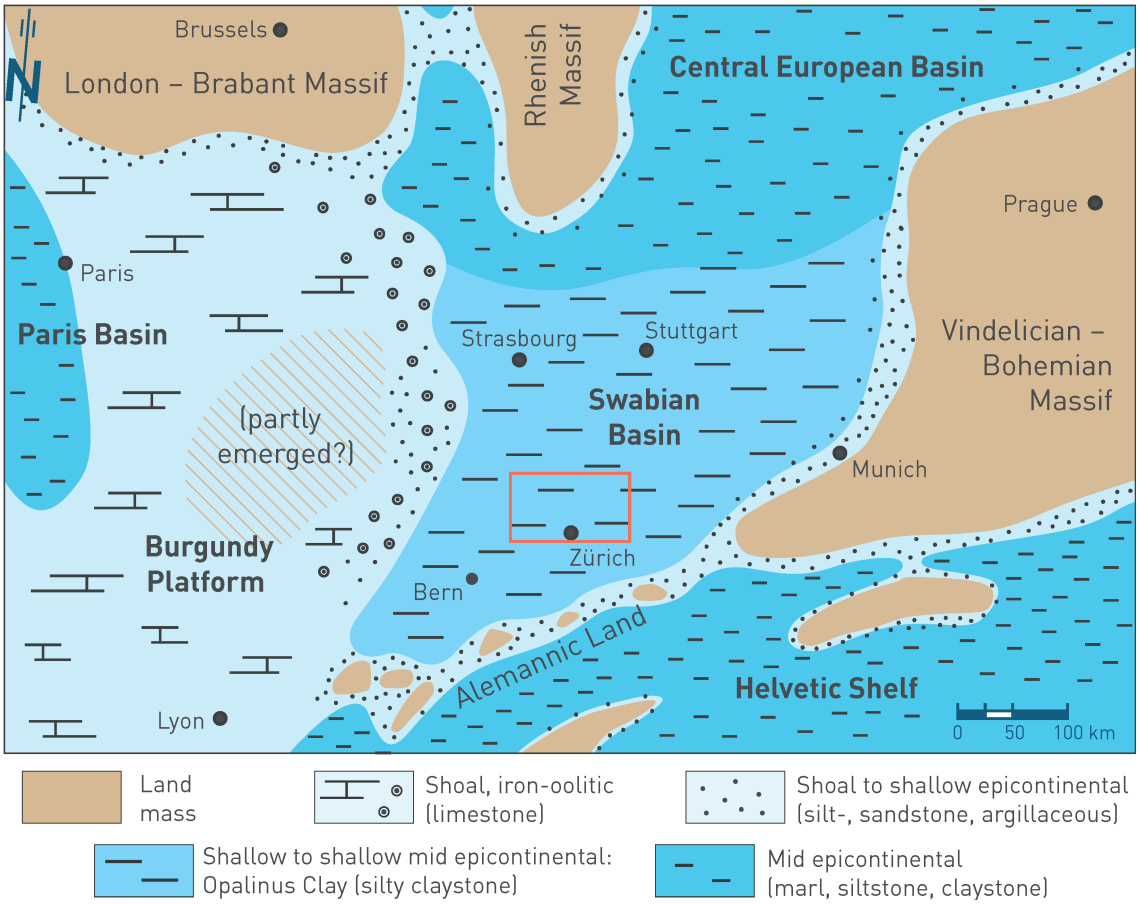


Fig. 3-8: Palaeogeographic situation of Western to Central Europe in the Aalenian during the sedimentation of the Opalinus Clay and its time equivalents

The red rectangle shows the extent of the detailed palaeoenvironment maps (Section 4.2). Map based on Etter (1990) and Lauper et al. (2021a). The north arrow refers to present-day geographic north. The approximate locations of the cities are shown to simplify orientation.

In a second phase of deposition, the Celtic Platform extended into Northern Switzerland and oolitic and bioclastic limestone interbedded with some more marly interlayers (Hauptrogenstein) (Fig. 3-9) were deposited in a shallow marine environment. Towards the Swabian Basin in the east calcareous marl with interfingering oolitic limestone prevailed (Klingnau Formation) while argillaceous marl, siltstone and claystone dominated further offshore («Parkinsoni-Württembergica-Schichten»). In NL, these sediments, probably in the form of sediment drifts, filled the basin and finally also covered the isolated carbonate platform, so that the «Herrenwis Unit» is embedded in clay-mineral-rich sedimentary rocks. The third phase of deposition is again characterised by a condensed succession of often fossiliferous, iron-oolitic marl and limestone (mostly Ifenthal and Wutach Formations; Bitterli-Dreher 2012, Bläsi et al. 2013).

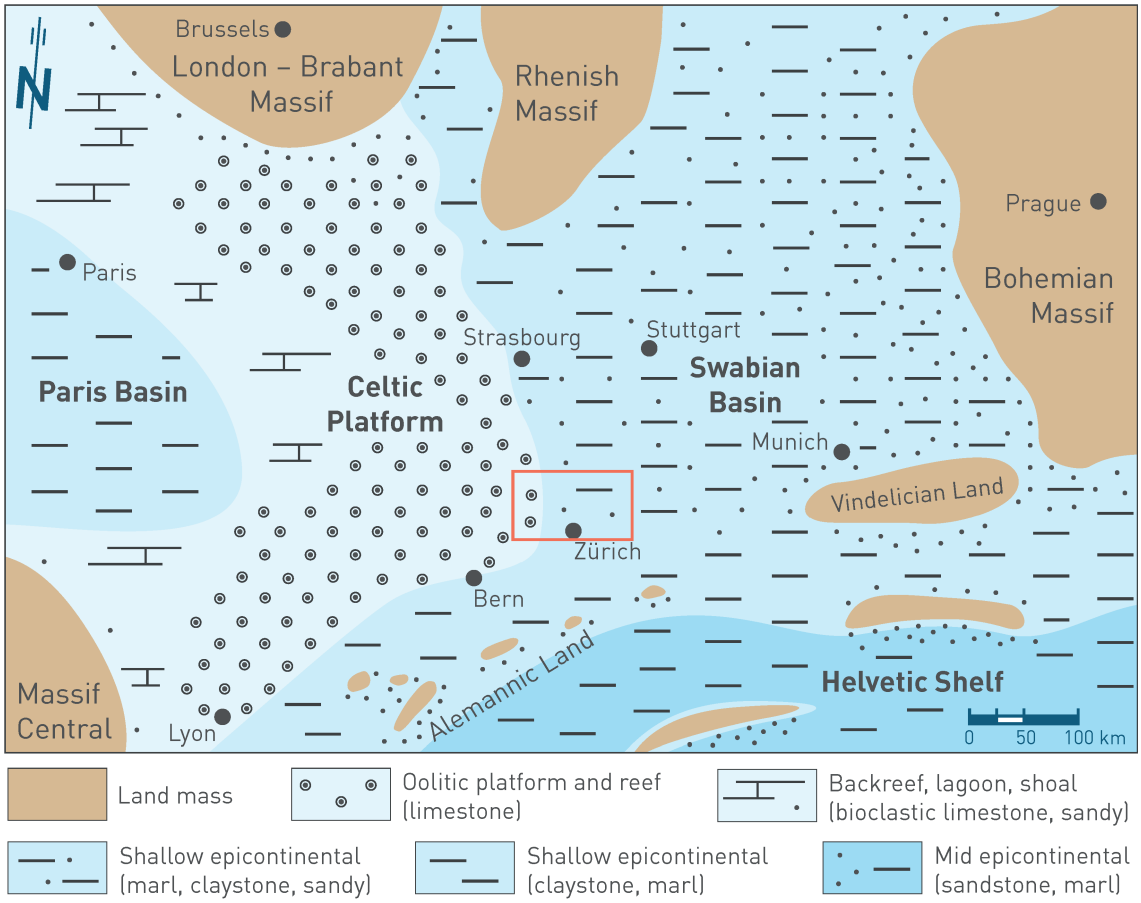


Fig. 3-9: Palaeogeographic situation of Western to Central Europe in the Bajocian during the sedimentation of the Hauptrogenstein and «Parkinsoni-Württembergica-Schichten» and their time equivalents

The red rectangle shows the extent of the detailed palaeoenvironment maps (Section 4.2). Map based on Barron et al. (2012), Correia (2018), Geyer et al. (2023), Gonzalez & Wetzel (1996), Krakow & Schunke (2017), Munier et al. (2021) and Védrine & Strasser (2009). The north arrow refers to present-day geographic north. The approximate locations of the cities are shown to simplify orientation.

3.3.2.3 Late Jurassic

During Late Jurassic times (Malm Group), the Swabian Basin including Northern Switzerland formed part of a shallow epicontinental sea (Fig. 3-10). The nearest landmasses were the London – Brabant, Rhenish and Bohemian Massifs in the north and east. To the south, the shelf sea merged into the Piemont – Liguria Ocean (Geyer et al. 2023). Overall, the Late Jurassic formations show considerably less lateral variability than the underlying succession (Dogger Group above Opalinus Clay).

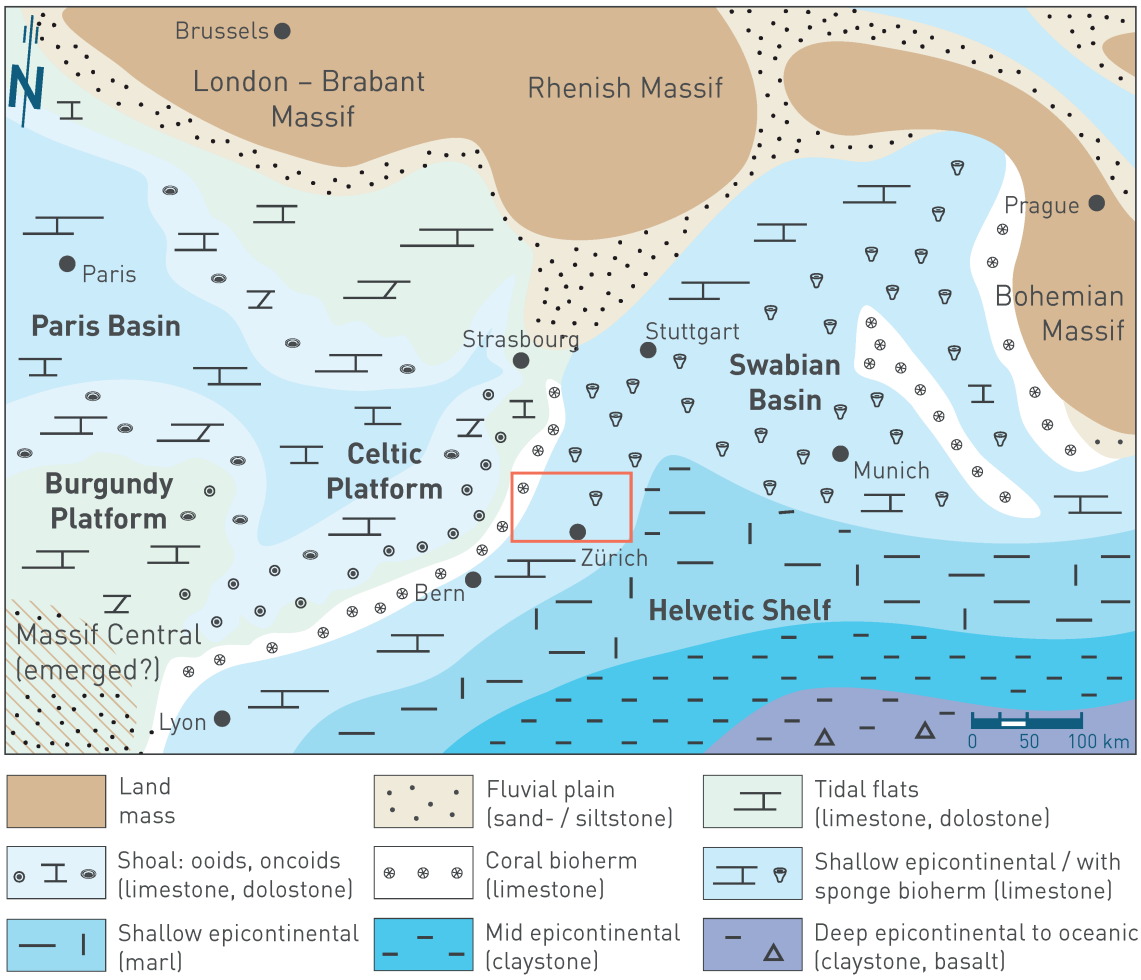


Fig. 3-10: Palaeogeographic situation of Western to Central Europe in the Kimmeridgian during the sedimentation of the Burghorn Formation, «Felsenkalke» and «Massenkalk» and their time equivalents

The red rectangle shows the extent of the detailed palaeoenvironment maps (Section 4.2). Map based on Diedrich (2011), Geyer et al. (2023), Gouffon (2024), Gygi (2012), Jank et al. (2006), Koppka (2015), Krakow & Schunke (2017), Marty et al. (2007), Meyer & Schmidt-Kaler (1996), Püntener et al. (2015), Rauhut et al. (2017) and Schmid et al. (2005). The north arrow refers to present-day geographic north. The approximate locations of the cities are shown to simplify orientation.

Late Jurassic deposition started with a phase of reduced sedimentation that was followed by deposition in a more basinal setting or carbonate ramp (Swabian facies realm) adjacent to a carbonate platform located farther to the northwest (Celtic facies realm). The sedimentary rocks are dominated by calcareous marl and limestone, where regular interlayering is thought to reflect variations in climate and sea level (Wildegg Formation). In Northern Switzerland, the depositional centre was situated in the west, and sediment thicknesses decreased considerably towards the east. The region with the thickest sediment successions might reflect highest differential subsidence and/or highest accumulation by bottom currents (Allenbach 2002). Subsequently, predominantly micritic limestone (Villigen Formation, «Felsenkalke») with local bioherms (sponge reefs, «Massenkalk»), intercalated with more marly sediments (Schwarzbach Formation), were

deposited in the shallow Swabian Basin. The youngest preserved Mesozoic sedimentary rocks in Northern Switzerland are of Kimmeridgian age; younger Mesozoic sedimentary rocks were eroded (Fig. 3-4, Fig. 3-6b, Section 3.3.3; Gygi 2012).

3.3.3 Cretaceous

Cretaceous deposits in Northern Switzerland are either eroded or have not been deposited. However, Cretaceous times saw the development of the Alps. The Alps can be subdivided into two domains. The Eastern Alps and the Western Alps. The Eastern Alps are the result of two orogenies (Eo-Alpine and Alpine) and the Western Alps only of the Alpine orogeny. The Alps evolved in response to collision of the Adriatic promontory of the African plate with the European continent. Collision involved the decoupling of the subducting European slab from the Alpine nappe stack and tectonic underplating / accretion of the European upper crust to the Alpine wedge (Schmid et al. 1996, Escher et al. 1997, Schmid et al. 2004, Schlunegger & Mosar 2011). N- to NNE-directed convergence of the Adriatic plate started during the Cretaceous, leading to the progressive closure of the Piemont – Liguria and Valais Oceans (Stampfli et al. 1998).

3.4 Paleogene and Neogene

3.4.1 Paleocene

The main phase of the Alpine orogeny occurred during the Paleogene and Neogene (e.g. Schmid et al. 2004. Paleocene times saw continued closure of the Piemont – Liguria and Valais Oceans as well as troughs such as for instance the Cormoz High, a NNE-SSW-trending Paleozoic line in the Bresse Graben (Schori 2021).

3.4.2 Eocene

In the Central Alps, emplacement of the Penninic nappes occurred in the Early Eocene, whereas the Helvetic domain was affected by N- to NNE-directed thrusting from the Late Eocene onwards (Pfiffner 2009). In the Late Eocene to Early Oligocene, the opening of the Upper Rhine Graben, part of the European Cenozoic Rift System (ECRIS), was accompanied by subsidence and associated with uplift of the graben shoulders (Rotstein & Schaming 2011). This extensional system extended from the Bohemian Massif to the Mediterranean Sea (Bourgeois et al. 2007). The development of the Upper Rhine Graben can be subdivided into an early extensional phase which was followed by a transtensional phase. The transtensional phase is characterised by a NW-SE-oriented maximum horizontal stress axis and is thus comparable to the present day. The closure of the Piemont – Liguria and Valais Oceans that initiated in the Late Cretaceous was completed in the Eocene, marking the onset of continental collision (Handy et al. 2010). Lithospheric folding resulting from the continental collision is proposed to result in surface uplift of the North Alpine Foreland (Fig. 3-4; Dèzes et al. 2004, Bourgeois et al. 2007).

During the Eocene (Fig. 3-5e), a humid and warm (sub-) tropical climate formed an extensive karst landscape on the exposed Mesozoic bedrock. The residual material of the strong chemical weathering, consisting of mostly clay minerals, quartz sand, and ironhydroxide pisoids, was accumulated in palaeokarst depressions and infills (Siderolithic Group). The surface topography was probably hills and valleys partly covered by tropical forest with a species-rich fauna including primates and crocodiles (Rosselet 1991).

The change to erosive conditions between the Late Cretaceous and Early Eocene preluded a ca. 50-Myr-long period of recharge of meteoric waters in Northern Switzerland. This caused karstification extending several decametres into the Malm Group (filled palaeokarst). Over the long timescale, the freshwater conditions in the Malm aquifer caused an overprinting of the initial marine porewaters in the Opalinus Clay and the confining units (Section 4.6.5).

3.4.3 Oligocene

The Oligocene represents the time of major deformation in the Helvetic domain of the Central Alps with the emplacement of the Helvetic nappes (Pfiffner 2009). The development of the Alpine Foreland basin can be explained by flexural bending of an elastic lithospheric plate as a response to crustal loading resulting from internal build-up of the Alps (e.g. Willett & Schlunegger 2010) or slab roll-back and associated buoyancy-driven uplift (Schlunegger & Kissling 2015).

During the Early Oligocene, Northern Switzerland was still characterised by a karst landscape. Locally, nodular and crustal limestone formed under arid to semiarid conditions («Ältere Krustenkalke»; Hofmann et al. 2000). At this time, the emerging Alps led to an increased sediment supply and deposition in the northern Alpine foredeep, firstly as deep marine North-Helvetic Flysch Group and then as shallow marine to littoral sediments of the Lower Marine Molasse Group (UMM; e.g. Kuhlemann & Kempf 2002).

During the Late Oligocene (Fig. 3-5f), the increasing crustal loading or slab dynamics resulted in foredeep migration and migration of Molasse deposition from southeast to northwest (Allen et al. 1991, Sinclair & Allen 1992, Kuhlemann & Kempf 2002, Ford et al. 2006, Schlunegger & Kissling 2015). The adjacent forebulge also migrated northwards and was associated with erosion and normal faulting (e.g. Laubscher 1985, Jordan et al. 2015).

The former marine Alpine Foreland basin was progressively infilled, passing into terrestrial fluvial systems. The Lower Freshwater Molasse Group (USM) was deposited on large debris fan systems, which drained towards northeast to east. Deposition from Alpine River systems migrated over time towards the northwest. In a NNW-SSE cross-section, a wedge-shaped sedimentary body developed with coarse clastic debris fan series with conglomerates («Nagelfluh») in the near-Alpine, proximal area and silty-sandy-marly sediments of rivers and floodplains in the distal area (Schlunegger et al. 1997). No deposits of USM occur in the JO siting region (eroded or not deposited), except for the southeastern-most part near Villnachern. USM is preserved in distal facies in the NL and ZNO siting regions.

3.4.4 Miocene

Continued uplift of the Upper Rhine Graben rift shoulders (i.e. Black Forest and Vosges Massifs) in the Miocene caused local extensional reactivation of inherited structures. Furthermore, it resulted in tilting of the pre-Mesozoic basement towards the south, which was further enhanced by the flexural lithospheric bending and folding (e.g. Laubscher 1992, Dèzes et al. 2004, Berger et al. 2005). As a consequence, the Mesozoic sedimentary cover of the Black Forest area was emergent and eroding. The eroded material was deposited in conglomeratic units containing Mesozoic detritus in parts of Northern Switzerland and adjacent Germany (Jura Nagelfluh). As a result of the uplift and erosion in the Black Forest area, meteoric waters could directly infiltrate into increasingly deep aquifers.

At the beginning of the Miocene, deposition of USM continued with interruptions. In Northern Switzerland, USM, dominated by Alpine material, is found up to a line from Brugg via Schaffhausen into the Hegau (Fig. 3-2), where it partly interfingers with conglomerates of the Malm Group limestone from the Black Forest area («Ältere Juranagelfluh»).

In the Early Miocene (since ca. 21 Ma), subsidence led to transgression of the sea from the Rhone Valley. Eventually, it formed the narrow, around 100-km-wide Burdigalian seaway connecting the Mediterranean in the southwest (Lyon) with the Paratethys in the northeast (Vienna). The Upper Marine Molasse Group (OMM) was deposited in a shallow marine coastal environment. It comprises glauconitic sandstone and marl with scattered units of fossiliferous conglomerate («Quarzit Nagelfluh», «Austernnagelfluh»), some containing pebbles of Jurassic origin («Mittlere Juranagelfluh»; Jost et al. 2016). The OMM is characterised by facies changes over small distances and several erosional unconformities. In the latest Early Miocene (after ca. 17 Ma), the sea had largely retreated, and a river system formed running SW across the Hegau and Schaffhausen (Fig. 3-2). This locally incised up to 100 m deep into the older Molasse deposits. At this time, extensive quartz-rich sandstone was deposited in the so-called "Graupensandrinne" in a brackish depositional environment (Bolliger 1999). Overall, the OMM is commonly missing in the JO siting region, presumably because this area was located outside or near the northern coastline of OMM and affected by later erosion. Relicts of OMM can also be found in the eastern part of JO (Diebold et al. 2006).

The marine to brackish conditions during the Upper Marine Molasse Group (OMM) deposition were the latest marine phase in Northern Switzerland. Remnants of these marine waters can be sampled in deep boreholes from the Molasse (OMM, USM) and from the Malm aquifer (Section 4.5.5.2). Additionally, calcite veins in the Upper Jurassic Effingen Member in the Oftringen (OFT) borehole are related to the infiltration of OMM groundwater (de Haller et al. 2011, Mazurek et al. 2018).

From the beginning of the Middle Miocene, continental conditions prevailed again throughout the Alpine Foreland in Northern Switzerland and the terrestrial deposits of the Upper Freshwater Molasse Group (OSM) were deposited. Large debris fans built up at the Alpine front, flowing N and NW into a broad southwest-flowing stream system, the "Glimmersandrinne" (Zaugg & Vogel 2014). The NL and ZNO siting regions are situated in a distal setting of these debris fans ("Hörnli-Schuttfächer"), which are dominated by marl, silt- and sandstone. In JO, fluvial conglomeratic layers («Jüngere Juranagelfluh») with pebbles of Malm and Dogger Groups from the southern Black Forest were also deposited. These are intercalated with marly, silty and sandy sedimentary rocks (Diebold et al. 2006).

Activity of the Hegau – Bodensee Graben located northeast of the study area is dated to Early to Middle Miocene based on correlation of OMM sedimentary rocks across the Randen Fault (Schreiner 1992, Hofmann et al. 2000, Egli et al. 2017, Ibele 2015). The main tectonic activity in the Hegau – Bodensee Graben occurred between the Late Miocene and the Pliocene in a transtensional manner (e.g. Ibele 2015, Egli et al. 2017). Volcanic activity dated to 19 to 6.9 Ma accompanied the early extension-dominated phase of the Hegau – Bodensee Graben (Ibele 2015 and references therein).

Early to Middle Miocene (20 to 13 Ma) thrusting of the External Crystalline Massifs over the sedimentary cover resulted in their exhumation (Herwegh et al. 2017, 2020). It is a likely cause for the NW propagation of the Alpine thrust front along the Triassic evaporites, which are generally considered as décollement horizons (Fig. 3-6d; Marro et al. 2023, Burkhard 1990, Sommaruga et al. 2017, Jordan & Nüesch 1989). The front of the detached Mesozoic strata strikes north of the JO and NL siting regions and runs through the southern part of ZNO. Thermochronological data from the Schafisheim (SHA) borehole located south of the Jura Main Thrust show that tectonic activity along the basal décollement is constrained to have started during the Middle Miocene (Fig. 3-6d; 14.3 Ma; Looser et al. 2021). Similar age ranges were documented for the western Jura (Smeraglia et al. 2021). No evidence for shortening related to the Alps in the distal foreland is known east of Zürich; the shortening was most probably accommodated within the Subalpine Molasse (Burkhard 1990, von Hagke et al. 2012, Ortner et al. 2024).

The combination of age dating and 2D geometric balancing of selected cross-sections indicated maximum shortening rates during the main thin-skinned Jura Fold-and-Thrust Belt formation of around 0.5 mm/yr (for the time period 14.3 to 4.5 Ma, i.e. linked to the décollement activity in the SHA borehole) for the western part of JO (Jordan et al. 2015, Madritsch et al. 2024).

The youngest preserved Molasse sedimentary rocks in Northern Switzerland are approximately 11.5 Ma old (Rahn & Selbekk 2007). However, sedimentation continued within the Swiss Molasse Basin that evolved from a flexural foreland basin to a wedge-top basin as a result of the formation of the Jura Fold-and-Thrust Belt (e.g. Cederbom et al. 2004, Schlunegger & Mosar 2011, Schlunegger & Kissling 2015, Willett & Schlunegger 2010). Deposition of the Cenozoic sedimentary rocks resulted in a second burial of the Mesozoic strata (Mazurek et al. 2006), whereby maximum temperatures decreased with increasing distance from the Alpine front, reflecting the wedge geometry of the Molasse deposits. For the distal margin of the Molasse, thermal history modelling based on vitrinite reflectance and thermochronological data suggests that, before the onset of Miocene erosion, the Molasse thickness in the Weiach – Benken area was approximately 1 km greater than today (e.g. Mazurek et al. 2006).

3.4.5 Pliocene

The main phase of thin-skinned deformation within the Jura Fold-and-Thrust Belt is thought to extend from the Middle Miocene until the Early Pliocene (Fig. 3-6d; e.g. Becker 2000, Schlunegger & Mosar 2011, Mosar 1999). Undeformed infilled karst features in folded Malm limestones of the Vue-des-Alpes Anticline (located in the Central Jura Fold-and-Thrust Belt, i.e. west of the study area) were dated from 4.2 to around 3 Ma and thus locally represent the end of the main deformation phase in the Internal Jura (Bolliger et al. 1993, Steininger et al. 1996). Nonetheless, several studies examining the front of the Jura Fold-and-Thrust Belt have identified evidence of moderate post-Pliocene tectonic thick-skinned (i.e. involving the substratum beneath the décollement horizon) activity (e.g. Giamboni et al. 2004, Madritsch et al. 2010). Geodynamic considerations support that the more recent deformation also affects the units below the décollement rather than being exclusively thin-skinned deformation (e.g. Mosar 1999; Fig. 3-6e). In fact, interpretations of seismic reflection data from west of Basel indicate a component of thick-skinned deformation starting from the Late Pliocene onwards (Ustaszewski & Schmid 2007, Madritsch et al. 2008). This inferred basement involvement is also observed in the latest 3D seismic reflection data obtained by Nagra (Section 4.3; Nagra 2024b).

From the latest Miocene into the Pliocene (ca. 7.3 – 4.2 Ma), the North Alpine Foreland drained towards the northeast to the Black Sea via the Aare-Danube River system (Fig. 3-11; Heuberger et al. 2014, Yanites et al. 2013, Ziegler & Fraefel 2009). This river system is documented by gravel relicts up to 270 m above the recent valley floor of the upper Danube River mostly between Blumberg and Ulm (Aare – Donau Höhenschotter; Villinger 2003). Later in the Pliocene (ca. 4.2 – 2.9 Ma), the Aare – Doubs System draining towards the Rhone and the Mediterranean Sea was established when the Aare-Danube River was captured by the proto-Doubs River in the region of Waldshut. This river reorganisation is potentially related to the sea-level drop in the Medi-terranean Sea during the Messinian salinity crisis resulting from isolation from the Atlantic Ocean (ca. 5.5 Ma; Krijgsman et al. 1999) and a successive backward incision of the palaeo-Rhone and Doubs systems. Alternatively, the headward erosion along the proto-Doubs River could have been caused by strong subsidence in the Bresse Graben (Schlunegger & Mosar 2011). Part of the eroded material was deposited west of Basel and is partially preserved in the form of the Sundgau Gravel (Liniger 1967) and its equivalents in the Forêt de Chaux (northeastern Bresse Graben; Petit et al. 1996).

Towards the end of the Pliocene at the transition to the Quaternary, the Aare – Rhine System, draining towards the North Sea, was established when the Aare-Doubs River was captured by the proto-Rhine River in the region north of Basel. This gave rise to the first deposition of Alpine sediments in the Upper and Lower Rhine Graben (ca. 2.8 – 2.6 Ma; Hagedorn & Boenigk 2008, Westerhoff et al. 2008). The timing and course of these river systems in the Pliocene are subject to larger uncertainty because of sparse sedimentological records and scarce chronological information.

The flow distance from the study area along the Danube towards the Black Sea is considerably larger compared to the flow distance of the Rhine River towards the North Sea. The modern Danube catchment is located more than 200 m higher compared to the Rhine catchment. This difference may have been even more pronounced in the past when the water divide was located farther to the west. For this reason, the change from the Danube to the Rhine system led to a significant baselevel fall and triggered a subsequent incision wave across the study area and the Central Swiss Molasse Basin (Schlunegger & Mosar 2011, Heuberger et al. 2014, Yanites et al. 2013).

The groundwater flow systems in the bedrock aquifers are influenced by the evolution of topography and of the river network. The Pliocene incision of the Rhine and Aare Rivers affected the regional discharge zones for the deep groundwaters of the Swiss Molasse Basin and of the sedimentary cover of the Black Forest (e.g. Waber & Traber 2022).

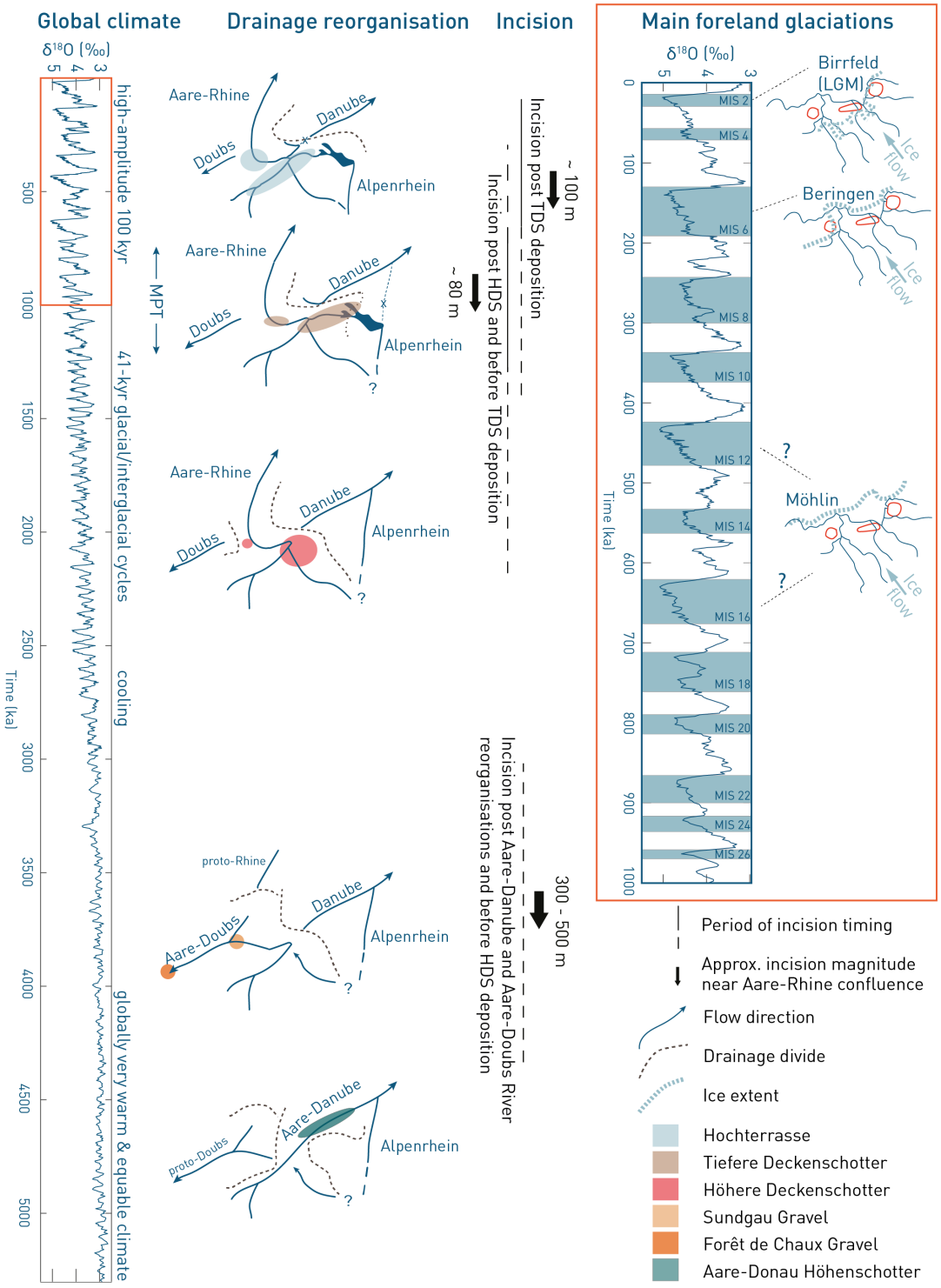


Fig. 3-11: Main landscape-forming events in Northern Switzerland during the past 5 Myr

Compilation shows global and regional events linked to the Pliocene-Quaternary landscape evolution in Northern Switzerland. $\delta^{18}O$ record with marine isotope stages (MIS) based on Lisiecki & Raymo (2005). Incision magnitudes of major drainage reorganisations are based on visual inspection of the Aare – Rhine confluence area based on Heuberger et al. (2014) and yield ~ 300 – 500 m for the Aare-Doubs incision, ~ 80 m between HDS (Höhere Deckenschotter) and TDS (Tiefere Deckenschotter) deposition and ~ 100 m after TDS deposition. Maps with ice extents show present-day river network for orientation.

3.5 Quaternary

The Quaternary landscape evolution is driven mostly by tectonics, climate, and river drainage reorganisations in Northern Switzerland (Nagra 2024k). The tectonic setting is determined by ongoing Alpine orogeny, transtensional deformation within the Upper Rhine Graben, tectonic activity of the Jura Fold-and-Thrust Belt and the Hegau – Bodensee Graben. The dominant Alpine-related uplift produced a general uplift gradient oriented perpendicularly to the Alpine front with rates that decline towards the NNW (Nagra 2024l).

The Quaternary climate is globally characterised by a series of glacial and interglacial periods. These glacial/interglacial cycles are mainly driven by oscillations in the Earth's orbit and axial tilt, which affect the distribution of solar radiation. Cooling and warming periods have been divided into marine isotope stages (MIS) based on isotope data derived from deep-sea core samples (Lisiecki & Raymo 2005). Alpine glaciers advanced and retreated dynamically in concert with the global climate cycles and largely depended on local Alpine temperature and humidity. During pronounced global glacial periods, the Alpine glaciers reached the Alpine Foreland (Fig. 3-5g, Fig. 3-11; Nagra 2024j). During the so-called Mid-Pleistocene Transition (ca. 1.25 – 0.7 Ma; Clark et al. 2006), the principal glacial/interglacial cycle changed from a dominant 41-kyr to a 100-kyr period (Fig. 3-11). The cause for this transition remains debated, potential candidates include ice-dynamic, oceanic and atmospheric feedbacks (Berends et al. 2021). Large glaciations have reached the foreland since the Early Pleistocene (Schlüchter et al. 2021) but probably had their largest erosion potential only within the last one million years, when cyclicity changed to a high-amplitude 100-kyr glacial/interglacial cycle (e.g. Preusser et al. 2011). At that time, glaciers eroded into the bedrock below the fluvial baselevel, creating major overdeepened valleys in the Swiss Plateau Molasse.

During the Quaternary, the Rhine River system evolved in several phases of drainage reorganisation that resulted in significant drops in the local baselevel (Fig. 3-11). The drainage divide between the Rhine and the Danube system continued to shift eastwards because of the headward erosion of the Rhine River and its precursors. This shift was probably facilitated by glacial erosion and deposition. Since late Early Pleistocene to Middle Pleistocene, the Alpenrhein River no longer drains northwards into the Danube River, but towards the Hochrhein River (Ziegler & Fraefel 2009, Heuberger et al. 2014).

In the Early Pleistocene (2.6 – 0.77 Ma), the Alpine glaciers advanced into the Alpine Foreland for the first time. Rare findings of ice-contact sediments indicate that some Early Pleistocene glaciers advanced to similar extents to that reached, for instance, during the Last Glacial Maximum (LGM; Fig. 3-5g). Downstream of these glaciers, extensive plains with fluvioglacial gravels were aggraded in wide channel systems (Graf 1993). Fluvial incision resulted in the development of gravel terraces, leaving behind flat-topped hills in the landscape, the so called Höhere and Tiefere Deckenschotter ("Higher and Lower Cover Gravels"; Fig. 3-11). In this progressively incising fluvial system, older gravel terraces are generally preserved at higher elevation, while younger terraces are at lower elevation (Burbank & Anderson 2012). Many of the Deckenschotter terrace bodies are further characterised by a composite internal structure (including cut-and-fill sequences) interpreted as climatically controlled depositional–erosional phases (Graf 1993). Continued fluvial baselevel lowering during the Early Pleistocene into the Middle Pleistocene caused incision into accumulated gravels and, more importantly, into bedrock (Kuhlemann et al. 2013, Dieleman et al. 2022a, Thew et al. 2024).

During the Middle Pleistocene (0.77 Ma – 130 ka), global glacial/interglacial cycles (now dominated by the 100-kyr periodicity) continued to cause expansion and retreat of Alpine glaciers including the most extensive glaciation (Fig. 3-11). During this period, large volumes of fluvioglacial gravel were deposited in the forefield of the glaciers and the downstream valleys, together forming the Hochterrasse ("High Terrace"). Interglacial sediments are rarely preserved.

The most extensive glaciation of the Swiss Alpine Foreland is represented by the Möhlin Glacial (Graf 2009b; Fig. 3-11), which is tentatively assigned to MIS 16 to MIS 12 (676 – 424 ka; Preusser et al. 2021, Dieleman et al. 2022b). It left behind extended overdeepened troughs in the Alpine Foreland (Buechi et al. 2024). The subsequent glaciations during the Habsburg Glacial (ca. MIS 10, 374 – 337 ka) had a smaller extent, but also eroded overdeepened troughs. Fewer constraints exist for the glaciations of the Hagenholz Glacial (ca. MIS 8, 300 – 243 ka), that had an even smaller extent and left comparatively minor traces in the landscape (Graf 2009b). The main glaciations of the following Beringen Glacial (MIS 6, 191 – 130 ka; Lowick et al. 2015) were again extensive and eroded new and reactivated existing overdeepened troughs.

During the Birrfeld Glacial (corresponding to the Late Pleistocene after the Eemian, 115 – 12 ka), several periods of glacier advance and retreat are well documented in Northern Switzerland, forming the Niederterrasse ("Low Terrace"). An early and limited glacier advance into the foreland occurred during MIS 4 (71 – 57 ka). The Rhine glacier reached its maximum extent (LGM) between ca. 26 and 22 ka ago (Gaar et al. 2019, Kamleitner et al. 2023; Fig. 3-11). The LGM ice extent is reduced compared to the maximum extents of the Beringen Glacial. It did not reach JO, only reached into the southeastern part of NL but covered ZNO completely.

Probably as a result of gravel accumulation in front of the small Black Forest ice cap, the Wutach River formerly draining to the Danube was diverted after ca. 18 ka towards the Rhine system, triggering a rapid incision of "up to 150 m" within only 6 kyr and producing a deep gorge (Einsele & Ricken 1995, Hebestreit 1995). This incision has potentially impacted the recharge into the Muschelkalk aquifer (Section 4.5.5.5).

With the disappearance of the glaciers in the foreland around 16 – 17 ka ago, fluvial, lacustrine and hillslope processes dominated on a pre-sculptured, locally glacially overdeepened landscape (12 ka – recent). The Rhine catchment is still growing at the expense of the Danube River (Winterberg & Willett 2019).

Total bedrock incision since deposition of the Deckenschotter reaches ~ 180 m (since HDS deposition) and ~ 100 m (since TDS deposition) at the location of the Aare confluence (Fig. 3-11). Incision values in the realm of the siting regions generally decrease from east to west and from south to north (Fig. 6-6c and d) with values generally decreasing from east to west and from north to south (Nagra 2024k) with regionally averaged incision between ~ 200 – 300 m since HDS and ~ 130 – 200m since TDS deposition, respectively. The incision probably occurred stepwise, with the highest values achieved as a response to the Mid-Pleistocene Transition (ca. 1.25 – 0.7 Ma). The reason for this incision is probably a combination of (1) a colder climate with frequent extensive glaciations reaching the Alpine Foreland, (2) drainage reorganisations and (3) rock uplift.

Quaternary incision and the related eastward enlargement of the Rhine catchment with the new drainage of the Alpenrhein from the Bodensee area towards the west (Hochrhein) probably shifted the discharge areas for the Malm aquifer north of the ZNO and NL siting regions in an east- to southeastward direction. This may have influenced the groundwater circulation to the north of the siting regions and potentially also in the northwestern part of ZNO.

The glaciations of the Pleistocene led to locally increased subglacial recharge; for example, numerous groundwater samples with cold climate signatures (Section 4.5.5.2) from the Bodensee area have been preserved in the Malm aquifer and in the Molasse (Fig. 3-3). Here, the ice cover caused a temporary reversal of the hydraulic gradient, whereby water flowed across the USM into the Malm aquifer (see Section 4.5.5.2 or Waber & Traber 2022). Many of the deep Molasse groundwater samples represent a mixture between a Pleistocene cold-climate water and an OMM marine component.

3.6 Present-day geodynamic situation

Present-day Northern Switzerland is considered to be located within the rigid domain of Central Europe (Fig. 3-5h; Nocquet & Calais 2004). With respect to seismicity, Switzerland has a well-documented historical record of seismicity and represents a transition between high rates south of the Alps and sparse seismicity within and north of the Alps (Houlié et al. 2018). The overall distribution of seismicity in Switzerland follows large tectonic domains, with seismicity clustering within the Upper Rhine Graben or the Valais for instance. A detailed description of the seismicity in Northern Switzerland is provided in Chapter 5.

The overarching geodynamic setting of Central Europe is influenced by ongoing convergence between the African and Eurasian Plates (Fig. 3-12). The largest geodetic velocities are measured in the eastern part of the African – Eurasian plate boundary zone in Greece and Turkey (e.g. Serpelloni et al. 2022). Rates decline significantly towards the Alps. While some ongoing shortening is detected across the Eastern Alps, shortening rates across the Swiss Alps are very low to non-existent (e.g. Sánchez et al. 2018).

The vertical velocity field of the Alps based on GNSS measurements is in the order of ~ 2 mm/yr along the Alpine arc (e.g. Piña-Valdés et al. 2022). Vertical velocity generally correlates positively with topography (e.g. Serpelloni et al. 2022). Tectonic drivers of ongoing Alpine uplift are overlain by buoyancy forces (e.g. Sternai et al. 2019, Piña-Valdés et al. 2022). Low uplift rates (positive < 1 mm/yr to stable zero rates) are observed in the Jura Mountains and the Molasse Basin, but a weak signal extends further into the area of the Upper Rhine Graben shoulders (i.e. the Black Forest and Vosges Mountains; Sánchez et al. 2018, Henrion et al. 2020). This could be associated with observed subsidence within the Upper Rhine Graben north of Basel and west of the Upper Rhine Graben towards the Bresse Graben (e.g. Sánchez et al. 2018, Henrion et al. 2020.

It is anticipated that Northern Switzerland will be subject to ongoing deformation at low rates. This is influenced by the Alpine orogeny, the Upper Rhine Graben and tectonic activity of the Jura Fold-and-Thrust Belt.



Fig. 3-12: Present-day geodetic movements relative to Eurasia

For detailed present-day geodetic velocities, see Section 6.2.

Geodetic velocities are taken from Nocquet (2012). The plate boundaries are modified after Pfiffner (2009).

4 Detailed geological framework

Key points:

- All three siting regions show areas devoid of seismically mappable faults. In NL this area is the largest. The observed differences between the siting regions relate to their position with respect to tectonic domains (Konstanz – Frick Trough, Jura Fold-and-Thrust Belt, Hegau – Bodensee Graben and Upper Rhine Graben).
- The Opalinus Clay host rock shows similar characteristics in all the siting regions (100 to 120 m thick, clay-mineral-rich, small lithological variability). This can be attributed to deposition in an epicontinental marine basin characterised by clay-mineral-rich input, generally high sedimentation rates and a relatively homogeneous environment.
- The confining units with overall high clay-mineral content surround the host rock. Compared to Opalinus Clay these units show more variability (e.g. intercalated sandy and calcareous beds). This is the result of more variable, mostly marine depositional environments (e.g. variations in subsidence, water depth, sediment input, currents).
- The low hydraulic conductivity interval comprising host rock and confining units is well constrained by hydraulic field and laboratory data in all the siting regions. The interval is sandwiched in between regional and local aquifers. It is thickest in NL and thinnest in JO.
- The aquifers above the confining units (Malm, Hauptrogenstein) include groundwaters of high residence time. Quasi-stagnant conditions are observed in the Malm aquifer in NL. The Keuper aquifer delimiting the lower confining units is also characterised by high residence times, except for parts of JO. In contrast, the Muschelkalk aquifer further below represents a continuous and comparably dynamic flow system in all the siting regions.
- Porewater investigations provide independent evidence for the hydraulic barrier effect and for diffusion-dominated transport at formation scale over geological times. NL shows highest Opalinus Clay porewater values of stable water isotopes indicating a comparably large old component.

4.1 Introduction

This chapter is dedicated to the characterisation of the study area in Northern Switzerland with respect to sedimentation, diagenesis, tectonic deformation, current stress field, hydrogeological and hydrochemical characteristics and current temperature conditions. The focus is on the safety-relevant geological units from the base of the Schinznach Formation (upper Muschelkalk Group) to the top of the «Felsenkalke» and «Massenkalk» (upper Malm Group). This sequence includes the host rock, the surrounding low-permeability confining units and the bounding aquifers. The chapter provides a description of the present situation, but frequently refers to the past evolution because this is key for understanding the current situation. For example, the lateral variability of properties of a certain unit is closely related to its depositional environment.

The chapter highlights similarities and differences between the three siting regions and forms the framework for Chapter 5, which focuses on safety-relevant properties and processes in the clay-mineral-rich core of the geological barrier (the Opalinus Clay and adjacent low-permeability rocks). The detailed description of the geological barrier also forms the basis for the assessment of its future evolution, which is discussed in Chapter 5.

Fig. 4-1 visualises the topics covered in this chapter. Section 4.2 focuses on the sedimentology and stratigraphy of the geological units of main interest (base of the Schinznach Formation to the top of the «Felsenkalke» and «Massenkalk»). Section 4.3 describes the tectonic situation in the siting regions and in a larger regional context. In Section 4.4, the recent stress field is characterised. Section 4.5 addresses the hydrogeological and hydrochemical situation in the aquifer – aquitard sequence. Past transport in the host rock and confining units is discussed in Section 4.6 (investigations of profiles of natural tracers in the porewater) and in Section 4.7 (investigations of secondary mineralisations). Section 4.8 describes the current temperature conditions. The final Section 4.9 summarises the most important project-specific conclusions, including a site-specific definition of the extent of the lower and upper low-permeability confining units.

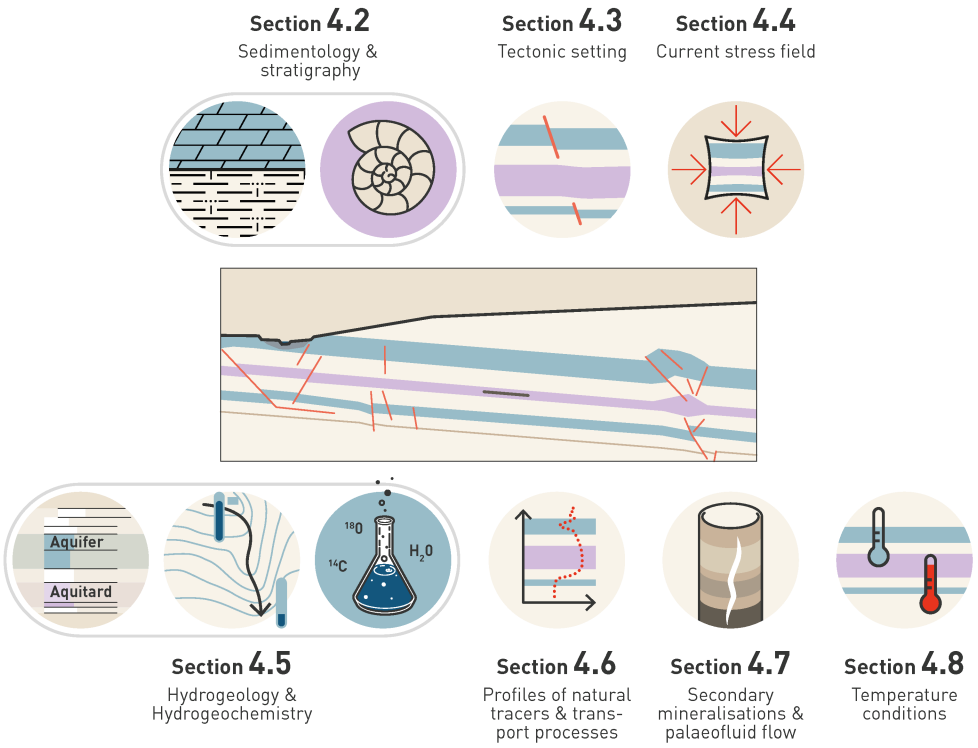


Fig. 4-1: Schematic overview of the content and structure of the chapter

4.2 Sedimentology and stratigraphy

Key points:

- The Opalinus Clay host rock shows thicknesses of about 100 to 120 m in the three siting regions. Lithological characteristics are similar due to a common, relatively homogeneous marine depositional environment characterised by clay-mineral-rich input and high sedimentation rates.
- The units directly below and above the Opalinus Clay are, in general, also characterised by high clay-mineral contents, but they show more variable thickness and facies. This reflects locally more varying depositional environments.
- While the marine Staffelegg Formation directly below the host rock is similar between the siting regions, some prominent differences occur in the underlying partly shallow marine to mostly terrestrial Klettgau Formation.
- The marine deposits of the Dogger Group above Opalinus Clay are characterised by lateral thickness and facies changes. The deposits include decametre-thick clay-mineral-rich units as well as intercalated sandy-calcareous beds, condensed horizons and carbonate build-ups reflecting changes in sediment input, water depth and ocean currents.

4.2.1 Overview

In this section, the sedimentological and stratigraphic evolution of the study area for selected units is interpreted with respect to changing tectonic and climatic conditions and associated processes such as sea-level variations and ocean currents. The geological conditions of the investigated area during the Permo-Carboniferous, following the Variscan orogenesis, were dominated by regional crustal extension and erosion (refer also to Chapter 3 for further context). The troughs were filled with fine- to coarse-grained sediments in a terrestrial depositional environment under mostly arid and partly humid climate conditions. During the Mesozoic, the break-up of Pangaea and the opening of the North Atlantic Ocean and the Piemont – Liguria Ocean led to extension-dominated tectonics in Northern Switzerland. Accommodation space for sediments was created by subsidence in the Central European Basin. In a shallow marine epicontinental sea to partly terrestrial setting, 800 to 900 m[10] of predominantly argillaceous to calcareous sediments were deposited under subtropical climate conditions (Fig. 4-2). The characteristics of the specific depositional environments (Fig. 4-3) and later diagenesis of the sediments deposited in the study area have determined many of their fundamental barrier properties (e.g. lithology and the vertical as well as lateral variability). The spatial and temporal characteristics of the sedimentary processes and the resulting rock units furthermore provide the basis for a better understanding of the similarities and differences between the siting regions (Fig. 4-4, Fig. 4-5, Fig. 4-6).

This section is divided into further subsections arranged from older to younger selected lithostratigraphic units. The Opalinus Clay and its confining units below and above are especially emphasised because of their importance as the host rock and barriers of the repository system. Additionally, the regional Muschelkalk and Malm aquifers are discussed. The sections are divided into the following paragraphs: introduction, facies and lithostratigraphy, variability, chronology, and depositional evolution. Interpreted timelines are given as red dashed lines in this section (e.g. Fig. 4-2). Information on the other lithostratigraphic units below and above the regional Muschelkalk and Malm aquifers can be found in Chapter 3 and the literature cited therein.

[10] 800 – 900 m refers to the current compacted thickness of sedimentary rocks.

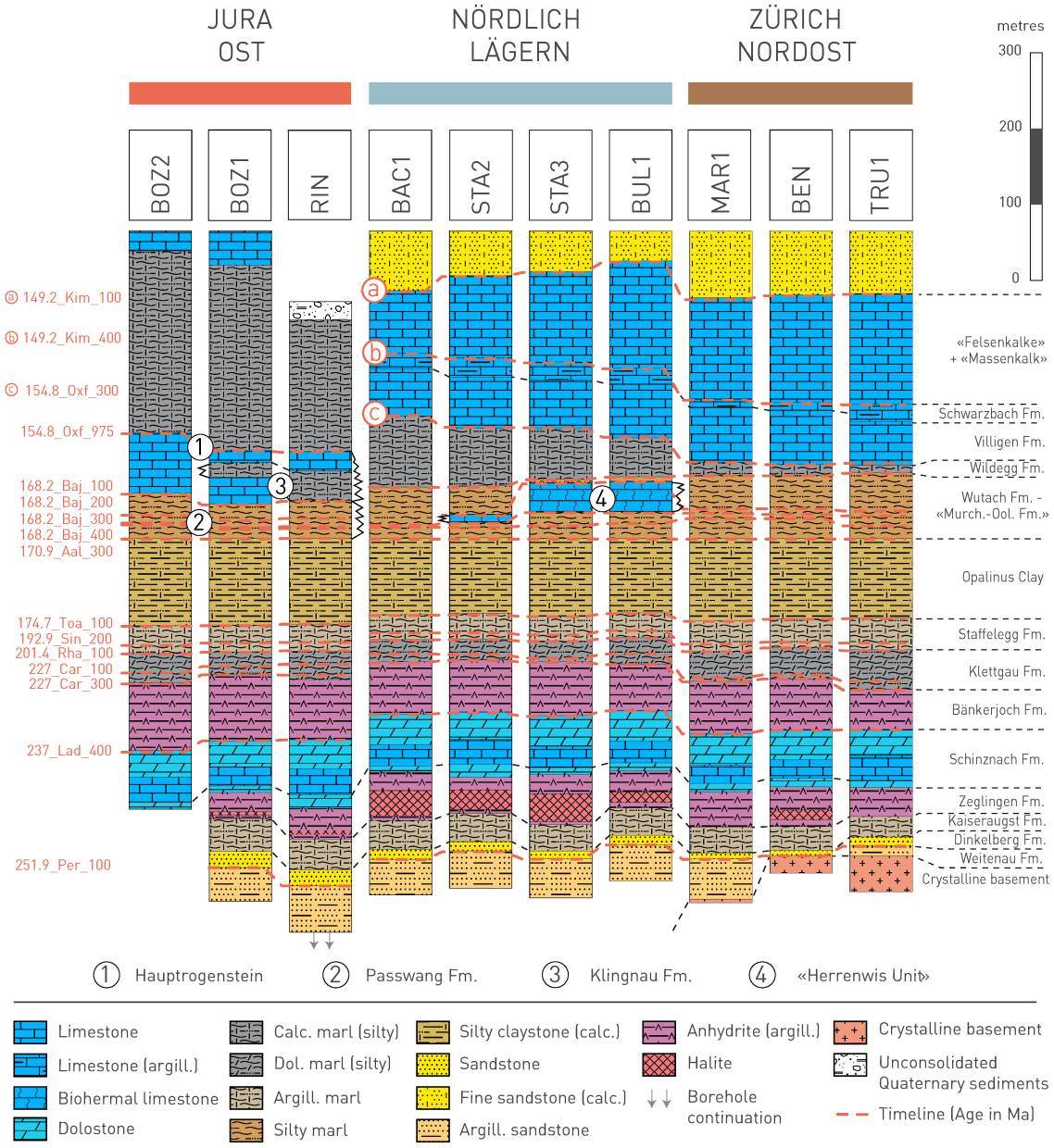
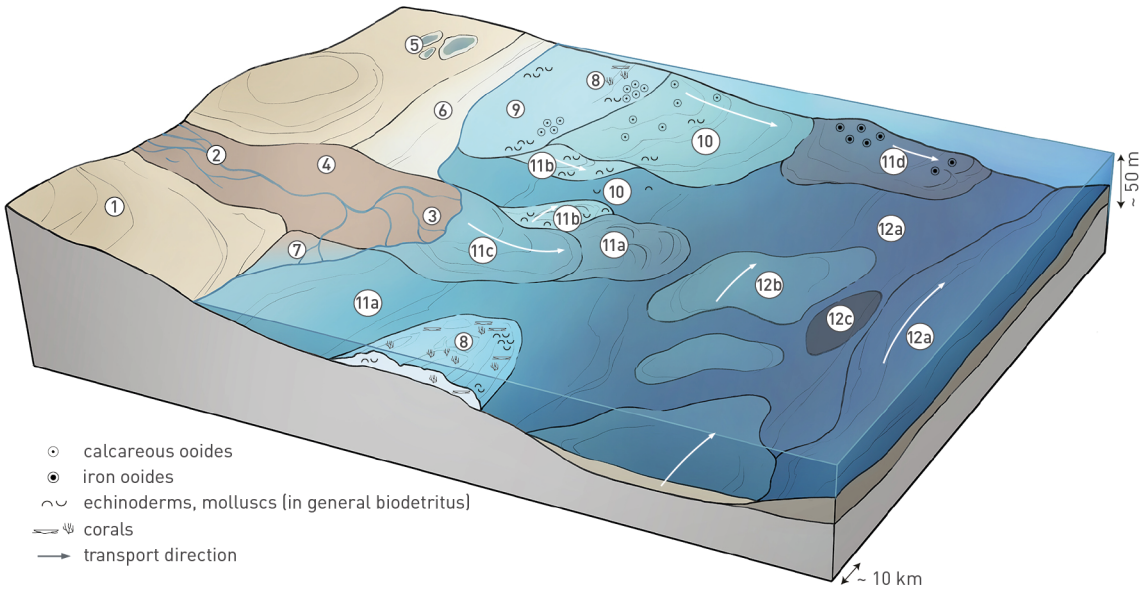


Fig. 4-2: Lithological overview correlation with the focus on Mesozoic sedimentary rocks of the three siting regions

Boreholes are aligned to Top Opalinus Clay. Simplified lithological legend according to Naef et al. (2019). Black dashed lines indicate lithostratigraphic boundaries. Red dashed lines indicate timelines. Their names consist of three elements (e.g. 170.9_Aal_300): 1) start age of the corresponding chronostratigraphic stage (International Chronostratigraphic Chart, v 2022/10, e.g. 170.9 Ma for start of the Aalenian), 2) name of corresponding chronostratigraphic stage and 3) three-digit number. The given age in the name should therefore not be understood as depositional age but rather as a general temporal orientation based on the corresponding chronostratigraphic stage. The temporal resolution or number of timelines was chosen regarding potential horizons in seismic interpretation and for a basic stratigraphic analysis. Therefore, many more timelines could be identified, and the three-digit numbers are not sequential but were chosen to enable later additional picking of lines without changing the numbering scheme.



	Depositional Environment	Examples
Terrestrial	① gap (no sedimentation/erosion)	Triassic/Jurassic Boundary
	② fluvial, channel	Ergolz, Gruhalde and Seebi Members (Klettgau Formation)
	③ fluvial, overbank	
	④ floodplain, partly lacustrine	
	⑤ playa	Seebi Member (Klettgau Formation)
	5a dolomitic, partly siliciclastic	
	5b dolomitic, porous	
	⑥ sabkha (coastal)	Zeglingen Formation, Bänkerjoch Formation
	⑦ brackish to shallow lagoon	Belchen Member (Staffelegg Formation)
Shallow marine epicontinental basin	⑧ carbonate platform/ramp, shoal (backreef) /bioherm (coral)	Schinznach Formation, «Herrenwis Unit», Hauptrogenstein
	⑨ carbonate platform/ramp, shallow epicontinental /bioherm (sponge)	Villigen Formation, «Massenkalk»
	⑩ epicontinental mixed carbonate-siliciclastic	Klingnau Formation, Wildegg Formation
	⑪ shallow epicontinental	
	11a siliciclastic (silty/argillaceous)	Opalinus Clay
	11b bars and bed sequences (siliciclastic (sandy/silty) and/or calcareous)	Passwang Formation, Wedelsandstein Formation
	11c siliciclastic (sandy/silty)	Dogger Group above Opalinus Clay
	11d sediment starvation (often condensed, e.g. iron-oolite)	«Humphriesioolith Formation», Wutach Formation
	⑫ shallow mid epicontinental	
	12a siliciclastic (silty/argillaceous)	Opalinus Clay
	12b bars and bed sequences (siliciclastic (sandy/silty) and/or calcareous)	Opalinus Clay
	12c siliciclastic (silty/argillaceous), bituminous, anoxic	Rietheim Member (Staffelegg Formation)

Fig. 4-3: Schematic representation of depositional environments of Mesozoic sedimentary rocks in Northern Switzerland

This sketch conceptually summarises the main characteristics of depositional environments and serves as an orientation for the respective maps below. Note that the sketch is strongly vertically exaggerated.

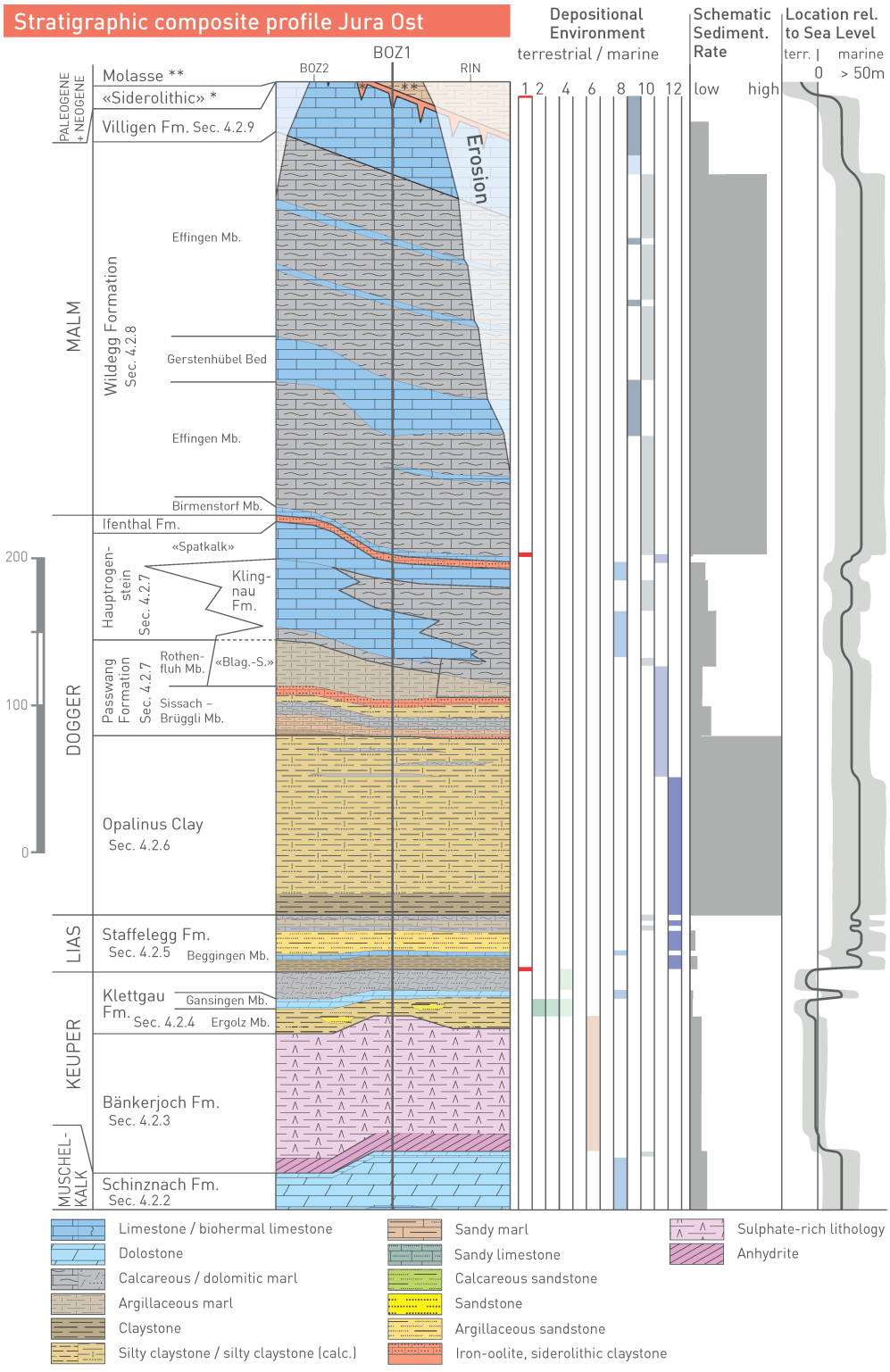


Fig. 4-4: Schematic lithostratigraphic column for JO with depositional environments, schematic sedimentation rates and estimated location relative to sea level

Refer to Fig. 4-3 for depositional environments. Boreholes are aligned to the base of the Opalinus Clay. Stratigraphic thicknesses in three right panels according to BOZ1. Sedimentation rates were estimated by dividing the thickness by the deposition period (including hiatuses) of a unit. Fm. = Formation, Mb. = Member.

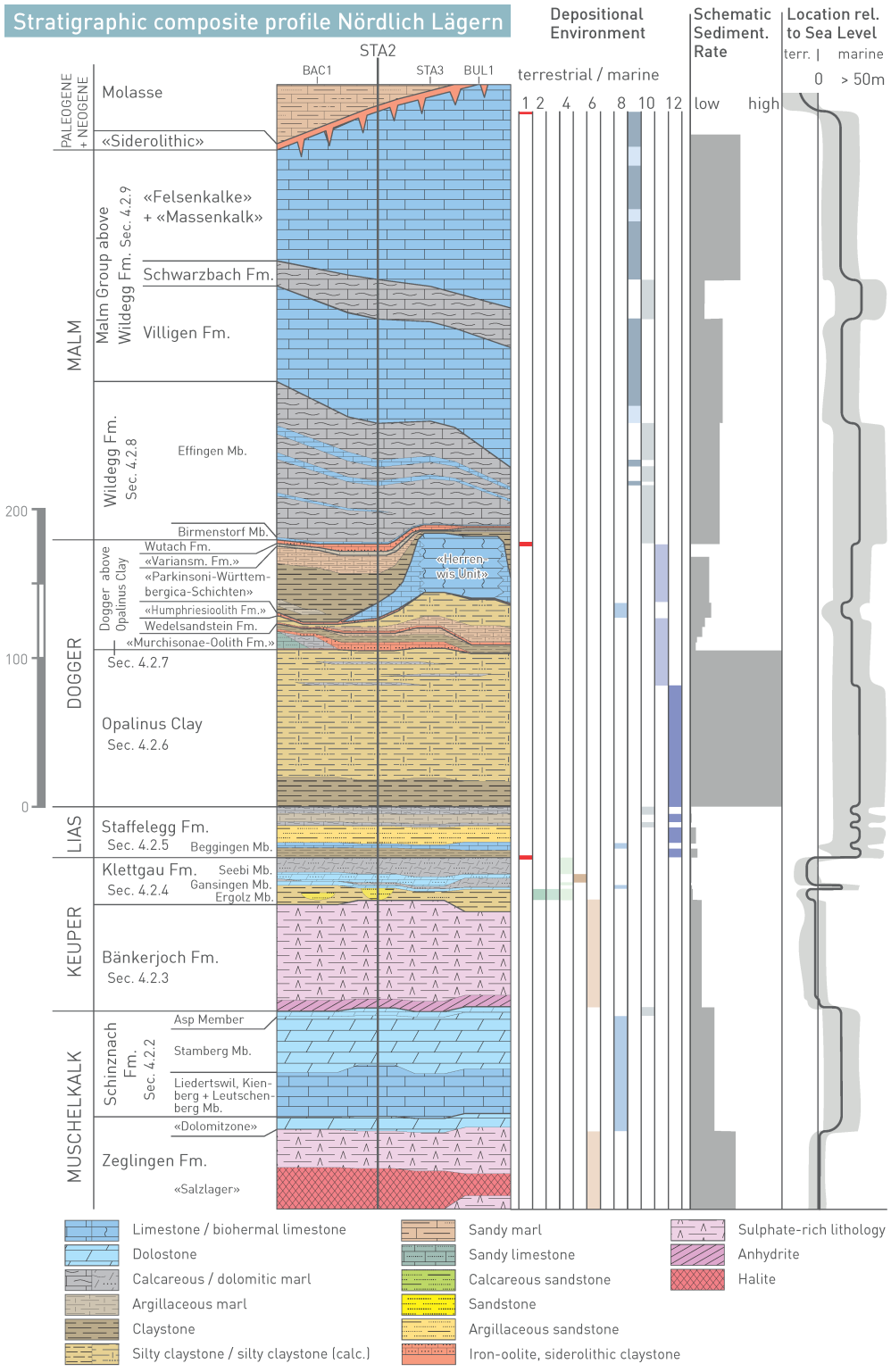


Fig. 4-5: Schematic lithostratigraphic column for NL with depositional environments, schematic sedimentation rates and estimated location relative to sea level

Refer to Fig. 4-3 for depositional environments. Boreholes are aligned to the base of the Opalinus Clay. Stratigraphic thicknesses in three right panels according to STA2. Sedimentation rates were estimated by dividing the thickness by the deposition period (including hiatuses) of a unit. Fm. = Formation, Mb(s). = Member(s).

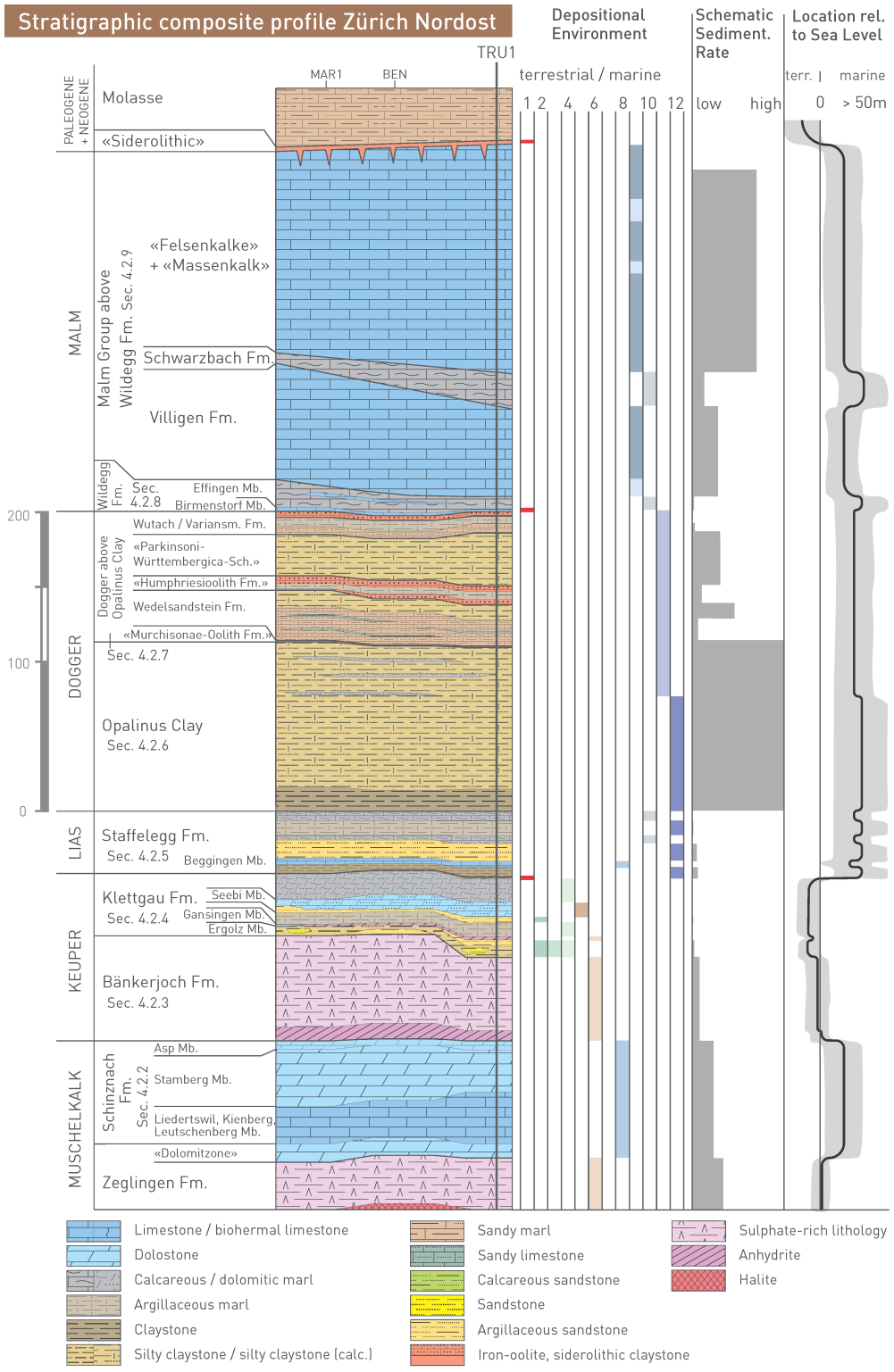


Fig. 4-6: Schematic lithostratigraphic column for ZNO with depositional environments, schematic sedimentation rates and estimated location relative to sea level

Refer to Fig. 4-3 for depositional environments. Boreholes are aligned to the base of the Opalinus Clay. Stratigraphic thicknesses in three right panels according to TRU1. Sedimentation rates were estimated by dividing the thickness by the deposition period (including hiatuses) of a unit. Fm. = Formation, Mb. = Member.

4.2.2 Schinznach Formation

4.2.2.1 Introduction

The Schinznach Formation forms the regional aquifer below the potentially lowermost confining units of the Bänkerjoch Formation (Section 4.5.3.12). During the Middle Triassic, the study area was part of the Central European Basin (Chapter 3). The mostly carbonate sediments were deposited in a shallow marine depositional environment (Merki 1961, Pietsch et al. 2016, Adams & Diamond 2017).

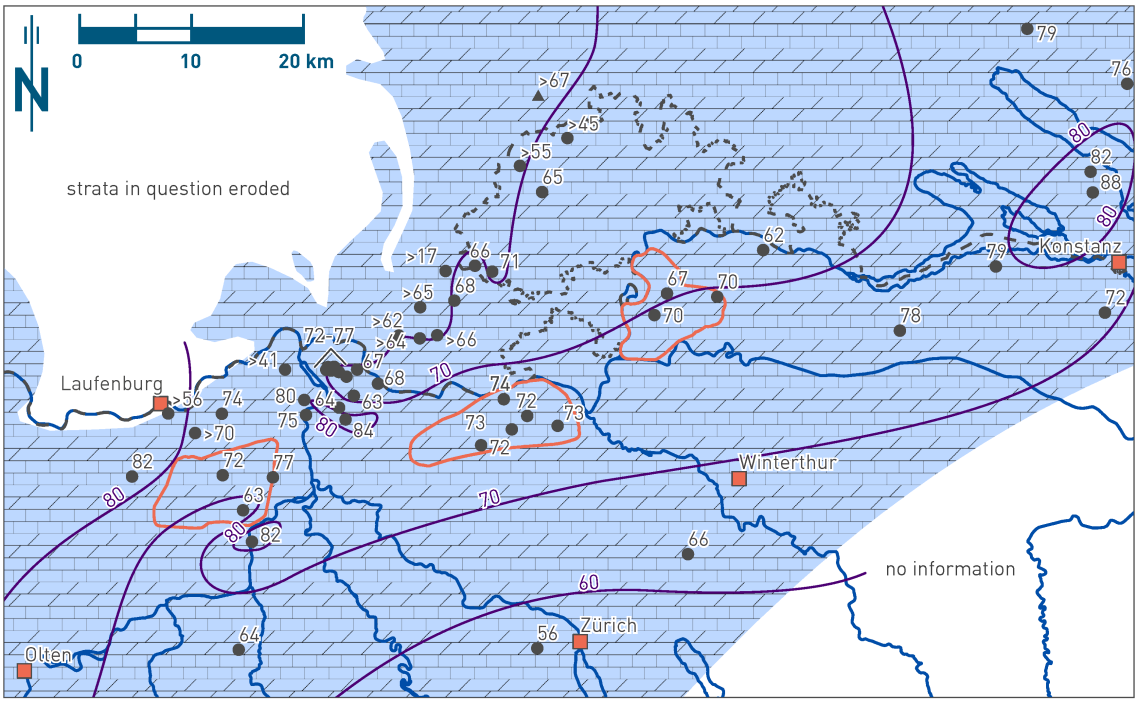


Fig. 4-7: Map of depositional environments during the Middle Triassic (Anisian – Ladinian) preserved in the Schinznach Formation

Refer to Fig. 4-3 for a schematic representation of depositional environments. The north arrow refers to present-day geographic north.

4.2.2.2 Facies and lithostratigraphy

The Schinznach Formation (Upper Muschelkalk Group, former «Hauptmuschelkalk», «Trigonodusdolomit» and «Lettenkohle») exists in all three siting regions and is about 65 to 75 m thick (Fig. 4-7; Pietsch et al. 2016). It consists of macrofossil-poor to bioclastic limestone and local macrofossil-rich dolostone (Fig. 4-8). Intervals with oncoids and ooids may occur locally. Later diagenesis led to a partial or complete dolomitisation and successions of cementing and leaching events determine the remaining porosity. Especially in dolomitised bioclastic or oolitic beds,

reduced sectors of open porosity exist. However, the porous shoal facies is relatively rare compared to southern Germany (Adams & Diamond 2017). The Schinznach Formation was subdivided into five members:

Leutschenberg and Kienberg Members (lower and middle part of the former «Hauptmuschelkalk»): In the study area, the two lowermost members of the Schinznach Formation are generally hard to separate in the boreholes and are combined in the present study (Jordan & Deplazes 2019). The combined thickness varies between ca. 20 and 30 m. They consist of a bedded succession of limestone (micrite, mudstone) with a varying content of bioclastic limestone (biomicrite, wackestone, packstone) (Fig. 4-9a & b). Ooids and oncoids also occasionally occur. Some parts of the succession are dolomitised.

Liedertswil Member (upper part of the former «Hauptmuschelkalk»): The thickness of this member varies between ca. 2 and 12 m. It consists mostly of a thin- to medium-bedded succession of partly bioturbated, glauconitic limestone (micrite, mudstone) with some bioclasts mostly concentrated in coquinas (Fig. 4-9c). The upper boundary to the overlying unit of the Stamberg Member is defined by the onset of post-sedimentary, persistent and complete dolomitisation (Pietsch et al. 2016). This petrographic, diagenetic boundary is therefore diachronous.

Stamberg Member (approx. former «Trigonodusdolomit»): The thickness of this member varies between ca. 30 and 40 m. In the lower part it comprises bedded, macrofossil-poor dolostone (mudstone, wackestone), which resembles the Liedertswil Member but is fully dolomitised (Fig. 4-9d). The upper part is characterised by partly porous dolostone with chert nodules and is locally sandy or anhydritic. In the porous dolostone, vugs with a size of up to 3 cm occur, which may originate from dissolved shells (Fig. 4-9e). Additionally, oolite horizons may occur (Fig. 4-8).

Asp Member (ca. former «Lettenkohle»): The thickness of this member varies around ca. 5 m. The Asp Member can generally be separated into two parts. The lower part consists of a fossiliferous, often bituminous shale or claystone with thin dolostone interbeds (Fig. 4-9f). The upper part is characterised by dolostone with anhydrite nodules and nodular layers (Fig. 4-9g).

4.2.2.3 Variability

The overall facies variability of the Schinznach Formation is similar in all boreholes of the siting regions and mainly concerns varieties of dolostone and limestone (Fig. 4-8). The depth of dolomitisation varies laterally, depending on local diagenesis.

4.2.2.4 Chronology

The Schinznach Formation was deposited in the Middle Triassic (Anisian to Ladinian; Pietsch et al. 2016, Bernasconi et al. 2017). Sequence stratigraphic analysis of the Schinznach Formation below the Asp Member identified a variable number of cycle sets (transgressive-regressive / regressive-transgressive hemicycles) as seen in the drill cores retrieved from the siting regions (Pietsch et al. 2016, Warnecke 2018, Adams & Diamond 2019).

4.2.2.5 Depositional evolution

The Schinznach Formation was deposited in the southern part of the Central European Basin between the London Brabant Massif in the west and the Vindelician – Bohemian Massif with its Alemannic promontory in the east and southeast (note: for cardinal points the present geographic reference system is used as plotted in the depositional maps). During the Middle Triassic, the basin was temporarily connected to the Neotethys by seaways in the east (Silesia and Eastern Karpathian Gates) and west (Burgundy Gate). The depositional environment was characterised by a carbonate platform to ramp transition in a shallow epicontinental sea (Adams & Diamond 2019, Warnecke & Aigner 2019). The Schinznach Formation is characterised overall by medium sedimentation rates (Fig. 4-4, Fig. 4-5, Fig. 4-6); however, sedimentation rates must have varied temporarily.

Together with its neighbouring lithostratigraphic units, the Schinznach Formation comprises two major transgressive to regressive sequences (Adams & Diamond 2019). *The first transgression* is expressed by the evaporitic sedimentary rocks of the upper Zeglingen Formation and continues

through the deposits of the Leutschenberg and Kienberg Members (Fig. 4-8). *The first regression* is expressed by the sedimentary rocks of the Stamberg Member and ends with the strata at the top of the Stamberg Member; the top also corresponds to an unconformity. 3D seismic facies interpretation could indicate exposure-related dissolution in the Stamberg Member (Nagra 2024a, 2024b, 2024c). The *second transgression* led to the deposition of the Asp Member in a brackish to deltaic environment as expressed by strata at the base and inter- to subtidal coastal sediments towards the top. The *second regression* is mainly represented by the evaporitic sabkha environment of the overlying Bänkerjoch Formation.

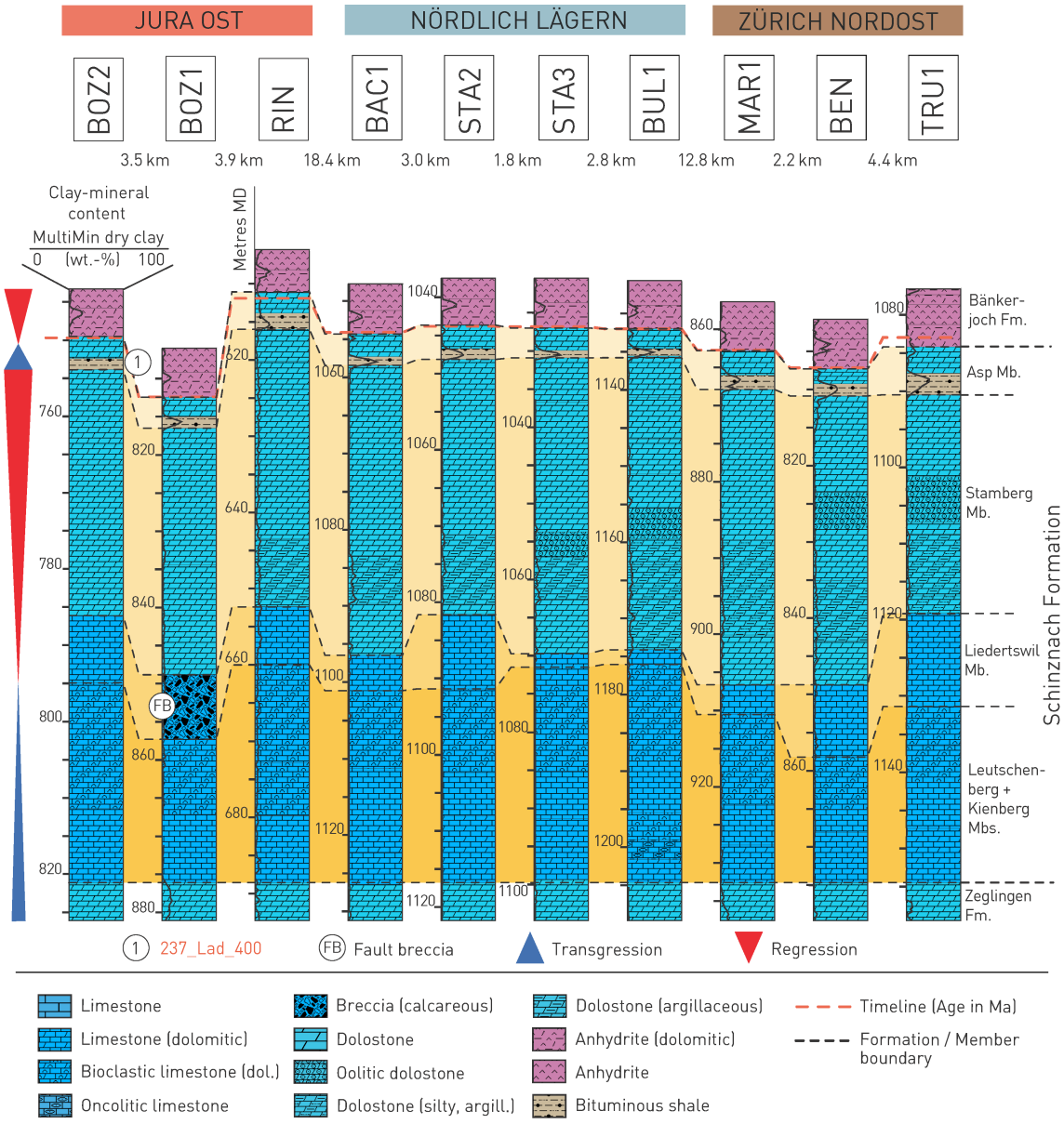


Fig. 4-8: Stratigraphic borehole correlation of the Schinznach Formation

For lithological nomenclature refer to Naef et al. (2019). Clay-mineral content after Becker & Marnat (2024). Some of the boundaries and lithologies as discussed in the original reports were adjusted to integrate all presented borehole data.

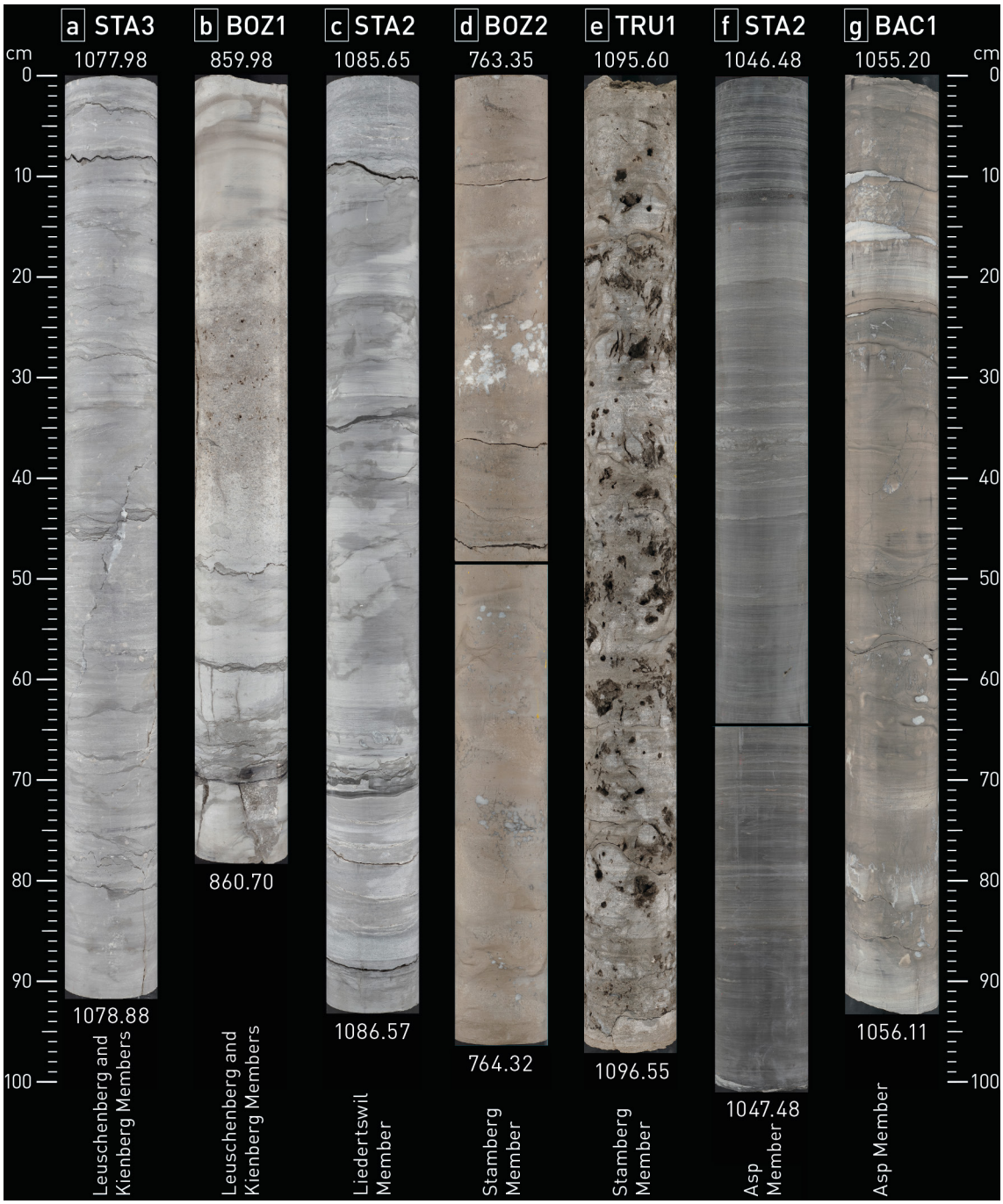


Fig. 4-9: Selected core photos of the Schinznach Formation

(a) Grey, moderately fossiliferous (crinoids) limestone, slightly to moderately bioturbated, stylolites with thin argillaceous coatings; **(b)** light grey limestone and medium grey calcareous marl, bioturbated with grey, porous, bioclastic limestone bed; **(c)** grey, partly bioturbated and glauconitic limestone; **(d)** beige dolostone with white irregularly shaped anhydrite nodules; **(e)** beige grey dolostone with abundant vugs; **(f)** dark grey bituminous shale; **(g)** greyish brown dolostone with white anhydrite nodules and nodular layers.

4.2.3 Bänkerjoch Formation

4.2.3.1 Introduction

The Bänkerjoch Formation (lower unit of the Keuper Group) underlies the Klettgau Formation. Where the local Keuper aquifer (part of the Klettgau Formation) is absent, the Bänkerjoch Formation is part of the lower confining units (Sections 4.5.3.11, 4.9). The Bänkerjoch Formation was deposited during the Triassic, when Northern Switzerland was located at the southern border of the Central European Basin (Chapter 3). It was deposited in vast sabkha plains with sporadic marine ingressions in an arid climate setting (Dronkert et al. 1990).

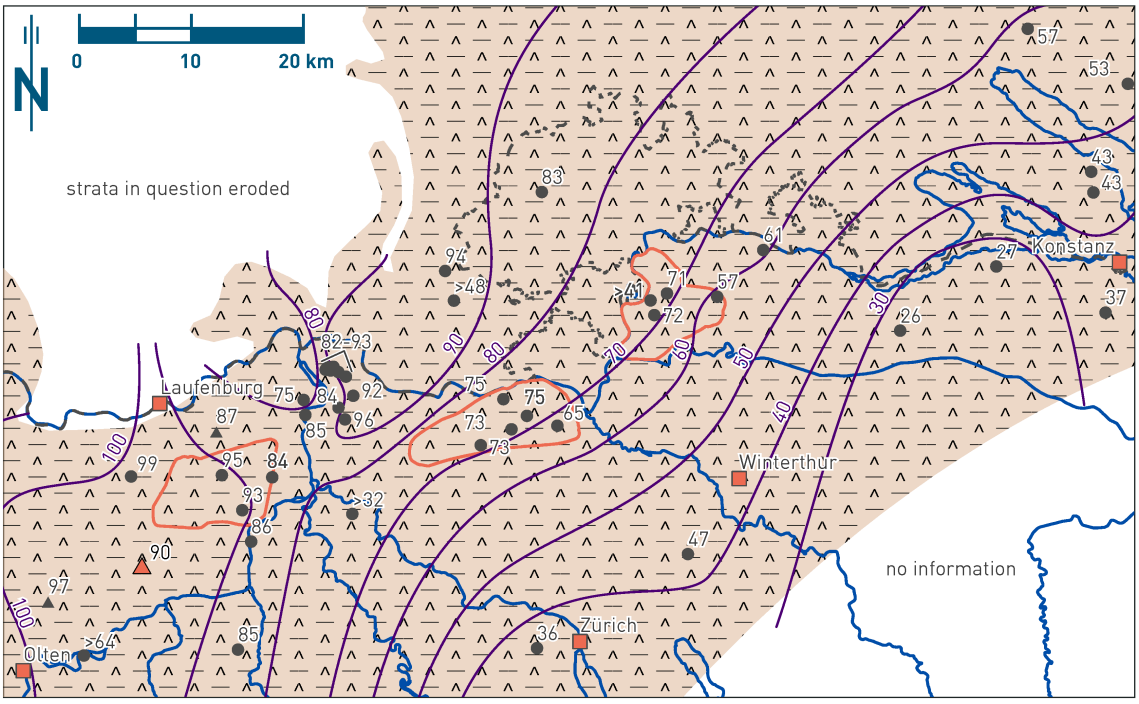


Fig. 4-10: Map of depositional environments during the Middle Triassic (Late Ladinian – Early Carnian) preserved in the Bänkerjoch Formation

Refer to Fig. 4-3 for a schematic representation of depositional environments. The north arrow refers to present-day geographic north.

4.2.3.2 Facies and lithostratigraphy

The Bänkerjoch Formation (former «Gipskeuper», part of the Keuper Group) exists in all three siting regions with similar characteristics and a thickness in the range between ca. 55 and 95 m (Fig. 4-10). The unit mostly consists of anhydrite (close to the surface and in outcrops also gypsum), claystone and dolostone (Fig. 4-11). From bottom to top, the formation comprises cyclic successions of chicken-wire anhydrite, dolomitic claystone with thin anhydritic layers and claystone (Dronkert et al. 1990; Fig. 4-12).

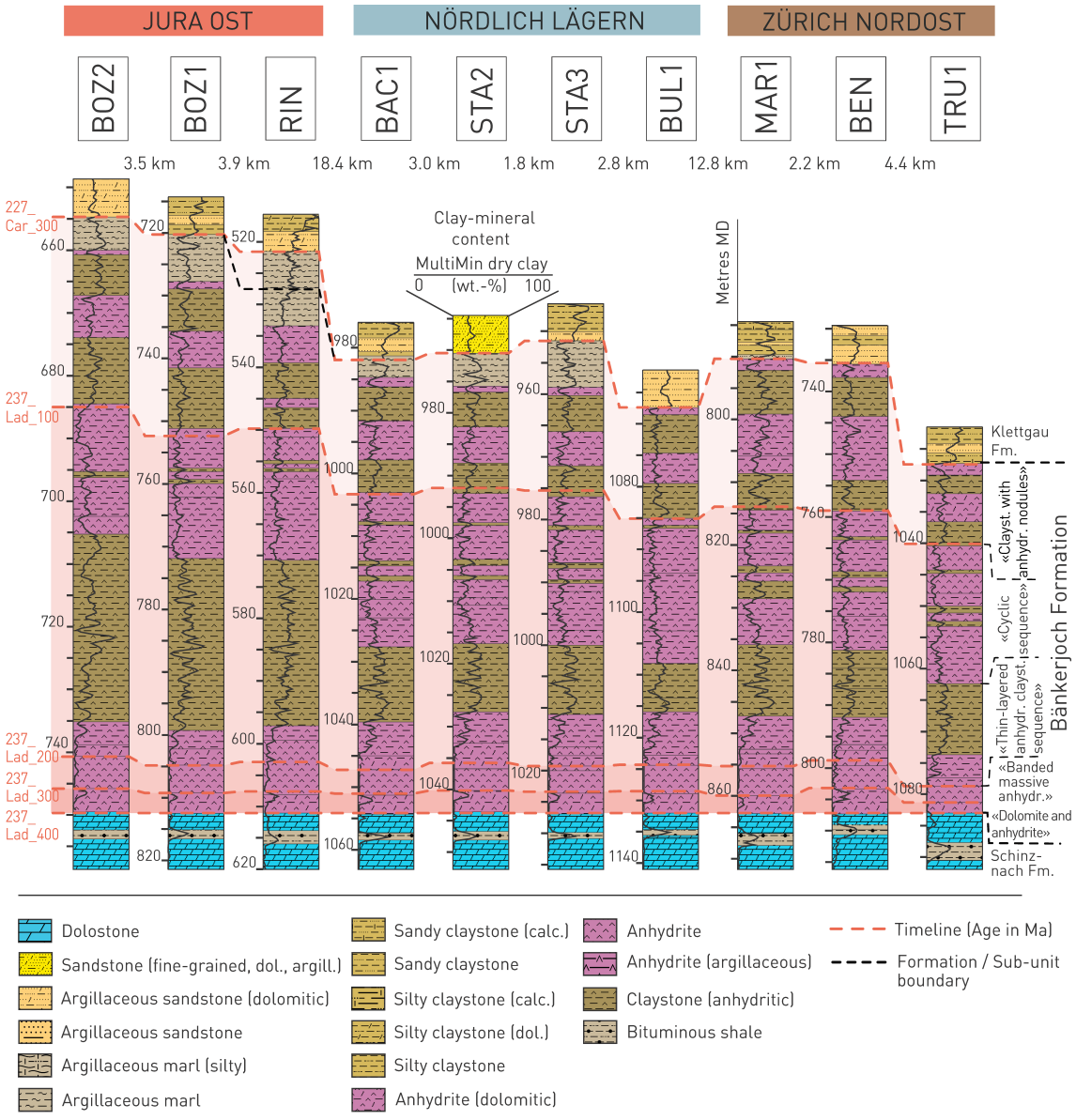


Fig. 4-11: Stratigraphic borehole correlation of the Bänkerjoch Formation

For lithological nomenclature refer to Naef et al. (2019). Clay-mineral content after Becker & Marnat (2024). Some of the boundaries and lithologies as discussed in the original reports were adjusted to integrate all presented borehole data.

The Bänkerjoch Formation has been subdivided into five informal subunits (Jordan et al. 2016a, 2016b):

«Dolomite and anhydrite»: The lowermost subunit of the Bänkerjoch Formation consists of an intercalation of dolomitic and anhydritic layers with some argillaceous marls with anhydritic nodules (Fig. 4-12a).

«Banded massive anhydrite»: This subunit mostly consists of massive to banded anhydrite with some argillaceous to dolomitic interbeds (Fig. 4-12b).

«Thin-layered anhydrite claystone sequence»: This subunit mostly consists of a succession of finely laminated anhydritic claystone, argillaceous, dolomitic marl and anhydrite (Fig. 4-12c). The anhydrite occurs mostly in the form of beds with a nodular to chicken-wire fabric.

«Cyclic sequence»: This subunit includes sedimentary rocks that represent complete and mostly incomplete cycles with a thickness of mostly a few decimetres (Fig. 4-12d & e). A typical complete cycle starts with chicken-wire anhydrite with anhydritic nodules in a matrix of claystone (anhydritic). It is followed by dolomitic claystone and nodular to laminated anhydrite and ends with a claystone (anhydritic) traversed by anhydrite veins.

«Claystone with anhydrite nodules»: This uppermost subunit of the Bänkerjoch Formation is lithologically the most heterogeneous (Fig. 4-12f & g). It is mostly characterised by silty claystone (anhydritic or dolomitic) with interbeds of anhydrite and dolostone (anhydritic) to dolomitic marl. The anhydrite occurs in form of single nodules of mm to > 1 dm size, veins and densely packed nodular beds.

4.2.3.3 Variability

The general facies variability determined by sulphatic, argillaceous and dolomitic intercalations in the Bänkerjoch Formation is similar and is correlatable between all boreholes of the siting regions (Fig. 4-11). For example, the interval with massive anhydrite in the lowermost part of the Bänkerjoch Formation is very well expressed and can be traced well laterally (defined by low clay-mineral contents between 237_Lad_300 and 237_Lad_200). However, in detail the expression, thickness and number of the lithological cycles vary depending on local conditions in the former sabkha environment. Additionally, lateral differences exist in the uppermost subunit where the overlying fluvial facies of the Ergolz Member (Klettgau Formation) is separated from the Bänkerjoch Formation by an erosional unconformity as observed in the TRU1 borehole.

4.2.3.4 Chronology

The Bänkerjoch Formation was deposited during the transition between Middle and Late Triassic (Ladinian to Early Carnian; Kozur & Bachmann 2008, Bernasconi et al. 2017). Three timelines have been picked within the Bänkerjoch Formation (237_Lad_300, 237_Lad_200, 237_Lad_100). The two older timelines approximately follow the «Banded massive anhydrite» facies, which is interpreted as being deposited during roughly the same period (Fig. 4-11). The younger timeline approximately follows the top of the «Cyclic sequence».

4.2.3.5 Depositional evolution

The Bänkerjoch Formation was deposited in vast sabkha plains at the southern border of the Central European Basin under arid conditions. The depositional environment was characterised by subaerial flats, ephemeral and saline ponds to lagoons subjected to sporadic marine ingressions. 3D seismic facies interpretation indicates that the Bänkerjoch Formation is characterised by a complex depositional history with potentially one or more evaporite dissolution events (Nagra 2024a, 2024b, 2024c). The sedimentation rates are overall medium, but fluctuated significantly between phases of deposition and non-deposition (Fig. 4-4, Fig. 4-5, Fig. 4-6). The Bänkerjoch Formation formed during a large-scale regressive cycle with many superimposed small-scale regressive cycles (Dronkert et al. 1990). In the Bänkerjoch Formation, no halite and dissolution breccias such as in the Zeglingen Formation have been found; this reflects deposition in a marginal position of the basin with a relatively high argillaceous input. Conversely, coeval

sedimentary rocks exposed in the present-day French Jura Mountains formed in a more basinal environment where halite was deposited. The depositional evolution of the Bänkerjoch Formation is subdivided here into four time intervals (Fig. 4-11):

The first time interval (237_Lad_400 to 237_Lad_300) approximately corresponds to the «Dolomite and anhydrite» subunit. During this time, the depositional environment was characterised by saline ponds and lagoons, with anhydritic to dolomitic sedimentation as well as argillaceous input.

The second time interval (237_Lad_300 to 237_Lad_200) approximately corresponds to the «Banded massive anhydrite» subunit. This time interval was characterised by depositional environments ranging from saline ponds to lagoons, with generally anhydritic sedimentation.

The third time interval (237_Lad_200 to 237_Lad_100) approximately corresponds to the «Thin-layered anhydrite claystone sequence» and «Cyclic sequence» subunits. During this time interval, thick successions of sediments were deposited in shallow and ephemeral ponds as well as subaerial flats. In subaerial flats, pedogenic processes in combination with groundwater fluctuations and periodic flooding led to the formation of nodular to bedded sulphate horizons (cycles).

The fourth time interval (237_Lad_100 to 227_Car_300) approximately corresponds to the «Claystone with anhydrite nodules» subunit. This time interval is dominated by subaerial, more argillaceous sediments. Pedogenesis and groundwater fluctuations led to the formation of nodular anhydrite.

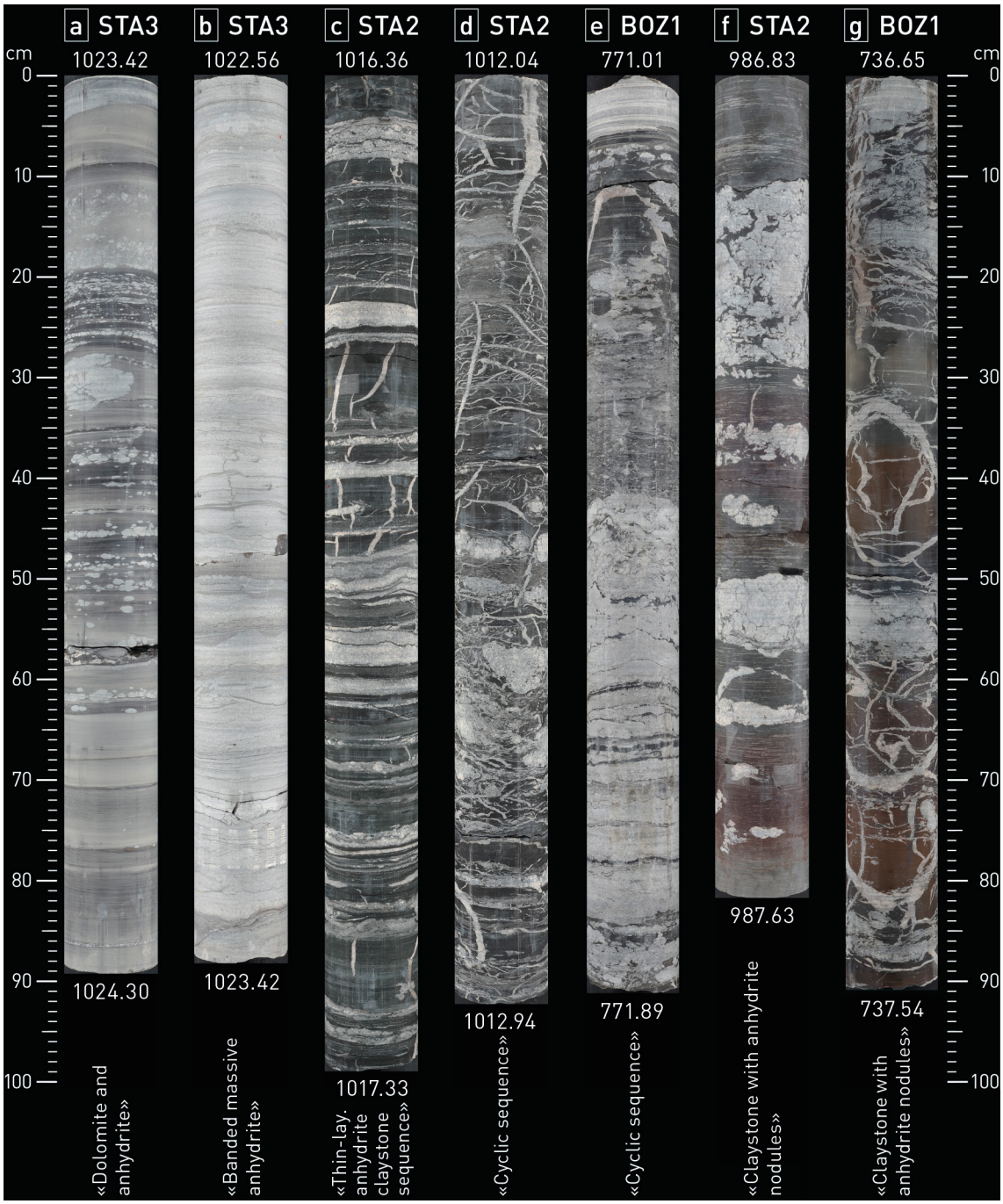


Fig. 4-12: Selected core photos of the Bänkerjoch Formation

(a) & **(b)** beige to dark grey dolomitic marl with white anhydrite nodules and beds of beige grey argillaceous dolostone, above 1'023.45 m: white massive to thin-bedded anhydrite with fine layers of dark grey dolomitic claystone; **(c)** alternating laminated layers of white dolomitic anhydrite and black anhydritic claystone with few white anhydrite veins; **(d)** white nodular anhydrite (chicken-wire) with frequent anhydrite veins and black anhydritic claystone; **(e)** from bottom to top: cyclic sequence of white nodular anhydrite (chicken-wire), dark grey dolomitic claystone with nodular to laminated beds of anhydrite and black anhydritic claystone with anhydrite veins; **(f)** & **(g)** dark grey to brown anhydritic claystone with white nodular anhydrite partly enriched in beds traversed by anhydrite veins.

4.2.4 Klettgau Formation

4.2.4.1 Introduction

The Klettgau Formation (upper unit of the Keuper Group) underlies the Staffelegg Formation and belongs, at least partly, to the lower confining units. In JO and ZNO and partly in NL, it includes the local Keuper aquifer (Section 4.5.3.10). The Klettgau Formation was deposited in the southern part of the Central European Basin during the Late Triassic (Chapter 3). At this time, Northern Switzerland was dominated by variable, mostly terrestrial depositional environments (Fig. 4-13).

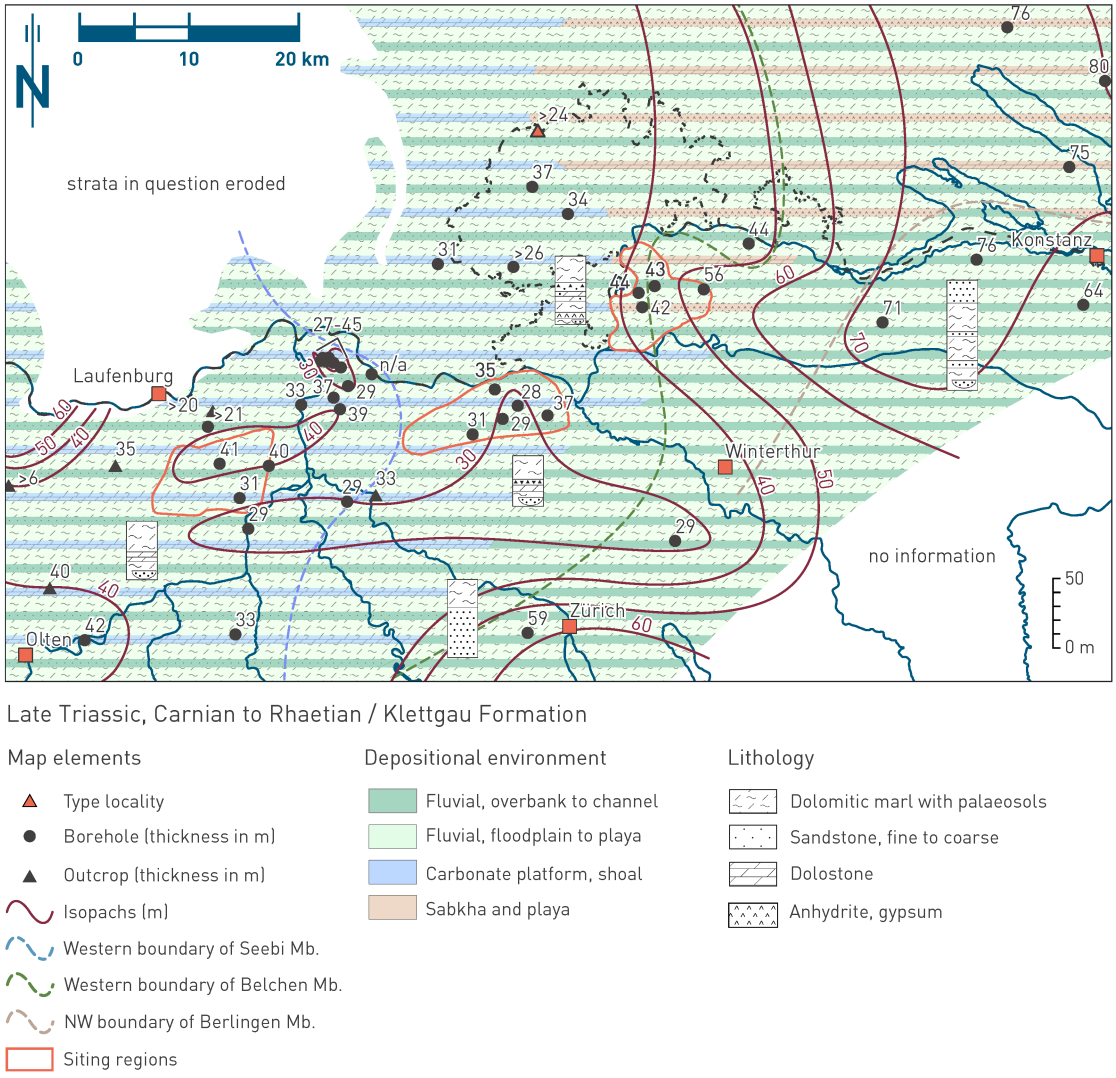
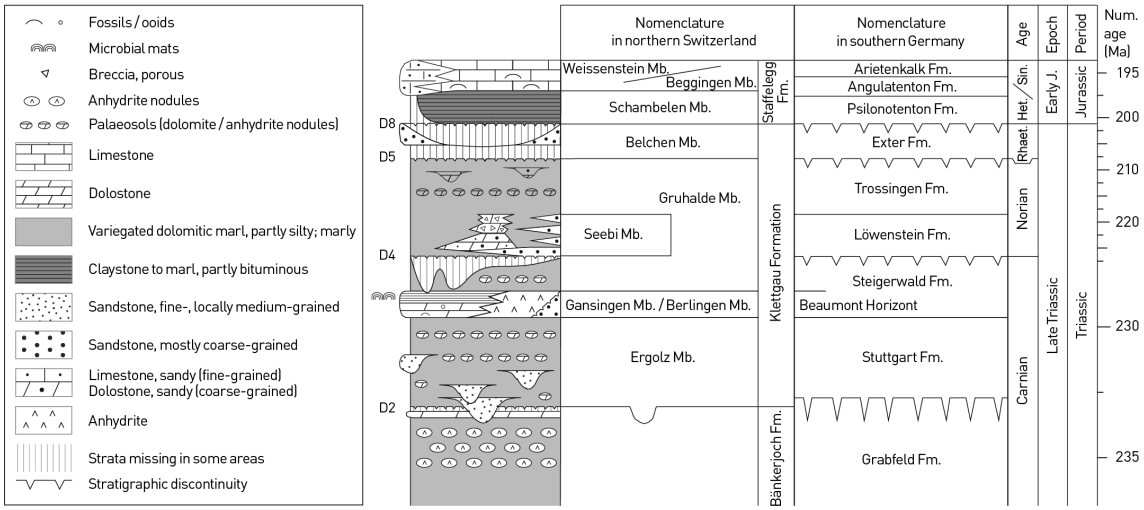


Fig. 4-13: Map of depositional environments during the Late Triassic (Carnian to Rhaetian) preserved in the Klettgau Formation

Refer to Fig. 4-3 for a schematic representation of depositional environments. The north arrow refers to present-day geographic north. Mb.: Member.



Unconformities: D2: Intra-Carnian, D4: Old Cimmerian, D5: Infra-Rhaetian, D8: Jurassic; Fm.: Formation; Mb.: Member; Rhaet.: Rhaetian; Het.: Hettangian, Sin.: Sinemurian; J.: Jurassic

Fig. 4-14: Schematic synoptic section of the Klettgau Formation with its different members

On the right, comparison with correlative stratigraphic units in Germany (Etzold & Schweizer 2005, Geyer et al. 2023). Modified after Jordan et al. (2016b).

4.2.4.2 Facies and lithostratigraphy

The Klettgau Formation has a thickness varying between ca. 30 and 55 m (Fig. 4-13). It is a heterogeneous succession dominated by dolomitic and argillaceous marls with intercalations of dolostones and partly porous sandstones (Fig. 4-16). In some intervals this unit also includes porous dolomitic breccias and anhydrite. The Klettgau Formation can be divided into five members (Fig. 4-14) in the three siting regions (Jordan et al. 2016b; Fig. 4-16):

Ergolz Member (former «Schilfsandstein (sensu lato)» or «Schilfsandstein Formation», «Untere Bunte Mergel»): This member is the lowermost unit of the Klettgau Formation. Its thickness varies between ca. 6 and 21 m (Fig. 4-17). It is dominated by dolomitic and argillaceous marl of the floodplain facies («normal facies»; Fig. 4-16a). In this facies there are pedogenic nodular beds and nodules of dolostone. There are also partly porous sandstones and siltstones with cross- and flaser-bedding as well as ripples that were deposited in fluvial channels («channel facies»; Fig. 4-16b, Fig. 4-18, Fig. 4-19). The sandstones of the Ergolz Member contain a significant proportion of lithic clasts, particularly up to ca. 30% of schistose clasts. As a transition between floodplain and channel facies deposits there are overbank facies deposits with a heterolithic association of fine, partly porous and silty sandstone and marl. Within the siting regions the most distinctive cross-bedded fluvial channel facies has been drilled in the STA2 borehole in western NL, but, based on its former depositional environment, it is likely that it also exists in all three siting regions. Channel-proximal overspill and overbank facies have been identified in boreholes of all three siting regions.

Gansingen Member (former «Gansinger Dolomit (sensu lato)»): The thickness of the overlying Gansingen Member generally decreases from west to east (JO: ca. 4.5 to 7 m, NL: ca. 1 to 3 m, ZNO: ca. 1.5 to 2 m; Fig. 4-20). In JO, the Gansingen Member consists in the lower part of a dolostone locally with bivalves and ooids. This lower part is partly porous (up to cm-wide vugs and druses; locally brecciated and fractured (Fig. 4-16c). The upper part is mostly laminated, consisting of dolostone, dolomitic and argillaceous marl, locally with microbial mats, teepee structures and desiccation cracks. The NL siting region appears to lie in a transitional area between the depositional environments of JO and ZNO. In general, the facies is similar to JO, but thinner and with lower macroporosity. In the eastern boreholes of NL, the Gansingen Member includes an anhydritic facies at the base similar to ZNO, where it mostly consists of anhydrite (Fig. 4-16d). In the lower part of the Gansingen Member of ZNO, interlayers of claystone and marl occur.

Gruhalde Member (former «Obere Bunte Mergel» and «Knollenmergel»): This unit is separated into a lower and upper part by the Seebi Member in NL and ZNO (Fig. 4-15). In JO the Seebi Member does not occur or is thinner than one metre (Riniken borehole, RIN). The Gruhalde Member in JO has a thickness of ca. 14 to 19 m. The thickness of the lower part of the Gruhalde Member is up to ca. 6 m in NL and varies between ca. 7 to 10 m in ZNO. The thickness of the upper part varies between ca. 11 and 14 m in NL and ca. 16 and 18 m in ZNO. The Gruhalde Member mostly consists of variegated dolomitic marls («normal facies») with argillaceous marl and partly nodular pedogenic dolostone (argillaceous, partly silty to sandy; Fig. 4-16g). Desiccation cracks, local brecciation, bioturbation and plant root tubes are typical phenomena for these deposits.

Seebi Member (former «Stubensandstein (sensu lato)»): The thickness generally increases from southwest to northeast (JO: not occurring or less < 1 m, NL: < 1 – ca. 6 m, ZNO: ca. 9 – 14 m; Fig. 4-21). In NL it consists mostly of dolostone (partly argillaceous), partly brecciated sandy dolostone, argillaceous marl and few interlayers of dolomitic sandstone. The dolostone is partly brecciated. In ZNO, the Seebi Member consists of three parts. In the lower part, argillaceous, dolomitic and partly porous sandstone with interbedded dolostone prevails (Fig. 4-16e). In the middle part, fine-grained dolostone, partly brecciated, is found. In the upper part, dolomitic breccia or dolocrete dominate with partly significant porosity and with vugs up to 10 cm (Fig. 4-16f). The occurrence of brecciated dolocretes with elevated macroporosity seems to increase within ZNO from west to east (Fig. 4-15).

Belchen Member (former «Rhät»): It occurs in the deep boreholes within the siting regions only in Benken (BEN) and TRU1 with a thickness of 0.6 and 1.4 m respectively. It consists mostly of partly bituminous and fossiliferous (thin bone beds) claystone.

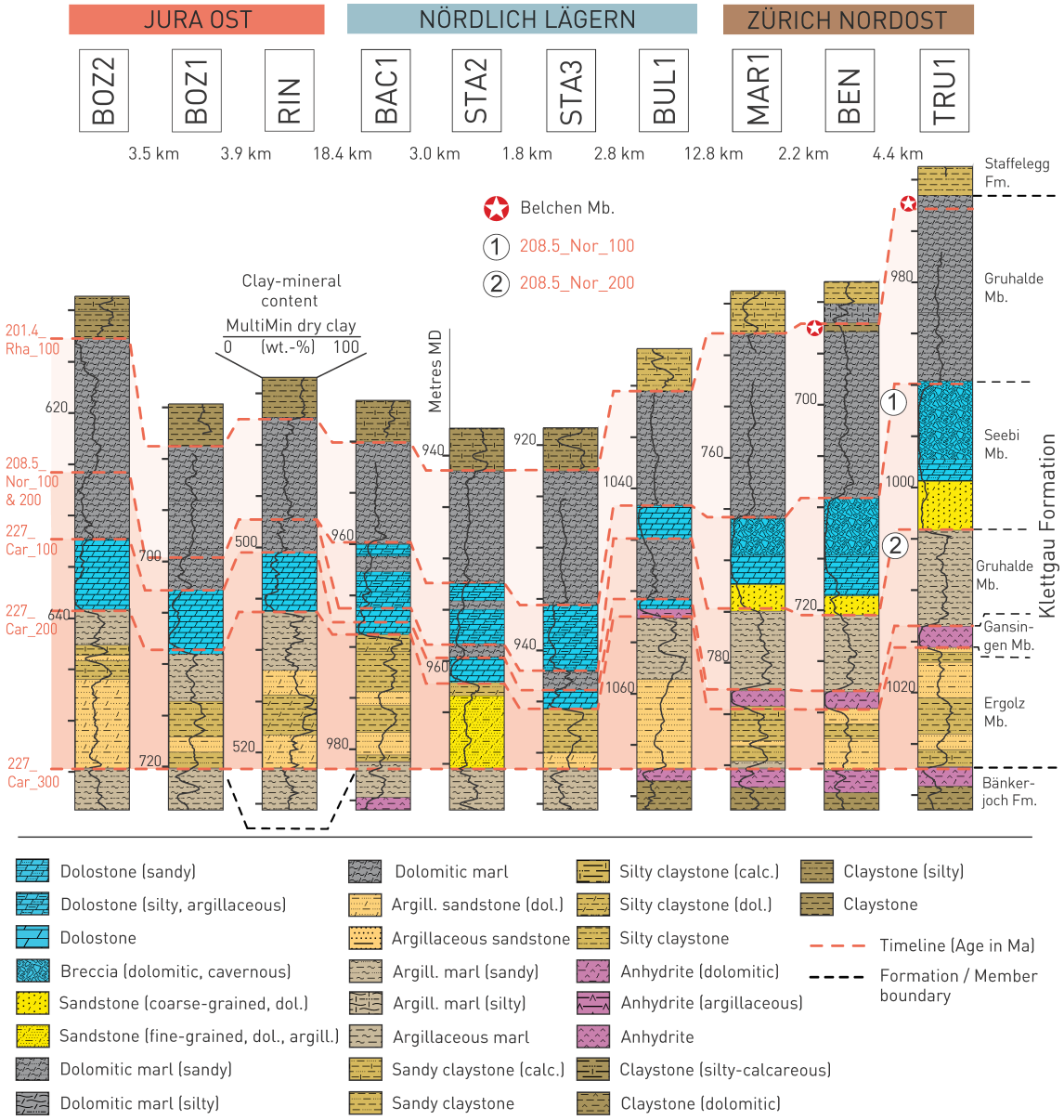


Fig. 4-15: Stratigraphic borehole correlation of the Klettgau Formation

For lithological nomenclature refer to Naef et al. (2019). Clay-mineral content after Becker & Marnat (2024). Some of the boundaries and lithologies as discussed in the original reports were adjusted to integrate all presented borehole data.

4.2.4.3 Variability

The Klettgau Formation is a heterogeneous sedimentary succession with prominent lateral facies changes. In the Ergolz Member, channel, overbank and floodplain facies associations alternate laterally. The sandstones show a great variability in terms of composition, degree of diagenesis and porosity. The «channel facies» is incised in, or flanked by, the overbank and floodplain facies. The most typical channel facies was drilled in STA2, but, based on the inferred depositional environment, it is assumed that this facies may potentially occur in all the siting regions. The Gansingen Member decreases in thickness and shows a general facies trend from dolostone to anhydrite from west to east (along the siting regions). The Gruhalde Member exhibits a similar facies in all three siting regions, but the Seebi Member can be defined only in NL and ZNO. The Seebi Member shows a general facies change from west to east (along the siting regions) with both increasing thickness and macroporosity. Partly porous sandstones in the lower part of the Seebi Member and brecciated dolocretes with vugs have only been found in the boreholes of ZNO, and their occurrence seems also to increase towards the east.

4.2.4.4 Chronology

The Klettgau Formation spans a long time period from the Middle Carnian to the Rhaetian in the Late Triassic, covering up to around 30 million years (Jordan & Deplazes 2019). It has generally only limited age constraints. Four timelines were picked within the Klettgau Formation (227_Car_200, 227_Car_100, 208.5_Nor_200, 208.5_Nor_100) that broadly follow corresponding lithostratigraphic boundaries (Top Ergolz Member, Top Gansingen Member, Top lower part of Gruhalde Member, Top Seebi Member; Fig. 4-15). Between the top of the terrestrial Klettgau Formation and the overlying marine Staffelegg Formation there is a major diachronous unconformity that may encompass more than the entire Rhaetian, i.e. more than seven million years. However, also at the base and within the Klettgau Formation there are several unconformities that seem to have a supraregional character; the most prominent being the Old Cimmerian unconformity that encompasses a gap of several million years (Fig. 4-14). They emphasise the discontinuous character of sedimentation in this depositional environment (Beutler 2005, Jordan et al. 2016a).

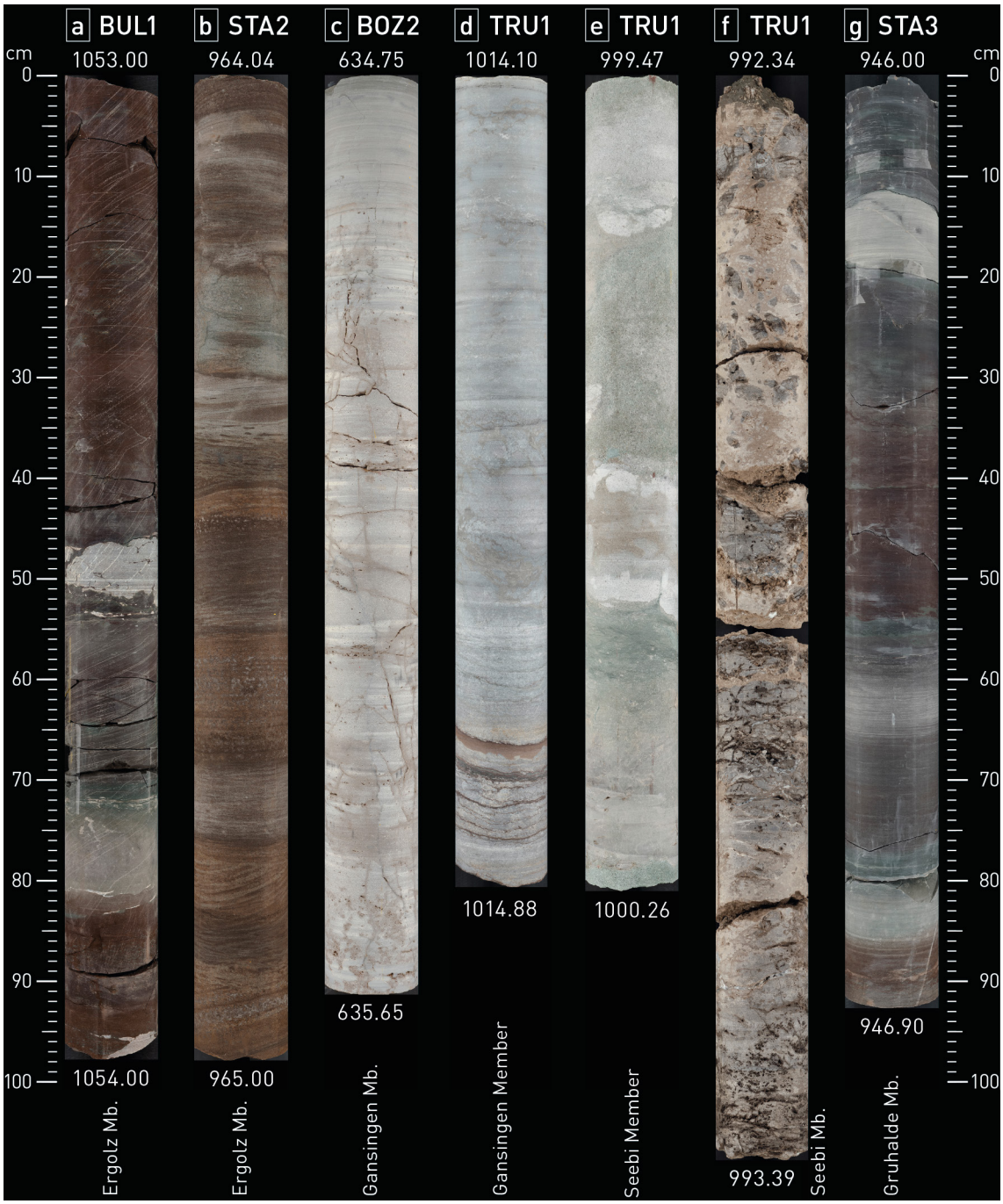
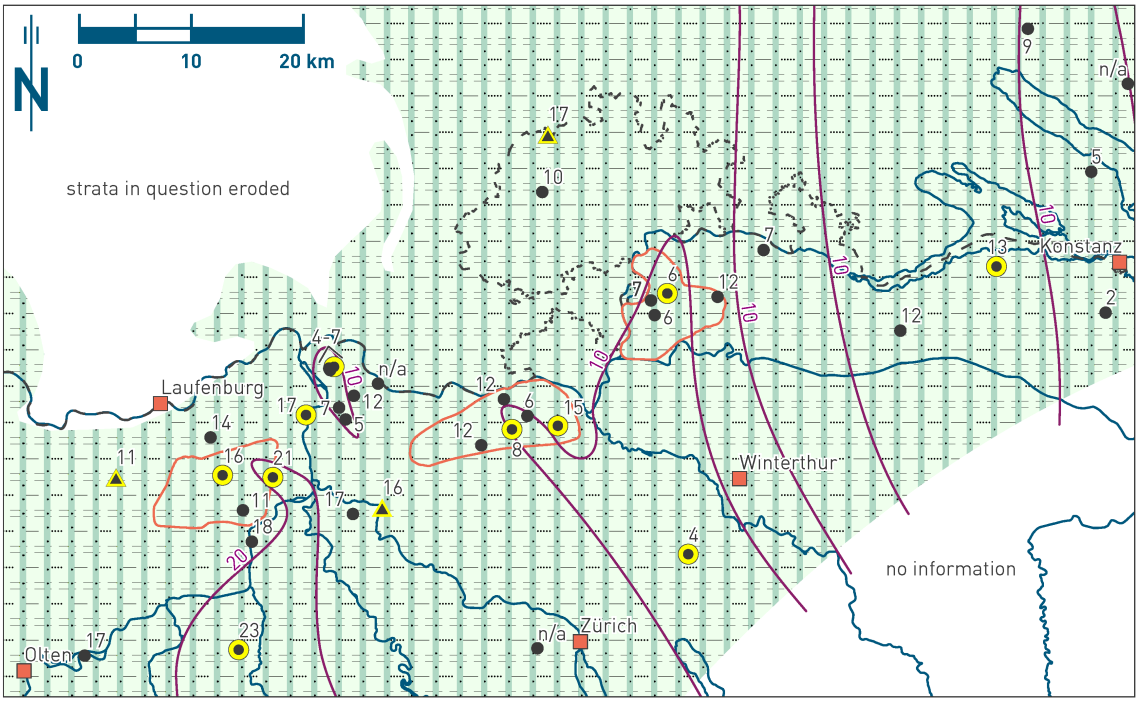


Fig. 4-16: Selected core photos of the Klettgau Formation

(a) Grey violet, red to grey green dolomitic marl (silty) with light grey pedogenic anhydritic nodules (possibly partly dolomitised); **(b)** reddish brown to grey sandstone (dolomitic, argillaceous); fine- to medium-grained, with cross-bedding; **(c)** beige grey dolostone with bivalves, vugs and fracture network; **(d)** light grey to white anhydrite, laminated to nodular with reddish brown, argillaceous laminae at bottom; **(e)** light greenish sandstone (dolomitic), medium- to coarse-grained, with very light grey dolocrete nodules; **(f)** dark grey and pale pink brecciated dolostone, subordinate sandstone and limestone with a texture similar to rauhwacke and frequent vugs; **(g)** pale green and violet argillaceous marl (dolomitic, silty) with light grey nodules and nodular layers, at base reddish brown argillaceous sandstone.



Late Triassic, Middle Carnian / Klettgau Formation, Ergolz Member

Map elements
- Borehole (thickness in m)
- Borehole / outcrop with significant amount of channel and overbank facies (thickness in m)
- Isopachs (m)
- Siting regions

Depositional environment
- Fluvial, channel and overbank
- Fluvial, floodplain

Lithology
- Sandstone, fine
- Sandy claystone to sandstone, fine

Fig. 4-17: Map of depositional environments during the Late Triassic (Middle Carnian) preserved in the Ergolz Member of the Klettgau Formation

Refer to Fig. 4-3 for a schematic representation of depositional environments. The north arrow refers to present-day geographic north.

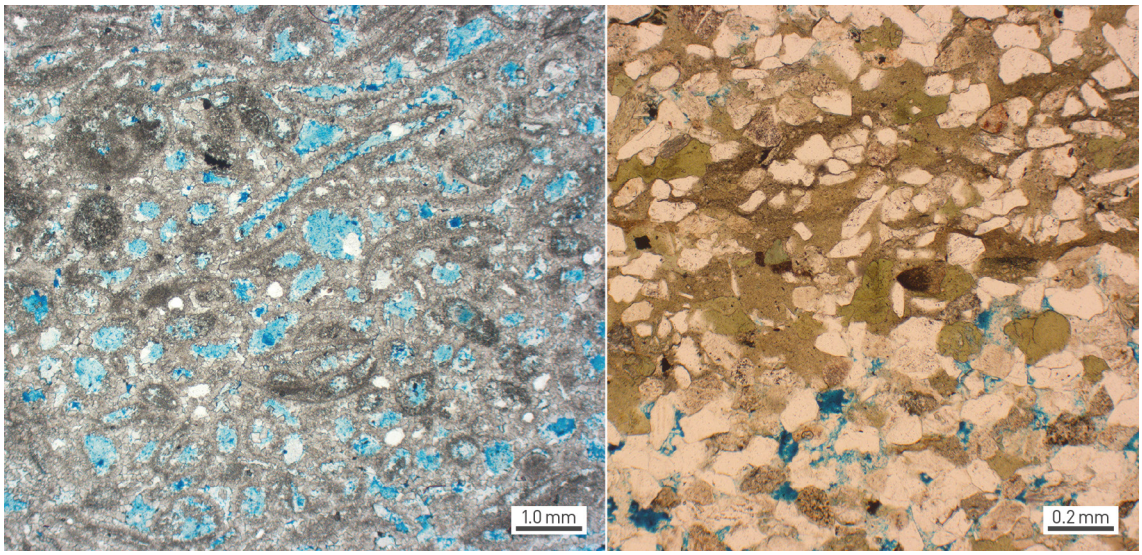


Fig. 4-18: Microfacies of porous dolostone and sandstone with argillaceous matrix and open pores

Pore space filled with blue coloured glue. Left: Originally bioclastic, oolitic limestone which was dolomitised and leached, leading to open pores (leached ooids and bivalves); example from Gansingen Member, BOZ1-1-706.90 (Nagra (ed.) 2022a, Dossier IV). Right: Sandstone (argillaceous) composed of quartz grains and numerous rock fragments (greenish and brown components), as well as argillaceous matrix and open pores. Example from Ergolz Member, BAC1-1-975.74 (Nagra (ed.) 2023a, Dossier IV).



Fig. 4-19: «Channel facies» intercalated with «floodplain facies» in the Ergolz Member at Steigrabe in Hemmiken

«Channel facies» on the right as weathering-resistant sandstone, «floodplain facies» on the left as non-weathering-resistant dolomitic marl (Jordan et al. 2016a).

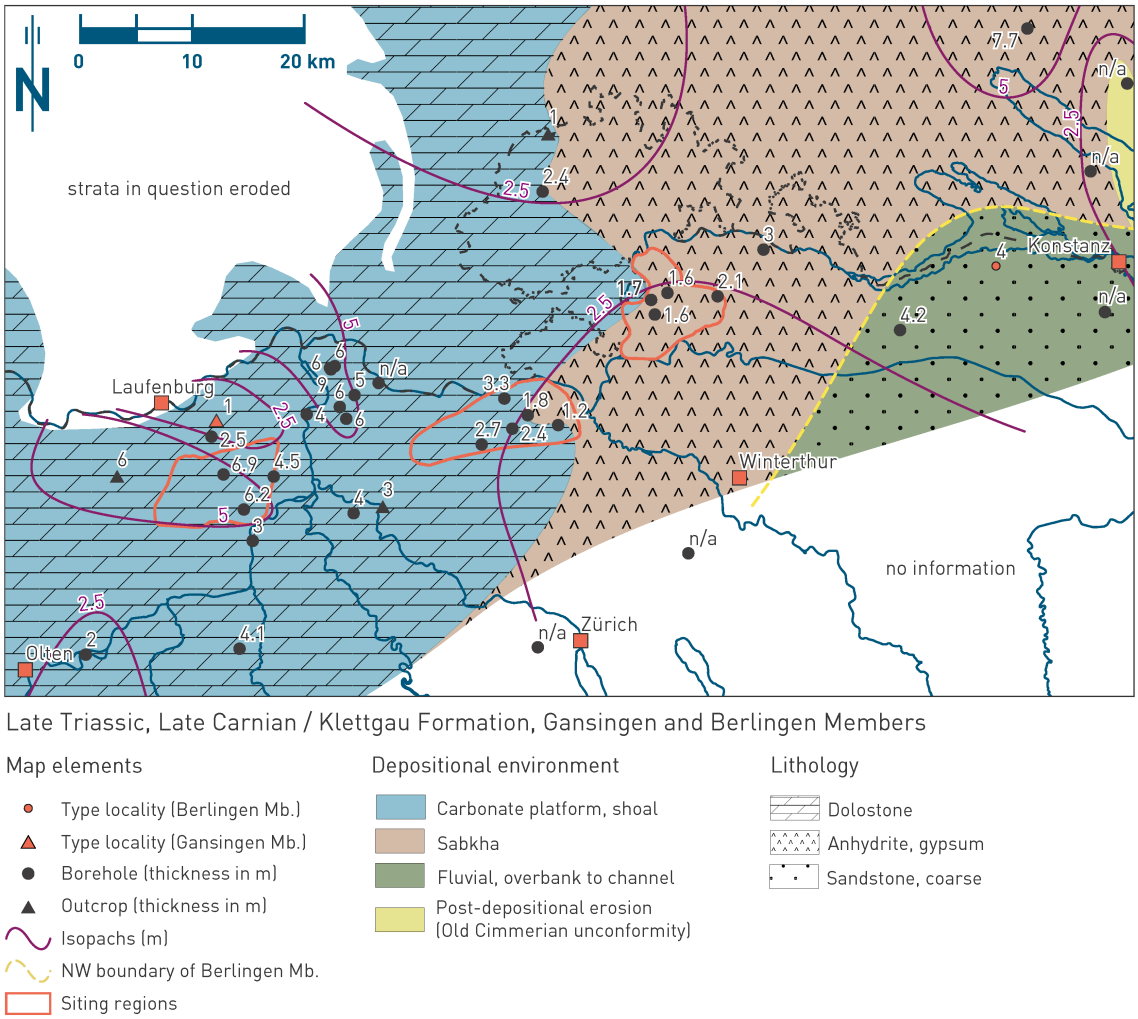


Fig. 4-20: Map of depositional environments during the Late Triassic (Late Carnian) preserved in the Gansingen and Berlingen Members of the Klettgau Formation

Refer to Fig. 4-3 for a schematic representation of depositional environments. The north arrow refers to present-day geographic north.

4.2.4.5 Depositional evolution

The Klettgau Formation was deposited in the southern part of the Central European Basin. During the long time span (some 30 Myr) from Middle Carnian to end Rhaetian, this basin underwent a very complex evolution resulting in a variety of different facies realms (Fig. 4-13). They include terrestrial fluvial and playa environments as well as short marine ingressions. Sedimentary provenance also varies throughout the depositional evolution of the formation. At the beginning it was mostly the southern Norwegian Caledonides (Paul et al. 2008), later the Vindelician – Bohemian Massif (Wurster 1968). During the fluvial periods, channel fill sediments as well as overbank and evaporite sediments have been deposited in a vast continental playa under (semi)arid conditions (Fig. 3-7). The marine ingressions are characterised by up to several metre-scale, partly stromatolitic carbonate layers, anhydrite sabkha sediments and estuarine sandstone. Despite the long period of deposition, the preserved succession is thin. As the deposits are not condensed, it can be assumed that most of the time is represented by gaps in sedimentation. Several erosive phases during deposition can be distinguished that partly resulted in deep incisions into the underlying strata. Even though channel-fill intervals of the Klettgau Formation were associated with very high sedimentation rates, the unit, including the erosive gaps, is characterised by low to very low sedimentation rates (Fig. 4-4, Fig. 4-5, Fig. 4-6). The depositional evolution of the Klettgau Formation is subdivided here into five time intervals:

The first time interval (227_Car_300 to 227_Car_200, Middle Carnian) corresponds approximately to the deposition of dolomitic marls of the Ergolz Member (Fig. 4-15). These dolomitic marls originated in vast floodplains of a playa system («floodplain facies»), which were intersected by fluvial channels («channel facies»; Fig. 4-17). The channels reach depths of at least 7 m (STA2). Between these two facies associations, in a channel-proximal position and in overspills sand and silt layers are interbedded with dolomitic marls («overbank facies»). Dolomitic nodules, desiccation cracks, bioturbation and plant root tubes demonstrate relatively stable phases of soil formation and the development of vegetation covers in the floodplain.

The second time interval (227_Car_200 to 227_Car_100, Late Carnian) primarily corresponds to the Gansingen Member and reflects deposition during a transgression from the southwest, from the Burgundy Gate (Jordan et al. 2016b). From west to east, a shallow marine to lagoonal depositional environment existed (mostly carbonate deposition) that transitioned into a sabkha environment (mostly sulphate deposition), which is bordered by a terrestrial proximal fluvial fan (sandstone deposition, Berlingen Member; Fig. 4-20). This suggests clastic input from the Vindelician – Bohemian Massif. The marine character of the Gansingen Member is also evidenced by the fossil record (Wildi 1976). Locally, the thickness of the Gansingen Member is significantly reduced, and its top is erosive (Jordan et al. 2016a).

The third time interval (227_Car_100 to 208.5_Nor_200, Late Carnian to Norian) corresponds approximately to the deposition of the strata in the lower part of the Gruhalde Member. The prevailing dolomitic marls document a return of a fluvial depositional environment similar to the Ergolz Member. However, at this time the «floodplain facies» were mostly deposited.

The fourth time interval (208.5_Nor_200 to 208.5_Nor_100, Norian) approximately corresponds to the Seebi Member. Proximal fluvial fans reached Northern Switzerland from the northeast and probably from the south (Fig. 3-7, Fig. 4-21). The source was the Vindelician – Bohemian Massif in the northeast and probably its promontory, the Alemannic Land, in the south. The influence of these fans is most evident in the lower part of the Seebi Member in ZNO and decreases towards the west; in JO the Seebi Member is < 1 m thick. In the ZNO siting region the sandy facies was superseded by a more dolomitic facies with brecciated dolocretes with vugs representing a playa environment. In NL the Seebi Member is also dominated by a dolomitic facies but without vugs. In the light of this, it is postulated that particularly the eastern sector of ZNO was dominated by

a playa depositional environment in which evaporitic minerals were formed that were subsequently dissolved leading to the formation of vugs. Towards the west less evaporites were formed, which resulted in reduced macroporosity.

The fifth time interval (208.5_Nor_100 to 201.4_Rha_100, Norian up to Rhaetian) approximately corresponds to the deposition of the strata in the upper part of the Gruhalde Member and the thin Belchen Member, where it survived later erosion. During this time period, mostly dolomitic and argillaceous marls were deposited in floodplains («floodplain facies»), which formed the habitat for plateosaurs (Hofmann & Sander 2014). This terrestrial depositional environment was terminated by a transgression during the Rhaetian (e.g. Schneebeli-Hermann et al. 2018). The sedimentary rocks of the Belchen Member were deposited in an estuarine to shallow marine depositional environment (Looser et al. 2018). Finally, the top of the Klettgau Formation constitutes a major erosive unconformity.

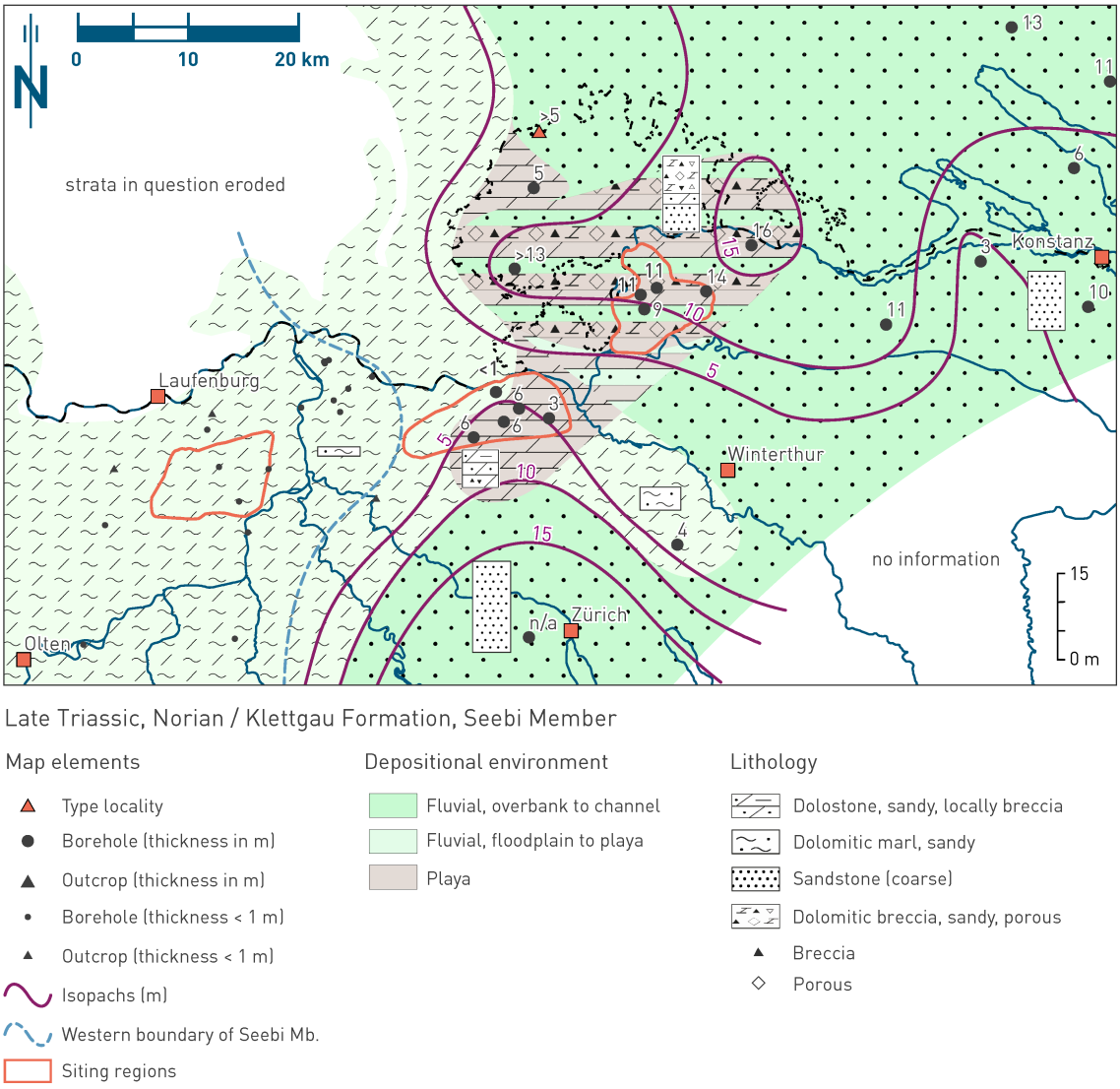


Fig. 4-21: Map of depositional environments during the Late Triassic (Norian) preserved in the Seebi Member of the Klettgau Formation and its western equivalent (part of the Gruhalde Member of the Klettgau Formation)

Refer to Fig. 4-3 for a schematic representation of depositional environments. The north arrow refers to present-day geographic north.

4.2.5 Staffelegg Formation

4.2.5.1 Introduction

The Early Jurassic Staffelegg Formation immediately underlies the Opalinus Clay and is therefore the uppermost stratigraphic element of the lower confining units (Section 4.5.3.9). It corresponds in Northern Switzerland to the Lias Group. The Jurassic was characterised by continued N-S-directed extension during the opening of the Piemont – Liguria Ocean (Chapter 3). The study area was located in a shallow marine epicontinental sea.

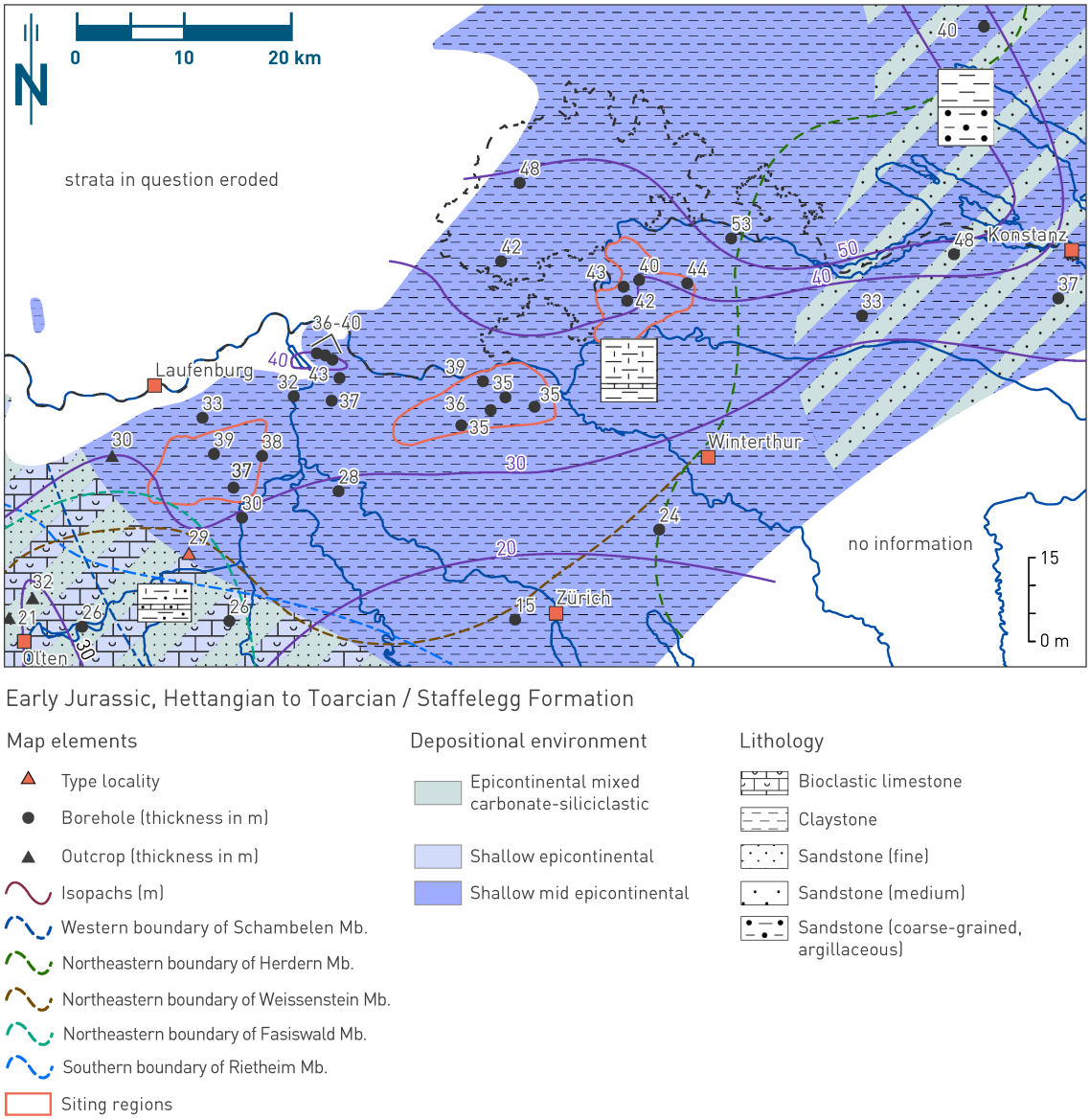


Fig. 4-22: Map of depositional environments during the Early Jurassic (Hettangian to Toarcian) preserved in the Staffelegg Formation

Refer to Fig. 4-3 for a schematic representation of depositional environments. The north arrow refers to present-day geographic north.

4.2.5.2 Facies and lithostratigraphy

The Staffelegg Formation exists in all the siting regions, with generally similar characteristics and a thickness that reaches 35 to 45 m (Fig. 4-22). It consists mostly of claystone, siltstone and marl (Fig. 4-23), but it also comprises limestone and iron-oolite (Fig. 4-24). The Staffelegg Formation can be separated into eight members in the three siting regions (Reisdorf et al. 2011, Kiefer et al. 2015):

Schambelen Member (former «Insektenmergel», «Psiloceras-Schichten»): The lowermost unit of the Staffelegg Formation is the Schambelen Member (Fig. 4-24a). Its thickness varies between ca. 5 and 10 m. It is dominated by sandy/silty claystone (partly bituminous) and siltstone, also fossiliferous marl (mainly bivalves) occurs. These strata are intercalated with dm-thick limestone beds, partly in the form of hardgrounds.

Beggingen Member (former «Arietenkalk» and «Angulatenschichten»): This unit has a thickness of ca. 3 to 4 m (Fig. 4-26) and is dominated by fossiliferous limestone (partly iron-oolitic, limonitic and phosphatic) with interbeds of claystone and argillaceous marl (Fig. 4-24b & c). Various surfaces with borings and/or hardgrounds can be identified. In outcrops such as at the clay pit of Frick Gruhalde Fig. 4-25) cross-bedded limestone occurs, which is generally bioturbated (Reisdorf et al. 2011). A lower limestone succession with iron-oolitic interbeds and an upper limestone succession with abundant ammonites and *Gryphaea* oysters separated by a clay-mineral-rich interval are generally expected. However, this succession is not equally well developed in all boreholes across the siting regions.

Frick Member (former «Obtusus-Ton»): This unit has a thickness between ca. 11 and 16 m and is characterised by monotonous argillaceous siltstone and silty claystone (Fig. 4-24d); macrofossils are rare.

Grünschholz (former «Obliqua-Schichten»), *Breitenmatt* (former «Numismalis-Schichten») and *Rickenbach Members* (former «Amaltheen-Schichten») (from bottom to top): These three units represent highly condensed intervals (Fig. 4-24e). They are often described as one informal stratigraphic unit, as the unambiguous recognition of the three members is difficult. In some boreholes the lowermost Grünschholz Member was identified based on the presence of *Gryphaea obliqua* and its nodular look. The three members reach a total thickness between ca. 2 and 5 m. They are characterised by a fossiliferous (predominantly belemnites) succession of limestone, calcareous and argillaceous marl (all glauconitic) with nodules of phosphorite, siderite and pyrite. Bored surfaces and/or hardgrounds are common.

Rietheim Member (former «Posidonienschiefer»): This unit has a thickness between ca. 4 and 10 m. Its lower part is characterised by laminated bituminous shale with fossiliferous horizons (e.g. bivalves) and distinct cm- to dm-scale, partly laminated and bituminous limestone beds (e.g. «Unterer Stein»; Fig. 4-24f). The upper part is characterised by argillaceous to calcareous marl which is still rich in organic matter.

Gross Wolf Member (former «Jurensis-Mergel»): This unit has a thickness of ca. 3 to 7 m and is dominated by silty to sandy argillaceous to calcareous marl, and decimetre-scale nodular interbeds of fossiliferous limestone (mostly belemnites) (Fig. 4-24g).

To the west and east of the three siting regions, more sandy intercalations occur in the Staffelegg Formation, such as in the Weissenstein and Herdern Members (Fig. 4-26). These members were not identified in the boreholes within the siting regions.

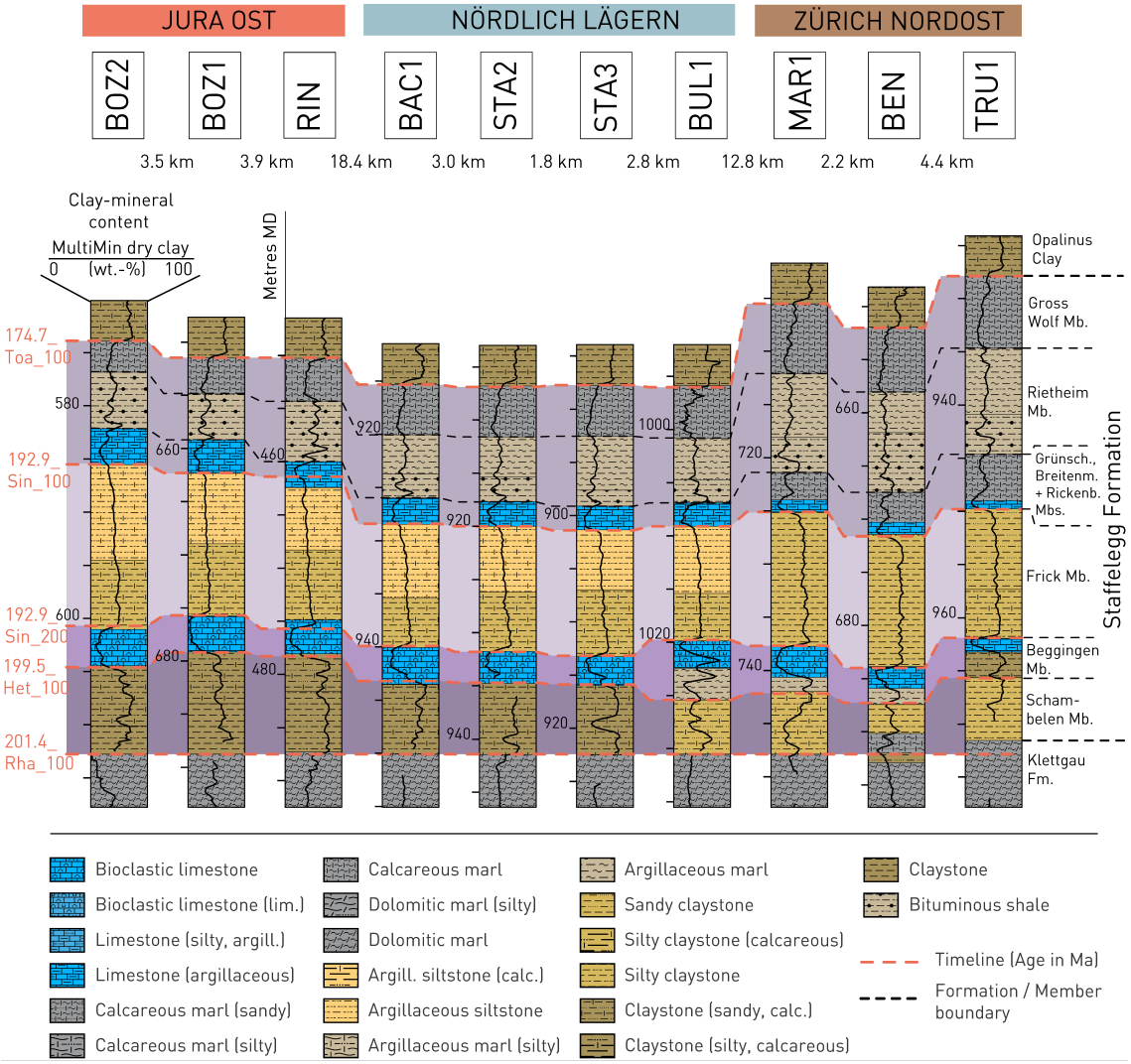


Fig. 4-23: Stratigraphic borehole correlation of the Staffelegg Formation

For lithological nomenclature refer to Naef et al. (2019). Clay-mineral content after Becker & Marnat (2024). Some of the boundaries and lithologies as discussed in the original reports were adjusted to integrate all presented borehole data.

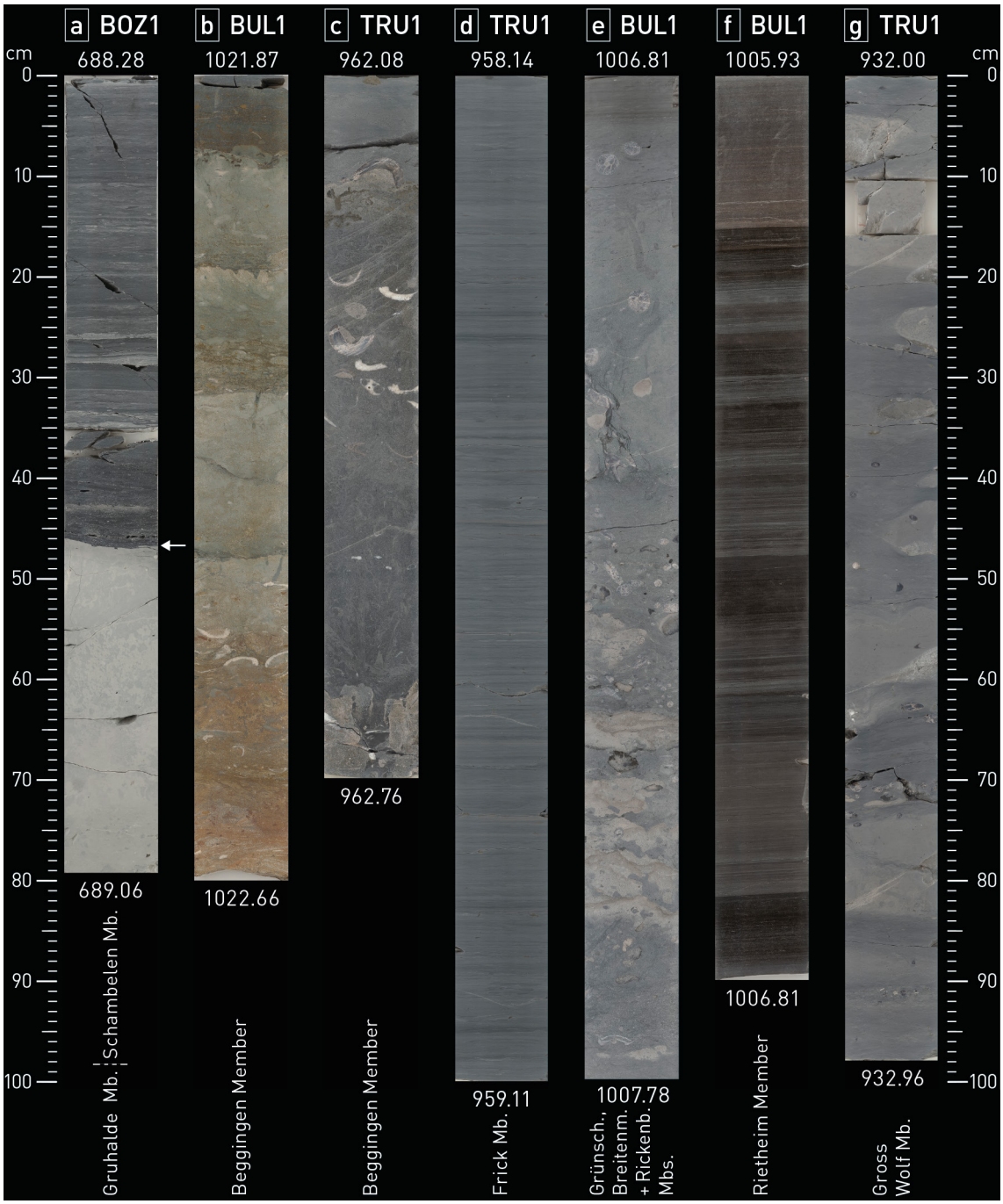


Fig. 4-24: Selected core photos of the Staffelegg Formation (slabbed cores)

(a) Triassic/Jurassic discontinuity with change from terrestrial, light grey, dolomitic marl to marine, dark claystone with silty layers; **(b)** grey to ochre brown limestone (iron-oolitic), fossiliferous with various bored hardgrounds; **(c)** grey bioclastic limestone (partly argillaceous), fossiliferous, phosphatic concretions and two hardgrounds (962.19 m and 962.67 m); **(d)** grey, laminated silty claystone (calcareous); **(e)** grey limestone (partly argillaceous), glauconitic, fossiliferous (belemnites), with several bored and phosphatic hardgrounds; **(f)** dark grey to black, laminated, bituminous shale with limestone bed at top («Unterer Stein»); **(g)** grey calcareous marl with intercalated nodular limestone (both fossiliferous).

4.2.5.3 Variability

The members of the Staffelegg Formation are correlatable between all boreholes (Fig. 4-23). Some lateral facies changes occur, but in general the different facies can be identified in all boreholes. In relation to other Mesozoic formations, thickness variations of the different members are small.



Fig. 4-25: Outcrop of the Staffelegg Formation in the Frick Gruhalde clay pit

The Beggingen Member forms a few-metre-thick limestone succession between the clay-mineral-rich Schambelen and Frick Members. The red arrow denotes a normal fault, which displaces the Beggingen Member (see Section 5.5.4 and Fig. 5-36 for further information). Modified after Nagra (2014b).

4.2.5.4 Chronology

The Staffelegg Formation spans the entire Early Jurassic and thus represents a protracted period of deposition of nearly 30 million years. Three timelines picked within the Staffelegg Formation (199.5_Het_100, 192.9_Sin_200, 192.9_Sin_100; Fig. 4-23) approximately follow lithostratigraphic boundaries (Top Schambelen Member, Top Beggingen Member and Top Frick Member). Within the very bituminous lower part of the Rietheim Member, the negative carbon-isotope excursion of the Toarcian Oceanic Anoxic Event is recognised (e.g. Fantasia et al. 2019). This global Toarcian Oceanic Anoxic Event, together with the C-isotope chemostratigraphy, allows a high-resolution correlation for the boreholes presented here (Wohlwend et al. 2024).

4.2.5.5 Depositional evolution

The Early Jurassic Staffelegg Formation was deposited in a shallow epicontinental sea in a subtropical to tropical climate. The Early Jurassic was characterised by a N-S-directed extension during the opening of the Piemont – Liguria Ocean (Chapter 3). The base of the Staffelegg Formation is a major unconformity (Section 4.2.4). In nearly 30 million years only 35 – 45 m of sedimentary rocks are preserved; the overall sedimentation rates are thus low to very low

(Fig. 4-4, Fig. 4-5, Fig. 4-6). The Early Jurassic is globally characterised by a marine transgression (Haq 2018). The associated deposits in the study area are related to phases of strong condensation, reworking, hiatuses and some intermittent episodes with relatively elevated sedimentation rates (Reisdorf et al. 2011, Kiefer et al. 2015). To the east and south, the epicontinental sea was bordered by the Vindelician Land and its promontory, the Alemannic Land, which successively became an island because of continuous lowering and flooding. These topographically high zones were potential sources for siliciclastic input (Trümpy 1959, Jordan 1983). Overall, the depositional environment appears to have evolved similarly over the entire study area. Lateral facies variability points to the presence of a smaller-scale palaeo-relief on the sea floor and different bottom current conditions. The depositional evolution of the Staffelegg Formation is subdivided here into four time intervals:

The first time interval (201.4_Rha_100 to 199.5_Het_100, mostly Hettangian) approximately corresponds to the strata of the Schambelen Member. This time interval represents the first fully marine depositional environment after the mostly terrestrial Triassic Klettgau Formation. The sedimentary rocks reflect phases with elevated siliciclastic input. More proximal settings with coastal sands of the Alemannic Land and the Vindelician Land characterise areas towards the east and are inferred to exist south of the siting regions.

The second time interval (199.5_Het_100 to 192.9_Sin_200, mostly lower part of Sinemurian) mainly corresponds to the Beggingen Member. During this time interval, calcareous sedimentation dominated (Fig. 4-26). Evidence for condensation such as hardgrounds, iron-oolites and phosphatic nodules is common, supporting the notion of very low sedimentation rates. Sedimentary structures and fossils document the past existence of a shallow, partly very shallow marine setting with potential, localised, short-term emergence (Jordan 1983, Wetzel et al. 1993, Reisdorf & Wetzel 2018), with high current activity and diverse marine fauna.

The third time interval (192.9_Sin_200 to 192.9_Sin_100, within the upper part of the Sinemurian) mainly corresponds to the Frick Member. The depositional environment was characterised by fine-grained siliciclastic input from the Alemannic Land and the Vindelician Land (similar situation as shown in Fig. 3-8). During the deposition of the Frick Member sedimentation rates temporarily increased.

The fourth time interval (192.9_Sin_100 to 174.7_Toa_100, uppermost part of the Sinemurian to end of the Toarcian) corresponds to the time interval during which the Grünschholz up to the Gross Wolf Members were deposited. The first part of this time interval, at the end of the Sinemurian and the Pliensbachian, is again characterised by the deposition of condensed successions indicated by phosphatic hardgrounds and reworked nodules (Grünschholz, Breitenmatt and Rickenbach Members). After a hiatus, the depositional environment was characterised by sedimentation rich in clay minerals and organic material during the Early Toarcian (Rietheim Member). This depositional environment has been extensively studied in Southern Germany, including famous fossil sites such as Holzmaden (Posidonienschiefer Formation). A shallow marine, warm, partly hypersaline and oxygen-poor environment can be reconstructed for the deposition during this interval (Riegraf 1985). Röhl & Schmid-Röhl (2005) favoured a depositional model involving a slow increase of the sea level in a "silled basin" that resulted in stagnant conditions. Alternative depositional models were also discussed. After a further hiatus with pronounced erosion, a phase of condensed deposition in a shallow marine, distal setting with an increased calcareous content is reflected by the Gross Wolf Member.

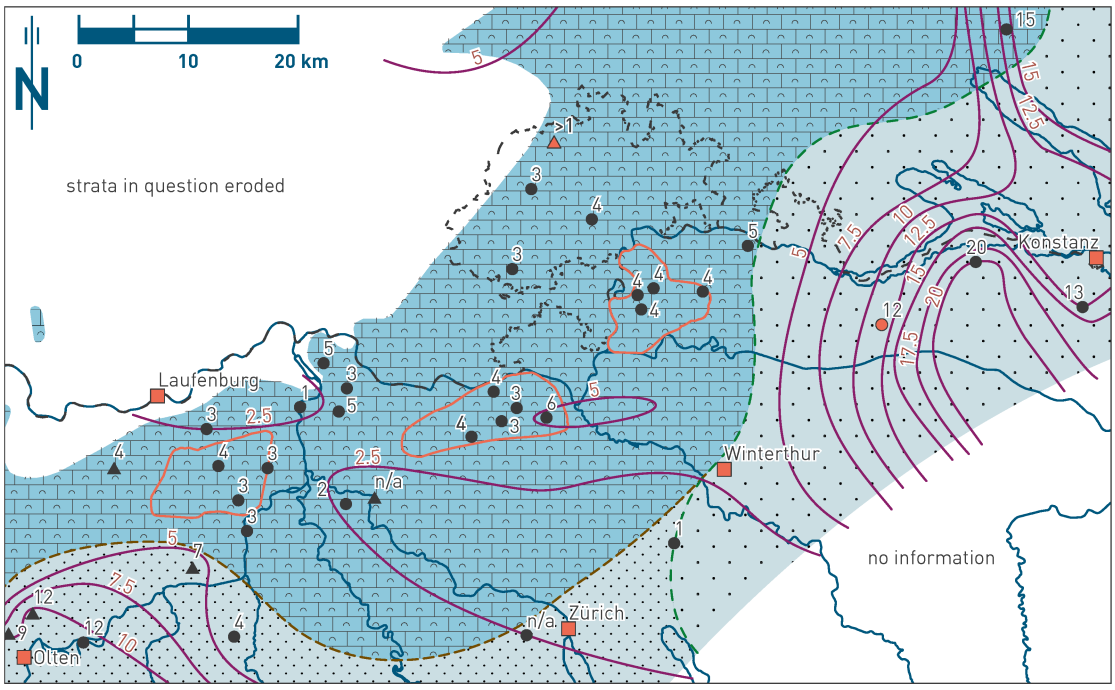


Fig. 4-26: Map of depositional environments during the Hettangian to Sinemurian preserved in the Beggingen and Weissenstein Members and part of the Herdern Member

Refer to Fig. 4-3 for a schematic representation of depositional environments. The north arrow refers to present-day geographic north.

4.2.6 The Opalinus Clay

4.2.6.1 Introduction

The Opalinus Clay host rock exists in all three siting regions with similar facies characteristics and thickness. It was deposited during the Aalenian at the beginning of the Middle Jurassic. During this time period, Central Europe was affected by continued N-S-extension during the opening of the Piemont – Liguria Ocean (Chapter 3). These processes led to subsidence and created accommodation space for the deposition of the thick Opalinus Clay succession. This unit was deposited in a shallow marine epicontinental sea.

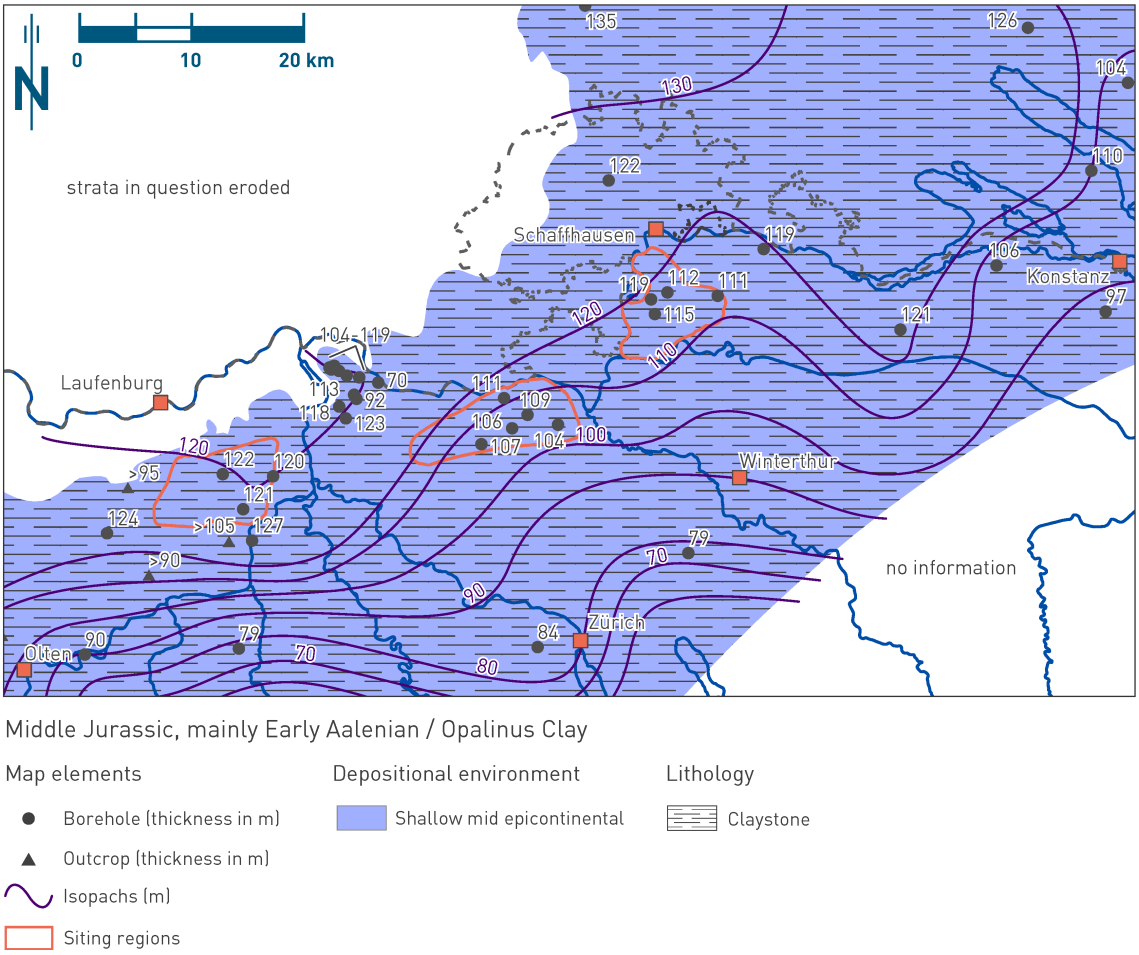


Fig. 4-27: Map of depositional environment during the Middle Jurassic (mainly Early Aalenian) preserved in the Opalinus Clay

Refer to Fig. 4-3 for a schematic representation of depositional environments. The north arrow refers to present-day geographic north.

4.2.6.2 Facies and lithostratigraphy

The Opalinus Clay has the lithostratigraphic rank of a formation (Remane et al. 2005) and forms the lower part of the Dogger Group. The thickness of the Opalinus Clay is ca. 120 m in JO (BOZ2: 122 m, BOZ1: 121 m, RIN: 120 m), ca. 105 – 110 m in NL (BAC1: 107 m, WEI: 111 m, STA2: 106 m, STA3: 109 m, BUL1: 104 m) and ca. 115 m in ZNO (MAR1: 115 m, RHE1: 119 m [calculated true vertical depth TVD], BEN: 112 m, TRU1: 111 m) (Fig. 4-27). The Opalinus Clay consists mostly of a fine sandy and silty claystone and claystone (sandy/silty, calcareous) (Fig. 4-28, Fig. 4-29).

There is no formal subdivision for the Opalinus Clay. In the past it had been subdivided into several dm- to m-scale subunits. This subdivision scheme was applied to the Opalinus Clay strata in the Nagra boreholes drilled in the 1980s and in the Mont Terri rock laboratory (e.g. Matter et al. 1988, Nagra 2001, Hostettler et al. 2017). This subdivision was refined by Mazurek & Aschwanden (2020) and applied to the TBO drilling campaign (Dossier III of TBO reports listed in Tab. 2-1, Fig. 4-28). From bottom to top this subdivision includes the following units: «Clay-

rich sub-unit», «Mixed clay-silt-carbonate sub-unit», «Upper silty sub-unit» and «Sub-unit with silty calcareous beds». The additional «Carbonate-rich silty sub-unit» and the «Lower silty sub-unit» were only identified to the west of the study area.

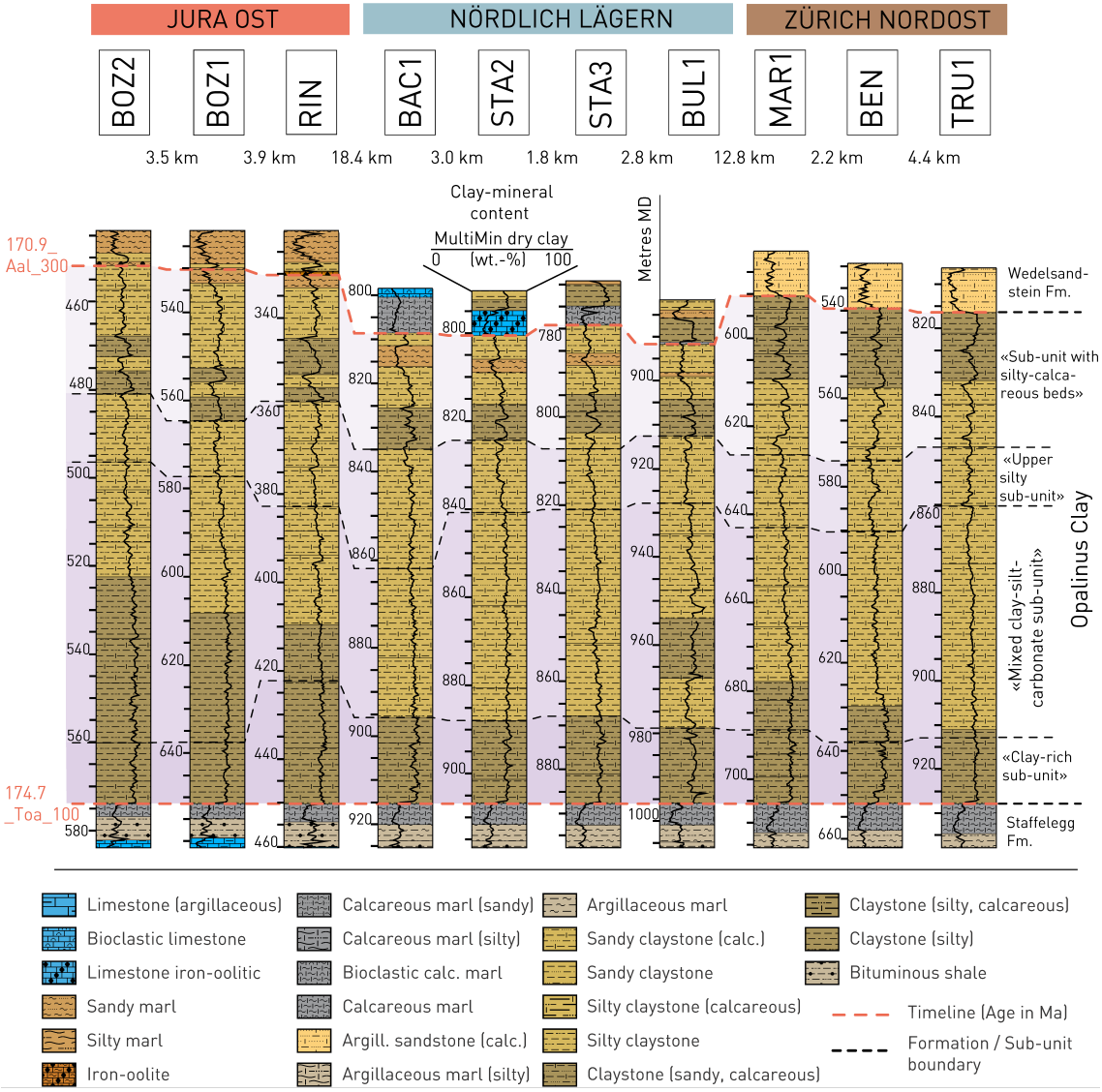


Fig. 4-28: Stratigraphic borehole correlation of the Opalinus Clay

For lithological nomenclature refer to Naef et al. (2019). Clay-mineral content after Becker & Marnat (2024). Some of the boundaries and lithologies as discussed in the original reports were adjusted to integrate all presented borehole data.

Recent multi-proxy studies combining petrographic, petrophysical, geochemical and mineralogical analyses consider lithological heterogeneity on a cm- to dm-scale. Based on these analyses, a new subfacies classification scheme was developed at the Mont Terri rock laboratory by Lauper et al. (2018). This classification was also applied in the study area and developed further by Lauper et al. (2021b) and Zimmerli et al. (2024); the geosynthesis follows these principles. In the study area, the Opalinus Clay is dominated by three subfacies (Fig. 4-30). The argillaceous subfacies 1 (SF1) consists of a dark grey, homogeneous claystone (sandy/silty, calcareous) (Fig. 4-29a to c). Dispersed quartz, mica, feldspar grains and bioclastic fragments occur within the argillaceous matrix. SF1 dominates the lower half of the Opalinus Clay and repeatedly occurs in boreholes of NL and ZNO in the approximately uppermost part of this unit. The laminated subfacies 2 (SF2) is a silty claystone with lenticular bedding (Fig. 4-29d and e). It shows an alternation of a dark grey, argillaceous matrix and continuous to discontinuous, light grey, quartz and bioclastic-rich lenses (thickness: few mm to few cm). Most lenses are cemented by a sparitic Fe-calcite. The lenticular subfacies 3 (SF3) consists of a silty and fine sandy claystone. This subfacies has a lenticular to wavy-bedded texture. The lenses become thicker from a few mm to several cm and the argillaceous matrix contains more quartz grains and bioclastic fragments than the previous subfacies types. SF2 and SF3 may occur over the entire thickness of the Opalinus Clay, except in the lowermost part (Fig. 4-30). Additionally, sideritic nodules and layers (Fig. 4-29b) may be found throughout the Opalinus Clay; they occur particularly frequently in approximately the second quarter of the Opalinus Clay (from the bottom). The sandy subfacies 4 (SF4) and the bioclastic subfacies 5 (SF5), as defined by Lauper et al. (2018) in the Mont Terri rock laboratory, were not identified in the boreholes of the study area. Zimmerli et al. (2024) define an additional homogeneous/deformed subfacies 6 (SF6). This subfacies is characterised by homogenised, folded, deformed or tilted structures related to soft-sediment deformation. It is dominated by clay minerals, calcite and quartz grains and may occur in approximately the second and third quarters of the Opalinus Clay. In the approximately uppermost quarter of the Opalinus Clay, additional cm- to dm-scale beds of silty limestone and limestone (iron-rich) (Fig. 4-29f and g) occur. The silty limestone consists of silt- to sand-sized quartz grains, with micas, feldspars, bioclastic fragments, clay minerals, pseudosparitic calcite cement, and minor pyrite, and is highly bioturbated. The iron-rich or ferruginous limestone contains abundant bioclastic debris, lithoclasts, and some concretions.

4.2.6.3 Variability

Overall, the Opalinus Clay has similar sedimentological characteristics in all investigated boreholes of the three siting regions. The lateral and vertical lithological variability is generally small compared with other Mesozoic formations of Northern Switzerland. The succession of sub-units or subfacies trends can generally be correlated over all borehole sites (Fig. 4-28, Fig. 4-30). However, local facies differences occur and the possibility to correlate units improves with a detailed look at the individual siting regions. For example, the approximately uppermost part of the Opalinus Clay retrieved from the boreholes of JO is richer in fine sand and silt, and less argillaceous compared to NL and ZNO. Special attention must be paid to the occurrence of characteristic calcareous and/or iron-rich beds to further investigate correlatable strata within the Opalinus Clay. Wohlwend et al. (2024) and Zimmerli et al. (2024) propose six potential marker beds or horizons, at least at local scale (Fig. 4-30). Most of these beds occur in the approximately uppermost quarter of the Opalinus Clay. Within the NL and ZNO siting regions, the correlation of these beds appears to be quite robust, with the exception of Bed-II which represents a correlation with high uncertainty. The correlation towards and within JO is generally less reliable.

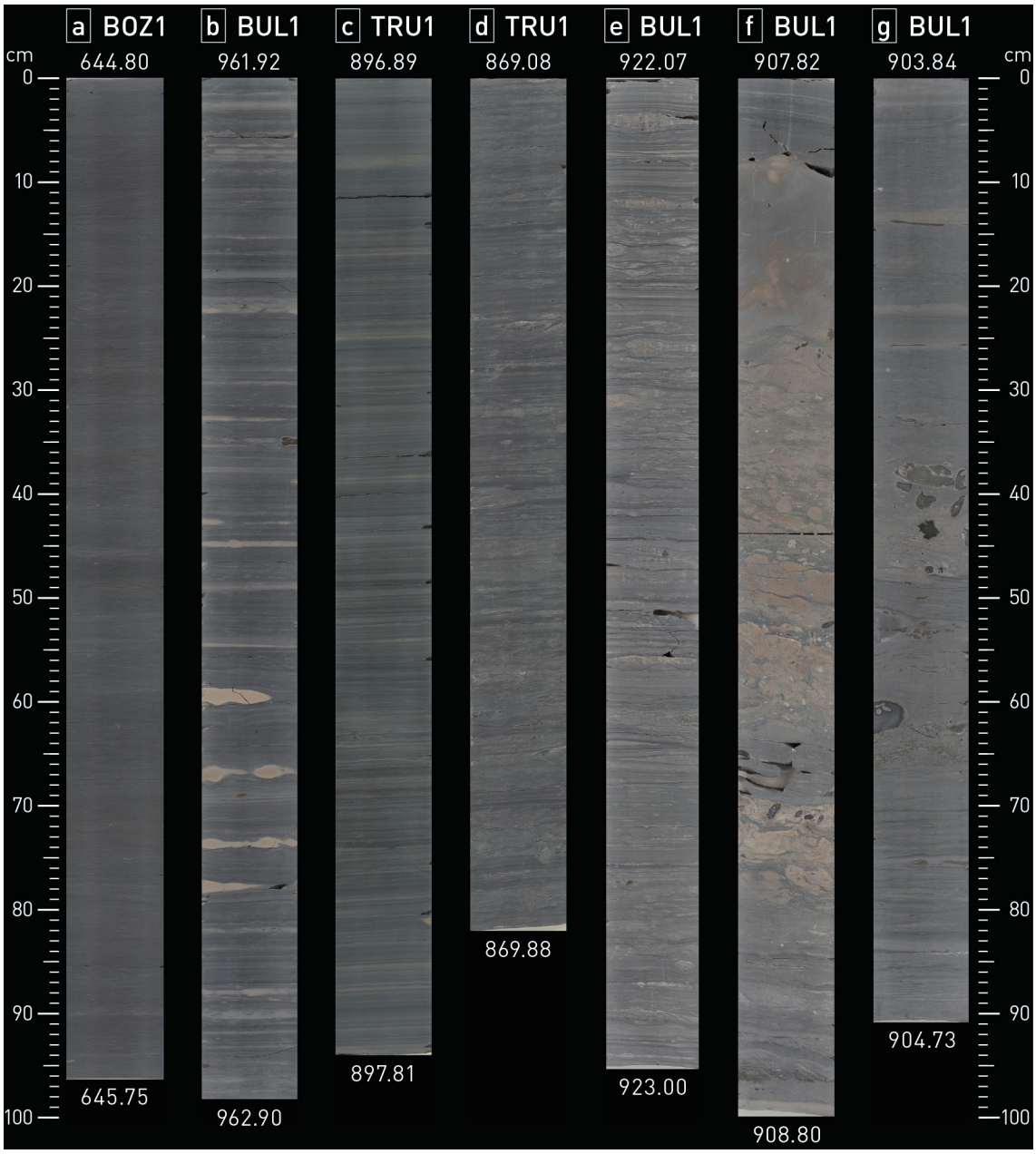


Fig. 4-29: Selected core photos of the Opalinus Clay (slabbed cores)

(a) Dark grey claystone (silty), sparsely pyritic, scattered fine bioclasts and pyritised burrows (SF1); **(b)** dark to medium grey, laminated claystone (silty) with light grey layers and lenses of siltstone with beige siderite nodules (SF1); **(c)** dark to medium grey, laminated silty claystone (calcareous) with light grey, more silty to sandy layers (SF1); **(d)** dark grey sandy claystone with lenticular-bedded light grey lenses of siltstone and light grey sandy marl, rippled, bioturbated (SF2); **(e)** medium grey laminated to bioturbated sandy claystone (silty), with abundant light grey lenses of silt to sand, rippled (mostly SF2, towards SF3); **(f)** partly iron-rich succession of several firm- to hardgrounds, lithoclasts, calcareous marls and bioclastic limestone (argillaceous), ooids (former iron-mineral composition replaced by calcite); **(g)** medium to dark grey silty to sandy claystone (calcareous), with light grey lenses of mostly siltstone, rippled with beige limestone lithoclasts (904.18 to 904.48 m), densely bored (SF1 to SF2 with iron-rich limestone).

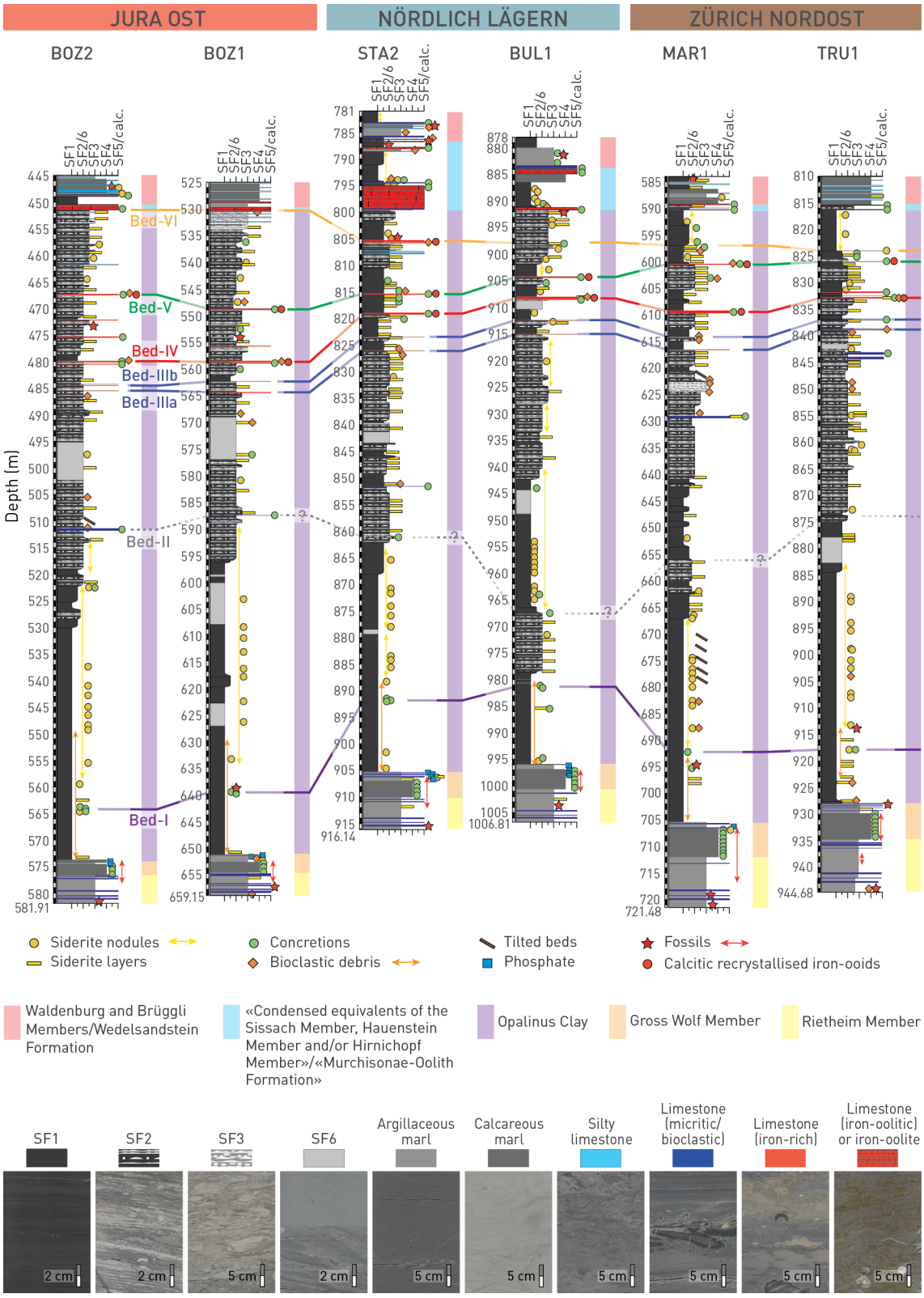


Fig. 4-30: Subfacies classification and lithologies of the Opalinus Clay and adjacent formations in boreholes of Northern Switzerland

Modified after Zimmerli et al. (2024).

The Middle Jurassic Opalinus Clay was mainly deposited during the Opalinum ammonite Zone of the Early Aalenian. To improve the chronology within the Opalinus Clay, the combination of biostratigraphy, based on ammonites and palynomorphs, and stable carbon-isotope chemostratigraphy, measured on inorganic carbonates and organic matter, was applied (Wohlwend et al. 2024). In the uppermost part of the Staffelegg Formation (Rietheim Member), the global negative carbon-isotope excursion of the Toarcian Oceanic Anoxic Event was detected in all boreholes of the three siting regions. This demonstrates the reliability of C-isotopic chemostratigraphy (Section 4.2.5). In the lower part of the Opalinus Clay, an additional, slightly less negative C-isotope shift in the organic matter was detected in the Opalinum Subzone of the Opalinum Zone. This negative shift is as well correlatable across all boreholes of the three siting regions. Within most of the Opalinus Clay, the C-isotopes of the organic matter are very constant or only show slight changes. However, a clear increase in C-isotope values of organic matter can be traced in the uppermost part of the Opalinus Clay that can be allocated to the Bifidatum Subzone of the Opalinum Zone by ammonites and palynomorphs. The positive isotope increase coincides with a calcareous, iron-rich bed and is well expressed in the boreholes of NL (Bed-VI in Fig. 4-30). The facies (e.g. amount of iron-oolites) and thickness of this bed change laterally, but it apparently marks a more or less synchronous event of condensation in all boreholes. Therefore, these types of beds can be used in a first step to define timelines on a local to regional scale. In the Opalinus Clay, six beds were picked in the boreholes that might represent timelines (Fig. 4-30). Bed-I, -III to -VI have a medium to good confidence level, whereas Bed-II has a low confidence level.

4.2.6.4 Depositional evolution

The Middle Jurassic Opalinus Clay was deposited in a shallow epicontinental sea in a subtropical to tropical climate (Wetzel et al. 2003, Lauper 2021, Wetzel & Allia 2003). During the Middle Jurassic, Europe continued to be affected by the development of the Piemont – Liguria Ocean (Chapter 3). For the Early Aalenian, an overall regressive trend was suggested for the epicontinental Central European Basin (Lauper et al. 2021a, Zimmermann et al. 2018). The epicontinental sea was surrounded by the Rhenish Massif to the north, the Vindelician – Bohemian Massif to the east, the Alemannic Land to the south and the very shallow area in the Burgundy area to the west (Fig. 3-8). Siliciclastic input to the epicontinental basin could have come from the nearby landmasses or long-distance transport from Fennoscandia. Absolute water depth was estimated to about 20 to 50 m (Allia 1996, Wetzel & Allia 2003), but may also have been deeper at least temporarily (Fig. 4-31). The large accommodation space needed to deposit the thick Opalinus Clay in a relatively shallow water environment – particularly considering uncompacted sediment thicknesses – was provided by regional subsidence (Wetzel & Allia 2003). Subsidence led to a depositional environment that became differentiated into subtle swells and depressions, thought to have had an important impact on thickness and facies variations of the Opalinus Clay (Wetzel & Allia 2000, 2003, Lauper et al. 2021a).

The lower lithostratigraphic boundary of the Opalinus Clay coincides with the Toarcian-Aalenian boundary within the available biostratigraphic resolution in the study area in Northern Switzerland. Towards the west, in the Mont Terri rock laboratory, the deposition of the Opalinus Clay had already begun by the Late Toarcian (Hostettler et al. 2017). In general, the entire Opalinus Clay exhibits a shallowing-upward trend, with more homogeneous claystone at the bottom and increasing silt and fine sand towards the top, which may reflect the overall regressive trend observed in the Early Aalenian. Different authors have postulated additional cyclic facies trends such as coarsening-upward cycles ("Dachbankzyklen") (Allia 1996, Wetzel & Allia 2003, Lauper et al. 2021a, Leu et al. 2023). The intervals between the correlatable beds presented here (Fig. 4-30) have been interpreted as coarsening-upward cycles that correspond to shallowing-upward regressive trends (Zimmerli et al. 2024). As pointed out earlier, the definition of such trends is more difficult in the lower and middle parts of the unit compared to the uppermost

sectors; in the upper layers, calcareous and iron-rich beds are more common and can be correlated at local to regional scales. These beds appear to trace phases of reduced sedimentation and slight stagnation to condensation. The increased occurrence of these calcareous beds in the upper part could indicate that sedimentation rates decreased towards the top. Conversely, the sedimentation rates of the thicker, lower part of the Opalinus Clay were probably very high (Fig. 4-4, Fig. 4-5, Fig. 4-6).

Zimmerli et al. (2024) defined an additional homogeneous/deformed subfacies 6 (SF6) characterised by homogenised, folded, deformed or tilted strata. It is interpreted to reflect mass-wasting events of different scales within the basin.

The more sandy-silty expression of the uppermost part of the Opalinus Clay as seen in the boreholes of JO could indicate an additional or stronger input of quartz- and feldspar-rich detritus (interval between marker bed Bed-V and Top Opalinus Clay; Fig. 4-30). The upper boundary of the Opalinus Clay was correlated to a regression discontinuity (Burkhalter 1996). Lauper et al. (2021a) also identified the top of the Opalinus Clay as a diachronous discontinuity (Fig. 4-34) and linked its genesis to sediment bypassing.

The Opalinus Clay is generally described as a tempestite-dominated deposit (Allia 1996, Wetzel & Allia 2003, Lauper et al. 2018; Fig. 4-31a). During storm events, continental detritus and bioclastic elements were inferred to have been mobilised, reworked, and transported into the basin. In this model, coarser and finer lithologies reflect more proximal and distal tempestites, respectively. Depending on the position relative to the storm-wave base and bathymetry, facies and thickness variations developed. Modern analogues can be found in the North Sea and the Baltic Sea (Aigner & Reineck 1982, Milkert 1994, Wetzel & Allia 2003).

Recently, alternative depositional models have been postulated, including drift deposits (Zimmerli et al. 2024; Fig. 4-31b). Drift deposits are in general fine-grained sedimentary bodies that develop due to the interaction of continuous bottom currents and bathymetry of the sea floor. Potential past analogues of such drift deposits exist, albeit in deeper settings, in the hemipelagic Early Jurassic Laurasian Seaway in the Cardigan Bay Basin, UK (Pieńkowski et al. 2021) or in the deposits of the Upper Jurassic/Lower Cretaceous Vaca Muerta Formation in the Argentine Neuquén Basin (Paz et al. 2022). Muddy shallow-water drifts (ca. 150 – 300 m) can for example be found on the south-western shelf of Mallorca (Verdicchio & Trincardi 2008, Vandorpe et al. 2011). The evidence for the occurrence of drift deposits on top of the Opalinus Clay below the «Herrenwis Unit» in a similar general setting (Section 4.2.7.5) supports the importance of currents for sediment transport and deposition in the environment of the Opalinus Clay.

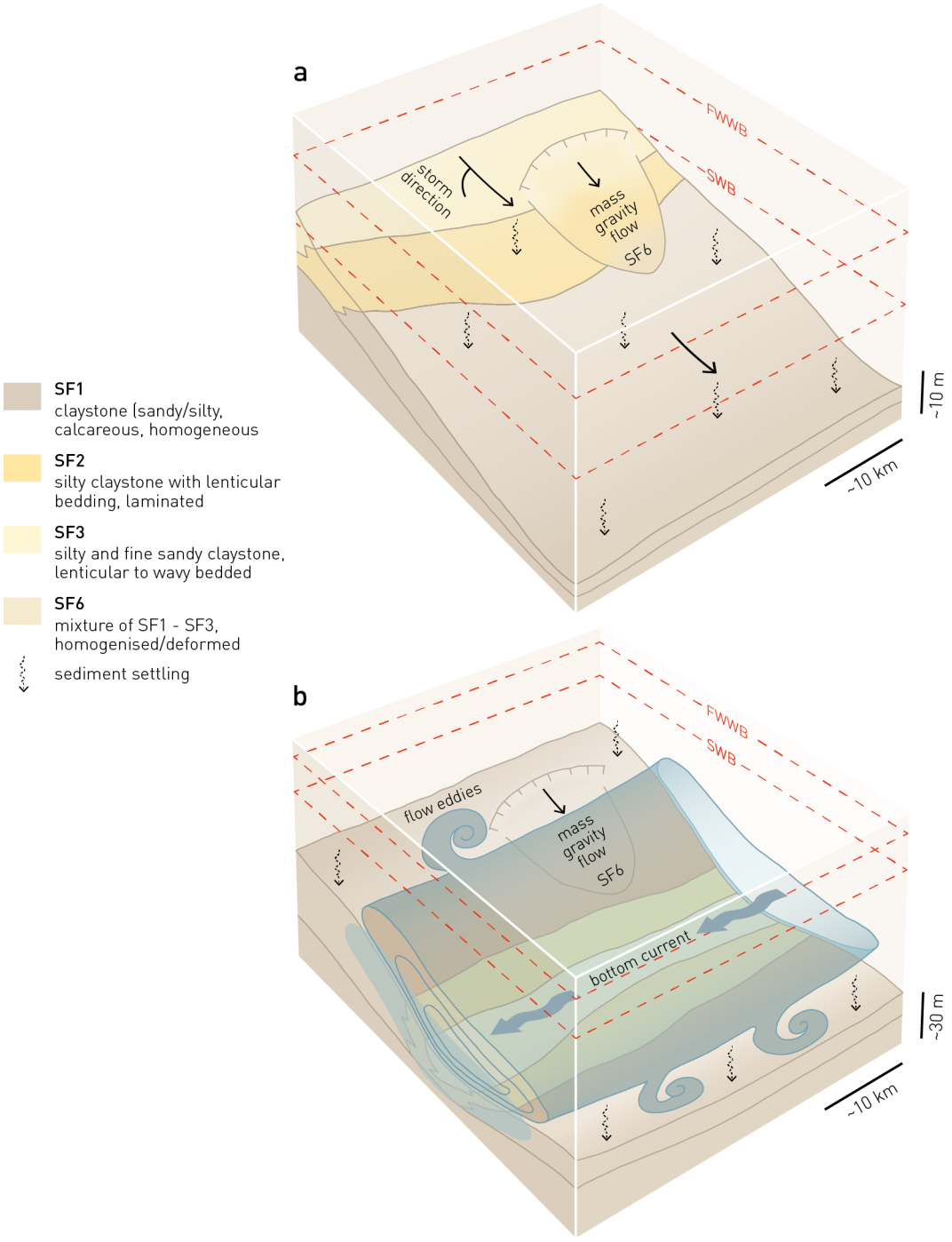


Fig. 4-31: Block diagrams showing depositional models of the Opalinus Clay in Northern Switzerland

Sediment transport dominated by (a) storm events (tempestites) or (b) bottom currents (drift deposits). The depositional models are inspired by investigations of Lauper et al. (2018), Rebesco et al. (2014), Wetzel & Allia (1996, 2003) and Zimmerli et al. (2024). SF: subfacies, FWWB; fair-weather wave base, SWB; storm wave base.

4.2.7 Dogger Group above Opalinus Clay

4.2.7.1 Introduction

The sedimentary units of the Dogger Group that directly overlie the Opalinus Clay form the lowermost and most important part of the upper confining units (Section 4.5.3.5). They were deposited in the Middle Jurassic. At this time, Central Europe was affected by the development of the Piemont – Liguria Ocean, resulting in large-scale N-S-directed extension leading to subsidence (Chapter 3). The Dogger Group above Opalinus Clay was deposited in a shallow epicontinental sea with some lateral and vertical facies variability (Fig. 4-32).

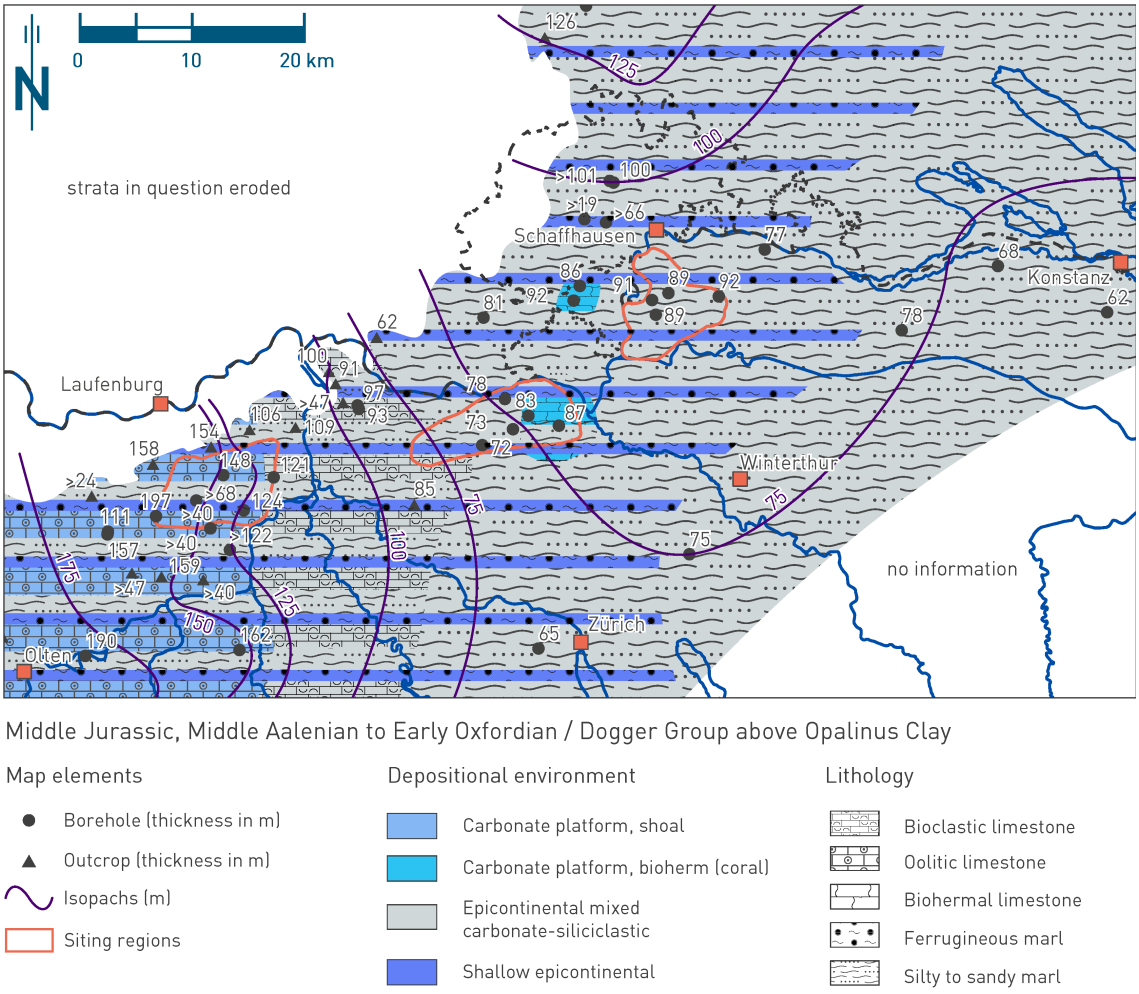


Fig. 4-32: Map of depositional environments during the Middle Jurassic (Middle Aalenian to Early Oxfordian) preserved in the Dogger Group above Opalinus Clay

Refer to Fig. 4-3 for a schematic representation of depositional environments. The north arrow refers to present-day geographic north. Map shows the setting during the time interval 170.9_Aal_300 to 154.8_Oxf_975 as discussed in the text.

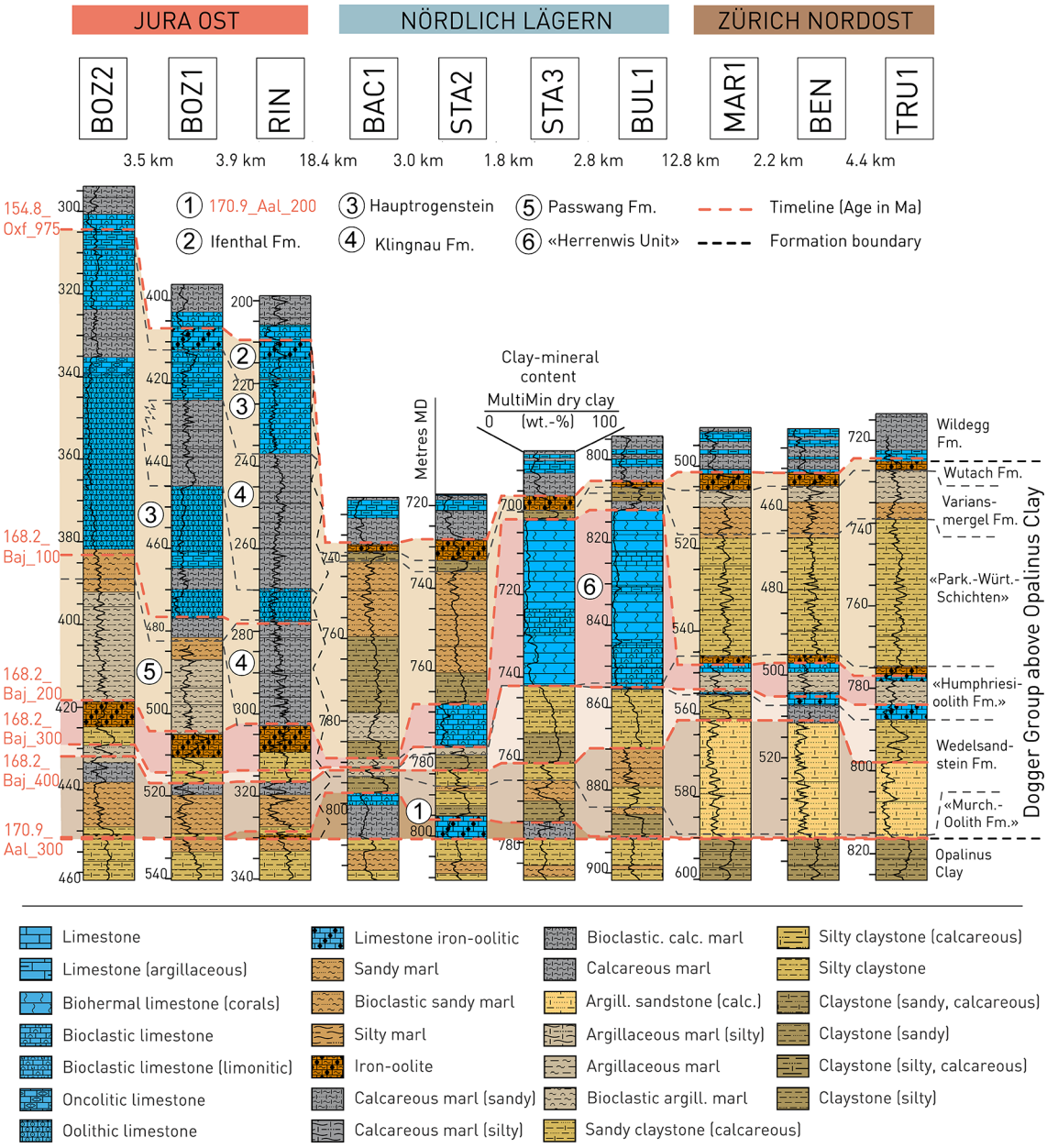


Fig. 4-33: Stratigraphic borehole correlation of the units of the Dogger Group above Opalinus Clay

For lithological nomenclature refer to Naef et al. (2019). Clay-mineral content after Becker & Marnat (2024). Some of the boundaries and lithologies as discussed in the original reports were adjusted to integrate all presented borehole data.

4.2.7.2 Facies and lithostratigraphy

For the Dogger Group above Opalinus Clay, a different lithostratigraphic nomenclature is used for the JO compared to the NL and ZNO siting regions (Fig. 4-33, Fig. 4-34, Fig. 4-35). In the lower part this is partly because of historical reasons (e.g. Bläsi et al. 2013). In the middle part, a general facies trend from a more proximal to distal setting relative to the Celtic Platform (Fig. 3-9) emphasises the usefulness of different nomenclature (Fig. 4-32). In the upper part, starved sedimentation dominates in the three siting regions. The lithostratigraphy of the Dogger Group above Opalinus Clay integrates several informal units (marked with chevrons) and will likely be revised in the near future.

With the exception of the Hauptrogenstein and the «Herrenwis Unit», the Dogger Group above Opalinus Clay consists mostly of silty to sandy claystone (partly calcareous) and argillaceous, calcareous to silty or sandy marl (Fig. 4-36). Intercalated in these clay-mineral-rich sedimentary rocks are single or successions of more weathering-resistant "hard beds" (Bläsi et al. 2013). In general, three types of "hard beds" can be distinguished that are mainly based on their lithology: 1) biomicritic limestone, 2) silty to sandy, bioclastic limestone, and 3) iron-oolite or iron-oolitic beds.

Dogger Group above Opalinus Clay in JO

In JO the Dogger Group above Opalinus Clay starts with the Passwang Formation (Burkhalter 1996). It consists mostly of silty claystone, argillaceous siltstone and silty to sandy marl with non-porous, calcareous and iron-oolitic interbeds. Its thickness decreases from ca. 60 m (BOZ2) in the west to ca. 30 m (Riniken borehole, RIN) in the east (Fig. 4-33). The Passwang Formation is overlain by the strata of the carbonate platform of the Hauptrogenstein (Gonzalez & Wetzel 1996), which mostly consist of bedded oolitic and bioclastic limestone and some calcareous marl. The Hauptrogenstein platform interfingers towards the east with its more basinal counterpart of the Klingnau Formation. The composite thickness of the Hauptrogenstein decreases from ca. 80 m (BOZ2) in the west to 26 m (RIN) in the east. The Klingnau Formation consists mostly of calcareous and argillaceous marl. It is classified as a formation, but only if it reaches a thickness of > 15 m (Nagra (ed.) 2022a, Dossier IV) and has a composite thickness of ca. 60 m in the east (RIN). The Dogger Group above Opalinus Clay is completed with the Ifenthal Formation (Bitterli-Dreher 2012), which consists of a 5 – 10 m thick succession of partly iron-oolitic limestone and calcareous marl.

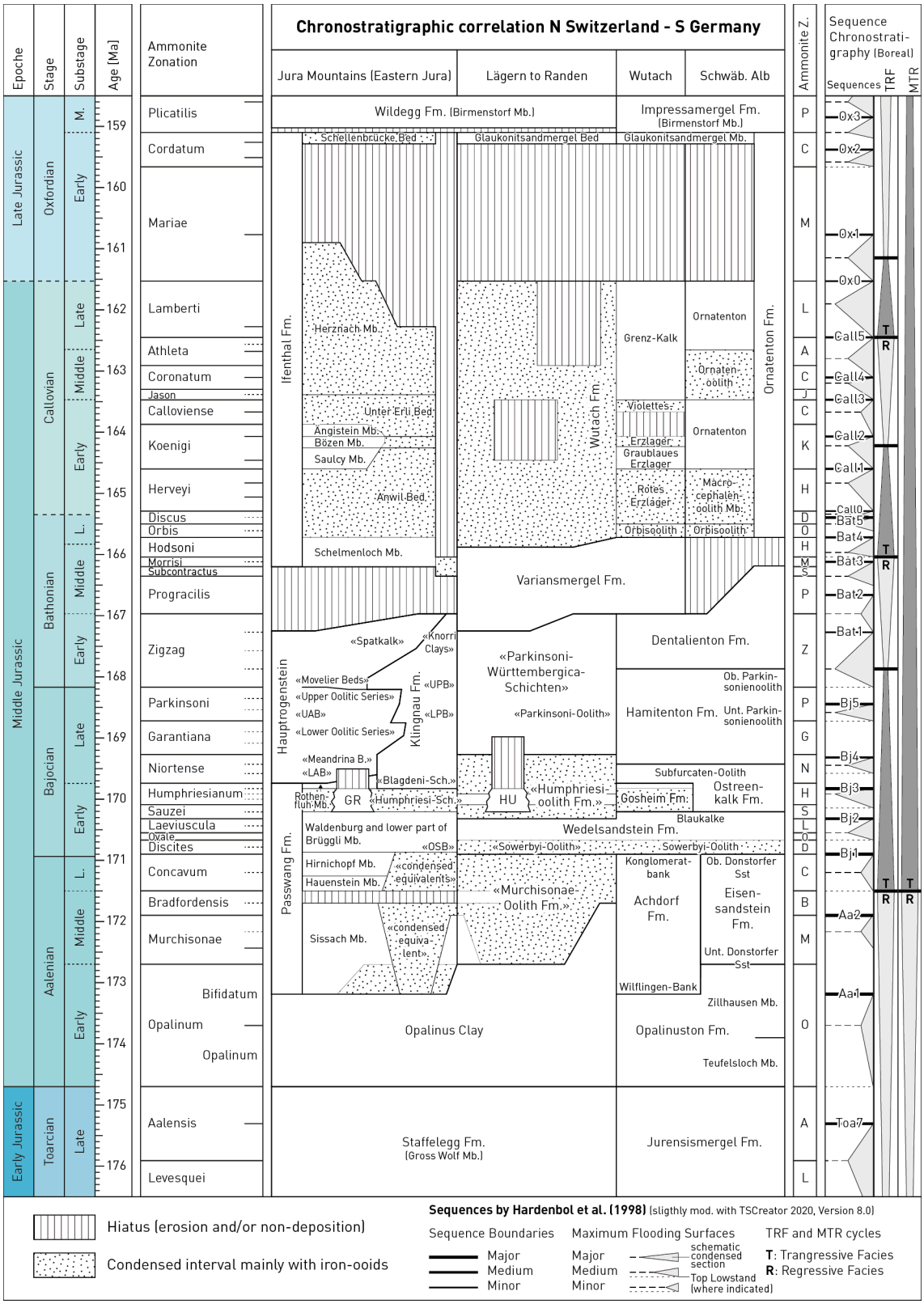


Fig. 4-34: Stratigraphy of the Middle Jurassic of Northern Switzerland and the correlation with neighbouring Southern Germany

For figure explanations see next page.

Chronostratigraphy is based on the chronostratigraphic chart of the International Commission of Stratigraphy, v. 10/2020, Hesselbo et al. (2020) and TSCreator 2020 (Version 8.0); Ammonite zonation after Cariou & Hantzpergue (1997), Dietze et al. (2011, 2014, 2021); sequence chronostratigraphy and nomenclature are after Hardenbol et al. (1998) and slightly modified using TSCreator 2020 (Version 8.0). German stratigraphy after Bloos et al. (2006), Dietl (2006, 2007, 2008, 2010), Franz & Nitsch (2009). Abbreviations: L. = Late, M. = Middle, Fm. = Formation, Mb. = Member, B. = Beds, LAB = «Lower Acuminata Beds», UAB = «Upper Acuminata Beds», OSB = «Obere Sublata-Bank», LPB = «Lower Parkinsonien Bank», UPB = «Upper Parkinsonien Bank», GR = Gisliflue Reef, Sch. = Schichten, HU = «Herrenwis Unit», Unt. = Untere(r)/Lower, Ob. = Obere(r) /Upper, Sst = Sandstein/Sandstone, Z. = Zonation, TRF = Transgressive-Regressive Facies Cycles, MTR = Major Transgressive-Regressive Cycles. Modified after Bläsi et al. (2013) and Meier & Deplazes (2014).

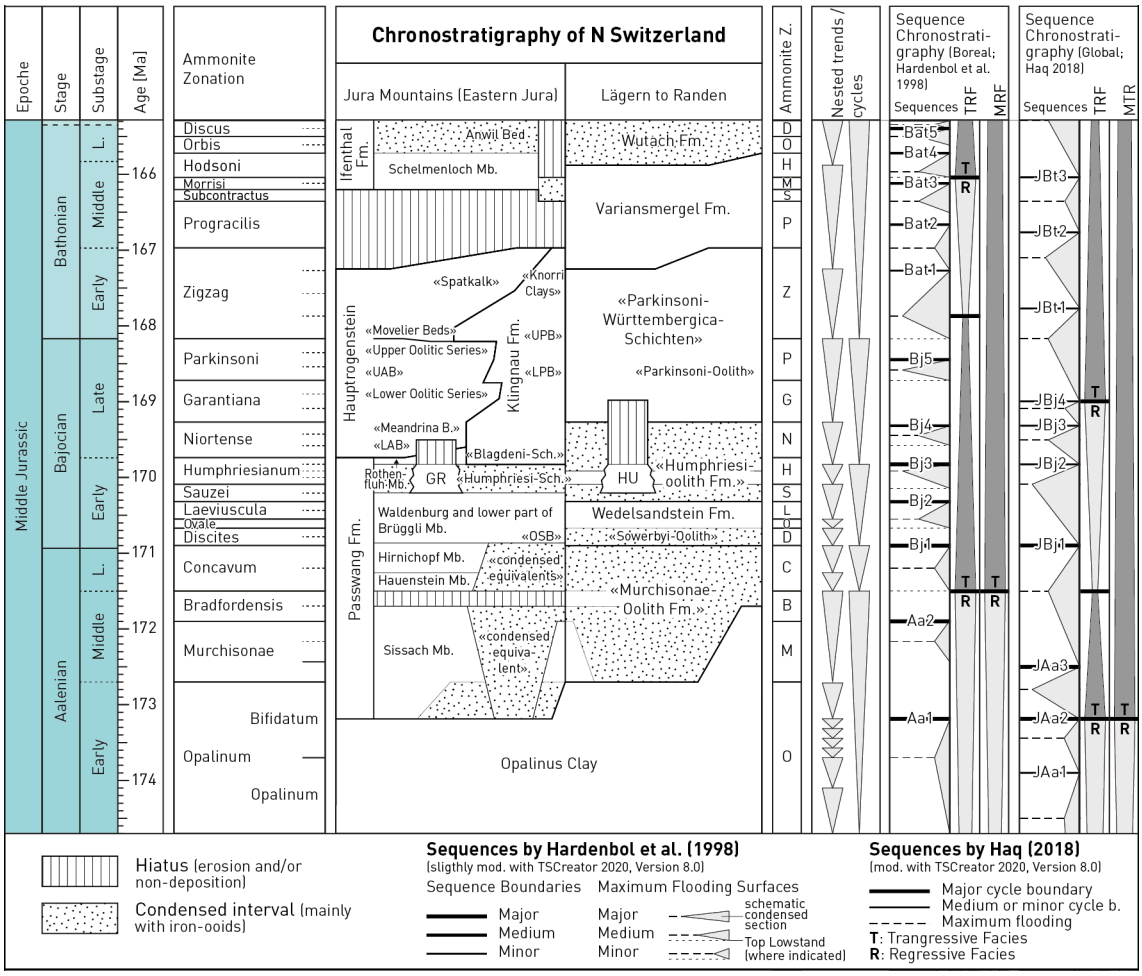


Fig. 4-35: Biostratigraphy and lithostratigraphy of the Middle Jurassic (Aalenian to Bathonian) of Northern Switzerland with sequence stratigraphic correlation

Biostratigraphy and lithostratigraphy based on Bläsi et al. (2013) and Meier & Deplazes (2014). Chronostratigraphy is based on the chronostratigraphic chart of the International Commission of Stratigraphy, v. 10/2020, Hesselbo et al. (2020) and TSCreator 2020 (Version 8.0); Ammonite zonation after Cariou & Hantzpergue (1997), Dietze et al. (2011, 2014, 2021); Sequence chronostratigraphy and nomenclature after Hardenbol et al. (1998), Haq (2018) and slightly modified using TSCreator 2020 (Version 8.0). Abbreviations: refer to Fig. 4-34.

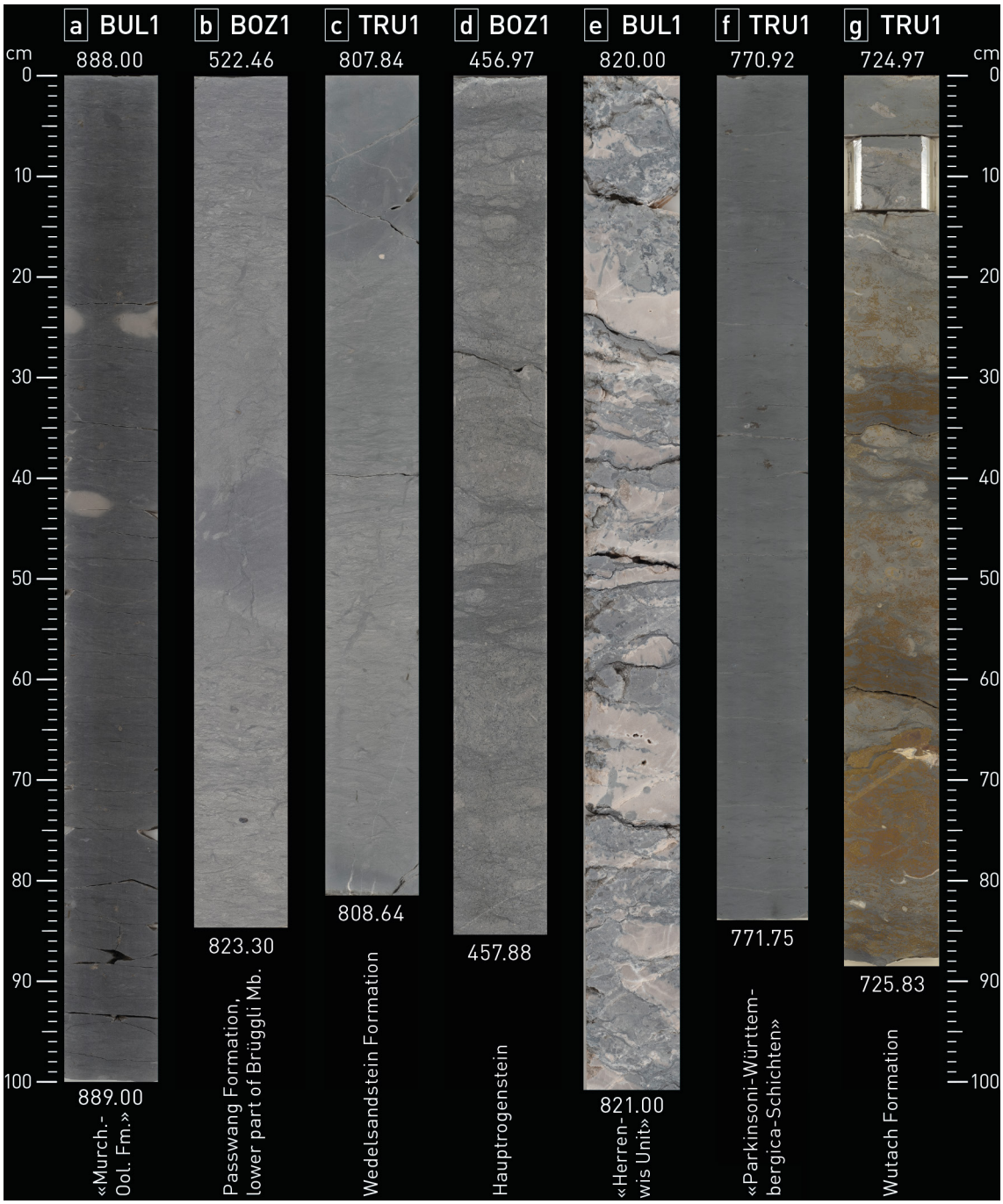


Fig. 4-36: Selected core photos of the Dogger Group above Opalinus Clay (slabbed cores)

(a) Dark grey, silty to sandy claystone with siderite nodules; **(b)** light grey, silty to sandy limestone, bioclastic and bioturbated, and dark grey silty marl, bioturbated; **(c)** dark grey sandy limestone, bioclastic, bioturbated, and dark grey sandy marl, bioturbated; **(d)** light grey oolitic limestone, bioclastic, irregularly wavy bedded, ooids with black coatings and with interbeds of medium grey calcareous marl; **(e)** beige grey (matrix) to pale pink (corals) coral limestone, fossiliferous matrix (echinoderms, bivalves), corals often bored and few vugs; **(f)** dark grey silty claystone (calcareous), moderately fossiliferous (e.g. belemnites), pyrite; **(g)** repeated gradual transition of light grey iron-oolitic limestone to dark grey, iron-oolitic marl, reddish brown iron-ooids, very fossiliferous (esp. oysters).

In JO, the Dogger Group above Opalinus Clay can be subdivided into the following units:

«Condensed equivalents of the Sissach Member, Hauenstein Member and/or Hirnichopf Member»: In JO, the lowermost members of the Passwang Formation are condensed and only up to ca. 2 m thick. They consist of undulating, fossiliferous, iron-oolitic and calcareous hardgrounds (Wohlwend et al. 2019).

Waldenburg Member and lower part of Brüggli Member: These two members are treated as one ca. 20 – 25 m thick stratigraphic unit (Wohlwend et al. 2019), which can be subdivided into two parts in the boreholes of JO. The lower and larger part consists mostly of silty to sandy marl with numerous dm- to m-scale beds of mainly bioturbated, partly bioclastic, silty to sandy limestone (Fig. 4-36b). The facies and thickness of the dm- to m-scale beds show nested trends, which are at least partly cyclic in nature. These trends or cycles can generally be correlated within JO (Fig. 4-37). Based on thin sections of the TBO campaign, these beds show no elevated porosity. Towards the upper part, silty claystone with some interbeds of partly iron-oolitic limestone dominate.

«Humphriesi-Schichten» (upper part of Brüggli Member): This ca. 5 m thick unit is a prominent marker unit in the upper part of the Passwang Formation (Bläsi 1987, Wohlwend et al. 2019). It consists of fossiliferous iron-oolitic limestone and marl that stand out because of their reddish colour (Fig. 4-37).

Rothenfluh Member: This lithostratigraphic unit is part of the Passwang Formation, where it is overlain by Hauptrogenstein (BOZ2 and BOZ1); outside the platform, the equivalent unit becomes part of the Klingnau Formation (RIN) (Gonzalez & Wetzel 1996). The Rothenfluh Member consists of an alternation of mostly bioclastic argillaceous, silty to sandy marl with decimetre-scale, partly nodular beds of bioclastic limestone.

Klingnau Formation: This unit consists mostly of fossiliferous, often nodular, calcareous, and argillaceous marl with some decimetre-scale beds of limestone. Sparse calcareous ooids are evidence of the adjacent oolitic facies of the Hauptrogenstein from which they were transported.

Hauptrogenstein: This formation was subdivided into up to eight informal subunits (Schmassmann 1945, Gonzalez & Wetzel 1996). In JO only the easternmost part of the strata of the Hauptrogenstein carbonate platform is encountered and – depending on the interfingering with the Klingnau Formation – a different succession of lithostratigraphic units can be distinguished. In general, the lower and larger part decreases in total thickness from 54 m in the west (BOZ2) to ca. 8 m in the east (RIN). It is characterised by predominantly oolitic and bioclastic limestone (Fig. 4-36d) with dm- to m-scale beds of sandy marl in the lowermost section, otherwise calcareous marl with some ooids dominates. The ooids show typically black coatings. In BOZ2 the upper part of the Hauptrogenstein consists of «Movelier Beds», the lateral equivalent of the Klingnau Formation in BOZ1, and «Spatkalk» with a total thickness of 26 m; in BOZ1 and RIN only «Spatkalk» with a thickness of 12 m and 18 m is present. These units consist of bioclastic calcareous marl, bioclastic limestone and limonitic bioclastic limestone with some iron-ooids towards the top.

Ifenthal Formation: This formation was subdivided into several members by Bitterli-Dreher (2012). However, most of the members seem to be condensed in the study area. In JO, the lower part is characterised by fossiliferous limestone and bioclastic calcareous marl with some iron-ooids. This lower part may correspond to the Schelmenloch Member. The upper part is characterised by iron-oolite and iron-oolitic limestone with several hardgrounds (Fig. 4-34).

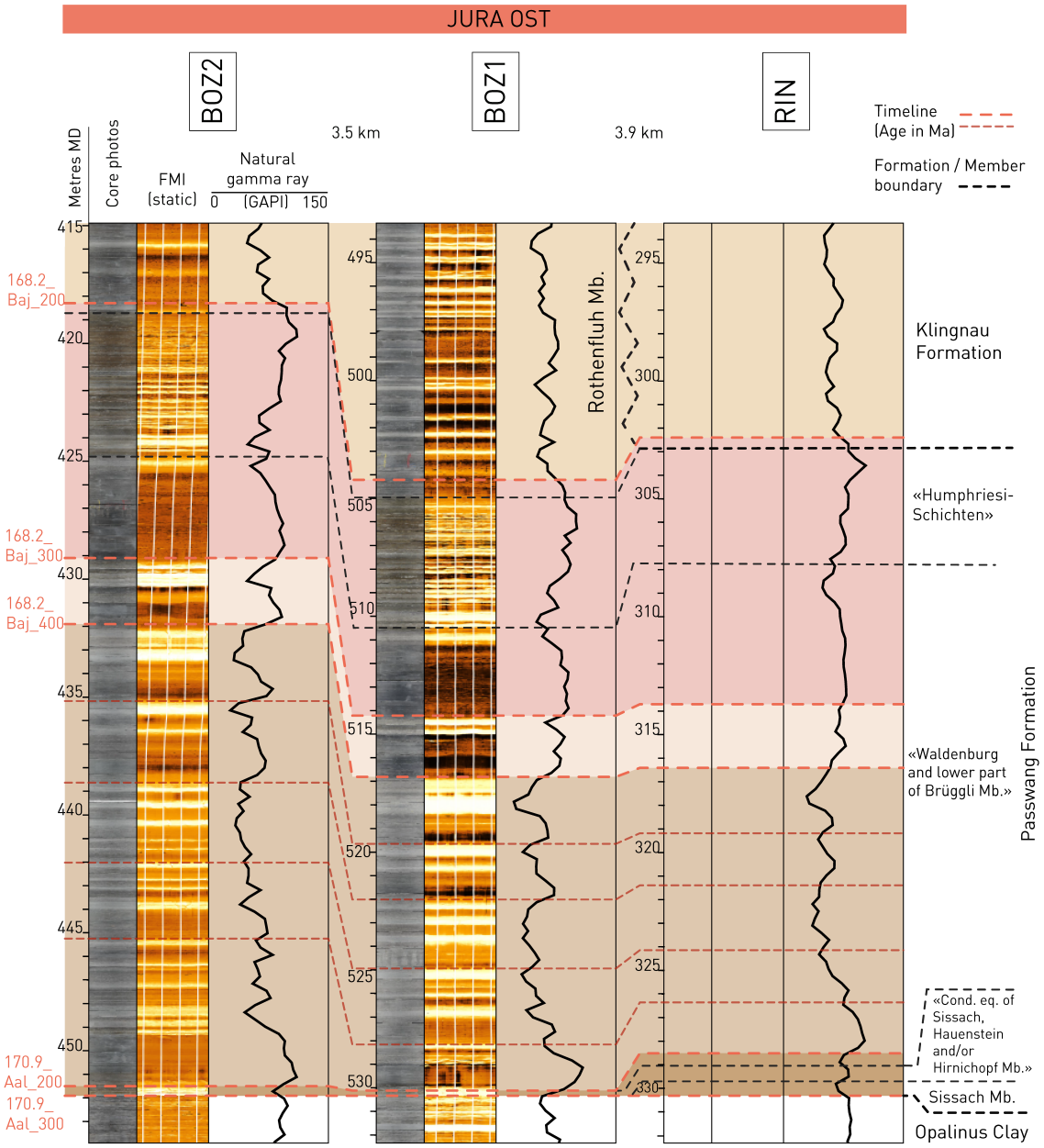


Fig. 4-37: Detailed correlation of the sedimentary succession directly above the Opalinus Clay in boreholes of JO

In the formation microresistivity imaging (FMI) data, more conductive lithologies appear darker (e.g. claystone), whereas more resistive lithologies appear lighter (e.g. limestone or sandstone).

Dogger Group above Opalinus Clay in NL and ZNO

In NL and ZNO, the Dogger Group above Opalinus Clay starts with the «Murchisonae-Oolith Formation». The thickness decreases from western NL (ca. 15 m) to eastern NL (7 m) and is condensed in ZNO (≤ 1 m) (Fig. 4-33). It consists of several nested trends or cycles of claystone, siltstone, marl, limestone and iron-oolite. Some of these nested facies trends might be similar to the 'coarsening-upward' or 'shallowing upward' successions as described by Burkhalter (1996). Some of these nested trends seem to correspond to boreal or global sequences as proposed by Hardenbol et al. (1998) or Haq (2018) (Fig. 4-35).

In NL, the overlying Wedelsandstein Formation increases significantly in thickness from the west (2 m in BAC1) to the area where it underlies the «Herrenwis Unit» in eastern NL (28 m in BUL1). It mainly comprises claystone and silty claystone with a few decimetre-scale calcareous beds. In ZNO, the thickness varies between ca. 25 and 35 m and mainly consists of silty marl and argillaceous siltstone with many beds of argillaceous, silty to sandy limestone (Fig. 4-33).

The following «Humphriesioolith Formation» is only up to 2 m thick in NL and consists predominantly of iron-oolitic to limonitic, argillaceous to calcareous beds. In ZNO this formation reaches a thickness of ca. 10 – 13 m and consists in the lower and upper part of iron-oolitic and bioclastic limestone to marl and iron-oolite and, in the middle part, of calcareous to argillaceous marl.

The «Herrenwis Unit» is found only in the eastern part of NL. It consists of ca. 40 m thick strata associated with an isolated carbonate platform that is embedded in argillaceous strata (Fig. 4-33) and extends over several square kilometres. It consists in STA3 and BUL1 of coral limestone intercalated with marl and up to several-metre-thick bioclastic limestone (encrinite) and occasional beds of argillaceous marl. In STA2, the basinal part of the «Herrenwis Unit» comprises a medium- to thick-bedded succession of bioclastic limestone, bioclastic calcareous marl and bioclastic argillaceous marl.

The overlying unit «Parkinsoni-Württembergica-Schichten» fills up the positive relief created by the «Herrenwis Unit» in NL. Accordingly, this unit decreases in thickness from BAC1 with 48 m to STA3 with 2 m (including the overlying Variansmergel Formation). In ZNO, the thickness of the «Parkinsoni-Württembergica-Schichten» unit varies between ca. 30 and 35 m. It consists of (silty) claystone and silty marl with some decimetre-scale beds of bioclastic limestone.

The Variansmergel Formation has a thickness of ca. 2 – 5 m in NL and ca. 12 m in ZNO. Its composition is similar to the «Parkinsoni-Württembergica-Schichten», but generally with more decimetre-scale bioclastic limestone beds.

Finally, the Wutach Formation has a thickness of ca. 1 – 5 m and consists of a very fossiliferous succession of (iron-oolitic) argillaceous marl, iron-oolitic, bioclastic limestone and iron-oolite with several hardgrounds.

In NL and ZNO the Dogger Group above Opalinus Clay can be subdivided into the following units:

«Murchisonae-Oolith Formation»: In general, this formation can be separated into two parts (Fig. 4-33, Fig. 4-38). The lower part reaches the largest thickness in eastern NL, with 11 m at BAC1. It consists of an alternation of dm- to m-scale beds of calcareous marl and sandy, silty to bioclastic limestone with some iron-ooids and limonitised components. This part terminates with cross-bedded limonitic limestone to iron-oolite and a hardground at the top. The lower part is similar to corresponding outcrops of the Sissach Member at the Surb River or Acheberg east of NL (Wohlwend et al. 2019). Within NL, the lower part decreases in thickness and is condensed to a calcareous bed in BUL1 as well as in ZNO. The upper, ca. 4 – 11 m thick part of the «Murchisonae-Oolith Formation» consists in NL of silty claystone (Fig. 4-36a) and argillaceous marl with bioclastic limestone and hardgrounds in the upper part. In ZNO the corresponding unit has a thickness of ≤ 1 m and consists of an argillaceous siltstone with a calcareous, iron-oolitic hardground at the top.

Wedelsandstein Formation: In NL the Wedelsandstein Formation consists of at least two facies trends or cycles of predominantly claystone to silty claystone, some argillaceous marl and decimetre-scale calcareous beds at the top, often including a hardground (Fig. 4-38). Towards the west in NL, and especially as seen in the drill cores of BAC1, the Wedelsandstein Formation is strongly reduced and difficult to delineate solely based on lithological criteria; for this reason biostratigraphic evidence was additionally considered (Nagra (ed.) 2023a, Dossier IV). In ZNO the lower and larger part of the Wedelsandstein Formation mainly comprises argillaceous to calcareous siltstone with many dm- to m-scale beds of mostly bioturbated and bioclastic, partly micritic, silty to sandy limestone (Fig. 4-36c). The dm- to m-scale beds show nested facies trends or cycles, which can be at least partly correlated within ZNO (Fig. 4-39). Based on the thin sections from cores retrieved during the TBO drilling campaign, these beds show no elevated porosity. Towards the upper part, silty claystone with some calcareous interbeds dominate. The Wedelsandstein Formation is almost time-equivalent to the Waldenburg Member and lower part of the Brüggli Member in JO (Fig. 4-37).

«Humphriesioolith Formation»: In NL this formation is thin (2 m) and even missing in STA3. Its composition varies in terms of content of iron-ooids, limonitic components, carbonate and silt from borehole to borehole, but is dominated by marl. In ZNO the «Humphriesioolith Formation» can be divided into three parts by the occurrence of iron-ooids: a lower iron-oolitic interval, a marly interval with calcareous beds without iron-ooids, and an upper iron-oolitic interval (Fig. 4-39).

«Herrenwis Unit»: In the eastern part of NL, the first evidence for the presence of the «Herrenwis Unit» was provided by 2D seismic data, resulting in the description of a sedimentary body forming a positive relief on top of the underlying sedimentary rocks (Meier & Deplazes 2014 and references therein, Fig. 4-40, Fig. 4-41). This unit was recognised for the first time during the BUL1 campaign. The term «Herrenwis Unit» was introduced as an informal stratigraphic unit of undefined rank named after the BUL1 borehole locality "Herrenwis" (Nagra (ed.) 2021a, Dossier III). The «Herrenwis Unit» could already have been drilled in the Eglisau-2 borehole from 1957 (Cadisch 1959) if the final depth is taken into account and the rudimentary recording is reinterpreted. In STA3 and BUL1, the isolated carbonate platform is dominated by coral and bioclastic limestones, which are partly porous, and some beds of argillaceous marl (Fig. 4-36e). The 40-metre-thick coral reef exhibits a large number of specimens and low species diversity (i.e. consisting of a few taxa), which is typical for Bajocian reef environments (Ruchat et al. 2024). At least two notable decreases in species diversity exist that partly coincide with increased clay-mineral contents in this unit. The «Herrenwis Unit» terminates with a prominent hardground. The more argillaceous basinal part of the «Herrenwis Unit» or the periplatform wedge was drilled in STA2 and its north-westernmost extent also in the Weiach borehole.

«Parkinsoni-Württembergica-Schichten»: This unit mostly consists of an alternation of lenticular- to flaser-bedded claystone and silty marl with decimetre-scale beds that occur more frequently towards the top (Fig. 4-36f). In the lower or lowermost part, iron-oolitic to limonitic horizons can occur that may partly correspond to the «Parkinsoni-Oolith».

Variansmergel Formation: This formation has a similar facies to the «Parkinsoni-Württembergica-Schichten», but it is generally more fossiliferous, including brachiopods, bivalves and crinoids partly concentrated in coquina beds.

Wutach Formation: This formation corresponds partly to the Ifenthal Formation in JO (Fig. 4-34) and represents a condensed succession of iron-oolite, iron-oolitic limestone and marl (Fig. 4-36g).

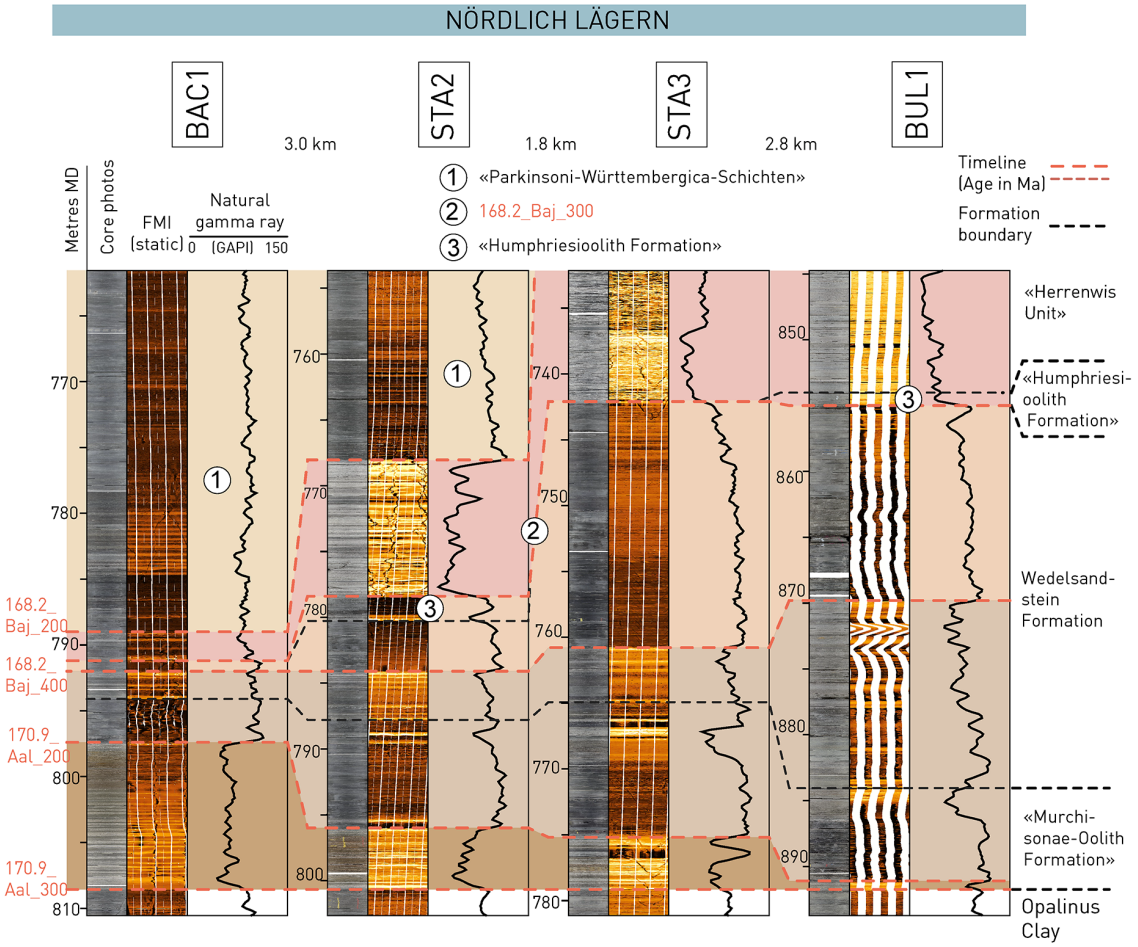


Fig. 4-38: Detailed correlation of the sedimentary succession directly above the Opalinus Clay in boreholes of NL

In the formation microresistivity imaging (FMI) data, more conductive lithologies appear darker (e.g. claystone), whereas more resistive lithologies appear lighter (e.g. limestone or sandstone).

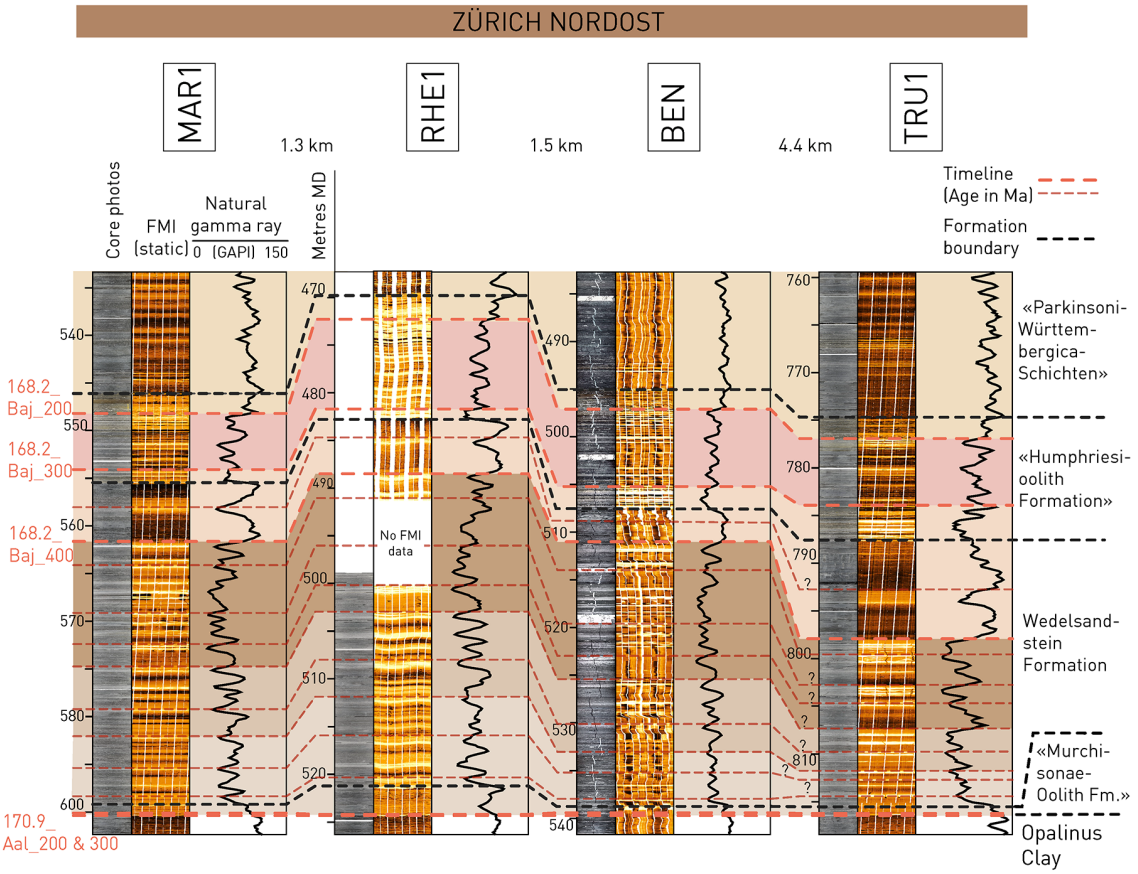


Fig. 4-39: Detailed correlation of the sedimentary succession directly above the Opalinus Clay in boreholes of ZNO

In the formation microresistivity imaging (FMI) data, more conductive lithologies appear darker (e.g. claystone) whereas more resistive lithologies appear lighter (e.g. limestone or sandstone). In RHE1, thicknesses are larger because it is an inclined borehole.

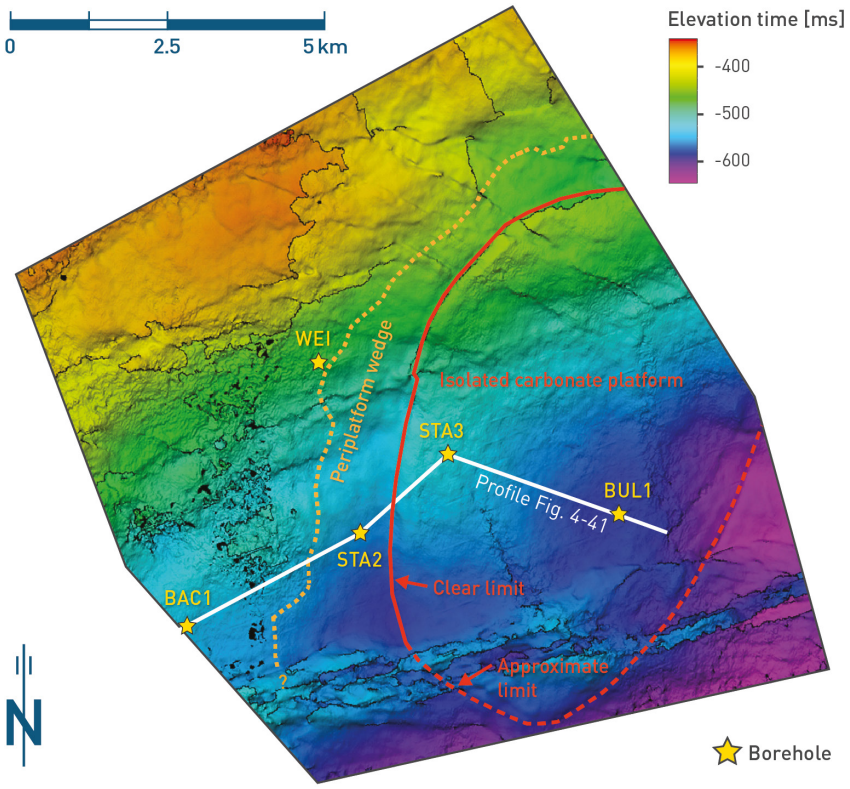


Fig. 4-40: Subcrop map (top reflection of the «Herrenwis Unit») of the geophysical survey area acquired in NL with seismically derived extent of the isolated carbonate platform and of the periplatform wedge

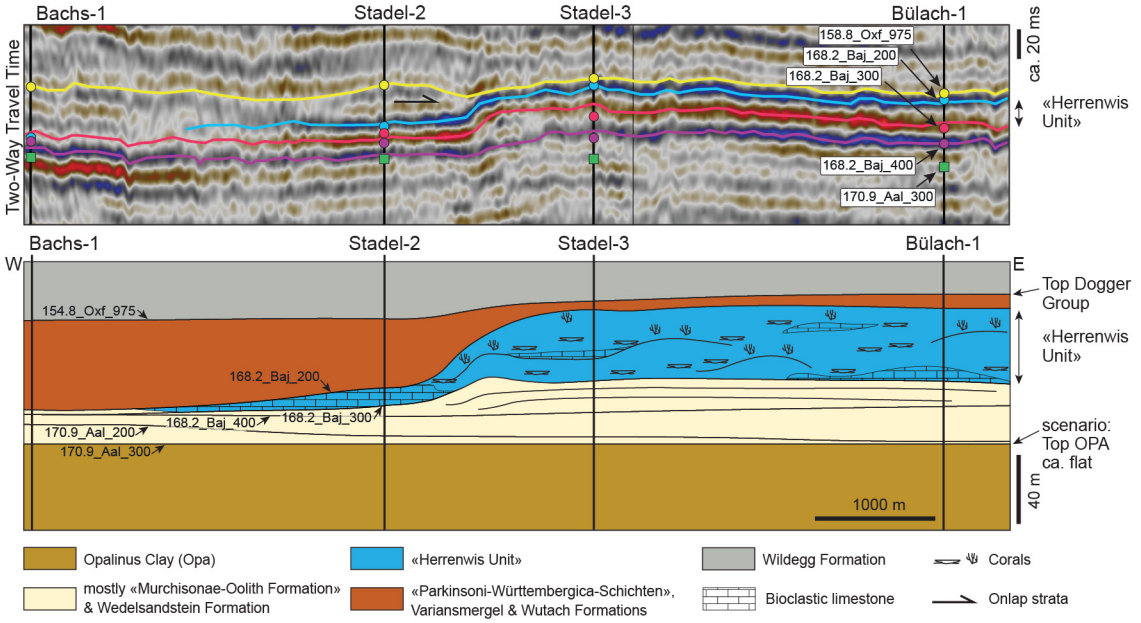


Fig. 4-41: E-W-oriented seismic profile across the western edge of the «Herrenwis Unit» and conceptual sketch of the extent of the «Herrenwis Unit» and adjacent units

The upper panel is flattened to ca. Top Keuper Group, the lower panel to Top Opalinus Clay. Refer to Nagra (2024b and 2024f) for discussion of the seismic reflection data.

4.2.7.3 Variability

Compared to the Opalinus Clay, the overlying units of the Dogger Group generally exhibit increased vertical and lateral variability in thickness and facies, reflecting locally diverse depositional environments. This is also expressed by the high number of different lithostratigraphic units at formation and member levels (Fig. 4-34). A significant portion of these units is organised by nested facies trends or cycles, which typically start with argillaceous sedimentary rocks that become more silty and finally calcareous to iron-oolitic at the top (Fig. 4-35). However, the thickness of the elements of the individual facies trends may vary strongly laterally depending on basin bathymetry and bottom currents.

The first interval from the Top Opalinus Clay to Top «Humphriesioolith Formation» / «Herrenwis Unit» / « Humphriesi-Schichten» of the Passwang Formation shares more similarities in JO and ZNO than in NL (Fig. 4-33). In JO and ZNO, the «Condensed equivalents of the Sissach Member, Hauenstein Member and/or Hirnichopf Member» and the «Murchisonae-Oolith Formation» are strongly condensed. This succession is dominated by an argillaceous to silty sediment with few calcareous, iron-oolitic beds. In contrast, in western NL the «Murchisonae-Oolith Formation» starts with an up to 11 m thick more calcareous interval that thins out towards the east. The overlying Wedelsandstein Formation and equivalent parts of the Passwang Formation (Fig. 4-37, Fig. 4-38, Fig. 4-39) are very similar in JO and ZNO, whereas in NL this unit is more similar to the Opalinus Clay and is dominated by claystone and silty claystone, with less calcareous, sandy beds. In eastern NL, this interval terminates partly with the thin «Humphriesioolith Formation» and is then overlain by the 40-metre thick «Herrenwis Unit», an isolated coral reef carbonate platform embedded in argillaceous sedimentary rocks.

The second interval, which extends to the Top Dogger Group above Opalinus Clay, has, in terms of facies, more similarities in NL and ZNO compared to JO. It is dominated by relatively homogeneous claystone and silty marl of the «Parkinsoni-Württembergica-Schichten» (Fig. 4-33). The thickness varies strongly; thickness is minimal over the «Herrenwis Unit» and is much greater outside of the isolated carbonate platform of the «Herrenwis Unit» (Fig. 4-41). In JO, the second interval has different characteristics; generally, the strata have an increased carbonate content, and oolitic and bioclastic limestone related to the extended Hauptrogenstein platform appear.

4.2.7.4 Chronology

The Dogger Group above Opalinus Clay spans most of the Middle Jurassic, from the Middle Aalenian to the Callovian and partly also to the earliest part of the Late Jurassic (Early Oxfordian). Within this interval, five timelines were picked (170.9_Aal_200 to 168.2_Baj_100; Fig. 4-33). These timelines were picked based on the integration of detailed biostratigraphic, chemostratigraphic and lithofacial (e.g. hardground) criteria (for data please refer to Dossiers III and IV of data reports of the TBO campaign, see Tab. 2-1). The timelines generally follow lithostratigraphic boundaries, but partly cross or are within lithostratigraphic boundaries, reflecting lateral facies changes in time-equivalent periods (Fig. 4-33).

4.2.7.5 Depositional evolution

The Dogger Group above Opalinus Clay in the study area was deposited in a shallow epicontinental sea bordered by the Vindelician Land in the east, the Alemannic Land to the south, the Celtic Platform to the west and the London-Brabant Massif and Rhenish Massif to the north (Fig. 3-9). The transgression of the sea onto the Alemannic Land, which began in the Late Toarcian, continued and the last small remnants or islands on the former southern edge (e.g. Windgällen) were also flooded in the course of the Aalenian and Bajocian (Trümpy 1959). Overall, the depositional environment is dominated by fine-grained siliciclastic input from these land-

masses and/or from even farther source areas to the north, leading to relatively high sedimentation rates (Fig. 4-4, Fig. 4-5, Fig. 4-6). Additionally, also shallow marine environments dominated by in-situ carbonate production were associated with high sedimentation rates (Hauptrogenstein, «Herrenwis Unit»). Periods with high sedimentation rates are interrupted by intervals with condensation with very low sedimentation rates or even no net deposition. In several intervals, the vertical facies associations are organised in nested facies trends or cycles, which start with argillaceous sedimentary rocks that become more silty and finally calcareous to iron-oolitic at the top. Some of these facies trends seem to reflect changes in relative sea level and/or climate variability, and their boundaries might be partly related to boreal or global sequence boundaries (Fig. 4-35). However, these facies trends are often not complete. Their strata may strongly vary laterally in thickness and facies depending on basin bathymetry and bottom currents causing sediment mobilisation, transport, and accumulation. The depositional evolution of the Dogger Group above Opalinus Clay is subdivided here into four time intervals (Fig. 4-33):

The first time interval (170.9_Aal_300 to 170.9_Aal_200) spans the Middle Aalenian (Murchisonae to lower part of Bradfordensis ammonite Zones; Fig. 4-33, Fig. 4-42). It includes, in JO, the interval from the Top Opalinus Clay to the top of the lower part of the Passwang Formation (Sissach Member to lower part of the Waldenburg Member, Fig. 4-37). In NL and ZNO, it corresponds to the interval from the Top Opalinus Clay to the top of the lower part of the «Murchisonae-Oolith Formation» (Fig. 4-33, Fig. 4-38, Fig. 4-39). This first time interval is characterised by strong condensation in JO, eastern NL (BUL1) and ZNO, which is reflected in the occurrence of calcareous and iron-oolitic hardgrounds. Only in the western part of NL was an interval several metres thick and comprised of marl, bioclastic limestone and iron-oolite deposited (BAC1). A similar succession exists ca. 10 km to the east of NL at the Surb River and Acheberg (Wohlwend et al. 2019), indicating a potential eastward extension of this facies. The interval in NL also includes cross-bedded limonitic limestone, suggesting transport by bottom currents. This interval could have accumulated in a local depression, or it could have accumulated by local carbonate production (e.g. crinoids) and transport by bottom currents forming a positive relief.

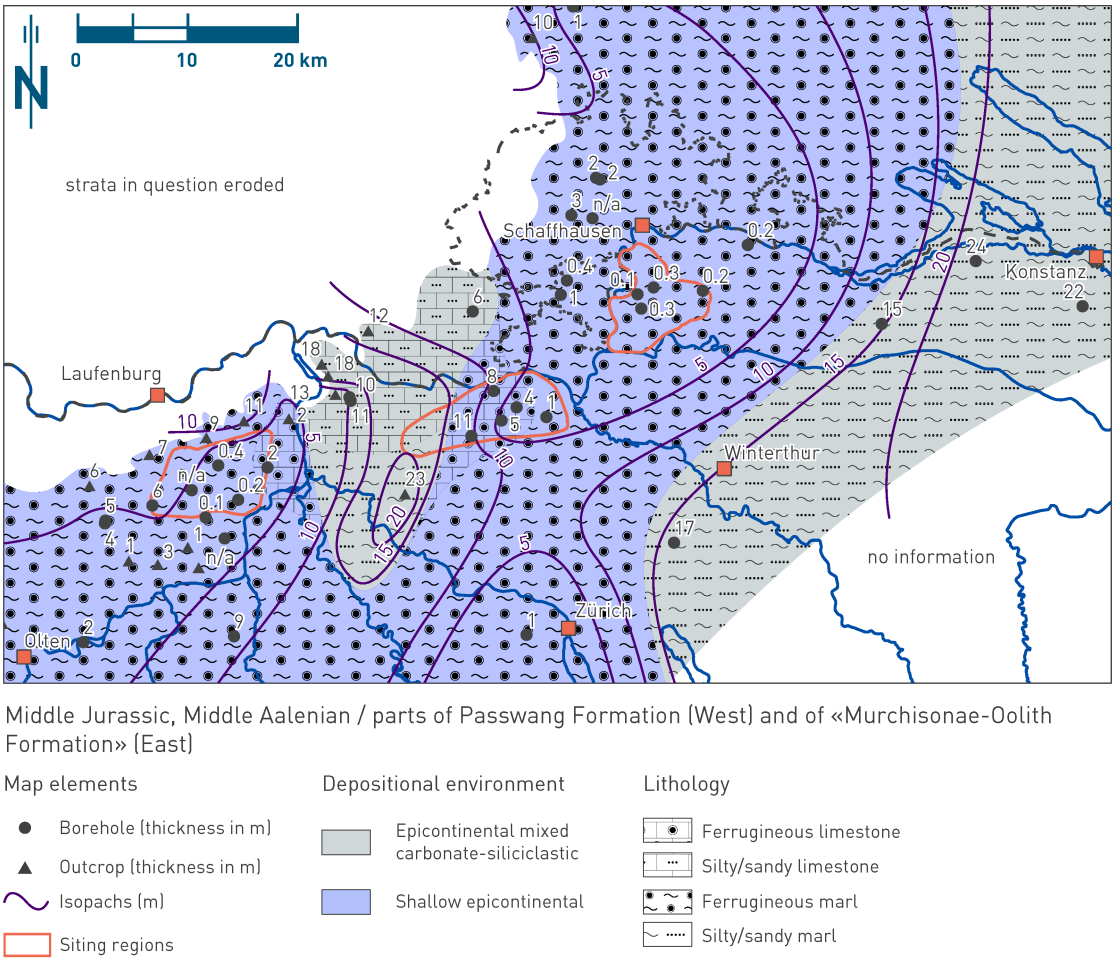
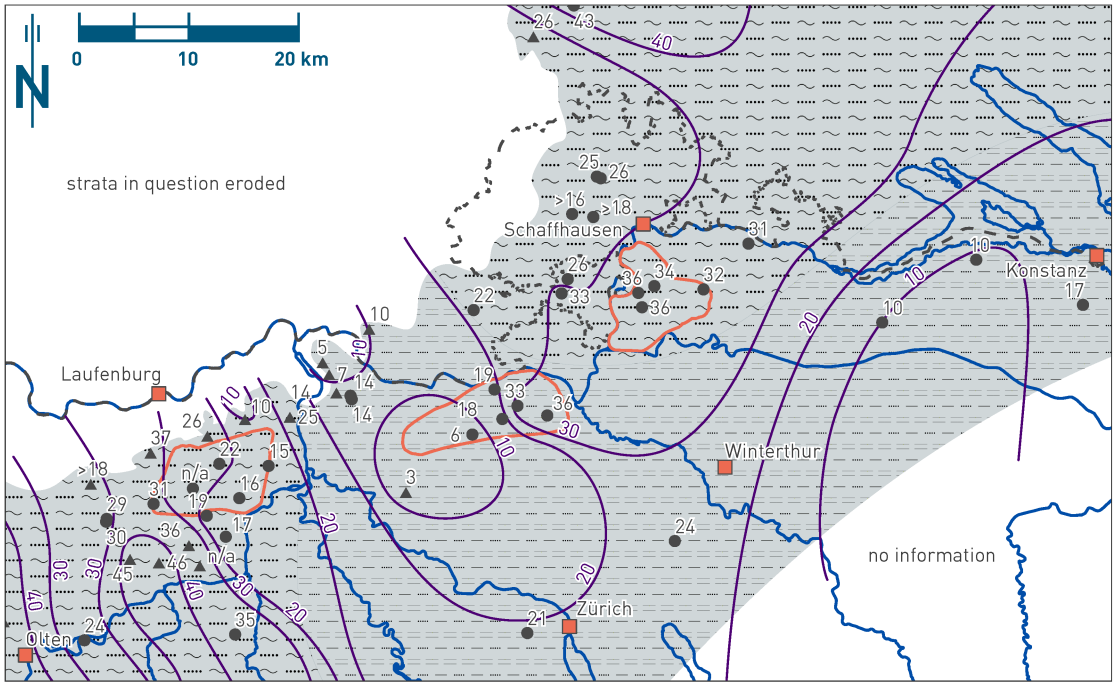


Fig. 4-42: Map of depositional environments during Middle Aalenian

Refer to Fig. 4-3 for a schematic representation of depositional environments. The north arrow refers to present-day geographic north. Map shows the setting during the "first time interval" (170.9_Aal_300 to 170.9_Aal_200) as discussed in the text.

The second time interval (170.9_Aal_200 to 168.2_Baj_300) spans the late Middle Aalenian to Early Bajocian (Bradfordensis to Laeviuscula Zones; Fig. 4-33, Fig. 4-43). In JO, it corresponds to most of the middle part of the Passwang Formation (i.e. most of the Waldenburg Member and lower part of the Brüggli Member), whereas in NL and ZNO, mostly to the Wedelsandstein Formation and the lower iron-oolitic part of the «Humphriesioolith Formation». Within this interval, an additional timeline (168.2_Baj_400) was identified at the top of calcareous beds that enables this interval to be separated into at least two facies trends or cycles. In the second time interval, the depositional environments in JO and ZNO show many similarities with a mainly silty and argillaceous sediment with many calcareous (mostly bioclastic but also micritic) to sandy beds. These beds or successions of beds can be partly correlated on a local scale, i.e. between boreholes within the siting regions (Fig. 4-37, Fig. 4-39). However, these beds do not represent regional marker beds such as some of the calcareous and iron-oolitic hardgrounds. The beds of the Wedelsandstein Formation might trace storm events or phases with elevated transport that brought sediments e.g. from carbonate platforms in the west into the area and formed sheet-like deposits. Locally, production of carbonates (crinoids) may also have occurred. Generally, these successions were formed during times of high sedimentation. In NL this interval is dominated by

claystone to silty claystone and shows a clear thickness increase from west to east (Fig. 4-38). For example, there are pronounced thickness increases for the uppermost facies trend (168.2_Baj_400 to 168.2_Baj_300) from ca. 6 m in STA2 to 19 m in STA3 over a distance of only 1.8 km. Assuming that this facies trend represents the same time interval, sedimentation rates must have increased significantly from west to east. In combination with seismic facies analysis (Fig. 4-41), this sediment body is interpreted as an argillaceous drift deposit that formed a positive relief and basis for the following depositional processes that generated the «Herrenwis Unit».



Middle Jurassic, late Middle Aalenian to Early Bajocian / parts of Passwang Formation (West) and most of Wedelsandstein Formation (East)

Map elements
- Borehole (thickness in m)
- Outcrop (thickness in m)
- Isopachs (m)
- Siting regions

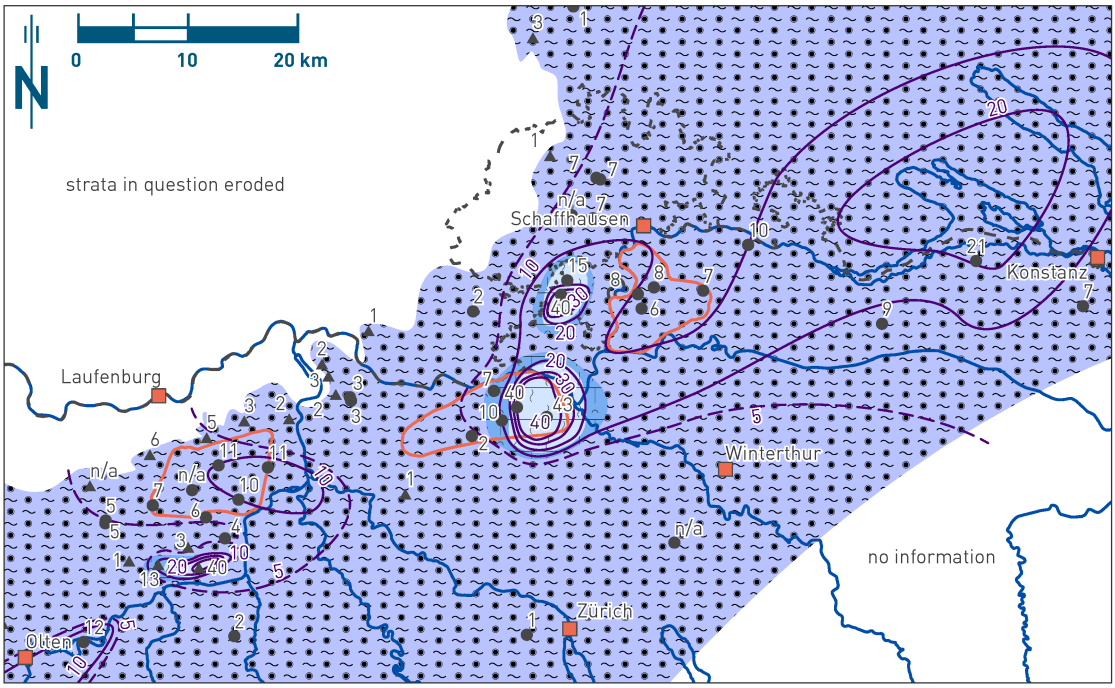
Depositional environment
- Epicontinental mixed carbonate-siliciclastic

Lithology
- Silty/sandy marl
- Silty/sandy claystone

Fig. 4-43: Map of depositional environments during late Middle Aalenian to Early Bajocian

Refer to Fig. 4-3 for a schematic representation of depositional environments. The north arrow refers to present-day geographic north. Map shows the setting during the "second time interval" (170.9_Aal_200 to 168.2_Baj_300) as discussed in the text.

The third time interval (168.2_Baj_300 to 168.2_Baj_200) spans the Early Bajocian (Sauzei to Humphriesianum Zones; Fig. 4-33, Fig. 4-44). In JO it corresponds to an interval in the upper Passwang Formation (uppermost part of the Brüggli Member and the «Humphriesi-Schichten»), in western NL (BAC1) mostly to the «Humphriesioolith Formation», in eastern NL to the «Herrenwis Unit», and in ZNO to the middle and upper parts of the «Humphriesioolith Formation» (Fig. 4-33). In JO the third time interval is mostly characterised by low sedimentation rates. Iron-oolitic sediments were partly produced in situ during phases of sediment starvation, perhaps in relatively elevated regions and transported and accumulated in depressions or as offshore bars. In eastern NL, the isolated carbonate platform of the «Herrenwis Unit» developed during this time interval (Fig. 4-40, Fig. 4-41). The carbonate platform, as found in STA3 and BUL1, mainly consists of in-situ grown coral bioherms (plate- and pillarstone sensu Insalaco 1998), but also some bioclastic limestone (rudstone; Ruchat et al. 2024). In STA2 the more basinward part of the carbonate platform, the periplatform wedge, was drilled with an intercalation of siliciclastic and calcareous sedimentary rocks that contain few transported coral fragments (Fig. 4-38). The carbonate platform developed on top of the positive relief of the underlying argillaceous units, probably a sediment drift deposit (mostly Wedelsandstein Formation). On top of this positive relief, the conditions for coral growth were more favourable, probably because of better light conditions (shallower water depth) and oxygen availability (current circulation). The carbonate platform is interpreted to consist of several horizontally 100 m- to decametre-scale mounded coral bioherms or patch-reefs with flanking or intercalated bioclastic limestone as observed in time-equivalent reefs in Lorraine and Burgundy (Geister & Lathuilière 1991, Brigaud et al. 2024; Fig. 4-45) and central Morocco (Ait Addi 2015). Regional time-equivalent reefs (Fig. 4-44) can be found at the Gisliflue ca. 20 km northeast of Olten (Wullschleger 1966, Gonzalez & Wetzel 1996) and potentially in the less well documented boreholes around Jestetten north of NL (Franz 2022, Geyer et al. 2023). Within the «Herrenwis Unit», several phases can be distinguished which can be traced by changes in the ecological associations and seem to be partly also mimicked by clay-mineral content. The coral growth, and correspondingly the «Herrenwis Unit», end with a prominent unconformity which might be correlated with a major transgression ('Vesulian Transgression' in eastern France; Durlet & Thierry 2000). The build-up of the biohermal «Herrenwis Unit» represents deposition during a phase of high sedimentation rate, which was followed by a phase of strong condensation, reworking, and partly infilling of the underlying «Herrenwis Unit». During the third time interval, western NL was characterised by a siliciclastic basinal depositional environment outside of the «Herrenwis Unit», with low sedimentation rates. In ZNO, the third time interval was dominated firstly by similar fine-grained siliciclastic sedimentation with medium to low sedimentation rates. Secondly, a succession of iron-oolitic accumulations or hardgrounds were formed, indicating low to very low sedimentation rates.



Middle Jurassic, Early Bajocian / mostly «Humphriesi-Schichten» (West), «Herrenwis Unit» and parts of «Humphriesioolith Formation» (East)

Map elements
- Borehole (thickness in m)
- Outcrop (thickness in m)
- Isopachs (m)
- Intermediate Isopachs (selection)
- Siting regions

Depositional environment
- Isolated carbonate platform, bioherm (coral)
- Carbonate periplatform
- Shallow epicontinental

Lithology
- Bioclastic limestone
- Biohermal limestone
- Ferrugineous marl

Fig. 4-44: Map of depositional environments during the Early Bajocian

Refer to Fig. 4-3 for a schematic representation of depositional environments. The north arrow refers to present-day geographic north. Map shows the setting during the "third time interval" (168.2_Baj_300 to 168.2_Baj_200) as discussed in the text.

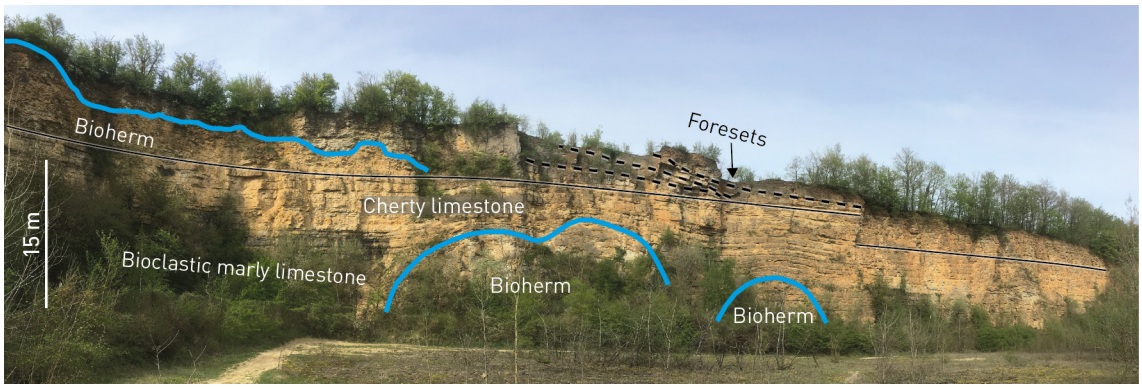


Fig. 4-45: Bioherms at two levels (Calcaire à polypiers inférieur et supérieur) shown as a time-equivalent analogue for the bioherms of the «Herrenwis Unit»

Quarry near Malancourt-la-Montagne (Lorraine, France; see Geister & Lathuilière 1991; photo and interpretation by A. Ruchat).

The fourth time interval (168.2_Baj_200 to 154.8_Oxf_975) spans the Late Bajocian to Early Oxfordian (Fig. 4-33, Fig. 4-46). In JO it corresponds to the upper Passwang Formation, Hauptrogenstein, Klingnau and Ifenthal Formations. In NL and ZNO it corresponds to the «Parkinsoni-Württembergica-Schichten», Variansmergel and Wutach Formations. In JO the fourth time interval is dominated by the progression of the oolitic and bioclastic Celtic Platform (Hauptrogenstein) from the west (Fig. 3-9). The carbonate platform interfingers to the east with a more basinal depositional environment, which is characterised by a mixture of calcareous input from the platform and siliciclastic "background" sedimentation in the basin. The Hauptrogenstein comprises three shallowing-upward successions, each capped by a hardground (Gonzalez & Wetzel 1996; Fig. 4-35). Within these successions, the oolitic and bioclastic platform advances from west to east. This phase of the fourth time interval is dominated by high to very high sedimentation rates. This contrasts with the deposits of the overlying Ifenthal Formation that was formed during a time interval characterised by low to very low sedimentation rates (Fig. 4-4). In NL the depositional environment of the fourth time interval must have been strongly influenced by the underlying «Herrenwis Unit». The basin west of the isolated carbonate platform was filled by mostly argillaceous sediments associated with high to very high sedimentation rates. This is corroborated by onlaps of the corresponding «Parkinsoni-Württembergica-Schichten» and Variansmergel Formation on the «Herrenwis Unit» as seen in seismic profiles (Fig. 4-41). In the area above the isolated carbonate platform of the «Herrenwis Unit», this phase was characterised by non-deposition, condensation (hardgrounds) and episodes of minor argillaceous deposition, reflecting low to very low sedimentation rates. In ZNO the depositional environment during this time interval was similar to the conditions in western NL, with siliciclastic basinal deposition and high sedimentation rates. In JO, NL and ZNO, the fourth time interval ends with condensation, i.e. with a phase characterised by low to very low sedimentation rates (Wutach and Ifenthal Formations respectively; Fig. 4-4, Fig. 4-5 and Fig. 4-6).

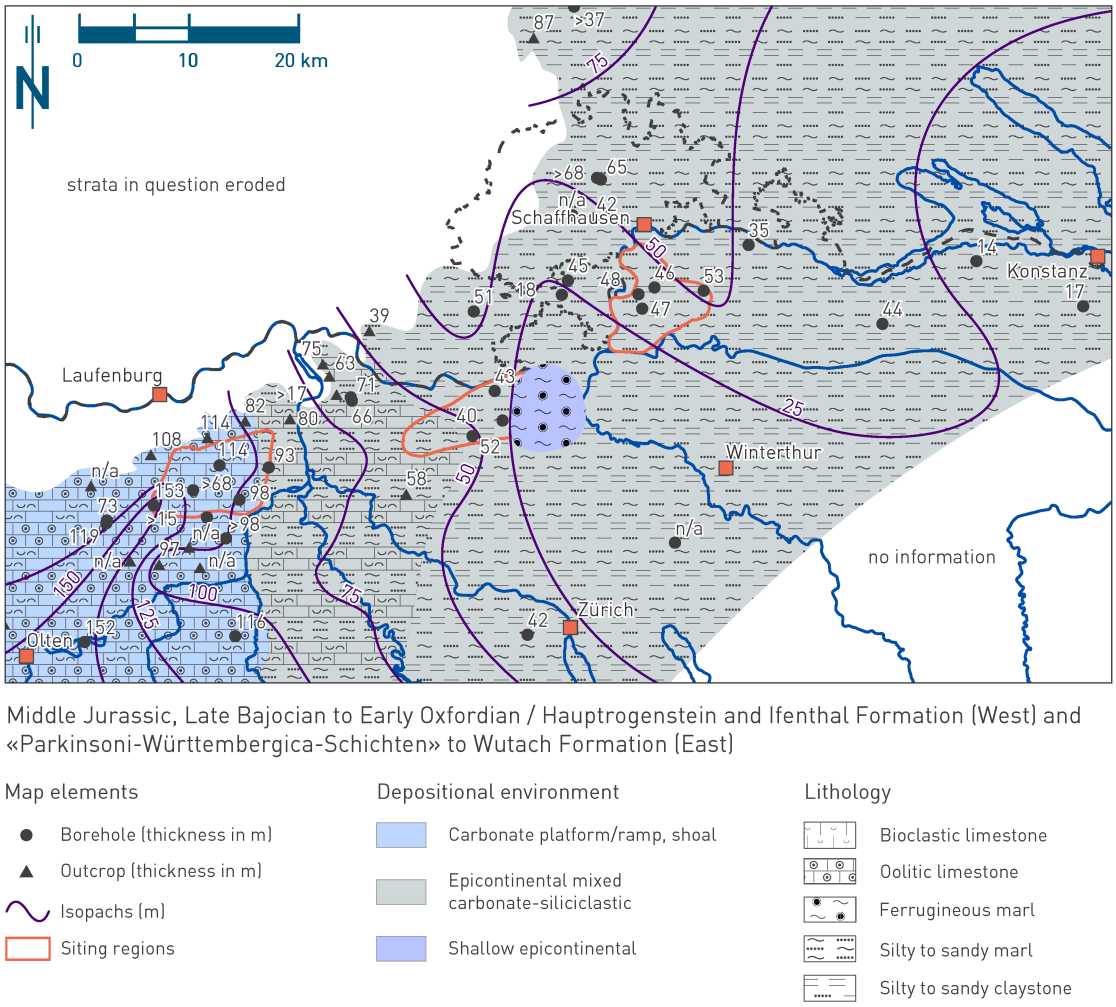


Fig. 4-46: Map of depositional environments during Late Bajocian to Early Oxfordian

Refer to Fig. 4-3 for a schematic representation of depositional environments. The north arrow refers to present-day geographic north. Map shows the setting during the "fourth time interval" (168.2_Baj_200 to 154.8_Oxf_975) as discussed in the text.

4.2.8 Wildegg Formation

4.2.8.1 Introduction

The Wildegg Formation forms the uppermost part of the upper confining units in the NL and ZNO siting regions (Section 4.5.3.4). It was deposited during the Late Jurassic in a shallow marine epicontinental setting (Chapter 3). The depositional environment corresponded to a mixed carbonate-siliciclastic setting with a depositional centre between Olten, Aarau and Brugg. In the JO siting region, the upper part of the Wildegg Formation is partly eroded.

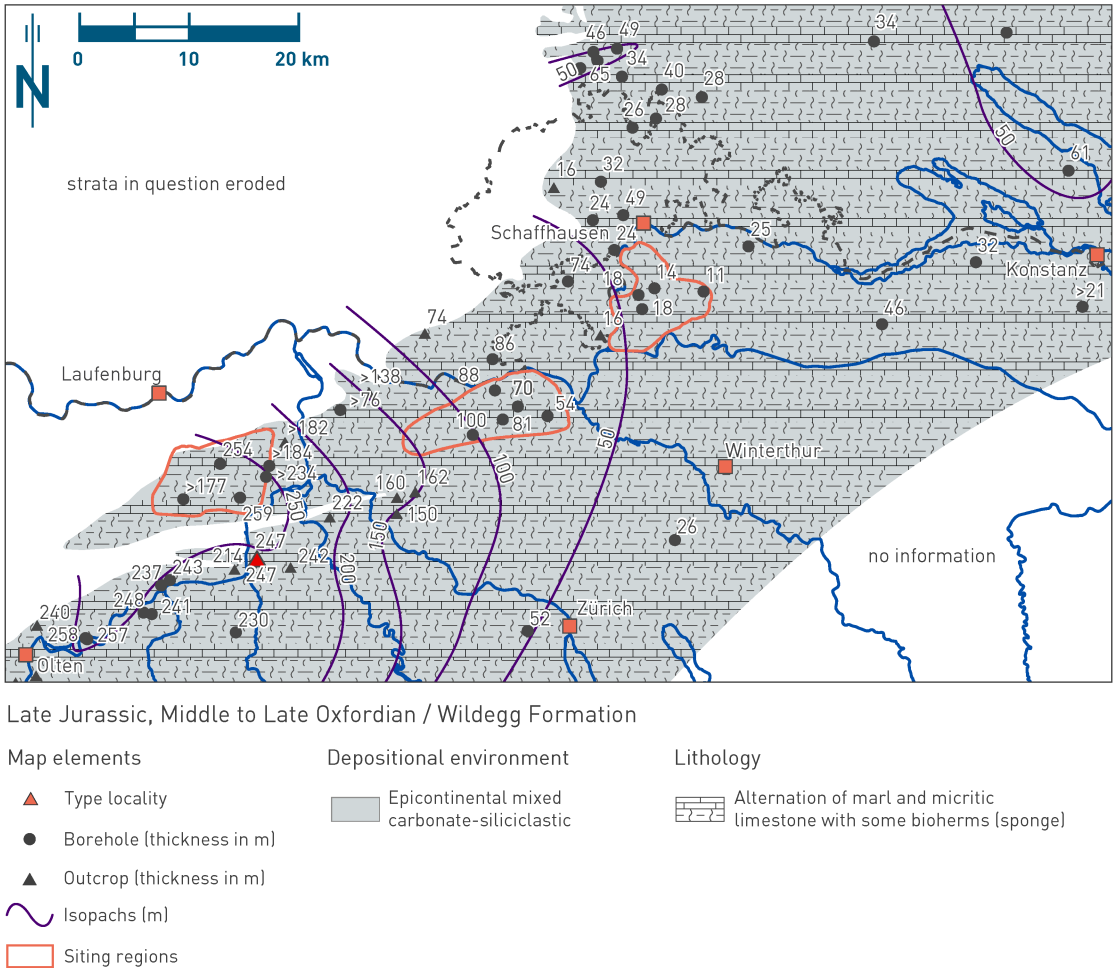


Fig. 4-47: Map of depositional environment during the Late Jurassic (Middle to Late Oxfordian) preserved in the Wildegg Formation

Refer to Fig. 4-3 for a schematic representation of depositional environments. The north arrow refers to present-day geographic north.

4.2.8.2 Facies and lithostratigraphy

In Northern Switzerland, the thickness of the Wildegg Formation decreases from west to east (Fig. 4-47). In the JO siting region, it has a thickness of a ca. 250 to 260 m, in NL ca. 50 to 100 m, and in ZNO ca. 10 to 20 m. The Wildegg Formation consists mostly of limestone, argillaceous limestone and calcareous marl (Fig. 4-48, Fig. 4-49; Allenbach 2001, Deplazes et al. 2013). Individual limestone beds are mostly bundled in few metre- to decametre-scale thick successions which alternate with calcareous marl successions. The most characteristic, the Gerstenhübel Bed, and also the thinner of these limestone successions (Fig. 4-48) can be followed over large distances of 25 km or more in the study area (Gygi & Persoz 1986, Deplazes et al. 2013).

The Wildegg Formation can be subdivided into the Birmenstorf Member (only up to few metres thick) at the base and the younger Effingen Member, which makes up the vast majority of the formation:

Birmenstorf Member: In the JO siting region, the Birmenstorf Member has a thickness of up to ca. 4 m. It consists of bioclastic and glauconitic limestone (biomicrite) and is very fossiliferous, with sponges, ammonites and belemnites (Fig. 4-49a). At the base it may include some iron-ooids. Towards the east, the Birmenstorf Member is gradually replaced by condensed units from bottom to top: «Glaukonitsandmergel Bed», «Mumienkalk Bed» and «Mumien-mergel Bed» (Gygi 2012). The latter two units were incorporated into the Birmenstorf Member by Jordan & Deplazes (2019); together they generally reach a thickness of mostly ca. 1 m, rarely up to few metres (e.g. TRU1). They consist of fossiliferous, glauconitic, partly iron-oolitic to oncolitic calcareous to argillaceous marl and argillaceous limestone (biomicrite) (Fig. 4-49b). Characteristic for some parts of this interval are so-called "Mumien" (mumies) consisting of partly encrusted, subangular to rounded limestone oncolites and lithoclasts.

Effingen Member: This member forms by far the largest part of the Wildegg Formation. The principal lithologies of (argillaceous) limestone (micrite) and calcareous marl are partly bioturbated, bioclastic, often pyritic and contain some quartz and feldspar (silty-sandy) (Fig. 4-49d – g). In the lower part of the Effingen Member, sponge bioherms may also occur (Fig. 4-49c).

4.2.8.3 Variability

The Wildegg Formation is dominated by an alternation of (argillaceous) limestone and calcareous marl successions which have similar characteristics over Northern Switzerland (Fig. 4-48). However, the thickness of the entire formation and its individual stratal successions decreases strongly from west to east in the study area. Some of these successions can be partly correlated over large distances of more than 25 km (Deplazes et al. 2013). The most prominent limestone succession, the Gerstenhübel Bed, may even be correlated over the entire study area, although its thickness and facies change laterally. Additionally, especially in the interval below the Gerstenhübel Bed, the correlation of the succession is less clear compared to the interval above the Gerstenhübel Bed.

4.2.8.4 Chronology

The Wildegg Formation was deposited in the Late Jurassic during the Middle to the Late Oxfordian (Gygi 1969). Timelines were picked mostly near the Gerstenhübel Bed (154.8_Oxf_750 and 154.8_Oxf_700). The top of the Wildegg Formation is diachronous (Deplazes et al. 2013).

4.2.8.5 Depositional evolution

The Wildegg Formation was deposited in a shallow epicontinental sea in the carbonate-siliciclastic Swabian facies realm, with a depositional centre that corresponds to the present-day area between Olten, Aarau and Brugg (Chapter 3). Mass wasting deposits, especially in the lower Effingen Member, indicate relief contrasts in the basin. Towards the west, the Effingen Member was bounded by the eastern part of the Celtic Platform consisting of a carbonate shoal with oolites and coral bioherms (Günsberg Formation) and a backreef environment with a lagoonal facies (Vellerat Formation; Gygi 2000a, Strasser et al. 2012). The patch-reef belt migrated southeastwards towards the basin during the Oxfordian (Gygi 1986). To the south, the shelf sea merged into the open Piemont – Liguria Ocean. The nearest mainlands were the London-Brabant, Rhenish and Bohemian Massifs in the north and east. During the first phase of the deposition of the Wildegg Formation, sedimentation rates were low to very low, particularly in the eastern Birmenstorf Member. In contrast, during the deposition of the Effingen Member sedimentation rates were very high within the depositional centre between Olten, Aarau and Brugg, although with an eastward-decreasing trend (Fig. 4-4, Fig. 4-5, Fig. 4-6). During the Late Jurassic, accommodation space was created by subsidence as the compacted sedimentary rock thickness exceeded the estimated water depth of ca. 50 – 100 m. The development of the depositional centre can be explained by differential subsidence (Allenbach 2001, 2002). The sediment accumulation pattern may also have been characterised by reworking by bottom current systems, perhaps along the eastern side of the carbonate platform (sediment drift deposits). The partly correlatable limestone and calcareous marl successions might reflect climate cycles in combination with relative sea level changes (Allenbach 2001, Deplazes et al. 2013). The depositional evolution of the Wildegg Formation is subdivided here into three time intervals (Fig. 4-48):

The first time interval (154.8_Oxf_975 to 154.8 Oxf_750) approximately corresponds to the Birmenstorf Member and the Effingen Member below the Gerstenhübel Bed. This time interval starts with a phase of condensation especially in the east, where only a succession of hardgrounds is preserved. In the west, a somewhat thicker succession with sponge bioherms was deposited. The Effingen Member below the Gerstenhübel Bed is mainly interpreted as a deposition formed during relatively low sea-level conditions (Gygi et al. 1998, Allenbach 2001). In this setting, more siliciclastic sediment must have reached the basin that led to an overall increase in the deposition of siliciclastics. At the same time, the area of carbonate production in the shelf environment decreased, leading to a lower calcareous input.

The second time interval (154.8_Oxf_750 to 154.8 Oxf_700) approximately corresponds to the deposition of the Gerstenhübel Bed. It was possibly deposited during relatively high sea-level conditions. With a higher sea level, more siliciclastic material was trapped in the flooded coastal plains and the transport distances of the siliciclastics to the shallow basin increased. On the platform, carbonate production may have increased as accommodation space increased, and as the siliciclastic input may have decreased (less turbidity); at the same the increased calcareous production may have caused an increased calcareous export into the shallow basin.

The third time interval (154.8_Oxf_700 to 154.8 Oxf_300) approximately corresponds to the Effingen Member above the Gerstenhübel Bed. It may correspond to a second phase of deposition during relatively low sea-level conditions that was followed by a second phase of deposition during relatively high sea-level conditions, which is reflected by the uppermost Effingen Member and the overlying Villigen Formation. The top of the Effingen Member is probably diachronous. In the east the mostly carbonate-dominated sedimentation of the Villigen Formation started slightly earlier, whereas in the west the mixed siliciclastic-carbonate facies lasted longer.

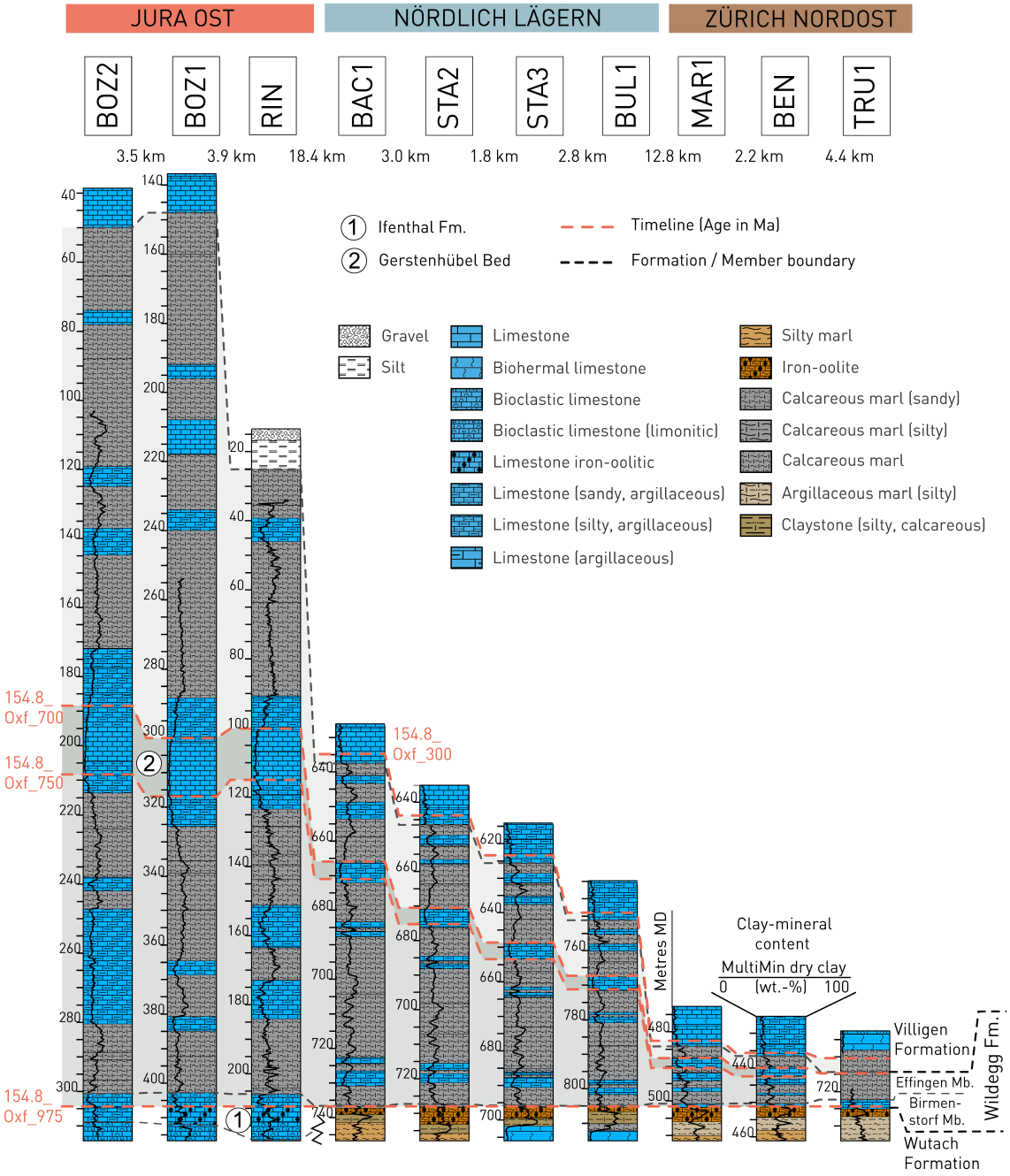


Fig. 4-48: Stratigraphic borehole correlation of the Wildegg Formation

For lithological nomenclature refer to Naef et al. (2019). Clay-mineral content after Becker & Marnat (2024) Some of the boundaries and lithologies as discussed in the original reports were adjusted to integrate all presented borehole data.

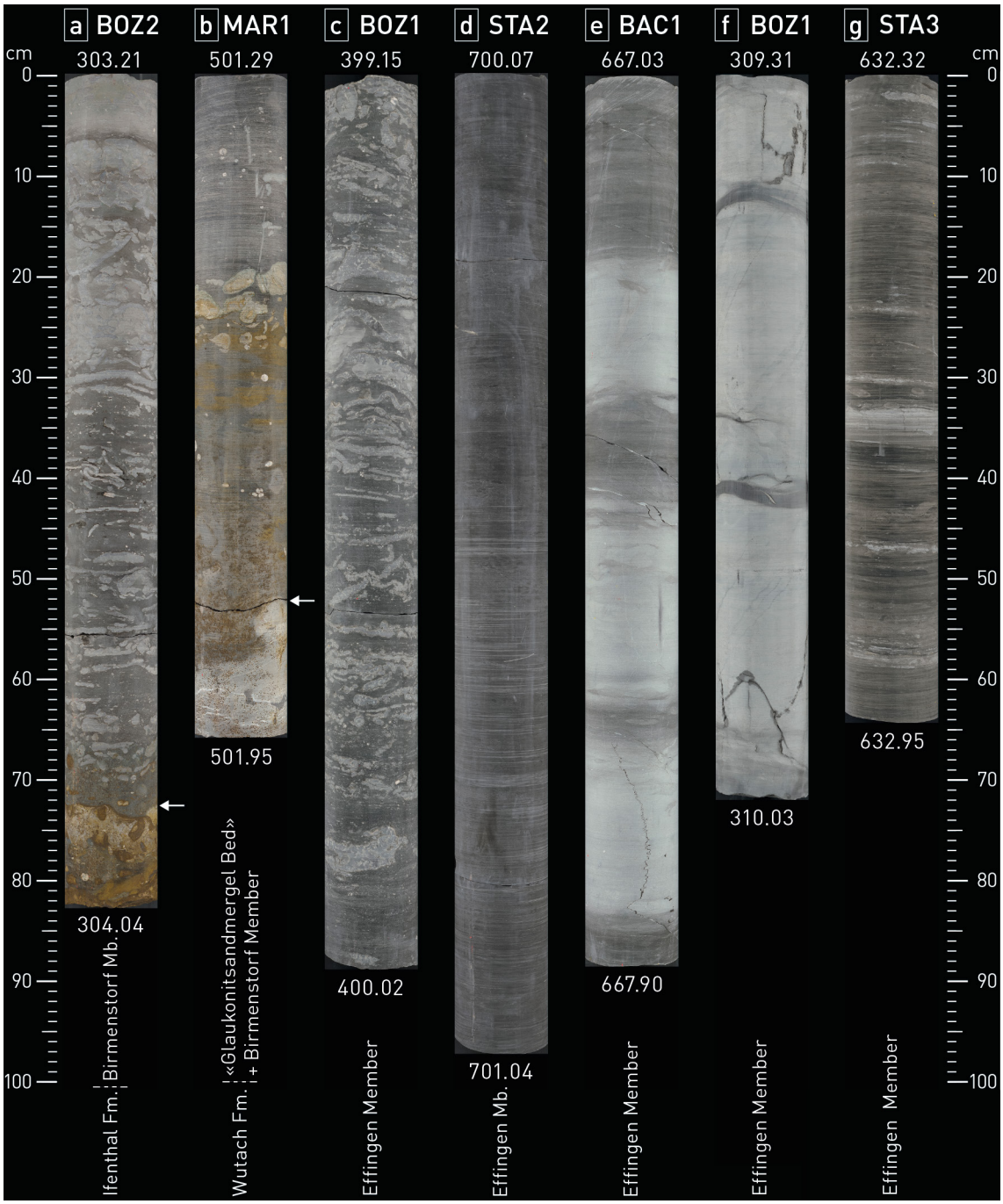


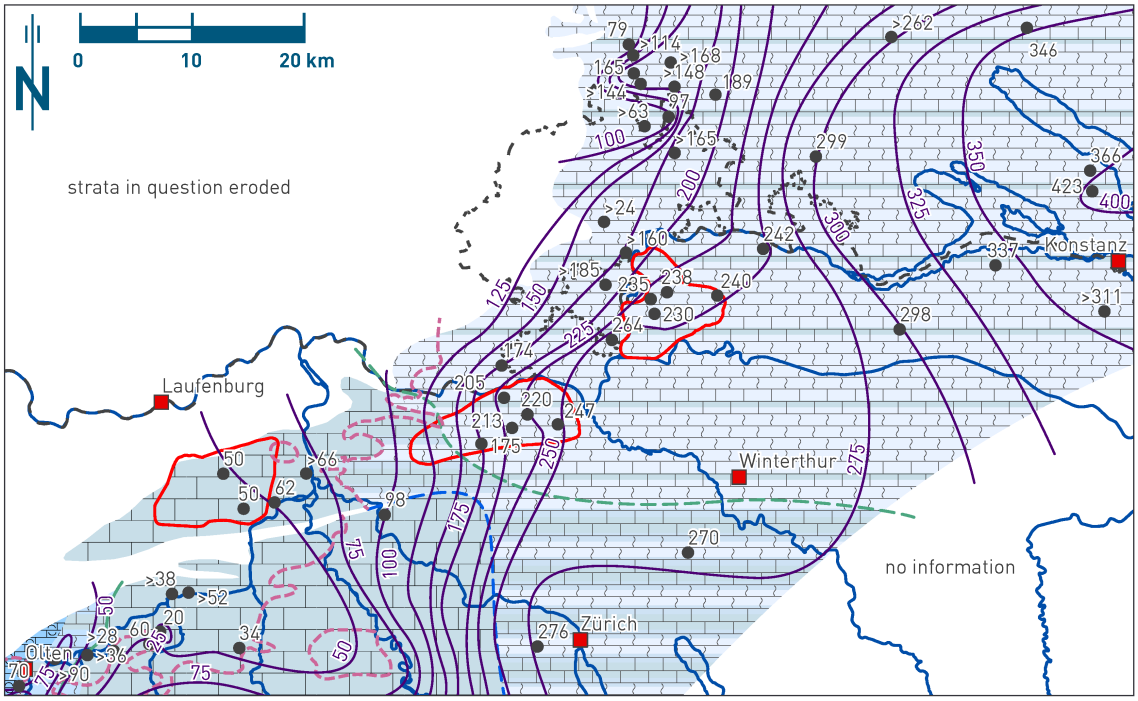
Fig. 4-49: Selected core photos of the Wildegg Formation

(a) Reddish brown iron-oolite (hardground) below glauconitic, bioclastic argillaceous to calcareous marl and limestone with many light grey sponges; **(b)** Reddish grey iron-oolitic limestone (hardground) below grey glauconitic argillaceous marl with reworked iron-ooids in the lower part and oncolitic limestone bed; **(c)** dark grey bioclastic, glauconitic, argillaceous marl with many light grey sponges; **(d)** dark grey calcareous marl; **(e)** & **(f)** intercalation of light grey limestone with cm- to dm-scale beds of calcareous marl; **(g)** dark grey argillaceous marl, silty with centimetre-scale limestone layers.

4.2.9 Malm Group above Wildegg Formation

4.2.9.1 Introduction

The Malm Group above Wildegg Formation overlies the upper confining units of the host rock. It forms the Malm aquifer in NL and ZNO; in JO this aquifer exists in part of the siting region at shallow level (Section 4.5.3.3, Fig. 4-50). The sedimentary succession was deposited during the Late Jurassic in a shallow marine epicontinental sea (Chapter 3).



Late Jurassic, Late Oxfordian to Early Tithonian / Villingen and Balsthal to Reuchenette and Burghorn Formations, «Felsenkalke» + «Massenkalk» and Obere Bankkalk Formation (DE)

Map elements

- Borehole (thickness in m)
- Outcrop (thickness in m)
- Isopachs (m)
- Erosional Limit of Late Kimmeridgian
- Eastern boundary of transition to Balsthal Formation
- Southwestern boundary of Hornbuck Member
- Limit between Burghorn Formation and «Felsenkalke» + «Massenkalk»
- Siting regions

Depositional environment

- Carbonate plattform, shoal (backreef)
- Carbonate plattform, bioherm (coral)
- Carbonate ramp, shallow epicontinental
- Carbonate ramp, bioherm (sponge)

Lithology

- Micritic, partly bioclastic limestone
- Bioclastic, partly oolitic limestone
- Biohermal limestone (coral, sponge)

Fig. 4-50: Map of depositional environments during the Late Jurassic (Late Oxfordian to Early Tithonian) preserved in the Malm Group above Wildegg Formation

Refer to Fig. 4-3 for a schematic representation of depositional environments. The north arrow refers to present-day geographic north.

4.2.9.2 Facies and lithostratigraphy

In the three siting regions, the Malm Group above Wildegg Formation comprises the Villigen Formation, Schwarzbach Formation as well as the «Felsenkalke» and «Massenkalk» (Fig. 4-51). The top of this unit is truncated by a major diachronic erosive unconformity, overlain by residual deposits from the Eocene («Siderolithic Group»; Chapter 3). At the northeastern boundary of the map of Fig. 4-50 in southern Germany, the last preserved Mesozoic rocks are of Early Tithonian age (Hangende Bankkalke Formation; Zaugg et al. 2008, Koch 2019). In the southwest of the map, the erosion has nearly reached the base of the Villigen Formation. North of Olten, at the western edge of the map, even the Wildegg Formation is missing, and the erosion has reached late Middle Jurassic sediments. In the JO siting region, an approximately 50 m succession of the Malm Group above Wildegg Formation, i.e. Villigen Formation, was found in the BOZ1, and BOZ2 boreholes (Fig. 4-50). In the NL and ZNO siting regions, parts of the «Felsenkalke» and «Massenkalk» are preserved beneath the unconformity. The thickness of the Malm Group above Wildegg Formation has been confirmed in boreholes, between 175 and 250 m in NL and between 230 and 240 m in ZNO.

The Villigen Formation mostly consists of well-bedded limestone (mudstone, packstone, (bio-) micrite) with generally similar characteristics in all the siting regions (Fig. 4-51, Fig. 4-52a – c). Some of the layers are glauconitic and some fossiliferous with sponges (boundstone), crinoids, bivalves, and ammonites. In NL and ZNO, the Villigen Formation has a thickness between ca. 60 and 80 m (Fig. 4-51). The Villigen Formation is subdivided into the Geissberg, Crenularis, Wangen and Letzi Members in the western part of Northern Switzerland, and into the Hornbuck, Küssaburg and Wangental Members in the eastern part (Gygi 1969, 2000b).

The Schwarzbach Formation (former «Mittlere Malmmergel») consists mostly of a bedded succession of glauconitic limestone (argillaceous) and some glauconitic, calcareous marl (Fig. 4-52d). It has similar characteristics in the NL and ZNO siting regions and is a lateral equivalent of the Baden Member of the Burghorn Formation. The limestones consist of different carbonate textures (mudstone, wackestone, some packstone) and lithotypes (micrite, biomicrite, biopelmicrite). The Schwarzbach Formation has an increased clay-mineral content in comparison to the underlying and overlying formations (Fig. 4-51). The boundary to these formations is gradual rather than abrupt. The Schwarzbach Formation is fossiliferous and comprises sponges, ammonites, belemnites, bivalves, and some crinoids. Traces of bioturbation are common. It has a thickness in the range between ca. 10 and 25 m.

The «Felsenkalke» (former «Quaderkalk», «Plattenkalk» or «Bankkalk») and «Massenkalk» represent two different facies units that were deposited next to each other. They are regarded here in combination as an informal unit in the rank of a formation and have a thickness in the range between ca. 85 and 155 m (Fig. 4-51). They share similar characteristics in NL and ZNO. The «Felsenkalke» unit largely consists of typically micritic, mostly well-bedded limestone (mud-stone, wackestone to packstone, micrite, biopelmicrite) with decimetre-scale marl and limestone (argillaceous) interbeds (Fig. 4-52e). Many horizons of the «Felsenkalke» are fossiliferous, including ammonites, some sponges, belemnites, crinoids, and brachiopods. The «Massenkalk» consists of massive limestone with algal sponge bioherms (boundstone, packstone, biomicrite to pelmicrosparite) up to decametres in size (Fig. 4-52f). Additionally, benthic fauna such as echinoderms can be found. The strata of the «Massenkalk» are originally dominated by siliceous sponges and also diagenetic siliceous nodules may occur. In some intervals, the sponges are no longer visible because of dolomitisation and dedolomitisation, leading to a saccharoidal limestone (Koch 2011). Such saccharoidal limestones are characterised by brown-yellow colour, variable dolomitic content and vugs (Geyer et al. 2023). These processes can also spread from the «Massenkalk» into the «Felsenkalke». The differentiation between the two facies units in bore-holes can be gradual. «Felsenkalke» and «Massenkalk» also contain palaeokarst features that are filled with siderolithic claystone («Boluston»; Fig. 4-52g, Chapter 3).

4.2.9.3 Variability

The Villigen Formation is dominated by limestone and shows relatively low variability (Fig. 4-51). Lateral correlation of calcareous successions can be guided by marker beds such as the «Knollen Bed», which, however, could not be identified in all boreholes. Occurrence of sponges, especially in the Hornbuck Member, may lead to lateral and vertical variability as they can form bioherms of very local extent.

The Schwarzbach Formation shows relatively low variability and can be laterally well correlated (Fig. 4-51). Additionally, the general succession of more calcareous to argillaceous beds within the Schwarzbach Formation seems to be correlatable, especially in the boreholes of NL.

The facies units of the «Felsenkalke» and «Massenkalk», interfinger laterally and vertically, but both facies units are dominated by limestones. The sponge bioherms of the «Massenkalk» probably formed mounds that were surrounded by the well-bedded «Felsenkalke». These mounds can have lateral extents of few decametres to several kilometres (Geyer et al. 2023). Additionally, beds particularly enriched in fossils and glauconite exist. One of these beds, the «Glauconitic Marker Bed», was identified as a marker horizon by Gygi (2000a).

4.2.9.4 Chronology

The Villigen Formation was deposited in the Late Jurassic during the Late Oxfordian to Early Kimmeridgian (Gygi 2000a). The Schwarzbach Formation was deposited mainly in the later Early Kimmeridgian and the «Felsenkalke» and «Massenkalk» in the Late Kimmeridgian. Timelines were picked approximately at the boundaries of the formations (154.8_Oxf_300, 149.2_Kim_700, 149.2_Kim_400, 149.2_Kim_100). However, the top of the «Felsenkalke» and «Massenkalk» is a major unconformity and is therefore diachronous.

4.2.9.5 Depositional evolution

The Villigen Formation, Schwarzbach Formation, «Felsenkalke» and «Massenkalk» were deposited in a basinal domain of the epicontinental sea that connects the Celtic or Rauracian Platform in the west and the Swabian Basin in the northeast (Fig. 3-10). The nearest mainlands were the London-Brabant and Rhenish Massifs in the north and the Bohemian Massif in the east. To the south, the Helvetic and Briançonnais shelf margin merged into the Piemont – Liguria Ocean (Gouffon 2024). Calcareous oolites were deposited on the carbonate platform to the west and mostly at the platform margin coral bioherms also grew (Olten Member of the Balsthal Formation; Gygi 1990). The depositional environment of the study area was dominated by a carbonate ramp, locally with bioherms partly in a basinal setting and sedimentation rates that were generally high (Fig. 4-5, Fig. 4-6). However, glauconitic, fossiliferous and nodular horizons indicate depositional phases with reduced sedimentation rates. Sponges occur throughout the Malm Group above Wildegg Formation, particularly extensive sponge bioherms exist in the Hornbuck Member of the Villigen Formation and in the «Massenkalk». In comparison to the Early Oxfordian, the environment documents a general decrease in terrestrial input and an increase in carbonate production also in deeper water. An exception is the time interval during which the deposits of the Schwarzbach Formation were formed, which reflects an intermittent relative increase in argillaceous input relative to carbonate production and input. The variations in terrestrial and carbonate input could reflect variations related to climate and eustatic sea level changes (Gygi 2000b).

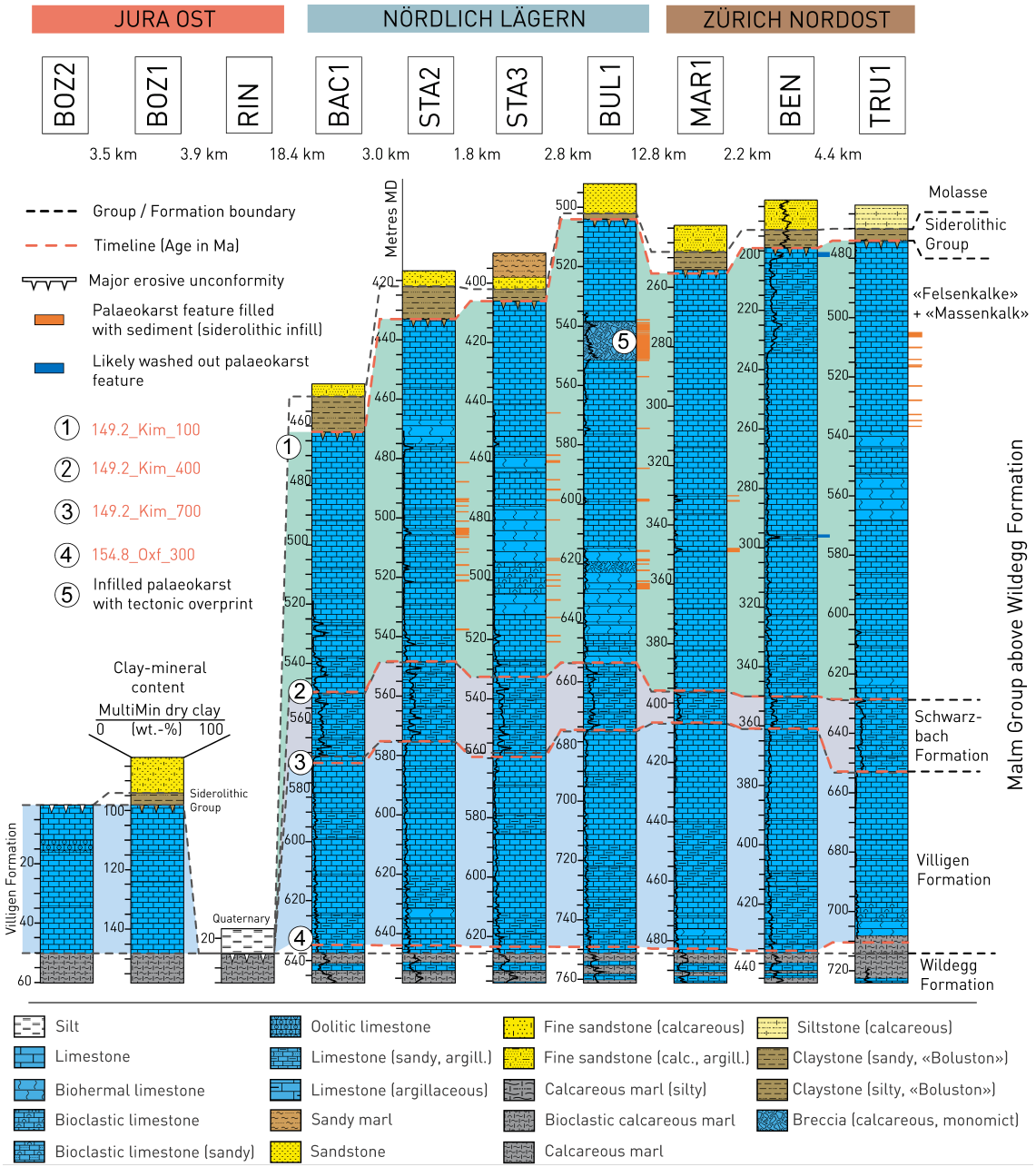


Fig. 4-51: Stratigraphic borehole correlation of the Malm Group above Wildegg Formation

For lithological nomenclature refer to Naef et al. (2019). Clay-mineral content after Becker & Marnat (2024). Some of the boundaries and lithologies as discussed in the original reports were adjusted to integrate all presented borehole data.

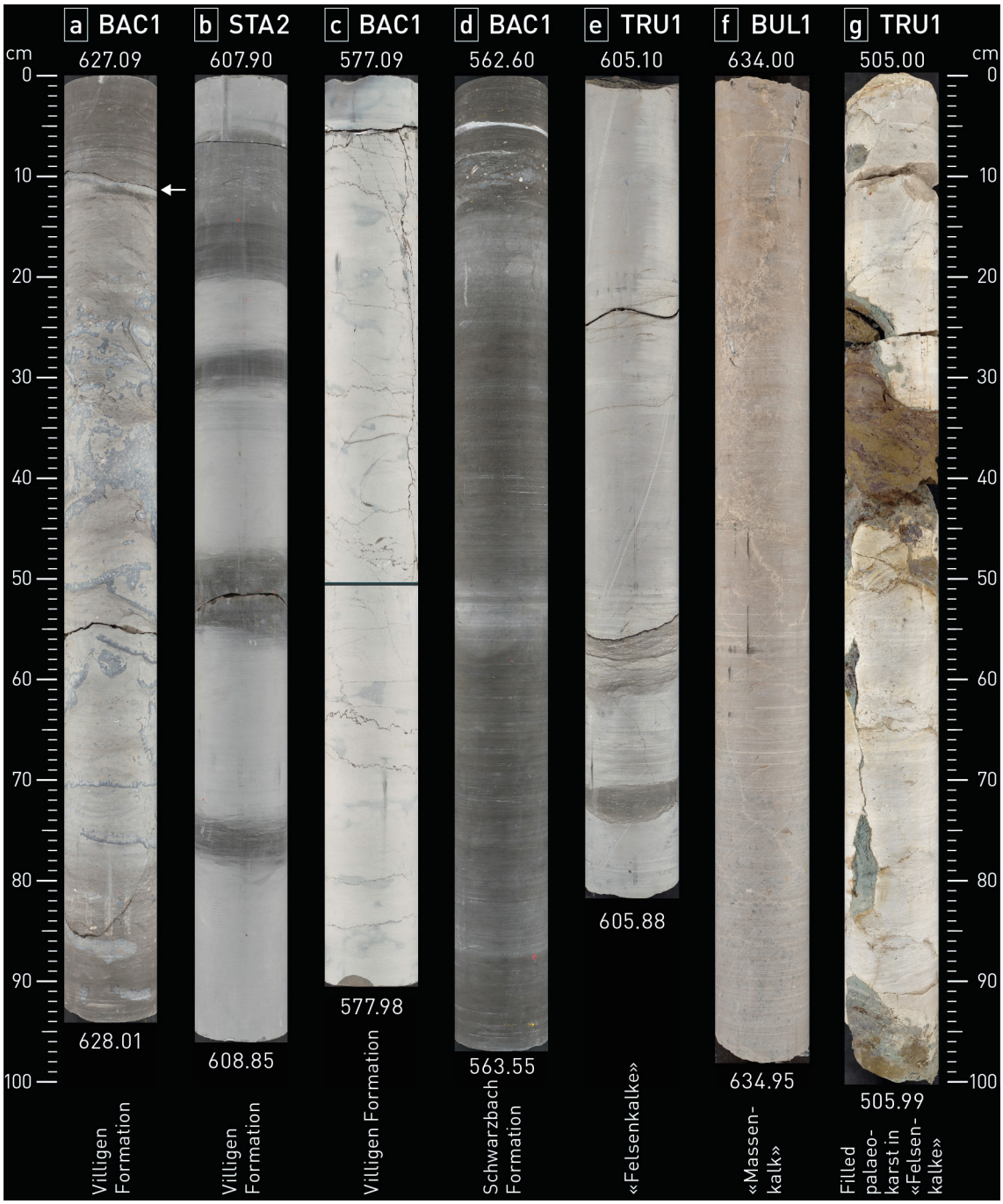


Fig. 4-52: Selected core photos of the Malm Group above Wildegg Formation

(a) Top Hornbuck Member (627.20 m) with grey to beige biohermal limestone, very fossiliferous (sponges, echinoderms) and dark grey bioclastic calcareous marl; **(b)** medium light limestone, with interlayers of dark grey argillaceous to calcareous marl; **(c)** light grey limestone, strongly bioturbated with thin seams of claystone, mostly reduced to stylolites; **(d)** dark grey bioclastic calcareous marl, glauconitic, fossiliferous (bivalves, belemnites, crinoids), bioturbated, with grey interlayers of limestone, argillaceous, bioturbated; **(e)** medium grey limestone, with thin beds of calcareous marl; **(f)** beige-grey, massive limestone, fossiliferous (many sponges); **(g)** beige limestone with palaeokarst fissures filled with variegated claystone.

4.2.10 Conclusions

- The Opalinus Clay exhibits similar characteristics in all the siting regions, with high clay-mineral content and relatively small vertical and lateral variability. This can be attributed to deposition in an epicontinental marine basin characterised by clay-mineral-rich input, generally high sedimentation rates and a relatively homogeneous environment. The thickness of the Opalinus Clay is similar in all three siting regions (104 – 122 m). In NL, the Opalinus Clay is slightly thinner compared to JO and ZNO, but the layers directly above the Opalinus Clay have a higher clay-mineral content compared to the other siting regions (> 35% over large sections). In the eastern part of NL, the clay-mineral-rich zone including Opalinus Clay and these overlying rocks reaches thicknesses > 130 m.
- In all the siting regions, the lower and upper confining units of the Opalinus Clay have an overall high clay-mineral content but are more variable (e.g. intercalated sandy, calcareous, or dolomitic interlayers).
- Underlying the Opalinus Clay, the Staffelegg Formation is dominated by strata rich in clay minerals, including more calcareous intercalations. These units reflect marine conditions with changing depositional environments. The lateral extent of the individual units is large, therefore the differences between the siting regions and the variability within the siting regions are small in this formation.
- The stratigraphic succession further below (Klettgau Formation) is more variable and preserves intercalated terrestrial and marine sedimentary rocks. The stratigraphically uppermost, potentially water-conductive unit is the Seebi Member, which is thickest and most porous in ZNO (sandstone and dolomitic breccia), thinner and less porous in NL (mainly dolostone) and absent in JO. The next prominent unit with low clay-mineral content is the Gansingen Member. It is thickest, dolomite-rich and most porous in JO and increasingly thinner and more anhydritic towards the east. Sandy intercalations lower in the succession (Ergolz Member) were deposited in fluvial channels in a floodplain environment. These facies are local, difficult to predict, and can be present in all the siting regions.
- Further down-section, above the regional Muschelkalk aquifer (Schinznach Formation), the Bänkerjoch Formation is represented by an evaporitic to clay-mineral-rich succession, mainly deposited in a sabkha environment.
- The successions above the Opalinus Clay differ between the three siting regions. In JO and ZNO, the generally clay-mineral-rich units following the Opalinus Clay contain numerous calcareous and sandy beds. In NL, the decametre-thick interval above the Opalinus Clay exhibits a higher clay-mineral content compared to JO and ZNO. In the eastern part of NL, this clay-mineral-rich succession is interpreted to result from a depositional positive relief formed by marine bottom currents during the Bajocian. This topographically high area favoured the growth of an isolated carbonate platform several square kilometres in size («Herrenwis Unit»). Up-section, clay-mineral-rich deposits dominate in NL and ZNO with thickness variations reflecting the filling of the basin around the carbonate platform. As a result of this depositional succession, the «Herrenwis Unit» represents an isolated body embedded in clay-rich rocks.
- In contrast, in JO carbonate deposition is represented by strata in the upper part of the Dogger Group (Hauptrogenstein). The easternmost part of the carbonate platform and its margin are recognised in the JO siting region (platform in the west, basin towards the east).
- The uppermost unit (Wildegg Formation) below the regional Malm aquifer is represented by successions of limestone and calcareous marl with a pronounced reduction in thickness from west to east in the study area.

4.3 Tectonic setting

Key points:

- The tectonic evolution of Northern Switzerland is linked to the evolution of the surrounding tectonic domains. These are the Konstanz – Frick Trough (and in general the pre-structured Paleozoic basement), the Jura Fold-and-Thrust Belt, the Upper Rhine Graben and the Hegau – Bodensee Graben.
- In general, inherited faults act as zones of weakness within the less deformed rock volume and later deformation preferentially localises along them.
- The geodynamic evolution is summarised by two phases of sedimentation and burial (Mesozoic and Paleogene – Neogene) separated by a phase of subaerial exposure. Miocene NW propagation of the Alps formed the Jura Fold-and-Thrust Belt.
- The Triassic salt layers acted as décollement level during the NW-propagation of the Alpine front in the eastern Jura Fold-and-Thrust Belt. No evidence for a secondary décollement within the Opalinus Clay was observed within the siting regions.
- All the siting regions show areas devoid of seismically mappable faults. NL includes the largest of such areas.

4.3.1 Overview

In this section, the structural setting of the three siting regions within the framework of the tectonic setting of Northern Switzerland is described. In the context of the siting process for a deep geological repository, knowledge of the occurrence and architecture of faults is relevant as such structures may affect the properties of the rock volume. The following sections are focused on the siting regions and the framework of consideration is enlarged only sporadically. The chapter starts with a terminology section (Section 4.3.2), as structural geology terms might have slightly different meanings within different scientific communities. Section 4.3.3 provides an overview over the regional tectonic setting, with the focus on the larger tectonic structures such as the Konstanz – Frick Trough. Section 4.3.4 provides a description of the structures encountered during the characterisation of the siting regions, taking into account the interpretation of the 3D seismic reflection data and the observations from the recently drilled deep boreholes (Tab. 2-1). A focused description of deformation in the Opalinus Clay is given in Section 5.5.

The general geological evolution of Northern Switzerland has briefly been introduced in Chapter 3. Section 4.3.5 elaborates on the tectonic evolution since Early Jurassic times in more detail and adds insights gained from the structural investigations during SGT Stage 3 and from recent investigations of the burial and temperature history by analyses of veins from outcrops and drill cores. Section 4.3.6 characterises key factors that influenced the present-day structural inventory in the siting regions. The chapter concludes with Section 4.3.7. Neotectonic activity (i.e. indications for post-Pliocene tectonic deformation) are discussed in Section 6.2.

4.3.2 Terminology of structures

Considering the different spatial scales of geological structures observed in the three siting regions, it is necessary to use a unifying terminology for a comparative analysis of the siting regions. For the sake of consistency with previous work carried out by Nagra, in this chapter the terminology originally employed for the description of structures recorded in the cores of the TBO boreholes is adapted (Tab. 2-1).

Generally, a distinction is made between Mohr-Coulomb brittle failure and ductile deformation. Stylolites, shear zones and mylonites as defined in Ebert & Decker (2019) were identified as ductile structures. The Mohr-Coulomb brittle failure structures are called fractures as an over-arching term. Extensional fractures are called joints; these may be barren or veins when filled. The term fault refers to fractures that have experienced shearing detectable on the scale of observation (e.g. in hand specimens). To better convey the variable dimension covered by the term fault, faults were subdivided according to their size into regional fault zones, local faults, small-scale faults and micro faults (Fig. 4-53). The structural terminology used in this report is summarised in Tab. 4-1.

Tab. 4-1: Summary of the structural terminology for faults across the observation scales

Tectonic structure	**Definition**	**Dimensions**
Regional tectonic elements	Regional tectonic element is an overarching term encompassing (i) regional fault zones and (ii) zones of increased tectonic complexity.	km-scale length
Regional fault zone	Regional fault zones encompass seismically mappable, relatively closely spaced and clustered faults in the Mesozoic strata associated with established Northern Switzerland tectonic elements.	km-scale length Displacement is variable among the structures and dependent on structural style (typically 10 m to 10s of metres)
Zones of increased tectonic complexity	Overarching term including (a) zones characterised by an increased number of local faults mapped in seismic reflection data, but devoid of a distinct regional trend, (b) zones with diffuse deformation linked to a regional fault zone and (c) structural setting known to bear the potential for increased sub-seismic deformation, e.g. in connection with major regional basement structures.	km-scale length
Local fault	Seismically mappable faults or faults identified in outcrops that are solitary structures and are not part of the regional fault system.	100s of metres scale length Displacement is dependent on structural style (typically m to few 10s of m)
Seismically mappable fault	Seismically mappable faults are faults matching the criteria defined by a number of fault diagnostic signatures in seismic reflection data (Nagra 2024a, 2024b, 2024c).	Faults with vertical offset > 5 – 10 m can be detected consistently in the central part of the three siting regions. In many cases, also smaller features can be detected by 3D seismic reflection data
Sub-seismic faults	Faults that are too small to be detected by faulting diagnostic signatures in seismic reflection data.	Maximum vertical offset of subseismic fault is < 10 m in the central part of the three siting regions. In many cases, also smaller features can be detected by 3D seismic reflection data (Nagra 2024a, 2024b, 2024c)

Tab. 4-1: (continued)

Tectonic structure	Definition	Dimensions
Small-scale fault	A small-scale fault is a complex planar structural discontinuity with a significant width that is characterised by displacement and shear indicators. A small-scale fault is further characterised by (i) the occurrence of multiple structures, (ii) different structure types (e.g. micro faults or veins) and / or (iii) the formation of fault rock (clay gouge, cataclasite, dilation breccia etc.).	10s of metres to few m estimated length Displacement dependent on structural style (typically cm to m)
Micro fault	Plane of shear failure, i.e. slickensides with evidence for plane-parallel movement. A micro fault is a single, thin, planar and sharp structural discontinuity with negligible volume. Micro faults show shear indications such as different types of striation.	< few m estimated length Measured displacement is dependent on structural style (typically mm to a few cm)
Joint	A barren, closed fracture on which there is no measurable slip or dilation at the scale of observation (Hancock 1985).	< few m estimated length
Vein	Mineral infill of a fracture with a dilatational component.	< few m estimated length
Fracture	General term for any type of Mohr-Coulomb failure, i.e. it is applicable to structures formed by extension or shear. Fractures include approximately planar discontinuities such as faults, joints and veins (Peacock et al. 2016).	< few m estimated length
Stylolite	Irregular, commonly jagged surface in a rock formed by local removal of material by pressure solution (Passchier & Trouw 1998).	< few m estimated length

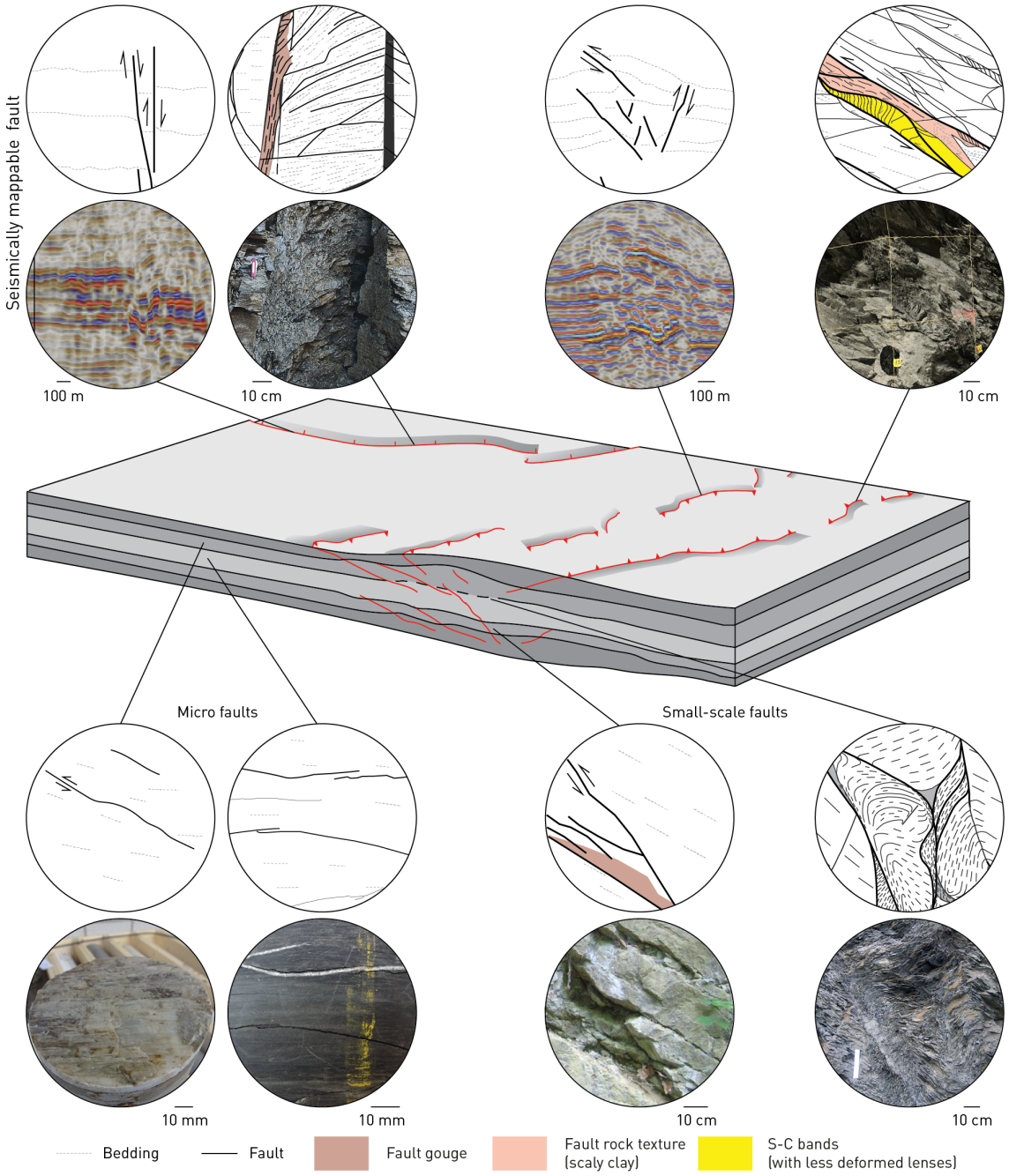


Fig. 4-53: Conceptual block diagram showing fault terminology across the observation scales

Note the mechanical stratigraphy indicated by the grey shading and the highly segmented faults. The seismically mappable normal fault represents the Neuhausen Fault with outcrop in Siblingen. The seismically mappable reverse fault is the Baden – Irchel – Herdern Lineament and the "Main Fault" in the Mont Terri rock laboratory as an outcrop example (modified after Jaeggi et al. 2017).

4.3.3 Tectonic situation of Northern Switzerland

As elaborated in Chapter 3, the study area is situated in the North Alpine Foreland. The siting regions sit between the Upper Rhine Graben in the west, the Hegau – Bodensee Graben in the northeast and the Jura Fold-and-Thrust Belt in the south (Fig. 4-54). In addition, Jura Ost and Nördlich Lägern are located above the Konstanz – Frick Trough, whereas Zürich Nordost is mostly north of it. As the regional tectonic domains strongly control the structural inventory encountered in the siting regions, they are introduced below.

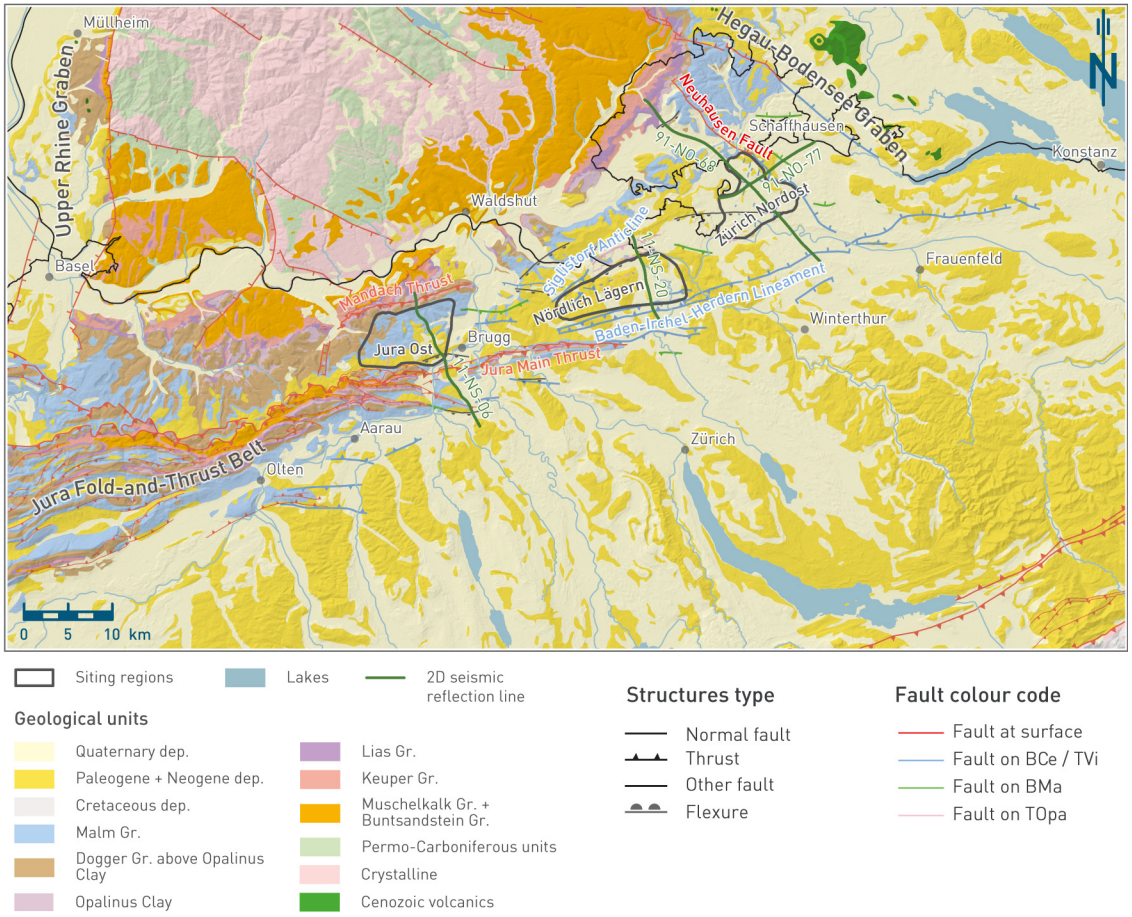


Fig. 4-54: Geological map of Northern Switzerland with the siting regions and major faults

Geological units from 1:500'000 geological map with the addition of the Opalinus Clay outcrops in Northern Switzerland (©swisstopo). Fault traces from seismic interpretation are based on 2D seismic reflection (Madritsch et al. 2013, Meier et al. 2014) and 3D seismic reflection interpretation (Nagra 2024a, 2024b, 2024c). They are shown on the highest stratigraphic horizon where the specific fault segment was picked (different colours in the map view). Only horizons from Top Opalinus Clay and higher stratigraphic levels are shown. Note that only a selection of the structures from 3D seismic interpretation is shown to highlight the structural trends of regional importance. See Fig. 4-61, Fig. 4-65 and Fig. 4-69 for the complete fault pattern.

Konstanz – Frick Trough (Permo-Carboniferous Trough)

The oldest tectonic domain, thought to have acted as an inherited zone of crustal weakness for an extended period of time, is the so-called Konstanz – Frick Trough, which is a graben filled with Permo-Carboniferous sedimentary rocks (Chapter 3). Available knowledge on the buried Konstanz – Frick Trough is derived from boreholes, 2D seismic reflection lines and 3D seismic reflection surveys (e.g. Diebold et al. 1991, Marchant et al. 2005, Madritsch et al. 2013, Naef & Madritsch 2014). Despite extensive subsurface data across the area under consideration, the robustness of the delimitation of the Konstanz – Frick Trough varies considerably (Madritsch et al. 2018). Its northern boundary is well constrained by boreholes, seismic reflection data and outcrops of crystalline basement in the neighbouring Black Forest Massif. The southern boundary is less well defined. It is suspected to roughly coincide with the front of the Internal Jura (Diebold & Noack 1997, Laubscher 1985, Malz et al. 2016). A tentative map of potential Carboniferous troughs underneath the entire Swiss Molasse Basin was presented by Leu (2008).

The Konstanz – Frick Trough is subdivided into a western segment (between Frick and the lower Aare Valley) and an eastern segment (east of the lower Aare Valley; Diebold et al. 1991). The transition between the two segments occurs across a system of NW-SE-trending faults (Fig. 4-55, Vorwald Fault). The western segment is characterised by a wider and deeper central depocentre, whereas the eastern segment has wider trough shoulders with decreased sedimentary infill. JO is located above the western segment, whereas NL and the S-SW corner of ZNO are located above the eastern segment (Fig. 4-55). The transition between the western and eastern segments occurring around an inherited fault system provides evidence for the major control exerted by such inherited faults – and by the pre-structured basement in general – on later deformation.

The main understanding of the tectonic evolution of the Konstanz – Frick Trough derives from the analysis of its sedimentary filling. From this, a three-stage subsidence history has been proposed (Diebold et al. 1991). Late Carboniferous deposition of organic-rich sediments was followed by the main subsidence phase in the Early Permian (~ 295 Ma onwards; Madritsch et al. 2018). Deposition of Late Permian sediments occurred during the late- to post-rifting stages of trough formation (~ 265 Ma).

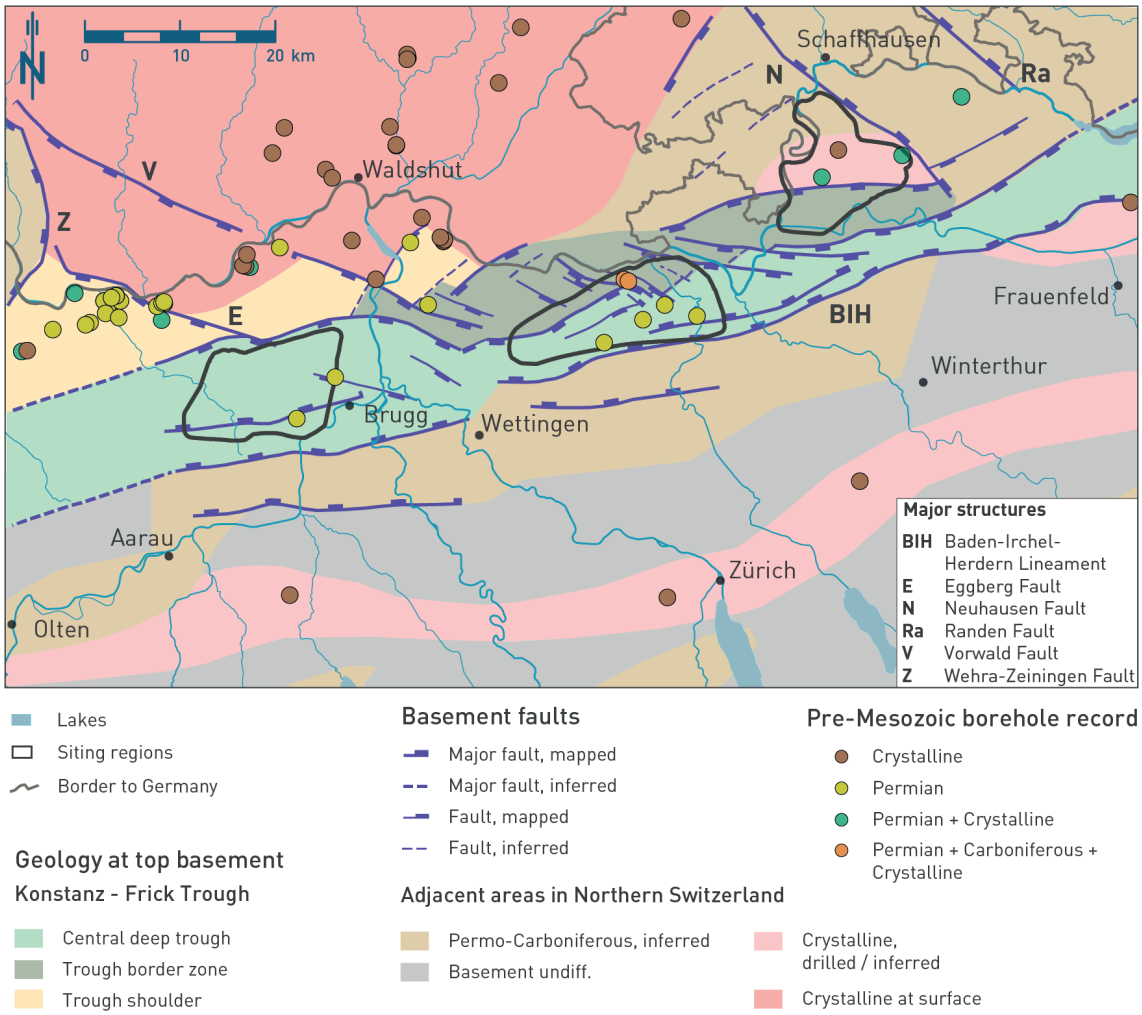


Fig. 4-55: Conceptual tectonic map at top basement showing the main faults and the extent of the Konstanz – Frick Trough

Modified after Madritsch et al. (2018) and Naef & Madritsch (2014). The borehole symbol refers to the pre-Mesozoic record encountered in the borehole.

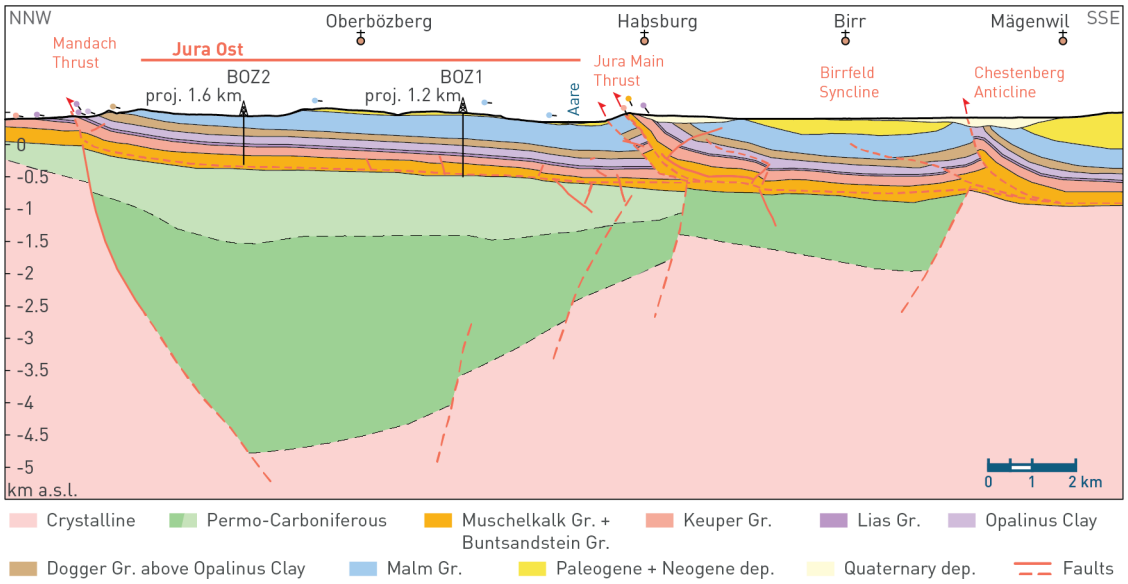


Fig. 4-56: Large-scale geological cross-section through Jura Ost

Geological section drawn along the 2D seismic reflection line 11-NS-06. Section trace located in Fig. 4-54. The section is based on Meier et al. (2014). Results from 3D seismic reflection interpretation were integrated within the 3D seismic perimeter (Nagra 2024a). The symbols above the topographic profile indicate bedding dip measured in nearby outcrops. Gr.: Group, Dep.: deposits.

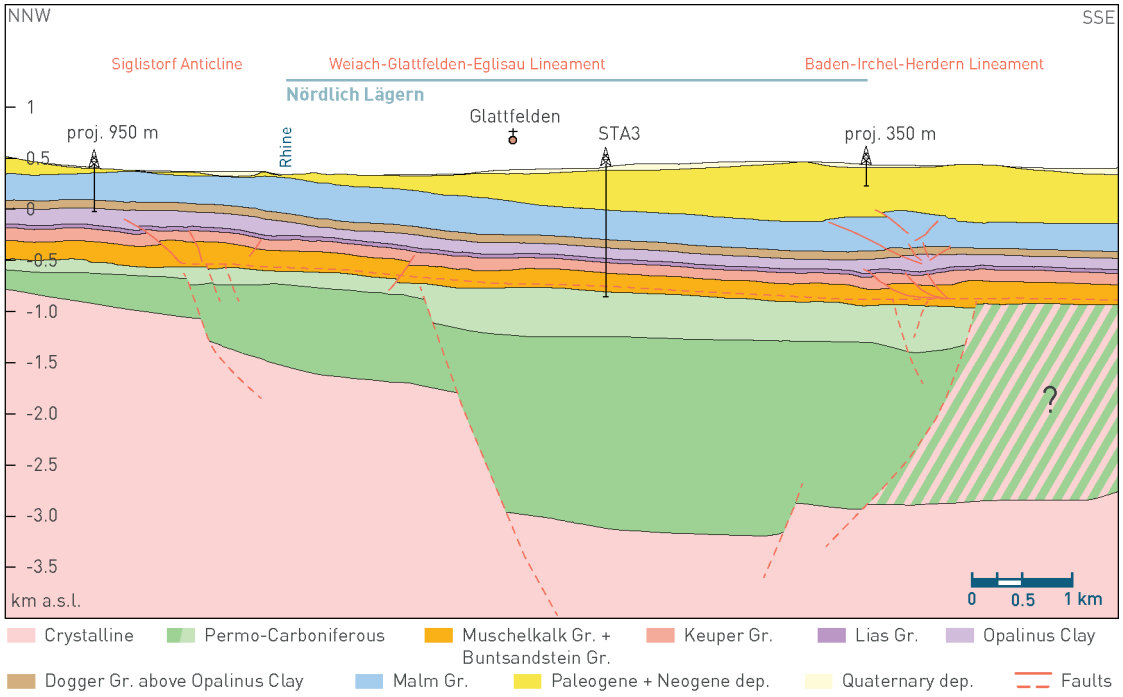


Fig. 4-57: Large-scale geological cross-section through Nördlich Lägern

Geological section drawn along the 2D seismic reflection line 11-NS-20. Section trace located in Fig. 4-54. The section is based on Meier et al. (2014) and Jordan et al. (2015). Results from 3D seismic reflection interpretation were integrated within the seismic perimeter (Nagra 2024b). Gr.: Group, Dep.: deposits. Green hatched area refers to either crystalline or Permo-Carboniferous deposits.

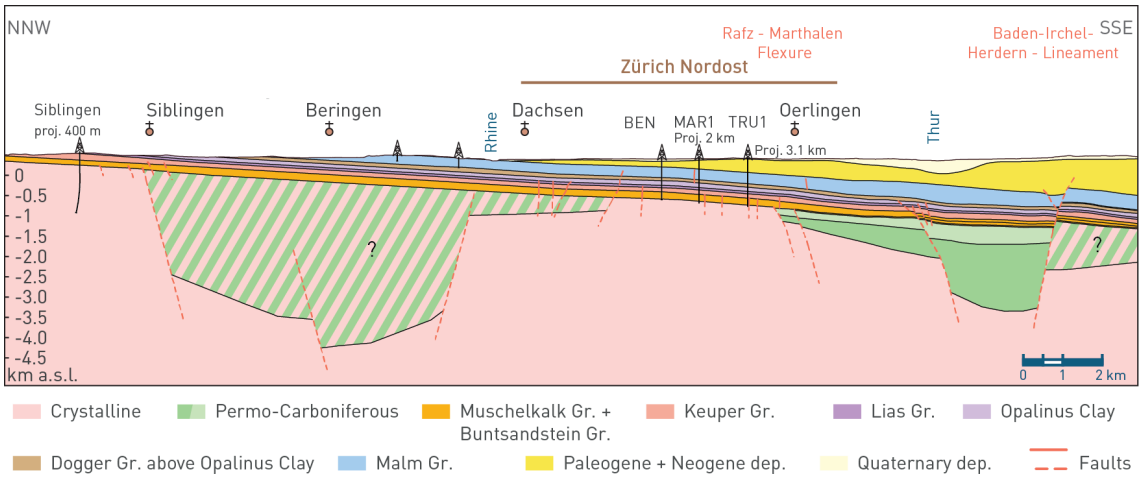


Fig. 4-58: NNW-SSE large-scale geological cross-section through Zürich Nordost

Geological section drawn along the 2D seismic reflection line 91-NO-68. Section trace located in Fig. 4-54. The section is based on Meier et al. (2014) and Jordan et al. (2015). Results from 3D seismic reflection interpretation were integrated within the seismic perimeter (Nagra 2024c). Gr.: Group, Dep.: deposits. Green hatched area refers to either crystalline or Permo-Carboniferous deposits.

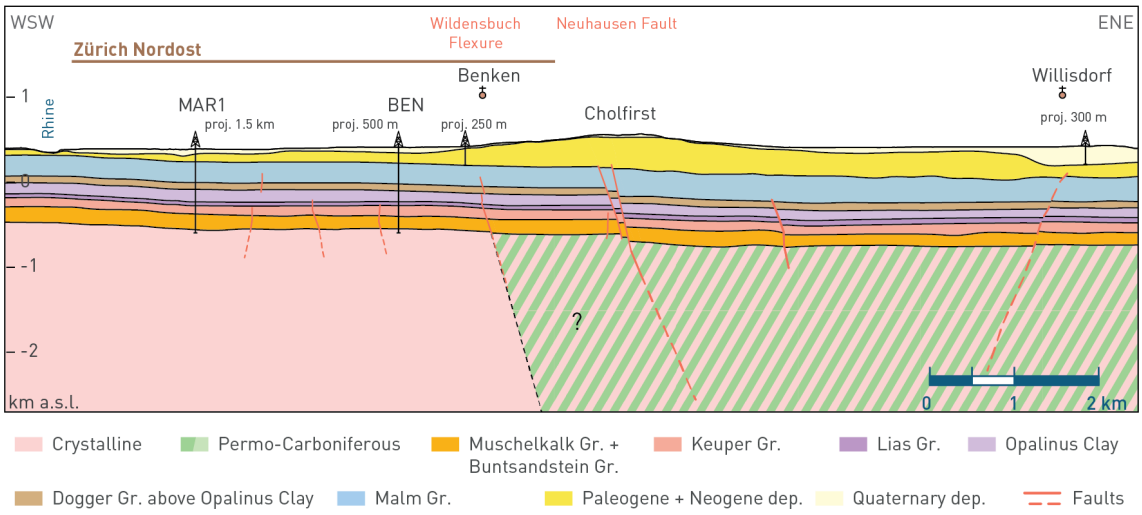


Fig. 4-59: WSW-ENE large-scale geological cross-section through Zürich Nordost

Geological section drawn along the 2D seismic reflection line 91-NO-77. Section trace located in Fig. 4-54. The section is based on Meier et al. (2014) and Jordan et al. (2015). Results from 3D seismic reflection interpretation were integrated within the seismic perimeter (Nagra 2024c). Gr.: Group, Dep.: deposits. Green hatched area refers to either crystalline or Permo-Carboniferous deposits.

Jura Fold-and-Thrust Belt (Internal and External Jura)

The Jura Fold-and-Thrust Belt forms some of the hills around the siting regions Jura Ost and Nördlich Lägern. It is an arc-shaped mountain range of ~ 300 km length and a maximum transect width of ~ 75 km (e.g. Marro et al. 2023, Schori 2021) and represents the outermost fold-and-thrust belt segment of the central and western European Alps. It is subdivided into a more deformed (i.e. shortened) Internal Jura (also referred to as the Folded Jura) and a substantially less deformed but still detached external domain (External Jura, formerly referred to as the "deformed Tabular Jura" or "Vorfaltenzone"; Gouffon 2024). The autochthonous part of the Jura is referred to as Tabular Jura (e.g. Sommaruga 1997).

The Internal Jura is estimated to be displaced up to 30 km to the NW in its central segment consisting of well-developed fault-bend and fault-propagation folds that resulted in local duplication of the Mesozoic cover (e.g. Laubscher 1965, Burkhard 1990, Philippe et al. 1996, Sommaruga 1997, Affolter & Gratier 2004, Ortner et al. 2024). The External Jura is composed of more deformed zones characterised by thrusts and narrow anticlinal folds that are termed "faisceaux", and of gently folded, broad synclinal blocks (i.e. plateau in Sommaruga 1997). The faisceaux (i.e. regional fault zones) were used to delimit the siting regions in previous stages of the Sectoral Plan (Nagra 2008b, 2014b). The plateaux of the External Jura (from the central and western Jura) are represented in Northern Switzerland by less deformed Mesozoic blocks. JO and NL are located within such types of blocks. The Mesozoic block hosting JO is referred to as the Herznach – Bözberg Tafel (Diebold et al. 2006). Zones of gently dipping to flat-lying Mesozoic strata are encountered in all the siting regions (Fig. 4-54 to Fig. 4-59). In ZNO only the SW corner (i.e. south of the Rafz – Marthalen Flexure) is part of the detached sedimentary cover. The majority of ZNO is autochthonous.

The flexural North Alpine Foreland, which encompasses the Jura Fold-and-Thrust Belt, was formed during the Alpine orogenesis. In addition to the contractional folding and thrusting of the Jura, the build-up of the Alps resulted in an extensional overprint prior to the contraction in relation with the northward propagation of the foreland. The formation of the Jura Fold-and-Thrust Belt is associated with the NW propagation of Alpine deformation along Middle Triassic evaporites (e.g. Burkhard 1990). Deformation in Northern Switzerland initiated around 14.3 Ma, as documented by, for instance, décollement-related calcite cements in the Schafisheim borehole (Looser et al. 2021). The general evolution of the Jura Fold-and-Thrust Belt is further elaborated in Section 4.3.5.

Hegau – Bodensee Graben

The tectonic domain of the Hegau – Bodensee Graben exerts a major control on the structural setting of the ZNO siting region. The Hegau – Bodensee Graben is a NW-SE oriented graben controlled by multiple faults extending to the NW from the Bodensee. Its southwestern border coincides with the Neuhausen Fault, which affects the northeastern edge of ZNO. The Hegau – Bodensee Graben formed as part of the Freiburg – Bonndorf – Bodensee Fault Zone, which extends from the Bodensee to the Upper Rhine Graben and forms a conjugate fault system with the latter (Egli et al. 2017). The central part of the Hegau – Bodensee Graben experienced a few hundred metres of tectonic subsidence (Ibele 2015).

Field evidence indicates that the Freiburg – Bonndorf – Bodensee Fault Zone evolved within the framework of strike-slip tectonics at least since the Middle Miocene along inherited structures (Egli et al. 2017). Deformation also resulted in the development of predominantly NE-SW-trending normal faults, which are kinematically compatible with the overall dextral character. The graben structures are considered as a local kinematic response to crustal scale strike-slip tectonics induced by the far field Alpine compression, with extension occurring on suitably oriented pre-existing structures (Egli et al. 2017).

The main tectonic activity in the Hegau – Bodensee Graben occurred during Late Miocene to Pliocene times (Schreiner 1992). Early stages were accompanied by volcanic activity (Schreiner 1992, Wittmann 1937). Volcanic activity in the Hegau region has been dated to Middle to Late Miocene (Schreiner 1992). Tectonic activity in the graben has increased syn- and post-rift sedimentation of the Upper Marine Molasse (Ibele 2015). The NE-dipping Randen Fault, located ~ 10 km NE of Zürich Nordost, has experienced a total of 170 m normal offset since the Middle Miocene (Schreiner 1992).

Upper Rhine Graben

The Upper Rhine Graben is part of the European Cenozoic Rift System (ECRIS), which extends from the Bohemian Massif to the Mediterranean Sea (e.g. Dèzes et al. 2004, Bourgeois et al. 2007). The formation of the southern Upper Rhine Graben started in the Late Eocene (Rotstein & Schaming 2011, Dèzes et al. 2004). The main rifting phase ended in Rupelian times, although localised extension continued during the Miocene and until the present day (Giamboni et al. 2004, Rotstein & Schaming 2011).

The Upper Rhine Graben is partly controlled by inherited structures stemming from the Variscan orogeny and the subsequent Permo-Carboniferous extensional tectonics (that also formed the Konstanz – Frick Trough; Giamboni et al. 2004, Rotstein & Schaming 2011). According to Rotstein & Schaming (2011), the tectonic evolution of the Upper Rhine Graben can be subdivided into two phases, including an early rifting stage and a later transtensional – transpressional stage. The rifting phase was controlled by a normal faulting stress regime with an E-W-trending, horizontal minimum principal stress axis (S_{hmin}), whereas the strike-slip-dominated later stage was characterised by a NNW-SSE-trending, horizontal maximum principal stress axis (S_{Hmax}). Uplift of the graben shoulders (i.e. Black Forest and Vosges Massifs) accompanied rifting. This uplift resulted in a general southward dip of Mesozoic strata in Northern Switzerland, which is preserved in the less deformed blocks of the region (e.g. Müller et al. 2002).

Summary

In summary, the tectonic evolution of the siting regions is conceptualised as the interplay among the tectonic processes responsible for the development of the major tectonic domains described above. The Variscan orogeny and the formation of the Konstanz – Frick Trough resulted in NW-SE, NNE-SSW, and ENE-WSW-trending structures, which are zones of weakness in the basement. The formation of the Upper Rhine Graben resulted in uplift of the Black Forest Massif, which in turn produced tilting of the Mesozoic strata and normal faulting. Further tilting and extensional overprint were induced by the northward migration of the Alpine forebulge. The development of the Hegau – Bodensee Graben influenced mainly ZNO, which was affected by oblique extension within the framework of transtensional deformation. On the other hand, the development of the Jura Fold-and-Thrust belt produced shortening of the Mesozoic strata, with a decreasing intensity from west to east (Fig. 4-60).

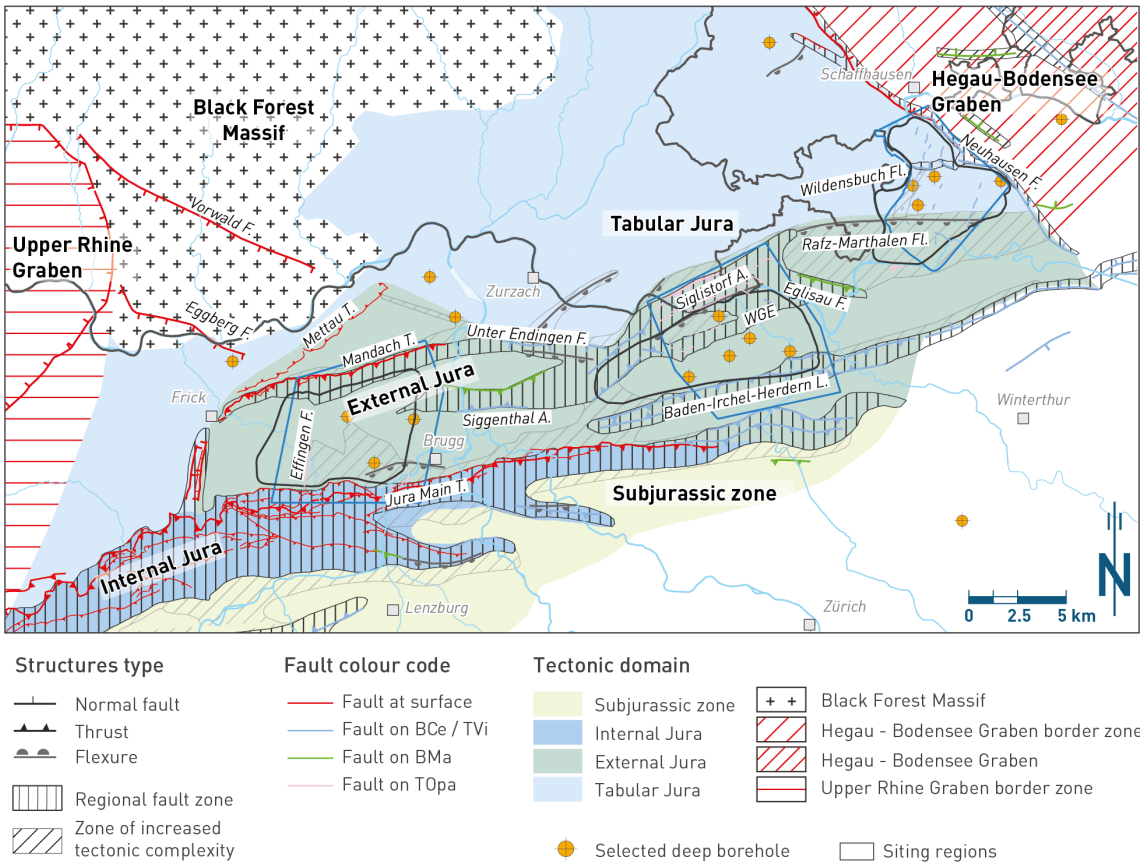


Fig. 4-60: Tectonic map of Northern Switzerland showing regional fault zones and regional tectonic domains

This report uses historic names of tectonic structures to ensure continuity with the existing literature. Surface fault traces are based on Nagra (2014b). Fault traces from seismic interpretation are based on 2D seismic reflection (Madritsch et al. 2013, Meier et al. 2014) and 3D seismic reflection interpretation (Nagra 2024a, 2024b, 2024c). They are shown on the highest stratigraphic horizon where the specific fault segment was picked (different colours in the map view). Only horizons from Top Opalinus Clay and higher stratigraphic levels are shown. Note that only a selection of the structures from 3D seismic interpretation is shown to highlight the structural trends of regional importance. See Fig. 4-61, Fig. 4-65 and Fig. 4-69 for the complete fault pattern. A.: Anticline, F.: Fault, Fl.: Flexure, L.: Lineament, T.: Thrust. WGE: Weiach – Glattfelden – Eglisau Lineament.

4.3.4 Structural inventory in the siting regions

As shown in the previous section, the siting regions are located away from major deformation zones and are bounded by regional fault zones (Section 4.3.3, Fig. 4-54). The central part of all the siting regions is characterised by gently SSE-dipping to flat-lying Mesozoic strata (Fig. 4-56, Fig. 4-57, Fig. 4-58, and Fig. 4-59). The central areas are typically several square kilometres in size.

In the following section, the inventory of structures encountered in the siting regions is described from west (JO) to east (ZNO). The focus is on the interpretation of the seismic reflection data and the data from retrieved core material.

Jura Ost

Within Jura Ost, the Jura Main Thrust and the Mandach Thrust delimit the southern and the northern border of the siting region, respectively (Fig. 4-54, Fig. 4-56, Fig. 4-61). In between, the Mesozoic units form a less deformed block of gently SSE dipping strata (Diebold et al. 2006). Fault trace maps based on the interpretation of 3D seismic reflection data (Fig. 4-61) show a limited number of discrete, seismically mappable faults in the less deformed block. Furthermore, they show a higher number of fault segments at the Near Top Muschelkalk Group horizon compared to the Near Top Lias Group and Top Opalinus Clay horizons (Fig. 4-61). Similarly, fracture frequency measured in the BOZ1 and BOZ2 boreholes shows higher values in the mechanically competent units (e.g. Muschelkalk Group) and lower ones in the less competent units (clay-mineral-rich units, e.g. Opalinus Clay). Small-scale faults (referred to as fault zones in Nagra (ed.) 2022a and 2022b, Dossier V) were encountered predominantly in the Triassic units (9 out of 16 in BOZ2 and 18 out of 30 in BOZ1, Fig. 4-61). The observation of a higher number of low-angle small-scale faults in the Triassic evaporites supports the concept of a décollement horizon within the Triassic evaporites allowing strain from the Alpine orogeny to be transferred NNW-wards.

Of the micro faults observed in the two boreholes 69% show reverse shear sense indicators. Normal faulting was described for 27% of the micro faults, whereas strike-slip dominated movement was found in 4% of the cases (Fig. 4-61). The predominance of thrust-related structures encountered in the boreholes is associated with the shortening related to the formation of the Jura Fold-and-Thrust Belt overprinting the precursor geological history.

The Jura Main Thrust, which is exposed in the southernmost portion of JO, represents the northern boundary of the Internal Jura (Fig. 4-60). As it is located close to the margin of the 3D seismic perimeter, the fault geometry is not well imaged within the 3D seismic volume; therefore, its interpretation is based on regional 2D seismic reflection lines and surface mapping (Fig. 4-61). The Jura Main Thrust consists of an imbricate fan soling out in the Triassic evaporites (Fig. 4-56). It accommodated 2 to 5 km of shortening during Jura-related folding and thrusting, as estimated from balanced geological sections. These also show that the shortening decreases towards the east (Jordan et al. 2015). The Jura Main Thrust is roughly located over the southern border fault of the western segment of the Konstanz – Frick Trough (Diebold et al. 1991, Madritsch et al. 2018). East of JO, the Lägern Anticline, located south of NL, represents the eastern continuation of the Jura Main Thrust (Fig. 4-60).

The Mandach Thrust is known from surface mapping (Diebold et al. 2006, Bitterli-Dreher et al. 2007). It is located approximately 6 km north of the Jura Main Thrust and strikes roughly E-W. It can be traced at the surface for ~ 15 km (Diebold et al. 2006, Bitterli-Dreher et al. 2007). In the fault trace maps obtained from seismic reflection data, fault traces associated with the Mandach Thrust can be mapped up to the Near Top Lias Group but not above, mainly due to near-surface effects altering the seismic reflection image (Fig. 4-61; Nagra 2024a). The Mandach Thrust is interpreted as a thrust ramp splaying out from the Muschelkalk Group evaporite décollement (e.g. Laubscher 1985, Nagra 2019b). Consequently, the strata above the décollement and south of the Mandach Thrust are considered as detached (i.e. part of the External Jura). About 500 m of shortening was accommodated by the Mandach and the Mettau Thrusts located further to the north during folding and thrusting of the Jura (Fig. 4-60; Malz et al. 2020). The Mandach Thrust is located along the northern edge of the Paleozoic graben. The northern boundary fault of the Konstanz – Frick Trough within JO also offsets the Base Mesozoic unconformity, as a result of Paleogene extensional reactivation (Laubscher 1986). The step below the décollement level (i.e. Muschelkalk evaporites) appears to have localised later deformation, in particular by controlling thrust ramp development at this site (Fig. 4-62).

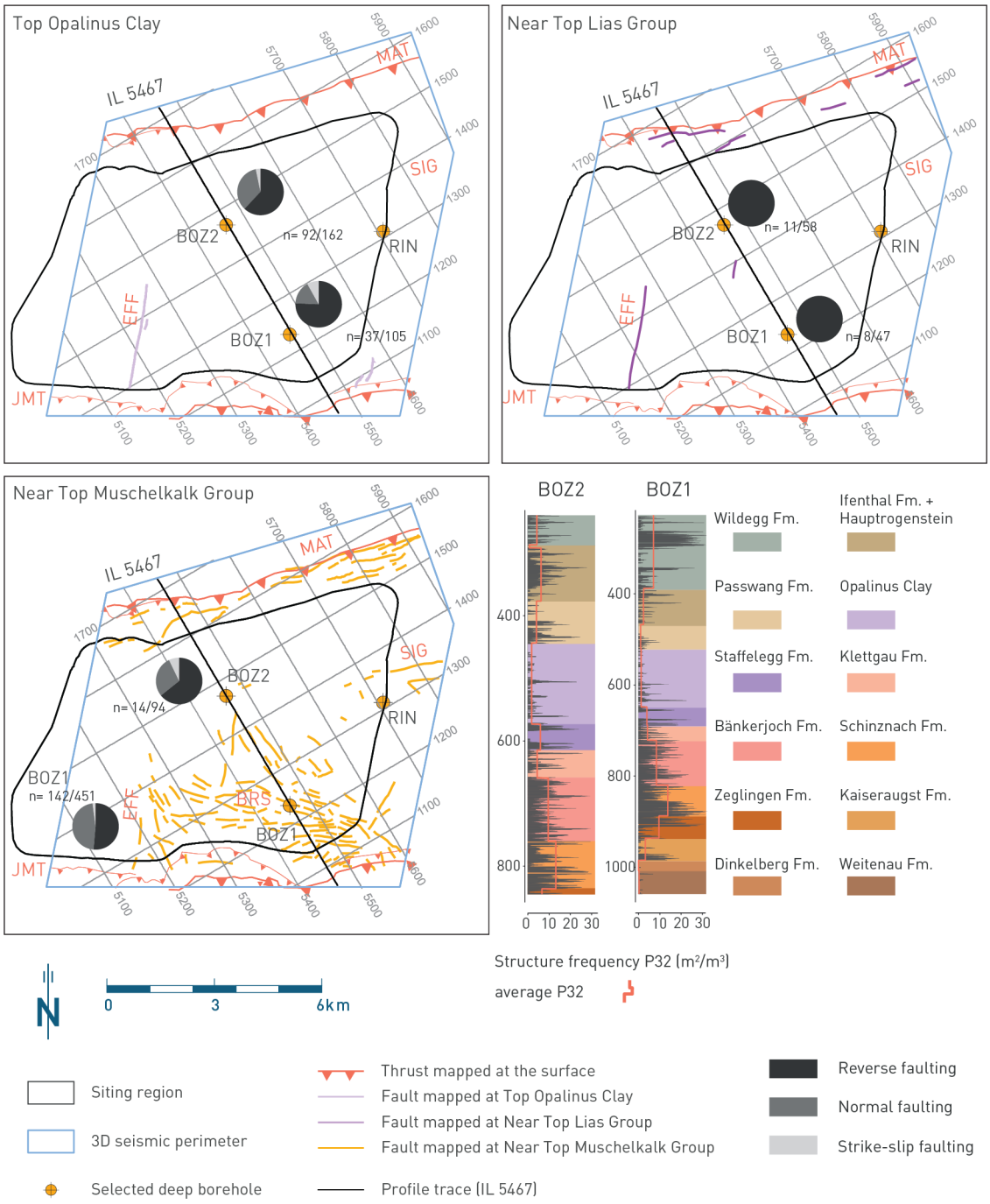


Fig. 4-61: Fault map for JO (shown on three stratigraphic levels) and fracture frequencies in the recent deep boreholes

Fault maps based on seismic reflection interpretation reported in Nagra (2024a). Pie charts show the distribution of shear sense indicators within the Opalinus Clay, the Lias Group and the Muschelkalk Group, respectively. The numbers after 'n=' represent the total number of micro faults with shear sense indication ratio to total number of micro faults. Reverse faulting encompasses all dip-slip upward movements. P32 values refer to the fracture area in a unit volume, i.e. the intersection area of the plane with the cylindrical core and, as such, represents a non-directional intrinsic measure of the degree of rock mass fracturing, incorporating both a frequency measure and a fracture-size component (Ebert & Decker 2019, Dershowitz 1985, Dershowitz & Herda 1992). MAT: Mandach Thrust; SIG: Siggenthal Anticline, EFF: Effingen Fault: JMT: Jura Main Thrust, BRS: "Brugg Strukturzone".

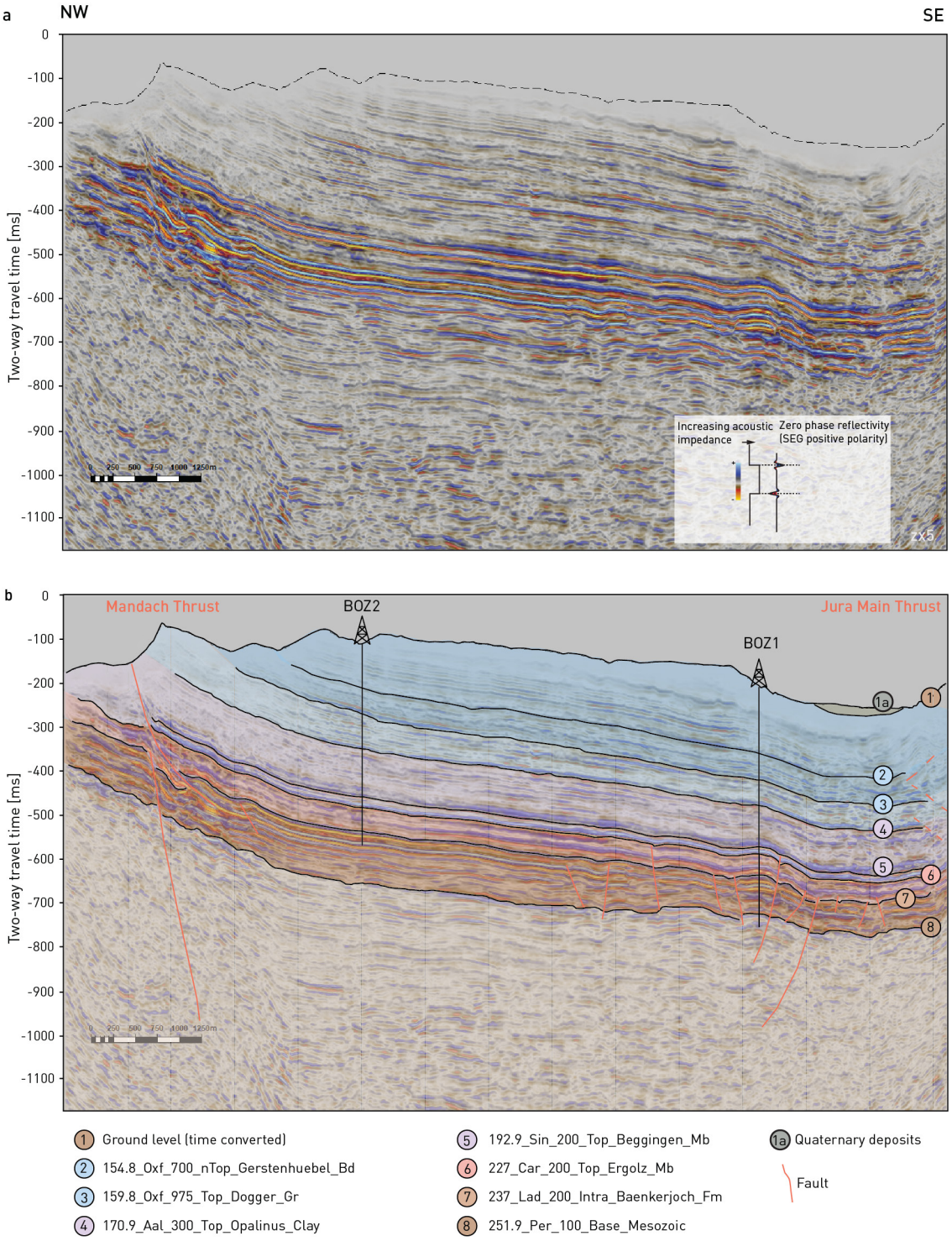


Fig. 4-62: NW-SE cross-section in time domain extracted from 3D seismic reflection data through Jura Ost

View is along acquisition inline 5467, modified after Nagra (2024a). (a) Uninterpreted. (b) Interpreted. Note that the recognition of fault signatures within the Opalinus Clay is strongly hampered by the presence of multiples. The vertical axis was stretched 5 times (Z × 5). Seismic display is PreSTM-ref reflectivity with an overlay of relative acoustic impedance. Profile trace shown in Fig. 4-61. Bd: Bed; Gr: Group; Mb: Member; Fm: Formation.

In the easternmost sector of JO, the western termination of the Siggenthal Anticline occurs between the Jura Main Thrust and the Mandach Thrust (Fig. 4-61; Bitterli-Dreher et al. 2007). This structure continues – and is well exposed – east of the 3D seismic perimeter. It is a north-vergent anticline associated with a thrust ramp rooting in the Triassic evaporites (Nagra 2019b, 2024a). No major Paleozoic structures occur beneath this structure, and nucleation does not appear therefore to be controlled by inherited structures underlying the décollement (Nagra 2024a, Madritsch et al. 2024). Seismic reflection interpretation in the NE corner of JO is hampered by data quality inhibiting a more detailed analysis (Nagra 2024a). Seismically mappable fault segments associated with the Siggenthal Anticline are mapped on Near Top Muschelkalk Group and concentrate at the corner of the siting region. However, a few fault segments showing a similar orientation are mapped at a close distance from the BOZ2 borehole (Fig. 4-61). Micro faults in BOZ2 are predominantly ENE-WSW-trending, hence displaying a similar orientation (Nagra (ed.) 2022b).

Located in the SW sector of the block, the Effingen Fault represents a major structural element in JO. It is a normal fault known from seismic reflection data interpretation and reaching from the pre-Mesozoic basement into the Wildegg Formation (Fig. 4-63; Nagra 2019b). It strikes NNE-SSW and dips towards the E.

A cluster of faults is observed on Near Top Muschelkalk Group in the central to south-eastern part of the 3D seismic survey and grouped under the term "Brugg Strukturzone" (Fig. 4-61; Nagra 2024a). They display only a mild expression at the level of the Near Top Lias Group (Fig. 4-61). They encompass thrust imbricates from the Jura Main Thrust in the south as well as a NW-SE-trending zone with a change from contractional features to extensional features indicative for a strike-slip-dominated deformation. Micro faults mapped in BOZ1 within the Muschelkalk Group show comparable orientations (NW-SE-trending and subordinate NE-SW-trending) to the faults detected in the 3D seismic reflection data (Fig. 4-61; Nagra (ed.) 2022a).

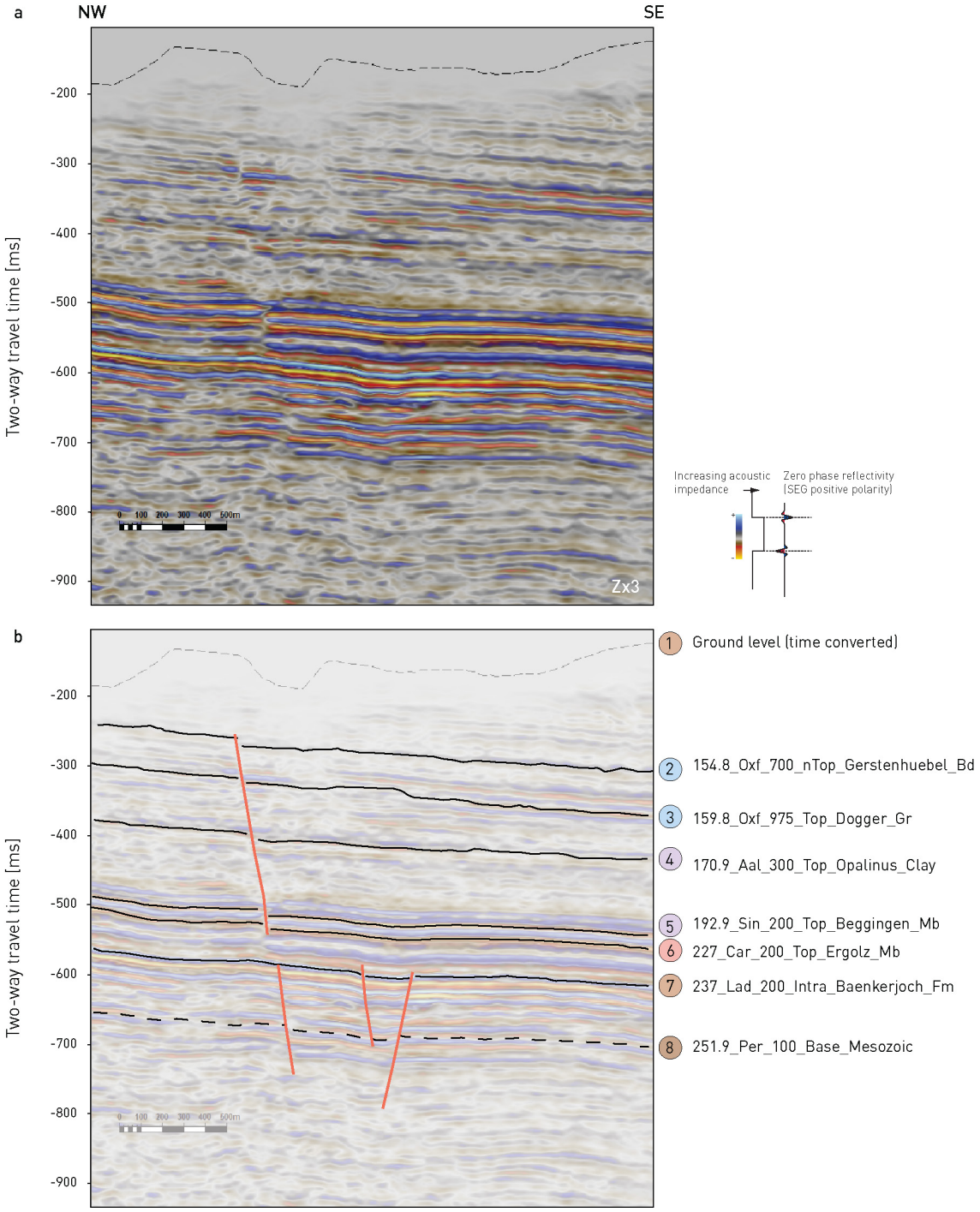


Fig. 4-63: Cross-section extracted from 3D seismic reflection data showing the Effingen Fault

Modified after Nagra (2024a). (a) Uninterpreted. (b) Interpreted. Seismic display is PreSTM-ref reflectivity with an overlay of relative acoustic impedance. Note the slight normal fault offset along the Effingen Fault for instance at the Top Ergolz Member. The vertical axis was stretched 3 times (Z × 3). Bd: Bed; Gr: Group; Mb: Member; Fm: Formation.

Nördlich Lägern

Nördlich Lägern is characterised by a relatively large (compared to JO and ZNO) less deformed block located between the Baden – Irchel – Herdern Lineament to the south and the Weiach – Glattfelden – Eglisau Lineament to the north (Fig. 4-64). Discrete seismically mappable faults are predominantly observed at the level of the Top Muschelkalk Group (Fig. 4-65). Less numerous fault segments are seen in the seismic reflection dataset at Near Top Lias Group and Near Top Opalinus Clay levels. This agrees well with the observed differences in fracture frequencies in the boreholes (Fig. 4-65). Similarly to JO, a strong influence of mechanical stratigraphy is shown by higher fracture frequencies in the competent units (e.g. Malm and Muschelkalk Groups) and lower fracture frequencies in the less competent units (clay-mineral-rich units, e.g. Opalinus Clay). Small-scale faults (referred to as fault zones in Nagra (ed.) 2023a, 2022c, 2022d, 2021a, Dossier V) were encountered predominantly in the Triassic units (9 out of 15 in BAC1, 17 out of 25 in STA2, 17 out of 31 in STA3 and 34 out of 50 in BUL1). As in JO, the observed higher number of small-scale mostly low-angle faults in the Triassic evaporites provides supporting evidence for strain localisation within the main Jura décollement level in this region.

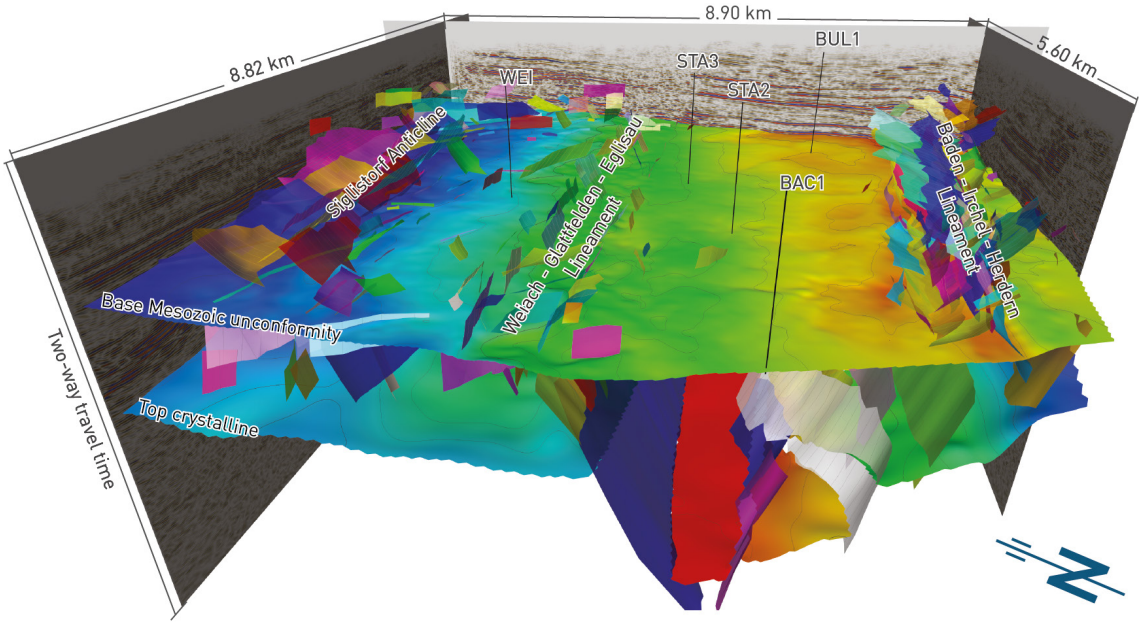


Fig. 4-64: 3D view showing the less deformed block in NL between the regional fault zones

Modified after Zambrano et al. *submitted*. Two horizons are shown for orientation. North is indicated by the blue arrow. Note that the z axis is in time.

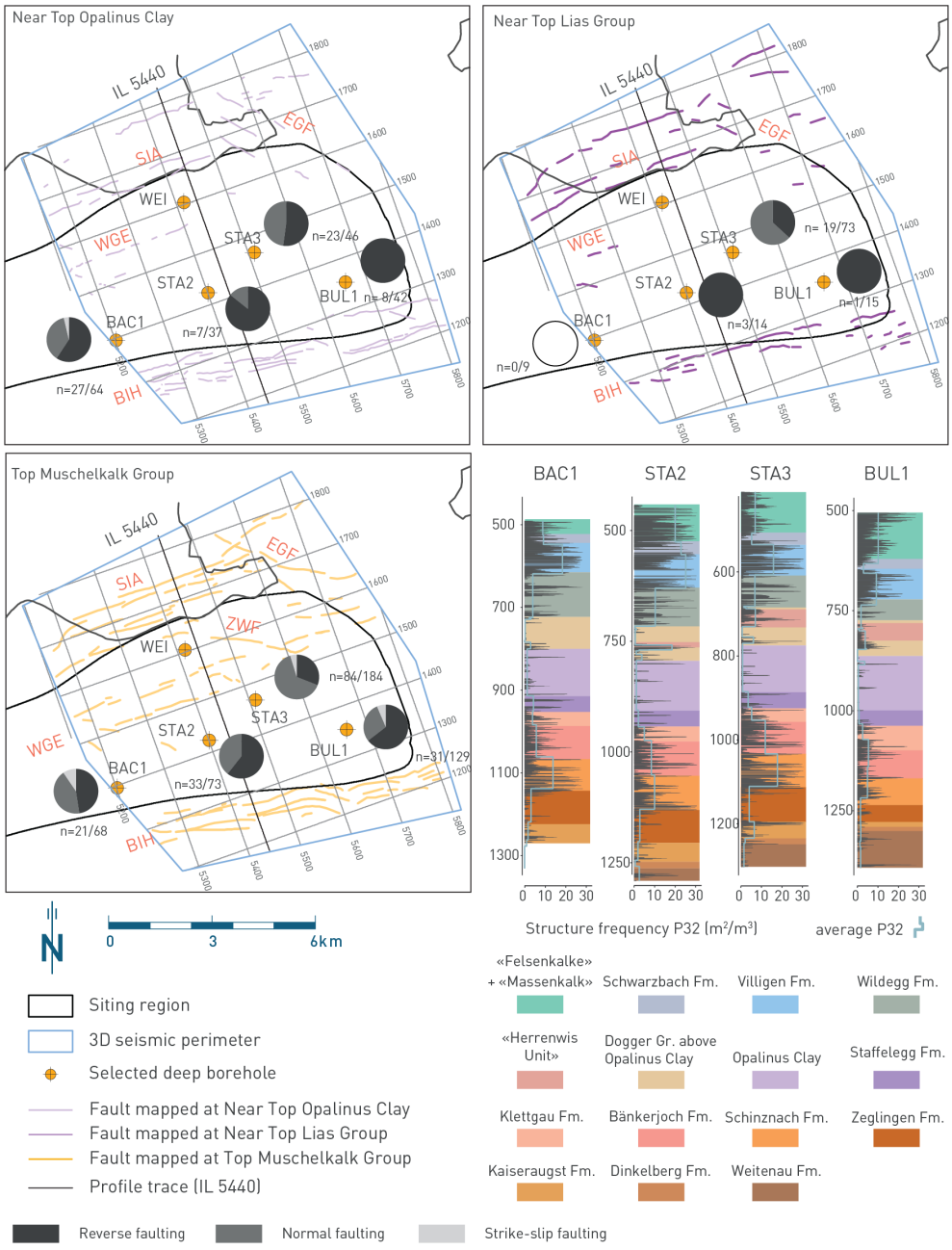


Fig. 4-65: Fault maps for NL (shown on three stratigraphic levels) and fracture frequencies in the recent deep boreholes

Fault maps based on seismic reflection interpretation reported in Nagra (2024b). Pie charts show the distribution of shear sense indicators within the Opalinus Clay, Lias Group and Muschelkalk Group, respectively. The numbers after 'n=' represent the total number of micro faults with shear sense indication/total number of micro faults. Reverse faulting encompasses all dip-slip upward movements. P32 values refer to the fracture area in a unit volume, i.e. the intersection area of the plane with the cylindrical core and, as such, represents a non-directional intrinsic measure of the degree of rock mass fracturing, incorporating both a frequency measure and a fracture-size component (Ebert & Decker 2019, Dershowitz 1985, Dershowitz & Herda 1992). SIA: Siglistorf Anticline, EGF: Eglisau Fault, ZWF: Zweidlen Fault, WGE: Weiach – Glattfelden – Eglisau Lineament, BIH: Baden – Irchel – Herdern Lineament.

All recent boreholes were drilled within the less deformed block. Shear sense indicators on micro faults show a predominance of reverse faulting with approximately 71% reverse shear sense mapped. Normal faulting was described for 23% of the micro faults, whereas strike-slip faulting was found in 6% of the cases (Fig. 4-65). Thrust-related features are consistent with shortening related to the formation of the Jura Fold-and-Thrust Belt. Multiple micro faults showing two different sets of striae/shear fibre lineation on a single slickenside were observed in the drill cores. This indicates two slip directions, both probably related to thrusting during the formation of the Jura Fold-and-Thrust Belt. NNE- and NNW- thrusting directions inferred from these micro faults are consistent with shortening directions reported from outcrops in Northern Switzerland (Madritsch 2015).

North of the Lägern Anticline, the Baden – Irchel – Herdern Lineament is located above faults of the underlying Konstanz – Frick Trough (Fig. 4-66). It is composed of multiple thrusts and back-thrusts arranged in a narrow, steep belt (Fig. 4-67; Zambrano et al. *submitted*). Several authors have interpreted it as a composite triangle zone including a series of fish-tail structures (Laubscher 1985, Malz et al. 2016, Nagra 2024b). Within this structure, the Opalinus Clay allowed significant decoupling of the deformation between a lower competent layer (thick-bedded to massive limestones and dolostones of the Upper Muschelkalk Group) and an upper competent unit (thick-bedded to massive limestones of the Malm Group). The Opalinus Clay appears to have been shortened and locally thickened by roughly coaxial strain between the two disharmonically folded, competent rock panels located above and below it. The upper competent panel is antiformally folded, while the lower competent panel is synformally folded, resulting in a tectonically thickened Opalinus Clay in the core of both folds (Nagra 2024b). It should be noted that, although within the Baden – Irchel – Herdern Lineament the Opalinus Clay acted as a decoupling unit, no evidence was found within the siting regions along the boreholes for a décollement in the Opalinus Clay. This shows that, within the less deformed block, the Opalinus Clay did not act as décollement level.

The link of the Baden – Irchel – Herdern Lineament to the substratum (i.e. strata below the décollement in the Triassic evaporites) has been conceptualised differently over time. Malz et al. (2016) proposed an evolution of the Baden – Irchel – Herdern Lineament influenced by pre-thrusting normal faulting affecting the Base Mesozoic unconformity and overlying Mesozoic succession. These authors interpreted no faults cutting from the Paleozoic units into the Mesozoic strata. Recent structural interpretation of the 3D seismic reflection data indicated the occurrence of reverse faults offsetting both the upper part of the Paleozoic succession and Mesozoic strata, therefore cutting across the Base Mesozoic unconformity (Nagra 2024b). Consequently, the formation of the Baden – Irchel – Herdern Lineament is proposed to have occurred by post-detachment shortening involving both the Mesozoic succession and the underlying Upper Paleozoic sedimentary fill of the Konstanz – Frick Trough. This would be associated with late-stage bulk shortening triggering mild basin inversion of the Konstanz – Frick Trough (Zambrano et al. *submitted*).

The structural style of the Baden – Irchel – Herdern Lineament varies along strike. The contractional structure characterising the Baden – Irchel – Herdern Lineament south of NL, clearly related to Jura shortening, deamplifies progressively and fades away eastwards. South of ZNO, the composite triangle zone is no longer present, and a pronounced normal fault occurs instead in the Mesozoic succession (hard- linked with the underlying Late Paleozoic fault). This normal fault was extensionally reactivated, propagating into and offsetting the overlying Mesozoic units (Fig. 4-60). The extensional reactivation was probably associated with the northward migration of the flexural forebulge (Chapter 3).

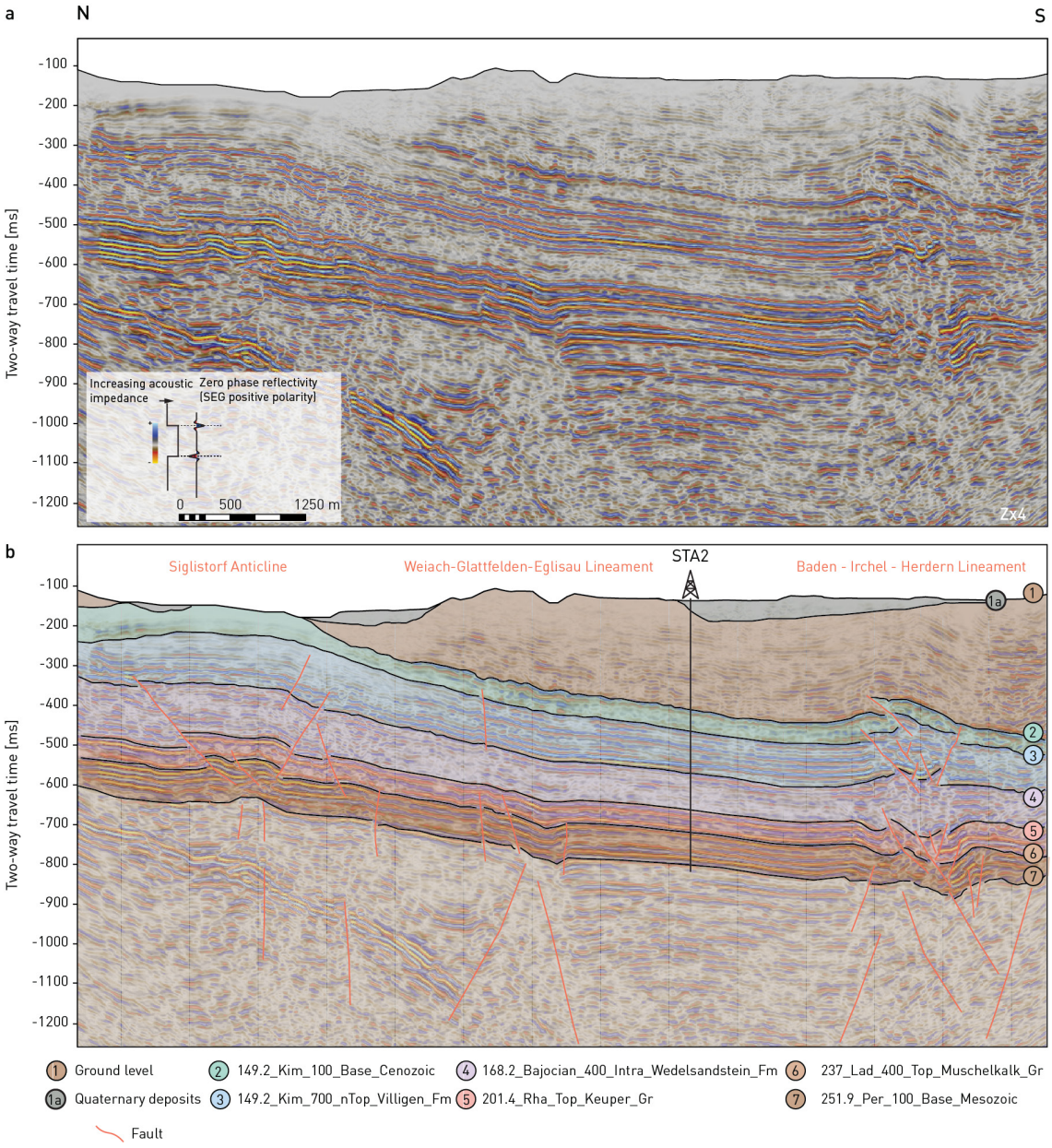


Fig. 4-66: N-S cross-section in time domain through the 3D seismic reflection data across NL

View is along the acquisition inline 5440, modified after Nagra (2024b). (a) Uninterpreted. (b) Interpreted. Note that the recognition of fault signatures within the Opalinus Clay is strongly hampered by the presence of multiples. The vertical axis was stretched 4 times (Z × 4). Seismic display is PreSTM-ref reflectivity with an overlay of relative acoustic impedance. Note that Top Opalinus Clay could not be picked. Colour shade is given to a larger interval including clay-mineral-rich units above and below the Opalinus Clay with a similar rheology. Profile trace shown in Fig. 4-65.

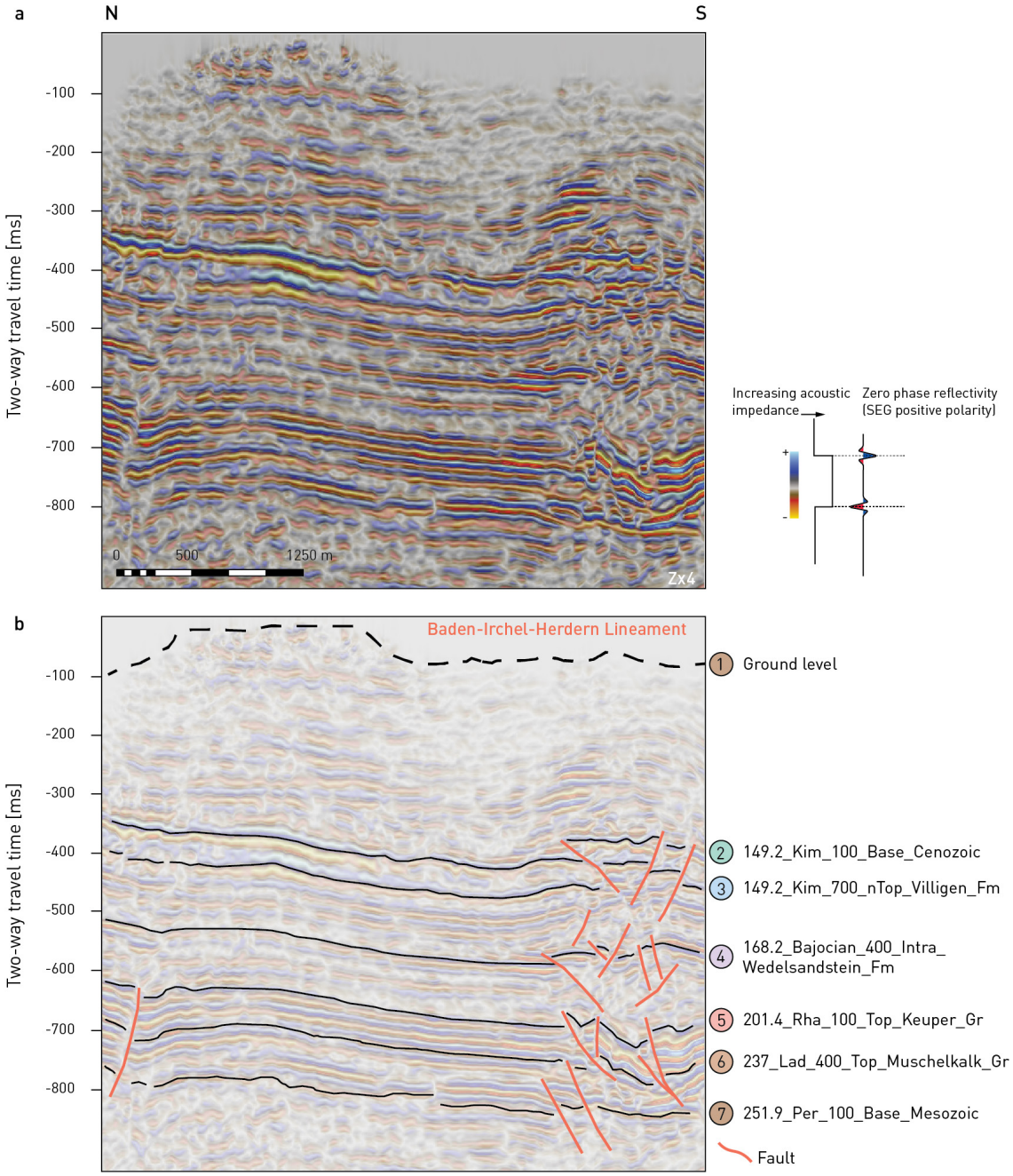


Fig. 4-67: Focused view in time domain showing interpreted fault geometries in the Baden – Irchel – Herdern Lineament

View is along the acquisition inline 5403, modified after Nagra (2024b). (a) Uninterpreted. (b) Interpreted. Seismic display is PreSTM-ref reflectivity with an overlay of relative acoustic impedance. Note the antiform and synform above 168.2 Bajocian 400 and below 201.4 Rha 100, respectively. The vertical axis was stretched 4 times (Z × 4).

In NL, the Konstanz – Frick Trough is more symmetric than in JO (Fig. 4-56 and Fig. 4-57). In particular, the northern shoulder of the trough is wider and characterised by the occurrence of several normal faults (Fig. 4-55). These faults appear to have controlled the localisation of later deformation during the Jura-related shortening episodes, which resulted in the development of multiple deformed zones including the Siglistorf Anticline and the Weiach – Glattfelden – Eglisau Lineament in the Mesozoic cover (Fig. 4-66). Therefore, structural development in the northern sector of NL shows a striking difference with respect to JO, where a narrower deformation zone (associated with the Mandach Thrust) developed at a substratum step produced by a single normal fault of the Konstanz – Frick Trough. The Weiach – Glattfelden – Eglisau Lineament is well imaged at the Top Muschelkalk Group level (Fig. 4-65). It is a high-angle, strongly segmented, ENE-WSW-trending fault array. From west to east, fault segments can be seismically mapped with a length ranging from 300 m to 1 km (Fig. 4-65). Vertically, the high-angle faults mostly terminate below Near Top Lias Group. Only a few segments affect the units above the Opalinus Clay (Fig. 4-66). Multiple seismic reflection interpretations identified a hard linkage of the Weiach – Glattfelden – Eglisau Lineament between the substratum (i.e. strata below the décollement level in Middle Triassic evaporites) and the sedimentary cover (Fig. 4-66). This hard linkage suggests a formation of the Weiach – Glattfelden – Eglisau Lineament postdating décollement-related deformation north of it (i.e. at a distal position with respect to the Alps), as it would otherwise be transported foreland-ward during activity along the décollement.

The Siglistorf Anticline consists of an up to ~ 2-km-wide, composite pop-up including highly segmented thrust and backthrust splays (Fig. 4-68). In the Malm Group, deformation is accommodated by folding rather than faulting (Fig. 4-60). 2D cross-section balancing revealed shortening of approximately 200 m across it (Jordan et al. 2015). Although the control exerted by normal fault-related substratum steps on later thrust ramp development appear evident, it remains unclear to what degree the faults that controlled the localisation of the Siglistorf Anticline are linked across the Base Mesozoic unconformity. Schöpfer et al. (2024) discuss multiple scenarios involving both décollement-related deformation and deformation involving the basement. However, Nagra's current 3D seismic reflection interpretation favours a model, where the faults in the Upper Paleozoic succession, control the localisation of the Siglistorf Anticline and the faults above the Triassic evaporites, as the geometry of the latter faults is consistent with décollement-related deformation (Nagra 2024b).

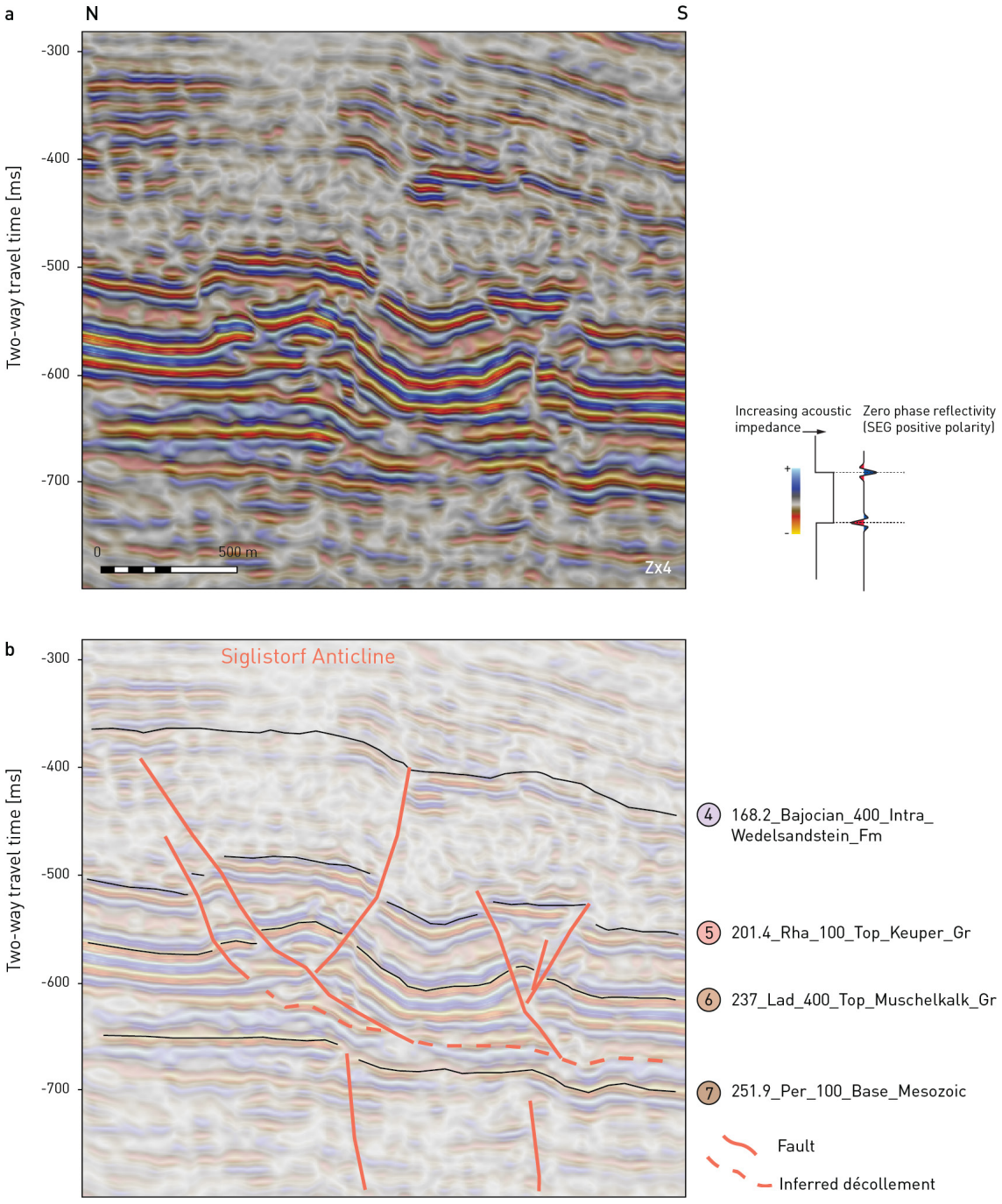


Fig. 4-68: Focused view in time domain showing the relationship of thrusting in the Siglistorf Anticline and the underlying faults in the Paleozoic strata

View is along the acquisition inline 5239, modified after Nagra (2024b). (a) Uninterpreted. (b) Interpreted. Seismic display is PreSTM-ref reflectivity with an overlay of relative acoustic impedance. The thrust affecting the Mesozoic sequence appears to flatten within the Triassic evaporite interval. The faults in the Paleozoic strata produced the steps at the Base Mesozoic unconformity as a result of minor Paleogene extensional reactivation. The vertical axis was stretched 4 times (Z × 4).

The Eglisau Fault and the Zweidlen Fault are known only from seismic reflection interpretation (Fig. 4-65; Nagra 2014b, 2019c). They strike roughly NW-SE in a Hercynian orientation. These structures can be traced from the pre-Mesozoic substratum into the sedimentary cover (Fig. 4-65). This indicates a strong influence of inherited Paleozoic faults on faulting within the sedimentary cover. They are mainly expressed at Top Muschelkalk Group level, but indications are found up to Base Malm Group for the Eglisau Fault and Near Top Lias Group for the Zweidlen Fault (Fig. 4-65; Nagra 2019c, 2024b). The Eglisau Fault can be subdivided into two segments (Nagra 2019c, Madritsch et al. 2013). The northern one (i.e. north of the Siglistorf Anticline and north of the contractional deformation front of the Alps) is a steeply dipping normal fault. The southern segment shows evidence for contractional deformation, with still observable normal faulting at the Base Mesozoic unconformity level. The Zweidlen Fault appears to terminate at its intersection with the Weiach – Glattfelden – Eglisau Lineament. It is in its present-day geometry mostly a steep reverse fault dipping towards the NE, rooting in the Paleozoic basement.

Zürich Nordost

Zürich Nordost differs tectonically from JO and NL as the Mesozoic here is mostly autochthonous (Nagra 2014b, Birkhäuser et al. 2001). However, the proximity to the Hegau – Bodensee Graben affected the siting region with transtensional deformation expressed by an increased number of high-angle faults (Fig. 4-58 and Fig. 4-59). Major tectonic structures are the Neuhausen Fault, which represents the northeastern boundary of the siting region, and the Rafz – Marthalen Flexure (Fig. 4-69). The predominance of normal faulting is recorded by the shear sense indicators observed in the boreholes, mainly in the Muschelkalk Group in MAR1 (Fig. 4-69) but also in general, with approximately 55% normal faulting observed, particularly within the Opalinus Clay (Fig. 4-69). Reverse faulting was described for 37% of the micro faults, whereas strike-slip faults represent 8% of the cases, homogeneously distributed over the entire stratigraphic column (Fig. 4-69). In addition to extension associated with the Hegau – Bodensee Graben, normal faulting related to the northward migration of the Alpine flexural forebulge and Miocene contraction related with folding and thrusting of the Jura in the SW corner of ZNO is also likely to have occurred within ZNO. The Rafz – Marthalen Flexure is considered the northern front of this contractional deformation (south of the deep boreholes, e.g. Birkhäuser et al. 2001, Müller et al. 2002, Marchant et al. 2005, Nagra 2019d). The mechanical stratigraphy observed in JO and NL is confirmed in ZNO. Higher fracture frequencies are observed in the competent units and lower frequencies in the less competent units (e.g. Opalinus Clay; Fig. 4-69). Small-scale faults (referred to as fault zones in Dossier V of TBO reports, see Tab. 2-1) were encountered predominantly in the Triassic units (21 out of 26 in MAR1, 4 out of 4 in RHE1 and 11 out of 17 in TRU1).

The Neuhausen Fault is the most prominent fault in ZNO. It is a NE-SW-trending normal fault exposed at the surface north of ZNO (Fig. 4-70; Hofmann 1981). Its vertical offset is about 60 m (Birkhäuser et al. 2001). Kinematically linked to the Neuhausen Fault is the Wildensbuch Flexure, which is a WNW-ESE-trending normal fault (Nagra 2024c). The Wildensbuch Flexure was intensively studied as a case example of a soft-linked fault and to analyse in detail fault architecture in relation to mechanical stratigraphy (Roche et al. 2020).

The Rafz – Marthalen Flexure (Fig. 4-60) developed in the Mesozoic strata overlying the northern rim of the Konstanz – Frick Trough or southern border of the Benken Horst (Fig. 4-55; Nagra 2014b, Birkhäuser et al. 2001). It is expressed as a mild change in dip azimuth of the Mesozoic strata (Nagra 2024c).

Prominent local faults identified in the 3D seismic reflection data are the Rheinau Fault, the Trüllikon Fault and the Uhwiesen Fault (Fig. 4-69; Nagra 2024c, 2019d). The Uhwiesen Fault appears as a NW-SE-trending subvertical fault mainly expressed at Near Top Muschelkalk Group and Top Lias Group levels. The Trüllikon Fault (formerly referred to as Trüllikon Anticline), is a N-S-trending fault best imaged at the Near Top Muschelkalk Group level. The orientation of micro faults observed in TRU1 in the Muschelkalk Group are well aligned with the Trüllikon Fault traces from seismic reflection interpretation (Fig. 4-69; Nagra (ed.) 2021c).

The Near Top Muschelkalk Group is also affected by numerous fault segments, especially in the "Strukturzone von Niderholz", that are not discretely observable above the Opalinus Clay (Birkhäuser et al. 2001, Nagra 2024c, 2019d). They represent high-angle faults that might be linked to the transtensional opening of the Hegau – Bodensee Graben. The high-angle faults, producing discrete strain (i.e. displacement) accumulation mostly evident in the Muschelkalk Group, are accompanied by folds. Folding also affects unfaulted strata at higher stratigraphic levels. However, it is characterised by fold amplitudes progressively decreases at higher stratigraphic levels (Nagra 2024c).

Typically, no evidence for seismically mappable faults was observed above the Opalinus Clay for the high-angle faults, which indicates that strain was accommodated in a more distributed manner in the Opalinus Clay and above (Section 5.5). The Rheinau Fault represents an exception, as fault segments were seismically mapped also above the Opalinus Clay (Fig. 4-72). Therefore, the segments above and below the Opalinus Clay are conceptually connected in the seismic interpretation. The Rheinau Fault, which consists of a nearly vertical fault in the competent units above (Malm Group) and below the Opalinus Clay (Muschelkalk Group), was investigated by the means of a deviated borehole (RHE1). The borehole was deviated to sample the Opalinus Clay between the two nearly vertical seismically mapped fault segments above and below the Opalinus Clay. Within the structural record of the borehole, no major faulted interval was encountered. The micro fault frequency is comparable to the vertical boreholes (TBO reports in Tab. 2-1). At the measured depth of approximately 650 m MD, a fault with indications for oblique slip and a dip of approximately 40° was encountered. This micro fault could be kinematically related to the conceptually interpolated Rheinau Fault segments between the above and below the Opalinus Clay (Fig. 4-72). The observations in the Rheinau borehole are consistent with the deformation behaviour of Opalinus Clay, where strain tends to be more distributed (Section 5.5.4).

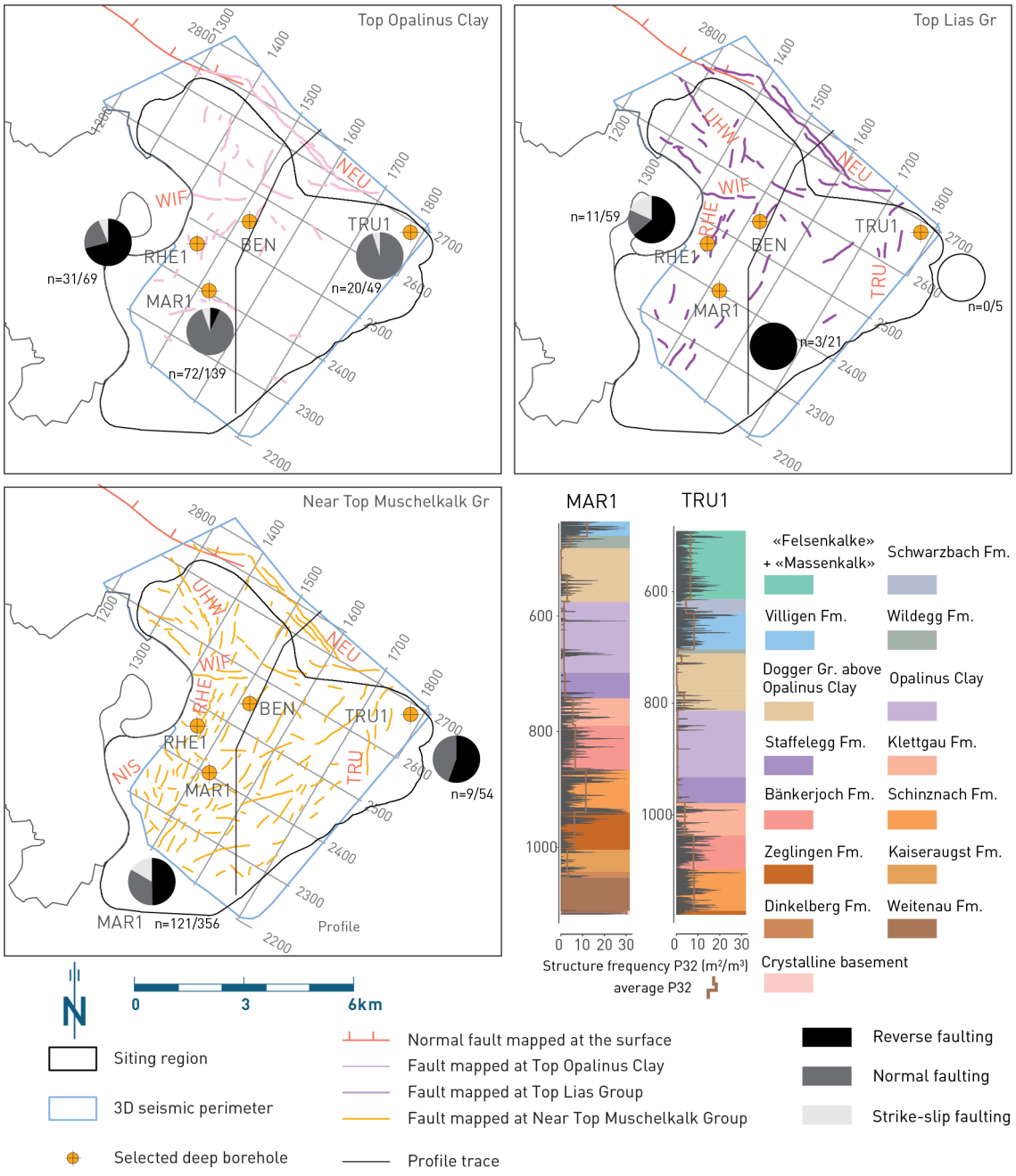


Fig. 4-69: Fault map for ZNO (shown on three stratigraphic levels) and fracture frequencies in the recent deep boreholes

Fault maps based on seismic reflection interpretation reported in Nagra (2024c). Pie charts show the distribution of shear sense indicators within the Opalinus Clay, the Lias Group and the Muschelkalk Group, respectively. The numbers after 'n=' represent the total number of micro faults with shear sense indication / total number of micro faults. Reverse faulting encompasses all dip-slip upward movements. P32 values refer to the fracture area in a unit volume, i.e. the intersection area of the plane with the cylindrical core and, as such, represents a non-directional intrinsic measure of the degree of rock mass fracturing, incorporating both a frequency measure and a fracture-size component (Ebert & Decker 2019, Dershowitz 1985, Dershowitz & Herda 1992). NEU: Neuhausen Fault, NIS: "Strukturzone von Niderholz", RHE: Rheinau Fault, TRU: Trüllikon Fault, UHW: Uhwiesen Fault, WIF: Wildensbuch Flexure.

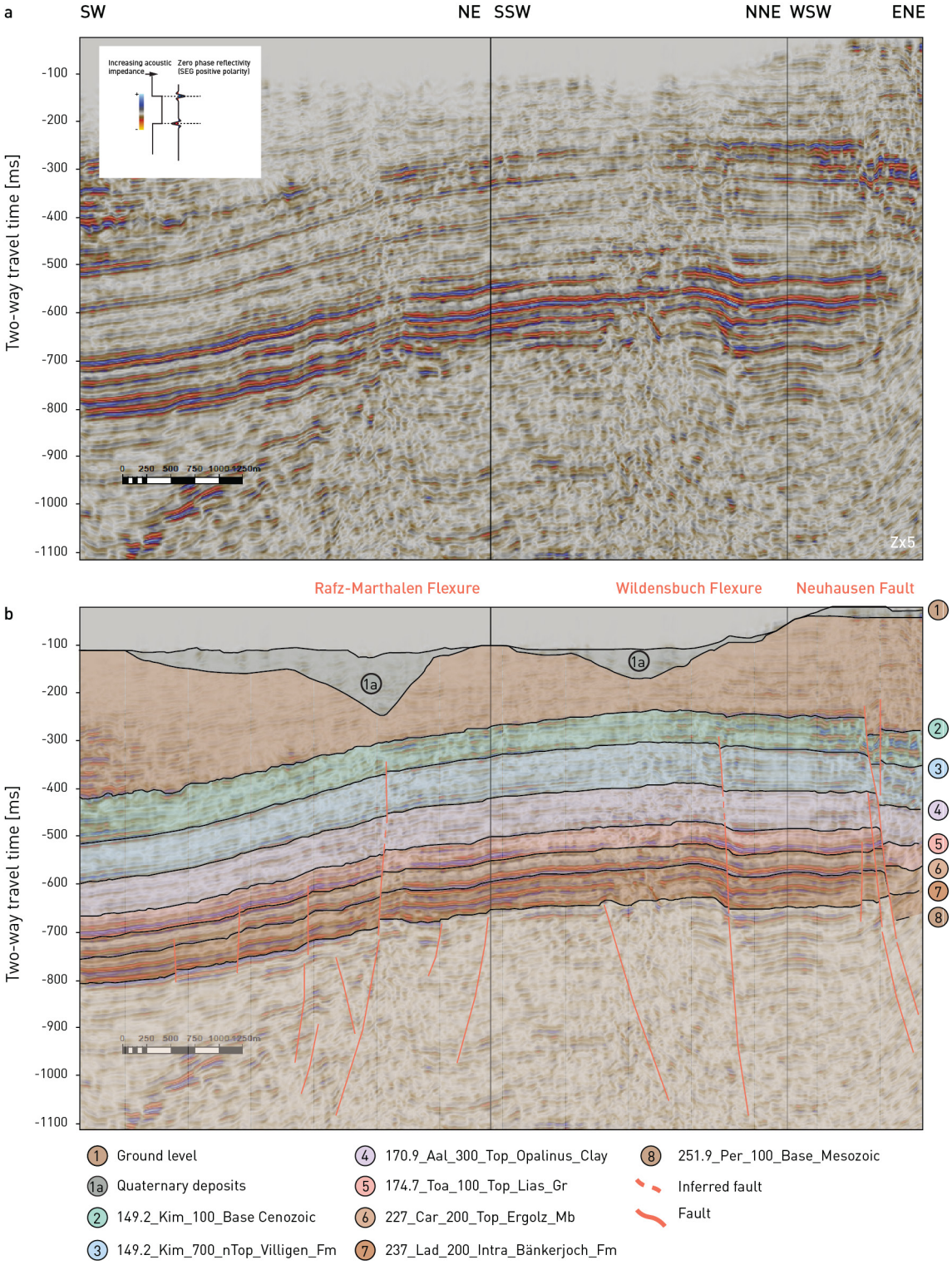


Fig. 4-70: 2D seismic reflection line extracted from 3D seismic reflection data across major structures in ZNO

Modified after Nagra (2024c). (a): Uninterpreted. (b): Interpreted. Seismic display is PreSTM-ref reflectivity with an overlay of relative acoustic impedance. Profile trace shown in Fig. 4-69. The vertical axis was stretched 5 times (Z × 5).

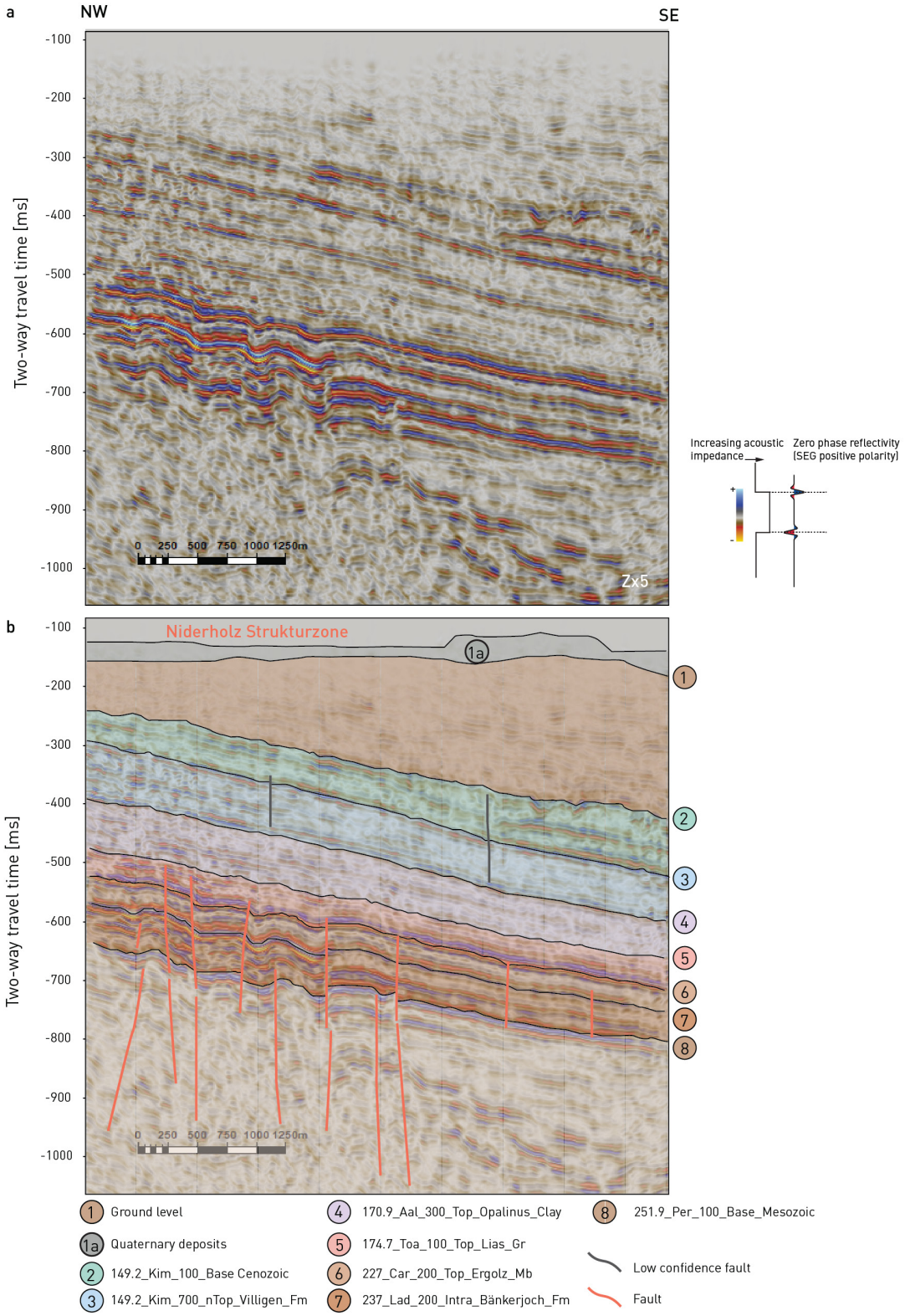


Fig. 4-71: 2D seismic reflection showing high-angle faults in the "Strukturzone von Niderholz"

View is along acquisition crossline 2320, modified after Nagra (2024c). (a): Uninterpreted. (b): Interpreted. Seismic display is PreSTM-ref reflectivity with an overlay of relative acoustic impedance. Profile trace shown in Fig. 4-69. The vertical axis was stretched 5 times (Z × 5).

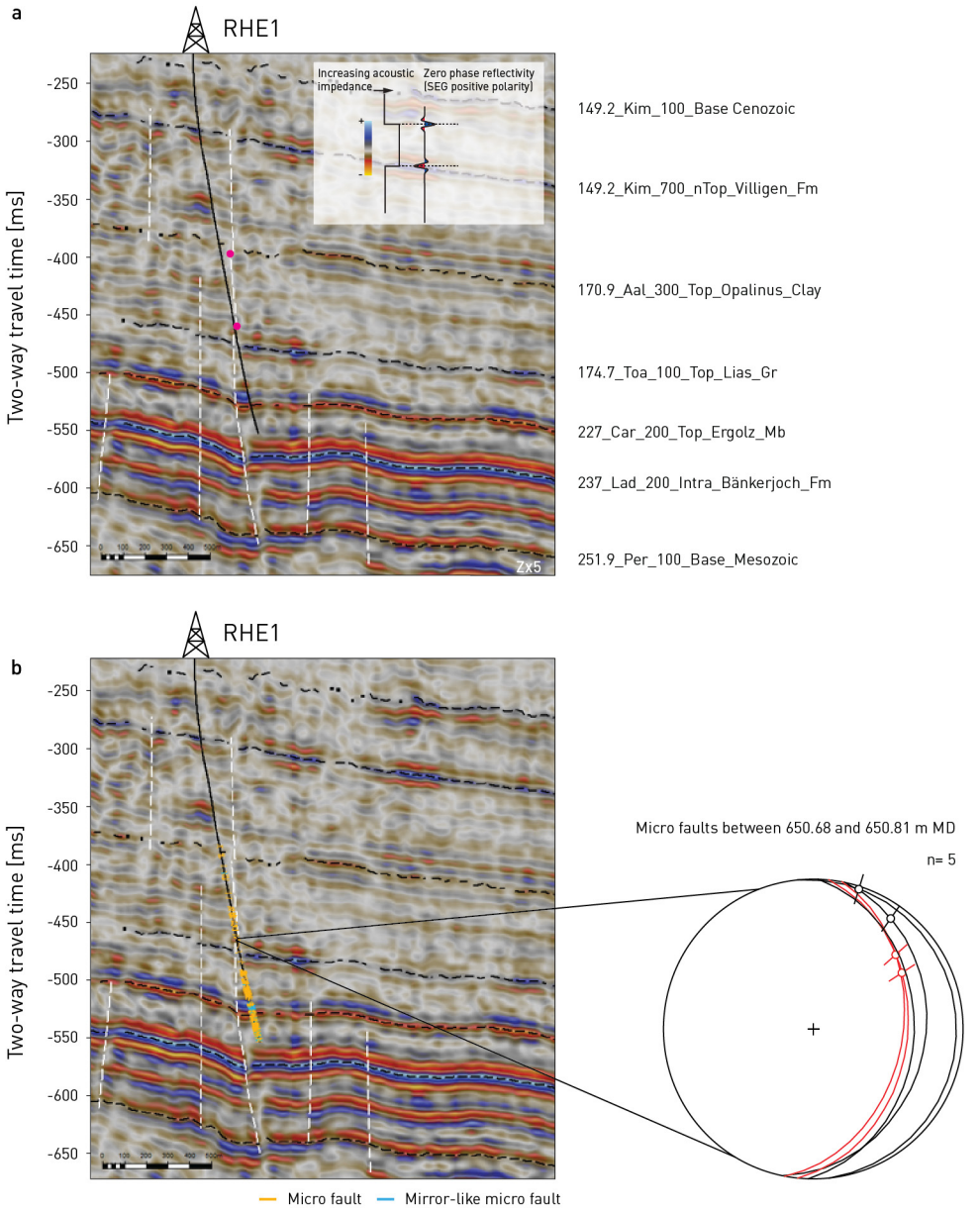


Fig. 4-72: Rheinau Fault in a 2D seismic reflection line oriented parallel to the borehole path

Modified after Nagra (2024c). White dashed lines refer to interpreted fault segments. For the Rheinau fault, the segments mapped above and below the Opalinus Clay were conceptually connected with a separate fault stick (magenta dots) to indicate that the fault cannot directly be seen on the seismic data here in the Opalinus Clay (see Nagra 2024c for more details). (a) 2D seismic reflection line oriented parallel to the borehole path. (b) 2D seismic reflection line oriented parallel to the borehole path including structural inventory from borehole, and a lower hemisphere equal area projection showing orientation and slickenlines of micro faults encountered in the drill core at the depth of 650.7 – 650.8 m MD. The two micro faults highlighted in red could be related to the seismically mappable Rheinau Fault. Seismic display is PreSTM-ref reflectivity with an overlay of relative acoustic impedance (Nagra 2024c). The vertical axis was stretched 5 times (Z × 5).

4.3.5 Detailed tectonic and burial temperature evolution since the Early Jurassic

The general geological evolution of Northern Switzerland since the Paleozoic has been introduced in Chapter 3. In the following, more details regarding the tectonic and burial temperature evolution since the Early Jurassic are presented based on the observations reported in Section 4.3.4 combined with temperature and absolute age constraints obtained by clumped isotope thermometry coupled with U-Pb and U-Th dating of carbonate cements in veins and diagenetic structures such as pore fillings. The analysis of multiple generations of carbonate cements allows tracking of the evolution of burial temperature and pore fluids across geological timescales. The elemental and isotopic compositions of such carbonate cements record both the timing of precipitation as well as the temperature and composition of the mineral-forming fluid and thereby provide information on the ambient conditions at a specific point in time (e.g. Looser et al. 2021). Time of crystallisation is recorded by the incorporation of uranium into the carbonate lattice and the temperature of crystallisation by the clumped isotope composition. The carbonate clumped isotope palaeothermometer (Δ_{47}) allows the direct reconstruction of the formation temperature and of the oxygen isotopic composition of the mineral-forming fluid ($\delta^{18}O_{fluid}$). Δ_{47}/(U-Pb/U-Th) thermochronometry thus contrasts other burial temperature proxies such as apatite fission tracks and (U-Th)/He thermochronometers, vitrinite reflectance, or maturation-dependent biomarkers, which yield an integrated temperature signal over time.

In the following, the geodynamic evolution since the Early Jurassic is discussed with the focus on the younger evolution as it has a more direct impact on the present-day setting and its extrapolation to the future. Oxygen isotope data of pore fluids are included in the discussion as these provide additional information on the burial setting. Details on palaeo-fluid flow are discussed in Sections 4.5 to 4.7. The present-day temperature conditions in the siting regions are elaborated in Section 4.8.

Deposition, early diagenesis and onset of burial during the Early Jurassic

In the Early Jurassic, sedimentation occurred in an epicontinental sea (Chapter 3) with lithospheric stretching creating accommodation space. Deposition rates were very low throughout the Early Jurassic, resulting in a present-day thickness of the Lias Group of only 30 – 50 m in Northern Switzerland and shallow burial conditions until the beginning of the Middle Jurassic (Section 4.2.5; Reisdorf & Wetzel 2018, Müller et al. 2002). Void-filling calcite cements in ammonites, aragonite replacement cements in bivalves, and veins in the Beggingen Member (lower Lias Group) yield U-Pb ages overlapping with the stratigraphic age of the host rocks and thus document the early Jurassic geodynamic evolution (Fig. 4-73). In the case of the early veins, this indicates that lithification of calcareous units in the Lias Group initiated shortly after deposition. The $\delta^{18}O_{fluid}$ signatures of these cements document earliest diagenesis with the mineral-forming fluids sourcing from seawater (Fig. 4-73). One sample from the Frick clay pit (Fig. 4-60) indicates mixing with meteoric waters infiltrated during localised temporary emergence of the Beggingen Member during the Early Jurassic, in agreement with sedimentological evidence (Section 4.2.5, Reisdorf & Wetzel 2018 and references therein). Despite overlapping U-Pb ages, the temperatures of these early calcite phases show an inconsistent picture, with values ranging between 25 and 50 °C and, in the case of one outlier, even of 70 °C. While seawater-like Δ_{47} temperatures are in good agreement with marine to very shallow burial conditions, the extent of the observed high temperatures of other calcite phases as well as the coeval occurrence of very different temperatures raises questions about their plausibility. The observed high temperatures may result from near-surface related kinetic effects (e.g. degassing) and should thus be interpreted with caution.

Middle Jurassic to Early Cretaceous extension and thermal anomaly

Because of the absence of the Late Jurassic and Cretaceous sedimentary rocks due to non-deposition and/or erosion, the burial and thermal evolution during the Late Jurassic and Cretaceous has been debated. Several studies reported indications for heating during the Late Jurassic and Cretaceous, but the timing of occurrence and associated temperatures could not be precisely constrained (e.g. Schegg & Leu 1998, Mazurek et al. 2006, Timar-Geng et al. 2006, Omodeo-Salé et al. 2021, Villagómez Díaz et al. 2021). It thus remained unclear whether high temperatures resulted from deep burial under (later eroded) the latest Jurassic and Cretaceous sediments or from high basal heat flow. The presented Δ_{47}/(U-Pb) data of calcite and saddle dolomite veins and pore-filling cements indicate that, between the Middle Jurassic and Early Cretaceous, burial temperatures increased to peak temperatures of 60 °C in the upper Malm Group, 80 – 85 °C in the middle Dogger Group, and up to 100 – 115 °C in the lower Lias Group at 150 – 135 Ma (Fig. 4-73). Primary fluid inclusions in the same cements suggesting similar or even higher temperatures corroborate these Δ_{47} temperatures (i.e. pressure-corrected trapping temperatures of 80 °C for the upper Malm Group, 85 – 90 °C for the middle Dogger Group, and up to 110 – 115 °C for the lower Lias Group). These temperatures are in good agreement with temperatures of up to 104 ± 9 °C obtained from calcite veins in the Opalinus Clay reported by Akker et al. (2023), although U-Pb dating of those veins was unsuccessful.

The U-Pb ages of the carbonate cements recording these temperatures overlap within error or are only slightly younger than the depositional age of the youngest preserved Jurassic sediments (Wettingen Member, «Felsenkalke» and «Massenkalk») which have a Late Kimmeridgian stratigraphic age corresponding to 150 – 149 Ma. This suggests relatively shallow burial depths for the time of occurrence of peak burial temperatures and confirms high basal heat flow as the reason for the observed heating, as proposed by Mazurek et al. (2006), rather than deep burial. The $\delta^{18}O_{fluid}$ signatures of the cements recording the peak burial temperatures reflect pristine to only slightly modified seawater and contradict extensive interaction between pore fluids and host rocks at high temperatures. Instead, the observed marine-like $\delta^{18}O_{fluid}$ compositions document comparably short residence time of the fluids at the recorded high temperatures, in agreement with the inferred shallow burial depths. Low (non-radiogenic) $^{87}Sr/^{86}Sr$ signatures of these cements consistent with Jurassic to Early Cretaceous seawater show no indication for interaction of the pore fluids with the crystalline basement and/or Triassic formations and speak against hydrothermal fluid ascent into the Jurassic succession (Looser 2022). Therefore, the fluids sourced either externally from downward migrating Late Jurassic to Early Cretaceous seawater or internally from marine formation waters present in the host rocks and heated rapidly due to abruptly increased basal heat flow.

The temperature anomaly diminished during the early Middle Cretaceous, as recorded by 30 °C cooling in the lower Lias Group until 120 Ma, although burial depths are thought to have remained constant or even increased during that time (Crampton & Allen 1995, Schegg & Leu 1998, Mazurek et al. 2006). Although the general thermal evolution is comparable, the peak burial temperatures indicated by carbonate cements were hotter and reached earlier than suggested previously based on thermal modelling using apatite thermochronology, vitrinite reflectance and biomarker isomerisation data. For instance, Omodeo-Salé et al. (2021) estimated peak temperatures of ~ 95 °C for the lower Dogger Group that were reached at 110 Ma and Mazurek et al. (2006) estimated peak temperatures of ~ 60 °C for the top of the uneroded Malm Group, ~ 80 °C for the lower Dogger Group, and, interpolated from their estimates for the top of the crystalline basement, ~ 85 – 90 °C for the Lias Group at 120 – 105 Ma (Fig. 4-73).

The time frame for the occurrence of high basal heat flow coincides with continental-scale crustal extension related to continued ocean opening and spreading at the Piemont – Liguria Ocean and Atlantic Ocean in the Late Jurassic – Early Cretaceous (e.g. Ziegler 1990, Handy et al. 2010). This tensional stress resulted in widespread extension tectonics (e.g. Trümpy 1980, Stampfli &

Borel 2002) and accelerated subsidence of large parts of central Europe (Chapter 3, Section 4.2, e.g. Wildi et al. 1989). In Northern Switzerland, subsidence rates increased drastically at the beginning of the Middle Jurassic Era, as evidenced by orders of magnitude higher net sedimentation rates for the Dogger and Malm Groups compared to the Lias Group (Section 4.2; Müller et al. 2002). In this extensional regime, pre-existing Paleozoic fault systems in Northern Switzerland, such as the Konstanz – Frick Trough, are thought to have been episodically reactivated across the Jurassic (Allenbach 2002, Wetzel et al. 2003, Reisdorf & Wetzel 2018). The observed high basal heat flow could thus well have occurred related to thermal disturbances along such basement-rooted faults. Further evidence for thermal disturbances during the Jurassic and Early Cretaceous is provided by hydrothermal veins and mineral alterations in the pre-Mesozoic units in the Black Forest Massif, with radiometric ages covering the entire Jurassic and Early Cretaceous (Wernicke & Lippolt 1997, Pfaff et al. 2009, Staude et al. 2012, Brockamp et al. 2015 and references therein). As elaborated above, hydrothermal activity in Northern Switzerland would have been restricted to the pre-Mesozoic units and the lowermost Triassic sedimentary rocks without cross-formation fluid flow into the Jurassic succession whereby massive Triassic evaporites could have acted as effective seal (Mazurek et al. 2006, Looser 2022).

Eocene exhumation and evolution during the Oligocene

Cessation of the first interval of burial during the Late Mesozoic is recorded by a major erosional unconformity spanning ~ 100 Ma from the latest Jurassic to Eocene times (Herb 1988). Combined Δ_{47}/(U-Pb) data show cooling of 25 °C at 55 to 50 Ma, which can be correlated with exhumation (Fig. 4-73). Calcite cements precipitated in the Malm Group between Late Cretaceous and Early Eocene times show $\delta^{18}O_{fluid}$ signatures overlapping with those of Jurassic porewaters. This indicates that the Mesozoic succession remained hydrologically undisturbed until the onset of exhumation at ~ 55 Ma. Starting at 50 Ma and continuing until 20 Ma, however, $\delta^{18}O_{fluid}$ signatures gradually shifted to meteoric signatures with values as low as -7 ‰ resulting from infiltration of meteoric fluids and mixing with Jurassic marine porewaters. Possible transport processes are discussed in Section 4.7.

The earliest preserved deposits after erosion are continental karst infills in the uppermost Malm Group consisting of Siderolithic clays with a Middle Eocene to Early Oligocene depositional age (Mammal Paleogene zones MP13 – MP22, corresponding to 45 – 33 Ma (Rosselet 1991, Gradstein et al. 2020).

During the Oligocene, closure of the Piemont – Liguria and Valais Oceans was completed (e.g. Schmid et al. 1996). Subsequently, collision involved basal accretion of European upper crust into the Alpine wedge (Handy et al. 2010, Gleißner et al. 2021). Increased crustal loading of the lower plate resulted in down bending of the lithosphere and the consequent formation of a wedge-shaped foreland basin referred to as the Molasse Basin (Pfiffner 1986). Alternatively, it has been suggested that not flexural loading, but slab rollback is responsible for bending of the lower plate (Schlunegger & Kissling 2022). Whichever mode is preferred, the flexural foreland basin was deepest close to the orogenic front and became progressively shallower towards the north, resulting in a wedge geometry. Basin width (i.e. N-S extent) as well as possible formation of a distal forebulge is a function of the elastic thickness of the lower plate. The forebulge marked an area dominated by uplift and erosion. The lithospheric flexure resulted in a SE-directed tilting of the Mesozoic strata in Northern Switzerland (Fig. 4-56, Fig. 4-57 and Fig. 4-58).

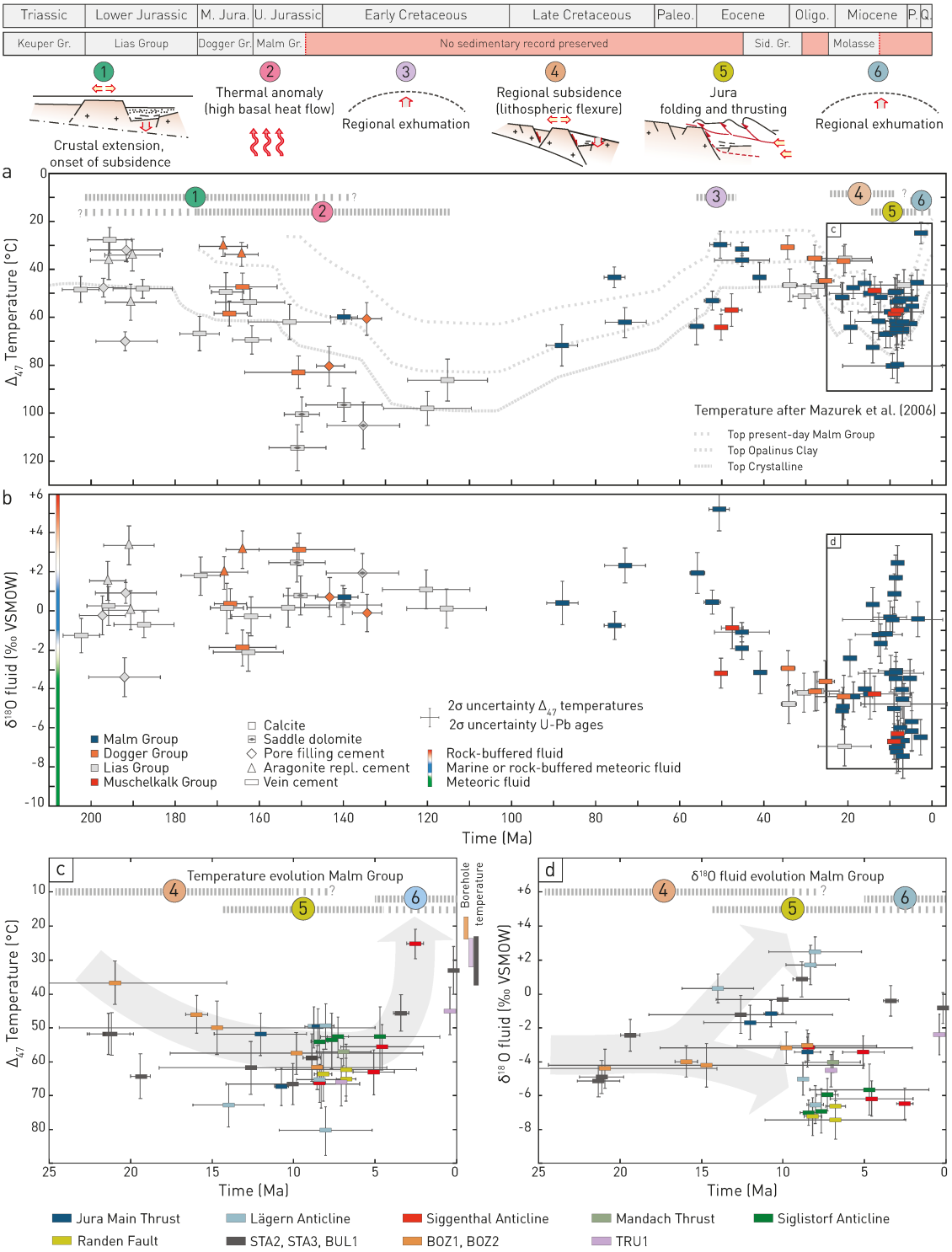


Fig. 4-73: Evolution of burial temperature and oxygen isotope composition of pore fluids ($\delta^{18}O_{fluid}$) since the Early Jurassic

(a) Evolution of temperature since the Early Jurassic (after Mazurek et al. 2006). (b) Evolution of the oxygen isotope composition of mineral-forming fluids since the Early Jurassic. (c) Temperature evolution in the Malm Group since 25 Ma. (d) Evolution of the oxygen isotope composition of mineral-forming fluids in the Malm Group since 25 Ma. M.: Middle, U.: Upper, Paleo.: Paleocene, Oligo.: Oligocene, P.: Pliocene, Q.: Quaternary, Gr.: Group, Sid.: Siderolithic, VSMOW: Vienna standard mean ocean water, repl.: replacement.

Furthermore, flexing of the lower plate including pre-Mesozoic basement and Mesozoic cover resulted in extensional tectonics in Northern Switzerland during the Paleogene (e.g. Laubscher 1985). This normal faulting phase is recorded in Northern Switzerland, for instance, in the Mesozoic strata north of the Mandach Thrust which are at higher elevation than south of the Mandach (Nagra 2024a), in the present-day net normal offset preserved along the eastern continuation of the Baden – Irchel – Herdern Lineament (Fig. 4-60; Meier et al. 2014) or in the normal faulting observed along the cores of the recent deep boreholes (Tab. 2-1).

Preceded by Late Cretaceous volcanism, rifting in the southern Upper Rhine Graben started in Late Eocene times (42 – 31 Ma; Henrion et al. 2020, Ziegler 1992, Rotstein & Schaming 2011, Dèzes et al. 2004). The main rifting phase ended in the mid-Rupelian but localised extension related to a strike-slip-dominated deformation continued at least into the Pliocene (Giamboni et al. 2004, Rotstein & Schaming 2011). Rift-related surface uplift of the graben shoulders (i.e. Black Forest and Vosges Massifs) further increased southward tilting of the Mesozoic strata in Northern Switzerland (e.g. Müller et al. 2002).

Evolution during the Miocene

During the Miocene, the Alps grew by frontal and basal accretion. This has been attributed to either plate convergence (e.g. Bonnet et al. 2007, Schlunegger & Mosar 2011, Willett & Schlunegger 2010), or slab rollback and associated buoyancy-driven uplift (Schlunegger & Kissling 2015). NW-propagation of the Alpine deformation occurred along an intra-Triassic décollement level rooting underneath the External Crystlline Massifs (e.g. Buxtorf 1916, Laubscher 1961, Burkhard 1990, Ortner et al. 2024). Low strength Triassic evaporites acted as a décollement horizon facilitating the formation of a narrow taper as observed in the Jura Fold-and-Thrust Belt (e.g. Mosar 1999). Folding and thrusting in the Jura mountains 50 – 80 km north of the front of the Alpine nappes is inferred to have started in the Middle Miocene (Fig. 4-74; Becker 2000, Looser et al. 2021, Smeraglia et al. 2021). Stratigraphic evidence from mammalian fauna place onset of Jura folding and thrusting at about 12 Ma (Becker 2000). Tectonic activity along the décollement (i.e. thin-skinned) is estimated from U-Pb calcite dating to 14.3 to 4.5 Ma in the Schafisheim borehole located south of the Internal Jura (Looser et al. 2021). Dating of regional fault zones in Northern Switzerland confirmed this age range and specifies that the main thin-skinned structures were established at 8 Ma (Fig. 4-74; Madritsch et al. 2024). For instance, the Mandach Thrust, the Siggenthal Anticline and the Jura Main Thrust in JO and the Lägern Anticline in NL are associated with décollement-related (i.e. thin-skinned) deformation (Section 4.3.4).

Shortening north of the Subalpine Molasse generally decreases eastwards in the central North Alpine Foreland (e.g. Ortner et al. 2024 and references therein). This is also seen in the shortening estimates decreasing from JO to NL and in general from the shortening around 25 – 30 km in Central Jura and the maximum 5 km shortening estimated in JO (Fig. 4-74; Burkhard 1990, Jordan et al. 2015). The eastward decrease of shortening and finally the change from allochthonous to autochthonous sedimentary rocks in the North Alpine Foreland can be associated with the strength of the décollement, where the thin-skinned salient of the Jura Mountains is associated with the distribution of evaporites.

As described by Madritsch et al. (2024), no clear trend of in-sequence or out-of-sequence thrusting can be deduced from the dense age data for the deformation sequence in the External Jura in Northern Switzerland (Fig. 4-74). This is expected for a growing wedge, as it maintains its critical taper geometry (e.g. Willett 1999, Buiter 2012, Caër et al. 2018).

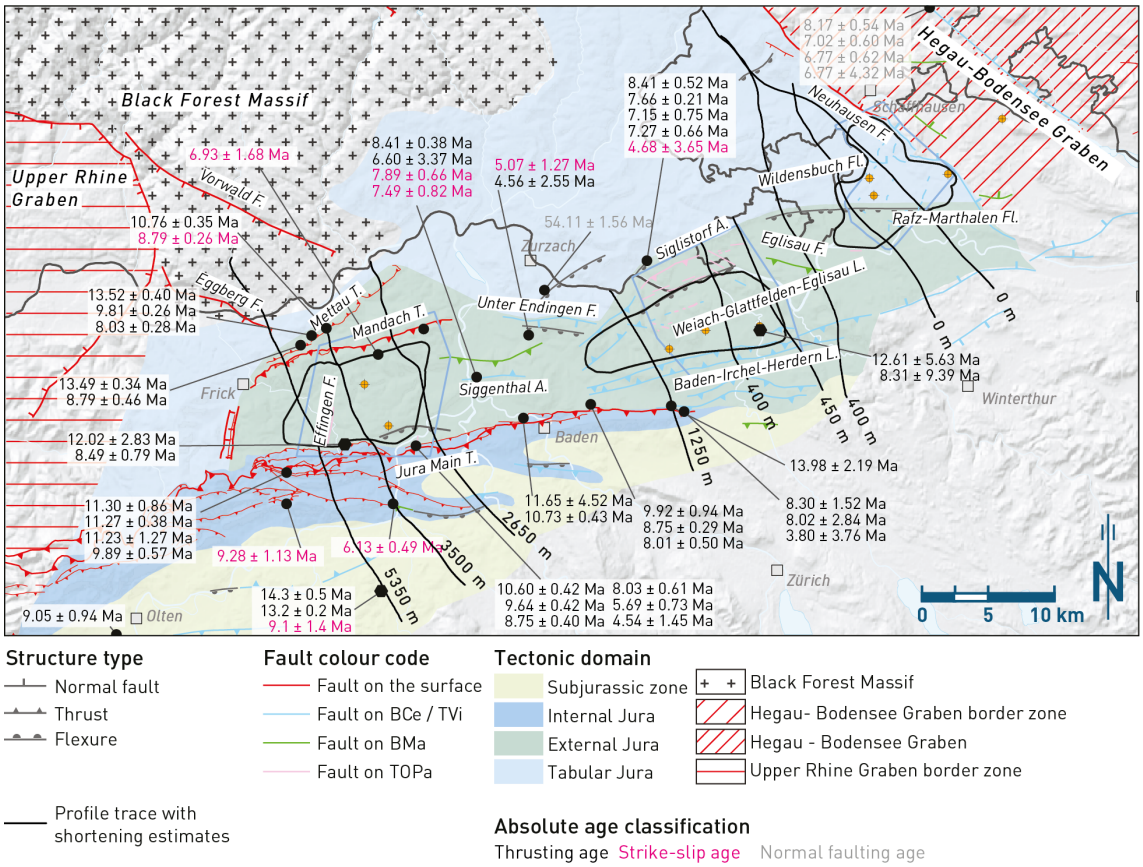


Fig. 4-74: Simplified tectonic map of Northern Switzerland showing absolute ages obtained from veins sampled in outcrops and drill cores and shortening estimates

Surface fault traces based on Nagra (2014b). Fault traces from seismic interpretation are based on 2D seismic reflection (Madritsch et al. 2013, Meier et al. 2014) and 3D seismic reflection interpretation (Birkhäuser et al. 2001, Nagra 2024a, 2024b, 2024c). They are shown on the highest stratigraphic horizon where the specific fault segment was picked (different colours in the map view). Only horizons from Top Opalinus Clay and higher stratigraphic levels are shown. Note that only a selection of the structures from 3D seismic interpretation is shown to highlight the structural trends of regional importance. See Fig. 4-61, Fig. 4-65 and Fig. 4-69 for the complete fault pattern. Absolute ages are from Madritsch et al. (2024) and Looser et al. (2021). Colour coding indicates the kinematic association of the sampled veins. Profile traces with shortening estimates are taken from Jordan et al. (2015) and refer to shortening estimates from kinematic 2D balancing.

The Hegau – Bodensee Graben also initiated during the Early Miocene with a period of transtension (Ibele 2015 and references therein). This was followed by a main phase of strike-slip tectonism in the Late Miocene to Pliocene (Schreiner 1992, Hofmann et al. 2000, Egli et al. 2017). U-Pb age dating of calcite showed that the Randen Fault, which is part of the Hegau – Bodensee Graben, was active at the same time as the main phase of the Jura folding and thrusting (Fig. 4-74; Madritsch et al. 2024).

Continuing lithospheric flexure during the Late Miocene (e.g. Kuhlemann & Kempf 2002, Ford et al. 2006) led to a second interval of burial of the Mesozoic formations accompanying deposition in the Molasse Basin. Maximum burial temperatures during the Miocene decreased with increasing distance from the Alpine front, which is associated with the thinning of the Molasse sedimentary wedge towards the north (e.g. Pfiffner 1986, Kuhlemann & Kempf 2002). This

second interval of burial is documented in calcite cements by a temperature increase starting at ~ 20 Ma and resulting in peak burial temperatures between 10 and 5 Ma, in broad agreement with the timing suggested by previous thermochronological data (Mazurek et al. 2006, Villagómez Díaz et al. 2021) and in agreement with the maximum age for the cessation of Molasse sedimentation of ~ 11.5 Ma in Northern Switzerland (Rahn & Selbekk 2007). Peak temperatures in the Malm Group ranged between 50 – 80 °C and are thus in broad agreement with previous estimates (Fig. 4-73; Mazurek et al. 2006).

The southward rise in temperature and the development of the Jura Fold-and-Thrust Belt, which led to localised surface uplift along thrusts and consequently the creation of new fluid migration pathways, caused local variations in the temperature and oxygen isotopic composition of calcite cements. This is reflected by calcite veins formed coevally between 10 and 8 Ma in the Malm Group at different locations that show large variability in Δ_{47} temperatures and the evolution of $\delta^{18}O_{fluid}$. After relatively uniform compositions until 15 Ma, both Δ_{47} temperatures and $\delta^{18}O_{fluid}$ data show diverging trends contemporaneously with the formation of the Jura Fold-and-Thrust Belt (Fig. 4-73).

Evolution during the Pliocene

During Pliocene times, the Alpine deformation front continued propagating northwestwards, reaching into the Plateau Jura (Schlunegger & Mosar 2011). The major thin-skinned deformation phase of the Jura Fold-and-Thrust Belt (i.e. Miocene evolution) has been followed by a thin- and thick-skinned deformation at low strain rates until the present day (e.g. Philippe et al. 1996, Pfiffner et al. 1997, Mosar 1999, Giamboni et al. 2004, Ustaszewski & Schmid 2007, Madritsch et al. 2008, Schlunegger & Mosar 2011, Lacombe & Bellahsen 2016, Caër et al. 2023). Deformation involving the substratum below Middle Triassic décollement level is corroborated by interpretations from the recent 3D seismic reflection database (Section 4.3.4, Fig. 4-66; Zambrano et al. *submitted*). For instance, the Weiach – Glattfelden – Eglisau Lineament roots in the Paleozoic strata but cuts through the décollement horizon and a footwall shortcut (i.e. thrusting cutting through the fault's footwall) affecting the Paleozoic basement underneath the Mandach are evidence for the substratum involvement (Section 4.3.4). Caër et al. (2023) proposed lateral changes in deformation style along the Jura arc as the basement-involving deformation front follows the Alpine Front which has a different shape than the Jura arc. This results in deformation involving the basement in the eastern Jura Fold-and-Thrust Belt.

Miocene burial was followed by exhumation resulting in the present-day setting. The youngest preserved sedimentary rocks in Northern Switzerland are Upper Freshwater Molasse sedimentary rocks dated to 11.5 Ma and thus constrain the initiation of net erosion in the Molasse Basin (Rahn & Selbekk 2007). Based on existing data von Hagke et al. (2015) showed that exhumation may have commenced sometime between about 12 and 4 Ma and heat flux probably increased over time. Numerous studies propose onset of large-scale foreland exhumation to occur between 6 and 4.5 Ma (Kuhlemann & Kempf 2002, Cederbom et al. 2004, 2011, Schlunegger & Mosar 2011, von Hagke et al. 2014, Looser et al. 2021). Reported Δ_{47}/(U-Pb) data from calcite cements of the Siggenthal Anticline and STA2 record cooling from 63 to 25 °C between 5.0 and 2.5 Ma (Fig. 4-73) agreeing with the aforementioned estimates. This in turn is in agreement with rapid incision pulse triggered by capture of the former Aare-Danube River by the Rhone-Doubs system at 4.2 – 2.9 Ma with incision of 300 – 500 m in the lower Aare Valley (Chapter 3, Fig. 3-11). The recorded 25 °C at 2.5 Ma suggests a remaining sedimentary overburden, in agreement with incision of another 100 – 200 m during the Pleistocene as recorded by gravel deposits in the lower Aare Valley (Chapter 3, Fig. 3-11).

Quaternary tectonic activity

Tectonic deformation within the Quaternary has been postulated for Northern Switzerland. The present-day seismicity suggests that deformation in the North Alpine Foreland is ongoing (Kastrup et al. 2004, Lanza et al. 2022, Diehl et al. 2023). The inversion of focal mechanisms implies a strike-slip to normal faulting tectonic regime for the majority of the North Alpine Foreland. Indications for contraction to oblique contraction related seismicity are rare and restricted to the northwestern front of the Jura Mountains, where there is also geomorphic evidence for ongoing folding (Nivière & Winter 2000, Madritsch et al. 2010, Lanza et al. 2022). In addition, two samples provide U-Th ages within the Quaternary (Fig. 4-73). The sample from the Villigen Formation (0.41 ± 0.01 Ma) was obtained from a slickenfibre indicating strike-slip faulting in TRU1. The other sample documents Quaternary fluid flow but is not related to tectonic activity. Further, discussion of the present-day tectonic activity (including vertical and horizontal velocities) is provided in Section 6.2 and in Nagra (2024l).

4.3.6 Deformational style and tectonic domains

This section is dedicated to summarising key factors that influenced the present-day structural inventory. It focuses first on the encountered deformation style (i.e. influence of Paleozoic faults and mechanical stratigraphy) and then on the impact of the tectonic domains surrounding the siting regions on the structural inventory within the siting regions.

Influence of Paleozoic fault inventory on later deformation

The importance of geometric steps affecting the Base Mesozoic unconformity for subsequent deformation has been previously proposed for the Jura Fold-and-Thrust Belt (e.g. Laubscher 1961, Homberg et al. 2002, Schori et al. 2021, Schori 2021. The pre-Mesozoic tectonic evolution resulted in the formation of three distinct fault orientations (Hercynian or NW-SE-trending, Rhenish or NNW-SSW-trending, and Erzgebirgian or ENE-WSW-trending, Fig. 4-55). These faults have acted as zones of weakness within the less deformed surrounding rock volume and were repeatedly reactivated throughout the tectonic evolution of Northern Switzerland (Section 4.3.5). Comparison of fault traces at various stratigraphic levels as performed by Schöpfer et al. (2024) indicates a strong control of these orientations on deformation in the sedimentary cover. In JO and NL, regional fault zones, with exception of the Siggenthal Anticline, are located above structures related to the Konstanz – Frick Trough (ENE-WSW-trending). This spatial coincidence calls for being consequential rather than coincidental. For NL, Butler et al. (submitted) investigated the influence of the basement topography and highlighted differences between the eastern and western segment of the Baden – Irchel – Herdern Lineament within the 3D seismic perimeter that could be associated with differences in the underlying Paleozoic fault geometry. Other examples of faults in the Mesozoic sedimentary cover with a typical Paleozoic orientation are the Neuhausen Fault, the Eglisau Fault and the Zweidlen Fault (NW-SE-trending). The Effingen Fault and the Trüllikon Fault and the Rheinau Fault are examples of faults trending NNE-SSW (Rhenish trend).

The influence of step morphology in the Base Mesozoic unconformity is further testified by a comparison between the Mandach Thrust and the Siglistorf Anticline. The Mandach Thrust is expressed throughout the Mesozoic succession as a rather narrow deformation zone. In contrast, deformation in the Mesozoic strata overlying the northern border of the Konstanz – Frick Trough in NL affects a broader zone. This marked difference is probably linked to the pronounced, single Paleozoic normal fault underlying the Mandach Thrust, whereas the Siglistorf Anticline is underlain by various smaller and more distributed Paleozoic faults (Nagra 2024a, 2024b).

The aforementioned examples from seismic reflection data interpretation provide supporting evidence for the proposed influence of the Upper Paleozoic trough and its fault pattern on the localisation of later deformation.

Mechanical stratigraphy and décollement horizons

In addition to the aforementioned stepped geometry of the Base Mesozoic unconformity, the variable mechanical properties of the Mesozoic strata also strongly influenced strain accommodation in Northern Switzerland. The overall stratigraphic column was introduced in Chapter 3 and Section 4.2. It is characterised by strong contrasts in the mechanical competence between the different units, with for instance the carbonates of the Malm Group and the Muschelkalk Group representing competent units and the clay-mineral-rich Opalinus Clay representing a less competent unit. The detailed geomechanical properties are reported in Sections 4.4 and 5.5 focusing on the Opalinus Clay. The mechanical competence contrast among different formations, also termed mechanical stratigraphy, is reflected in the fracture frequency distribution (Section 4.3.4), but also in the stress field characteristics (Section 4.4).

Two key observations in Northern Switzerland with respect to the understanding of the tectonic evolution are related to the mechanical stratigraphy. Firstly, the mechanical stratigraphy influences the fault architecture in the different units. In general, faults in Northern Switzerland appear highly segmented not only in map view, but also in vertical sections (Section 4.3.4). For instance, the surface expression of the Mandach Thrust varies along strike, being influenced by the mechanical stratigraphy and local changes in the stepped geometry of the Base Mesozoic unconformity (Malz et al. 2020). The mechanically less competent, clay-mineral-rich units are characterised by an even higher fault segmentation, with soft-linkage and fault relay zones (Roche et al. 2020, Zwaan et al. 2022). Fault architecture of these units is further detailed in Section 5.5.4.

Secondly, the typical stratigraphic column in Northern Switzerland contains multiple horizons that could act mechanically as décollement levels (e.g. Marro et al. 2023, for a recent compilation for the western Jura). Décollement level refers to the observation that the total strain accommodated above it differs from that below it. The evaporites in the Zeglingen Formation and in the Bänkerjoch Formation are considered as main décollement for the Jura Fold-and-Thrust Belt (e.g. Sommaruga et al. 2017). Additionally, the Opalinus Clay has also been proposed as a subsidiary décollement level (Matter et al. 1987, Marro et al. 2023). The detailed fault pattern observed in the Baden – Irchel – Herdern Lineament (Fig. 4-67) requires an interval around the Opalinus Clay capable of decoupling the mechanical panel above from that below it (Laubscher 1985, Malz et al. 2016, Nagra 2024b). However, the competent panels above and below the incompetent Opalinus Clay, although independently folded in the Baden – Irchel – Herdern triangle zone in NL, are characterised by similar amounts of deformation. Therefore, at least in the siting regions, the Opalinus Clay did not allow the rock panel overlying it to be transported forelandward more than the rock panel underlying it. Also the overall degree of tectonic deformation observed within the Opalinus Clay in the boreholes within the siting regions shows that it was not acting as a secondary décollement north of the Baden – Irchel – Herdern Lineament (Section 5.5 and fracture frequency distribution in Fig. 4-61, Fig. 4-65, Fig. 4-69).

As mentioned above, the evaporites in the Zeglingen Formation are considered as décollement level in the eastern Jura Fold-and-Thrust Belt. The halite intervals encountered in the recent deep boreholes vary substantially in vertical thickness (Fig. 4-2). While the halite thickness reaches only 1.4 m in BOZ1, several decameter-thick halite deposits have been drilled in the central part of NL. In general, the halite is only slightly deformed with minor horizons of intense deformation (i.e. shear zones). Shortening estimates from the halite intervals are in broad agreement with the shortening estimates for the area north of the boreholes (distal with respect to the source of deformation, i.e. the Alps) based on balanced and restored cross-sections (Jordan et al. 2015). The halite interval in BOZ1 is more strongly deformed along with a generally more deformed Triassic

evaporitic sequence than in NL (Madritsch et al. 2024; TBO reports in Tab. 2-1). It is concluded that the Triassic evaporites encountered in the boreholes in the External Jura provide evidence for a décollement particularly in JO but also in NL. This observation based on the borehole records is well aligned with the proposed fault geometry from seismic reflection interpretation for the Siglistorf Anticline and the Mandach Thrust (Section 4.3.4).

Tectonic domains in Northern Switzerland

As introduced in Chapter 3 and detailed in the sections above, Northern Switzerland is at the interplay of the Konstanz – Frick Trough, the Jura Fold-and-Thrust Belt, the Hegau – Bodensee Graben and the Upper Rhine Graben. The following section is dedicated to illustrating the influence of these tectonic domains onto the structural inventory of the siting regions.

Paleogene to Early Neogene normal faulting in response to the uplift of the Black Forest related to the opening of the Upper Rhine Graben, the northward migration of the Alpine flexural forebulge and the lithospheric flexural bending in response to the Alpine orogeny affected Northern Switzerland (Section 4.3.5). This is recorded inter alia by (i) the general south dip of the Mesozoic strata; (ii) the net normal offset observed within Mesozoic strata along the eastern segment of the Baden – Irchel – Herdern Lineament; and (iii) the bending of the Mesozoic strata south of the Mandach Thrust, which is clearly related to a post-Mesozoic but pre-thrusting extensional reactivation of the master fault bounding the Konstanz – Frick Trough to the north. The occurrence of shear sense indicators indicative for normal faulting in the boreholes can be considered as additional evidence for this deformation stage (Fig. 4-75).

The contractional deformation related to folding and thrusting associated with the Jura Fold-and-Thrust Belt is depicted foremost in surface topography. Its decrease towards the east is shown by the decreasing shortening estimates along 2D geological profiles across Northern Switzerland (Fig. 4-75; Jordan et al. 2015). In addition, the relative abundance of reverse faulting shear sense indicators in the boreholes in JO and NL is also considered as evidence of the contraction-dominated deformation affecting the siting regions. The overall higher frequency of subseismic fracturing in the boreholes in JO (BOZ2, BOZ1) compared to the other boreholes is probably related to the stronger contractional overprint due to its more internal position with respect to the central Jura. The occurrence of the seismically mappable "Brugg Strukturzone", expressed in the Muschelkalk Group in the vicinity of BOZ1, could also influenced the subseismic fault density encountered along the entire borehole.

The Neuhausen Fault, marking the northeastern border of ZNO (Fig. 4-75), is linked to the Hegau – Bodensee Graben. The oblique extension of the Hegau – Bodensee Graben probably resulted in the formation of high-angle faults in ZNO. It could further be the cause for the increased amount of normal faulting observed in the drill cores in ZNO compared to JO and NL (Fig. 4-75).

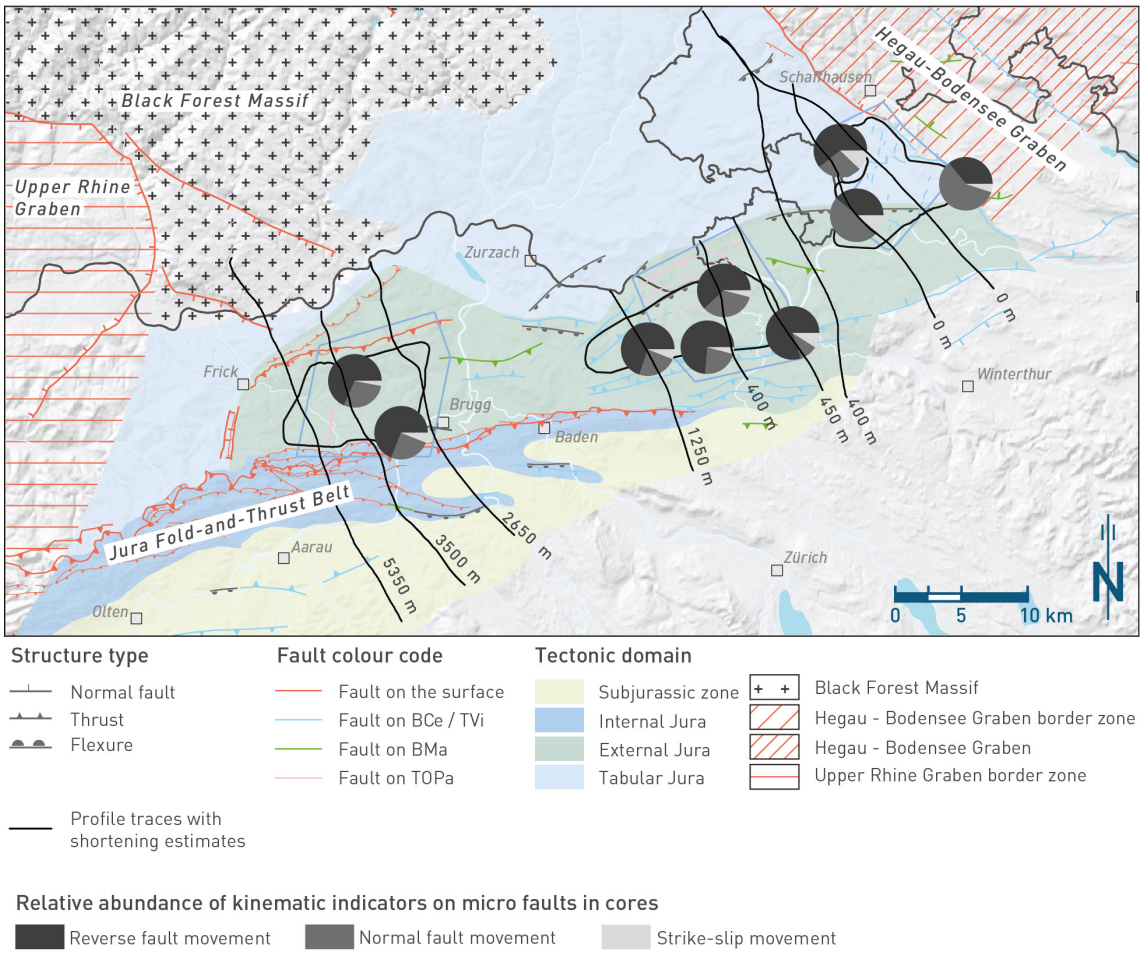


Fig. 4-75: Tectonic map of Northern Switzerland showing the influence of the neighbouring tectonic domains

Surface fault traces based on Nagra (2014b). Fault traces from seismic interpretation are based on 2D seismic reflection (Madritsch et al. 2013, Meier et al. 2014) and 3D seismic reflection interpretation (Birkhäuser et al. 2001, Nagra 2024a, 2024b, 2024c). They are shown on the highest stratigraphic horizon where the specific fault segment was picked (different colours in the map view). Only horizons from Top Opalinus Clay and higher stratigraphic levels are shown. Note that only a selection of the structures from 3D seismic interpretation is shown to highlight the structural trends of regional importance. See Fig. 4-61, Fig. 4-65 and Fig. 4-69 for the complete fault pattern. The shortening estimates were calculated based on geometric 2D section restoration along 2D seismic reflection lines documented in Jordan et al. (2015). The pie charts show the relative abundance of shear sense indicators observed in the full cored sections. Micro faults with undefined shear sense are not displayed. The charts show the influence of the Jura Fold-and-Thrust belt with a predominance of reverse faulting or thrusting in JO and NL, the influence of the trans-tensional activity in the Hegau – Bodensee Graben with an increased portion of normal faulting in ZNO as well as the Paleogene extension related to the migration of the Alpine forebulge.

4.3.7 Conclusions

- All three siting regions show areas devoid of seismically mappable faults that are bounded by well-defined deformed areas (i.e. seismically mappable faults and folded domains). In NL, the area free of seismically mappable faults is largest.
- The tectonic history of Northern Switzerland is influenced by the evolution of the Jura Fold-and-Thrust Belt, the Hegau – Bodensee Graben and the Upper Rhine Graben. The influence on the structural inventory of each tectonic domain decreases with distance from it as demonstrated for instance by the decreasing eastward shortening related to the Jura Fold-and-Thrust Belt.
- The basement underlying Northern Switzerland is pre-structured with (i) the Upper Paleozoic Konstanz – Frick Trough (controlled by ENE-WSW-trending faults), (ii) Hercynian faults (NW-SE-trending), and (iii) Rhenish faults (NNE-SSW-trending). The geological past provided numerous evidence that these inherited structures exerted a strong control on the localisation of later tectonic deformation.
- Observations made at multiple scales (seismic interpretation, macroscopic and microscopic core description) provide evidence that inherited structures acted as zones of weakness within the less deformed rock volume, localising later strain (i.e. by fault reactivation).
- Fracture distribution testifies to the control of mechanical layering: higher fracture frequencies characterise the mechanically competent units (Malm and Muschelkalk Groups), whereas lower fracture frequencies are observed in the less competent units (Opalinus Clay, Lias Group).
- In all three siting regions, no evidence for a secondary décollement within the Opalinus Clay was found.
- Geodynamically, Northern Switzerland evolved from a first burial to exhumation resulting in terrestrial conditions in the Eocene. The incorporation of Northern Switzerland into the flexural foreland basin of the Alps resulted in a second burial. With the NW-propagation of the Alpine deformation front and the formation of the Jura Fold-and-Thrust Belt, Northern Switzerland evolved towards a wedge-top basin. ZNO, north of the Rafz – Marthalen Flexure (i.e. in the part considered as autochthonous), remained part of the flexural foreland basin. Neogene exhumation resulted in the present-day situation.
- Detailed temperature data gained from the analysis of calcite cements provide evidence for locally higher temperatures and thermal gradients than previously estimated for the Mesozoic evolution. Final cooling after burial beneath the Molasse sedimentary rocks is suggested to have occurred essentially after 5 Ma.

4.4 Current stress field

Key points:

- The dominant azimuth of the maximum horizontal stress magnitude (S_{Hmax}) is oriented NNW-SSE. This orientation is consistent in all the siting regions in the Mesozoic sediments and the pre-Mesozoic basement rocks.
- Characteristics of the stress field are similar in all three siting regions, with depth and mechanical layering coupled to tectonic loading controlling stress magnitudes.
- Tectonic loading has led to higher stress magnitudes in more competent calcareous layers and can explain why tectonic overprint in these layers is often more pronounced than in the weaker clay-mineral-rich layers.
- In the three siting regions the spatial characteristics of the present-day stress field can be predicted with geomechanical-numerical models with the same degree of reliability.
- The Opalinus Clay exhibits very consistent gradients of the stress magnitudes, irrespective of the siting region considered. Minor differences in the stress regime (i.e. ratios of horizontal to vertical stress) between regions arise mainly from the different depths of the Opalinus Clay.

4.4.1 Overview

The stress field is an important state variable and exerts strong control on the mechanical behaviour and stability of the rock mass. For a deep geological repository, the quantification of the undisturbed present-day stress field is relevant for both short-term (construction of underground and access structures) and the long-term (thermal stresses and gas migration) considerations.

Here it is assumed that the vertical stress $S_v = g \cdot \rho \cdot z$ is a principal stress (g = gravitational acceleration, ρ = rock bulk density, z = depth). Based on this assumption, the maximum and minimum horizontal stresses, S_{Hmax} and S_{hmin}, respectively, are also principal stresses. This simplified stress tensor has only four unknowns: the orientation of S_{Hmax} and the magnitudes of S_{hmin}, S_{Hmax} and S_v (Nagra 2024o).

In Northern Switzerland, the assumption that the vertical stress S_v is a principal stress is reasonable and can be demonstrated by 3D geomechanical-numerical models (Nagra 2024o). The minimum principal stress (S_{hmin}) was measured by means of microhydraulic fracturing (MHF) tests, and the maximum horizontal stress (S_{Hmax}) was derived from sleeve reopening (SR) tests. The detailed evaluation and assignment to stress magnitudes are explained in Nagra (2024o).

This section summarises the key results of the 3D stress tensor description in the various regions. It focuses first on stress data of the S_{Hmax} orientation (Section 4.4.1) and secondly on stress magnitude estimates (Section 4.4.2). Section 4.4.3 illustrates the results of geomechanical-numerical models that integrate all rock property and stress data for a continuous description of the stress state in 3D, before concluding with the main insights (Section 4.4.4). A detailed overview and evaluation of stress data and model results are provided in Nagra (2024o). The quantification of the ambient stress field is also of direct importance for other aspects covered in this report, in particular for the robust self-sealing of the Opalinus Clay (Section 5.7) and scenarios of future tectonic evolution (Section 6.2).

4.4.2 Stress orientations

The prevailing orientation of S_{Hmax} in the siting regions was constrained by new borehole data using the orientation of borehole breakouts, drilling-induced tensile fractures and fractures generated as a result of MHF testing (Section 4.4.3). The results (Fig. 4-76) are very much consistent with those predating the new boreholes (Heidbach & Reinecker 2013):

- S_{Hmax} trends in a NNW-SSE orientation, with a small counter-clockwise rotation of S_{Hmax} from east to west. The mean S_{Hmax} orientation based on the borehole data is 172 ± 9.3° (ZNO), 166 ± 10.8° (NL) and 163 ± 7.6° (JO) (Fig. 4-76), indicating that S_{Hmax} is approximately perpendicular to the arc-shaped Jura Fold-and-Thrust Belt.
- The dominant S_{Hmax} orientation is also stable in the vertical direction, i.e. orientations derived from boreholes (to a depth of 1.3 km) are in general agreement with S_{Hmax} orientations derived from earthquake focal mechanisms at much greater depths (up to 30 km; Nagra 2024o).
- In individual boreholes, the S_{Hmax} orientation is relatively stable across the Mesozoic sediments, and across the Opalinus Clay in particular. The few exceptions presenting local variations of S_{Hmax} orientations are discussed in Nagra (2024o).
- A comparison with palaeo-strain data (Madritsch & Hammer 2012) indicates broad consistency of the S_{Hmax} orientation with deformation features since Miocene times.

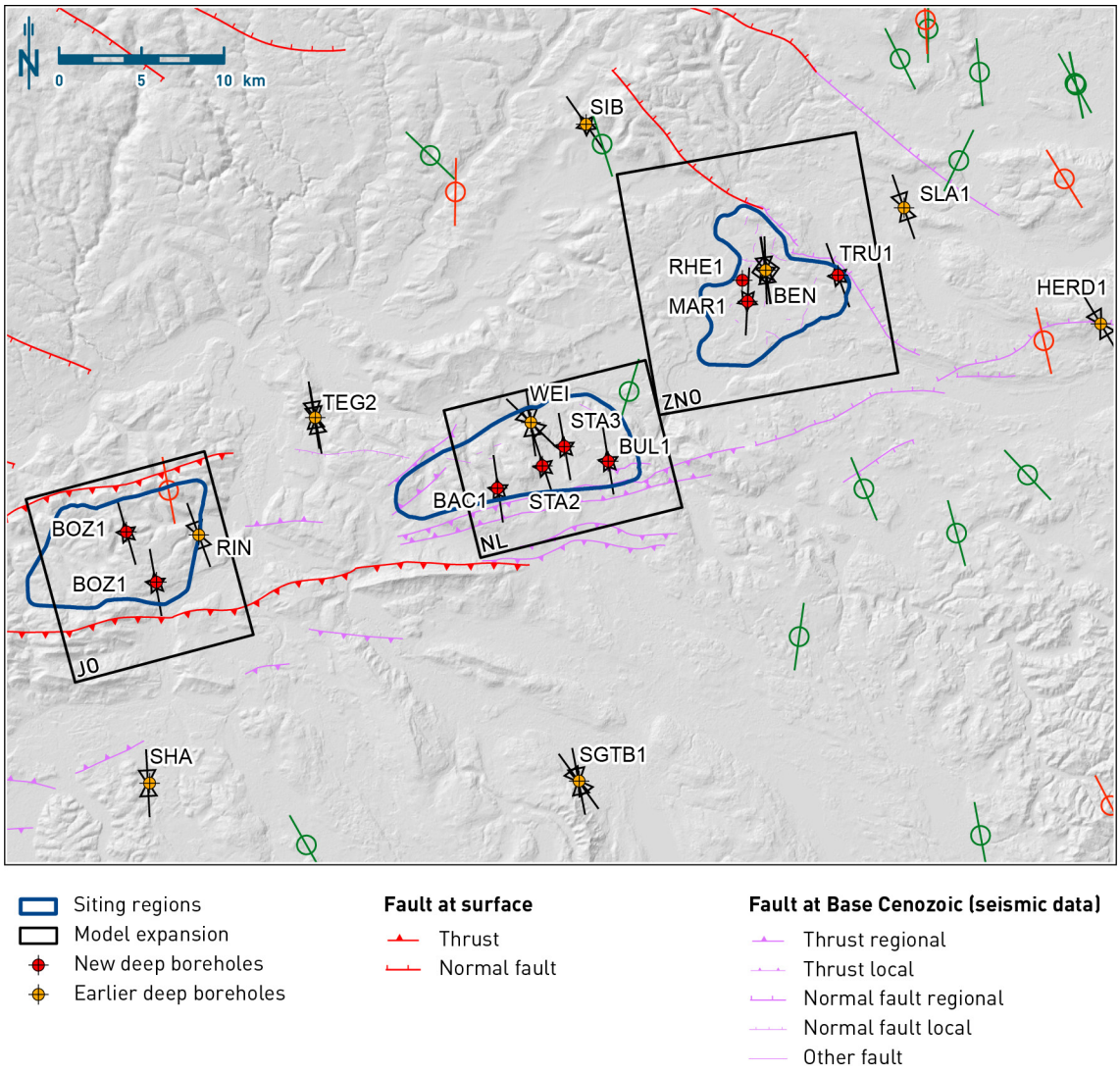


Fig. 4-76: Orientation of maximum horizontal stress S_{Hmax} in the siting regions

Black lines indicate S_{Hma} orientations derived from borehole data. Red lines (normal faulting stress regime) and green lines (strike-slip stress regime) indicate S_{Hmax} orientations derived from earthquake focal mechanisms. Black squares indicate the extent of site-specific 3D geo-mechanical-numerical models. Note that only a selection of the structures from the 3D seismic interpretation on Top Villigen Formation were projected to Base Cenozoic and are shown to highlight the structural trends of regional importance.

4.4.3 Stress magnitudes and stress regime

The vertical stress S_v is estimated by integrating the bulk density of the drilled formations. Micro-hydraulic fracturing (MHF) tests were performed in vertical boreholes to provide quantitative information on the S_{hmin} magnitude, and in a few cases also served to independently verify values of S_v from logs (Nagra 2024o). In comparison to previous stress testing campaigns (e.g. Nagra 2001), dry sleeve reopening (SR) tests on previously induced fractures were also performed to derive values of the S_{Hmax} magnitudes (Nagra 2024o for details).

From the 139 successful MHF tests in eight of the nine new boreholes and the following SR tests, 121 reliable S_{hmin} magnitudes and 65 reliable S_{Hmax} magnitudes were estimated. In addition to the new tests, two measurements from the Benken borehole were also re-analysed (Nagra 2024o). This unique dataset from the three siting regions has increased the number of stress magnitude data by an order of magnitude since 2019 (Fig. 2-3).

A representative example of the stress data obtained is shown for the STA3 borehole in Fig. 4-77. The figure shows that values of S_{hmin} are close to values for S_v in the shallow subsurface but become increasingly lower than S_v with greater depth. Similarly, S_{Hmax} values are greater than S_v closer to the surface while becoming lower than S_v as depth increases. This can be explained by topographic effects (Nagra 2024o).

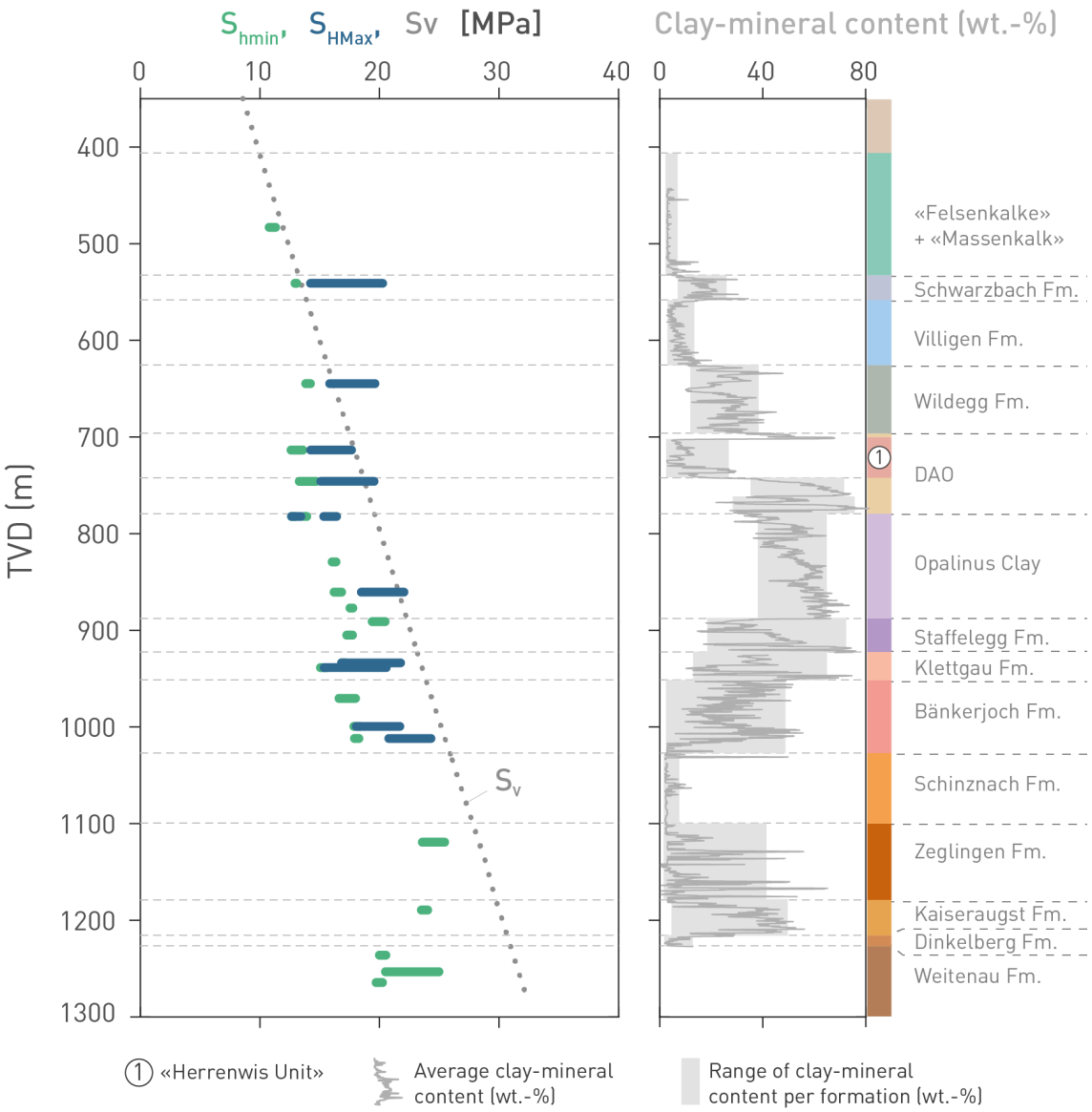


Fig. 4-77: Stress magnitudes and comparison to clay-mineral content (proxy for layer stiffness)

Shown are data for the STA3 borehole (Nagra 2024o). Continuous line of average clay-mineral content is from Becker & Marnat (2024), and ranges per formation in grey represent the P5 to P95 interval according to Nagra (2024m). Fm.: Formation, DAO: Dogger Group above Opalinus Clay.

Hence, depth exerts an important control on the absolute stress magnitudes. It is noted that the value bands for S_{Hmax} (blue bars) are always wider than those of S_{hmin}, because the method used to determine S_{Hmax} implies a range at least three times that of S_{hmin} (Nagra 2024o).

Another important control on the stress magnitudes stems from mechanical stratigraphy. This is illustrated by the clay-mineral content in Fig. 4-77 showing clear variations between formations. Formations with lower clay-mineral content, e.g. the limestones of the «Felsenkalke» and «Massenkalk» or the anhydrite-dominated Zeglingen Formation have a different gradient of S_{hmin} (closer to S_v) than the clay-mineral-rich units of the Opalinus Clay and adjacent formations.

MHF and SR tests sample stresses of the formation on a metre scale. Hence, variability of material properties within the formation and relative contrasts between formations also impact the resulting stress magnitudes. This is highlighted in Fig. 4-78, which summarises all obtained S_{hmin} values as gradients of S_{hmin}, i.e. magnitudes normalised by depth per formation and siting region. The figure indicates a relatively large variation of S_{hmin} gradients in the Klettgau, Bänkerjoch and Zeglingen Formations. This is also consistent with the larger variation in stiffness compared to other formations (Fig. 4-77). For the Bänkerjoch Formation two ranges were estimated to account for the bimodal nature of the data because of strongly contrasting bands of weak clay-rich rocks and stiffer anhydrites. The latter is also responsible for the Bänkerjoch and Zeglingen Formations standing out with some S_{hmin} gradients above typical gradients for the vertical stress (24 to 25 MPa/km), whereas the Schinznach Formation exhibits consistently very low values. In the shallower formations above the Opalinus Clay, S_{hmin} gradients tend to increase significantly, as effects of shallow burial superimpose the effects of mechanical layering, especially in the Malm limestones in the NL region, and the Hauptrogenstein and Wildegg Formation in JO.

The sketch in Fig. 4-79 highlights how absolute depth and mechanical layering can exert a fundamental control on the stress field at different stages of tectonic loading in a highly simplified, alternating limestone and claystone sequence. With only gravitational loading (uniaxial strain condition) and assuming an elastic model, the horizontal stress S_h increases by $\upsilon/(1-\upsilon)*S_v$, where υ is the Poisson's ratio (e.g. Thiercelin & Plumb 1994). Since υ is greater in the claystone than in the limestone, the gradient of S_h is smaller in the latter, leading to initially lower S_h values than for claystone at the formation boundaries (Fig. 4-79a). However, with lateral tectonic loading (e.g. Miocene times, Section 3), S_h grows proportionally to the Young's moduli in each layer, leading to much larger stress increments in the limestone than in the claystone for the same amount of lateral shortening (Fig. 4-79b). With further tectonic loading, this initially leads to a homogenisation in stress magnitudes across the different lithologies, and eventually to a reversal of the initial situation, where the S_h values in the limestone are greater than those in the claystone. Fig. 4-79c also highlights that S_h can exceed S_v in the shallow subsurface, as is observed with the high gradients in the Malm limestones in the NL siting region and in the Hauptrogenstein in the JO siting region (Fig. 4-78). The simplified model also illustrates that S_h in competent layers at greater depth remains lower than S_v, even with stronger tectonic loading, as the depth effect still dominates, i.e. the shift of S_h by tectonic loading is less than the difference from initial gradients.

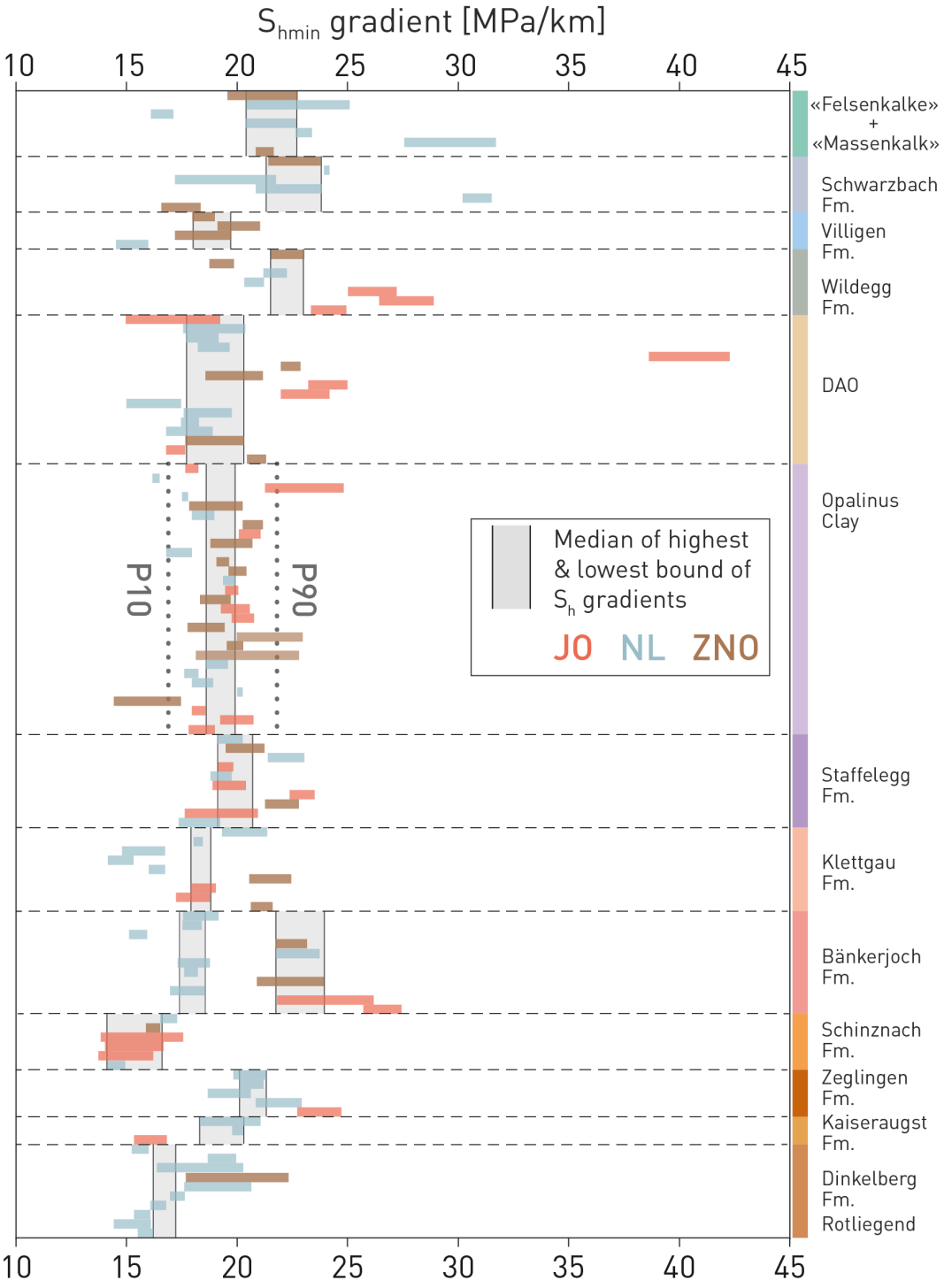


Fig. 4-78: Control of mechanical layering on stress magnitude data

This figure displays the gradients of 121 reliable measurement of S_{hmin} from MHF tests from the TBO campaign and two reanalysed MHF tests for the Opalinus Clay from the Benken borehole. Data are grouped by the three siting regions and sorted according to the distance to the top of each formation. Grey vertical bars show the range between the medians of the upper and lower bounds of the S_{hmin} gradients for each formation. For the Bänkerjoch Formation two ranges are estimated. The vertical axis does not show absolute depth, just relative depth. The very high gradient of one measurement in JO in the Upper Dogger comes from a very stiff section of the Hauptrogenstein and is not representative of the entire formation.

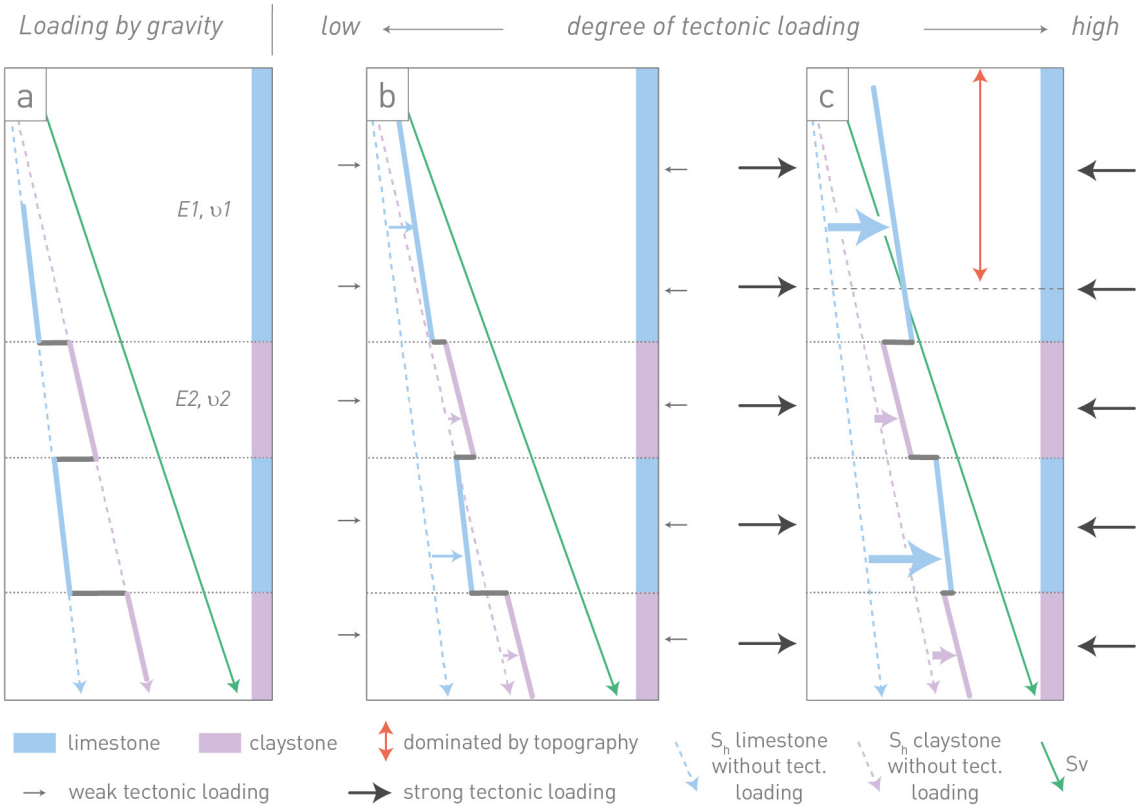


Fig. 4-79: Conceptual sketch of the evolution of the horizontal stress magnitude S_h in a mechanically layered limestone – claystone sequence

(a) Overburden stress (S_v) is translated laterally through Poisson's ratio, which is higher in claystones than in limestones ($\upsilon 2 > \upsilon 1$), leading to a steeper gradient (higher S_h values) in claystones in comparison to limestones. (b) Uniform horizontal tectonic loading leads to larger S_h increments in limestones because of larger stiffness ($E1 > E2$), and eventually to homogenisation of S_h values across the layers. (c) Further tectonic loading can lead to higher S_h values in limestones than claystones, and to $S_h > S_v$ in the shallow subsurface.

In the Opalinus Clay, the stress measurements show a consistent linear trend with increasing depth, irrespective of the siting region (Fig. 4-80). In other words, the gradient of S_{hmin} is similar for all sites. The magnitude of S_{hmin} in the Opalinus Clay is clearly lower than S_v, and the ratios of S_{hmin}/S_v range between approximately 0.6 and 0.9. Measurements close to or outside the bounds depicted in Fig. 4-80 can be explained as local outliers and are discussed in Nagra (2024o). Note that MHF and SR tests sample on a metre scale and thus S_v is generally the largest of the principal stress magnitudes in the Opalinus Clay, followed by S_{Hmax} and S_{hmin}. Given the larger bandwidth of S_{Hmax}, it cannot be ruled out that in some cases S_{Hmax} reaches a value similar to S_v or, in rare cases, even larger than S_v. Overall, this translates into a stress regime that is dominated by normal faulting to strike-slip faulting in the Opalinus Clay.

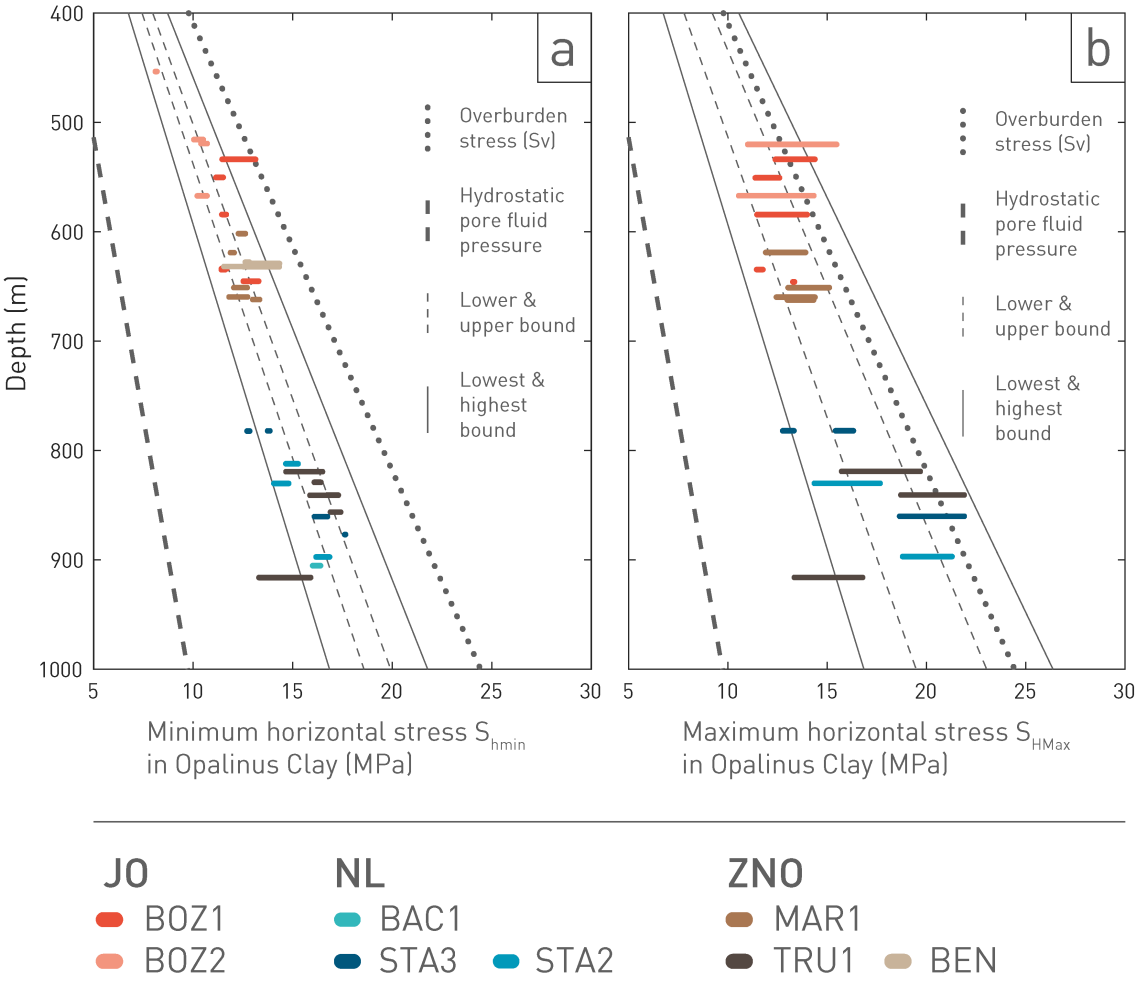


Fig. 4-80: Compilation of stress magnitude data in the Opalinus Clay across siting regions

Bars denote values of S_{hmin} (a) and S_{Hmax} (b) for the various stations including the value range from test interpretation. Lower and upper bounds refer to the median of the lower and upper values of the estimated range, and lowest and highest bounds to the P10 and P90 percentile range of all measurements. Pore fluid pressure and vertical stress S_v are approximated with constant densities (1'000 kg/m^3 and 2'450 kg/m^3, respectively).

4.4.4 3D geomechanical-numerical models of the siting regions

To provide a continuous description of the 3D stress state in the siting regions, geomechanical-numerical models are set up that use point-wise stress magnitude measurements for the model calibration. These models, hereafter "stress models", integrate all geomechanically relevant rock properties of the drilled formations and structural elements. The lateral extent of these stress models is depicted in Fig. 4-76 and further technical details can be found in Nagra (2024o).

Given that the stiffness distribution, i.e. Young's Modulus *E*, exerts a key control on the stress field, the stress models account for stiffness variability. An example of modelling input and results is shown in Fig. 4-81, with the range of stiffness values on 95% probability (i.e. stiffness value within this range) on the right. The result is a bandwidth of the horizontal stress magnitudes rather than a single line indicating the best fit to the stress magnitude data used as model calibration points. Using this stiffness variation for sensitivity analyses in stress model runs, Fig. 4-81 shows

the resulting 95% probability of stresses that should be expected. This 95% probability band should contain the stress measurements of S_{hmin} and the derived S_{Hmax} values, as they also reflect the stiffness variability within the formations. Indeed, except for a few outliers that sampled the formation outside the 95% probability range, most data points are covered by the derived stress band.

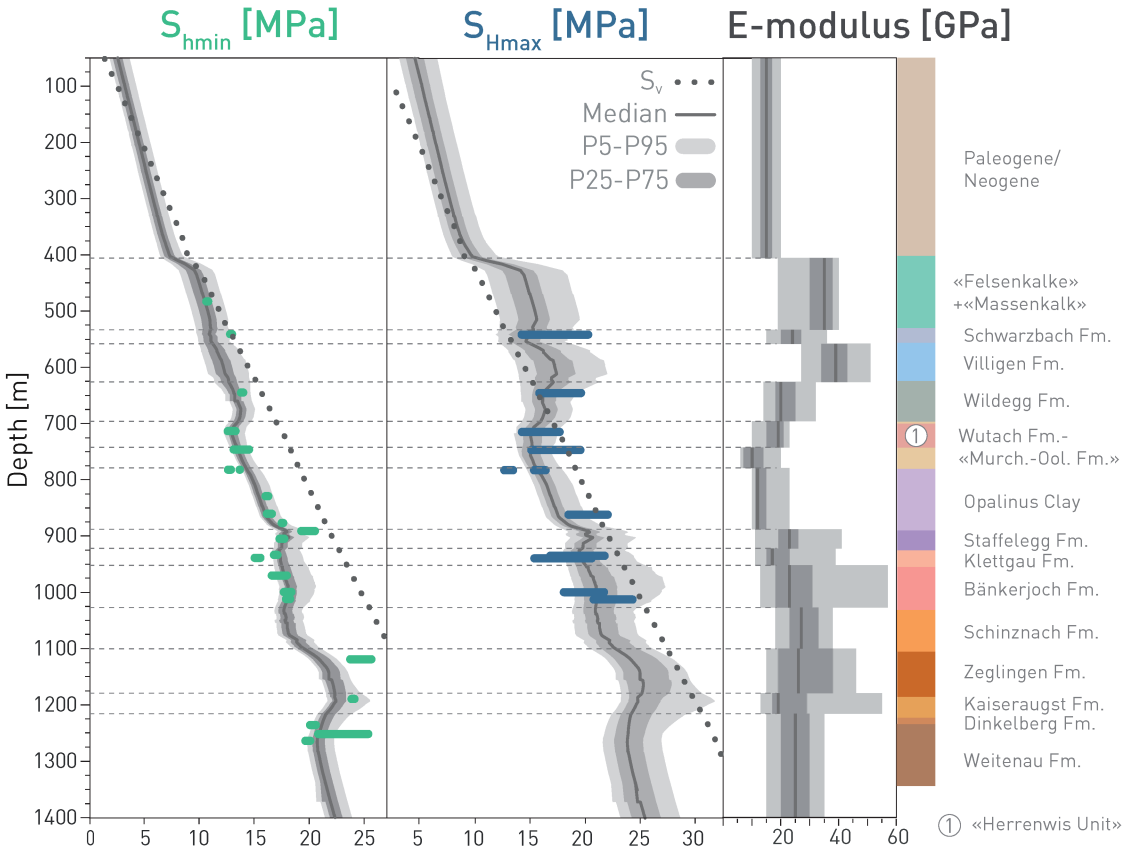


Fig. 4-81: Stress magnitude data from MHF/SR tests and modelled stress bandwidth

Green and blue bars represent bandwidths of S_{hmin} and S_{Hmax} magnitudes from MHF and SR test results from the STA3 borehole. The dotted line depicts S_v. Dark and light grey bands represent the P25 to P75 and P5 to P95 percentile, respectively, and the dark line in the centre represents the P50 value for both, Young's Modulus *E* on the right, and the track of the S_{hmin} and S_{Hmax} from the stress models.

Stress models were also used to explore the effect of faults on the stress field. It can be shown that this effect is relatively small and is not present a short distance away from the faults (Nagra 2024o, Reiter et al. 2024).

The model results also provide the bandwidth of the stress regime in all formations grouped by site as displayed in Fig. 4-82. For site comparison, stress values were extracted from the site-specific stress models along a vertical trajectory into the approximate location of the current repository project. The stress regime is expressed using the continuous regime stress ratio (RSR) value (Simpson 1997). As discussed above for the MHF field data only, the stress model runs suggest a normal faulting stress regime for the Opalinus Clay, especially for the NL siting region. For ZNO and especially JO, the dominant stress regime transitions from normal faulting to strike-

slip faulting because of the progressively shallower position of the Opalinus Clay. This trend to a higher lateral stress relative to the vertical stress is particularly manifested in the formations above the Opalinus Clay and can reach thrust faulting stress regime conditions ($S_{Hmax} > S_{hmin} > S_v$) in the Malm.

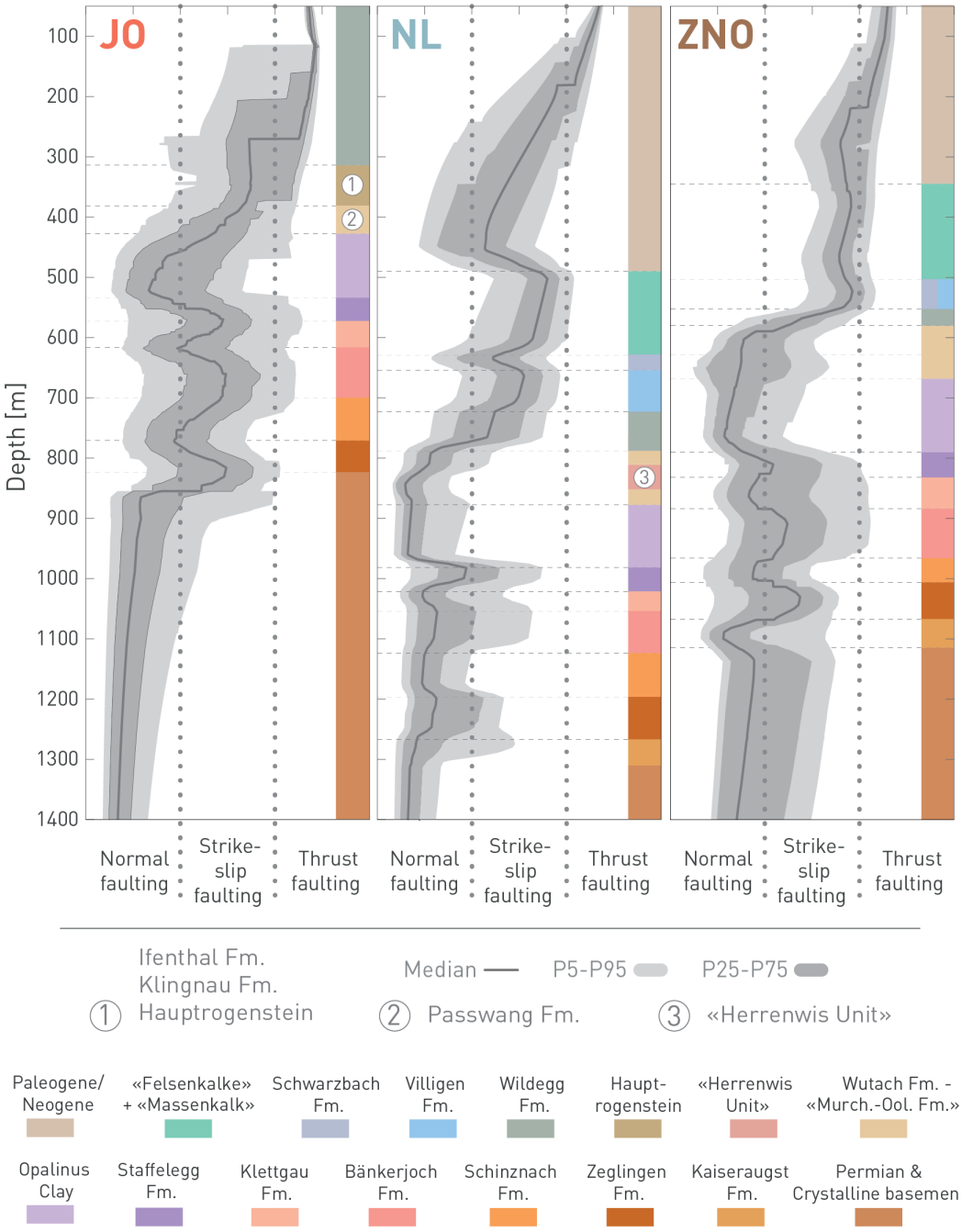


Fig. 4-82: Comparison of stress regimes within the rock formations across the different siting regions

Values are extracted from stress model runs at a vertical trajectory into the approximate location of the high-level waste section of the current repository project in each site. To assign continuous values of stress regime (x-axis) the classification according to the regime stress ratio is used (details can be found in Nagra 2024o).

4.4.5 Conclusions

- The stress field in all three siting regions is well defined. This conclusion is based not only on the high density of in-situ borehole tests (MHF, SR), but also on the consistency of observed trends and bandwidths from the stress models.
- The prevailing S_{Hmax} orientation is NNW-SSE, approximately perpendicular to the Jura Fold-and-Thrust Belt, with a small counterclockwise rotation by approximately 10° from the ZNO region to the JO region. Broad consistency of current S_{Hmax} orientation with Miocene deformation features indicates relative stability of the dominant horizontal stress orientation over the past few million years.
- Continuity of the orientation of S_{Hmax} across Mesozoic sediments (vertically and laterally) derived from boreholes is an indicator of good stress coupling. Significant discrete stress rotations are generally not observed in boreholes in the siting regions.
- The stress field is similar in all three siting regions, primarily related to depth and secondarily to mechanical layering, which is coupled to tectonic loading.
- The higher stress magnitudes from tectonic loading in more competent layers explains why the stronger formations often exhibit stronger tectonic overprint than the clay-mineral-rich layers (Section 4.3.4). This is amplified closer to the surface (especially in Malm limestones).
- The Opalinus Clay exhibits consistent gradients of stress magnitudes, irrespective of the site provenance. Given the differences in tectonic history at the three sites, this finding indicates that the stress field in the Opalinus Clay is relatively insensitive to tectonic loading.
- The level of predictability of the stress field beyond the boreholes using 3D geomechanical-numerical models is similar in all three siting regions. Furthermore, the models show that faults do not have any relevant impact on the stress field in the far-field.
- The stress regime in all three siting regions can be considered similar. It changes with depth from a thrust faulting stress regime closer to the surface, to a strike-slip and normal faulting stress regimes at greater depth. Where the Opalinus Clay is located at greater depth (in the NL siting region), a stress regime causing normal faulting is dominant, whereas it is normal to strike-slip faulting where at more shallow position (ZNO and especially in JO siting regions).

4.5 Hydrogeology and hydrogeochemistry

Key points:

- The low-permeability sequence around the Opalinus Clay is delimited at the top by the regional Malm (NL, ZNO) and Hauptrogenstein (JO) aquifers. The lower limit is formed by the complex Keuper aquifer or, where it is absent, by the regional Muschelkalk aquifer.
- The Na-Cl type Malm groundwaters in NL are remnants of seawater from the Upper Marine Molasse Group (OMM) and are characterised by particularly high residence times > 500 kyr. The quasi-stagnant conditions can be explained by slow groundwater recharge through seepage from the Molasse. In ZNO, the seawater component of the Malm groundwater is increasingly displaced by freshwater recharging further to the north.
- The limestones of the Hauptrogenstein constitute the aquifer above the host rock in JO. Because of a lithological facies transition and a thickness change the hydrogeological importance decreases from west to east.
- The local Keuper aquifer is characterised by a large variation in hydraulic conductivity that results from the lithological complexity of these sediments deposited in a mainly continental setting. While it probably represents a continuous aquifer in JO and ZNO, water flow is constricted to locally occurring fluviatile sandstone channels in NL.
- In the ZNO and NL siting regions, the Muschelkalk aquifer hosts a continuous dynamic flow system with ^{81}Kr model ages of the individual groundwater samples ranging from 23 – 115 kyr. In JO, there is a more local flow system related to the local topographic and structural situation.

4.5.1 Overview

This section addresses the characterisation of the hydrogeological system within which the repository will be constructed. The complete aquifer – aquitard system is described with a particular focus on the deep aquifers situated above and below the Opalinus Clay host rock and the surrounding confining units. These aquifers define the boundary conditions for transport in the low-permeability units between them and represent a potential connection to shallow aquifers and, ultimately, to the biosphere. A more detailed characterisation of transport phenomena and properties of the host rock and the confining units is given in Chapter 5. This section focuses on the present-day state and partly on the past evolution. Scenarios for future evolution of the aquifer – aquitard system are included in Section 6.5.

Structure of this section

- Section 4.5.2 provides an overview of the relevant elements of the hydrogeological system, namely the topography, the river network, the hydrostratigraphic units and the main tectonic features.
- The hydrostratigraphy section (Section 4.5.3) subdivides the sedimentary succession by hydrogeological criteria and presents the transport properties.
- The analysis of the flow systems in the aquifers is presented in Section 4.5.4. The steady-state hydrodynamic model allows the consistency of the hydrogeological datasets to be checked, identification of recharge and discharge zones, and calculation of water fluxes and hydraulic gradients.
- The hydrogeochemistry section (Section 4.5.5) provides information on the dynamics of the flow systems in the aquifers, notably on residence times. The chemical composition of the groundwater contains information on the units that the water has been in contact with and, therefore, may evidence interaction with other aquifers along faults (*cross-formation flow*). In addition, deep groundwater geochemistry provides the boundary conditions for the interpretation of natural tracer profiles in porewater (Section 4.7) and is used to check consistency with the flow fields computed with the hydrodynamic model.

4.5.2 Regional hydrogeological situation

The relevant elements of the hydrogeological system comprise the topography, the river network, the sedimentary succession and the properties of each unit within it and the tectonic situation including the fault systems (Fig. 4-83).

The regional aquifers of interest comprise the Malm aquifer, Hauptrogenstein aquifer (JO and the area to the west) and Muschelkalk aquifer and are described further in the hydrostratigraphy section below (Fig. 4-84, Section 4.5.3). Potential recharge areas of the aquifers of interest are located in the hilly area to the north of the NL and ZNO siting regions (Fig. 4-83), notably the large zones of Malm Group outcrop in Canton Schaffhausen and the Wutach Valley area for the Muschelkalk aquifer. For the JO region, the aquifers of interest outcrop along the Internal Jura (Folded Jura) in the south and in the External and Tabular Jura in the north. Additional outcrops of the regional aquifers occur in the Alps and may contribute to the recharge of the southern Molasse Basin (Nagra 2024n).

The potential discharge areas are located where the river valleys cut into the mostly SSE-dipping aquifer units. Regional scale discharge areas are located along the Rhine River and in the lowermost Aare Valley. Additional potential discharge areas exist in smaller valleys. The river valleys are typically filled with highly permeable unconsolidated sediments which host important groundwater resources used for water supply. These aquifers are often characterised by intensive interaction with the rivers.

The Jurassic rocks are covered by increasingly thick Molasse units towards the south-east because of the general dip of the strata. In the southern part of the basin, the Malm aquifer is covered by a several kilometre thickness of Molasse (Fig. 3-2).

Regional fault systems delimit the geological siting regions, affect the outcrop situation and the continuity of units of interest. The Jura Main Thrust is an important example (Fig. 3-3, Fig. 4-54 and Fig. 4-83). Discharge areas are located where it is cut by the valleys of Limmat, Reuss and Aare. At these locations, the spas of Baden and Bad Schinznach use thermal water ascending in the Muschelkalk aquifer from deep parts of the (southern) Molasse Basin.

The lithological diversity of the sedimentary succession results in important variations in the hydraulic conductivities in the vertical direction. That is, there are different aquifer levels separated by aquitards. The importance of regional fault zones and potential cross-formation flow is evaluated with the hydrodynamic model (Nagra 2024n) and discussed based on hydrogeochemical arguments (Section 4.5.5).

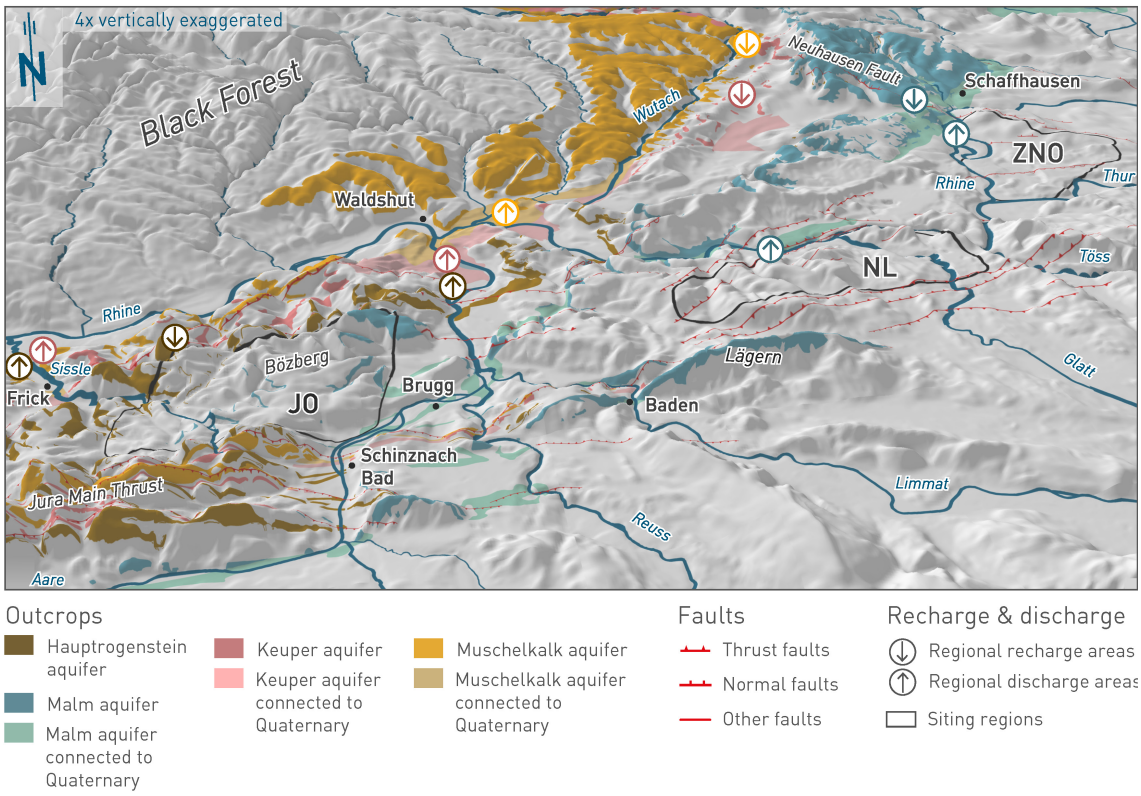


Fig. 4-83: Aquifer outcrops, river network, regional fault zones and potential recharge and discharge areas relevant for the siting regions

The digital elevation model is vertical exaggerated by a factor 4. Regional recharge areas: Malm aquifer: Südranden and Randen areas; Hauptrogenstein aquifer: Frickberg and adjacent outcrops; Keuper aquifer: Hallauerberg and adjacent areas; Muschelkalk aquifer: Upper Wutach Valley. Regional discharge areas: Malm aquifer: Rheinfall area, Rhine Valley near Kaiserstuhl; Hauptrogenstein aquifer: Lower Aare Valley, Sissle Valley; Keuper aquifer: Lower Aare Valley, Sissle Valley; Muschelkalk aquifer: Confluence of Aare and Rhine River area, Sissle Valley.

4.5.3 Hydrostratigraphy

4.5.3.1 Introduction

This section subdivides and describes the sedimentary stack based mainly on hydrogeological criteria. Primarily, it differentiates between aquifers, where hydraulic conductivity is typically sufficiently large to allow for groundwater sampling, and aquitards. In addition to the hydraulic properties, this section gives indications on the nature of water flow.

As a result of the earlier investigation programmes by Nagra in Northern Switzerland, the regional hydrostratigraphy was already well established and has now been updated with the new data (Fig. 4-84). The units are divided into regional and local aquifers separated by aquitards.

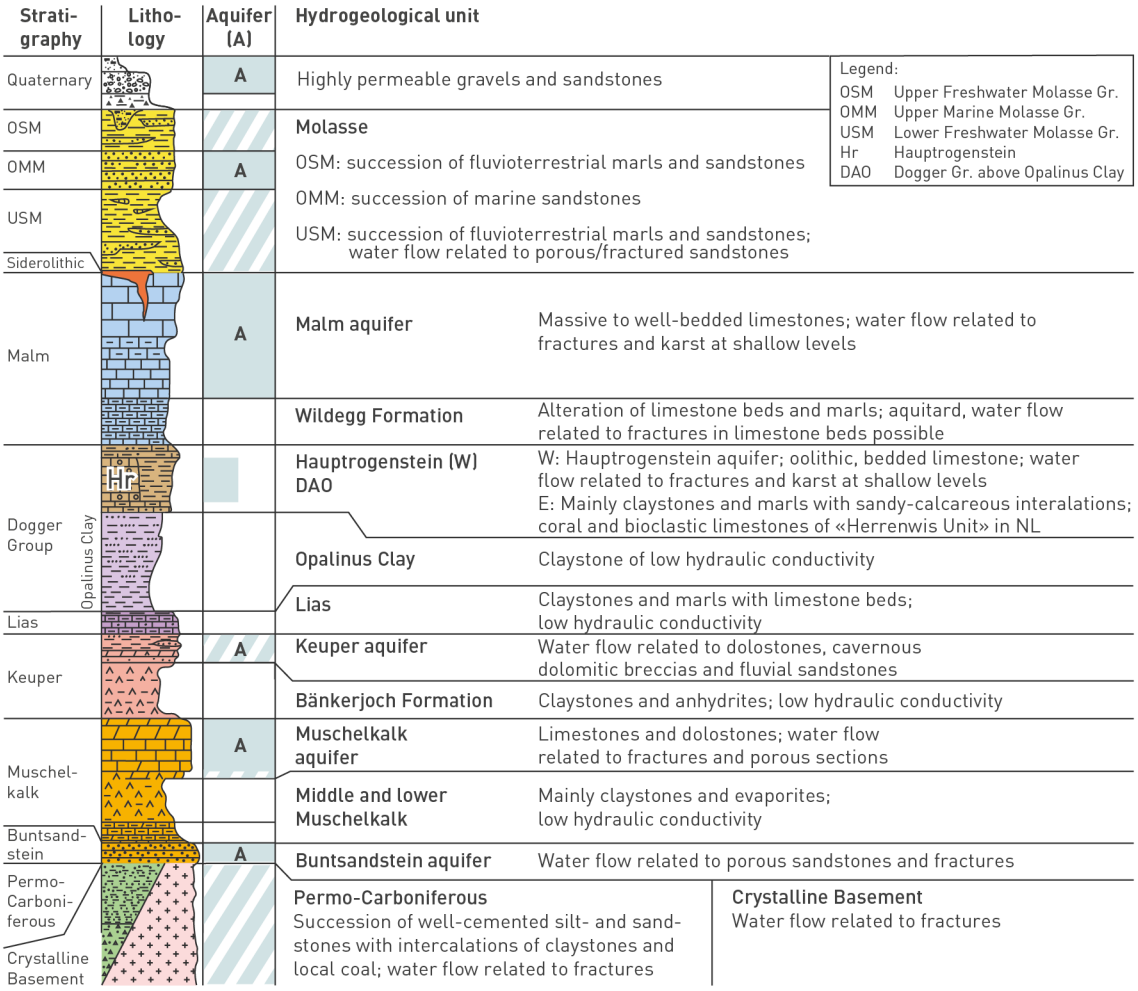


Fig. 4-84: Hydrostratigraphic units of Northern Switzerland

The figure focuses on the situation relevant in siting regions. For the Dogger Group, it illustrates the facies change from the carbonate-rich Hauptrogenstein in the west to more clay-mineral-rich units further eastwards (Section 4.2.7). Hatched areas indicate local aquifers or units in which the water flow is linked to a specific lithology (e.g. sandstones in the USM). Gr.: Group.

Groundwater flow occurs either in the porous matrix or along discontinuities such as fractures or karst features. The links to lithofacies (Section 4.2) and to the structural overprint (Section 4.3) are important in understanding fluid flow. The clay-mineral content is used as a proxy for the mechanical competence and thus deformation behaviour of the rock (i.e. the more clay minerals the less prone to brittle deformation; see also Sections 4.9, 5.5 and 5.6).

The regional aquifers refer to the thick and brittle carbonate rocks, namely the Malm aquifer, Hauptrogenstein aquifer (JO and the area to the west) and Muschelkalk aquifer. These aquifers are termed regional because of their comparably uniform lithology in Northern Switzerland. The units between these regional aquifers are mostly aquitards rich in clay minerals (Fig. 4-84), except for the local Keuper aquifer and the «Herrenwis Unit» which are discussed later in more detail.

Specifically, the following characterisation focuses on the section between the Opalinus Clay and the regional aquifers above and below. These aquifers, together with the occurrence of the local Keuper aquifer, define the maximum thickness of the low-permeability units and provide the hydrogeochemical and hydraulic boundary conditions to the aquitards in between.

Additional aquifers occur in shallower units (e.g. Upper Marine Molasse Group (OMM), sandstone channels in the Lower Freshwater Molasse Group (USM)) and in deeper units (e.g. Buntsandstein Group, crystalline basement; Fig. 4-84). These were detailed in many earlier reports and publications (e.g. Thury et al. 1994, Klemenz et al. 2000, Küpfer 2005, Gander 2004, Plum et al. 2008, Waber & Traber 2022).

4.5.3.2 Overview

The new TBO boreholes allowed the hydrogeological understanding of the siting regions and of the regional flow systems to be complemented and refined (Fig. 4-85). Elevated hydraulic conductivities were observed as expected in the regional Malm and Muschelkalk aquifers, which in most cases allowed for groundwater sampling. The Hauptrogenstein aquifer is only observed in Jura Ost and is affected by a facies transition (details in Section 4.2.7). Transmissive lithofacies of the local Keuper aquifer were tested in several boreholes and groundwater sampling was partly feasible. The existence of the Keuper aquifer is evident in many natural tracer profiles (Section 4.6).

The transmissivities observed in the different aquifers reflect their lithological variation, structural overprint and indicate their hydrogeological importance (Fig. 4-86). The transmissivities observed in the Muschelkalk aquifer are comparably uniform in the siting regions and about one order of magnitude higher than in the Malm aquifer. Groundwater residence times also reflect this (Section 4.5.5). In contrast, the observed transmissivities in the Keuper aquifer scatter over eight orders of magnitude.

Between these aquifers, the mostly clay-mineral rich rocks are characterised by low hydraulic conductivities. The units directly above and below the Opalinus Clay include so-called "hard beds" which were controversially discussed in earlier project phases (e.g. Nagra 2014f; see also Section 4.2.7). Intensive testing of the TBO boreholes provides no evidence that these "hard beds" allow for larger-scale groundwater flow.

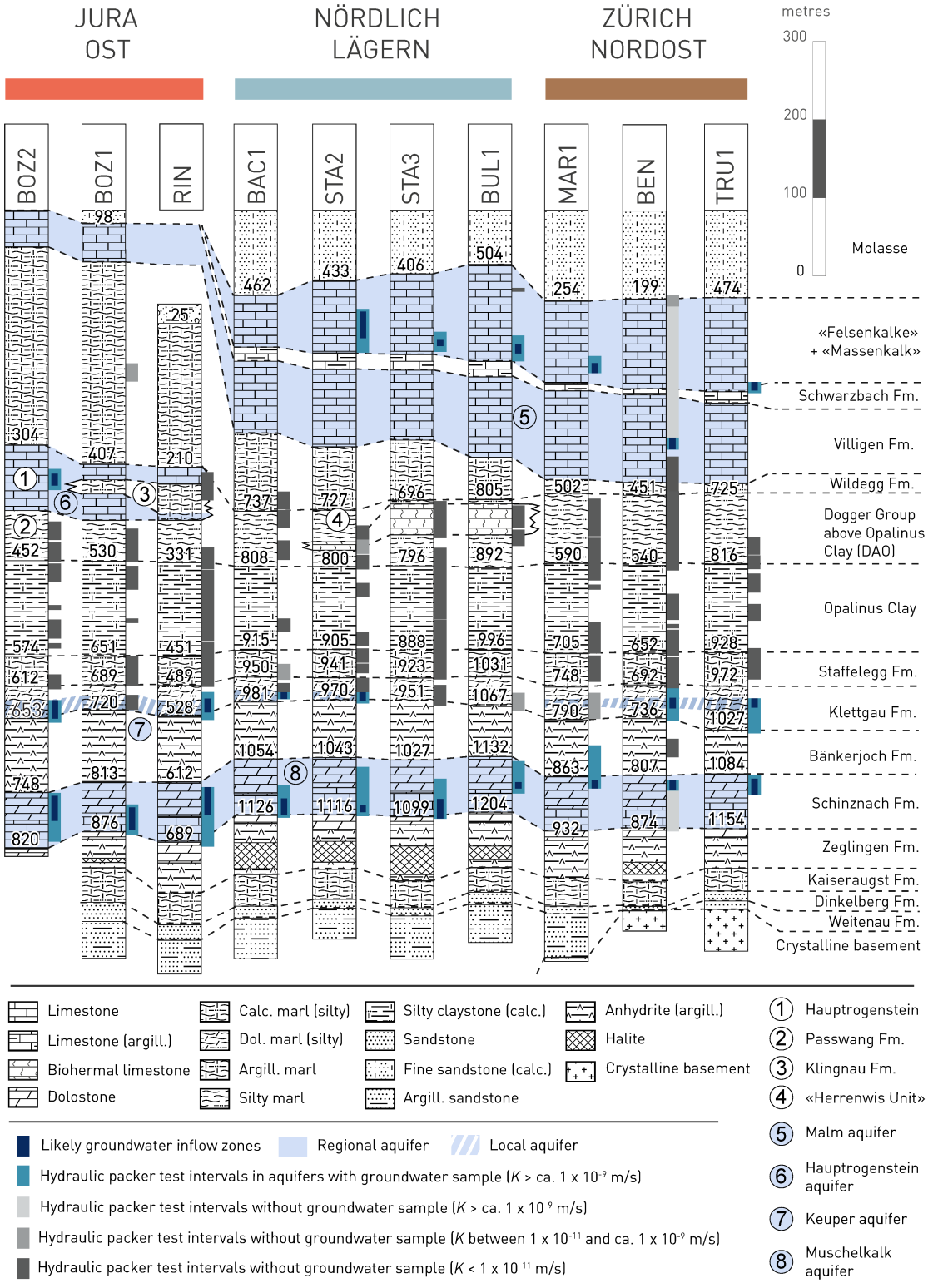


Fig. 4-85: Hydrogeological correlation of key boreholes with summarised results of hydraulic packer tests and location of regional and local deep aquifers

Correlation of the Keuper aquifer in JO and ZNO additionally takes profiles of natural tracers into account (see Section 4.5.3.10 for details). The likely groundwater inflow zones within the test intervals were identified based on e.g. drilling fluid losses, observations on drill cores and image logs or – where available – on fluid logging.

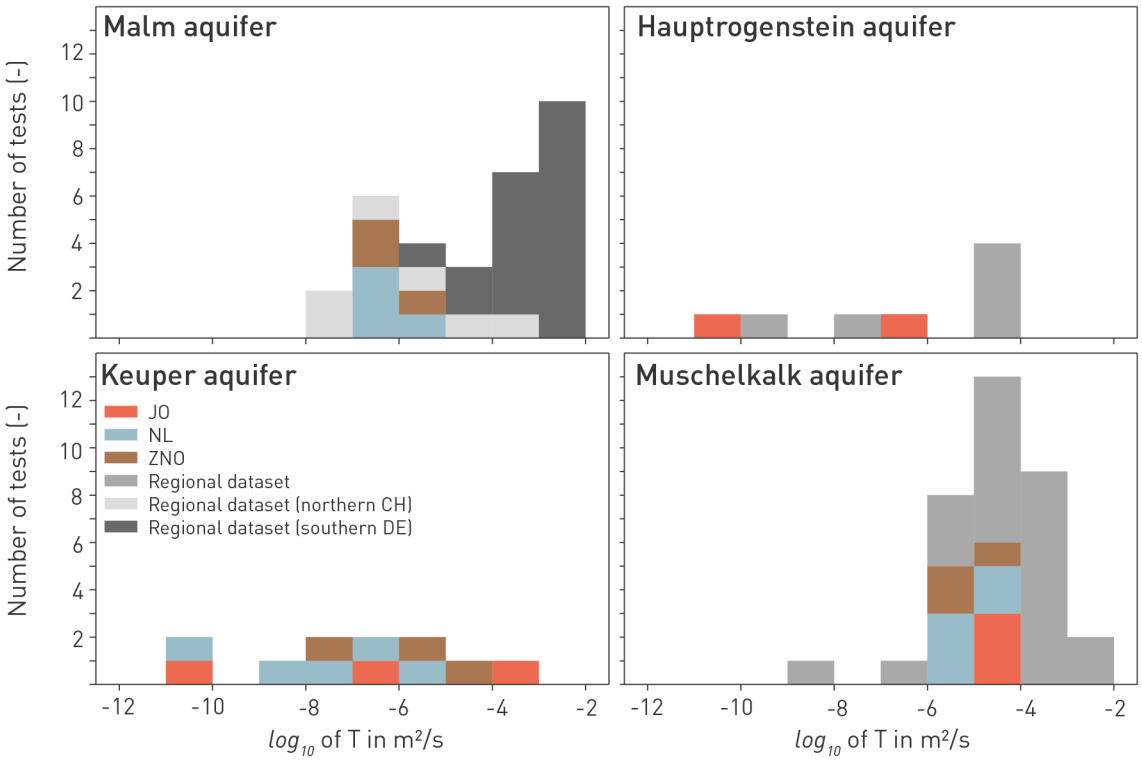


Fig. 4-86: Histogram of the transmissivities measured in the aquifers

The displayed dataset of the regional aquifers includes results of hydraulic tests carried out inside and outside the siting regions. The latter is referred to as the regional dataset. For the Keuper aquifer, test data from the siting regions are shown. The highest transmissivity is shown for boreholes where more than one test per hydrogeological unit was performed (e.g. to estimate properties of different members of the Klettgau Formation). Note the large variability of the transmissivities for the local Keuper aquifer, particularly compared to the regional Muschelkalk aquifer.

4.5.3.3 Malm aquifer

The Malm aquifer relates to the thick limestone units above the Wildegg Formation, that is the «Felsenkalke» and «Massenkalk» and the Villigen Formation. The latter formations are separated by the marly Schwarzbach Formation (Fig. 4-85, see also Section 4.2.9). The upper limit of this hydrogeological unit is defined by the Eocene Siderolithic Group and the Lower Freshwater Molasse Group (USM).

The hydrogeological definition of the vertical extent of the Malm aquifer unit comes mainly from outcrop observations in the Internal Jura, in Canton Schaffhausen and in the Swabian Alb area of Southern Germany. Here, the aquifer can have a high hydraulic conductivity and a large vertical extent because of the structural overprint and karstification. The extent of karstification depends on many aspects and is known to decrease with depth and with overburden of Molasse (e.g. Plum et al. 2008).

The situation below the thick Molasse cover, notably in the siting regions ZNO and NL, is different. Here, the units were affected by karstification during the Eocene (Chapter 3). Such palaeokarst features are typically filled with clay-mineral-rich sediments and can be observed several decametres into the limestones. This palaeokarst seems hydraulically not relevant today

(e.g. BUL1 borehole hydrotest, Fig. 4-87) but a locally incomplete filling of the palaeokarst by siderolithic clay cannot be excluded. The thick cover of Molasse units currently prevents further karstification. In this zone, water flow is essentially restricted to fractures.



Fig. 4-87: Drill core pictures from the hydraulic test interval in the «Felsenkalke» and «Massenkalk» of the BUL1 borehole

Hydraulic test BUL1-1-MAL1 (537.2 – 545.0 m) yields low T of 1×10^{-11} m^2/s ($K = 2 \times 10^{-12}$ m/s). Test interval includes limestone with silty-clay-filled palaeokarst voids with a tectonic overprint (see also Nagra (ed.) 2021a, Dossier V).

Tectonic overprint and recent karstification close to the surface are probably the dominant features affecting the regional distribution of hydraulic conductivity (Fig. 4-88). In addition, the Malm aquifer is partly composed of sponge algae reefs in which cavernous dedolomite is encountered (e.g. Plum et al. 2008, Stober et al. 2013). On the regional level, the differing relevance of these features results in a scatter of around six orders of magnitude in the hydraulic properties (Fig. 4-86, Fig. 4-88).

In the siting regions in Northern Switzerland, these rocks consist in many cases of almost pure calcite. The dolomite/ankerite component is typically below a few wt.-% and is more commonly detected in the Villigen Formation. Pyrite contents are low, with a trend to somewhat higher values in the marly sections (rarely exceeding 1 wt.-%).

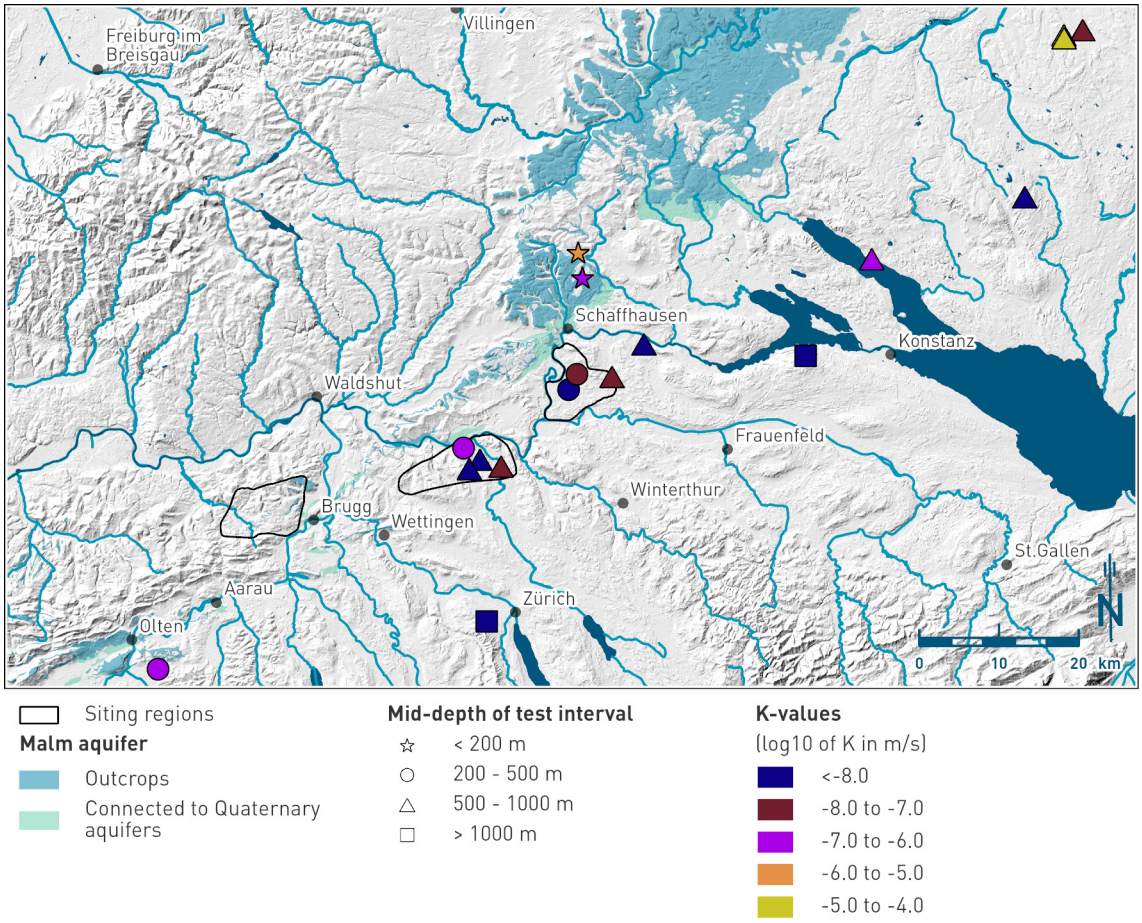


Fig. 4-88: Hydraulic conductivities from in-situ hydraulic tests in the Malm aquifer in Northern Switzerland and Southern Germany

The length of the test intervals varies between < 10 and > 100 m. The displayed dataset includes results of hydraulic tests performed in closed intervals as well as in open boreholes.

In the majority of the TBO boreholes in NL and in ZNO, fluid logging was carried out over the major parts of the Malm aquifer. These allow the transmissive sections to be localised and quantified as well as a comparison with the structural inventory from the drill cores and from the image logs. The investigations show highly localised groundwater flow related to fractures. The results of the fluid logging also served to position the packers for the hydraulic tests (that included the aim of sampling groundwater). The majority of the most transmissive sections were identified in the «Felsenkalke» and «Massenkalk», that is above the marly Schwarzbach Formation (Fig. 4-85). This suggests that the water flow may be related to solution-enhanced fracture networks that developed above the Schwarzbach Formation, most likely at the time of palaeokarst formation. However, the hydraulic packer tests in the NL and ZNO siting regions indicate, compared to the regional dataset and to the Muschelkalk aquifer (Section 4.5.3.12), relatively low hydraulic conductivities with typical values around 10^{-8} m/s. This is consistent with the much

higher residence times of the Malm groundwaters in comparison to the Muschelkalk groundwater (Section 4.5.5). In contrast to the fractured zones, the matrix is characterised by low porosity (Fig. 5-10) and low hydraulic conductivity.

The Malm aquifer exists in part of the JO siting region at shallow level. It is not discussed in this report because the focus in JO is on the Hauptrogenstein aquifer which is closer to the host rock.

4.5.3.4 Wildegg Formation

The Wildegg Formation is subdivided into the Birmenstorf Member and the much thicker Effingen Member (Section 4.2.8). The latter is considered an aquitard of regional extent with strongly decreasing thickness from the west (more than 200 m in JO) to the east (below 10 m in ZNO) (Fig. 4-85). It was studied in detail during SGT Stage 2 as a potential host rock for low- and intermediate-level waste disposal in the former Jura-Südfuss siting region (Nagra 2014f, Dossier VI). To the east of the occurrence of the Hauptrogenstein aquifer, in the NL and ZNO siting regions, it is part of the upper confining units of the Opalinus Clay.

The Effingen Member consists of sandy calcareous marls and argillaceous limestone interbeds. The regional packer test dataset of SGT Stage 2 shows hydraulic conductivities < 10^{-11} m/s at an overburden thickness larger than ca. 300 m (Nagra 2014f, Dossier VI). At shallower depths, higher hydraulic conductivities are measured and indicated by water inflows into tunnels or by groundwater samples. In SGT Stage 2, notably the thicker limestone beds were assessed critically regarding the potentially increased permeability related to tectonic overprint (lack of self-sealing properties).

In SGT Stage 3, the hydrogeological database for the Effingen Member was complemented in view of its contribution as a confining unit by packer tests (Fig. 4-85), fluid logging partly covering this unit and by the profiles of natural tracers (Section 4.6). The investigations confirmed the generally low hydraulic conductivities, e.g. expressed by the absence of relevant excursions in the profiles of the natural tracers. A transmissive zone was detected related to the tectonic overprint of the most prominent limestone bed (Gerstenhübel Bed; Section 4.2.8) at around 310 m depth in BOZ1; the transmissivity of 3×10^{-8} m^2/s is well within the values expected in SGT Stage 2. Note that the thickness of this limestone bed strongly decreases towards the east (BOZ1 ~ 37 m, BAC1 ~ 6 m).

The Birmenstorf Member is a thin carbonate-rich horizon located at the base of the Wildegg Formation. In Northern Switzerland, its thickness decreases from west to the east (e.g. OFT ca. 15 m, BOZ2 ca. 4 m, BAC1 0.7 m, TRU1 ca. 2.6 m) and the lithofacies changes. In the NL and ZNO siting regions it occurs at depths greater than 500 m and is dominated by marly lithologies. In this area, there is no indication of water flow in this unit, and it is part of the natural barrier. In contrast, it occurs in the Aarau – Solothurn area as a much thicker limestone (with sponges or sponge bioherms). In the Internal Jura, the Birmenstorf Member is an aquifer at shallow depth (e.g. Herold 1997) and in boreholes in the Aarau and Gösgen area groundwater could be sampled up to ca. 340 m depth.

4.5.3.5 Clay-mineral-rich aquitard units above the Opalinus Clay (Dogger Group)

The Dogger Group above the Opalinus Clay is characterised by contrasting lithologies (Section 4.2.7). There is an important vertical variation along individual boreholes and there are also lateral facies changes between the different boreholes. In this section, the mostly clay-mineral-rich units of the Dogger Group above the Opalinus Clay are discussed. The Hauptrogenstein aquifer and the «Herrenwis Unit» are presented in separate sections.

For the NL and ZNO siting regions, this unit refers to the clay-mineral-rich «Brauner Dogger» studied in detail during SGT Stage 2 (Nagra 2014f). With the new TBO boreholes, the hydrogeological dataset was substantially complemented, notably by hydraulic packer testing (see also Section 5.6) and by investigations of natural tracers in the porewater (Section 4.6). The hydraulic conductivities from the boreholes within the siting regions are very low ($< 10^{-11}$ m/s; Fig. 4-85)[11] and the profiles of the natural tracers in the porewater show no anomalies. That is, these units are part of the zone with diffusion-controlled transport and thus additionally contribute to the geological barrier. This is particularly robust in the eastern part of the NL siting region where the section below the «Herrenwis Unit» is characterised by high clay-mineral contents ensuring substantial self-sealing behaviour (Fig. 4-33). In ZNO, the clay-mineral contents in the section above the Opalinus Clay are significantly lower but, at the resolution of the geophysical logs (ca. 0.4 m), are in a range where some self-sealing limits the transmissivities of fractures (Sections 5.2.3 and 5.6.3.2). Here, the Wedelsandstein Formation is characterised by a layered sequence of clay-mineral-rich sediments and thin so-called "hard beds" consisting of silty to sandy limestones (Section 4.2.7). The hydraulic significance of the latter was controversially discussed in SGT Stage 2 (Nagra 2014f) and was of particular interest in the TBO investigations. The new investigations do not provide evidence for hydraulically active fracture networks or a permeable matrix. The low hydraulic conductivities indicated from the in-situ tests and from matrix tests (Section 5.6) can be explained by cementation of these "hard beds" giving rise to particularly low porosity (example shown in Fig. 4-89). Above the Wedelsandstein Formation in ZNO, the clay-mineral-rich section (Fig. 4-85) comprising the «Parkinsoni-Württembergica-Schichten» and the Variansmergel Formation constitutes a caprock of significant thickness (Section 4.2.7).

[11] In the BAC1 borehole the section directly above the Opalinus Clay was affected by a drilling-induced fracture. In the SLA1 borehole east of ZNO, a test indicated 1×10^{-9} m/s. The cause for this increased K value is unclear.

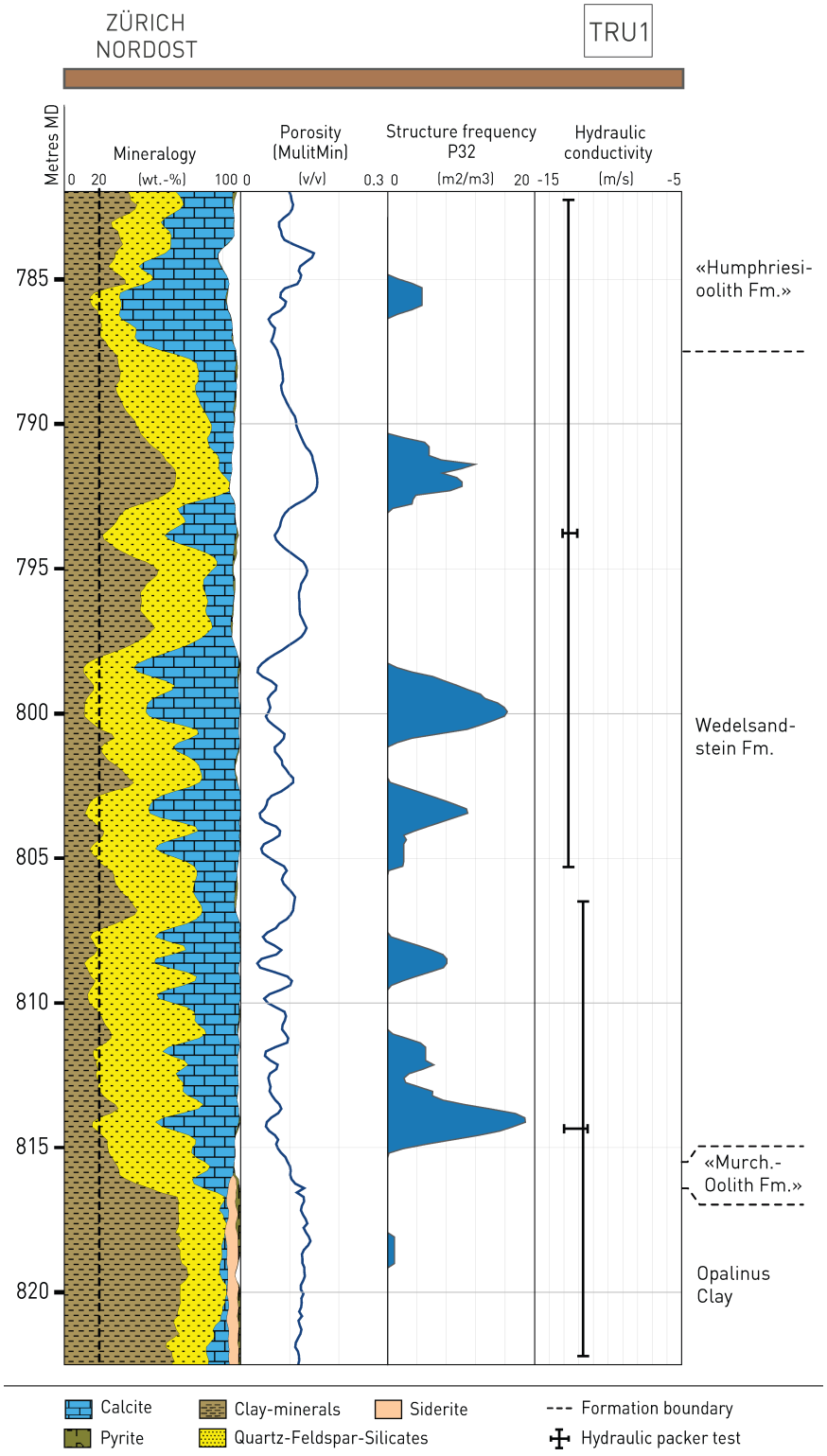


Fig. 4-89: Profile of the Wedelsandstein Formation in the TRU1 borehole: mineralogical composition, porosity, structural inventory and hydraulic conductivity

The black dashed line (20 wt.-% clay content) is used to highlight the clay-poor intervals. Sections poor in clay minerals ("hard beds") are characterised by low porosity. The hydraulic conductivities are very low despite the partly low clay-mineral contents and the increased structure frequency.

In JO, the Passwang Formation is located between the Opalinus Clay host rock and the Hauptrogenstein aquifer. It has some similarities to the Wedelsandstein Formation in ZNO in terms of a succession of clay-mineral-rich sediments with interlayered "hard beds" (Section 4.2.7). The low hydraulic conductivities (Fig. 4-85) and the absence of significant excursions in the profiles of the natural tracers (Section 4.6) confirm the aquitard character and that this unit is part of the low-permeability geological barrier. As in the case of the Wedelsandstein Formation in ZNO, the lower clay-mineral contents compared to the equivalent unit in NL below the «Herrenwis Unit» indicate a lower self-sealing potential.

4.5.3.6 Hauptrogenstein aquifer

The biodetritic and oolitic limestones of the Hauptrogenstein constitute a fractured and partly karstic aquifer in the Jura Mountains (Jäckli & Kempf 1972). The facies transition towards the clay-mineral-rich Klingnau Formation in the east occurs within the JO siting region (Section 4.2.6), i.e. the Hauptrogenstein is a relevant aquifer only in JO.

A comparatively small dataset is available on the hydrogeological properties (Fig. 4-86). The highest transmissivities in the range of 10^{-5} m^2/s relate to test depths < 270 m. In the BOZ2 borehole, fluid losses occurred related to a fracture at around 350 m depth (Nagra (ed.) 2022b). The transmissivity of 4×10^{-7} m^2/s allowed groundwater to be sampled (Section 4.5.5.3). This transmissive zone is also nicely expressed in the profiles of the natural tracers in porewater (Section 4.6). In the BOZ1 borehole, only a minor inflow zone was detected by fluid logging (2×10^{-9} m^2/s) which is without expression in the tracer profiles. In the easternmost Riniken (RIN) borehole, the Hauptrogenstein is characterised by a low hydraulic conductivity and a reduced thickness (Fig. 4-85).

Overall, the hydraulic properties mirror the facies change from west to east. The eastern limit of the Hauptrogenstein aquifer is only vaguely defined.

4.5.3.7 «Herrenwis Unit»

The «Herrenwis Unit» occurs only in the eastern part of NL, as a ca. 40 m thick isolated carbonate platform that is embedded into clay-mineral-richer units above and below and also laterally (Section 4.2.7, Fig. 4-41). This unit is characterised by a substantial variability along the boreholes and also within an individual core section (Fig. 4-36). At the CT-scan scale, carbonate and clay-mineral-rich zones can be identified and isolated macroporosity can be shown (Fig. 4-90). These observations and the complex internal architecture of this unit show that a substantial variability of matrix permeability must be expected.

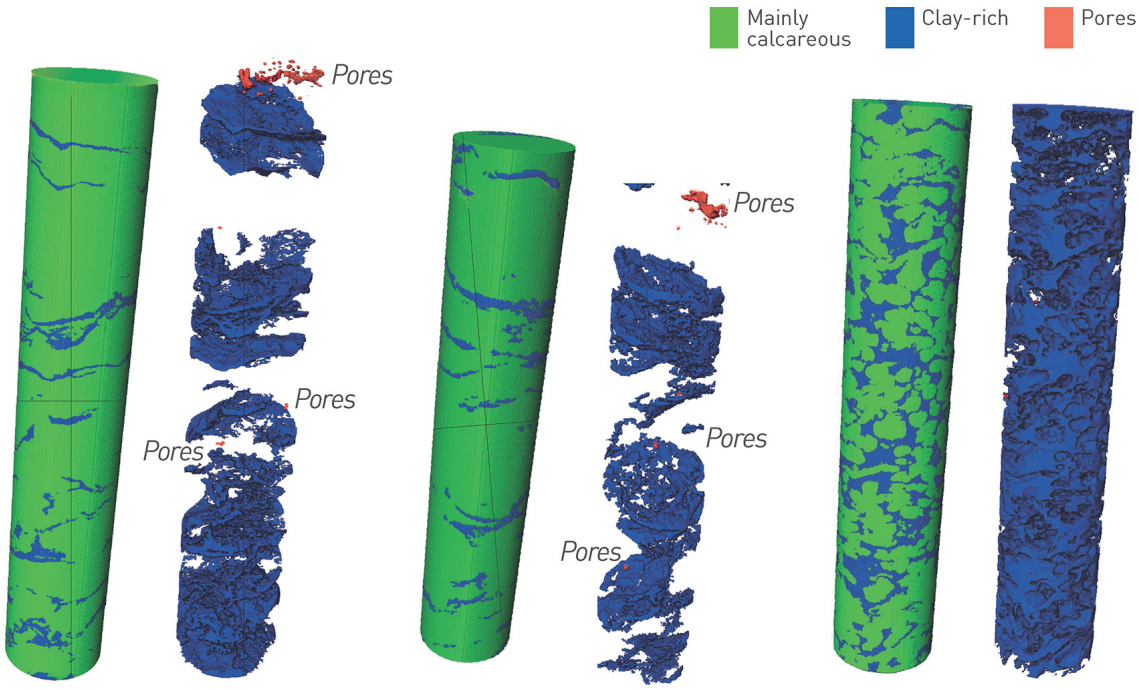


Fig. 4-90: «Herrenwis Unit» of the BUL1 borehole: CT-scan-based visualisation of mainly calcareous and clay-mineral-rich zones and macropores

Drill core diameter is 95 mm. Displayed are core samples BUL1-1 816.60 GM, BUL1-1 818.55 GM and BUL1-1 842.10 GM (number denotes the depth of the top of the core section).

The hydraulic conductivities from the in-situ testing in the BUL1 and STA3 boreholes are very low (< 10^{-11} m/s;Fig. 4-92). This probably relates to the burial history (mechanical and chemical compaction) and the absence of relevant dolomitisation or of dissolution-enhanced hydraulic conductivity. A higher conductivity was observed related to a sub-vertical joint (Fig. 4-92) in the basinal part (periplatform wedge, Section 4.2.7) drilled by the STA2 borehole (3×10^{-10} m/s). Hydraulic heads lower than the potential discharge area (Fig. 4-91) are a strong argument in support of the hydraulically isolated nature of the «Herrenwis Unit» (for a detailed discussion see Section 5.6.5). The profiles of the natural tracers in porewater, in particular Cl and Br, are affected by increased scatter in this heterogeneous low-porosity unit. The profiles of the stable isotopes, the Br/Cl ratio and ^{4}He that are considered most robust in this unit do not show significant excursions (Section 4.6).

To conclude: The «Herrenwis Unit» is an isolated carbonate platform embedded in clay-rich rocks. There are no indications of an active aquifer, e.g. it has no direct recharge or discharge areas. Hydraulic conductivities are low for the tested lithofacies but may be debatable given the heterogeneity of this unit. However, the hydraulic properties of the unit may locally be influenced by tectonic overprint as indicated by the test in the STA2 borehole.

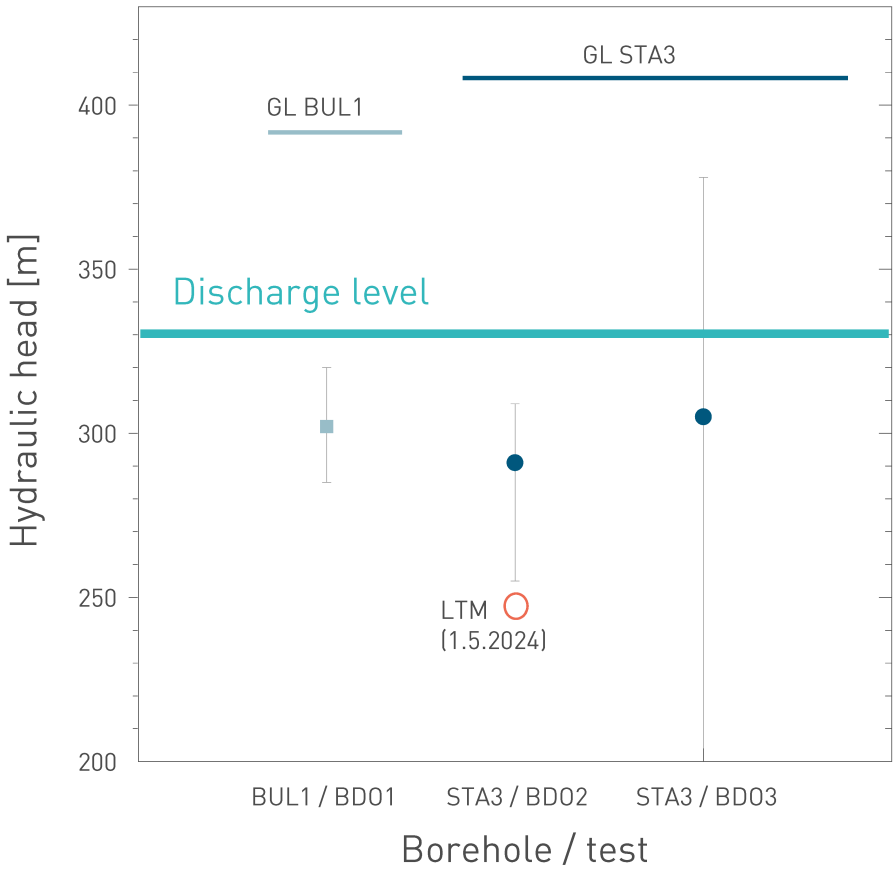


Fig. 4-91: Hydraulic heads in the «Herrenwis Unit» observed by packer testing and comparison with data from the long-term monitoring system (LTM) in STA3

The data are compared to the ground level (GL) of the drillsites and to the altitude of the potential discharge area along the Rhine River (Section 4.5.3.3, Malm aquifer). The figure shows the results from packer test intervals (almost) completely located within the «Herrenwis Unit». Tests are not shown if the intervals include important parts of other formations (STA2-BDO2, BUL1-BDO2). See also Fig. 4-85.

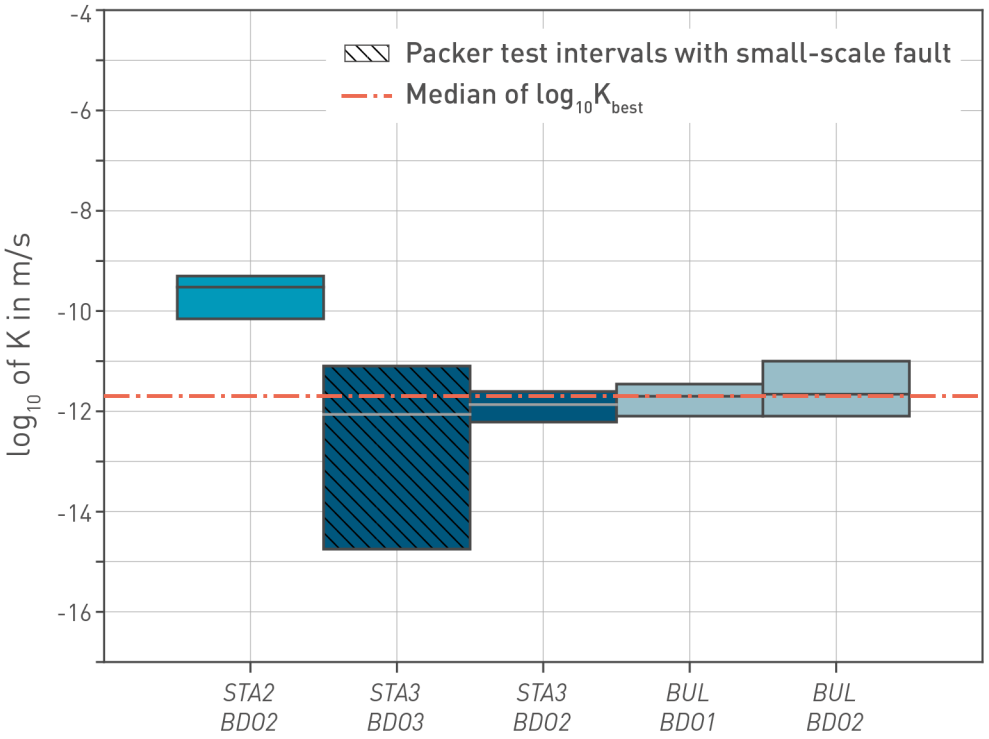


Fig. 4-92: Hydraulic conductivity from in-situ hydraulic packer tests in the «Herrenwis Unit»
The test interval STA2/BDO2 includes a sub-vertical joint.

4.5.3.8 Opalinus Clay

The Opalinus Clay constitutes a major aquitard of regional extent in Northern Switzerland that stands out from its confining units for the remarkable uniformity of its mineralogical, petrophysical and hydraulic properties (Section 4.2.6, Chapter 5). Along with adjacent units, the Opalinus Clay is an efficient barrier to flow between the regional aquifers, as supported by hydrogeochemical evidence (Sections 4.5.5, 4.6).

Hydraulic conductivities measured in situ (i.e. from hydraulic packer tests) and in laboratory tests are low (mainly < 10^{-12} m/s) and vary in a narrow range if the overburden thickness is larger than about 200 m (10^{-14} to 10^{-12} m/s for the hydraulic packer tests; Section 5.6). Observations from the boreholes in Northern Switzerland are well supported by hydrogeological investigations carried out in the Mont Terri rock laboratory (e.g. Marschall et al. 2004).

The Opalinus Clay is characterised by its high and uniform clay-mineral content, which is typically well above 40 wt.-% (Fig. 4-28, Section 5.2). The clay-mineral-rich matrix is fundamental for many properties, notably self-sealing. The in-depth characterisation of the Opalinus Clay is presented in Chapter 5.

4.5.3.9 Lias Group and uppermost Keuper

This section characterises the hydrogeological unit between the Opalinus Clay and the Keuper aquifer, i.e. the Staffelegg Formation and the uppermost part of the Klettgau Formation (in SGT Stage 2 termed 'clay-rich Keuper'). The unit includes important lithological variation in the vertical direction but shows good lateral correlation on the regional scale (Section 4.2.5 and partly 4.2.4). The lithologies mainly comprise dolomitic marls, limestone beds with individual thicknesses of less than 5 m and clay-mineral-rich intervals with good self-sealing properties (Fig. 5-3).

A focus of the in-situ hydraulic testing was on the Staffelegg Formation because of its position directly below the Opalinus Clay (Fig. 4-85). The observed hydraulic conductivities are generally $\leq 10^{-11}$ m/s, with the majority of the best estimate values being $< 10^{-12}$ m/s (Fig. 4-93). The comparison with matrix hydraulic conductivities suggests that some tests were affected by fractures. The highest value relates to an interval that includes fractures in the Beggingen Member (BAC1/LIA1 $T = 2 \times 10^{-10}$ m^2/s). The low hydraulic conductivities are supported by the absence of relevant anomalies in the profiles of the natural tracers (Section 4.6). These observations show that this unit is part of a low-permeability sequence in which diffusion dominates mass transport.

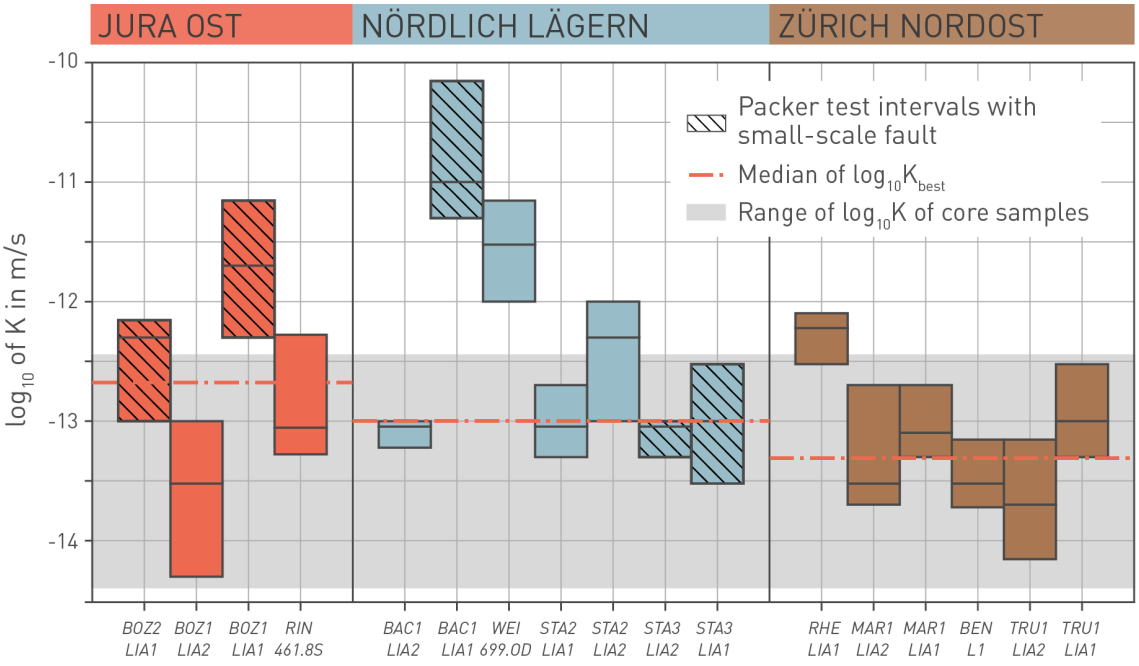


Fig. 4-93: Results of in-situ hydraulic packer tests in the Staffelegg Formation and comparison to values from laboratory tests on drill cores

The best estimate of the hydraulic conductivity is displayed with a thick black line. The associated uncertainty is shown with the vertical extent of the bars. The range of matrix hydraulic conductivity is shown in light grey (11 measurements).

For the recent TBO boreholes, the figure indicates test intervals that include small-scale faults. Note that no such detailed structural inventory is available for the historical boreholes Riniken (RIN) and Weiach (WEI).

4.5.3.10 Keuper aquifer

The Keuper Group consists mainly of low-permeability clay-rich rocks and evaporites. Only the Klettgau Formation in its upper part includes some transmissive lithologies. At the time of deposition, the study area was dominated by variable mostly terrestrial depositional environments, resulting in high variability of the deposited sediments and of their thickness (Section 4.2.4, Fig. 4-15). This variability affects the hydrogeological properties of the potential aquifer units, with a variation of hydraulic test transmissivities over eight orders of magnitude (Fig. 4-86). To address this variability and to make a distinction from the regional Malm and Muschelkalk aquifers, the term local aquifer is used (Nagra 1988, 2002).

The following section focuses on the potential aquifer units in the Klettgau Formation that are of particular interest for the siting regions in Northern Switzerland, i.e. the Seebi Member, the Gansingen Member and the Ergolz Member (Fig. 4-94). In Southern Germany, additional units may be of interest (Plum et al. 2008). The Keuper aquifer is of particular relevance because it is the aquifer closest to a potential repository in the Opalinus Clay (JO: similar distance to the Hauptrogenstein).

In the JO siting region, the Keuper aquifer was sufficiently transmissive to sample groundwater (Section 4.5.5.4) in the RIN and BOZ2 boreholes (and also in the nearby Beznau borehole, BEZ), with a particularly high transmissivity in the range of 10^{-4} m^2/s in BOZ2 (Fig. 4-86). In BOZ1, low transmissivity was observed but the characteristic shape of the profiles of the natural tracers (notably stable isotopes of water and chloride) shows a clear excursion (Section 4.6). This means that there is evidence for an active Keuper aquifer in all of the boreholes of this siting region. Based on the hydrogeological dataset and taking into account lithology (Fig. 4-15) and tectonic overprint, the permeability is most probably associated with the Gansingen Member which is particularly thick in JO. Groundwater flow probably occurs in fractures and may be facilitated by the partly well-developed macroporosity (Fig. 4-16).

In the NL siting region, the test transmissivities of 2×10^{-7} and 1×10^{-6} m^2/s in the BAC1 and STA2 boreholes allowed sampling of groundwater. In the other three boreholes, transmissivities were too low (range of 2×10^{-8} to 1×10^{-10} m^2/s; Fig. 4-86). In the case of the BUL1 and STA3 boreholes, the lower values are in line with an absence of significant excursions in the profiles of the natural tracers. From the packer test position and supported by other evidence, it is shown that the conductive zones relate to fluvial sandstone sections in the Ergolz Member. A particularly thick (ca. 7 m) quartz-rich channel was observed in the STA2 borehole (Fig. 4-94). In NL, the other members of the Klettgau Formation have not been observed to significantly contribute to transmissivity, probably because of local lithofacies and thickness (Section 4.2.4 and Fig. 4-95). In the Ergolz Member, the positive trend of transmissivity with quartz and feldspar content and intervals devoid of carbonate cement suggest that the matrix significantly contributes to overall transmissivity. The connectivity of the individual sandstone channels is probably limited as indicated by the differences in the hydrogeochemistry of the groundwater samples (Section 4.5.5.4) and by different extents of aquifer-aquitard interaction indicated by the profiles of the natural tracers in the BAC1 and STA2 boreholes (Section 4.6). Overall, the observations indicate that groundwater flow in NL is restricted to such channel systems and not as extensive as, for example, in the case of the Seebi Member in ZNO. The mostly low hydraulic test transmissivities in NL (Fig. 4-86) are in line with the outcome of the calibration of the simplified representation of the Keuper aquifer in the hydrogeological model (Section 4.5.4.4).

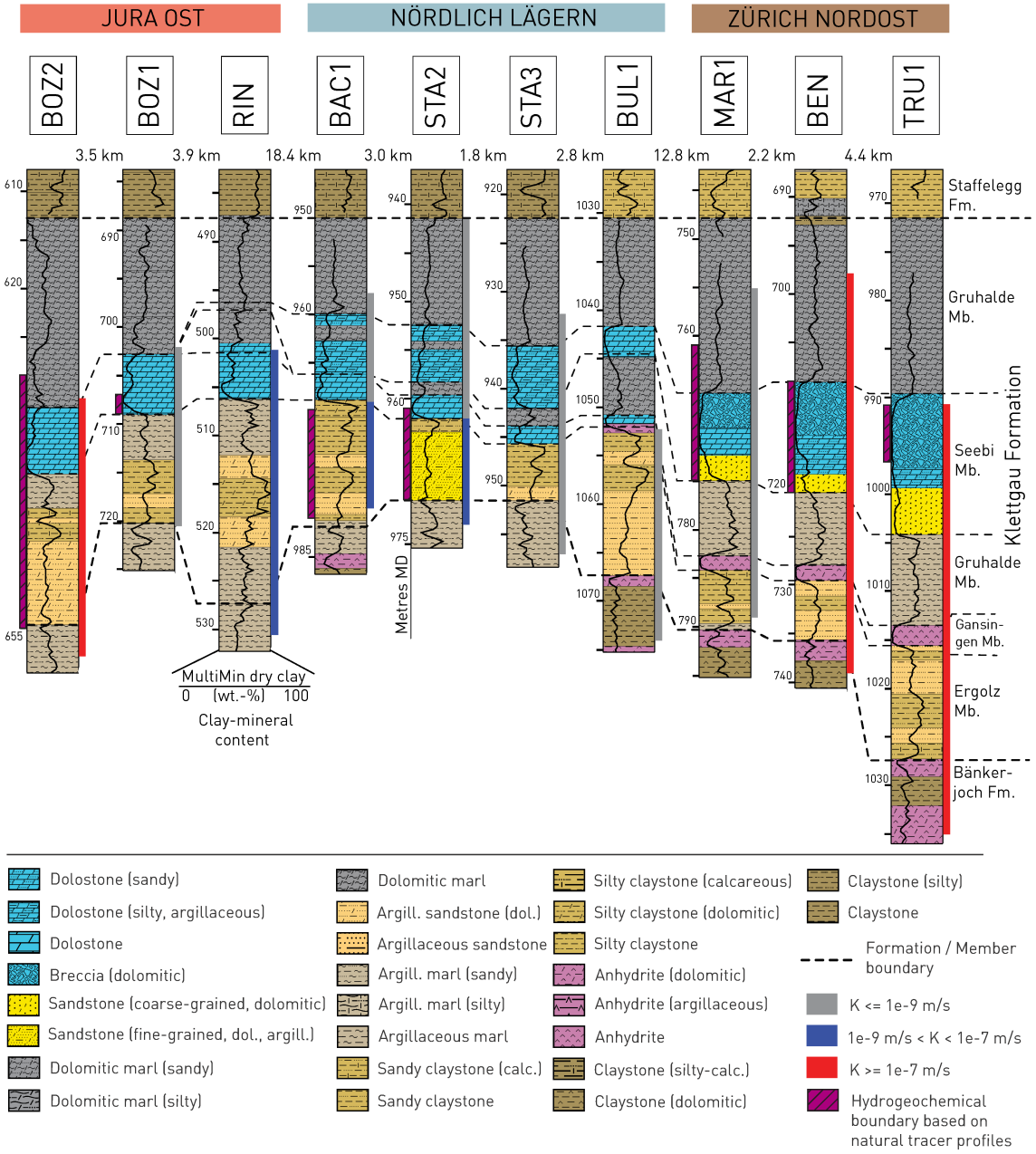


Fig. 4-94: Results of the hydraulic packer testing and hydrogeochemical investigations in the Klettgau Formation

The vertical extents of the hydraulic packer tests are shown on the right of the stratigraphic profiles. The colour code refers to the magnitude of the hydraulic conductivity (see legend) calculated from the transmissivity and the length of the test intervals. The vertical extents of the hydrogeochemical boundaries as estimated based on observations on natural tracer profiles (and complemented by drill core observations) are displayed on the left of the stratigraphic profiles (purple hatched intervals). The latter represent the hydrogeochemical boundaries at the Keuper aquifer used for the modelling of the natural tracer profiles in the aquitards (Sections 4.6.2 and 4.6.3).

In the ZNO siting region, the new TBO boreholes confirmed the earlier investigations related to the Keuper aquifer as the major hydrogeochemical boundary for the Opalinus Clay. High test transmissivities (4×10^{-6} and 6×10^{-5} m^2/s) allowed sampling of groundwater of similar composition from the Benken (BEN) and TRU1 boreholes (Section 4.5.5.4). In MAR1 the transmissivity was lower (1×10^{-8} m^2/s; Fig. 4-86), but the profiles of the natural tracers show a clear excursion with a characteristic change to a low-chloride meteoric composition (Section 4.6). The same systematic pattern was observed in the RHE1 borehole and also in the nearby Schlattingen-1 geothermal borehole (Wersin et al. 2016). Overall, the available hydrogeological dataset indicates there is an active Keuper aquifer across the entire ZNO siting region. The transmissive zone relates to the Seebi Member (former 'Stubensandstein') which exclusively includes in ZNO and the nearby areas a partly macroporous dolomitic breccia (Section 4.2.4).

At the regional level, permeable sandstone channels of the Ergolz Member must be expected in all the siting regions (Fig. 4-95). They are of limited extent and occur only locally, but their position is difficult to predict. In contrast, the permeable, cavernous dolomitic breccia of the Seebi Member is a particular feature of ZNO, and the thick Gansingen Member exists in JO.

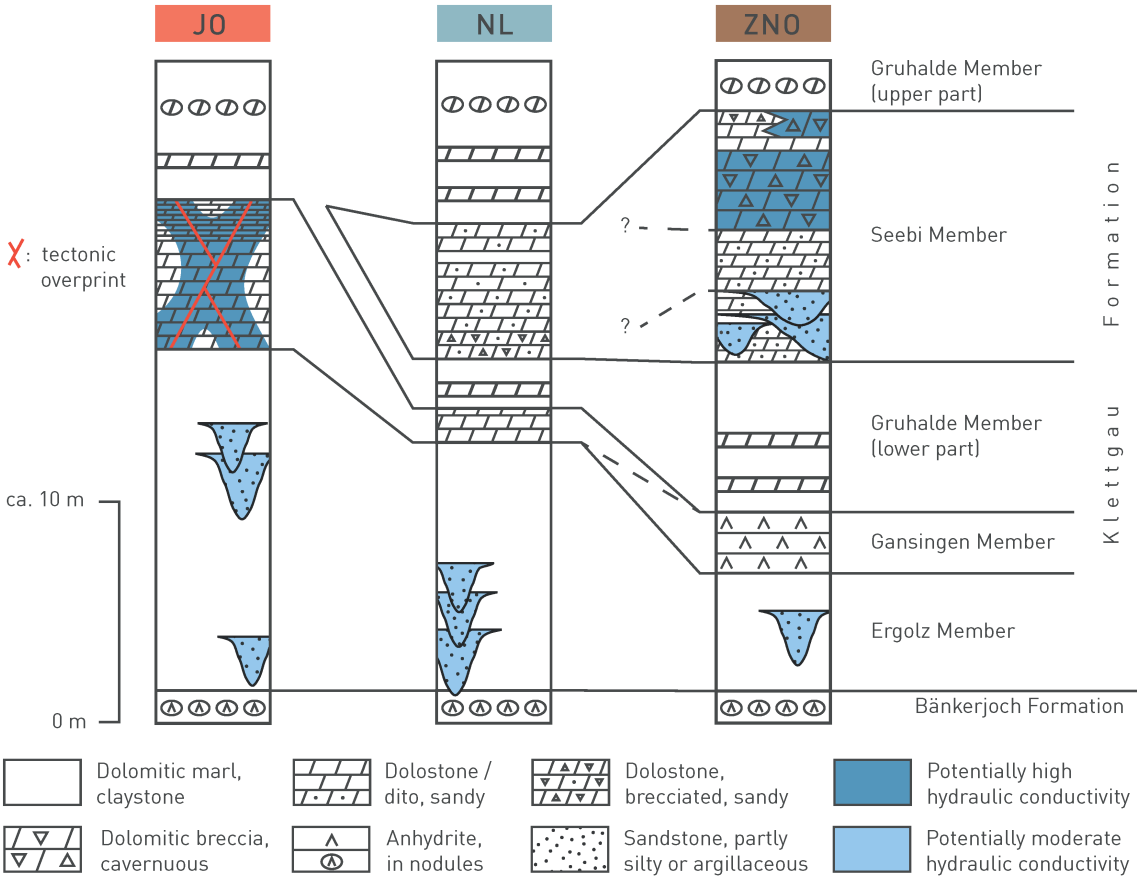


Fig. 4-95: Hydrogeological synopsis of the Keuper aquifer indicating the permeable lithofacies of the Klettgau Formation in the different siting regions

4.5.3.11 Bänkerjoch Formation

The Bänkerjoch Formation («Gipskeuper») is a thick aquitard of regional extent (Fig. 4-10) between the Keuper aquifer and the regional Muschelkalk aquifer (Fig. 4-84). It consists mainly of anhydrite (which at shallow levels may be hydrated to gypsum), clay minerals and dolomite (Section 4.2.3). Where the Keuper aquifer is not active, it is part of the low-permeability confining units below the Opalinus Clay.

At the relevant depths, the hydraulic conductivities are very low: tests on drill cores showed values of $< 10^{-11}$ m/s and a packer test in the BEN borehole indicated 1.1×10^{-13} m/s (Klemenz et al. 2000). The anhydrite-rich sections have good self-sealing properties because of the volume expansion caused by reaction with groundwater resulting in the hydration to gypsum ($T <$ ca. 42 °C). The profiles of the natural tracers indicate diffusion as the dominant transport mechanism between the Keuper and the Muschelkalk aquifer (Section 4.6). Particularly steep concentration gradients are mostly observed in the lowermost Bänkerjoch Formation related to the occurrence of massive anhydrite units which are an efficient transport barrier. In this subunit, porosity trends to zero if the anhydrite content exceeds ca. 60 to 80 wt.-% (Fig. 5-8; Mazurek et al. 2023a).

The interpretation of 3D seismic data provides indications for dissolution processes in the Bänkerjoch and / or the Schinznach Formation probably related to subaerial exposure (Nagra 2024a, 2024b, 2024c). Under current conditions, the development of gypsum karst is restricted to the outcrop zone (Plum et al. 2008, Ufrecht 2017).

4.5.3.12 Muschelkalk aquifer

The Muschelkalk aquifer consists of the carbonate rocks of the Schinznach Formation. As a result of the large-scale uniform lithology (Fig. 4-7), it is a regional aquifer in Northern Switzerland (e.g. Nagra 2014e, Dossier V) and Southern Germany (e.g. Stober & Villinger 1997, Ufrecht 2018) with a typical thickness around 70 to 80 m in the siting regions. The aquifer is bounded at the top by the Bänkerjoch Formation and at the bottom by the Zeglingen Formation (Fig. 4-8, Section 4.2.2). Note that the uppermost dolomite of the Zeglingen Formation can be part of the aquifer (former 'Dolomit der Anhydritgruppe').

In the boreholes in Northern Switzerland, the unit mainly consists of dolomite and calcite in varying proportions. In addition, sulphate minerals (anhydrite, celestite) are locally observed.

As a result of the comparably high hydraulic conductivities, the Muschelkalk aquifer is exploited in many wells, including for the spas of Baden and Bad Schinznach (e.g. Burger 2011, Waber & Traber 2022 and further references therein).

Water flow in the deep Muschelkalk aquifer is mainly related to fractures in combination with a partly porous and permeable rock matrix (Fig. 4-9). Of the four different members of the Schinznach Formation (Section 4.2.2), the dolomitic Stamberg Member is most relevant for water conductivity via the rock matrix. This is mainly because of 1) the early diagenetic dolomitisation (classical ‘Trigonodus-Dolomit'; Adams et al. 2019, Aschwanden et al. 2019a) and 2) the presence of macropores formed by local dissolution of anhydrite nodules by upwelling of groundwater from the Buntsandstein and/or the crystalline basement during the different geodynamic situations in the Oligocene and the Miocene (Aschwanden et al. 2019b; see also Section 4.5.5.5). At present, the porosity of the Stamberg Member in the TBO boreholes can locally exceed 20 vol.-% based on geophysical logging (Fig. 5-10). Fractures increase the hydraulic conductivity by 1 – 3.5 orders of magnitude compared to the rock matrix (Aschwanden et al. 2017). Depending on where brittle deformation has occurred, the most transmissive intervals can also be located in the Liedertswil Member or the Leutschenberg and Kienberg Members where limestones dominate (see Section 4.2.2). With increasing overburden, mechanical and chemical compaction cause a substantial decrease in the hydraulic conductivity (Fig. 4-96).

Epigenic karst is observed in shallow situations, where the overlying units were eroded or where the cover is only thin or patchy (e.g. Hoehn 1979, Plum et al. 2008). Hypogenic karstification under thick overburden has only been observed where carbon dioxide of magmatic or volcanic origin is upwelling along fractures extending to a greater depth, leading to carbonate dissolution; such conditions have only been reported north of the investigation area in Baden-Württemberg (Plum et al. 2008, Ufrecht 2006). In the siting regions in Northern Switzerland, no expressions of, or drivers for, such hypogenic karst development have been observed. The interpretation of 3D seismic data provides indications for dissolution processes in the Bänkerjoch and / or the Schinznach Formation probably related to subaerial exposure (Nagra 2024a, 2024b, 2024c).

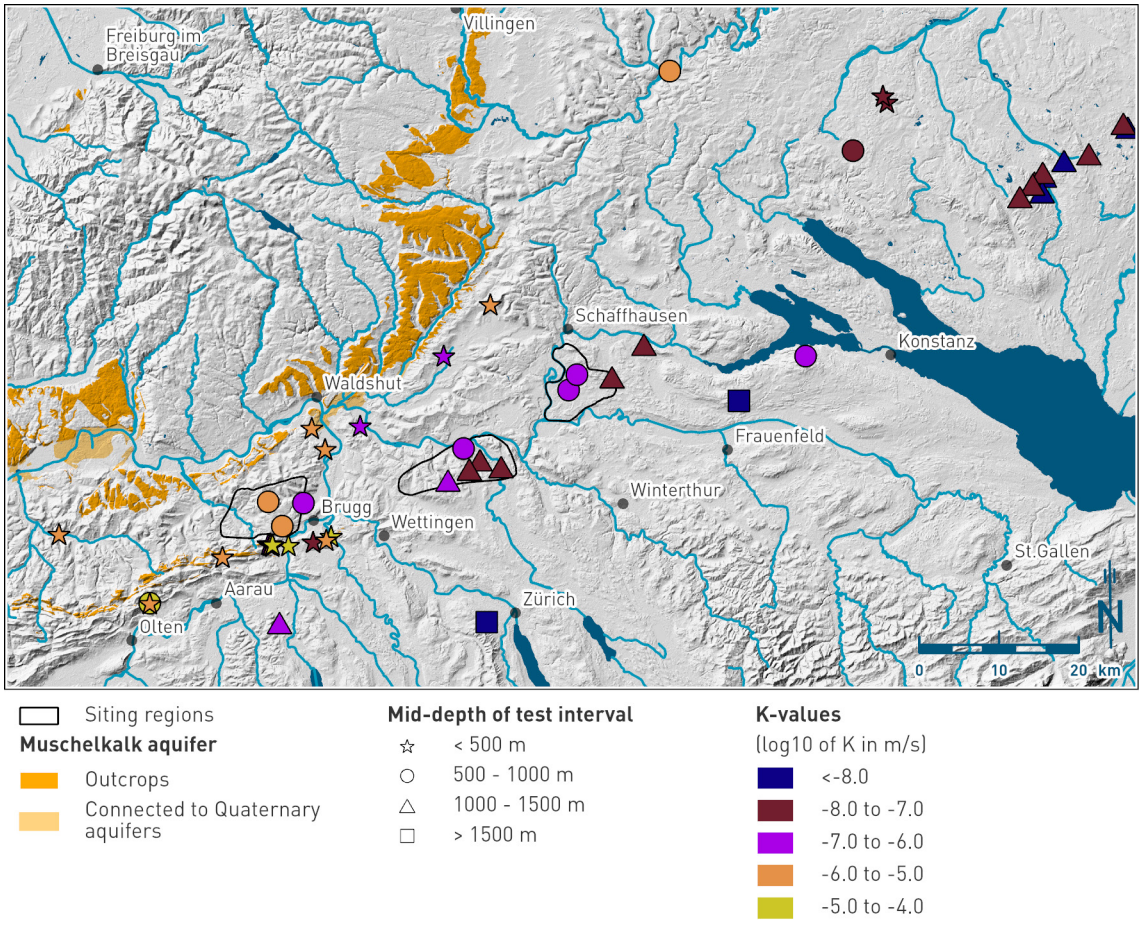


Fig. 4-96: Hydraulic conductivities from in-situ hydraulic tests in the Muschelkalk aquifer in Northern Switzerland and Southern Germany

The length of the test intervals varies between approximately 10 and > 100 m. The figure shows the regional distribution of hydraulic conductivity and its dependence on depth (see text for further details).

The test transmissivities show a comparably uniform distribution of the values, i.e. no large regional differences are evident (Fig. 4-86). The overburden thickness seems to exert a major control on the properties (Fig. 4-96).

In the siting regions, the Muschelkalk aquifer was tested in all boreholes and the hydraulic conductivity was sufficiently high in all cases to sample groundwater. The location and lengths of the test intervals were chosen based on indications such as losses of drilling fluid and observations on drill cores (fractures, porous zones). From the resulting distribution of the packer test positions, no particular subunit with elevated hydraulic conductivity is evident (Fig. 4-85). In comparison to the Malm aquifer, the conductive sections seem to be more distributed throughout the entire unit and are probably linked to subvertical fractures and joints. The hydraulic properties in the siting regions agree with the regional dataset, particularly if the depth-dependence is taken into account (Fig. 4-96). The typical test transmissivity in the siting regions is around 10^{-5} m^2/s and the values scatter within the narrow range of ± 1 order of magnitude. Despite the larger overburden resulting from the stratigraphic position, the transmissivity is approximately one order of magnitude larger than in the Malm aquifer (Fig. 4-86). This enables a large-scale connected deep flow system (Section 4.5.5.5).

4.5.4 Analysis of the flow system based on the regional hydrodynamic model

This section develops an understanding of the hydrogeological system based on the regional hydrodynamic steady state model (Nagra 2024n) and the hydraulic heads in the aquifers measured in the deep boreholes. Piezometric maps of the main aquifers are presented, and recharge and discharge areas are identified. Finally, large-scale hydraulic head differences between aquifers are discussed.

4.5.4.1 Model description

The three-dimensional steady state numerical groundwater flow model (extract of the 3D model shown on Fig. 4-97) aims to test the consistency of the hydrogeological dataset and provide insights into the groundwater flow systems. It is also a tool to investigate the impact of different conceptualisations, for example with respect to the properties of the hydrogeological units and of the regional faults.

The focus of Sections 4.5.4.2 to 4.5.4.5 is on the identification of the recharge and discharge areas of the main aquifers. These will also feed into the interpretation of the hydrogeochemical data of the groundwater samples to develop a consistent understanding (Section 4.5.6). Note that the hydrogeochemical dataset may also include information on transient processes (e.g. old seawater components) – in contrast to the steady state groundwater flow model.

Technical details on the model are provided by Nagra (2024n). The model extent and the boundary conditions were defined based on available data and earlier modelling results (e.g. Gmünder et al. 2014). The modelling procedure included a sensitivity analysis of the boundary conditions to investigate their impact on the groundwater flow field. The outcome of this analysis led to the selection of a base-case model for further calibration. The calibration was carried out using the PEST algorithm (Doherty 2004) focusing on the hydraulic parameters of the Malm, Hauptrogenstein, Keuper, and Muschelkalk aquifers (Nagra 2024n). The hydraulic properties of the faults were related to the hydraulic properties of the hosting units using multiplicative factors. The latter were adjusted during the final phase of the calibration to further enhance the quality of the fit.

The base-case model includes a no flow boundary condition at the southern limit of the model reflecting the low hydraulic conductivities of the aquifers expected at several kilometres depth. The importance of this choice needs to be put into perspective. Indeed, the sensitivity analysis showed that the hydraulic conditions assigned to the southern boundary have no significant impact on the northern part of the model where the siting regions are located.

The recharge and discharge areas of the aquifers are visualised using backward and forward particle tracking (Fig. 4-98, Fig. 4-100, Fig. 4-101, Fig. 4-102). These were calculated by post-processing the model results using the simulated groundwater velocity field and generic porosities. The calculation of the particle paths was stopped after an arbitrarily selected time frame of 5 million years. Note that this is not intended to serve as a long-term prediction (steady state model).

Particles were released in the middle of the aquifer horizons above and below the Opalinus Clay in the perimeter of the siting regions. While the released particles usually travel within the bounds of the thick aquifers during the considered time frame, particles released in thin aquifer layers may be trapped in the adjacent aquitards (Nagra 2024n).

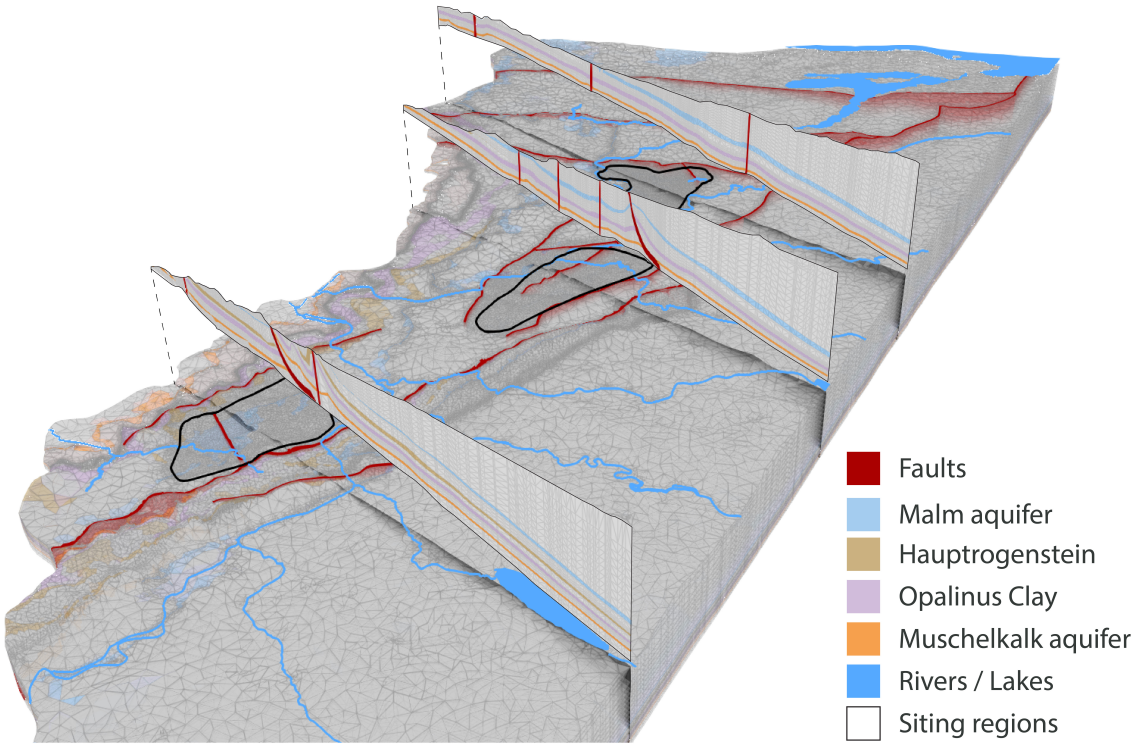


Fig. 4-97: 3D view of the northeastern part of the hydrogeological model, with respective cross-sections showing the main regional aquifers, together with the Opalinus Clay

Model is vertically exaggerated 2×, cross-sections are exaggerated 3×. The Malm aquifer (top of the «Felsenkalke» + «Massenkalk» to the base of the Villigen Formation), Hauptrogenstein aquifer, Opalinus Clay and Muschelkalk aquifer (Schinznach Formation), as well as a simplified regional fault pattern are displayed.

4.5.4.2 Malm aquifer

The Malm aquifer is the nearest aquifer above the Opalinus Clay in the NL and ZNO siting regions. The model was implemented based on the hydraulic conductivities observed in the boreholes and a depth dependence. In addition, tectonic overprint was taken into account (Nagra 2024n).

The piezometric map (Fig. 4-98) shows that the zone north of the Jura Main Thrust and the Baden – Irchel – Herdern Lineament is mainly affected by the local topography and the outcrop situation. The flow system in this zone is well supported with borehole data, notably within the siting regions. The area further to the south is less constrained by borehole data, but the sensitivity analyses show that the detailed situation in the southern part of the model is of little importance for conditions in the siting regions (Nagra 2024n).

The regional situation of the Malm aquifer is characterised by a piezometric dome in the northeasternmost corner of the model perimeter (Fig. 4-98). The groundwater then flows towards the southeast driven by a steep hydraulic gradient. High hydraulic heads also exist in the Bodensee area, reflecting groundwater inflow from the east. Recharge also occurs locally along the Internal Jura where the Malm is outcropping.

The main discharge areas are located along the Rhine River where the Malm aquifer is in contact with the river and/or associated Quaternary aquifers (e.g. Rhine Falls and Rheinau area northwest of the ZNO siting region, the area of Kaiserstuhl – Hohentengen in the Rhine Valley north of the NL siting region, and at the confluence of the Aare, Reuss and Limmat Rivers near the town of Brugg). South of the Jura Main Thrust, Malm groundwater discharges in the Reuss and Aare Valleys where the associated rivers cut the Internal Jura (Fig. 4-98).

The topography and outcrop position of the Malm aquifer in the northern part of the model leads to site-specific hydrogeological situations. Backward particle tracking from the ZNO siting region shows that the recharge of the Malm aquifer mainly takes place along Malm outcrops in the north. The model results indicate that the Randen fault acts as a drain, channelling the groundwater further to the southeast. Recharge also occurs locally along the Malm outcrops of the Südranden area. These groundwater flow systems then discharge in the Rhine Falls and Rheinau areas.

In the NL siting region, the recharge of the Malm aquifer mainly takes place through the thick Molasse units north of the Jura Main Thrust (i.e. northern part of the Lägern Anticline; Fig. 4-98). This is indicated by the hydraulic head differences at the interface between the Malm aquifer and the USM (Fig. 4-99). Note that the differences are more pronounced in the western part of the siting region than in the eastern part due to the topographical effect. The Jura Main Thrust and the Baden – Irchel – Herdern Lineament do not act as preferential pathways.

The groundwater discharge zone is located near Kaiserstuhl – Hohentengen north of the siting region where the Malm is in contact with the Rhine River (Fig. 4-98).

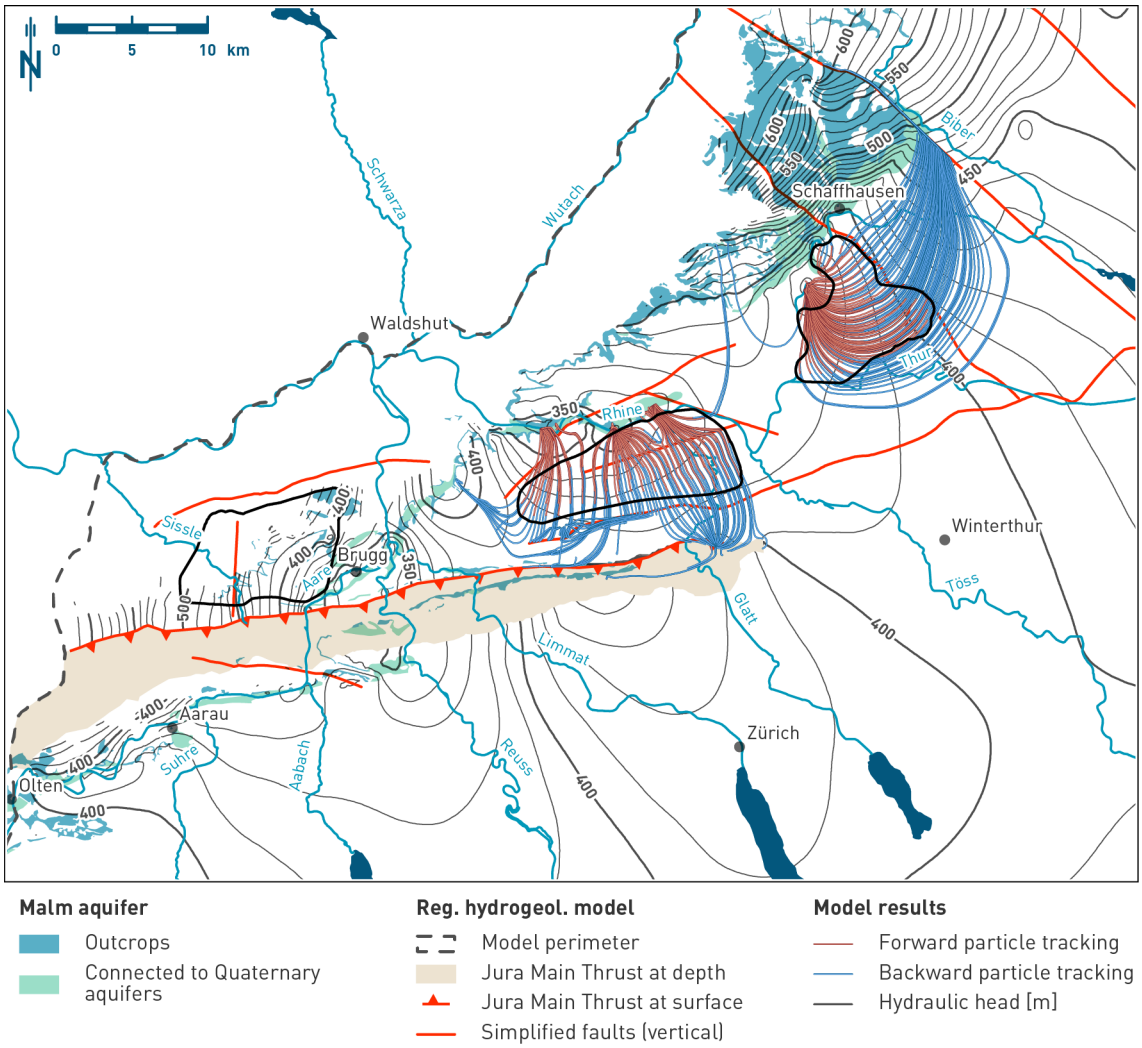


Fig. 4-98: Simulated hydraulic heads and the particle paths identifying recharge and discharge areas in the Malm aquifer

Hydraulic head situation at the top of the Villigen Formation horizon of the hydrogeological model. The map also shows the outcrops and the simplified regional fault pattern used in the model. The displayed particle paths are a 2D projection of the 3D particle traces. Note the site-specific groundwater flow systems.

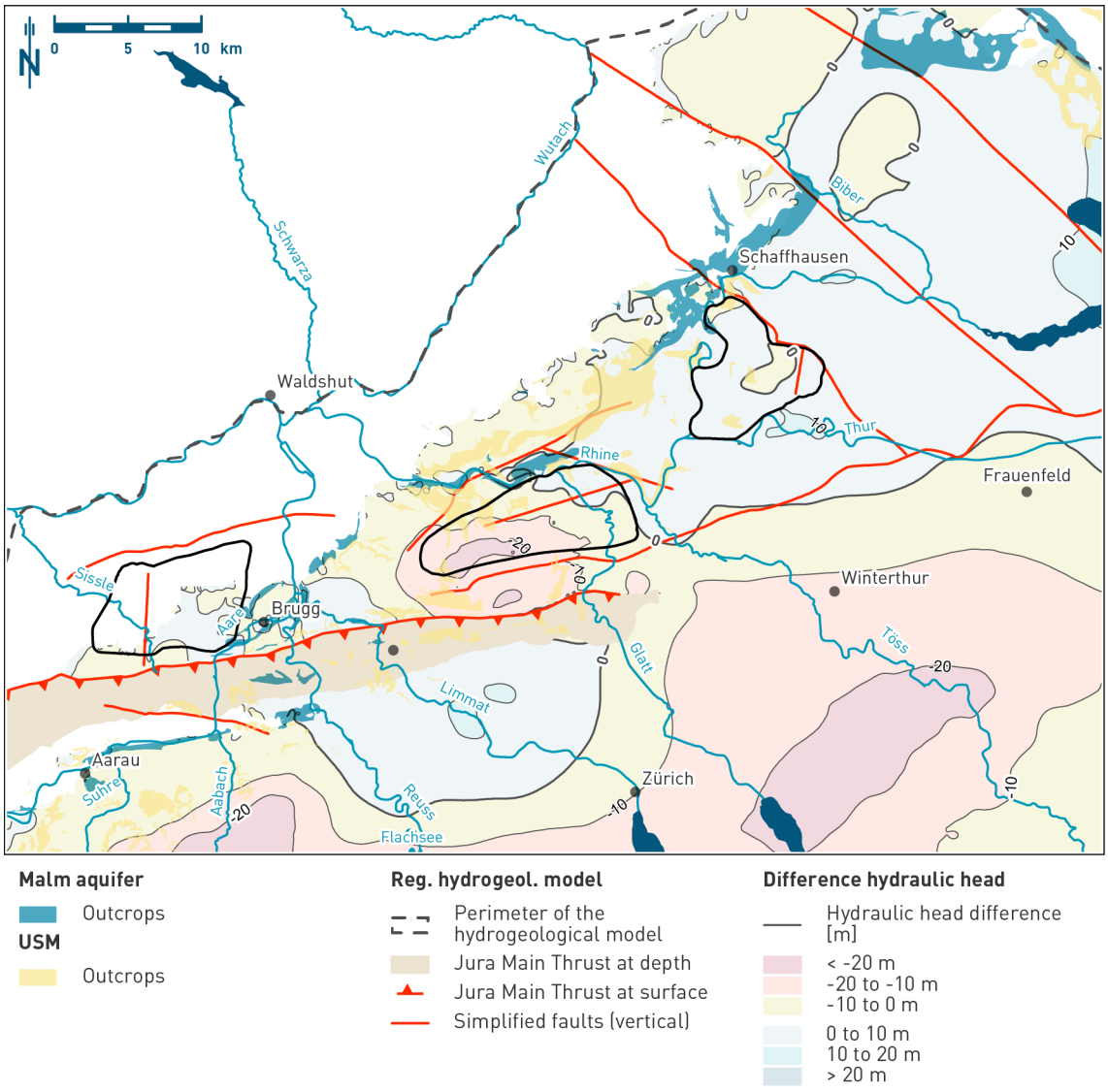


Fig. 4-99: Head difference map between the Malm aquifer and the Lower Freshwater Molasse Group (USM)

Positive and negative head differences indicate upward and downward hydraulic gradients respectively. Hydraulic head difference were calculated using the results of the base case (Nagra 2024n). The top of the Villigen Formation and the top of the lowermost USM horizons of the model were considered. The map also shows the outcrops and the simplified regional fault pattern used in the model. Note the negative hydraulic head difference in the NL siting region indicating vertical recharge of the Malm aquifer through the Molasse deposits.

4.5.4.3 Hauptrogenstein aquifer

The Hauptrogengestein is the nearest aquifer above the Opalinus Clay in the JO siting region. The flow system is affected by the local topographic situation and by the facies transition towards units with higher clay-mineral contents towards the east (Sections 4.2.7 and 4.5.3.6).

Potential recharge areas are the outcrops located north and west of the siting region (Fig. 4-100). The location of the discharge areas depends on the assumptions regarding the continuity and properties of the aquifer. Assuming that the permeable facies reach the lower Aare Valley to the east, discharge mainly occurs along the Aare River and, to a lesser extent, in the Quaternary aquifer of the Sissle Valley to the west.

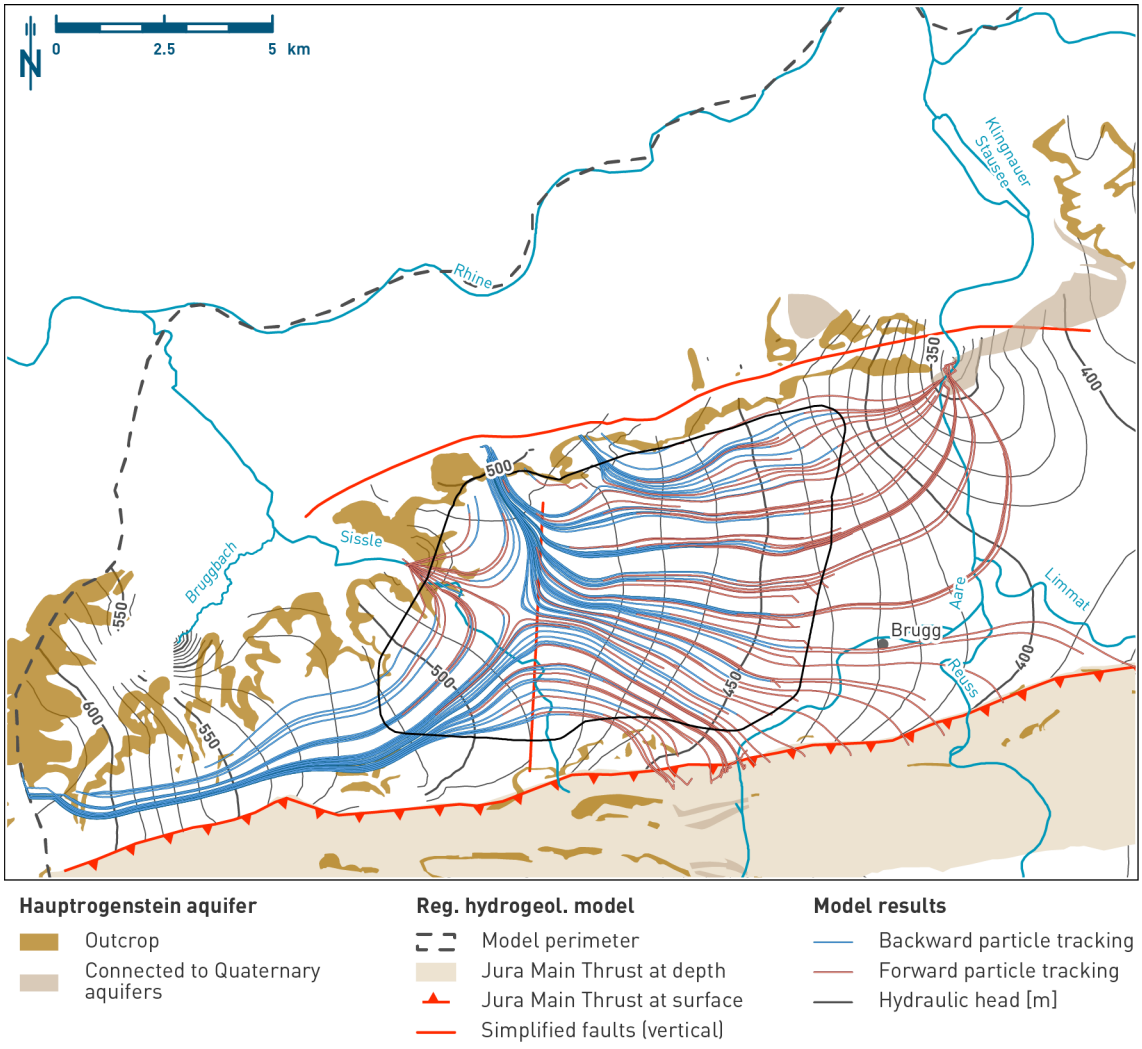


Fig. 4-100: Simulated hydraulic heads and particle paths identifying recharge and discharge areas in the Hauptrogenstein aquifer

Hydraulic head situation at the top of the Hauptrogenstein aquifer of the hydrogeological model. The map shows the outcrops and the simplified regional fault pattern used in the model. The displayed particle paths are a 2D projection of the 3D particle traces. Note the west to east orientation of the groundwater flow. Particles that stop close to the eastern boundary of the site do not display any further displacement as they are trapped in the overlying low permeability formation (see discussion in Nagra 2024n).

4.5.4.4 Keuper aquifer

Where present, the Keuper aquifer is the nearest aquifer below the Opalinus Clay. It is characterised by important lithological variations (Section 4.2.4) and a large variability of its hydraulic properties (Section 4.5.3.10, Fig. 4-95). In the regional groundwater flow model, the Keuper aquifer unit is abstracted in one layer. The local complexity of the associated groundwater flow systems was regionally evaluated through the following cases (Nagra 2024n):

- Base case: It includes an almost site-specific parametrisation of the Keuper aquifer. The area north of the Jura Main Thrust and the Baden – Irchel – Herdern Lineament is subdivided into different zones based on hydrogeological observations, facies maps, and tectonic overprint (Nagra 2024n). The zone surrounding the ZNO siting region is linked to the occurrence of the brecciated, cavernous lithofacies of the Seebi Member (Section 4.5.3.10). Another zone approximates the extent of the comparably thick transmissive facies of the Gansingen Member as observed in the JO siting region (Section 4.5.3.10). Around the NL siting region, another zonation aims to represent an area of the Keuper aquifer dominated by fluviatile channels of the Ergolz Member.
- Homogeneous isotropic case: To evaluate the impact of a less compartmentalised model on the groundwater flow system (i.e. in comparison to the base case), a homogeneous and isotropic medium was considered as an alternative to the base case (Fig. 4-101).

The two cases were calibrated leading to a comparable fit between simulated and observed hydraulic heads. However, the base case results in a slightly better agreement between modelled and observed hydraulic heads for the siting regions (Nagra 2024n).

While the two cases show a distinct hydraulic head distribution (Nagra 2024n), both provide a consistent image of the main hydrogeological features of the Keuper aquifer:

- Two different regional flow domains are recognised on Fig. 4-101. A first groundwater flow system exists north of the Jura Main Thrust and the Baden – Irchel – Herdern Lineament. It is well constrained by the outcrops to the southeast of the Wutach River, but also in the lower Aare Valley and in the Tabular Jura north of JO (Fig. 4-101). A second regional flow domain exists south of the Jura Main Thrust and the Baden – Irchel – Herdern Lineament.
- The potential recharge areas are located between the Wutach and the Klettgau Valleys north of the NL and ZNO siting regions, and locally on Keuper outcrops north of the JO siting region (Fig. 4-101). Similar to the Muschelkalk aquifer, the Keuper aquifer discharges in the lower Aare Valley as well as in the Quaternary aquifer of the Sissle Valley west of the JO siting region.
- Calibration of the base case and the alternative homogeneous isotropic case led to low hydraulic conductivities in the area north of the Jura Main Thrust and the Baden – Irchel – Herdern Lineament. Values are between 10^{-8} and 10^{-10} m/s for the base case and approximately 10^{-9} m/s for the alternative case (Nagra 2024n). Particularly low values are found in the NL siting region for the base case (approximately 10^{-10} m/s), in agreement with the results of the hydraulic packer tests (Fig. 4-94).
- The two calibrated models (Fig. 4-101) show similar groundwater flow patterns in the siting regions despite their difference in the distribution of hydraulic conductivities. Backward particle tracking indicates groundwater flow in the ZNO siting region towards the south-southeast impacted by the presence of the recharge area in the north. This agrees with the flow direction inferred from the hydraulic head data.

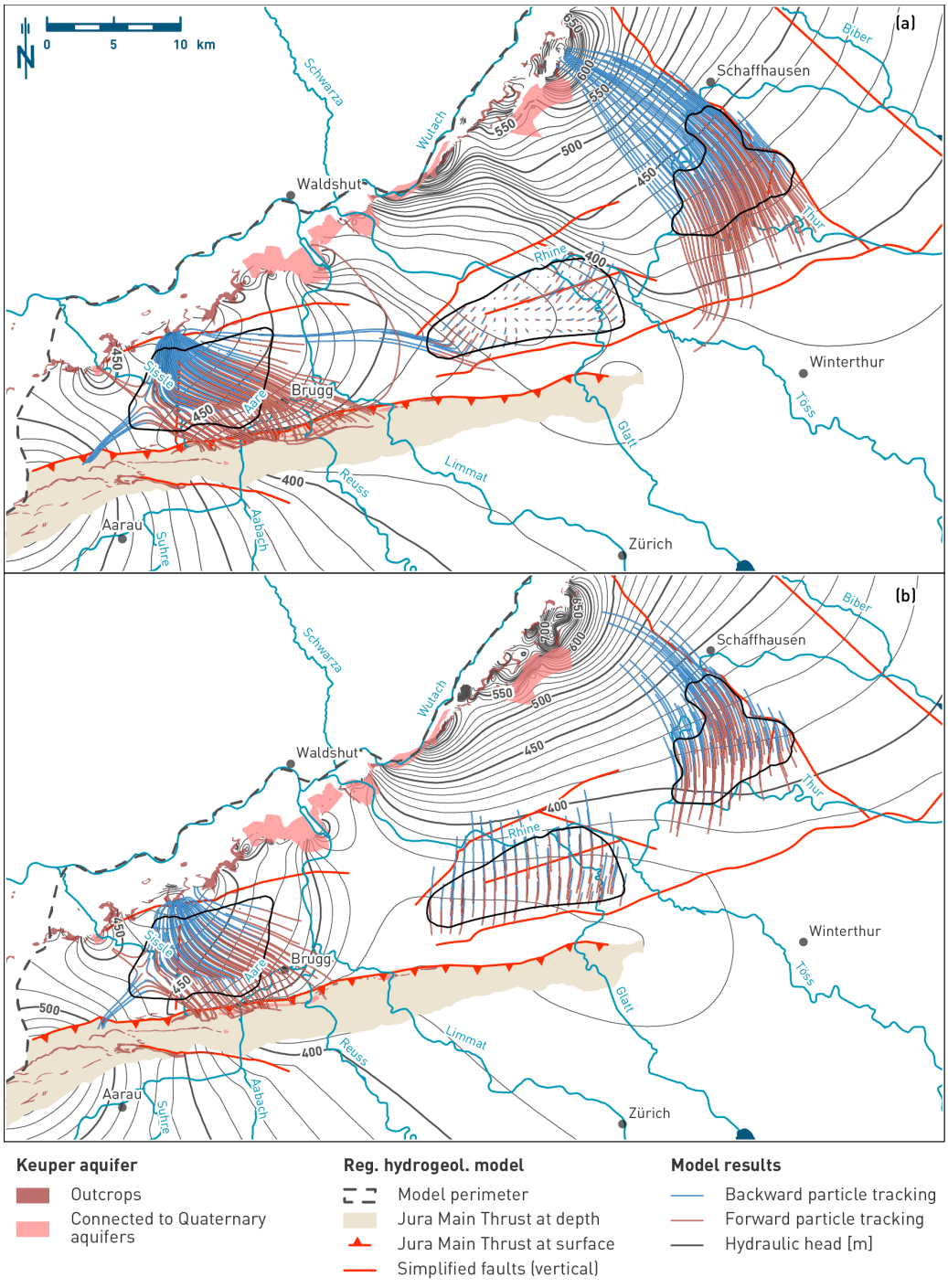


Fig. 4-101: Simulated hydraulic heads and particle tracking in the Keuper aquifer identifying recharge and discharge areas for the base case (upper figure) and alternative homogeneous isotropic case (lower figure)

Hydraulic head situation at the top of the Keuper aquifer horizon of the hydrogeological model. Base case with different domains of hydraulic properties, alternative homogeneous isotropic case assuming uniform properties north of the Jura Main Thrust and the Baden – Irchel – Herdern Lineament. See text for detailed discussion. The map also shows the outcrops and the simplified regional fault pattern used in the model. The displayed particle paths are a 2D projection of the 3D particle traces. Note the short distances travelled by the particles released in the NL siting region during the considered time frame for the particle tracking indicating very slow flow velocities, particularly in the base case (see discussion in Nagra 2024n).

For the NL siting region, the two model cases indicate only small flow distances during the time frame considered for the particle tracking, highlighting the low hydraulic gradients and the comparably lower hydraulic conductivity in the base case. The major recharge areas are located in the north or northeast in both cases. From the siting region, the particles migrate towards the regional discharge area in the lower Aare Valley or towards the low hydraulic head zone in the Limmat north of the Jura Main Thrust.

Both models also show consistent results in the vicinity of the JO siting region: The hydraulic head distribution is mainly constrained by the presence of the Keuper outcrops to the north, where water is recharging, and the regional and local discharge areas in the lower Aare Valley and in the Sissle Valley respectively.

4.5.4.5 Muschelkalk aquifer

The Muschelkalk aquifer was implemented based on the hydraulic conductivities observed in the boreholes and a depth-dependence (Fig. 4-96). In addition, tectonic overprint was taken into account (Nagra 2024n).

As for the Malm aquifer, the groundwater flow system in the zone north of the Jura Main Thrust and the Baden – Irchel – Herdern Lineament is controlled by the topography and the outcrop situation. The flow system in this zone is well supported with borehole data, notably within the siting regions. The area further to the south is less constrained by borehole data, but the sensitivity analyses show that the detailed situation in the southern part of the model is of little importance for conditions in the siting regions (Nagra 2024n).

In the northeastern part of the domain, the recharge of the Muschelkalk aquifer mainly occurs in the Wutach Valley where the Muschelkalk aquifer is outcropping at the valley flanks. The important groundwater inflow from the north leads to a regional groundwater divide roughly oriented northwest-southeast, the impact of which in the model is visible down to the southern model area. Such a divide has already been identified in earlier work (e.g. Nagra 2002). West of the groundwater divide, the flow system is aligned towards the discharge area near the confluence of the Aare and Rhine Rivers. Muschelkalk groundwater south of the Jura Main Thrust discharges in the lower Reuss and Aare Valleys, as well as in the Limmat Valley in the Baden area (i.e. discharge of thermal water), where the associated rivers cut through the Jura Main Thrust (Fig. 4-102). This is in agreement with earlier work (Gmünder et al. 2014, Nagra 2014e).

Forward and backward particle tracking indicates that the groundwater flow in the NL and ZNO siting regions shares a similar pathway (Fig. 4-102). It infiltrates in the northern Wutach Valley area, turns towards the southwest, flowing through the siting regions before exfiltrating after several tens of kilometres at the convergence of the Rhine and Aare Rivers.

The flow system in the JO siting region is controlled by the local tectonic situation, topography and the nearby discharge areas (Fig. 4-102). Particle tracking indicates that the Muschelkalk aquifer is recharging at outcrops to the north of the siting region and by vertical recharge of water along the Jura Main Thrust to the south. Groundwater is discharging in the lower Aare Valley to the east, and the lower Sissle Valley to the west where outcrops meet Quaternary aquifers.

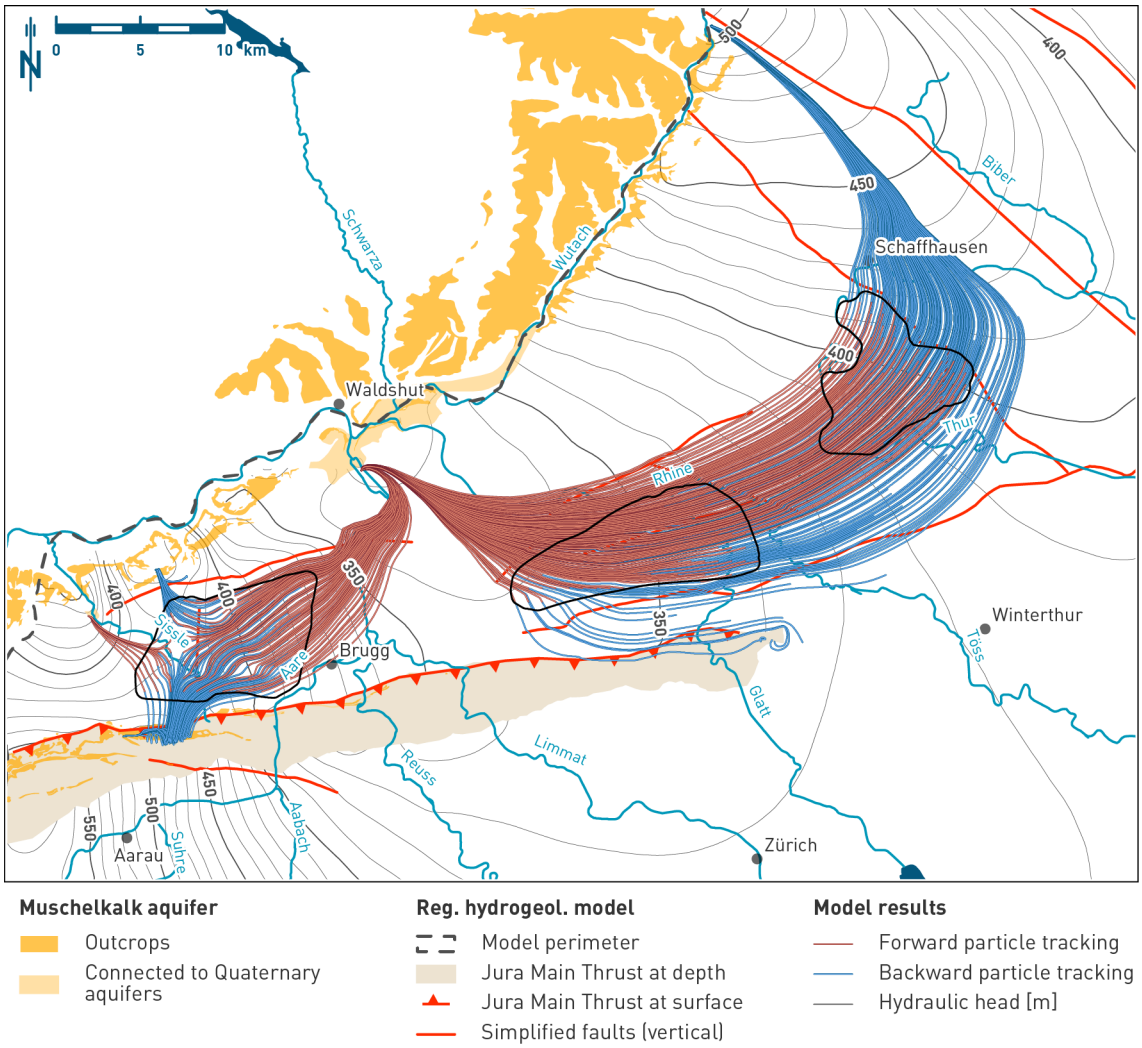


Fig. 4-102: Simulated hydraulic heads and particle tracking identifying recharge and discharge areas in the Muschelkalk aquifer

Hydraulic head situation at the top of the upper Muschelkalk aquifer of the hydrogeological model. The map shows the outcrops and the simplified regional fault pattern used in the model. The displayed particle paths are a 2D projection of the 3D particle traces. Note the well-defined regional flow paths of the groundwater flowing through the NL and ZNO siting regions, and the more local groundwater flow system around the JO siting region.

4.5.4.6 Differences in hydraulic heads between the aquifers

The difference in hydraulic heads between aquifers below and above the Opalinus Clay was regionally evaluated based on the result of the hydrogeological model (Fig. 4-103; Nagra 2024n). This gives valuable information on transport dynamics under steady-state hydraulic conditions in the host rock and the confining units. In combination with the distance between the considered aquifers and the vertical distribution of hydraulic conductivities in the aquitards, it helps to constrain the magnitude and direction of the steady-state vertical hydraulic gradient in the host rock and confining units.

The Hauptrogenstein and Malm aquifers are the nearest aquifers above the Opalinus Clay approximately west and east of the Aare Valley, respectively. The presence or absence of the Keuper aquifer below the Opalinus Clay can potentially shorten or increase the distance that separates the over- and underlying aquifers. The hydraulic difference is thus evaluated considering the possible combinations (i.e. Malm – Keuper, Malm – Muschelkalk, Hauptrogenstein – Keuper and Hauptrogenstein – Muschelkalk) as illustrated in Fig. 4-103.

The absolute magnitude of the hydraulic head difference is mainly below ca. 100 m (Fig. 4-103) in the area of the siting regions but can be higher close to the main recharge boundaries of the aquifers. From a site-specific perspective, downward gradients are calculated in the JO siting region. Upward hydraulic gradients are, however, inferred in the northeastern part of the siting region in the case where the Hauptrogenstein and the Keuper aquifers are considered.

In the ZNO siting region, head differences involving the Malm aquifer and the Keuper or Muschelkalk aquifers indicate upward gradients. This agrees with the artesian conditions observed for the Keuper aquifer in the BEN borehole and low hydraulic heads in the Malm. The head difference tends to increase towards the northwest, reaching a value greater than 50 m.

In the NL siting region, hydraulic head differences are comparably small. While the combination Malm and Muschelkalk shows overall downward gradients, the northern part of the siting region indicates weak upward gradients when the Keuper aquifer is considered.

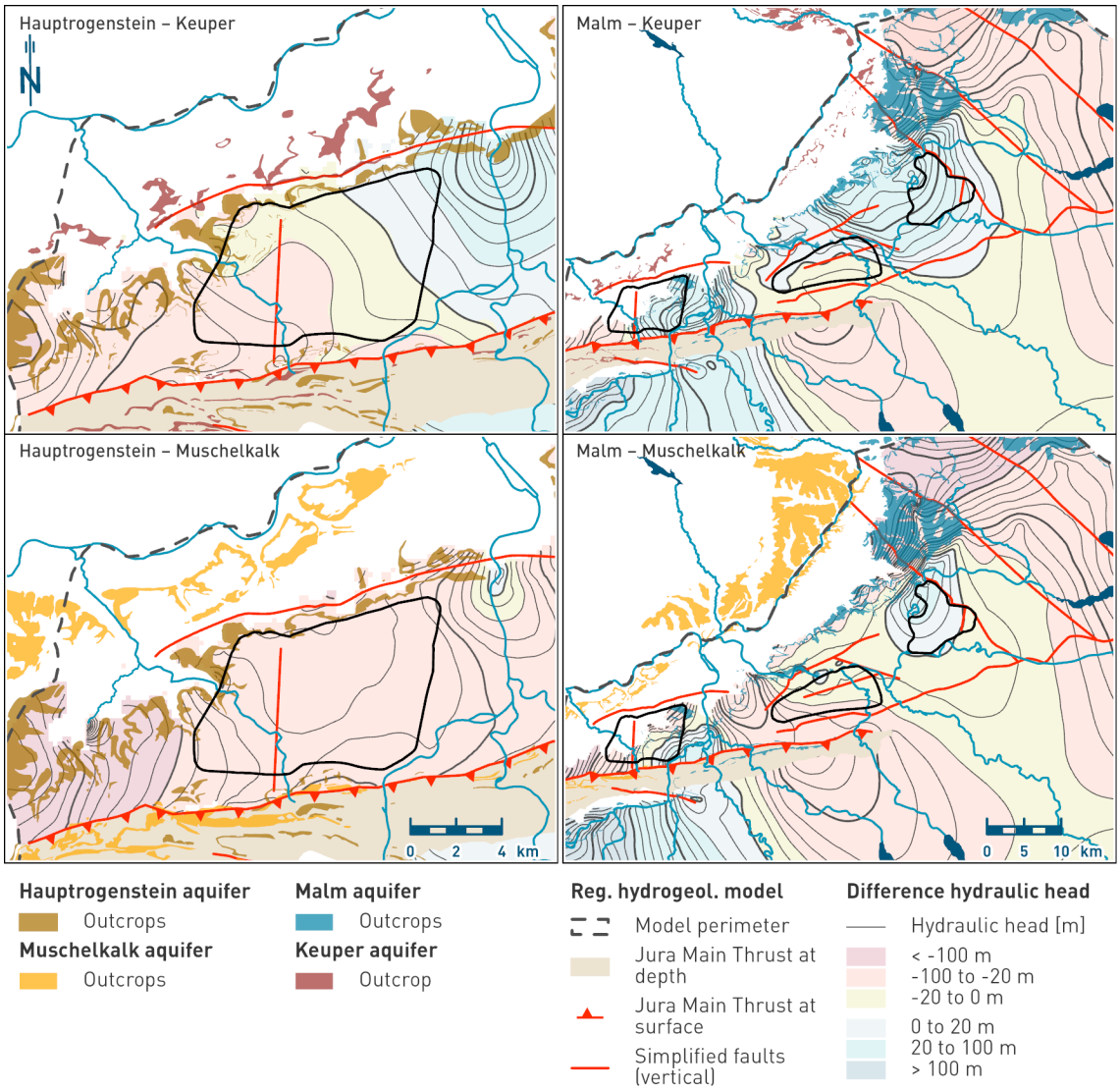


Fig. 4-103: Difference in hydraulic heads between aquifers above and below the Opalinus Clay

Negative and positive values indicate upward and downward gradients, respectively. The maps show the outcrops and the simplified regional fault pattern used in the model.

4.5.5 Hydrogeochemistry of deep groundwaters

4.5.5.1 Introduction

This section presents the major hydrogeochemical data of the deep aquifers situated above and below the repository host rock. As detailed in Section 4.5.3, these are the Malm and Hauptrogenstein aquifers above, and the Keuper and Muschelkalk aquifers below the host rock. Using major solute concentrations, stable isotopes, age tracers and dissolved gas concentrations, this section discusses groundwater origin, the governing mineral reactions, regional flow systems including subsurface residence times, and the origin of dissolved gases for the different aquifers. As such, this section provides independent evidence for testing and improving the understanding of the regional flow systems derived from the steady-state hydrodynamic simulations (Section 4.5.4).

The hydrogeochemical data are presented and discussed for each aquifer in the regional context of Northern Switzerland, with particular emphasis on the three siting regions. A comparison of the different aquifers is presented in a concluding section, discussing indications for both the absence and occurrence of cross-formation flow and providing explanations for the different hydrogeochemical conditions in the relevant aquifers.

While this section focuses on the aquifers above and below the repository host rock, it also contains limited hydrogeochemical information on the aquifers of the Molasse units located above the Malm aquifer, as well as the crystalline basement aquifers located below the Muschelkalk aquifer. This information is useful for evaluating potential hydraulic and hydrogeochemical connections between these aquifers. Accordingly, hydrogeochemical information on these additional aquifers is provided in the description of the aquifers with which there is a potential hydraulic communication.

A regional overview of existing hydrogeochemical data for the aquifers above and below the repository host rock as well as other deep aquifers including the Molasse, Buntsandstein, Permo-Carboniferous and crystalline basement aquifers is provided in Waber & Traber (2022) and in the individual TBO borehole reports (Tab. 2-1).

4.5.5.2 Malm aquifer

A) Hydrogeochemical characterisation and groundwater origin

Groundwater samples from the Malm aquifer in Northern Switzerland and adjacent areas display a large range in composition and mineralisation (Fig. 4-104). Low-salinity groundwaters with concentrations of total dissolved solids (TDS) below 2 g/L show a depth-dependent water composition. Samples taken from shallow boreholes ranging down to about 300 m below surface are of the Ca-HCO_3 or Ca-Mg-HCO_3 type. At greater depths, Na^+ may become the dominant cation and groundwaters also relate to the Na-HCO_3 type. In contrast, high salinity groundwaters with TDS concentrations of up to 19 g/L are of the Na-Cl type. In the Malm aquifer of Northern Switzerland, Na-Cl type groundwaters are almost exclusively observed in the ZNO and NL siting region. Moreover, they are closely related to Na-Cl type groundwaters from the Molasse aquifers located above (i.e. USM, OMM). Since Na-HCO_3 type waters from the Malm and the Molasse aquifers also show strong similarities, both types of Molasse groundwaters are shown together with the Malm groundwater samples (Fig. 4-104, open symbols).

The Na-Cl type groundwaters plot on or close to the seawater dilution line in the Br-Cl and Na-Cl plots (Fig. 4-104). Accordingly, they represent diluted seawater, which means that Cl and Na are of marine origin. In the stable water isotope plot, all Na-Cl type groundwaters are shifted to the right of the Global Meteoric Water Line (GMWL; Fig. 4-104), which is consistent with a non-meteoric origin. In contrast, the low-salinity groundwaters (i.e. Ca-HCO_3, Ca-Mg-HCO_3, Na-HCO_3 type groundwaters) plot on the GMWL although actual values of stable water isotopes show quite large variations with $\delta^{18}O$ ranging from -12 to -8 ‰. Values below -11 ‰, indicating meteoric water recharge during cold, glacial periods, are measured for the Na-HCO_3 type groundwaters mainly occurring in the Bodensee region (Fig. 4-105). In contrast, all Ca-HCO_3 type groundwaters display $\delta^{18}O$ values between -10 and -8 ‰ typical for recharge during climatic conditions similar to today.

The different water types are also reflected in groundwater residence times inferred from ^3H and ^{14}C activities. The Ca-HCO_3 and Ca-Mg-HCO_3 type groundwaters show significant ^{14}C activities (Fig. 4-104) and are often ^3H-bearing, indicating that meteoric water recharge occurred in the recent past. In contrast, all Na-Cl type groundwaters and some of the Na-HCO_3 type groundwaters are ^{14}C-free, suggesting a residence time of more than ca. 40 kyr.

Na-Cl type groundwaters show elevated ^{4}He concentrations up to 6×10^{-2} ccSTP/g (Fig. 4-104). Based on the low ^{4}He production rates of the Malm carbonates (Waber & Traber 2022), such ^{4}He concentrations cannot result from in-situ ^{4}He underground production over reasonable geological timescales. It follows that the ^{4}He in the Na-Cl type groundwaters is of allochthonous origin. The most likely source is the diffusive ^{4}He exchange between the Malm aquifer and the porewater of the adjacent aquitards. However, the observations that the ^{4}He concentrations in the Malm aquifer at TRU1 and MAR1 are above those in the adjacent porewater (Rufer et al. 2024) demonstrate that other ^{4}He sources are relevant as well (Ballentine & Burnard 2002). The most likely candidate is radiogenically produced ^{4}He infiltrating into the Malm aquifer along deep-reaching faults.

B) Regional groundwater systems

The different hydrochemical signatures of the Malm groundwaters in Northern Switzerland reflect different stages in their hydrogeochemical evolution. This is discussed below for the three major water types.

Ca-HCO_3 and Ca-Mg-HCO_3 type waters: Shallow groundwaters close to outcrops

The chemical composition of the Ca-HCO_3 and Ca-Mg-HCO_3 type groundwaters is almost exclusively controlled by the chemical equilibrium between water, calcite ($CaCO_3$), CO_2 and, if present, dolomite ($CaMg(CO_3)_2$). Thus, they fully reflect the carbonate-dominated mineralogical composition of the Malm aquifer (Section 4.5.3.3). In Northern Switzerland, Ca-HCO_3 type groundwaters occur at shallow depths (< 300 m) where the Malm units outcrop at the surface or where the Malm outcrops are in contact with unconsolidated rock aquifers such as at the southern margin of the Black Forest (Fig. 4-105). Accordingly, they represent the first stage of the hydrogeochemical evolution when meteoric water infiltrates into the Malm aquifer. This is consistent with short residence times inferred from the detection of ^{3}H, their high ^{14}C activities and δ^{18}O signatures overlapping with recent recharge signatures (Fig. 4-104).

The Ca-Mg-HCO_3 type waters are closely related to the Ca-HCO_3 type. As a result of the comparatively slow reaction kinetics of dolomite (Lüttge et al. 2003), significant Mg concentrations are only observed if the residence time is sufficiently high to reach equilibrium with respect to dolomite. Accordingly, Ca-Mg-HCO_3 type groundwaters reflect a slightly more evolved state than Ca-HCO_3 type groundwaters, which is consistent with their lower ^{14}C activity, less negative ^{13}C values indicating more carbon isotopic exchange with Malm carbonates, and occurrence at greater depth (Fig. 4-104).

Na-HCO_3 type waters: Ca-exchanged groundwaters in the Bodensee region

In addition to the dissolution of carbonates and CO_2, the chemical composition of Na-HCO_3 type groundwaters is controlled by Ca-exchange reactions with Na-exchanged clays (Waber & Traber 2022), resulting in excess Na and the deviation of these groundwaters from the seawater dilution line in the Na – Cl plot (Fig. 4-104). Based on the low abundance of clay minerals in the Malm aquifers, the chemical signature of Na-HCO_3 type groundwaters is a clear indication for a hydraulic communication with the above-lying clay-mineral-rich Molasse units. This is well supported by the strong hydrogeochemical similarities between Na-HCO_3 type groundwaters from the Malm and those from the Molasse aquifers (Fig. 4-104). δ^{18}O values below -11 ‰ indicate cold-time climatic recharge conditions (Fig. 4-104). Together with their low or absent ^{14}C activities (Fig. 4-104), this suggests that in the Bodensee region vertical recharge of most Na-HCO_3 groundwaters occurred during the last glaciation between 12 and 115 kyr ago (Section 6.3; Schlüchter et al. 2021).

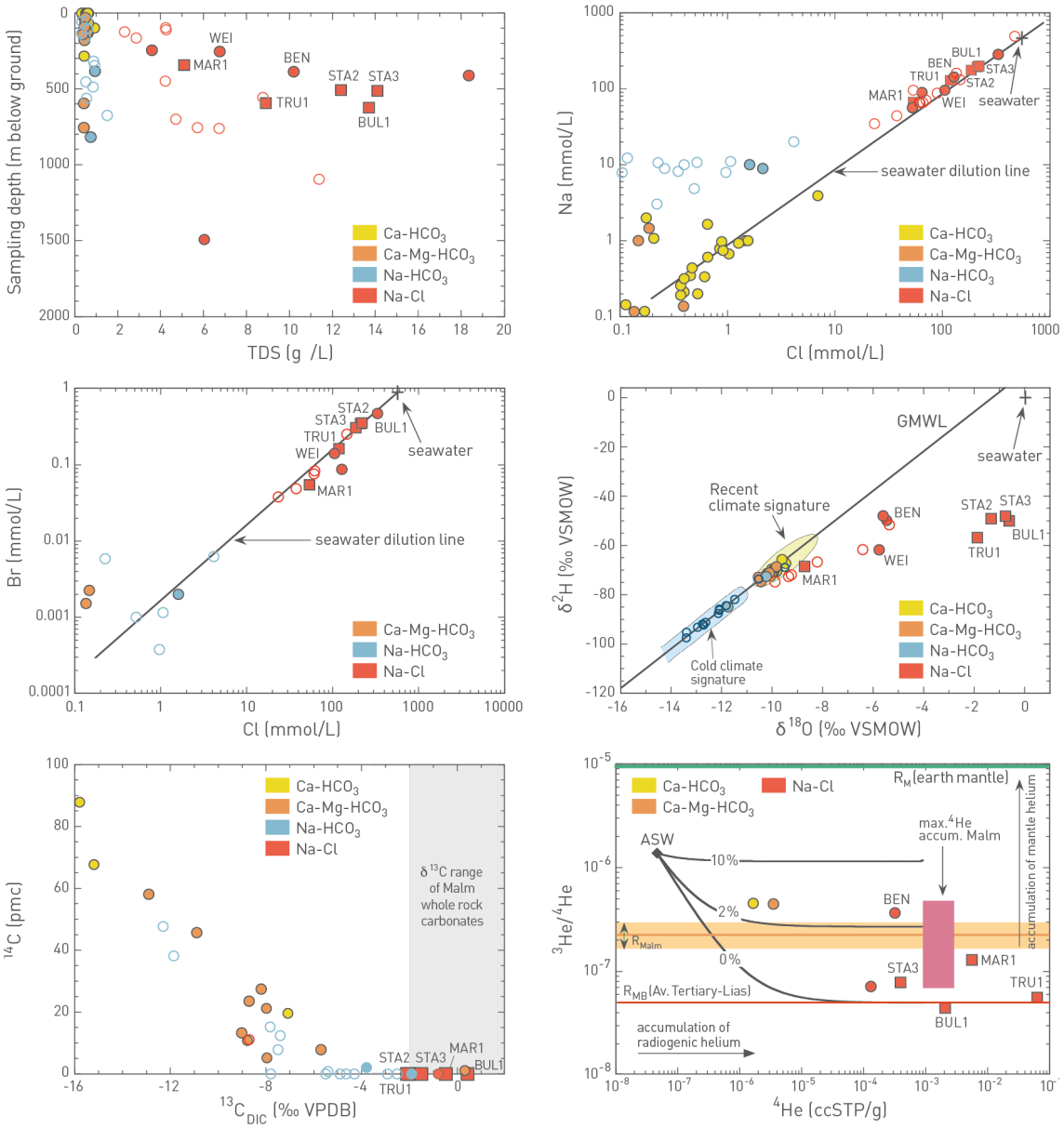


Fig. 4-104: Cross-plots illustrating the behaviour of key hydrogeochemical parameters in groundwaters collected from the Malm (closed symbols) and Molasse aquifers (open symbols) in Northern Switzerland and Southern Germany

Filled circle and square symbols represent samples reported in Waber & Traber (2022) and collected during the TBO campaign, respectively. Open circle symbols refer to samples collected from Molasse aquifers to illustrate the similarity of Na-Cl and Na-HCO_3 groundwaters collected from the Malm and Molasse aquifers. Sampling locations are only provided for the samples collected in the three siting regions.^{14}C activities are corrected for drilling mud contamination and other sampling artefacts. R_{MB}: average $^3He/^4He$ production ratio of Molasse to Lias Group sedimentary rocks in the Swiss Molasse Basin. R_{Malm}: $^3He/^4He$ ratio (average and range) in Malm limestone of the BEN, OFT and SLA1 boreholes. Max. ^4He accum. Malm: range of maximum accumulation of underground produced ^4He in porewater under closed system conditions. ASW: air-saturated water (Kipfer et al. 2002). Black lines in the He-plot indicate the behaviour of hypothetical mixtures between ASW and R_{MB} as well as different proportions of mantle helium (R_M).

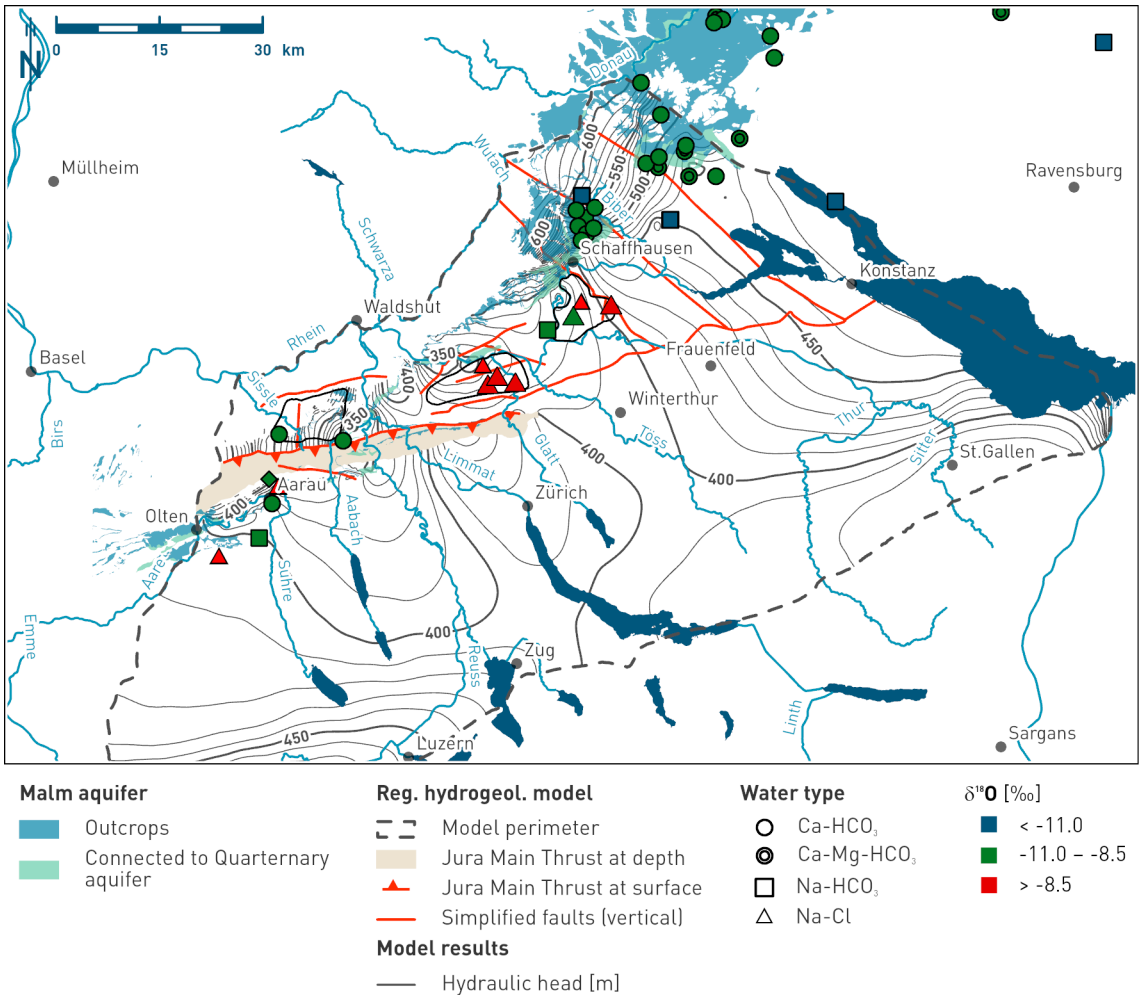


Fig. 4-105: Map showing the spatial distribution of $\delta^{18}O$ values in groundwaters collected from the Malm aquifer as an indication for the origin of the different water types

The symbols represent the water types while the colour of the fillings indicate the $\delta^{18}O$ value range of the samples. The data range of $\delta^{18}O$ of -11.0 to -8.5 ‰ VSMOW is representative for recent groundwaters of the region. Green colour denotes groundwater formed during climatic conditions similar as today in the study area. Groundwater samples marked in blue formed under colder climatic conditions. Groundwater samples marked in red ($\delta^{18}O$ > -8.5 ‰ VSMOW) contain a significant amount of a modified seawater component (see text for details). The map also shows the Malm outcrops, the simplified regional fault pattern and the hydraulic heads according to the regional hydrogeological model (Section 4.5.4.2).

Na-Cl type waters: ZNO and NL siting regions

In contrast to the Ca-HCO_3, Ca-Mg-HCO_3, and Na-HCO_3 type groundwaters, the chemical composition of the Na-Cl type groundwaters is dominated by an ancient seawater component overprinted by rock – water interaction processes. Hence, they represent the most evolved groundwaters of the Malm aquifer. In the ZNO and NL siting regions, all Malm groundwaters are of the Na-Cl type (Fig. 4-104). Accordingly, understanding its hydrogeochemical evolution is of major interest. In general, the literature agrees that Na-Cl type groundwaters in the Malm aquifers originate from marine or brackish conditions prevailing during the sedimentation of the Upper Marine Molasse Group (OMM; Waber & Traber 2022 and references therein). Based on the hydrogeochemical similarity of Na-Cl and Na-HCO_3 groundwaters from the Molasse (OMM, USM) and Malm aquifers (Fig. 4-104), the OMM seawater penetrated downwards into the USM and eventually into the Malm aquifer. This is consistent with the hydrodynamic model indicating a vertical hydraulic gradient from the Molasse (USM) down to the Malm aquifer (Section 4.5.4.2).

In the plot of the stable isotopes of water (Fig. 4-104), the Malm groundwaters from the ZNO and NL siting regions plot on a straight line to the right of the GMWL that is unable to match the composition of stable isotopes of current seawater. This suggests that they represent a mixture between an isotopically modified seawater and meteoric water. Based on the intersection of this correlation with the GMWL at a $\delta^{18}O$ value of around -10.5 ‰, the meteoric water endmember probably infiltrated during an interglacial period similar to today. The proposed mixture is confirmed by excellent linear correlations between $\delta^{18}O$ and Cl as well as $\delta^{2}H$ and Cl (Fig. 4-106). While the $\delta^{2}H$ vs. Cl correlation falls on the seawater dilution line, the $\delta^{18}O$ vs. Cl correlation is far off. This demonstrates that a process in addition to the dilution of seawater has modified $\delta^{18}O$ values. The correlations between stable isotopes of water and Cl, as well as their relation to seawater, can be explained by a three-step hydrogeochemical evolution (Fig. 4-106):

- Dilution of seawater originating from OMM times with meteoric water during its downward migration into the Malm aquifer caused a shift of $\delta^{18}O$ and $\delta^{2}H$ values from seawater towards the GMWL. The amount of dilution and hence the resulting stable isotope values and Cl concentrations are unknown. The concentration of Cl, however, was higher than the maximum value measured in the two siting regions (ca. 200 mmol/L; Fig. 4-104).
- After emplacement of the groundwater in the Malm aquifer, the diluted and $\delta^{18}O$- and $\delta^{2}H$-modified seawater chemically and isotopically interacted with the Malm carbonates. Harrison et al. (2022) showed in laboratory experiments that the rate of oxygen isotope exchange between calcite and aqueous solutions is quite high, even under ambient conditions and chemical equilibrium, causing a measurable O isotope exchange over timescales of as little as weeks to months. Given that, after emplacement in the Malm aquifer, the groundwater interacted for at least several million years with the corresponding mineral phases, the groundwater $\delta^{18}O$ values probably approached the O isotopic equilibrium with respect to calcite. Large temperature variations in the geological past (Mazurek et al. 2006), the unknown timing of the re-equilibration process, the strong temperature dependence of the oxygen isotope fractionation factor (Füger et al. 2018) and the variation of $\delta^{18}O$ values of Malm carbonates (de Haller et al. 2011, Mazurek et al. 2018) means that the $\delta^{18}O$ values after equilibration are not precisely constrained. Considering all uncertainties yields a re-equilibrated $\delta^{18}O$ value in the range from 0 to 7 ‰. In contrast to $\delta^{18}O$, $\delta^{2}H$ values are unaffected by the long-term interaction with calcite.
- The infiltration of meteoric water during an interglacial period similar to today caused the dilution of the $\delta^{18}O$ modified and diluted seawater. This eventually resulted in the observed correlations between $\delta^{2}H$ and $\delta^{18}O$, $\delta^{2}H$ and Cl, and $\delta^{18}O$ and Cl (Fig. 4-106).

The three-step model discussed above is fully consistent with the regional hydrogeological model proposed for the Malm aquifer (Section 4.5.4.2). For the northern parts of the ZNO and NL regions, the hydrogeological model implies that recharge occurs through the Malm outcrops north of the Rhine River (Fig. 4-107). Accordingly, $\delta^{18}O$ values are lower, the closer the sampling locations are to these outcrops. Based on the linear correlation between $\delta^{18}O$ and Cl (Fig. 4-106), the same applies for the Cl concentrations. It follows that the contribution of meteoric water in the groundwater mixture of the Malm aquifer increases with decreasing distance from the current recharge locations. Thus, the mixing ratio between the modified seawater and the meteoric water component is controlled by the current regional hydrogeological flow system.

Based on the lack of ^{14}C in the in-situ groundwater samples from the ZNO and NL siting regions (Fig. 4-104) and the signatures of stable water isotopes suggesting an interglacial composition similar to today, the meteoric component of the Malm groundwaters in the ZNO and NL siting regions has infiltrated in a previous interglacial period. This means that the corresponding residence time corresponds at least to the Eemian interglacial period 115 – 130 kyr ago (Preusser et al. 2011). This minimum results from the fact that the climatic signatures of cold climate recharge older than the last glaciation are likely to be masked by long-term mixing with multiple meteoric water components infiltrating under different climatic conditions, which could well be the case for the meteoric water component of the Malm groundwater in the ZNO and NL siting regions. Moreover, it should be noted that the minimum residence time estimate (115 – 130 kyr) also applies for the groundwater sample from MAR1, showing the highest contribution of the second, more recent meteoric water component of all Malm samples in the ZNO and NL siting regions.

The ^{81}Kr model ages of groundwaters collected from the two siting regions range from 143 to 608 kyr and show a linear correlation with $\delta^{2}H$ and hence with $\delta^{18}O$ and Cl (Fig. 4-106). Because the residence time of the modified seawater component from OMM times is of the order of several million years and the low solubility of Kr in seawater, the modified seawater component is probably ^{81}Kr-free. Gerber et al. (2017) have shown that, for such mixing scenarios with an ^{81}Kr-free endmember, ^{81}Kr model ages are close to the model age of the younger ^{81}Kr-bearing endmember. Accordingly, the residence time of the meteoric water component in the Malm aquifer of the ZNO and NL siting regions refers to the derived ^{81}Kr model ages. In analogy to $\delta^{18}O$ and Cl, the derived ^{81}Kr model ages are consistent with the regional hydrogeological flow model (Section 4.5.4) A comparably low ^{81}Kr model age of 148 kyr was obtained for MAR1, which is close to the Malm outcrops north of the Rhine River where recharge of meteoric water occurs (Fig. 4-107). In contrast, the highest ^{81}Kr model ages (> 519 – 608 kyr) are observed at STA2, STA3 and BUL1 where the hydraulic connection with the recharge location north of the Rhine River is poor, which fits well with a higher residence time of the diluting meteoric water component.

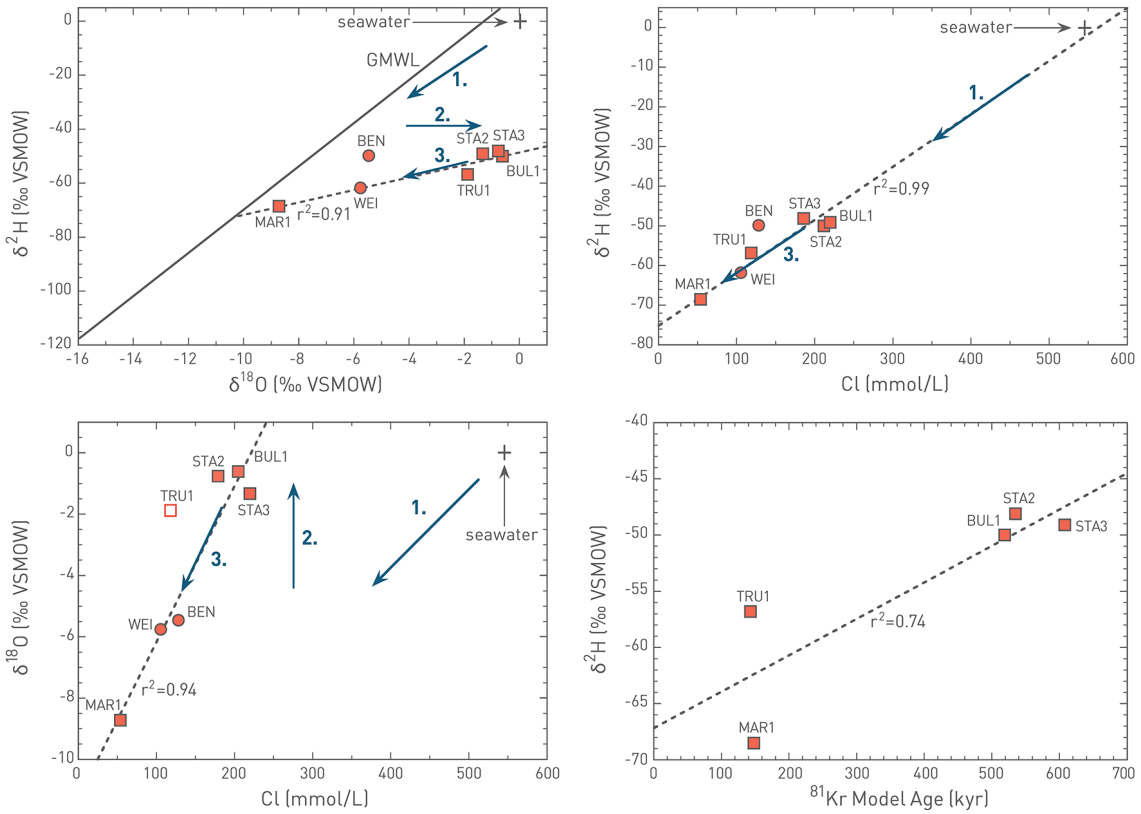


Fig. 4-106: Correlations between values of stable isotopes of water and Cl concentrations as well as ^{81}Kr model ages of Na-Cl type Malm groundwaters collected in the ZNO and NL siting regions

Circle and square symbols represent samples reported in Waber & Traber (2022) and collected during the TBO campaign, respectively. The linear correlations, plotted as dashed lines, were derived exclusively using the samples collected during the TBO campaign. The sample from TRU1 was not considered for calculating the linear correlation between $\delta^{18}O$ and Cl because it probably experienced a slightly more complex hydrogeochemical evolution. The figure illustrates the evolution of the Na-Cl type groundwaters collected in the ZNO and NL siting regions. Numbers 1. – 3. refer to the steps in the hydrogeochemical evolution of these samples as described in the text.

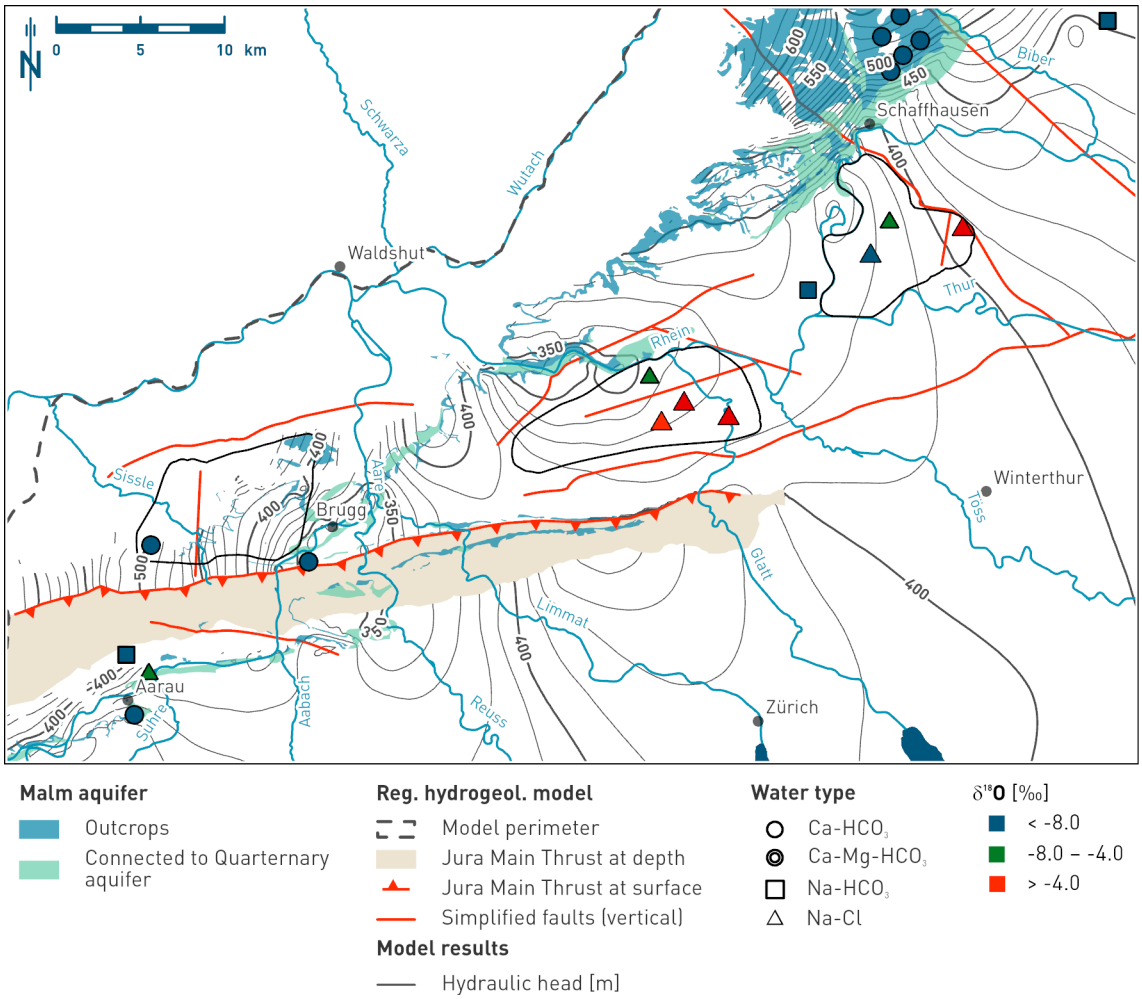


Fig. 4-107: Map showing the spatial distribution of the $\delta^{18}O$ values of the Malm groundwaters as an indication for dilution of the modified seawater component with meteoric water

The symbols represent the water types while the colour of the fillings indicates the $\delta^{18}O$ value range of the samples. Groundwater samples with a large proportion of the modified seawater component are marked in red. For Na-Cl type samples, green and blue denote samples increasingly diluted with a meteoric component. Note the different classes compared to Fig. 4-105. The map also shows the Malm outcrops, a simplified regional fault pattern, and the hydraulic head isolines according to the regional hydrogeological model (Section 4.5.4.2).

Summary for the Malm aquifer in the siting regions

In conclusion, the Malm groundwaters in the ZNO and NL siting regions represent mixtures between i) diluted and isotopically modified seawater residing at least several million years in the aquifer and ii) meteoric water that infiltrated at least 115 kyr ago probably through the Malm outcrops along the Rhine River. Based on the very high groundwater residence times observed in the siting regions, flow rates are very low, and groundwater behaves almost like a stagnant water body. This is in agreement with the small geochemical gradients between pore- and groundwater observed notably in the NL siting region (Section 4.6). In other regions where the hydraulic conductivity of the Malm aquifer is much higher because of, for example, karstification, hydrochemically less evolved groundwaters (Ca-Mg-HCO_3) are observed at the same depth as the Na-Cl water samples in ZNO and NL (Fig. 4-107). This comparison emphasises the strong control of the hydraulic conductivity on groundwater residence time and composition.

4.5.5.3 Hauptrogenstein aquifer including Birmenstorf Member

A) Hydrogeochemical characterisation and groundwater origin

As a result of the facies change from the Hauptrogenstein in the west to the clay-mineral-rich Klingnau Formation in the east (Sections 4.2.7 and 4.5.3.6), the Hauptrogenstein aquifer is only relevant for the JO siting region and groundwater samples have only been obtained west of the Aare River (Fig. 4-108). Their composition is variable, with TDS concentrations ranging from about 1 to about 11 g/L (Fig. 4-109). Shallow groundwaters in the top 300 m are of the Ca-HCO_3, Ca-Mg-HCO_3 or Na-HCO_3 type and show TDS concentrations below 1 g/L. In the investigated region, there are only two samples collected below 300 m. Both of them show much higher TDS concentrations of 5 and 11 g/L, respectively, and they are characterised as Na-SO_4 or Na-Cl type groundwaters.

In the Br – Cl plot, the deep and saline Na-Cl and Na-SO_4 type groundwaters plot on or close to the seawater dilution line (Fig. 4-109). These groundwaters represent diluted seawater, which means that Na and Cl are of marine origin with an additional SO_4 source for the Na-SO_4 type groundwater collected at BOZ2 (see below). In the stable water isotope plot, Na-Cl and Na-SO_4 type groundwaters are shifted slightly to the right of the GMWL (Fig. 4-109), which is consistent with a non-meteoric origin. In contrast, the low-salinity groundwaters (i.e. Ca-HCO_3, Ca-Mg-HCO_3 or Na-HCO_3 type waters) plot on the GMWL with values ranging between -11 and -9 ‰ typical for the infiltration of meteoric water under similar climatic conditions to today.

In the Na – Cl plot almost all groundwaters deviate from the seawater dilution line (Fig. 4-109), indicating that Ca-exchange reactions with Na-rich clay minerals are relevant for almost all Hauptrogenstein groundwaters.

Information on the groundwater residence time is only available for the deep Na-SO_4 type groundwater from BOZ2. While the sample is ^{14}C-free, the derived ^{81}Kr model age is 273 kyr. Such elevated residence times are consistent with the elevated ^{4}He concentration of 2.33×10^{-4} ccSTP/g.

B) Regional groundwater evolution

Similarly to the Malm aquifer, the different hydrogeochemical signatures of shallow and deep groundwaters reflect different stages in their hydrogeochemical evolution. While the shallow groundwaters of the Ca-HCO_3, Ca-Mg-HCO_3 or Na-HCO_3 type are mainly controlled by the dissolution of carbonates and ion exchange reactions, the composition of deep Na-Cl and Na-SO_4 type groundwaters is additionally affected by an ancient seawater component as well as a SO_4 source and hence reflect more evolved groundwaters (Fig. 4-109). With the limited dataset available for the Hauptrogenstein aquifer it is not possible to conclusively identify the origin of these additional components.

Based on their elevated residence time and the similar stable isotope shift to that observed for Na-Cl type groundwaters from the Malm aquifer (Fig. 4-109), the Na-Cl and Na-SO_4 type groundwaters may have experienced a similar hydrogeochemical evolution. Thus, deep Hauptrogenstein groundwaters from the JO siting region may contain a diluted and isotopically modified seawater component such as discussed above for the Malm aquifer. Alternatively, high concentrations of Na, Cl and SO_4 could be the result of a long-lasting exchange with porewater of the underlying aquitards. These porewaters are of marine origin and show higher concentrations of Na, Cl and SO_4 than the Hauptrogenstein groundwaters (Fig. 4-108, Fig. 4-109, Section 4.6; Nagra (ed.) 2022b, Dossier VIII, Wersin et al. 2023) causing a diffusive flux towards the Hauptrogenstein aquifer. Since cation exchange reactions occur in clay-mineral-rich aquitards, the shift of almost all groundwaters from the seawater dilution line in the Na – Cl plot may be a manifestation of the importance of such a porewater contribution.

In either case, based on the long groundwater residence times inferred from the high ^{81}Kr model ages (273 kyr) as well as the simulated tracer profiles for BOZ2 (Section 4.6), the Hauptrogenstein aquifer in the JO siting region is probably characterised by slow flow rates and a limited contribution of meteoric water that has infiltrated through the outcrops of the Hauptrogenstein in the Jura Mountains. Based on their signatures of the stable isotopes of water and the high ^{81}Kr model age, recharge occurred under climatic conditions similar to today and hence in a previous interglacial period (i.e. at least 115 kyr ago).

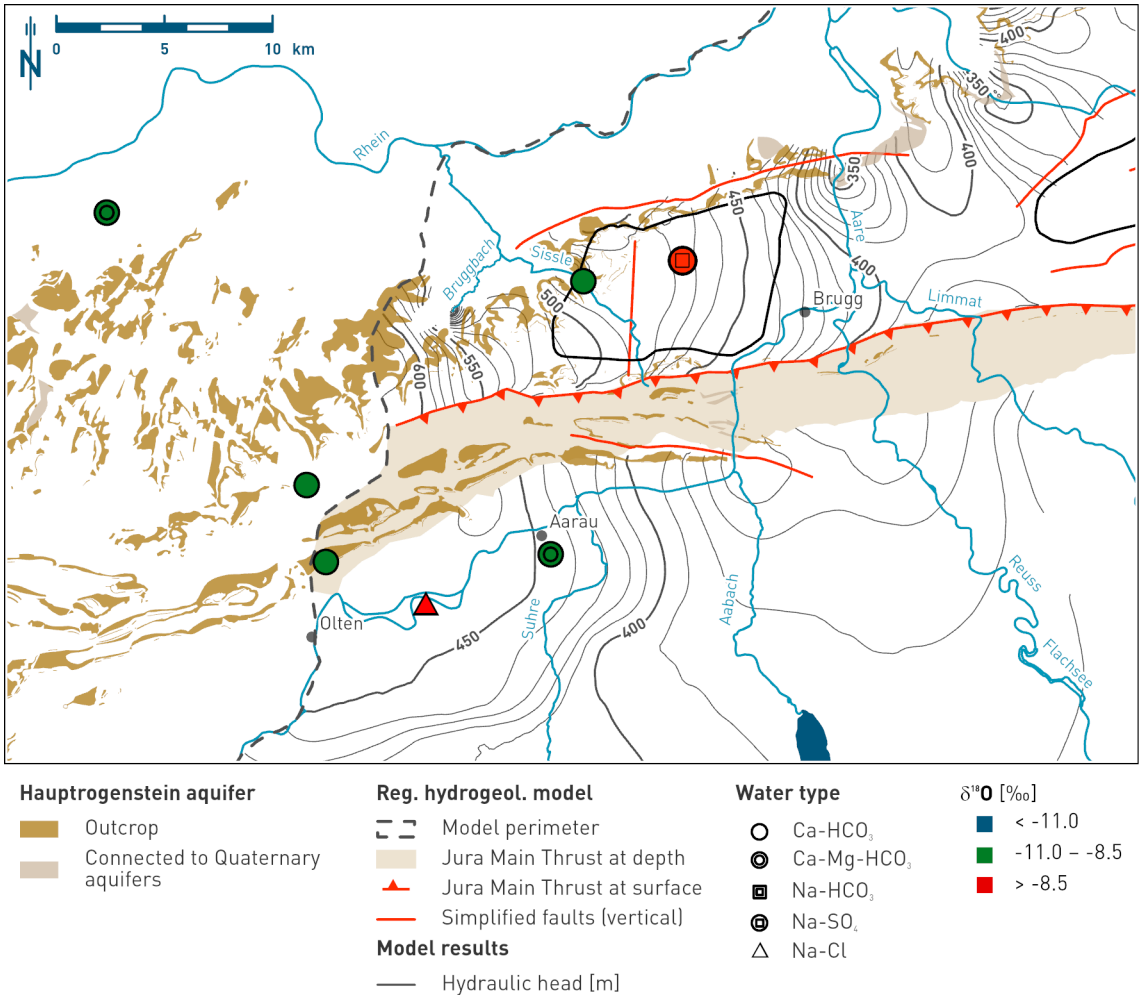


Fig. 4-108: Map showing the spatial distribution of $\delta^{18}O$ values in groundwaters collected from the Hauptrogenstein aquifer and the overlying Birmenstorf Member in Northern Switzerland

The symbols represent the water types while the colour of the fillings indicate the $\delta^{18}O$ value range of the samples (see legend). The data range of $\delta^{18}O$ of -11.0 to -8.5 ‰ VSMOW is representative for recent groundwaters of the region. Green colour denotes groundwater formed during climatic conditions similar as today in the study area. The map also shows the Hauptrogenstein outcrops, a simplified regional fault pattern, and the hydraulic head isolines according to the regional hydrogeological model (Section 4.5.4.3).

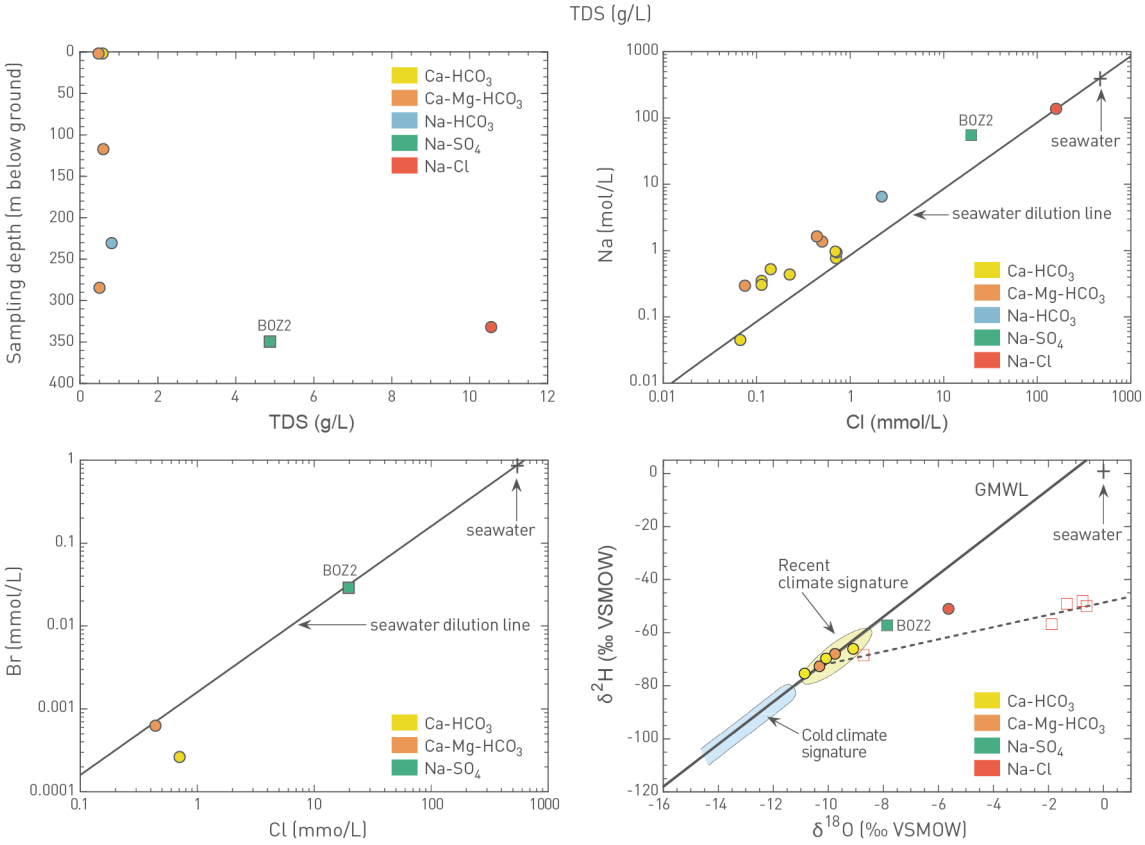


Fig. 4-109: Cross-plots illustrating the behaviour of key hydrogeochemical parameters in groundwaters collected from the Hauptrogenstein aquifer in Northern Switzerland

Circle and square symbols represent samples reported in Waber & Traber (2022) and collected during the TBO campaign, respectively. Sampling locations are provided for the samples collected in the three siting regions. For stable isotopes ($\delta^{18}O$, $\delta^{2}H$), Na-Cl type groundwaters collected from the Malm aquifer in the ZNO and NL siting regions, and the corresponding linear correlation are plotted as well (open symbols) to illustrate that deep Na-Cl and Na-SO_4 type groundwaters from the Hauptrogenstein aquifer may follow a similar trend. Samples from the overlying Birmenstorf Member are plotted as well.

4.5.5.4 Keuper aquifer

A) Hydrogeochemical characterisation and groundwater origin

Groundwater samples from the Keuper aquifer in Northern Switzerland display a marked variation in their composition, with TDS concentrations ranging from about 2 to more than 20 g/L (Fig. 4-110). Shallow groundwaters mainly occurring west of the Aare River in the Jura Mountains (Fig. 4-111) are of the Ca-SO_4 type and show TDS values below 3 g/L. Groundwaters from depths below 100 m mostly refer to the Na-SO_4 type and display TDS concentrations up to 16 g/L. The only exception is the Keuper groundwater retrieved from the BAC1 borehole, which refers to the Na-Cl type with a TDS concentration of 21 g/L.

The Ca-SO_4 type groundwaters as well as the Na-Cl groundwater from BAC1 plot close to or on the 1:1 correlation between the concentrations of Ca^{2+} and SO_4^{2-} (Fig. 4-110). This demonstrates that Ca and SO_4 in these groundwaters are mainly inherited from the dissolution of gypsum or anhydrite. In addition, these waters may show significant Mg concentrations indicating a dedolomitisation reaction where gypsum/anhydrite and dolomite dissolve and calcite precipitates. Consequently, depending on the residence time the groundwaters are at or close to saturation with calcite, dolomite and gypsum or anhydrite.

In contrast, the Na-SO_4 type groundwaters strongly deviate from the 1:1 correlation between Ca^{2+} and SO_4^{2-}. These groundwaters are controlled by processes in addition to the dissolution of anhydrite. The most likely candidate is the diffusive exchange with porewater of the above-lying aquitards coupled with cation exchange reactions in these clay-mineral-rich units. The porewaters show higher concentrations of Na and Cl than the Keuper groundwaters, causing a diffusive flux towards the aquifer (Wersin et al. 2023).

The ratios of stable isotopes of water of shallow Ca-SO_4 type groundwaters fall within the range of meteoric water infiltrating under similar climatic conditions to today. Together with significant ^3H activities of selected samples and the occurrence of Keuper outcrops in the Jura Mountains (Fig. 4-111), this indicates short residence times of a few years to a few decades. In contrast, about half of the deeper Na-SO_4 groundwaters as well as the Na-Cl type groundwater from BAC1 display signatures of stable isotopes inconsistent with recharge under current climatic conditions. The sample from RIN plots on the GMWL at higher $\delta^{18}O$ and δ^2H values than currently observed, indicating that recharge occurred during warmer climatic conditions. The samples from STA2 and BAC1 plot slightly below the GMWL (Fig. 4-110), which is probably caused by the diffusive exchange with porewater in the above-lying aquitards as described above. Based on the Br/Cl ratio, this porewater is likely of marine origin (Section 4.6.3).

With the exception of the Keuper sample from BOZ2, Na-SO_4 and Na-Cl type groundwaters show ^{81}Kr model ages ranging from 400 to 929 kyr. Inferred residence times in the order of several 100 kyr for these groundwaters compare well with their elevated ^4He concentrations and $^3He/^4He$ ratios (Fig. 4-110). Interestingly, the sample from BOZ2 shows a much lower ^{81}Kr model age of < 22 kyr, which is consistent with the ^{14}C model age of 10 – 14 kyr.

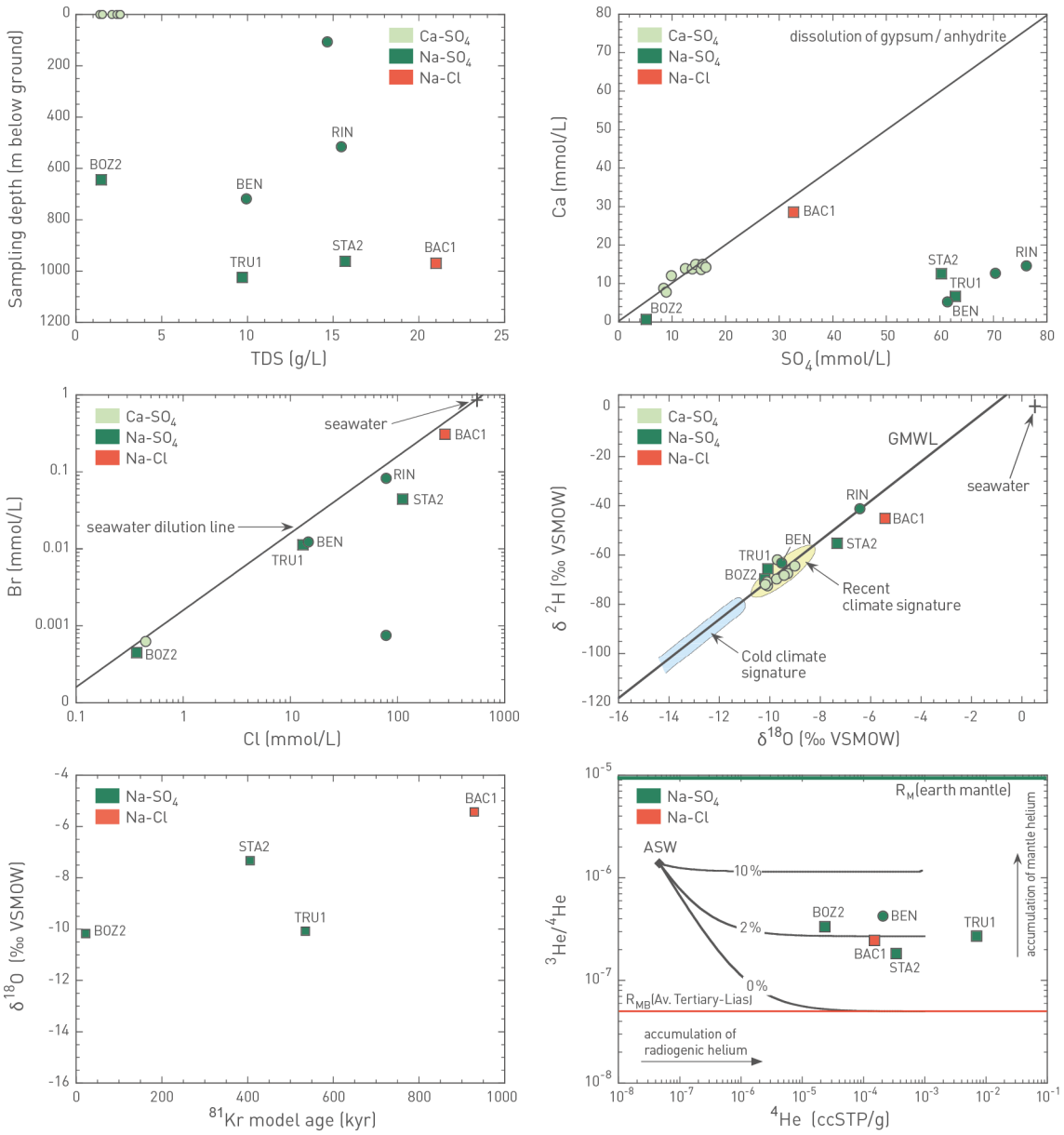


Fig. 4-110: Cross-plots illustrating the behaviour of key hydrogeochemical parameters in groundwaters collected from the Keuper aquifer in Northern Switzerland

Circle and square symbols represent samples reported in Waber & Traber (2022) and collected during the TBO campaign, respectively. Sampling locations are only provided for the samples collected in the three siting regions. Samples from hydrocarbon exploration wells in the central Molasse Basin have limited datasets and are not shown. R_{MB}: average $^3He/^4He$ production ratio of Molasse to Lias Group sediments in the Swiss Molasse Basin. ASW: air-saturated water (Kipfer et al. 2002). Black lines in the He-plot indicate the behaviour of hypothetical mixtures between ASW and R_{MB} as well as different proportions of mantle helium (R_M). The Br/Cl ratio of the groundwater from TRU1 is affected by a high uncertainty of the Br analysis.

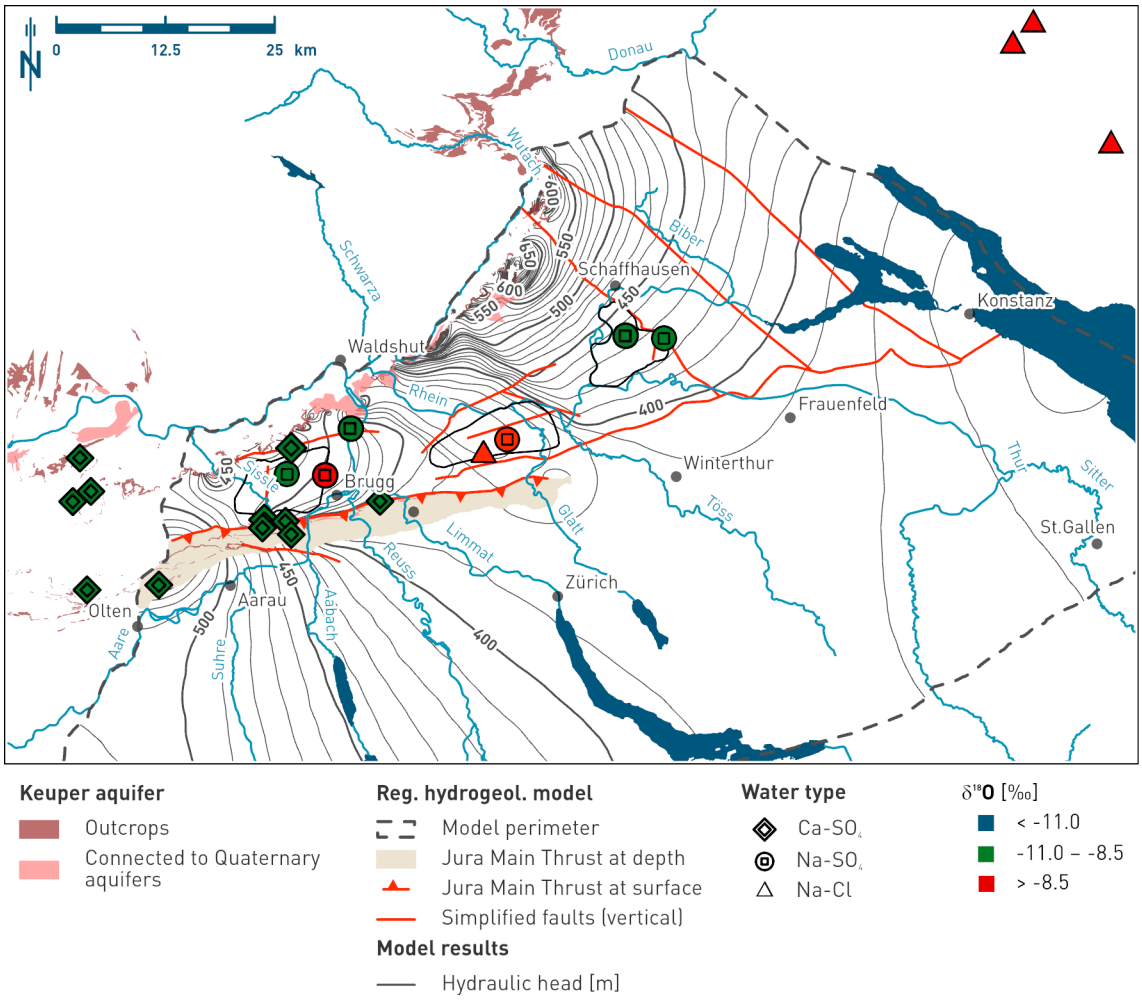


Fig. 4-111: Map showing the spatial distribution of $\delta^{18}O$ values in groundwaters collected from the Keuper aquifer as indication of the recharge conditions of the different water types

The symbols represent the water types while the colour of the fillings indicates the $\delta^{18}O$ value range of the samples (see legend). The data range of $\delta^{18}O$ of -11.0 to -8.5 ‰ VSMOW is representative for recent groundwaters of the region. Green colour denotes groundwater formed during climatic conditions similar as today in the study area. The map also shows the Keuper aquifer outcrops, a simplified regional fault pattern, and the hydraulic head isolines according to the regional hydrogeological model (base case model, Section 4.5.4.4).

B) Regional groundwater evolution

The different hydrogeochemical signatures of the Keuper groundwaters in Northern Switzerland reflect different stages in their hydrogeochemical evolution. This is discussed below for four major groups of water types representing shallow groundwater close to outcrops as well as deep groundwater in the three siting regions.

Ca-SO_4 type groundwaters: Shallow groundwater close to outcrops

These groundwaters are controlled by the dissolution of gypsum and/or anhydrite present in the Bänkerjoch Formation (Section 4.5.3.11) or in the Klettgau Formation. Accordingly, the Ca-SO_4 type groundwaters represent the first stage of the hydrogeochemical evolution when meteoric water infiltrates into the Keuper aquifer. This is consistent with short residence times inferred from the detection of ^{3}H and stable isotope signatures overlapping with recharge signatures observed today.

Na-SO_4 type groundwaters without stable isotope shift: Deep groundwater in the ZNO siting region

In the ZNO siting region, groundwater samples from the Keuper aquifer were retrieved from the TRU1 and BEN boreholes. Both samples are of Na-SO_4 type and show a stable isotope signature consistent with recharge under similar climatic conditions to today (Fig. 4-110). Moreover, the chemical composition of the two samples is very similar. In addition to the dissolution of anhydrite, these groundwaters are controlled by the diffusive uptake of Na and Cl from the porewater of the above-lying aquitards. The strong hydrogeochemical similarity of the two samples suggests that, in the ZNO siting region, the Keuper operates as a well-connected aquifer. This is consistent with the observation that, in this region, the Seebi Member regionally occurs as dolomitic breccia with frequent macropores, probably causing the high transmissivities observed in the Klettgau Formation of the BEN and TRU1 boreholes (Sections 4.5.3 and 4.2). Additional evidence for a regionally well-connected Keuper aquifer is provided by the tracer profiles along the MAR1, TRU1 and BEN drill cores, all showing strong concentration gradients between the Keuper aquifer and porewater of the above-lying aquitards (Section 4.6), typical for a single hydraulic activation of the aquifer. Despite these observations, the flow velocities appear to be very slow based on the relatively high ^{81}Kr model age of the TRU1 groundwater (535 kyr; Fig. 4-110), which is consistent with the corresponding porewater tracer simulations suggesting an activation of the aquifer some 650 kyr ago (Section 4.6.2).

Na-SO_4 and Na-Cl type groundwater with stable isotope shift: Deep groundwaters in the NL siting region

In the NL siting region, groundwater samples from the Keuper aquifer were retrieved from the boreholes STA2 and BAC1. While the sample from STA2 is of Na-SO_4 type, the one from BAC1 relates to Na-Cl type. In contrast to the two samples from the ZNO siting region, their stable isotope composition is shifted to the right of the GMWL, suggesting diffusive uptake of ^{2}H and ^{18}O with a marine signature from the porewater of the above-lying aquitards, in addition to the uptake of Na and Cl. Accordingly, the Keuper groundwaters in the NL region represent a hydrogeochemically more evolved state than those from the ZNO siting region. This is probably caused by the fact that Keuper groundwater samples in NL were retrieved from individual sandstone channels of the Ergolz Member (Sections 4.5.3.10), which probably does not represent a well-connected regional aquifer. Consequently, the tracer profiles of the STA2 and particularly BAC1 boreholes show lower concentration gradients between the Keuper groundwater and porewater of the above-lying aquitards than the corresponding profiles in the ZNO siting region (Section 4.6). Despite the different hydrogeochemical signature, the ^{81}Kr model ages of Keuper groundwaters from the ZNO and NL siting regions are in the same order of magnitude (406 – 929 kyr; Fig. 4-110). This may result from a younger, ^{81}Kr-bearing water component of similar mean residence time in both siting regions but different mixing proportions with an older, ^{81}Kr-free and more saline component (higher contribution of the more saline component in NL than in ZNO).

Na-SO_4 type groundwaters without stable isotope shift but strongly contrasting signature: Deep groundwater in the JO siting region

In the JO siting region, groundwater samples from the Keuper aquifer could be retrieved from the RIN and BOZ2 boreholes. Both samples are of the Na-SO_4 type, display similar Ca/SO_4 and Br/Cl ratios close to the anhydrite dissolution and seawater dilution trends, respectively, and their stable isotope signatures fall on the Global Meteoric Water Line GMWL (Fig. 4-110). Besides these similarities, there are notable differences despite the two boreholes being located only about 5 km apart. The most prominent ones include a much higher TDS concentration of the RIN sample and a corresponding stable isotope signature, which is inconsistent with the infiltration of meteoric water under current climatic conditions. Based on the chemical similarity but much lower salinity (RIN: 15 g/L; BOZ2: 1.5 g/L), the groundwater from BOZ2 can be interpreted as a strongly diluted version of the RIN sample. Consequently, the Keuper aquifer at BOZ2 is probably much more active hydraulically than at RIN. This is consistent with ^{14}C and ^{81}Kr model ages of < 14 kyr and < 22 kyr, respectively, as well as the signature of stable isotopes, suggesting that the diluting water component infiltrated in the current Holocene interglacial period. The large presence of a young groundwater component at BOZ2 also agrees well with high tracer concentration gradients between the Keuper groundwater and porewater of the above-lying aquitards in the corresponding tracer profiles (Section 4.6) and may relate to groundwater from the outcrops to the north of BOZ2. It follows that there are almost stagnant conditions at RIN, while at BOZ2 the Keuper aquifer appears to be much more active hydraulically.

Summary of the Keuper aquifer in the siting regions

The Keuper aquifer represents spatially limited and partly isolated local aquifers with often quasi-stagnant conditions, as manifested by the fact that, in the three siting regions, Keuper groundwater could only be retrieved from about half of the deep boreholes. The isolated and local nature is linked to the local lithofacies (Section 4.5.3.10) of the potential transmissive layers.

In the JO siting region, the hydrogeochemical data evidence large differences in flow dynamics between BOZ2 and RIN. The characteristics of the RIN sample point to high residence times. The BOZ2 sample is more dilute and has a ^{81}Kr model age < 22 kyr. Overall, these characteristics agree with the general NW-SE flow direction suggested by the hydrodynamic model (Fig. 4-111).

In the NL siting region, groundwater could only be sampled in 2 out of 5 boreholes. Both samples are characterised by high ^{81}Kr model ages (STA2 406 and BAC1 929 kyr) but distinct chemical differences. Their stable isotope composition is shifted to the right of the GMWL, suggesting diffusive uptake from the porewater of the above-lying aquitards. This exchange is particularly evolved in the case of BAC1. Overall, these are hydrogeochemically highly evolved groundwaters pointing to quasi-stagnant conditions.

In the ZNO siting region, the groundwater samples from BEN and TRU1 have similar hydro-chemical composition and plot on the Global Meteoric Water Line in the range of recent groundwaters. The similarity is in agreement with a well-connected aquifer in this siting region. However, the ^{81}Kr model age of the TRU1 groundwater (535 kyr) point to very low flow velocities.

4.5.5.5 Muschelkalk aquifer

A) Hydrogeochemical characterisation and groundwater origin

Groundwater samples from the Muschelkalk aquifer in Northern Switzerland and adjacent areas display very large variations in their composition, with TDS concentrations ranging from 0.5 to 156 g/L (Fig. 4-112). Groundwaters with TDS concentrations above 8 g/L are of Na-Cl type. If the TDS concentration is between 2 and 8 g/L, groundwaters are mainly of Ca-SO_4 type. Exceptions are the thermal waters of the Baden/Ennetbaden and Schinznach Bad groups and the groundwater from the Schlattingen-2 borehole (SLA2), which are of [Na/Ca]-[SO_4/Cl] type. Groundwaters with TDS concentrations below 2 g/L are of Ca-HCO_3 or Ca-[Mg]-[HCO_3/SO_4] type.

All groundwaters plot on or close to the 1:1 correlation between the concentrations of alkaline earth metal cations (Ca^{2+} + Mg^{2+}) and SO_4^{2-} (Fig. 4-112). This indicates that Ca and SO_4 are mainly inherited from the dissolution of gypsum in the recharge areas and anhydrite at greater depth in the aquifer (Section 4.5.3), resulting in a typical dedolomitisation scenario where gypsum/anhydrite and dolomite ($CaMg(CO_3)_2$) dissolve while calcite precipitates. Consequently, the Muschelkalk groundwaters are at, or are close to, saturation with respect to calcite, dolomite and gypsum/anhydrite.

Compared to seawater, the Na-Cl type groundwaters display an excess of Cl over Br and hence strongly deviate from the seawater dilution line (Fig. 4-112). In addition, the groundwater collected in the BUL1 borehole displays a TDS concentration of 145 g/L, strongly exceeding that of seawater (Fig. 4-112). These observations demonstrate that the Na-Cl signature is because of the dissolution of halite occurring in the Zeglingen Formation, ca. 100 m below the Muschelkalk aquifer (Section 4.2) and not from a seawater-like water component such as described above for the Malm aquifer. This is consistent with the observation that, in terms of stable water isotopes, all Muschelkalk groundwaters plot on or very close to the GMWL, confirming the meteoric origin of these groundwaters (Fig. 4-112).

The different water types are also reflected in groundwater residence times inferred from ^3H and ^{14}C activities. The Ca-HCO_3 and Ca-[Mg]-[HCO_3/SO_4] type groundwaters are ^3H-bearing and show ^{14}C activities generally above 15 pmC (Fig. 4-112), suggesting that meteoric water recharge occurred in the recent past. This is consistent with the signature of stable isotopes in these groundwaters, which fall within the range of meteoric water for today's climatic conditions (Fig. 4-112). Most of the Ca-SO_4, [Na/Ca]-[SO_4/Cl] and Na-Cl type groundwaters show corrected ^{14}C activities below 15 pmC. In the case of the groundwater sample from STA2, it is below detection. This is consistent with $\delta^{18}O$ values below -11 ‰ of groundwaters collected in the ZNO and NL siting regions, indicating that meteoric water recharge occurred during a cold glacial period (Fig. 4-113). It follows that, in these two siting regions, Muschelkalk groundwaters infiltrated during the last glacial cycle (i.e. 12 – 115 kyr ago; Schlüchter et al. 2021).

Helium analyses are available for the Ca-SO_4, [Na/Ca]-[SO_4/Cl] and Na-Cl type groundwaters. The Ca-SO_4 type groundwaters show ^4He concentrations ranging from 10^{-7} to 10^{-5} ccSTP/g (Fig. 4-112). In groundwaters of the other two types ([Na/Ca]-[SO_4/Cl] and Na-Cl), ^4He concentrations are up to two orders of magnitude higher, with the highest concentration being measured at BOZ2. In terms of $^3He/^4He$ ratios, all groundwaters from the three siting regions show elevated values above those of the Mesozoic sedimentary rocks, indicating the presence of a few percent of mantle-derived He.

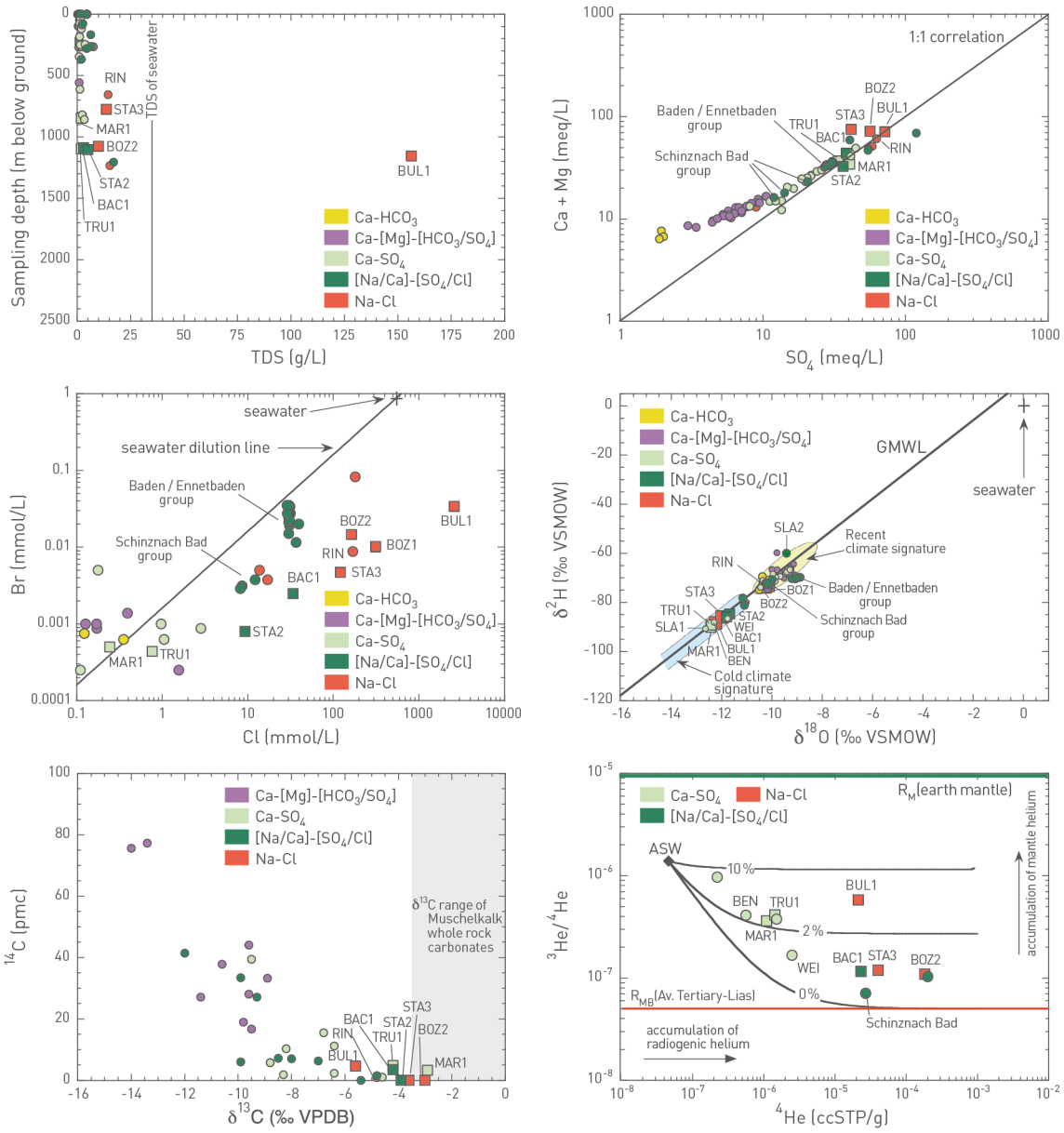


Fig. 4-112: Cross-plots illustrating the behaviour of key hydrogeochemical parameters in groundwaters collected from the Muschelkalk aquifer in Northern Switzerland and Southern Germany

Filled circle and square symbols represent samples reported in Waber & Traber (2022) and collected during the TBO campaign, respectively. Sampling locations are only provided for the samples collected in the three siting regions as well as those from the Baden and Bad Schinznach geothermal areas to emphasise that these all relate to [Na/Ca]-[SO_4/Cl] type groundwaters. Samples from hydrocarbon exploration wells in the central Molasse Basin have limited datasets and are not shown. ^{14}C activities are corrected for drilling mud contamination and other sampling artefacts. R_{MB}: average $^3He/^4He$ production ratio of Molasse to Lias Group sedimentary rocks in the Swiss Molasse Basin. ASW: air-saturated water (Kipfer et al. 2002). Black lines in the He-plot indicate the behaviour of hypothetical mixtures between ASW and R_{MB} as well as different proportions of mantle helium (R_M).

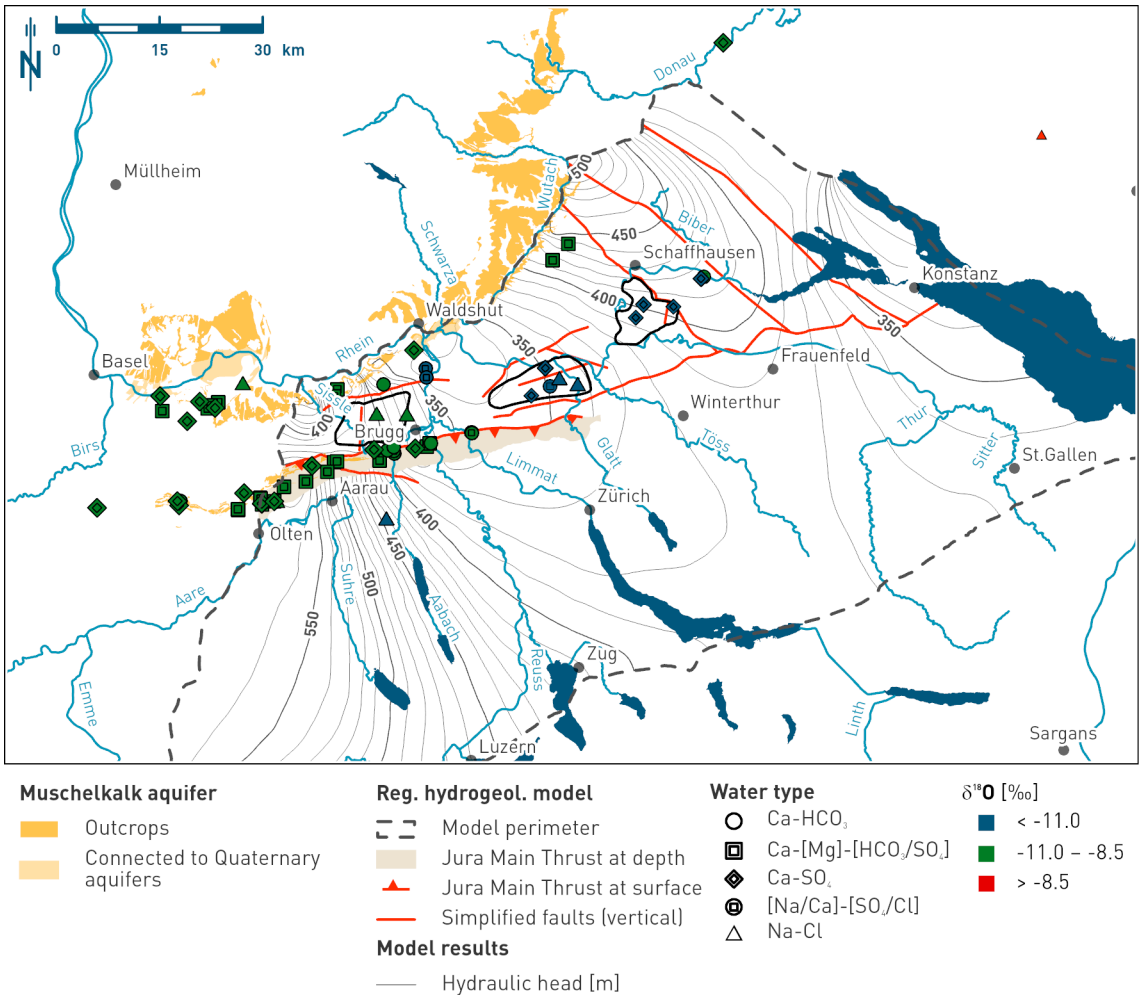


Fig. 4-113: Map showing the spatial distribution of $\delta^{18}O$ values in groundwaters collected from the Muschelkalk aquifer as indication of the recharge conditions of the different water types

The symbols represent the water types while the colour of the fillings indicates the $\delta^{18}O$ value range of the samples (see legend). The data range of $\delta^{18}O$ of -11.0 to -8.5 ‰ VSMOW is representative for recent groundwaters of the region. Green colour denotes groundwater formed during climatic conditions similar as today in the study area. Groundwater samples marked in blue formed under cold climatic conditions. The map also shows the outcrops of the Muschelkalk aquifer, a simplified regional fault pattern and the hydraulic head isolines according to the regional hydrogeological model (Section 4.5.4.5).

B) Regional groundwater evolution

The different hydrogeochemical signatures of the Muschelkalk groundwaters in Northern Switzerland reflect different stages in their hydrogeochemical evolution. This is discussed below for the three major groups of water types.

Ca-HCO_3 and Ca-[Mg]-[HCO_3/SO_4] type groundwaters: Shallow groundwaters close to outcrops

In Northern Switzerland, Ca-HCO_3 and Ca-[Mg]-[HCO_3/SO_4] type groundwaters occur at relatively shallow depths where the Muschelkalk units outcrop at the surface or where they are in contact with Quaternary gravel aquifers such as at the southern margin of the Black Forest or north of the Aare River in the Jura Mountains (Fig. 4-113). They represent the first stage of the hydrogeochemical evolution when meteoric water infiltrates into the Muschelkalk aquifer. This is consistent with their short residence times inferred from ^{3}He and ^{14}C activities as well as their $\delta^{18}O$ signatures, which fall within the range of meteoric water infiltrating under similar climatic conditions to today (Fig. 4-112). High recharge rates through the Muschelkalk outcrops and the high solubility of gypsum probably lead to a depletion of gypsum with time. Accordingly, these groundwaters deviate from the 1:1 correlation between alkaline earth metal cations (Ca^{2+} + Mg^{2+}) and SO_4^{2-} (Fig. 4-112), and their chemical composition is mainly controlled by the dissolution of calcite and dolomite with a variable contribution from the dissolution of gypsum or anhydrite.

Ca-SO_4 and [Na/Ca]-[SO_4/Cl] type groundwaters: ZNO and NL siting regions

Compared to the Ca-HCO_3 and Ca-[Mg]-[HCO_3/SO_4] type groundwaters, the chemical composition of Ca-SO_4 groundwaters is more strongly controlled by the dissolution of anhydrite/ gypsum and dolomite as well as the precipitation of calcite as manifested by the 1:1 correlation of alkaline earth metal cations (Ca^{2+} + Mg^{2+}) and SO_4^{2-} (Fig. 4-112). They represent a more evolved state, which is consistent with their lower ^{14}C activity and less negative ^{13}C values, indicating more carbon isotope exchange with Muschelkalk carbonates (Fig. 4-112). Stable isotope ratios in Ca-SO_4 and [Na/Ca]-[SO_4/Cl] type groundwaters from the ZNO and NL siting regions show strong linear correlations with a series of other hydrogeochemical parameters including ^{81}Kr model ages, $^{87}Sr/^{86}Sr$ ratios, as well as Li and Cl concentrations (Fig. 4-114). Accordingly, they imply that the Muschelkalk groundwaters in the ZNO and NL siting regions represent a mixture of at least two components:

- A younger meteoric water component of Ca-SO_4 type characterised by $\delta^{18}O$ values below -12.5 ‰ typical for cold climatic recharge conditions, non-radiogenic $^{87}Sr/^{86}Sr$ ratios below 0.7083 and Li and Cl concentrations below 0.2 and 5 mmol/L, respectively. This is the major component (> 80%).
- An older meteoric water component of Na-Cl type characterised by $\delta^{18}O$ values above ca. -9 ‰, radiogenic $^{87}Sr/^{86}Sr$ ratios above 0.7150 and higher Li and Cl concentrations than the meteoric water component described above (i.e. above 0.2 and 5 mmol/L, respectively).

The second component may indicate a contribution from deeper aquifers, e.g. a groundwater similar to the WEI sample from the crystalline basement (Fig. 4-114). This component may i) still ascend along faults or ii) be present in the matrix porewater with an origin related to earlier cross-formation flow under different geodynamic conditions (Fig. 4-115). Note that similar observations have previously been used to postulate upwelling of groundwater from the crystalline basement into the Muschelkalk aquifer north of the Bodensee (Stober et al. 2023) and that, in the two Schlattingen (SLA1 and SLA2) boreholes, the sample from close to the Randen Fault

indicates higher $\delta^{18}O$ and chloride as well. It is important to note here that the most mineralised groundwater from BUL1 (Na-Cl type) is affected by salt dissolution but is devoid of particular indications of a basement component (see separate discussion below).

The mixing model discussed above is fully consistent with the regional hydrogeological model for the Muschelkalk aquifer in the ZNO and NL siting regions. Fig. 4-116 shows that $\delta^{18}O$ values increase with increasing distance from the Muschelkalk outcrops along the SE margin of the Black Forest in Southern Germany (e.g. Wutach Valley) probably operating as the main recharge location of the younger meteoric water component. Based on their linear correlations with $\delta^{18}O$ values (Fig. 4-114), the same applies to the ^{81}Kr model ages, the $^{87}Sr/^{86}Sr$ ratios and the concentrations of Li and Cl. The proportion of the younger meteoric water component decreases along the groundwater flow path inferred from the regional hydraulic flow model (Fig. 4-116). In contrast, the proportion of the older meteoric water component increases, although in most cases it never reaches more than a few percent based on the correlations shown in Fig. 4-114. The strong spatial control of the proportion of the two water components demonstrates that the Muschelkalk aquifer in the ZNO and NL siting regions represents a large and regionally well-connected aquifer. This is in strong contrast to the other deep aquifers such as the Malm aquifer where the flow rates are much slower and almost stagnant conditions prevail. The differences occur because the transmissivity of the Muschelkalk aquifer is higher (Fig. 4-86). In addition, the hydraulic head gradient is higher because the Muschelkalk outcrops on the southern margin of the Black Forest occur at a higher altitude than those of the Malm aquifer (Fig. 4-105 vs. Fig. 4-113).

While ^{14}C activities, ^{81}Kr model ages and $\delta^{18}O$ values are fully consistent with recharge of the younger meteoric water component during the last glaciation period (12 – 115 kyr), the residence time of the older meteoric water component is less constrained. Based on the inferred endmember $\delta^{18}O$ value around -8.5 ‰ indicating climatic conditions similar to today and the increase in ^{81}Kr model ages with increasing contribution of this water component, the corresponding minimum residence time relates to the previous Eemian interglacial period some 115 – 130 kyr ago (Preusser et al. 2011). However, the residence time of this water component could be much higher. Unfortunately, there are no ^{81}Kr analyses available for the groundwaters from SLA2 and WEI to better constrain the residence time of this second, upwelling groundwater component. Also, it remains unclear whether the vertical connection between the Muschelkalk aquifer and the underlying crystalline units is still active today. Alternatively, the recharge of the younger meteoric water component during the last glaciation period (12 – 115 kyr ago) could have caused the displacement of the older one, which may have infiltrated into the Muschelkalk aquifer along deep-reaching faults a long time ago. Overall, the strong linear correlation between $\delta^{18}O$ values and the ^{81}Kr model ages (Fig. 4-114) suggests that the older meteoric water component is Kr-bearing and that the ^{81}Kr model ages reflect the mean residence time of the mixture of the two components.

Na-Cl type groundwaters in NL siting region

The composition of Na-Cl type groundwaters in the NL siting region (particularly BUL1; Fig. 4-112) is mainly controlled by the dissolution of halite (NaCl) locally occurring in the Zeglingen Formation, around 100 m below the Muschelkalk aquifer (Section 4.2). Such dissolution does not affect hydrogeochemical parameters other than the concentrations of Na and Cl and the Br/Cl ratio, thus these groundwaters have simply experienced an additional chemical process in comparison to the Ca-SO_4 and [Na/Ca]-[SO_4/Cl] type groundwaters described above. Their hydrogeochemical evolution, however, could be very similar. This is manifested in the ZNO and NL siting regions where the Na-Cl type groundwaters plot on the same correlations between $\delta^{18}O$ and other hydrogeochemical parameters (Fig. 4-114) and thus belong to the same regional flow system.

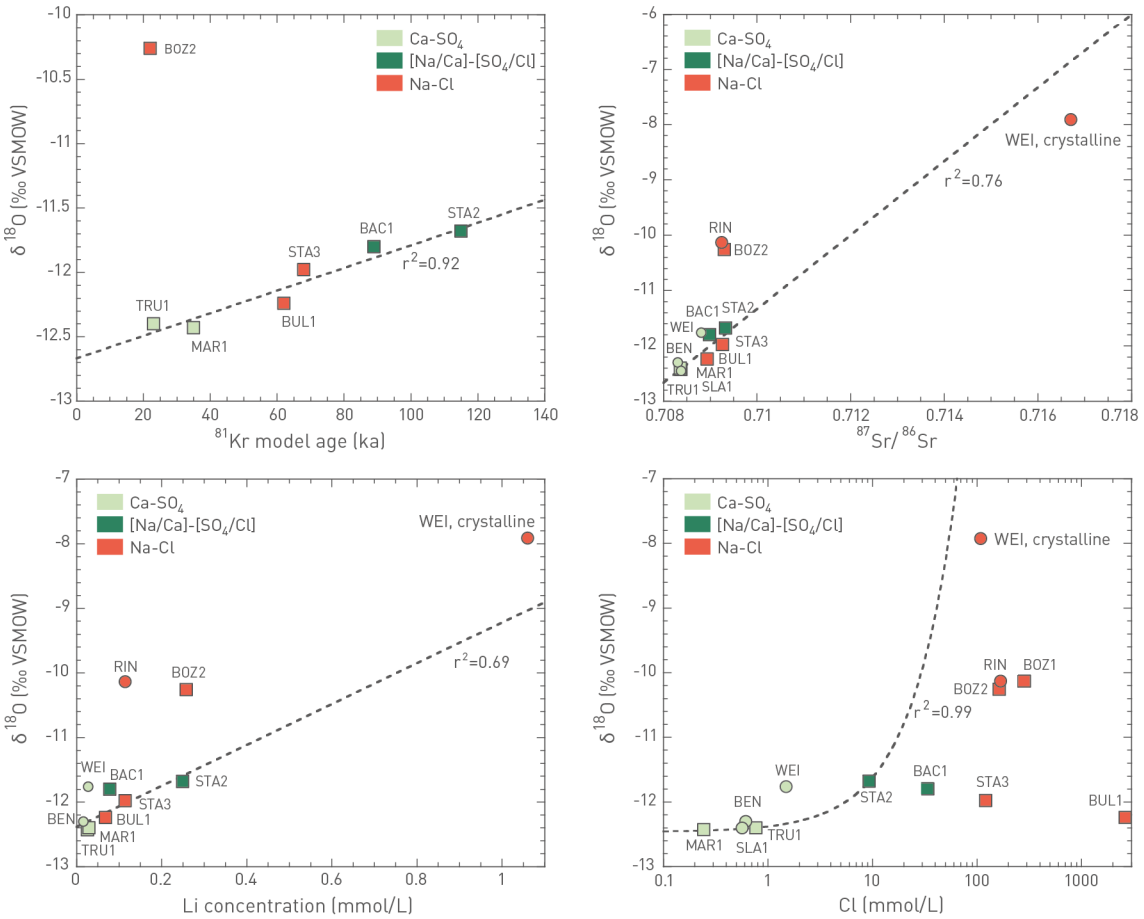


Fig. 4-114: Correlations between $\delta^{18}O$ values and selected other parameters of Muschelkalk groundwaters collected in the siting regions as well as comparison to a potential endmember of the mixing trend (WEI, crystalline)

Circle and square symbols represent samples reported in Waber & Traber (2022) and collected during the TBO campaign, respectively. The linear correlations, plotted as dashed lines, were derived using the samples collected during the TBO campaign in the NL and ZNO siting regions. For the $\delta^{18}O$ vs. Cl correlation, the Na-Cl type Muschelkalk groundwaters were not used because they are affected by the local dissolution of halite. Also discarded was the [Na/Ca]-[SO_4/Cl] type groundwater collected from the BAC1 borehole because it is also likely affected by local halite dissolution.

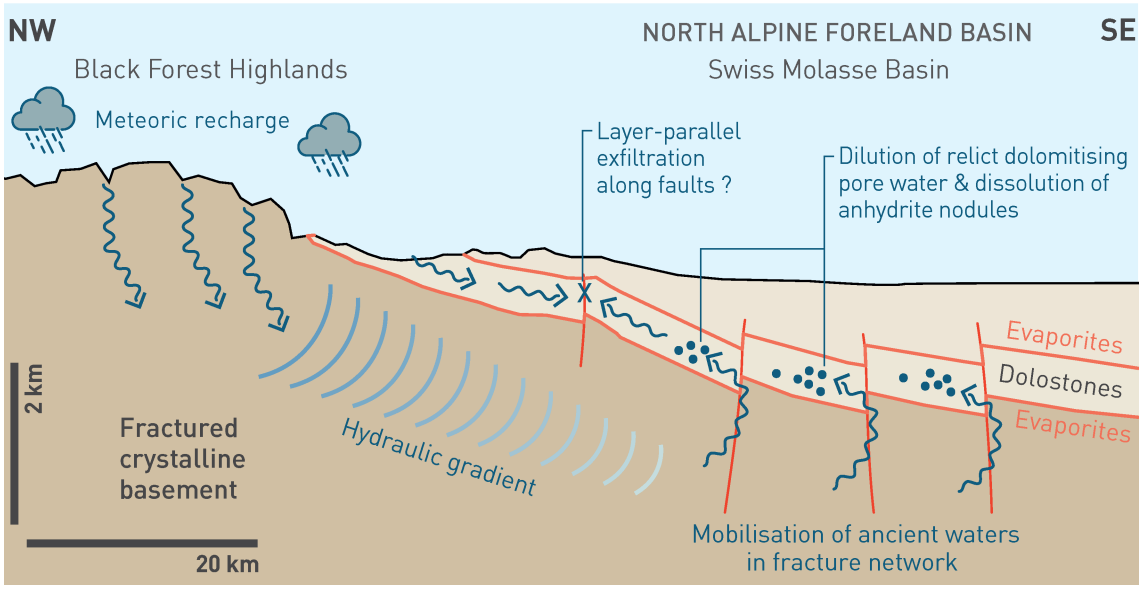


Fig. 4-115: Sketch illustrating the upwelling of groundwater from the crystalline basement into the Muschelkalk aquifer along regional fault zones some 8 – 13 Myr ago

Modified from Aschwanden et al. (2019b).

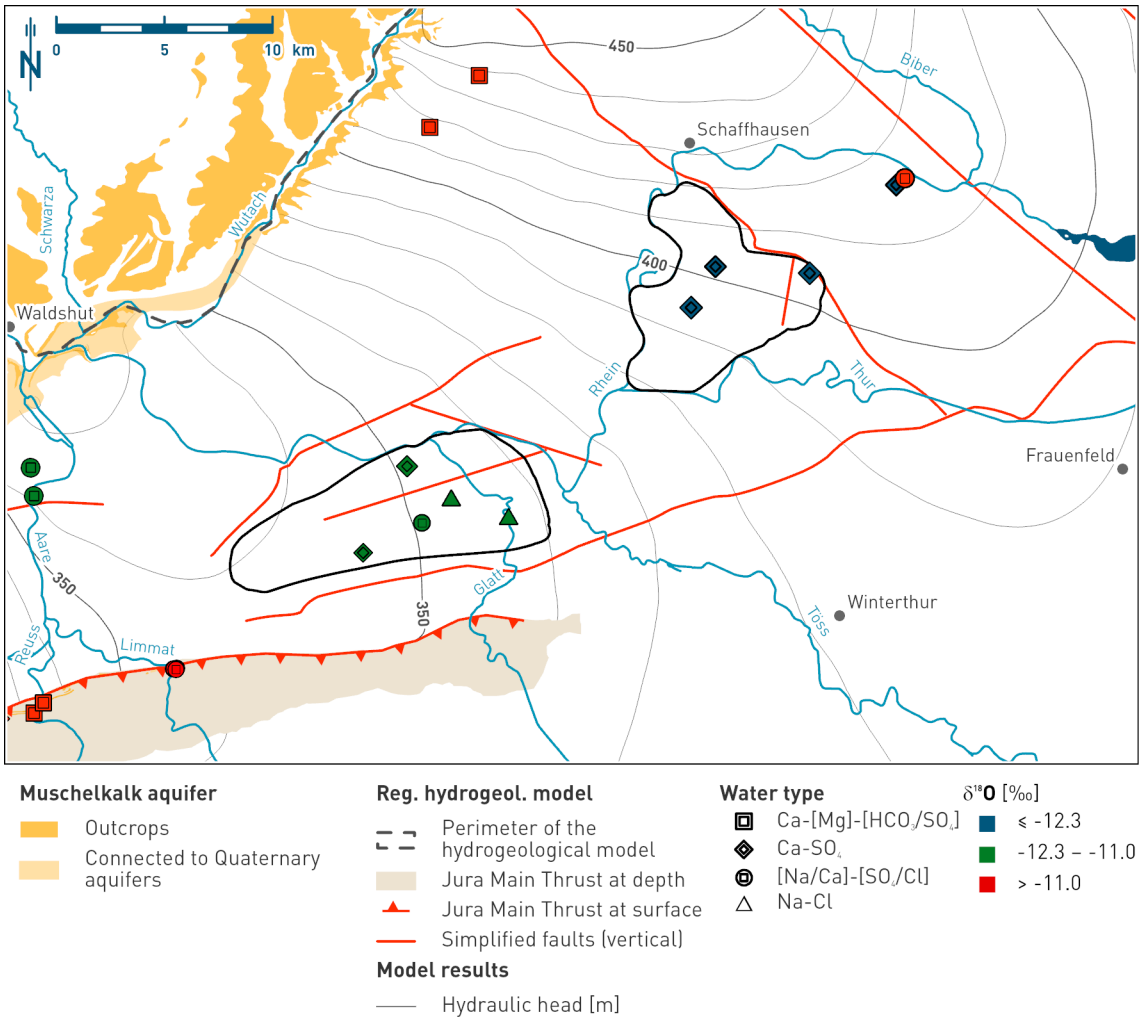


Fig. 4-116: Map showing the distribution of the $\delta^{18}O$ values in groundwaters of the Muschelkalk aquifer as manifestation of the regional groundwater flow system in the ZNO and NL siting regions

The general flow direction is illustrated in Fig. 4-102. The symbols represent the water types while the colour of the fillings indicates the $\delta^{18}O$ value range of the samples (note the different classes compared to Fig. 4-113). The map illustrates the evolution from the particularly negative isotopic composition of the groundwater in the ZNO area to less negative values in NL (see text for details). The map also shows the Muschelkalk outcrops, a simplified regional fault pattern and the hydraulic head isolines according to the regional hydrogeological model (Section 4.5.4.5).

Na-Cl type groundwaters in the JO siting region

All groundwaters from the JO siting region are of Na-Cl type (Fig. 4-112), which may be explained by a saline component reaching the Muschelkalk aquifer probably along the Jura Main Thrust south of the JO siting region. Based on strongly contrasting $\delta^{18}O$ values and the lack of correlations with other chemical parameters plotted in Fig. 4-114, they have probably experienced a contrasting hydrogeochemical evolution than the Muschelkalk groundwaters in the NL and ZNO siting regions. Hence, they do not belong to the same flow system as the one active in the ZNO and NL siting regions (Section 4.5.4.5) suggesting that, in the JO siting region, recharge occurs through the outcrops in the Jura Mountains to the south and not along the SE margin of

the Black Forest as for the other two siting regions (Fig. 4-113). In addition, based on the ^{81}Kr and ^{14}C model ages of the BOZ2 sample of less than 22 kyr and 14 kyr, respectively, also the mean groundwater residence time in the JO siting region may be quite different. Together with the $\delta^{18}O$ value of around -10 ‰, these model ages point towards recharge occurring in the current Holocene interglacial period. Accordingly, the flow system in the Muschelkalk aquifer in the JO siting region may be more active than in the two other siting regions. This could be a result of the local tectonic setting (Section 4.3).

Summary of the Muschelkalk aquifer in the siting regions

In conclusion, the Muschelkalk aquifer in the ZNO and NL siting regions represents a regionally well-connected aquifer consisting of two main water components: (i) Ca-SO_4 type groundwaters originating from meteoric water that infiltrated through the Muschelkalk outcrops along the SE margin of the Black Forest during the last glacial period (12 – 115 kyr) and a minor component of (ii) an older Na-Cl type groundwater of meteoric origin that upwelled into the Muschelkalk aquifer from the underlying crystalline basement along deep reaching faults (see discussion in following section). Locally, the dissolution of halite may lead to high concentrations of Na and Cl exceeding those of seawater; however, this is not necessarily related to cross-formation flow. In the JO siting region, the Muschelkalk aquifer belongs to a different, much more active hydraulic system where recharge probably occurred in the current interglacial period (< 12 kyr ago).

4.5.5.6 Cross-formation flow

In the three siting regions, the deep aquifers situated above and below the potential repository host rock (Malm, Hauptrogenstein, Keuper, Muschelkalk) are separated by low-permeability aquitards such as the Opalinus Clay below the Malm/Hauptrogenstein aquifers and the anhydrite-rich Bänkerjoch Formation below the Keuper aquifer (Section 4.5.3). These aquitards act as highly efficient barriers and thus cause a pronounced separation in the behaviour of the aquifers. Based on the distinct hydrogeochemical properties of the aquifers discussed above, there is no indication for any advective groundwater flow across these aquitards. This is particularly manifested by the chloride concentration and ^{81}Kr model age profiles shown in Fig. 4-117. In each borehole, the two parameters differ by up to two orders of magnitude, whereas similar values are observed in each borehole for the same aquifer. In general, groundwater from the Muschelkalk aquifer displays the lowest ^{81}Kr model ages and Cl concentrations, except for the samples affected by local halite dissolution (e.g. BUL1; Fig. 4-117). In contrast, groundwater samples from the Malm aquifer show the highest ^{81}Kr model ages and a preserved marine Na-Cl component, although it is located at the shallowest depth compared to the other deep aquifers relevant for the repository host rock. The profiles shown in Fig. 4-117 thus emphasise that the deep groundwaters in the three siting regions experienced a highly distinct, aquifer-specific evolution and do not communicate hydraulically across the aquitards. Accordingly, the chemical signature of deep groundwaters is controlled by the local mineralogy as well as the corresponding, aquifer-specific hydrogeochemical evolution. The hydrogeochemical evolution is mainly affected by the regional connectivity, the transmissivity and the hydraulic head gradient driving groundwater flow. For instance, because of the higher hydraulic head gradient, higher transmissivity and better connectivity (Section 4.5.3), the Muschelkalk groundwaters display a lower mean residence time than groundwaters from the other three aquifers. Consequently, signatures of stable isotopes of the Muschelkalk groundwaters fall almost exactly on the Global Meteoric Water Line whereas significant shifts may be observed in samples of deep groundwaters from the other aquifers.

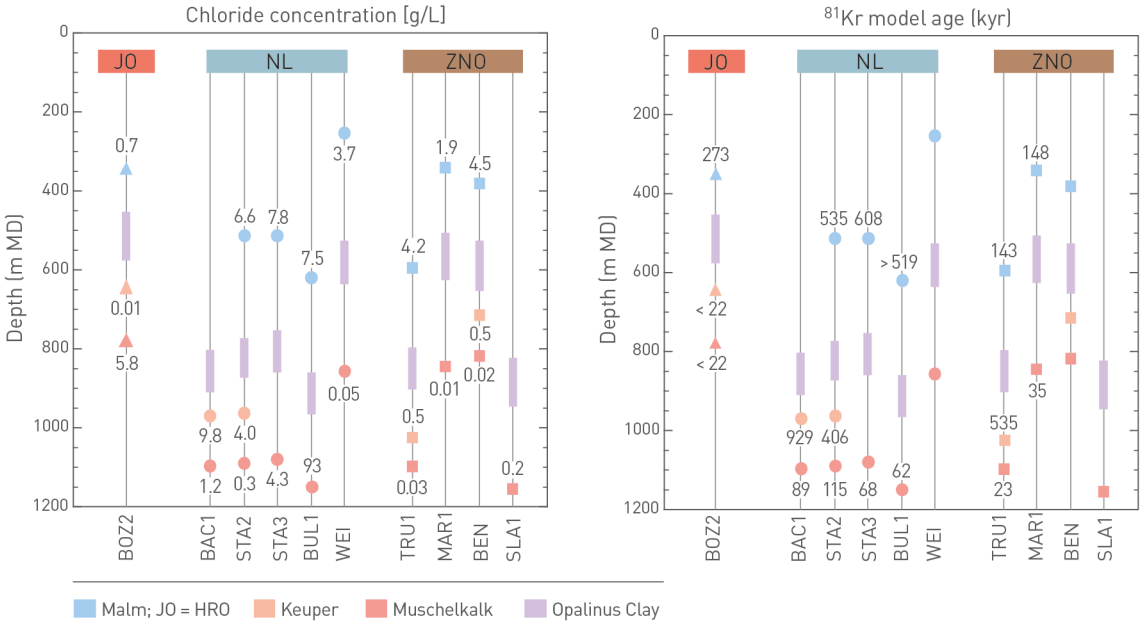


Fig. 4-117: Chloride concentrations and ^{81}Kr model ages in groundwater collected from boreholes in the three siting regions

The symbol colours (blue, orange, red) denote the aquifer from which the groundwaters were sampled and the adjacent number displays the corresponding chloride concentration in g/L and ^{81}K model ages in kyr. The depth range of the Opalinus Clay in the different boreholes is shown as a reference in purple. High chloride concentrations observed in the Muschelkalk samples from BUL1 and STA3 are inherited from the dissolution of local halite occurrences and thus cannot be discussed in the regional context. For JO, data for the Hauptrogenstein aquifer (HRO) are shown (which is closer to the Opalinus Clay than the Malm aquifer).

Despite the strong aquifer-specific signature of deep groundwaters occurring in the aquifers above and below the Opalinus Clay and the lack of mutual hydrogeochemical interaction, three types of cross-formation flow appear to be relevant between this Mesozoic sedimentary sequence and the underlying crystalline basement as well as with the Molasse units located above. These exceptions are described below.

i) Downward migration into the Malm aquifer

Based on the strong similarity of Na-HCO_3 and Na-Cl type groundwaters from the Molasse and Malm aquifers (Fig. 4-104), the high salinity and Na-Cl type nature of the Malm groundwaters in the ZNO and NL siting regions is probably inherited from the penetration of seawater from OMM times into the USM and eventually into the Malm aquifer. While the downward migration of seawater from the OMM probably occurred several million years ago during Pliocene times, it appears to also be facilitated during glacial periods. This is manifested by $\delta^{18}O$ values below -11 ‰ typical for recharge under cold climatic conditions of Na-HCO_3 type groundwaters collected from the Malm and Molasse aquifers in the Bodensee region in Southern Germany (Fig. 4-104, Fig. 4-105). A potential explanation for the accelerated downward migration during glacial periods is that the water pressure at the base of large glaciers is high because it represents the thickness (i.e. the topography) of the entire glacier (e.g. Schintgen & Moeck 2021). Accordingly, the recharge of glacial meltwater through the underlying units of the Molasse sequence into the Malm aquifer may be promoted during glacial periods (Section 6.5). This hypothesis is consistent with the extent of glaciers during the last few glacial periods covering the

locations showing Na-HCO_3 type Malm groundwaters in the Bodensee region today (Preusser et al. 2011). Schintgen & Moeck (2021), however, have shown that the penetration of meteoric water through the entire Molasse sequence during glacial periods requires elevated permeability of the Malm aquifer. The low permeability of the Malm aquifer in the ZNO and NL siting regions (Section 4.5.3) is probably another reason why, in Northern Switzerland, such downward migration did not reach the Malm aquifer during the last glaciation, as evidenced from the lack of cold climate stable isotope signatures, high ^{81}Kr model ages and high salinities (Fig. 4-104, Fig. 4-106). In other words, it allowed the preservation of the Na-Cl type waters in the Malm.

ii) Upwelling of groundwater from the crystalline basement into the Muschelkalk aquifer

The correlations between hydrogeochemical parameters of Muschelkalk groundwaters collected from the ZNO and NL siting regions (Fig. 4-114) provide evidence for the upwelling of groundwater from the crystalline basement into the overlying Muschelkalk aquifer (see Section 4.5.5.5: Muschelkalk aquifer). It is unclear, however, whether upwelling still occurs today or only happened in the geological past. In either case, the upflow of water from the crystalline basement is driven by the hydraulic head gradient caused by the Black Forest Highlands and is restricted to fault zones (Fig. 4-115). Upwelling rates, however, are low as manifested by the mean residence time inferred for the upwelling water component of at least 115 kyr, as well as the low proportion of a crystalline groundwater endmember inferred from the correlations shown in Fig. 4-114.

iii) Episodic upwelling of gases from deep sources

^4He concentrations in Na-Cl type Malm groundwaters from the ZNO and NL siting regions are above the maximum values expected from in-situ ^4He production (Fig. 4-104). In the case of TRU1 and MAR1 they even exceed the concentrations measured in the adjacent porewater (Rufer et al. 2024). In addition, deep sedimentary groundwaters from all three siting regions show $^3He/^4He$ ratios above those expected for Mesozoic sedimentary rocks. It follows that locally there are external ^4He sources for the Na-Cl type Malm groundwaters whereas a regionally relevant external ^3He source affects the $^3He/^4He$ ratio of all deep groundwaters.

For the Malm aquifer, ^4He concentrations above those measured in the adjacent porewater suggest that He and other gases (e.g. CO_2, CH_4, N_2) originate from the episodic upflow of gases along deep-reaching faults connecting the Malm aquifer with deeper units and bypassing the Mesozoic sedimentary sequence in between (Rufer et al. 2024).

The few percent of mantle-derived He identified in all deep aquifers is caused by the diffusive background ^3He flux from the earth's mantle into the crust, which may be variable in the three siting regions based on the different tectonic setting. For instance, the influence of the Hegau – Bodensee Graben decreases from east to west (Section 4.3). Elevated $^3He/^4He$ ratios are expected for the Hegau volcanic area. A regional decrease of the mantle-derived ^3He flux may have caused the east-west trend of decreasing $^3He/^4He$ ratios in the Muschelkalk groundwaters, with highest values in the ZNO and lowest values in the JO siting region (Fig. 4-112). In the case of the Muschelkalk aquifer, the $^3He/^4He$ ratio may be additionally affected by elevated dissolved ^3He and/or ^4He concentrations in the upwelling groundwater component and hence by advection (Fig. 4-115). In any case, in contrast to the ^4He input into the Malm aquifer, there is no evidence that the diffusive or advective ^3He input occurs as gaseous He.

4.5.6 Concluding summary hydrogeology

Thanks to the new boreholes of the TBO campaign, the hydrogeological understanding of the siting regions could be supplemented and refined. The combination of the hydrogeological dataset with the lithostratigraphic and structural geological investigations is the basis for the development of the 3D model understanding and the evolution with time. The major differences between the

siting regions regarding hydrostratigraphy relate to the occurrence of the Hauptrogenstein aquifer exclusively in JO and the site-specific differences regarding the local Keuper aquifer. The siting regions NL and ZNO share many commonalities regarding the Muschelkalk aquifer and in some aspects also regarding the Malm aquifer. In the JO siting region flow systems are of a more local scale due to the tectonic and topographic situation.

The combination of the steady state hydrogeological model together with the hydrogeochemical dataset is the basis for the analysis of the flow systems. The combined dataset can be used for consistency checks and helps to identify transient states.

Malm aquifer: There is a well-established hydrodynamic understanding of the regional flow pattern in the Malm aquifer which can consistently be supported with the hydrogeochemical data. The Na-Cl type groundwaters in the NL and ZNO siting regions include variable contents of fossil OMM seawater. The fact that such an old water component is preserved can only be explained by comparatively low hydraulic conductivities and a quasi-stagnant area in the flow system. For the ZNO siting region, the groundwater model suggests recharge from the Malm outcrops in the north-east (Fig. 4-105). This means that the current Na-Cl type groundwater will be increasingly displaced by freshwater in the future (Section 6.5). This is consistent with the observed mixing trends including the different salinities and model ages observed in the ZNO region, with MAR1[12] clearly more strongly influenced, while in BEN, and even more so in TRU1, more of the old component has been retained. A large fraction of the OMM seawater is preserved in the NL siting region where the samples from BUL1, STA3 and STA2 indicate a comparably uniform composition characterised by high salinities, high $\delta^{18}O$ values and high ^{81}Kr model ages (> 519 kyr; Fig. 4-106). For this zone, the hydrodynamic model indicates low horizontal gradients and slow recharge via seepage from the overlying Molasse into the Malm, which is in agreement with earlier conceptual ideas of Molasse – Malm interaction (e.g. Schmassmann et al. 1990, Balderer 1990). Here, the findings consistently indicate a zone of quasi-stagnant conditions where the recharge into the Malm is limited by the low vertical hydraulic conductivity of the Molasse. Further to the north, in the Weiach borehole, the groundwater salinity is about 50% lower. This indicates a significant contribution of a freshwater component which might be related to the thinner Molasse cover here (top Malm is at a comparably shallow depth of 186 m).

Hauptrogenstein aquifer: There is a comparably small-scale flow system because of the local topography including the related outcrops and the regional faults delimiting the siting region in the south and in the north. In addition, the facies change from the Hauptrogenstein in the west to the clay-mineral-rich Klingnau Formation in the east affects thickness and the hydraulic conductivity of the aquifer. The groundwater sample from the BOZ2 borehole is of generally Na-SO_4 type, characterised by a high ^{81}Kr model age of 273 kyr, and displays a high total dissolved solid concentration of 4.5 g/L. No groundwater could be sampled in the boreholes BOZ1 and RIN. Overall, the location of the eastern boundary of the Hauptrogenstein aquifer is only weakly known.

Keuper aquifer: The Keuper aquifer is considered a local aquifer because of its lithological variability. Therefore, a site-specific discussion and evaluation is needed. In the framework of the hydraulic modelling, a base case and alternative model cases were considered to mimic the different permeable lithofacies and to explore the flow system.

---

[12] In contrast to what is indicated by the hydrodynamic model, groundwater from MAR1 contains a stronger meteoric component. This might point to a more important flow from the outcrops in the NW to the westernmost ZNO region or an influence related to the overdeepened valley extending to the SE of Marthalen.

- **JO:** All boreholes provided evidence for the existence of a Keuper aquifer. Permeability in JO is probably related to a fracture network in the comparably thick Gansingen Member. The flow system is affected by the tectonic and topographic situation. Recharge occurs via nearby outcrops. Based on the measured heads, topographic considerations and the model scenarios, potential discharge areas are located in the Sissle or the Aare Valley and near the confluence of Aare, Reuss and Limmat. The hydrogeochemical data suggest large differences in flow dynamics between RIN and BOZ2 (the latter is close to outcrops in the north).
- **NL:** In the NL siting region, the observed permeable zones relate to the channel facies (STA2) or the overbank deposits (BAC1) of the Ergolz Member. In the BUL1 and STA3 boreholes, hydraulic conductivities are low to very low. Overall groundwater flow therefore depends heavily on the internal structure and connectivity of these fluvial deposits. This was accounted for by different model cases in the hydrogeological modelling (Nagra 2024n). The calibration resulted in a base case model with about one order of magnitude lower hydraulic conductivity in NL compared to ZNO. All modelled cases indicate recharge from the outcrops in the north, which is consistent with the hydraulic heads measured in the boreholes. In detail, the hydraulic head distribution strongly depends on the assumption regarding the hydraulic conductivity distribution, but the discharge area indicated by all cases is located in the lower Aare Valley. The hydrogeochemical dataset indicates low flow dynamics and a correlation with lithofacies: The groundwater sampled from the channel facies of the Ergolz Member in STA2 is characterised by a high ^{81}Kr model age of 406 kyr. For the sample from the somewhat less permeable overbank deposits in borehole BAC1, even a much higher residence time is indicated. Here, the quasi-stagnant conditions resulted in groundwater geochemistry largely equilibrated with the adjacent porewater. To conclude, the hydrogeological data can be explained by only limited to partly absent groundwater flow in the Keuper aquifer in NL.
- **ZNO**: The Keuper aquifer in ZNO is closely related to the occurrence of the Seebi Member as a cavernous dolomite breccia. All boreholes of the region indicate an active Keuper aquifer by high hydraulic conductivities (and pumped groundwater samples) and/or anomalies of the natural tracers in the porewater. The similar hydrogeochemical composition of the groundwater samples from BEN and TRU1 agree with a well-connected aquifer in this siting region. The measured hydraulic heads and the hydrogeological model consistently indicate a general groundwater flow direction south to southeast with recharge in the Klettgau area (ca. 15 km to the northeast). Residence times in the system are high as indicated by the ^{81}Kr model age of the TRU1 sample of 535 kyr.

Muschelkalk aquifer: The flow pattern modelled for the Muschelkalk aquifer is in good agreement with the borehole hydraulic head data. The large-scale flow system from the recharge area in the northern Wutach Valley across the ZNO and NL siting regions to the discharge area near the confluence of Aare and Rhine is also consistent with the hydrogeochemical data. There is a much more dynamic flow system compared to Malm aquifer as indicated by the hydrogeochemical data (e.g. ^{81}Kr model ages MAR1 35 kyr and STA3 68 kyr) that include groundwaters of Ca-SO_4 to the general [Na/Ca]-[SO4/Cl] type and locally also of Na-Cl type. The groundwater in this flow system can be explained by mixture of Ca-SO_4 type water with a subordinate amount (< 20%) of an older component (Li, Cl, Sr isotopes) from the porewater of the rock matrix or from small amounts of water from deeper aquifers. In addition, the groundwaters are locally affected by dissolution of halite (notably BUL1). In the JO siting region, the flow systems are strongly affected by topography and the tectonic situation. The hydrogeochemical tracers point to a comparably active flow system, e.g. ^{81}Kr model age of BOZ2 < 22 kyr. All groundwaters are of Na-Cl type, which are probably explained by a saline component reaching the Muschelkalk aquifer along the Jura Main Thrust south of the JO siting region.

4.6 Solute transport in the host rock and confining units demonstrated by the profiles of natural tracers

Key points:

- Porewater investigations allowed derivation of profiles of natural tracers (including δ^2H, $\delta^{18}O$, Cl, Br, ^4He, $^3He/^4He$) across the Mesozoic sedimentary column.
- These tracer profiles provide insight into the palaeohydrogeological evolution and dominant transport processes, as well as independent evidence for the hydraulic barrier effect of the host rock and the confining units.
- Transport modelling shows that the curved segments of the profiles result from diffusion-dominated exchange between the porewater and groundwater in aquifers, which were activated in the Pleistocene (variable times depending on the aquifer).
- The highest stable isotope values of the porewater are found in the central part of the Opalinus Clay host rock in NL and are interpreted as the oldest.
- Concentrations of the dissolved noble gas isotope ^4He are more than 4 orders of magnitude higher than for air-saturated water. More than 65% of the He produced in Opalinus Clay since deposition is still present, which demonstrates the strong barrier efficiency of the system.

4.6.1 Overview

This section discusses data for mobile (i.e. non-retarded) natural tracers (stable isotopes of water, Cl, Br, He) obtained at the different sites investigated. From the shape of the tracer profiles, it is often possible to identify the hydrochemical boundaries of the low-permeability zone (aquitard) and to delineate the thickness of this zone. Furthermore, the relevance of transport processes (diffusion, advection) or of episodic events may be assessed by comparing data and model calculations. A careful analysis of the profiles and the palaeo-hydrogeological setting, including transport modelling, allows the past evolution of the groundwater-porewater interaction to be constrained and to test whether transport parameters obtained in the laboratory are applicable at larger scales.

It is advantageous to consider several different tracers to obtain more robust interpretations. The information provided by each tracer may differ. Tracers such as stable isotopes of water or anions are mostly influenced by processes at hydrogeological boundaries, while a tracer such as He is also affected by the internal production and release rate within the aquitard. Furthermore, transport parameters are not identical. For example, He diffusion coefficients in water are about three times higher, and effective He diffusion coefficients D_e in the Opalinus Clay are more than five times higher than those of a water tracer (Jacops et al. 2017), while D_e values of Cl are about four to five times lower than those of a water tracer. Also, during advective transport, anions typically experience a higher effective flow velocity because they are mostly located in larger pores (i.e. further away from negatively charged surfaces) with a higher local flow velocity. He transport tends to be more dominated by diffusion, while anion transport is more sensitive to advection compared to a water tracer. Finally, boundary conditions for the different tracers can vary independently, depending on the hydrogeological and climatic conditions. For example, freshwater recharge is characterised by low anion contents, while the signature of stable isotopes of such water depends also on the climatic conditions. The lack of unique relationships between boundary conditions for different tracers may, in turn, also complicate the definition of consistent sets of boundary conditions for the past.

The spatial distribution of tracer concentrations across low-permeability formations is the result of flow and solute transport processes that have acted over geological timescales. The composition of porewater in aquitards is affected by the initial water composition at the time of sediment deposition (connate water), by water-rock interactions and by solute exchange with adjacent aquifers. If the groundwater composition in an aquifer in contact with an aquitard changes as a result of a palaeo-hydrogeological event (e.g. new discharge zones, new recharge of meteoric water, different climatic conditions etc.; Fig. 4-118), the changing groundwater signature propagates over time into the aquitard. As solute transport in an aquitard is generally slower than that in an aquifer, tracer profiles across the aquitard have a longer memory. They record situations in the distant past, in particular in their central region where signals from changing boundary conditions in the aquifers are most strongly retarded and attenuated. If molecular diffusion dominates transport across the aquitard, the trends of tracer concentrations are anticipated to be relatively smooth, while advection across the aquitard could (depending on other parameters) lead to sharper tracer fronts.

A tracer profile obtained in a given borehole can represent a steady-state situation, but more often it represents a snapshot of a slowly evolving, transient situation. The profile can be interpreted by transport modelling. The modelling tries to simulate the observed tracer pattern assuming suitable initial and boundary conditions in the past and using transport parameters that were derived from laboratory experiments. Before doing so, it is appropriate to be aware of the approximate 'field of view', that is of the approximate time and space scales of observation. For one-dimensional diffusive transport, a diffusive timescale t_d for the propagation of a mobile (non-retarded) tracer over a distance x can be obtained as:

$$t_d = \frac{x^2}{D_p}$$

where D_p is the pore diffusion coefficient. If we assume a thickness x of an aquitard of 100 m and a D_p of 10^{-10} m^2 s^{-1} (e.g. the Opalinus Clay at in-situ temperature), a change at the boundary of the aquitard would roughly propagate up to the centre of the aquitard in a time frame of about 0.8 Myr. For a thickness of 300 m, the characteristic time would increase ninefold, i.e. to 7.2 Myr. That is, it would still be expected to see a (transient) response of a change in boundary conditions within a formation of 100 or 300 m thickness if this change happened less than about 1 Myr or 7 Myr ago, respectively. In contrast, the new signature would already have affected large parts of the formation if the change had happened several Myr or several tens of Myr ago, respectively. The detailed response would also depend on the variability of diffusion properties or on any influence of advection, but this simple calculation sets a time frame for the interpretation of tracer profiles. It also shows that, during the long time since deposition of the Opalinus Clay, its porewater composition has definitively been altered, inter alia by exchange with groundwater in bounding aquifers and with porewater in embedding formations.

Different methods are required to obtain the concentrations of tracers. Values of the stable isotopes of water (δ^2H, δ^{18}O) were mainly obtained by diffusive isotope exchange experiments (Aschwanden et al. 2024, Gimmi et al. 2024). This method is well established and provides robust data for clay-mineral-rich samples but is more challenging and leads to slightly larger uncertainties for low-porosity samples (e.g. limestones or evaporites). Anion (Cl, Br) contents of the porewater were mainly obtained from aqueous leachates (Zwahlen et al. 2024, Wersin et al. 2023), but a substantial dataset from advective displacement (AD) and squeezing (SQ) experiments is also available. The aqueous leachate data have to be scaled by the anion-accessible porosity fraction in order to obtain concentrations per anion-accessible pore volume (as needed for transport modelling, see Section 5.4.2 and Zwahlen et al. 2024). The required scaling was done based on data from diffusion experiments or based on the combined data from advective displacement and squeezing experiments. The scaling leads in the end to increased uncertainties of the Cl

or Br concentrations per accessible porewater, especially for low-clay samples (Wersin et al. 2023). The Br/Cl ratios, in contrast, are not affected by the uncertainty regarding the accessible pore fraction, which is probably very similar for the two ions and thus cancels out in their ratio. Noble gas contents in porewater were obtained by outgassing experiments (Rufer et al. 2024). Helium in particular is characterised by a low abundance in air and air-saturated water, an in-situ geogenic production through radioactive decay of U and Th in the rock matrix as well as a high diffusivity in the porewater. The resulting enrichment of helium in the aquitard porewater relative to (most) groundwaters and its efficient diffusive redistribution makes it a useful tracer to investigate and temporally constrain even younger hydrogeological disturbances.

Diffusive transport of δ^2H, $\delta^{18}O$, Cl, and Br across the formations between the Malm and Muschelkalk was modelled using the numerical code PFLOTRAN (www.pflotran.org). Sensitivity calculations including advection were previously undertaken for data from the Benken (BEN) borehole in the ZNO region; they indicated the lack of any signature of an advective component (Gimmi & Waber 2004, Gimmi et al. 2007). Similar sensitivity calculations are being done for the new tracer profiles. Unlike the earlier simulations for data from the BEN (Gimmi et al. 2007) and Schlattingen-1 boreholes (Wersin et al. 2018), porosities and pore diffusion coefficients were varied with depth in the current modelling campaign, based on measured diffusion data (Van Loon et al. 2023) and temperature logs (Section 4.8).

Simulating the detailed evolution of the porewater in the low-permeability sequence since the time of deposition is not considered meaningful because of the collective uncertainties. It is likely that the changing boundary conditions since deposition and the prolonged interaction times have led to profiles with comparably smooth trends with depth, before more recent changes at the currently active boundaries left their signatures in the aquitard. Based on the tectonic and burial history of Northern Switzerland (Section 4.3.5), modelling concentrated on the last ~ 10 Myr, starting by using the δ^2H and $\delta^{18}O$ data that have comparably small analytical uncertainties. The procedure was as follows: First, approximate initial conditions for these simulations were fixed (constant value for δ^2H based on maximum values towards the centre of the profiles, decreasing values with depth for $\delta^{18}O$ based on the general trend in the central part, see Section 4.6.2). Then, step changes of the boundary conditions to the different aquifers (when present) to present-day values were applied. The times of these step changes were treated as unknowns; they were fitted so that a good match of the simulations with the overall shape of the profile was obtained. In some cases, two step changes of the boundary condition were considered, in order to account for observed trends. The evolution times derived in this way from the profiles of the water tracers were then used for the subsequent simulations of the profiles of Cl and Br (also setting their constant initial concentrations at the maximum values found in the central part).

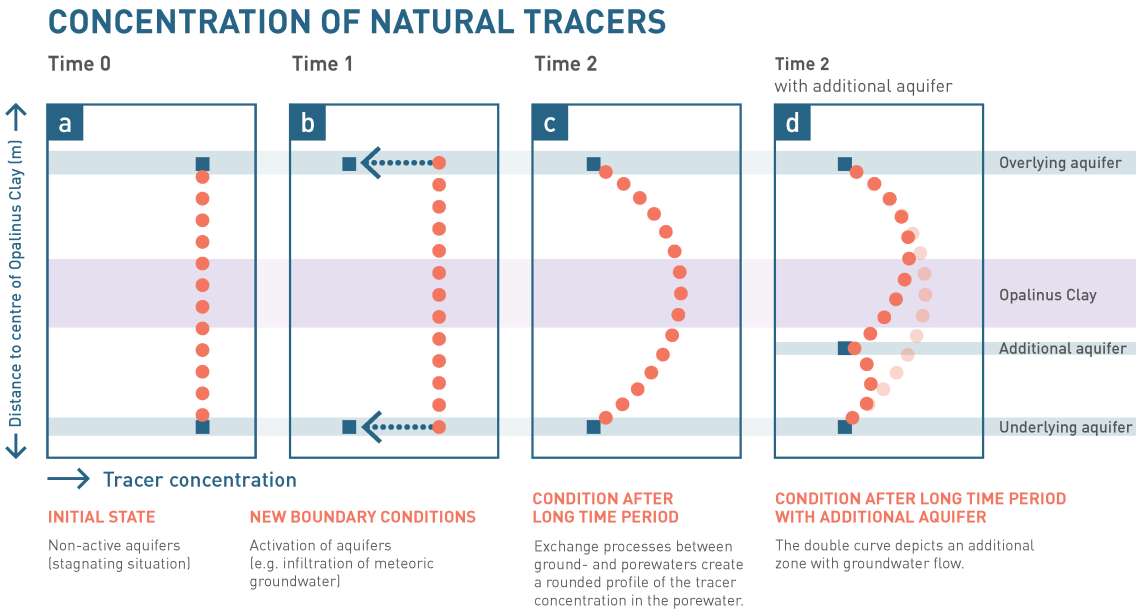


Fig. 4-118: Illustration of possible evolution of tracer profiles across an aquitard sequence driven by concentration changes in two or more bounding aquifers

Example of a tracer without in-situ production.

4.6.2 Profiles of stable isotopes of water

General observations

The measured depth profiles of stable isotopes of water (δ^2H, $\delta^{18}O$; Gimmi et al. 2024) of the eight sites of the TBO campaign with vertical boreholes together with the BEN borehole are presented in Fig. 4-119 and Fig. 4-120. The data show trends which are thought to be indicative of diffusive transport (Gimmi et al. 2007). The scatter and uncertainties are largest in regions of low porosity such as in the Malm limestones, in the heterogeneous «Herrenwis Unit» of the Upper Dogger, or in the anhydrite-bearing zones of the lower part of the Keuper (Bänkerjoch Formation). This is mainly because of experimental difficulties associated with these lithologies (Aschwanden et al. 2024). Scatter is much smaller in clay-mineral-rich units with larger porosity, such as in the Opalinus Clay.

Porewater isotope results for depth intervals of the aquifers generally agree well with those obtained for corresponding groundwater samples (when available). This corroborates the quality of the porewater dataset, as local equilibrium in these intervals can be assumed (diffusion is fast over short distances, and groundwater residence times are generally > 10 kyr; Section 4.5.5). In some intervals with potential aquifers, no groundwater could be sampled during packer tests because the hydraulic conductivity was too low. This was the case in the Malm in BAC1, in the Hauptrogenstein in BOZ1, and in the Keuper in BOZ1, STA3, BUL1 and MAR1.

The profile shapes of δ^2H and $\delta^{18}O$ can be roughly classified into three types. Type 1, exemplified by those of BAC1, STA3 and BUL1, is characterised by more or less linear profiles down to the lower part of the Keuper. Type 3, the other endmember type, is characterised by clearly curved profiles or profile parts, especially towards the top of the Keuper. This group includes the profiles

from BOZ2, STA2, TRU1, and BEN. Type 2 is intermediate, with less pronounced curved profiles towards the top of the Keuper. It includes BOZ1 and MAR1. Note that this classification is based on the profiles of δ^2H and $\delta^{18}O$. The profiles of Cl or Br at the latter two sites exhibit more pronounced curvatures compared to the hydrogen and oxygen isotopes of the water.

Interactions with groundwater in aquifers

The distinction of the three profile types is clearly related to the occurrence of flowing groundwater in aquifers. Notably, Keuper groundwater could be sampled in all clearly curved profiles of type 3 (BOZ2, STA2, TRU1 and BEN; see Section 4.5). In contrast, no Keuper groundwater could be sampled in two of the three more or less straight profiles of type 1 (STA3, BUL1). Interestingly, the hydraulic conductivity was also too low to sample groundwater in the Keuper packer interval in the intermediate type 2 profiles (BOZ1, MAR1) with a weak excursion only, while sampling was possible in the type 1 profile of BAC1 showing hardly any curvature towards the Keuper. Type 1 profiles (no excursion towards the Keuper) are found in NL, type 2 and type 3 profiles are found in all study areas, with most strongly curved profiles in the ZNO region (Section 4.5).

The observations regarding the influence of flowing groundwater in the Keuper are consistent with the general understanding of this aquifer. They corroborate the lateral variability in this aquifer mentioned earlier (Gimmi & Waber 2004, Gimmi et al. 2007) when presenting the tracer profiles from the BEN borehole. The variability is related to the regionally changing lithofacies of this formation (more sheetlike water-conducting structures in ZNO, more sandy fluvial channels in NL, probably a dolomitic member in JO; Section 4.5.3.10). As a result, hydraulic conductivity and flow velocity are locally very variable, in particular in NL, leading to the different profile types.

Groundwater in the Malm (or in the Hauptrogenstein in the case of BOZ2) could be sampled in all profiles except BOZ1 and BAC1. This groundwater clearly influenced the shape of the upper part of these profiles (in MAR1, the porewater dataset is limited as only the lowermost part of the Malm was cored). In BAC1, no Malm groundwater could be sampled, but the uppermost porewater values start to decrease again upwards; it is possible that water flow occurred further above. The transmissive zones in the Malm are generally (except for BEN) located above the Schwarzbach Formation (Section 4.5.3.3), that is near to or above the uppermost porewater data point of BAC1.

The profile trends towards the Malm aquifer are mostly relatively flat, less curved than towards the Keuper groundwater. This indicates long-term stable boundary conditions and comparatively long interaction times (as diffusion coefficients are not especially large in these massive limestones; Van Loon et al. 2023), probably longer than those towards the Keuper groundwater. A prominent exception is TRU1, where a possibly more recent change in the Malm groundwater composition may have caused the bending of the upper part of the $\delta^{18}O$ (but not δ^2H) profile towards higher values. To a lesser degree, STA2 and possibly also STA3 show a similar feature. The curvature towards the Hauptrogenstein groundwater in BOZ2 is relatively steep, indicating a shorter interaction time compared to those for the interaction with the Malm groundwater at the other sites (assuming diffusion coefficients are of similar order). In BAC1, the comparatively flat profile above the Keuper groundwater could indicate a longer interaction time between groundwater and porewater but, combined with the less negative groundwater signature in the Keuper than at other sites, it could also hint at a comparably small volume of interacting groundwater because of slow flow of groundwater and/or a small extent of the transmissive zone (consistent with a zone away from the main water flow, Section 4.5), both leading to stronger alteration of the groundwater signature by exchange with the porewater.

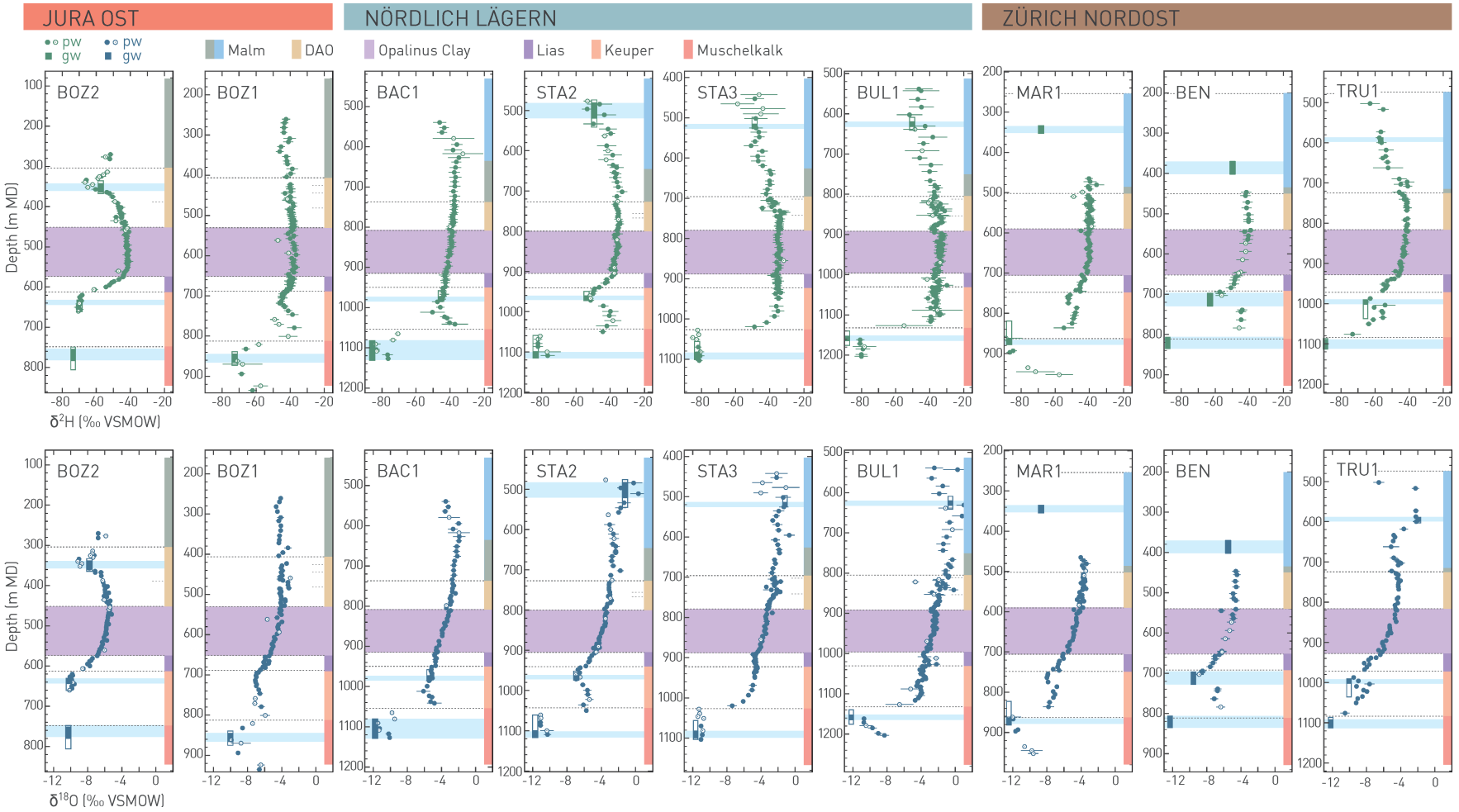


Fig. 4-119: Profiles of δ^2H (top row) and $\delta^{18}O$ (bottom row) in porewater (pw) and groundwater (gw) in the different siting regions

Porewater data were derived from diffusive isotope exchange experiments; open symbols: less reliable (potential artefacts or contamination with drilling fluid). Where groundwater could be sampled, open rectangles show packer intervals, closed rectangles and light blue bars most likely inflow zones. DAO: Dogger Group above Opalinus Clay. Light blue background indicates the location of the transmissive zone in the aquifers.

At depth, all profiles are then clearly influenced by groundwater in the Muschelkalk aquifer, where minima of δ^2H and $\delta^{18}O$ are observed. The steep gradients of porewater δ^2H and $\delta^{18}O$ towards the most negative values in the Muschelkalk aquifer indicate a comparatively late change of the signature in this aquifer, and/or very low diffusion coefficients in the overlying Bänkerjoch Formation (containing clay-bearing to massive anhydrite beds; Section 4.2.3, Mazurek et al. 2023a).

Relationship between δ^2H and $\delta^{18}O$ values

The δ^2H and $\delta^{18}O$ pore- and groundwater data can be compared with respect to their position relative to the Global Meteoric Water Line (GMWL). This provides information regarding the origin of – and interactions between – pore- and groundwaters. The Malm groundwaters plot distinctly to the right of the GMWL (see Fig. 4-121 with ground- and porewater of four boreholes; see also Fig. 4-104 in Section 4.5.5.2 for Malm groundwater in all boreholes). This indicates generally long residence times (see discussion in Section 4.5.5). The Hauptrogenstein, Keuper and Muschelkalk groundwaters are located on or near the GMWL (see also Fig. 4-109, Fig. 4-110, Fig. 4-112 and Fig. 4-121). Keuper waters – except at BAC1 and STA2 – have a modern recharge signature, indicating recharge under climatic conditions similar to recent conditions (e.g. during an interglacial period in the Quaternary). The values slightly to the right of the GMWL in BAC1 and STA2 could indicate a more pronounced interaction with the aquitard porewaters, for instance because of a lower thickness of transmissive zones and/or lower water flow velocity. Muschelkalk waters in JO have a modern recharge signature, while those in NL and ZNO indicate a colder recharge temperature than at present. The porewater values evolve from the Malm or Hauptrogenstein through an intermediate peak in the lower Malm, Dogger Group above Opalinus Clay or the Opalinus Clay with maximum δ^2H values (but not maximum $\delta^{18}O$ values, Fig. 4-121) towards the Keuper or Muschelkalk waters. The curved depth trends demonstrate that the porewater data in the aquitard represent a transient situation and not a steady tracer distribution between the bounding aquifers. This also means that the values in the aquitard (and especially in the central part) do not originate from the presently measured groundwater values, but from an earlier evolution.

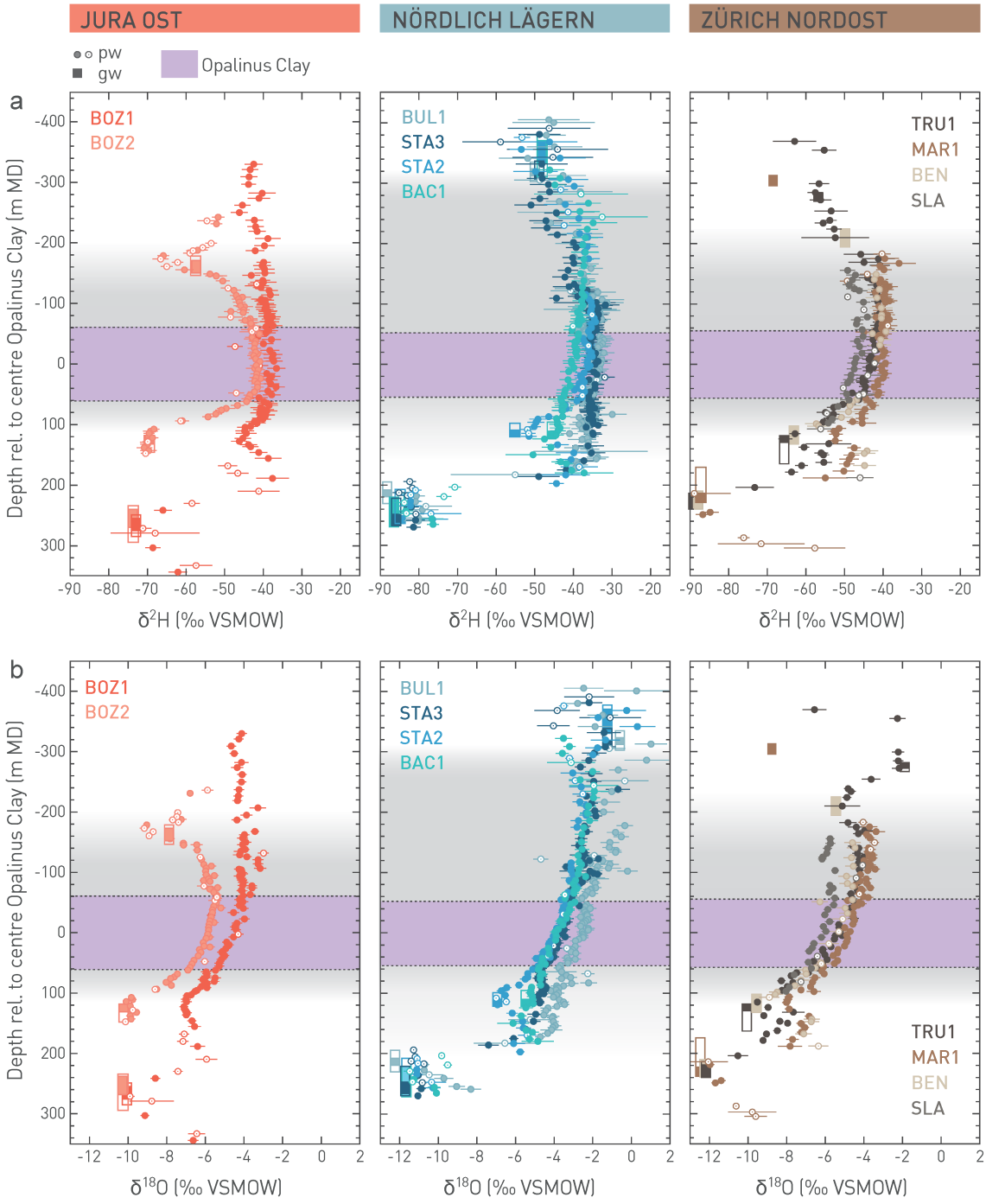


Fig. 4-120: Comparison of profiles of δ^2H (a) and $\delta^{18}O$ (b) in porewater (pw) and groundwater (gw) of the different geological siting regions

For the groundwater, open rectangles show packer intervals, closed rectangles most likely inflow zones. Porewater data were derived from diffusive isotope exchange experiments; open symbols denote less reliable data (because of potential artefacts or contamination with drilling fluid). The grey background illustrates in an approximate way the extent of the low-permeability sequence between bounding aquifers in each region.

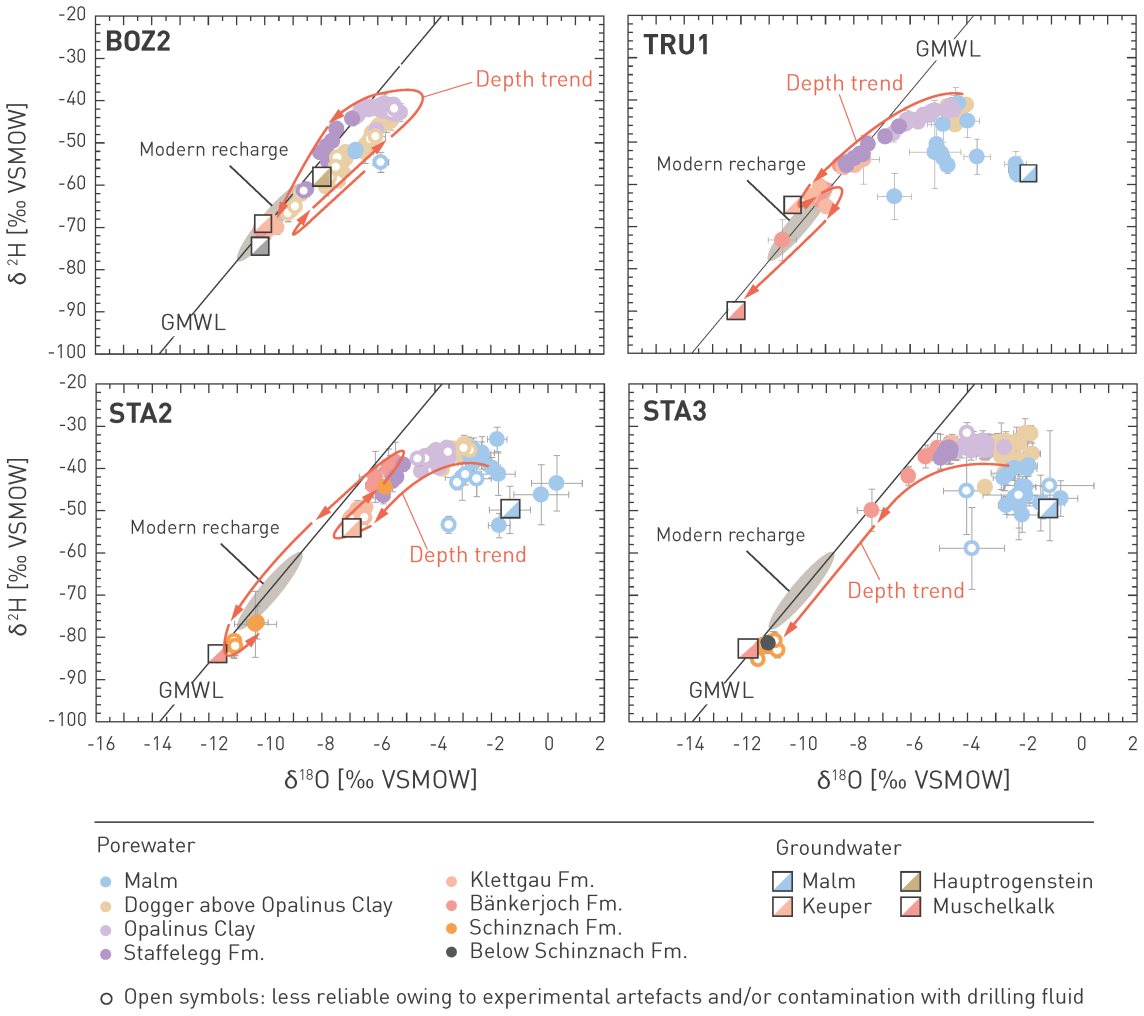


Fig. 4-121: Signatures of stable water isotopes for BOZ2, STA2 and TRU1 (all influenced by Keuper groundwater) as well as for STA3 (no Keuper groundwater)

Graphs show the evolution from the Malm groundwater (STA2, STA3, TRU1) or the close to meteoric Hauptrogenstein groundwater (BOZ2) towards meteoric, modern recharge groundwater (BOZ2, TRU1) or a mixture of meteoric and older groundwater (STA2) in the Keuper aquifer (if present), and then towards modern recharge groundwater (BOZ2) or colder climate meteoric water (TRU1, STA2, STA3) in the Muschelkalk aquifer.

Qualitative interpretation of the profiles of δ^2H and $\delta^{18}O$

The good similarities between the different siting regions in terms of maximum observed δ^2H or $\delta^{18}O$ values and 'background' trends in the central parts become obvious in Fig. 4-120, as well as the similarities and differences in terms of bounding aquifers. The similarities demonstrate that the isotopic signatures in the different siting regions share a largely common evolution. The area has been continental probably since the Late Cretaceous (except for the short Upper Marine Molasse Group period) and erosion occurred down into the karstified Malm limestones (Section 3.4.2). The contact with meteoric water at the surface during that time led to negative isotope values as observed today in the central parts of the aquitard sequence. The later deposition of the Upper Marine Molasse Group (OMM, which has affected the groundwaters in the Malm aquifer in the NL and ZNO siting regions, see Section 4.5.5.2) probably had only a minor

influence on the isotope signatures in the deeper aquitard sequence. The more recent evolution of the profiles was triggered by contact with flowing groundwater in aquifers. The specific evolution is related to the timing of events in the groundwater (such as the activation of flow by erosion in the recharge and/or discharge areas), to the specific local groundwater values in each aquifer, as well as to the thickness of the low-permeability sequence, which is schematically shown as grey background in Fig. 4-120. The thickness is largest for NL and smallest for JO. This difference, as well as the difference in hydrogeological situation and topography, may partly be responsible for the generally lower isotope values of the profiles in JO compared to those in other areas, and also for their comparatively low Cl contents (Section 4.6.3). However, for instance for BOZ2, the isotope gradients towards the Keuper and Hauptrogenstein are steep, and it appears that the maximum values in the central part are not yet affected by the present-day boundary conditions. This means that the lower values in the central part in BOZ2 and also in BOZ1 compared to those in other profiles cannot be the result of the present-day boundary conditions, but probably evolved at earlier times. This also becomes evident when plotting only the values from the Opalinus Clay in a $\delta^2H - \delta^{18}O$ diagram (Fig. 4-122). Slightly different trends are seen in the different areas. The data in NL start from values furthest to the right of the GMWL, while the data in JO and in ZNO start at values closer to the GMWL. At the same time, the lowest values in JO and ZNO reach or nearly reach, respectively, the GMWL, while the lowest values in NL still remain to the right of the GMWL. The trend lines for NL and ZNO are also similar, while that for JO has a shallower slope.

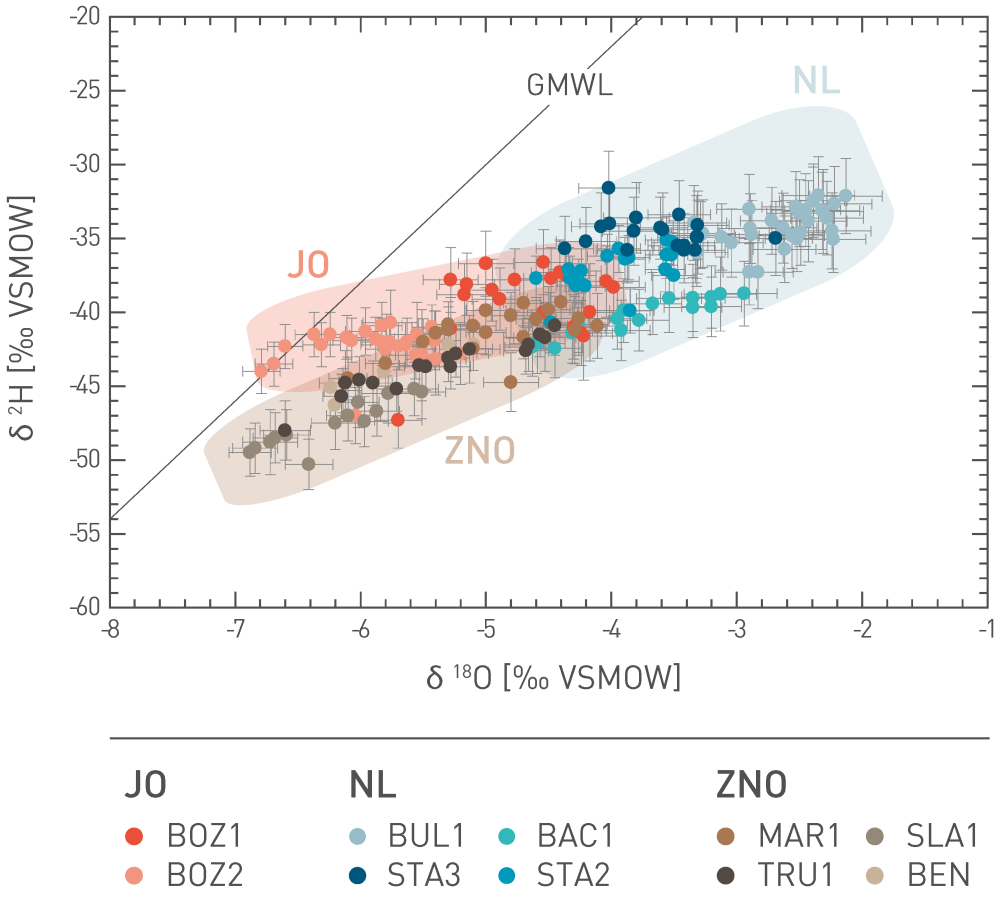


Fig. 4-122: Signatures of stable isotopes in porewater of the Opalinus Clay in the different siting regions

For groundwater values, see Fig. 4-121.

Results of modelling of the profiles of δ^2H and $\delta^{18}O$

As noted in Section 4.6.1, modelling concentrated on the more recent evolution (the last ~ 10 Myr), starting from constant values with depth (δ^2H) or values slightly decreasing with depth ($\delta^{18}O$) that match the trends in the central parts of the profile. The boundary values at each aquifer were then changed in a single step to present-day values (or, in a few cases only, in two steps, to account for observed trends). The times of the changes, that is the evolution times, were fitted for each aquifer in order to obtain a good match between simulations and measurements.

The simulations for pure diffusion match the data well, especially in the part between the Malm or Hauptrogenstein and Keuper aquifer, as shown for four examples in Fig. 4-123. Evolution times in the range of ~ 1.5 – 3 Myr were obtained for the Malm aquifer in NL and ZNO (when ignoring the second step) or of 0.45 Myr for the Hauptrogenstein aquifer in JO of ~ 0.1 – 0.7 Myr for the Keuper aquifer (where present), and of ~ 0.02 – 0.15 Myr for the Muschelkalk aquifer (Tab. 4-2).

Tab. 4-2: Evolution times derived from the modelling of the δ^2H and $\delta^{18}O$ profiles

* Second step. ** Poorly constrained, no data in lower part.

Evolution times [Myr] **based on modelling of the δ^2H and $\delta^{18}O$ profiles**				
	JO BOZ2	**NL** STA2	**NL** STA3	**ZNO** TRU1
Malm aquifer		1.6	2.65	2.15 0.15*
Hauptrogenstein aquifer	0.45			
Keuper aquifer	0.15	0.1		0.65
Muschelkalk aquifer	0.05**	0.08	0.15	0.02

The derived evolution times for all aquifers depend to some degree on the initial conditions selected and the local diffusion coefficients (which are uncertain for the Bänkerjoch Formation above the Muschelkalk). However, in general, the simulations indicate that changes in the Malm occurred at earlier times than those in the Keuper, while the Muschelkalk boundary only changed comparably late in its history to present-day values.

These results are in line with those from earlier simulations for the BEN profile in the ZNO siting region (Gimmi et al. 2007), where diffusive evolution times of ~ 0.55 Myr were estimated for the signature towards the Keuper. The estimated time for TRU1 in this work is well within the range of 0.2 − 1.5 Myr given by Gimmi et al. (2007) when considering various uncertainties for the less comprehensive dataset at BEN.

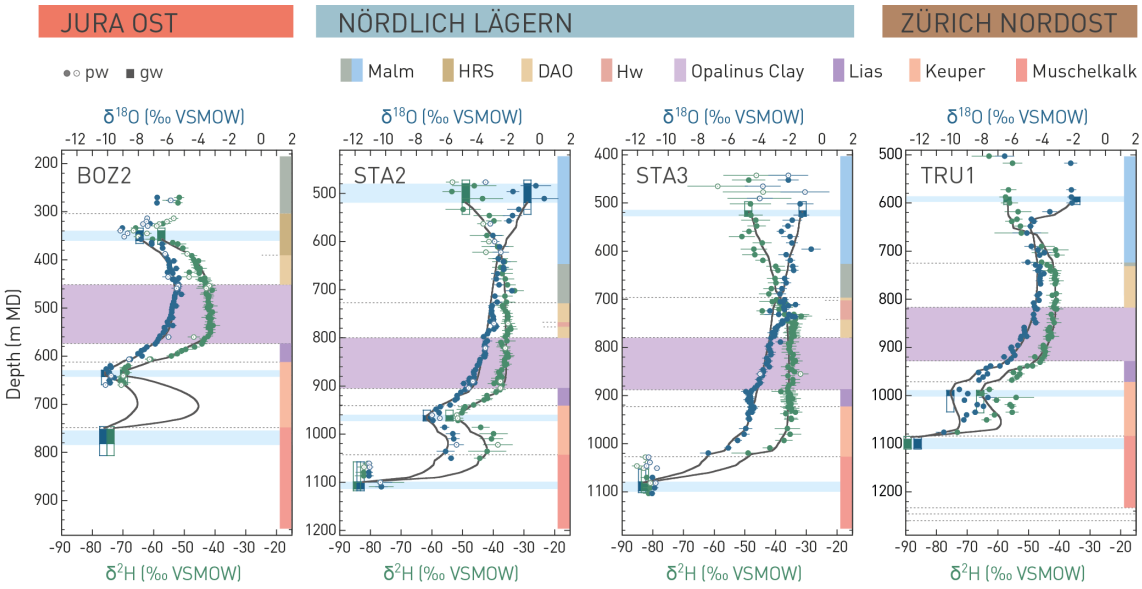


Fig. 4-123: Comparison of measured and simulated profiles of stable water isotopes in BOZ2, STA2, STA3 and TRU1

The solid black lines show the simulation results. Porewater data were derived from diffusive isotope exchange experiments; open symbols: less reliable (potential artefacts or contamination with drilling fluid). Where groundwater could be sampled, open rectangles show packer intervals, closed rectangles and light blue bars most likely inflow zones. DAO: Dogger Group above Opalinus Clay, HRS: Hauptrogenstein, Hw: «Herrenwis Unit». The evolution times used for the simulations are shown in Tab. 4-2. Light blue background indicates the location of the transmissive zone in the aquifers.

The example simulations demonstrate typical results for evolution times towards the aquifers. While specific evolution times derived for each profile and each aquifer vary to some degree (also depending on the assumed initial conditions and local diffusion coefficients), the observed general tendencies appear plausible. For instance, the evolution times for the Malm and Keuper signature in ZNO and NL could relate to the creation of new recharge and discharge zones related to the eastward migration of the Aare – Rhine catchment including diversion of the initially eastward flowing Alpenrhein through the Klettgau Valley (Section 3.4.5). Also, the variability of the local Keuper aquifer properties (Section 4.5.3.10) is reflected in the broad range of the evolution times. In addition, the hydraulic situation in the more western JO area is different from that in the more eastern regions, influenced by topography and the tectonic situation.

The tendency of having mostly longer evolution times for the Malm boundary condition, intermediate times for the Keuper boundary condition and shortest time for Muschelkalk appears also to be plausible. The short times derived for the Muschelkalk boundary condition could be related to the diversion of the Wutach River (Section 3.5) and infiltration of glacial melt water. However, the large uncertainty in the diffusion coefficients for the lowest part of the profile (anhydrite with possibly very low diffusion coefficients) propagates into large uncertainties for the Muschelkalk evolution times.

4.6.3 Chloride profiles and Br/Cl ion ratios

Profiles of chloride in porewater

The chloride profiles across the sampled Jurassic and Triassic sequence of the eight TBO boreholes and the BEN borehole are depicted in Fig. 4-124. Looking at the Opalinus Clay porewaters, which generally reflect maximum Cl concentrations and salinities, the lowest Cl concentrations occur in JO boreholes (~ 2 – 5 g/L; Fig. 4-124), whereas the Cl concentrations from the NL and ZNO boreholes are higher, in the range of ~ 7 – 14 g/L, the highest concentrations being encountered in the BUL1 borehole. In general, porewater data from aqueous leachates scaled with the anion accessibility derived from diffusion data are shown, as well as data directly obtained from advective displacement (AD) or from squeezing (SQ). A scaling of aqueous leachate data based on the anion accessibility from the combined AD and SQ data leads to almost identical results for the profiles in the NL and ZNO regions. For the JO profiles with the lowest salinities, however, the different scalings lead to different results, and both derived porewater datasets are shown (only for the Opalinus Clay, as no AD and SQ data are available for the other formations).

All boreholes exhibit similar Cl patterns, in particular across the Jurassic sequence, where continuous profiles, albeit with some scatter, are manifested. This is in line with the corresponding $\delta^{18}O$ and $\delta^{2}H$ profiles. Further similar features of the chloride profiles and the stable water isotope profiles are evident:

- Porewater concentrations mostly agree well with those of groundwaters in the same area.
- Profile shapes are influenced to different degrees by the Keuper aquifer in a similar way to those of the stable water isotopes where three types were defined (see above). Thus, BUL1, STA3 and BAC1 profiles show flat shapes down to the lower part of the Keuper (type 1). Conversely, BOZ1, BOZ2, TRU1, MAR1 and BEN show a clear curvature towards the Keuper aquifer (type 3). STA2 lies somewhere in between, displaying less prominent curvature towards the Keuper aquifer (type 2).

The Cl profiles also indicate some dissimilar features and generally more scatter with regard to the profiles of stable water isotopes, mostly related to the uncertainties in the anion-accessible porosity fraction, as also exemplified by the different scalings shown for JO (see Section 5.4.2). Furthermore, relative errors in water contents increase in low-porosity rocks, in particular for lithologies with small-scale heterogeneity. For example, some variation is manifested in the upper confining units which are both vertically and laterally more heterogeneous than the Opalinus Clay. In this context, the «Herrenwis Unit» in the middle Dogger Group, a low porosity limestone with strong variations in clay-mineral content, is noteworthy. Considerable scatter is also seen in the lithologically heterogeneous Triassic rocks in the lower part of the sequence. Despite this scatter, different trends between the lower Keuper and the Muschelkalk aquifer can be discerned (e.g. decreasing with depth in BAC1, STA2 and STA3, increasing in BOZ1 and BUL1).

The different trends in the lower Triassic section are related to compositional differences in the Muschelkalk aquifer, in which Cl concentrations in the groundwater vary between < 1 g/L to 86 g/L. In contrast, variations in stable water isotope signals are small in this aquifer, all suggesting a strong meteoric component. Available porewater data below the Muschelkalk aquifer point to high Cl concentrations. Locally, the Cl data in the lower part of the Triassic and groundwater data in the Muschelkalk aquifer indicate the influence of halite dissolution from the laterally heterogeneous salt layer in the Zeglingen Formation. This is corroborated by the Br/Cl ratios (see below) and the $\delta^{37}Cl$ data (Wersin et al. 2023).

Overall, the ensemble of Cl profiles suggests diffusive exchange between the porewaters and the bounding aquifers in a similar way as indicated for the data of stable water isotopes.

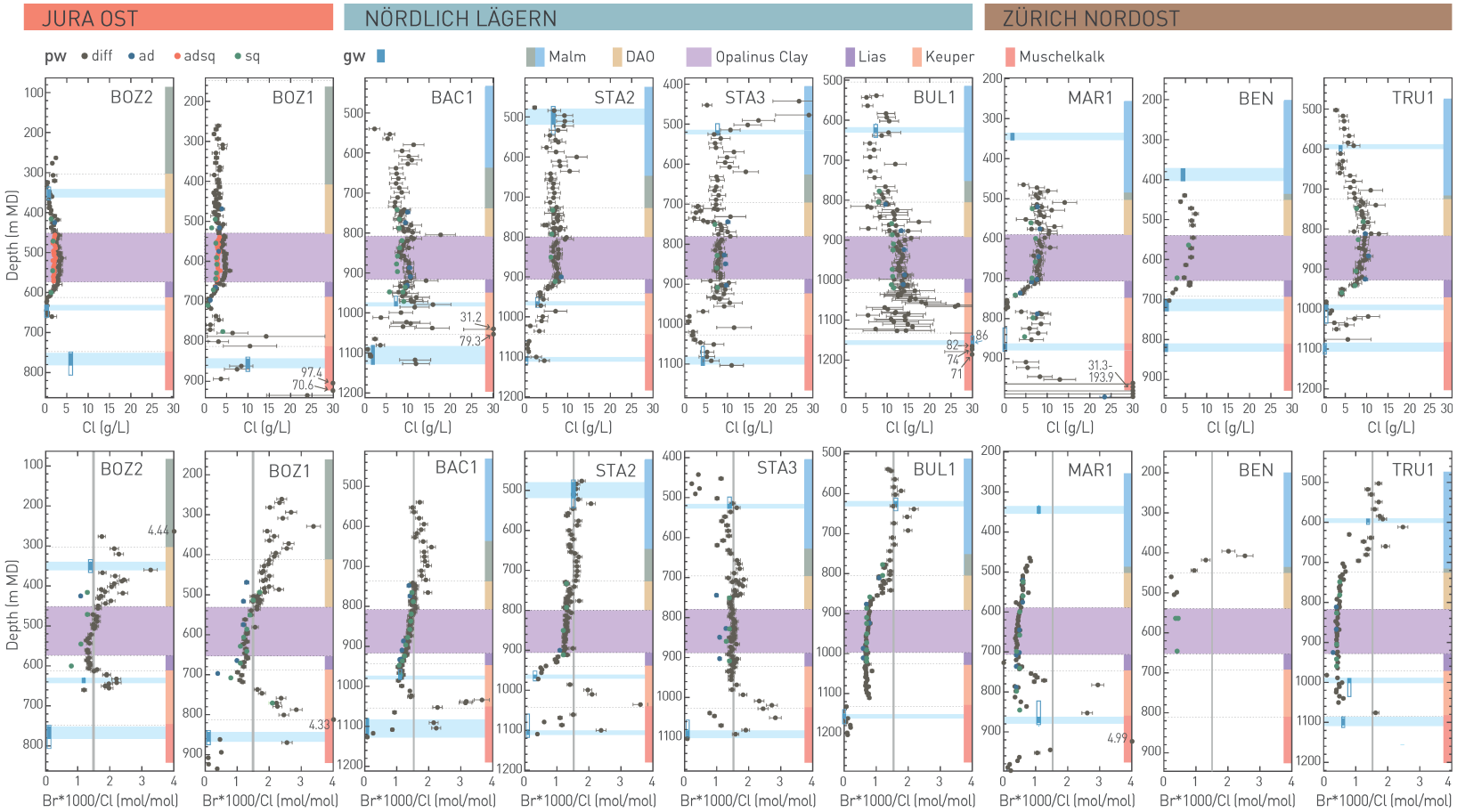


Fig. 4-124: Profiles of chloride (top row) and Br/Cl ratios (bottom row; grey vertical lines indicate seawater ratio) in porewater of the different boreholes

Porewater data were derived from aqueous leaching and scaled based on diffusion data (diff) or based on advective displacement and squeezing data (adsq), or directly from advective displacement (ad) or squeezing (sq) data. For groundwater samples (gw), open rectangles show packer intervals, closed rectangles and light blue bars most likely inflow zones. DAO: Dogger Group above Opalinus Clay. Light blue background indicates location of transmissive zone in the aquifers.

Profiles of Br/Cl ratio of porewater

The Br/Cl profiles (Fig. 4-124) are much smoother and uncertainty ranges are smaller when compared to the single anion profiles. This is because the ratios can be calculated directly from the aqueous extraction data without scaling to the accessible pore space.

The agreement between porewater and adjacent groundwater is again evident in most cases, but in some cases differences occur. Moreover, the continuity of the Br/Cl ratios across the largest part of the profiles, and particularly in the Opalinus Clay, is manifested. This further supports the very similar diffusion behaviour of Cl and Br in the porewater. Regional differences in the Br/Cl ratios can be observed and a trend with Br/Cl ratios in the Opalinus Clay and confining units close to that of seawater in the west (comprising BOZ2, BOZ1, BAC1, STA2, STA3), shifting to ratios below seawater in the east (BUL1, MAR1, TRU1) can be inferred.

The top part of the sequence in the Malm displays Br/Cl ratios close to seawater for all boreholes except for MAR1 (note, however, that for this borehole no porewater data are available in most of the Malm section).

In the centre of the low-permeability sequence, the porewater of the Lias and Dogger (sometimes extending into the upper Keuper) shows a trend from marine Br/Cl ratios in the western boreholes to lower values in the east. There is no obvious correlation with the chloride concentration, the occurrence of halite in the lower Muschelkalk or the hydrogeological conditions in the adjacent aquifers. The Br/Cl ratio in the Opalinus Clay probably reflects conditions that predate the current hydrogeochemical environment in the embedding aquifers. The scatter of the data in this section is conspicuously low, and the Br/Cl values are constant or show only limited trends with depth.

In the lower part of the sequence, there is a tendency towards lower Br/Cl ratios but strong variations with positive anomalies in the anhydrite-bearing Bänkerjoch Formation (BOZ1, BAC1, STA2, STA3, MAR1) can be seen in most of the boreholes, sometimes reaching the upper Schinznach Formation (STA3, MAR1). Br/Cl ratios in the Muschelkalk aquifer are well below the marine value, further supporting the influence of dissolution of halite from the underlying Zeglingen Formation (which has a very low Br/Cl ratio, see Kharaka & Hanor (2014). This interpretation is supported by $\delta^{37}Cl$ data, which yielded similar values for the underlying halite in the three siting regions where analyses were performed (BOZ1, STA3, BUL1). Note that mixing of the groundwater by dilute meteoric water hardly affects the Br/Cl signals.

Results of modelling

The modelling of the Cl profiles followed the same procedure as that described above for the water tracers, also with initial conditions set to approximately maximum values in the central parts of the profiles. However, the evolution times were not fitted. Instead, the times derived from the stable water isotopes were directly applied for Cl and Br/Cl. For BOZ2, the two different variants of the porewater data were considered: the one with the anion accessibility based on diffusion data, the other based on advective displacement and squeezing data. The differences between the two sets simply represent the uncertainty of the porewater data.

The modelling of four example profiles is presented in Fig. 4-125. Approximate matches with the data could be obtained in all cases for transport by diffusion. For BOZ2, however, the timing had to be slightly adjusted compared to that obtained from the water isotopes when modelling the Cl and Br/Cl porewater contents based on the accessibilities obtained from diffusion experiments. Also, compared to the stable isotopes of water, considerable deviations between data and simulations appear in some zones, especially where Cl or Br show a large scatter (e.g. drop to low Cl concentrations in the «Herrenwis Unit» or above the Muschelkalk for STA3). As these zones

do not show any peculiarities, either in the stable isotope values or in the Br/Cl ratios or in the He values, it is believed that these deviations are mainly related to an increased uncertainty in the porosity and the anion-accessible fraction for the more heterogeneous limestone formations, and/or because of contributions from fluid inclusions.

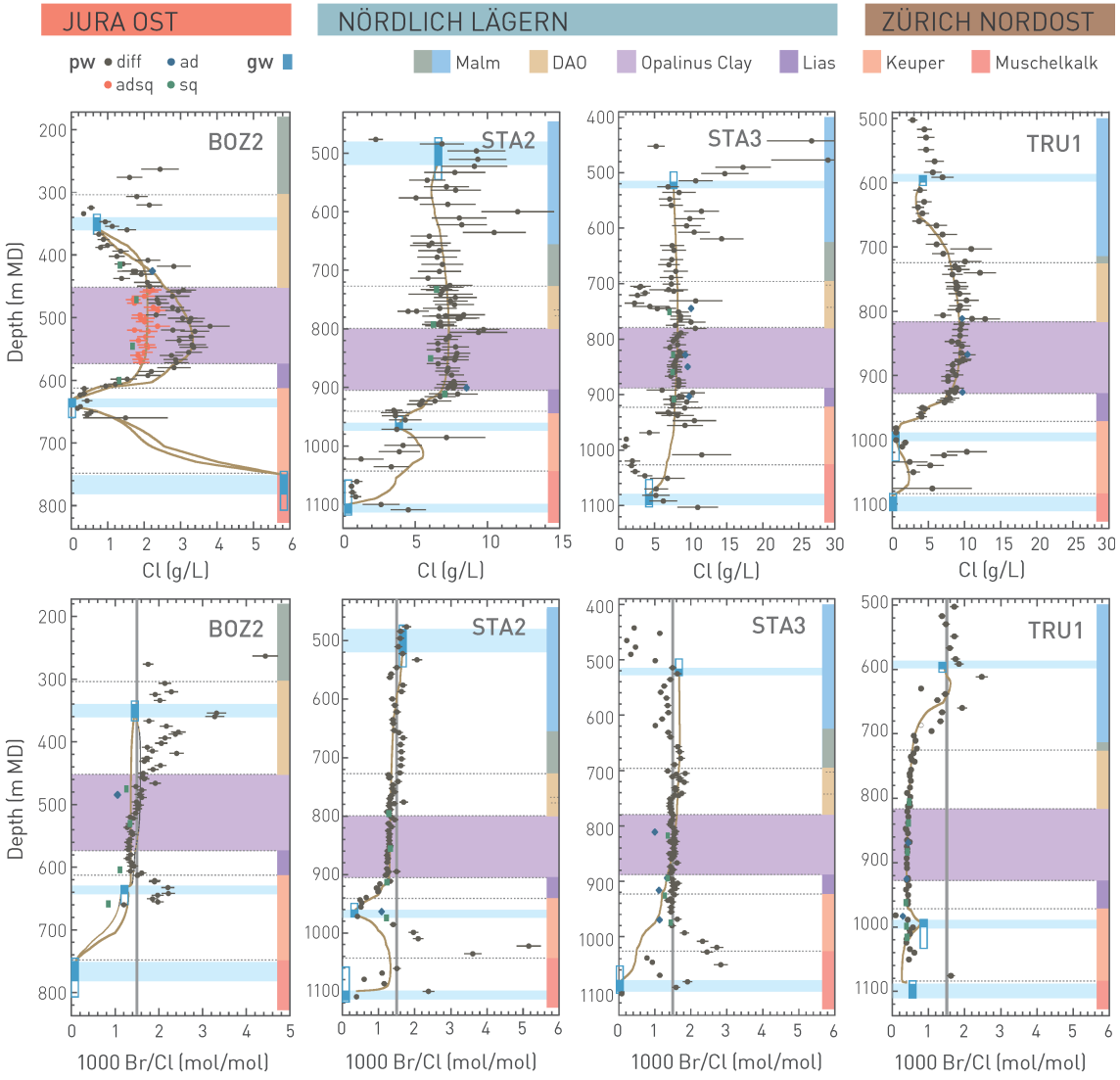


Fig. 4-125: Comparison of measured and simulated profiles of chloride (top row) and of the Br/Cl ratio (bottom row; grey vertical lines indicate seawater ratio) at BOZ2, STA2, STA3 and TRU1

The brown solid lines show the simulation results (data and simulations for two variants for BOZ2, see text). Porewater (pw) data were derived from aqueous leaching and scaled based on diffusion data (diff) or based on advective displacement and squeezing data (adsq), or directly from advective displacement (ad) or squeezing (sq) data. Where groundwater (gw) could be sampled, open rectangles show packer intervals, closed rectangles and light blue bars most likely inflow zones. DAO: Dogger Group above Opalinus Clay. Light blue background indicates the location of the transmissive zone in the aquifers.

4.6.4 Profiles of helium in porewater

Two boreholes per siting region were investigated for dissolved helium in porewater (JO: BOZ1, BOZ2; NL: BUL1, STA3; ZNO: TRU1, MAR1), with the results summarised here and discussed in more detail in Rufer et al. (2024).

General observations

The porewater helium profiles from all six boreholes (Fig. 4-126) show generally smooth trends above the Muschelkalk – interpreted to be indicative of diffusive transport – and are largely comparable in shape to the δ^2H and $\delta^{18}O$ profiles (Section 4.6.2). Over the low-permeability, clay-mineral-rich Lias – Dogger sequence, all profiles show similar concentrations of ^4He in the porewater and predominantly flat profile shapes with depth. As an exception, the BOZ2 profile is influenced in the upper part of this section by the groundwater of the Hauptrogenstein aquifer. $^3He/^4He$ porewater signatures from the central aquitard section show similarly flat profiles with well -constrained isotope ratios. It is noteworthy that helium shows no discernible anomalies in the «Herrenwis Unit» of NL.

Interactions with groundwaters

All helium profiles extend to the Keuper aquifer (Klettgau Formation) or beyond. In two boreholes, transmissivities in the Klettgau Formation were sufficiently large to sample groundwater (BOZ2, TRU1; see Fig. 4-85, Section 4.5.3.10). The associated ^4He porewater profiles show a curvature from higher ^4He concentrations in the hanging units towards lower values close to the groundwater, indicating helium transport in this direction in the past. In BOZ2, the groundwater has a lower ^4He concentration compared to the adjacent porewater, supporting such an interpretation also at the present time. In TRU1, however, the presently measured ^4He groundwater value exceeds that of the adjacent porewater by an order of magnitude, contrasting the observed curvature of the ^4He porewater profile (see discussion below). The $^3He/^4He$ ratios of the porewater in both boreholes match the $^3He/^4He$ ratios of the Keuper groundwater. In the other four boreholes, hydraulic transmissivities in the Klettgau Formation were too low to obtain groundwater samples, and the ^4He porewater profiles show no apparent anomalies. The $^3He/^4He$ profiles of the BOZ1 and MAR1 porewaters, however, do show clearly higher values for samples measured from the Klettgau Formation, indicating some exchange with an isotopically different groundwater, consistent with the observations of the δ^2H and $\delta^{18}O$ profiles (Section 4.6.2). In NL, while a singular slightly higher porewater $^3He/^4He$ value was obtained from the Keuper in the BUL1 borehole, the limited spatial resolution of these profiles in both boreholes does not allow a conclusive interpretation.

Towards the top, all helium profiles (except MAR1) extend to the depth of the Malm (NL, ZNO) or Hauptrogenstein (JO) aquifer, and groundwater samples could be obtained in all investigated boreholes except BOZ1. The small anomalies in the porewater ^4He value of BOZ2 towards the lower groundwater value, and the lack of any excursion in the $^3He/^4He$ porewater profile, suggests an exchange between the porewater and – in terms of helium – an isotopically similar but lower concentration groundwater. No excursion is seen in BOZ1. In NL and ZNO, the STA3 and TRU1 porewaters tend to higher ^4He concentrations and lower $^3He/^4He$ values with shallower depth. In both boreholes, the $^3He/^4He$ value of the Malm groundwater is similar ($\sim 1 \times 10^{-7}$) and matches the porewater $^3He/^4He$ values at the same depth. This congruence, however, contrasts with the mismatch between the ^4He concentrations of the groundwater and adjacent porewater, with the groundwater concentration being roughly 10 times lower in STA3 and 10 times higher in TRU1 compared to the porewater. These observations could indicate a past exchange with a groundwater having a $^3He/^4He$ signature similar to the present-day groundwater but a different ^4He concentration (higher in STA3 and lower in TRU1). As the $^3He/^4He$ ratio of the groundwater is lower

than that of the porewater in the central aquitard, the helium of the groundwater must originate from a source with a more radiogenic (lower $^3He/^4He$ ratio) signature than the sampled aquitard lithologies (see discussion below). BUL1 shows somewhat divergent profile shapes, with porewater ^4He concentrations being elevated in the lower Malm, but then returning to values near identical to the groundwater in the aquifer. The $^3He/^4He$ ratio of the present-day Malm groundwater in BUL1 is also lower than that of the central aquitard porewater, again indicating an external source for (at least a part of) the helium in the groundwater. The porewater $^3He/^4He$ ratios, however, increase from the central aquitard towards the groundwater, suggesting past exchange with a groundwater characterised by a higher $^3He/^4He$ ratio. A former contact with a groundwater with an admixture of air-saturated water ($^3He/^4He$ of 1.38×10^{-6}; Kipfer et al. 2002) or with helium derived from a subcontinental mantle-like reservoir ($^3He/^4He$ of $6.5 – 8.5 \times 10^{-6}$, Ballentine et al. 2002 and references therein) would allow this observed $^3He/^4He$ increase to be explained.

At depth, five of the porewater helium profiles intersect the Muschelkalk aquifer, from which groundwater with roughly one (JO), two (NL) and three (ZNO) orders of magnitude lower ^4He concentration compared to the respective central aquitard porewater was encountered. These five contiguous ^4He porewater profiles show steep gradients towards very low values close to the groundwater depth, generally the lowest observed porewater ^4He concentrations in the profiles. These gradients mimic the δ^2H profiles (Section 4.6.2) and are also similarly observable in the anion tracer profiles (Section 4.6.3). They are interpreted to be the result of either very low porosity (Mazurek et al. 2023a) and diffusivity in the anhydrite-rich lithologies in that interval and/or of recent changes in the groundwater composition. The corresponding porewater $^3He/^4He$ profiles from the central aquitard to the Muschelkalk groundwater are mostly flat and roughly match the $^3He/^4He$ ratio of the groundwater in NL and ZNO. In JO, the basal part of the porewater $^3He/^4He$ profiles trend to lower values towards the Muschelkalk, again matching the groundwater signature in the aquifer.

Discrepancy between ^4He concentrations in the Keuper and Malm groundwater and adjacent porewater in the TRU1 borehole

In this borehole, the sampled ^4He concentration in the Malm and Keuper groundwater exceeds that of the adjacent porewater samples by roughly a factor of 10, while the corresponding $^3He/^4He$ signatures are nearly identical. With the groundwater ^4He concentration also exceeding the values of the central aquitard porewater, it cannot be explained by diffusive flux from the aquitard into the groundwater as the sole source but requires a helium source external to the investigated aquitard/aquifer sequence. A pervasive helium flux from depth across the Mesozoic sediment stack can be excluded because it would contradict the observed low ^4He concentrations in the aquitard porewaters and – at least recently – be restricted by the Muschelkalk groundwater with its very low ^4He concentration. In consequence, this external helium must be supplied to the different groundwater levels in a manner that largely bypasses the aquitard lithologies between them. Based on the groundwater chemistry, gas and isotope compositions of the groundwaters in the Malm, Keuper and Muschelkalk aquifers, a possible pathway along a steep tectonic fault crosscutting the entire sediment stack, such as the NW-SE-trending Neuhausen Fault situated at distance of less than 1 km to the northeast was suggested (Rufer et al. 2024) and references therein). In such a scenario, potential source lithologies for such a radiogenic (low $^3He/^4He$) helium component could be the units of the Permo-Carboniferous Trough and the crystalline basement.

Enrichment of the different groundwaters by such a helium component migrating upwards along a fault would, to a large extent, be controlled by the relation between the ascending helium flux and the groundwater flux. Groundwaters with low flow rates and high residence times would become more enriched in helium and have their $^3He/^4He$ signature lowered compared to faster

flowing aquifers with lower residence times. With the groundwater residence times gradually increasing from the Muschelkalk to the Keuper and Malm aquifers in ZNO, the observed groundwater concentrations and $^{3}He/^{4}He$ signatures qualitatively fit with this conceptual enrichment model.

In-situ production of ^{4}He, minimum accumulation times and diffusion timescales of the observed porewater helium system

The calculated in-situ production of radiogenic ^{4}He shows broadly comparable ranges over most of the stratigraphic stack (Rufer et al. 2024), with notably lower production rates (compared to the more clay-mineral-rich central aquitard) in the evaporitic strata of the Bänkerjoch and the Zeglingen Formation and in the dolostones and limestones of the Schinznach Formation and the Malm. In the carbonate dominated lithologies, these lower ^{4}He production rates are compensated by higher release coefficients of helium from the rock matrix to the porewater. As a result, ^{4}He accumulation rates in e.g. the limestones of the «Herrenwis Unit» in NL are similar to those in more clay-rich units (Rufer et al. 2024). Over all three regions, both, ^{4}He in-situ production and accumulation rates of specific lithotypes are very comparable between boreholes and correspond well to established data such as e.g. from the BEN borehole (Rufer & Waber 2015) or the compilation given in Waber & Traber (2022).

Minimum necessary accumulation times for the presently observed ^{4}He in the porewater over the stratigraphic column clearly indicate that in-situ produced helium is diffusively redistributed along the concentration gradient, generally from the units of the Lias – Dogger via the over- and underlying units into the bounding groundwaters with significantly lower ^{4}He concentrations (at least in the past for Malm and Keuper in TRU1). As such, the porewater of all these aquifer/ aquitard units must be considered an open system with respect to diffusive transport of dissolved gas.

Based on calculated diffusion timescales, helium would require at least 1.8 Myr to diffuse from the centre of the Opalinus Clay to the under- or overlying aquifers (assuming an aquitard thickness of 300 m). These values are much shorter than the minimum ^{4}He porewater accumulation times in the Opalinus Clay (~ 115 Myr in JO, ~ 149 Myr in NL and ZNO; Rufer et al. 2024). This, together with the observed flat ^{4}He and $^{3}He/^{4}He$ porewater profiles in the clay-mineral-rich central sections, implies that the porewater helium inventory across the Lias – Dogger aquitard is the result of a long-term evolution of the porewater system driven by He production and diffusion towards the boundaries.

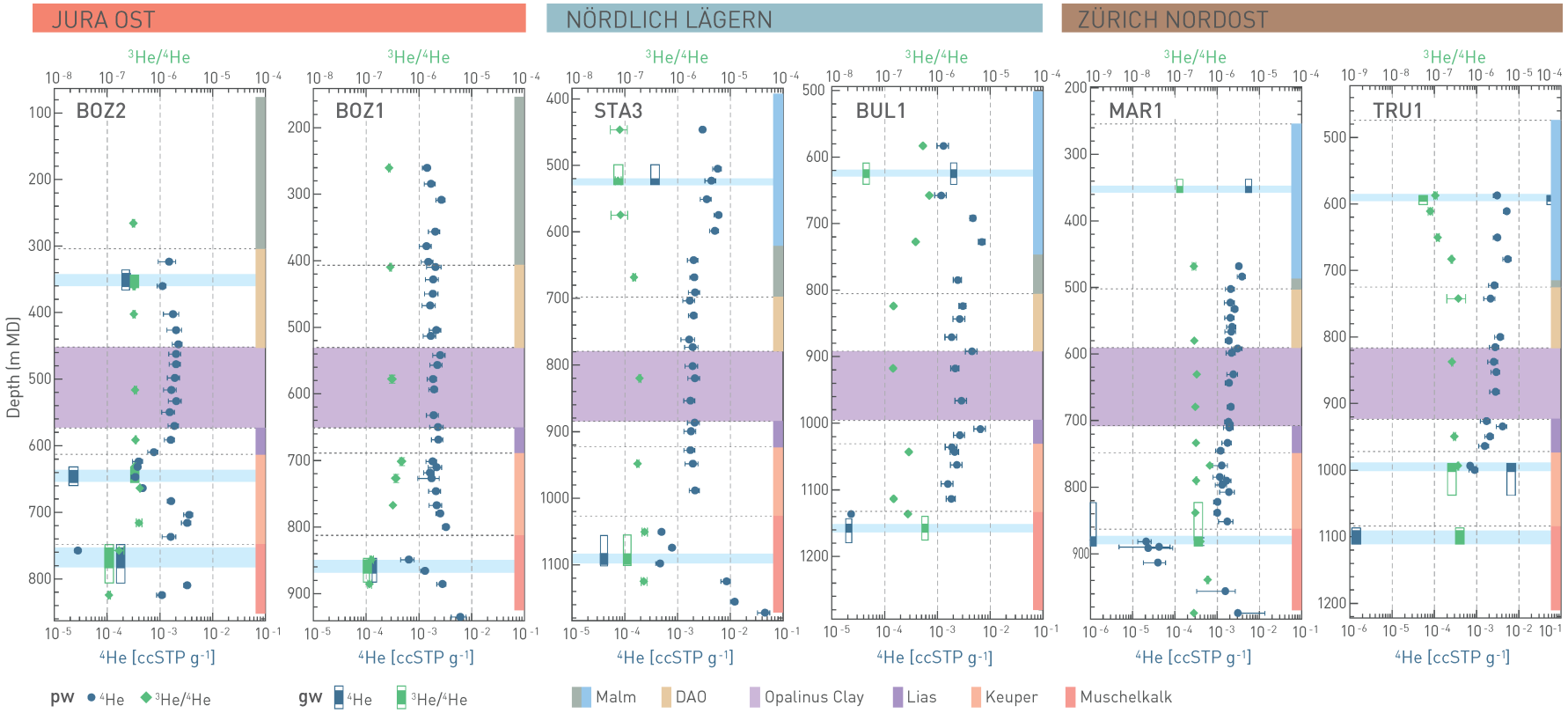


Fig. 4-126: Profiles of ^{4}He concentrations and $^{3}He/^{4}He$ ratios in porewater (pw) and groundwater (gw) for the BOZ2 and BOZ1 (JO), STA3 and BUL1 (NL) and MAR1 and TRU1 (ZNO) boreholes

For the groundwater, open rectangles show packer intervals, closed rectangles most likely inflow zones. DAO: Dogger Group above Opalinus Clay.

4.6.5 Concluding summary of natural tracer profiles

Tracer profiles support the hydrogeological understanding of the siting regions

The profiles of each of the different natural tracers (stable isotopes of the water molecule, Cl and Br/Cl, ^{4}He and $^{3}He/^{4}He$) across the Mesozoic sequence are influenced by various processes that occurred in the past. Most of the profiles are clearly affected by the tracer signatures in an overlying aquifer (the Malm aquifer in ZNO/NL and the Hauptrogenstein aquifer in JO) and in an underlying aquifer in the Muschelkalk, while only some profiles are also clearly affected by the signatures in an aquifer in the upper part of the Keuper (Fig. 4-119, Fig. 4-124, Fig. 4-126). This is consistent with the general hydrogeological knowledge in this area, where the aquifers in the Malm and in the Muschelkalk are known to be of regional extent, while the aquifer in the Keuper has a more local and more variable character (Section 4.5.3.10).

In most cases where porewater tracer profile shapes suggest the presence of an active aquifer and flowing groundwater, the latter could be sampled. In two cases (BOZ1, MAR1), the profile shapes of the stable water isotopes and the anions (and to a limited extent $^{3}He/^{4}He$) indicate the presence of an active aquifer in the Keuper, but no groundwater could be sampled from packer tests because of too low hydraulic conductivity. In two other profiles (STA3, BUL1) where no groundwater could be sampled in the Keuper, no signature of flowing groundwater is seen. These comparisons demonstrate the additional value of profiles of natural tracers in characterising the hydraulic situation.

Characteristic shapes of the tracer profiles are strongly influenced by the Pleistocene landscape evolution

The groundwaters in the aquifers generally show signatures more evolved towards freshwater, that is lower δ values of stable water isotopes and lower Cl concentrations compared to the 'older' porewater signatures in the aquitards between the aquifers. This results in curved profiles of these tracers towards the aquifers, with signatures of the tracers in the porewater approaching those of the groundwater of the aquifers. The noble gas tracer ^{4}He shows partly similar curved profiles to the water tracer $\delta^{2}H$, from higher values in the centre of the aquitard towards lower values in the aquifers.

It is evident, and corroborated by tracer transport simulations, that the more recent evolution (mostly during the Pleistocene) of the profiles occurred due to changes in the boundary conditions in the aquifers, probably following the creation of new recharge and discharge zones for the aquifers. 1D transport simulations were performed for all profiles, taking into account the vertical heterogeneity in porosities and diffusion coefficients according to measured data. The simulations demonstrate that diffusive transport dominated the development of the tracer profiles, and they provide estimates for evolution times of the profiles towards the Keuper aquifer, and partly also for evolution times towards the Malm or Hauptrogenstein and the Muschelkalk aquifers. Specific evolution times derived for each profile and each aquifer vary to some degree (also depending on the initial conditions and parameters used) but are mostly consistent between the water and anion tracers. The trends in evolution times for the different aquifers (longer times of ~ 1.6 – 2.6 Myr for the Malm boundary, intermediate times of ~ 0.7 – 0.1 Myr for the Keuper boundary, shortest times of ~ 0.15 – 0.02 Myr for the Muschelkalk boundary) appear also plausible. These times are broadly in line with the overall understanding of the hydrogeological system and the landscape evolution. The eastward migration of the drainage divide between Rhine and Danube, including the diversion of the Alpenrhein to the west through the Klettgau Valley and a stepwise lowering of the baselevel (Sections 3.5, 6.4.1.2), probably affected recharge and discharge areas in the Malm and Keuper aquifers. The much shorter evolution time of the Muschelkalk aquifer in ZNO may be related to the diversion of the Wutach from the Danube into the Rhine system (Chapter 3,

Section 6.4.1.3) and possible infiltration of glacial melt water. The higher variability of evolution times in the Keuper aquifer compared to the Malm and even more so to the Muschelkalk aquifer probably reflects the more variable nature of the local Keuper aquifer (Section 4.5.3.10).

Long-term geochemical stability evidenced by the near-linear, similar central parts of the profiles

The tracer values in the central parts of the aquitard sequence are interpreted to be 'older' compared to those towards the aquifer boundaries, but they are clearly no longer those of the original seawater at the time of sediment deposition. This means that these porewaters were affected by solute exchange with the overlying or also underlying porewater or groundwater during the long time since deposition, and by production in the case of He. For the water tracers and the anions, an exchange with freshwater has obviously occurred, probably by diffusive exchange with water in shallow aquifers (the surface was exposed to continental, meteoric conditions most of the time since the Late Cretaceous). This led to the observed lower values compared to the original seawater in the central part. In addition, the porewater in the central parts also shows some signs of modification by water-rock interactions (for $\delta^{18}O$) and by exchange with porewater having been affected by precipitation and dissolution reactions (e.g. halites, for Cl and Br concentrations). This earlier history of the profiles is more difficult to reconstruct quantitatively, but the near-linear segments of the profiles in the central parts indicate geochemical stability over very long geological periods (millions to tens of million years).

Remarkably, the signatures of $\delta^{18}O$, $\delta^{2}H$, or of He in the Opalinus Clay are relatively similar between the different sites (Fig. 4-119, Fig. 4-126). The comparably small differences are probably related to a large part to the older, pre-Pleistocene history and not to differences in the present-day signatures of the groundwaters, because these do not yet affect the central parts of the profiles. The overall similarities demonstrate that the porewaters at the different sites experienced a largely common development. That is, they were influenced by the same processes over very long times (millions to tens of million years).

For Cl, the differences in the central part of the profiles (e.g. in the Opalinus Clay) are – in relative terms – larger than for the water tracers. This is interpreted as being related to an earlier, more local input of Cl from the dissolution of underlying evaporitic formations in some of the profiles, i.e. from the dissolution of halite from the underlying Zeglingen Formation. This interpretation is supported by $\delta^{37}Cl$ data, which yielded similar values in the porewater and for the underlying halite. The localised character of the Cl input is probably related to the heterogeneous distribution of halite beds, and possibly also to discrete faults across the overlying low-permeability anhydrite beds. In any case, the Cl input mainly in BUL1 in NL and TRU1 and MAR1 in ZNO must have occurred a very long time ago, because the signatures reach comparably high up in the profiles. It should also be noted that high Br/Cl ratios significantly above that of seawater were observed approximately at the base of Bänkerjoch Formation in some boreholes, which may originate from the evaporation of seawater beyond the saturation of Br salts. The preservation of such high ratios, together with the presence of highly soluble evaporitic minerals remaining since the time of deposition in this zone, is remarkable but in line with the extremely low porosity (and therefore low diffusion coefficients) in the anhydrite-rich rocks.

The He data also support the long-term geochemical stability of the system. While relevant fractions of the He produced in situ in the central part of the low-permeability sequence (i.e. in the Opalinus Clay) have been lost most probably by diffusion, concentrations of the dissolved noble gas isotope ^{4}He are still more than 4 orders of magnitude higher than in air-saturated water. For the Opalinus Clay, build-up times of > 115 Myr can be calculated from these concentrations and the in-situ production rates. More than 65% of the He produced in the Opalinus Clay since deposition is still present, which demonstrates the strong barrier efficiency of the system.

4.7 Palaeo-fluid flow reconstructed by geochemical investigations of secondary mineralisations

Key points:

- Mineralised fractures (veins) can be observed in all stratigraphic units. The Opalinus Clay in particular shows only few. They are thin (thickness mostly 0.5 – 3 mm) and are mainly found in narrow zones (1 – 2 metres thick). Between such zones, the Opalinus Clay is essentially free of veins.
- The combination of U-Pb dating, clumped isotope thermometry and isotope signatures of vein minerals allow constraining the palaeohydrogeological evolution and the behaviour of the geological barrier over timescales beyond the memory window of the porewater tracer profiles.
- In general, the data indicate evolutions of the mineral-forming fluids from modified seawater-type prior to the Eocene times towards meteoric waters in the Cenozoic.
- The investigated veins in the Opalinus Clay precipitated from fluids with less negative $\delta^{18}O$ values compared to the present-day porewater and/or at higher temperatures. This suggests vein formation prior to Pliocene cooling.
- Based on $\delta^{13}C$ and Sr-isotope data, an internal evolution of the mineral-forming fluids is conceivable for the Opalinus Clay, however, they could also attest to an efficient rock-buffering.

4.7.1 Overview

Mineralised fractures (veins) record the composition of the fluid at the time of mineral precipitation, that is they are archives of the evolution of ground- and porewater. The combination of U/Pb and U/Th dating, clumped isotope thermometry (see also Section 4.3.5) and other isotope proxies allows reconstruction of the palaeohydrogeological evolution, notably for the time period older than the memory window of the porewater tracer profiles (Section 4.6) or from the analyses of groundwater composition (Section 4.5.5). Comparing such information to present-day values for pore- and groundwater provides an insight into the long-term behaviour of the aquitards (geological barriers), particularly with respect to fluid flow along fractures. Note that hydromechanical processes leading to self-sealing of fractures are discussed in detail in Section 5.7.

This section summarises the investigations of vein mineralisation in the TBO drill cores and draws conclusions on past transport in the aquifer-aquitard systems. It builds on previous studies on palaeo-fluid flow in the Mesozoic cover in Northern Switzerland by Pearson et al. (1991; old Nagra boreholes), Nagra (2001; Benken borehole), de Haller et al. (2011; Oftringen borehole), Mazurek & de Haller (2017; Mont Terri rock laboratory), Mazurek et al. (2018; Schlattingen borehole) and Looser (2022; clay pit of Frick).

4.7.2 Approach, methodology and limitations

The approach for reconstructing palaeo-fluid flow is based on the investigation of mineralised structures by 1) thin-section petrography to identify the inventory of different types of mineralisation, different mineral growth generations and paragenetic sequences and 2) using a set of selected isotope tracers ($\delta^{18}O$, $\delta^{13}C$, $\delta^{34}S_{SO4}$, $\delta^{18}O_{SO4}$, $^{87}Sr/^{86}Sr$) and clumped isotope thermometry (Meckler et al. 2014, Müller et al. 2017) of ~~s~~econdary minerals. Thus, knowing the $\delta^{18}O$ value of the mineral and the temperature of precipitation allows the calculation of $\delta^{18}O$ of the mineral-forming fluid. These results are then combined with information on the timing of mineral precipitation obtained from U-Pb and U-Th geochronology for reconstructing their evolution with time. The respective analytical protocols and methods are described by Dold & Spangenberg (2005), Waber (2020) and Looser (2022).

Challenges related to reconstructing palaeo-fluid flow in sedimentary sequences relate to the different behaviour of solutes/isotopes while interacting with the rock. In the case of carbon and strontium, the rock is the dominant reservoir and thus generally buffers the isotope composition of the fluid. This means that external fluid signals will be obliterated during migration, especially when fluid/rock ratios and fluid fluxes are low. In contrast, the oxygen isotope system is more robust to rock buffering as the water constitutes a very large reservoir for oxygen. Apart from concentration differences between rock and fluid, concentration differences between different fluids also have to be considered. For example, an infiltrating meteoric water with low strontium concentrations has a limited potential to change the Sr isotope signal of a local marine porewater showing high strontium concentrations (i.e. lever rule).

Ultimately, it has to be noted that geochemical data do not provide direct information on the transport mechanisms. These have to be deduced in the context of the regional hydrogeological evolution and be verified by transport simulations. Thus, for the remainder of this section, the term "migration" is used for solute movement in the underground by either advection or diffusion.

4.7.3 Investigated structures and inventory of mineralisations

In general, two different types of mineralisation were distinguished: 1) infills of primary macropores mainly observed in the Upper Dogger («Herrenwis Unit») and the Lias (Staffelegg Formation) and 2) tectonic mineralisations associated with fractures, i.e. veins. The latter are unevenly distributed over the Mesozoic sequence. The greatest density of veins is observed in the competent carbonates of the Malm Group (Section 4.3.4, Fig. 4-61, Fig. 4-65, Fig. 4-69), where they can attain thicknesses of a few centimetres (Fig. 4-127a, b). The less competent, clay-mineral-rich Dogger – Lias units show distinctly fewer veins, the Opalinus Clay in particular shows only few. Most of these veins are between 0.5 – 3 mm thick (Fig. 4-127c, d) and are mainly found in narrow zones (1 – 2 metres thick). Between such zones, the Opalinus Clay is essentially free of veins.

In general, mineralisation is associated with micro faults (i.e. slickenfibres) or within extensional joints and tension gashes (e.g. blocky calcite with no shear or slip indicators). The investigated veins exhibit a large variation in orientation, reflecting the polyphase deformation history of Northern Switzerland (Section 4.3 and Chapter 3; Akker et al. 2023).

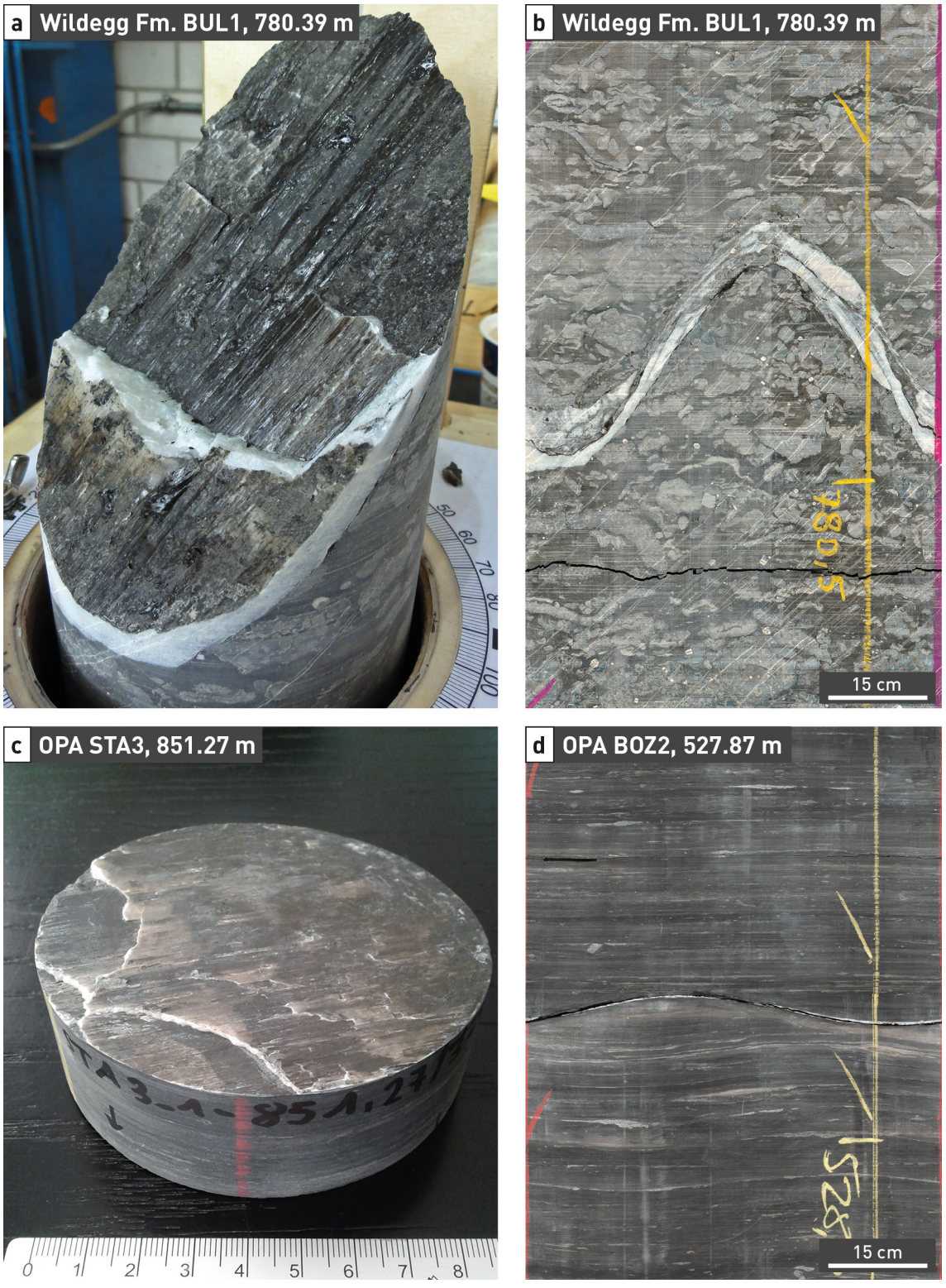


Fig. 4-127: Examples of veins from the TBO boreholes

(a) Reverse micro fault with cm-thick synkinematic calcite in the Malm Group of the BUL1 borehole (from Nagra (ed.) 2021a, Dossier V). (b) 360° core photograph of the same structure (from Nagra (ed.) 2021a, Dossier V). (c), (d) Reverse micro fault with mm-thick synkinematic calcite in the Opalinus Clay of the STA3 and BOZ2 boreholes, respectively.

Information on the petrography of secondary mineralisations in the Dogger – Keuper interval for various sites across Northern Switzerland (i.e. older boreholes of Nagra and SEAG, Mont Terri) is documented in a variety of reports and publications, which are compiled and summarised by Mazurek & Aschwanden (2020). The TBO boreholes yielded a similar inventory of vein-filling minerals as observed in nearby older boreholes, including calcite, which is consistently present at all investigated sites and constitutes the dominant infill of veins. Calcite vein-fillings are either single-phase (Fig. 4-128a) or they contain multiple generations, the latter reflecting polyphase deformation and precipitation (Fig. 4-128b; see also Akker et al. 2023). Additionally, there are minor occurrences of celestite (Fig. 4-128c) and pyrite as vein-infills, mainly in the Dogger Group above Opalinus Clay and in the Opalinus Clay itself. Also, there are minor occurrences of dolomite with saddle habitus as pore infills in the «Herrenwis Unit» (Fig. 4-128d).

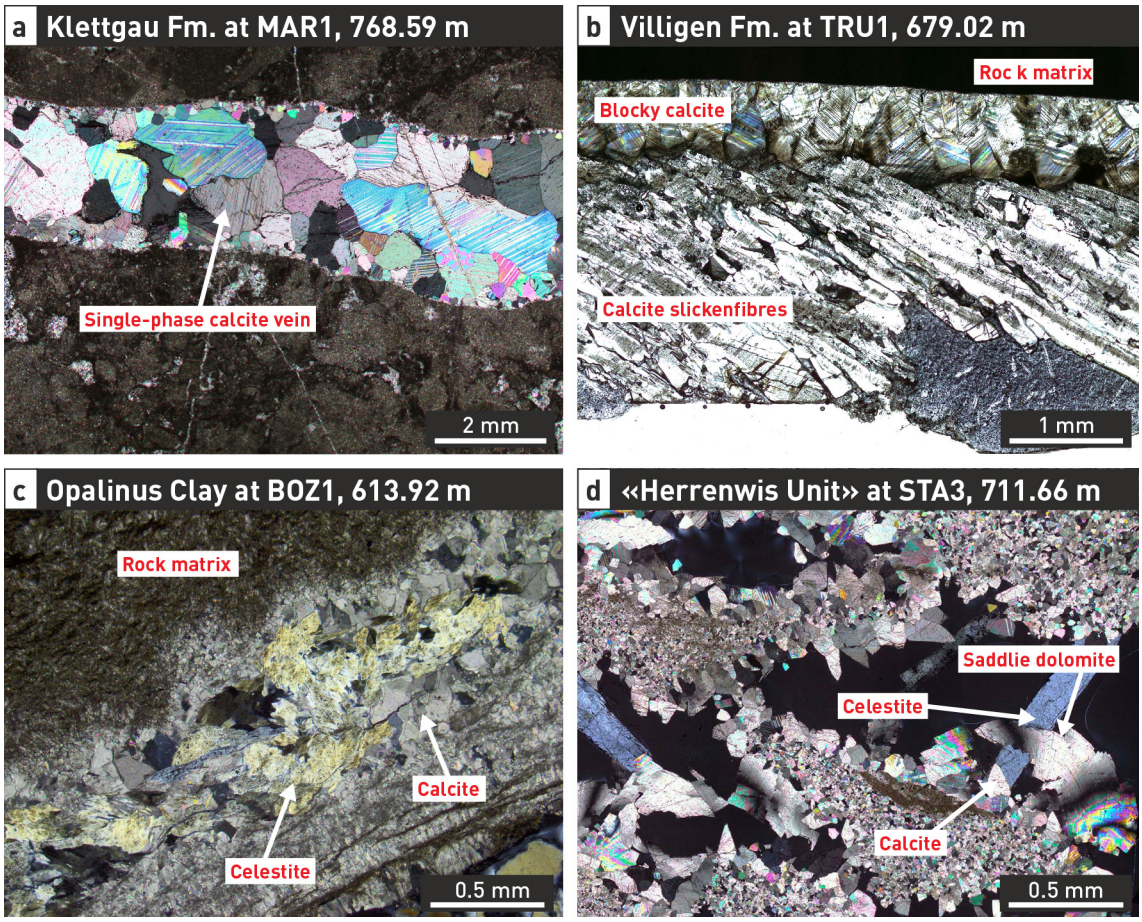


Fig. 4-128: Mineralised structures in the Opalinus Clay and other Mesozoic units

(a) Single-phase calcite vein (cross-polarised transmitted light microscopy). (b) Two calcite generations representing polyphase deformation (plane-polarised transmitted light microscopy). (c) Calcite-celestite intergrowth in a tension gash (cross-polarised transmitted light microscopy). (d) Saddle dolomite as pore filling. Saddle dolomite typically shows curved crystal faces (cross-polarised transmitted light microscopy).

4.7.4 Results of geochemical investigations of vein calcite

During the Jurassic and probably parts of the Cretaceous, marine conditions prevailed in Northern Switzerland (Mazurek & de Haller 2017). The $\delta^{18}O$ values of calcite-forming fluids (obtained from clumped isotope thermometry, see Section 4.3.5) in the Mesozoic strata for this period are mostly around 0 ‰ VSMOW or even slightly above (Fig. 4-129). They can be interpreted as remnants of old formation water that evolved from the original seawater by interaction with the rock in the course of geological history. The slightly negative $\delta^{18}O$ values of some early-diagenetic phases in the Lias Group may evidence localised, short-term emergence (Section 4.2.5; see also Reisdorf & Wetzel 2018).

In the Late Eocene, at around 52 Ma, the $\delta^{18}O$ values of calcite-forming fluids started to evolve towards meteoric signatures, reaching -4 to -5 ‰ VSMOW during the Oligocene – Early Miocene times (Fig. 4-129 and Fig. 4-130a). This trend resulted from subaerial exposure since at least Eocene times (Chapter 3, Section 4.3.5; Schegg & Leu 1998, Mazurek et al. 2006), which led to karstification in the top of the Malm Group, deposition of the Bohnerz Formation (Siderolithic Group) and, ultimately, direct recharge and in-diffusion of meteoric water into the Mesozoic strata. Continental conditions persisted throughout the Oligocene and downward migration of meteoric water into the Mesozoic strata continued. Surficial freshwater for this time period showed $\delta^{18}O$ values (based on fossil bone and tooth apatite of vertebrates; Tütken et al. 2006, Tütken & Vennemann 2009, Héran et al. 2010, Tütken 2014, Tütken & Absolon 2015, Ring et al. 2020) that are in good agreement with those of the calcite-forming fluids observed in the Malm Group and the Dogger Group above Opalinus Clay.

Samples from the clay pit in Frick (Fig. 4-60) show meteoric $\delta^{18}O$ values in the Staffelegg Formation at 21 – 34 Ma (Fig. 4-130b). The processes by which the meteoric signals were transported to these levels of the strata are not yet fully understood. However, the Cenozoic evolution of the Frick area differs from the siting regions in the sense that Molasse deposits were substantially thinner. Whether this is due to non-deposition or due to OMM to post-OMM erosion remains unclear (Diebold et al. 2006). The erosional event removed not only possible older Molasse deposits but also locally Mesozoic units down to the Dogger Group (Diebold et al. 2006). That is, there were probably prolonged meteoric conditions, and the relevant overburden thickness was substantially thinner, resulting in a more direct transmission of meteoric signals. Furthermore, the relative proximity to the Upper Rhine Graben (Section 4.3.3) could have had an influence on vertical fluid flow by the formation of normal faults at that time. Based on the aforementioned reasons, these samples from Frick are not necessarily representative for the palaeohydrogeological evolution of the siting regions.

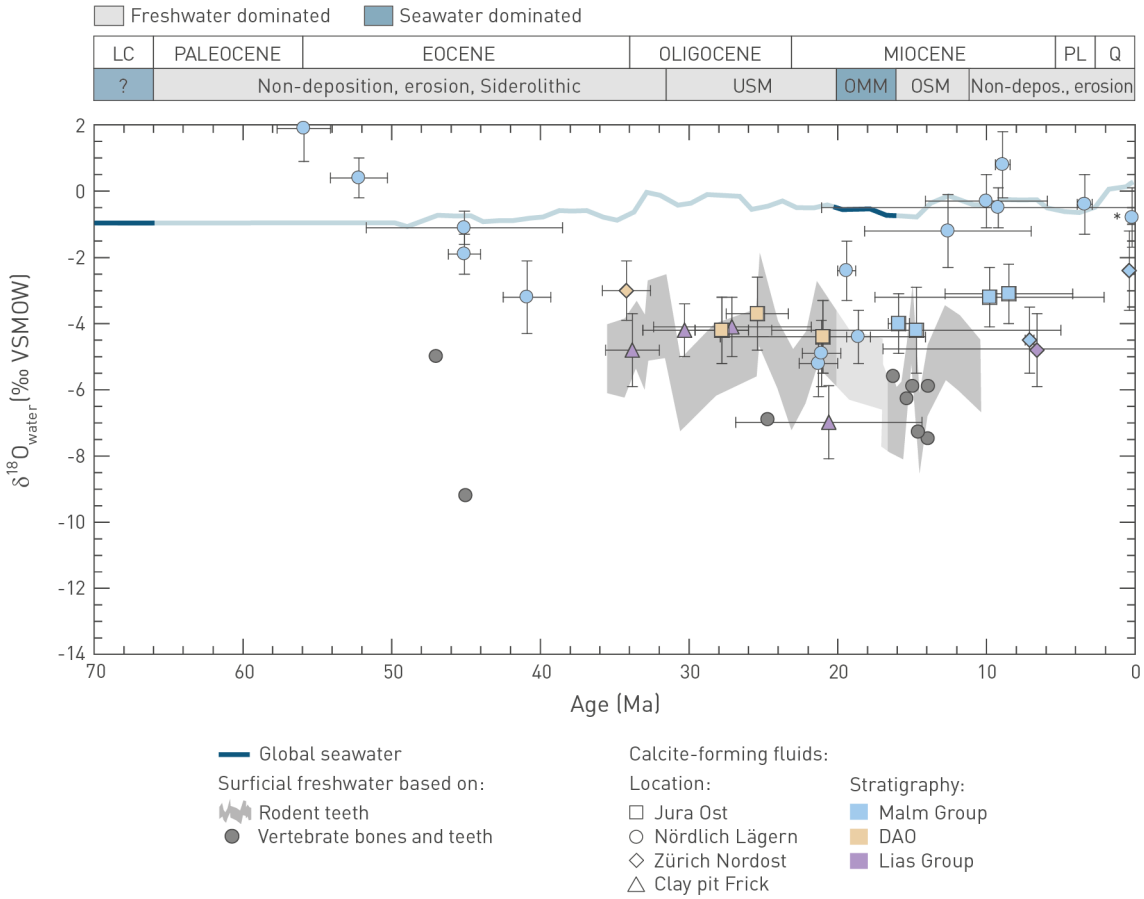


Fig. 4-129: Evolution of $\delta^{18}O$ of calcite-forming fluids over the last 70 Ma as obtained from coupled clumped isotope thermometry and U-Pb and U-Th dating of calcite cements

For comparison, literature data for seawater (Lear et al. 2000) and Eocene – Miocene surficial freshwater are also shown (Tütken et al. 2006, Tütken & Vennemann 2009, Héran et al. 2010, Tütken 2014, Tütken & Absolon 2015, Ring et al. 2020). As a result of consistently low U concentrations and high Pb contents (dominated by common Pb), no reliable U-Pb age data could be obtained for vein calcite in the Opalinus Clay (Akker et al. 2023). Data for the Lias at the Frick clay pit are from Looser (2022). Q: Quaternary, PL: Pliocene, LC: Late Cretaceous, DAO: Dogger Group above Opalinus Clay. Post-kinematic calcite (see text for details). Data of regional fault-related outcrops in the Eastern Jura (see Fig. 4-73) are not shown here because they are not considered representative for the fluid evolution in the comparably weakly deformed and deeply buried Mesozoic strata in the siting regions.

For the siting regions, the earliest occurrence of meteoric waters in the Lias Group is indicated by a vein in ZNO dated to 7 Ma (although the uncertainty on the age is large). The calcite-forming fluid shows similar negative $\delta^{18}O$ values as observed for the Dogger Group above Opalinus Clay (ZNO and JO) during the Oligocene. Thus, for the hydrogeological evolution of the Opalinus Clay in the siting regions, an influence of meteoric waters is indicated latest by Late Miocene times.

For the Malm Group, a large variability in $\delta^{18}O$ values is indicated for the Miocene Epoch (Fig. 4-129). This variability is interpreted to result from:

- Downward migration of seawater during the Burdigalian marine transgression and deposition of the Upper Marine Molasse Group (OMM) at around 16 – 20 Ma (Garefalakis & Schlunegger 2019; Chapter 3), which interrupted Miocene freshwater-dominated conditions. This is also evidenced by distinct trends of upwards decreasing $\delta^{13}C$ and increasing $^{87}Sr/^{86}Sr$ values from vein calcite in the top of the Malm Group at the Oftringen borehole (see also de Haller et al. 2011 and for the NL boreholes Fig. 4-132 and Fig. 4-133).
- After deposition of the OMM, freshwater-dominated conditions were re-established and meteoric water migrated into the Mesozoic strata. The Molasse deposits are relatively thin in JO (ca. 100 m in total), whereas in NL they reach a thickness of more than 400 m. For the latter siting region this results in higher burial temperatures (50 – 80 °C in NL vs. 45 – 60 °C in JO for the Malm Group) and longer transport distances, i.e. potentially longer subsurface residence time of the calcite-forming fluids during which their isotope composition is modified by the interaction with the rock.

For two of the veins in the Malm Group, U-Th geochronology yields Pleistocene ages. The corresponding vein calcite from ZNO (Villigen Formation, TRU1-1) is synkinematic, collected from a strike-slip fault that formed in response to contraction (Section 4.3.4). In contrast, the vein calcite from NL («Felsenkalke» and «Massenkalk», STA3-1) is post-kinematic, i.e. reflecting a fluid pulse with no concurrent deformation. The mineral-forming fluids of these two young vein calcites show the same difference in their $\delta^{18}O$ values as observed for Miocene times, i.e. with seawater-type $\delta^{18}O$ values in NL and distinctly more negative values in ZNO. Similarly, as explained above, variation in subsurface residence times, transport distances and burial temperatures can explain the difference in the $\delta^{18}O$ values of the calcite-forming fluids between the siting regions. Also, the groundwater in the Malm aquifer can play a role: At least for the vein from the Villigen Formation in ZNO (0.4 Ma; Fig. 4-130), a transient hydraulic connection with the Malm groundwater (i.e. as sampled at present) is evident. This is indicated by a distinct shift of the calcite-forming fluid towards a more positive $\delta^{18}O$ value (in good agreement with those of the groundwater) relative to the present-day porewater in the adjacent rock.

As observed for the confining units, calcite-forming fluids in the Opalinus Clay show a large variability in their $\delta^{18}O$ signatures ranging from modified seawater-type to distinctly negative values (Fig. 4-130e). The consistently low U concentrations and the high Pb contents of the vein calcites dominated by common Pb (Akker et al. 2023) result in no reliable U-Pb age data being obtained (except for two Jurassic ages; Fig. 4-73) that would help to better constrain the evolution of the calcite-forming fluids. Following the above observations for the confining units, i.e. involving a transition from modified seawater-type to meteoric $\delta^{18}O$ values during Eocene – Oligocene times, it is argued that the variability observed for the calcite-forming fluids in the Opalinus Clay reflects a similar evolution. Based on the temperature – depth history of the Mesozoic strata (Mazurek et al. 2006, Looser 2022; Section 4.3.5), the temperatures of vein formation of 57 – 102 °C for the modified seawater-type (Paleocene and older) and 50 – 81 °C for the meteoric waters (Eocene and younger) are consistent with such a hypothesis. This is illustrated in Fig. 4-131a, which shows the temperature and $\delta^{18}O$ values of calcite-forming fluids together with the timing of precipitation in veins of the confining units. Hence, for the Opalinus Clay, vein formation during Late Jurassic - Cretaceous, as well as later during Eocene – Miocene times, is indicated. Note that all calcite-forming fluids in the Opalinus Clay show less negative $\delta^{18}O$ values and/or higher temperatures compared to the present-day porewater in the adjacent rock matrix (Fig. 4-131b), suggesting that vein formation occurred before Pliocene cooling started at around 5 Ma (Section 4.3.5), i.e. beyond the memory window estimated for the porewater $\delta^{18}O$ profiles (Section 4.6.2).

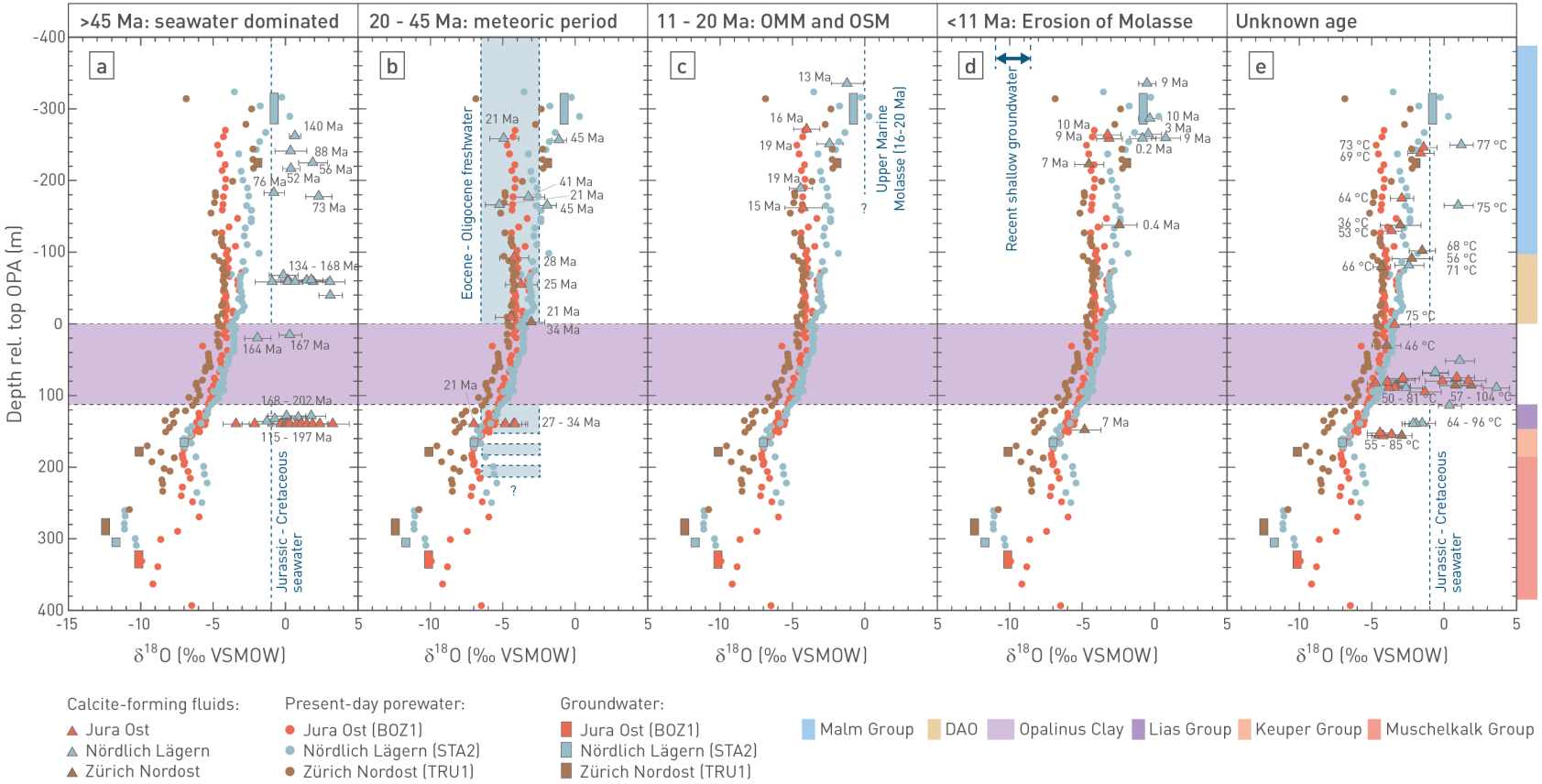


Fig. 4-130: Depth profiles of the oxygen isotope composition of calcite-forming fluids derived from clumped isotope thermometry for different time periods

Depths are relative to the top of the Opalinus Clay. For comparison, the oxygen isotope composition of the present-day porewater is also illustrated (Section 4.6), as well as the values for the groundwater in the confining aquifers (Section 4.5.5). The numbers indicate U-Pb/Th ages or clumped isotope temperatures for structures with no reliable age data. a) Time period for which calcite-forming fluids constitute remnants of old formation water that evolved from the original seawater by interaction with the rock. b) Time period during which meteoric waters migrated into the Mesozoic strata before deposition of the Upper Marine Molasse Group (OMM). c) Situation during deposition of the OMM and the Upper Freshwater Molasse (OSM) Groups. d) Situation after Molasse deposition. e) Samples with no reliable age data.

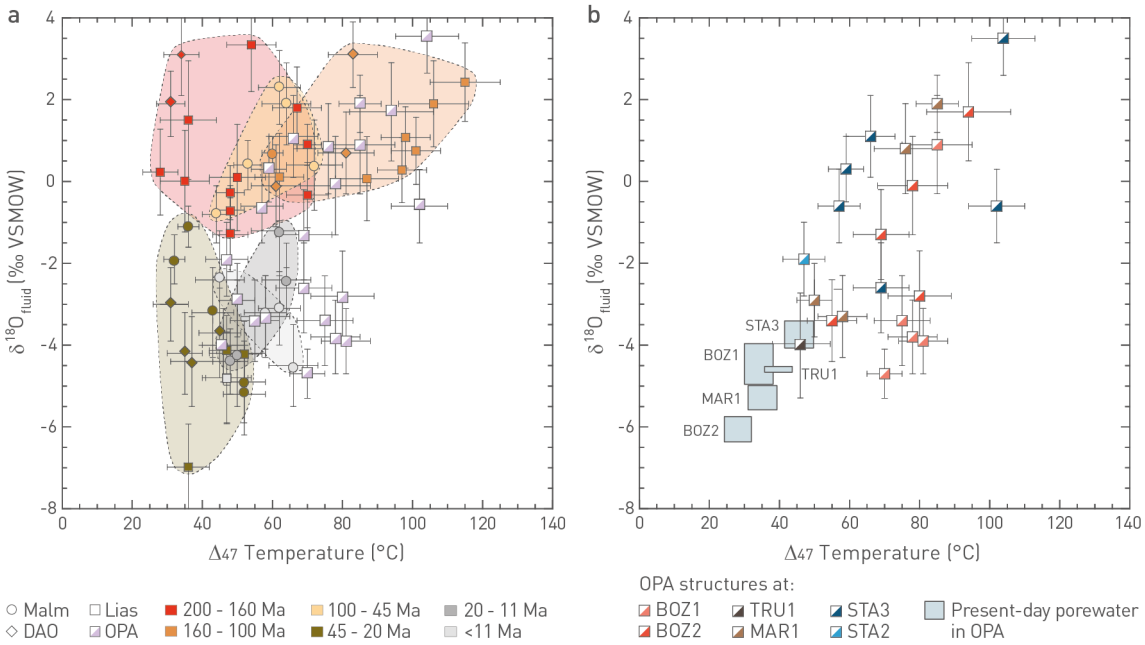


Fig. 4-131: Temperature and $\delta^{18}O$ values of calcite-forming fluids from clumped isotope thermometry

a) The coloured fields indicate the timing of vein formation in the units above and below the Opalinus Clay (based on U-Pb geochronology) to better constrain the timing of vein formation in the Opalinus Clay (no reliable U-Pb data; see text). Calcite-forming fluids from the Malm affected by relatively shallow, near-surface processes (e.g. downward migration of OMM seawater) are not shown in this graph (see Section 4.7.6). b) Calcite-forming fluids in the Opalinus Clay compared to the $\delta^{18}O$ values and temperatures of the present-day porewater in the adjacent rock matrix. DAO: Dogger Group above Opalinus Clay, OPA: Opalinus Clay.

Regarding the $\delta^{13}C$ of vein calcite, the Opalinus Clay generally shows similar values to the matrix carbonate (except for JO; see below), but at lower levels compared to the Malm Group (Fig. 4-132). This difference probably reflects the relatively higher content of organic material in the clay-mineral-rich lithologies (e.g. Nagra (ed.) 2021a, Dossier VIII), which provides a source for isotopically light carbon. Thus, an internal evolution of the calcite-forming fluids is conceivable for the Opalinus Clay. However, the coherence of $\delta^{13}C$ of veins and rock matrix is a necessary but not a sufficient argument. Fracture apertures in the clay-mineral-rich lithologies are generally very narrow and potential fluid fluxes were supposedly low; thus, rock buffering is considered very effective, and any external carbon isotope signal could be obliterated by the interaction with the rock (see Section 4.7.2). Vein calcite in the Opalinus Clay in JO is somewhat exceptional because $\delta^{13}C$ values of vein calcite and matrix carbonate are clearly different, with the former showing distinctly more negative values. The reason for this is yet to be resolved. Potentially, it reflects an external signal, but it could also result from, for instance, the decomposition of organic material (Harrison et al. 2022), similarly to what was suggested for the very negative $\delta^{13}C$ values of early diagenetic calcite in the underlying Staffelegg Formation.

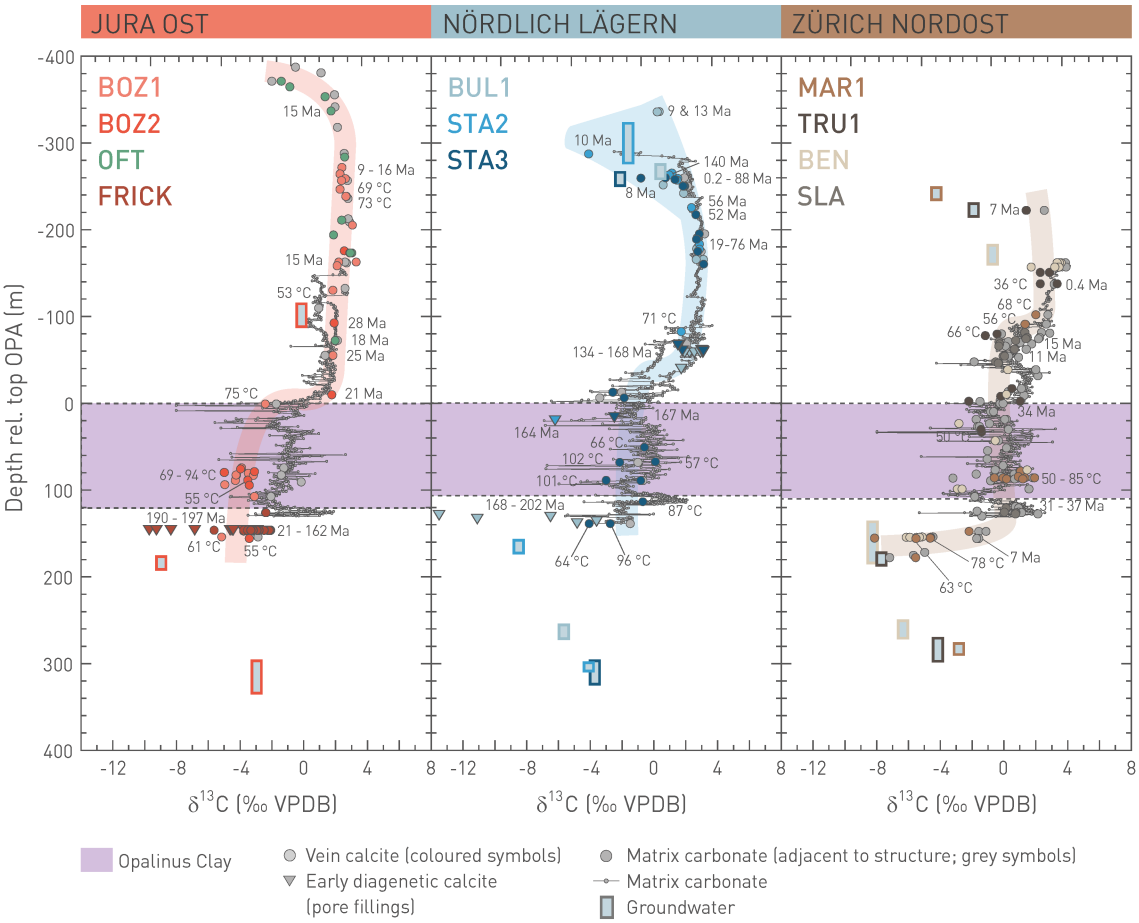


Fig. 4-132: Depth profiles of the carbon isotope composition of vein calcite and matrix carbonate

Depths are relative to the top of the Opalinus Clay. For comparison, the carbon isotope composition of the groundwater samples is also shown. The black numbers indicate U-Pb ages (Ma) or clumped isotope temperatures (°C) for samples with no reliable U-Pb age. The coloured fields highlight the trends observed for vein calcite. Data for the older Benken (BEN), Oftringen (OFT) and Schlattingen (SLA) boreholes are from Nagra (2001), de Haller et al. (2011) and Mazurek et al. (2018). The data from the clay pit of Frick are from Looser (2022). Note that the OFT data are illustrated in the JO plot although the borehole is located ca. 27 km southwest of the siting region. Matrix carbonate composition based on Ruf et al. (2005), Nagra (ed.) 2023a, Dossier IV) and Wohlwend et al. (2024). OPA: Opalinus Clay.

In the Opalinus Clay, $^{87}Sr/^{86}Sr$ ratios of vein calcite and celestite are all higher compared to the overlying more calcareous lithologies (Fig. 4-133; except for the top of the Malm Group where downward migration of Burdigalian seawater is evident). Also, $^{87}Sr/^{86}Sr$ ratios of vein calcite are higher compared to the matrix carbonate. This implies that the mineral-forming fluids in the Opalinus Clay evolved within rubidium-bearing lithologies where they picked up radiogenic strontium from continuous rubidium decay. An evident source for radiogenic strontium is the rubidium associated with clay minerals. As for the carbon isotopes, an internal evolution of the mineral-forming fluids is conceivable for the Opalinus Clay (bulk rock $^{87}Sr/^{86}Sr$ ratios up to 0.714052; Nagra 2001) but again this could also simply attest to an effective rock buffering (see Section 4.7.2).

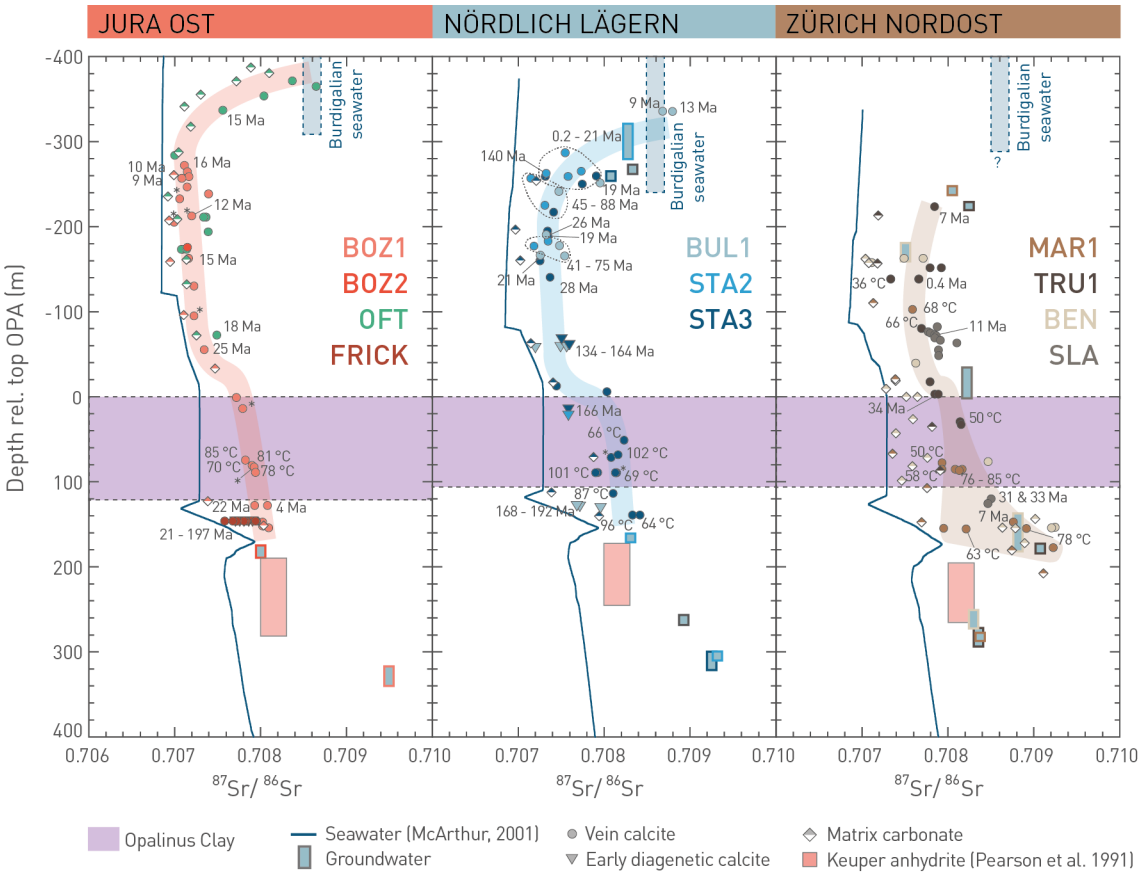


Fig. 4-133: Depth profiles of strontium isotope ratios of vein calcite, vein celestite and present-day porewater

Depths are relative to the top of the Opalinus Clay. For comparison, the palaeo-seawater line is also illustrated (McArthur et al. 2001), as well as the present-day groundwater in the confining aquifers (Section 4.5.5) and Keuper anhydrite (Pearson et al. 1991). The black numbers indicate U-Pb ages (Ma) or clumped isotope temperatures (°C) for samples with no reliable U-Pb age. The coloured fields describe the general trends observed for the mineral-forming fluids (see text for details). Data for the Benken (BEN), Oftringen (OFT) and Schlattingen (SLA) boreholes are from Nagra (2001), de Haller et al. (2011) and Mazurek et al. (2018). The data from the clay pit of Frick are from Looser (2022). Note that the OFT data are illustrated in the JO plot although the borehole is located around 27 km southwest of the siting region. OPA: Opalinus Clay. Samples marked with an asterisk refer to vein celestite.

4.7.5 Results of geochemical investigations of vein celestite

Fig. 4-134 shows the $\delta^{34}S$ and $\delta^{18}O$ isotope signatures for vein celestite observed in the BOZ1 and STA3 boreholes. For comparison, isotope data for marine sulphate during different geological periods are also illustrated (Claypool et al. 1980), as well as $\delta^{34}S$ and $\delta^{18}O$ values of evaporites in the Bänkerjoch Formation and the Muschelkalk Group (Rick 1990, Pearson et al. 1991, Bernasconi et al. 2017). The vein celestite in all of the investigated samples shows $\delta^{18}O$ versus $\delta^{34}O$ outside the range of marine sulphate at all times at which seawater was potentially present in the region, indicating modification by sulphate reduction. This is further evidenced by the occurrence of pyrite as vein infill (Section 4.7.3). The slope of the resulting isotope enrichment in a plot of $\delta^{34}S$ versus $\delta^{18}O$ varies as a function of different factors (bacterial vs. abiotic reduction, open vs. closed system, effects of Rayleigh distillation) but mostly lies in the range of 0.25 – 0.4

(Pierre 1989, Clark & Fritz 1997). Fig. 4-134 shows that such a slope fits reasonably well with the isotope data of celestite in the Malm Group, with Jurassic seawater as a likely source of the sulphate (i.e. internally sourced, pre-dating Eocene – Oligocene influx of meteoric water). One sample (marked with an asterisk in Fig. 4-134) falls off this general trend by showing a distinctly lower $\delta^{18}O$ value. The sulphate of this vein celestite potentially originates from Burdigalian seawater associated with the deposition of the Upper Marine Molasse Group. A similar hypothesis was proposed by de Haller et al. (2011) for vein celestite in the Malm Group of the Oftringen (OFT) borehole.

For vein celestite in the Opalinus Clay, a slope of 0.25 – 0.4 in the $\delta^{34}S$ versus $\delta^{18}O$ plot also fits reasonably well the isotope data, however, with sulphate originating in the underlying evaporites of the Keuper. Based on similar trends, Mazurek & de Haller (2017) also proposed Keuper-sourced sulphate for vein celestite in the Opalinus Clay at the Mont Terri rock laboratory. This does not necessarily imply advective communication between the Keuper units and the Opalinus Clay, it could result from diffusive exchange over long timescales. Present-day porewaters in the Opalinus Clay – Lias interval show increasing sulphate concentrations with increasing depth (e.g. Nagra (ed.) 2023a, Dossier VIII), thus, this concentration gradient makes upward diffusion of sulphate a plausible scenario.

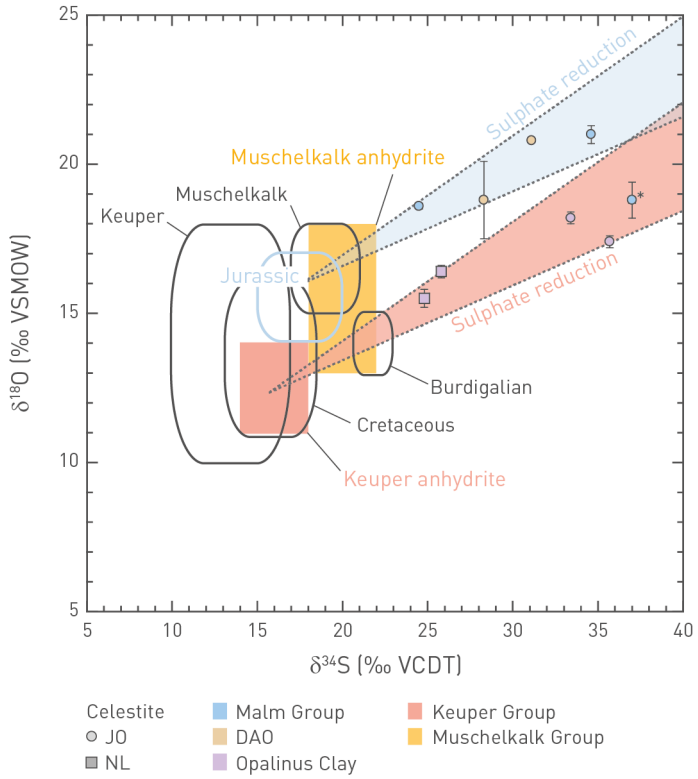


Fig. 4-134: $\delta^{18}O$ and $\delta^{34}S$ values for vein celestite observed in boreholes in Northern Switzerland

Solid lines represent ranges for marine sulphate during different geological periods (Claypool et al. 1980). Data for anhydrite in the Gipskeuper and Muschelkalk are from Rick (1990), Pearson et al. (1991) and references therein and Bernasconi et al. (2017). DAO: Dogger Group above Opalinus Clay. The two fans bordered by dotted lines indicate the trends of sulphate reduction (Pierre 1989, Clark & Fritz 1997). These trends fit the isotope data of vein celestite reasonably well, suggesting Jurassic (and Burdigalian) seawater as the source of sulphate for vein celestite in the Malm and DAO, whereas vein celestite in Opalinus Clay seems to be sourced from Keuper anhydrite. Celestite occurrences at ZNO were generally too small to be analysed.

4.7.6 Implications for palaeo-transport processes and distances

Isotope investigations combined with U-Pb geochronology show that, during the Eocene – Oligocene, downward migration of meteoric surface waters affected the Malm Group – Dogger Group above Opalinus Clay interval. At the clay pit of Frick, similar negative $\delta^{18}O$ values are observed for calcite-forming fluids in the Lias Group below the Opalinus Clay. Neither the origin nor the process(es) by which these signals were transported in the vertical dimension are fully understood. In any case, evidence from U-Pb dating, the general geodynamic evolution and structural mapping suggest that the fluid evolution at Frick is not necessarily representative for the siting regions further east.

Downward migration of Burdigalian seawater during deposition of the Upper Marine Molasse Group is evidenced for the top 100 – 200 m of the Malm section at the Oftringen (OFT) and NL boreholes. In contrast, at JO, mineral-forming fluids from similar depth and age do not show any seawater signals. Most likely, such regional differences reflect the location of the palaeo-shoreline during OMM deposition. Müller et al. (2002) show that the transgression of the Burdigalian sea covered both NL and ZNO, whereas JO was largely unaffected (Section 3.4.4). Moreover, during late Burdigalian and Langhian times an erosive phase affected the JO area, eroding parts of the older Molasse deposits and in places cutting channels into Mesozoic units (Diebold et al. 2006). It is thus likely that possible marine porewaters would have been rapidly displaced by meteoric waters.

For one of the youngest Pleistocene structures in the Malm Group, a hydraulic connection with the groundwater in the Malm aquifer (i.e. as sampled at present) is evidenced. Minimum transport distances estimated from the isotope profiles are in the range of 80 – 100 m. Advection was the likely transport mechanism, however, transient fluid fluxes must have been short-lived, affecting only the porewater in close proximity to the water-conducting structures, otherwise anomalies in the porewater isotope profiles would be expected, which is not the case.

For the time period pre-dating the evolution times of the porewater tracer profiles (Section 4.6), the hydrogeological history of the Opalinus Clay remains poorly constrained, because veins are infrequent, thin and U-Pb geochronology was unsuccessful. In general, a similar evolution as for the confining units is likely, involving modified seawater-type mineral-forming fluids prior to the Eocene, followed by a change towards meteoric waters in the Cenozoic. However, the underlying transport process(es) of this change are not exactly known. In general, $\delta^{13}C$ and $^{87}Sr/^{86}Sr$ values of vein calcite are consistent with an internal evolution of the mineral-forming fluids, however, the isotope signals could also result from an effective rock buffering by which external signals were possibly obliterated. Thus, thin veins in the Opalinus Clay can be explained by external or by internal fluid sources. The underlying mechanisms for the latter include local pressure drops in response to slip induced by tectonic deformation (Diamond 1998) or mixing of chemically different waters (Sanz et al. 2011).

Based on the observed regional cooling at around 5 Ma (Section 4.3.5), clumped isotope temperatures of vein calcite in the Opalinus Clay (Akker et al. 2023) suggest a minimum Pliocene age for these veins, thus documenting for at least this time the efficient barrier properties of the Opalinus Clay. Further constraints on the timing of vein formation in the Opalinus Clay derived from rock-mechanical considerations are presented in Section 5.7.6.

4.8 Current temperature conditions

Key points:

- Temperatures in the Opalinus Clay and in the deep aquifers correlate well with depth below surface.
- In the siting regions, measured temperatures for mid Opalinus Clay are in the expected range from 28 °C (510 m below surface, borehole BOZ2) to 45 °C (940 m below surface, BUL1 borehole).
- For the aquifers, temperatures vary between 6 – 32 °C for mid Malm and 45 – 58 °C for mid Muschelkalk.
- Clay-mineral-rich units show considerably higher temperature gradients than limestones, reflecting the different thermal conductivities of the rocks.
- The new temperature data are in agreement with the expectations. The known anomalies southeast and northeast of the JO siting region can be explained by the local hydrogeological and tectonic setting.

This section provides an overview of the temperature conditions in the three siting regions. Further information related to the geothermal conditions, including details on the thermal properties of the relevant units and on the thermo-hydraulic conditions at site scale, can be found in Nagra (2024w).

Formation temperatures have been obtained from wireline temperature logging performed in the BOZ1, BOZ2, BUL1, STA2, STA3, MAR1 and TRU1 TBO boreholes several months after borehole completion (see Tab. 2-1 for references to the corresponding data reports). In addition, in the BOZ1, STA3 and MAR1 boreholes, long-term temperature monitoring systems were installed (Longridge et al. 2024). The temperatures show the expected depth dependence (Fig. 4-135) with gradients dependent on the respective lithologies and, in the case of the potential aquifers, also possible flow (and hence transmissivities). The temperature profiles do not provide evidence for previously unknown significant transmissive zones.

For boreholes with a long-term monitoring system, geothermal gradients have been calculated under the assumption of a yearly average surface temperature of 10 °C, resulting in average gradients of 44 and 47 °C/km (BOZ1: 47 °C/km, STA3 and MAR1: 44 °C/km). These values are in the expected range for Northern Switzerland and there are no relevant site-specific differences.

Geothermal gradients within the lithological units correlate well between the boreholes. For the Opalinus Clay, the gradients are comparably high (7 – 7.5 °C/100 m). Such high gradients are typical for clay-rich rocks with a low thermal conductivity (~ 1.5 W/mK for the Opalinus Clay; Nagra 2024w), whereas carbonates display a low thermal gradient and high thermal conductivity (~ 4 W/mK for carbonates from the Muschelkalk aquifer; Nagra 2024w).

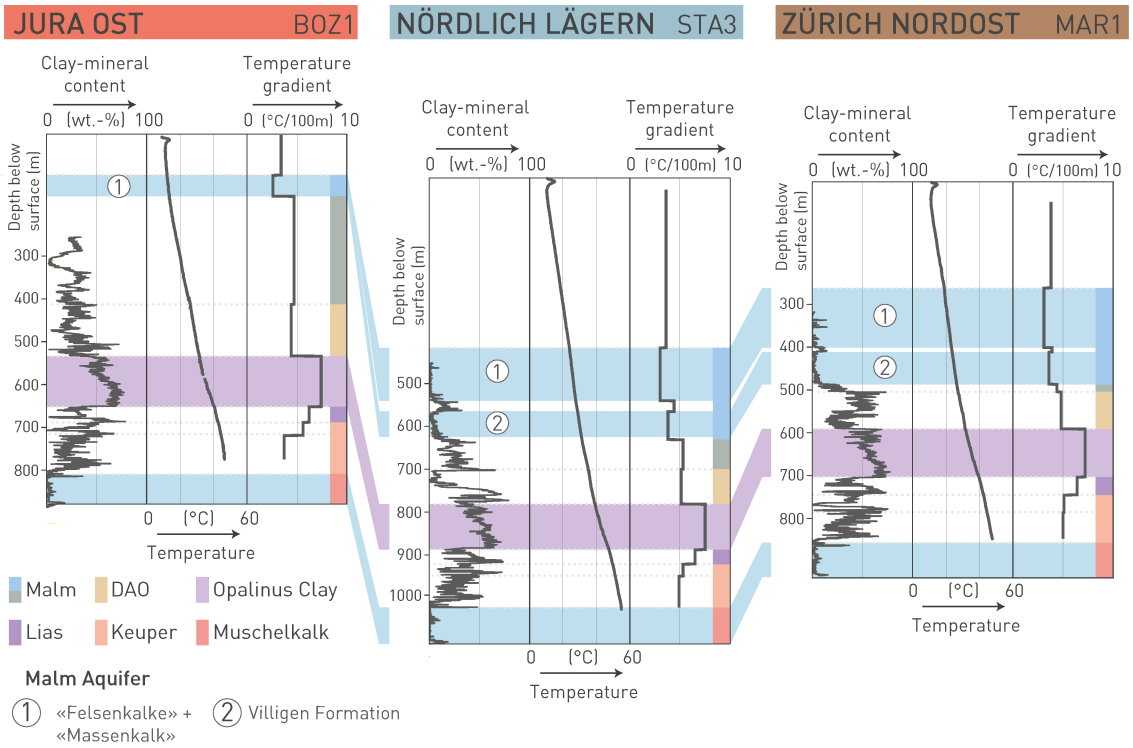


Fig. 4-135: Temperature profiles and lithology-dependent temperature gradients

Shown here are temperature measurements from the fibre-optic long-term monitoring system together with calculated temperature gradients (for the borehole and for each unit) and the corresponding clay-mineral content. Note the increased temperature gradients in units with high clay-mineral contents.

Measured temperatures for mid Opalinus Clay in the siting regions correlate well with depth and range from 28 °C (510 m below surface, BOZ2 borehole) to 45 °C (940 m below surface, BUL1 borehole) (Fig. 4-136). For mid Malm and mid Muschelkalk aquifers, the observed temperatures are 6 – 32 °C and 45 – 58 °C for, respectively (Fig. 4-136).

The heatflow map of Northern Switzerland (Schärli & Rybach 2002, published in Nagra 2002), shows two distinct thermal anomalies:

- The first anomaly is located south to southeast of JO, approximately between Baden and Schinznach. This anomaly is located along the Jura Main Thrust and the southern limit of the Konstanz – Frick Trough (Fig. 4-55). Hydrogeologically, this zone reflects the regional discharge area for the Muschelkalk aquifer south of the Jura Main Thrust (Fig. 4-102; Nagra 2024n). The upwelling thermal waters feed the well-known thermal springs of Baden and Bad Schinznach which are located where the Limmat and Aare cut through the easternmost Internal Jura.
- The second anomaly is located to the northeast of JO, in the lower Aare Valley, just north of the Konstanz – Frick Trough. This is slightly to the south of the regional discharge area of the Muschelkalk aquifer for the flow system north of the Jura Main Thrust (Fig. 4-102). In addition, it is an area with known upward-directed hydraulic gradients in the crystalline basement. These can be explained by recharge in the Black Forest hilly area and the overall low hydraulic conductivity of the Konstanz – Frick Trough preventing further southbound flow (Voborny et al. 1994). See Nagra (2014g, Dossier VII) and Rybach (2009) for further discussion.

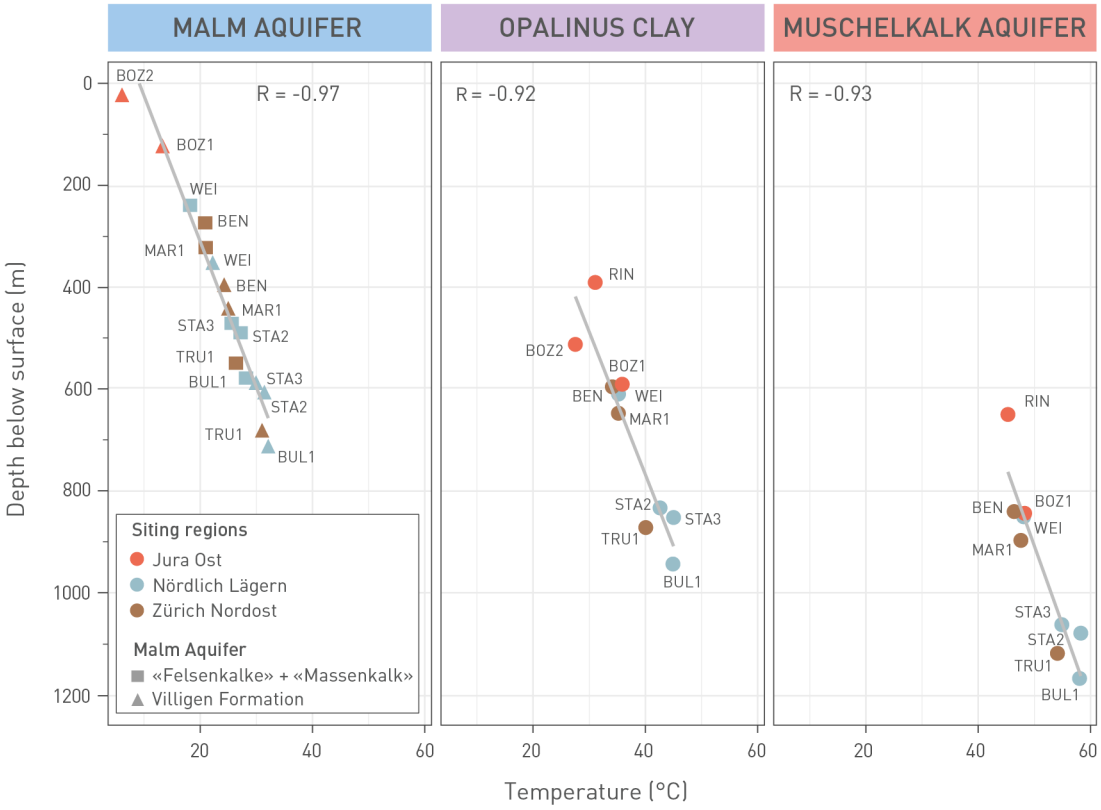


Fig. 4-136: Cross-plots of temperature (°C) vs. depth below surface (m) for the Malm aquifer, Opalinus Clay and Muschelkalk aquifer

Data points are colour-coded according to the siting regions. Temperature values were taken from the centre of the respective unit. For the Muschelkalk aquifer of STA3, the given temperature corresponds to the top of the unit, as no data are available for the deeper part. Where data from the long-term monitoring system and temperature logging exist, the data from the long-term monitoring system were selected. Note that the value for the Malm aquifer in BOZ2 is influenced by seasonal temperature variation. The data show linear relationships between depth and temperature.

To conclude, these thermal anomalies can be explained by the local hydrogeological and tectonic setting favouring heat transport towards these zones. The situation in the potential disposal zones of the three siting regions is different. Here, the observed temperature profiles can be modelled reasonably well with a constant basal heat flow (Nagra 2024w).

4.9 Detailed geological framework: Summary

This section summarises important findings of Chapter 4. Observations from deep boreholes and key parameters are compiled site-specifically by projection to a reference borehole (Fig. 4-137, Fig. 4-138, Fig. 4-139). This forms the basis for the site-specific delineation of the low-permeability confining units (Fig. 4-140).

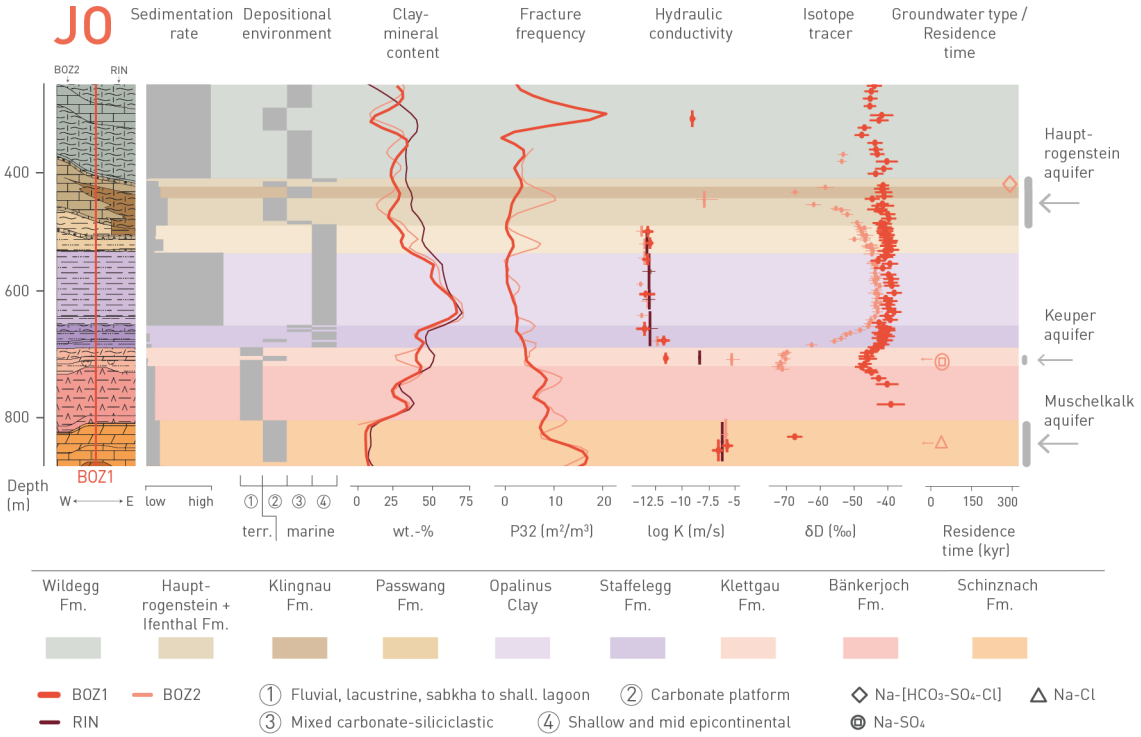


Fig. 4-137: Key observations between Muschelkalk and Hauptrogenstein aquifers in JO

Data from the BOZ2 and RIN boreholes are projected to the reference borehole BOZ1. The arrows next to the groundwater symbols indicate maximum residence times. Fracture frequency and clay-mineral-content regression lines were smoothed with a moving average. shall.: shallow.

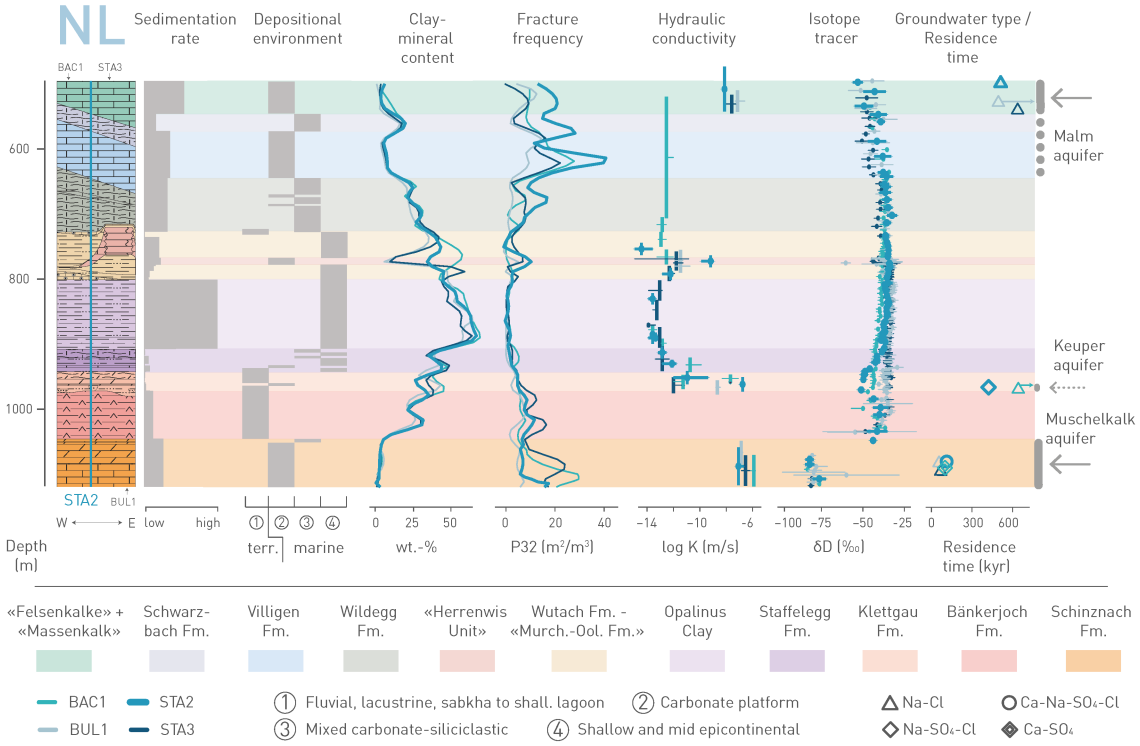


Fig. 4-138: Key observations between Muschelkalk and Malm aquifers in NL

Data from the BAC1, BUL1 and STA3 boreholes are projected to the reference borehole STA2. The arrows next to the groundwater symbols indicate minimum residence times. Fracture frequency and clay-mineral-content regression lines were smoothed with a moving average. shall.: shallow.

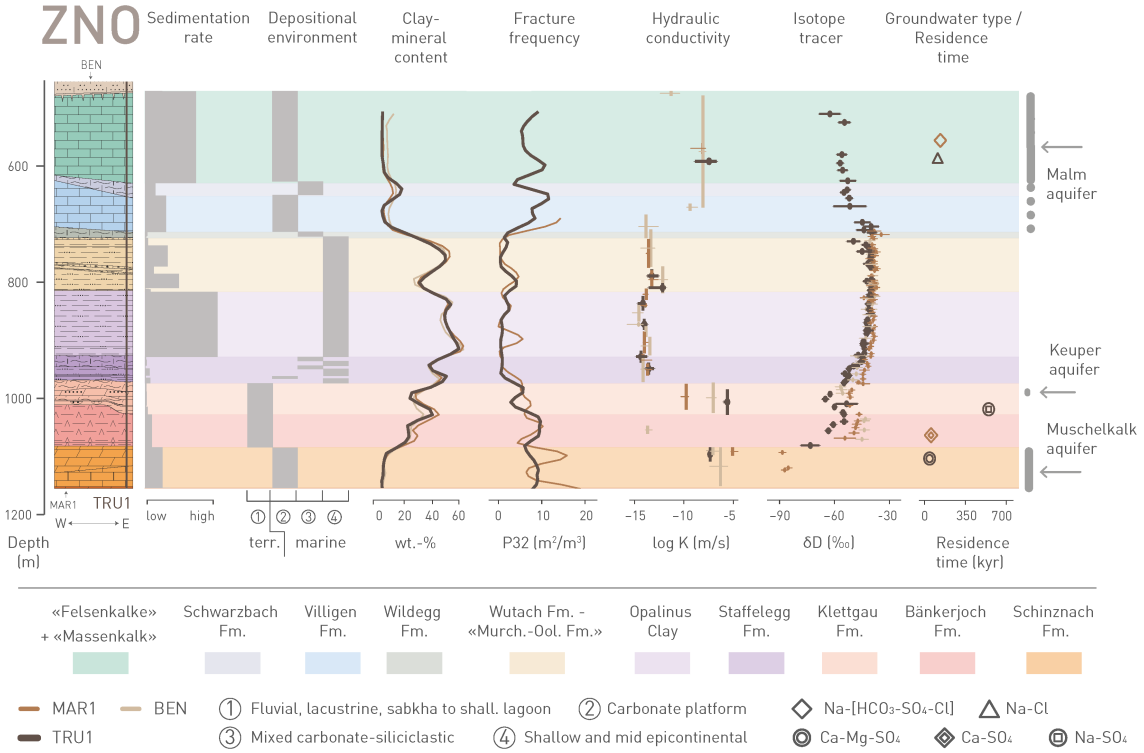


Fig. 4-139: Key observations between Muschelkalk and Malm aquifers in ZNO

Data from the MAR1 and BEN boreholes are projected to the reference borehole TRU1. Fracture frequency and clay-mineral-content regression lines were smoothed with a moving average. shall.: shallow.

With regard to the barrier function, the geological units presented in Fig. 4-137, Fig. 4-138 and Fig. 4-139 can be allocated to three groups with similar characteristics: Host rock, low-permeability confining units and deep aquifers:

- The Opalinus Clay host rock is the core of the transport barrier. It is characterised by a small lateral variability compared to other Mesozoic formations in Northern Switzerland. This is related to the depositional environment represented by a shallow epicontinental sea with a high clay-mineral input (comparably high sedimentation rates). The general subfacies succession can be correlated between all boreholes across the siting regions. The fracture frequency is lower compared to more competent units. Numerous hydraulic packer tests demonstrate a very low hydraulic conductivity. This is consistent with the straight profiles of isotope tracers, with no indications for localised flow.
- Above and below the host rock, the natural barrier is complemented by low-permeability confining units in all the siting regions. Overall, these show characteristics similar to the host rock, but with greater lithological heterogeneity (e.g. intercalated sandy and calcareous beds) and larger differences between the siting regions, particularly in the Dogger Group above Opalinus Clay. For example, the clay-mineral-rich units directly above the Opalinus Clay include more calcareous and sandy beds in JO and ZNO compared to NL and are generally more clay-mineral-rich in NL. In the eastern part of NL, particularly clay-mineral-rich units are overlain by a ca. 40 m thick isolated carbonate platform («Herrenwis Unit»). The lithological differences in the confining units reflect local changes in the depositional environment, which were strongly influenced by bottom currents. The clay-mineral content in the confining units is more variable but, overall, still high. This favours a more ductile defor-

mation behaviour and is consistent with low overall fracture frequency, as observed in the Opalinus Clay. The hydraulic tests show low hydraulic conductivities, which is consistent with the shape of tracer profiles with no indication for groundwater flow. This indicates diffusion-dominated transport in the host rock and confining units over long timescales.

- The confining units are bounded at the top and at the base by deep aquifers. The situation differs across the siting regions:

  JO: The low-permeability zone is located between the regional Hauptrogenstein aquifer and the local Keuper aquifer. The carbonate platform of the Hauptrogenstein, known as a regional aquifer further to the west, extends into the JO siting region. This is demonstrated by the measured enhanced hydraulic conductivities and by the shape of the natural tracer profiles in the BOZ2 borehole. To the east, there is a facies transition to the clay-mineral-rich Klingnau Formation. Probably related to the facies transition, no transmissive section was drilled in the eastern boreholes (RIN and BOZ1). Residence times of the groundwater sample of the BOZ2 borehole is high, but the salinity and the water isotope composition indicate more interaction with meteoric waters in the past compared to most of samples from the Malm aquifer in NL and ZNO. The lower confining units are bounded by the Keuper aquifer, which is probably linked to the fractured dolomitic Gansingen Member, as indicated by hydraulic tests and tracer profiles. The ^{81}Kr model age for the BOZ2 Keuper aquifer groundwater are low, probably due to sampling close to the recharge area.

  NL: The regional Malm and the local Keuper aquifer, which was observed in some boreholes only, define the vertical extent of the low-permeability zone. In the stiffer limestone units of the Malm Group, fracture frequencies are higher compared to the weaker units below (e.g. the Opalinus Clay, Staffelegg Formation). The hydraulic tests indicate water flow related to fractures, mainly in the upper part of the limestone series («Felsenkalke» and «Massenkalk»). The Malm groundwaters contain varying contents of fossil Na-Cl water of marine origin. In NL, the marine component is particularly large and, together with long groundwater residence times, indicates quasi-stagnant conditions. In contrast to the other siting regions, indications for water flow in the Keuper aquifer are limited to sandstone channels (Ergolz Member), which only occur locally. Indications for enhanced hydraulic conductivities were only observed in two boreholes, however, with high groundwater residence times. The very local occurrence of the Keuper aquifer means that it is possible that stratigraphically deeper units, down to the Muschelkalk aquifer, contribute to the barrier function in NL (potential additional confining units in Fig. 4-140).

  ZNO: The low permeability zone is delimited by the Malm and the Keuper aquifers, respectively. As in NL, water flow in the Malm aquifer is related to fractures and is located mainly in the upper part («Felsenkalke» and «Massenkalk»). The water isotopic composition and the residence times indicate a slightly more active system compared to NL, particularly in the eastern part which is characterised by lower overburden thickness. In the Keuper aquifer, there are consistent indications for water flow in the Seebi Member from all boreholes in this area (hydraulic tests and/or tracer profiles). The Seebi Member is relatively thick in ZNO and includes a porous dolomitic breccia and sandstones. Groundwater residence times are large.

  The regional Muschelkalk aquifer occurs in all the siting regions and represents the most dynamic flow system as demonstrated by comparably high hydraulic conductivities, clear signatures in tracer profiles and comparably low groundwater residence times.

A comparison of the lithological and hydrogeological situation between the three siting regions is shown in Fig. 4-140. Regarding the barrier efficiency, the thickness of the host rock and confining units is an important characteristic. The distance between the centre of the host rock and the next overlying aquifer is largest in NL and smallest in JO. The distance between the centre of the host rock to the closest underlying aquifer (Keuper aquifer) delimiting the lower confining units is similar in all the siting regions. However, because of the peculiar, very local nature of the Keuper aquifer in NL, the units down to the Muschelkalk aquifer could contribute to the barrier function.

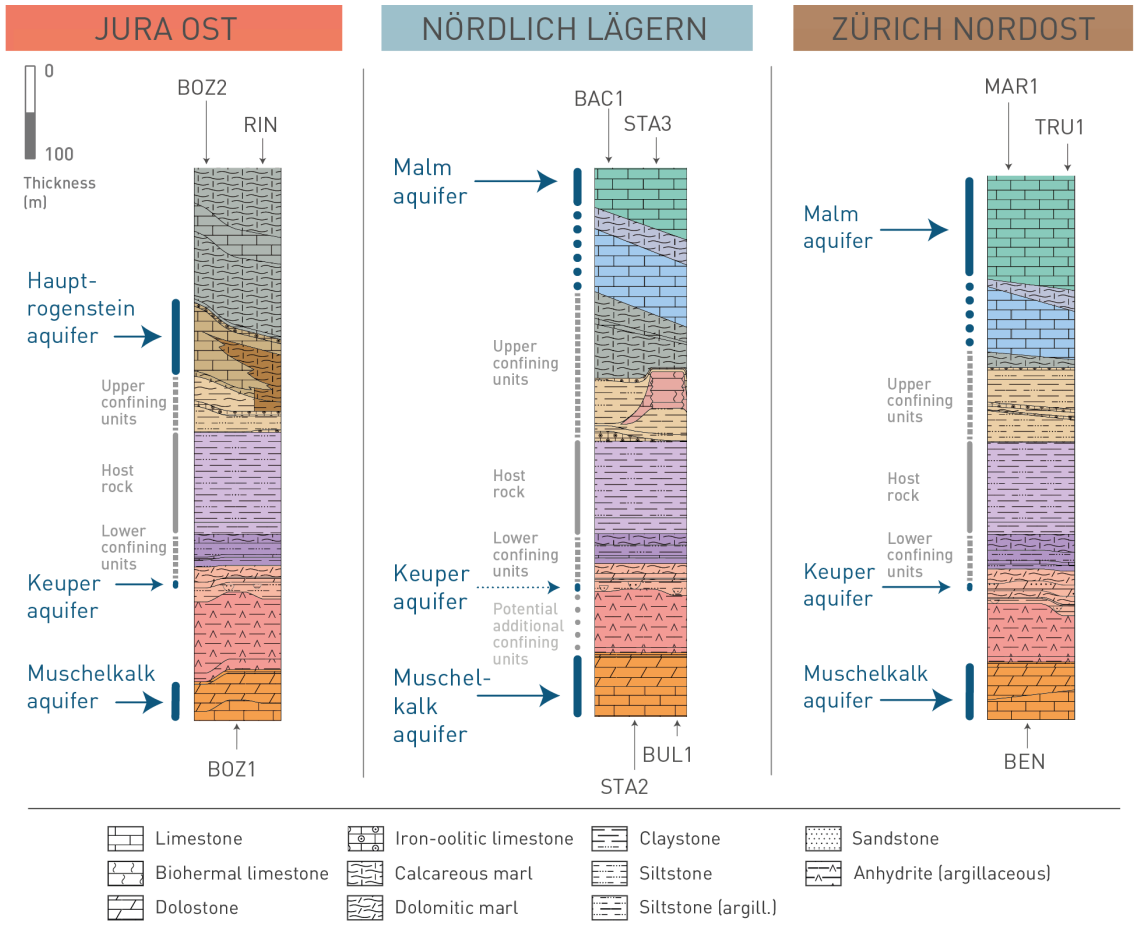


Fig. 4-140: Extent of host rock and low-permeability confining units and location of neighbouring aquifers for the JO, NL and ZNO siting regions

Key datasets guiding the extent of the host rock and confining units are shown in Fig. 4-137, Fig. 4-138 and Fig. 4-139. Note that the distance between the centre of the host rock and the next aquifer above is largest in NL. The distance to the lower aquifer is similar in all the siting regions. As a result of the peculiar, much more local nature of the Keuper aquifer in NL (see discussion in text), the anhydrite- and clay-mineral-rich units of the lower Keuper may contribute to the barrier function as additional confining units.

Besides these observations, the following aspects discussed in Chapter 4 are regarded as particularly relevant:

- With respect to the lateral extent of the potential repository zone and the flexibility for the placement of the disposal areas, all the siting regions show areas devoid of seismically mappable faults. In NL this area is the largest.
- The geological past provided numerous evidence for reactivation of larger structures, such as the regional fault zones, during later deformation episodes. This preference to reactivate pre-existing structures over the formation of new faults is anticipated to continue in future (Section 6.2).
- Present-day orientation of S_{Hmax} was confirmed and is roughly NNW-SSE-trending in all the siting regions. The orientation of S_{Hmax} across the entire Mesozoic sequence and especially across the evaporitic units and the Opalinus Clay is indicative of a relatively stable present-day stress field.
- Overall, the independent evidence gained from ground- and porewater investigations provides valuable insights into the past transport processes in the aquitard/aquifer system in the siting regions over timescales spanning several orders of magnitudes (ca. 10^4 to 10^7 years). In all the siting regions, the barrier efficiency is demonstrated by the profiles of natural tracers in porewater, which are best explained by molecular diffusion being the dominant transport mechanism. The isotopic composition of the Opalinus Clay porewater indicates a larger fraction of old porewater and a smaller overprint by meteoric water in NL, compared to the other siting regions.
- The high contents of the noble gas isotope ^4He in Opalinus Clay porewater demonstrate the strong barrier efficiency: Concentrations are more than 4 orders of magnitude higher than for air-saturated water. More than 65% of the He produced in Opalinus Clay since deposition is still present.
- The study of mineral-filled fractures ('veins') indicates the evolution of the mineral-forming fluids from modified seawater-type prior to the Eocene times towards more meteoric waters in the Cenozoic. This trend resulted from subaerial exposure since at least Eocene times, which led to karstification in the top of the Malm Group, deposition of the Bohnerz Formation (Siderolithic Group) and downward migration of meteoric surface waters. The investigated veins in the Opalinus Clay were precipitated from fluids with less negative $\delta^{18}O$ values than today's porewater at higher temperatures. This suggests vein formation prior to Pliocene cooling.
- Temperatures in the Opalinus Clay and in the Malm and Muschelkalk aquifers correlate well with depth below surface. In the siting regions, no distinct local temperature anomalies are indicated by the new boreholes and by comparison with temperature modelling. The previously known local temperature anomalies in the lower Aare Valley are restricted to the southeast and to the northeast of the JO siting region and can be explained by the local hydrogeological and tectonic setting (probable heat transport in the Muschelkalk aquifer and along basement faults).

5 Key characteristics of the host rock and clay-mineral-rich confining units as geological barriers

Key points:

- The Opalinus Clay is characterised by consistently high clay-mineral contents (> 40 wt.-%). This mineralogical composition controls the pore structure and ensures very low hydraulic conductivities and efficient self-sealing of faults. Consequently, solute transport in the Opalinus Clay is diffusion-dominated.
- Moderate salinity and neutral pH of the porewater, and chemical conditions buffered by mineral equilibria provide highly stable geochemical conditions in the Opalinus Clay.
- Tectonic strain in clay-rich rocks is accommodated by more distributed and segmented deformation, which impedes continuous flow paths.
- Confining units above and below the Opalinus Clay also exhibit low hydraulic conductivity and contribute to the barrier function but show larger variability in hydraulic properties and a lower self-sealing potential.

5.1 Introduction

Clay-rich rocks are widely recognised as providing excellent barrier properties for radioactive waste containment. The two key characteristics of these geomaterials are i) very small pore sizes, and ii) significant clay-mineral content. The small pore sizes result in extremely low hydraulic conductivities, and the abundance of clay minerals is responsible for high retention and high self-sealing potential.

The Opalinus Clay has pore sizes in the nm range, and the clay-mineral content in all the siting regions is high throughout the formation (> 40 wt.-% when averaged over metre scale). These properties are similar to those of other clay-rich rocks, notably the Callovo-Oxfordian, the designated host rock for the French deep geological repository, and the Toarcian-Domerian at the Tournemire rock laboratory (OECD/NEA 2022). The mineralogy and basic properties of these rocks are also comparable with many top seals of hydrocarbon reservoirs (Fisher et al. 2023).

This chapter provides a detailed characterisation of the host rock in terms of the properties and processes relevant for its efficiency as a geological barrier to fluid transport. In the various sections, the clay-mineral-rich confining units are characterised in comparison with the Opalinus Clay to highlight their potential to contribute to the geological barrier of a repository in the Opalinus Clay. In a few cases, the comparison is extended to limestones of the aquifer units to better emphasise the favourable barrier properties of the Opalinus Clay and its related confining units.

- Section 5.2 explores the spatial variability of the mineralogy of both the whole rock and the clay fraction, and diagenetic mineral sequences. The clay-mineral content is of great relevance, because transport properties and the self-sealing potential directly correlate with it, as will be summarised in Section 5.10.
- Section 5.3 is dedicated to porosity and pore-size distributions, including correlations with mineralogy. The pore network controls transport properties but also clay mineral – porewater interactions, which in turn affect the porewater chemistry.
- As will be shown in Section 5.4, the porewater chemistry, rock mineralogy and porosity network provide a very stable geochemical environment in the Opalinus Clay.
- Section 5.5 summarises key geomechanical properties, deformation behaviour of and typical fault architecture in the Opalinus Clay. The volumetric behaviour, notably the volumetric expansion from unloading (swelling) is relevant for self-sealing (Section 5.7). The main features of the deformation behaviour of the Opalinus Clay are also put into context with the relatively low tectonic overprint.
- Sections 5.6 to 5.9 provide detailed information on the transport properties of the Opalinus Clay. The hydraulic conductivities (Sections 5.6) are low, and mass transport is dominated by diffusion (Section 5.8). The section on self-sealing (Section 5.7) provides further evidence and a conceptual explanation for the absence of significant fracture- or fault-related transmissivities in the rock.

For the various sections, the properties and behaviour of the Opalinus Clay were examined across different scales (e.g. microscale, core, borehole, tunnel). Considerable effort went into correlating geochemical, hydrogeological and geomechanical properties with basic properties such as density, porosity and clay-mineral content. A high clay-mineral content stands out as the fundamental characteristic ensuring favourable barrier properties. In contrast to the continuously clay-mineral-rich Opalinus Clay, the low-permeability confining units are characterised by a higher mineralogical variability, including layers with reduced clay-mineral content and thus limited self-sealing potential.

Although the chapter sequentially addresses the rock microstructure (porosity and mineralogy), deformation behaviour and transport properties, it is noted that all these aspects are strongly interdependent (hydromechanical coupling) as emphasised in Fig. 5-1. This figure also provides an overview of the sections included in this chapter (see numbers in brackets).

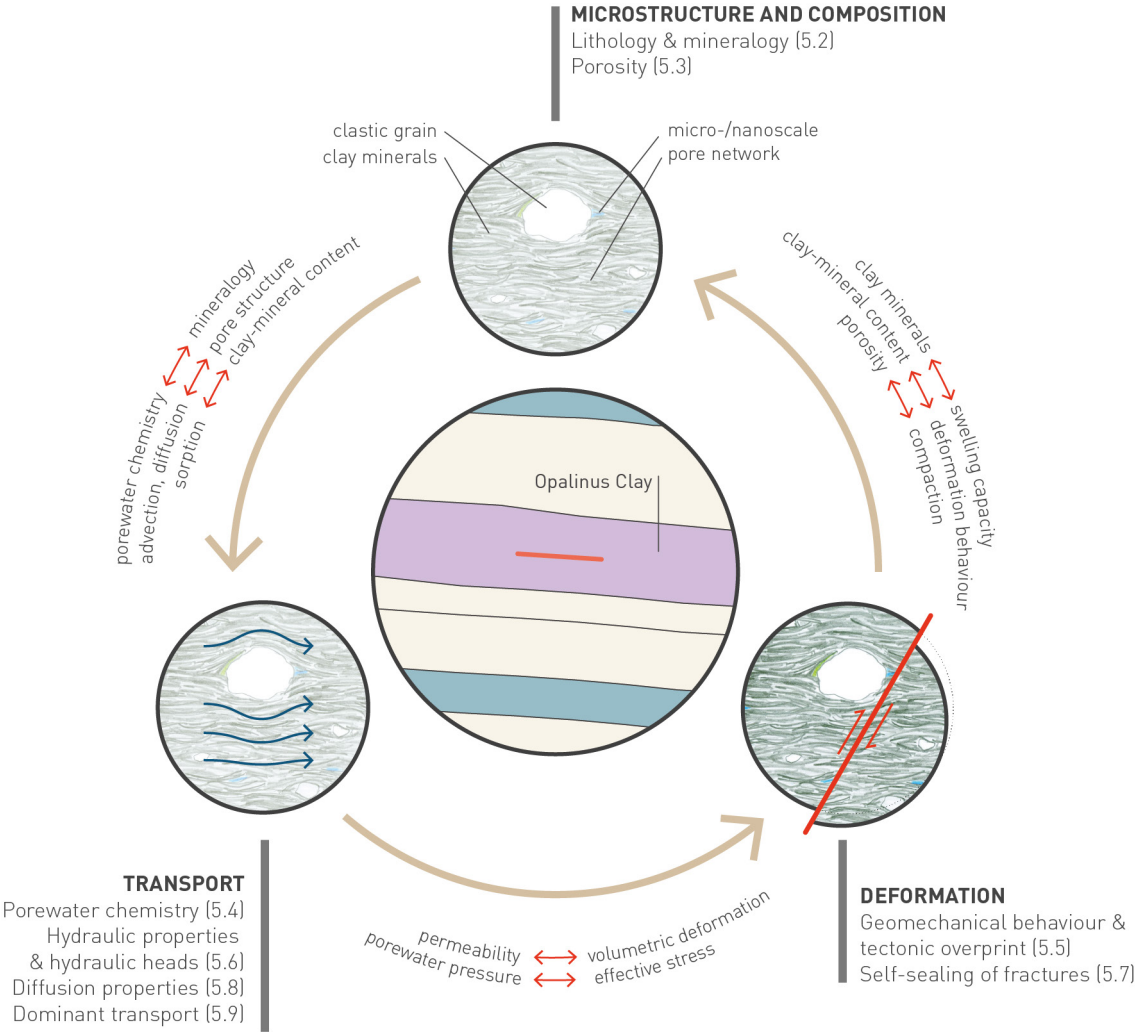


Fig. 5-1: Coupling between structure, deformation behaviour and transport properties in the Opalinus Clay

Numbers in brackets relate to sections dedicated to the various topics in this chapter.

5.2 Lithology and mineralogy

Key points:

- The Opalinus Clay is characterised by average clay-mineral contents between 55 and 60 wt.-%. There is no relevant difference between the siting regions.
- In the study area, the Opalinus Clay is characterised by comparably minor lithological and mineralogical variations in the vertical dimension. Characteristic depth trends in the different boreholes can be correlated at regional scale, that is, the composition is predictable.
- The composition of the clay-mineral fraction in the Opalinus Clay varies only slightly in the vertical dimension and is also consistent laterally. No relevant spatial variability must be expected regarding swelling or sorption behaviour.
- The similar mineral composition in the Opalinus Clay across the study areas allows the use of the same set of equilibrium phases in the porewater model for all siting regions.
- The confining units are mostly clay-mineral-rich, but show a larger variability compared to the Opalinus Clay. They include layers with low clay-mineral contents and thus reduced self-sealing potential.

5.2.1 Overview

The mineralogical composition of the host rock and the confining units is directly correlated to several safety-relevant aspects and serves as a good proxy for many relevant barrier properties. It provides direct input for estimating the sorption of radionuclides and for defining the porewater composition. In this context, it affects the speciation of solutes and therefore the mobility of radionuclides and the stability of the engineered barriers. Mineralogy, notably the clay-mineral content, correlates with porosity and geomechanical properties and thus plays a key role for self-sealing behaviour, permeability, and diffusion coefficients.

5.2.2 Lithology and structure of the Opalinus Clay from microscopic to formation scale

The sedimentological and stratigraphic features of the Opalinus Clay are presented in Section 4.2.6.

The structure of the Opalinus Clay on scales between tens of km to 1 nm, i.e. a scale ranging over 13 orders of magnitude, is illustrated in Fig. 5-2. The main methods and sources of information include, in order of decreasing scale, geophysical borehole logs, macroscopic core inspection, thin-section analysis, scanning electron microscopy (SEM) and transmission electron microscopy (TEM). More detail is provided in Mazurek & Aschwanden (2020).

On a regional scale, several Opalinus Clay subunits can be distinguished and correlated laterally (Section 4.2.6). The same subunits can be identified in all three siting regions, and only a minor variability of the total thickness of the Opalinus Clay can be seen.

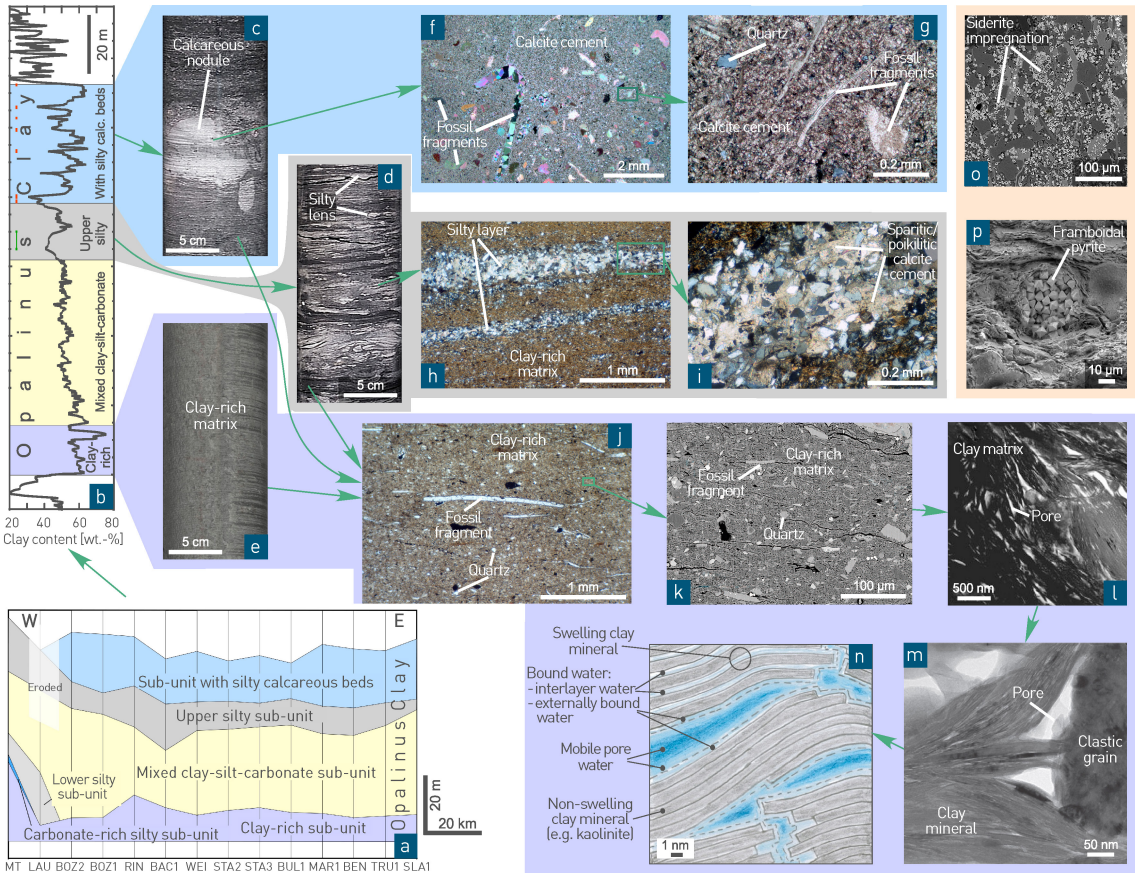


Fig. 5-2: Conceptual representation of the structure of the Opalinus Clay over a length scale range of 13 orders of magnitude

Adapted from Mazurek & Aschwanden (2020). MT: Mont Terri.

(a) Regional distribution of subunits
(b) Typical borehole profile with subunits, discrete heterogeneities and clay-mineral log (Benken borehole, BEN)
(c) Calcareous nodule in the «Sub-unit with silty calcareous beds» (BEN 549.22)
(d) «Upper silty sub-unit» (BEN 582.83)
(e) «Clay-rich sub-unit» (Mont Terri rock laboratory, MT BDB-1 220.74)
(f) Thin-section photograph of a calcareous nodule from the «Sub-unit with silty calcareous beds» (Schlattingen borehole, SLA 852.80, transmitted light, crossed polars)
(g) Detail from (f)
(h) Thin-section photograph from the «Upper silty sub-unit» showing two silty lenses (BEN 575.35, transmitted light, parallel polars)
(i) Thin-section photograph from the «Upper silty sub-unit» showing a close-up of a silty lens cemented by sparitic/poikiloblastic calcite (MT 808.40, transmitted light, crossed polars)
(j) Thin-section photograph from the «Clay-rich sub-unit» (MT 968.50, transmitted light, parallel polars)
(k) SEM image from the «Clay-rich sub-unit» (MT FE tunnel, from Seiphoori et al. 2017)
(l) TEM image of the clay matrix (from Keller & Holzer 2013)
(m) TEM image of the clay matrix (MT sample, from Keller et al. (2013)
(n) Artist's view of the clay structure on the nanometre scale (from Nagra 2002)
(o) Siderite impregnation in a concretion (SLA 833.69, from Wersin et al. 2013)
(p) Pyrite framboid (MT FE tunnel, from Seiphoori et al. 2017).

On the borehole scale (Fig. 5-2b), discrete heterogeneities such as calcareous beds/nodules with a thickness in the range of 0.1 – 0.6 m (Mazurek & Aschwanden 2020) occur in the upper part of the formation in all the siting regions. It should be noted that, even in sections with calcareous beds/nodules present, the average clay-mineral content at the metre scale is > 40 wt.-%. Individual heterogeneities often cannot be correlated between boreholes, indicating limited lateral extent. At the base of the Opalinus Clay, a particularly clay-rich layer extends across the whole study area, with average clay-mineral contents well above 50 wt.-%.

On this basis, the Opalinus Clay illustrated in Fig. 5-2c – e can be conceptually simplified to:

- Clay matrix with variable contents of disseminated quartz and calcitic fossil fragments in all subunits
- Calcareous beds/nodules
- Silty lenses, most frequently occurring in the silty subunits.

The small-scale calcareous and silty heterogeneities are embedded in a clay-rich matrix, which is the dominant building block. This fact is illustrated by arrows pointing from Fig. 5-2c – e towards Fig. 5-2j. Calcareous beds/nodules are illustrated in Fig. 5-2f – g on the thin-section scale. They consist of fossil fragments, silty particles and a calcite cement, with only small amounts of clay minerals. Fig. 5-2h – i illustrate silty lenses on a microscopic scale. These can contain clay minerals or, as shown in Fig. 5-2h – i, consist of almost pure quartz ± feldspars. Given the originally large pore apertures, the lenses are mostly cemented by sparitic and/or poikilitic calcite cement.

The clay-rich matrix is the quantitatively dominant building block of the Opalinus Clay and is illustrated in Fig. 5-2j – n. It contains varying amounts of disseminated quartz and calcitic fossil fragments (Fig. 5-2j – k). Note that, under the SEM, only a small fraction of the pore space can be visualised, given the limited resolution (at best around 10 nm). Fig. 5-2l – m visualises the clay matrix under TEM. Visible pores are due to geometric incompatibilities between clay aggregates or between clay and non-clay minerals. Pores with even smaller, nanometric apertures constitute a substantial part of the pore space. These apertures are difficult or impossible to image and are thus illustrated by a conceptual sketch in Fig. 5-2n. Porosity is also present in the interlayer space of swelling minerals, particularly smectite (within illite/smectite mixed-layer minerals).

Apart from the cementation by several calcite generations, siderite and pyrite are the only quantitatively relevant diagenetic neoformations (Section 5.2.5) and occur in all subunits of the Opalinus Clay (Fig. 5-2o – p). Siderite can be found in concretions with sizes in the range of centimetres or as disseminated crystals in the clay matrix. Pyrite occurs in the form of 1 – 10 µm-size framboids or as larger crystals. Pyrite concretions are also found, even though much less frequently than in the case of siderite.

5.2.3 Whole-rock mineralogy

The Opalinus Clay is the most clay-mineral-rich unit throughout the study area, with no systematic differences in the mineralogical composition between the siting regions (Fig. 5-3, Fig. 5-4). Vertically, the clay-mineral content increases slightly with depth. Remarkably, the occurrence of siderite is almost exclusively limited to the Opalinus Clay. As shown in Fig. 5-4, the average clay-mineral content is well above 50 wt.-% at all studied locations.

Limestones and marls are the main lithologies present in the Malm Group.

The Dogger Group above Opalinus Clay is also clay-mineral-rich, but includes heterogeneities such as Fe-rich oolites, sandy lithologies (mainly in ZNO) or limestones such as the «Herrenwis Unit» in NL and the Hauptrogenstein in JO (see also Sections 4.2.7 and 4.5.3).

The Staffelegg Formation (Lias Group) below the Opalinus Clay consists of six generally clay-mineral-rich members showing consistent mineralogical compositions throughout the study area, but with substantial vertical heterogeneity (Mazurek et al. 2023a). Clay-mineral contents tend to be slightly higher in the ZNO siting region, particularly in the Frick Member. The underlying Triassic units are mineralogically heterogeneous, given the presence of evaporitic minerals (mainly anhydrite) and dolomite.

Additional figures showing mineralogical variability are included in Nagra (2024m).

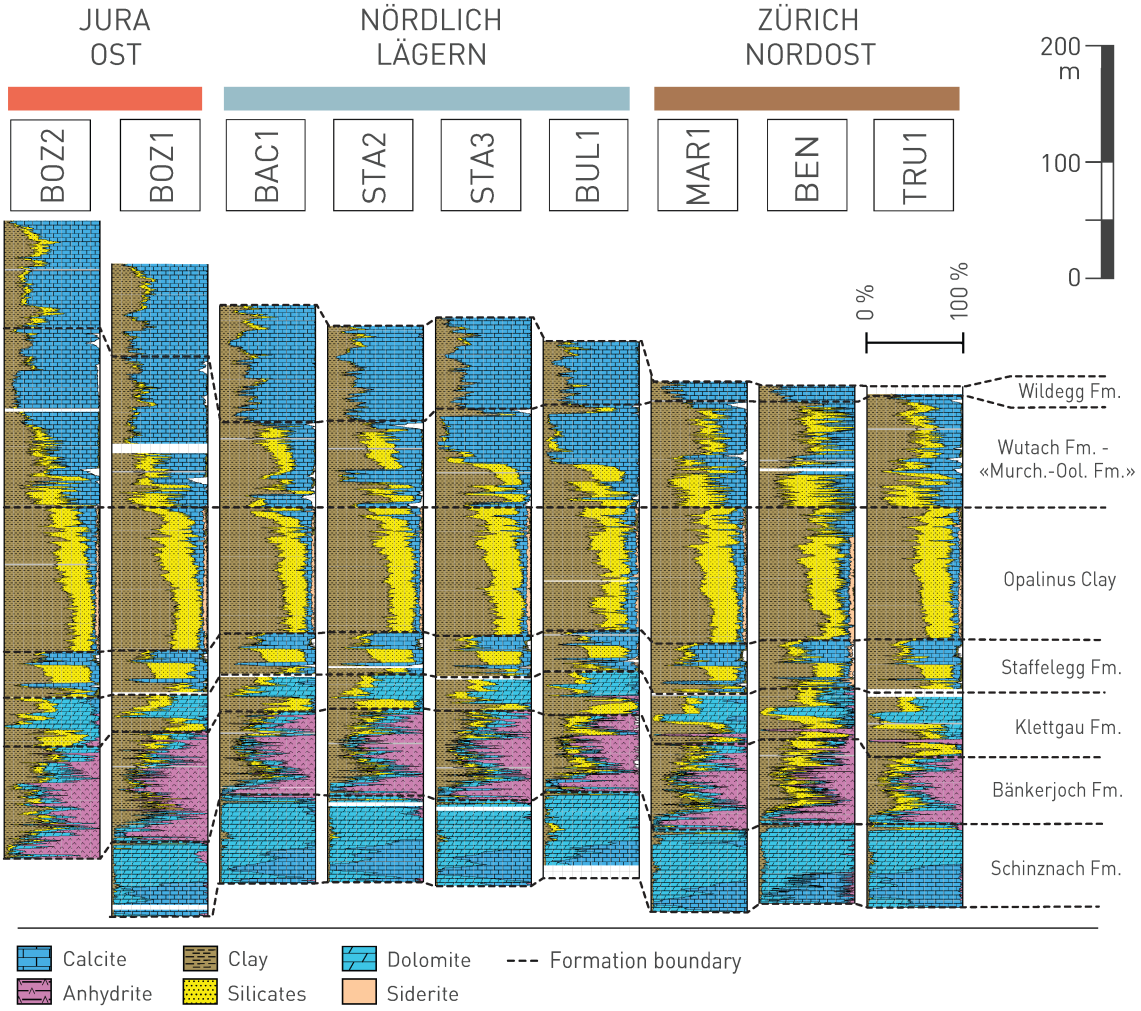


Fig. 5-3: Mineralogical composition of formations in boreholes of the siting regions

Continuous mineralogy from core-calibrated geophysical logs (Becker & Marnat 2024).

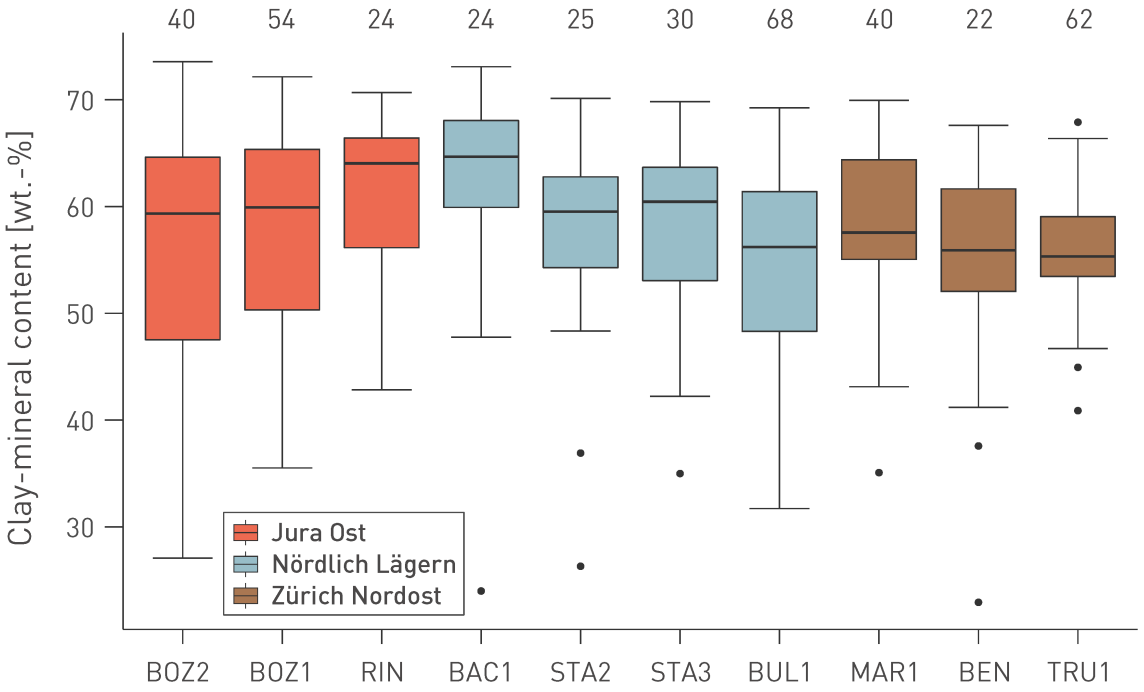


Fig. 5-4: Clay-mineral content of the Opalinus Clay in boreholes of the siting regions, based on laboratory data

Each box encloses 50% of all measured values. The horizontal line in the box indicates the median, and the whiskers (error bars) the minimum and maximum values (min: 25th percentile – (1.5 × interquartile range); max: 75th percentile + (1.5 × interquartile range)). The black dots indicate outliers. The values above the boxplots denote the number of samples.

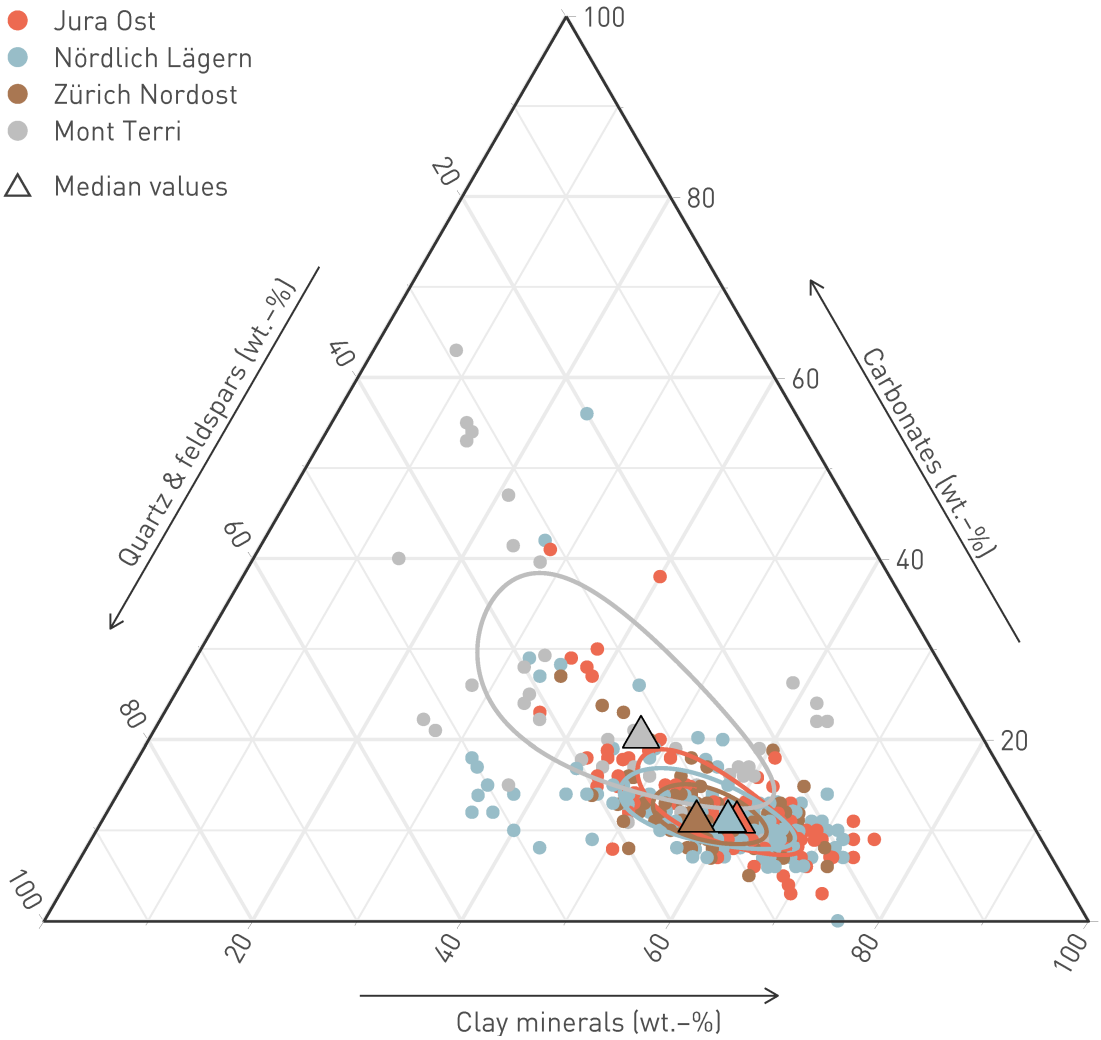


Fig. 5-5: Mineralogical composition of the Opalinus Clay based on laboratory data from X-ray diffraction

Data are shown for all TBO boreholes and for Mont Terri (BDB1 borehole). Triangles and ellipses show median values and variance for each region. Note the small differences between the three siting regions. The Mont Terri samples with low clay-mineral content relate to the carbonate-rich silty facies, which is absent in Northern Switzerland.

5.2.4 Composition of the clay-mineral fraction

The composition of the clay-mineral fraction is of importance for the evaluation of processes such as sorption or swelling. In the Mesozoic profile, it includes illite, illite-rich illite/smectite mixed layers, kaolinite, chlorite, and small proportions of chlorite/smectite mixed layers. Trace amounts of smectite may also occur. In the Opalinus Clay, the relative proportions of endmember clays[13] show only slight variability (Fig. 5-6). Only a slight upward increase in the illite/kaolinite endmember ratio is observed (Fig. 5-6). This means that relevant properties such as swelling and sorption behaviour can be considered constant throughout the formation. Above and below the Opalinus Clay, the illite/kaolinite endmember ratio increases substantially.

[13] For the endmember compositions, the illite, chlorite and smectite components of mixed-layer phases were added to the respective pure phases. The smectite endmember refers almost exclusively to mixed-layer phases.

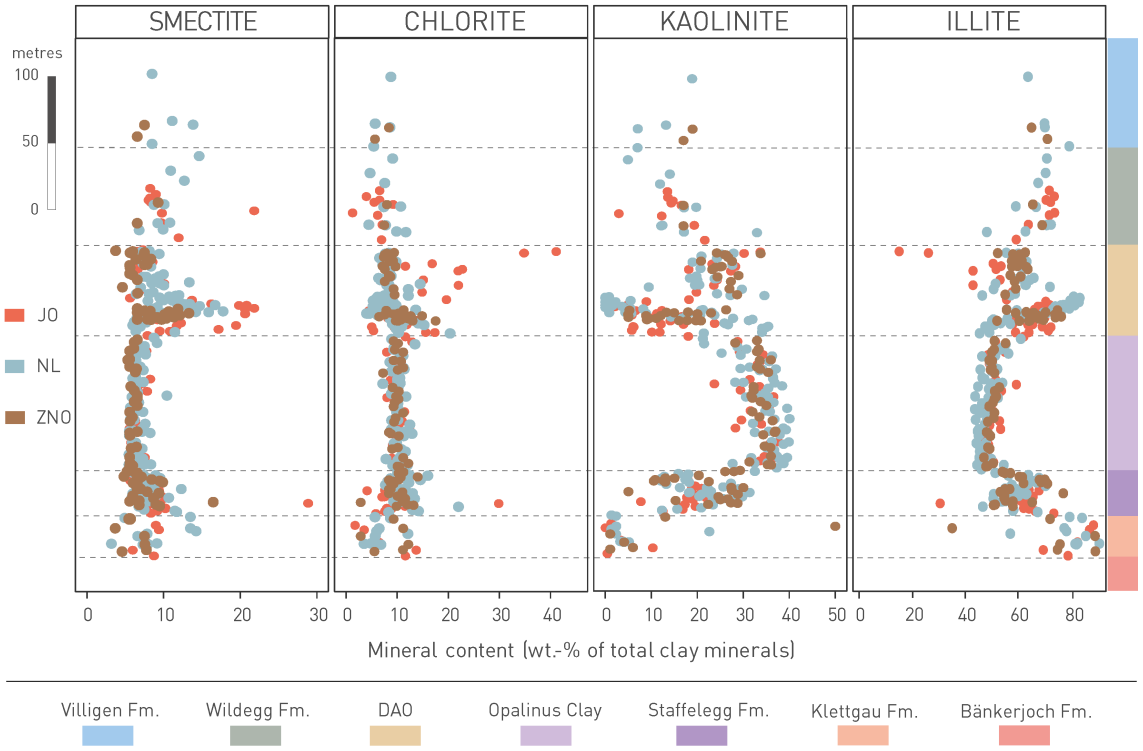


Fig. 5-6: Composition of the clay-mineral fraction in the TBO boreholes in profile view

Clay endmembers are shown. Data are projected to profile STA2. DAO: Dogger Group above Opalinus Clay.

5.2.5 Trace and diagenetic minerals

After deposition on the seafloor, sediments were compacted during burial (Chapter 3, Fig. 3-4) and affected by dissolution – precipitation reactions that influenced the mineralogical composition and porosity. These coupled processes caused cementation, affected the pore-size distribution and resulted in a modification of the initial (typically marine) porewater. Fig. 5-7 provides a summary of the diagenetic evolution of the Opalinus Clay and its confining units based on the summary of Mazurek & Aschwanden (2020). Mineralisation in veins is described separately in Section 4.7.

The effects of early diagenesis (eogenesis), i.e. processes that occur within the first 100 m of burial, are quantitatively particularly important and mainly include the precipitation of aragonite/Mg-calcite, pyrite I, siderite, calcite I and dolomite I (Fig. 5-7). The precipitation of framboidal pyrite I and dolomite I affected all lithologies, including those that are clay-mineral-rich. In contrast, precipitation of aragonite/Mg-calcite and calcite I only occurred in areas rich in bioclastic material whose early diagenetic dissolution provided the solutes for pore-occluding cement precipitation. Siderite was mainly detected in the Opalinus Clay. Note that, from a quantitative perspective, diagenetic cements in the clay-rich matrix of the Opalinus Clay are only minor. Later cements related to burial diagenesis (mesogenesis), such as authigenic quartz and poikilitic calcite II, are more strongly expressed in silty/calcareous lithologies but only weakly in the clay-rich bulk of the rock. Diagenetic celestite and Ba-Sr sulphate have been detected by conventional transmitted light microscopy in both the Opalinus Clay and in the confining units. They mainly occur as fillings of interstices and as xenomorphic, fibrous cement in the rock matrix (Fig. 5-7). It was argued that the solutes of these cements were supplied by dissolution of bioclasts (Lerouge et al. 2014).

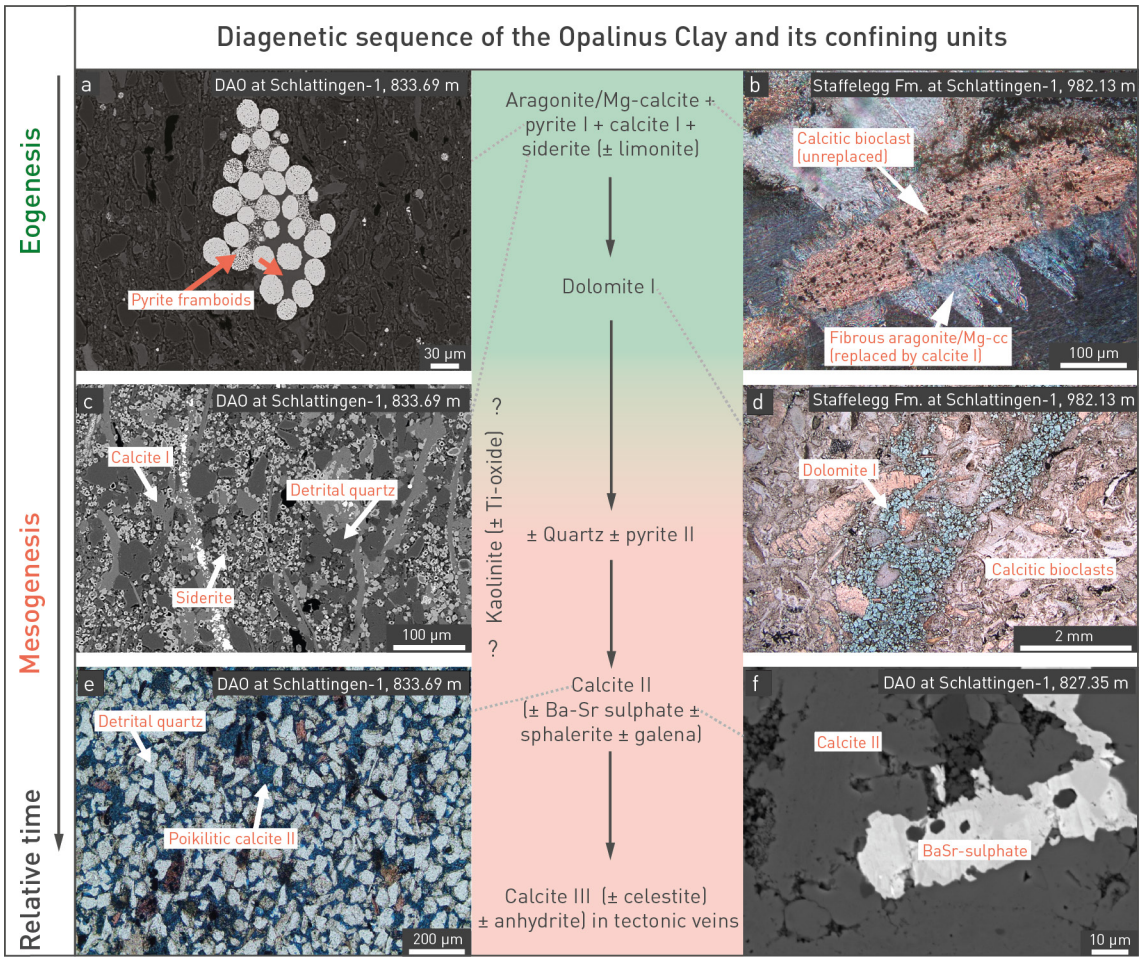


Fig. 5-7: Diagenetic minerals and their relative temporal sequence of precipitation in the Opalinus Clay and its confining units in Northern Switzerland

Modified after Mazurek & Aschwanden (2020): (a) Agglomerated framboids of pyrite. (b) Blocky (Fe-)calcite I replacing early fibrous aragonite/Mg-calcite cements in bioclast-rich zones. (c) Siderite concretion in a silty lens cemented with calcite II. (d) Dolomite I in a bioclast-rich zone. (e) Poikilitic calcite II cementing a silty lens. (f) Ba-Sr sulphate filling residual intergrain pore space after cementation by calcite II (a), (c), (f): Scanning electron microscope backscattered electron image (SEM-BSE); (b), (d), €: transmitted light microscopy). All photos from Mazurek & Aschwanden (2020) and Wersin et al. (2013). DAO: Dogger Group above Opalinus Clay.

There are no major systematic differences in the diagenetic cements and their relative timing over the study area, and no evident distinctions between the Opalinus Clay and the confining units can be made except for the fact that diagenetic effects are quantitatively more strongly expressed in the latter.

Implications for porosity and pore-size distribution in the Opalinus Clay: Based on the spatial homogeneity of diagenetic effects and the regionally consistent occurrence of different subunits, porosity and pore-size distribution can be considered to depend mainly on the maximum burial depth and on the current depth (i.e. the degree of uplift and decompaction). This implies that corresponding data are transferrable among sites with comparable burial and uplift histories.

Implications for porewater chemistry of the Opalinus Clay: As the inventory of detrital and diagenetic minerals present in the Opalinus Clay does not vary over the study area, it can be concluded that the mechanisms by which the rock controls the chemical composition of the porewater are regionally constant and can be treated in one single porewater model.

5.2.6 Conclusions

- The combination of numerous laboratory analyses and calibrated data from geophysical borehole logs provides detailed, unbiased and highly resolved information on the mineralogical composition of the Opalinus Clay and its confining units.
- The mineralogical composition of the Opalinus Clay shows no systematic variability laterally, i.e. the three siting regions are equivalent in this respect. Vertically, a slight upward decrease in the clay-mineral content and a slight increase in the illite/kaolinite ratio can be observed consistently throughout the study area. Overall, the mineralogy of the Opalinus Clay is homogeneous and predictable in the study area.
- Large parts of the confining units are also clay-mineral-rich but show higher variability. The underlying Staffelegg Formation (Lias Group) shows little heterogeneity horizontally but consists of several members with distinct properties vertically, including subordinate limestones and silt-/sandstones. The Dogger Group above Opalinus Clay shows heterogeneity both vertically and horizontally and, apart from clay-rich lithologies, also includes limestones, silt-/sandstones and iron-rich oolites.
- Diagenetic effects on the Opalinus Clay include some degree of cementation by calcite, mainly localised in silty, calcareous and bioclastic beds and lenses. Siderite occurs in cm-sized lenses or disseminated in the rock. The clay-rich matrix is very weakly cemented, which is a favourable feature from the perspective of self-sealing potential.
- Diagenetic mineralisation in the rock matrix is more strongly developed in the confining units. Various diagenetic trace phases were formed, some of which are relevant as controls of the porewater composition (e.g. Ba-Sr sulphate and celestite).
- The inventory of detrital and diagenetic minerals present in the Opalinus Clay does not markedly vary over the study area. The mechanisms by which the rock controls the chemical composition of the porewater are thus regionally constant and can be treated in one single porewater model.

5.3 Porosity

Key points:

- The Opalinus Clay in the siting regions is characterised by a porosity of 10 – 13 vol.-% with low variability and only minor differences with depth.
- The mean pore size of the Opalinus Clay is in the range of a few nanometres.
- A general increase of porosity with increasing clay-mineral content is observed for most clayrocks.
- Clay-mineral-poor sections of the confining units are typically characterised by low porosity and larger pore sizes than in the Opalinus Clay.

5.3.1 Overview

Porosity and pore-size distribution are relevant determining factors for a number of rock properties and states, such as permeability (Section 5.6), porewater chemistry (Section 5.4), diffusion coefficients (Section 5.8), and various geomechanical parameters (Section 5.5). The three-dimensional architecture and connectivity of different pore types also determine the anisotropy of many rock properties. Clay-rich rocks in general, and the Opalinus Clay in particular, are characterised by a relatively large porosity but, at the same time, extremely small pore apertures (the average value for the Opalinus Clay is around 2 – 3 nm).

5.3.2 Porosity profile

Several laboratory methods were used to quantify porosity, including the measurement of water content upon heating to 105 °C (yielding water-loss porosity), density measurements (yielding pycnometer porosity), or based on diffusive isotope exchange experiments (yielding porosity from isotope exchange). The methodologies are documented in Waber (2020). While the physical basis for the porosity determination differs substantially between these methods, the results converge, despite small method-specific differences. In addition to laboratory-based methods, porosity was also quantified from borehole logs (Becker & Marnat 2024).

Along the investigated profiles (Fig. 5-8), porosity is mostly below 0.15 (expressed as the fraction of pore space relative to bulk rock volume). The Opalinus Clay shows little variation in the continuous log-derived porosity profiles. Porosities are generally very low in the Malm Group section (< 0.05), pointing to well cemented rock. Particularly low porosities are also observed at the base of the Bänkerjoch Formation, in the zone where typically massive anhydrite occurs. A substantial variation is seen within the Muschelkalk aquifer, with higher values in the upper, dolostone-dominated part (Sections 4.2.2 and 4.5.3.12).

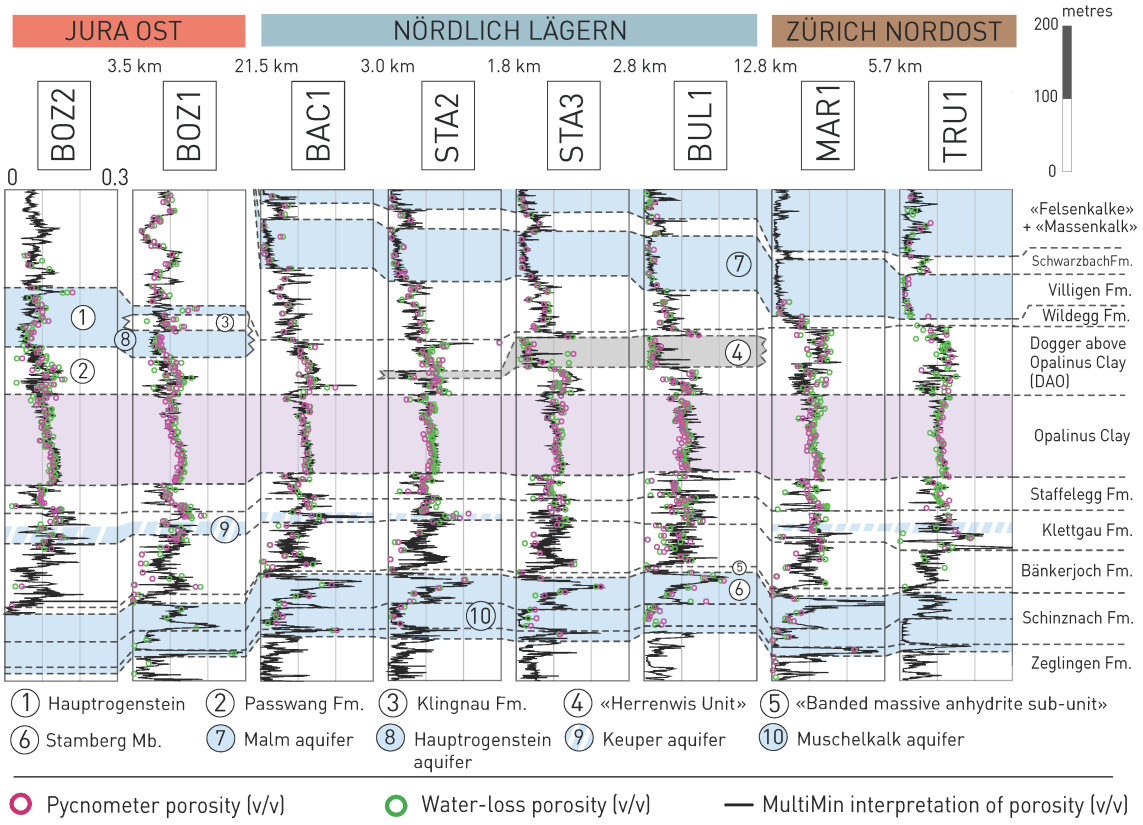


Fig. 5-8: Porosity profiles from selected boreholes in the siting regions

Blueish shading depicts the regional and local aquifers while the purple shading depicts the Opalinus Clay. The continuous MultiMin-porosity profiles (Becker & Marnat 2024) are computed from geophysical logging data and are calibrated with drill-core analyses.

The typical range for porosity in the Opalinus Clay in the siting regions is 0.10 – 0.13 (Fig. 5-9). At the Mont Terri rock laboratory (Fig. 5-10), the porosity is somewhat higher (0.12 – 0.15), which can be explained by the external position relative to the Alpine front and therefore shallower Miocene burial and compaction (details in Mazurek et al. 2006). There is a moderate correlation between the current depth of the Opalinus Clay and its porosity (Fig. 5-10). The median porosity is around 0.11 for the BUL1 and TRU1 boreholes, where the Opalinus Clay occurs at 820 – 1'000 m depth, while it is around 0.12 at shallower depth in boreholes BOZ1 and BOZ2 (450 – 650 m depth). The porosity increase associated with unloading from 1'000 m to 400 m depth can be estimated from oedometric test results (Section 5.5.2). This yields an approximately 0.002 to 0.007 increase in porosity. It is therefore conceivable that other factors in the burial history contributed to the slightly different porosities observed at the different depth intervals, for example a lower maximum burial depth during Miocene times, where Molasse sediments are mostly absent in the JO siting region (Section 3.4.3).

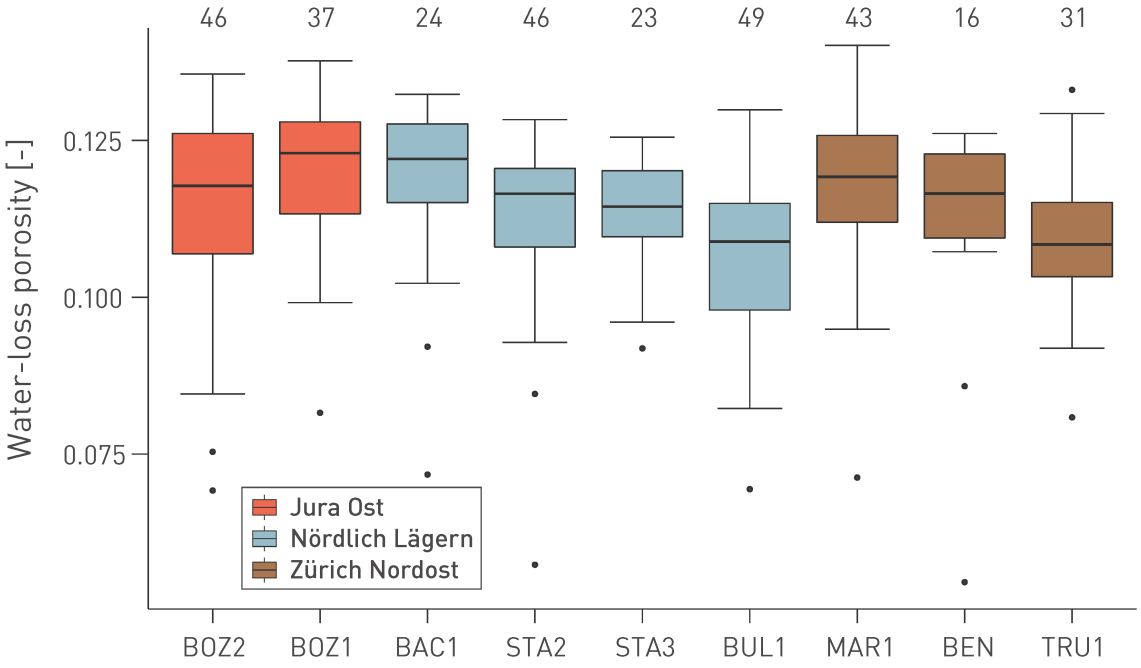


Fig. 5-9: Water-loss porosity of the Opalinus Clay

Each box encloses 50% of all measured values. The horizontal line in the box indicates the median, and the whiskers (error bars) the minimum and maximum values (min: 25th percentile – (1.5 × interquartile range); max: 75th percentile + (1.5 × interquartile range)). The black circles indicate outliers. The values above the boxplots denote the number of samples.

The scatter of porosity is remarkably low (1σ deviations are 0.010 – 0.016) within the Opalinus Clay. Outliers towards lower porosity are related to clay-poor, often well cemented beds in the upper part of the formation (Fig. 5-10). At Mont Terri, the most prominent outliers occur in the «Carbonate-rich silty sub-unit», which is not observed in the siting regions in Northern Switzerland.

The increased variability of porosity in the Dogger Group above Opalinus Clay reflects the higher lithological heterogeneity of this sequence both vertically and laterally (Fig. 5-8). Particularly low matrix porosities are found in the limestones of the «Herrenwis Unit» of STA3 and BUL1, and in the Hauptrogenstein of BOZ1 and BOZ2. Nevertheless, the average porosity is relatively high (0.10), given the generally clay-rich lithologies present in the Dogger Group above Opalinus Clay.

Porosity in the Staffelegg Formation also varies over a wide range, but the variability shows a systematic vertical pattern over the area of the siting regions, reflecting variation in clay-mineral contents (Mazurek et al. 2023a). The lowest porosity values are found in the limestones of the Beggingen and the Grünschholz, Breitenmatt and Rickenbach Members, whereas all other members yield averages of 0.08 – 0.11.

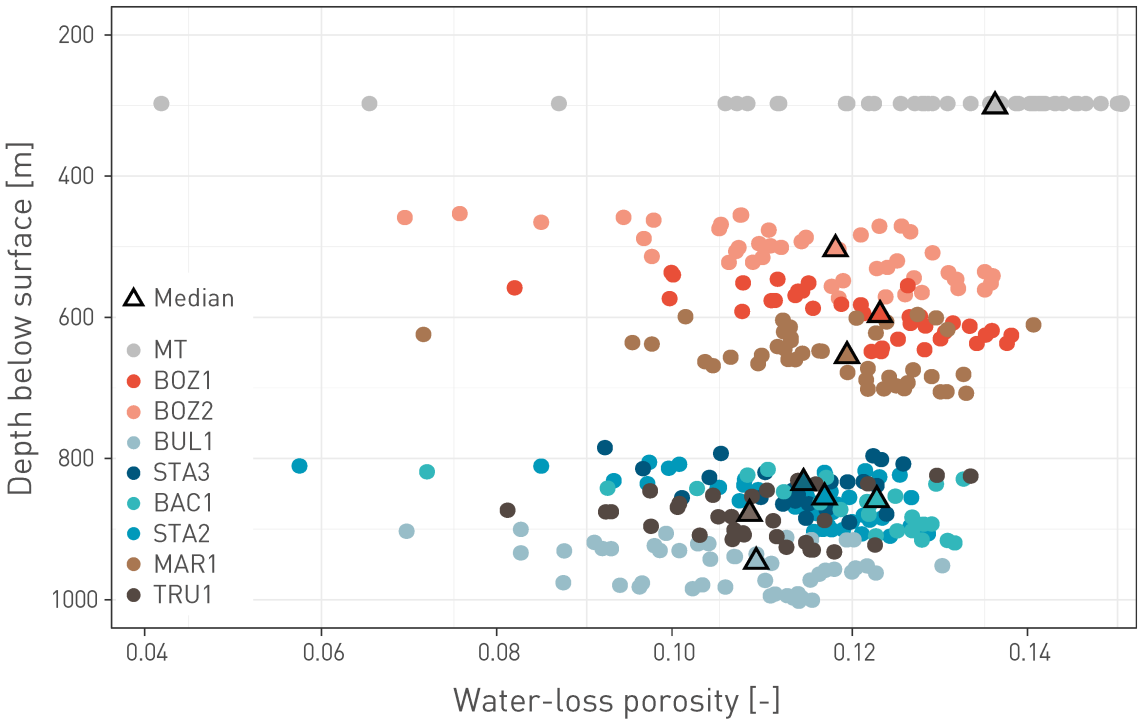


Fig. 5-10: Water-loss porosity of the Opalinus Clay in different boreholes as a function of current depth

Triangles indicate the borehole-specific median values (plotted at mid formation depth).

Mont Terri (MT) data refer to the BDB1 borehole (complete profile) and are shown at a nominal depth of 300 m.

5.3.3 Correlation of porosity with other rock properties

In the Jurassic profile, a good correlation is found between clay-mineral content and porosity, even though several outliers towards higher porosity can be identified (Fig. 5-11). These originate from Fe-rich oolites (e.g. Wutach Formation, «Humphriesioolith Formation», «Murchisonae-Oolith Formation»), from the Hauptrogenstein (oolitic limestone) and from the reef facies of the «Herrenwis Unit». All samples from these units are shown with open symbols in Fig. 5-11, together with sandstones (but not the more clay-mineral-rich lithologies) of the Wedelsandstein Formation. All these units have in common that, at the time of deposition, they contained large mechanically competent grains, such as ooids, abundant quartz in the sand fraction and coarse-grained calcite from the reef. As suggested by Mazurek et al. (2023a) and following earlier work (e.g. Revil & Cathles 1999), it is conceivable that the compaction of such grain-supported lithologies led to less reduction of porosity when compared with the other, in general matrix-supported units (clay and micrite). When these outliers are screened out, a power-law function provides a good fit of the measured data (Fig. 5-11). The slope of the fit curve is 0.010 – 0.016 at low clay-mineral contents but flattens out to < 0.0015 at contents > 40 wt.-%. As discussed in more detail in Mazurek et al. (2023a), considering pore-size distributions based on N_2 ad-/desorption isotherms (see below), the porosity data shown in Fig. 5-11 can be considered to consist of two contributions: 1) *Clay porosity* between clay aggregates, with sizes of a few nm, and 2) *porosity related to geometric incompatibilities* between platy and granular minerals, with sizes in the range of tens of nm (Fig. 5-12). Clay porosity can be assumed to be proportional to the clay-mineral content, whereas porosity due to incompatibilities is present in clay – carbonate

mixtures but not in pure clay or carbonate. Extrapolating the trend line fitting the measured data in Fig. 5-11 to pure clay leads to a porosity of 0.17. The red line then reflects the clay porosity, considering proportionality with the clay-mineral content. The curvature in the fit line reflects the additional pore type that occurs in lithologies in which platy clay minerals occur together with more isometric grains of calcite. The contribution of this pore type is at a maximum when both mineral types occur in comparable proportions and is of lesser relevance towards the pure clay and non-clay compositions.

The scatter that remains in the correlation between clay-mineral content and porosity even after screening out lithologies with grain-supported fabrics indicates that clay-mineral content is not the only parameter that controls porosity. The following additional factors probably play a role:

- While the studied Jurassic sequence is dominated by mixtures of clay minerals and carbonates (i.e. claystones, marls and limestones), silty/sandy lithologies also occur but are less frequent. The decrease in porosity from claystone towards the quartz/feldspar corner as shown in Fig. 5-13 is less strong compared to that towards the carbonate corner, indicating that the compaction behaviour of clay-mineral – quartz mixtures differ from that of clay-mineral-carbonate mixtures.
- It can also be seen in Fig. 5-11 that, even at the same clay-mineral content, systematic differences in porosity exist between different geological units. For example, the Opalinus Clay has a lower porosity than the overlying Dogger units of comparable clay-mineral content, a finding that cannot be explained by the only marginally different maximum burial depths. Rock fabric and porosity thus depend on other parameters as well, such as the rate of sediment deposition as this is related to the time available for early diagenesis. A low deposition rate means that the time over which early diagenesis acted on the unconsolidated sediment was longer, potentially leading to more extensive mineral reactions, such as dissolution and cementation, with consequences for the rock fabric and its compactional behaviour during later burial. The Opalinus Clay was deposited at a rate of about 50 – 60 m/Myr (referring to the current thickness in the compacted state), which is more than for any of the other Dogger units (see Section 4.2). The rapid burial is consistent with the observation that the Opalinus Clay is only weakly cemented and disaggregates when immersed in pure water, except in silty lenses in which sparitic calcite fills the pore space. In comparison, the average deposition rates for the underlying Staffelegg Formation and the Dogger Group above Opalinus Clay were 1.3 – 1.6 and 10 – 14 m/Myr, respectively, thus leaving more time for early diagenetic cementation and leading to a stiffer behaviour during compaction.

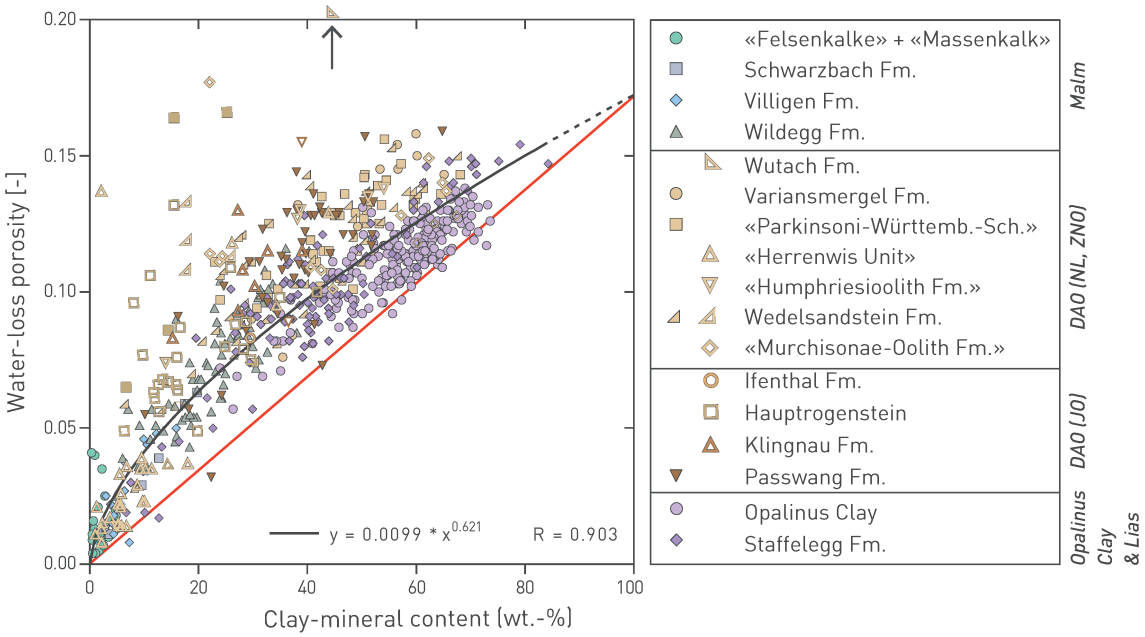


Fig. 5-11: Relationship between clay-mineral content and porosity in the Jurassic section

Redrawn from Mazurek et al. (2023a). Points with open symbols were not considered for the calculation of the black fit curve (see text). The red line reflects the clay porosity, considering proportionality with the clay-mineral content. Arrow points to a sample with a porosity of 0.30. DAO: Dogger Group above Opalinus Clay, Fm.: Formation.

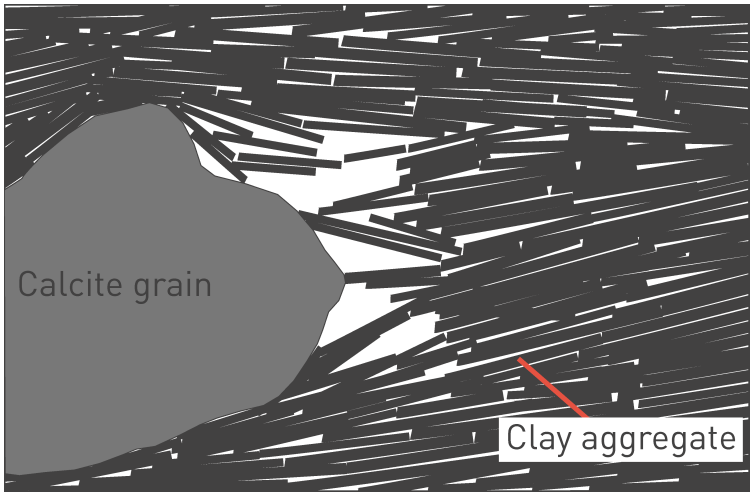


Fig. 5-12: Conceptual view of the porosity types (white) in clay-carbonate mixtures

Redrawn from Mazurek et al. (2023a). Sketch width is ~ 1 µm.

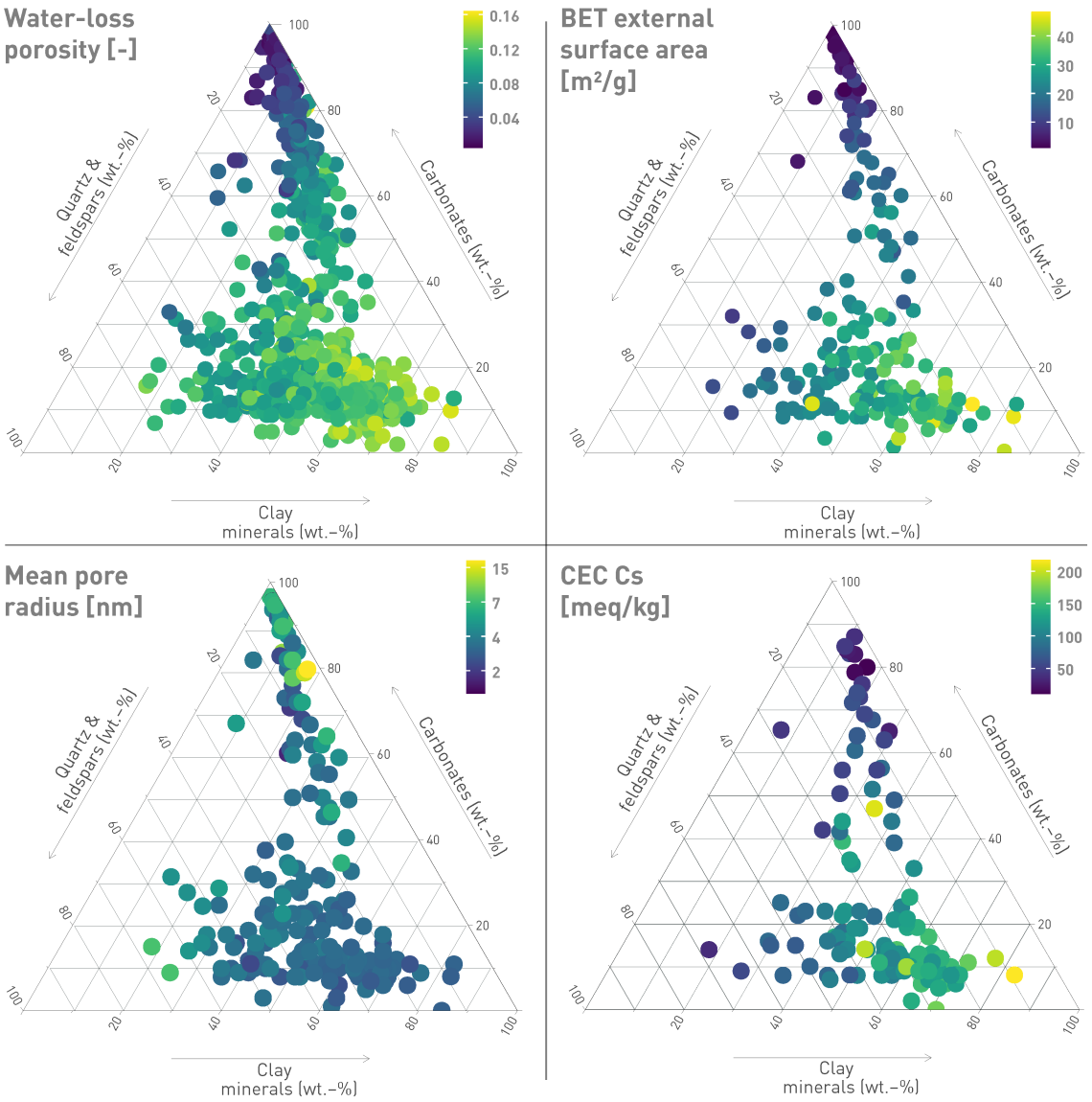


Fig. 5-13: Key rock data for Jurassic samples from TBO boreholes shown in the Füchtbauer triangle

Axes are in wt.-%. Samples with > 10 wt.-% minerals other than those represented by the triangle are excluded. After Füchtbauer (1988).

Fig. 5-14 shows the relationship between clay-mineral content and porosity for a number of formations under investigation in the context of radioactive waste disposal (OECD/NEA 2022). The Opalinus Clay is among the units richest in clay minerals and exhibits some of the lowest porosities of the clay-rich rocks shown. The absence of a correlation between clay-mineral content and porosity is because the maximum burial depth and therefore degree of compaction varies widely among the different units (e.g. < 500 m for the Belgian clays, 4'000 m for the Boda Claystone Formation in Hungary).

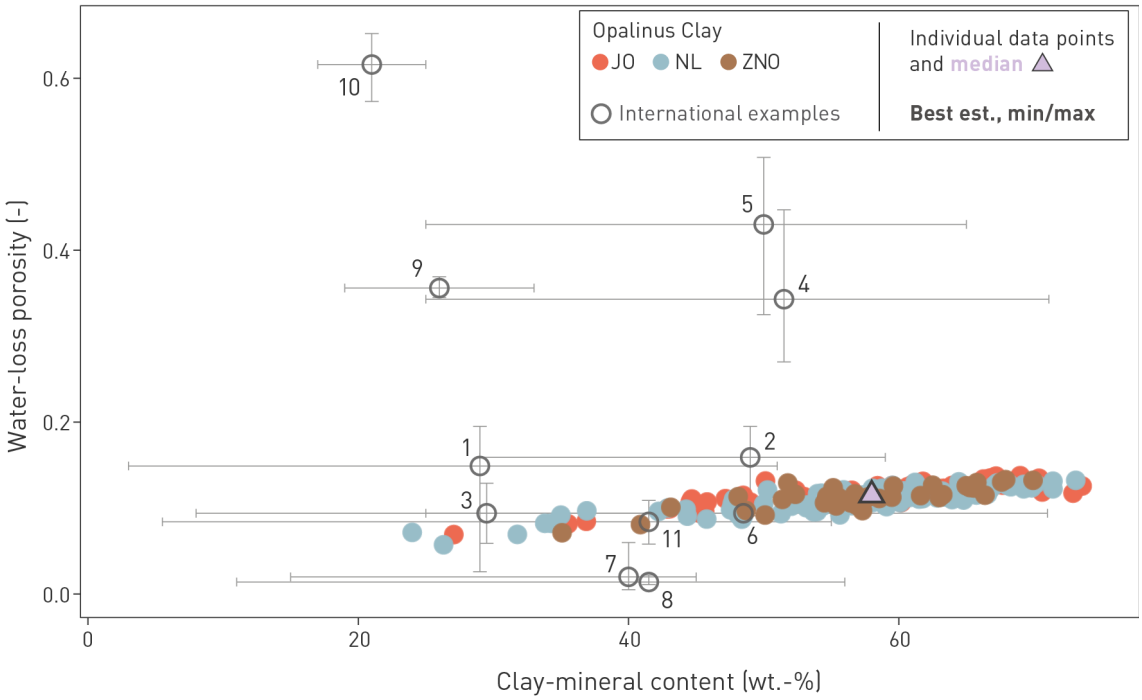


Fig. 5-14: Water-loss porosity of the Opalinus Clay as a function of clay-mineral content and comparison to other clay-rich rocks

The figure shows drill-core analyses of the Opalinus Clay from the TBO boreholes and the related median value. International data are from the Clay Club Catalogue (OECD/NEA 2022). 1: Callovo-Oxfordian at Meuse/Haute Marne, silty-calc. unit (F); 2: Callovo-Oxfordian at Meuse/Haute Marne, clay-rich unit (F); 3: Toarcian-Domerian at Tournemire (F); 4: Boom Clay at Mol (B); 5: Ypresian Clay at Kallo/Doel (B); 6: Georgian Bay Formation at Bruce nuclear site (CDN); 7: Boda Claystone Formation, Gorica block (H); 8: Boda Claystone Formation, Boda block (H); 9: Wakkanai Formation at Horonobe (JP), 10: Koetoi Formation at Horonobe (JP), 11: Queenston Formation (CDN). est.: estimate.

5.3.4 Pore-size distribution and external surface area

Together with porosity, the surface area of minerals and the distribution of pore sizes are key parameters that affect numerous rock properties. Clay-mineral-rich lithologies are known to have small pore apertures and large mineral surface areas, with major consequences for solute transport (low permeability, substantial cation-exchange capacity and sorption on clay surfaces etc.). N_2 ad-/desorption tests provide the basis for obtaining the external surface area of minerals (i.e. not considering clay interlayers that are not accessed by N_2; Brunauer et al. 1938), as well as the pore-size distribution in the range 2 – 200 nm (Barrett et al. 1951). More detail on methodology and results is provided in Mazurek et al. (2023a).

As expected, the external surface area shows a good correlation with the clay-mineral content (Fig. 5-15a), illustrating the fact that clay minerals are by far the most relevant contributors to surface area. The average value for the Opalinus Clay is 30 m^2/g. The trends for all lithologies represented in the Füchtbauer triangle are shown in Fig. 5-13. Mean radii of external pores (assuming cylindrical geometry) can be estimated by dividing the water content relative to dry weight by the external surface area and the water density. The data trends are shown in Fig. 5-13, and all data from the Jurassic profile are shown as a function of the clay-mineral content in Fig. 5-15b. For lithologies with > 50 wt.-% clay minerals, the mean pore radius is remarkably constant at 3 nm. More scatter is found for clay-mineral-poor rocks, illustrating the textural heterogeneity of limestones in particular. While the oolitic Hauptrogenstein (and all Fe-rich oolites) have large mean pore apertures, other limestones with often micritic fabrics (such as the Wildegg Formation) may have mean apertures even smaller than clay-mineral-rich lithologies.

Examples of the full pore-size distributions for different lithologies are illustrated in Fig. 5-15c. In clay-mineral-rich lithologies, the size distribution based on the adsorption branch shows a prominent peak at 2 – 3 nm, which can be associated with clay minerals as its amplitude decreases with decreasing clay-mineral content. In carbonate-rich lithologies (most of which still contain a small proportion of clay minerals), a broad peak in the range of 40 – 100 nm dominates. Bimodal distributions with both peaks at comparable amplitude are found for intermediate, more quartz-rich lithologies, while silt-/sandstones towards the quartz corner-show a broad plateau over a wide range of pore sizes. Thus, pore-size distributions vary systematically between lithologies, and clay-mineral-rich lithologies tend to be dominated by the smallest pore diameters in the range of a few nm.

N_2 adsorption is insensitive to pore radii larger than about 200 nm. Samples from the Opalinus Clay were also studied using NMR cryoporometry (Fleury et al. 2022, Mazurek et al. 2023a), a method that can capture even larger pores. As shown in Fig. 5-15d, such pores were not identified by this method and probably do not exist. Another advantage of the cryoporometry technique is the fact that samples are tested in their natural state, i.e. no drying is needed prior to or during analysis, in contrast to most other methods (e.g. Hg intrusion porosimetry, H_2O ad-/desorption). It is concluded that many, if not most, pores resolvable in the clay-mineral-rich matrix under the SEM are not present in the formation but are artefacts of drying and sample preparation.

As already noted in previous studies (e.g. Mazurek 2011), an excellent correlation can be found between the external surface area and the cation-exchange capacity (Fig. 5-16). This is also shown in Fig. 5-13.

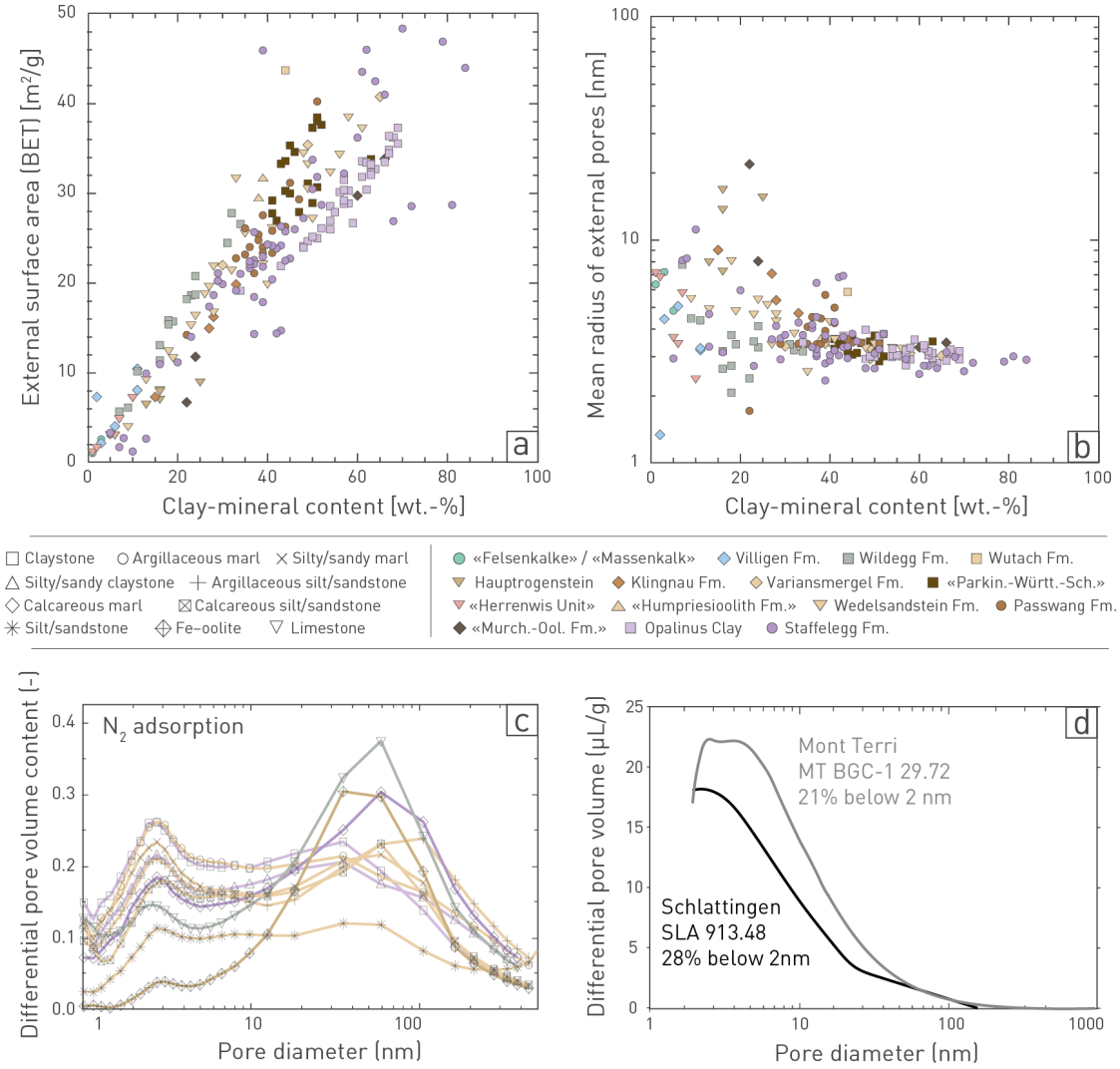


Fig. 5-15: Mineral surface areas and pore-size distributions in the Jurassic profile

(a) External (BET*) surface area as a function of clay-mineral content.

(b) Mean radius of external pores as a function of clay-mineral content.

(c) Examples of pore-size distributions based on the N_2 adsorption branches, normalised to the water content of the samples (BJH** algorithm). Claystone = TRU1 923.34, Opalinus Clay, «Clay-rich sub-unit»; Argillaceous marl = BUL1 808.92, «Parkinsoni-Württembergica-Schichten»; Silty/sandy claystone = BUL1 965.46, Opalinus Clay, «Mixed clay-silt-carbonate sub-unit»; Argillaceous silt/sandstone = TRU1 788.76, Wedelsandstein Formation; Silty/sandy marl = STA3 748.38, Wedelsandstein Formation; Calcareous marl = MAR1 717.76, Staffelegg Formation, Rietheim Member; Limestone = BOZ1 323.16, Wildegg Formation, Effingen Member; Calcareous silt/sandstone = MAR1 588.40, Wedelsandstein Formation; Silt-/sandstone = TRU1 812.24, Wedelsandstein Formation; Fe-rich oolite BOZ2 313.13, Hauptrogenstein, Spatkalk.

(d) Pore-size distribution for two samples of the Opalinus Clay obtained from NMR cryoporometry. Adapted from Fleury et al. (2022).

* Method to derive the (external) surface area of solid materials based on gas adsorption (typically N_2). BET stands for the names of the developers of the method (Brunauer, Emmet, Teller).

** Barrett – Joyner – Halenda algorithm (a procedure for calculating pore volumes and pore-size distributions from experimental isotherms, using the Kelvin equation).

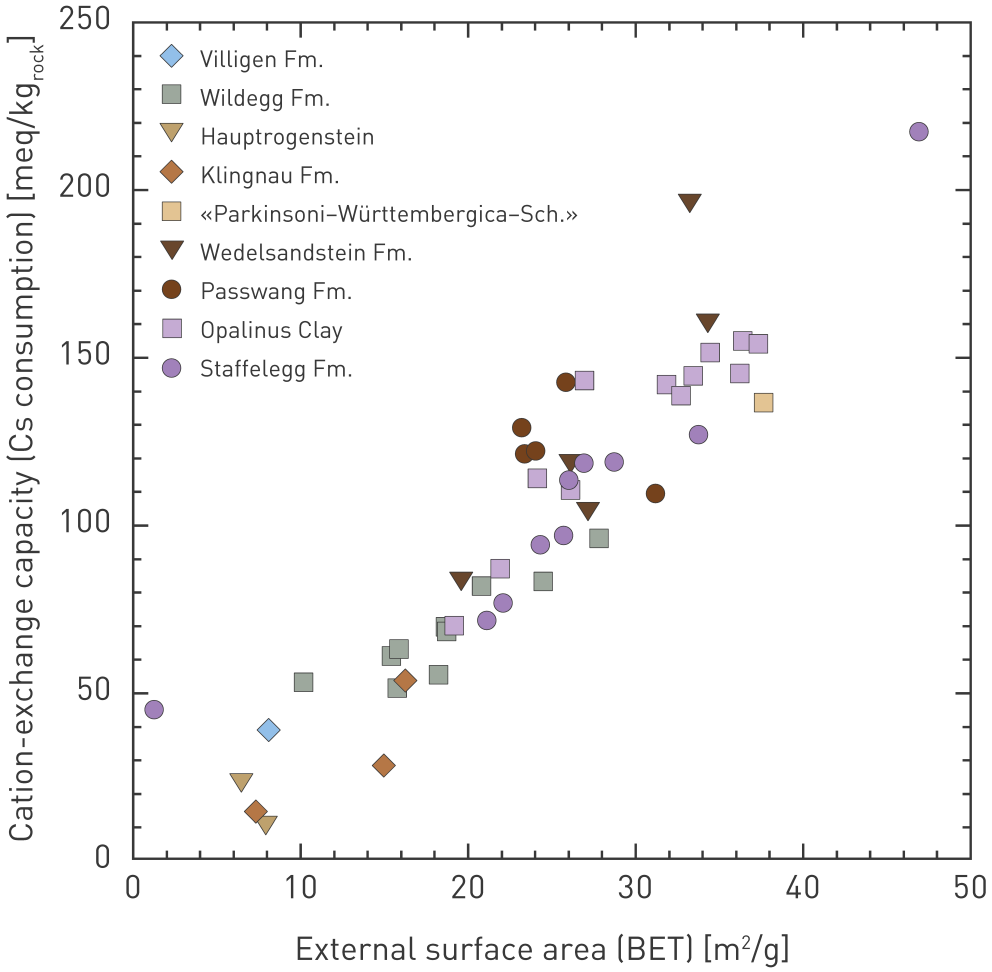


Fig. 5-16: Correlation between external surface area and cation-exchange capacity based on Cs consumption

Only data for the Jurassic profile are shown. Cs data from Baeyens & Fernandes (2022). BET: see explanations in Fig. 5-15.

5.3.5 Conclusions

- Porosity and pore-size distribution are relevant determining factors for a number of rock properties and states. The presented data contribute to the interpretation of permeability, pore-water chemistry, diffusion coefficients and various geomechanical parameters and moduli.
- Porosity of the Opalinus Clay was quantified by laboratory methods and geophysical log analyses and the results show consistent values in the range 0.10 to 0.13, with only a low correlation with current burial depth. Local excursions to lower porosities occur mainly in the upper part of the formation.
- In the Jurassic section, a good correlation exists between clay-mineral content and porosity. Exceptions include (Fe-)oolitic lithologies, reef limestones of the «Herrenwis Unit» and silty/sandy beds in the Wedelsandstein Formation.

- Apart from the clay-mineral content, the nature of the other constituents (e.g. carbonate/quartz ratio) also affects porosity, and the degree of cementation affects compaction behaviour and therefore porosity. The Opalinus Clay has a lower porosity than other units of comparable clay-mineral content in the confining units, which is probably because of its high deposition rate and therefore much shorter time over which early diagenetic cementation could occur.
- The pore-size distribution in clay-rich rocks such as the Opalinus Clay shows a peak at pore radii in the range of only a few nm. In contrast, the pore-size distribution of limestones shows a broad peak in the range of 40 – 100 nm. Marls, i.e. mixtures between clay and carbonate minerals, show bimodal distributions. Thus, the mean pore size is negatively correlated with the clay-mineral content.
- The external surface area correlates linearly with the clay-mineral content and cation-exchange capacity.

5.4 Porewater chemistry (geochemical conditions)

Key points:

- In the Opalinus Clay, the anion-accessible porosity fraction relevant for the transport of negatively charged species is well constrained and depends on porewater ionic strength. In JO it is about 30%, in NL and ZNO in the range of 40 – 50% of the total porosity.
- In the confining units, the anion-accessible porosity fraction is partly larger. This is explained by the partly lower clay-mineral contents and larger pore sizes.
- Opalinus Clay porewater chemistry can be robustly constrained based on complementary datasets and approaches. The porewater of the general Na-Cl type is of moderate ionic strength (0.15 – 0.37 molal), the pH is in the near-neutral range and the redox conditions are buffered by mineral equilibria in the reducing range.
- Porewater ionic strength is lowest in JO because of the different palaeo-hydrogeological evolution. For ZNO and NL, the similar data allow the same reference porewater model to be used to evaluate radionuclide mobility and the stability of the engineered barriers.

5.4.1 Overview

The mobility of radionuclides (sorption, solubility, diffusion) and the long-term stability of the engineered barriers strongly depend on the geochemical conditions in the host rock, notably the porewater chemical composition, pH and redox state. In addition, porewater chemistry can be used as independent evidence for the hydraulic barrier effect; this topic is addressed in Section 4.6.

There is a strong interaction between the mineral surfaces and the porewater in the nanometric pore space of clay-rich rocks. The section on solute distribution in the pore space (Section 5.4.2) introduces relevant concepts needed for the interpretation of porewater data and the pertinent dataset. Porewater cannot be directly sampled because of the very low hydraulic conductivities but requires laborious, dedicated experiments. The section on porewater chemistry (Section 5.4.3) presents the modelling approach used to integrate the available data and illustrates sensitivities of the model with respect to temperature and the choice of equilibrium phases.

5.4.2 Solute distribution in the pore space

The pore space of clay-rich rocks has a nanometric architecture (see also Mazurek et al. 2023a), with clay-mineral grain and interlayer surfaces representing a substantial part of the water – mineral contact (Fig. 5-17). These surfaces interact with the solutes of the porewater. Most of these clay-mineral surfaces are negatively charged, which leads to the repulsion of anions and to the attraction of cations that balance the surface charge. In contrast, the electrostatic force does not affect neutral species. Generally, the concentration of anions increases with increasing distance to the negatively charged surface until, at a certain distance, a charge-balanced electrolyte solution persists, which is often termed free porewater (Bresler 1973, Tournassat & Steefel 2021) (white in Fig. 5-17). The spatial distribution of the ions in the remaining fraction of the porewater affected by charged surfaces (blue in Fig. 5-17) is complex and depends on various parameters, such as the charge of the ion itself, the charge density of the clay surfaces (electrostatic potential), the ionic strength of the free porewater and the microstructure (e.g. Tournassat & Steefel 2019, 2021, Wigger 2017, Appelo et al. 2010). This anion-depleted porosity may constitute a large fraction of the total porosity, such that a significant portion of the pore space is barely accessible to anions (Pearson 1999).

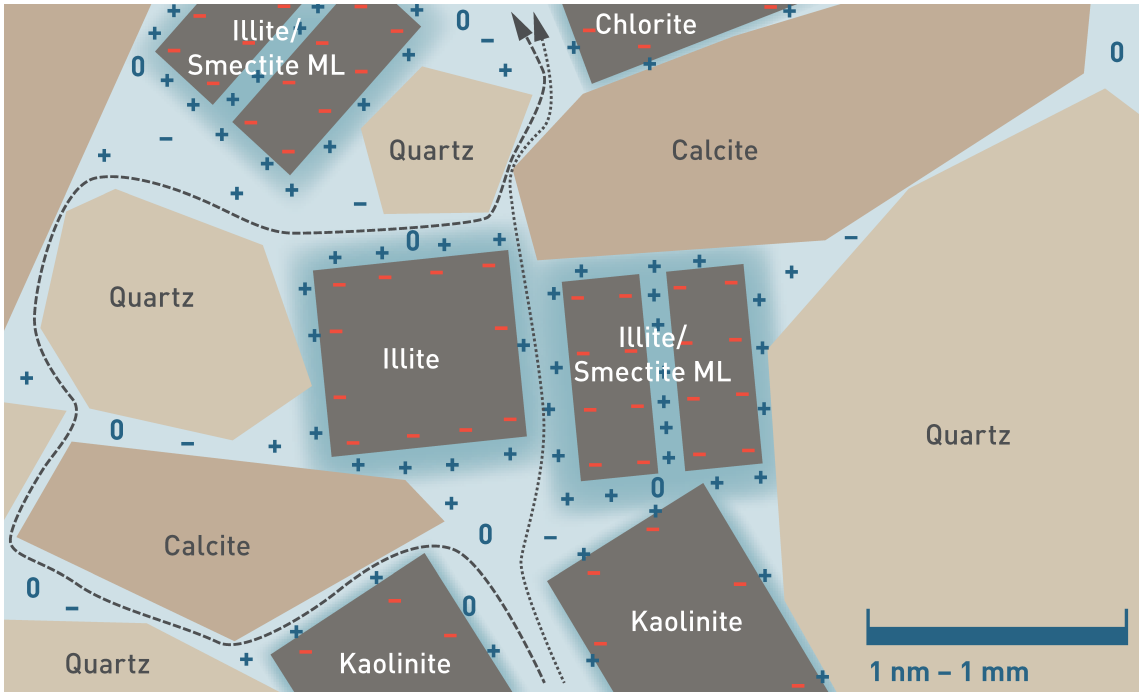


Fig. 5-17: Conceptual model of anion-accessible porosity (white), anion-depleted porosity (blue), cations, anions, neutral species (+, -, 0, in dark blue) and the negative charge on clay mineral surfaces (red)

Model is not to scale. To illustrate the effect on transport, the dashed line indicates a hypothetical diffusion path of an anion and the dotted line for a neutral species, respectively. Note that the schematic abstraction covers a range of scales, given the fact that the bound, anion-depleted water layer has a thickness in the order of 1 nm, while the grain size of calcite and quartz is more likely in the range of µm to mm.

Diffusive transport is further explained in Section 5.8.

Profiles of anion concentrations across clay-rich lithologies contribute to the understanding and quantification of diffusive transport between clay-rich formations and the bounding aquifers (Section 4.6.3) but require the concentrations in the free porewater for obtaining local concentration gradient and the computation of solute-mineral equilibria. In order to scale the concentrations of anionic tracers determined for the bulk porewater (blue and white zones in Fig. 5-17) to the free porewater concentration, a scaling factor termed anion-accessible porosity fraction (f_a) is required. This factor accounts for the overall anion depletion present in the rock. It can be approximated as the ratio of the anion concentration in the bulk porewater determined by aqueous extraction divided by the concentration in the free porewater obtained by advective displacement (AD), high pressure squeezing (SQ) or borehole sampling (Zwahlen et al. 2024, Wersin et al. 2020). Alternatively, f_a can be inferred from species-specific porosities obtained from through-diffusion experiments, e.g. for ^{36}Cl and HTO (Van Loon et al. 2023).

Zwahlen et al. (2024) compiled a large dataset of experimentally derived chloride-accessible porosity fractions (f_{Cl}) for the sedimentary sequence in the three siting regions. Two empirical models for extrapolating the experimental f_{Cl} values of the entire profiles were tested. The first model is based on the clay-mineral content of the rock (e.g. Wersin et al. 2013, 2016, Mäder & Wersin 2023) while the second model considers formation-specific averages of the experimental data. In heterogeneous formations, several formation-specific averages are calculated based on mineralogical constraints. Both models present two different sets of f_{Cl} values, one for JO and one for ZNO & NL, because of the differences in ionic strength of the free porewater (Fig. 5-18a). The second model was found to be more suitable because of the impact of the rock texture on the extent of anion exclusion, in particular evident for lithologies with a low clay-mineral content. The comparison of these models underlines that clay-mineral content is an important, but not the only, factor that determines anion accessibility in the pore space. For the Opalinus Clay, the recommended f_{Cl} values in JO range from 0.28 to 0.34 and in NL and ZNO from 0.42 to 0.52. Examples of scaled Cl profiles as obtained from measured bulk Cl concentrations and the formation-specific f_{Cl} values are detailed in Fig. 5-18b.

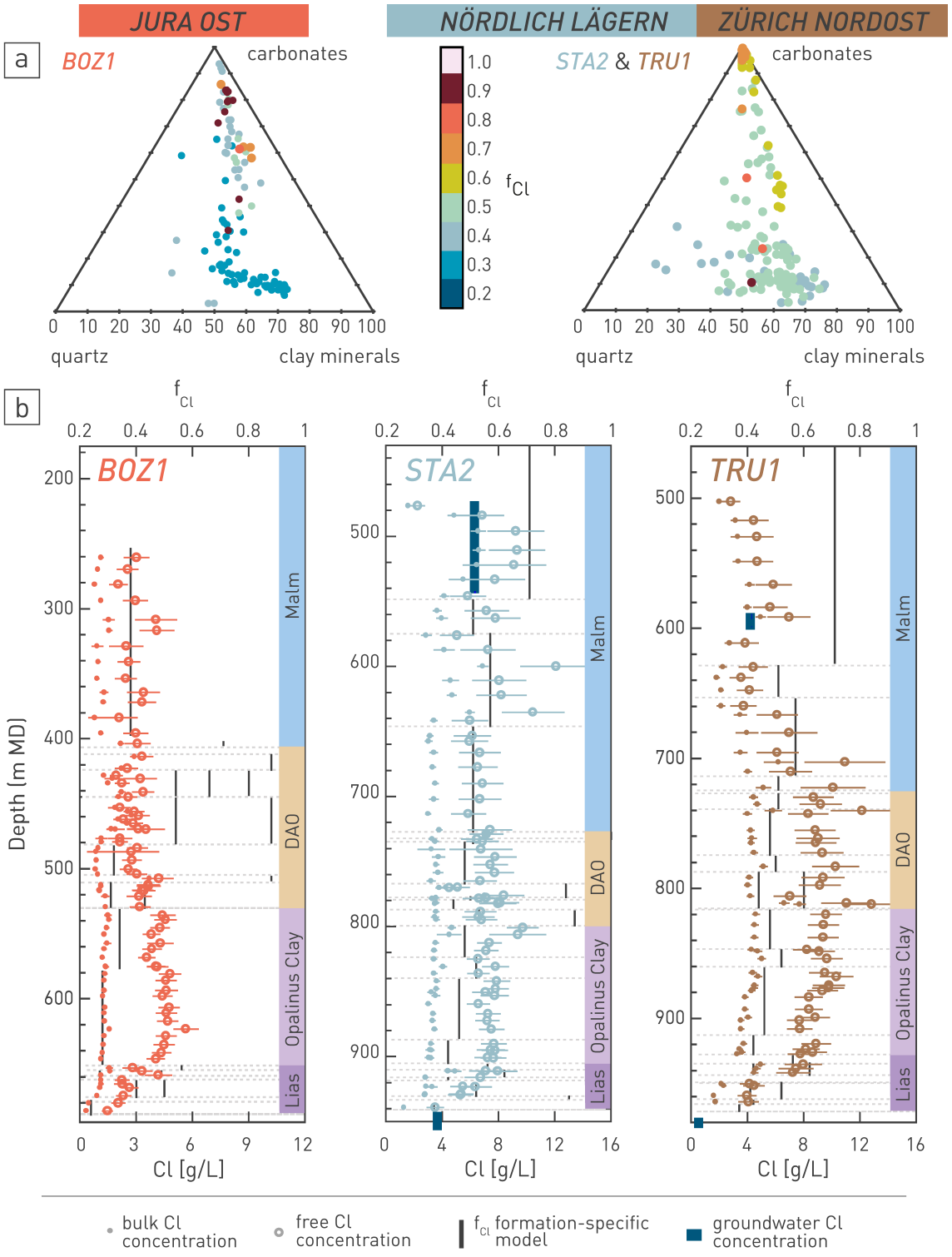


Fig. 5-18: Chloride-accessible porosity fraction (f_{Cl})

a) Mineralogical composition and f_{Cl} values of samples from JO (BOZ1), NL (STA2) and ZNO (TRU1) in the left and right triangle, respectively. b) Formation-specific f_{Cl} values (black lines) used to scale bulk Cl concentrations (filled circles) derived by aqueous extraction to free porewater Cl concentrations (hollow circles).

5.4.3 Porewater composition in the Opalinus Clay and the confining units

Given the physico-chemical complexity of the pore space, different extraction methods are used to sample different fractions of the porewater. Comprehensive porewater compositions that are considered to be close to the free porewater composition are obtained by direct sampling methods such as advective displacement and high-pressure squeezing of rock samples (Kiczka et al. 2023, Mazurek et al. 2015, Mäder 2018).

The specific characteristic porewater compositions in JO, NL and ZNO are consistently reflected in the porewaters obtained by advective displacement and high-pressure squeezing (Fig. 5-19). Porewaters of the Opalinus Clay and the confining units (Dogger Group above Opalinus Clay and Lias Group) in NL and ZNO are of Na-Cl type, whereas the porewaters in JO are more dilute and of Na-Cl-(SO_4) type. Cl concentrations in the Opalinus Clay are in the range of ~ 7 – 14 g/L in NL and ZNO but significantly lower in JO (~ 2 – 3 g/L). The different salinities reflect the local hydrogeological controls, for example the larger influence of a younger meteoric groundwater component in the comparably shallower JO siting region (Section 4.6). The difference between the Opalinus Clay porewaters in JO and NL and ZNO is also manifested in the distinctly higher SO_4/Cl ratios in the former region. Within the Opalinus Clay, vertical chemical gradients are small, but in some profiles (e.g. in ZNO and JO) a slight decrease in Cl concentrations with depth in the lower part of this unit is manifested due to the influence of the underlying Keuper aquifer (Section 4.6.3).

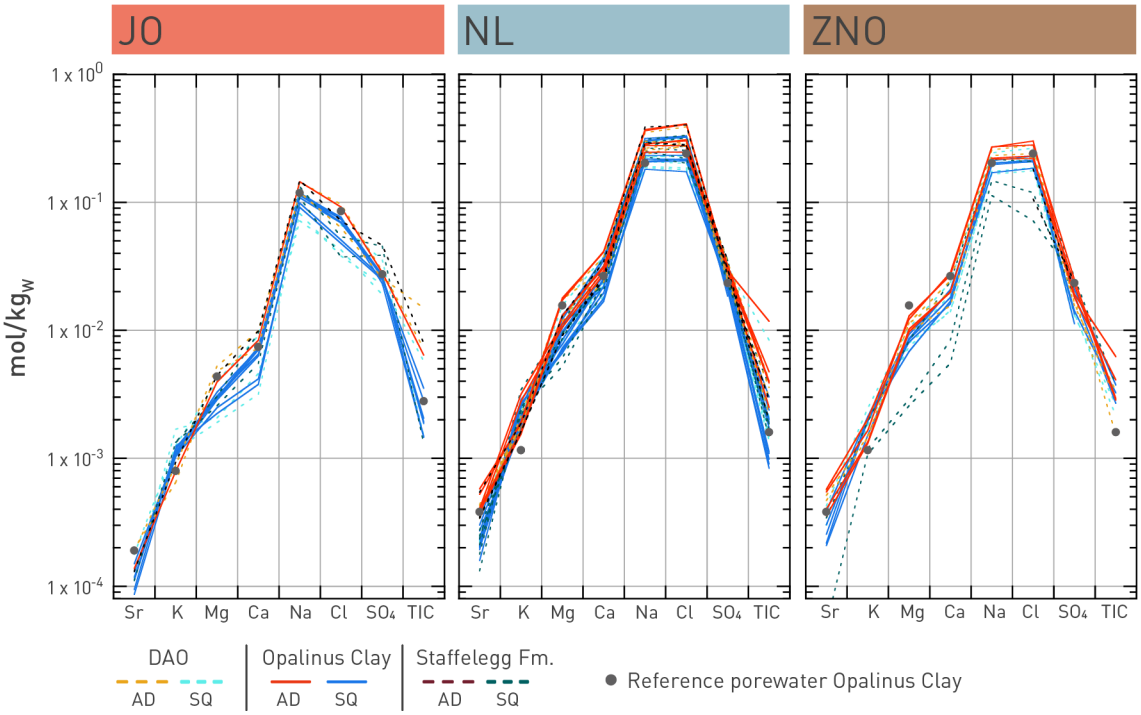


Fig. 5-19: Schoeller plots visualising the chemical composition of porewater in the Opalinus Clay and in the adjacent confining units in the three siting regions

Data from advective displacement (AD) and high-pressure squeezing (SQ) are shown (Kiczka et al. 2023) and compared to the respective reference porewater for the Opalinus Clay as defined in Mäder & Wersin (2023). DAO: Dogger Group above Opalinus Clay, Fm.: Formation.

5.4.4 Reference porewaters for the Opalinus Clay

Reference porewaters constitute an abstraction of the ensemble of the experimentally derived data, constraints from other data (e.g. mineralogy, aqueous extraction, cation exchange experiments) and modelling (Mäder & Wersin 2023).

A consistent thermodynamic porewater model is an important component in the derivation of the reference porewaters (Mäder & Wersin 2023) and, generally speaking, in the derivation of the in-situ porewater compositions of the Opalinus Clay and its confining units in the different siting regions (Kiczka et al. 2023). The model takes into account the "free" solutes (conservative species, such as Cl, not affected by mineral reactions), dissolved gases, cation exchange reactions and equilibria with relevant rock-forming minerals (Kiczka et al. 2023, Mäder & Wersin 2023). Such calculations, commonly carried out with a geochemical code like PHREEQC, have been shown to yield consistent results with regard to squeezing and advective displacement data (Wersin et al. 2016, Mäder & Wersin 2023, Kiczka et al. 2023), thus providing an independent measure for the robustness of the experimentally obtained data. Uncertainties with respect to key parameters (e.g. pH – pCO_2 – alkalinity, or sulphate) were addressed by defining model variants for the reference porewater that are also thermodynamically consistent in the same way as the reference porewater (Mäder & Wersin 2023).

An integral part of the model is the phase rule in which – at constant temperature and pressure – each component is constrained by fixed concentrations, mineral or cation exchange equilibria, respectively. The constraints used for the calculation of the reference porewater and for an alternative model approach are illustrated in Tab. 5-1. The purpose of the alternative model is related to the uncertainty in pCO_2 and pH. In fact, the experimental determination of pH and partial pressure of CO_2 is generally difficult and prone to experimental artefacts and changes between in-situ and laboratory conditions, such as temperature and pressure (Kiczka et al. 2023) (outlined below). The two models constrain pH and the partial pressure of CO_2 (pCO_2) in different ways, i.e. (i) fixing pCO_2 according to expert judgement based on earlier work or (ii) assuming a pair of equilibria of clay minerals (Kiczka et al. 2023, Mäder & Wersin 2023). The latter approach does not require an a priori assumption on pCO_2 but requires a judgement on the selected mineral pair and the thermodynamic data for such phases (illite, illite/smectite, chlorite) that are still uncertain as e.g. discussed in Wersin et al. (2020). The two models show similar results for calculations at 25 °C for most underlying mineral pairs and databases (Fig. 5-20).

Tab. 5-1: Constraints on major component concentrations used for modelling of reference porewaters (Mäder & Wersin 2023)

Component	**Constraint**	
	Reference porewater fixed pCO_2	**Alternative model** clay-mineral equilibria
pH	calcite eq.	pair of clay-mineral eq. [f)]
$CO_{3,t}$	fixed $pCO_2 = 10^{-2.2}$ bar [a)]	calcite eq.
Cl	fixed [b)]	fixed [b)]
SO_4	fixed SO_4/Cl [b)]	fixed SO_4/Cl [b)]
Sr	celestite eq.	celestite eq.
Na	fixed exchanger [c, d)]	fixed exchanger [c)]
K	fixed exchanger [c, d)]	fixed exchanger [c)]
Ca	fixed exchanger [c, d)]	fixed exchanger [c)]
Mg	dolomite eq.	dolomite eq.
Si	quartz eq.	quartz eq.
Al	kaolinite eq.	clay-mineral pair eq. [f)]
Fe	siderite eq.	siderite eq.
Eh	pyrite-siderite eq. [e)]	pyrite-siderite eq. [e)]

[a)] best estimate expert judgement based on available data

[b)] based on data obtained from squeezing and advective displacement experiments

[c)] based on data obtained from cation exchange experiments

[d)] only initial estimate, later adjusted slightly by model simultaneously to mineral equilibria

[e)] S(VI)/pyrite redox couple assumed to be active

[f)] kaolinite/chlorite or kaolinite/illite or illite/chlorite equilibrium

5.4.5 Extrapolating from standard conditions to in-situ temperature and pressure

Reference porewaters used for safety assessment are commonly defined at standard temperature and pressure conditions (i.e. 25 °C, 1 bar). Thus, porewater chemistry data obtained from laboratory experiments at room temperature closely reflect such conditions. In-situ temperatures and hydrostatic pressures of the Opalinus Clay porewater, however, are higher, and may reach up to 50 °C and 90 bar, depending on the location and depth of the repository.

Thermodynamic equilibria are rather insensitive to temperature in the range of interest (in-situ temperature 30 – 50 °C) as indicated by both experimental and modelling studies from the French programme (Beaucaire et al. 2012, Gailhanou et al. 2017) and modelling of the Opalinus Clay porewaters (Wersin et al. 2020, Mäder & Wersin 2023). An example of a modelling exercise is illustrated in Fig. 5-20 in which the effect of temperature on the reference porewater composition (Mäder & Wersin 2023) is shown in the range of 25 – 80 °C. The main aqueous components Na, Ca, Mg, Cl and SO_4 show very little change within this temperature range. The largest change is indicated for pH and pCO_2, which is because of the change in CO_2 solubility and the dissociation constant of H_2O with temperature. Thus, pH is shifted to about 0.5 units lower values when passing from 25 to 50 °C.

The effect of pressure on the Opalinus Clay porewater composition has also been evaluated by thermodynamic modelling (Wersin et al. 2020). In these calculations, it was shown that an increase in pressure up to 90 bars results in only very minor changes in the composition in spite of the higher solubility of CO_2.

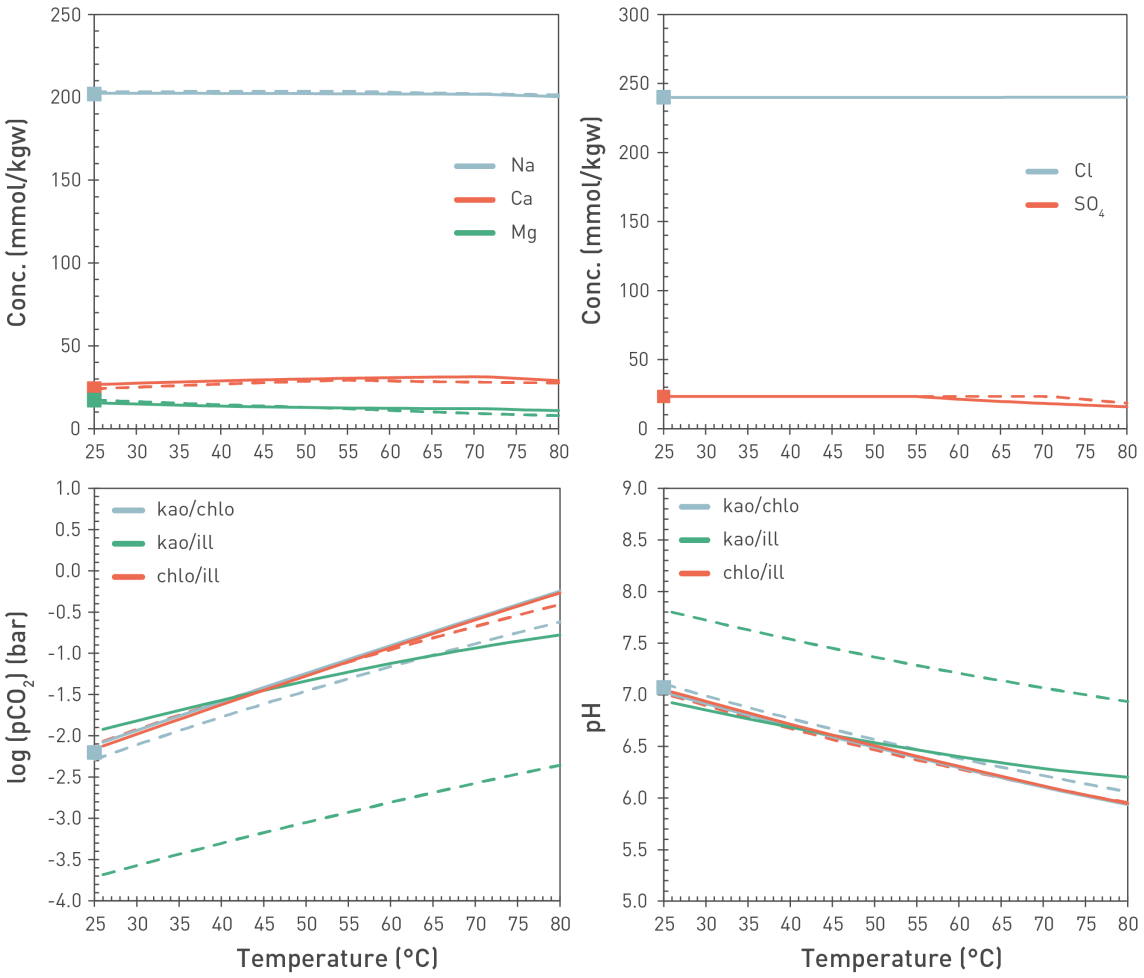


Fig. 5-20: Modelled concentrations of main porewater components (upper panel) as well as log(pCO_2) (bar) and pH (lower panel) as a function of temperature using an alternative porewater model including clay mineral phases (curves)

Squares allow comparison to the reference model (25 °C, fixed $pCO_2 = 10^{-2.2}$ bar; Mäder & Wersin 2023).

Model runs performed for three different sets of clay-mineral equilibria: kaolinite/chlorite, kaolinite/illite, chlorite/illite. Solid lines: The PSI Thermodynamic Database (Hummel & Thoenen 2023), dashed lines: ThermoChimie (Giffaut et al. 2014, Rodriguez et al. 2022). Both databases indicate very similar results in ion composition but some differences regarding simulated pH/pCO_2. The latter point is related to different thermodynamic data of clay minerals used in the two databases.

5.4.6 Geochemical stability and buffering capacity of the Opalinus Clay

The Opalinus Clay acts as an effective chemical buffer because of its mineralogical-chemical properties (Wersin et al. 2020). Thus, the very large cation exchange capacity (in the range of 100 meq/kg) compared to the porewater inventory helps to keep the exchanger composition nearly constant and thus also the dissolved cation ratios over a wide range of salinities. The buffering of pH to near-neutral values is provided by rapid calcite dissolution/precipitation and surface protonation/de-protonation reactions. Silicate weathering reactions occur at much lower rates but may be effective in buffering pH over timescales of years and longer (Wersin et al. 2020). It should be noted that, under alkaline conditions (e.g. induced by cementitious materials in the repository), silicate reaction rates are enhanced and the contribution of these minerals to buffering becomes more important.

The Opalinus Clay has a large reducing capacity because of its ferrous- and sulphide-bearing minerals (siderite, ankerite, pyrite) and organic matter. The reducing character of the porewater was confirmed by earlier measurements (Wersin et al. 2020, Mäder & Wersin 2023).

5.4.7 Conclusions

- The Opalinus Clay provides a stable geochemical environment for hosting a repository for radioactive waste.
- In clay-rich rocks, only part of the porosity is accessible to anions. In the Opalinus Clay, the accessible fraction is well constrained and depends primarily on porewater salinity. For JO the accessible fraction is ca. 30% and for NL and ZNO it is in the range of 40 to 50% of the porosity. This fraction is partly larger in the confining units: This is explained by the partly lower clay-mineral contents and larger pore sizes.
- The Opalinus Clay porewater chemistry can be robustly constrained based on complementary datasets and approaches. The model includes mineral and cation exchange equilibria and concentrations of free solutes such as chloride. The porewater of the general Na-Cl type is of moderate ionic strength (0.15 – 0.37 molal), pH is in the near-neutral range and the redox conditions are buffered by pyrite and siderite equilibria to the reducing range.
- The porewater ionic strength of the Opalinus Clay is lowest in JO because of its different palaeohydrogeological evolution. The equivalent data from ZNO and NL allow the same reference porewater model to be used.

5.5 Geomechanical behaviour and tectonic overprint

Key points:

- Geomechanical properties of the Opalinus Clay are comparable in all three siting regions. The high clay-mineral content in combination with deep maximum burial and significant overburden today (> 400 m) contribute to the low variability in mechanical properties (e.g. compared to Mont Terri).
- The relatively low stiffness and low «brittleness» of the Opalinus Clay and clay-mineral-rich confining units is consistent with more distributed deformation compared to more competent Mesozoic units.
- Localised fault-related flow is generally impeded by this type of deformation and is further counteracted by the expansive volumetric behaviour of clay-rich rocks when unloaded.

5.5.1 Overview

The position of larger seismically mappable faults will be taken into account when planning the location of the disposal areas. However, subseismic faults (small-scale and/or micro faults, Tab. 4-1) may also occur in areas free of seismically mappable faults. The effects of tectonic overprinting on the Opalinus Clay and the confining units are less pronounced than in the more competent over- and underlying formations (Section 4.3), which can be related to the mechanical layering (Section 4.6) at larger scale.

Here the focus is on the deformation behaviour and typical fault geometries of the Opalinus Clay and clay-mineral-rich confining units. It is emphasised that these are favourable to maintaining barrier integrity over longer timescales, consistent with hydraulic packer test results (Section 4.5). Compaction and moderate diagenesis of the Opalinus Clay in the siting regions has led to overall higher strength than at the Mont Terri rock laboratory (Section 5.5.3), whilst still maintaining good swelling capacity (Section 5.5.2).

The understanding of the detailed constitutive behaviour of the Opalinus Clay (e.g. Nagra 2014h, Marschall & Giger 2016) has not changed significantly with the recent exploration campaign. However, the mechanical database in the siting regions is now substantially improved, much more robust and demonstrates a relatively small variation in mechanical properties for the Opalinus Clay. Numerical modelling of the constitutive behaviour was further advanced to integrate both anisotropic stiffness and strength (Section 5.5.3).

In Section 5.5.4, the low tectonic overprint in the Opalinus Clay is discussed. Only small-scale or micro-scale faults were encountered in the deep boreholes. Analyses of outcrops and 3D seismic reflection data and comparison with similar rocks shows that deformation in clay-rich rocks is generally soft-linked, and fractures poorly interconnected. The expansive volumetric behaviour of the Opalinus Clay and clay-mineral-rich confining units as elaborated in Section 5.5.2 further counteracts fracture-dominated flow, as will be emphasised in Section 5.7 (self-sealing).

5.5.2 Volumetric deformation behaviour

Geomaterials subjected to load change experience deformation, either volumetric and/or distortional. When compressed, the Opalinus Clay experiences both irreversible and reversible volumetric deformation. After loading and unloading, a part of the deformation is recovered in an elastic rebound (Fig. 5-21 in Section 5.5.3). The amount of plastic (irreversible) and elastic (reversible) deformation can be investigated in oedometric tests: a cylindrical sample is loaded in the axial direction, while radial strains are prevented (i.e. the specimen can only experience deformation in the loading direction) and porewater pressure is maintained.

Two curves obtained from oedometric tests in saturated conditions are reported in Fig. 5-21, one for the Opalinus Clay from the Mont Terri rock laboratory, and one from the BUL1 borehole. Both samples have a similar clay-mineral content (ca. 60 wt.-%), and the main difference between the two is the depth of extraction and porosity at the start of the tests. Initially, the sample is saturated in constant volume conditions (total stress is increased to constrain the swelling and keep deformation close to zero). Afterwards, samples are always kept saturated. The porosity evolutions with the load/unload increments are shown as a function of applied axial effective stress. Effective stress is defined here as the difference between the total stress (because of external loads) and the porewater pressure.

Each point corresponds to a loading (or unloading) step, where load is applied (or removed), and the evolution of axial displacement is measured. The evolution of the displacement is related to the porewater pressure build-up or reduction (depending on whether a load is applied or removed) and its dissipation in time. The response of a material is related to its hydromechanical properties, particularly the hydraulic conductivity, and its rigidity (through the oedometric modulus); these two properties combined define the consolidation coefficient. At the end of the porewater over-pressure dissipation, the sample is consolidated, and the corresponding porosity is assigned to that stress level (i.e. the points on the curve represent drained states). If the load is maintained beyond the time needed for the sample to consolidate, viscous deformation at constant load can be observed, referred to as secondary compression ("creep"). During the experiments, the extent of the creep deformation is usually minor compared to the amount of deformation due to changes in effective stresses.

While the overall response is similar, it is noted that the Opalinus Clay at Mont Terri shows generally higher porosity and higher compressibility (expressed by the slope of the curve upon loading at high stresses) within the investigated range of stress.

The unloading paths (highlighted in Fig. 5-21) allow calculation of the swelling index, C_s. It is worth highlighting that "swelling index" is a geotechnical term that indicates the slope of the unloading branch in oedometric conditions in the semi-logarithmic void-ratio (equivalent to porosity used in Fig. 5-21) versus vertical effective stress plane. This is related to the elastic properties of the saturated material upon unloading, and it is not to be confused with the swelling related to the saturation process. The higher the swelling index, the steeper the curve in the plot. A high swelling index corresponds to low stiffness and vice versa.

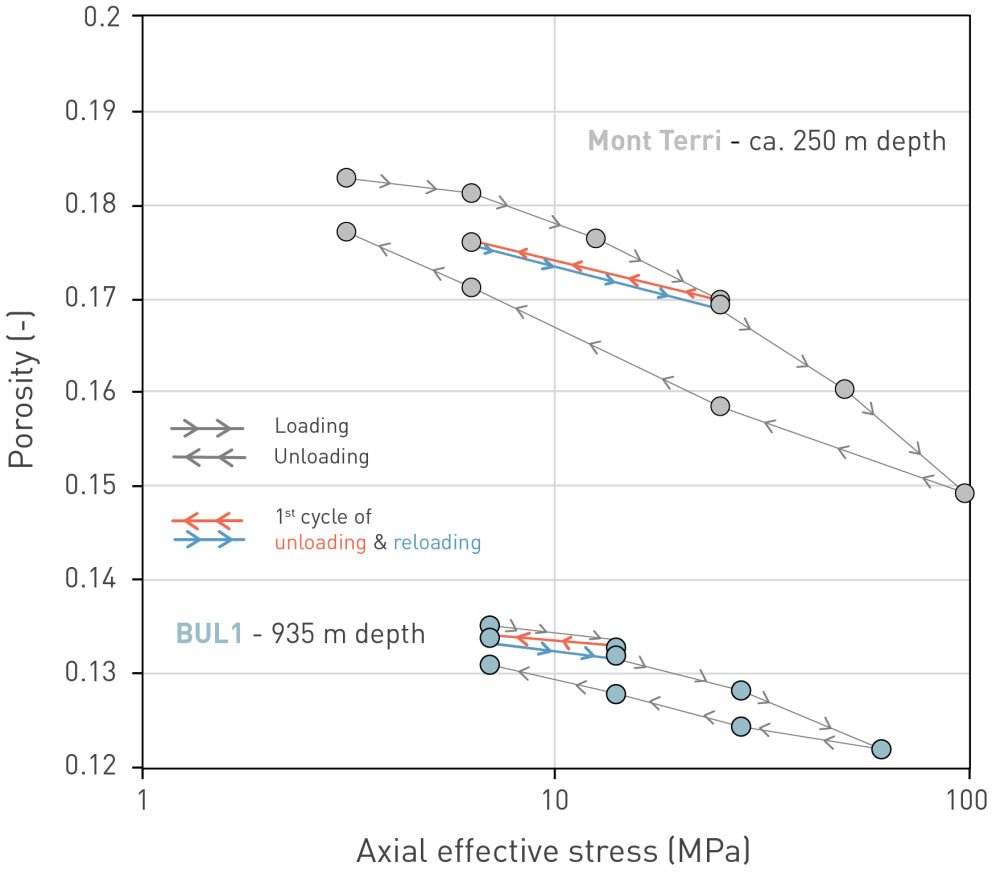


Fig. 5-21: Comparison of oedometric curves of the Opalinus Clay from Mont Terri and BUL1

Note that both samples have a similar clay-mineral content of approximately 60 wt.-% but a different initial porosity. The unloading path (adopted to calculate the swelling index C_s) is highlighted.

For geomaterials with a comparable range of porosity, a high C_s (i.e. low stiffness) is obtained for a high clay-mineral content. On the other hand, for low clay-mineral content material (< 40 wt.-%), the effect of the composition on the stiffness is limited, and additional aspects such as the porosity play a major role for the observed stiffness.

Obtained swelling indices from testing Opalinus Clay and confining units are summarised in Fig. 5-22 as a function of the clay-mineral content. The C_s are computed for unloading from stress levels of 20 – 15 MPa, down to a few MPa, and show a positive correlation with clay-mineral content. The upper limit of the stress range adopted for C_s calculation was chosen to be comparable with the expected maximum stress experienced by the formation.

In conventional unconstrained swelling tests (ISRM 1989, VSS 2019), axial swelling is measured on samples which are initially not fully saturated with water. Due to this partial saturation, such samples can experience a considerable amount of suction (equivalent to negative porewater pressure), resulting in strong hydraulic head gradients when the samples are exposed to water, and increased effective stress compared to fully saturated samples with positive porewater pressures under similar confining stress. Total expansion in such tests may therefore be greater than that measured in the unloading tests. For comparison of the two methods, a number of swelling tests were also done by starting from unsaturated conditions and a specified controlled load to assess the expansion over the low effective stress range (Fig. 5-23).

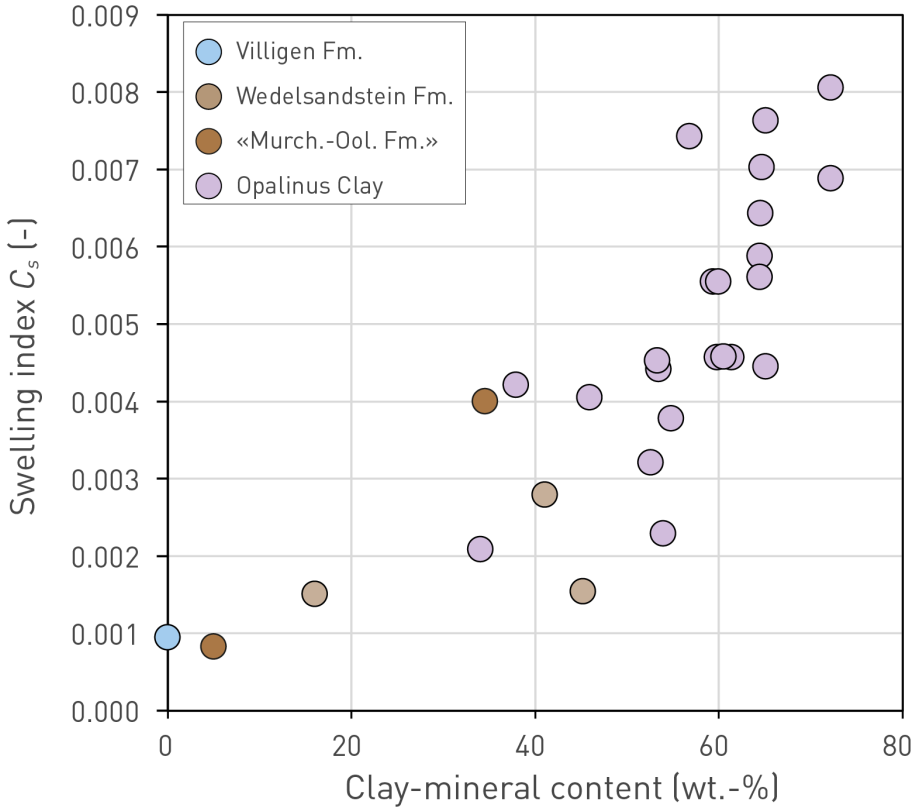


Fig. 5-22: Swelling index (C_s) as a function of the clay-mineral content

Values obtained from the unloading paths from 20 – 15 MPa, down to a few MPa (drained, saturated conditions). Fm.: Formation.

In such swelling tests under constant load, the following procedure was adopted. The initial sample saturation is "as prepared". A constant stress level was then applied to samples and, afterwards, the sample was put in contact with balanced porewater and allowed to swell under constant load.

The specimens first may undergo a compression because of the load applied, then an expansion because of the saturation (i.e. effective stress reduction). The stresses shown in Fig. 5-23 are those achieved at the end of the swelling phase, and the strains reflect the difference from the maximum compression (initial load) to the maximum expansion at the end of the test. At an axial effective stress of approximately 5 to 10 MPa, the swelling under constant load did not result in any relevant net swelling strain. Swelling under constant load was also examined under triaxial conditions (Crisci et al. 2024a) and resulted in similar slopes (swelling strain vs. logarithmic axial effective stress) as in oedometric conditions (Fig. 5-23).

The 10 MPa axial effective stress can be considered equivalent to a depth of approximately 700 m (in situ). Assuming the range of determined C_s values of Opalinus Clay (Fig. 5-22), typical unloading paths from saturated conditions are also plotted in Fig. 5-23. These indicate the amount of swelling strain for a specific axial effective stress starting from the assumed 10 MPa in-situ vertical (axial) effective stress.

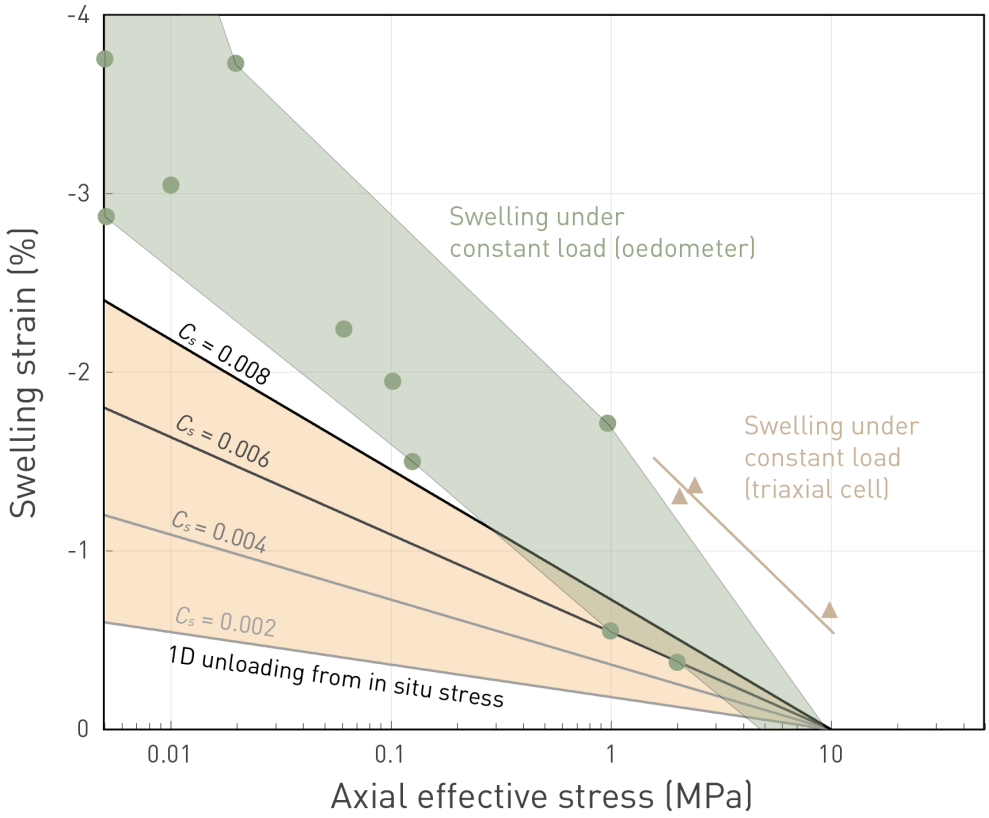


Fig. 5-23: Axial swelling strain in the Opalinus Clay constrained by different methods

Orange surface indicates range of swelling strains (negative values for expansion) from saturated conditions at an assumed in-situ axial effective stress of 10 MPa (equivalent to approximately 700 m depth), with C_s (swelling index) values from Fig. 5-22). Swelling from initially unsaturated conditions at constant load are also shown for comparison (both from oedometric tests and also trends from triaxial tests), with each data point reflecting a separate test. Note the even larger expansion for swelling tests at constant load.

Swelling under constant load shows greater overall swelling strains than unloading from saturated conditions, with one data point even plotting outside the limits of the graph (swelling strain of 5.6% at 0.05 MPa axial effective stress). Previous results of unconstrained swelling tests (also starting from unsaturated conditions) from the Benken (Nagra 2002) and Schlattingen boreholes (Ferrari et al. 2012) are also consistent with the new results, with swelling heaves up to 11%. For the very low effective stress range (< 1 – 3 MPa), swelling may induce microfissuring, i.e. enhancing the expansion (for the mechanism, see Section 5.7.3), compared to the saturated unloading.

In summary, the swelling capacity of the Opalinus Clay was assessed using different methods, and under various conditions and hydromechanical stress paths. All the methods highlight significant expansion, with most of that expansion occurring at very low or negligible effective confinement.

5.5.3 Shear deformation behaviour

A schematic of the mechanical response of the Opalinus Clay depending on effective stress paths is presented in Fig. 5-24, in the plane deviator stress versus mean effective stress. Deviator stress is intended here as the maximum minus the minimum principal stress applied, while mean effective stress is the average of the three principal effective stress components.

If the change in stress remains in the elastic domain, the deformation is reversible. Once the stress applied exceeds the elastic domain, part of the deformation will be reversible (elastic), and part will be irreversible (plastic and the elastic domain will expand).

The failure envelope defines the strength of the material, which is dependent on the mean effective stress. Along the failure envelope, the material is not able to sustain further stress increments without the formation of fractures.

Along the curved part of the envelope in the tensile strength domain, low deviator and mean effective stress provide conditions for the initiation of mode I tensile fractures, which might be induced by, e.g., pore pressure increments at low confining stress. For intermediate confinement levels and high deviator stress, shear fractures can be induced. Along the right-hand side of Fig. 5-24, compaction occurs for high mean and relatively low deviator stress. Some material compaction might be localised (as in a compaction band), while in plastic materials compaction results in a more irreversible volume decrease associated with porosity reduction. Combinations and arrangements between shear and dilation fractures (mixed mode I and II) and compaction structures will occur under intermediate stress conditions.

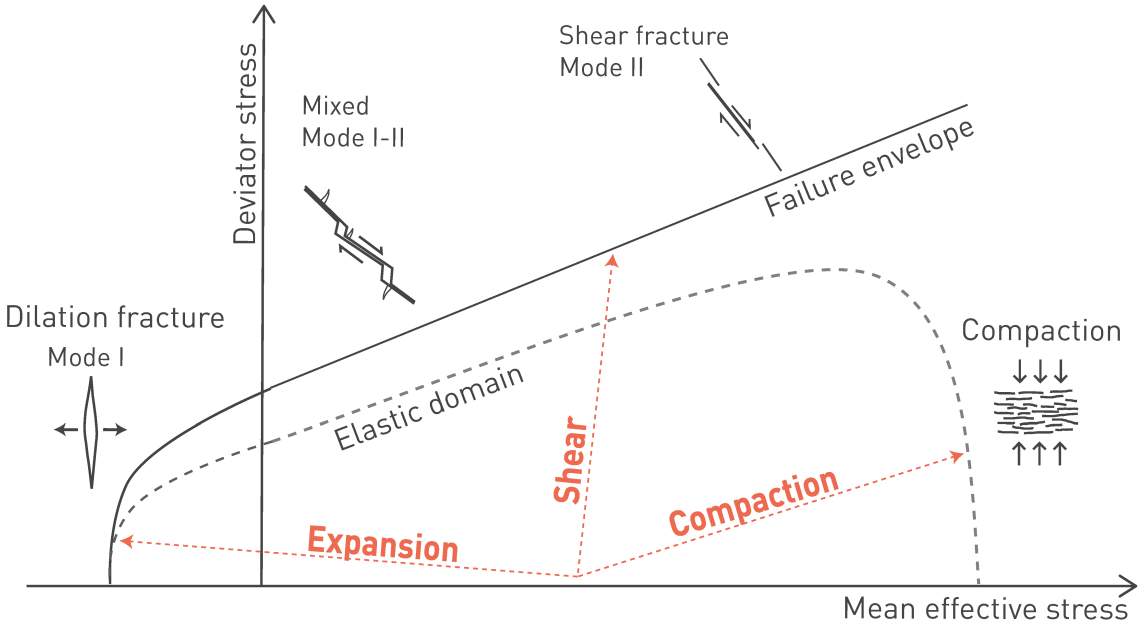


Fig. 5-24: Schematic of the mechanical response of the Opalinus Clay for different stress paths

Dilation is associated with extensional fractures (mode I) and shear fractures at low effective mean stress (mixed mode I and II). At higher mean effective stress, compactional shear dominates.

During fast loading (and unloading), the pore fluid contained in the pore space is subject to over- (or under-) pressure that dissipates over time. The dissipation of the pore pressure variation is strictly related to the formation permeability. To study the mechanical response of low-porosity geomaterial, it is necessary to analyse both the pore pressure and stress changes through the evolution of the effective stress.

The Opalinus Clay has a low stiffness compared to most other rocks, and high strain to failure. In contrast to other rocks, once the stress to which the material is subjected exceeds the elastic realm, the material can continue to sustain increased loading and accommodate deformation (hardening) before reaching the maximum deviator stress (strength). With further loading after reaching the strength value, the material does not dramatically lose its capacity to sustain load (as brittle response typical of rocks) but can still accommodate a significant deviator stress of approximately 50 to 70% of the strength value. This is commonly referred to as quasi-brittle behaviour.

Over 150 laboratory triaxial tests were conducted on the Opalinus Clay and confining units to characterise the hydromechanical response of these geomaterials in detail, and to explore material variability. Dedicated and benchmarked testing protocols (Minardi et al. 2021) were adopted. These testing protocols are also in accordance with new procedures suggested for triaxial testing of shales currently being finalised by the International Society of Rock Mechanics. The dedicated protocols ensure sufficient pore fluid pressure equilibration to derive effective material parameters, but also avoid damage to the specimens by swelling during the early saturation phase (Crisci et al. 2024a).

Examples of stress paths and stress-strain evolutions during triaxial testing of three contrasting Mesozoic sediments are shown in Fig. 5-25. For specimens of the Opalinus Clay and the Wedel-sandstein Formation, the initial linear elastic stress – strain response transitions into non-linear up to peak (strength). After peak, softening occurs, i.e. progressive reduction of the sustained stress as strain increases until reaching a relatively stable value (usually referred to as post-peak strength). At this point, a clear failure surface has been created within the sample, and further shearing will develop as movement along the surface.

Rocks such as the limestones of the Villigen Formation exhibit a much stronger increase in stress because of their high stiffness when shortening is applied and the elastic domain extends close to the failure envelope (Fig. 5-24). This is then followed by a more brittle response with a stronger reduction in sustained stress after peak. The differences in stiffness and plastic response between the Opalinus Clay and such competent rocks have implications for the stress concentration (Section 4.4) and the tectonic overprint (Sections 4.3.5 and 5.5.4).

The stress paths shown in Fig. 5-25 correspond to undrained tests, i.e. the pore fluid volume in the sample remains constant during loading. An increase (or decrease) in pore pressure is related to the specimen's attempt to reduce (or increase) its volume. Since water cannot escape (or enter) the sample in undrained conditions, pore pressure increases (or decreases). As loading progresses, pore pressure is increased until reaching a maximum value, then decreases. It is noted that, given the low permeability of the Opalinus Clay and the confining units, a slow shear rate needs to be used to ensure that the measured pore pressure is representative of the entire sample volume.

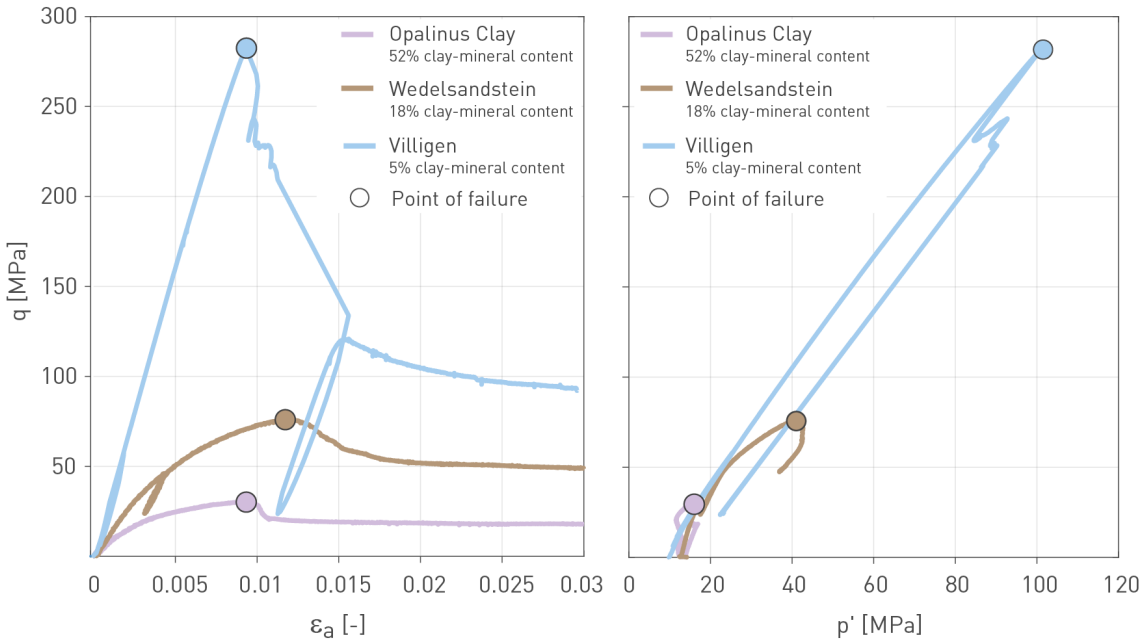


Fig. 5-25: Different mechanical response of Mesozoic sedimentary rocks with contrasting clay-mineral contents

Left side: deviator stress (q) vs. axial strain (ε_a). Right side: Deviator stress (q) vs. mean effective stress (p'). Data from Dossier IX of TBO reports in Tab. 2-1.

The Opalinus Clay shows a cross-anisotropic (or transversely isotropic) behaviour (Section 5.5.5), i.e. the response in the direction orthogonal to the bedding plane is different from the response in the bedding plane direction. Despite the heterogeneity of the formation, the shear strength shows limited variability in all the tested directions with respect to bedding (Crisci et al. 2024b).

The shear strength of all triaxial tests loaded perpendicular to the bedding direction (S-specimens) of the Opalinus Clay tested in the TBO campaign is reported in Fig. 5-26 by borehole, in terms of axial versus radial effective stress. Results are colour-coded by sample bulk density. Bulk density is adopted because it depends on both the effect of the mineralogical composition and the porosity of the sample. Despite the range of sourcing depth in the 7 boreholes (450 m – 1'000 m), the range of mineralogy (35% to 70% clay-mineral content) and porosity (0.10 to 0.14) tested, only minor strength differences emerge. The same observation was also made in the other testing directions (parallel and at an angle to bedding).

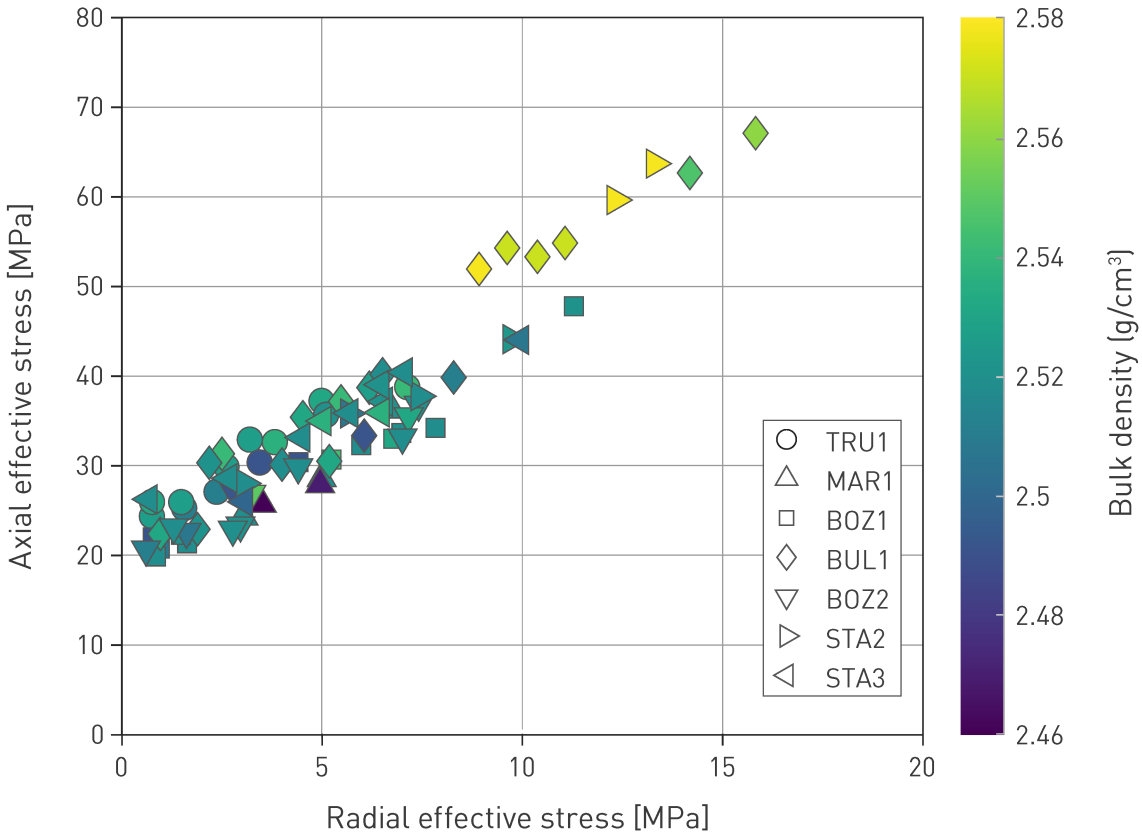


Fig. 5-26: Shear strength of the Opalinus Clay from the siting regions

Loading of the cylindrical specimens was in axial direction, prependicular to bedding. Note: The intersection of the regression line (not shown) with the y-axis would correspond to the calculated effective unconfined compressive strength (approximately 21 ± 5 MPa). Detailed data analysis can be found in Crisci et al. (2024b).

The shear strength values of the Opalinus Clay from the siting regions (TBO campaign) contrast with results obtained from the Mont Terri rock laboratory (FMT), particularly for samples with high clay-mineral contents (shaly facies; Fig. 5-27). This is related to the difference in porosity, especially between shaly facies and TBO results (approximately 0.12 to 0.17 vs. 0.10 to 0.13; Crisci et al. 2024b). Therefore, the different burial history and difference in current depth between TBO (400 to 1'000 m) and FMT (220 to 320 m) clearly influences the strength of the clay-mineral-rich endmember of the Opalinus Clay.

In contrast to shear strength of the intact material, no major discrepancy is seen for test results of TBO and FMT samples for post-peak strengths (Fig. 5-27 right), but differences appear to be related to facies type (mineralogy). In summary, where intact strength values are homogenised across the facies with greater burial, i.e. controlled by the burial history, post-peak strength seems to be controlled by mineralogy (Crisci et al. 2024b).

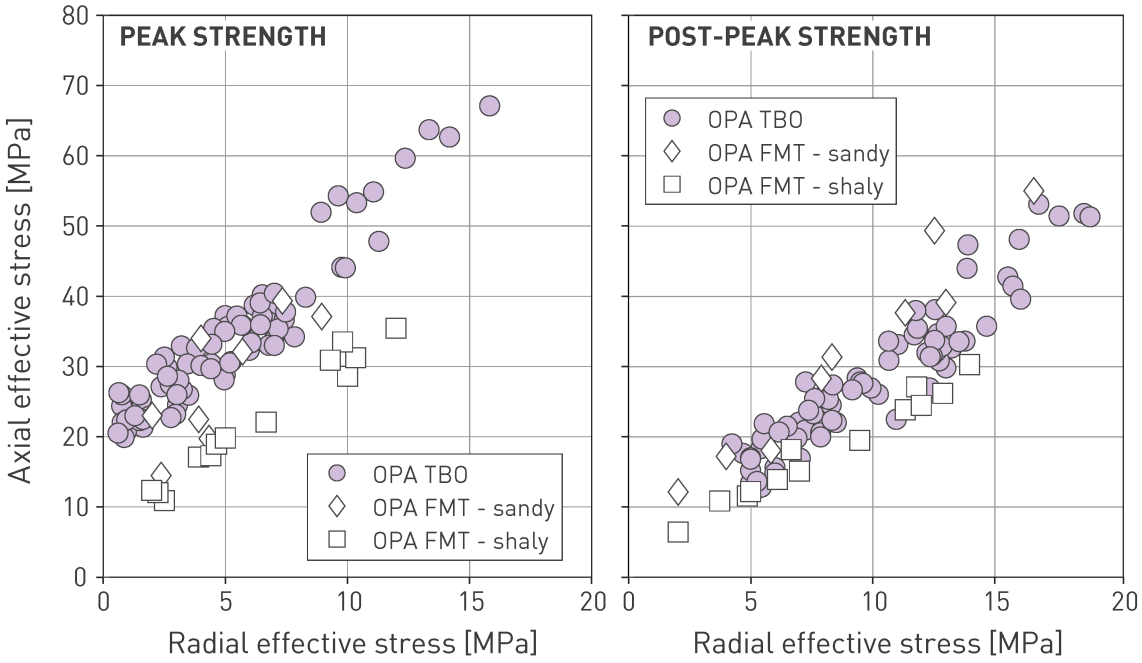


Fig. 5-27: Peak and post-peak strength of the Opalinus Clay in the siting regions in comparison to Mont Terri

All test results are for specimens loaded perpendicular to bedding, and each data point reflects stresses at point of failure (peak strength) or after development of deformation band (post-peak strength). TBO data are from Crisci et al. (2024b). Mont Terri rock laboratory (FMT) data are from Crisci et al. (2021), Favero et al. (2018) and Minardi et al. (2019).

No significant differences in shear strength were observed with depth or between siting regions. Fig. 5-26 and Fig. 5-27 also indirectly illustrate the strength differences of the Opalinus Clay compared to estimates prior to the TBO campaign. The estimation of the shear strength of the Opalinus Clay in Stage 2 of the Sectoral Plan (SGT) was mainly based on experience from Mont Terri (Marschall & Giger 2016) because of the small size of the database for the siting regions. This led to a relatively low reference value for the unconfined compressive strength (~ 10 MPa). In contrast, the unconfined compressive strength of the new TBO data varies between approximately 16 and 26 MPa. This is clearly greater than the reference value and partly even greater than the upper bound of SGT Stage 2 (20 to 22 MPa). The range of strengths of Opalinus Clay from the TBO results are also very similar to the Callovo-Oxfordian clay-rocks at Meuse / Haute Marne (OECD/NEA 2022).

Besides laboratory testing, elastic properties of the Opalinus Clay and confining units were also assessed through direct field measurements at larger scale, via pressure meter tests (Elkhoury et al. 2022, Elkhoury et al. *in press*). Pressure meter testing (PMT) is a formation test that consists of inflating a cylindrical packer inside a borehole, while measuring the radial deformation as a function of packer pressure. Measurement of fluid volume injected into the packer serves as a measure of borehole deformation, therefore changes in packer pressure associated with changes in injected fluid volume provide a direct measurement of formation stiffness. Results from five pressure meter stations allow a direct comparison between the laboratory and field determination of the shear modulus in the direction of the bedding plane ($G_{//}$). The impact of the difference in scales (a few cm in the laboratory, a few decimetres in the field) was investigated via dedicated numerical analysis and was found to be negligible. Field moduli compare well with moduli

derived from laboratory testing but were approximately 10 – 30% higher than the latter (Elkhoury et al. *in press,* Nagra 2024m). The main cause of the difference is identified in the strain dependency of the elastic moduli determination, in agreement with findings in similar investigations at Mont Terri (Liu et al. 2022).

Overall, there is an excellent database on the geomechanical properties of the Opalinus Clay from both laboratory and field measurements. The good understanding of the deformation behaviour of the Opalinus Clay is also reflected in detailed constitutive laws, which have been further improved over recent years (e.g. Parisio & Laloui 2017, Khaledi et al. 2023). An advanced elasto-plastic damage model was developed (Madaschi et al. 2023), accounting for the anisotropy in strength and stiffness. The good agreement of modelled evolution of stresses and pore pressure compared with laboratory test results is shown in Fig. 5-28.

Depending on the purpose of the investigation, somewhat simpler constitutive models have also been developed and calibrated on the new Opalinus Clay database (e.g. Nordas et al. 2024).

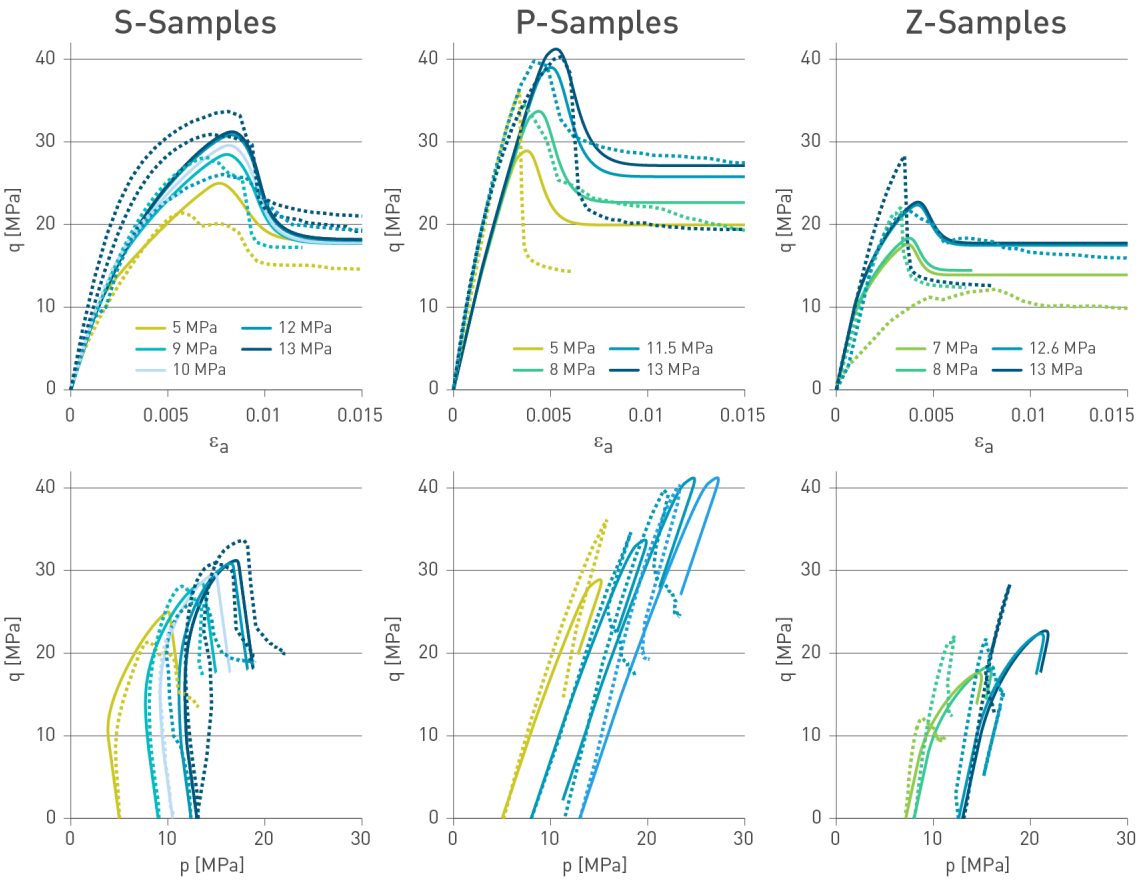


Fig. 5-28: Comparison of mechanical behaviour in numerical (bold lines) and laboratory test results (dashed lines)

Plots above show deviator stress q as a function of axial strain ε_a, and plots below show stress paths, i.e. q as a function of the mean effective stress p'. Results are grouped by loading direction with respect to bedding: S = 90°, P = 0°, Z = 30°. After Madaschi et al. (2023).

Transitioning from the peak to the post-peak phase in laboratory tests of the Opalinus Clay is associated with the formation and evolution of slip surfaces and linkage structures between them. A light microscope image showing the deformation feature of a laboratory-deformed specimen is shown in Fig. 5-29. This specimen contains mm-wide layers which are largely free of clay minerals and was loaded in the direction perpendicular to bedding. Deformation between the hanging wall cylinder and footwall cylinder is accommodated along several shear bands which form an anastomosing network of variable thickness and enclosing relatively undeformed rocks as lenses. The shear band can also be seen to deflect at mineralogical boundaries where dark grey shows clay-mineral-rich intervals and the white bands are quartz- and carbonate-rich layers. The following section relates this microstructural example to the rare field examples of faults in the Opalinus Clay.

The unconfined compressive strength (UCS) of the sedimentary rocks encountered in the deep boreholes varies strongly depending on the rock mineralogical composition. Low clay-mineral content formations generally show higher strength, while strength progressively reduces as the clay-mineral content increases and cementation decreases. The largest decrease in strength is observed for a clay-mineral content from 0 wt.-% to 20 wt.-%, while the decrease is moderate between 20 wt.-% and 40 wt.-%. The UCS remains relatively constant for clay-mineral content values above 40 wt.-%, i.e. in the range of the composition of the Opalinus Clay and many of its confining units (Fig. 5-30).

For the Opalinus Clay, the range of UCS values in Fig. 5-30 is extrapolated from triaxial tests (y-axis intercept in Fig. 5-26). For the other rock formations, UCS was measured via uniaxial compressive tests in the rock-mechanical testing programme.

Mineralogical composition was measured on the Opalinus Clay samples, while for the other rock samples it was constrained from the core-calibrated logs (Becker & Marnat 2024) for the location where the samples were sourced.

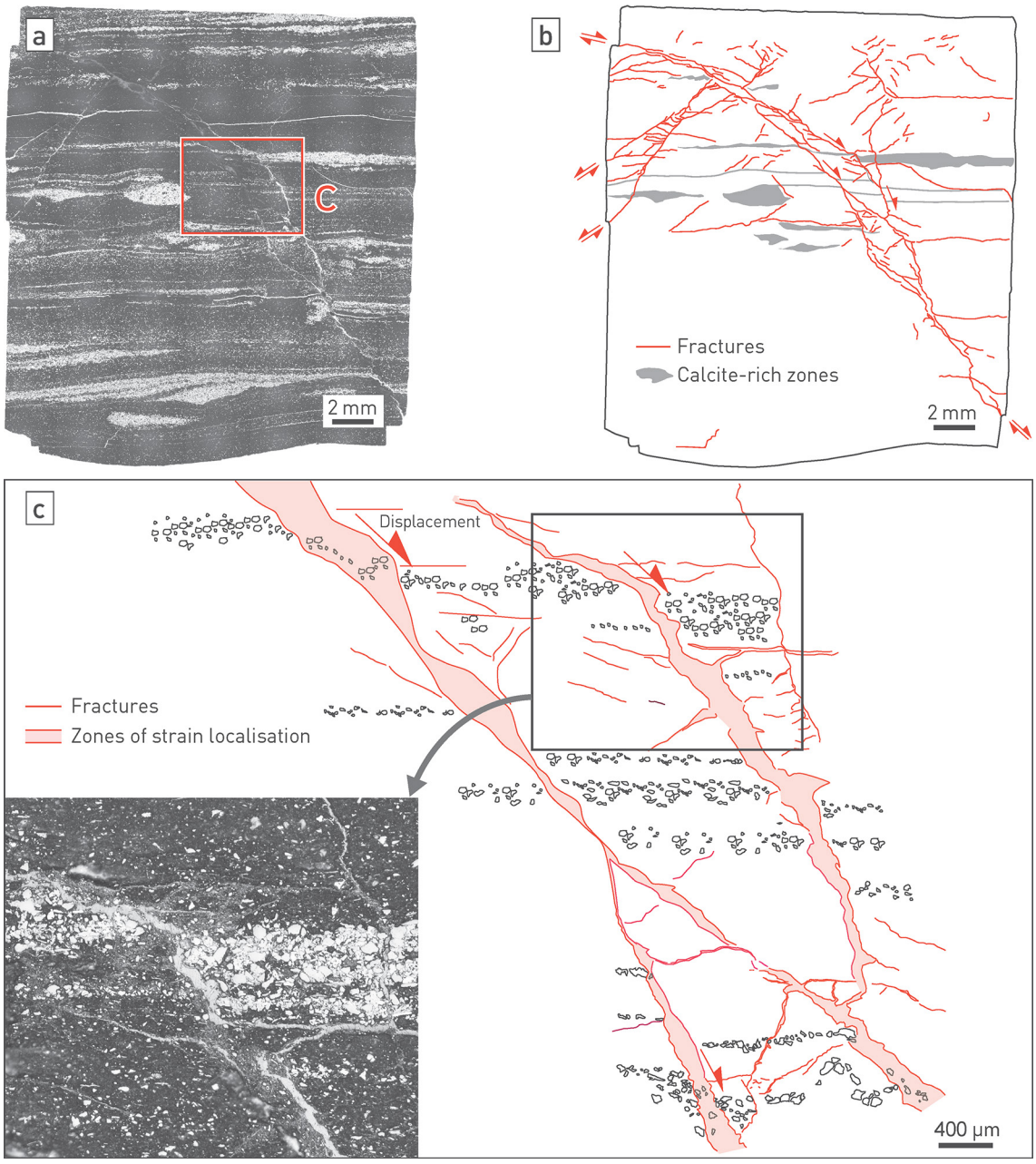


Fig. 5-29: Typical fault microstructure of the Opalinus Clay obtained in triaxial testing

Example of the Opalinus Clay from borehole BOZ2 (test C5_BOZ2_1_504.78S8CTCU).

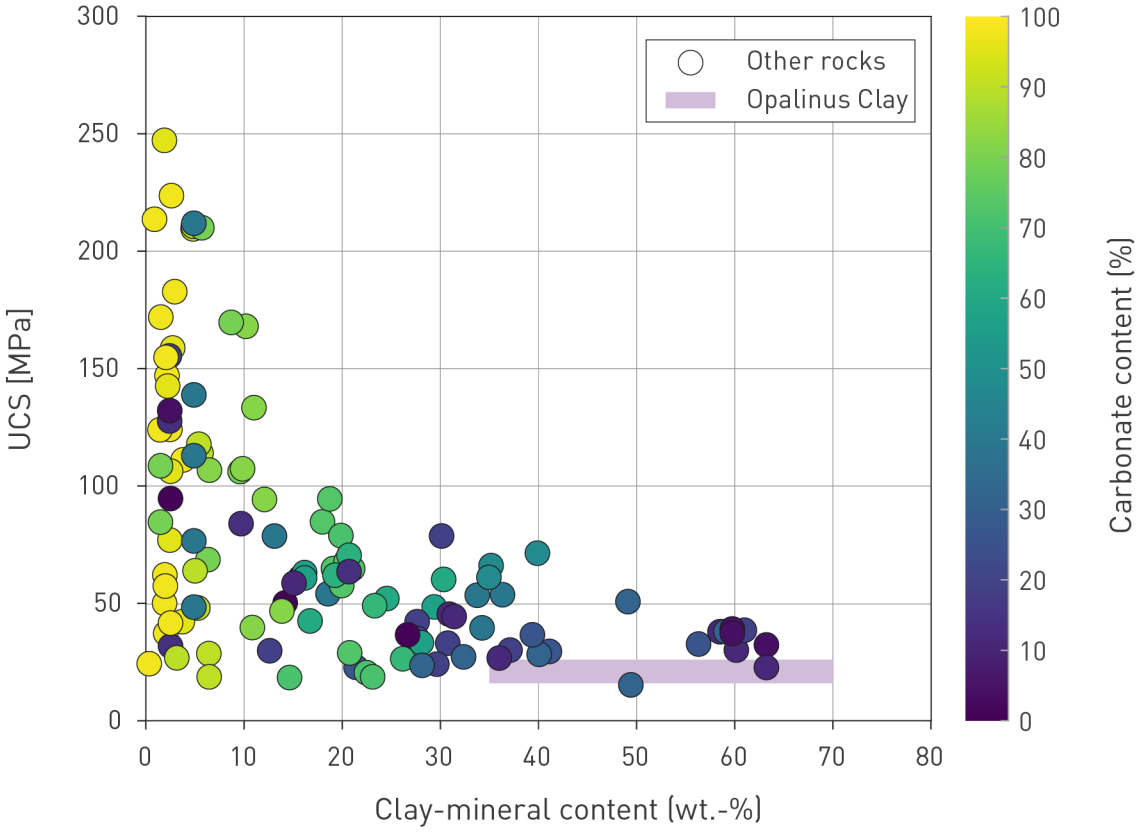


Fig. 5-30: Unconfined compressive strength (UCS) as a function of the clay-mineral content

Note the strong reduction in strength from 0 to approximately 20 wt.-% clay-mineral content. At higher clay-mineral contents, the changes are moderate, and almost negligible within the Opalinus Clay.

5.5.4 Tectonic deformation and fault architecture in the Opalinus Clay

The degree of tectonic deformation in the Opalinus Clay is small compared to the more competent units of the Malm Group and Triassic units (Section 4.3.4). Geomechanically stiffer units are more affected by tectonic loading (Section 4.4), i.e. the stress increase per increment of shortening is higher for limestones than for the Opalinus Clay (Fig. 4-79 and Fig. 5-25).

Most drill cores recovered from the Opalinus Clay during the TBO campaign were free of any fractures (Fig. 5-24). Nevertheless, some veins and smaller faults (below the seismically mappable scale) were encountered (Dossier V of TBOs, see Tab. 2-1). Based on borehole image analysis, all fractures are considered macroscopically closed in situ. A representative selection of encountered fractures is provided in Fig. 5-31 (see Tab. 4-1 for terminology).

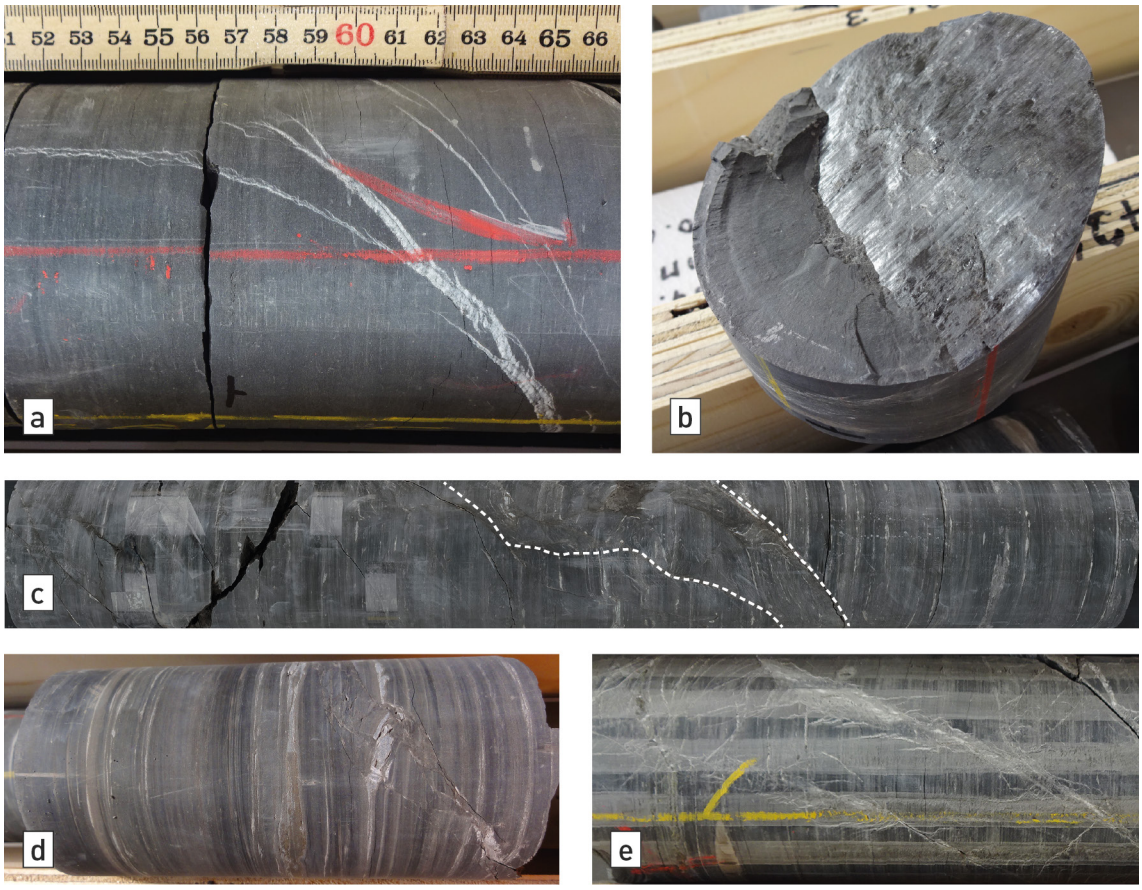


Fig. 5-31: Examples of tectonic deformation accommodated in the Opalinus Clay from the recent deep boreholes

(a) Vein or mineralised fracture (STA2, 821.86 – 822.15 m MD log depth). (b) Example of micro fault (shear fracture) with calcite slickenfibres (STA2, 855.61 m MD log depth). (c) Small-scale fault resulting in tilting of bedding (BOZ2, 510.02 – 510.70 m MD log depth). (d) Micro- to small-scale fault (BOZ2, 507.90 – 508.15 m MD log depth) with tilting of bedding and onset of fault breccia. Initial normal faulting was followed by a strike-slip-dominated faulting. (e) Multi-stranded veins (STA2, 885.93 – 886.33 m MD log depth).

Small-scale faults (i.e. faults below seismically mappable scale, but larger than an individual surface) consist of tilted and disturbed bedding and fault rock (Fig. 5-31c), or in some cases of a cluster of micro faults (i.e. individual surface with evidence for movement) including mineralisation of variable thickness (Fig. 5-31d) and were referred to as fault zones in Dossier V of the deep borehole reports (Tab. 2-1). Here, major clusters of micro faults are also included; these were highlighted and discussed in the respective reports in the total count of small-scale faults. Typically, one to a maximum of three small-scale faults are identified within each of the newly drilled boreholes in the Opalinus Clay section (Fig. 5-32a). No cohesionless fault rocks (e.g. gouges) were observed in any of these small-scale faults.

Micro faults (Tab. 4-1) are more common in the Opalinus Clay. In Dossier V of the deep borehole reports (Tab. 2-1), micro faults are either termed fault planes, mirror-like fault planes or stylolitic fault planes. Offsets constrained on the micro faults are typically very small, in the order of sub-mm to mm for examples of mirror-like fault planes.

These are typically only 1 – 2 mm thick and cannot be drawn to scale in Fig. 5-32a (i.e. the stroke width exaggerates the actual width of the micro fault). They are characterised by a single shear surface with striations (i.e. slickensides) and partly slickenfibres indicating sense of shear (Fig. 5-31b). The number of micro faults encountered in the boreholes varies between 162 micro faults in 122 m of the Opalinus Clay in BOZ2 (i.e. 1.3 micro faults per m) and 37 micro faults in 106 m of the Opalinus Clay in STA2 (0.4 micro faults per m). Overall, the micro faults show shallow dips below 30° (74% of the measured dips are below 30°, 91% are below a dip of 45°). The deviated borehole RHE1 (ca 30° from vertical) shows very similar dip values for the micro faults (71% of the micro faults have measured dips below 30° and 86% have dips below 45°). This comparability of dip angle between the deviated RHE1 borehole and the vertical boreholes can be interpreted in the sense that no systematic sampling bias by vertical boreholes was observed: if vertical micro faults were systematically undersampled in the vertical boreholes, a different dip distribution of micro faults in RHE1 would have been expected.

Veins (mineralised fractures) (Fig. 5-31a) are mostly very thin, with thicknesses of 1 – 2 mm (> 90% of all mapped veins have a thickness below 2 mm). These veins were further analysed regarding their microstructural and geochemical characteristics (Section 4.7). Detailed microstructural analyses highlighted several phases of vein growth from early compaction to Miocene shortening and extension related to the formation of the Jura Fold-and-Thrust Belt and the Hegau-Bodensee Graben (Akker et al. 2023). Mechanisms of formation and relevance of veins for the barrier integrity are further discussed in Section 5.7.6.

The overall fracture frequency (i.e. including veins) was statistically evaluated by the fracture area per unit volume (P32 value) in Section 4.3, and a detailed analysis for the Opalinus Clay is provided in Fig. 5-32b. The whisker plots in the figure are explained for the example of borehole BOZ2: the median P32 is 0.6 m^2/m^3, the average P32 is 1.9 m^2/m^3, with 75% of the 15 cm sampling intervals having a P32 lower than 2.1 m^2/m^3 and 95% of the 15 cm intervals lower than 5.3 m^2/m^3.

Comparing the analyses across all new boreholes shows generally very low P32 values; only for BOZ2 is the median value above 0 m^2/m^3. This means that the vast majority of the 15 cm sampling intervals in the Opalinus Clay are devoid of any fracture (excluding drilling-induced). For STA3, STA2, BUL1, MAR1 and TRU1, 95% of all sampling intervals have a P32 value of zero (i.e. box and whisker plots are located at zero in Fig. 5-32b). Larger continuous intervals free of any fracture (excluding drilling-induced) were encountered in each borehole. The longest intervals free of fractures for each borehole vary between 12.1 m in BOZ2 and 32.1 m in BUL1.

Furthermore, the whisker plots allow differentiation of the degree of clustering between the boreholes (Fig. 5-32b). For the boreholes STA3, STA2, BUL1, MAR1 and TRU1, the average P32 values are above the 95% interval of data, indicating a strong clustering with very few 15 cm intervals characterised by relatively high P32 values. In the boreholes BOZ2, BOZ1 and BAC1, this difference is less but the average values are still above the median values, indicating some degree of clustering. Generally, the boreholes BOZ2, BOZ1 and BAC1 are characterised by a more pervasive tectonic deformation and generally higher P32 values. The RHE1 borehole also has elevated P32 values, which might be associated with the seismically mappable Rheinau Fault located in the vicinity (Nagra 2024c). The more acute angle between the micro faults and the borehole path also leads to higher P32 for geometric reasons because dip distribution in RHE1 is comparable to that in the vertical boreholes (TBO reports in Tab. 2-1).

Outcrop-scale faults within the Opalinus Clay are known from quarries in Siblingen and Holderbank (Fig. 5-33), and the "Main Fault" in the Mont Terri rock laboratory (Fig. 5-34). These faults can be considered as transitional small-scale to local faults according to Tab. 4-1, and accordingly are at an intermediate scale between the structures encountered in the cores and the seismically mappable faults (Nagra 2024a, 2024b, 2024c).

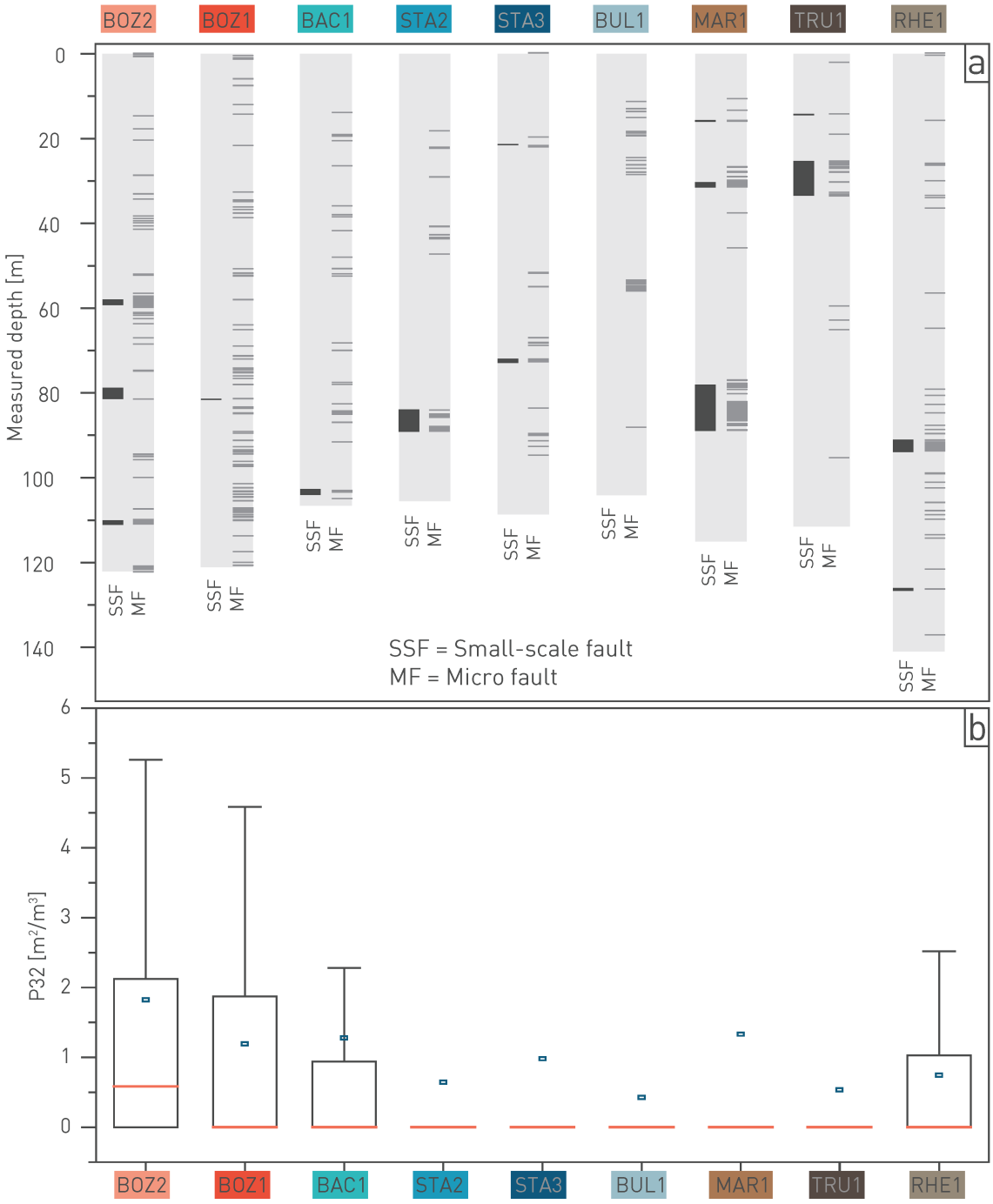


Fig. 5-32: Distribution of small-scale fault and micro fault frequency in the Opalinus Clay from new boreholes and overall fracture frequency

(a) Depth plot showing the distribution of small-scale faults and micro faults. Boreholes are arranged from W to E. Note that vertical extent is only to scale for the small-scale faults, but stroke width exaggerated the width of micro faults. (b) Whisker plots for fracture frequency in the Opalinus Clay (P32 values, see Section 4.3). Boreholes are arranged from W to E. Note that no box or whisker plots are shown for boreholes STA3, STA2, BUL1, MAR1 and TRU1, indicating that at least 95% of the sampling intervals (15 cm length) are devoid of any fractures (excl. drilling-induced fractures). The box extents to the 5% and 95% percentiles and the red line represents the median, while the blue marker depicts the mean of the distributions.

The outcrop-scale faults are characterised by strong heterogeneity, both in terms of width but also in terms of disturbance and accommodated deformation. Multiple micro faults often form an anastomosing network, also containing less deformed rock volumes. Similar fault geometries are also observed in the fairly wide deformation zones observed in triaxial testing at low strain (Fig. 5-32), with increasing strain leading to stronger rotation of bedding, fragmentation of the rock and potentially scaly clay and fault gouge along several slip surfaces (e.g. Laurich et al. 2014, 2018, Winhausen et al. 2022).

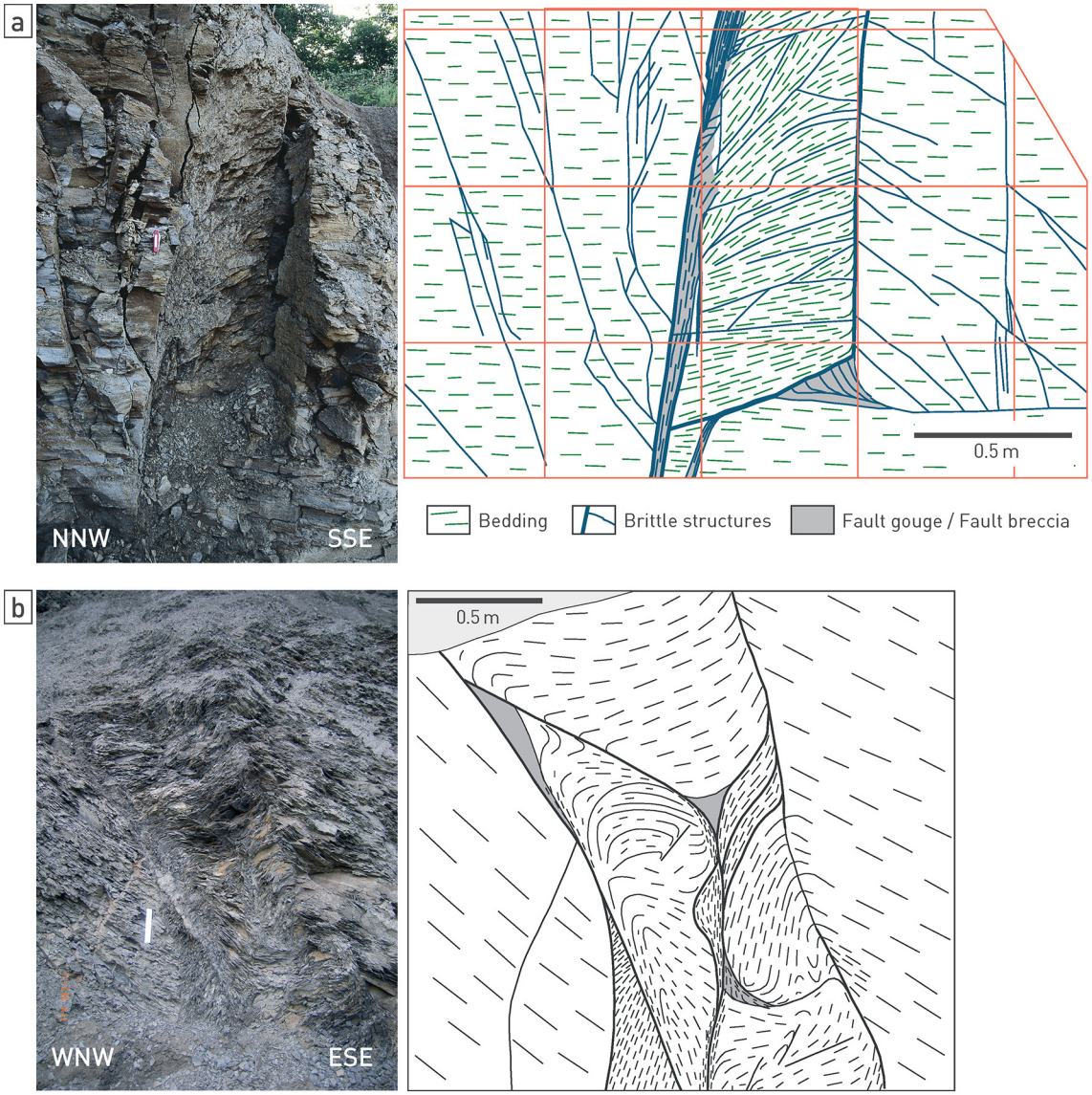


Fig. 5-33: Outcrop examples of fault structures in the Opalinus Clay

(a) Normal fault in a quarry near Siblingen, close to ZNO (Nagra 2002). (b) Thrust fault in a quarry near Holderbank, close to JO (Giger & Marschall 2014). Note: friable rock structure is affected by surface effects (swelling, drying, weathering) and not representative of in-situ conditions.

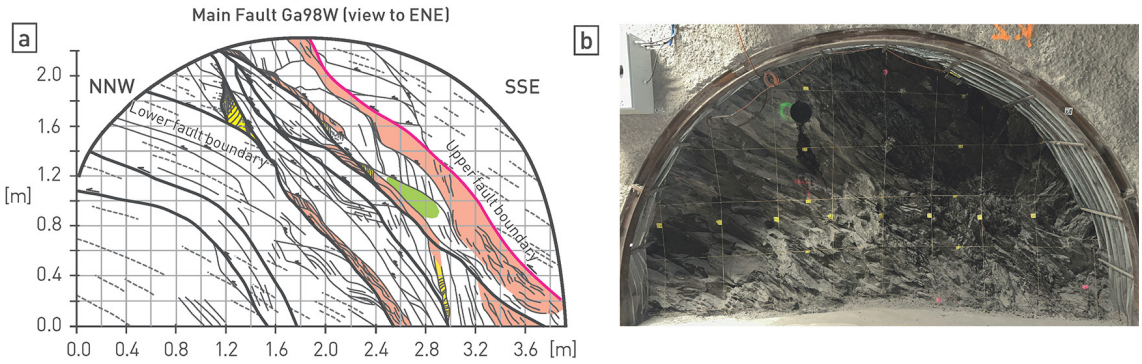


Fig. 5-34: Example of the "Main Fault" in the Opalinus Clay at the Mont Terri rock laboratory a) Interpretation according to Jaeggi et al. (2017). b) Photograph.

The strong variability in the degree of deformation in the Opalinus Clay is typical for so-called soft-linked sediments (e.g. Dahlstrom 1969, Walsh et al. 1999, Fossen & Rotevatn 2016). Based on vintage 3D seismic reflection data from ZNO, Roche et al. (2020) interpreted fault segmentation not only along strike, but also vertically across the Opalinus Clay in the Wildensbuch Flexure (Fig. 5-35 and Section 4.3.4). Localised deformation was found to be more partitioned across the Opalinus Clay, partly accommodated by folding. Similar observations are made from the Mont Terri rock laboratory (Fig. 5-34), where the "Main Fault" is segmented along strike (e.g. Jaeggi et al. 2017) and also in a vertical direction, as drilling experience in various experiments has shown. Partitioning of deformation by segmentation and soft-linkage thus reduces offsets along individual fault segments and affects the vertical connectivity of the segments. Overall, the segmentation hinders fault continuity and connectivity, and consequently also fault-related flow.

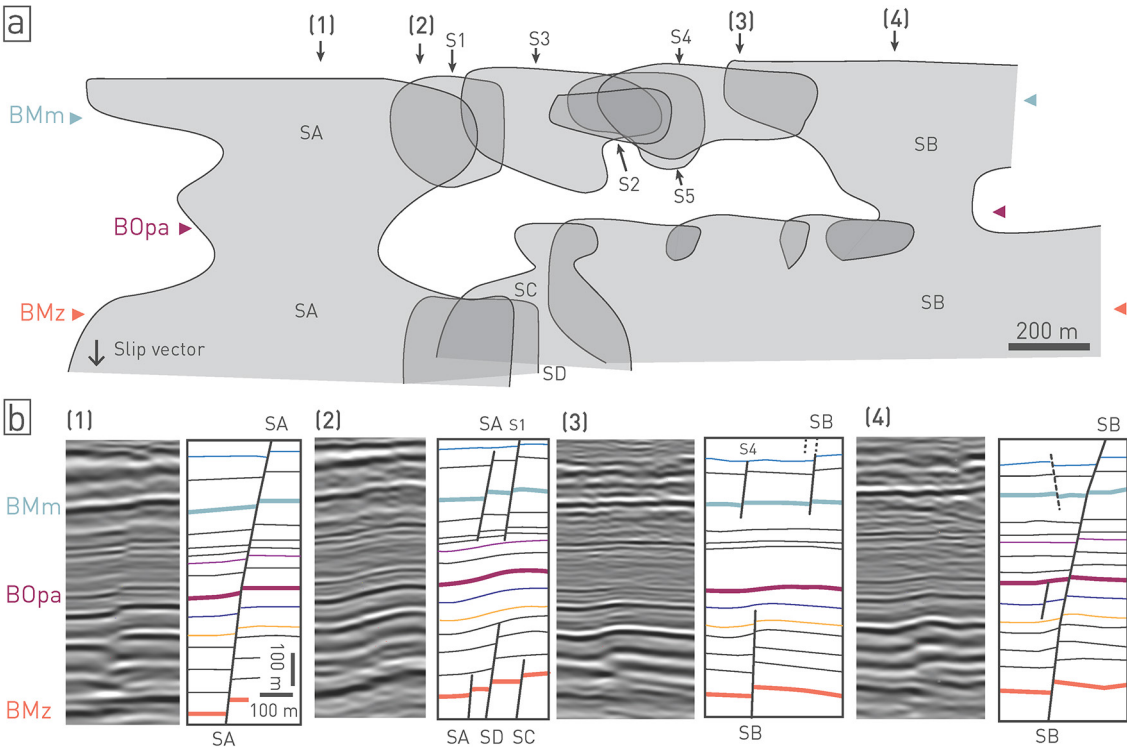


Fig. 5-35: Fault architecture of a seismically mappable fault (Wildensbuch Flexure in ZNO)

(a) Strike projection of the Wildensbuch Flexure (see also Section 4.3.4) with fault surfaces represented in grey. (b) Four seismic sections and their interpretations at the locations indicated in (a). BMm: Base Malm Group, Bopa: Base Opalinus Clay, BMz: Base Mesozoic unconformity. SA-SD and S1 to S5 indicate distinct fault segments. In sections (1) and (4) faults are continuous across the Opalinus Clay, whereas in sections (3) and (4) they are interpreted to be discontinuous at the seismic scale. Slightly modified after Roche et al. (2020).

Recent trenching and outcrop mapping around Frick (JO siting region) focused first on the Opalinus Clay in the Cheesleten quarry, but no tectonic fault could be mapped. However, in the nearby Gruhalde quarry, a normal fault in the underlying Staffelegg Formation was exposed. An offset between 1.5 to 2.5 m in two mechanically contrasting lithologies (the Beggingen Member and the Frick Member) is interpreted (Fig. 5-36, see also Fig. 4-25). In the fossiliferous limestones of the Beggingen Member, the fault is discrete, but then splays off into the mechanically softer and weaker clay-rich rocks of the Frick Member. The trench mapping highlighted that as the fault propagates into softer rock, the strain becomes more distributed. Softer rocks deform more easily and can accommodate strain over a larger area. The Frick Member is considered here as an analogue of the Opalinus Clay, where similar dispersion of strain accommodation is also indicated at the seismic scale in the siting regions (Nagra 2024a, 2024b, 2024c).

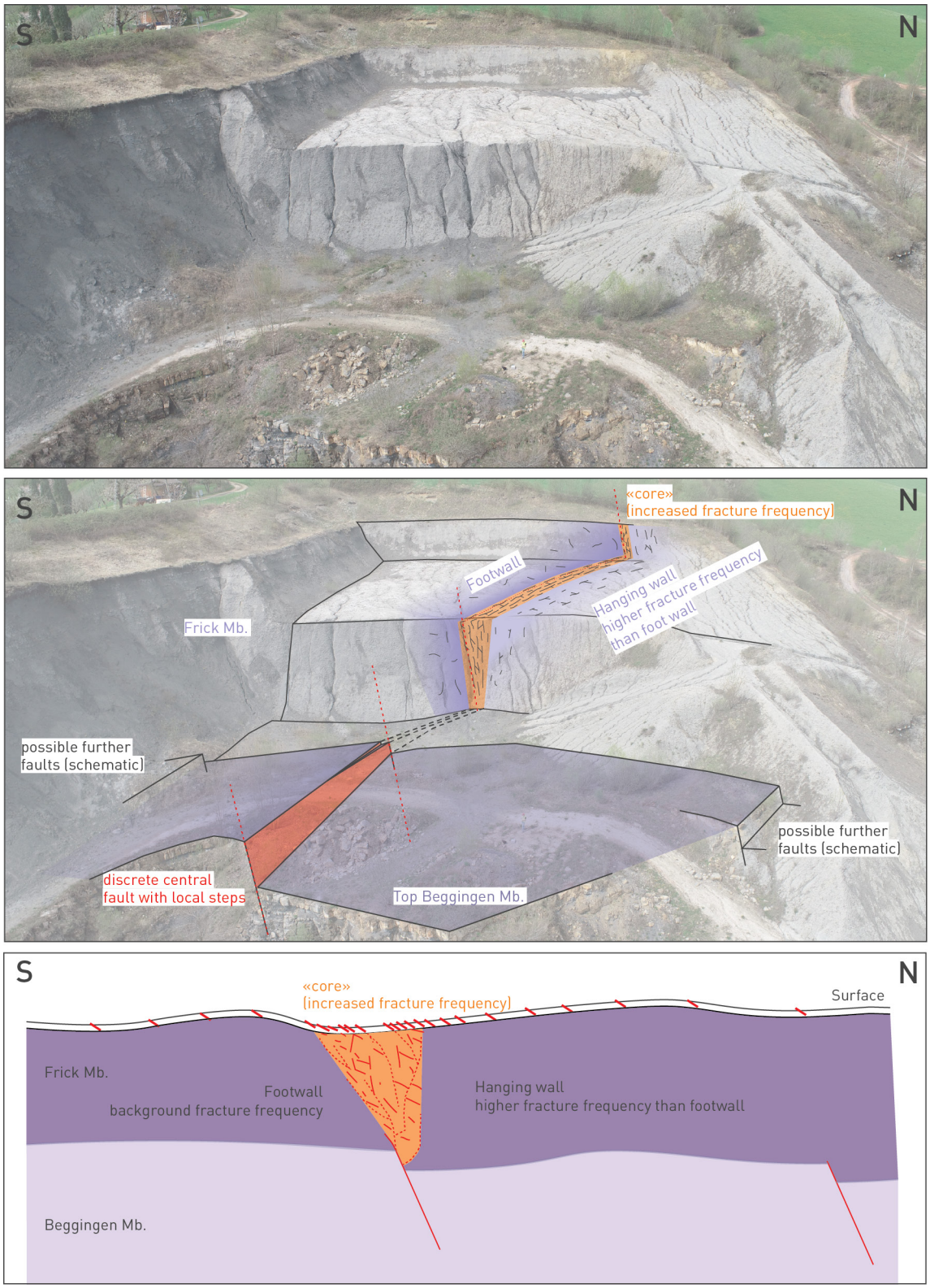


Fig. 5-36: Synthesis of trench mapping exposing fault propagation across mechanical layering

Highlighting the difference in strain accommodation between the Beggingen Member and the clay-mineral-rich Frick Member (Gruhalde quarry near Frick, Canton Aargau).

5.5.5 Conclusions

- The constitutive behaviour of the Opalinus Clay is well understood. Geomechanical properties and volumetric ("swelling") behaviour are particularly favourable for self-sealing (Section 5.7).
- The Opalinus Clay exhibits comparable mechanical properties in the three siting regions, but peak strengths are clearly different from the shaly facies of the Mont Terri rock laboratory. The different burial history (greater burial depth and lower tectonic overprint) has led not only to higher overall strength than in Mont Terri, but also to a lower variability.
- Deformation tests with the Opalinus Clay and confining units, as well as aquifer limestones, are consistent with observed effects of mechanical layering (Sections 4.3 and 4.4) and highlight that fracturing has a much greater effect on the more competent rocks than for the Opalinus Clay.
- Deformation in clay-rich rocks is typically expressed by more distributed strain and step-overs in contrast to more localised discrete strain accommodation in stiffer units.
- Segmentation of fault structures in the Opalinus Clay is expected to hinder fault-related flow.

5.6 Hydraulic properties and hydraulic heads

Key points:

- Hydraulic conductivity of the Opalinus Clay is very low and shows only little scatter. There is no relevant difference between the siting regions related to the different depth.
- The Opalinus Clay hydraulic conductivities from in-situ packer testing are in the same range as lab-tests on drill cores. That is, the tested faults do not act as preferential flow paths.
- The highest observed fault transmissivity at relevant depth in Northern Switzerland of 1×10^{-11} m^2/s is from a prominent thrust zone in the Schafisheim borehole outside the siting regions.
- Hydraulic conductivity in the confining units is also low but can be several orders of magnitude higher than in the Opalinus Clay. There is no indication of elevated matrix conductivities related to hard beds in the Lias Group – Dogger Group section.
- Formation hydraulic heads in the Opalinus Clay are affected by transient processes which are indicative of very low hydraulic conductivities.

5.6.1 Overview

The hydraulic barrier is ensured by low hydraulic conductivities, resulting in small water fluxes and low advective velocities. Very low hydraulic conductivities indicate mass transport dominated by molecular diffusion.

This section presents direct evidence on hydraulic properties. This includes laboratory tests on drill core samples (cm – dm scale) and in-situ hydraulic packer tests (metre to decametre scale). These are discussed in relation to rock mineralogy, porosity and structural inventory, and are complemented by observations from underground laboratories and tunnels.

Note that independent evidence on the hydraulic barrier effect such as natural tracers in porewater is presented in Section 4.6.

5.6.2 Small-scale properties from lab tests

Hydraulic tests on core samples have the advantage that effective stresses can be controlled, and the matrix properties can be related to a measurable mineralogy or porosity. A variety of methods such as constant head tests, consolidation theory (oedometer) and advective displacement with sample dimensions in the range of 1 to 10 cm were applied and provide an overall consistent picture (see Dossier IX of TBO reports in Tab. 2-1 and Waber 2020).

The matrix hydraulic conductivities perpendicular to bedding scatter over a relatively narrow range around 10^{-13} m/s (Fig. 5-37). There is no obvious correlation between hydraulic conductivity and mineralogy or porosity. Given the substantial lithological variability, this can be taken as an indication that diagenetic cementation of clay-poor samples is the cause for the low hydraulic conductivities. Note that a similar trend is observed by an in-depth interpretation of the in-situ hydraulic packer test dataset, for example the existence of a negative correlation between the measured bulk hydraulic conductivities with the carbonate content in the Passwang Formation in JO and the Wedelsandstein Formation in ZNO and NL (Nagra 2024m). The hydraulic packer test results in the latter formations also indicate that quartz and feldspar-rich layers that are poor in carbonates could show slightly enhanced matrix hydraulic conductivities (Nagra 2024m).

The systematic comparison of tests parallel and perpendicular to bedding on the centimetre-scale samples did not show a meaningful hydraulic anisotropy of the Opalinus Clay. Anisotropy depends on the scale of observation and the centimetre-scale samples are too small to directly derive formation-scale anisotropy. However, the dataset can be used for a geostatistical evaluation of equivalent horizontal and vertical hydraulic conductivities. The result indicates an anisotropy (K_h/K_v) ratio of ca. 5 (best estimate; Nagra 2024m).

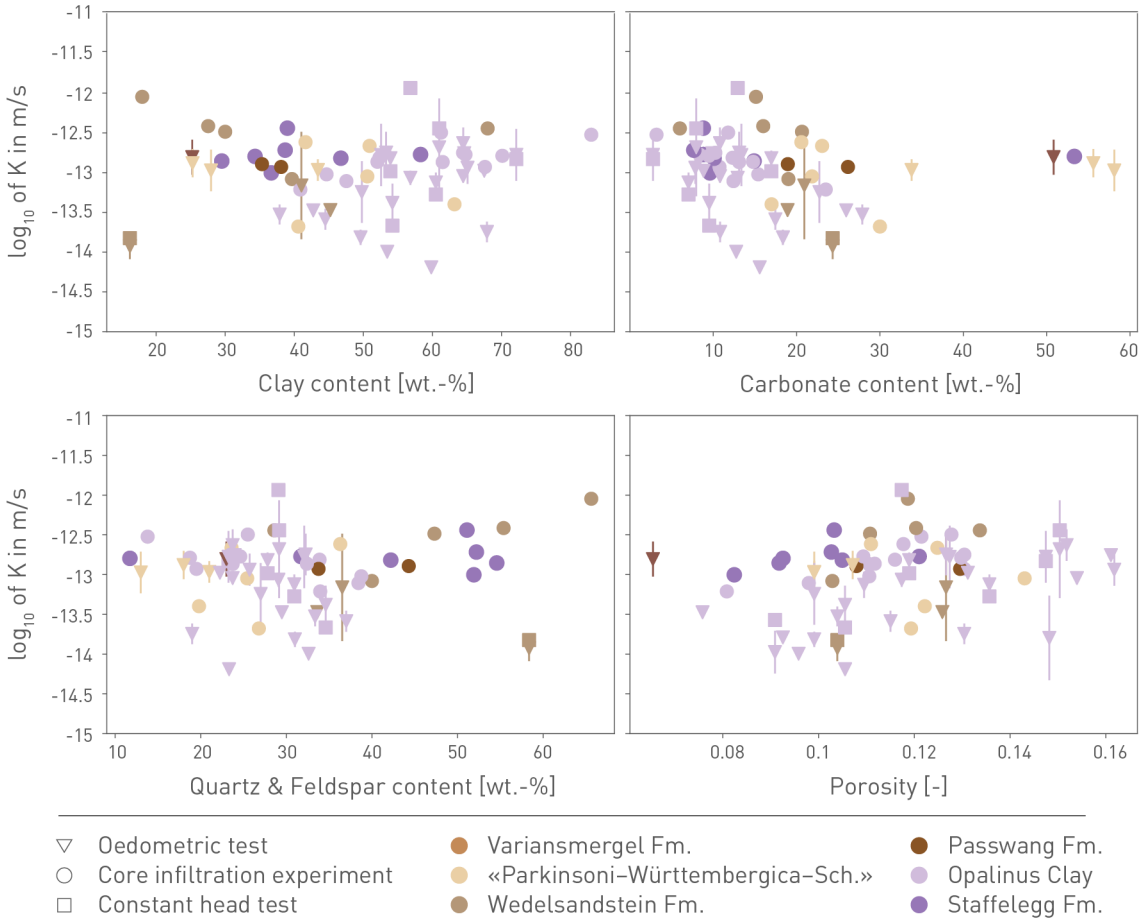


Fig. 5-37: Matrix hydraulic conductivity of the Opalinus Clay and clay-mineral-rich confining units as a function of mineral composition and porosity

All measurements were done with flow perpendicular to bedding. The figure displays the results of different test types. For the oedometric tests, the error bars show the range of measured hydraulic conductivities over a spectrum of effective stress representative for in-situ conditions (Dossier IX of TBO reports, see Tab. 2-1). The data shown are from the TBO boreholes plus Benken and Schlattingen-1 boreholes. The few drill core samples tested perpendicular to bedding, whose mineralogy and porosity are not available, show hydraulic conductivities scattering between 1×10^{-15} and 2×10^{-13} m/s.

5.6.3 Rock mass scale properties from in-situ hydraulic tests

In-situ hydraulic packer tests provide the transmissivity of the tested interval (length: several metres to a few decametres). This includes the contribution of the matrix and all discontinuities such as faults and joints in the test interval. The test data can be recalculated to average horizontal hydraulic conductivities.

5.6.3.1 Opalinus Clay

A comprehensive and robust database for the hydraulic properties is available from Nagra's investigations in the siting regions as well as from earlier investigation programmes, from the Mont Terri rock laboratory and from third party investigations.

Hydraulic properties are known to depend on overburden (stress). In the case of the overconsolidated Opalinus Clay, high values up to ca. 10^{-4} m/s are observed only in the uppermost decametres (Fig. 5-38) because of rock weathering and decompaction, as evidenced by the Lausen case study (Vogt et al. 2016, Mazurek et al. 2017) or the study of Hekel (1994). With increasing depth, the values decrease by several orders of magnitude, e.g. in the Mont Terri rock laboratory typical values are in the range of 1×10^{-12} to 1×10^{-13} m/s (see also Nagra 2014f). The best estimates of the hydraulic conductivities from hydraulic packer tests carried out in the JO, NL and ZNO boreholes plot in a narrow range, namely from 1×10^{-13} to 1×10^{-14} m/s. With this overburden thickness, no depth dependence is apparent (Fig. 5-38), i.e. the hydraulic properties of the Opalinus Clay are considered to be identical among the siting regions.

The hydraulic conductivities from the in-situ tests agree with the properties derived from the tests on drill core samples (see Section 5.6.2). In addition, there is a trend of a linear increase of the interval transmissivity with increasing test interval length, despite the possible presence of faults (Fig. 5-39). This indicates comparably homogeneous behaviour and shows that lithological variability, and in particular faults, have no major impact on hydraulic conductivity.

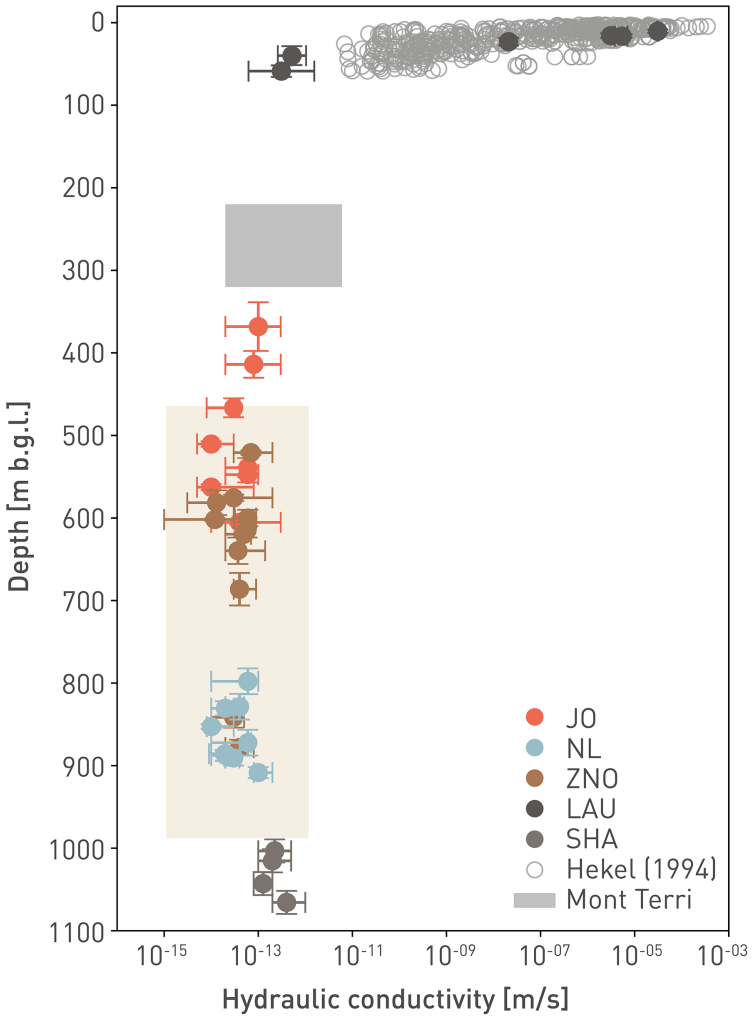


Fig. 5-38: Hydraulic conductivities of the Opalinus Clay as a function of depth

The beige zone indicates the range of hydraulic conductivities from lab tests on drill core samples performed parallel and perpendicular to bedding. The data range from Mont Terri is from Gautschi (2017). Fig. 6-46 illustrates the dataset at small overburden thickness in detail.

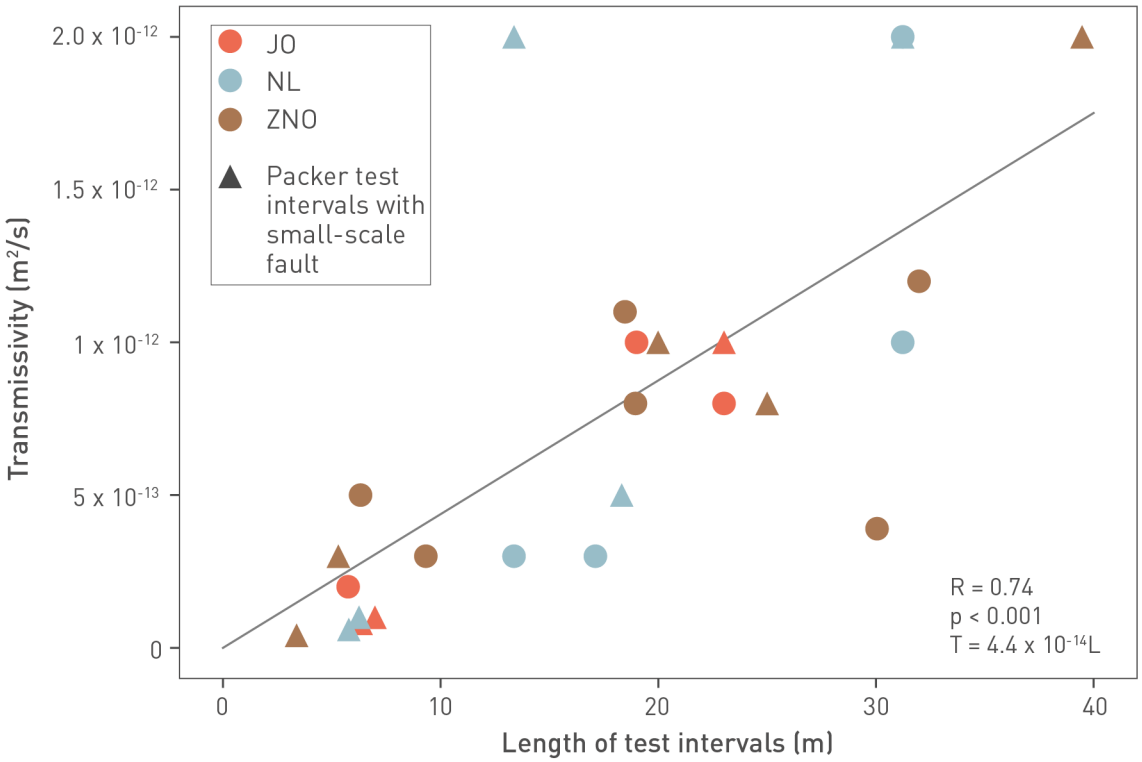


Fig. 5-39: In-situ test best estimate transmissivities of the Opalinus Clay derived from hydraulic packer tests as a function of the length of the test intervals

The figure shows data from the TBO boreholes plus the Benken borehole, which were tested using a similar state-of-the-art approach. "R" refers to the Pearson correlation coefficient of the regression line, "p" refers to the p value, "T" refers to the transmissivity, and "L" refers to the length of the test interval. The low calculated p value (< 0.001) indicates there is a statistically significant linear relationship between the transmissivity and the length of the test intervals. The bandwidth of the transmissivities is typically within an order of magnitude around the best estimate.

During the TBO campaign, hydraulic testing of fractures (faults, joints) was a primary target in all boreholes. The maximum transmissivities of the fractures can be estimated from the test results assuming one such discontinuity per interval. The histogram of the transmissivities shows generally low values of approximately 1×10^{-12} m^2/s ± one order of magnitude (Fig. 5-40). The maximum value of 10^{-11} m^2/s is from a long test interval at the base of the Opalinus Clay in the Schafisheim (SHA) borehole. This interval includes a major fault zone related to the folding and thrusting of the Jura mountains – such structures are absent in the siting regions. In the BAC1 borehole, a test on a small-scale fault indicated 2×10^{-12} m^2/s (Fig. 5-39). To summarise, fractures in the Opalinus Clay in the siting regions under present-day stress conditions have low transmissivity and are not considered to be preferential flow paths. This can be explained with the deformation and self-sealing behaviour (Sections 5.5 and 5.7).

The low hydraulic conductivity of the Opalinus Clay can also be well justified by comparison with international examples (Fig. 5-41). The values are of the same order of magnitude as in other clay-rich rocks of comparable porosity. The Opalinus Clay hydraulic conductivity is lower than in the high-porosity soft clays and lower than in highly indurated brittle clays.

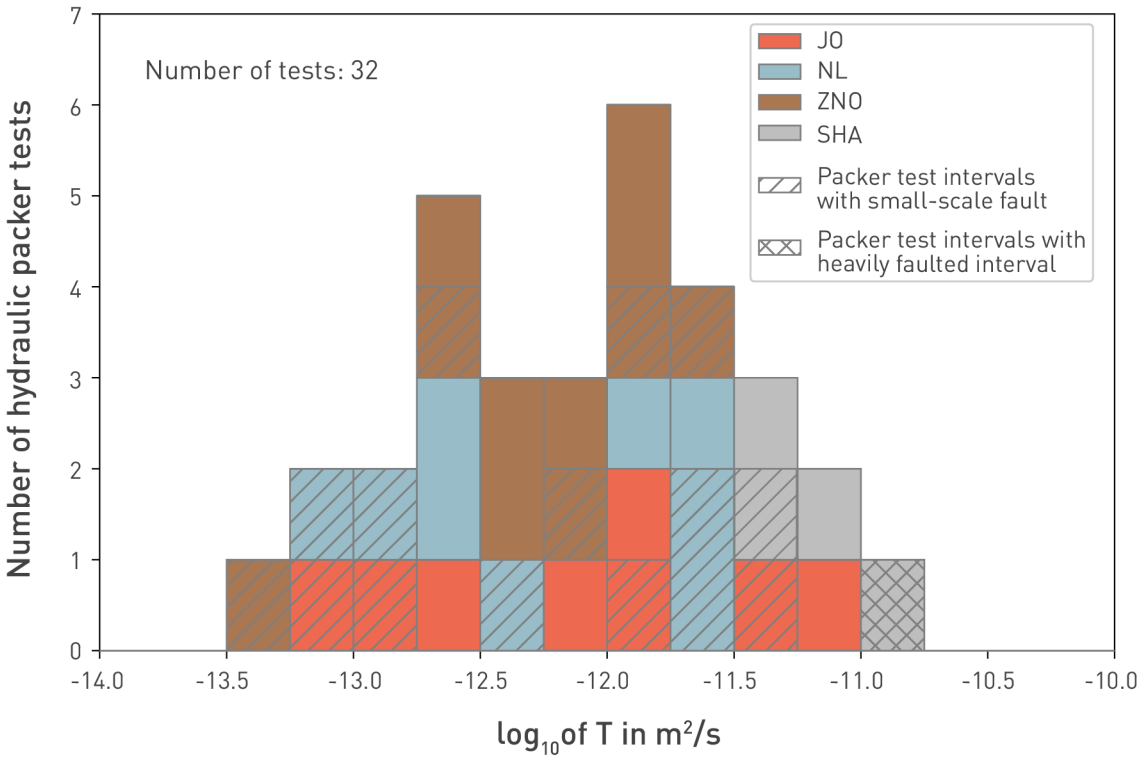


Fig. 5-40: Distribution of the logarithm of the best estimate of the in-situ hydraulic packer test transmissivities in the Opalinus Clay

The figure includes tests performed in the TBO boreholes plus the Benken (BEN) and Riniken (RIN) boreholes of the JO, NL and ZNO siting regions, and the tests in the Schafisheim borehole (SHA). Interval length of displayed tests varies between < 5 m and 60 m. Structural inventory of the BEN, RIN and SHA boreholes from Ebert (2014).

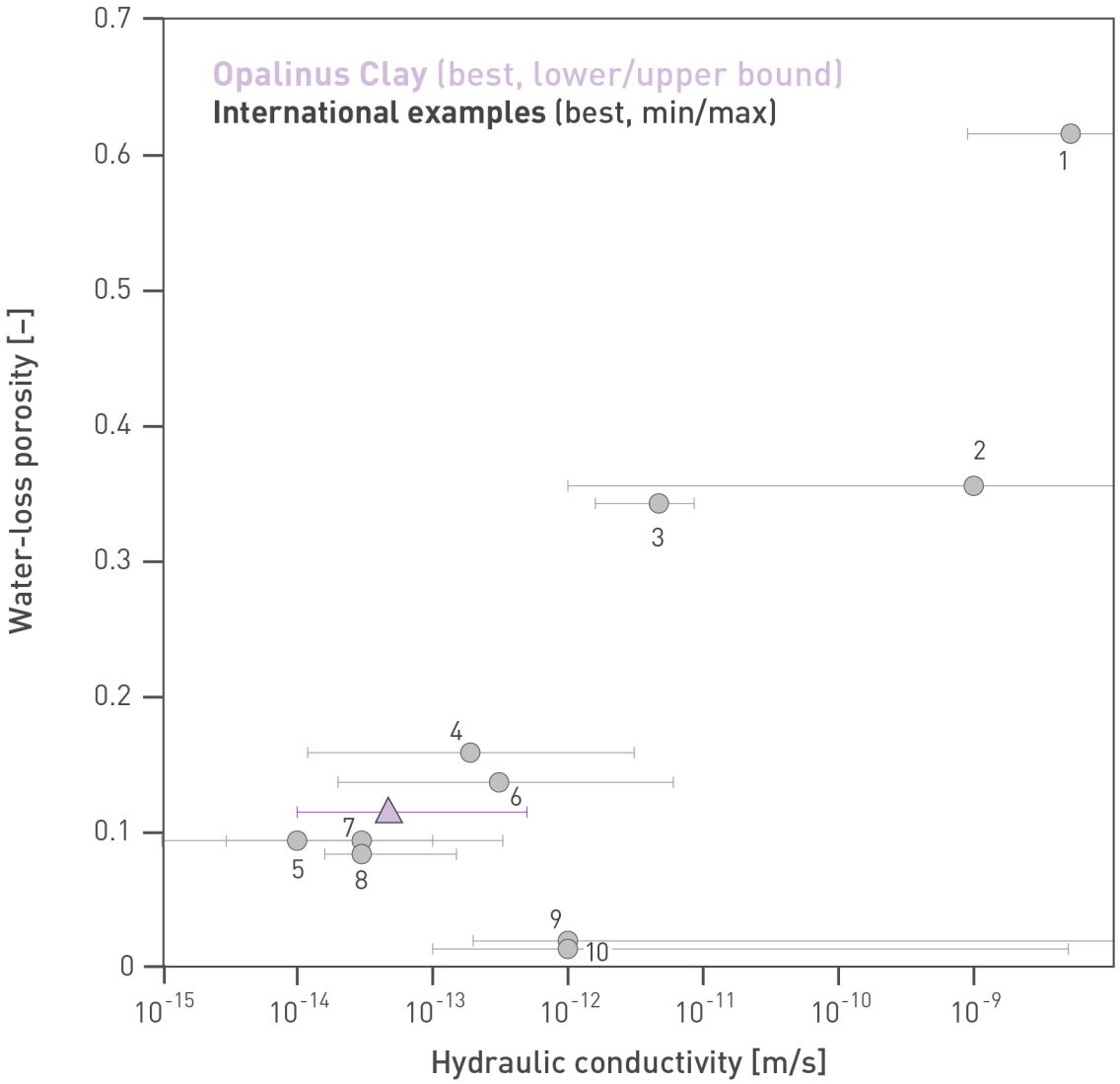


Fig. 5-41: Comparison of the horizontal hydraulic conductivity of the Opalinus Clay with examples of clay-rich rocks worldwide

Opalinus Clay data based on Nagra (2024m). Values are plotted at best estimate water-loss porosity. International data are from the Clay Club Catalogue (OECD/NEA 2022). Points indicate best estimates, bars represent minimum and maximum values. 1: Koetoi Formation at Horonobe (JP, max. burial: 1'000 m), 2: Wakkanai Formation at Horonobe (JP, 1'200 m), 3: Boom Clay at Mol (B, 215 m), 4: Callovo-Oxfordian at Meuse/Haute Marne (F, porosity UA unit, 850 m), 5: Toarcian-Domerian at Tournemire (F, 1'300 m), 6: Opalinus Clay Mont Terri (CH, upper bound K from Gautschi 2017, 1'350 m), 7: Georgian Bay Formation at Bruce nuclear site (CDN, 1520 m); 8: Queenston Formation (CDN, 1'450 m), 9: Boda Claystone Formation, Gorica block (H, 4000 m); 10: Boda Claystone Formation, Boda block (H, 4'000 m). Max. burial depths as indication for consolidation (best estimates or average values).

5.6.3.2 Confining units

A major effort was invested in the hydraulic characterisation of the confining units (see also Section 4.5.3). The in-situ hydraulic packer tests generally indicate hydraulic conductivities below 10^{-11} m/s and typical values around 10^{-13} m/s. The investigations do not provide evidence of significantly elevated matrix hydraulic conductivities in the confining units adjacent to the Opalinus Clay (Fig. 5-37, Nagra 2024m). Therefore, the focus is on constraining the impact of fractures for different lithologies. As in previous reports (e.g. Nagra 2014f), the clay-mineral content of the units is used as a proxy for brittle behaviour and self-sealing potential and thus as an additional argument to constrain the hydraulic properties. This is done in two empirical approaches:

- Evaluation of the hydraulic conductivity as a function of the clay-mineral content of the test interval: Given the lithological variability within the typical test intervals in the confining units, the data are displayed as a function of the lowest average clay-mineral content calculated over a 5 m window in the test intervals (Fig. 5-42).
- Evaluation of the hydraulic properties as a function of the thickness of the brittle, clay-poor units (i.e. clay-mineral content < 20 wt.-%; Fig. 5-43).

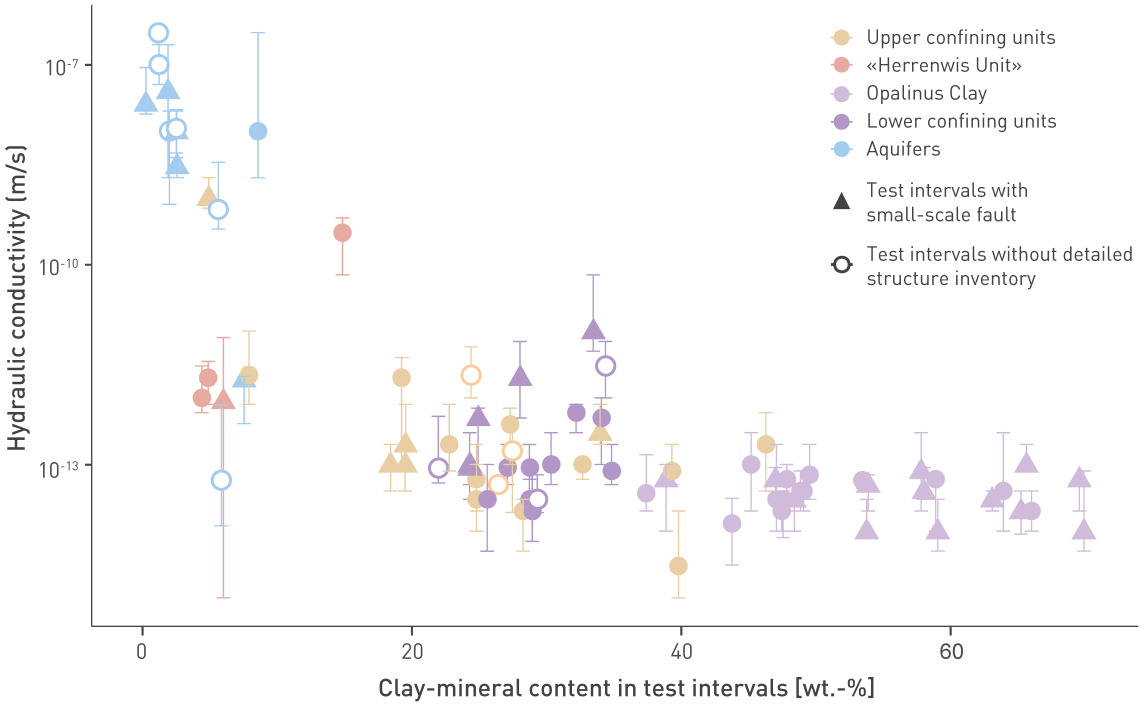


Fig. 5-42: Hydraulic conductivity of the in-situ hydraulic packer tests as a function of the clay-mineral content of the test interval

The dataset includes packer tests from the base of the Lias Group to the top of the Malm Group in the TBO boreholes plus RIN, WEI and BEN. The dataset for the confining units is supplemented by data from the Malm and Hauptrogenstein aquifers. See text regarding calculation of clay-mineral content.

The highest hydraulic conductivity (1×10^{-9} m/s) encountered in the upper confining units was measured in the Wildegg Formation of the BOZ1 borehole. This test interval includes the Gerstenhübel Bed. A hydraulic conductivity of 3×10^{-10} m/s was measured in the «Herrenwis Unit» of the STA2 borehole in association with a subvertical joint.

The hydraulic test results show a good correlation with the clay-mineral content (Fig. 5-42):

- Intervals with clay-mineral contents above about 35 – 40 wt.-% have consistently low hydraulic conductivities – similar to the Opalinus Clay – of < 10^{-13} m/s, demonstrating that the variable tectonic overprint is not associated with elevated transmissivities. This group corresponds not only to the Opalinus Clay but also to clay-rich formations in the upper confining units such as the «Parkinsoni-Württembergica-Schichten» or the clay-rich facies of the Wedelsandstein Formation in NL.
- Intervals with a minimum average clay-mineral content in the range of ca. 20 – 40 wt.-% are characterised by a somewhat larger scatter, while hydraulic conductivities remain in majority below 10^{-11} m/s, even for tests with tectonic overprint. This indicates a reduced but relevant self-sealing potential. The presence of thin hard beds in some test intervals has no visible impact on the measured transmissivities (Fig. 5-43), reflecting their small fracture inventory and low porosities. In summary, units corresponding to this group with a minimum clay-mineral content of 20 wt.-% contribute significantly to the hydraulic barrier effect. This group comprises the majority of packer test intervals of the upper confining units (with the exception of the «Herrenwis Unit» and the Wildegg Formation) and all the tests in the lower confining units.
- The group with minimum average clay-mineral contents below 20 wt.-% shows a broad range of hydraulic conductivities. Values greater than ca. 10^{-9} m/s refer to tests with a thickness of the clay-poor section of more than ca. 8 m (Fig. 5-43). This latter group includes the Malm and Hauptrogenstein aquifers, fractured intervals of the «Herrenwis Unit» and the Wildegg Formation (e.g. Gerstenhübel Bed). In contrast, test intervals with thinner clay-poor layers display average hydraulic conductivities below 10^{-11} m/s (Fig. 5-43) even in the presence of small-scale faults.

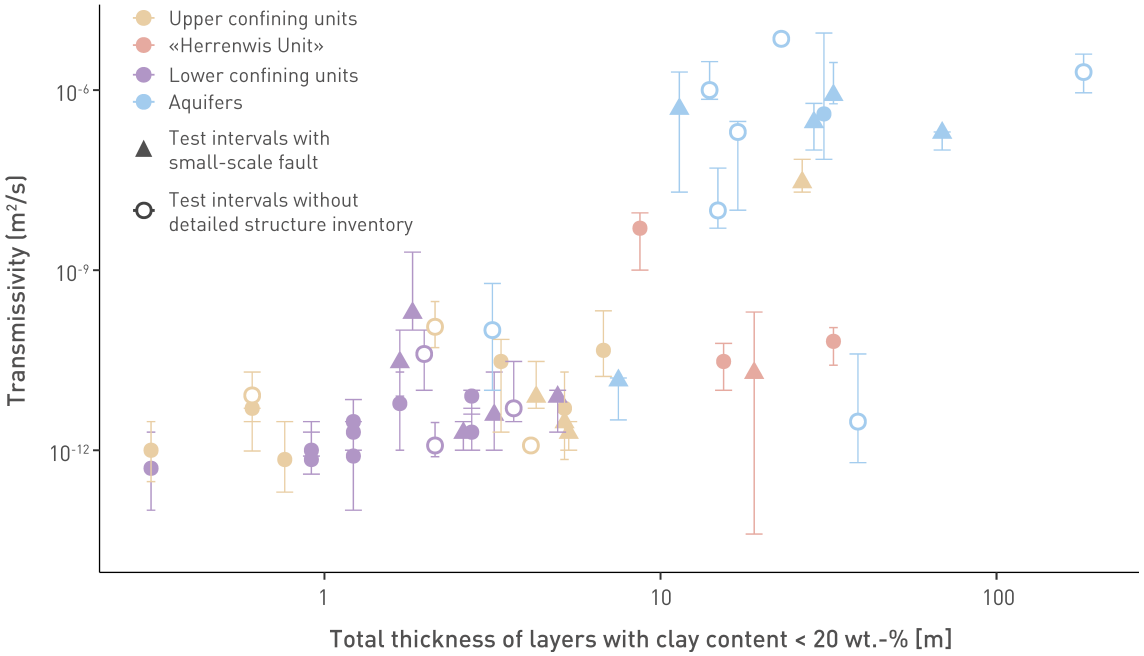


Fig. 5-43: Transmissivity as a function of the total thickness of a layer with clay-mineral content < 20 wt.-%

The dataset considered includes packer tests from the base of the Lias Group to the top of the Malm Group (except the Opalinus Clay) in the TBO boreholes plus RIN, WEI and BEN. The dataset of the confining units is supplemented with data from the Malm and Hauptrogenstein aquifers.

The highest transmissivity (3×10^{-8} m^2/s) encountered in the upper confining units was measured in the Wildegg Formation of the BOZ1 borehole. The test interval includes the Gerstenhübel Bed. A transmissivity of 5×10^{-9} m^2/s was measured in the «Herrenwis Unit» of the STA2 borehole in association with a subvertical joint.

5.6.4 Observations in tunnels

Tunnels and underground rock laboratories offer the opportunity to study the properties of the rocks of interest at larger scale compared to the deep boreholes. It is emphasised that the tunnels studied are constructed in areas of much stronger tectonic overprint than in the siting regions for the deep geological repository. This applies also to the Mont Terri rock laboratory, situated in the Folded Jura in Western Switzerland.

Gautschi (2001) and earlier literature cited therein screened the hydrogeological observations in the Opalinus Clay in five railway tunnels and five motorway tunnels. The overburden thickness at the locations in the Folded Jura ranges from 100 to 800 m. The level of mapped details in the available documentation is variable. Despite the complex tectonics, comprising numerous faults in a water-saturated environment, only two damp patches and three measurable water inflows are reported for a total of 6'600 m of tunnel length. All these indications of water flow are from sections with low overburden thickness (less than 200 m) and are either associated with a calcareous – sandy facies not observed in the siting regions in Northern Switzerland or with faults. The detection limit for visual identification of damp patches along faults in ventilated tunnels is estimated to a transmissivity of 10^{-9} m^2/s.

In the framework of the construction of the new Belchen motorway tunnel in the Folded Jura, pulse tests in two boreholes indicated rock mass transmissivities ranging from 1.3×10^{-9} to 4.3×10^{-11} m^2/s (Renz et al. 2019, Ziegler et al. 2022). These data refer to intervals with tectonic faults and are probably affected by the excavation damage zone of the large tunnel diameter.

Becker & Vogt (2020) studied the occurrence of so-called 'wet spots' in the Mont Terri rock laboratory, where overburden thickness above the tunnels in the Opalinus Clay ranges between 220 and 320 m. The term wet spot is used for damp patches observed on tunnel walls, dripping points or water inflows (also termed seepage waters). The study of Becker & Vogt (2020) focused on the BBB-3 borehole and provided evidence of localised flow along features with a maximum thickness of a few centimetres and local hydraulic conductivities in the range of 10^{-9} – 10^{-11} m/s. Hydraulic cross-borehole connections were observed over distances of 0.8 – 1.0 m, suggesting that the wet spots are a spatially limited phenomenon. The authors consider small-scale variations of lithological properties in the transition zone from the carbonate-rich to the sandy facies in conjunction with stress redistributions due to the extensive tunnelling activities in the URL as the probable cause. Whether fracture planes, e.g. originating from the excavation damage zone, in these low clay-mineral content layers also contribute to preferential flow paths could not be clarified. Overall, the occurrence of wet spots can be (at least partly) explained in the context of small-scale variation in hydraulic conductivity and the activation of these systems by the tunnel construction (high hydraulic gradients, possibly disadvantageous stress situation). The profiles of natural tracers provide evidence against large flow systems active over long periods of time. Both at Mont Terri and at the neighbouring Mont Russelin, the profiles of the natural tracers can be explained by diffusion as the dominant transport process, despite the stronger tectonic overprint compared to the siting regions in Northern Switzerland (e.g. Wersin et al. 2020, Waber & Rufer 2017, Mazurek et al. 2009).

5.6.5 Profiles of formation hydraulic heads

Hydraulic head profiles along boreholes can support the identification of potential release paths and are used to estimate vertical hydraulic gradients between the host rock and the confining units, and the local and regional aquifers (Nagra 2024m). In addition, the values recalculated to pore pressures feed into geomechanical interpretation.

In principle, formation hydraulic heads can be estimated in two ways: From the analyses of the hydraulic packer tests, and from the hydrogeological long-term monitoring systems, directly measured in selected boreholes and intervals.

Regarding the hydraulic packer tests, the test strategies and test design were optimised notably for testing low-permeability clay-mineral-rich rocks based on earlier experience (Nagra 2001, Nagra 2002, Marschall et al. 2004, Reinicke & Frieg 2021). The hydraulic packer test analyses provide reliable and well constrained estimates of the transmissivity and hydraulic conductivity. The formation hydraulic head in the units with low clay-mineral content, particularly in the Malm, Keuper and Muschelkalk aquifers, is also well defined by the hydraulic test results. Despite the improved testing strategy, the estimated hydraulic heads in test intervals located in low-permeability clay-mineral-rich rock are considered to be strongly biased by artefacts (see also Nagra 2002, Beauheim 2013) and are therefore termed 'apparent heads'. They are not representative of formation hydraulic heads and are therefore not further discussed here.

As in other investigation programmes of low-permeability clay-rich rocks (e.g. Distinguin & Lavanchy 2007, NWMO 2011), hydrogeological long-term-monitoring (LTM) systems are used instead of short-term hydraulic tests to derive representative hydraulic heads or formation pore pressures. In addition to the pre-existing LTM system in the Benken (BEN) borehole, three additional boreholes were equipped (MAR1, STA3, BOZ1), that is one per siting region. The LTM systems are intended to measure the undisturbed formation hydraulic heads and their

temporal fluctuations in the Opalinus Clay, the confining units and the deep aquifers. Measurements with the new LTM systems started in late spring 2022. While the pressures in many intervals are still evolving, the following conclusions can be formulated for the moment (with the focus on host rock and confining units):

- The monitoring system in the BEN borehole records the hydraulic heads since 2009 (installation of the Baker-Hughes system). After 15 years of operation, the values in the Opalinus Clay are still slowly declining and are the lowest in the monitored units. Currently (Longridge et al. 2024), the measured hydraulic head in the Opalinus Clay is ca. 335 m a.s.l., that is 69 m below hydrostatic and ca. 56 m lower than in the Malm aquifer.
- The hydraulic heads measured in the new boreholes seem to evolve like those measured in the BEN borehole. That is, the formation hydraulic heads in the Opalinus Clay are below hydrostatic (Fig. 5-44) and lower than in the adjacent aquifers.
- The hydraulic head in the «Herrenwis Unit» of the STA3 borehole is also subhydrostatic and lower than the discharge level of the Malm aquifer along the Rhine River (Fig. 4-91).

In the scientific literature, values of hydraulic heads that cannot be explained solely by gravity-driven flow are termed 'anomalous heads' or 'anomalous pore pressures' (e.g. Neuzil 1995, Birchall et al. 2022). Many examples worldwide have been reported. They are believed to arise when processes cause sufficiently large changes in pore volume or fluid volume that cannot be dissipated by flow in the low-permeability formation (Horseman et al. 1996). Typical processes invoked to cause underpressures are stress release either because of erosion or after melting of Pleistocene ice cover (e.g. Beauheim 2013, Normani et al. 2017). These anomalous heads are an indication of very low hydraulic conductivity.

The hydraulic diffusivity is the measure of the ability of a porous medium to dissipate pressure. For the Opalinus Clay it is estimated at ca. 10^{-8} s^{-1} ($K \sim 10^{-14}$ m/s, $Ss \sim 10^{-6}$ m^{-1}) and is well within the range of examples worldwide with observed anomalous pressures (literature overview in Vinard 1998, Neuzil 2015).

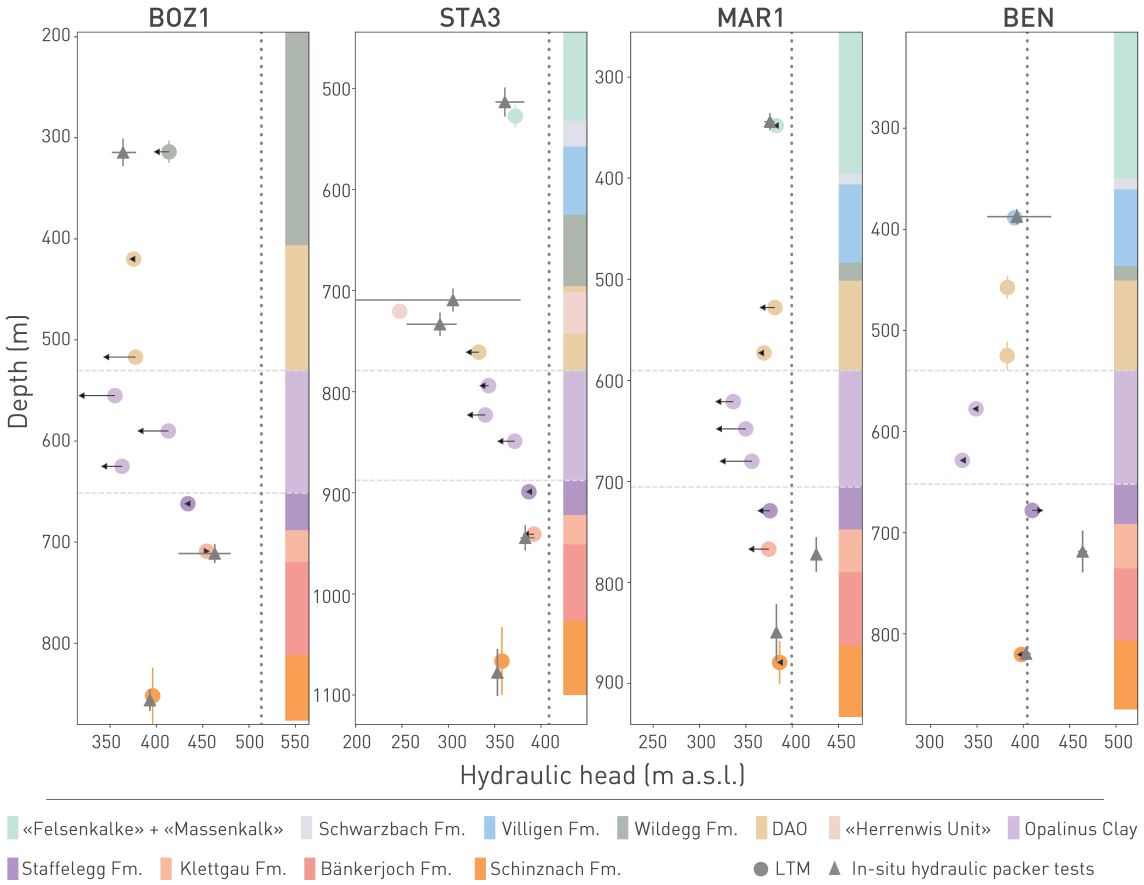


Fig. 5-44: Hydraulic head profiles based on hydrogeological long-term monitoring and in-situ hydraulic packer test data in the BOZ1, STA3, MAR1 and BEN boreholes

Status of the long-term monitoring data is 01.05.2024. Hydraulic heads of the long-term monitoring systems are displayed using full circles. The extent of the intervals in contact with the formation is shown with a vertical line (in many cases the interval is smaller than the size of the data points). Left-pointing and right-pointing arrows respectively indicate decreasing and increasing hydraulic head with time (i.e. not yet stabilised). The length of the arrows is proportional to the magnitude of the rate of change of the hydraulic head with respect to time. No arrows are displayed for intervals with an absolute rate of change smaller than approximately 3 mm/day (about 1 m/yr). Hydraulic heads estimated from hydraulic packer tests are displayed with grey triangles. The associated horizontal and vertical lines show the uncertainty range of the hydraulic head value and the extent of the tested interval respectively. Hydraulic head estimates from hydraulic packer tests in low-permeability clay-rich units are affected by artefacts and are not shown (see text). Vertical dotted lines indicate the ground level. DAO: Dogger Group above Opalinus Clay, Fm.: Formation.

5.6.6 Conclusions

- The hydraulic conductivities of the Opalinus Clay are uniformly low and comparable among the studied sites. The low values are supported by independent evidence such as natural tracers in porewater (Section 4.6) and are the reason for diffusion being the dominant transport process (Section 5.9).
- The Opalinus Clay fracture hydraulic properties as observed in in-situ tests in boreholes in Northern Switzerland are consistent with the range of values of the intact matrix. That is, fractures do not represent preferential flow paths. This is explained by self-sealing (Section 5.7).
- Hydraulic conductivities in the confining units are low and will contribute to the retardation of radionuclides. Tectonic overprint on clay-poor lithologies may result in locally elevated transmissivities – but it remains a hypothetical assumption that such units may provide a continuous release path.
- Hydraulic heads in the Opalinus Clay are lower than in the adjacent aquifers. This is probably caused by transient hydromechanical processes related to loading and unloading of the rock column. Such processes underpin the very low hydraulic conductivity.

5.7 Self-sealing of fractures

Key points:

- High self-sealing potential of the Opalinus Clay ensures that fractures, when and where formed, do not remain permeable and thus would not jeopardise the barrier integrity over relevant timescales.
- Clay-mineral content is a very good indicator for the self-sealing potential of the host rock and confining units, with values greater than approximately 40 wt.-% (e.g. the Opalinus Clay) exhibiting very high self-sealing and values less than approximately 20 wt.-% exhibiting low or negligible capacity.
- Besides clay-mineral content, sufficient effective stress (or equivalent depth) is required for robust self-sealing. This is achieved in the Opalinus Clay in all the siting regions.
- In view of the long-term development of the repository and related concerns about erosion, a residual overburden of 200 m can be considered as sufficient for robust self-sealing in the Opalinus Clay.

5.7.1 Overview

The term "self-sealing" broadly encompasses all hydromechanical, hydrogeochemical and hydrobiochemical processes that lead to a reduction in transmissivity of a fractured rock mass (Tsang et al. 2005). The term "sealing" implies that the reduction in hydraulic conductivity is so significant that transport properties are again comparable to the intact rock mass or simply so low that transport becomes diffusion-dominated (Section 5.8). The prefix "self" implies that the sealing processes occur spontaneously if access to water or brine is granted. Self-sealing can be considered as the key factor for the barrier integrity of the Opalinus Clay and other clay-rich rocks even in tectonically disturbed areas, which is a critical difference to other low-permeability rocks with lower clay-mineral content.

Section 5.7.2 first summarises selected empirical and phenomenological evidence for self-sealing in the Opalinus Clay. The key processes and mechanisms responsible for self-sealing are then explained in Section 5.7.3.

It was highlighted previously that hydraulic conductivity in the Opalinus Clay is low even in fractured and faulted intervals (Section 5.6). The most relevant evidence is results from the hydraulic packer tests in the new deep boreholes, which are consistent with matrix values of unfractured laboratory samples (Fig. 5-38). Besides the standard packer tests in deep boreholes, relevant new data were also acquired from dedicated special hydraulic tests in the deviated RHE1 borehole, which are discussed in Section 5.7.4.

Self-sealing potential correlates mainly with material properties such as clay-mineral content and bulk density or porosity but depends also on the effective stress field (see Section 5.7.3 for the mechanisms). This stress dependence explains why a landfill in the Opalinus Clay at a few tens of metres depth cannot rely on similar self-sealing potential as can a facility at repository depth. Effective stresses in all the siting regions currently ensure robust self-sealing (Section 5.7.4) for the Opalinus Clay at the level of a future repository. Self-sealing may be limited when the overburden thickness decreases to values < 200 m. This is not expected for the period under consideration (Sections 6.4 and 6.5).

Other factors affecting self-sealing are discussed in Section 5.7.5, and the relevance of mineralised fractures ("veins") for the self-sealing potential in the Opalinus Clay is addressed separately in Section 5.7.6.

5.7.2 Empirical evidence

A comprehensive summary of evidence for self-sealing in argillaceous formations in the context of geological disposal of radioactive waste was provided by Bock et al. (2010).

Specific to the Opalinus Clay, there is both phenomenological and direct evidence from active testing for self-sealing (Tab. 5-2). The phenomenological evidence stems from observations in tunnels and boreholes (see also Sections 5.6.3 and 5.6.4) that tectonic structures in the Opalinus Clay do not show significant changes in hydraulic properties in situ. In addition, experiments at the Mont Terri rock laboratory and in the RHE1 borehole in the ZNO siting region at potential repository depth provide direct evidence for self-sealing, as fissures are either generated or faults reactivated. These experiments have demonstrated that faulting or fault re-opening at low effective stress is associated with an increase in transmissivity by several orders of magnitude and followed by fault closure and a strong decrease in transmissivity over time and with an increase in effective stress.

The empirical findings are complemented by numerous laboratory experiments under controlled conditions, which describe the self-sealing behaviour in the Opalinus Clay phenomenologically and quantitatively:

- Small-scale tests with artificially induced cracks in core material show closure of the cracks within hours to days in the presence of water and confining stress of a few MPa (e.g. Seiphoori 2019a, Wenning et al. 2021a, Voltolini & Ajo-Franklin 2020; see Fig. 5-45).
- Direct shear and triaxial tests with measurements of hydraulic properties exhibit rapid disaggregation of the rock in the vicinity of fractures (e.g. Zhang et al. 2008, Cuss et al. 2011, Monfared et al. 2012, Zhang 2013, Seiphoori 2019a), and eventually their closure, with a significant reduction in conductivity (several orders of magnitude) reaching values close to (or slightly higher than) the intact material.
- Detailed studies of volumetric behaviour such as consolidation and swelling tests (Section 5.5.2) quantify the volumetric expansion or compaction due to effective stress changes as well as hydration.

Tab. 5-2: Empirical findings and key experiments on self-sealing in the Opalinus Clay

EDZ: Excavation damage zone.

Locality / Area	Findings	Conclusion	References
Indirect evidence for self-sealing (phenomenological evidence)			
Internal Jura	Geological gallery surveys in railroad and road tunnels: no dripping water or damp spots where overburden thickness greater than a few hundred metres (e.g. Mont Russelin with 300 – 400 m overburden).	Transmissivity of brittle structures at larger overburden thickness is very low, even in heavily faulted sections.	Gautschi (2001), Gautschi (2017)
Autochthonous cover, Alpine Foreland	At Lausen, Opalinus Clay outcrops beneath Quaternary. Drastic decrease in hydraulic conductivity within uppermost 30 m depth from the surface.	Low depth / stress sufficient to have a significant sealing effect.	Vogt et al. (2017) and Section 6.5.2
Central Molasse Basin	Strong tectonic overprint at Base Opalinus Clay in the Schafisheim borehole: no increased hydraulic conductivity.	Brittle structures do not differ significantly hydraulically from the rock matrix.	Gautschi (2017)
Siting regions	Diverse brittle structures of different sizes in numerous deep boreholes: no significantly increased hydraulic conductivity in packer tests.	Brittle structures do not differ significantly hydraulically from the rock matrix.	Gautschi (2017), Dossier VII of reports in Tab. 2-1
Whole of Northern Switzerland	In the Opalinus Clay, vein fillings are rare and volumetrically not relevant.	No significant water – rock interaction associated with advective water flow.	Nagra (2002), Mazurek et al. (2018)
Mont Terri rock laboratory	"Main Fault": no increased hydraulic conductivity in packer tests prior to fault reactivation.	Under undisturbed effective stress conditions, the "Main Fault" is not hydraulically effective.	Nussbaum & Bossart (2004), Guglielmi et al. (2020)
In-situ experiments with direct evidence for self-sealing			
Mont Terri rock laboratory	GS experiment: significant crack transmissivity is observed only at low effective normal stress (< 2 MPa).	Only low normal stress required for mechanical self-sealing of discrete deformation structures.	Nagra (2002)
Mont Terri rock laboratory	In the Selfrac experiment, the hydraulic conductivity of the EDZ decreased by about 2 orders of magnitude over a period of 2 years. At loads of up to 5 MPa, an additional decrease by 2 orders of magnitude is observed within 6 months. Various other experiments confirm the findings (HG-A, MB etc.).	Open fractures in the EDZ seal by contact with water (swelling) and by increasing the normal effective stress.	Nagra (2002), Marschall et al. (2017)
Mont Terri rock laboratory	FS experiment: rapid reduction of transmissivity by 2 orders of magnitude after stimulation (pressure pulse) at the "Main Fault", followed by a slow reduction and closure at sustained rate over a period of approximately 1 year.	Confirmation of the findings from the Selfrac experiment. Empirical evidence from EDZ can be transferred to larger fault zone.	Soom et al. (2021)
RHE1 deep borehole, 580 m depth	Head injection test: Increase in transmissivity by approx. 3 orders of magnitude by increasing pore pressure until reactivation of an existing disturbance. After reduction of the pore pressure, the transmissivity drops back to the level before stimulation (see Section 5.7.4).	Transmissivity only elevated near fracture opening pressure. High transmissivity only maintained at high pore pressure.	Dossier VII of Nagra (ed.) (2023b) and Section 5.7.4 of this report

The knowledge base is further supplemented by analogue studies of similar rocks:

- In particular, the Callovo-Oxfordian Claystone from the French investigation programme (e.g. OECD/NEA 2022, Wang et al. 2022, Zhang & Talandier 2023) with very similar hydro-mechanical properties to the Opalinus Clay.
- Experiments in the Tournemire rock laboratory with Toarcian-Domerian claystones (OECD/NEA 2022, Donzé et al. 2023).
- Very broad literature documenting clay-rich rocks (shales) with similar mineralogy and basic properties as to the Opalinus Clay acting as top seals or cap rocks of conventional hydro-carbon reservoirs over geological timescales (e.g. Fisher et al. 2013, 2023).

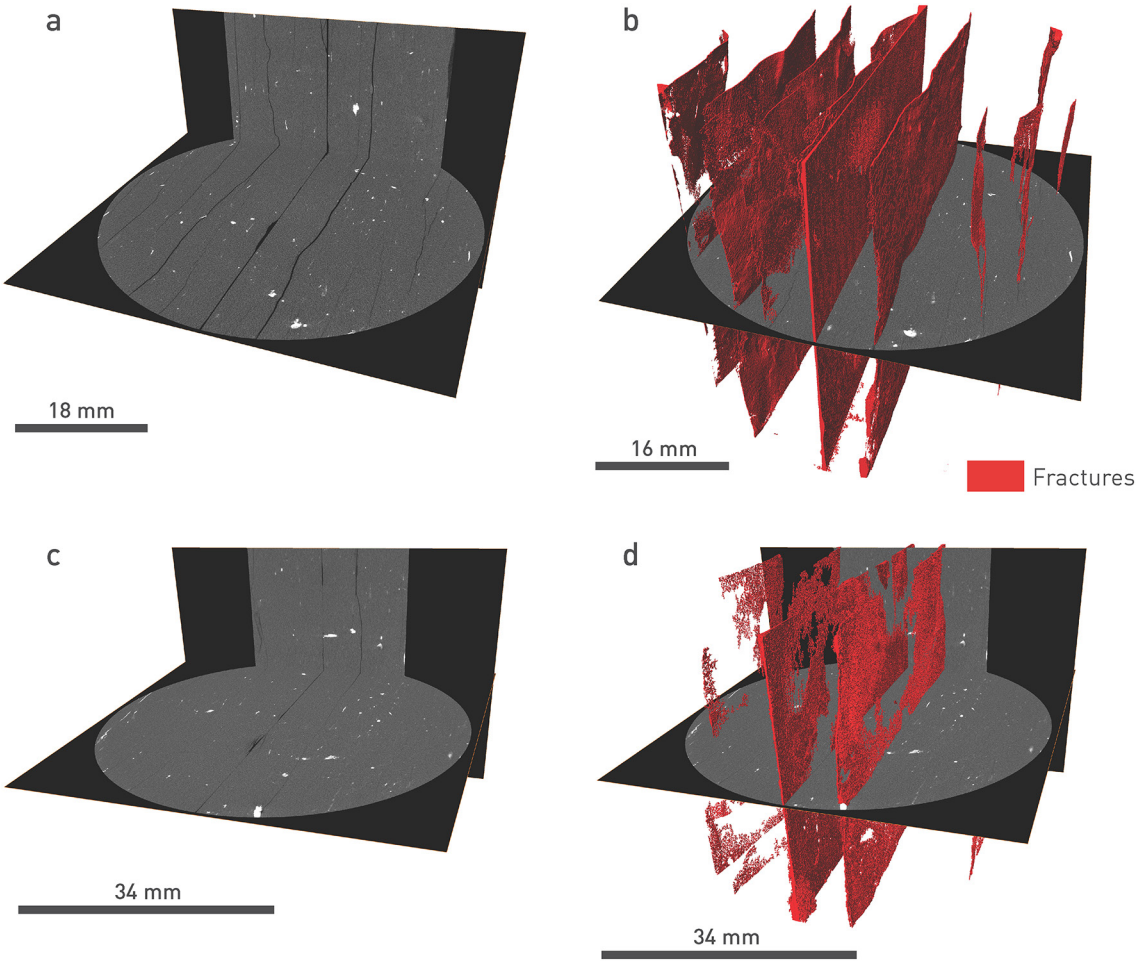


Fig. 5-45: Experimental evidence of self-sealing in laboratory experiments

X-ray images at the beginning (a), (b) and about 2 days after water injection (c), (d), with (b) and (d) illustrating the reconstructed 3D image of the fractures in red. The apertures of the original fractures (up to 200 µm) in (b) reduce partly to below the imaging resolution of about 30 µm in (d). Experimental details can be found in Seiphoori (2019a).

In contrast to cap rocks, the clay-mineral content and porosity in gas resource shales is much lower, and deformation response more brittle. However, successful production of gas from resource shales generally relies on injection of proppants to maintain flow after fracturing, demonstrating relatively rapid closure even in shales with low self-sealing potential (Fisher et al. 2013, 2023).

5.7.3 Relevant processes and mechanisms

The mechanisms contributing to self-sealing are of both physicochemical and hydromechanical nature. Bock et al. (2010) provides an empirical basis and some conceptual background for self-sealing in clay-rich rocks considered as host rocks for a deep geological repository.

For the Opalinus Clay, self-sealing processes were described in an earlier report by Nagra (2002). Since then, the understanding has been enhanced significantly, particularly at the Mont Terri rock laboratory, and using core material from the Schlattingen-1 (SLA1) deep borehole, drilled near the ZNO siting region. The summary of process understanding presented hereafter is based on the above-cited works, as well as on Mitchell & Soga (2005) and Laird (2006).

The fundamental pre-condition for self-sealing to occur is the generation of dilatant fractures (mode I or mixed mode I and II fractures, see Fig. 5-24) in a preceding deformation event. Development of these fractures is locally associated with a change in the fluid pressure and the stress state. Phenomenologically, self-sealing leads to progressive reduction of the fracture aperture, but the underlying processes involve a volumetric expansion of the rock mass in the vicinity of the fracture (or system of fractures). These key processes are of hydromechanical and physicochemical nature and act either (i) mainly at the fracture surface, or (ii) in the (intact) rock behind the fracture wall. In both cases, the main factors controlling the changes to fracture aperture are the changes in total stress, and the changes in fluid pressure in the fracture and the pore pressure in the rock matrix.

Along the fracture surface, changes in fluid pressure can equilibrate rapidly compared to the pore pressure in the rock matrix, especially at very low effective stress. In the case of fluid injection (e.g. injection tests, Section 5.7.4), the fluid pressure acts orthogonally to the fracture surface (i.e. the normal stress) and forces the opening of the fracture. However, in the absence of active injection, pore pressure in the fracture and behind the fracture wall will decrease with dilation associated with fracturing because of the low compressibility of water. Negative pore pressure (suction) could also develop.

At the end of active injection, once fluid pressure decreases, an increase in the effective stress along the fracture occurs and generally results in rapid closure. The response to the effective stress changes depends on the hydromechanical properties of the rock. Clay-rich rocks, and the Opalinus Clay in particular, have a relatively low stiffness and a capacity to deform plastically. The compliance of the material leads to the deformation of asperities along the fracture surface (e.g. contact points), which further favours the decrease in fracture transmissivity. In contrast, the rough surfaces of more competent rocks can sustain much higher stresses without a significant reduction in transmissivity.

In contrast, pore pressure in the adjacent rock behind the fracture wall changes slowly because of the low conductivity (low pressure diffusivity) of the intact Opalinus Clay. A reduction in fluid pressure (or suction increase) in the dilatant fracture generates a gradient in the fluid pressure from the adjacent rock (higher pore pressure) towards the fracture, enhancing the effective stress reduction and therefore the volumetric expansion (Section 5.5.2). At the particle level, mechanisms typical of expansive geomaterials such as clays in contact with water and brine occur. These are the crystalline swelling between clay-particle stacks (water hydration) and double-layer

swelling because of the repulsive electrostatic forces within the quasi-crystals (Laird 2006, Bourg & Ajo-Franklin 2017). These mechanisms also affect the clay minerals of the asperities at the fracture wall, and further contribute to fracture closure (Fang et al. 2017).

Swelling is considered the key process of fault transmissivity reduction over longer timescales of in-situ tests (months to years, e.g. Marschall et al. 2017, Soom et al. 2021). As emphasised in Fig. 5-23, the expansion is enhanced at low effective stress. Osmotic pressure gradients can further contribute to water movement. In partly saturated conditions, e.g. in the excavation damage zone (EDZ) of the tunnel, suction can also be an important driver from higher saturation rocks (the undisturbed rock mass) to those of lower saturation (the EDZ). Saturation increase also causes effective stress reduction and therefore volumetric expansion of the rock.

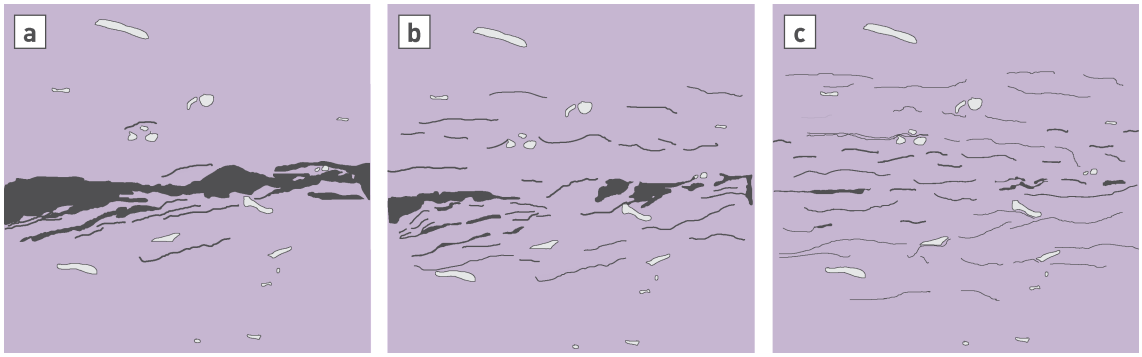


Fig. 5-46: Concept of self-sealing sequence in the Opalinus Clay

Fracture aperture in black, larger clastic grains in white, clay matrix in light grey: (a) Initial condition with existing large fracture in the centre. (b) Fracture closing comes at the expense of material expansion in the vicinity of the fracture where effective stresses can be particularly low (locally "unstressed fracture surface"). This creates new fissures and leads to material disintegration. (c) Further closure can lead to fissuring deeper into the initially undamaged rock, but this will be closed in a similar fashion. Drawing based on a synchrotron X-ray micro-tomography study of Voltolini & Ajo-Franklin (2020).

Self-sealing of faults and joints is typically accompanied by the formation of smaller subsidiary fractures in the intact rock (e.g. Seiphoori 2019a, Wenning et al. 2021b, Voltolini & Ajo-Franklin 2020, Di Donna et al. 2019, Crisci 2019) to compensate for the initial fracture porosity (Fig. 5-46). This is because of the locally unconstrained surfaces along the fracture, which can lead to swelling beyond the elastic limit and induce new fractures. Hence, the main fracture closes, but the fractured zone grows into the intact rock. Smaller fractures then close in similar fashion and self-sealing is complete when a hydromechanical and hydrochemical equilibrium is achieved in the near-field of the fracture. Hence, the initial fracture aperture is compensated by disintegration of the rock in a wider zone, and finally a homogenisation and local increase in "matrix" porosity compared to the undisturbed porosity. However, a local increase in matrix porosity equates to only very small or negligible changes in the overall transport properties (Section 5.7.5).

Additional mechanisms can further contribute to the sealing of fractures, but their contribution is subordinate to those described above. These involve "creep" defined as secondary compression (i.e. volumetric deformation with time at constant effective stress; Favero et al. 2016, Crisci et al. 2021) or the precipitation of secondary minerals ("veins", Section 5.7.6).

5.7.4 Importance of effective stress for robust self-sealing

Whereas the clay-mineral content exerts strong control on the swelling capacity of the Opalinus Clay (Section 5.5.2), a sufficient overburden thickness (Section 5.6.3) or critical effective normal stress is also required for robust self-sealing.

Experiments at Mont Terri and the Tournemire rock laboratories have shown that a relevant increase in fracture transmissivity is only obtained at very low effective normal stress on the fracture surface (Marschall et al. 2017, Donzé et al. 2023, Guglielmi et al. 2020) (Fig. 5-47). This "threshold" is referred to as fracture opening pressure (FOP) and was constrained at approximately 1 – 2 MPa. In Fig. 5-47, FOP is indicated in terms of the corresponding effective stress level.

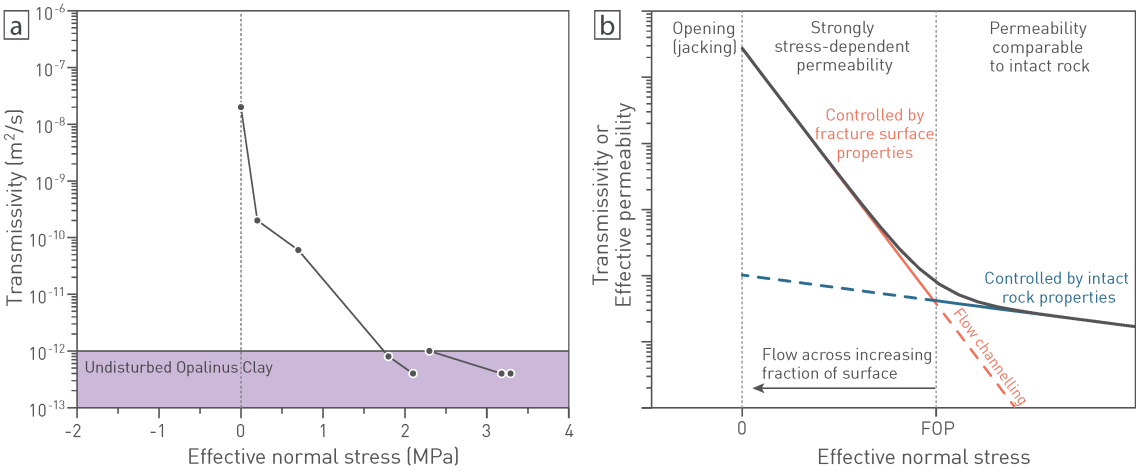


Fig. 5-47: Dependence of fracture transmissivity on the effective normal stress

(a) Example of the GS experiment at Mont Terri (Marschall et al. 2017). (b) Conceptual understanding of flow regimes (modified after Donzé et al. 2023).

Conceptually, the FOP separates an effective permeability field at high effective stress, which is only marginally dependent on stress, from a field at low effective stress, which is strongly dependent on effective stress (Fig. 5-47b). As the FOP is approached from initially higher effective stress, local dilatancy can occur, subsequently connecting dilatant parts of the fault and channelling fluid flow. Once fluid pressure achieves the critical value (FOP), transmissivities can increase by several orders of magnitude, as the effective confinement on the fault is gradually removed. It is important to note that the FOP is considered as a conceptual transition point, but absolute transmissivities may remain low (e.g. $T < 10^{-10}$ m²/s at 0.5 – 1 MPa) before effective opening at close to zero effective stress (Fig. 5-47a).

This conceptual understanding was recently confirmed in dedicated hydraulic tests in the Opalinus Clay in the RHE1 borehole at approximately 580 m depth below ground (Dossier VII, RHE1, Nagra (ed.) 2023b) (Fig. 5-48). The test suite consisted of stepped-constant differential head injection tests (HI), followed by a withdrawal test applying constant differential head (HW) in an interval consisting of several fault planes with typical azimuth of 130° and main dips of 30 to 60° (Dossier V, RHE1, Nagra (ed.) 2023b).

Even after raising pore fluid pressure by more than 3 MPa in the test interval, no significant change in the flow rate was observed (point HI303 in Fig. 5-48a). The stress field at the depth interval can be estimated from 3D geomechanical numerical modelling (Section 4.3 and Nagra 2024o). This is depicted by Mohr circles as initial condition in Fig. 5-48b, where different circles represent the uncertainty in the total stresses (pore fluid pressure in the formation is assumed to be hydrostatic), and the dark grey circle as the average. The minimum value of the "failure" envelope of the fault planes can be estimated from post-peak strength of triaxial tests (Fig. 5-27b). As illustrated in Fig. 5-48b, the corresponding average Mohr circle prior to raising the fluid pressure is at safe distance from the failure envelope.

After increasing the pore fluid pressure to more than 5 MPa in the test interval (point HI306), the Mohr circle approximately intersects with the failure envelope, especially considering the uncertainties in the stress field. This is associated with a flow rate increase by 1 – 2 orders of magnitude. Furthermore, the effective normal pressure of the fault planes with dips of 30 to 60 degrees (indicated by dashed lines on the Mohr circle) at this stage was approximately 2 MPa, in good general agreement with a FOP as constrained in Mont Terri.

Fault opening is indicated with a progressive interval pressure drop after the HI306 phase, despite increasing the flow rate by nearly one order of magnitude. This was then followed by a pressure recovery after a constant head withdrawal test (HWS), where the pressure equilibrated to approximately 1 MPa above hydrostatic. The subsequent HW phase again allowed measurement of the flow rate, demonstrating major reduction to close to pre-stimulation values. The high transmissivities observed in the in-situ experiments (RHE1 and underground laboratories) followed by rapid reduction when injection is stopped is consistent with rapid pore fluid pressure equilibration across the fracture plane (Section 5.7.3). Over longer periods of time (months to years), "swelling" will dominate the self-sealing process and further reduce fracture transmissivity (Section 5.7.3).

Assuming a typical effective stress gradient of 0.01 – 0.015 MPa/m, a very similar range of effective stress (2 – 3 MPa) is reached for a FOP threshold at approximately 200 m overburden thickness. This is consistent with packer test results (Fig. 5-41) and observations of water ingress and damp spots in tunnels (Gautschi 2017; Section 5.6.4).

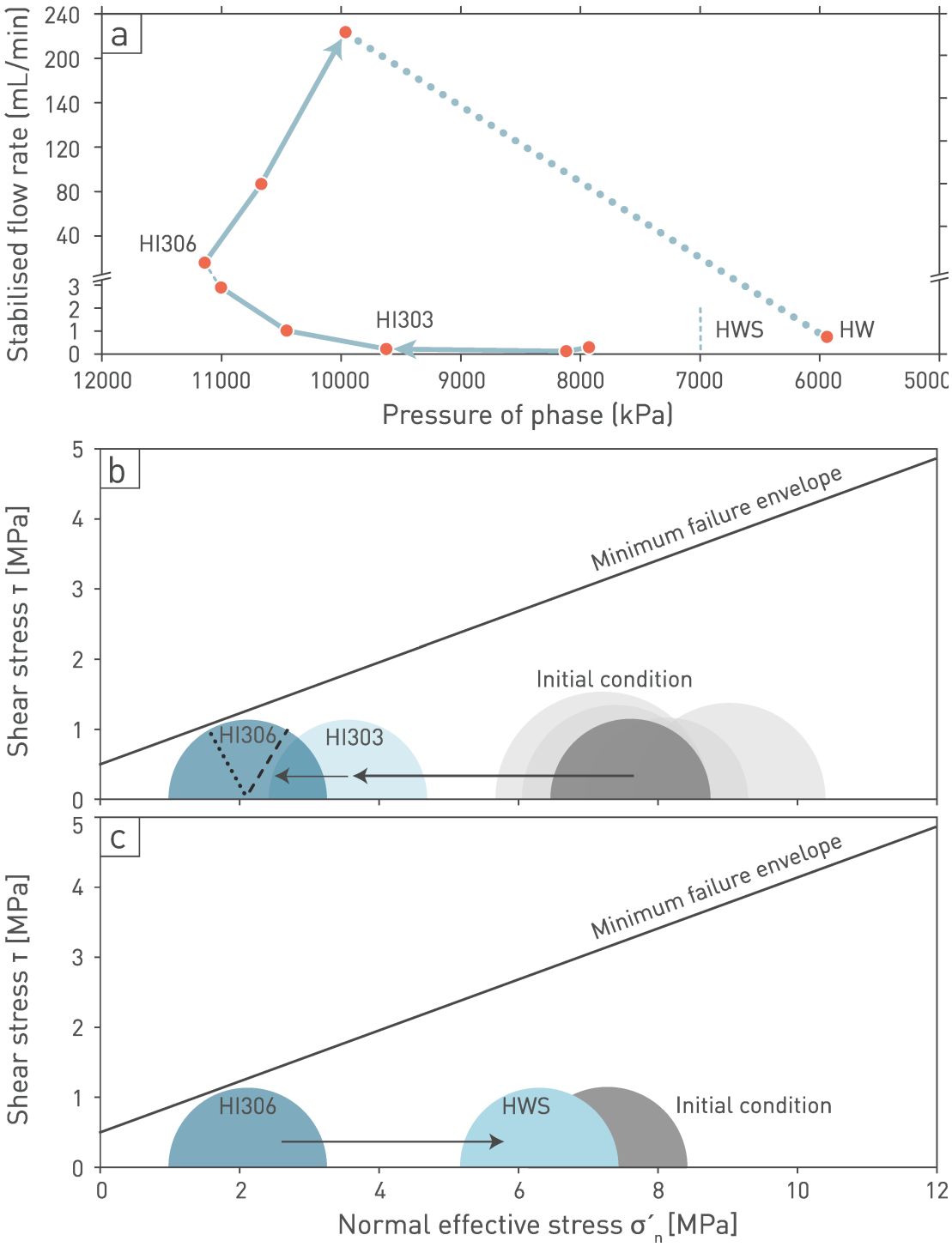


Fig. 5-48: Relationship of fault-related flow and effective stress in the Opalinus Clay at the RHE1 borehole at approximately 580 m depth below ground

(a) Flow rate as a function of interval pressure (Nagra (ed.) 2023b, Dossier VII, RHE1). (b) and (c) show changes to the effective stresses and relationship to the Opalinus Clay minimum failure envelope as constrained from triaxial testing (Section 5.5.3). Mohr circles show stress field according to stress modelling results (Nagra 2024o). Dashed lines in figure (b) depict positions of fault dips between 30 and 60° on the Mohr circles. HI: constant head injection test, HW: withdrawal test (applying constant differential head), HWS: pressure recovery after constant head withdrawal test.

5.7.5 Influence of other factors on the self-sealing potential

To summarise the points above, the critical factors for robust self-sealing are i) availability of water or brine, ii) a minimum effective stress, and iii) sufficient clay minerals in the rock matrix (Fig. 5-22). Points ii) and iii) relate predominantly to the swelling mechanism, which in turn may be influenced by other aspects that are briefly discussed here.

Water chemistry: It is standard practice at the Mont Terri rock laboratory to use only compressed air as "drilling fluid" to evacuate cuttings, because water-based drilling fluids are known to result in swelling and disintegration of the borehole wall. The water chemistry, or concentration of ions in the porewater (also termed ionic strength), exerts a certain control on the swelling behaviour of clays, affecting mainly the osmotic swelling (Madsen & Müller-Vonmoos 1989). However, studies on more compacted clay-rich rocks, and on the Opalinus Clay in particular, have demonstrated that salinity has a moderate influence on swelling capacity unless water with very different chemistry to the in-situ porewater chemistry (Section 5.4.3) is used (Hauber et al. 2005, Ewy 2015, Delage & Belmokhtar 2022, Favero 2017, Barakat et al. 2024), and the porewater in the Opalinus Clay is chemically buffered (Section 5.4.6). Conversely, immersion tests showed rapid swelling and degradation of the Opalinus Clay even with a balanced porewater (Seiphoori 2019a). Hence, swelling can only be prevented when non-reactive fluids are used (Ewy 2015, Wenning et al. 2021a). For this reason, non-polar, non-wetting and volatile hydrocarbons are also used for gentle sample preparation for laboratory tests.

Clay mineralogy: The more actively swelling clay minerals in the Opalinus Clay and the clay-mineral-rich confining units are the smectite-illite (Ill/Sm) interlayers, with approximately 20 – 25 wt.-% of total clay minerals. The amount of the smectite endmember is approximately 6 – 8 wt.-%, and this proportion is fairly constant in the Opalinus Clay both in the vertical direction and between boreholes and sites (Section 5.2.4). However, as pointed out by Madsen & Nüesch (1989), swelling is related not only to the activity of clay minerals but essentially to the water-accessible clay mineral surface, and therefore non-active clay minerals (e.g. kaolinite) also contribute to the process, but to a much lesser extent.

Temperature: Experiments on fractured Opalinus Clay and Callovo-Oxfordian claystone have demonstrated no significant effect on the swelling behaviour of samples heated up to 90 °C, other than the expected change in hydraulic conductivity because of viscosity change (e.g. Zhang 2013, Favero et al. 2016, Favero 2017, Gbewade et al. 2024). A temperature of 90 °C is roughly comparable to the maximum temperature that can be expected by future thermal loading in the vicinity of high-level waste drifts (Bosch et al. 2023). The maximum temperature of the Opalinus Clay in its geological history was slightly higher (just above 100 °C, Sections 4.3.5 and 4.7.4).

Fault gouge material: The bulk of the evidence from laboratory and in-situ tests detailed above relates to discrete fractures or displacement surfaces. Larger faults or fault zones additionally consist of variable, sometimes highly fractured and de-structured rock from mechanical wear ("fault gouge") with a higher porosity than the strongly compacted intact rock (e.g. Nagra 2002, Orellana et al. 2022). Similarly, swelling in the vicinity of fractures can de-structure the rock and lead to an overall porosity increase in the matrix (Fig. 5-45). Laboratory tests with ground and remoulded Opalinus Clay have demonstrated swelling indexes of approximately 0.03 to 0.08, i.e. approximately one order of magnitude greater than for intact material (Fig. 5-22; Favero et al. 2016, Crisci et al. 2019). The stronger swelling can be explained by the mechanical grinding process removing diagenetic features such as grain interlocking and bonding.

As emphasised in Section 5.7.3, swelling is associated with a local increase in porosity to compensate for the fracture-related void increase. Crushed and recompacted Opalinus Clay was also used to estimate corresponding conductivity values at different stages of compaction. These tests show very low hydraulic conductivities even at much greater (matrix) porosities than those observed in natural examples (boreholes and Mont Terri). Although the method of grinding and

compacting the material and the mineralogy led to some variability, it is found that, even for a porosity of 0.30, the hydraulic conductivity remains very low (< 1×10^{-11} m/s; Fig. 5-49). A value of 0.30 would be higher than the porosities reported for fault gouges in the Opalinus Clay at Mont Terri (< 0.23; Orellana et al. 2022, Nagra 2002).

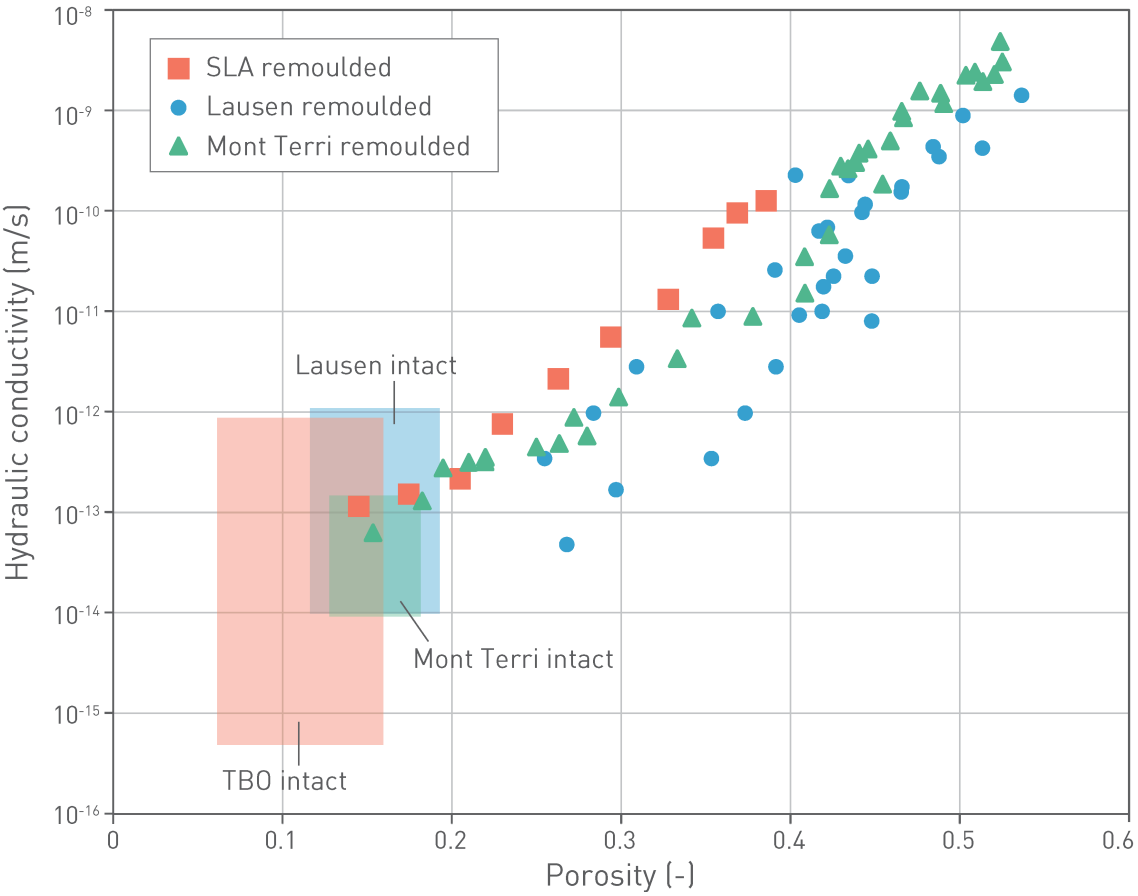


Fig. 5-49: Relationship between porosity and hydraulic conductivity in crushed and recompacted ("remoulded") Opalinus Clay

Individual points show results at different stages of reconsolidation (compilation after Seiphoori 2019b). Data points from Lausen cover two different tests. Rectangles show values of intact Opalinus Clay by provenance for comparison.

5.7.6 Relevance of veins for self-sealing potential

Mineralised fractures (veins) in the Opalinus Clay are found in all boreholes of the TBO programme (Sections 4.7.4, 4.7.5 and 5.5.4). They are very thin (> 90% are thinner than 2 mm; Sections 4.7.3 and 5.5.4), macroscopically closed and show no detectable effect on the results of hydraulic testing (Section 5.6.3). Larger veins (up to centimetres in thickness) as depicted in Fig. 5-31 are extremely rare and vary strongly in thickness and continuity even at the core scale.

Veins are observed in clay-rich rocks or shales worldwide (e.g. Cobbold et al. 2013, Gale et al. 2014). They are typically interpreted to have formed by precipitation from supersaturated aqueous solutions in the dilatational fractures (e.g. Bons et al. 2012), with precipitation and mineral growth leading to clogging of voids and essentially acting as a sealing mechanism (Bock et al. 2010;

Section 5.7.3). However, mineral growth may also have been concurrent with fracture opening, as has been proposed for bedding-parallel «beef» structures in shales (Cobbold & Rodrigues 2007, Cobbold et al. 2013), that is with no open space for veins to grow into. Irregular, multi-stranded veins have also been considered to represent dewatering structures during early burial of fluid-overpressured mudstones (Lorenz & Cooper 2018). What all the models seem to have in common is that the local effective stress at the time of vein formation was probably quite low to allow for volume expansion (Fig. 5-24), either with or without fluid overpressure.

Low effective stress conditions can occur during the early stage of burial, especially during rapid sedimentation (Section 4.1) and burial as inferred for the Middle Jurassic (Section 4.3.5). Together with the apparent thermal anomaly in the Late Jurassic to Early Cretaceous, this has probably caused temporary fluid overpressure from disequilibrium compaction. The geochemical signature of vein cements from the Lias and Dogger Groups and formation temperature (Akker et al. 2023) are consistent with such a conceptual model. Also, some of the matrix cement in the Opalinus Clay is attributed to such an early phase of burial (Section 5.2.5). Another phase of rapid burial occurred during the Oligocene and Early Miocene (Section 4.3.5).

Fluid overpressure may also have been triggered from the transformation of mineral reactions. For the Opalinus Clay, this could mainly concern the smectite to smectite-illite transformation with release of structurally bound water (Nadeau et al. 2005).

Tectonic loading may also have increased pore fluid pressure in the Opalinus Clay, provided that the loading rate was fast enough with respect to the drainage capacity or fluid dissipation rate (Section 5.5.3). But, as highlighted in the conceptual figure in Section 4.4, lateral tectonic loading has a stronger effect on stresses in the more competent layers (Malm, Keuper and Muschelkalk Groups). In other words, the stress field in the Opalinus Clay is somewhat shielded by these more competent layers. A certain degree of plastic deformation was also accommodated in the Opalinus Clay during the Miocene to present-day shortening.

There are substantial quantities of calcite in the Opalinus Clay (Section 5.2) and the porewater in the Opalinus Clay today is saturated in calcite and could therefore provide a local source for vein precipitates (Section 4.7). However, it remains unclear whether the existing veins formed in a closed system. Veins in the Opalinus Clay formed at higher or much higher temperatures than the present-day in-situ temperature, with plausible formation ages greater than 5 million years (Section 4.7.4), with most veins probably forming during the Late Jurassic – Cretaceous, and later during Eocene – Miocene times (Section 4.3.5).

Vein formation in the Opalinus Clay at low effective stress is also consistent with a minimum effective stress threshold required for robust self-sealing (see Section 5.7.4). Fracture closure is expected to occur quickly if low effective stress (high fluid pressure) is not maintained, and the rate of swelling is dependent on water supply. If the latter is slow, swelling is slowed down, but this can only occur in a tight ("closed") system, i.e. where water supply from the adjacent rock is low. In contrast, if water supply is ensured, a significant reduction in transmissivity will be fast, i.e. over days in laboratory experiments (e.g. Fig. 5-43) and weeks to months in field experiments (Nagra 2014d, Lanyon et al. 2014).

The rate of self-sealing by swelling also depends on the width of the fractures generated during deformation. But, as elaborated in Section 5.5, deformation in the Opalinus Clay is characterised by a relatively low brittleness (low softening, low dilation angle), and more distributed deformation with low fracture width. These aspects also favour rapid self-sealing.

In summary, keeping in mind that veins record the integrated burial and tectonic history since the time of deposition, the following conclusions can be drawn:

- Veins in the Opalinus Clay are rare, generally very thin, often discontinuous at core and outcrop scale and, because of soft-linked accommodation of deformation, are poorly interconnected, i.e. they are hydraulically insignificant.
- Their formation is probably associated with low effective stress conditions, which were particularly prevalent during early diagenesis and burial in the Middle and Late Jurassic, and again during the Oligocene and Miocene. As in the clay-rich rocks in the Lias and Dogger Groups, it is probable that many veins in the Opalinus Clay are old (> 5 Ma) to very old structures (> 100 Ma). This interpretation is also consistent with tracer profiles (Section 4.6), suggesting that transport is diffusion-controlled also across intervals of the Opalinus Clay containing veins.
- Today's porewater is saturated in calcite and could provide a local source of vein formation without the need for an external water source.
- At present depths in the siting regions, the effective stress conditions (Section 4.4) are well above the critical effective stresses of 2 – 3 MPa at which relevant modifications to the self-sealing potential could be expected (Section 5.7.4), and therefore the key mechanisms for robust self-sealing are expected to operate at the rate at which water can be supplied.

5.7.7 Conclusions

- As a result of the high self-sealing potential of the Opalinus Clay, and of clay-rich rocks in general, fractures have a much lower significance as a threat to barrier integrity than fractures in other low-permeability rocks also considered as host rocks for a deep geological repository (e.g. granitic rocks).
- Clay-mineral content is a very good indicator for the self-sealing potential of the Opalinus Clay and the confining units for the disposal depths considered in all the siting regions. Rocks with a clay-mineral content greater than about 40 wt.-% have a high self-sealing potential, and rocks with clay-mineral contents less than about 20 wt.-% have low or negligible self-sealing potential.
- At the tunnel scale (several metres), self-sealing potential in the Opalinus Clay is high throughout the formation at all the sites. In contrast, some facies in the confining units have low or even negligible self-sealing potential over distances much larger than the tunnel scale.
- The other key variable controlling the self-sealing potential is the stress field. The stress field can be considered favourable for robust self-sealing of the Opalinus Clay in all the siting regions at current depths.
- The timescale over which self-sealing mechanisms operate depends on the ability of the rock to equilibrate water pressure in the disturbed area. Fracture closure can occur immediately upon a reduction in fluid pressure (or effective stress) and is followed by slower time-dependent mechanisms (especially swelling) over days to years.
- For the long-term evolution of the repository, a residual overburden thickness of 200 m can be considered reliable for self-sealing in the Opalinus Clay. If the overburden thickness is reduced to 50 – 100 m, self-sealing may be limited, and if the overburden thickness is only 20 – 30 m, it is hardly or no longer effective.

5.8 Diffusion properties

Key points:

- In the Opalinus Clay, the diffusion coefficient for the water tracer HTO shows minor variation and is well comparable among the different sites. Owing to differences in porewater ionic strength, the effective diffusion coefficient D_e for chloride shows site-specific differences with lowest values in JO (more pronounced anion exclusion).
- The validity of diffusion properties is established at different scales of space and time: Consistent diffusion properties are observed in small-scale lab experiments and in-situ experiments in the Mont Terri rock laboratory.
- The laboratory diffusion coefficients contribute to plausible modelling of the formation-scale profiles of natural tracers in porewater that evolved over geological timescales.
- Diffusion properties can be estimated from clay-mineral content or porosity.

5.8.1 Overview

Hydraulic conductivities of the Opalinus Clay and the surrounding rocks are very low. Accordingly, molecular diffusion is an important, or even the major, process by which radionuclides may be transported towards aquifers.

The modelling of the diffusive solute flux relies on appropriate diffusion coefficients. Diffusion coefficients for weakly- or non-sorbing species are typically determined in the laboratory using small, centimetre-sized samples and experimental setups that last from weeks to a few months. Field experiments in underground rock laboratories provide larger spatial scales (dm – m) and longer timescales (up to a few years) to validate laboratory parameters. Finally, profiles of natural tracers from deep boreholes provide a possibility to deduce transport processes at the formation scale (Section 4.6). This section presents and discusses diffusion parameters obtained in laboratory and field experiments and relates them to other rock properties.

5.8.2 Diffusion properties at the laboratory scale (HTO and chloride)

This section forms the main basis for the parameterisation and process understanding.

At the laboratory scale, diffusion coefficients are most often estimated from through-diffusion experiments (e.g. Van Loon et al. 2023) that last over a few weeks to a few months. In such experiments, a rock sample with a thickness of one to a few centimetres is sandwiched between two solution reservoirs. The inlet reservoir is spiked with a tracer (e.g. HTO or ^{36}Cl), while the breakthrough and the flux of the tracer through the sample is observed in the outlet reservoir. One difficulty of such experiments is that the solution used in the reservoirs should match the porewater with respect to the main ions, to avoid geochemical reactions and effects of coupled diffusion of several ions (multi-component diffusion). From the analysis of the temporal evolution of the tracer flux, the effective diffusion coefficient D_e as well as the accessible porosity ε can be estimated. Slightly different setups exist that allow the diffusion coefficients to be derived either perpendicular or parallel to bedding.

Diffusion coefficients of solutes in rocks depend on the porosity of the rock and the tortuous pore pathway, and possibly also on interactions with the solid surfaces. The effective diffusion coefficient D_e of a non-sorbing solute can be given as:

$$D_e = \varepsilon D_p = \varepsilon \frac{D_w}{G}$$

with ε the (water-filled or accessible) porosity, D_p the pore diffusion coefficient, D_w the diffusion coefficient in bulk water, and G the geometric factor (often also called tortuosity) that depends on the pore structure and connectivity of the rock. The effective diffusion coefficient D_e is generally smaller than D_p as ε is smaller than 1. Because clays have negatively charged surfaces, anions are partly excluded from the pore space near the surfaces (Section 5.4). Thus, their accessible porosity is typically smaller than the water-filled porosity, and their tortuosity larger than that of a water tracer. As a result, the values of D_e and D_p of an anion (e.g. Cl) tend to be smaller than those of a water tracer (e.g. HTO), and the values of the geometric factor (tortuosity) G of an anion tend to be larger than those of a water tracer (conceptual model in Fig. 5-17).

No cation diffusion data are presented here. For the sake of completeness, it is simply noted that the negative surface charge of clay minerals is also responsible for the sorption of cations in clay-rich rocks, and thus diffusive transport of cations is typically retarded compared to diffusion of HTO. If non-specific sorption in the diffuse layer near charged surfaces is important (Fig. 5-17), the effective diffusion coefficient of cations such as, for instance, Na can be larger than that of a water tracer, as Na in the diffuse layer remains mobile and contributes to the total cation flux, in addition to the Na in the porewater. This effect depends on the ionic strength of the porewater (larger for low ionic strength, for instance Glaus et al. 2024).

A large number of laboratory diffusion experiments has been performed on samples from the deep drilling campaign in the three siting regions (Van Loon et al. 2024, 2023). Diffusion perpendicular to bedding was investigated. The HTO and ^{36}Cl diffusion coefficients perpendicular to bedding of all samples from the three regions are plotted as a function of depth (scaled to a reference profile for each region) in Fig. 5-50. The following is observed: D_e values for ^{36}Cl are lower than those for HTO, especially in clay-mineral-rich units. The differences tend to be larger for the JO siting region, which exhibits the lowest salinities of the porewater (Section 5.4). Both observations are related to the partial anion exclusion near the negatively charged clay-mineral surfaces, as noted above. The exclusion effect tends to be larger at the lower salinities in the JO region (lower salinities lead to thicker diffuse double layers that have low anion concentrations, or generally to larger anion exclusion, see for instance interpretation in Glaus et al. 2024). Lower diffusion coefficients of anions compared to those of the water tracer have already been reported in earlier studies for samples from the Opalinus Clay, Dogger Group above Opalinus Clay or Effingen Member in the Malm Group (see Table 2.6-1 in Nagra 2014f).

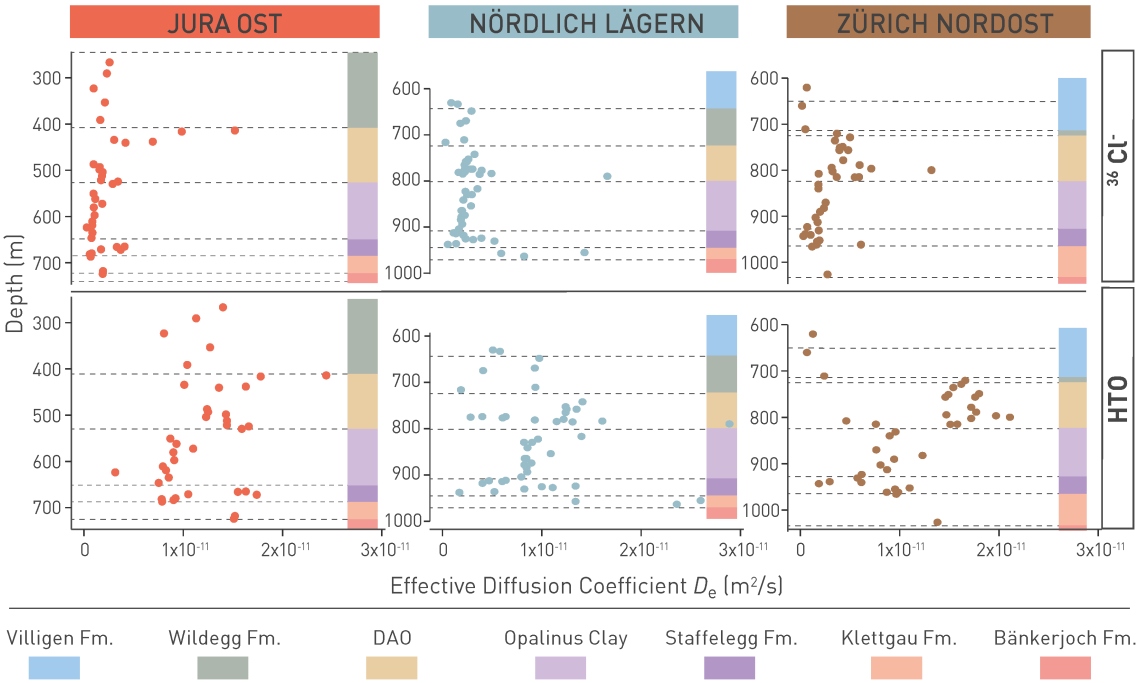


Fig. 5-50: Measured effective diffusion coefficients D_e for chloride and HTO of the investigated formations in the three siting regions

Measurements were done perpendicular to bedding. The samples of a siting region are projected to a reference profile: in the case of JO to BOZ1, in the case of NL to STA2 and in the case of ZNO to TRU1. DAO: Dogger Group above Opalinus Clay, Fm.: Formation.

Box plots illustrating the range of the diffusion coefficients D_e perpendicular to bedding obtained for HTO and Cl in the three siting regions are shown in Fig. 5-51. The data show again that D_e values for Cl are markedly smaller than those for HTO, especially in the Opalinus Clay. Furthermore, the diffusion properties of the Opalinus Clay scatter over a small range. Finally, D_e values for HTO are largely identical between different siting regions. For Cl, some region-specific differences result from different porewater salinities (ionic strength) as already noted above: D_e values of Cl in the Opalinus Clay are lower in JO than in other regions because of its lower salinity. For the less clay-mineral-rich units Dogger Group above Opalinus Clay and Lias Group, the D_e values of Cl scatter more, but no clear differences are seen between the different siting regions.

The anisotropy of diffusion in the Opalinus Clay from the Benken (BEN) borehole or Mont Terri was assessed with radial through-diffusion experiments in the laboratory. It is in the order of 4:1 to 6:1 (largest values for BEN), i.e. diffusion parallel to bedding is about a factor 4 to 6 faster than diffusion perpendicular to bedding (Van Loon et al. 2004a). This can be explained by the more tortuous pathway perpendicular to bedding, because the clay platelets have a large aspect ratio and tend to be aligned along the bedding.

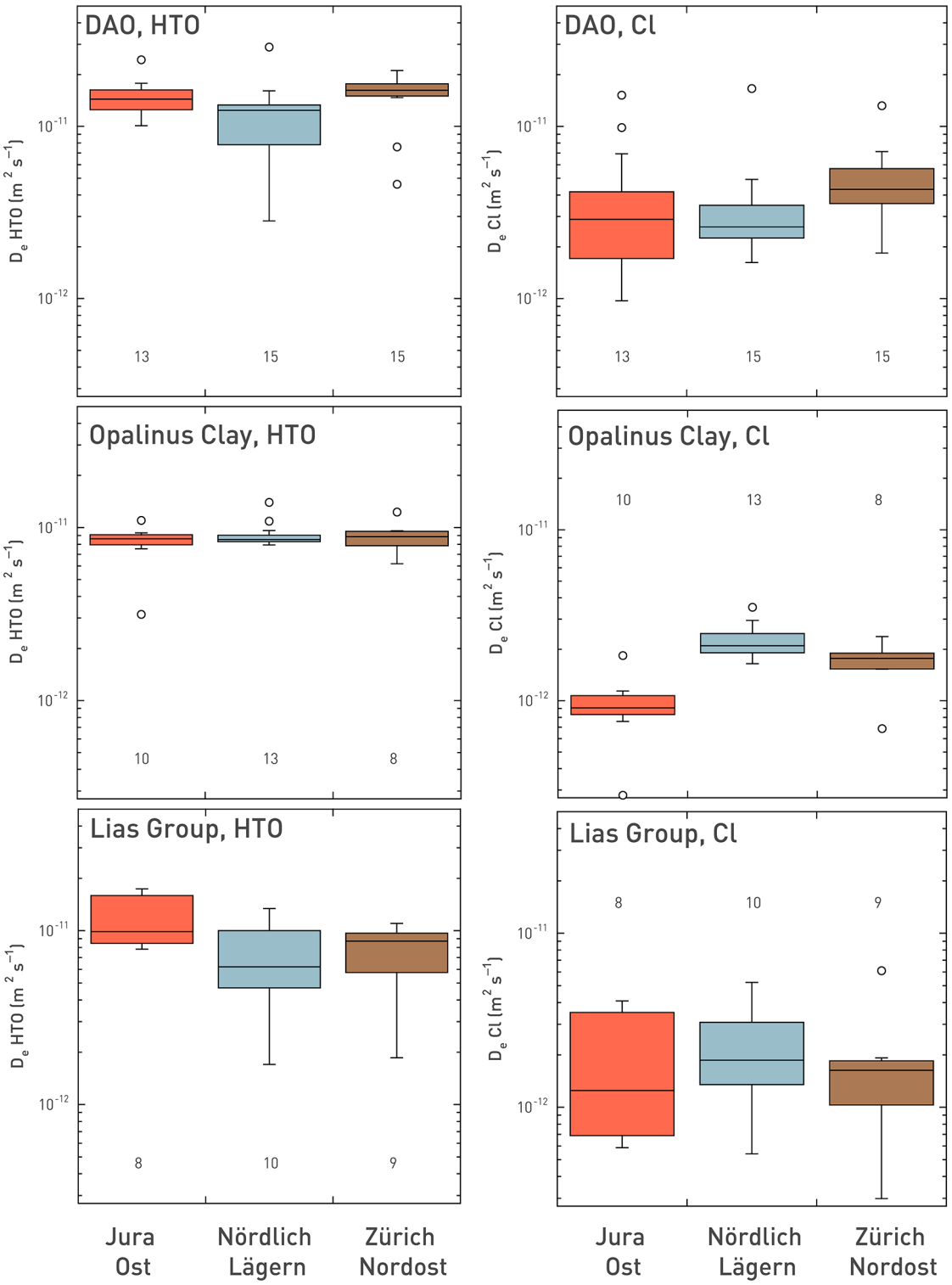


Fig. 5-51: Box plots illustrating the range of effective diffusion coefficients D_e for HTO (left column) and for Cl (right column), grouped by siting regions

Measurements were done perpendicular to bedding. DAO: Dogger Group above Opalinus Clay. Each box contains 50% of the values; the horizontal line shows the median, the whiskers the minimum and maximum values within an 'acceptable' range (from the upper or lower box limit to ± 1.5 times the box size), the circles values outside this range. The sample number for each group is also indicated.

The accessible porosities derived from the diffusion experiments with HTO and Cl are illustrated in Fig. 5-52. The results are also presented as box plots that show the typical range of values. It can be seen here that accessible porosities of HTO in the Opalinus Clay scatter over a small range and are very similar between the different siting regions. For the Dogger Group above Opalinus Clay and the Lias Group, the accessible porosities of HTO extend over larger ranges, which is related to the more pronounced lithological heterogeneity in these formations. The diffusion-accessible porosity of Cl in the Opalinus Clay is lower in JO compared to NL and ZNO, resulting from different porewater salinities (ionic strength effect). For the Dogger Group above Opalinus Clay and the Lias Group, the ranges are larger and no influence of the porewater salinity is seen.

Finally, the geometric factor G correlates with the clay-mineral content, both for HTO and for Cl (Fig. 5-53). The factor G becomes larger in a non-linear way with increasing clay-mineral contents. Thus, the D_e values inversely tend to become smaller with increasing clay-mineral contents. No simple relationship exists to fit all data. However, when excluding some outliers with comparably high tortuosity values (and corresponding low D_e), the relationship for G of HTO can be fitted for instance by an exponential function (R^2 of 0.77) or by a polynomial of degree 4 (R^2 of 0.79). Such a relationship can for instance be used to estimate G and then the diffusion coefficient D_e of a sample, provided its clay-mineral content and its porosity are available. Outliers with comparably large G values for HTO (and thus comparably low D_e values for HTO) are found in formations with specific pore configurations, such as the Rietheim Member containing considerable contents of organic matter, the Schambelen Member and the Beggingen Member of the Lias Group, or the Wedelstandstein Formation, the Passwang Formation, and the «Humphriesioolith Formation» belonging to the Dogger Group above Opalinus Clay. Many rock samples with comparably large G values for HTO (and thus low D_e) show at the same time some peculiarities in the pore-size distribution derived from N_2 adsorption.

Outliers with large geometric factors G for HTO tend to also have large tortuosities for Cl (and thus low D_e for Cl), with the exception of the two samples from the Beggingen Member and the Schambelen Member of the Lias Group. When excluding the same values as for the relationship for G for HTO (open symbols), the relationship for G for Cl can be fitted for instance by an exponential function (R^2 of 0.74) or by a polynomial of degree 4 (R^2 of 0.76). The geometric factors G for Cl for clay-mineral-rich samples are roughly a factor of 2 larger than those for HTO. For lower clay-mineral contents, the difference is smaller (about a factor of 1 – 2). This is related to the effects of anion exclusion in clay minerals, which lead to an increase in the tortuosity of the anion diffusion pathways compared to those for HTO in clay-mineral-rich samples.

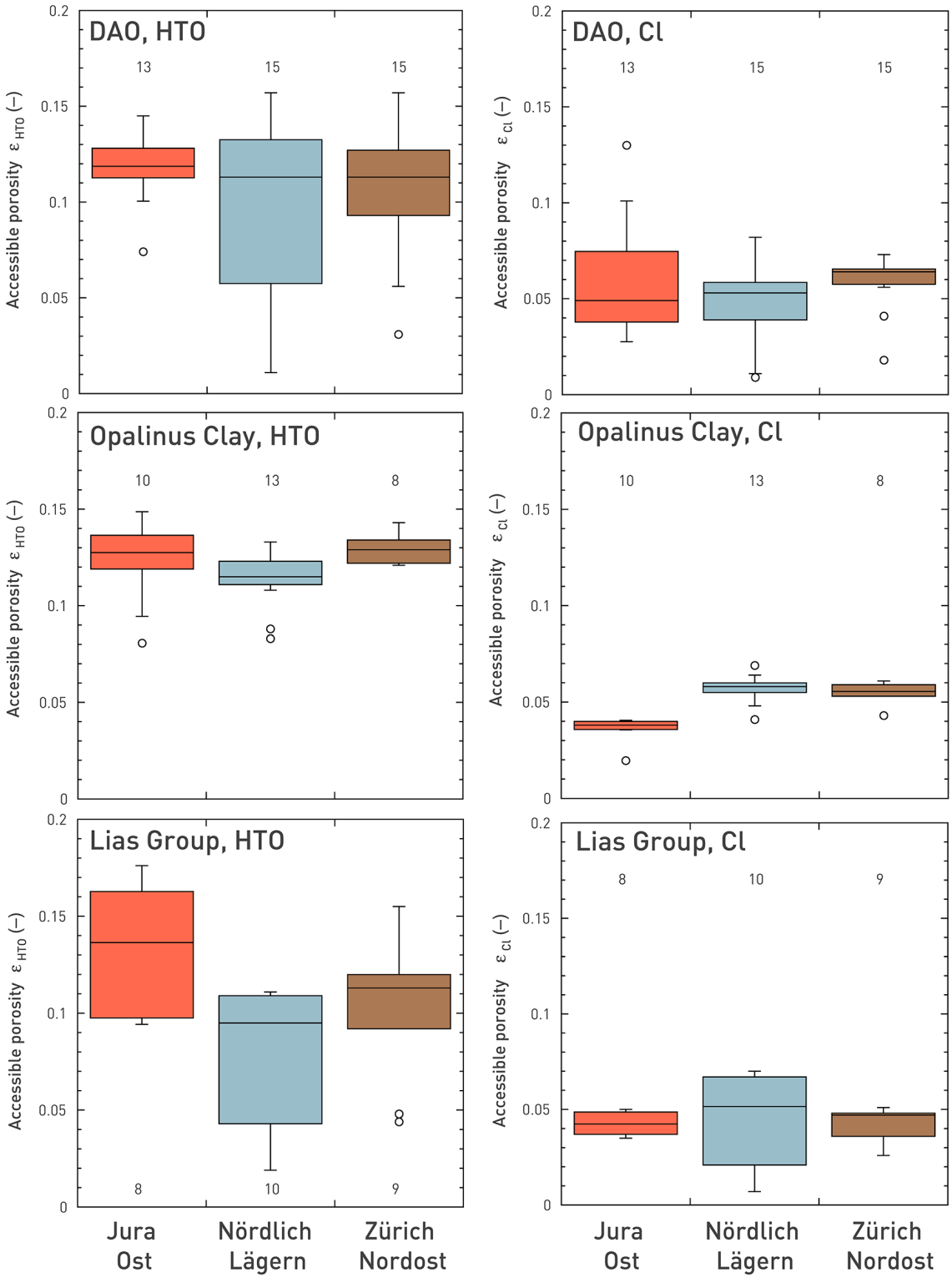


Fig. 5-52: Box plots illustrating the range of accessible porosities ε for HTO and for Cl, grouped according to the siting regions

DAO: Dogger Group above Opalinus Clay. Each box includes 50% of the values; the horizontal line shows the median, the whiskers the minimum and maximum values within an 'acceptable' range (from the upper or lower box limit to ± 1.5 times the box size), the circles values outside this range. The sample number for each group is also indicated.

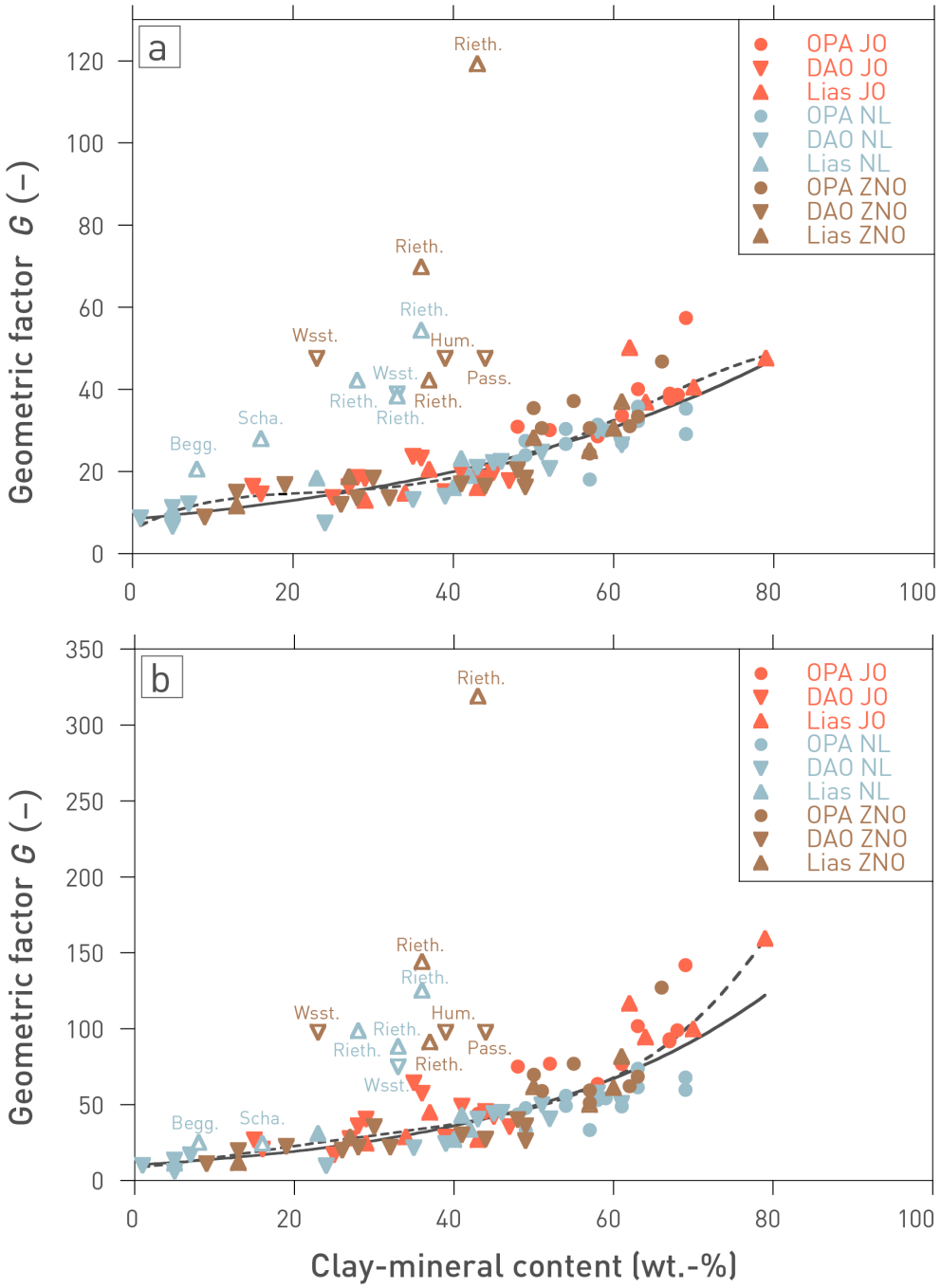


Fig. 5-53: Correlation of geometric factor G with clay-mineral content for HTO (a) and Cl (b) as a basis for estimating D_e of HTO and Cl for the Dogger Group above Opalinus Clay, the Opalinus Clay and the Lias Group

Measurements perpendicular to bedding. The solid line shows an exponential function, the dashed line a polynomial of fourth degree fitted to the solid symbols. Open symbols denote outliers defined as values with comparably high G for HTO (i.e. low D_e of HTO); they are located in the Rietheim Member (Rieth.), Schambelen Member (Scha.) and Beggingen Member (Begg.) of the Lias Group, and in the Wedelsandstein Formation (Wsst.), Passwang Formation (Pass.) and «Humphriesioolith Formation» (Hum.) of the Dogger Group above Opalinus Clay (DAO). In most cases, these outliers also have comparably high G for Cl (i.e. low D_e of Cl).

5.8.3 Diffusion at the underground rock laboratory scale

This section gives a short overview of results from in-situ diffusion experiments that typically cover larger scales than laboratory experiments (decimetre to metre, months to a few years).

In-situ diffusion experiments at the underground rock laboratory scale provide an important link between small-scale laboratory experiments and diffusion profiles at the formation scale (Altmann et al. 2012). They complement lab experiments by exploring a much larger rock volume under in-situ geochemical conditions (e.g. pH, redox, porewater composition) and in-situ pressures that are closer to the repository situation. Simultaneous diffusion in all directions (parallel and perpendicular to bedding) occurs during in-situ experiments, but – depending on the setup – diffusion parallel to bedding often dominates. In contrast, the substantial database from lab experiments contains mostly data normal to bedding. In-situ diffusion data for the Opalinus Clay exist from the Mont Terri rock laboratory as a result of a number of experiments carried out over the last ca. 25 years (Leupin et al. 2017). The first pioneering test was the DI experiment (carried out 1997 – 2001) where the basic design was developed (Palut et al. 2002, 2003). In this design, tracers (HTO, I^-) were continuously circulated between a reservoir and the borehole and were allowed to diffuse into the rock in a packed-off test interval via a porous screen. Tracers were monitored by regular sampling of the circulated solution. After termination, tracer profiles were analysed from the overcored sections. The DI design and methodology were successively refined in the later experiments (FM-C, DI-A1, DI-B, DI-A2, DR, DR-A) and additional non-reactive and reactive tracers were investigated (Gómez-Hernández et al. 2004, Wersin et al. 2006, Yllera et al. 2004, Wersin et al. 2010, Gimmi et al. 2014, Leupin et al. 2017, Soler et al. 2019; see also summary in Leupin et al. 2017). Most of the test boreholes were drilled straight down, i.e. oblique to the bedding (dip 30 – 45°) of the Opalinus Clay and had long test intervals (~ 1 m) such that diffusion parallel to the bedding plane dominated the experiments. The DR experiment was drilled perpendicular to bedding and, besides a short pressure monitoring interval at the bottom, had two short (0.15 m) test intervals (separated by ~ 40 cm) which allowed the effect of rock anisotropy on diffusion to be investigated. The FM-C test was carried out in the highly fractured "Main Fault". As for laboratory diffusion experiments, the solution composition in the reservoir (except for the second stage of the DR-A experiment) was chosen to more or less match the porewater with respect to the main ions, in order to prevent any geochemical reactions and avoid effects of coupled diffusion of several ions (multi-component diffusion).

All tests were accompanied by extensive modelling, yielding diffusion parameters including effective diffusion coefficients parallel to bedding, diffusion-accessible porosities, information on rock anisotropy (DR only) and sorption data. As mostly radioactive tracers were used in these experiments in a solution with a composition similar to the porewater (identical to laboratory experiments), individual tracers could be modelled separately. Tab. 5-3 summarises the diffusion parameters (D_e, ε) parallel to bedding obtained for conservative tracers (HTO, I^- and Br^-). Consistent values within their uncertainty ranges between the different in-situ tests are evident, regardless of their location, setup or diffusion time. The in-situ values are also consistent with those obtained from small-scale laboratory diffusion tests parallel to bedding with the Opalinus Clay samples from the Mont Terri (Tab. 5-3 and Fig. 5-54). The results from the DR experiments further confirm lab experiments regarding rock anisotropy. Thus, diffusion perpendicular to bedding in the Opalinus Clay from Mont Terri is lower by a factor of 3 – 5 relative to diffusion, parallel to bedding (Gimmi et al. 2014). The ensemble of results underlines the comparability between small-scale laboratory (e.g. Van Loon et al. 2004a, 2004b, Appelo & Van Loon 2008, Appelo et al. 2010) and larger-scale field experiments.

Tab. 5-3: Modelled diffusion data for the Opalinus Clay (parallel to bedding) for HTO, I^- and Br^- of in-situ diffusion experiments at the Mont Terri rock laboratory and comparison with data (parallel to bedding) from small-scale lab experiments with Mont Terri samples

Experiment	HTO		Iodide		Bromide		Anisotropy ratio	Duration	Ref.
	D_e	ε	D_e	ε	D_e	ε			
	$\times 10^{-11}$ m^2/s	–	$\times 10^{-11}$ m^2/s	–	$\times 10^{-11}$ m^2/s	–	–	yr	
DI-B	4 – 5	nc	0.83 – 1.2	nc				~ 1	[a]
DI-A1	5.4 – 6.5	0.17 – 0.2	1.2 – 2.0	0.08 – 0.09				~ 1	[b]
DI-A2	6.0	0.15	3.0	0.08	3.0	0.10		~ 1	[c]
DR-A	4.1	0.15	(1.2) [i]	(0.075) [i]				~ 0.5	[d]
DI	5	0.15	1 – 1.5	0.07 – 0.125				~ 1	[e]
FM-C	6.8	0.12	2.5	0.05				~ 0.7	[f]
DR	5.4	0.164	1.6	0.08	2.6	?	~ 5 (HTO) ~ 3 – 4 (I, Br)	~ 4	[g]
Lab exp.	5.4 – 5.7	0.1 – 0.17	1.44	0.06 – 0.08	1.7 – 4.5	0.08 – 0.15	~ 4	~ 0.1	[h]

[a] Yllera et al. (2004); [b] Van Loon et al. (2004b); [c] Wersin et al. (2008); [d] Soler et al. (2019), first stage; [e] Palut et al. (2003); [f] Tevissen & Soler (2003); [g] modelling in progress; [h] Van Loon et al. (2004b), Appelo et al. (2010); [I] D_e when assuming ε of 0.075; nc: not considered.

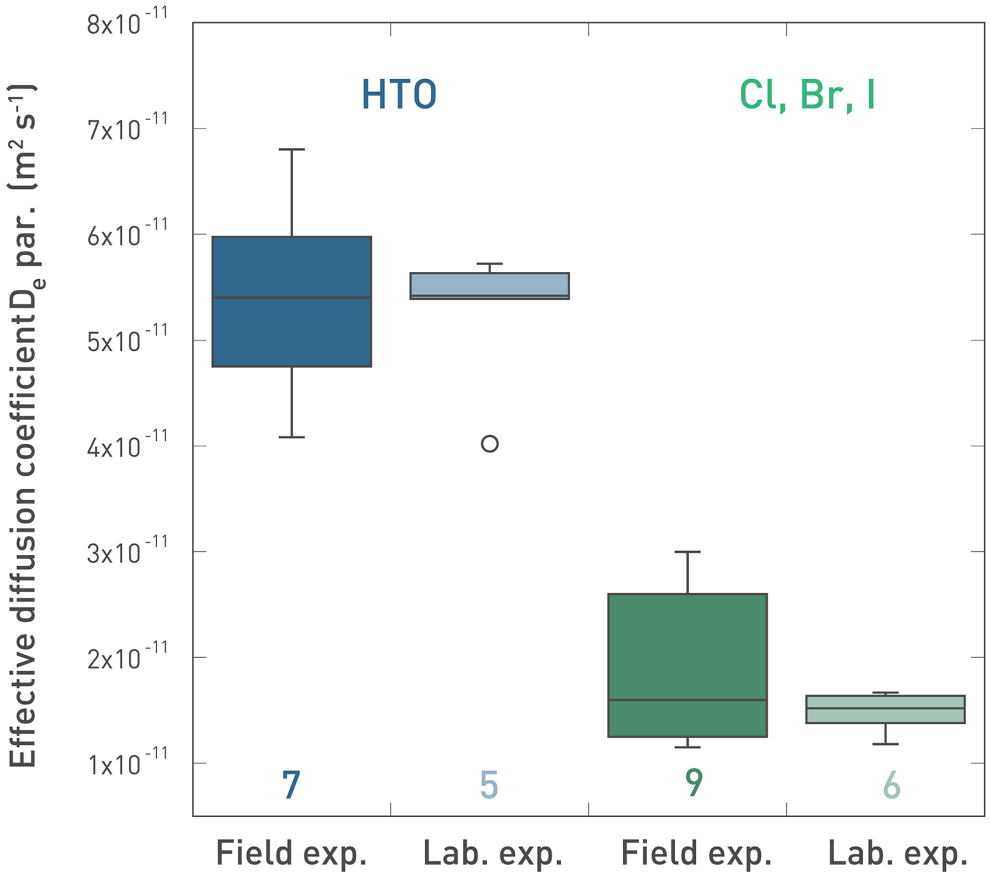


Fig. 5-54: Comparison of effective HTO and anion diffusion coefficients D_e for the Opalinus Clay obtained in Mont Terri field and laboratory experiments

Measurements are parallel to bedding. Laboratory tests were on small samples. Each box includes 50% of the values; the horizontal line shows the median, the whiskers the minimum and maximum values within an 'acceptable' range (from the upper or lower box limit to ± 1.5 times the box size), circles are values outside this range. The sample number for each group is also indicated.

5.8.4 Relevance at formation scale

Diffusion experiments cannot be performed at the formation scale because of time constraints. However, profiles of natural tracers (Section 4.6) offer an opportunity to test the applicability of transport properties derived in the laboratory on small samples. For instance, the observed profiles of stable water isotopes and of Cl in porewater in the Benken borehole have been modelled based on several assumptions. The following conclusions were drawn (Gimmi et al. 2007, Gimmi & Waber 2004): (1) No signature of advection could be detected in the profile shapes; the development of the profiles is dominated by molecular diffusion. (2) Using laboratory-derived diffusion coefficients adjusted for the higher in-situ temperature, an evolution time for the signature towards the Keuper aquifer consistent with the palaeo-hydrogeological history could be obtained. Thus, laboratory-derived diffusion coefficients are relevant also at the formation scale. Similar conclusions were drawn from a broad study that compared profiles of several natural tracers at various sites in several countries including the Mont Terri rock laboratory (Mazurek et al. 2011)

and from the recent modelling of profiles of e.g. stable water isotopes obtained in the three siting regions (Section 4.6). There, porosities and diffusion coefficients that vary with depth according to the measured laboratory parameters and the measured temperature trend for each site were used. This led to a good match with the measured tracer profiles for plausible timing of events (with respect to the palaeo-hydrogeological evolution) in each aquifer.

5.8.5 Comparison with data from other clay-rich rocks

The diffusion properties of the Opalinus Clay are comparable with those of other clay-rich rocks with similar porosity (Fig. 5-55). The porosity is related to the (maximum) burial depth, and the effective diffusion coefficient of a water tracer approximately follows a power law (Archie) relationship with the porosity.

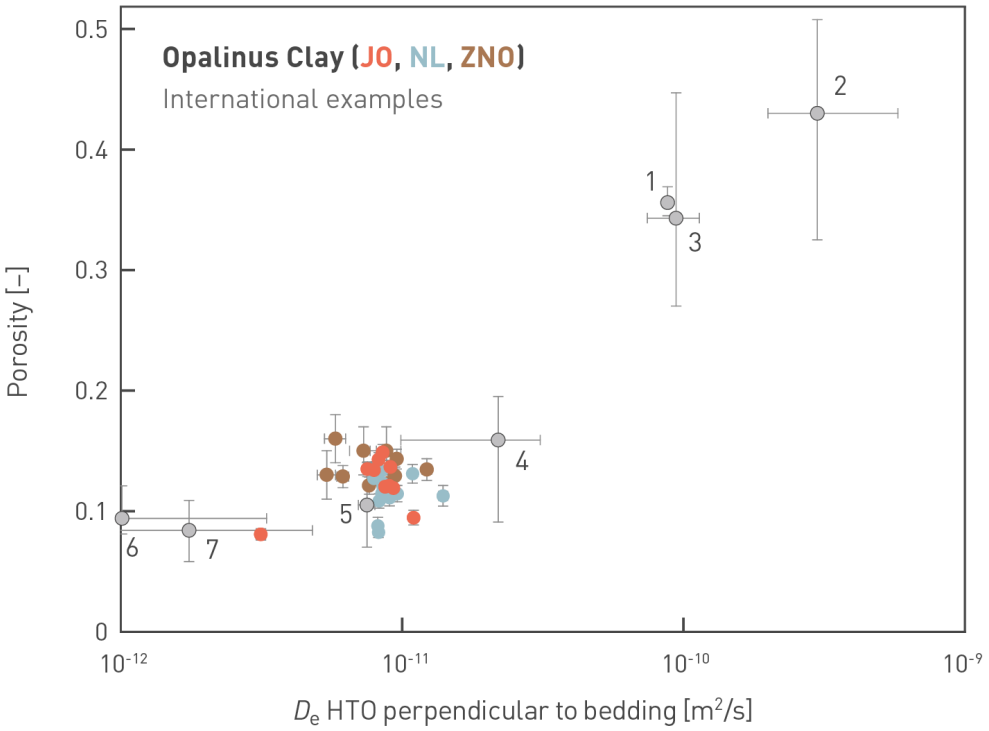


Fig. 5-55: Comparison of Opalinus Clay diffusion coefficients with data from other clay-rich rocks worldwide

D_e of HTO for Opalinus Clay from the JO, NL and ZNO siting regions plotted at the diffusion-accessible porosity. International examples are from the Clay Club Catalogue (OECD/NEA 2022) plotted at the indicated water-loss porosity. For the international samples, points indicate best estimates, bars represent minimum and maximum values. 1: Wakkanai Formation at Horonobe (JP, maximum burial depth: 1'200 m), 2. Ypresian Clay at Kallo/Doel (B, 450 m), 3: Boom Clay at Mol (B, 215 m), 4: Callovo-Oxfordian at Meuse/Haute Marne (F, UA unit, 850 m), 5: Toarcian-Domerian at Tournemire (F, 1'300 m), 6: Georgian Bay Formation at Bruce Site (CDN, 1'520 m); 7: Queenston Formation at Bruce Site (CDN, 1'450 m). Maximum burial depths as an indication for consolidation (best estimates or average values).

5.8.6 Conclusions regarding diffusion

- D_e values for HTO in the Opalinus Clay cluster within a small range and are almost identical for all three siting regions (Fig. 5-51).
- As a result of differences in porewater ionic strength, D_e for chloride shows site-specific differences, with lowest values in JO.
- The geometric factor G can be correlated to the clay-mineral content both for HTO and for Cl (Fig. 5-53). As (accessible) porosity is also correlated with the clay-mineral content (Fig. 5-11), D_e of HTO or Cl can be estimated from clay-mineral contents from Base Lias Group up to the Malm Group. Outlier lithologies can be identified and relate to rocks with special texture and pore architecture (pore-size distribution, pore connectivity) probably related to distinct diagenetic features, notably the Rietheim Member rich in organic matter («Posidonienschiefer»).
- The Dogger Group above Opalinus Clay and the Lias Group below the Opalinus Clay show more variability of diffusion properties, because of the more variable lithology (Fig. 5-51).
- For the Opalinus Clay, diffusion coefficients determined on small drill core samples in the laboratory match well with those derived from field-scale diffusion experiments in the Mont Terri rock laboratory (Fig. 5-54).
- The anisotropy factor for diffusion in the Opalinus Clay (values parallel to bedding compared to values perpendicular to bedding) is in the order of 3 – 6.
- Using laboratory diffusion coefficients (adjusted for increased temperature at greater depths) in simulations of the tracer profiles leads to good matches with the tracer profiles for plausible evolution times.
- No obvious scale dependence of diffusion properties of the Opalinus Clay between the lab, underground rock laboratory and formation scale was detected; local variations can be related to differences in the porosity or the clay-mineral content and the specific microstructure of samples from certain layers.

5.9 Dominant transport mechanisms in the Opalinus Clay

Key points:

- Molecular diffusion is the dominant transport mechanism in the Opalinus Clay and in adjacent low-permeability clay-rich rocks at formation scale.

The relative importance of diffusive compared to advective solute transport can be evaluated with the so-called Peclet number. This dimensionless number is defined as the ratio between the rate of advection to the rate of diffusion over a given characteristic length scale. Depending on the characteristic length used and the field of application, different definitions of the Peclet number exist in the literature (Huysmans & Dassargues 2005). To evaluate the importance of diffusion versus advection in the Opalinus Clay, a Peclet number similar to the one defined in de Marsily (1986) and Freeze & Cherry (1979) is considered:

$$Pe = \frac{|q|l}{D_e} = \frac{|v|l}{D_p}$$

where $|q|$ is the module of the Darcy flux [m/s], $|v|$ the module of the porewater velocity [m/s], l the characteristic length of the porous medium in [m] and D_e and D_P the effective and the pore diffusion coefficient, respectively, of a tracer in the porous medium in [m^2/s]. When this Peclet number equals 1, transport by advection is almost equally important as transport by diffusion. If Peclet numbers are < ~ 0.1 or > ~ 10, diffusion or advection, respectively, dominate.

Here, the main interest is in transport at the formation scale. Accordingly, a characteristic length l of 50 m, which reflects the distance between the deep disposal tunnels and the upper and lower limits of the Opalinus Clay, is chosen. The module of the Darcy flux $|q|$ was calculated using a vertical hydraulic conductivity of 1×10^{-14} m/s and hydraulic gradients i of 0.1 and 1.0. An effective diffusion coefficient D_e of 2×10^{-12} m^2/s for chloride was considered (Fig. 5-51).

The evaluation for chloride shows that, even for a high vertical hydraulic gradient of 1, advection is hardly important (Fig. 5-56). For more likely lower gradients (e.g. 0.1), the properties of the Opalinus Clay ensure dominance of diffusive transport. That is, the Peclet number for characteristic properties is well below 1.

Additional transport mechanisms were evaluated in earlier publications (Soler 1999, 2001, Nagra 2002, Marschall et al. 2004). The overall conclusion was that coupled phenomena will only have a very minor impact on radionuclide transport in the Opalinus Clay, in terms of fluid and solute fluxes. Recent work considered thermo-osmosis to explain pore pressures at Mont Terri (Gonçalvès et al. 2023). However, the study confirmed that diffusion remains the dominant transport mechanism also under consideration of this additional driving force.

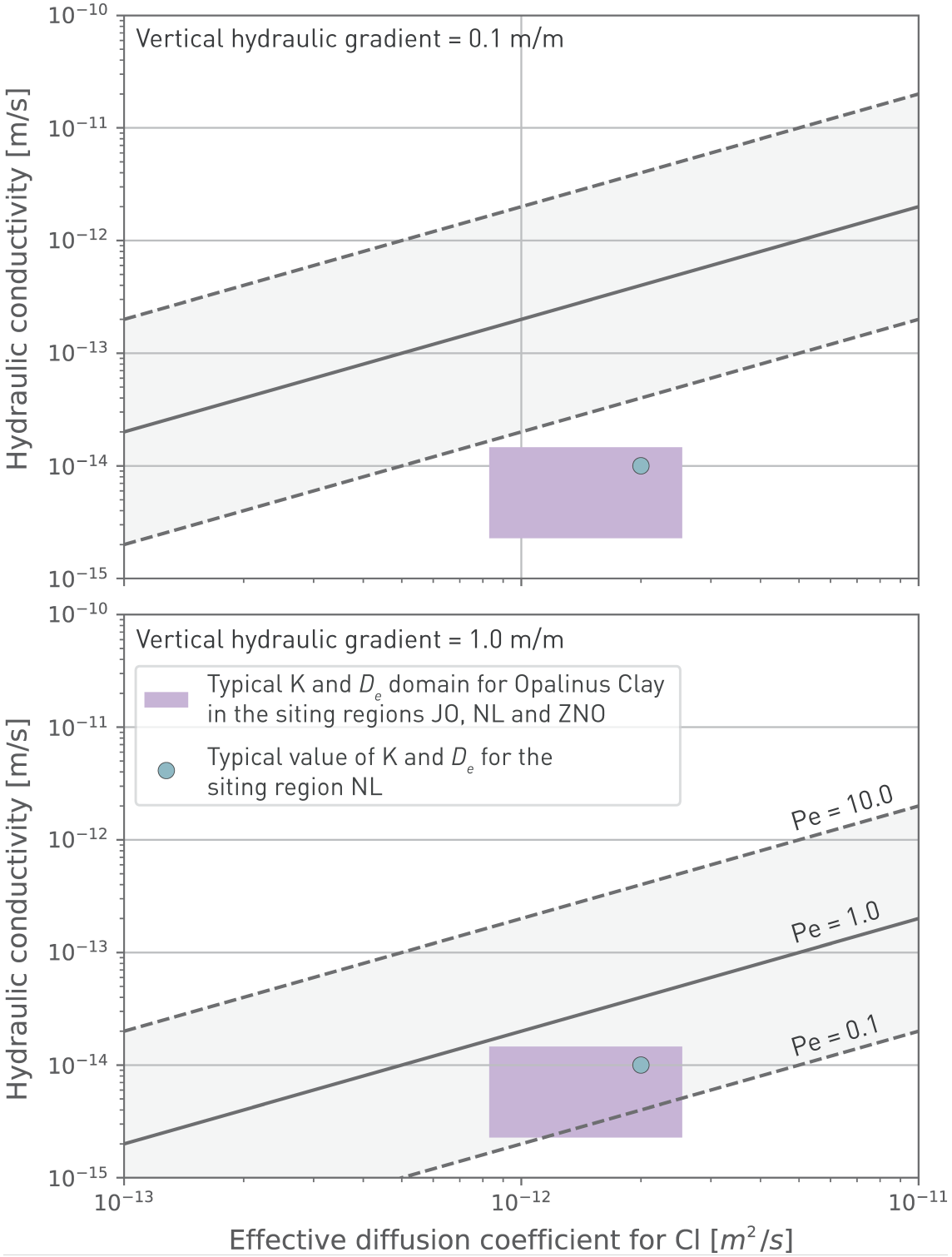


Fig. 5-56: Dominant transport mechanisms in the Opalinus Clay based on the Peclet number illustrated for chloride

The figure shows the range of hydraulic conductivity and effective diffusion coefficient compared to isolines of reference Peclet numbers Pe (i.e. 1.0 and bounding values of 0.1 and 10.0). The upper and lower figures consider a hypothetical hydraulic gradient across the Opalinus Clay of 0.1 and 1.0 respectively.

5.10 Overall conclusions on key characteristics of the host rock and confining units

For the long-term safety of a geological repository and for site comparison, the following aspects of the Opalinus Clay and its confining units are particularly relevant:

- The Opalinus Clay exhibits excellent and comparable barrier quality in all three siting regions. The consistently high clay-mineral content (> 40 wt.-%) leads to a clay-matrix-supported microstructure, which in turn dominates the mechanical behaviour and transport properties with relatively low variability.
- The porewater of the Opalinus Clay is of moderate ionic strength, pH near neutral and the redox conditions are buffered by pyrite and siderite equilibria to the reducing range. This translates to favourable geochemical conditions regarding the mobility of radionuclides and the stability of the engineered barriers.
- The difference in current burial depth in the three siting regions (approximately 400 to 900 m) results in only minor differences in basic properties (e.g. porosity). The Opalinus Clay can therefore be considered comparable across all regions. Depth-dependence of mechanical properties (strength and stiffness) is accounted for by the well-established dependence of these properties on effective stress.
- Deformation is accommodated in a more distributed manner than in more competent rocks with low clay-mineral content, with segmentation of fault planes and soft-linkage geometrically restricting continuous fracture flow paths.
- Measurements of extremely low hydraulic conductivity and porewater investigations provide evidence that mass transport in the Opalinus Clay is diffusion-dominated.
- The Opalinus Clay self-seals fractures at burial depths greater than approximately 200 m and therefore fractures do not compromise the barrier integrity over relevant timescales.
- The validity of diffusion properties is established at different scales of space and time: Consistent properties result from small-scale lab experiments and in-situ experiments in the Mont Terri rock laboratory. The laboratory diffusion coefficients lead to plausible matches of the formation-scale profiles of natural tracers in porewater that evolved over geological timescales.
- In the Opalinus Clay, the diffusion coefficient for the water tracer HTO shows very minor variation and is consistent across the different siting regions. As a result of differences in porewater ionic strength, the effective diffusion coefficient D_e for chloride shows some site-specific differences, with lowest values in JO.
- The confining units increase the effective containment of a future repository and also have very low hydraulic conductivities, but a lower self-sealing potential than the Opalinus Clay. Relative homogeneity, good spatial correlation and consistently high clay-mineral content are the major differences of the Opalinus Clay and its confining units, and a major advantage in terms of ease of characterisation.

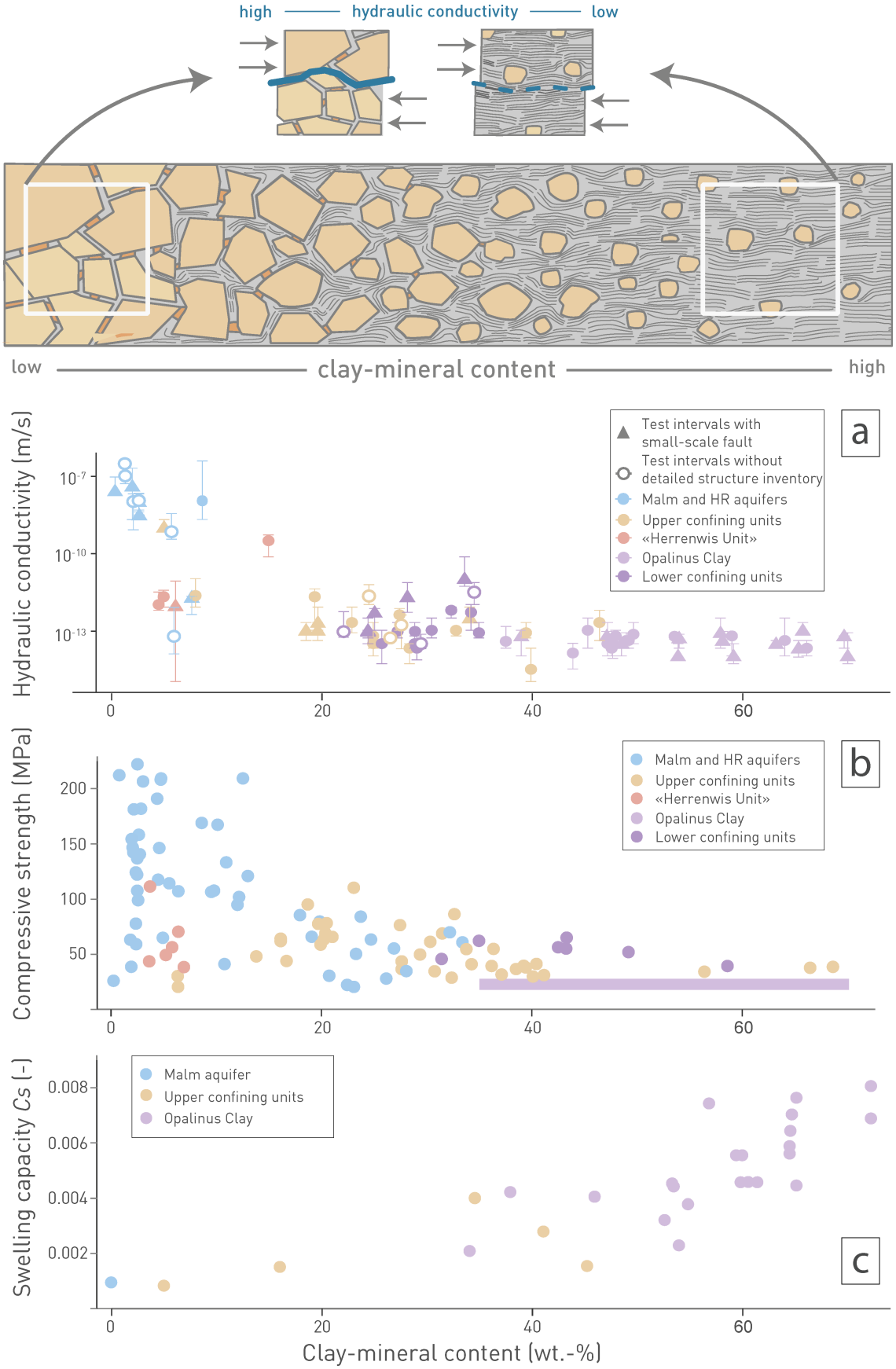

high
hydraulic conductivity
low
low
clay-mineral content
high
Hydraulic conductivity (m/s)
10-7
10-10
10-13
0
20
40
60
Test intervals with small-scale fault
Test intervals without detailed structure inventory
Malm and HR aquifers
Upper confining units
«Herrenwis Unit»
Opalinus Clay
Lower confining units
a
Compressive strength (MPa)
200
150
100
50
0
20
40
60
Malm and HR aquifers
Upper confining units
«Herrenwis Unit»
Opalinus Clay
Lower confining units
b
Swelling capacity Cs (-)
0.008
0.006
0.004
0.002
0
20
40
60
Malm aquifer
Upper confining units
Opalinus Clay
c
Clay-mineral content (wt.-%)

Fig. 5-57: Link of texture and clay-mineral content with key hydromechanical properties in Jurassic sediments of the siting regions (lower confining units to upper aquifers)

The uppermost figure depicts a highly simplified transition from a grain-supported framework (clastics or carbonate skeleton, with low clay-mineral content partially filling the pores) on the left side, to a clay-matrix-supported framework on the right. Transition to the clay-matrix-supported framework at approximately 20 to 40 wt.-% is consistent with the low hydraulic conductivity (a; see Fig. 5-42) because of the high swelling capacity (c; see Fig. 5-22), which in turn is possible because swelling is not hindered by strong diagenetic bonds, as indicated by low strength (b; see Fig. 5-30). Note figure shows data from the Lias Group to the Malm Group. HR stands for Hauptrogenstein.

The above observations are conceptually explained in relation to the clay-mineral content, and more specifically to the distribution of clay minerals at the microstructure scale (Fig. 5-57). At low clay-mineral content, the larger clastic grains (typically carbonates or quartz) are load-bearing and the microstructure can be referred to as *grain-supported*, whereas at higher clay-mineral content the microstructure is *clay matrix-supported* with clastic grains enclosed in clay minerals (Section 5.2). The transition between a grain-supported and matrix-supported microstructure for shales was interpreted to be around 30 to 40 wt.-% of clay and considered a threshold for robust barrier function with increasing clay-mineral content (Bourg & Ajo-Franklin 2017, Revil & Cathles 1999). This value is in good agreement with an increasing self-sealing potential observed from the confining units towards the Opalinus Clay, most notably with an increase in the swelling index (Fig. 5-57c).

In Fig. 5-57 only Jurassic sediments are shown (which have low matrix permeability), where elevated transmissivity can be related to fracture-dominated flow. It is noted that the hydraulic conductivity of the intact material is very low ($<< 10^{-10}$ m/s) in all formations shown in Fig. 5-57, in limestones of the Malm Group ("Aquifers") as well as in the Opalinus Clay. But while cementation of pores plays a dominant role in ensuring low permeability in intact limestones, flow in the clay matrix is controlled by the pore network of the small clay particles, i.e. a high tortuosity and narrow passages (constrictivity).

Fracturing in the Opalinus Clay has a much lower impact on changes in rock mass hydraulic conductivity because of the fundamentally different controls on its low permeability compared to limestones, where the brittle response during fracturing leads to relatively high surface roughness and localisation of deformation with hard linkage. As cement bonds and grains are broken during fracturing and swelling capacity is negligible, fracture permeability cannot easily be reversed.

Whereas the clay-mineral content in the Opalinus Clay is consistently high, the confining units show a larger variability, with clay-mineral contents transitioning from grain-supported to clay matrix-supported microstructures. At a clay-mineral content of approximately 20 to 40 wt.-%, this transition is associated with a decrease in strength and an increase in the swelling index towards higher clay-mineral contents. In the Opalinus Clay, packer tests show consistently low hydraulic conductivity ($< 10^{-12}$ m/s), regardless of whether clay-mineral contents are 40, 50 or even 70 wt.-%. In contrast, rocks with clay-mineral contents < 20 wt.-% exhibit rather high strength, negligible swelling indexes and partly very high, fracture-dominated hydraulic conductivities. Confining units in the transition zone with clay-mineral contents of 20 to 40 wt.-% generally also show low hydraulic conductivities but can occasionally be 1 – 2 orders of magnitudes above those measured in the Opalinus Clay.

6 Long-term geological evolution

Key points:

- Geological processes that may compromise the stability of the geological barrier and its function over the next one million years are assessed. These include tectonic faulting, climate change and ensuing erosion as well as their effect on hydraulic properties and gradients, and geochemical conditions.
- Northern Switzerland is tectonically active with very low deformation rates. Based on the geological history of the area, strain associated with future tectonic activity is expected to concentrate on existing larger fault zones. Movements on smaller faults are expected to be limited.
- Climate change has followed a predominant 100-kyr cycle since ~ 700 kyr at global scale. Repeated glaciations during cold phases strongly affected the landscape of Northern Switzerland, including the formation of deep glacial troughs. Due to anthropogenic CO_2 emissions future glaciations may be delayed by several 100 kyr compared to a natural scenario.
- The uncertainty regarding future erosion was assessed using a robust, structured hybrid-probabilistic approach. This approach includes different climate evolution scenarios and considers a broad range of uplift rates. The model parametrisation is based on a thorough reconstruction of past and present-day processes influencing landscape evolution.
- A critical reduction of the host rock overburden that would lead to a relevant change in the key barrier properties (hydraulic conductivity, diffusion properties, self-sealing capacity) is unlikely at all sites. NL is the most robust in this respect because of its greater depth.

6.1 Introduction

6.1.1 Aim and content of this chapter

This chapter addresses the changes in environmental conditions related to surface-driven, climate-driven, and geological processes that may affect the long-term stability of the geological barrier. Consequently, the principal topics to be addressed in this context are changes in transport properties (hydraulic conductivity, diffusion coefficients), hydraulic gradients, stress state and fault reactivation. Of particular importance in such an analysis is the consideration of the reduction in sediment cover thickness (referred to herein as overburden) above host rock under various tectonic and erosion scenarios. The latter is important because the barrier properties are "depth-dependent" and will persist as long as a minimum residual overburden is maintained above the rock units that host a future repository in the Opalinus Clay. Future erosion may reduce the overburden.

The assessment of future erosion potential considers the form and rate of processes in the past (Quaternary) as a basis for evaluating future variability in tectonic and surface processes that could affect the containment and isolation function of a repository or its geological barrier up to one million years into the future.

This assessment builds on the process understanding gained during earlier studies (e.g. Müller et al. 2002, Nagra 2014c, Dossier III). In SGT Stage 3 a targeted scientific field investigation programme was launched to provide a better understanding of the long-term Quaternary evolution of

Northern Switzerland (Section 2.4). These investigations were accompanied by numerical modelling studies and an in-depth literature review aimed at gaining a state-of-the-art process understanding of the main drivers for erosion of the landscape in Northern Switzerland. The erosion scenarios and argumentation from SGT Stage 2 (Nagra 2014c, Dossier III) were thus updated and improved to incorporate and illustrate uncertainties in a systematic and structured way. This effort includes the design of a new model cascade that allows the combination of numerical simulations and probabilistic calculations to estimate future repository overburden thickness and excavation probabilities. The most relevant results are presented and discussed in this chapter; further details are provided in additional reports (Nagra 2024l, 2024j, 2024k).

Chapter 6 is structured as follows (Fig. 6-1):

- Section 6.1.2 provides an overview of potentially relevant processes affecting the surface process and tectonic regimes of Northern Switzerland.
- Section 6.2 describes the geodynamic evolution of Northern Switzerland with a focus on (1) crustal uplift/subsidence patterns as drivers for erosion and sedimentation, and (2) the potential for faulting near the repository locations.
- Section 6.3 reviews the Quaternary climate evolution and its influence on the surface process regime in the light of recurring orbital changes and natural atmospheric CO_2 levels. This review forms the basis for a consideration of possible global future climate scenarios in the context of predicted orbital changes and anthropogenically influenced CO_2 levels. Subsequently, these climate states and cycles are reviewed with respect to their regional impact in Northern Switzerland, especially regarding glaciations and the occurrence of deep-reaching permafrost. Finally, the results of ice-flow modelling with respect to erosion potential and estimates of future glacial inception are discussed.
- In Section 6.4, changes in tectonic and climate processes are reviewed as potential drivers for erosion processes. In this context, the evolution of the principal drainage systems, the response of local topography to changes in tectonic and climate-driven processes, and particularly the character of glacial overdeepenings is presented in separate subsections. Subsequently, the new approach for estimating future erosion under consideration of uncertainties is introduced. Finally, the results of the assessment of future erosion (i.e. remaining overburden thickness and excavation probabilities) are summarised.
- Section 6.5 discusses the effects of tectonic and climate-driven processes and associated reduction in overburden thickness on hydrogeological conditions in the low-permeability geological barrier and surrounding aquifers. This discussion also considers changes in aquifer dynamics and host-rock properties, as well as the evolution of geochemical conditions in the host rock.
- The chapter concludes in Section 6.6 with a summary of the processes most relevant to the expected landscape and barrier evolution in the area of the deep geological repository. In addition, this section addresses findings that are relevant for site selection and long-term safety.

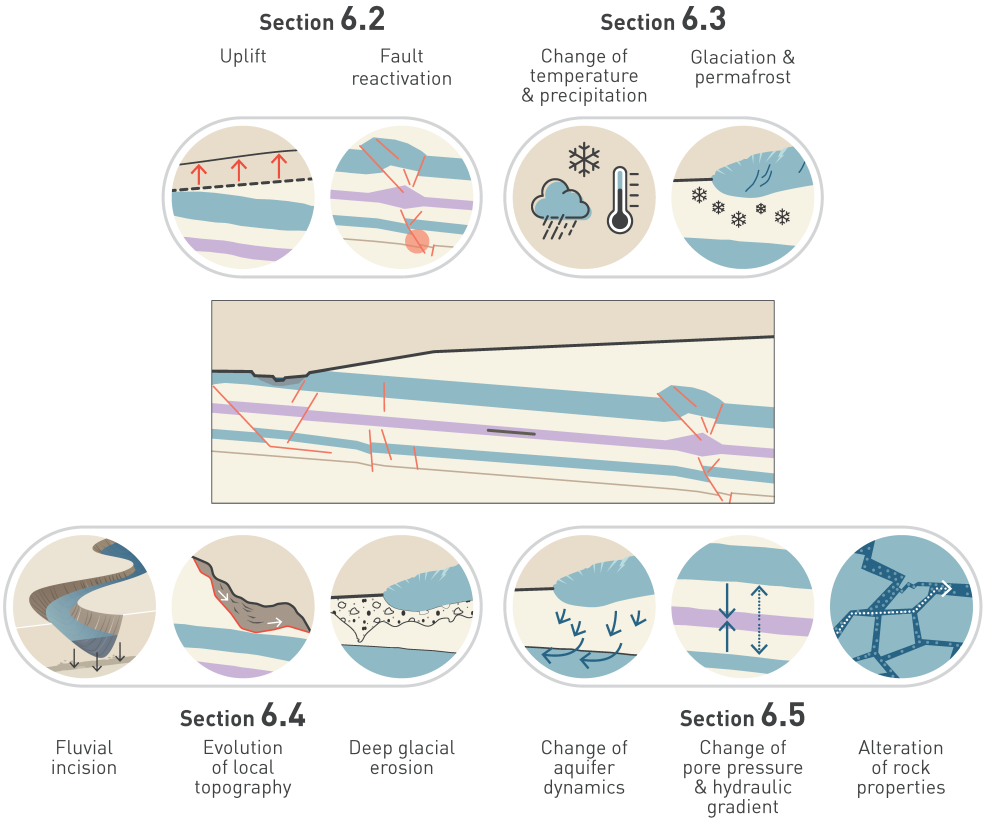


Fig. 6-1: Schematic visualisation of the principal geological processes potentially affecting the geological barrier and corresponding structure of the chapter

The main aspects that are addressed with respect to future repository performance and long-term safety are tectonic evolution with vertical motion as a driver of erosion and fault reactivation potential (Section 6.2); climate evolution as a driver of erosion and changes in hydrogeological conditions, such as changes in temperature and precipitation as well as ensuing glaciations and the formation of deep-reaching permafrost (Section 6.3); erosion with the three main components fluvial incision, evolution of local topography, and deep glacial erosion (Section 6.4); and the hydrogeological evolution including changes in properties of the aquifer flow system and pore pressure and thus in the flow system and the alteration of porewater and dissolution processes (Section 6.5).

6.1.2 Overview of the principal geological processes potentially affecting the geological barrier

Given the known process rates and the geological and geomorphological characteristics of the siting regions, it is expected that future tectonic and climatic forcing will drive fault movement and surface processes (Fig. 6-2) in Northern Switzerland, and the potential impact of these must be accounted for. This section provides an overview of the relevant processes, process interactions, and feedback to be expected in Northern Switzerland.

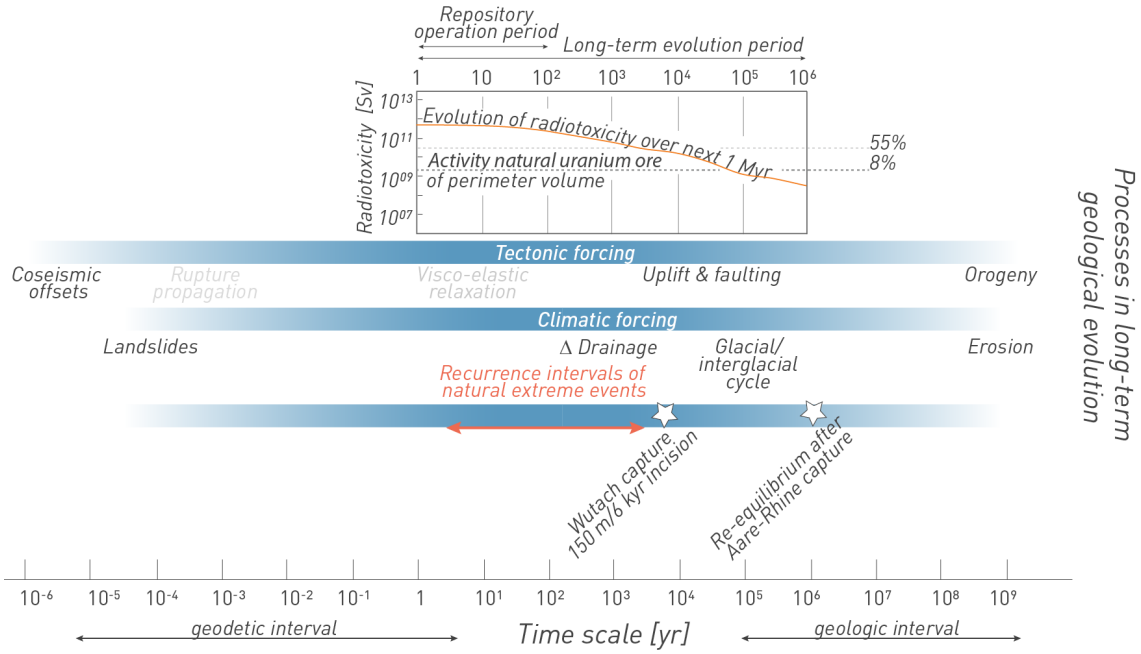


Fig. 6-2: Geological processes acting at different timescales compared with the time period relevant for repository safety

The geology and geomorphology in the vicinity of the repository are expected to be subjected to tectonic and climatic forcing that drive erosional processes or fault motion that could potentially affect the stability of the geological barrier. Given the period under consideration of one million years for HLW (see figure above), several of these processes need to be addressed. Note the log-scale for the time of observation. Radiotoxicity is based on the Swiss waste inventory and is a measure that allows the comparison between radioactive waste and natural rock compositions, such as U-rich (Cigar Lake [8%], La Creusaz [55%]) rock types, assuming a similar volume as the HLW waste in their perimeter of tunnels and caverns (see Nagra 2024d). Also indicated are two examples of geomorphic events that have influenced the process rates in Northern Switzerland on different timescales: the capture of the Wutach River resulted in strong incision of which the majority of up to 150 m may have occurred during the first approximately six thousand years after the capture (Einsele & Ricken 1995). The reorganisation of the Aare – Rhine Rivers impacted Northern Switzerland regionally. Re-equilibrium of the drainage system to a capture ~ 4.2 Ma ago was modelled to take approximately one million years.

Tectonic and climatic drivers act on a variety of timescales (Fig. 6-2), with short timescale events such as earthquakes or extreme climate-driven meteorological events, whether instrumentally or historically recorded, rarely being a good proxy for long-term behaviour. Conversely, studies that focus solely on geological archives and landforms on scales of 10^5 to 10^6 yr are often not precise enough to resolve discrete fault behaviour or to decipher the landscape response to climatic forcing. Therefore, earthquake and climate impact studies need to be integrated across multiple timescales, and observations extended to longer timescales spanning several thousand years to one million years to account for the potential future behaviour of different forcing factors that could reduce the efficiency of the geological barrier.

Consequently, any changes in topography and relief due to vertical crustal movements and super-imposed climate-driven changes in a tectonically active region will influence the form and rate of erosion processes. Thus, tectonic and climate-driven processes need to be identified, classified, and rated with respect to their relevance, timing, location, and potential impact on the geological

barrier function. In the light of these considerations, the specific forcing factors that have determined, and will continue to influence, the long-term geological evolution of Northern Switzerland involve low-strain tectonic processes, climate change, and protracted erosion (see Fig. 6-1). Taken together, these three components may influence the hydrogeology and geochemistry of the host rock and confining units, as explained below:

Tectonic evolution based on the present-day geodynamic configuration of the Alpine realm is expected to influence vertical and horizontal motion in the region. On a large scale, tectonic processes such as rock uplift of the Alpine Foreland and subsidence of the southern Upper Rhine Graben play an important role as they build topography and drive fluvial incision and denudation. Because the resulting erosion reduces the overburden thickness above the repository, the rates and patterns of such regional vertical motion have been assessed (see Section 6.2). Large-scale geodynamic processes, on geological timescales of millions of years (Chapter 3, Section 4.3), determine the orientation and magnitude of the regional tectonic stress regime, which might be altered on much shorter timescales by transient perturbations. These perturbations may, for instance, involve either lithospheric flexure because of regional loading and unloading during glacial advances and retreat or hydro-isostasy. Such processes can affect the aquifer flow system or hydraulic gradients (see Section 6.5), but they may also unclamp locked faults through the erosional reduction of normal stresses and trigger earthquakes with very long recurrence intervals (see Section 6.2.3).

Northern Switzerland is adjacent to a region where mantle-driven processes are responsible for magmatic activity and associated processes. Two of the closest centres of volcanic activity to Northern Switzerland are the Kaiserstuhl and Hegau Graben eruption centres in southern Germany. Volcanism at the Kaiserstuhl eruption centre occurred between ~ 21 and 13 million years ago, while volcanic activity in the neighbouring Hegau region ceased in the Late Miocene (Geyer et al. 2023). There has been no magmatic activity in Northern Switzerland for at least the last 5 million years (Schreiner 1992, Ibele 2015). Considering the current characteristics of the region, there are no indicators for dormant volcanic activity in Northern Switzerland, in contrast e.g. to the Eifel region in Germany. Seismicity in Northern Switzerland reflects low-rate tectonism (Diehl et al. 2023) with no documented volcanic tremors. Thus, volcanism in Northern Switzerland is considered very unlikely within the next one million years and is therefore of no concern and is not considered further here.

A characterisation of expected seismic or aseismic fault slip (see Section 6.2.3) is important to assess hydraulic changes and potential flow along faults in the low-permeability sequence. No relevant effects of seismic shaking on the integrity of the deep geological repository are expected because of the deep subsurface repository position and backfill (see Nagra 2024i). Seismic hazard during the operational phase is taken into account in the operational safety report (see Nagra 2024h and Nagra 2024g).

In this chapter, information is provided to answer the following questions:

- What uplift rates can be expected in the siting regions over the next 100'000 to one million years?
- What vertical motion is expected downstream and upstream of the siting regions along the main rivers, which may in turn influence future river incision?
- Where and to what extent is movement along faults possible?

Climate evolution in the northern sector of the Alpine region is expected to be influenced by recurring and protracted changes in the Earth's orbit and tilt, which has had a major influence on landscape evolution during Pleistocene glacial/interglacial cycles. Because of the recurrent nature of these forcing mechanisms, they are expected to continue to exert this influence in the future. In particular, the change from a predominant ~ 41-kyr cycle to the establishment of a 100-kyr-long cycle during the Mid-Pleistocene Transition (MPT) fundamentally impacted erosional and sedimentary processes and thus Quaternary landscape evolution in Northern Switzerland (see Section 6.4.1). This cyclicity modulates climate parameters such as temperature and precipitation, which in turn influence water and sediment discharge as well as the overall hydrogeological evolution in the subsurface.

The greatest past climate impact on the landscape was associated with Pleistocene glacial periods (see Section 6.3). Extensive foreland glaciations can change sediment routing, deposition and drainage pathways or erode overdeepened valleys. In Northern Switzerland, it is expected that long durations of extensive foreland glaciations can, for example, cause lithospheric depression in the North Alpine Foreland along with transient stress changes that could influence the seismogenic behaviour of inherited faults (see Section 6.2.4). Typically, postglacial rebound follows an exponential trend until isostatic equilibrium is restored. During this period, higher uplift rates and associated stronger fluvial incision can be expected (see Section 6.4.3.1). In addition, mechanical loading and compaction by the ice cover, as well as subglacial infiltration, are likely to impact the hydraulic system. Extensive foreland glaciations may be accompanied by deep-reaching permafrost, which might affect aquifers by groundwater freezing and increase hydraulic heads and/or change groundwater flow paths (see Section 6.5.1.3).

Questions to be answered with respect to climate forcing are:

- What timing and extent of future glaciations in Northern Switzerland might be expected, considering natural conditions and potential effects of anthropogenic CO_2 emissions?
- What ice thicknesses and duration of ice occupation are expected during future glaciations considering Pleistocene examples?
- To what depth could the subsurface be frozen during future ice ages (permafrost)?

Erosion is mainly driven by the effects of tectonic and climatic processes, as outlined above and illustrated in Fig. 6-2. In the area of the selected repository siting regions in Northern Switzerland, these processes may be characterised by slow vertical tectonic movements and glacial influences. The latter may involve significant erosional lag times between ice loading, topographic change, and deglaciation, as well as rate changes during isostatic readjustments. Ultimately, it is the synergistic interaction between long-term tectonic processes that build topography on the one hand and superimposed surface processes that are influenced by climate and vegetation cover on the other that sculpt landscapes (e.g. Burbank & Anderson 2012). The landscape of the three siting regions in Northern Switzerland has been primarily shaped by the stepwise fluvial incision of the Aare and Rhine Rivers, the evolution of a low-relief cuesta landscape, and repeated deep glacial erosion and depositional processes determined by the glaciations of the Alpine Foreland. Accordingly, the main drivers for these processes are the effects of glacial/interglacial cycles and long-term rock uplift associated with the vertical motion of the Alpine orogen and its foreland. However, the process rates are low in a global context and compared to seismically active plate-boundary settings.

To assess erosion with respect to the performance and long-term safety of the future repository, the following questions will be answered:

- To what extent will the overburden thickness be reduced at the repository sites? The answer to this question needs the following sub-questions to be addressed:
  - How will the fluvial system evolve? How much incision is expected during the period under consideration? Will the host rock and confining units remain below the local base-level?
  - How will the morphology around the repository evolve with regard to recharge and discharge areas?
  - How deep could future glacial erosion reach at the location of the future repository?

The cascade of driving forces outlined above leads to changes in the future landscape that also affect the **hydrogeology and hydrochemistry** in the rock column. Hydrogeological changes in areas subjected to multiple glaciations and tectonic uplift can be significant and the effects on the stability of the geological barrier are thus analysed in this regard. In hydrogeological systems, a geological barrier is typically subdivided into the host rock, the low-permeability confining units, and the surrounding deep aquifer systems. Not only do tectonic movements, climate change, and climate-driven surface processes (erosion) affect the recharge and discharge paths and gradients in deep aquifer systems, they can also impact the gradients in the low-permeability units. As a result of its high clay-mineral content (self-sealing capacity; Section 5.7) and low permeability (Section 5.6), there tends to be little impact of tectonics or erosion on transport in the Opalinus Clay. However, if overburden thickness decreases drastically because of erosion, decompaction effects may lead to less efficient self-sealing (Section 5.7), increased porosity and permeability (Section 5.6), and a change in host rock mineralogy and porewater chemistry.

The following main questions concerning the influences of tectonics, climate and erosion on the hydrogeology and barrier performance and thus the long-term safety of the future repository will be addressed:

- How could the dynamics in the deep aquifers evolve (flow velocity, flow direction, discharge paths)?
- Are the gradients across and along the low-permeability sequence (host rock and confining units) expected to change in a relevant way?
- What are the expected effects of the possible fault-slip scenarios?
- Will transport across the low-permeability units remain diffusion-dominated? Do diffusion and sorption properties change in a significant way?
- How might the porewater composition change in future and how might this impact diffusion and sorption of radionuclides?

6.2 Geodynamic evolution

Key points:

- Northern Switzerland is a tectonically active, low-strain domain.
- Various proxy data indicate uplift rates between 0.1 and 0.5 mm/yr, with strong dependency on the time interval. Average long-term uplift rates are < 0.3 mm/yr.
- Seismicity with an influence on Northern Switzerland is currently focused on the Upper Rhine Graben and the Hegau – Bodensee Graben. Around the siting regions, seismicity is sparse.
- Global navigation satellite system velocities measured in Northern Switzerland allow deduction of < 3 m/km/Myr of mean shortening.
- Faults inherited from earlier deformation episodes have acted as zones of weakness localising Cenozoic strain. Future tectonic activity is also expected to concentrate on large inherited faults.

Future tectonic activity in Northern Switzerland may affect the geological barrier properties of the host rock in the siting regions in two ways: (1) Rock uplift may increase topographic gradients and thus the potential for intensified erosion. (2) Seismic and aseismic fault slip may change the hydraulic properties along faults and thus the dominant transport mechanism. Consequently, both aspects need to be addressed and evaluated in detail.

This section summarises the knowledge on regional and local tectonic processes in Northern Switzerland. It builds on the geological evolution highlighted in Chapter 3 and provides additional detail about the present-day geodynamic context of Central Europe. Throughout the section, the term *neotectonics* is used to address seismogenic and aseismic deformation processes that have been active from Neogene times until the present day. This time period reflects the duration of the current stress regime, established since the last major tectonic reorganisation. In Northern Switzerland, this encompasses the period from the NW propagation of the Alpine deformation front (Early Miocene) and recorded décollement-related deformation in the eastern Jura Fold-and-Thrust Belt (Middle Miocene) until the present day (Section 4.3.5). The addressed period also includes the time of so-called active tectonics, i.e. as relevant for society (Wallace 1984, Nagra 2024l for more detail).

Section 6.2.1 starts with an overview of driving forces for neotectonic deformation within the European geodynamic framework. Seismicity, recent geodetic velocities, and the location of areas with potentially active tectonics in Northern Switzerland are introduced. This is followed by a brief outline of far-field tectonic drivers for the main erosion patterns and magnitudes that influence the siting regions (Section 6.2.2).

The focus of Section 6.2.3 is on regional neotectonic processes and rates in Northern Switzerland. Based on this, Section 6.2.4 discusses the future tectonic evolution and highlights the importance of reactivation of inherited faults, rather than formation of new faults. The main conclusions are summarised in Section 6.2.5. A more in-depth discussion of neotectonic observations is provided in Nagra (2024l).

6.2.1 Large-scale geodynamic framework

Overall, the geodynamic setting of Central Europe (Fig. 6-3a) is influenced by the convergence between the African and Eurasian plates (Chapter 3, Fig. 3-12). The largest geodetic velocities and highest strain rates are measured in the eastern part of the African – Eurasian plate boundary zone in Greece and Turkey (e.g. DeMets et al. 1990, Serpelloni et al. 2022). Rates decline significantly towards the western plate boundary zones, closer to the Alps. The highest rates of deformation within the western plate boundary zone have been recorded along wide, diffuse deformation zones, such as the Apennines, the Dinarides, or the Betic Cordillera (see Fig. 6-3a, b and c). Here, active deformation appears to be mainly influenced by independent microplate motion, such as the counterclockwise rotation of the Adriatic plate and Tyrrhenian and Aegean back-arc extension (e.g. Nocquet & Calais 2004, Piña-Valdés et al. 2022; see Fig. 6-3b for low geodetic rates, Fig. 6-3c for diffuse seismicity and Fig. 6-3d for S_{Hmax} indicators of stress regimes).

In the Alpine region, horizontal geodetic velocities are influenced by microplate deformation, but the rates are significantly lower and seismicity relatively sparse compared to the above-mentioned zones, despite considerable topographic relief and evidence for vertical motion (Fig. 6-3a, b, c, Fig. 6-4). Across the central Alps, shortening is low with values similar to the uncertainty (Sánchez et al. 2018).

Based on the global navigation satellite system (GNSS) measurements, the vertical velocity field of the Alps is in the order of ~ 2 mm/yr along the northward-convex border (Fig. 6-4), increasing towards the central Alps and characterised by a generally positive correlation with topography (Sánchez et al. 2018, Piña-Valdés et al. 2022, Serpelloni et al. 2022, Pintori et al. 2022). Total decadal-scale uplift is generally higher in the areas that undergo less horizontal shortening and, as such, is higher in the western and central Alps compared to the eastern part (Sternai et al. 2019). A tectonic contribution to rock uplift and exhumation appears to be pronounced in the eastern Southern Alps, where ~ 2 mm/yr movement between the Adriatic plate and stable Europe are accommodated (Sánchez et al. 2018, Sternai et al. 2019, Serpelloni et al. 2022). In addition to tectonic drivers, buoyancy forces associated with isostasy make a significant contribution to uplift (e.g. Sternai et al. 2019, Piña-Valdés et al. 2022). Isostatically driven processes, such as postglacial or erosional rebound/unloading, slab detachment, as well as the effects exerted by the formation of dynamic topography (upper mantle processes) and the establishment of horizontal gradients associated with gravitational potential energy are considered to play a role (Sternai et al. 2019). Isostatic adjustment in response to deglaciation or erosion might cause uplift and can be in the order of 10 – 30% and 10 – 20% in the western and central Alps and up to 50% and 30 – 40% in the eastern Alps, respectively.

Towards the northern and southern Alpine Forelands, vertical velocities decrease to positive sub-millimetre and even to stable, zero mm/yr rates (Sánchez et al. 2018, Henrion et al. 2020, Pintori et al. 2022; Fig. 6-4c). Low vertical velocities are observed in the Jura Mountains and the Molasse Basin (Fig. 6-4c).

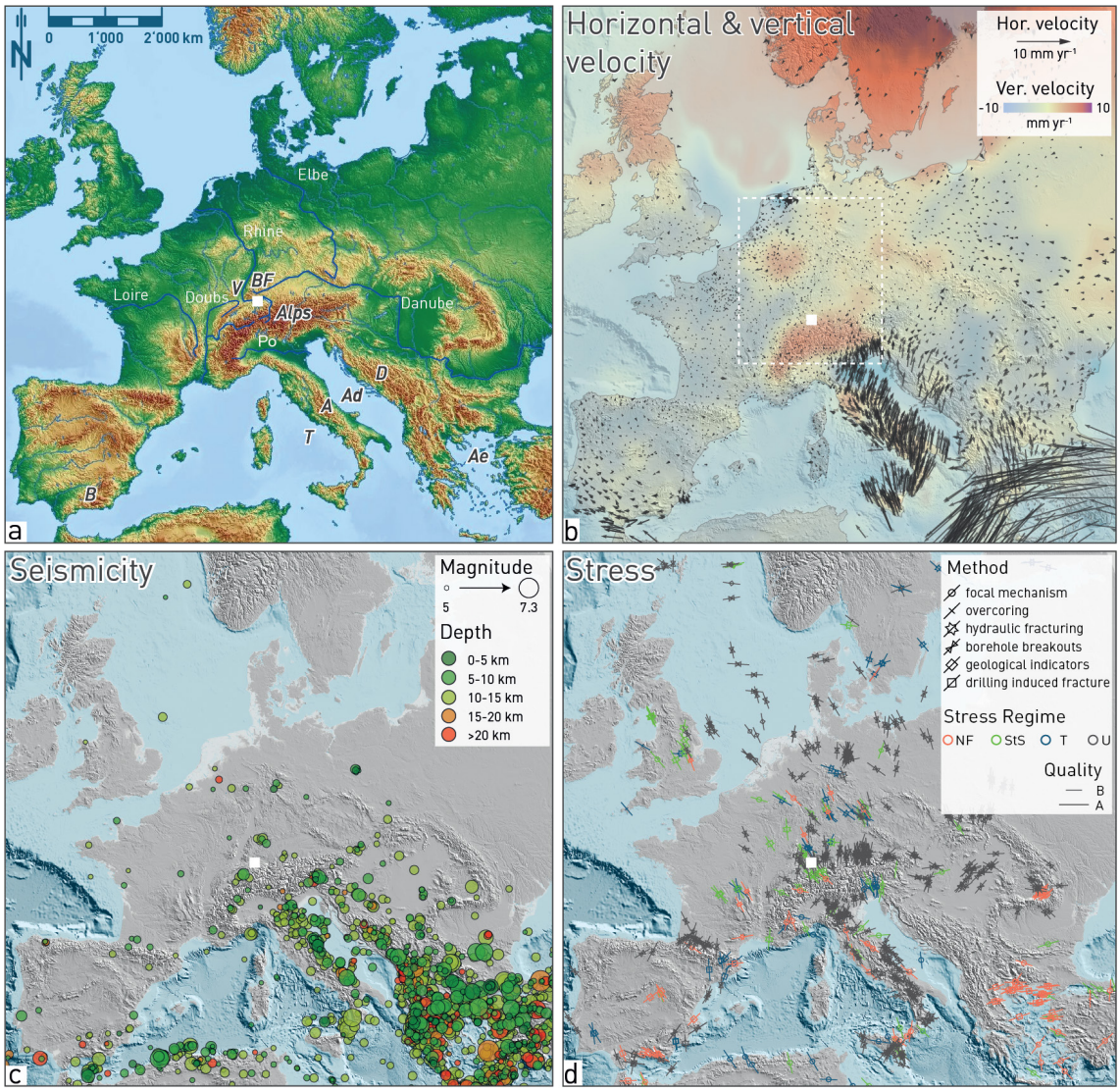


Fig. 6-3: Velocity fields, seismicity and stress vectors in Europe

(a) Hillshade and digital elevation map of the same area with labels of geographic features discussed in Section 6.2.1. V: Vosges, BF: Black Forest, A: Apennines, B: Betic Cordillera, D: Dinarides, Ad: Adriatic Ocean, T: Tyrrhenian Ocean, Ae: Aegean. (b) By combining and harmonising geodetic velocities of several European datasets, a smoothed 3D velocity field solution across Europe and with respect to a stable Europe framework was generated (Piña-Valdés et al. 2022). Dashed white rectangle outlines Fig. 6-4. (c) Earthquakes with magnitudes equal to and larger than 5 between 1900 and July 2023, colour-coded by depth (https://earthquake.usgs.gov/earthquakes/search/; retrieved July 10th 2023). High-seismicity regions in Europe (e.g. Greece and Italy) are associated with subduction processes and coincide with regions of large horizontal velocities. (d) Direction of maximum horizontal stress and stress regime (Section 4.4). The map is based on the World Stress Map project (CASMO) and shows data from focal mechanism solutions, borehole breakouts, hydrofractures etc. Stress indicators are colour-coded by their respective stress regime (Heidbach et al. 2016, 2018). NF: Normal fault, StS: Strike-slip fault, T: Thrust, U: Unknown. White solid square in all figures depicts the study area.

6.2.2 Uplift and subsidence domains along the route of the Rhine River

In this section, the regional geodynamic setting is reviewed with respect to its influence on erosion processes. Beyond the North Alpine Foreland, this primarily considers fluvial incision by the Rhine River system from source to sink. Here, it is considered how rates of deformation (mainly vertical motion) have driven baselevel changes of the Rhine on timescales similar to the future one million years. This information is important to assess future fluvial incision, as rock uplift is expected to exert a first-order control.

The Aare – Rhine River system hydrologically connects the Alps with the North Sea as the final baselevel (Fig. 6-4a). From source-to-sink, the Rhine crosses several tectonic domains that may influence erosion (Fig. 6-4b and Fig. 6-5). The siting regions are located along the Hochrhein section, between the Bodensee and Upper Rhine Graben (Fig. 6-4a).

The main neotectonic influence on erosion in Northern Switzerland are Alpine uplift, trans-tensional deformation in the Upper Rhine Graben and potential low-level movements of the Jura Fold-and-Thrust Belt and the Bodensee – Hegau Graben (see Section 6.2.3). Together these define the regional tectonic setting for fluvial erosion processes associated with rock uplift and baselevel drop.

Fluvial incision and erosion in Northern Switzerland are also influenced by far-field uplift of the Eifel area and the Rhenish Massif (Fig. 6-3b, Fig. 6-4, Fig. 6-5). The latter represents a regional intermediate baselevel of the Rhine. As long as the area continues uplifting, it is not expected that processes related to sea level changes will affect the siting regions on the relevant timescale of one million years. The main tectonic domains that are located between the Rhenish Massif and the Alpine Foreland, which control stream profile evolution of the Rhine River, are summarised below, starting at the relevant downstream locations (see Nagra 2024k for more detail).

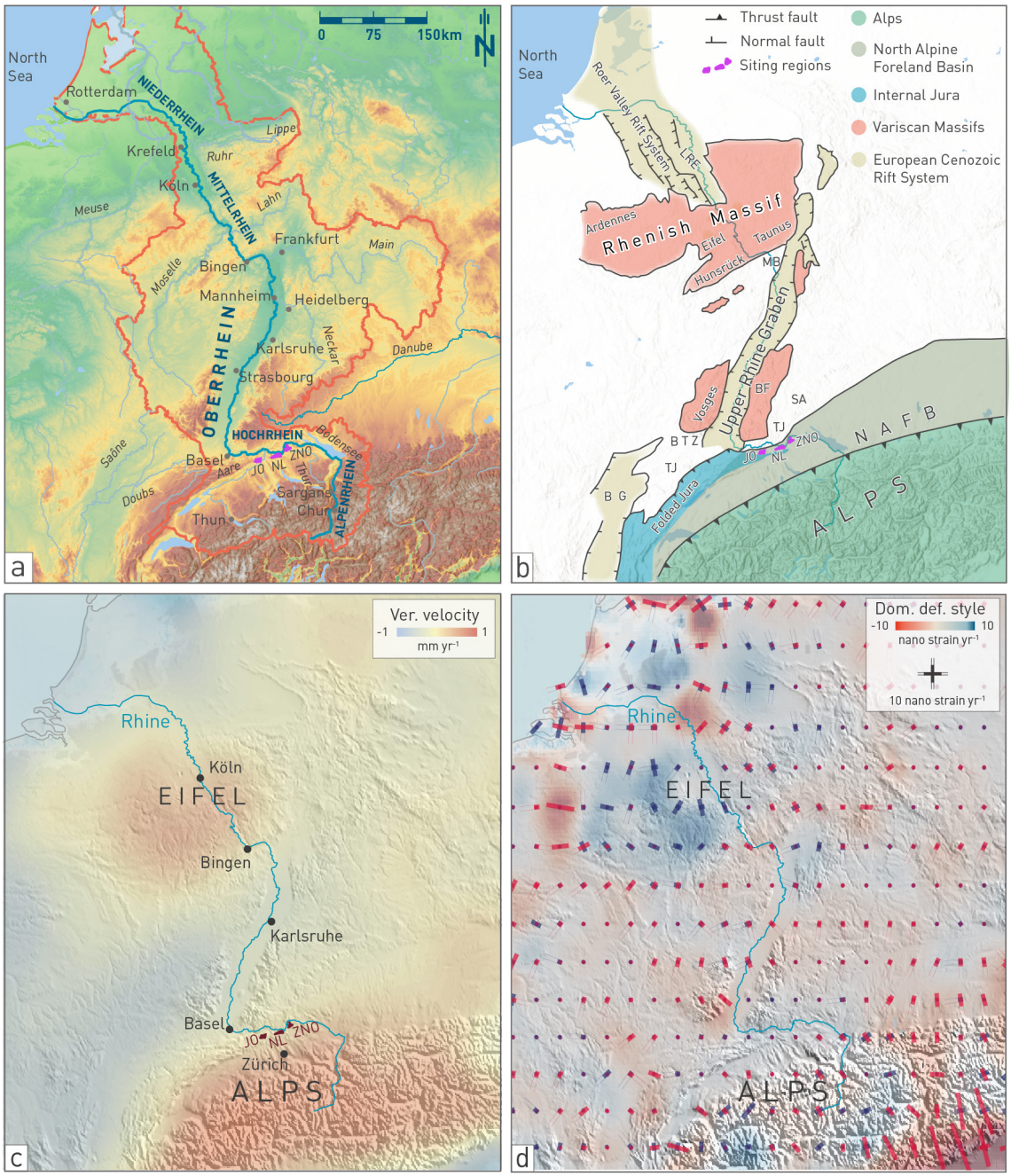


Fig. 6-4: Present-day Rhine catchment in a morphotectonic and geodynamic context for fluvial incision and sediment accumulation

(a) Rhine catchment (b) Morphotectonic domains. The course of the Rhine River is highlighted with dark blue line. BF: Black Forest, BG: Bresse Graben, BTZ: Bresse Transfer Zone, TJ: Tabular Jura, LRE: Lower Rhine Embayment, MB: Mainz Basin, NAFB: North Alpine Foreland basin, SA: Swabian Alb. Data source: EU-DEM (European Environment Agency), rivers based on European Environment Agency (2020), https://land.copernicus.eu/en/products/eu-hydro/eu-hydro-river-network-database. c) Geodetic velocities (redrawn from Piña-Valdés et al. 2022). Vertical motion relative to stable Europe is highlighted by red and blue colours (uplift and subsidence, respectively). The Alps and the Eifel area are prominent uplift regions that influence the profile of the Rhine River. (d) Strain rates (redrawn from Piña-Valdés et al. 2022) with red pins showing contraction and blue pins showing extension) are generally low within the Alpine Foreland.

Rhenish Massif, Upper Rhine Graben and Vosges and Black Forest Massifs

The Rhenish Massif represents an actively uplifting region, which is coincident with bedrock incision of the Rhine River (Mittelrhein, see Fig. 6-4 and Fig. 6-5). It has been uplifting since at least Oligocene times (Illies & Greiner 1979, Illies et al. 1979, Garcia-Castellanos et al. 2000, Ziegler & Dèzes 2005, 2007). Extensive volcanism in the area, spanning from the Oligocene (Westerwald) until the Late Quaternary (East and West Eifel; Schmincke 2007), is closely connected with asthenospheric upwelling associated with a plume (Ritter & Christensen 2007). Staircase river terraces document incision that has apparently accelerated since the Pliocene (Fuchs et al. 1983) or the latest Early to Middle Pleistocene (Meyer & Stets 1998), with the greatest amount of incision (up to 250 m) achieved during the past 880 kyr. While the aforementioned authors interpret the incision to be a response to uplift only, Demoulin & Hallot (2009) suggest that part of the total incision might be related to knickpoint retreat in tributaries rather than tectonic deformation. If correct, this process may reduce the total uplift to 140 m, yielding a Quaternary long-term uplift rate (since ~ 880 ka) of ~ 0.2 mm/yr (Demoulin & Hallot 2009). GNSS data of the Eifel area indicate an overall present-day uplift in the order of 0.5 – 1 mm/yr (Fig. 6-4c), which is likely related to mantle activity (Piña-Valdés et al. 2022, Henrion et al. 2020). Combined, these data suggest long-term and ongoing uplift of the Rhenish Massif – Eifel area at amounts that exceed eustatic sea-level changes. It is reasonable to assume that these processes will continue in the future. Under this assumption, the Mittelrhein section (Fig. 6-4a) would constitute an intermediate baselevel for the longitudinal profile of the Rhine.

The Upper Rhine Graben is part of the European Cenozoic Rift System (ECRIS). It is bordered to the northwest by the uplifting Rhenish Massif, to the south by the Jura Fold-and-Thrust-Belt, by the Vosges Mountains in the west and the Black Forest in the east (Fig. 6-4 and Fig. 6-5). Here, the Rhine (Oberrhein) drains a tectonic domain characterised by long-term intermittent subsidence, accompanied by erosion of the uplifting rift shoulders.

The present-day depositional centres (the northern, very deep Heidelberg Basin and the southern, less deep Geisswasser Basin) were established at least during the Pliocene – Quaternary. At this time, the central part of the Upper Rhine Graben was located in a restraining bend (Schumacher 2002) explaining the low subsidence and low sedimentation observed in this area (Karlsruher Swell; e.g. Gabriel et al. 2013, Edel et al. 2007, Hagedorn & Boenigk 2008, Rotstein & Schaming 2011). Importantly, the contrasting subsidence rates between Karlsruher Swell and Geisswasser Basin are expected to flatten the Oberrhein profile, leading to further deposition upstream. The Karlsruher Swell thus represents a buffer against increased incision. Quaternary subsidence rates are in the order of 0.1 – 0.3 mm/yr, increasing substantially towards the northern Upper Rhine Graben (Berger et al. 2005, Hagedorn & Boenigk 2008, Peters & van Balen 2007, Preusser et al. 2021).

Based on precise levelling data, Fuhrmann et al. (2014) inferred that the Upper Rhine Graben is mainly subsiding at rates between -0.2 and -0.5 mm/yr, which they attributed mainly to a combination of tectonic subsidence and sedimentary load (e.g. compaction and isostatic effects). This pattern is contemporaneous to slight uplift of up to 0.3 mm/yr of the graben shoulders at Black Forest and Vosges Massifs (relative to a reference point at the location of Freudenstadt in the eastern Black Forest Massif).

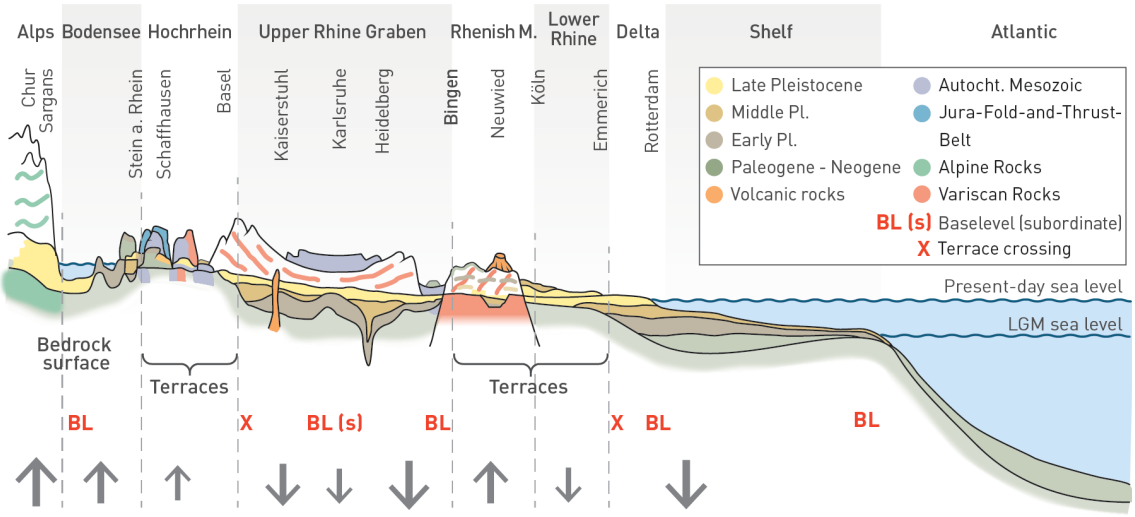


Fig. 6-5: Sketch of the Rhine River course with domains of Quaternary vertical motion

Schematic river course with simplified general geology, occurrence of fluvial terraces and location of terrace crossings, (intermediate) baselevels of regional relevance, and variability of sea level. Not to scale, after Neeb in Hinderer (2005) and Hinderer (2012). Tectonically driven rock uplift and basin subsidence (qualitatively marked by the grey arrows) influence the pattern and rates of fluvial incision along the Rhine. Northern Switzerland is mainly influenced by North Alpine Foreland rock uplift, subsidence of the Upper Rhine Graben, and rock uplift of the Rhenish Massif. Figure draft courtesy of H.A. Kemna.

North Alpine Foreland

The dominance of Alpine-related uplift (including tectonic and isostasy-driven processes) within the North Alpine Foreland results in a general surface uplift gradient oriented perpendicular to the Alpine front with rates that decline towards NNW (Fig. 6-6; Champagnac et al. 2009, Mey et al. 2016). This trend is also revealed by long-term thermochronology data (Fox et al. 2016), basin-wide erosion rates (Wittmann et al. 2007, Delunel et al. 2020) and measurements of present-day vertical motion (GNSS, precise levelling, e.g. Schlatter 2013, Nagra 2024l). The roughly north-south trend is also reflected by the principal flow direction of the larger rivers traversing Northern Switzerland, which suggests a long-term tectonic control on the geomorphic characteristics of this region.

Northern Switzerland is influenced by glacial/interglacial cycles with growth and decay of the Alpine Ice Field, including a number of large foreland glaciations (Section 3.5, Section 6.3; Nagra 2024j). Accordingly, Northern Switzerland is expected to undergo glacial isostatic adjustment (GIA), which affects the temporal and spatial uplift distribution (e.g. Craig et al. 2016). From studies related to large continental ice shields, it is known that GIA-related uplift after the Last Glacial Maximum (LGM) deglaciation shows a quasi-exponential form with fast and high-rate uplift shortly after deglaciation and continuously decreasing rates (see for instance Turcotte & Schubert 2014). A GIA effect might be still detectable in the Alpine Foreland, albeit to a lesser extent than in the Alps or in areas of large continental ice shields because of thinner ice and shorter duration of glaciation (see Section 6.3.2 and Nagra 2024j).

Long-term uplift proxies in Northern Switzerland (based on exhumation and incision rates)

Using exhumation or fluvial incision rates as proxy for rock uplift (which is the most important input parameter for the assessment of future erosion) is a simplification that requires the assumption of steady-state topography. Nevertheless, it allows a valuable first-order uplift estimate on long timescales, when short-term fluctuations level out. However, because of the complexities in tectonically active regions and the influence of climate fluctuations, this assumption needs to be treated with caution.

Past exhumation of the Molasse Basin is summarised in Section 4.3.5 and Chapter 3. Here the focus is on the second exhumation phase, which resulted in the present-day configuration. The amount of Miocene/Pliocene exhumation is generally estimated around 1 km (e.g. Mazurek et al. 2006, Villagómez Díaz et al. 2021, Omodeo-Salé et al. 2021, Schegg & Leu 1998). However, the timing of onset of exhumation is debated, with estimations ranging between 12 Ma and 5 Ma (von Hagke et al. 2015, Looser 2022, Mazurek et al. 2006, Villagómez Díaz et al. 2021). Under the simplest assumption of linear exhumation, inferred exhumation rates range between ~ 0.08 mm/yr and 0.20 mm/yr. However, it should be noted that several studies indicate heterogeneous exhumation rates in the past ~ 10 Myr.

Bedrock incision rates based on Quaternary geomorphic markers that are often used as proxy for rock uplift cannot be directly converted in Northern Switzerland. Here, effects of exhumation are complicated by the impact of baselevel lowering resulting from changes in drainage routing (see Sections 3.5 and 6.4.1.2). Nevertheless, a first-order assessment of bedrock incision can be calculated from bedrock elevation changes and the age of the Deckenschotter sediments (see Chapter 3 and Fig. 6-6c to e). Mean ages of 1.38 ± 0.31 Ma and 0.9 ± 0.13 Ma were assumed for the Höhere Deckenschotter (HDS) and Tiefere Deckenschotter (TDS), respectively to derive the incision rates shown in Fig. 6-6c to e (see Nagra 2024k for details on age determination). These rates (~ 0.1 – 0.2 mm/yr) are based on the elevation difference between the lowest data point of a respective Deckenschotter outcrop (Heuberger & Naef 2014) and the local erosion base (LEB). Incision rates increase slightly (mean rates HDS to LEB ~ 0.14 to 0.25 mm/yr and mean rates TDS to LEB ~ 0.2 to 0.32 mm/yr), if analysed along the valleys straddled by the Deckenschotter deposits and if using locally derived ages as well as the age ranges derived from samples across Northern Switzerland (see Nagra 2024k). Note that the incision signal not only includes a share from drainage reorganisation but is also a mixed signal stemming from rock uplift of the Alpine Foreland and baselevel fall at the transition to the Upper Rhine Graben. This may be seen in the the interpolated isolines of HDS to LEB and TDS to LEB heights (Fig. 6-6c and d) that are slightly rotated to a more NW-SE trend compared to levelling data and GNSS measurements (Fig. 6-6a and b).

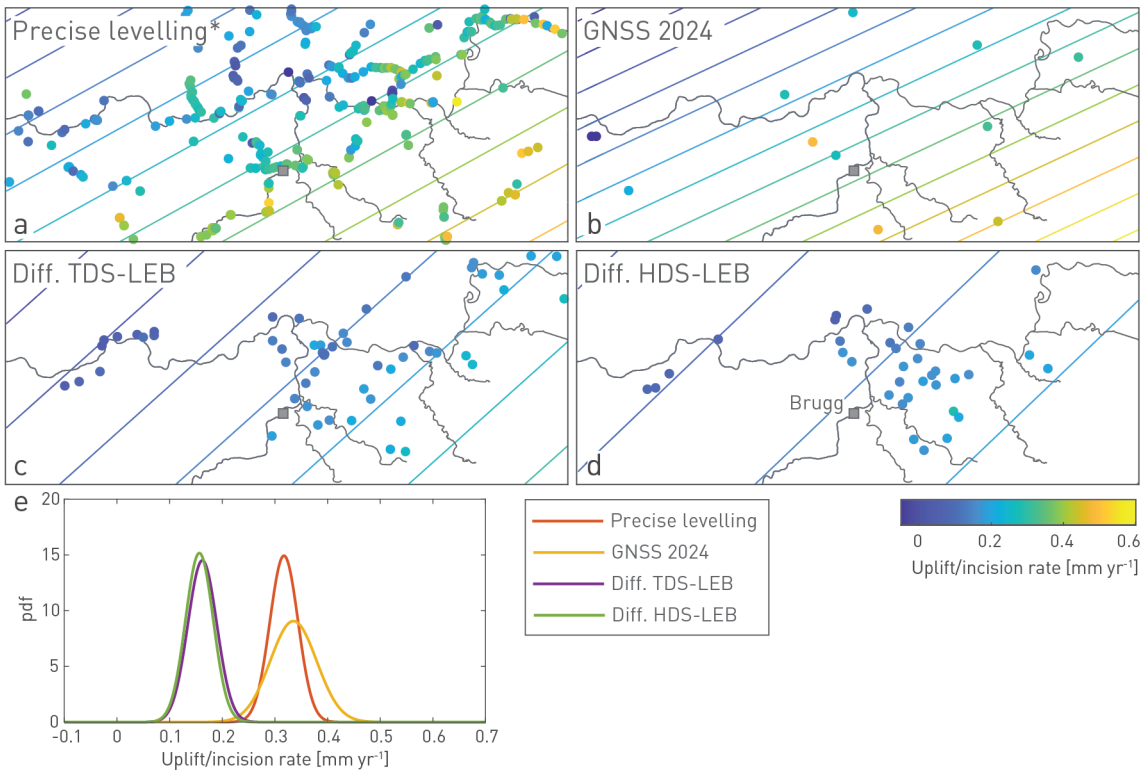


Fig. 6-6: Patterns and rates of surface uplift and incision proxies on different timescales

The uplift planes in (a) to (d) are calculated from point measurements based on a regression using the coordinates as independent variables. (a) The interpolation of precise levelling data shows a gradient at an azimuth of ~ 153°, perpendicular to the Alpine front and declining towards the foreland. Vertical rates are measured with respect to Laufenburg. * 0.28 mm/yr were added to the dataset of precise levelling, which corresponds to the GNSS-based rate at which Laufenburg is currently uplifting with respect to stable Europe. (b) Interpolation of the vertical GNSS data shows a similar pattern to precise levelling data at an azimuth of ~ 157°. (c) Interpolation of height differences between the geomorphic marker represented by the local erosion base (LEB, see Section 6.4.2.1 for definition) and the base of the Tiefere Deckenschotter (TDS) using a mean age of 0.9 Myr. (d) Similar to (c) but using the Höhere Deckenschotter (HDS) as marker and a mean age of 1.38 Myr. See Section 6.4.1.2 for a discussion of the age constraints for the Deckenschotter deposits. Note that the elevation differences are based on the lowest elevation of each mapped Deckenschotter occurrence (Heuberger & Naef 2014). (e) Probability density function of all uplift proxy data shown in the respective maps above calculated as an example for the location of the city of Brugg (square in maps). Note the higher rates of present-day geodetic surface uplift signals with respect to the longer-term incision rates. LEB: Local erosion base.

Short-term geodetic surface uplift rates in Northern Switzerland

Present-day surface uplift rates as derived from geodetic measurements (precise levelling and GNSS) are considerably higher compared to past exhumation rates or incision rates using these as proxy for long-term surface uplift. However, present-day surface uplift rates for Northern Switzerland agree with each other, when accounting for the different reference frames (Fig. 6-6a and b). The study area is currently uplifting at rates between ~ 0.2 and 0.5 mm/yr (Fig. 6-6 and Fig. 6-7). More detailed analyses are reported in Nagra (2024l).

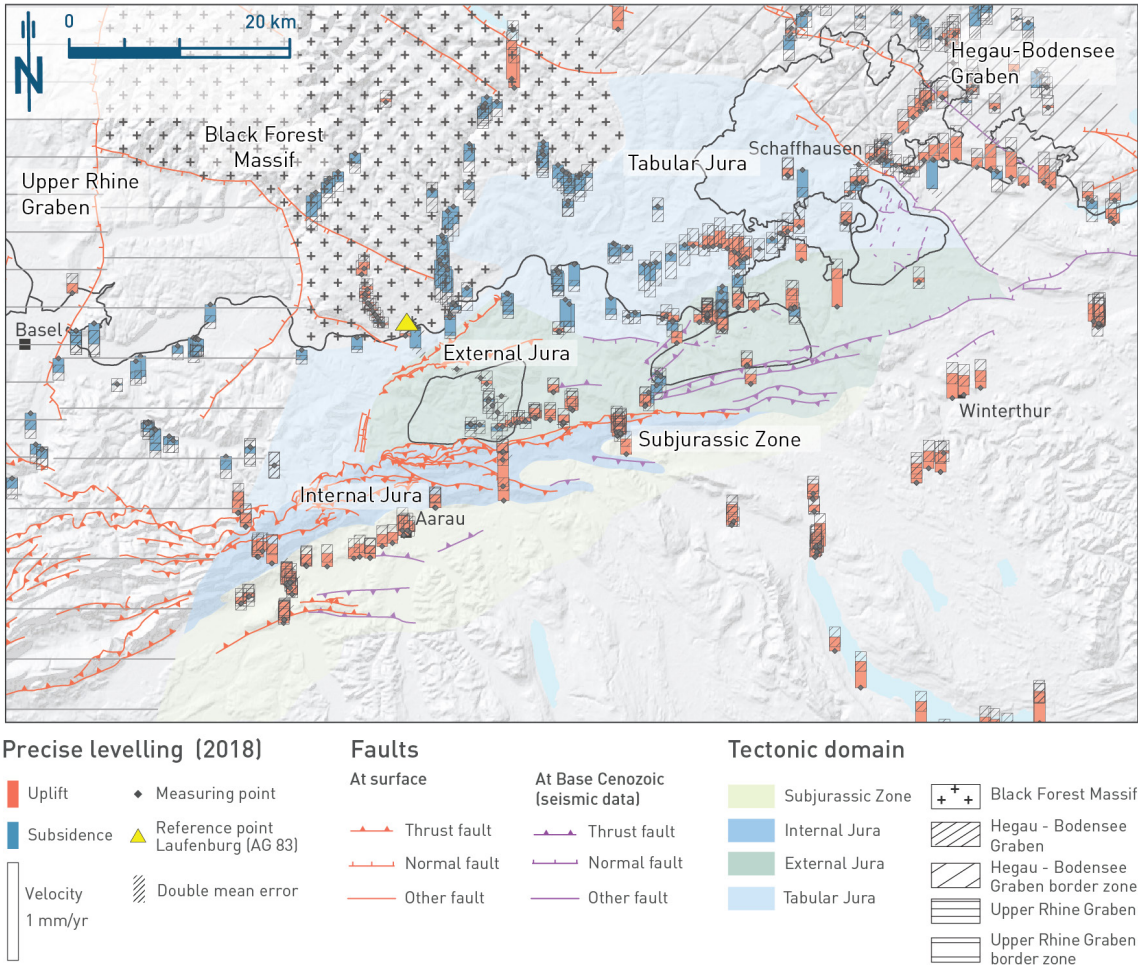


Fig. 6-7: Geodetic precise levelling data with measurement uncertainties

Precise levelling measurements (analysis NEOTEK2018 by swisstopo). Only data with a good geological quality ranking (> 8.5) are shown. Vertical velocities are based on levelling measurements relative to the fixpoint Laufenburg (yellow triangle). These data show a general trend of decreasing rates from the Alps towards the foreland. Note that only a selection of the structures from 3D seismic interpretation is shown to highlight the structural trends of regional importance. These were projected from Top Villigen Formation to Base Cenozoic.

Summarising the domains crossed by the Rhine River, it can be concluded that the main influence on the incision of the Hochrhein are low rates of North Alpine Foreland rock uplift, compared with low, potentially episodic subsidence within the Upper Rhine Graben. The longitudinal Rhine River profile is also influenced by continuous uplift of the Rhenish Massif and Eifel areas. Accordingly, the Hochrhein is presently buffered against fluvial processes approximately downstream of the city of Bingen (Fig. 6-5).

6.2.3 Present-day horizontal crustal movements in Northern Switzerland

All currently available data suggest that Northern Switzerland can be considered as an area characterised by low geodetic velocities. While the focus of the previous section was on vertical crustal motion (as a driver for erosion), this section highlights two additional datasets that provide evidence for ongoing tectonic activity in Northern Switzerland: (i) GNSS measurements at permanent stations, and (ii) the present-day earthquake distribution suggesting activity along major faults. The regions that record active deformation on multi-decadal timescales are the Upper Rhine Graben, the Hegau – Bodensee Graben and the Jura Fold-and-Thrust Belt.

Global navigation satellite system (GNSS)

Precise positioning measurements using permanently installed stations are used to monitor present-day motion (vertical and horizontal) at the Earth's surface. Such a network of permanent stations also exists in Switzerland and has been densified in Northern Switzerland (Nagra 2024l). It is observed that, in particular in the early time after installation, the stations are characterised by higher velocities which are probably related to artefacts. Stations with longer monitoring periods show more stable velocity fields (Nagra 2024l). Generally, the resolution for horizontal motion is difficult to quantify, but inferred to be close to 0.1 mm/yr or below (e.g. Fig. 6-8).

For a tectonic interpretation of the permanent stations located in Northern Switzerland, the horizontal motion is calculated in reference to stable Europe (Nagra 2024l). In general, horizontal velocity of the stations reveals a motion towards the NNE (Fig. 6-8). No differential movements above the general noise level between neighbouring stations are detectable. Thus, no significant tectonic activity above the detection limit or referable to specific regional faults can be detected via GNSS. The data are thus averaged over the entire Northern Switzerland to constrain average velocity anticipated to occur in the future.

To do so, the horizontal velocity vector from each permanent station is subdivided into a north component and an east component (Fig. 6-9). The east component is low, generally below 0.2 mm/yr for the considered stations. The north component is around 0.4 mm/yr. A slight decrease in the north component is observed in more northerly stations. The weak linear regression (Pearson's r = -0.30) indicates $1.4 \times 10^{-9} \pm 0.8 \times 10^{-9}$ yr^{-1} shortening or 1.4 ± 0.8 m/km/Myr (Nagra 2024l). The shortening amounts to $2.8 \times 10^{-9} \pm 0.9 \times 10^{-9}$ yr^{-1} if only the stations around the siting regions, which were built with focus on detecting potential tectonic activity (red in Fig. 6-9, Pearson's r = -0.71), are considered. This estimate is subject to substantial uncertainties and thus only serves for an order of magnitude estimation. The inferred strain rate agrees well with published data for Northern Switzerland also based on GNSS movements and is indicative for low rates of horizontal motion for Northern Switzerland (Sánchez et al. 2018, Houlié et al. 2018, Rabin et al. 2018, Piña-Valdés et al. 2022, Serpelloni et al. 2022). A very weak linear regression (Pearson's r = 0.03) indicates $0.1 \times 10^{-9} \pm 0.6 \times 10^{-9}$ yr^{-1} E-W directed extension (Nagra 2024l). It should be noted that the E-W directed trend with respect to station position along strike of the Alpes is not statistically robust but serves as estimate of order of magnitude. All recorded rates using GNSS are significantly lower than the typical time-averaged bulk strain rates in an orogen of 3×10^{-7} yr^{-1} as proposed by Fagereng & Biggs (2019). Therefore, it is concluded that Northern Switzerland is currently deforming at low rates.

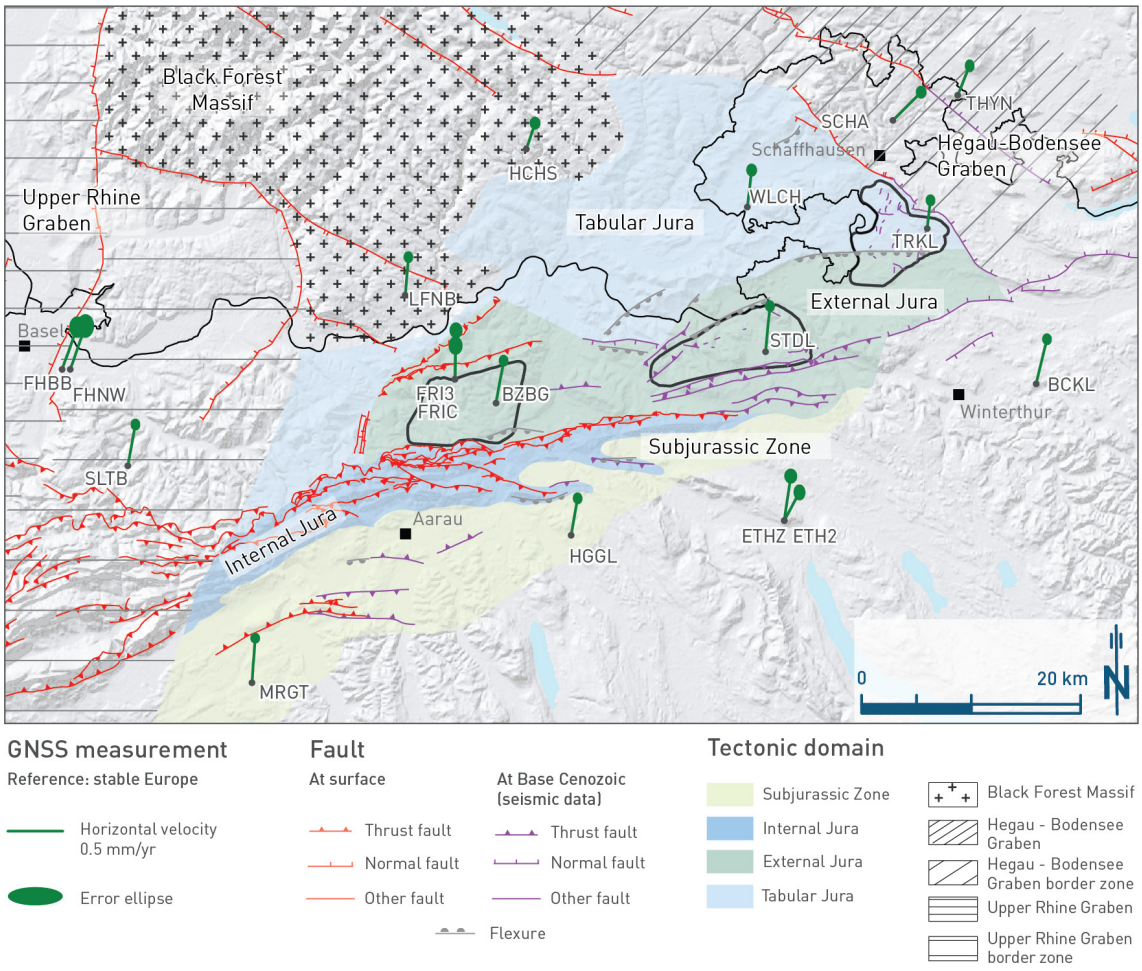


Fig. 6-8: Present-day horizontal motion of permanent GNSS stations in Northern Switzerland

Results are calculated in reference to the ETRF 2014 (i.e. relative to stable Europe representing a combination of the stations GRAS (Austria), JOZE (Poland), METS (Finland), ONSA (Sweden), POTS (Germany), WTZR (Germany), YEBE (Spain) and ZIMM (Switzerland). Stations with two vectors (ETHZ, ETH2, FRI3, FRIC) have two antennas at close distance. Fault inventory shows traces of faults mapped at the surface (red) or on Base Cenozoic (violet). Note that only a selection of the structures from 3D seismic interpretation is shown to highlight the structural trends of regional importance. These were projected from Top Villigen Formation to Base Cenozoic.

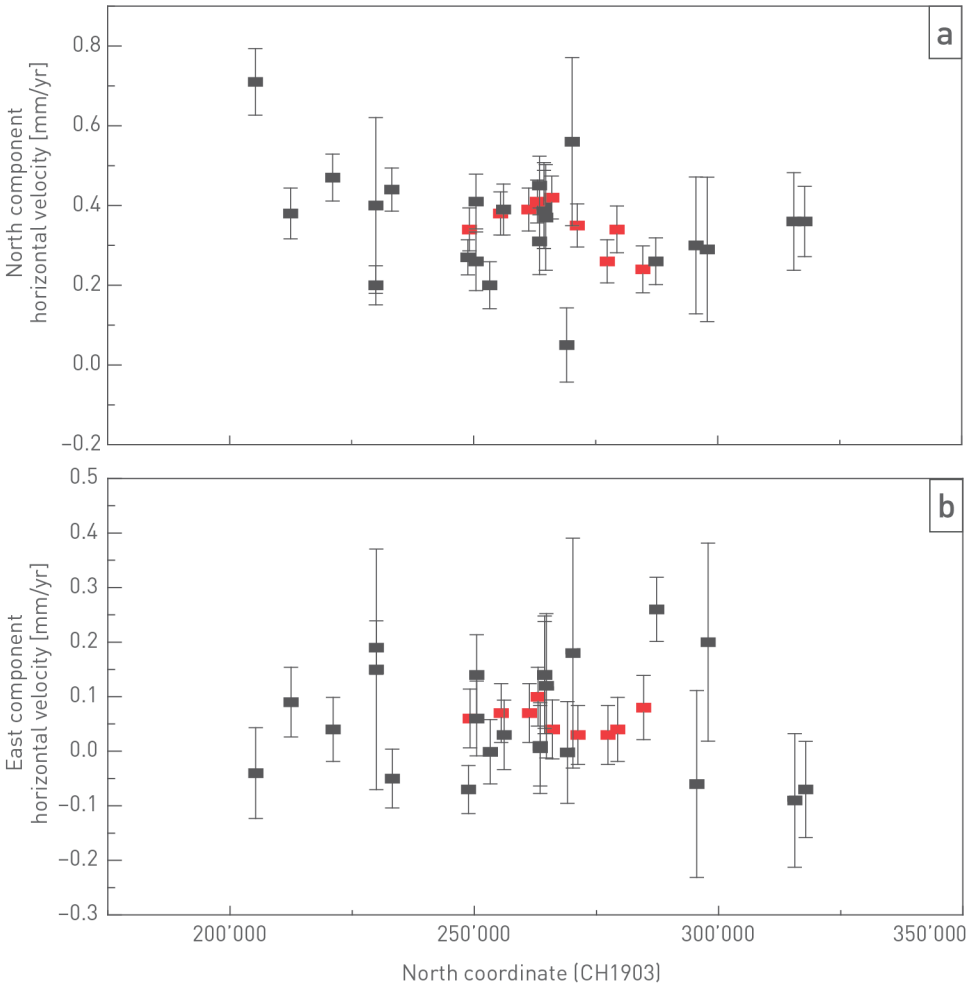


Fig. 6-9: Horizontal velocity components deduced from repeated GNSS measurements

Stations are located over approximately 120 km north-south and 200 km east-west extent centred over Northern Switzerland. (a) North component of horizontal velocity vector plotted against the north coordinate of the station. (b) East component of horizontal velocity vector plotted against the north coordinate of the station. Results are in reference to the ETRF 2014 (i.e. relative to stable Europe representing a combination of the stations GRAS (Austria), JOZE (Poland), METS (Finland), ONSA (Sweden), POTS (Germany), WTZR (Germany), YEBE (Spain) and ZIMM (Switzerland)). Red-labelled stations are NaGNet stations, whereas black-labelled stations are AGNES stations (AGNES: Automated GNSS Network for Switzerland). Stations are shown in Fig. 6-8. Stations with two vectors (ETHZ and ETH2, FRI3 and FRIC) have two antennas close-by.

Seismicity

Switzerland has a well-documented historical record of seismicity, which dates back several hundred years for felt seismicity (Fäh et al. 2011). The density of seismic stations was gradually increased over the past decades and now allows to determine earthquakes with magnitudes below 1.5 nearly everywhere in Switzerland and magnitudes even below 0.75 in the area comprising the siting regions (Nagra 2024l). Although earthquakes have been recorded in the area close to the siting regions, Northern Switzerland is one of the areas of lowest determined seismicity within the country (Fig. 6-10).

The largest known historical earthquake in the vicinity of the siting regions, located at the overlap between the Jura Fold-and-Thrust Belt and the Upper Rhine Graben, is the M_w 6.6 Basel earthquake in the year 1356 (Bakun & Scotti 2006, Fäh et al. 2011). Other historical and instrumentally recorded events had significantly smaller magnitudes (Fig. 6-10). The spatial distribution of seismicity in Northern Switzerland can be loosely correlated with the occurrence of the large tectonic domains. For example, the area around Basel with a comparatively higher level of seismicity is located in the Upper Rhine Graben (Fig. 6-10, see Section 4.3.3). Earthquakes in the Upper Rhine Graben have focal mechanisms typically indicating transtensional deformation (Fig. 6-10). Similarly, the Hegau – Bodensee Graben, which extends from the Bodensee to the NW (see Section 4.3.3), is characterised by increased present-day seismicity (Kahneman et al. 1982). Focal mechanisms of a series of earthquakes occurring between 2014 and 2019 located along the Neuhausen Fault within the Hegau – Bodensee Graben are characterised by predominant normal faulting (Fig. 6-10; see Diehl et al. 2023 and Nagra 2024l for more detail).

In the Jura Fold-and-Thrust Belt seismicity is concentrated in the central to western parts but is indicative of ongoing deformation in the Internal Jura (e.g. Lanza et al. 2022). Between these tectonic domains, seismicity in Northern Switzerland is sparse and earthquake hypocentres are distributed throughout the entire upper crust. A cluster of shallow, low-magnitude events occurs near the city of Eglisau (Fig. 6-10; see Nagra 2024l).

Glacial isostatic adjustment is known to influence not only the vertical surface velocities but also the horizontal velocity field. These effects are not only seen in the immediate vicinity of the glacial load, but also at long distances away (e.g. Grollimund et al. 2001), hence phases of increased fault activity need to be considered in association with glacial cycles, especially for a prolonged period following deglaciation. While glacial isostatic adjustment can perturb the overall stress field and thus inhibit or trigger faulting (e.g. Hetzel & Hampel 2005, Craig et al. 2016), it is unlikely that glacial isostatic adjustment alone is responsible for fault failure especially at a distance from the ice load (Craig et al. 2023).

Taking these considerations into account, it can be concluded that the timing of seismicity in Northern Switzerland might be predominantly caused by transient non-tectonic stress perturbations (e.g. related to glacial isostatic adjustment), while the overall mechanism of strain release follows the elastic long-term tectonic strain stored in the lithosphere. This tectonic strain is expected to be released along the pre-existing (regional) faults, as such faults have been repeatedly reactivated during the tectonic evolution (Section 4.3). In conclusion, Northern Switzerland is considered as tectonically active, but it is a low-strain area (see Nagra 2024l).

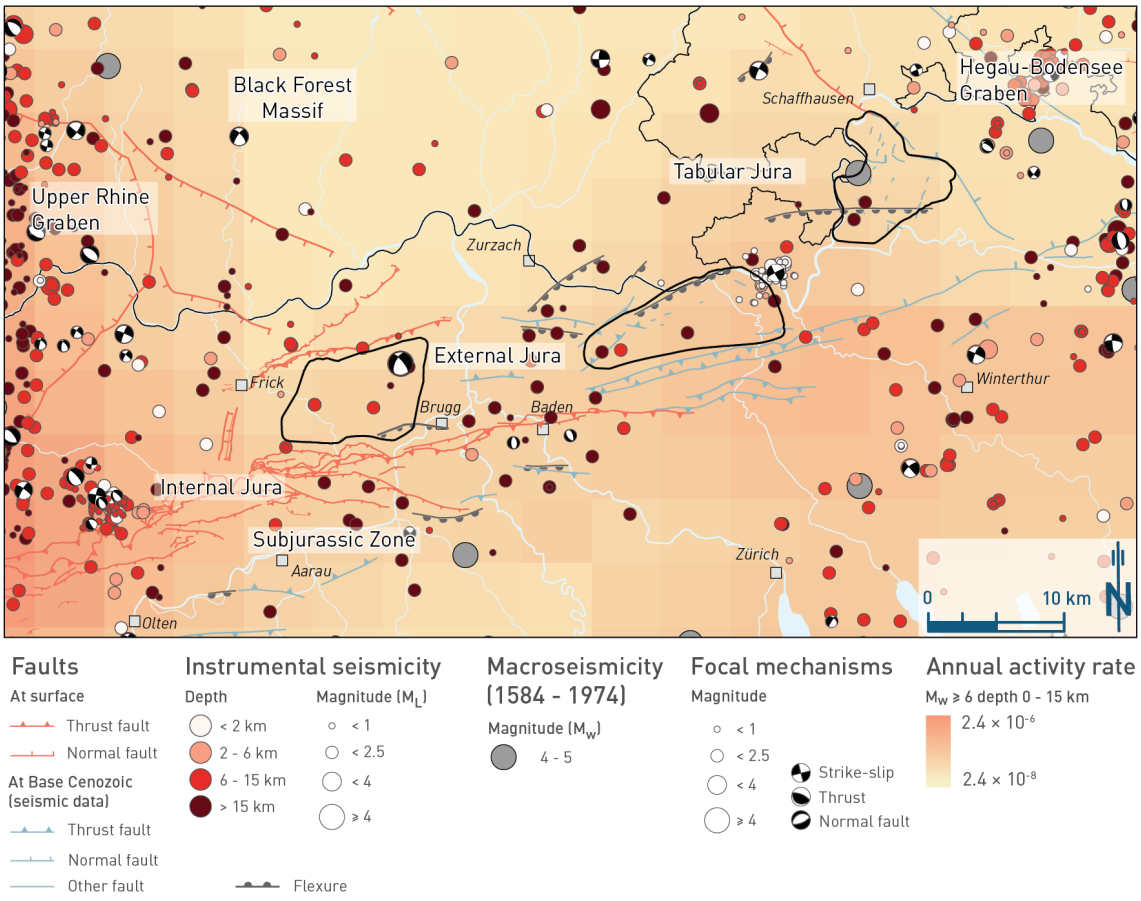


Fig. 6-10: Distribution of earthquakes and selected focal mechanisms

Recorded earthquakes (historical and instrumental) and modelled probability of earthquakes with $M_W \geq 6$ occurring in Switzerland, determined within the framework of the PRP project (swissnuclear 2013). The background colour indicates the annual probability of occurrence for earthquakes with $M_W \geq 6$ in an area of 0.05° longitude × 0.05° latitude (ca. 21 km^2) for hypocentral depths < 15 km. Seismicity is based on different catalogues: historical data prior to 1975 (Fäh et al. 2011) and instrumental data between 1975 and October 2023 (merged catalogue with data until 2023/10/03, including Swiss Instrumental Network, absolute re-localised events (following Diehl et al. 2021) and regional analyses of selected earthquake clusters; courtesy of T. Diehl). Focal mechanisms are shown for selected events of the instrumental catalogue. Note that only a selection of the structures from 3D seismic interpretation is shown to highlight the structural trends of regional importance. These were projected from Top Villigen Formation to Base Cenozoic.

6.2.4 Proposed tectonic evolution with respect to faulting

Tectonic deformation across Northern Switzerland is anticipated to continue at low rates in the future. The future evolution of Northern Switzerland with respect to tectonic loading is expected to be strongly controlled by the protracted effects of the Alpine orogeny, as the Swiss Molasse Basin and the Jura Fold-and-Thrust Belt are part of the North Alpine Foreland and form a mechanical wedge with the interior part of the Alps (Section 4.3).

With respect to the anticipated continued deformation in the siting regions three observations are particularly important:

(i) **The past tectonic evolution reactivated inherited faults acting as zones of weakness within the less deformed rock volume** (Section 4.3). It should be noted that the retrieved core material drilled within less deformed rock volume contains evidence for strain accumulation also in the rock volume in-between the regional fault zone. The accumulated strain is substantially lower than in the regional fault zones. This is exemplified in the small number of seismically mappable faults (Nagra 2024a, 2024b, 2024c). The phenomenon that inherited faults within the crust guide subsequent strain has been previously reported in literature (e.g. Cooke & Madden 2014, Bürgmann & Dresen 2008, Handy & Brun 2004, Cooke & Murphy 2004, Zoback et al. 2002, Townend & Zoback 2000, Kirby 1985).

(ii) **The overall geometry of the regional fault zones inferred from seismic reflection data seems suitable for allowing future slip along the fault plane and thus dissipation of strain**. Gently dipping fault segments are more prone to reactivation under thrusting, whereas steeper fault segments will preferentially accommodated strike-slip movements and normal faulting.

(iii) **Strain rates inferred from the recent GNSS measurements are low**. This implies that the anticipated total strain over the temporal and spatial scale considered for the deep geological repository is limited. Furthermore, the strain rates inferred from GNSS are comparable to strain rates inferred for the main folding and thrusting of the Jura Fold-and-Thrust Belt (Section 4.3.5).

Based on the aforementioned considerations, the most likely tectonic evolution for the next one million years is formulated with ongoing low-rate tectonic loading resulting in homogeneous N-S shortening and subordinate E-W extension across the siting regions. In addition, ice (un)loading and erosion are likely to predominantly affect the vertical component of the stress tensor and thus potentially impact fault reactivation. The predominant part of the anticipated strain will be dissipated along inherited regional fault zones.

The rock volume in-between the regional fault zones is likely to experience very limited amounts of strain. The evidence for reactivation of inherited faults and the concentration of instrumentally recorded seismicity along such structures provides a strong argument for tectonic stability of the potential disposal zones (Nagra 2024l). Nevertheless, the growth of new faults cannot be entirely excluded, but corresponding fault length and offset will be limited (Nagra 2024i).

6.2.5 Conclusions

The overall Cenozoic tectonic evolution of Northern Switzerland is an important driver for erosion, while seismicity and faulting are important factors that may affect long-term barrier performance. With respect to the assessment of future tectonic evolution, it can be concluded that:

- The neotectonic setting of Northern Switzerland is influenced by the effects of the ongoing Alpine orogeny in the south, transtensional deformation within the Upper Rhine Graben and the Hegau – Bodensee Graben, and tectonic activity of the Jura Fold-and-Thrust Belt. This setting defines the boundary conditions for erosion processes (low uplift rates and baselevel drop).
- The main neotectonic influence on the incision of the Hochrhein are low rates of North Alpine Foreland rock uplift, compared with low, potentially episodic subsidence within the Upper Rhine Graben. The longitudinal Rhine River profile is also influenced by continuous uplift of the Rhenish Massif and Eifel areas. Accordingly, the Hochrhein is presently buffered against fluvial processes approximately downstream of the city of Bingen.
- Uplift rates in Northern Switzerland are generally low and in sub-mm/yr, ranging between 0.1 and 0.5 mm/yr, with strong dependency on the time interval. Average long-term uplift rates are < 0.3 mm/yr.
- The trend of rock uplift reveals northward-decreasing rates perpendicular to the Alpine front. Thus, rock uplift is predominantly an Alpine signal, irrespective of the cause (tectonic vs. isostatic compensation).
- Northern Switzerland is a low-strain domain; Horizontal velocities show a slight decrease in their north component towards the north corresponding to the inferred strain rate (~ 1 – 3 m/Myr/km). Tectonic deformation rates are currently low and comparable to the past (Section 4.3), which increases confidence in their extrapolation.
- Seismicity in Northern Switzerland is sparse and generally at a low level compared to, for instance, the Upper Rhine Graben.
- Inherited faults have acted as zones of weakness that preferentially localise strain. It is anticipated that this will continue in the future and deformation will focus along the regional fault zones rather than forming new faults between these zones.

6.3 Climate evolution

Key points:

- Global climate-proxy data document that the Quaternary has been characterised by glacial/interglacial cycles with predominant 100-kyr cycles since at least ~ 700 kyr that influenced the formation of extensive ice covers in Northern Switzerland.
- Past glacial climate conditions in Northern Switzerland are modelled to a regional level using a nested approach. Ice flow models using these modelled climate conditions reproduce the maximum ice cover extent for the last glaciation as known from proxies, such as moraines.
- Coupled ice flow models allow estimation of the glacial erosion potential in Northern Switzerland during foreland glaciations. Key controlling factors are basal ice temperature, sliding speed and high subglacial water discharge.
- Future glacial inception and severity of glaciations depend on anthropogenic CO_2 emissions and may be significantly delayed, e.g. nearly 200 kyr for a present-day emission scenario.
- Each glacial period is expected to be associated with permafrost conditions during the phases of coldest temperatures. Permafrost is expected to reach maximum depths of 100 – 200 m.
- Due to the different distance to the Alps and different topography, ice thicknesses and the duration of ice occupation at the sites varied during past glacial cycles (ZNO > NL > JO). The same pattern will most likely be seen during future glaciations with ice thicknesses between 200 and 400 m and durations of ice occupation between 1'000 and 3'000 years.

The geology and geomorphology around the repository will be subject to erosional processes that are in turn influenced by climatic forcing. Large foreland glaciations may not only cause over-deepening of subglacial valleys but may also cause lithospheric depression and later isostatic rebound after deglaciation. These changes in mass may affect the local stress field as well as the hydrogeological system. Accordingly, this section provides the basis for climate as a driver of (deep glacial) erosion (Section 6.4.3.3). The coupling of climate to ice flow modelling allows derivation of a number of glacial parameters (e.g. ice thickness) which may be indicative for the evaluation of long-term hydrogeological changes (Section 6.5).

Section 6.3.1 starts with an overview of Quaternary climate evolution at a global scale (more regional aspects are summarised in Chapter 3). Past glacial cycles were important for the erosion history of Northern Switzerland, therefore the focus in Section 6.3.2 is on glacial conditions, including the occurrence of permafrost and knowledge about ice flow during extensive foreland glaciations. Based on the previous findings, changes in Earth's orbital parameters and anthropogenic CO_2 emissions, Section 6.3.3 provides model scenarios that were generated to better understand the onset of potential future glaciations. The main conclusions are provided in Section 6.3.4.

A more in depth discussion of climate evolution and ice flow is provided in Nagra (2024j).

6.3.1 Climate during the Quaternary

6.3.1.1 Global Quaternary climate

During the Quaternary Period, there have been multiple variations between cold and warm climates which gave rise to glacial and interglacial periods. During the glacial periods, ice sheets expanded across the globe, while interglacial periods reflect times of much-reduced ice-sheet extent. The glacial periods themselves comprise extremely cold intervals, known as stadials, and milder intervals that are referred to as interstadials.

These cycles of glacials and interglacial periods are commonly known as glacial cycles ("ice ages"). During at least the last ~ 700 kyr, i.e. after the Middle Pleistocene Transition, the glacial cycles lasted approximately 100 kyr (e.g. Clark et al. 2006).

Temperature-dependent O^{18}/O^{16} isotopic ratios ($\delta^{18}O$) in, for example, calcitic foraminifera from marine sediments, are typically used to identify glacials and interglacials in the geological record. Because foraminifera are in isotopic equilibrium with ocean water, $\delta^{18}O$ variations mainly reflect sea level (and hence global ice volume) and (water-) temperature if $\delta^{18}O$ records from different locations are combined (e.g. Ahn et al. 2017). Because of its higher vapour pressure, the H_2O^{16} molecule evaporates preferentially from the ocean surface. In the case of cold temperatures and expanding global ice, this results in seawater, which is residually enriched in ^{18}O. Conversely, lower $\delta^{18}O$ values typically correspond to warmer periods with a reduced ice volume.

Lisiecki & Raymo (2005) combined $\delta^{18}O$ values from 57 globally distributed sites into the LR04 stack database. From this record, marine isotope stages (MIS) were defined for the past 5.3 Myr. Even-numbered stages represent glacials, while odd numbers refer to interglacials (Fig. 6-11c, see Fig. 3-11 for a longer record).

Another important proxy of past global climate evolution is the greenhouse gas concentration, mainly CO_2, which can be measured from air trapped in gaseous bubbles in ice cores. Variation in CO_2 has been described for the last 800 kyr in ice cores from Antarctica (Vostok and EPICA; see Lüthi et al. 2008 and references therein). As well as greenhouse gas concentrations, orbital parameter variations have been proposed to be significant drivers for the change from glacials to interglacials (Ruddiman 2003). Since the early studies by Milankovitch in the 1920s, the orbital parameters of precession, eccentricity and axial tilt can be calculated accurately for the past and future and document changed cyclical orientations of the Earth towards the sun through time (Milankovitch 1941, Berger 1977, Roe 2006) and thus, the energy received by the Earth's surface (insolation).

Fig. 6-11 shows the measured $\delta^{18}O$ concentration from microorganisms in deep-sea sediments together with insolation (based on orbital parameters of the Earth), global mean temperature difference, CO_2 content and the estimated global ice volume for part of the Quaternary. The results show that CO_2 concentrations ranged between 300 ppm and 170 ppm during the last 800 kyr and correlate well with the MIS determined from the LR04 stack (Fig. 6-11). In general, high insolation correlates with warm periods, while low insolation values correlate with colder periods.

Currently, the Earth is in a relatively warm period (MIS 1). MIS 1 started approximately 14'000 years ago and has continued until today (Walker et al. 2009). It began with a gradual warming from the last glacial period, MIS 2, which lasted from 29'000 to 14'000 yr ago (Lisiecki & Raymo 2005). The Last Glacial Maximum (LGM, ~ 24'000 yr ago) is the term used to describe the most recent substantial ice sheets covering North America, Europe and Asia that caused global sea levels to fall by about 120 m (Clark et al. 2009). Shifts between glacial and interglacial periods were rapid, occurring within a few thousand years (Clark et al. 2007).

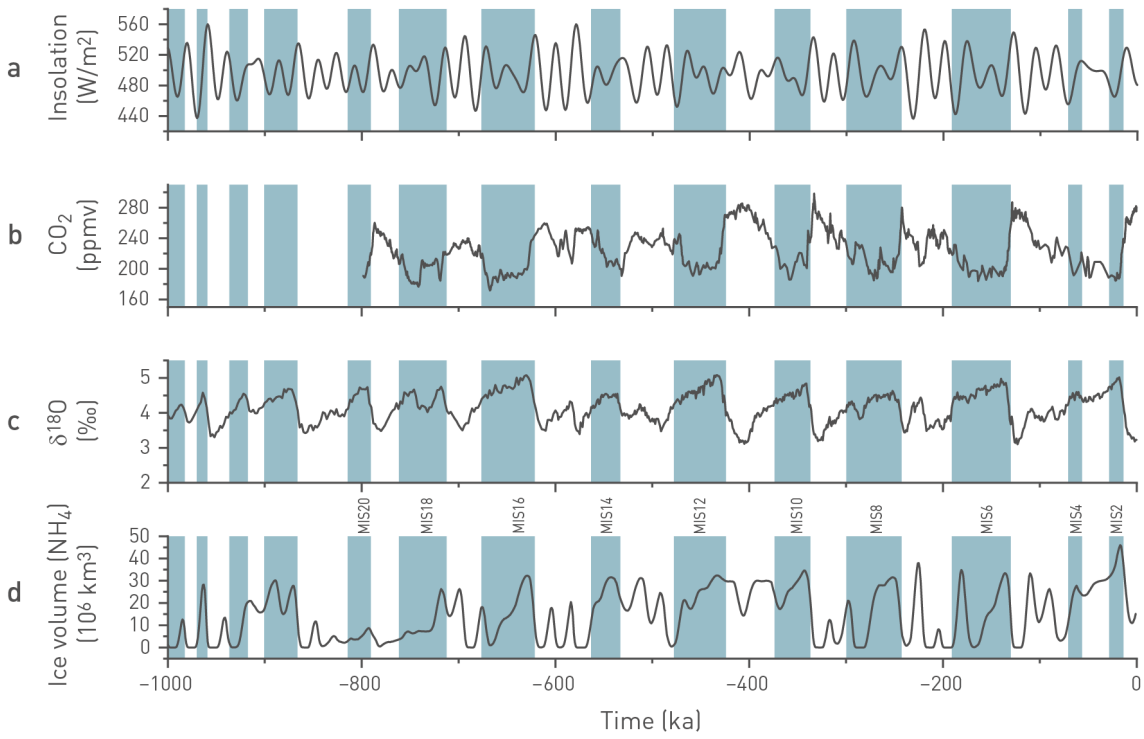


Fig. 6-11: Comparison of climate proxies for the northern hemisphere during the last million years

(a) Insolation is given for 65°N (July) according to Berger & Loutre (1991). (b) The CO_2 content follows the determinations from Lüthi et al. (2008) and is based on measurements from the EPICA ice core in Antarctica. (c) $\delta^{18}O$ was determined from 57 globally distributed benthic records, collected from the scientific literature (Lisiecki & Raymo 2005). (d) $\delta^{18}O$ was used to calculate a rough estimate of the northern hemisphere ice volume. Blue bars depict even-numbered MIS (periods of glaciations), white sectors correspond to interglacial stages.

6.3.1.2 Past climate conditions in Northern Switzerland

The short introduction to climate proxies on a global scale can be viewed as a general guideline to understanding the behaviour of climate and its potential impact at regional and local scales. On a local scale, climate is significantly influenced by e.g. local topographic conditions, distance to the ocean and poles and with respect to prevailing wind directions.

In Northern Switzerland, regional climatic conditions may have influenced the spatial and temporal evolution of foreland glaciations. Up to 15 Quaternary glaciations are assumed to have reached the foreland (Preusser et al. 2011, Ivy-Ochs et al. 2006). Of these, the potentially largest known may have occurred in the past ~ 800'000 years (see also Section 3.5, Section 6.4.1.4 and Fig. 6-12; Preusser et al. 2011). The advance and retreat of glaciers and their maximum extents for the Birrfeld, Beringen, Habsburg and Möhlin Glacials (Fig. 6-12) were reviewed by Preusser et al. (2011) and summarised in Nagra (2024k). The Möhlin Glacial is of particular interest because it reached the southern slopes of the Black Forest and is believed to be the most extensive glaciation (MEG) in the Swiss Alpine Foreland during the Quaternary (e.g. Graf 2009b). At that time, the different glaciers (Rhine, Linth, Reuss and Aare – Valais Glaciers) combined and formed a contiguous ice cover. Similarly, during the LGM, glaciers also reached far into the Alpine Foreland, forming a continuous ice cover but with a reduced north-western extent that was smaller

compared to that during the MEG. Ice extents of the Habsburg, Beringen and Birrfeld Glacials were smaller than the Möhlin Glacial and, at least during the Habsburg and Birrfeld Glacials, the ice is not believed to have formed a contiguous ice cover (Preusser et al. 2011). The ZNO siting region and partly also NL were covered during LGM-size glaciations, while JO remained ice-free. NL was covered during the Beringen glacial. JO is only covered by exceptionally large foreland glaciations, such as the Möhlin Glacial (Fig. 6-12) – these are considered key glacials in future erosion assessments.

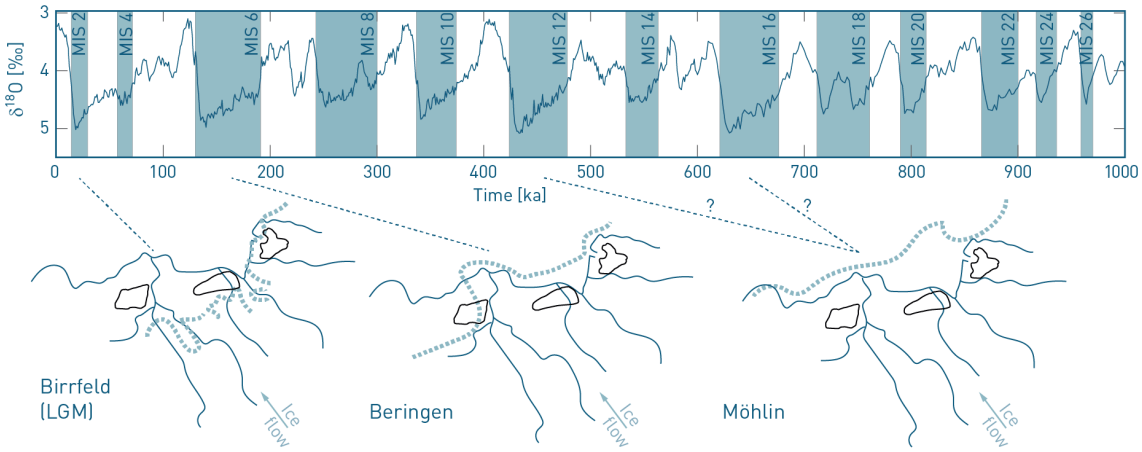


Fig. 6-12: Key glacials in Northern Switzerland

Glacials (MIS) of the past million years are highlighted together with the key glacials of Northern Switzerland. Sketches show the inferred maximum ice extent (dashed lines) during these times, together with the present-day main rivers and outlines of the siting regions. Ice extent during the LGM covered ZNO and the easternmost parts of NL. The Beringen Glacial is probably associated with MIS 6 and covered ZNO, NL and the easternmost part of JO, and the presumably most extensive glaciation (MEG, Möhlin) covered all three siting regions and is probably associated with MIS 12 or MIS 16 (Preusser et al. 2011).

To understand the regional behaviour of climate and climate-related processes for a specific region of interest, information from local proxies is needed. Such data are often based on analyses of pollen records in (lake) sediments or on measurements such as the $\delta^{18}O$ from dated speleothems (e.g. Luetscher et al. 2021). Proxy information for periods before the LGM is often sparse and more ambiguous but exists, for instance, from the Bergsee (Germany, e.g. Becker et al. 2006, Duprat-Oualid et al. 2017, Kämpf et al. 2022), Wehntal (Switzerland; e.g. Anselmetti et al. 2010, Dehnert et al. 2012), la Grande Pile (France, e.g. Woillard 1979, Rousseau et al. 2007), and Füramoos (Germany, e.g. Bolland et al. 2022).

Davis et al. (2024) compiled a large number of available pollen data for the LGM, including the Alpine realm, and determined mean seasonal values for temperature and precipitation. Russo et al. (2024) compared these values to climate simulations shown in the following figures. Although the exact timing of events between pollen proxy data and climate simulations is difficult to determine, Russo et al. (2024) showed that climate simulations for the LGM are in good agreement with parameter estimations from regional data (see also Nagra 2024j for more detail).

Together with the results of the climate simulations of MIS 4, MIS 6, MIS 8, and MIS 16 and their respective differences, details on the modelling approach can be found in Nagra (2024j). Their comparison suggests that the interplay between mean temperature changes and precipitation

changes as well as their seasonality and variabilities are important for the conditions that led to glacier advances into the Alpine Foreland of northeastern Switzerland. Below, illustrations of downscaled simulated climate conditions (temperature, precipitation, and climate classification) are presented for a comparison between pre-industrial (PI) and LGM conditions (Fig. 6-13). These simulations were further used for the ice-flow modelling (Section 6.3.2). Similar maps for older MIS are documented in Nagra (2024j).

Under pre-industrial conditions (PI) (Fig. 6-13c, d, g, h), a mean temperature of 8.3 °C (as averaged over 10 years in Switzerland) was simulated, which is slightly warmer, in particular during winter, than observations suggest. In this simulation, the difference in temperature between the coldest and the warmest month is 17.5 °C. The yearly mean precipitation is 4.39 mm/day, which is an overestimation compared to observations, again in particular in winter. The difference between the driest and the wettest month, a measure of the variability within a year, is 2.74 mm/day.

The simulated LGM (Fig. 6-13e, f, i, j) is, on average, much colder than PI, leading to a mean temperature of only -1 °C with a reduced difference of 15.7 °C between the coldest and warmest month. It is also drier than PI, showing a mean precipitation of 3.35 mm/day and a slightly reduced difference in precipitation of 2.65 mm/day over northeastern Switzerland.

Climate classifications can be derived based on such simulations (Fig. 6-13a and b). While, during the pre-industrial period, most of Switzerland experienced a temperate climate (except for the Alps), during the LGM most of Switzerland saw a polar climate (Fig. 6-13b).

During the glacials, polar climates (with ice cover or tundra) were likely to have been most prominent in Switzerland. Very low temperatures during the glacials would also have caused extensive permafrost conditions. Permafrost refers to a condition where subsurface material remains at negative temperatures (frozen) throughout the year and often over very long periods of time (centuries, millennia and more). Permafrost exists today at cold high latitudes and high altitudes. The fact that deep-reaching permafrost during past glacials also existed in wide parts of the European lowlands was documented by the analysis of characteristic deformation features (ice wedge casts and other cryoturbation phenomena) caused by former deep-reaching frost action in unconsolidated sedimentary deposits (Poser 1948, Washburn 1979, Lindgren et al. 2016). During the coldest time intervals, permafrost north of the Alps was continuous, cold (mean annual surface temperature about -5 °C with shorter-term extremes down to -10 °C; Duprat-Oualid 2019) and reached depths of about 100 to 200 m (Haeberli et al. 1984, Frenzel et al. 1992, Delisle et al. 2003).

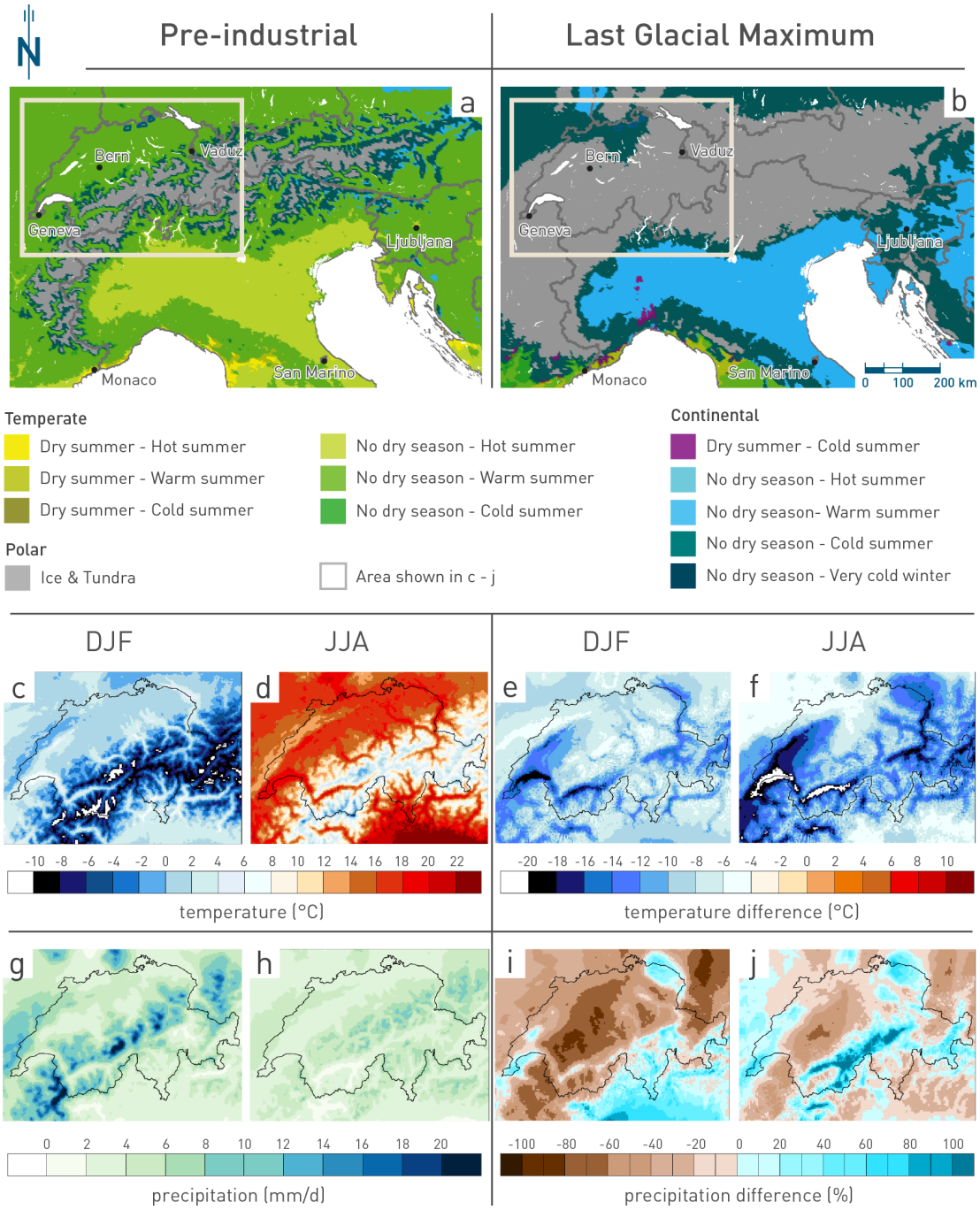


Fig. 6-13: Temperature, precipitation and climate classification for pre-industrial and LGM climates

The upper panels (a) and (b) show climate conditions from simulations of the pre-industrial period and the LGM (MIS 2), respectively. The climate classifications follow the Köppen classification scheme (Köppen 1918, see Nagra 2024j for more simulations). Note the extent of the polar climate, especially in Northern Switzerland. Below, the figures show simulated mean temperatures for the pre-industrial period in °C for (c) December, January, February (DJF) and (d) June, July, August (JJA), followed by temperature simulation for LGM, visualised as the difference with respect to pre-industrial values in °C (e and f). (g) Simulated precipitation for the pre-industrial period (DJF) as absolute values in mm/day, (h) same as (g) but for period JJA; (i) simulated precipitation for LGM for the period DJF, visualised as the difference with respect to pre-industrial in %; (j) same as (i) but for period JJA.

6.3.2 Glacier development and erosion potential in Northern Switzerland

Simulations of past climates (Section 6.3.1) are used to gain a better understanding of the potential development of glaciers in the Alps, with special focus on the northern central Alps and corresponding ice flow into the forelands of Northern Switzerland and adjacent Southern Germany. The climate simulations of PI, MIS 2, MIS 4, MIS 6, MIS 8 and MIS 16 and a climate signal proxy are combined to construct a transient climate over past glacial periods. This transient climate is used to force thermo-mechanically coupled, three-dimensional transient ice-flow models to simulate the dynamic evolution and basal conditions of glaciers in the Alps (see Nagra 2024j for further details).

The coupled climate and glacier modelling is used to assess the effects of ice-flow dynamics and related erosion potential in the siting regions during previous glacials. The assessment is based on quantitative criteria that incorporate the physical processes upon which glacial erosion depends (e.g. ice thickness, timing and duration of ice occupation, basal ice temperature, basal sliding velocity and subglacial routing of meltwater). These criteria can be derived from the numerical reconstruction of the ice surface geometry (see Fig. 6-14), flow dynamics and temperature field of the Alpine Ice Field and, in particular, the Rhine Glacier system (Fig. 6-16) during past glaciations.

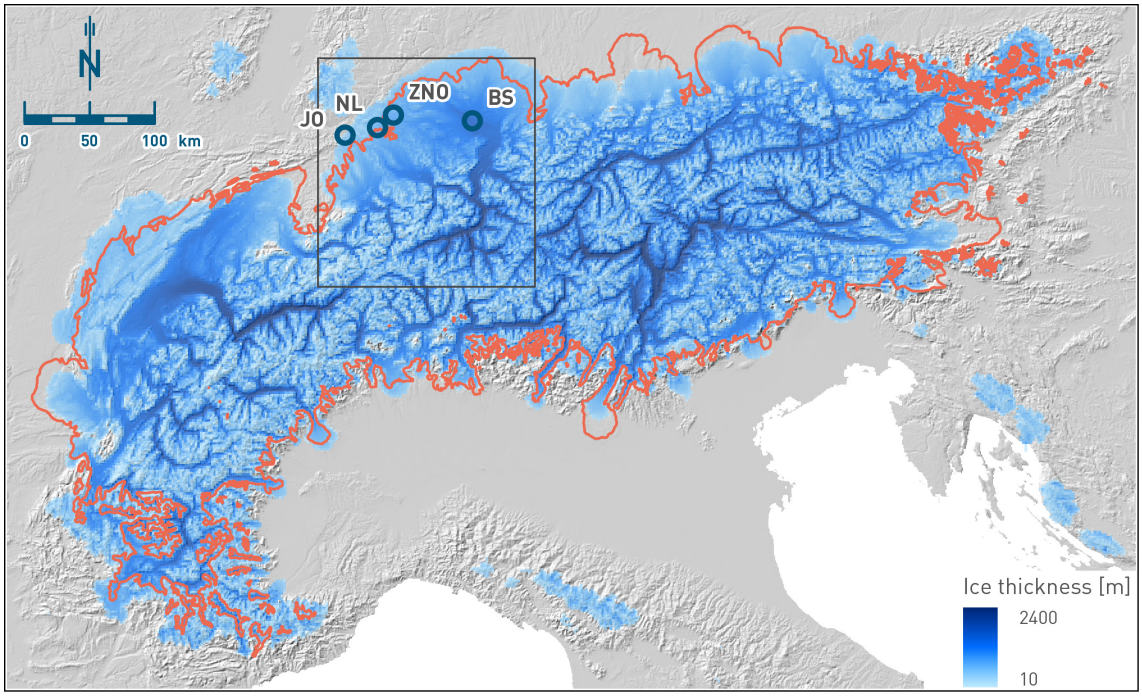


Fig. 6-14: Modelled maximum ice thickness and extent of the Alpine Ice Field during MIS 2

Geomorphologically reconstructed LGM outline is modified after Ehlers et al. (2011) (red line). Note that different glacier lobes reached their maximum ice thicknesses and extents at different times because fluctuations are controlled by the size of catchments and the resulting inertia of each glacier. The blue circles (JO = Jura Ost, NL = Nördlich Lägern, ZNO = Zürich Nordost, BS = Bodensee) indicate locations where ice thickness and duration of ice occupation have been evaluated (Fig. 6-15). The box shows the Rhine Glacier system (outline of Fig. 6-16). As basal topography for the model simulations, the publicly available NASA Shuttle Radar Topographic Mission (SRTM, http://srtm.csi.cigar.org/), the Digital Elevation Model (DEM), re-sampled at 2 km resolution and with major lakes and present-day glaciers removed (Farinotti et al. 2019) are used.

The modelled maximum east to west extent of the Alpine Ice Field during the LGM matches the geomorphological reconstruction of Ehlers et al. (2011) fairly well (Fig. 6-14). Furthermore, the results show that the flow dynamics of individual modelled glaciers agrees with several independent key geological observations, including moraine-based maximum reconstructed glacial extents, known ice transfluences and trajectories of erratic boulders of known origin and deposition (Jouvet et al. 2023).

The boxplots in Fig. 6-15 show the results from different simulations that were carried out as part of a sensitivity study (Nagra 2024j) and suggest a maximum ice thickness of ~ 200 – 400 m and a duration of ice occupation of ~ 1'000 – 3'000 yr in the ZNO and NL siting regions, while JO essentially remained ice-free. Ice thickness and ice occupation duration are significantly larger in the Bodensee region (BS in Fig. 6-15) due to its more proximal position to the Alpine front.

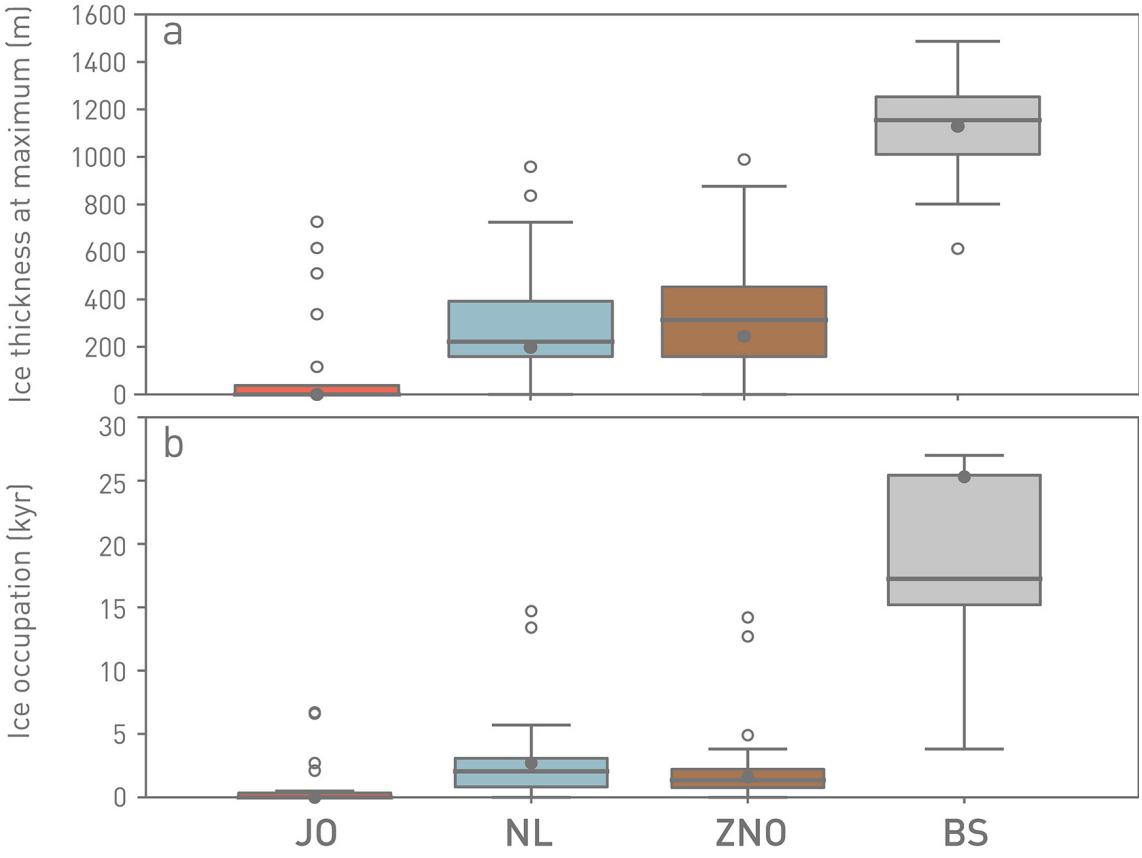


Fig. 6-15: Boxplots of modelled ice characteristics during the LGM

(a) Maximum ice thickness and (b) Duration of ice occupation. The boxes depict data between the first (25th percentile) and third quartile (75th percentile) known as the interquartile range (IQR), while the grey line in the box shows the median value (50th percentile). Black solid points indicate the result from the reference simulation. From above the upper quartile, a distance of 1.5 times the IQR is measured out and a whisker is drawn up to the largest point from the dataset that falls within this distance. Similarly, a distance of 1.5 times the IQR is measured out below the lower quartile and a whisker is drawn up to the lowest point from the dataset that falls within this distance. All other points are plotted as outliers. Data are based on 19 simulations. See Fig. 6-14 for the locations where ice thickness and duration of ice occupation were evaluated in the Jura Ost (JO), Nördlich Lägern (NL) and Zürich Nordost (ZNO) siting regions as well as for the Bodensee (BS) region.

These results are important for a variety of reasons. Firstly, they provide the boundary conditions for ice dynamics with respect to erosion potential. Secondly, ice loading affects mantle processes (e.g. Wu & Peltier 1982), which in turn cause transient perturbations of the stress field, including effects on uplift pattern and magnitudes (see Section 6.4 and Nagra 2024k) and may influence fault behaviour (see Section 6.2 and Nagra 2024l) and hydrogeological changes (Section 6.5). Assuming an ice density of 917 kg/m^3 and mantle density of 3'300 kg/m^3, a 400 m ice thickness could produce a lithospheric depression of up to ~ 110 m, if equilibrium is reached. Reaching equilibrium depends, in turn, upon the duration of the ice occupation and the viscoelastic response time influenced by the viscosity of the mantle. These parameters also influence the duration and magnitude of postglacial adjustment. Lithospheric glacial loading and unloading is accompanied by changes in vertical stress (σ_v) below the load but deviating horizontal stresses which extend beyond the ice cover (Grollimund et al. 2001, Steffen et al. 2022, Craig et al. 2023).

Basal ice temperature and sliding speed are two key variables that describe basal conditions relevant for glacial erosion (Fig. 6-16). Glacial erosion occurs where ice is warm-based (not frozen to the ground), which enables basal sliding and thus abrasion. Furthermore, where melt-water is able to flow along the bed, this promotes rapid sliding and stimulates quarrying (plucking) or may directly lead to subglacial meltwater erosion. Simulations for the LGM indicate that basal ice reached the pressure melting point over much of the piedmont lobes of the Rhine Glacier system, and also in the glacial valleys that fed these lobes (Fig. 6-16a). In the lobes, despite low surface slopes and low basal shear stresses in the Alpine Foreland, sliding dictated the main fluxes of ice, which closely followed bedrock topography. Ice was channelled between bedrock highs along troughs, some of which coincided with glacially eroded overdeepenings (Fig. 6-16b). These sliding conditions favoured glacial erosion by abrasion and quarrying.

Assuming that the glacial erosion rate scales with the basal sliding speed, the sliding distance calculated by time-integrating the sliding speed (Näslund et al. 2003, Staiger et al. 2005, Yanites & Ehlers 2016) yields a metric for glacial erosion by moving ice. Transient ice-flow modelling of the Rhine Glacier system over the course of the last glacial cycle indicates that the sliding distance is greatest at the base of Alpine valleys where sliding is fastest and where ice occupation time is longest (Fig. 6-16c). However, the sliding distance does not correlate well with the location of existing overdeepened valleys in the Alpine Foreland (Fig. 6-16c) owing to the smaller sliding speeds near the ice margin and the short time period during which ice covered the distal foreland (Fischer et al. 2021).

Based on computed time-dependent ice surface elevations, maps of hydraulic potential and associated flow accumulation area are calculated to estimate the location of subglacial water drainage routes and water fluxes (Chu et al. 2016). Time-integration of the flow accumulation area yields a metric for erosion by subglacial water flow. Larger values of time-integrated flow accumulation area indicate zones with significant subglacial water flow that has the potential to enhance sediment removal and increase subglacial fluvial erosion. Results from simulations of the Rhine Glacier system during advance and retreat in the foreland indicate that subglacial water discharge was high and focused along glacial valleys and existing overdeepenings (Fig. 6-16d), in particular when the water pressure underneath the Rhine and Linth Glacier lobes was close to the ice overburden pressure. These conditions are necessary for subglacial water to remove basal sediments, expose fresh bedrock, and favour further glacial erosion. Knowledge of the location and fluxes of subglacial water drainage is therefore useful for understanding patterns of erosion beneath ice masses that do not otherwise relate to the sliding of ice (Cohen et al. 2023).

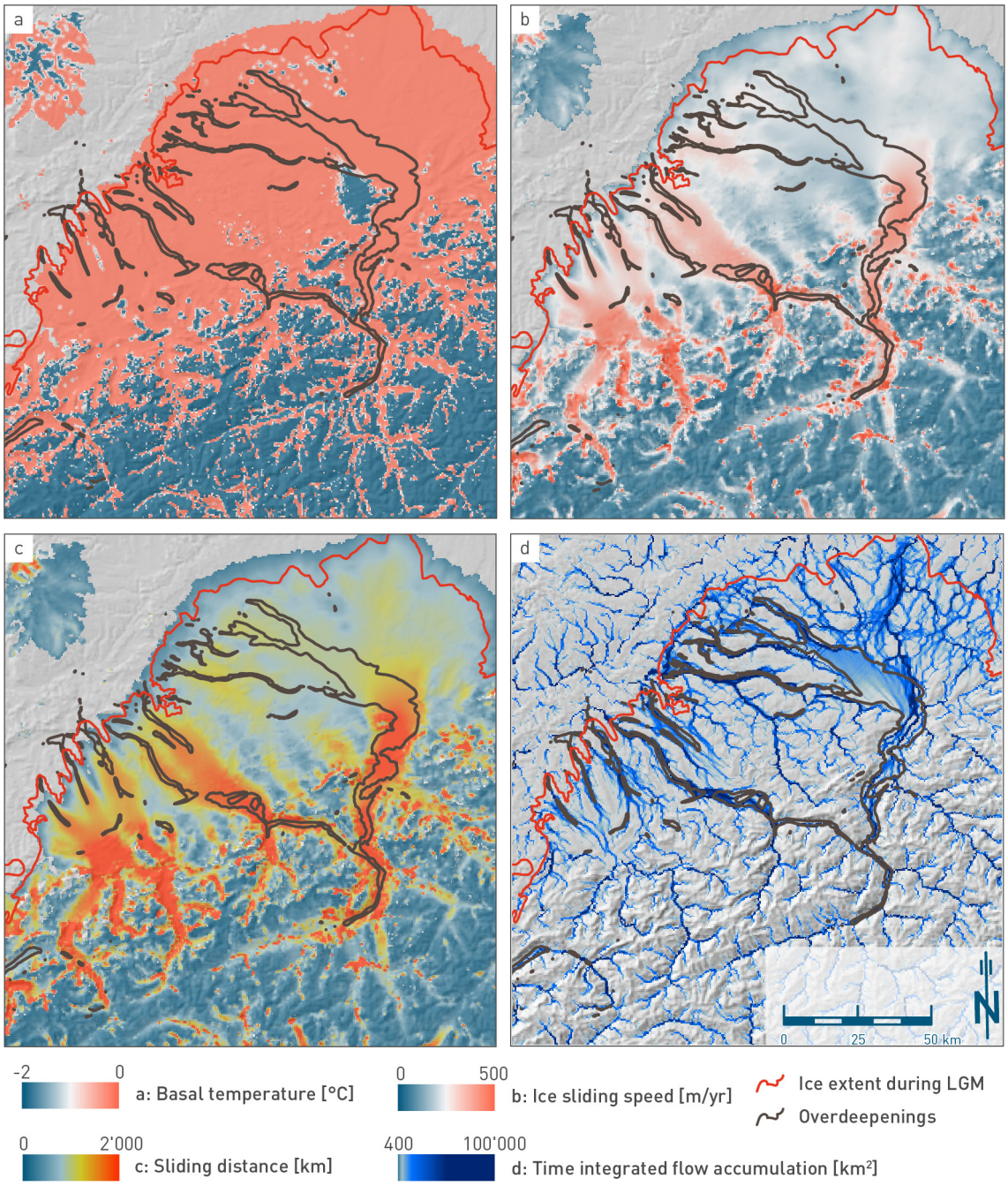


Fig. 6-16: The Rhine Glacier system and erosion potential at the LGM

(a) Basal ice temperature. (b) Ice sliding speed. (c) Sliding distance calculated by integrating the sliding speed over the course of the last glacial cycle as a proxy for glacial erosion by moving ice. (d) Time-integrated flow accumulation area over 12.8 kyr around the LGM as a proxy for glacial erosion by subglacial water flow (see Nagra 2024j for more details). See Fig. 6-14 for location. The brown lines denote the outlines of existing overdeepenings. The LGM extent is modified after Ehlers et al. (2011) and is shown by the red lines.

6.3.3 Future climate evolution

6.3.3.1 Timing of future glaciations

Important characteristics of climate with respect to repository safety are the timing and severity of future glaciations, as the related erosion may reduce the repository overburden thickness and thus modify the properties of the geological barrier (e.g. self-sealing properties, hydraulic conductivity; see Sections 6.4.1.4, 6.5). Hence, it is important to simulate future climate and analyse future climate scenarios explicitly with respect to these characteristics.

Parameters for orbital configurations can be calculated accurately for the past and future and are for example reported in Berger (1977, 1978) and Berger & Loutre (1997). However, the future atmospheric CO_2 content cannot be accurately estimated as the additional anthropogenic emissions cannot be easily forecast. To accommodate this uncertainty, several emission scenarios were used to cover a range of likely scenarios (Talento & Ganopolski 2021). Palaeo-reconstructions of the past 800 kyr (global mean surface temperature, CO_2 atmospheric concentration and normalised global landmass ice volume) were used as part of the training and validation set for the (predictive) model.

The first case is a natural scenario with no additional anthropogenic emissions (0 petagram Carbon [PgC]). This scenario also serves to determine the impact any additional anthropogenic emissions may have. For the period 1750 – 2017, fossil-fuel cumulative emissions and landuse in carbon equivalents are estimated to 660 PgC (Le Quéré et al. 2018). Future projections for additional cumulative emissions might reach between ~ 700 PgC (incorporating fossil-fuel reserves exploitable today) and ~ 3'000 PgC (considering resources that might become exploitable in the future) (McGlade & Ekins 2015). Accordingly, scenarios with additional cumulative emissions of 500, 1'000 and 3'000 PgC are analysed (for more detail see Nagra 2024j).

Talento & Ganopolski (2021) defined the occurrence of full glacial conditions and large glaciations at the 0.5 and 0.8 value of the normalised global landmass ice volume, respectively (see Fig. 6-17 for best solution scenarios). With respect to the long-term geological evolution of the repository sites, the main interest is in the potential future timing of large glaciations, as they may reach the Alpine Foreland. This timing is expected to correspond to the peaks above the 0.8-unit ice volume threshold in Fig. 6-17 (note that ~ 1 corresponds to the global equivalent of LGM ice volume).

In general, the higher the carbon concentration in the atmosphere, the later the next glaciation will occur (Fig. 6-17 for best solutions). In the natural scenario (E = 0 PgC), the next full glacial condition is simulated to peak around ~ 110 kyr (Fig. 6-17a). For the low emission scenario (E = 500 PgC), the next full glacial condition is postponed by ~ 90 – 100 kyr compared to the natural scenario, with a peak at ~ 220 kyr and simulated ice volumes of 0.8 (Fig. 6-17b). For the intermediate emission scenario (E = 1'000 PgC), full glacial conditions only occur the first time at ~ 650 kyr (Fig. 6-17c). Finally, with a cumulative emission of 3'000 PgC, simulations indicate mostly ice-free conditions for the next 800 kyr (Fig. 6-17d). In this scenario, full glacial conditions are not expected to occur before 850 kyr. Once the first larger glaciation has occurred, all scenarios show a cyclicity of approximately 100 kyr, similar to the glacial/interglacial cycles, established after the Mid-Pleistocene Transition; see Section 3.5).

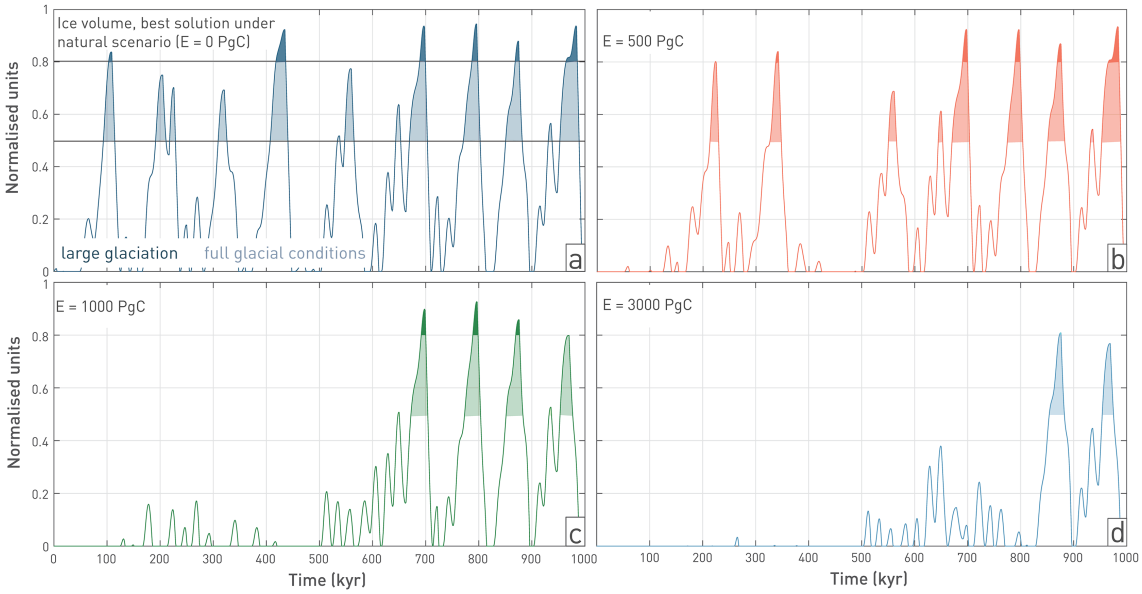


Fig. 6-17: Future climate simulations based on orbital configurations and different Anthropogenic CO_2 scenarios

The plots show the "best solution" simulations of global ice volume as proxy and are redrawn from Talento & Ganopolski (2021), using normalised global landmass ice volume as proxy for future glaciations. A value of 1 refers to approximately the same amount of ice as determined for the peak of the LGM. Full glacial conditions are suggested to occur at 0.5 units (filled parts), while a value of 0.8 may suggest a large glaciation (darker filled peaks). With respect to the long-term geological evolution of the repository sites, such large glaciations might reach the North Alpine Foreland. (a) Scenario with zero anthropogenic CO_2 emissions. A large (potentially reaching the North Alpine Foreland) glaciation occurs only after ~ 100 kyr from now. (b) Scenario with cumulative emissions of 500 PgC. In such a scenario, the next glacial inception is significantly delayed, with the next large glaciation occurring only after ~ 200 kyr. (c) The 1'000 PgC scenario considers consumption of all presently exploitable fossil fuel reserves and will further delay future large glaciations. (d) 3'000 PgC represents a worst-case scenario, including fossil fuel reserves that might become exploitable in the future.

6.3.3.2 Future climate characteristics during interglacials

Another important characteristic is the prevailing climate during the glacials and interglacials because it determines living conditions for humans directly above, or in the vicinity of, the repository.

Following the Köppen climate classification scheme (Köppen 1918), a typical climate at the start of a glaciation is a polar climate, followed by continental and temperate climates. Polar, continental and temperate climates have all occurred in the past and are well documented using proxy data and simulations (Nagra 2024j), and it is reasonable to assume that they are also representative for future glacial/interglacial cycles. At the height of an interglacial period, Switzerland may also experience a warmer-drier climate, especially if high carbon emissions are assumed. Simulations of the IPCC using Scenario RCP8.5, which is approximately equivalent to the 3'000 PgC scenario, predict warm-temperate climates for Switzerland by 2100. These climates are defined as having a mean temperature during the coldest month above 0 °C and above 22 °C for the warmest months, while 8 months have mean temperatures above 10 °C (IPCC 2023). A dry climate is defined as having very little precipitation and very high average monthly temperatures throughout the year. Currently, most of Spain experiences temperate to dry climates. According to Beck et al. (2018), the dry climate will advance north-eastwards in the next 100 yr and reach the Pyrenees while arid conditions are expected in parts of Spain. Under normal low or natural emission scenarios, a dry climate is not to be expected in Switzerland during a glacial/interglacial cycle. However, with continued carbon emissions and subsequent climate change a warmer-drier climate cannot be ruled out that, at least in the high-emission scenarios, such a dry climate may occur even in Switzerland in the future.

6.3.4 Conclusions

Climate is an important driver for erosion and has direct hydrogeological and geomorphological effects, in particular related to glacial erosive and depositional processes. Considering the present-day climate assessment and projected conditions regarding future climate states in the Alpine realm, the conclusions are:

- Glacials are of fundamental importance with respect to erosion processes in Northern Switzerland.
- The palaeoclimatic record and simulations of past Quaternary climates show that the global as well as the local climate evolution of Northern Switzerland was dominated by a succession of glacial/interglacial cycles. Before the Mid-Pleistocene Transition (between 1.25 and 0.7 Myr), these cycles lasted approximately 41 kyr, while after the transition 100-kyr cycles became dominant.
- Using the geological and geomorphological record, especially for the last glacial/interglacial cycle, the ice extent in the greater Switzerland area can be mapped and simulated. Glaciers reached far into the Alpine Foreland, repeatedly covering Northern Switzerland.
- The ZNO siting region and partly also NL were covered during LGM-size glaciations, while JO remained ice-free. ZNO and NL were covered by the Beringen Glacial. JO is only covered by exceptionally large foreland glaciations, such as the Möhlin Glacial.
- During the coldest time intervals, permafrost north of the Alps was continuous, cold (mean annual surface temperature about -5 °C with shorter-term extremes down to -10 °C) and reached depths of about 100 to 200 m
- Ice-flow modelling allows estimation of the erosion potential in Northern Switzerland during foreland glaciations; basal ice temperature and sliding speed are key variables for glacial erosion. Ice was channelled along troughs; these sliding conditions may have favoured glacial erosion. High subglacial water discharge is key to removing basal sediments, exposing bedrock and favouring further glacial erosion.
- A maximum ice thickness of ~ 200 – 400 m and a duration of ice occupation of ~ 1'000 – 3'000 yr in ZNO and NL were simulated and are expected for future foreland glaciations.
- Insolation is one of the main climate drivers and can be calculated accurately for the future. The atmospheric CO_2 concentration has a very strong influence on the timing and severity of future glaciations. Only if the greenhouse gas concentration is reduced to pre-industrial levels, will the next glaciation be expected to occur at around 100 kyr after present. An additional 500 PgC will postpone the next larger glaciation to > 200 kyr. Even higher total carbon emissions will move the onset of the next glaciation further into the future.
- After a glaciation, the climate warms, and climate conditions change from a polar climate (Switzerland largely covered by ice and/or permafrost conditions) towards a continental, temperate or potentially an even warmer-drier climate.

6.4 Erosion

Key points:

- The erosion assessment follows a modification of the actualistic principle. Here, proxy indicators of past processes serve as a key to the future behaviour of the erosional system.
- Future erosion in Northern Switzerland (glacial & non-glacial) is expected to be comparable in form to Pleistocene processes, but at lower rates (no major drainage reorganisation, smaller glaciers, delay in glacial inception, and resistant rocks).
- The comparably large uncertainty regarding future erosion was assessed with a robust, structured hybrid-probabilistic approach.
- A residual bedrock cover (remaining overburden) of 200 m thickness inferred to be necessary to maintain self-sealing properties of the Opalinus Clay can be shown to be sustained for the most likely scenarios in all the siting regions within the next one million years. Using the 5 – 95% range as reference, the JO siting region is least robust.
- Excavation of the repository by erosion within the next one million years can be considered extremely unlikely.

Erosion is the main process that can reduce the protective overburden thickness needed for sustained barrier functions (Section 6.1.2). In addition to information on the drivers of erosion (Sections 6.2 and 6.3), this section builds on Sections 3.4.5 and 3.5 and provides the key facts of past landscape evolution that allow a first-order assessment of past erosion processes and rates. To project these rates and processes under consideration of uncertainties into the future on a one-million-year timescale, a hybrid-probabilistic framework was established.

Section 6.4.1 summarises the main evidence needed to understand the Quaternary landscape evolution. It builds on site investigations (Section 2.4), but also incorporates general process understanding.

This information was used to derive probability distributions and arguments for parameters to be used in subsequent erosion modelling and assessments (Section 6.4.2). The main results and associated line of reasoning for each separate erosion process are presented briefly in Section 6.4.3.

Section 6.4.4 shows the combined results of the erosion assessment for the future one-million-year time frame. Discussed are the remaining overburden thickness for the expected geological evolution as well as, to show the robustness of the repository, the probability of repository excavation.

A summary of the main results is given in the conclusions of Section 6.4.5.

6.4.1 Key erosion processes and resulting landscape characteristics of Northern Switzerland

6.4.1.1 Erosion processes and landscape compartmentalisation

Tectonism and climate changes during the Quaternary have shaped the present-day landscape of Northern Switzerland (Chapter 3, Sections 6.2 and 6.3). The main erosion processes that are involved are the combined action of rivers and especially the drainage evolution of the Aare – Rhine River system, as well as erosion and sedimentation by repeated large foreland glaciations. These processes, in turn, control topographic slopes and mass movements, thus driving denudation of the topography.

The respective landscape forms derived from fluvial incision, evolution of hillslopes, and deep glacial erosion provide important geomorphic reference markers (Schnellmann et al. 2014). These markers allow the landscape to be divided vertically into different geomorphic compartments. Based on these markers, the geomorphic constraints at the respective repository sites can be determined and an assessment of future erosion made (Section 6.4.3). In the following, the three compartments and the main differences affecting the siting regions are briefly described (for more details see Nagra 2024k).

The main reference horizon, i.e. first landscape compartment, constitutes the *local erosion base* – the locally deepest fluvial incision level in bedrock (Fig. 6-18b). The local ersosion base is a virtual surface that is spanned between the thalwegs of the main river channels of the Rhine, Aare, Limmat, and Reuss and declines towards WNW. Some of these thalwegs are filled with sediments so that the bedrock interface defines the thalweg depth, and the local ersosion base is lower than the present-day river bed (see Pietsch & Jordan 2014 for more details[14]). No local river can significantly incise below this level. The local erosion base affecting the siting regions is gently inclined towards the WNW and is mainly defined by the paleochannels of the Rhine, Aare, Limmat and Reuss Rivers (Fig. 6-18b). The Quaternary fluvial incision history of Section 6.4.1.2 describes the past evolution of the local erosion base.

The local erosion base (LEB) separates the rocks (bedrock and unconsolidated sediments) above (here called *local topography*, Fig. 6-18c) from the unconsolidated Quaternary sediments that fill the glacially overdeepened basins (*glacial overdeepenings*, Fig. 6-18d) below.

Section 6.4.1.3 describes processes and rates that reflect the evolution of local topography in selected areas of Northern Switzerland and Section 6.4.1.4 summarises the Quaternary glacial history that led to deep glacial erosion and overdeepened basins. More details can be found in Nagra (2024k).

[14] The present adaptations on the bedrock model (version 2023) did not change the elevations of this reference.

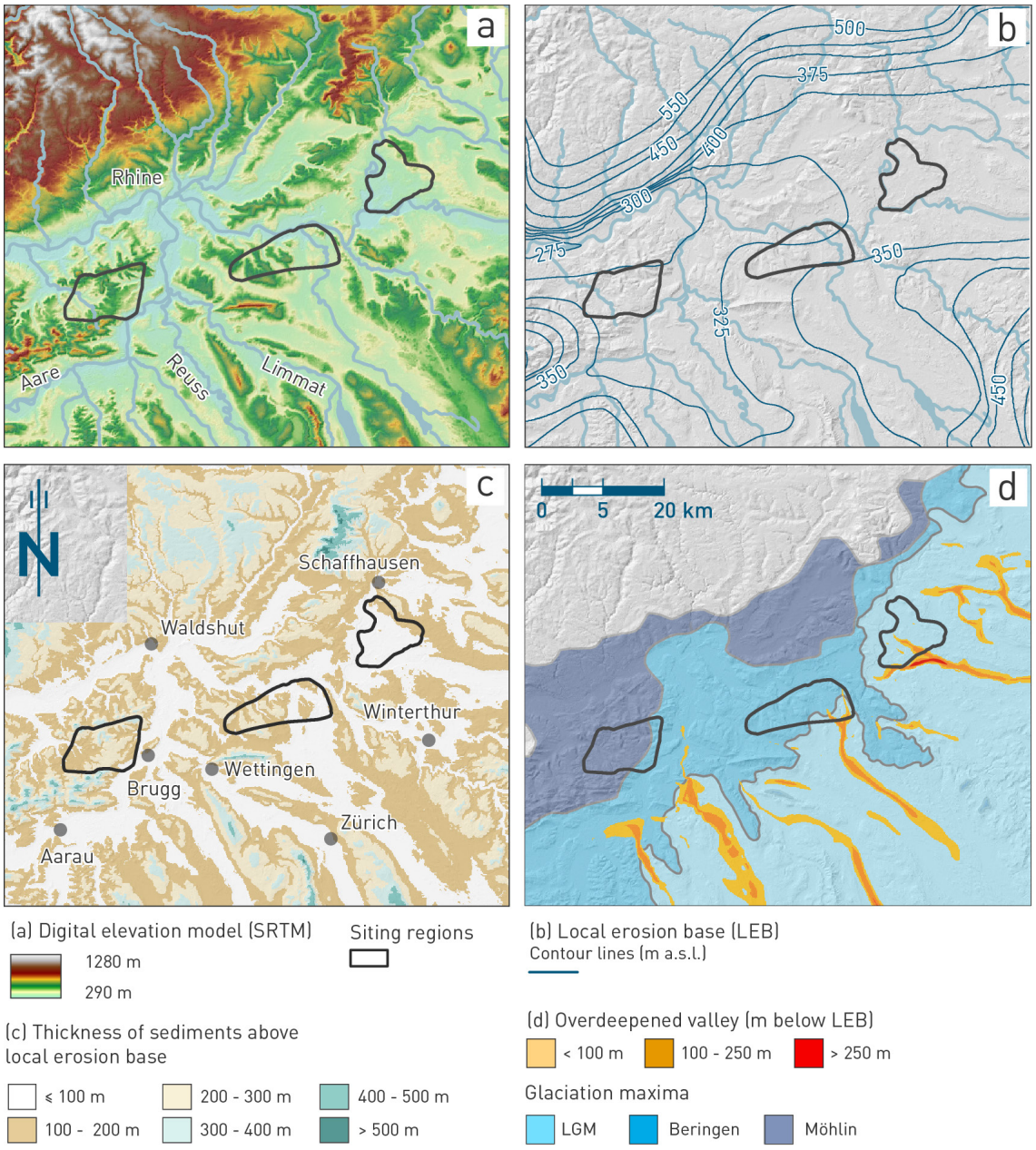


Fig. 6-18: Maps showing the main landscape compartments around the siting regions

(a) Digital elevation (NASA Shuttle Radar Topographic Mission SRTM, Digital Elevation Model) on a hillshade model showing the relief distribution around the siting regions and main rivers. (b) Contours of local erosion base (LEB) as derived by Pietsch & Jordan (2014). (c) Colour-coded thickness of local topography, i.e. the sedimentary rocks and unconsolidated Quaternary sediments above the LEB. (d) Ice extents of the three Quaternary key glacials (blue colours, see Section 6.4.1.4) and distribution and depth of glacial overdeepenings (orange colours). The siting regions are plotted in each subfigure for comparison.

6.4.1.2 Fluvial incision

The main parameters driving fluvial incision are uplift/subsidence, climate-driven water and sediment flux, and erodibility, with natural feedback between them.

Climate-driven water and sediment flux

The glacial/interglacial cyclicity (Section 6.3) has a major impact on the spatiotemporal sediment production and transport in Alpine source areas and their forelands (e.g. Antoniazza & Lane 2021). Sediment yield may be highly variable during phases of glacier advance, retreat, and readvance for instance. Antoniazza & Lane (2021) describe the highest sediment availability during early phases of glacial retreat and re-advance, before the sediment sources become exhausted at later stages.

Hinderer (2003) provided a source-to-sink case study from the Alpenrhein and Bodensee area, covering the Late Pleistocene and Holocene. They propose temporal storage of sediment in the source areas and the foreland during glacials. The highest sediment flux instead was observed during early melting (10× higher flux during the Late Pleistocene when compared to today). Importantly, the Bodensee as a large periglacial lake constitutes an efficient sediment trap and decouples further sediment flux into the foreland and the Hochrhein area (Hinderer 2003).

Upon filling of the Bodensee, incision in the Hochrhein is limited, because bedload is trapped within the lake and is not available as tools for fluvial impact erosion. The largely preserved knickpoint of the Rhine Falls seems indicative for this process. When bedload tools become available, it is expected that the local incision will strive towards equilibrating the longitudinal profile of the Hochrhein. However, at this point, further sediment flux from the Alpenrhein and the source region is no longer inhibited and large sediment supply may result in the opposite cover effect, i.e. shielding the riverbed from further vertical downcutting.

Rock uplift and stream piracy – process and Quaternary history

Rock uplift and subsidence of any landscape is mainly driven by neotectonic activity and/or isostatic compensation to mass redistribution by glacial processes (erosion and deposition). The effects of these processes dictate rates and locations of incision and sediment accumulation and thus can cause changes in river profiles (steepening, knickpoints), catchment changes by piracy, and variability in strength of the exposed rocks.

The influence of tectonic domains on the river profiles of the Aare and Rhine were explained in Section 6.2.2. Most important is the rock uplift of the Alpine Foreland. However, Rhine – Danube catchment competitions can also cause a sudden significant drop of the baselevel. As highlighted in Section 3.4.5, the past evolution of the Aare – Rhine River system occurred in several phases of drainage reorganisation that resulted in significant baselevel drops between tens of metres and up to several hundred metres (see Fig. 3-11 in Section 3.4.5). The present-day longitudinal profile of the Rhine is significantly shorter than that of the neighbouring Danube, which causes the Rhine catchment to grow at the expense of the Danube to achieve geometric equilibrium of the watersheds (e.g. Winterberg & Willett 2019). This relationship is illustrated in Fig. 6-19. The drainage divide has successively shifted further east as this process progresses. Importantly, fluvial geometric imbalance is often associated with variable erosion (incision) rates, and those rivers and tributaries that gain watershed experience an increase in rates (e.g. Willett et al. 2014). Most likely, the main pulse of increased incision based on past reorganisation has already propagated through the Hochrhein (range of the siting regions). This hypothesis is supported by the observation that the Hochrhein has attained an overall along-river gradient that is comparable to the Rhine River section draining the Upper Rhine Graben. Former river gradients need to be interpreted with care due to the possibility of tectonic tilting, but were still steeper than today, possibly showing a gradual adjustment since the emplacement of the Höhere Deckenschotter

(HDS; Fig. 6-19b). The relatively low gradients today suggest also that similar drainage changes in the future will most likely lead to minor if any increased incision. Any large events of fluvial incision in response to drainage reorganisations are therefore not to be expected within the next one million years.

The Quaternary incision history, which is an important parameter for evaluating future incision, probably reflects a combination of rock uplift and piracy-related baselevel lowering. In the following paragraph, the Quaternary incision history is briefly summarised based on four main morphostratigraphic units with fluvioglacial sediments (Fig. 6-20) that have been differentiated in the Swiss Alpine Foreland: Höhere Deckenschotter (HDS), Tiefere Deckenschotter (TDS), Hochterrasse (HT), and Niederterrasse (NT) (Graf 1993; Preusser et al. 2011), see also Section 3.5 and Nagra (2024k).

The HDS and TDS units are characterised by complex internal geometries (cut-and-fill sequences, see inset in Fig. 6-20), in which several depositional phases can be distinguished, for example based on clast petrography and orientation (Graf 1993). These deposits reflect protracted depositional phases, largely in proximity to former glaciers. In addition, interglacial overbank deposits occur for example in the HDS (Hasli Formation) at Irchel (Thew et al. 2024, Bolliger et al. 1996) and in the TDS at Hungerbol (Graf 2009a). The base of the HDS and TDS units may locally differ by several decametres (usually between 30 and 100 m), thus reflecting a period of net bedrock incision between the depositional phases (see also Fig. 6-19b). While the base of the relict HDS deposits is predominantly more or less planar, the TDS deposits are associated with pronounced channel forms. Accordingly, their base is highly irregular and has considerable relief differences (see for instance Fig. 6-20, inset). The incision between HDS and TDS accumulation might have been caused by increased subsidence of the Upper Rhine Graben, increased uplift of the external Alpine Foreland (Preusser et al. 2011), and/or by re-routing of the Alpenrhein from the Danube towards the 'recent' Rhine system through the Rhine Graben (see Section 3.4.5, Fig. 3-11); Claude et al. 2019). Age control of these units has improved considerably, but is still debated depending on different geochronometers (see Fig. 6-20a and Nagra 2024k for more detail).

Two main phases of sediment accumulation following bedrock incision occurred after the deposition of the HDS and TDS units (Fig. 6-19b and Fig. 6-20). The morphostratigraphically next lower level (Hochterrasse, HT) is located about 50 to 200 m below the TDS level, depending on the region. The difference significantly increases from west to east and from north to south (Preusser et al. 2011). It has been argued that this significant drop of the local erosion base after TDS accumulation could potentially be associated with the Mid-Pleistocene Transition (MPT, see Section 3.5). Preusser et al. (2011) speculated that these changes, including glaciations extending into the Alpine Foreland, might have led to reorganisation of the major drainage system. Accordingly, the Alpenrhein at the location of the Bodensee changed its course from previously draining towards the Danube towards a new Hochrhein direction.

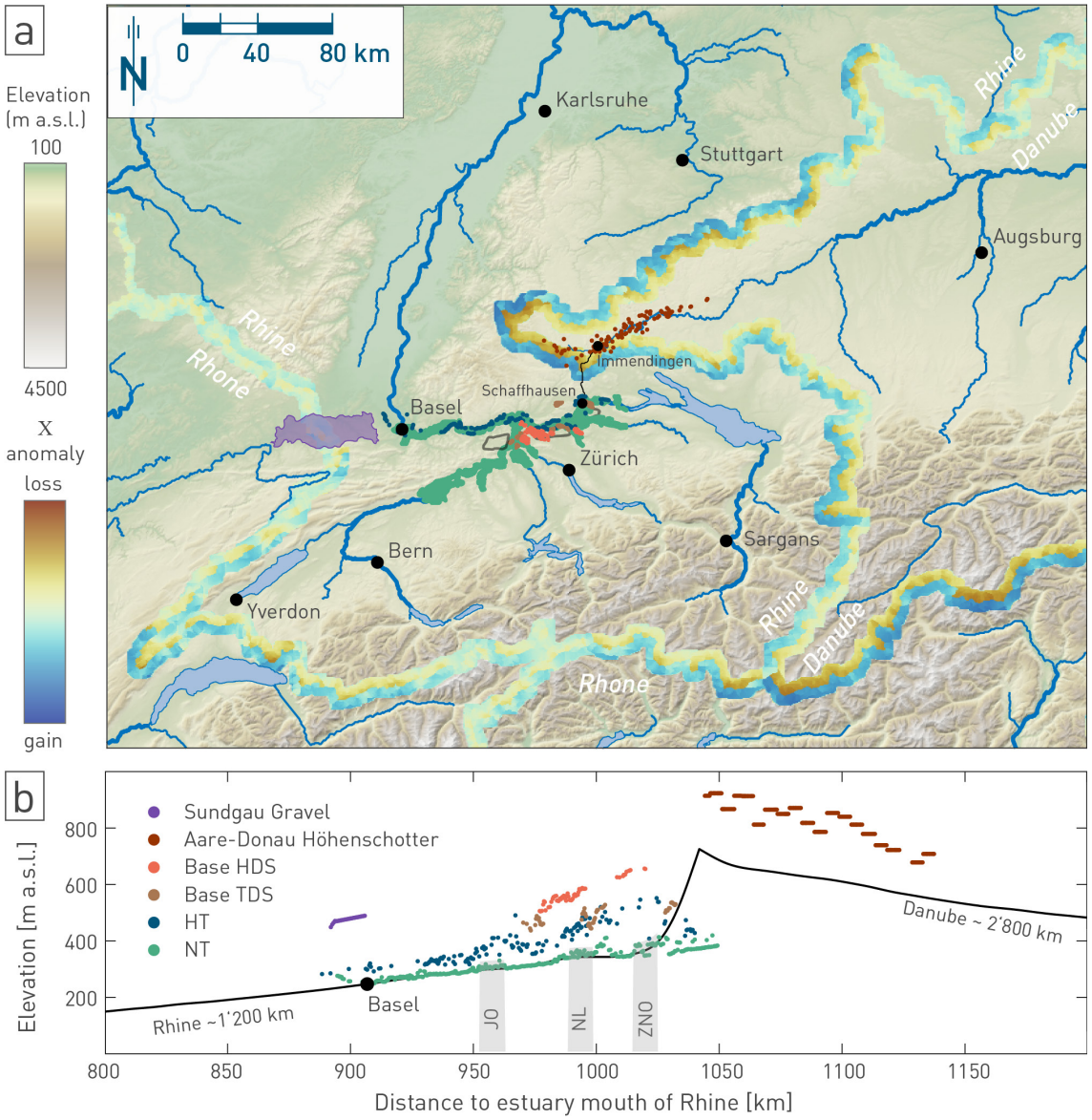

a
N
0 40 80 km
Elevation (m a.s.l.)
100
4500
X anomaly loss
gain
Karlsruhe
Stuttgart
Augsburg
Rhine
Danube
Rhine
Rhone
Immendingen
Schaffhausen
Basel
Zürich
Bern
Yverdon
Sargans
Rhine
Danube
Rhone
b
Sundgau Gravel
Aare-Donau Höhenschotter
Base HDS
Base TDS
HT
NT
Elevation [m a.s.l.]
800
600
400
200
Rhine ~1'200 km
Basel
JO
NL
ZNO
Danube ~ 2'800 km
800
850
900
950
1000
1050
1100
1150
Distance to estuary mouth of Rhine [km]

Fig. 6-19: Catchment competition between the Rhine and Danube watersheds and drainage reorganisation

Digital terrain model (a) with main river courses and their catchments. The drainage divide of the Rhine catchment is outlined by a visualisation of the direction of future catchment growth (calculation of a parameter X, e.g. Willett et al. 2014). The X anomaly quantifies the differences in the parameter X on either side of the divide. The X parameter is calculated for the river network and then projected onto the main upslope divides. Blue values indicate low X values and thus potential future gains in drainage area, whereas red values indicate potential losses. Sharp cross-divide contrasts thus highlight regions of potential future drainage reorganisation. In turn, similar anomaly values on both sides suggest stable divides. Also shown are locations of major fluvial to fluvioglacial deposits, see legend in (b) for colour-code. These deposits constitute important marker horizons for the past evolution of the drainage system. (b) Simplified comparison of partial longitudinal river profiles of the Rhine and Danube artificially connected along the black line between Immendingen and Schaffhausen in (a). The distance along the Rhine to the North Sea is remarkably shorter than the distance of the Danube to the Black Sea, resulting in a higher altitude of the Danube system. This difference resulted in a significant erosional pulse after capturing the Alpine-to-Danube River reaches and diverting them into the Rhine. The approximate position of the siting regions is indicated by the grey-coloured bars. The level of the Rhine is already clearly lowered at these positions (also visible from vertical the position of the fluvioglacial deposits) and is part of an equilibrated longitudinal profile, which suggests that the main pulse of the incision caused by the capture has already migrated through the Hochrhein and passed the repository sites.

On a more local scale, repeated drainage shifts were also observed during HT sediment accumulation. In an early phase, the higher Thur Valley drained via Stammheim, Schaffhausen and Klettgau towards Basel (northern HT occurrences), while the river's course via Eglisau and Koblenz (southern HT occurrences) probably became established only after the penultimate (Beringen) glaciation (Fig. 6-20; Graf 2009a). Clast provenance additionally provides evidence for an early drainage between Walensee and Klettgau (Graf 2009a). The vertical difference between the elevation of the deepest fluvial channel and the highest mapped gravel surface within the morpho-stratigraphic Hochterrasse unit can attain more than 100 m.

The lowest bedrock elevation attained prior to Hochterrasse deposition (e.g. Graf & Burkhalter 2016) is still considered the lowest regional level and constitutes the basis for the main reference used in evaluating future incision, the so-called local erosion base (see Section 6.4.1.1). Based on luminescence ages of the fluvial channel deposits, this depositional phase may fall within MIS 6 (onset ca. 190 ka ago, minimum age; e.g. Lowick et al. 2015).

No deeper vertical bedrock incision took place after MIS 6. The even younger Niederterrasse deposits were deposited onto the (partly incised) previous fill of Quaternary sediments or on bedrock at higher or approximately equal positions to the HT. In many places, these deposits are currently being incised by the Aare and Rhine Rivers and their tributaries (Fig. 6-20), locally more than 30 m (Nagra 2024k). About 14 m of postglacial incision (post-Würm glaciation) into Niederterrasse sediments are observed in the southern Upper Rhine Graben (Hillebrand & Frings 2017).

Mean values of incision rates derived for bedrock incision after HDS or TDS deposition (base HDS or base TDS to local erosion base, respectively), ranged between ~ 0.1 and ~ 0.3 mm/yr (see Section 6.2.2 and Nagra 2024k). This is based on simplified assumptions: firstly, the elevation of base of the deposits (i.e. the bedrock elevation) is used, to address the net lowering of the local baselevel over time, independent of intermediate aggradation phases. Secondly, it is assumed that the age range reflects the deposition at a late stage, i.e. shortly before the subsequent incision. Combining an age derived from sediment deposits accumulated up to several tens of metres with the elevation of the bedrock marker below these sediments requires the third assumption: a "quasi-instantaneous" incision through the unconsolidated Quaternary deposits.

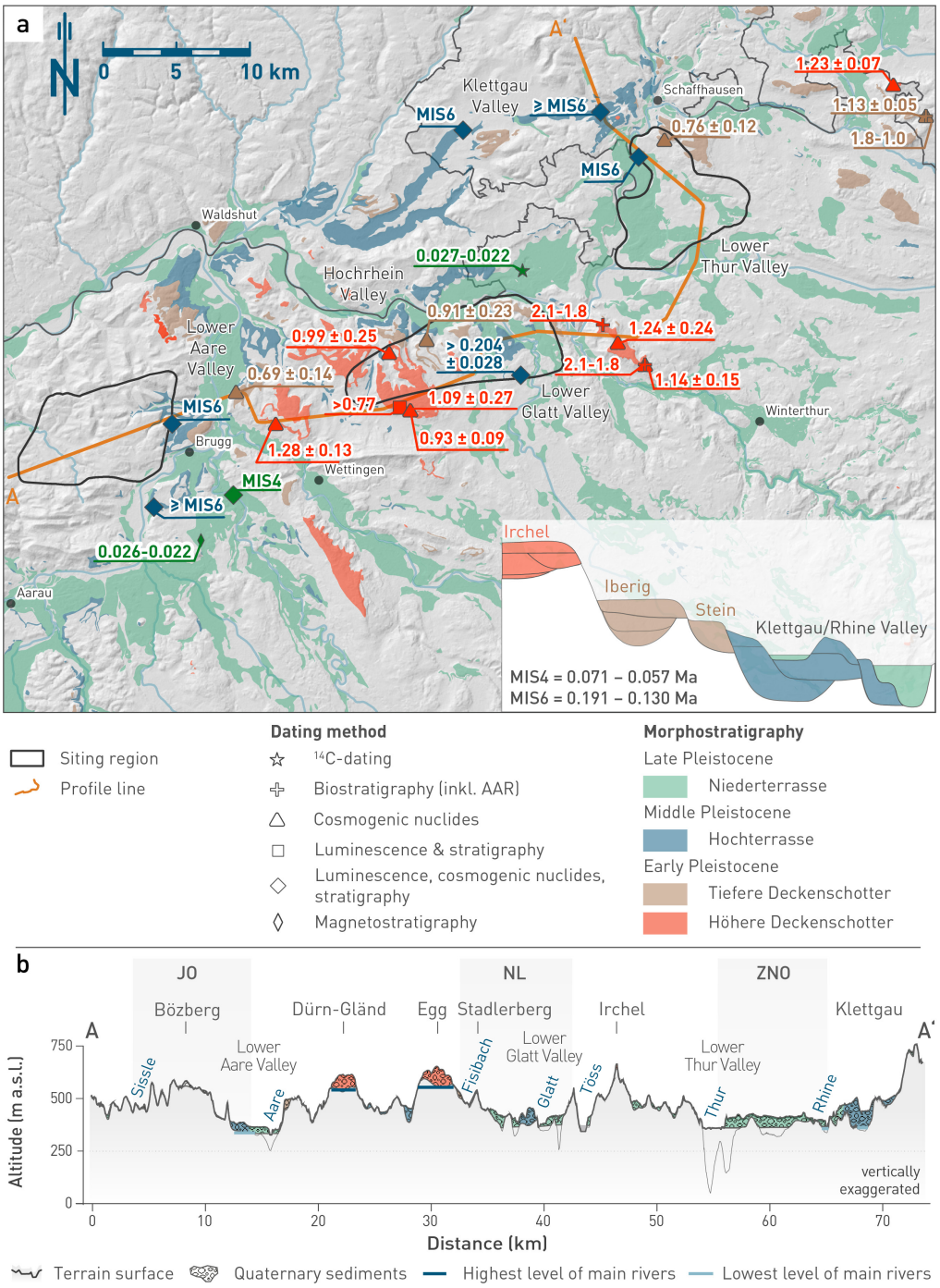


Fig. 6-20: Morphostratigraphic units in Northern Switzerland with selected age information

(a) Ages are colour-coded according to the morphostratigraphic unit of the respective deposits and listed with symbols according to dating method: biostratigraphy (Thew et al. 2024), AAR (Penkman et al. 2024), magnetostratigraphy (Scheidt et al. 2023), luminescence & stratigraphy (Mueller et al. 2024, Gegg et al. 2023, Kamleitner et al. 2023, Gegg 2021, Mueller et al. 2020, Gaar et al. 2019, Buechi et al. 2017, Lowick et al. 2015, Reber et al. 2014, Dehnert et al. 2012), cosmogenic nuclides (Dieleman et al. 2022a, Grischott et al. 2020, Knudsen et al. 2020). Inset shows sketch of morphostratigraphic relationship with complex cut-and-fill sequences within each unit (based on Graf 2009a). (b) Simplified profile (see a for location) through the siting regions and crossing several Deckenschotter deposits. Note highest fluvial level (dark blue) and lowest level (light blue).

Lithological control

Generally, two main counteracting processes are important for bedrock incision: (1) the "tool effect" when bedload (the tools) is available to erode the bed by impact, abrasion, or quarrying, and (2) the "cover effect", when the riverbed is protected from erosion by a critical sediment cover (e.g. Turowski et al. 2007). Erodibility, which defines the rock resistance against erosion[15], has an impact on sediment production and discharge, grain size, and bedload in the channel. The main influences on erodibility, in turn, are lithological contrasts, often defined by their rock compressive and tensile strengths (e.g. Fig. 6-21a, c).

The lithologies that form the stratigraphic column in Northern Switzerland comprise variable degrees of rock resistance (erodibility) with respect to the influence of fluvial impact erosion, as determined by abrasion mill experiments (Fig. 6-21b; Turowski et al. 2023). Resulting erosion rates derived from these experiments varied over about six orders of magnitude. Uncertainties scale with measured erosion rates.

Erosion rates measured on samples from the same lithostratigraphic unit revealed variability, most notably (for the given dataset) within the Lower Freshwater Molasse Group. Nevertheless, as expected, weakly consolidated sandstones or mudstones show the highest erosion rates and lowest tensile or compressive strength, and crystalline rocks such as granite tend to show the lowest erosion rates and highest tensile or compressive strength (Fig. 6-21).

[15] High erodibility corresponds to low rock resistance against erosion, and vice versa.

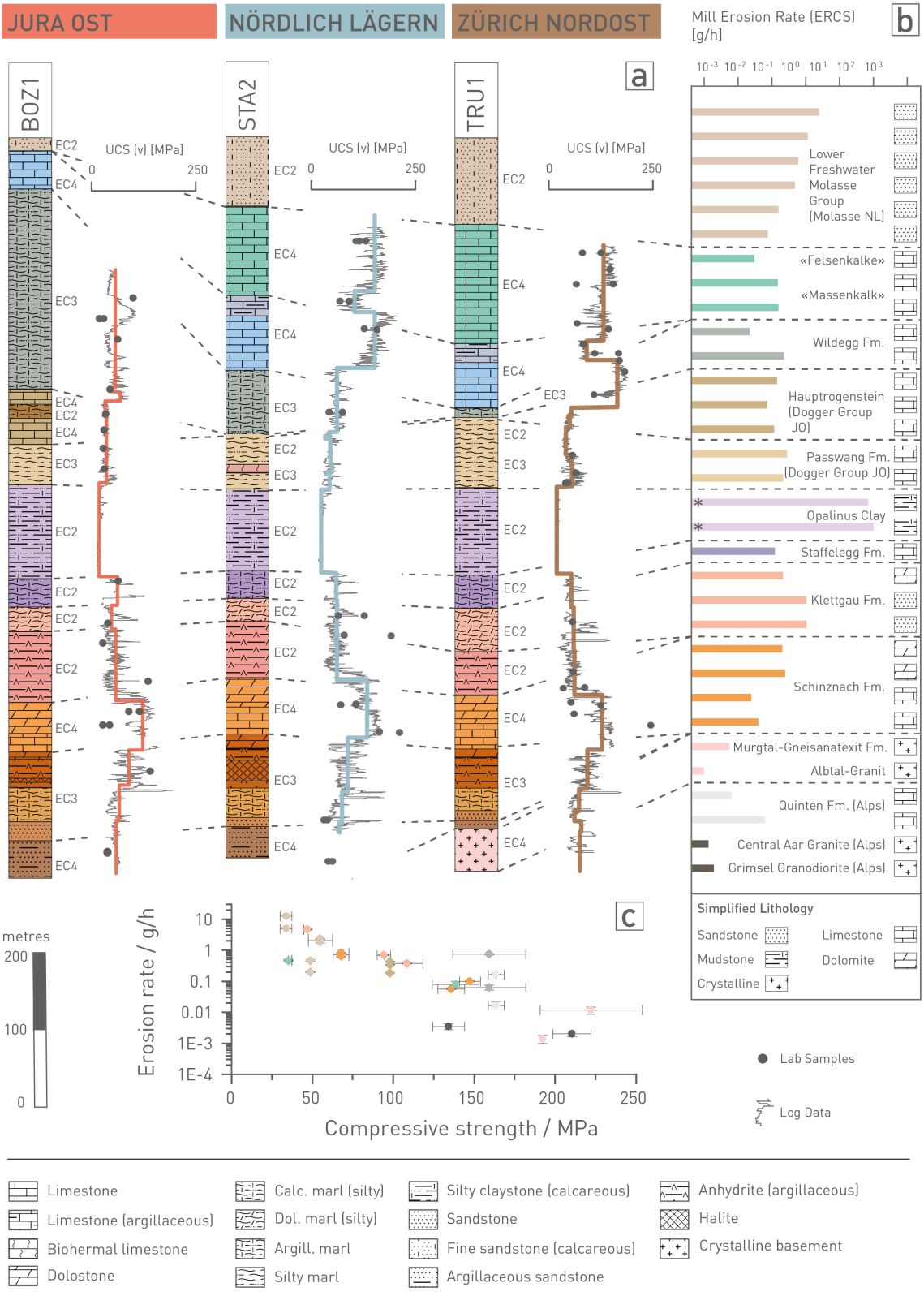

JURA OST
NÖRDLICH LÄGERN
ZÜRICH NORDOST
BOZ1
STA2
TRU1
UCS (v) [MPa]
0
250
EC2
EC3
EC4
a
b
c
Mill Erosion Rate (ERCS) [g/h]
10-3 10-2 10-1 100 101 102 103
Lower Freshwater Molasse Group (Molasse NL)
«Felsenkalke»
«Massenkalk»
Wildegg Fm.
Hauptrogenstein (Dogger Group JO)
Passwang Fm. (Dogger Group JO)
Opalinus Clay
Staffelegg Fm.
Klettgau Fm.
Schinznach Fm.
Murgtal-Gneisanatexit Fm.
Albtal-Granit
Quinten Fm. (Alps)
Central Aar Granite (Alps)
Grimsel Granodiorite (Alps)
Simplified Lithology
Sandstone
Limestone
Mudstone
Dolomite
Crystalline
metres
200
100
0
Erosion rate / g/h
10
1
0.1
0.01
1E-3
1E-4
0
50
100
150
200
250
Compressive strength / MPa
Lab Samples
Log Data
Limestone
Limestone (argillaceous)
Biohermal limestone
Dolostone
Calc. marl (silty)
Dol. marl (silty)
Argill. marl
Silty marl
Silty claystone (calcareous)
Sandstone
Fine sandstone (calcareous)
Argillaceous sandstone
Anhydrite (argillaceous)
Halite
Crystalline basement

Fig. 6-21: Unconfined compressive strength and abrasion mill erosion rates as quantitative indicators of bedrock erodibility

(a) Stratigraphic columns based on the BOZ1, STA2, and TRU1 boreholes with measured and estimated unconfined compressive strength (UCS) from selected deep boreholes in the three siting regions. Measured data points are based on core samples tested in the laboratory (Dossier IX in Nagra (ed.) 2022a, 2022c, 2021c). Continuous curves were approximated by combining the laboratory measurements with borehole log data from Nagra (2024m). Erodibility classes (EC) along the stratigraphic columns reflect the abstraction of the lithostratigraphic units as used for erodibility-related parameterisation in Model B of the erosion assessment model cascade described in Section 6.4.2.3 (Fig. 6-29). Quaternary deposits (not displayed here) are assigned to EC 1. (b) Relative erodibility in fluvial impact erosion as represented by erosion rates from abrasion mill experiments (Turowski et al. 2023; see further details there). Measurements were conducted on intact rock samples in the laboratory (ERCS method = erosion rate from the concentration of solids), from lithostratigraphic units as labelled. Asterisks denote results for highly erodible Opalinus Clay samples, where deviations from the standard experimental procedure were necessary. Samples were collected from surface outcrops, except for the Opalinus Clay and Alpine crystalline rock samples that were taken from the FMT and GTS rock laboratories, respectively. Due to technical limitations, there is a sampling bias towards harder rock types. This is mostly important for more heterogeneous formations, where samples focus on the harder beds (e.g. cemented sandstone layers in the Molasse units and limestone layers within the Wildegg Formation). Note the simplified lithological classification. (c) Strong negative correlation between abrasion mill erosion rate and UCS is suggested by paired laboratory measurements by Turowski et al. (2023). Error bars are only discernible if larger than the data point symbols. Colours correspond to figure part (b). Note that data for the Opalinus Clay and the Passwang Formation from (b) are missing in (c) because of a lack of UCS measurements on these samples.

An impressive example of the effect of variable erodibility on a river's longitudinal profile is the Rhine Falls knickpoint that is located within resistant limestones. However, besides the lithological contrast, the present-day incision efficiency needed to erode this knickpoint seems to be hampered by trapping of the Alpine sediments (i.e. the tools for efficient bedrock erosion) within large glacially overdeepened lakes, e.g. the Bodensee. Accordingly, a major control on the tool and cover effects and thus on the sediments and fluvial dynamics of Northern Switzerland is the glacial/interglacial cyclicity.

6.4.1.3 Evolution of local topography

Channel-hillslope coupling

Fluvial incision and deep glacial erosion processes determine the pace at which hillslopes respond to baselevel changes. Topographic slope stability depends for instance on the slope angle, controlled by the fluvial baselevel and associated mass movements. Thus, the nature of channel-hillslope coupling will drive denudation of the topography (Fig. 6-22a). This coupling also provides the link between the landscape compartments that define the *local erosion base* and *local topography* (see Section 6.4.1.1).

Rock properties (e.g. rock strength, fracture spacing, orientation of discontinuities with respect to slope), vegetation cover, and climate factors add to the control on hillslope stability or failure and can influence denudation rates. The distinct morphology and different geomorphic process rates that define a landscape need to be incorporated into any future assessment of erosion.

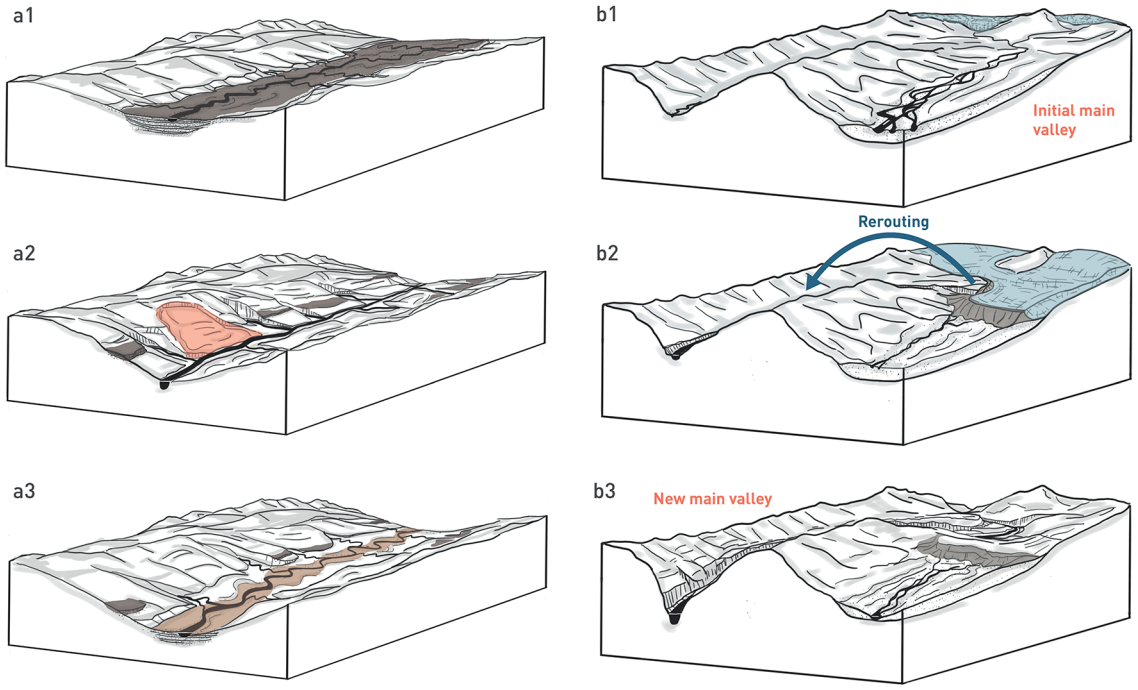


Fig. 6-22: Conceptual figures of local landscape evolution by (a) local baselevel fall of a main river, and (b) the formation of a breakthrough channel in an ice-marginal setting

Sequence (a) starts with a mature main river valley characterised by a wide aggraded valley floor (a1; dark brown). A pulse of fluvial incision of the main river through the former valley infill and into the bedrock (local baselevel fall) follows in (a2). This stage includes the formation of terrace relicts above the former valley floor (dark brown), propagation of the incision signal along tributary streams and hillslope response (e.g. landslides; red). More advanced adjustment to the new local baselevel is indicated in (a3), with the formation of a new main valley floor (light brown) and a general widening of the valley shape by continuing local erosion. Sequence (b) starts with a pro-glacial main valley (b1; glacier shown in light blue). Glacial advance in (b2) causes blocking of the former main valley by a terminal moraine (greyish brown), and subsequent rerouting of the ice-marginal main drainage into an adjacent valley. The new drainage erodes the former ridge at the location of overspill, thereby creating a breakthrough channel that evolves to a new main river valley after glacial retreat (b3).

Local topography in the greater Bözberg area of Northern Switzerland – a qualitative and quantitative comparison with the Wutach area of the Swabian Alb

The majority of the terrain in Northern Switzerland is characterised by a low-relief cuesta landscape (see Fig. 6-23a as an example). Wide fluvial channels and extended terrace systems define the postglacial terrain of Northern Switzerland. While both Höhere and Tiefere Deckenschotter deposits are preserved in isolated relicts, the Hochterrasse and Niederterrasse deposits follow a continuous and traceable fluvial network (Fig. 6-20). However, deviations from these general patterns of a distinct long-lived fluvial network exist at various scales. Small-scale lateral channels (breakthrough channels), for instance, are observed throughout Northern Switzerland. Evidence exists for temporary features (e.g. Wangetel between Jestetten and Wilchingen or Herblingertal between Thayngen and Schaffhausen) or persistent channels (e.g. Rhine Valley between Rüdlingen and Tössegg). Most of these channels developed in association with large

foreland glaciations, either by glacial or postglacial impoundment of a present drainage and subsequent overspill or by ice-marginal drainage (compare Fig. 6-22b; e.g. Keller & Krayss 2000). Such local changes in the drainage can have a profound influence on the adjusting landscape.

Holocene geomorphological process rates (e.g. shallow landsliding, overall denudation processes) in the Bözberg area of the JO siting region seem low based on a morphological landscape assessment (Fig. 6-23a and c; Ludwig 2018). Present-day terrain elevation within the extended study area ranges from around 700 m a.s.l. at the highest hilltops of the External Jura (Schinberg, Geissberg) to 300 m a.s.l. at the outlet of the Sissle River into the Rhine. Given this comparably high local relief, hillslope processes play a relevant role in shaping the landscape of the JO siting region and its surrounding areas. For instance, historical landslides from the study area have been documented by Baltzer (1876), Hartmann (1928, 1950) and Haefeli (1940). Fig. 6-23 shows that, in general, the central part of the siting region appears "quiet" with respect to landsliding. A large proportion of this region consists of the "upland low-relief area" of the "Bözbergplateau" and "presumably unfailed hillslopes", associated with the lithostratigraphic domains of Tertiary sediments (Molasse), Villigen Formation and Wildegg Formation (compare Fig. 6-21). On the other hand, landslides within the mapping area appear to be clustered within Tertiary sediments (Molasse) along the Aare River, i.e. the southern margin of the Bözbergplateau (southeastern corner of the siting region) and within various lithostratigraphic units along the Mandach Thrust north of the siting region, from Frickberg in the west to Böttstein next to the Aare in the east (Fig. 6-23c).

A prominent example of a larger-scale landscape adjustment to drainage changes is represented by the Wutach Gorge in the Swabian Alb (Fig. 6-23b and d), where a stream capture by a tributary of the Rhine River some 18 kyr ago has caused a significant baselevel drop (Einsele & Ricken 1995, Hebestreit 1995). From its headwaters at Feldberg (the highest elevation of the Black Forest, 1'493 m a.s.l.), the Wutach approximately flows in an east direction until reaching the location of the Late Pleistocene stream deflection near the village of Achdorf. Prior to drainage reorganisation, the former *Donau-Wutach*[16] here continued its eastward course along the present-day Aitrach Valley (Fig. 6-23d) towards the Danube. This changed when the *Donau-Wutach* was captured by the Rhine Basin from the south, as a result of headward erosion by a pre-existing Rhine tributary, referred to as the *Rhine-Wutach*.

Alternatively, coeval aggradation by the former *Donau-Wutach* leading to an overflow across the drainage divide has been presented as an additional explanation for the stream deflection, at least as a final trigger mechanism (Hebestreit 1995). Such aggradation may have been favoured by glacially enhanced sediment flux from the former *Feldberg Glacier* that occupied the *Donau-Wutach* headwater region during the last glaciation. As determined by the course of the former *Rhine-Wutach*, the present-day Wutach is directed to the south / southwest at Achdorf (Fig. 6-23d), until finally joining the Rhine to the south at an elevation of ~ 315 m a.s.l. This elevation of the Rhine corresponds to a much lower local erosion base than was set by the Danube prior to drainage reorganisation.

The adjustment of the drainage system to this lower local baselevel is expressed by the remarkable incision of the Wutach stream, which reached its present-day level by an incision of up to 150 m within only 6 kyr (Einsele & Ricken 1995). Both upstream and downstream from this point, the incision of the Wutach has produced deep valleys and gorges in the present-day landscape. The adjustment of local topography to the local baselevel fall is further expressed by an attenuated, but still ongoing hillslope response by landsliding along these incised valleys (Fig. 6-23b, d).

---

[16] The names *"Donau-Wutach"* and *"Rhine-Wutach"* are adopted from Einsele & Ricken (1995). Donau = Danube.

In the following paragraphs, the transient landscape around the Wutach gorge and the neighbouring Randen area is briefly compared with the landscape of the Bözberg (JO siting region) using denudation and chemical weathering rates based on cosmogenic radionuclides (^{10}Be, ^{36}Cl), alongside weathering rates from stream water chemistry (Fig. 6-23e and f for a simplified synthesis). Both areas share a comparable stratigraphy, with alternations of slightly inclined erosion-resistant (e.g. limestones) and more easily erodible units. A total of 26 samples of ^{36}Cl and 11 samples of ^{11}Be concentrations for catchment-average and hillslope[17] denudation rates in calcite and quartz were measured, respectively. More information on the method and sampled sub-catchments are provided in Nagra (2024k).

Catchment-wide denudation rates indicate the lowest rates in the low-relief areas of the Bözbergplateau and the incised carbonate valleys of the Randen area (0.05 – 0.1 mm/yr), similar to that described earlier by analogy with surrounding areas (Schnellmann et al. 2014). In these areas, weathering accounts for ~ 75% and 50% of the denudation, respectively (based on measurements of denudation and weathering rates outlined in paragraph above). Along the flanks of the Bözbergplateau, where hillslope channel processes are more active, these rates double and are within the range of long-term incision of the Rhine and Aare (Fig. 6-23e). Erosion and weathering each contribute ~ 50%. Highest rates (0.3 – 0.5 mm/yr with < 20% weathering) were measured in the rapidly incising Wutach gorge upstream of the capture point (Fig. 6-23f). Such high rates reflect adjustments to the transient process of the upper Wutach catchment capture but will reduce with increasing maturity of the landscape, as observed in the neighbouring Randen area.

Combined, the data show that, in areas of low relief (e.g. Bözbergplateau), weathering dominates over physical erosion. In areas of intermediate slopes (Randen, Bözberg flanks), the amounts of erosion and weathering are similar. In contrast, the rapidly incising upper Wutach is dominated by pronounced physical erosion processes.

These new quantitative data confirm the range of previously reported intermediate-term denudation rates from the North Alpine Foreland (usually below 0.3 mm/yr) or adjacent regions, such as the Black Forest (~ 0.01 – 0.1 mm/yr), which are also based on catchment-wide denudation rates, measured using cosmogenic nuclides (see Schnellmann et al. 2014 and Nagra 2024k for a summary). It is concluded that, on average, intermediate-term denudation rates below 0.1 mm/yr can be expected in the area of the siting regions. In the case of future modulation of the drainage system with baselevel drop or if exposure of different rock types leads to increased local relief, these rates can multiply locally but for a limited period in time.

[17] In the Bözberg region, two ^{36}Cl samples of amalgamated colluvium from the bottom of two hillslopes were collected for comparison with nearby streams.

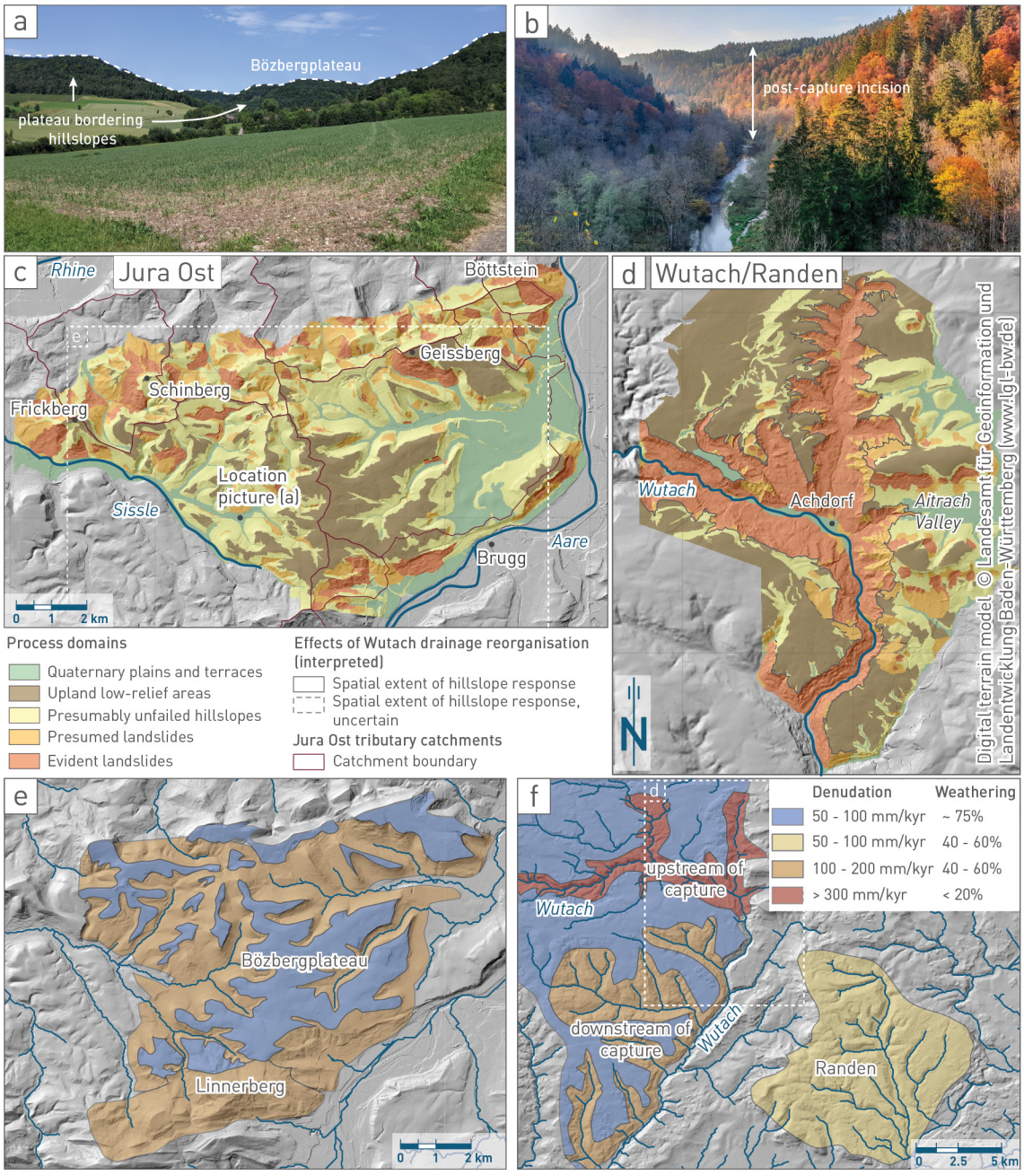


Fig. 6-23: Comparison of a geomorphically quiet (JO) with a highly active landscape (Wutach)

Comparison of the study areas. (a) Field picture of a valley carved into the Bözbergplateau. Note the relatively straight mountain tops of the plateau. (b) Field picture of the narrow Wutach gorge cut into Muschelkalk carbonates after the river capture event ~ 18'000 years ago. (c) Map of (hillslope) process domains for the JO study area (Ludwig 2018; see details there for definition and criteria of individual process classes). (d) Map of (hillslope) process domains for the Wutach catchment around Achdorf (digital elevation model: LGL 2010). (e) Simplified synthesis of interpreted denudation rates based on basin-wide and hillslope sampling of cosmogenic nuclides of the Bözberg area. (f) Interpreted denudation rates of the Wutach and Randen area. The colours also indicate the approximate percentage of weathering contributing to the total denudation rate (Fig. 6-23a, b, e, and f are courtesy of R. Ott, see also Nagra 2024k).

6.4.1.4 Deep glacial erosion

Glacially overdeepened, often back-filled troughs in Northern Switzerland are distinct features that have been eroded below the *local erosion base*. Areas with vestiges of *deep glacial erosion* constitute the third important reference compartment (see Section 6.4.1.1) for the erosion assessment.

Main glacial and subglacial erosion processes

The main processes of direct glacial erosion are abrasion and quarrying, which depend on the temperature and velocity of the basal ice, debris concentrations, bedrock properties, ice thickness and subglacial water pressure (e.g. Iverson 2002, Bennett & Glasser 2009, Burki 2009, Swift et al. 2015). Significant wear to the glacier bed can also be caused by subglacial fluvial action, similar to the bedrock incision by subaerial streams. The efficiency of subglacial drainage not only affects meltwater erosion but also likely plays a predominant role in evacuating sediments produced by erosion and thus keeping bed surfaces accessible for further erosion. Concerning integrated effects over large areas, abrasion and quarrying may be largely responsible for the overall eroded volumes (e.g. Drewry 1986, Burki 2009). However, with respect to maximum possible erosion depths, subglacial fluvial action likely plays an important role (Fischer & Haeberli 2010).

The latter view is supported by climate-driven ice-flow modelling (see Section 6.3.2, Fig. 6-16). Transient ice-flow modelling of the Rhine Glacier system over the course of the last glacial cycle indicates that the sliding distance is greatest at the base of Alpine valleys where sliding is fastest, and the duration of ice occupation is longest (Fig. 6-16c). However, the sliding distance does not correlate well with the location of existing overdeepenings in the Alpine Foreland owing to the smaller sliding speeds near the ice margin and the short time period during which ice covered the distal foreland (Fischer et al. 2021). On the other hand, time-integration of the flow accumulation area yields a metric for erosion by subglacial water flow. Results from simulations of the Rhine Glacier system during advance and retreat in the foreland indicate that subglacial water discharge is high and focused along glacial valleys and existing overdeepenings (Fig. 6-16d).

The formation of glacial overdeepenings is likely the result of the combined action of ice and basal water flow and depends on the extent to which processes and feedbacks are able to focus erosion and maintain the evacuation of water and sediment (Cook & Swift 2012). The deeply incised troughs and overdeepened valleys in the Swiss Plateau therefore presumably formed time-transgressively during periods of ice advance, when the steep surface slope of the ice margin provided the large hydraulic gradients necessary for a vigorous subglacial water flow and an efficient sediment evacuation from the ice-bed interface. They may also have formed during the retreat phase by the outburst of subglacial meltwater dammed behind a cold-based ice margin or a marginal permafrost wedge (Piotrowski 1994, Hooke & Jennings 2006, Stumm 2010, Kehew et al. 2012, van der Vegt et al. 2012).

Deep glacial erosion is expected to slow down within more erosion-resistant rocks (such as limestone). Good examples for such behaviour are observations from the lower Aare Valley (Fig. 6-25), but also from the Finger Lakes in New York (e.g. Mullins et al. 1996). The Cayuga Lake Basin, for instance, seemingly shows a limiting effect on incision when reaching the Onondaga limestone (Mullins et al. 1996, Bloom 2018, see also Nagra 2024k for more detail). When space is available, subglacial erosion tends to widen the overdeepening within the softer material instead of vertically incising into the harder rocks. In contrast, inneralpine overdeepenings carved in harder-to-erode rocks can reach a significant depth (e.g. Magrani et al. 2020). Here, however, topographic steering inside the preconditioned Alpine valleys may dominate over lithological control. Limited efficiency of erosion in limestone might also be the case, for example, because large amounts of subglacial water may be lost into the underlying limestone karst if available

(a process known as underdraining; Grust 2004, Gremaud & Goldscheider 2010, Braakhekke et al. 2017) thereby preventing the build-up of high water pressures that are favourable for active erosion, and the energetic water flow necessary for sediment evacuation.

Sills within the overdeepenings may locally lead to the formation of narrow inner gorges/canyons (e.g. Bandou et al. 2023) but very limited data is available about the abundance of such features in the distal Alpine Foreland.

Glacial overdeepenings in Northern Switzerland

The glaciations in Northern Switzerland caused deep erosion into the bedrock (mainly Molasse, but in the Aare Valley lime- and marlstone were also affected) and the formation of overdeepened troughs (Fig. 6-24). The glacially eroded Molasse assemblage in Northern Switzerland comprises a variety of different, yet mostly easily erodible, rock types. On the rare occasion where over-deepening in Northern Switzerland reached limestone (Fig. 6-25), the depth is considerably reduced. Furthermore, visual inspection of the map pattern (Fig. 6-24, east of Aarau and south of Brugg) suggests that overdeepening tends to widen within the easier erodible Molasse assemblage rather than to extend into the harder limestone units. Although a multitude of reasons could be considered for this effect (e.g. distance to ice margin, topography of Internal Jura as a barrier), lithological control seems reasonable (see Section 6.4.3.3 for more detail).

Some of the troughs in Northern Switzerland, such as the Strassberg Trough (Fig. 6-26b), show a multiphase filling, whereas the fillings of others seem to be dominated by only one phase (e.g. Gebenstorf – Stilli Trough, Fig. 6-25, Fig. 6-26a; Gegg et al. 2021). There is evidence for a multiple reactivation of the same trough by several glaciations (e.g. Bodensee Trough, Strassberg Trough), but in other cases troughs can occur side by side (e.g. Strassberg and Bülach Troughs, Fig. 6-26b), indicating a temporal and lateral shift of the overdeepening process.

The finding of pre-LGM sediments preserved within many overdeepenings (e.g. Dehnert et al. 2012, Buechi et al. 2018) suggests that not all glaciations were able to excavate the postglacial sediment infill of the previous glaciation and cause renewed overdeepening (Buechi et al. 2018). In ice-marginal areas of the North Alpine Foreland this preservation is often a result of changes in spatial focus and magnitude of subglacial erosion between different glacial periods (Buechi et al. 2024). On the other hand, progressive deepening over successive glacial cycles may also have taken place because ice flow is likely to be diverted from hills and ridges into already existing troughs and valleys (Kessler et al. 2008). This topographic steering is part of a positive feedback mechanism that causes the thicker and faster-flowing ice to generate more basal melting, which in turn will further increase basal sliding and sediment evacuation and consequently result in enhanced erosion. The glacial overdeepenings in the foreland often show a system of branching troughs (e.g. in eastern NL and ZNO, see Fig. 6-24). Breakthrough channels or ice-marginal drainage (Fig. 6-22b) can lead to new passages for ice that might subsequently focus (sub)glacial erosion with overdeepening. This process is thought to be more likely with repeated glaciations.

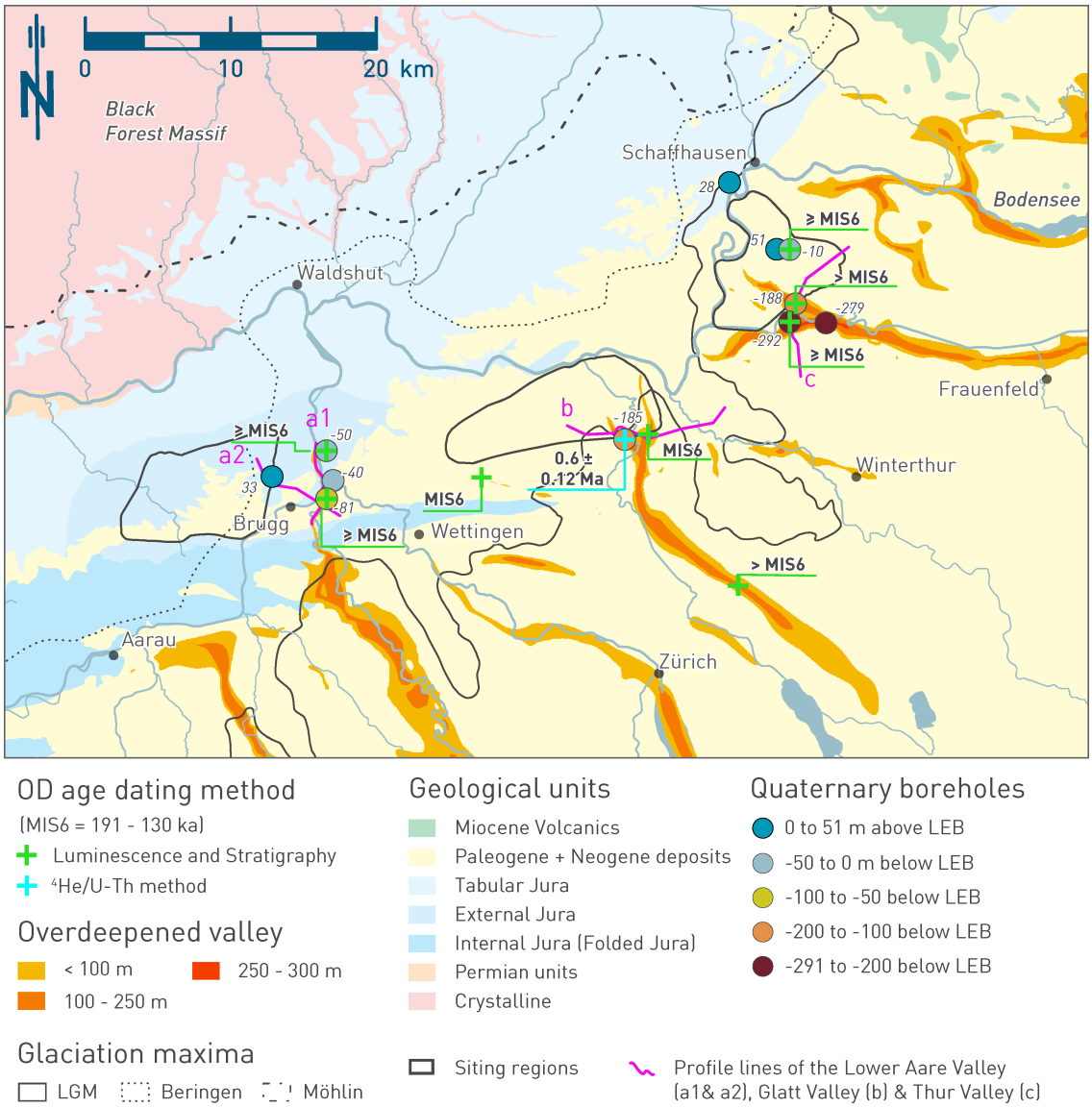


Fig. 6-24: Overview map showing the glacial overdeepenings and the underlying rock units

Overdeepening depth is depicted by sediment thickness below the local erosion base. The LGM (Bini et al. 2009) and the Beringen and Möhlin ice extents (Preusser et al. 2011) are drawn as solid, dotted and dash dotted black lines, respectively. It is conspicuous that almost exclusively the more easily erodible Molasse sediments were overdeepened (yellow colours). An exception is the lower Aare Valley, east of the JO siting region, where, amongst others, erosion-resistant Malm limestones were glacially overdeepened (Fig. 6-25). The locations of boreholes drilled during Nagra's Quaternary investigation programme are colour-coded and labelled with respect to their depth below the local erosion base. Selected ages reveal the timing of filling and thus postdate the deep glacial erosion event (e.g. Tomonaga et al. 2024, Mueller et al. 2024, Gegg et al. 2021). Also shown are the locations of the four interpretative cross-sections (a) through and across the lower Aare Valley, (b) across the Glatt Valley, and (c) across the Thur Valley which are shown in Fig. 6-25 (a1) and Fig. 6-26 (a2, b and c).

It is not always clear whether the observed multiphase backfilling cycles represent single advances within one glacial or different glacial stages. In general, the glacial sediments of over-deepened troughs are difficult to date, and available ages have large uncertainties. Evidence for significant overdeepening in Northern Switzerland exists for the Beringen and Möhlin glaciations. The oldest age so far, derived for the older part of the filling of the Strassberg trough, revealed a minimum age of 610 ± 120 ka applying the ^{4}He/U-Th dating method on porewaters (see Nagra 2024k, Tomonaga et al. 2024). Few glacial troughs are known to have been eroded into the bedrock during the LGM, although at positions closer to the Alpine chain (e.g. perialpine lakes). In contrast, mostly inlaid terminal glacial overdeepenings were formed in the distal foreland (Buechi et al. 2024). However, the Habsburg glaciation was of similar glacial extent and may be responsible for overdeepening in the study area such as the Birrfeld Trough. Dating efforts accompanying Nagra's Quaternary drilling programme are summarised and discussed in Nagra (2024k).

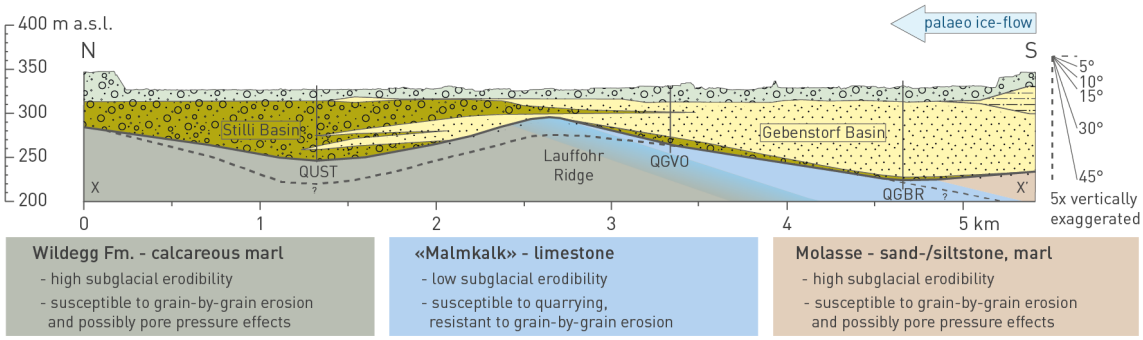


Fig. 6-25: Longitudinal profile through the Gebenstorf – Stilli Trough close to Brugg

The section (see Fig. 6-24; a1) is based on seismic cross-sections and boreholes (Gegg et al. 2021) . The orientation of the profile and relative amounts of erosion indicate that the Malm limestone forms a resistant zone in which the overdeepening capacity decreases relative to the Molasse to the south and calcareous marls to the north.

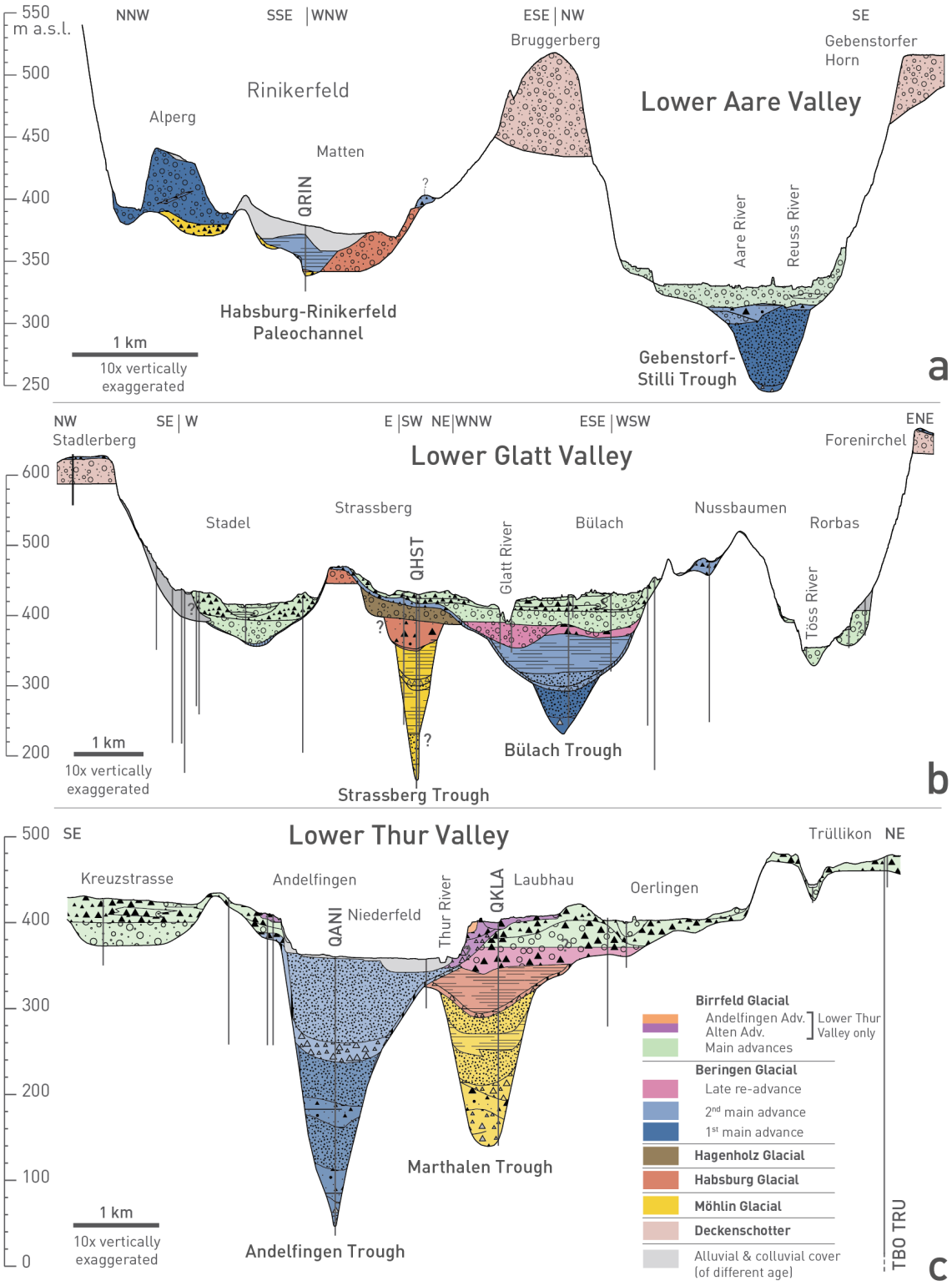

550 m a.s.l.
500
450
400
350
300
250
NNW
SSE | WNW
ESE | NW
SE
Rinikerfeld
Alperg
Matten
QRIN
Bruggerberg
Gebenstorfer Horn
Lower Aare Valley
Aare River
Reuss River
Habsburg-Rinikerfeld Paleochannel
Gebenstorf-Stilli Trough
1 km
10x vertically exaggerated
a
NW
Stadlerberg
SE | W
E | SW
NE | WNW
ESE | WSW
ENE
Forenirchel
Lower Glatt Valley
600
500
400
300
200
Stadel
Strassberg
QHST
Glatt River
Bülach
Nussbaumen
Rorbas
Töss River
Strassberg Trough
Bülach Trough
1 km
10x vertically exaggerated
b
500
400
300
200
100
0
SE
Lower Thur Valley
Trüllikon
NE
Kreuzstrasse
Andelfingen
QANI
Niederfeld
Thur River
QKLA
Laubhau
Oerlingen
Marthalen Trough
Andelfingen Trough
TBO TRU
1 km
10x vertically exaggerated
Birrfeld Glacial
Andelfingen Adv.
Alten Adv.
Lower Thur Valley only
Main advances
Beringen Glacial
Late re-advance
2nd main advance
1st main advance
Hagenholz Glacial
Habsburg Glacial
Möhlin Glacial
Deckenschotter
Alluvial & colluvial cover (of different age)
c

Fig. 6-26: Cross-sections characterising the Quaternary deposits in the lower Aare Valley, the Glatt Valley and the Thur Valley

The sections represent an integrated interpretation of high resolution 2D seismic data, borehole and outcrop data (Nagra 2018). The 10× vertically exaggerated profiles highlight forms, depths and filling of selected and representative glacial overdeepenings. (a) Lower Aare Valley with the fluvioglacial Habsburg – Rinikerfeld Palaeochannel (QRIN) and overdeepened Gebenstorf – Stilli Trough (after Gegg et al. 2021). (b) Glatt Valley with the overdeepened Strassberg (QHST) and Bülach Troughs. (c) Lower Thur Valley with the overdeepened Andelfingen (QANI) and Marthalen (QKLA) Troughs (Buechi et al. 2024). See Fig. 6-24 for location.

6.4.2 From past to future erosion

In this section, the concept of landscape compartmentalisation introduced in Section 6.4.1.1 and the erosion history highlighted in Sections 6.4.1.2 to 6.4.1.4 are used to derive a brief summary of the present landscape and to interpret the main differences between the three siting regions (Section 6.4.2.1). Combined with the respective repository depths, these differences provide site-specific constraints (Section 6.4.2.2) for the erosion assessment. Section 6.4.2.3 provides a brief introduction to the model cascade and the specific approach, including an introduction to the methodology of structured expert elicitation, to incorporate uncertainties in the assessment of future erosion. This assessment forms the basis for evaluating future erosion processes (Section 6.4.3), with the focus on the evolution of repository overburden thickness. Results are presented in Section 6.4.4.

6.4.2.1 Interpretation of present landscape characteristics in the siting regions

In Sections 6.4.1.2 to 6.4.1.4, it has been shown that the Quaternary landscape of Northern Switzerland is shaped by the effect of multiple glacial/interglacial cycles with phases of sediment accumulation and vertical incision (including multiphase deep glacial erosion). The distance from the Alpine chain and from the ice margins, as well as the erodibility of the outcropping rocks led to marked differences between the present-day landscapes of the three siting regions. These differences are highlighted along the summary profile through all the siting regions (Fig. 6-27). The consequences which these differences have with respect to the siting regions (e.g. depth of the Opalinus Clay) and which thus define the different boundary conditions are further described in the following Section 6.4.2.2.

Mainly because of the general SSE-ward dip of the strata in Northern Switzerland different lithologies crop out in the three siting regions, i.e. mainly Mesozoic rocks in JO and Paleogene/ Neogene rocks in NL and ZNO. The bedrock underlying Quaternary unconsolidated sediments in NL and ZNO, i.e. the rocks that are subject to erosion, are comprised of easy-to-erode assemblages of Molasse sediments of Northern Switzerland. Harder-to-erode rocks (e.g. Malm limestone) are located only at depths of several hundreds of metres. JO, in comparison, is characterised by a cuesta landscape with alternating harder- and easier-to-erode rocks (Fig. 6-21). Harder rock types (see Fig. 6-27) are presently located close to the surface and probably influenced the present stability of the plateau-like landscape in JO.

No glacial overdeepening is located within the HLW perimeter of JO; the closest occurrences can be found in the lower Aare Valley east of JO. In contrast, in the NL and ZNO siting regions, glacial overdeepenings are significantly deeper than in the lower Aare Valley. This observation can be attributed to two factors. On the one hand, the glacial troughs in NL and ZNO were cut into more erodible sedimentary rocks of the Molasse (Fig. 6-24), while the hard limestone layers in the lower Aare Valley slowed down erosion (Fig. 6-25). On the other hand, glaciations during past ice ages have impacted the three siting regions to varying degrees. The map of the ice extent shown in Fig. 6-18d, Fig. 6-24 and the simplified bars in Fig. 6-27 illustrate these differences based on three extensive and relatively well-known glacials in Northern Switzerland (Möhlin, Beringen and Birrfeld). Only the most extensive glaciations reached the JO siting region, and the glaciers were presumably less thick than in NL and ZNO. During the last ice age, the ice cover in ZNO was thicker and more extensive than in NL. Such patterns can be expected during future glaciations.

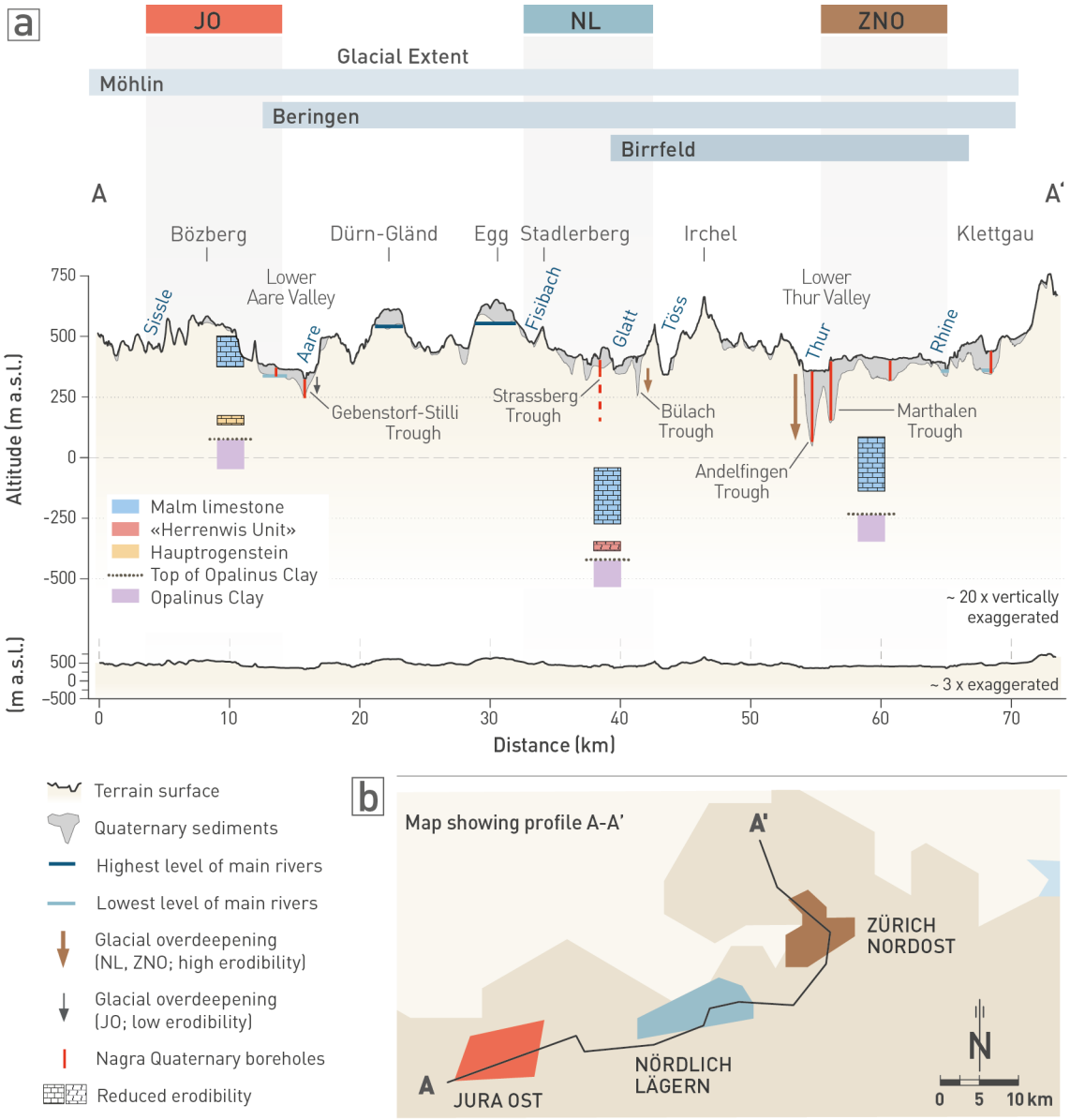


Fig. 6-27: Cross-section through the siting regions with the morphological and geological conditions that are key to assessing future erosion processes

The synthesis cross-section (a) shows the present-day topography, the main palaeoriver levels (highest fluvial level in dark blue and lowest level in light blue, the latter corresponds to the LEB) and glacial overdeepenings. Quaternary boreholes drilled during Nagra's investigation programme are shown (Strassberg Trough borehole dashed because it is not located at the cross-section position, see Fig. 6-26b for comparison), as well as a simplified stratigraphy focusing on the host rock (Opalinus Clay) and erosion-resistant rock types above it (Fig. 6-21). The blue bars above the figure show comparatively well-known extents of earlier glaciations (Fig. 6-18d). The extent of the Birrfeld glaciation marks the LGM of the most recent ice age around 21'000 years ago. The Beringen and Möhlin glaciations formed during earlier ice ages that probably occurred between 100'000 and 650'000 years ago (Fig. 6-12). (b) Simplified map showing the location of the cross-section with respect to the siting regions.

6.4.2.2 Site-specific constraints with respect to future erosion assessment

The differences illustrated above (e.g. occurrence of glacial overdeepenings or local topography) become effective when considering the depth-dependent barrier function (Sections 6.1.2, 6.5.2.2) of the host rock and potentially relevant tectonic- and climatic-driven surface processes. Fig. 6-28 exemplifies this effect by showing the fractions of the different landscape elements (compartments) with respect to the depth of the Top Opalinus Clay (i.e. the repository host rock) for each siting region. These fractions are shown for (1) the entire HLW siting regions, (2) the provisional disposal area (reflects the ~ 1 km^2 outline of the repository project for high-level waste; for location see Fig. 6-34) and (3) the provisional disposal area including spatial reserves (see Nagra 2024e for further information). Note that the final calculations of the erosion assessment refer to the provisional disposal areas.

The depth of the provisional disposal area (approximately 50 m below the Top Opalinus Clay; see Fig. 6-28, brown boxes) with respect to the local erosion base is deepest in NL (794 m at centre, 764 m at most shallow location), and considerably less deep in JO (291 m at centre, 270 m at most shallow location). On the other hand, the amount of local topography is significantly larger, both as median (206 m) and as range, in JO than in NL (median 113 m) or ZNO (median 84 m, red boxes). This local topography adds additional overburden thickness above the repository needed to maintain the barrier effect (Section 6.1.2).

The distribution of glacial overdeepenings in the siting regions varies significantly. As already highlighted above, no overdeepening is observed in the entire HLW siting region of JO. The box plots for glacial overdeepenings in NL and ZNO (blue boxes in Fig. 6-28) not only show the occurrence of such feature in the siting regions or the spatial reserves but also show that they can be very deep (> 150 m below local erosion base [LEB] in the entire HLW areas of NL and ZNO); more often or in larger parts, however, they do not reach more than about 70 m below LEB with median values around 30 m. This is an important observation when addressing this effect in the future assessment.

Accordingly, to compare the three sites with their different boundary conditions in an unbiased way, the landscape compartmentalisation into local erosion base, local topography, and glacial overdeepenings was transformed into a model cascade (see next section).

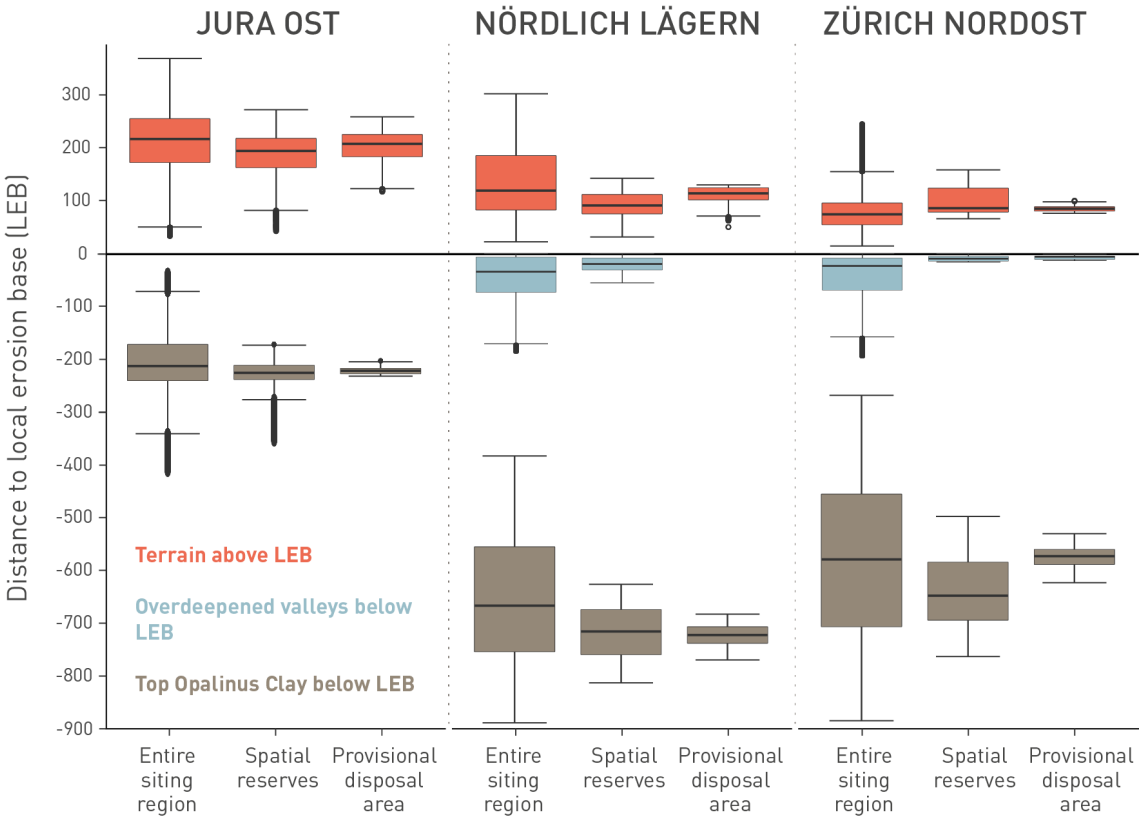


Fig. 6-28: Site-specific constraints of the landscape compartments within the siting regions

Depth profiles showing boxplot statistics on the main compartments with respect to the local erosion base (0 m line). Boxes entail the interquartile range between 25th – 75th quantiles, the whiskers the extreme values, as derived from multiplying the interquartile by 1.5. Values outside the whiskers are considered statistical outliers. The siting regions share different portions of the landscape compartments. The depth of the provisional disposal area with respect to the local erosion base (LEB) is deepest in NL, and considerably less deep in JO. On the other hand, JO is covered by significant terrain above the LEB (local topography) and this site is less affected by glaciations. JO has no overdeepened area within the siting region.

For the calculation of the difference raster LEB – Top Opalinus Clay, raster datasets of the LEB (Pietsch & Jordan 2014) and the horizon Top Opalinus Clay (Nagra 2014b) were used. In comparison to the local model Top Opalinus Clay of 2014 (Nagra 2014b), the more recent 3D horizon model of the sites (Nagra 2024m), covering the zones of the spatial reserves and the provisional disposal areas, shows the following average differences: 18 m deeper in JO, 12 m deeper in NL, 6 m shallower in ZNO. Note that the assessment of future erosion presented in Section 6.4.3 is based on the recent 3D horizon model documented in Nagra (2024m).

6.4.2.3 Approach to assessing future erosion

Managing knowledge and uncertainties in the context of assessing the long-term safety of a deep geological repository is challenging, in particular because of the long time span to be considered. In this section, the main procedure used is highlighted.

The model cascade

Two main questions are addressed to ensure barrier integrity and long-term safety with respect to future erosion: (i) how much remaining overburden thickness is expected in the siting regions after the periods under consideration and (ii) what is the probability of excavation at the end of one million years? Accordingly, the data provided here are used for the safety-based comparison of the siting regions and as input for safety analysis. The remaining overburden in metres and excavation probability in percent are the main outputs of the erosion model (Fig. 6-29). Both outputs can be calculated for any position within the area of interest. The focus is on the location of the provisional disposal area and its anticipated depth within the host rock Opalinus Clay.

The structure of the erosion model resembles a "Roman Fountain" where the output of Model A (Fluvial incision, i.e. future evolution of the local erosion base) generates input for Model B (Evolution of local topography) and Model C (Deep glacial erosion). The separate consideration of each of the three processes and subsequent combination in the model cascade allow future erosion in the siting regions to be critically assessed and compared.

Model A starts with simulations of the fluvial incision along the Hochrhein. Model B incorporates the 3D geology and simulates the response of local rivers and hillslopes to the derived incision of Model A, extracted at three selected points downstream of each siting region (Section 6.4.3.1). Both stable drainage networks and plausible alternative drainage scenarios (Section 6.4.3.2) are included to account for uncertainties in future channel dynamics, especially in JO. The latter considers the development of new valleys cutting across topographic highs, such as the Bözberg-plateau, in conjunction with large future foreland glaciations. Output of Model B provides the remaining overburden thickness and an excavation probability with excluding glacial over-deepening. Incision of Model A and the different drainage scenarios of Model B are input data for Model C. The calculation chain of Model C (Section 6.4.3.3) combines several aspects to be evaluated with respect to future deep glacially eroded troughs. The output of Model C provides estimates of remaining overburden thickness and excavation probabilities including glacial overdeepening.

To consider uncertainties for timescales of 100'000 and one million years, a hybrid approach was developed with as much probabilistic treatment as possible. Where a probabilistic treatment was not feasible, scenarios were specified covering what was considered a critical range of possibilities. The whole process was guided by a sensitivity analysis to identify critical parameters and processes in the model cascade. Models A and B are based on numerical simulation, while Model C processes the uncertainties analytically.

Expert elicitation

In the context of future erosion modelling, like in many other areas of science and engineering, modelling has to be carried out against a background of pronounced uncertainties. Whenever there is not enough observational data to determine these uncertainties quantitatively, it is unavoidable to employ expert knowledge for this purpose (Oppenheimer et al. 2016). Within the solid-earth-geosciences, this is particularly the case for seismic and volcanic hazard and risk assessments, in particular when nuclear facilities are involved. However, more recently, expert elicitation has

been used in assessment of climate parameters and models (e.g. Yucca Mountains; Dewispelare et al. 1995, Sebok et al. 2022, Bamber et al. 2019) or even in upcoming topics as carbon capture and sequestration (Moore et al. 2024).

Inclusion of expert knowledge must be carried out in a structured manner, as otherwise the results can easily become unreliable and not reproducible (Budnitz et al. 1997, Oppenheimer et al. 2016). This realisation has led to the development of a number of methodological approaches to structured expert elicitation, of which the protocol of the Senio Seismic Hazard Analysis Committee (or *SSHAC*; Budnitz et al. 1997) and the Sheffield Elicitation Framework (*SHELF*; Gosling 2018) are two well-tested examples. The aim of both methods is to describe uncertain quantities of interest (QoI) as probability distributions that represent the expert knowledge of a group, based on *expert judgment* of their members. It is important to note that there is a certain vocabulary inherent that may be uncommon. To avoid misunderstandings, brief explanations of the most common terms are added below (O'Hagan 2019).

Expert judgement (also expert opinion) describes the individual representation of one (or a group of) expert's scientific judgement on a specified topic, in this case for instance the uncertainty of a model input parameter. This rational judgement is based on available data and the expert's scientific know-how and experience and is provided after a training on the influence of cognitive biases (Kahneman et al. 1982) in decision making, especially such as anchoring, availability bias or overconfidence but also the more general aspect of group dynamics.

The probability concept behind expert judgement is that of *subjective probability*. Subjective probabilities (Cooke 1991) are the expert's *degrees-of-belief* formally expressed as probabilities. They are called "subjective" because they follow individual (or group's) judgements. These probabilities are nevertheless informative and scientific (O'Hagan 2019) and one of the existing legitimate probability concepts that meet Kolmogorov's axioms (Galavotti 2005).

Elicitation describes the process of gaining the expert's judgement. The uncertainty elicitations for the parameters relevant for the erosion assessment at Nagra followed the SHELF protocol (Gosling 2018), which is a two-step structured group elicitation framework for carrying out the elicitation of subjective probability distributions for quantities of interest (QoI). The actual elicitations are done in workshops which are led by an experienced facilitator (moderator) who has been trained in all aspects of the SHELF protocol.

The first step requires the individual elicitation of a set of quantiles (e.g. median, tertiles/quantiles, upper and lower bounds) for the uncertainty distribution of interest, one for each expert. In the second step, the expert group derives a single group distribution, which reflects an integrated view of the uncertain quantity. This means that all arguments brought up during the group discussions are considered, as they would be seen through the eyes of a *rational impartial observer (RIO)* (Gosling 2018, O'Hagan 2019) and it requires that all experts exchange their individual judgments with the role of RIO. The RIO perspective takes into account the combined knowledge of the group but gives some (perhaps more convincing) arguments more weight than others. The facilitator "acts" on behalf of the RIO (and thus in agreement and collaboration with the experts), when aggregating the distributions.

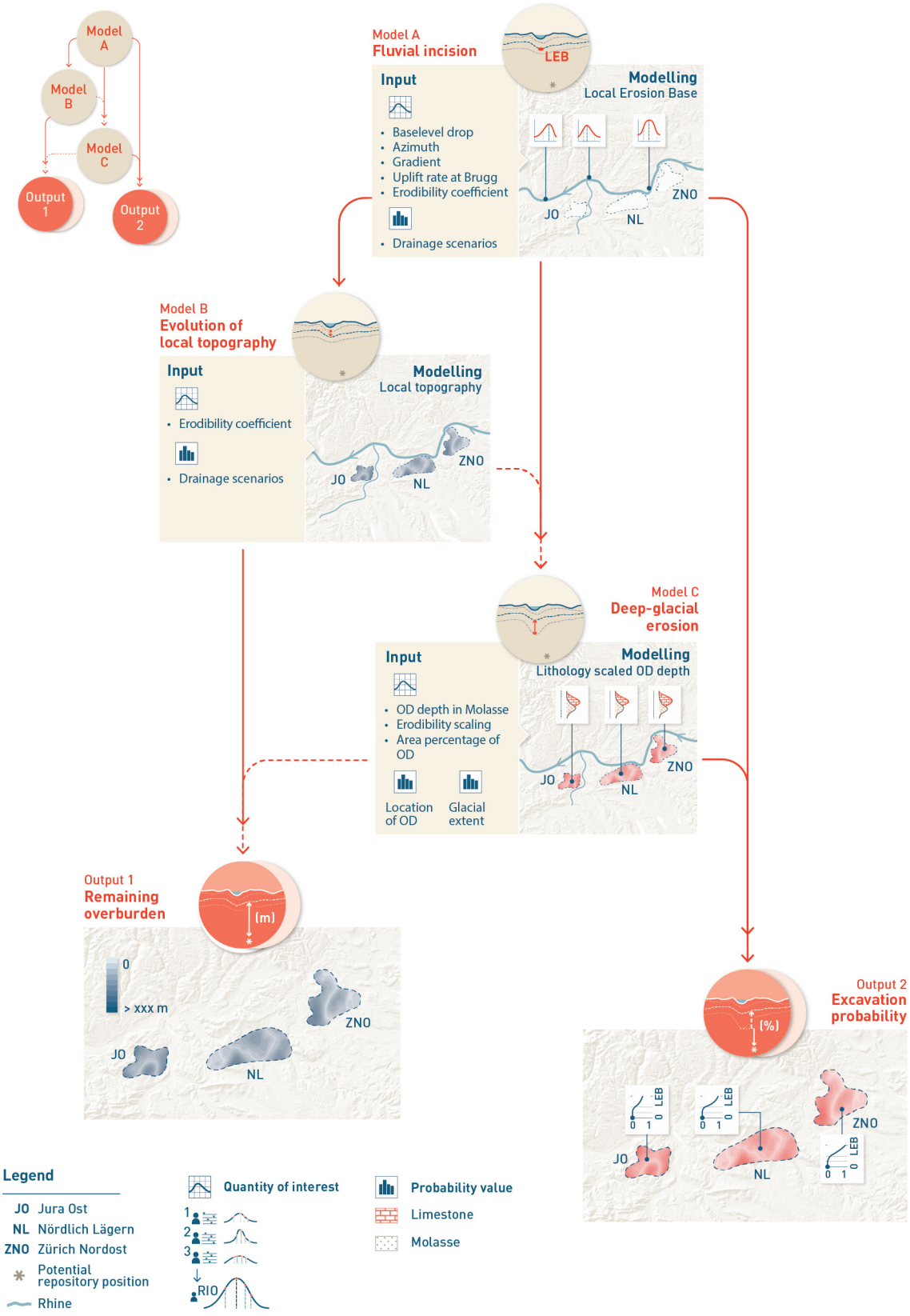

Model A
Model B
Model C
Output 1
Output 2
Model A
Fluvial incision
Input
Baselevel drop
Azimuth
Gradient
Uplift rate at Brugg
Erodibility coefficient
Drainage scenarios
LEB
Modelling
Local Erosion Base
JO
NL
ZNO
Model B
Evolution of local topography
Input
Erodibility coefficient
Drainage scenarios
Modelling
Local topography
JO
NL
ZNO
Model C
Deep-glacial erosion
Input
OD depth in Molasse
Erodibility scaling
Area percentage of OD
Location of OD
Glacial extent
Modelling
Lithology scaled OD depth
JO
NL
ZNO
Output 1
Remaining overburden
(m)
0
> xxx m
JO
NL
ZNO
Output 2
Excavation probability
(%)
LEB
JO
NL
ZNO
Legend
JO Jura Ost
NL Nördlich Lägern
ZNO Zürich Nordost
Potential repository position
Rhine
Quantity of interest
RIO
Probability value
Limestone
Molasse

Fig. 6-29: Simplified flowchart for calculating the remaining overburden thickness and probability of excavation at time T_x

The hybrid probabilistic model consists of three submodels: Model A: simulation of the local erosion base (LEB), Model B: accounting for the effects of local topography, Model C: assessing the probability of glacial overdeepening (OD) and evaluates the combined (glacial and fluvial) probability of incision below a certain vertical position (e.g. the level of the provisional disposal area). Both Model B and Model C depend on the output of Model A. The glacial part of Model C does not depend on the output of Model B. It is based on the LEB and does not account for local topography, i.e. Model C only takes glacial overdeepening events into account that cause an overdeepening below the LEB. However, Model C does depend on scenarios of alternative drainage networks that are developed within/for Model B. Note that final distributions of remaining overburden thickness and excavation probabilities are calculated for selected locations only. Also note that all listed input parameters (left side of subfigures) are quantities of interest for which uncertainties were assessed by elicitation following the SHELF protocol. Finally, it is possible to calculate non-glacial excavation probabilities (parallel to Indicator 1) and combined non-glacial and glacial distributions of remaining overburden thickness (parallel to Indicator 2).

The *RIO distributions* were fitted with parametric distributions that best reflected the elicited quantile values. Importantly, these RIO distributions comprise the uncertainty that is propagated into the model (Fig. 6-29). In Fig. 6-29, all input parameters (left side of each Model) are quantities of interest for which the uncertainties were assessed in SHELF-based elicitation workshops. A total of 34 parameter uncertainties have been evaluated to be used in the modelling or for plausibility checks (see Nagra 2024k for more details). Not all quantities, however, were assessed as probability distributions, some were provided as scenario weights or event probabilities. Because the elicitations were conducted within the erosion team at Nagra with usually 3 – 5 experts per workshop, it was particularly important to include both, the expertise in local geology and geomorphology, as well as expertise in process understanding. The facilitator was supported by an external expert with a strong background on statistics and probabilities, who was trained on all SHELF aspects. The high number of parameter uncertainties required prioritisation regarding, which parameters to treat with most effort (e.g. a higher number of experts, more time etc.). This prioritisation was supported by a sensitivity study. In exceptional cases, a pragmatic deviation from the protocol was allowed (see Nagra 2024k for more detail).

It is important to recapitulate that a rigorous evaluation of prior and present conditions of the landscape and the processes that shaped it was conducted by an extensive scientific programme over several years. The available outcomes of this programme (see also Nagra 2024k for more detail) were provided to all the experts prior to the workshops to ensure that all experts were 'reading from the same page' and that they had access to the same factual basis. In this report, the main evidence is provided in the previous Sections 6.2, 6.3, 6.4.1, as well as Sections 3.4.5 and 3.5.

In the following sections, RIO distributions are provided for the most important parameters used in the respective models only. They are provided with a brief reasoning, which in turn is based on the evidence provided before, partly supported by additional global data or more process-related expertise, which might then be shown or cited individually. More detail on the modelling and parameters can be found in Nagra (2024k).

Presentation of results

In this report, the results are shown only for the one-million-year timescale, with the exception of the intermediate results of future fluvial incision. The final calculations are provided for the provisional disposal areas of each site. To allow a more qualitative comparison within the wider areas containing the spatial reserves, an abridged calculation was used for a set of additional coordinates (Nagra 2024k) in each siting region. To follow the general procedure of the safety-based site comparison, different outputs were generated to evaluate criterion 2.2 (Erosion) and criterion 3.3 (Predictability of long-term changes) of the Sectoral Plan (SFOE 2008). These outputs, as well as considerations beyond one million years, are only reported in Nagra (2024k). Of the full range of uncertainties presented by the total assumed probabilities, the 5 – 95% range is considered the "expected range" in this assessment.

6.4.3 Future erosion processes and rates

In general, it is expected that future erosion processes (both glacial and non-glacial) will be comparable to those prevalent during the Quaternary with a few exceptions:

- The fluvial incision rates are predicted to be lower because the main pulse of incision caused by large-scale drainage reorganisation has diminished (Section 6.4.1.2).
- The most important variations between aggradation and incision periods are expected to be caused by future glacial/interglacial cycles. The long-term incision driven by vertical motion of the rock column will thus be modulated by phases of sediment accumulation with no net vertical incision, comparable Quaternary evolution (Section 6.4.1.2).
- The next glacial inception might be delayed because of the anthropogenic atmospheric CO_2 content (Section 6.3.3).
- The stratigraphic column above the repository sites NL and ZNO contains harder-to-erode rock types (limestones of the Malm) compared to the Molasse, which is currently the outcropping lithology at these sites (Fig. 6-27, see Sections 6.4.1.4 and 6.4.2.1).
- In addition, further erosional downcutting might decrease the accumulation area of future glaciers, which in turn might result in smaller glacial extents, even with similar climate forcing (Egholm 2022). On the other hand, as a result of the drainage divide shift between Rhine and Danube, the Rhine Glacier might undergo a westward shift with less ice being able to cross the divide and drain towards the Danube (Ellwanger et al. 2011), which in turn might increase the erosion potential in the study area.

For the future erosion assessment, evidence from Quaternary landscape evolution together with process understanding was used to derive probability distributions for the parameters to be applied in the modelling (see Section 6.4.2.3 for a brief overview on expert elicitation). An overview of the main results and associated line of reasoning for each separate erosion process (i.e. model part) is presented in this section. More details are provided in Nagra (2024k).

6.4.3.1 Future fluvial incision

Future evolution of the local erosion base

The analysis of future fluvial incision of the Hochrhein (i.e. approximately between the cities of between Stein am Rhein and Basel) and thus lowering of the local erosion base is based on the stream power incision model (SPIM) (for more detail see Nagra 2024k). The SPIM is frequently used in landscape evolution models that include tectonic uplift U. The main advantage is the low model complexity and its relatively straightforward numerical implementation, which allows its application to long timescales (10^5 – 10^6 years) and to investigate different boundary conditions. According to the SPIM, the rate at which rivers incise is a function of the drainage area A and channel slope $S = dz/dx$ raised to the power exponents m and n, respectively, and multiplied by a bulk parameter K which is a dimensional coefficient of erosion often simply termed erosional efficiency or erodibility coefficient (for more detail see Nagra 2024k).

When addressing the future, it is expected that parameters such as rock uplift U (Section 6.2.2), erodibility coefficient K or upstream drainage area A might change over time. Consequently, the evolution of the intermediate baselevel at the transition from the Alpine Foreland to the Upper Rhine Graben near Basel needs to be considered (Section 6.2.2). These parameters were elicited independently as subjective probabilities (see Fig. 6-29: Model A, Section 6.4.2.3 and Nagra 2024k).

Rock uplift

Spatial rock uplift is approximated here by a plane, i.e. rock uplift is modelled as a linear function of longitude and latitude. The main assumption is that the Alpine uplift provides the dominant cause for the geometry of the uplift plane. In simplified terms, the main gradient causes higher rates from the external foreland towards the Alps along a direction that is roughly perpendicular to the Alpine chain. However, the plane is based on the uncertain parameters of rock-uplift rate at one position (here Brugg), the gradient at which uplift is rising, and the azimuth direction along which the gradient is applied (see Nagra 2024k for more information). Based on the plane, calculated from these elicited parameter distributions, the uplift can be evaluated for any coordinate within the investigated area, for instance, for the locations of the siting regions (Fig. 6-30, Tab. 6-1). Note the higher rates for the shorter time frame of 100'000 years that includes similar values as measured using geodetic methods (Section 6.2.2).

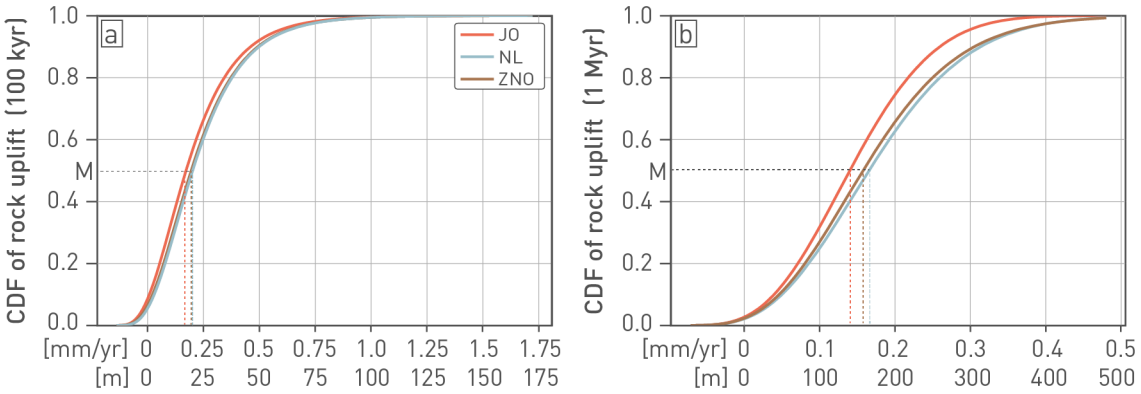


Fig. 6-30: Inferred future rock uplift rates in the three siting regions over the next 100'000 and one million years

Rock uplift rate is defined as the total rate of bedrock uplift in mm/yr that is expected as a response to tectonic processes and as an isostatic response to loading or unloading, including the response to loss of ice cover. The reference level for rock uplift is the geoid. The estimates are based on the assumption of a planar uplift pattern caused primarily by Alpine uplift. The results are calculated for the location of the provisional disposal areas and shown as cumulative distribution function (CDF), where the value of 1.0 (y-axis) equals to 100% cumulative probability. The letter M at both y-scales refers to the median value, i.e. the 50% quantile (value 0.5). The corresponding median values can be read at the x-axes (compare Tab. 6-1). (a) CDF of estimates for the time frame of 100'000 years. (b) CDF of estimates for one million years. Note that the shorter time frame of 100'000 years allows higher rates (see Nagra 2024k for more details). The lower x-axis translates the rates to cumulative amount of rock uplift for the respective time frames.

Tab. 6-1: Inferred future rock uplift rates

Rates are estimated at the locations of the provisional disposal areas of the siting regions for 100'000 and one million years, respectively (see Fig. 6-30). The location of the provisional disposal area is shown in Fig. 6-34. Values are rounded to the second digit. The 5 – 95% of the total probabilities are considered the expected range in this assessment

Quantile	**Uplift rates in JO** [mm/yr]		**Uplift rates in NL** [mm/yr]		**Uplift rates in ZNO** [mm/yr]	
	100 kyr	1 Myr	100 kyr	1 Myr	100 kyr	1 Myr
5%	-0.02	0.02	-0.04	0.02	-0.01	0.02
25%	0.07	0.08	0.10	0.10	0.09	0.10
50%	0.17	0.14	0.20	0.17	0.19	0.16
75%	0.30	0.20	0.34	0.24	0.33	0.23
95%	0.58	0.30	0.62	0.36	0.61	0.36

Erodibility coefficient

The rock types of Northern Switzerland comprise a variety of assumed resistance against erosion. They were divided into four erodibility classes (EC) based on lithological considerations and the lithostratigraphic units differentiated in the 3D geological model "Nagra Regionalmodell 2012" (Gmünder et al.. The classes comprise EC 1 = Quaternary unconsolidated sediments, EC 2 = Bedrock Class "soft", EC 3 = Bedrock Class "medium", and EC 4 = Bedrock Class "hard" (Fig. 6-21). It is generally assumed that the classification of erodibility follows the trend of EC 1 > EC 2 > EC 3 > EC 4. This allows distributions to be assigned for the erodibility coefficient (*K* values) needed for modelling fluvial incision and later local topography (see Section 6.4.3.2) using the SPIM equations.

The geological map of Northern Switzerland 1:100'000 (Isler et al. 1984) was first used to map spatially variable values of the erodibility coefficient *K* (depending on rock type) on the present-day topography, focusing on the JO siting region and surrounding area (Graf 2022). This first-order assessment was done by extracting ranges of apparent *K* values from the present-day landscape based on drainage area and gradient along the channel network. Lithological mapping along the Hochrhein is less distinct than within the 3D geological model. Here, rock types of EC 2 and EC 3 were combined into one class (here ECb) of weak to intermediate resistance to erosion (see Nagra 2024k for more detail).

Importantly, an uplift value of 0.1 mm/yr was spatially uniformly applied to the area used for the *K* mapping (Graf 2022). Simplified, this means it was assumed that the present-day landscape has evolved under a background rock uplift rate of 0.1 mm/a. Under the chosen SPIM assumption (n = 1, m = 0.45; Nagra 2024k), uplift and *K* values scale linearly. Accordingly, the elicited distributions for the *K* values of the four erodibility classes included ranges that were scaled to include variability in the uplift value. These ranges are consistent with the previously elicited one million years RIO distribution for uplift at Brugg (*UBR*, see above and Nagra 2024k for more detail).

The elicitation followed a rather pragmatic, systematic procedure. First, the general assumption was that the median value of each erodibility class, which was derived by the landscape inversion (Graf 2022), reflects the most robust *K* value of the respective class. The uncertainty distribution around this value should then reflect the scatter (excluding artefacts originating from low gradients at plateau areas or within flood plains). It should also be accounted for transient effects from spatially non-uniform uplift or incision within the landscape and for the uncertainty caused by the uplift assumption of 0.1 mm/yr (see above).

The mean values of the elicited parameter distributions vary by a factor ~ 1.5 and follow the pattern EC 1 > EC 2 > EC 3 > EC 4. The variability of *K* values within a distribution can be in the order of one magnitude (see Nagra 2024k).

Baselevel changes

In addition, to account for the downstream change from the tectonic domain of the Alpine Foreland into the subsiding domain of the Upper Rhine Graben, the parameter baselevel drop (*BL*) was introduced and elicited (Fig. 6-31). Baselevel in this context is considered with respect to sea level. Here, negative values reflect net baselevel gain. Accordingly, baselevel gain would mainly correspond to sediment accumulation, while baselevel drop can be both rock subsidence, which is not balanced by sedimentation, or incision into the present Quaternary fill.

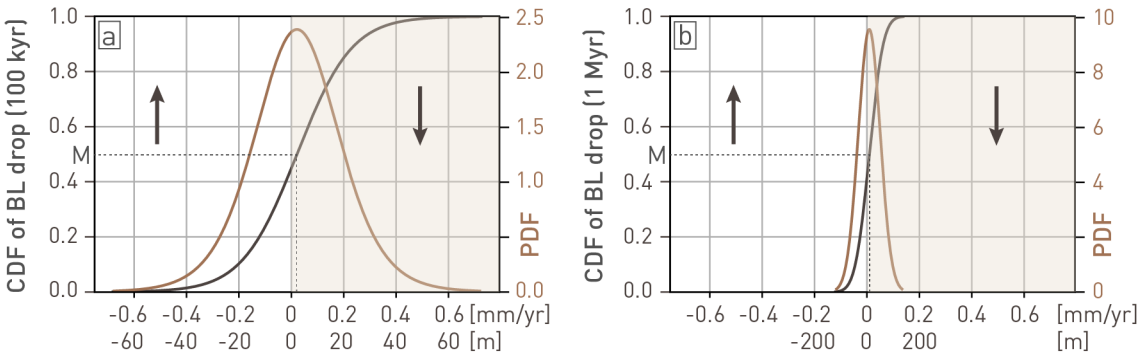


Fig. 6-31: Total assumed probabilities for baselevel drop downstream of Basel

The total assumed probabilities of the rate of baselevel drop are based on expert judgement (see Nagra 2024k). Probabilities are shown as cumulative distribution function (CDF, see caption of Fig. 6-30 for explanation) and as probability density function (PDF, brown colour). PDF visualisations allow to assess the most probable values, which are identified by the bulge of the curve (here close to 0 mm/yr). In contrast, lowest probabilities are reflected in the tails (a) 100'000-yr time window and (b) one-million-year time window. Negative values correspond to net baselevel gain. For both time frames, the baselevel downstream of Basel is expected to be stable with a very slight tendency towards baselevel drop. The letter M reflects the median value. The lower x-axis translates the rates to cumulative amount of baselevel change after the respective period under consideration, i.e. 100'000 yr in (a) and one million yr in (b). Note the similar x-axis to highlight the higher rates allowed during shorter periods.

Based on the present-day longitudinal profile and terrace distribution in the Hochrhein and near Basel (Fig. 6-19 and Fig. 6-20), the baselevel downstream of Basel is expected to be stable with a very slight tendency towards baselevel drop. However, fluctuations in the order of ~ 30 m (5 – 95%) within the next 100'000 years and up to ~ 60 m gain and ~ 80 m drop (5 – 95%) after one million years appear to be possible in light of the future dynamics of the Upper Rhine Graben and Rhenish Massif (Section 6.2.2) as well as climate-driven sediment flux (Sections 6.3.1 and 6.4.1.2) and were thus included in the uncertainty estimates for future fluvial incision. A baselevel gain of ~ 30 m would roughly reflect the thickness of the Niederterrasse deposits at the location around Basel. Allowing for an additional sediment pulse (e.g. after filling of the Bodensee and Zürichsee), such sediment accumulation seems to be a plausible scenario for a time span of 100'000 years. Yet another plausible scenario would be that, after filling of these peri-Alpine lakes, the sediment pulse fails to appear because of a prolonged interglacial and exhausted sediment sources in the catchments (see Section 6.3.3.1). In such a case, incision into the fill as seen today in large parts of the Hochrhein and Upper Rhine Graben could be expected to continue. Such a scenario could cause net baselevel drop down to the base of the Niederterrasse deposits. Higher fluctuations are allowed in the million-year time window, as it is more likely that larger glaciations will occur (Sections 6.3.3.1 and 6.4.3.3) and supply large amounts of sediment. A baselevel gain of no more than the approximate difference between the top of the Hochterrasse deposits and the river surface and a baselevel drop of approximately half the elevation difference between Bingen and Basel were considered as reasonable assumptions. This estimate is based on the assumption of continued rock uplift of the Rhenish Massif and preservation of the intermediate baselevel near the city of Bingen (see Section 6.2.2).

Changes in drainage area

Based on geometric considerations of the fluvial landscape (Section 6.4.1.2), far-reaching effects influencing the drainage system of Aare and Rhine, similar to those experienced during Pliocene-Quaternary times, are not to be expected at this location for the next million years. A larger piracy scenario that would theoretically be possible late in the period under consideration considers the capture and diversion of the Iller River. Simulations show that such a scenario does not have a major impact on discharge and the vertical erosion potential of the Hochrhein (see Nagra 2024k for more detail). Yet another scenario considers the future increase of the Rhine discharge at the expense of the Danube via karst sinkholes along the Danube. However, even with the full incorporation of the upper Danube catchment into the Rhine catchment, this increase makes only a minor contribution to the fluvial erosion and the longitudinal river profile evolution in the Hochrhein for the next one million years (Nagra 2024k).

Another reasonable scenario would be the diversion and shortcut of the Alpenrhein across a few metre high swell at Sargans, subsequently following a path through the Walensee.

While the Rhine catchment in the area of the siting regions grows at the expense of the Danube, it might lose area towards the Rhone River within the westernmost reaches east of Lac Léman. Headward erosion might capture the Upper Aare, e.g. in the area west of Yverdon (Fig. 6-19a, see also Nagra 2014c, Dossier III). Such a scenario could cause a baselevel drop with further headward erosion because the Rhone River with ~ 800 km length is significantly shorter than the Rhine River. However, it is not expected that headward erosion would reach the Hochrhein area within the period under consideration. Instead, the loss of Aare catchment would considerably reduce the incision potential of the Hochrhein.

Using a variety of scenarios for changes in future discharge/catchment, as mentioned above (capture of Iller, capture of Upper Danube, diversion of Upper Aare towards west, and diversion of the Alpenrhein across the swell of Sargans) that are ranked by their plausibility, and variants for the parameters based on expert degree of belief, SPIM was used in a Monte Carlo environment to generate probable future river profiles between the outflow of the Bodensee and Basel (i.e. the Hochrhein) at time T_x (100'000 years and one million years) from all parameter combinations (see Nagra 2024k for more detail).

Modelling results

The results are visualised in Fig. 6-32a for incision after 100'000 years and Fig. 6-32c for incision after one million years. The left panel shows the realisations of future longitudinal Hochrhein profiles in grey with the present-day river profile (in blue) and the elevations of Bingen and sea level as reference regional baselevels. The darker the future river profiles appear, the more likely is the amount of incision at this position. Baselevel gain flattens the profiles, while baselevel drop allows stronger incision. Because of the more proximal position with respect to the intermediate baselevel in Basel, this influence is largest within the area of JO. The orange boxplots in Fig. 6-32a and c describe the uncertainty distributions of the rock uplift that the provisional disposal areas (circles) might undergo during the same respective time. Using these distributions of rock uplift and future incision, the remaining overburden thickness above the repository location with respect to the local erosion base can be determined (Fig. 6-32b and d). In these plots, the boxes correspond to specific quantiles (see legend) and the violins reflect the distributions, such that the range of the violins extends past the extreme data points. The bulge corresponds to the most likely values.

The SPIM simulations using all parameter combinations show that fluvial incision itself is not expected to present any threat to the barrier function at ZNO and even less at NL. However, they reveal a considerable number of scenarios in which the repository in JO would be uplifted to, or

even above, the future local erosion base (i.e. at the position of the Sissle outlet) after one million years (Fig. 6-32d). JO would need to rely on the preservation of the additional topography situated above the local erosion base. The results of simulations of the evolution of this local topography are discussed in the next section (Section 6.4.3.2).

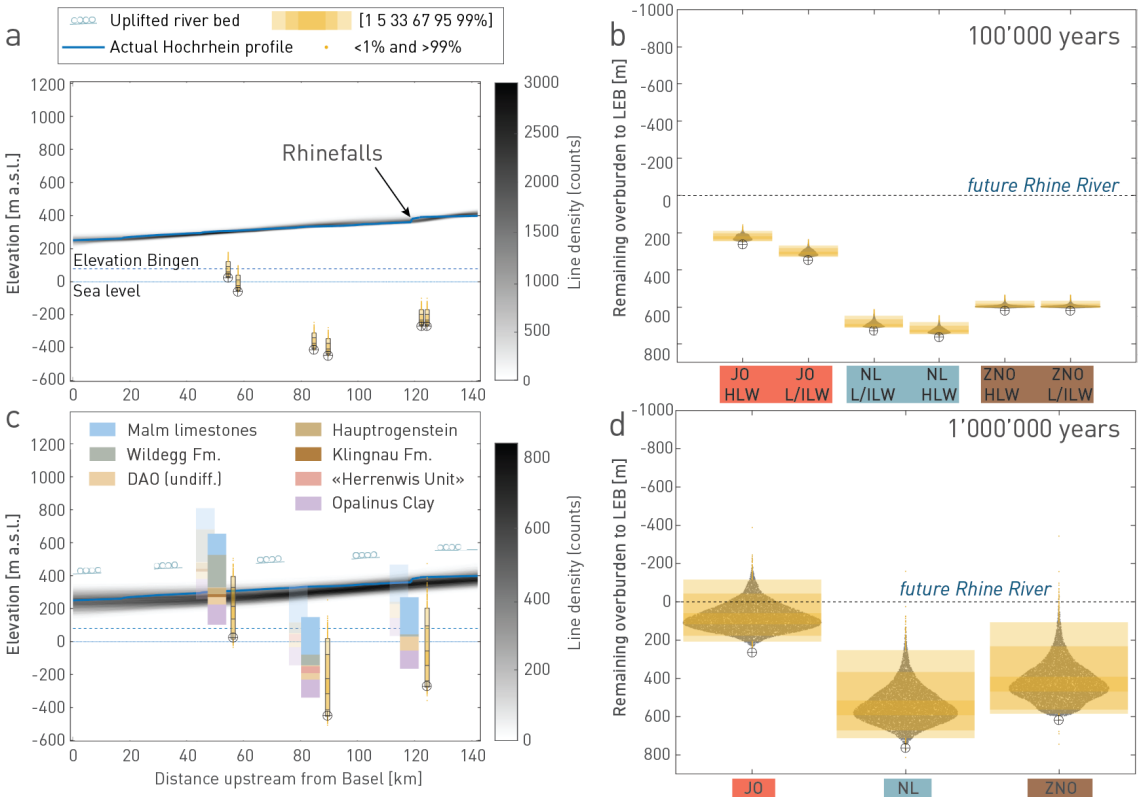


Fig. 6-32: Results of fluvial incision modelling using the Stream Power Incision Model (SPIM)

The left panel shows the realisations of future longitudinal Hochrhein profiles in grey for 100'000 years (a) and for one million years (c). Also shown are the present-day river profiles (in blue) and the elevations of Bingen and sea level as reference baselevels. The circles correspond to the depth of the provisional disposal areas at the time of emplacement. The orange boxplots above the circles describe the uncertainty distributions of the rock uplift that the disposal areas might undergo in these times. As an example, the stratigraphic columns at the locations of the provisional disposal areas are uplifted according to the median and the 95th percentile (transparent) – highlighting which units might be incised after one million years, if the Hochrhein or another main river were to flow directly across the disposal area by that time. Also shown are symbolised gravel deposits assuming they were also uplifted uniformly according to the median uplift value (and subsequently incised equally along the profile). As such, they represent the present-day riverbed that becomes remnants of a future terrace surface. The remaining overburden thickness above the repository with respect to the local erosion base is shown in the right panel for 100'000 years (b) and one million years (d). Note that these distributions are calculated for downstream positions along the Hochrhein (i.e. the Sissle confluence for JO, the Aare confluence for NL, and the Thur confluence for ZNO, see Fig. 6-29). DAO: Dogger Group above Opalinus Clay.

6.4.3.2 Future evolution of local topography

Local topography considers bedrock and unconsolidated sediments above the local erosion base. Because the characteristics of local topography vary between the sites, it is important to evaluate under what circumstances such additional overburden thickness can counterbalance potential disadvantages of a shallower site with respect to the local erosion base (Section 6.4.3.1).

It is likely that erosion rates will always be unevenly distributed in a cuesta landscape of alternating highly erodible and less erodible strata as in Northern Switzerland, and that the landscape will remain in disequilibrium (e.g. Forte et al. 2016, Perne et al. 2017, Yanites et al. 2017, Darling et al. 2020). The most resistant units can have both the steepest (cliff forms) and shallowest (plateau) gradients, and, locally, transient erosion rates can vary greatly and in either direction from the controlling rate of the main channel. Such processes render a forecast of the topographic evolution difficult.

Modelling the evolution of future local topography

The evolution of local topography was modelled with the landscape evolution model MuddPILE (Mudd et al. 2022) in a simplified approach using the SPIM equations described in Section 6.4.3.1. In an upstream working process, these equations are solved until the topography reaches equilibrium ("snap-to-steady"), i.e. the elevations stop changing, and until drainage divides no longer migrate (Graf 2022, Nagra 2024k).

The main input considers the SPIM-based modelled incision rates of the Rhine River and the total assumed probabilities of the erodibility coefficient K from Section 6.4.3.1 (Fig. 6-29, Model B). Lateral changes in the main drainage network (Fig. 6-34) were varied and incorporated as selected scenarios that were ranked based on expert judgement. Moreover, reference hillslope angles for the respective lithologies were determined based on the median values of associated lithostratigraphic units in Ludwig (2018), as they were considered to be a representative measure of hillslope relief observed in the present-day landscape. As an example, Fig. 6-33 shows the histograms and corresponding median values of hillslope gradients for the contrasting Villigen Formation and the Opalinus Clay.

Because the modelling approach is computationally intensive, a surrogate model (Nagra 2024k) was generated to allow all possible parameter combinations to be tested and to calculate a probabilistic distribution of remaining overburden thickness at the location of the provisional disposal area. Accordingly, the remaining overburden thickness was calculated for the future scenarios of local topography in all three siting regions, using the present-day drainage networks and a selection of parameter combinations (Fig. 6-35 and Fig. 6-36). Additionally, for JO, four alternative drainage scenarios were analysed (examples in Fig. 6-37 and Fig. 6-38). The output from surrogate model at the location of the provisional disposal areas is shown in Fig. 6-39.

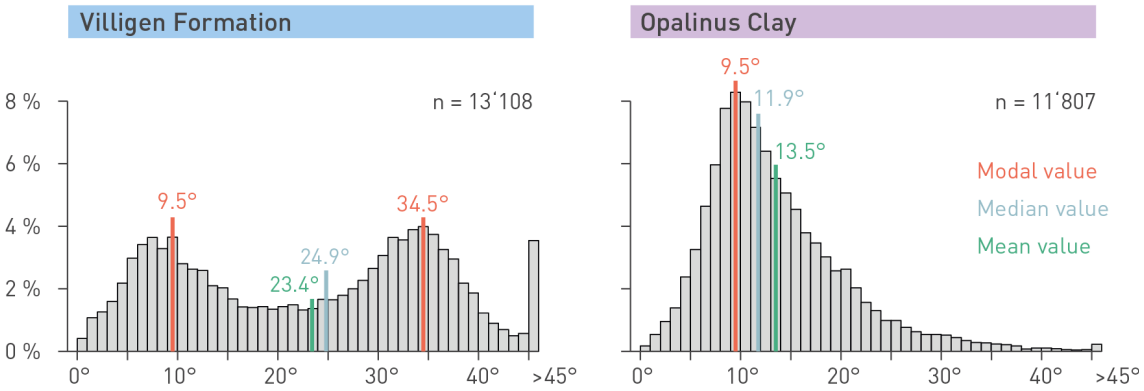


Fig. 6-33: Histogram and statistical measures of slope gradients within the hillslope domain of JO and surrounding area: two examples

The examples refer to the Villigen Formation (EC 4) and the Opalinus Clay (EC 2) (Ludwig 2018). Slope gradients correspond to pixel-based values from DTM-AV (2-m grid size; © swisstopo). Number ‘n’ indicates the number of pixels for each lithostratigraphic unit. Note that frequencies of values steeper than 45° are summarised in the histograms.

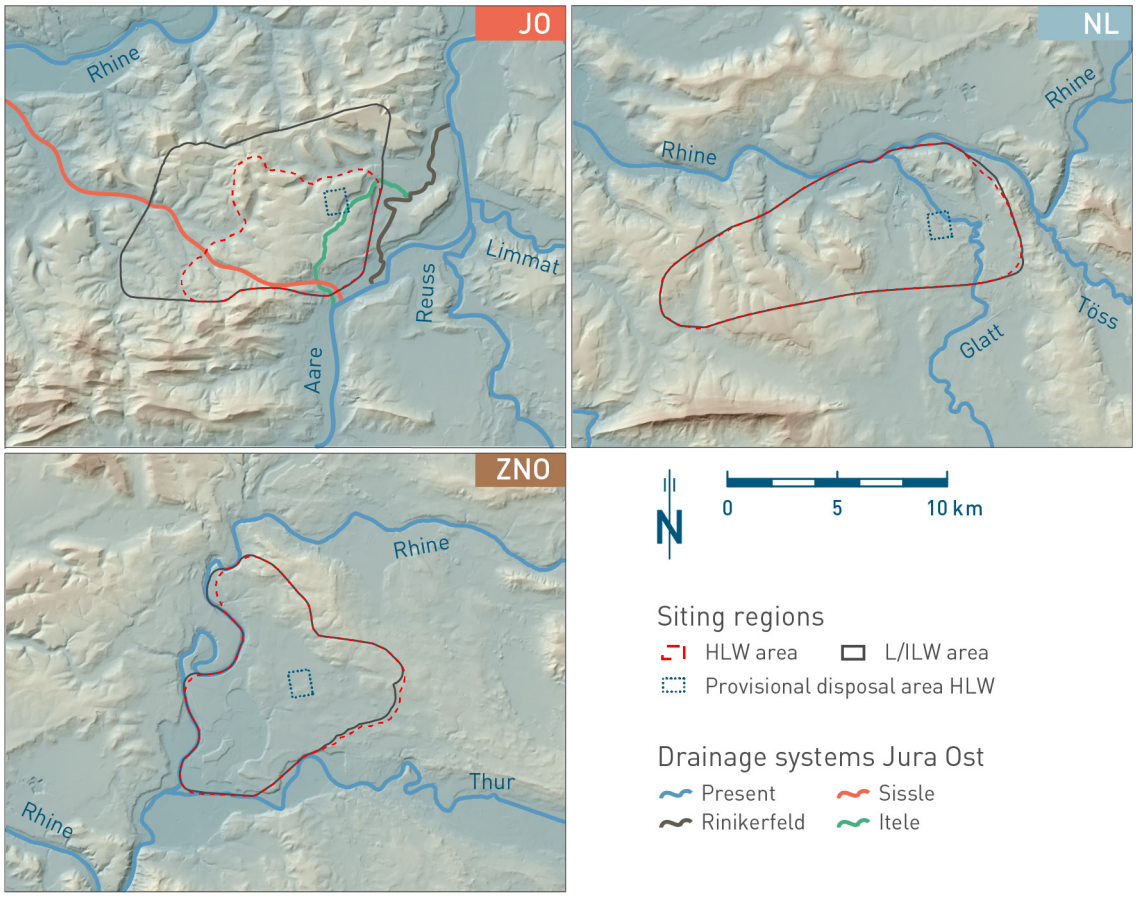


Fig. 6-34: The siting regions with present-day and alternative main drainage network scenarios

Local topography scenarios based on present-day (all sites) and alternative drainage networks (JO) are considered for the assessment of erosion in the provisional HLW disposal areas at one million years. Potential for lateral changes in drainage scenarios can be drawn from knowledge of fluvial or fluvioglacial processes and denudation.

Lateral migration and changes in main drainage

Lateral migration of the main and tributary rivers, particularly in connection with glacial processes, can lead to the formation of new drainages by cutting through bedrock relief. These processes are more likely in lower relief landscapes and under the influence of large foreland glaciations (see Fig. 6-22b in Section 6.4.1.3). However, even in areas of high local topography, corresponding scenarios cannot be excluded over long time periods and are thus considered as alternative evolutions, especially for JO (Fig. 6-34). Modelled scenarios are the reactivation of the Rinikerfeld Channel, an Aare shortcut using the Sissle drainage with and without incorporation of the Reuss and Limmat Rivers along this new route, and a breakthrough channel following the Itele Valley. Because the relief (local topography) in the relevant parts of NL and in ZNO is too low to provide meaningful alternative scenarios for modelling of future landscape evolution, a (worst-case) scenario is added that assumes a main drainage developing just above the provisional disposal area. In this case, the remaining overburden thickness is directly derived from the SPIM output of fluvial incision modelling (Section 6.4.3.1).

Modelling results

The first set of results considers a stable main drainage system (Fig. 6-35, Fig. 6-36). Such a situation may be expected in an evolution lacking major foreland glaciations. Compared to the results of remaining overburden thickness with respect to the local erosion base (Section 6.4.3.1, Fig. 6-32), the integration of local topography has a significant positive effect for JO.

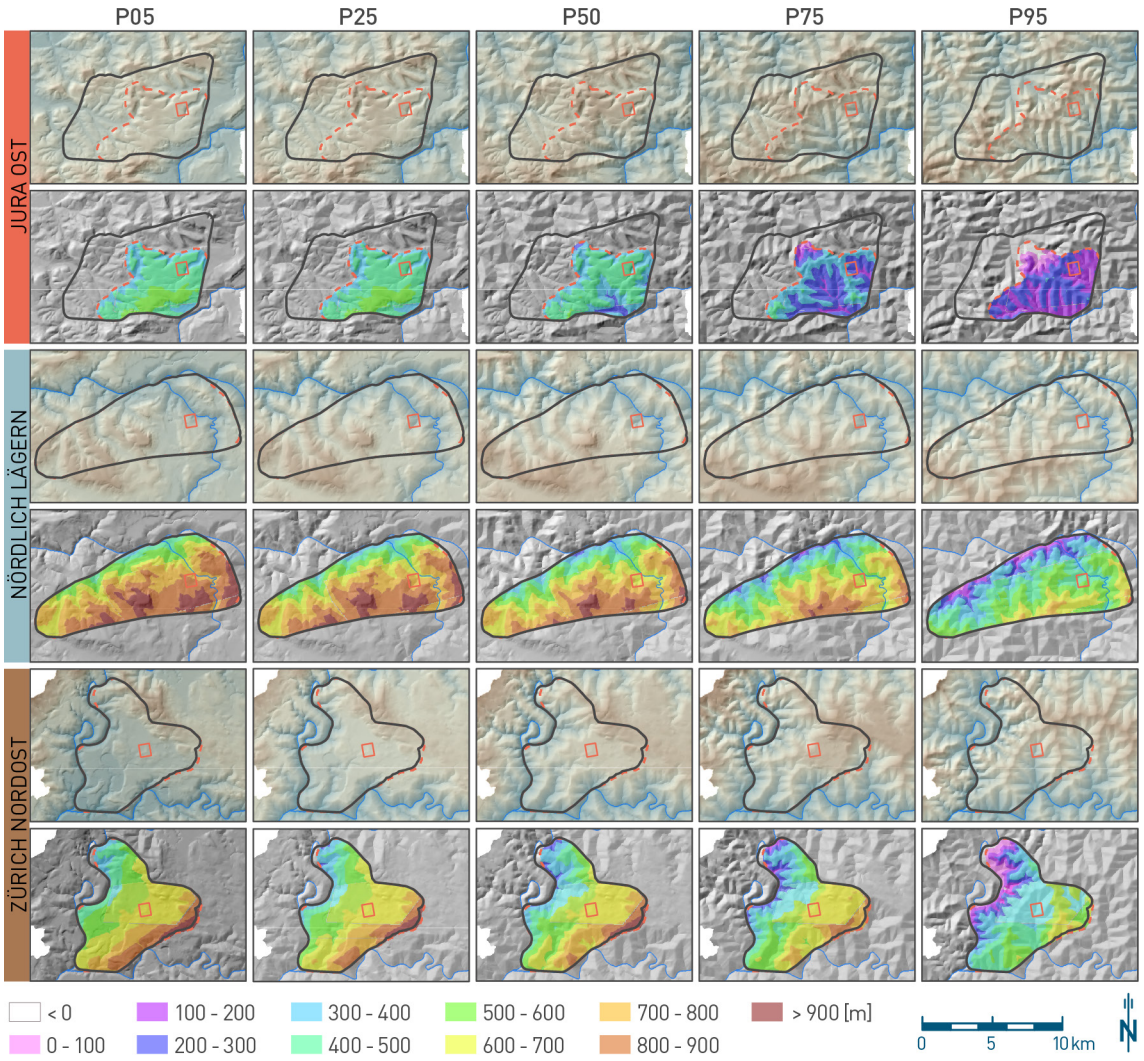


Fig. 6-35: Results of modelling the evolution of local topography at one million years using the present-day drainage network

Shown are examples of synthetic future landscapes and colour-coded remaining overburden thickness for each siting region and for certain quantiles of parameter combinations (e.g. 25th percentile of fluvial incision after one million years as derived from the SPIM modelling, combined with the 25th percentile of the erodibility distributions). Remaining overburden thickness is shown with respect to the Top Opalinus Clay. Red square shows the location of the provisional HLW disposal area.

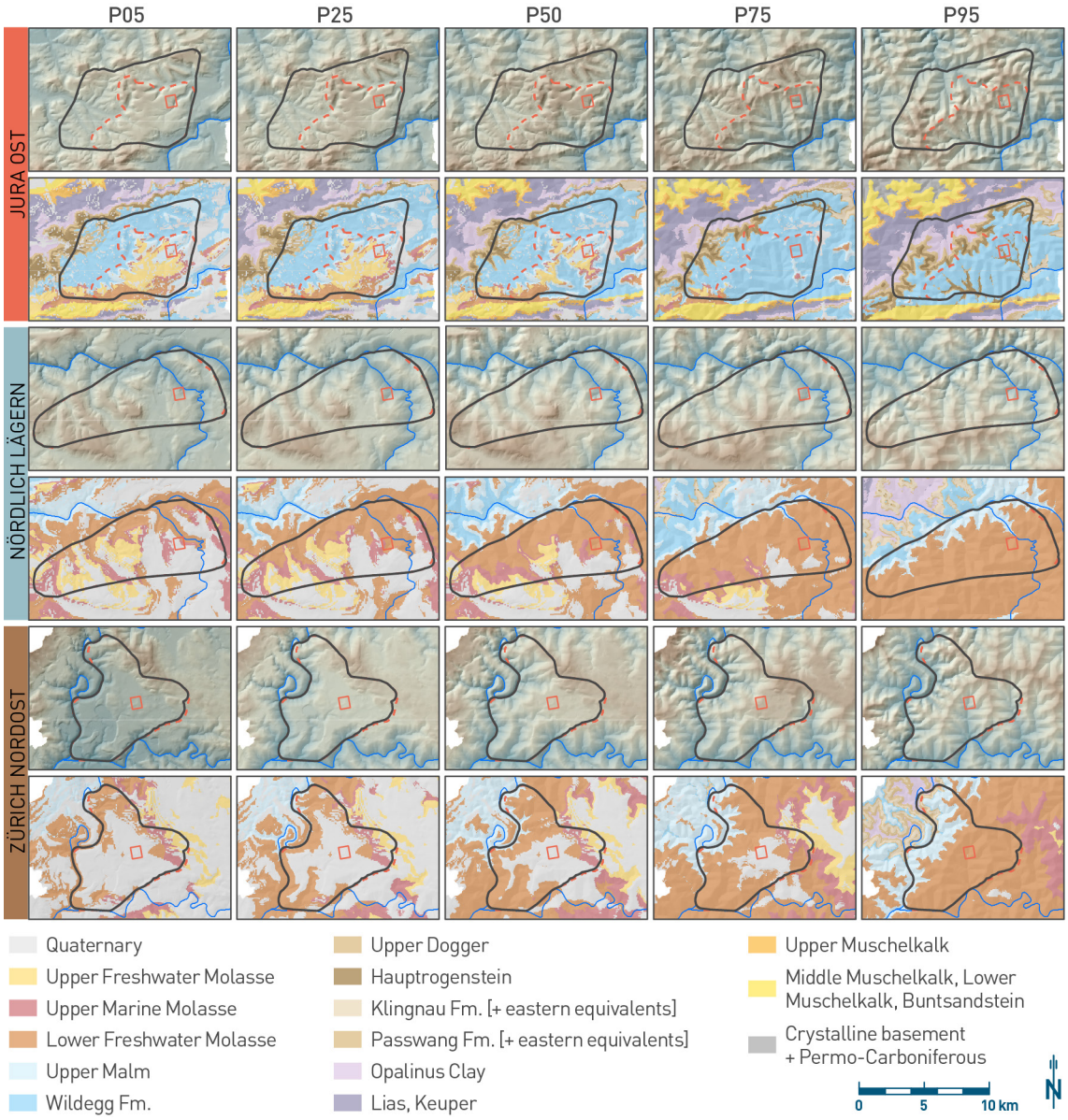


Fig. 6-36: Outcrop maps representing the evolution of local topography at one million years using the present-day drainage network

Shown are examples of synthetic future landscapes and colour-coded geological outcrop maps for each siting region and for certain quantiles of parameter combinations (e.g. 25th percentile of fluvial incision after one million years as derived from the SPIM modelling, combined with the 25th percentile of the erodibility distributions). The outcrop map is based on the Regional 3D Geological Model 2012 (Gmünder et al. 2013) used within MuddPILE. Red square shows the location of the provisional HLW disposal area.

In a second step, changes in the main drainage routing in JO (Fig. 6-34), which might be linked to future foreland glaciations, have been evaluated (Fig. 6-37 and Fig. 6-38). When including these alternative drainage networks, it can be seen that the Itele scenario in particular modifies the topography above the provisional disposal area in JO significantly and reduces the remaining overburden thickness considerably (Fig. 6-37). The probability of occurrence of this scenario, however, is low and depends on the development of a large foreland glaciation (Nagra 2024k).

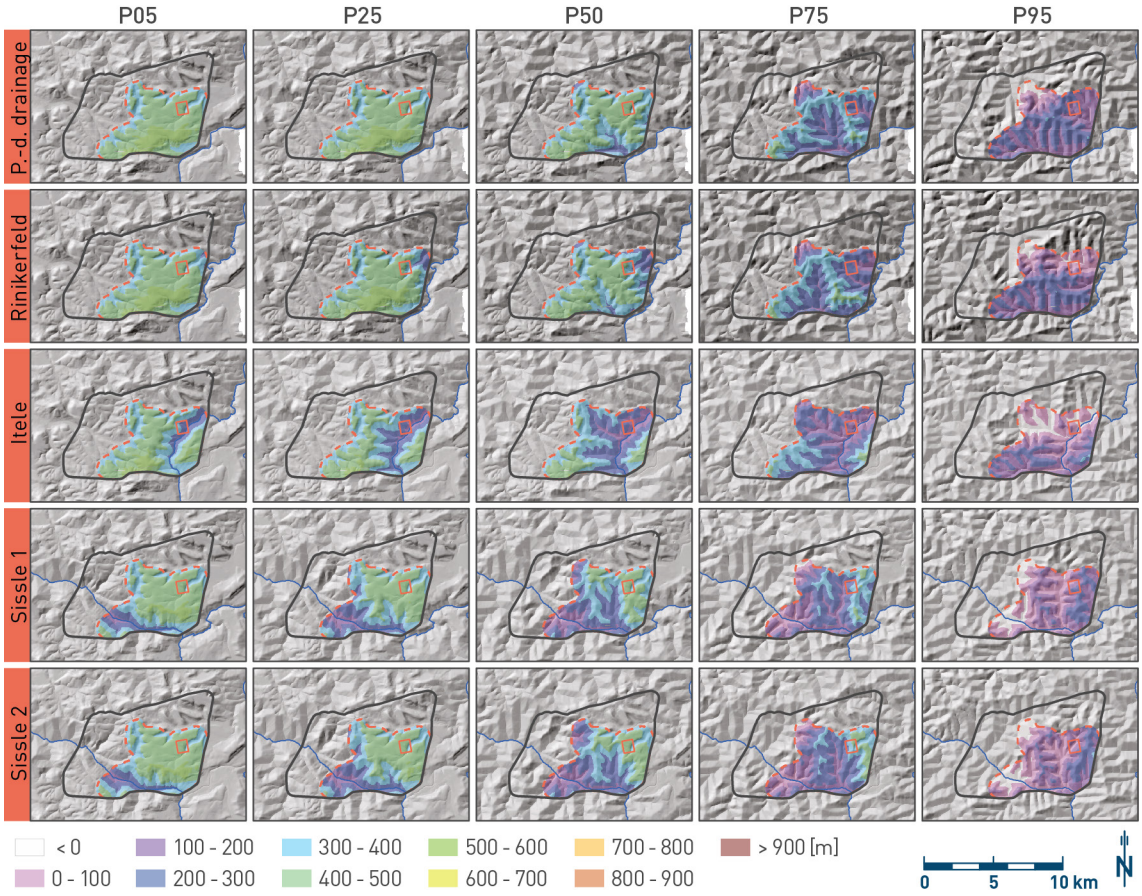


Fig. 6-37: Results of modelling the evolution of local topography at one million years using alternative drainage networks for JO

Shown are examples of synthetic future landscapes and colour-coded remaining overburden thickness for certain quantiles of parameter combinations (e.g. 25th percentile of fluvial incision after one million years as derived from the SPIM modelling, combined with the 25th percentile of the erodibility distributions) for the present-day main drainage network (upper panel) and alternative drainage networks (reactivation of the Rinikerfeld channel, break-through channel through the Itele Valley, a shortcut of the Aare through the Sissle Valley with [Sissle 1] and without [Sissle 2] diversion of Limmat and Reuss). Remaining overburden thickness is shown with respect to the Top Opalinus Clay. Red square shows the location of the provisional HLW disposal area.

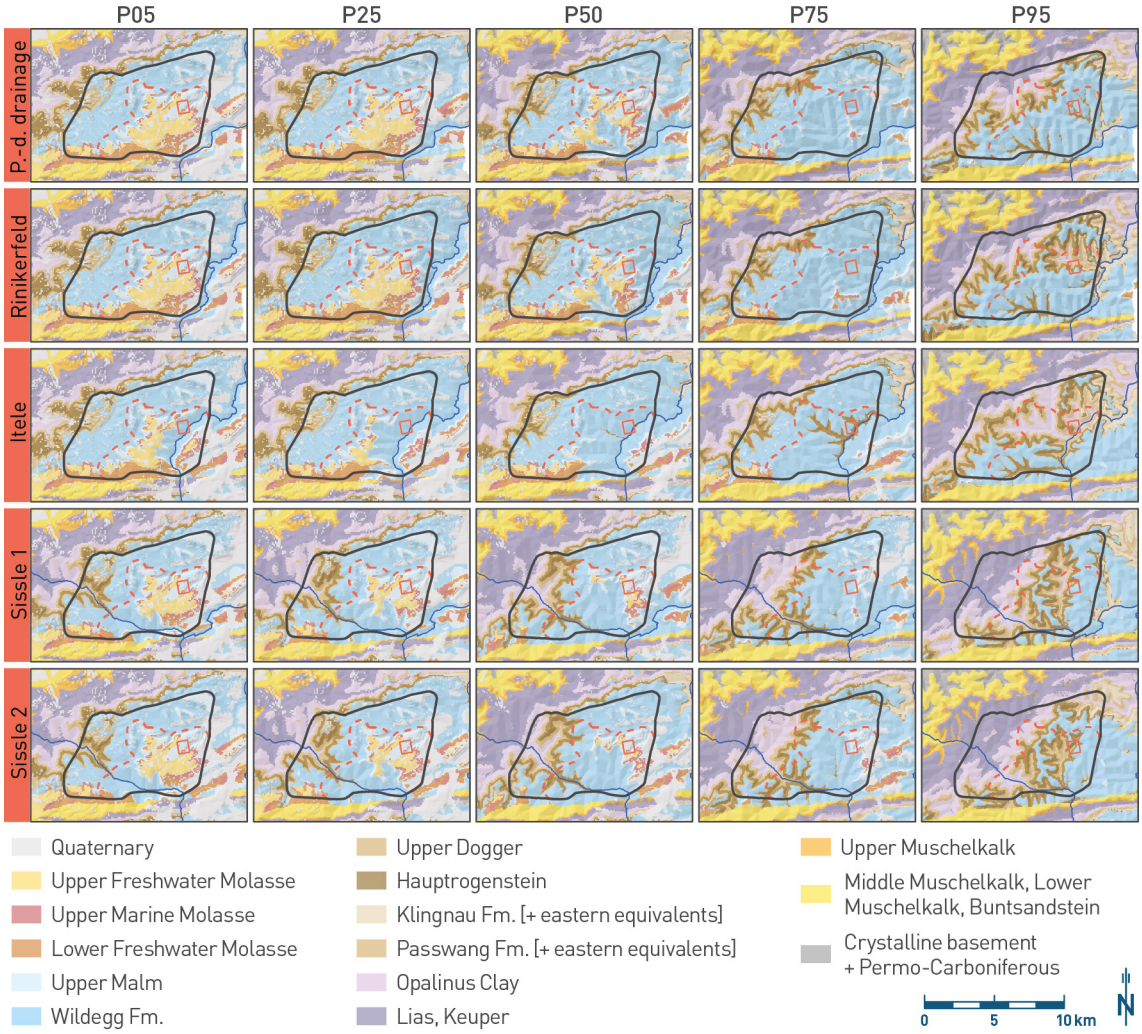


Fig. 6-38: Outcrop maps representing the evolution of local topography at one million years using alternative drainage networks for JO

Shown are examples of synthetic future landscapes overlain by colour-coded geological outcrop maps for certain quantiles of parameter combinations (e.g. 25th percentile of fluvial incision after one million years as derived from the SPIM modelling, combined with the 25th percentile of the erodibility distributions) for the present-day main drainage network and alternative drainage networks (reactivation of the Rinikerfeld Channel, breakthrough channel through the Itele Valley, a shortcut of the Aare through the Sissle Valley with [Sissle 1] and without [Sissle 2] diversion of Limmat and Reuss). The outcrop map is based on the Regional 3D Geological Model 2012 (Gmünder et al. 2013) used within MuddPILE. Red square shows the location of the provisional HLW disposal area.

The actual overburden assessment of the provisional disposal areas with respect to local topography uses the probability distribution of remaining overburden thickness provided by the surrogate model (see above, and Nagra 2024k). Results are shown in Fig. 6-39 for the local topography scenarios in each siting region based on (a) preservation of the present-day drainage network, and (b) including alternative drainage networks. For JO, the latter combines the results for the present-day and alternative drainage networks, as weighted by the expected probability of occurrence (Nagra 2024k). For JO, including local topography in both (a) and (b) has a significant positive effect as compared to accounting for the LEB only (Fig. 6-32).

For NL and ZNO, alternative drainage networks are assessed based directly on the output of the SPIM model (Section 6.4.3.1), reflecting the probability distribution of the future LEB. For NL, results in (a) and (b), i.e. accounting for local topography vs. for LEB only, are quite similar. The reason is the proximity of the NL provisional disposal area to the present-day main drainage system (defining the LEB), in this case represented by the Glatt River (Fig. 6-34). Accordingly, less local topography develops at the specific location in the case of a stable main drainage network. In contrast, ZNO shows a higher median value of remaining overburden thickness assuming the present-day drainage compared to NL (Fig. 6-39a), as its provisional disposal area is more distant to the present-day main rivers. Remaining overburden thickness (including the median), however, is largest in NL among the three sites when including alternative drainages (Fig. 6-39b). Given the low present-day relief in the eastern part of NL and ZNO, this represents a valid case to compare the two sites with respect to the evolution of local topography. The results are incorporated in the combined assessment of glacial and non-glacial erosion in Section 6.4.4.

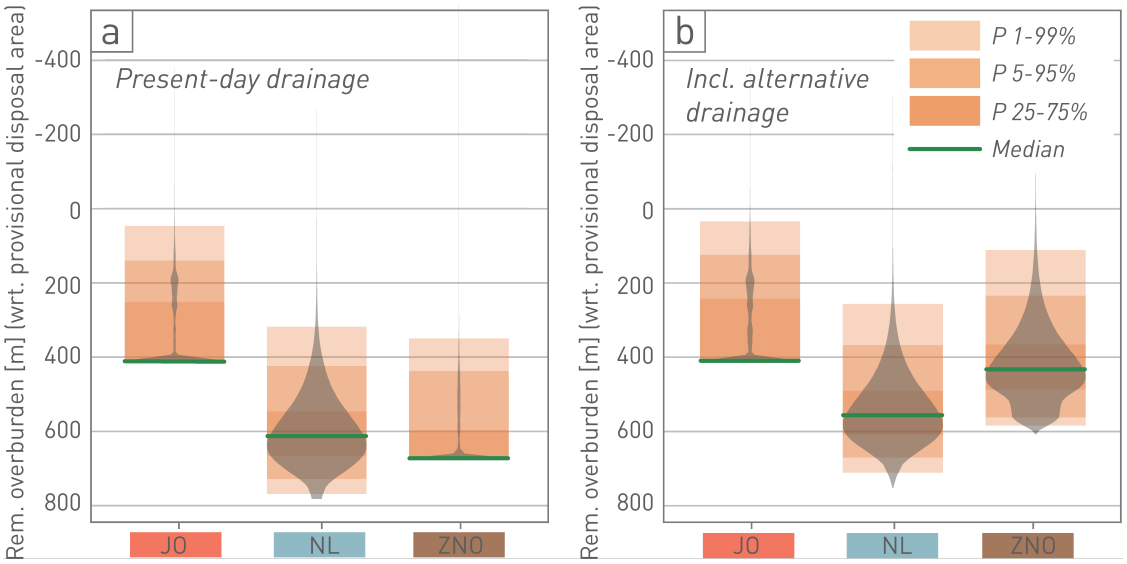


Fig. 6-39: Distributions of remaining overburden thickness after one million years including local topography for JO

Violin plots and boxes with selected percentiles of remaining overburden thickness at the location of the provisional disposal areas (see caption of Fig. 6-32 for explanation). (a) Distributions with respect to the evolution of local topography, assuming preservation of the present-day drainage network (i.e. main rivers remain laterally at the same position as today (Fig. 6-34). Including local topography has a significant effect, especially for JO, if compared to the distribution shown in Fig. 6-32d. Distributions for JO and ZNO "converge" at the value of the present-day overburden thickness, because of a modelling step that "caps" the model elevation as a function of the present-day terrain surface (further details in Nagra 2024f). (b) Several plausible alternative drainage scenarios were tested for JO (Fig. 6-34). A respective weighting by the probability of occurrence of the present-day and alternative drainage scenarios is incorporated into the uncertainty estimates for the evolution of local topography in JO. In NL and ZNO, scenarios for alternative drainage networks cannot be reasonably derived because of the low relief. Distributions are calculated using the (worst case) assumption of a main river positioned at the repository location (corresponding to direct output from the SPIM modelling, Fig. 6-32d).

6.4.3.3 Future deep glacial erosion

For future deep glacial erosion to affect the geological barrier of a deep geological repository, a series of events must occur. First, a future glaciation has to cover the siting region. Second, the eroded overdeepening must be deep enough to reach the level of the disposal area. This depth is a combination of the future local erosion base, the size and erosion potential of the glaciation, and the incised rock type. Third, the overdeepening must incise at the location of the future repository.

Unlike the simulation of the future local erosion base and local topography, the assessment of deep glacial erosion did not include numerical process modelling. Instead, a chain of calculations using expert knowledge-based parameter distributions link the above outlined aspects of depth, location, and erodibility. These will be summarised in the following paragraphs. For more information see Nagra (2024k).

Key glaciations and future climate

The specific extents of the known principal Quaternary glacials Birrfeld (including LGM), Beringen (probably MIS 6), and Möhlin (probably MIS 12/16) were used as key glacial stages in the future assessment of erosion with respect to the three siting regions (Fig. 6-18d, Fig. 6-24, Sections 6.3.1 and 6.4.1.4). The comparison of their respective ice extents with the locations of the siting regions suggests that JO will only be covered by a future glaciation of Möhlin-size, whereas NL would be affected by Möhlin- and Beringen-size glaciers, and ZNO would be affected by glaciers that would correspond to the size of all three principal glaciations. For a full assessment it is also considered that a foreland glaciation might occur, but it is smaller than LGM, i.e. in this context smaller than reaching ZNO. Such a glaciation will not have any impact on the estimated deep glacial erosion. The concept of key glacials was used to (1) estimate the probability of occurrence of alternative drainage scenarios (see Section 6.4.3.2) conditional on the occurrence of a key glacial; (2) to estimate the overdeepening depth for each of the key glacials; and (3) to estimate the probability of occurrence of future glaciations with similar extents as the key glacials over a time span of one million years. The Quaternary glaciation history of Northern Switzerland and the model results estimating ice volume in the next one million years (Talento & Ganopolski 2021; see Fig. 6-17 in Section 6.3.3.1) served as guidance for the latter argumentation.

According to Figure 19 in Preusser et al. 2011, there may have been four larger ice advances of "key glacial" size (1× Möhlin-size, 1× Beringen-size, 2× LGM-size [Habsburg and LGM]), see also Section 3.5. Earlier glaciations did reach the foreland, as rarely indicated by intercalated till within Deckenschotter deposits. It seems, however, that the above-mentioned four larger glaciations took place only after the accumulation of the TDS and probably after (or associated with) the Mid-Pleistocene Transition (MPT), when glacial cyclicity switched from a dominant 41-kyr to a 100-kyr cycle (Section 6.3.1). The ages of the Möhlin and Beringen Glacials are not unambiguously resolved, but the Möhlin Glacial is tentatively assigned to MIS 16 or MIS 12 and the Beringen Glacial to MIS 6 (see Section 3.5). Because of the age uncertainty and general poor preservation of continuous geomorphic markers for the Möhlin ice extent, it cannot be excluded that the ice advanced far to this position during both, MIS 16 and MIS 12 times. Many of the overdeepened throughs observed in the external Swiss Alpine Foreland are thought to be associated with these abovementioned large glaciations (Section 6.4.1.4). In summary, this suggests that the overdeepenings observed in Northern Switzerland are the cumulative result of recurrent processes that have affected Northern Switzerland during the past ~ 800 kyr or more, which corresponds roughly to the time frame to be assessed for the future. Accordingly, the observed overdeepening depth could be considered an "implicit stack", i.e. overdeepening depth at one million years may similarly reflect the cumulative result of multiple foreland glaciations. Because the depth distribution is placed below the future local erosion base, the most influential

overdeepening with respect to its potential to erode down to the repository level, is one that occurs late (when the local erosion base is already lowered significantly), and which stems from a large glaciation with high glacial erosion potential (see Nagra 2024k for more details).

Because of continuous erosional downcutting and subsequent decrease of the accumulation area of future glaciers, future foreland glaciations may be smaller even with similar climate forcing (Egholm 2022).

Overdeepening depth and dependence on rock type

The glacially eroded Molasse assemblage in Northern Switzerland comprises a variety of different, yet mostly easily erodible rock types. Because most of the observed glacial overdeepenings were carved into Molasse rocks (Section 6.4.1.4), these strata were considered as the base unit, when evaluating the potential depth of future overdeepenings. For each key glacial to be considered per site, a reference (i.e. for Molasse rocks) depth distribution for future glacial overdeepening occurring within each HLW perimeter, respectively was established during SHELF-based workshops (Fig. 6-40; see Nagra 2024k for detailed distributions and discussion).

The main evidence used to estimate the uncertainty of future glacial overdeepenings is based on the statistics of observations in Northern Switzerland, supported by global observations (Nagra 2024k). In this context, it is important to note that for instance the overdeepening depth drilled in the Nagra boreholes is contained within the total assumed probability but may correspond to a less likely percentile (Fig. 6-40; e.g. QHST in NL would be near the 70% percentile of the assessed probabilities for a future Beringen or Möhlin key glacial). These boreholes were explicitly located to drill the deepest parts, while the majority of the glacial overdeepenings in the distal foreland is shallower (e.g. Section 6.4.1.4, Fig. 6-24, Fig. 6-25, Fig. 6-26, Fig. 6-28, see Nagra 2024k for more statistics). The width of the total assumed probabilities allows no overdeepening at all on the lower bound and a depth similar to the exceptionally deep Bodensee Trough on the upper bound (Fig. 6-40). Such large depths, however, are considered very unlikely.

The assumed total probabilities of reference overdeepening depth for Möhlin and Beringen key glacials in NL and ZNO closely resemble each other but for a slight shift towards larger depth for future Möhlin-size glacials. The argumentation here is based on the remaining age uncertainty with respect to the sediment fill of the overdeepenings and thus the preceding glacial erosion event. In addition, the close proximity of similarly sized troughs, which may reflect different glacials (e.g. Strassberg Through [presumably Möhlin erosion] next to the Bülach Trough [presumably Beringen erosion] in the lower Glatt Valley or Marthalen Through [presumably Möhlin erosion] next to the Andelfingen Trough [presumably Beringen erosion] in the lower Thur Valley; Fig. 6-26b and c; Buechi et al. 2024) does not allow a clear distinction between the erosional efficiency of Beringen and Möhlin Glacials. The limited bedrock incision of an LGM-size glacial is also reflected in the total assumed probabilities but allowing also deeper values with less likely occurrence, because of the observation of glacial erosion during the similarly sized Habsburg Glacial in the Birrfeld Trough (Section 6.4.1.4).

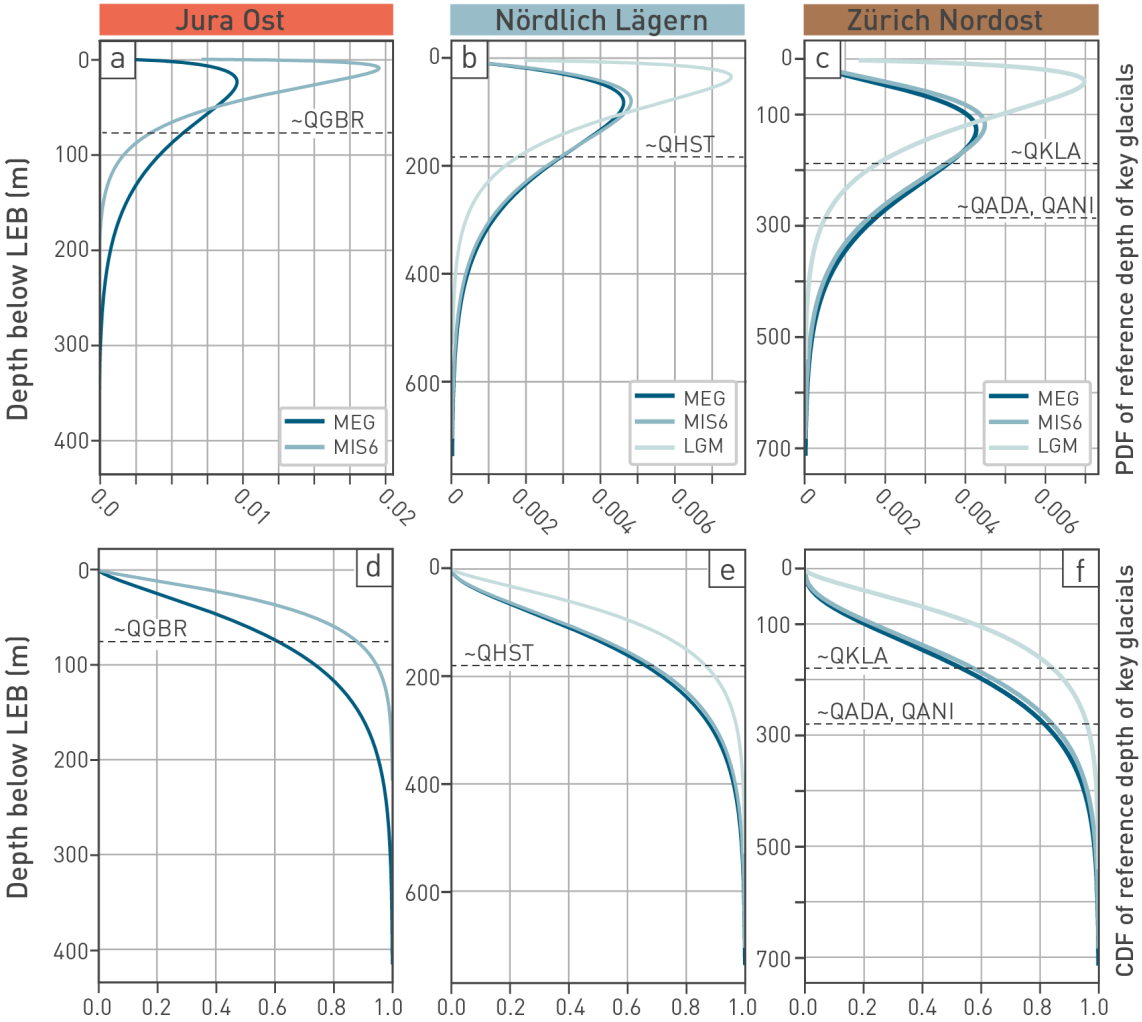


Fig. 6-40: Total assumed probabilities for reference overdeepening depth per key-size glaciation

Total assumed probabilities for reference depth distributions (Molasse) for each site and the respective key glacial. Note that MIS 6 refers to the Beringen glaciation and MEG to Möhlin. Figures in the upper panel show the probability density function (PDF), those in the lower panel show the respective cumulative distribution function (CDF) for Jura Ost (left), Nördlich Lägern (centre), and Zürich Nordost (right). Horizontal dashed lines correspond to the approximate depths (below LEB) of Quaternary boreholes that Nagra drilled within the wider areas of the siting regions (Section 6.4.1.4). QGBR: Gebenstorf-Brüel borehole is located within the lower Aare Valley but not within the HLW area of JO. QHST: Hochfelden-Strassberg borehole is located in the southernmost part of NL. QKLA: Kleinandelfingen-Laubhau borehole is located in the southernmost part of the ZNO-HLW area. QADA: Adlikon-Dätwil borehole is located in the south, just outside of the ZNO-HLW area. QANI: Andelfingen-Niederfeld borehole is also located in the south, just outside of the ZNO-HLW area (for references, see Tab. 2-2).

Because observations show that overdeepenings tend to incise into easily erodible rocks, if they are not additionally restricted by topography (see Section 6.4.1.4), and are less deep within more resistant rocks in such cases, a scaling was introduced leading to a stretching or shortening of the reference depth distribution if incision reaches a different rock type. Accordingly, the erodibility classes were scaled with respect to the Molasse assemblage (Fig. 6-41). For example, rock types that are part of EC 4 (e.g. Malm limestones) were considered on average only half as erodible as Molasse-type rocks.

Nevertheless, even if less likely, certain conditions might occur where resistance to erosion per class differs from the bulk of the material. The consideration of such possibilities is visible in the overlaps between the probability density functions (PDF; Fig. 6-41a, see Nagra 2024k for more detail).

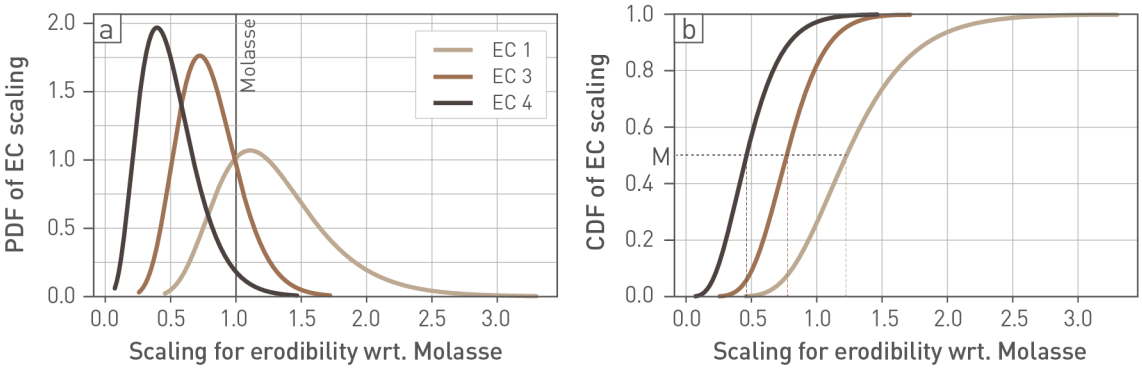


Fig. 6-41: Total assumed probabilities of erodibility scaling with respect to the Molasse of Northern Switzerland

The sediments of the Molasse assemblage of Northern Switzerland with their variety were considered as the base unit with the scaling value of 1.0 (labelled in a). Molasse sediments are in erodibility class (EC 2). Accordingly, rock types in EC 1 are generally easier to erode, and rocks in EC 3 and EC 4 are harder to erode. Probability (a) and cumulative distribution function (b) are based on expert judgement under the prerequisite that the median values (M, labelled in b) follow the assumption of M(EC 1) > M(EC 2 [equals Molasse]) > M(EC 3) > M(EC 4).

By taking the rock types at a certain overdeepened point into account and by scaling the reference depth of incision based on these rock types, the distribution for the actual depth of overdeepening at that point can be evaluated. Note that this distribution is conditional on glacial overdeepening occurring at the selected point (and conditional on a specific LEB). For evaluating the unconditional probability of repository excavation due to glaciation, additionally, the probability of future glaciation events, the spatial occurrence of glacial overdeepening and the actual over-deepened area must be taken into account (see next subsection). The full stepwise procedure to evaluate probabilities of incision (fluvial and deep glacial) at a certain point is illustrated in Fig. 6-42.

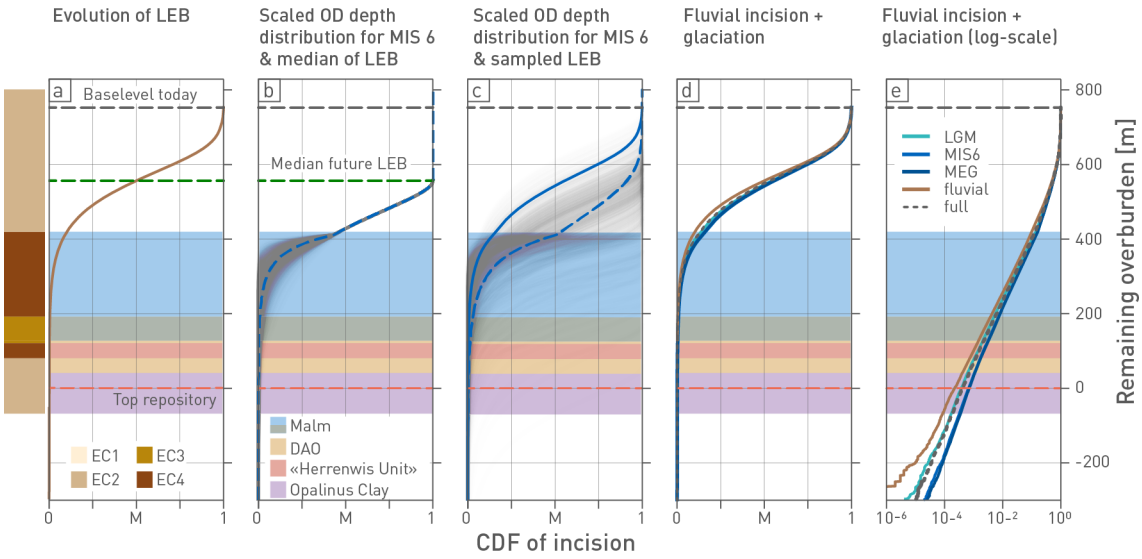


Fig. 6-42: Step-wise illustration of procedure to evaluate the probabilities of fluvial and deep glacial erosion at a certain point

The illustration represents a step-wise visualisation of the probabilistic approach for the example of NL and the timing of one million year. The stratigraphic column below the Molasse is shown in all subfigures. The (colour-coded) associated erodibility classes are visible on the left. (a) Cumulative distribution function (CDF) of the future local erosion base (LEB, dashed green line shows median value). (b) Scaled depth distribution (CDF), exemplarily shown for a future MIS 6 (Beringen-size) glaciation linked to the median of the future LEB (dashed green line), derived by scaling the reference depth distribution (dashed blue CDF) with different sets of scaling factors sampled from their distributions (Fig. 6-41). The variability resulting from the scaling starts at the depth of the stratigraphic step between Molasse rocks and rocks of EC4 (grey lines). Note that this is a subset of the full samples and plotted only for illustration purposes. (c) Scaled depth distributions (grey CDF) for different samples of the future LEB (blue solid CDF). The blue dashed line corresponds to the resulting CDF conditional on the glaciation and the occurrence of an overdeepening (OD) scenario at the location of the provisional disposal area. It does not involve the condition of an actual OD at the location[18]. This distribution is calculated conditional on the occurrence of a glaciation comparable to the one during MIS 6. (d) Probability of incision (fluvial and glacial) for a certain remaining overburden thickness, including all key glacials with their probabilities of causing overdeepening within the provisional disposal area. The process termed fluvial erosion ('fluvial') describes the case of no glacial OD, e.g. for glaciations of a size smaller than during the LGM and corresponds to the distribution of the future LEB. (e) For better visibility, the incision probability (same as in d) is illustrated in log-scale. Note that in this illustration it is assumed that glacial overdeepening occurs directly above the provisional disposal area.

[18] The probability for a point being actually overdeepened within an overdeepening scenario is below 100%. This is especially important for scenarios that allow random occurrence of new breaching channels within a relatively large area – not all of this area will be overdeepened.

Locations of future glacial overdeepenings

Besides the occurrence of a glaciation with a certain (key-size) extent and the depth of a future overdeepening, the potential location of future overdeepenings must be assessed. This is done by combining and weighting different scenarios.

The multiphase infilling history of many deep glacial troughs suggests a tendency for reoccupation of existing overdeepenings. Present overdeepenings as potentially preconditioned pathways for future reoccupation are thus one scenario. A spatial buffer around the present-day overdeepenings to account for growth in length or width and allowing a lateral shift of the axis, and thus the location of deepest erosion, can be applied. However, the potential for glacially diverted channels with new overdeepenings cannot be excluded as a scenario and this is thus integrated within the probabilistic model. Although the future topography cannot be precisely forecasted, there are certain assumptions that help in deriving such potentially additional scenarios. Topographic steering of ice through pre-existing valleys (ice is probably steered away from hills and ridges into already existing troughs and valleys; Kessler et al. 2008) is considered in the scenario building. On the contrary, the lower the relief, the more degrees of freedom or randomness need to be accounted for. This is especially important for ZNO but also the eastern part of NL, where the present relief is low. A set of plausible scenarios for each site was ranked during SHELF-based workshops, which in turn provided the input for scenario maps (Fig. 6-43, see Nagra 2024k for more details). The darker the colour in these maps appears, the more likely a certain scenario becomes. Calculations of remaining overburden thickness that incorporate the influence of overdeepening locations are shown in Section 6.4.4.

Finally, it is important to note that while the coloured parts of the maps highlight where overdeepening might plausibly occur, the actual dimension of the overdeepenings within such a zone is significantly smaller (compare the present-day occurrences in Fig. 6-24). For instance, ~ 5% of the NL siting region and less than 18% in ZNO are actually overdeepened. Because of a narrowing of the overdeepening forms towards depth, this number decreases, if considering only deeper troughs. For instance, overdeepenings of more than 50 m below LEB constitute ~ 2% area in NL and ~ 6% area in ZNO (see Nagra 2024k for more details). Such fraction of actual overdeepening with a potential overdeepening scenario is considered in the model (see Nagra 2024k) and results in an additional reduction of overdeepening probability.

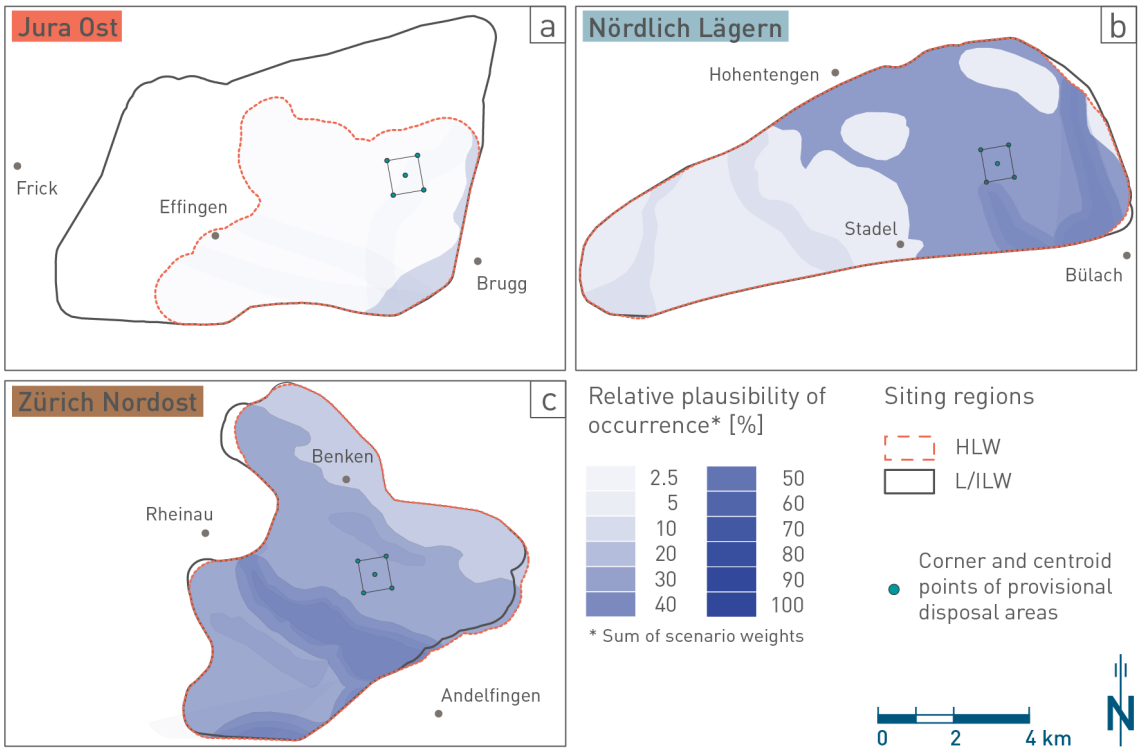


Fig. 6-43: Scenarios for spatial occurrence of future overdeepenings within the siting regions, one million years

Shown are colour-coded maps with darker colours reflecting a higher plausibility of occurrence of future glacial overdeepenings in the JO (a), NL (b) and ZNO (c) siting regions. The provisional disposal areas are shown with their respective corner and centroid points. For JO, overdeepening to occur is less likely for the next one million years. Here, the generally less likely occurrence of overdeepening is strongly linked to the (alternative) drainage scenarios (see Section 6.4.3.2).

6.4.4 Remaining overburden thickness and potential for repository excavation

This section presents the combined results of the erosion assessment for a 1-million-year time frame. Discussed are the remaining overburden thickness for the expected geological evolution as well as the probability of combined glacial and non-glacial repository excavation. The example below considers the full range of uncertainties as elicited for the locations and depth of the provisional HLW disposal areas over the period of one million years. Of this full range of uncertainties, the 5 – 95% range is considered as "expected range" of future evolutions. In Nagra (2024k), additional calculations are shown for subsets of scenarios that feed into site comparison (site comparison criteria 2.2. and 3.3; Nagra 2024t).

Fig. 6-44 shows the total probabilities of remaining overburden thickness distributions after one million years. Remaining overburden thickness is calculated in a Monte-Carlo approach using one million samples (Section 6.4.2.3, Fig. 6-29) and is provided with respect to the respective provisional disposal areas (i.e. the worst case of their four corner- and one midpoint[19]). The respective probabilities to incise to the depth of the provisional disposal areas are deduced from the Monte Carlo samples. Fig. 6-44 is tripartite for better accessibility: the upper panel provides probability density functions (PDF), from which the most likely scenarios can be deduced (bulk of the curves, highlighted by the vertical arrows). The middle panel shows the same distributions as cumulative distribution function (CDF). The shaded areas represent the 5 – 95% probability (x-axis) and associated overburden thickness amounts (y-axis), which are considered here as "expected range" of future evolutions. Very low probabilities are not distinguished in the upper and middle panels. Therefore, the lower panel shows the CDF in log-space. The intercept with the position of the provisional disposal area (red dashed line) reveals the probability of excavation.

The most likely scenarios show at least ~ 400 m of remaining overburden thickness above the repository after one million years at all sites (vertical arrows in Fig. 6-44a). In NL, nearly 600 m of overburden thickness is likely to be preserved. At the 5 – 95% probability range, between ~ 125 and 410 m of overburden thickness might be expected in JO, between ~ 350 and 670 m in NL and between ~ 220 and 560 m in ZNO (shaded area and vertical arrows in Fig. 6-44b). Considering the required 200 m of overburden thickness for efficient self-sealing (Section 5.7), the JO site (i.e. at the position of the provisional disposal area) shows more limitations within this range than the other sites. However, suitable conditions in JO are available in the immediate surroundings of this provisional disposal area (Nagra 2024k), such that JO can also reliably provide sufficient overburden thickness to secure the barrier function over the period under consideration.

Excavation of the repository within one million years was estimated to be highly unlikely at the provisional disposal areas in all three siting regions. This fact is best seen in the log-scale visualisation of the distribution (vertical arrows in Fig. 6-44c, see grey box showing the 5 – 95% range for comparison). This likelihood is about an order of magnitude lower for the provisional disposal area in NL than in JO and ZNO. Excavation probabilities were calculated to show the robustness of the repository. A discussion on the plausibility of the corresponding results, especially considering the extreme values contained in the tails of the total probability can be found in Nagra (2024k).

Fig. 6-44 also shows the main contributor with respect to the distributions of remaining overburden thickness. Although deep glacial erosion is capable of incising strongly into the overburden, its probability to incise at the position of the repository is strongly reduced. The main contributors consequently are fluvial incision driven by rock uplift and, in case of JO, associated evolution of local topography. The present-day low relief in ZNO and in the east of NL does not

[19] Note, in the case of Model B (modelling of local topography), the remaining overburden thickness is determined by the minimum value within the entire perimeter of the provisional disposal area.

allow to reasonably consider and rank scenarios for future evolution of local topography. Instead, remaining overburden is considered with respect to the local erosion base (see Section 6.4.3.2). However, it cannot be excluded that the location of the main drainage will be shifted away from the provisional disposal area and a significant protective relief will develop in the future. Accordingly, the remaining overburden thickness might be further increased, and the probability of excavation further reduced in NL and ZNO.

Consequently, considering the three erosion processes, NL provides the best protection against future erosion.

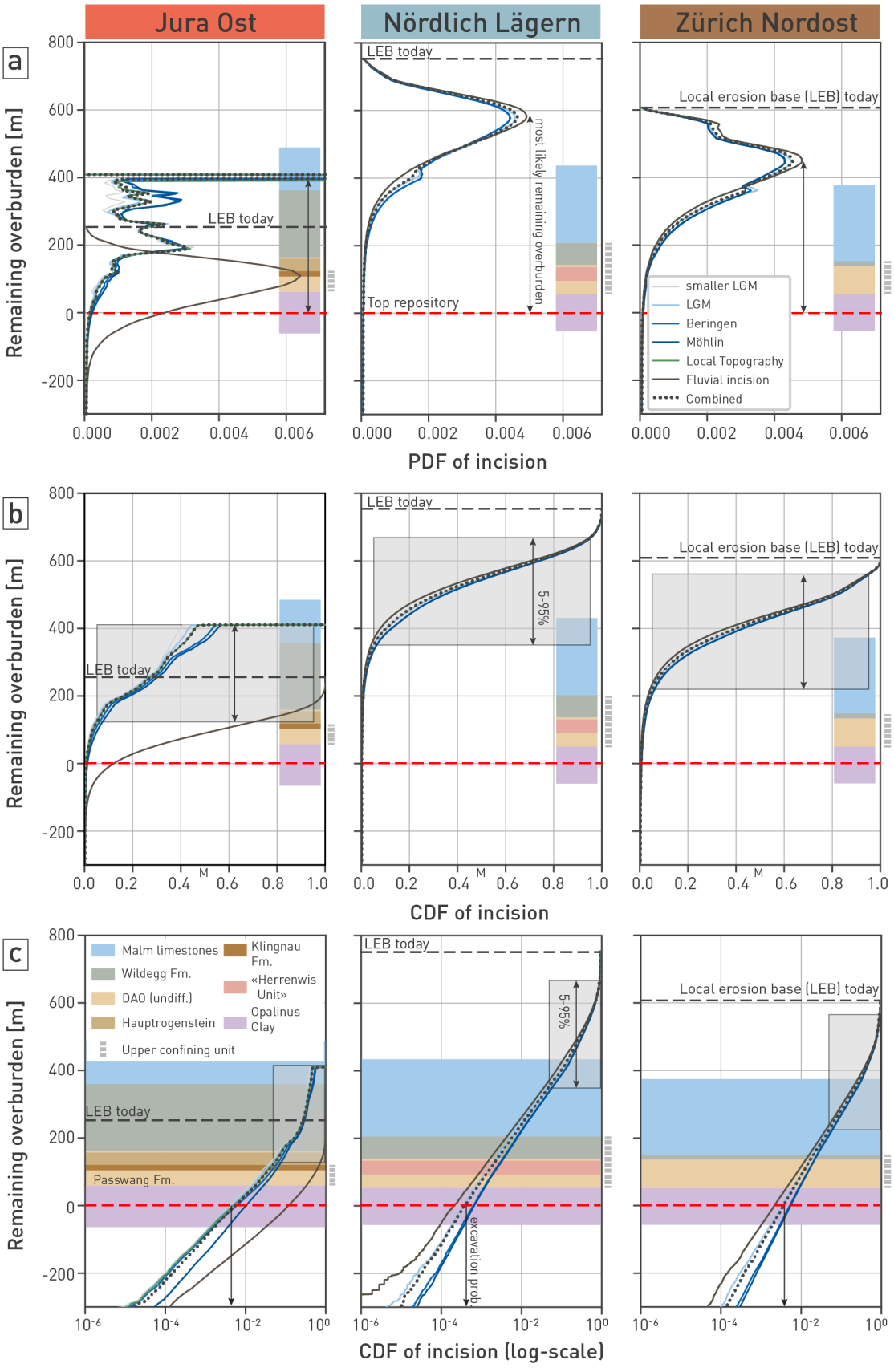

Jura Ost
Nördlich Lägern
Zürich Nordost
a
b
c
Remaining overburden [m]
LEB today
Local erosion base (LEB) today
most likely remaining overburden
Top repository
smaller LGM
LGM
Beringen
Möhlin
Local Topography
Fluvial incision
Combined
PDF of incision
5-95%
M
CDF of incision
Malm limestones
Wildegg Fm.
DAO (undiff.)
Hauptrogenstein
Klingnau Fm.
«Herrenwis Unit»
Opalinus Clay
Upper confining unit
Passwang Fm.
excavation prob.
CDF of incision (log-scale)

Fig. 6-44: Estimated probabilities of remaining overburden thickness above the provisional disposal area in the three siting regions

The same outputs are displayed in three different formats for better visualisation (a) as probability density function (PDF), (b) as cumulative distribution function (CDF), and (c) as CDF, transferred onto a logarithmic scale. Results are shown with respect to the depth and location of the provisional disposal area (red dashed line). The thick black dotted line represents the final combined probability. That is, it integrates over (i) both glacial and non-glacial processes and (ii) the occurrence of all considered key glacials. The lines "smaller LGM", "LGM", "Beringen" and "Möhlin" integrate over both glacial and non-glacial processes but are restricted to the occurrence of the specific key glacial. The line "Local Topography" integrates over all considered key glacials for determination of alternative drainage networks but is restricted to non-glacial processes (output Model B, i.e. no glacial overdeepening). The line "Fluvial incision" describes the modelled LEB (local erosion base) from Model A.

For JO, the final combined curve is a combination of the fluvial incision by main rivers (line "Fluvial incision"), evolution of local topography (including ranked scenarios) and deep glacial erosion (output Model C; conditional on the occurrence of key glacials). Local topography was not included in the case of NL and ZNO. Here, a main river (defining the local erosion base) was assumed to be located directly above the provisional disposal area (see Section 6.4.3.2). The vertical arrows in (a) highlight the most likely amount of remaining overburden thickness at the location of the provisional disposal area, in (b) the 5 – 95% range (also shaded), see M for position of median values, and in (c) the probability of excavation, which is about an order of magnitude lower in NL (see grey shaded box showing the 5 – 95% range for comparison). Simplified lithostratigraphic columns are provided with these images, allowing to visualise the incision depth. DAO: Dogger Group above Opalinus Clay. The grey dotted bar at the right of each subfigures represents the upper confining units.

6.4.5 Conclusions

Considering the erosion assessment aimed at ensuring uncompromised barrier properties during the period under consideration, the following conclusions are drawn:

- The overall knowledge about the capability, timescales, form and rate of erosion processes, and the erosion history of Northern Switzerland have been improved considerably by detailed field and laboratory work during recent years. The effects of recurring climate-driven erosion processes superposed on the low-strain domain of Northern Switzerland have been identified and analysed with respect to landscape evolution. Nevertheless, age determination and the limited availability of dated Quaternary geomorphic markers and sediments (e.g. Deckenschotter, infills of glacially overdeepened valleys) remain a challenge. Consequently, the age uncertainties of Quaternary landforms and deposits are accounted for in a systematic assessment of future erosion.
- Future erosion processes (glacial and non-glacial) are expected to be generally comparable to processes that have repeatedly influenced the area of the siting regions during the Quaternary, but they are inferred to operate at lower rates. One main argument for slower future process rates is the formation of smaller glaciers and a delay in glacial inception because of anthropogenic CO_2 emissions. In addition, analyses of the fluvial topography show that the catchment of the Rhine River will grow at the expense of the Danube catchment, thus no major pulse of drainage reorganisation will cause deep incision as the major wave of retrogressive erosion of the Rhine has already passed by the area of the three siting regions. In addition, less erodible rocks in the stratigraphic sequence below the Molasse strata are predicted to slow down erosion further.

- The assessment of future erosion was done using a robust, structured hybrid-probabilistic approach, based on available field data, rate determinations, laboratory tests and modelling, to evaluate the behaviour of the erosional system in Northern Switzerland for different future scenarios.
- A residual cover thickness of 200 m as required for maintaining the self-sealing properties of the Opalinus Clay can be shown for the most likely scenarios in all the siting regions for the period under consideration. Using the 5 – 95% range as reference, the JO site shows more limitations for such a 200 m criterion at the location of the provisional disposal area. However, suitable conditions in JO are available in the immediate surroundings of this provisional disposal area, such that JO can also reliably provide sufficient overburden thickness to secure the barrier function over the period under consideration. Nevertheless, because of the comparably small distance between the repository depth and the local erosion base, JO is dependent on the preservation of the local topography and is thus more sensitive to changes in the fluvial network compared to the other sites. The NL site is a well-suited location for the development of a repository because it is protected against future erosion from all of the principal erosion processes capable of causing deep incision by the large emplacement depth.
- Fluvial incision, driven mainly by rock uplift, dominates the modelled overburden thickness assessment on a timescale of one million years. Although deep glacial erosion can greatly increase the degree of incision, it is less likely at the sites. This is because of the low probability of glacial overdeepenings occurring at the location of the provisional disposal area, the more resistant rocks below the Molasse strata, and the longevity of elevated atmospheric CO_2 concentrations that are predicted to delay future foreland glaciations. Because of continuous erosional downcutting and subsequent decrease of the accumulation area of future glaciers, foreland glaciations might be smaller even with similar climate forcing.
- Excavation of the repository by erosion within the next one million years can be considered extremely unlikely in all the provisional disposal areas but is nearly an order of magnitude lower in NL.

6.5 Long-term hydrogeological and hydrogeochemical evolution

Key points:

- Deep flow systems are affected by large changes in morphology and / or by high subglacial water pressure. This may affect deep aquifer exfiltration paths, water fluxes and residence times, notably in the aquifers above the host rock (Malm, Hauptrogenstein).
- Robust and efficient self-sealing of reactivated faults in Opalinus Clay are maintained as long as the overburden remains > 200 m. This is the case for all sites over the next one million years in the most likely erosion scenario. For certain less likely evolutions in JO these conditions are not met. A substantial increase of hydraulic conductivity only occurs for overburden lower than ca. 30 – 50 m, this is very unlikely at all sites.
- Changes in porewater chemistry and diffusion properties of Opalinus Clay will be small during the period under consideration.
- The loading and unloading of the host rock with a few hundred metres of ice will result in only a minor change in host-rock porosity. Associated changes in pore pressure will result in a short-term increase in hydraulic gradient from the host rock towards the aquifers. The effect can be constrained and shown to be not relevant for overall tracer transport.
- Dissolution processes are unlikely to affect properties and long-term stability of the host rock and confining units because of small driving forces, low hydraulic conductivity and appropriate repository placement with respect to larger tectonic faults.

Future geodynamic evolution (Section 6.2), changing climate (Section 6.3) and morphological changes due to erosion (Section 6.4) can alter hydrogeological and hydrogeochemical conditions (states, properties) and might ultimately affect barrier efficiency. Consequently, the evolution of the barrier system over the period under consideration needs to be addressed. This section discusses the most relevant hydrogeological and hydrogeochemical changes in the aquifer-aquitard system:

- Changes in flow systems in the deep aquifers (Malm, Hauptrogenstein, Keuper and Muschelkalk aquifers; Section 6.5.1)
- Changes in hydraulic barrier efficiency of the host rock and low-permeability confining units (Section 6.5.2)
- Changes in diffusion properties (Section 6.5.3)
- Changes in porewater composition and related effects on solute mobility (Section 6.5.4)
- Changes related to dissolution processes below the host rock (Section 6.5.5)
- Alteration of host rock mineralogy (Section 6.5.6)

Note that the evolution of the biosphere, including scenarios and parameters for the evolution of shallow aquifers and surface waters, is discussed in a separate report (Nagra 2024q).

6.5.1 Changes in deep aquifer flow systems

The host rock and confining units are sandwiched between aquifers that provide the hydraulic and hydrogeochemical boundary conditions to the low-permeability sequence (Section 4.5.3.1, Fig. 4-84). Malm and Hauptrogenstein constitute the relevant aquifers above the host rock. Below the host rock, the local Keuper and the regional Muschelkalk aquifer are relevant. During the period under consideration, the flow systems in these deep aquifers can be affected by a variety of processes. In the following subsections, the impact of the most important drivers is briefly discussed.

6.5.1.1 Variations in groundwater recharge as a result of climate change

Groundwater recharge is dependent on climatic conditions, in particular temperature and precipitation. Changes in these parameters strongly impact water flux and residence time in shallow aquifers. In comparison, the impact on deep flow systems is dampened because of the lower hydraulic conductivities and because the overall differences in hydraulic head driving these deep systems are not strongly affected by recharge. Climate-related changes in recharge conditions thus have a subordinate influence on deep flow systems compared to other processes of the long-term geological evolution. Note that the impact of glaciations and permafrost is discussed separately (Section 6.5.1.3).

6.5.1.2 Changes due to erosion and changing morphology

Over timescales of 10^5 to 10^6 years, erosion may significantly modify the morphology of Northern Switzerland (Section 6.4). There will be a general lowering of the river network with respect to the repository depth (Fig. 6-32) and a decrease in the overburden thickness above the different aquifers (Fig. 6-35 to Fig. 6-38). The hydrogeological system will tend towards increasing flow rates in the aquifers as well as decreasing groundwater salinity and groundwater residence times over a timescale of 10^6 years because of the increasingly shallower situation and related decompaction effects. Ultimately, when the carbonate rocks have been uplifted above the baselevel (Fig. 6-32; e.g. Hauptrogenstein in JO), they may be affected by epigenic karst development.

Over the period under consideration, erosion will drive the development of more active flow systems and a shortening of discharge path lengths for the Malm aquifer in the NL and ZNO siting regions. This effect will probably be smaller or occur later in NL because of the greater depth of the Malm aquifer (see also Section 4.5.6).

In the JO siting region, the aquifer above the host rock (Hauptrogenstein) may be affected by decompaction effects and by potential dissolution as river incision may position the aquifer above the local baselevel (Fig. 6-32, Fig. 6-38). The less likely drainage evolution scenario assuming a direct connection of the Aare Valley to the Sissle for instance (Section 6.4.3.2) may result in an important reorganisation of the local hydrogeological system, with the new valley acting as a major discharge area for the Hauptrogenstein aquifer.

For the aquifers below the host rock, the remaining substantial overburden thickness will result in negligible changes in the aquifer properties within the siting regions (see also Section 6.4.4).

6.5.1.3 Changes related to glaciations and permafrost

During cold climate periods, the hydrogeological conditions may be affected by glaciation and permafrost (Section 6.3).

Water pressure below glaciers (warm-based, Section 6.3.2) increases with increasing ice thickness. A synthesis of studies in North America and Europe suggests that subglacial recharge may be increased by as much as 2 – 6 times compared to modern levels (Person et al. 2012). Such recharge may induce substantial changes in terms of water fluxes, hydraulic gradients, residence times and flow directions, as well as isotopic composition of the groundwaters. The depth to which this water infiltrates depends on numerous factors, such as the thickness of the ice, the duration of the glaciation and the hydraulic properties of the units below the glacier.

There is evidence from the study area of the effects of past glaciations on the hydrogeological system. In the Bodensee area, which was covered by substantial ice thicknesses in the past (Section 6.3.2), the groundwaters from the Malm and Molasse aquifers show a distinct cold climate isotopic signature, probably caused by increased subglacial recharge during the last glaciation period (Section 4.5.5.2, Fig. 6-45). Note that today this area is considered to be a discharge area. In the Swiss Molasse Basin further to the south, water types change with increasing depth and include Molasse groundwaters that infiltrated during Pleistocene cold time periods (Waber & Traber 2022). In the siting regions, no evidence exists for such glaciation-induced cross-formation recharge processes into the Malm aquifer (Section 4.5.5.2). This may be because of lower ice thickness and shorter duration of glaciation (Fig. 6-15), thick coverage by the Molasse sediments or differences in hydraulic conductivities of the Molasse and the Malm aquifer. Numerical simulations for a comparable geological setting in the Bavarian Molasse Basin show that a lower permeability aquifer below the Molasse cover may significantly reduce the depth of subglacial recharge (Schintgen & Moeck 2021). The fact that Malm permeabilities defined in these simulations compare well with the hydraulic conductivities measured in the siting regions of Northern Switzerland (Fig. 4-88) indicates that the low permeability of the Malm aquifer minimises glaciation-induced cross-formation flow across the Molasse deposits into the Malm.

However, a reduction in overburden thickness and subsequent decompaction effects may lead to increased hydraulic conductivities in the Malm aquifer (Section 6.5.1.2), allowing for higher water fluxes and reduced residence times during future glaciations, in particular in the western part of ZNO. In JO, future glaciations are less likely (e.g. Sections 6.4.2.1 and 6.4.3) but could nevertheless affect the Hauptrogenstein aquifer.

In the past, Northern Switzerland was repeatedly affected by permafrost (Section 6.3). Permafrost may reduce or locally prevent recharge and/or discharge through freezing of pathways (e.g. Jost et al. 2007, McIntosh et al. 2012) and thus affect the flow systems mainly in terms of reducing water fluxes and increasing residence times. During the period under consideration, such changes are temporarily expected in all the siting regions.

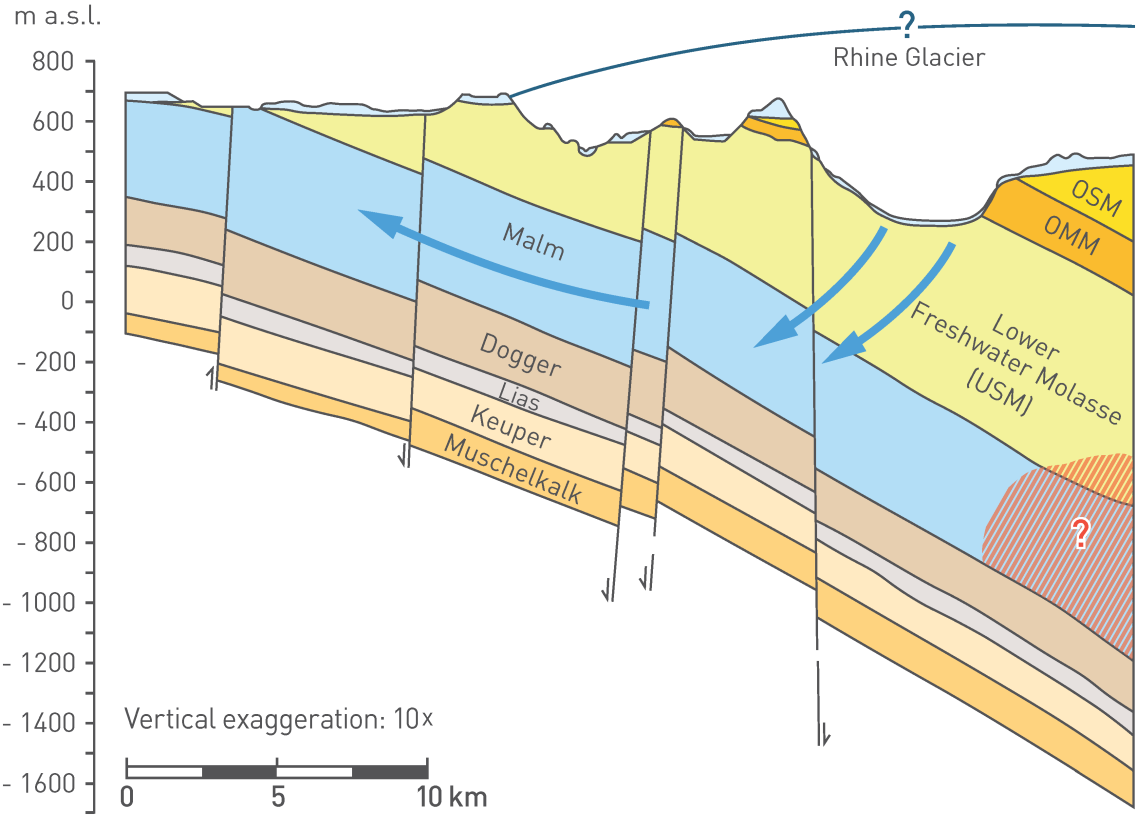


Fig. 6-45: Schematic representation showing Pleistocene subglacial meltwater recharge into the Malm aquifer in the Bodensee area

Figure from Waber & Traber (2022), based on earlier work of Bertleff & Watzel (2002). Blue arrows indicated recharge of subglacial meltwater into the Malm aquifer. Red hatched area indicates remnants of saline deep groundwaters. Note that there is no indication for such Pleistocene cross-formation meltwater flow across the Molasse in the siting regions. However, cross-formation flow across the Molasse and Malm could become more relevant in the future after reduction of the Malm overburden thickness (see text for discussion).

6.5.1.4 Changes in deep aquifer flow systems due to neotectonic activity

Strong earthquakes, even with distant epicentres, can induce changes in the groundwater system as evidenced by changed discharge rates of groundwater springs or fluctuations in groundwater levels in boreholes (Nagra 2024i, Wang & Manga 2010). Such changes may be the result of stress changes and related dilation, or contraction of cracks or enhanced permeability produced by seismically induced fractures. The effect generally diminishes over the timescale of a few years. It is thus not expected that effects of single earthquakes would fundamentally and persistently change the flow system.

Accumulated slip along faults can also affect aquifer pathways. Fundamental persisting changes to the aquifer flow system due to fault slip on regional or local faults are not anticipated during the period under consideration as deformation rates are generally low (Section 6.2). Nevertheless, the impact of flow across and along faults on the deep aquifer system and on discharge paths and the effects on flow paths and discharge areas are discussed in Nagra (2024n).

6.5.2 Changes regarding the hydraulic barrier efficiency of the Opalinus Clay and confining units

6.5.2.1 Change of porewater pressure and hydraulic gradient

The magnitude of the vertical hydraulic gradient across the host rock and the entire aquitard sequence influences the advective water flux. In this section, two bounding cases are discussed: In the first one, the hydraulic gradient is controlled by the difference in hydraulic head between the aquifers above and below the low-permeability sequence. This case would be relevant for water flux along a hypothetical steep fault connecting these aquifers. The second case discusses the effects related to mechanical loading and unloading of the host rock by a significant ice cover. Note that while the hydraulic heads in the aquifers will quickly react to changing conditions on the surface, the low-permeability host rock (and confining units) may need substantial time to re-equilibrate to new boundary conditions (see also Section 5.6.5).

Changes in aquifer hydraulic heads can be caused mainly by erosion and by recharge below glaciers (Section 6.5.1.3). In the absence of significant glaciations, the magnitude of expected changes is limited by the expected overall moderate evolution of topography over the period under consideration. In the case of significant (warm-based) glaciations, hydraulic heads in the aquifers and consequently also the hydraulic gradient across the aquitard sequence may be more affected. However, for the siting regions NL and ZNO, maximum ice thickness is estimated at 400 m and the duration of the ice coverage at a few thousand years (Section 6.3.2). Therefore, the increase in gradient is limited in magnitude and to a comparably short duration. The overall effect on advective flow in the host rock is small to negligible.

Mechanical loading and unloading of the host rock due to glaciation and deglaciation can affect the pore pressure in very low-permeability units such as the Opalinus Clay. The pore pressure and therefore also the hydraulic gradient are influenced by transient hydromechanical processes (Section 5.6.5). The currently measured underpressures in the Opalinus Clay (e.g. in the Benken borehole ca. 70 m subhydrostatic, Fig. 5-44) indicate vertical hydraulic gradients directed from the confining units towards the centre of the Opalinus Clay. During glaciation periods, the additional loading can result in an increase in hydraulic head in the Opalinus Clay relative to the confining units. During these episodes, the hydraulic gradient may therefore change direction from the centre of the Opalinus Clay towards the confining units. Conversely, a glacial retreat will again induce low pore pressures which will remain low for a longer time in the Opalinus Clay than in the more permeable confining units. Therefore, the hydraulic gradient after a deglaciation will again be directed from the confining units to the Opalinus Clay. The temporary increase in advective flux due to glacial loading was already studied in earlier work and was considered insignificant (Nagra 2002, Kosakowski 2004).

The effects of changing porewater pressures and hydraulic gradients are considered small at all sites, but the probability of a significant ice thickness above the repository is smaller in JO compared to the other sites.

6.5.2.2 Change in hydraulic conductivity due to reduction of overburden thickness

Future uplift and subsequent erosion will reduce the overburden thickness of the Opalinus Clay (Section 6.4.4). This may influence the geomechanical and hydrogeological properties of the host rock and confining units, and the self-sealing of fractures.

As long as the overburden thickness above the Opalinus Clay remains greater than 200 m, erosional unloading has only a very minor impact on the hydraulic conductivity (Section 5.6). This is because unloading of the Opalinus Clay is not associated with brittle deformation (Nagra 2014h), because existing fractures are held sufficiently tightly closed (Section 5.7.4). Furthermore, changes in porosity when unloading from repository depth to 200 m would be negligible (of the order of 0.5 to 1 vol.-%, Sections 5.3.2 and 5.5.2) and would not result in a relevant change in matrix hydraulic conductivity. However, with progressive erosional unloading to shallower depth, fractures may be induced and effective normal stress on the fractures may be insufficient for robust self-sealing.

For the most likely erosion scenario, reliable self-sealing conditions are predicted for all sites, as the host rock overburden thickness remains > 200 m during the time under consideration (Section 6.4.4). The full range of erosion scenarios shows that NL is the most robust in this regard. In JO, the remaining overburden thickness depends more substantially on the evolution of the drainage system and associated topography (Section 6.4.4, Fig. 6-44 and Fig. 6-47).

A study evaluating numerous hydraulic tests in various shallow boreholes in the Opalinus Clay demonstrates a marked increase in hydraulic conductivity of the Opalinus Clay when the overburden thickness is less than approximately 30 – 50 m, with the exact depth of this transition depending on multiple factors, in particular the topographic setting (Hekel 1994). Detailed investigations in the Lausen borehole revealed that a significant increase in hydraulic conductivity (the uppermost 30 m) broadly coincides with the depth at which significant decompaction-induced fracturing starts to occur (Fig. 6-46; Vogt et al. 2017, Crisci 2019, Mazurek et al. 2023b). The investigations also show that a significant increase in matrix porosity occurs only at very low effective stress (< 1 MPa), equivalent to an overburden thickness of just a few tens of metres (Fig. 6-46). The mineralogy and rock geochemistry were only altered in the uppermost few metres, and substantial geochemical evidence was gathered indicating that transmissive fractures self-sealed even in the lower weathered zone (approximately 15 m depth; Mazurek et al. 2023b). In summary, a substantial increase in hydraulic conductivity in the Opalinus Clay only occurs for overburden thicknesses < 30 – 50 m.

The clay-mineral-rich confining units are predicted to show a similarly low sensitivity of hydraulic conductivities to unloading as the Opalinus Clay. For carbonate-rich parts of the upper confining units, the depth-dependent hydraulic conductivity is less constrained. In the Effingen Member (Wildegg Formation), for example, the increased hydraulic conductivities observed down to a depth of around 300 m can possibly be explained by decompaction effects (Nagra 2014f).

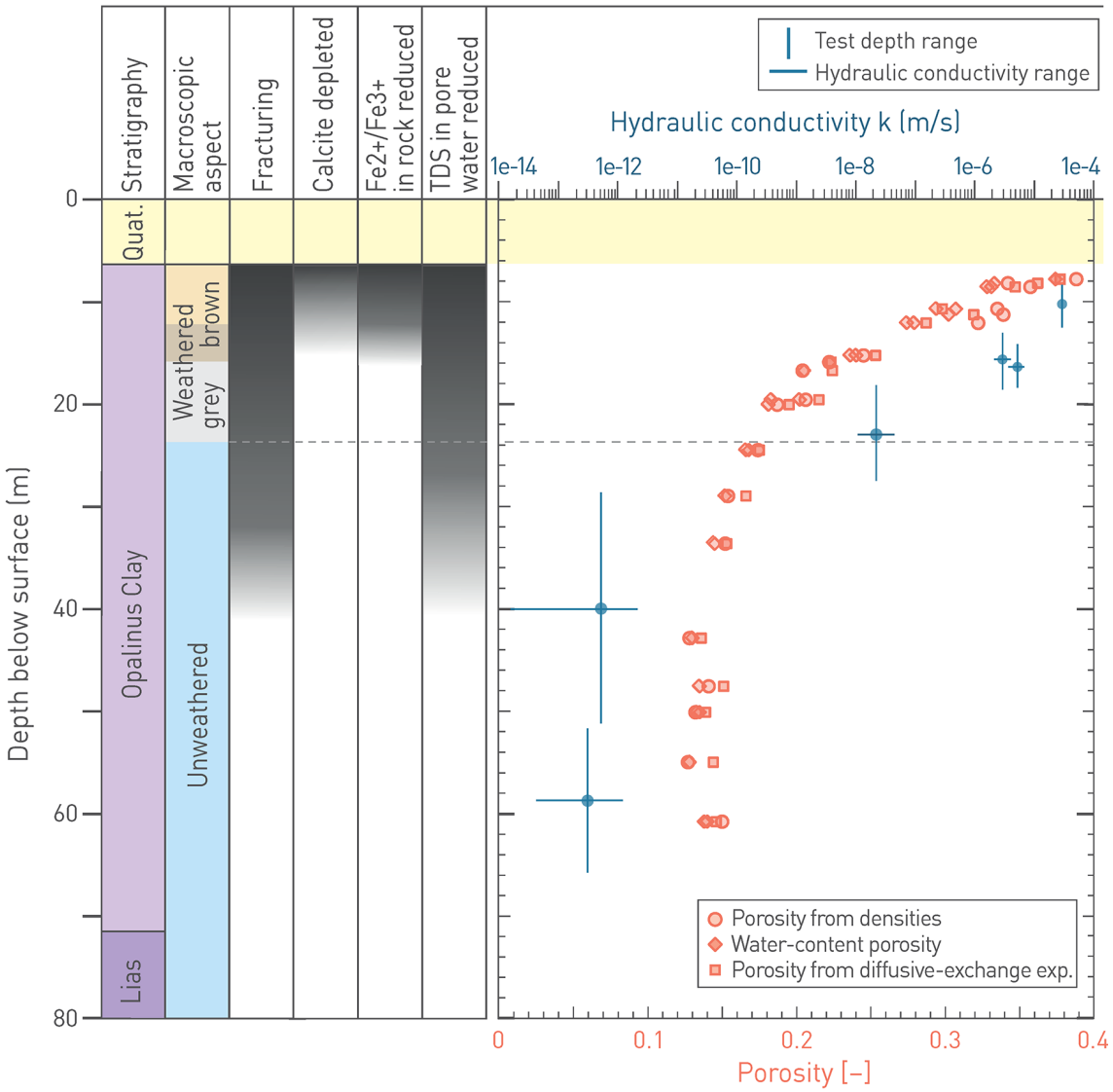


Fig. 6-46: Rock properties of the Opalinus Clay in the shallow decompaction zone: Synopsis of the observations in the Lausen case study

Figure based on Mazurek et al. (2023b) and Vogt et al. (2017). Dark colours indicate the depth range of alteration. TDS: Total dissolved solids.

6.5.2.3 Changes of hydraulic conductivity due to dissolution processes in host rock and confining units

Dissolution processes have the potential to alter the hydraulic conductivity of a rock. The host rock and confining units are characterised by varying amounts of clay, quartz and carbonate minerals and by porewaters in thermodynamic equilibrium with these minerals (Section 5.4). Of these, calcite is the most soluble mineral. Groundwaters in the adjacent aquifers are also characterised by calcite mineral equilibria (Section 4.5.5, no particular high-pCO_2 waters), that is there is no important driving force for dissolution. Other potentially soluble minerals (rock salt,

anhydrite) are not present in either the host rock or confining units[20] in significant quantities (Section 5.2). For the Opalinus Clay, dissolution of rock-forming minerals is not considered relevant over the period under consideration, mainly because of the limited amount of soluble minerals and their disseminated distribution (Section 5.4) and because of the very low hydraulic conductivity (Section 5.6).

The upper confining units are generally clay-mineral-rich but include sections with increased carbonate content. The clay-mineral-rich sections are less affected by dissolution processes and will most probably show a similar decompaction behaviour to the host rock. However, for the carbonate-rich sections, decompaction and related carbonate dissolution may result in an increased horizontal permeability. A more pronounced increase in hydraulic conductivity (karstification) may occur if the confining units are uplifted above the relevant local discharge level (~ local baselevel; Section 6.4).

In the provisional disposal areas of all the siting regions, the remaining overburden thickness above the upper confining units is at least 300 m thick in the most likely scenario (Fig. 6-44), in which no relevant decompaction effects are expected.

An uplift of the upper confining units above the local baselevel is considered very unlikely in NL and ZNO (Fig. 6-32). For JO, however, fluvial incision of the Aare River may cause lowering of the local erosion base to a level below the top of the Passwang Formation, potentially enhancing carbonate dissolution.

6.5.3 Change in diffusion properties of the host rock due to reduction of the overburden

Diffusion properties are closely related to porosity and the pore space architecture (Section 5.8). Porosity depends on overburden thickness (Section 5.2) and consequently also the diffusion properties. However, measurements of the Opalinus Clay porosity in boreholes in Northern Switzerland, where overburden thickness varies between 450 and 1'000 m, indicate only a very weak increase with decreasing overburden thickness (Fig. 5-10).

The diffusion properties measured in the different TBO boreholes for the Opalinus Clay using tritiated water (HTO) tracers are almost identical (median values differ by less than 4% with no relationship to overburden thickness; Fig. 5-51). The Opalinus Clay at Mont Terri, where the overburden thickness is less, i.e. ca. 300 m, has an approximately two times higher effective diffusion coefficient (D_e) value compared to the siting regions, which is attributed to the higher porosity at Mont Terri (Section 5.8.3).

A marked porosity-related increase of D_e is to be expected when erosion reduces the thickness of the overburden to a few decametres (Fig. 6-46). Note that for the transport of anions and cations, D_e is also influenced by the porewater chemistry, which may change slightly over time (Section 6.5.4).

For all the siting regions, the most likely overburden thickness above the provisional disposal areas after the period under consideration (Fig. 6-44) is a minimum of 400 m, sufficient to prevent an increase in the effective diffusion coefficient D_e in the Opalinus Clay (increase < a factor of ca. 2). The full range of erosion scenarios shows that NL is the most robust with respect to preserving this (or even larger) overburden thickness. In JO, this considerably depends on the evolution of the drainage system and associated topography (Section 6.4.4, Fig. 6-44).

---

[20] Note that the potential additional lower confining units in NL (Bänkerjoch Formation; Fig. 4-140) include considerable quantities of anhydrite. The dissolution potential of these rocks is discussed in Section 6.5.5.

6.5.4 Alteration of porewater composition by diffusive exchange with aquifers and effects on radionuclide mobility

Porewater chemistry of the host rock is a major constraint on radionuclide mobility (speciation, sorption, solubility) and the stability of the engineered barriers. Furthermore, porewater composition affects the diffusion behaviour (Van Loon et al. 2023), with lower salinity (lower ionic strength) leading to lower anion and higher cation diffusion coefficients (Glaus et al. 2024; Section 5.8), the latter mainly for cations undergoing ion exchange reactions.

Porewater constituents can be subdivided into free constituents such as chloride and elements buffered by thermodynamic equilibria with host rock minerals. While the mineralogical composition can be considered constant over the period under consideration (Section 6.5.6), the free porewater constituents are affected by the diffusive interaction with bounding aquifers. The modelling of the tracer profiles (Section 4.6) shows that the Opalinus Clay porewater may slowly evolve towards lower salinity on a timescale of hundreds of thousands of years. Forward modelling of the Benken dataset suggests a decrease in chloride concentration of less than 1 g/L in the centre of the Opalinus Clay within 1 Myr (see Section 8.6.2 in Nagra 2002). The slowly changing porewater chemistry results in slightly decreasing diffusion coefficients for anions and a slight increase for cations that undergo mainly ion-exchange reactions.

The impact of decreasing porewater salinity on solubility is specific for each radionuclide and depends on the changing ion concentrations. A qualitative comparison of solubilities based on the NL and ZNO reference porewater with the one based on the dilute JO porewater yields only minor differences (Kulik & Miron 2024).

6.5.5 Dissolution processes below the host rock

The prerequisites for dissolution processes are the presence of relevant quantities of easily soluble minerals in the rock and circulation of significant quantities of groundwater that is undersaturated with respect to these minerals. Some units below the host rock contain soluble carbonate and evaporite minerals and dissolution phenomena are observed in near-surface positions (Sections 4.5.3.11 and 4.5.3.12). Therefore, the question arises as to whether large-scale dissolution processes (‘karstification’) at relevant depth could affect the long-term stability of the repository above (Jeannin et al. 2015).

Carbonate dissolution in the Muschelkalk aquifer: Given the position in the sedimentary succession, the relevant zone below the repository will be at significant depth at the end of the period under consideration and certainly below the discharge area of this aquifer. This indicates that the Muschelkalk will not be affected by major decompaction effects and will not be exposed to direct recharge of weakly mineralised waters. Therefore, deep Muschelkalk groundwaters will remain saturated with calcite and near or at saturation with respect to dolomite in the future. That is, there is no or only little driving force for dissolution of the carbonate minerals. Hydrogeochemical investigations (Section 4.5.5) evidence a large-scale dedolomitisation process with a reaction progress probably controlled by slow diffusive interaction with the adjacent sulphate-mineral-rich units. In addition, water flow in the Muschelkalk aquifer occurs along a comparably large number of fractures and partly in the porous matrix (Section 4.5.3.12). Overall, there are only negligible to small driving forces for dissolution. Given the nature of water flow and the generally small and limited water fluxes at this depth, the evolution of large cavities is unlikely.

Carbonate dissolution in the Muschelkalk aquifer could also be triggered by cross-formation flow (hypogenic karst development), i.e. caused by groundwater ascending along faults from deeper aquifers such as the Buntsandstein or the crystalline basement. These groundwaters are of different chemical composition, that is they would have some potential to dissolve carbonate minerals. There is evidence for cross-formation flow between the crystalline basement and the Muschelkalk aquifer in structurally highly affected areas related to earlier periods of geological

history (Section 4.5.5.5). Within the NL and ZNO siting regions, increasing concentrations of elements such as Li along the flow path (Section 4.5.5.5) indicate mixture with a component that might reside in the matrix of the Muschelkalk aquifer or indicate minor admixture (< ca. 20%) of deeper groundwater along the regional flow path. In contrast, Muschelkalk groundwaters with elevated concentrations of Na and Cl in NL (i.e. Na-Cl type waters) are devoid of particular indications of a basement component (Section 4.5.5.5). In JO, Muschelkalk groundwaters are all of Na-Cl type and may show elevated concentrations of ^{4}He and Li (Fig. 4-114). Here, the Na-Cl type groundwater signature may thus indicate cross-formation flow from deeper units to the Muschelkalk aquifer. Overall, cross-formation flow may occur locally, e.g. along regional fault zones, and cause some dissolution, but this is mostly a subordinate process in the genesis of the deep Muschelkalk groundwaters. In any case, it is a slow process given the residence times of these waters. Cavities of significant size are not expected.

Dissolution of anhydrite (Bänkerjoch Formation) and related loss of barrier function is not expected because of remaining large overburden thickness and self-sealing by anhydrite – gypsum transformation (Section 4.5.3.11). In addition, the groundwaters in the adjacent aquifers are at or near to saturation with respect to the relevant sulphate minerals. In a field study near Stuttgart (Ufrecht 2017), an overburden thickness larger than ca. 40 – 80 m was found sufficient to maintain the original anhydrite component. This agrees with the observations in the Böttstein borehole in Northern Switzerland, where the transformation to gypsum is essentially restricted to less than 60 m depth (data compilation by Mazurek 2017). These observations underline that the Bänkerjoch Formation will maintain its aquitard character as long as this minimum overburden is maintained.

The local salt deposits (halite) in the Zeglingen Formation are also readily soluble. Dissolution is imaginable in the case of direct contact with the strongly halite-undersaturated groundwaters in the aquifers above and below. This might occur, for example, along a transmissive fault connecting these aquifers. Hydrogeochemical indications for such processes come from the JO area (Section 4.5.5.5) and from the area closer to the Rhine Graben (Waber & Traber 2022). The high Na and Cl concentrations observed in borehole BUL1 are likely explained by a lateral contact with the salt deposit (Section 4.5.5.5). The halite deposits are sandwiched in between anhydrite-rich rocks (including some clay-rich layers), that is these rocks have a self-sealing potential, and the faults are therefore not likely to have high transmissivity (where vertical displacement is small). In any case, the dissolved volume of rock is expected to be small and deformation related to collapse of dissolution cavities is not expected to reach the level of the repository located ca. 300 m above.

Overall, adverse effects due to dissolution below the host rock are considered very unlikely. There are no major drivers for carbonate and anhydrite dissolution. Furthermore, the positioning of the disposal areas takes into account the location of larger faults.

6.5.6 Alteration of host rock mineralogy

The mineralogical composition of the Opalinus Clay host rock is relevant for the sorption of radionuclides and the buffering of the porewater chemistry. Unaltered host rock also ensures, for example, unaltered diffusion properties (Section 5.8) and hydraulic conductivity (Section 5.6).

A number of studies show that the mineralogical composition of the Opalinus Clay is only altered if the overburden thickness is less than a few decametres (Hekel 1994, Mäder & Mazurek 1998, Mazurek et al. 2023b; Fig. 6-46).

Given the expected erosion and the remaining overburden thickness (Fig. 6-44), these processes are not relevant during the period under consideration. The host rock provides a stable and predictable system regarding porewater chemistry, sorption, diffusion properties and hydraulic conductivity.

6.5.7 Conclusions on long-term hydrogeological and hydrogeochemical evolution

- Overburden thickness is a determining factor for the long-term hydrogeological evolution of the sites and the ability to maintain the barrier function. A remaining overburden thickness of 200 m is required to ensure efficient self-sealing of fractures in the Opalinus Clay. At the end of the period under consideration, the most likely scenarios at the location of the provisional disposal areas of all sites show at least ~ 400 m of remaining overburden above the host rock. The full range of erosion scenarios shows that NL is the most robust in this regard. In JO, the remaining overburden thickness depends more substantially on the evolution of the drainage system and associated topography.
- Only subordinate changes in diffusion properties of the Opalinus Clay are expected over the period under consideration, related to decreasing overburden thickness or because of changing porewater chemistry.
- Transient effects related to glaciations may affect the geological barrier in terms of pore pressures, hydraulic gradients and advective flux. The impact of these transient processes can be constrained and will result in a short-term but not relevant increase in advective flux out of the Opalinus Clay.
- Aquifers are more strongly affected by long-term evolution, notably the aquifers above the host rock. This mainly affects transport in the aquifers (water fluxes and residence times). Where the aquifers are at greater depth, the effects are smaller or occur later.
- Dissolution processes are not expected to affect the barrier properties of the host rock. This is mainly because the low hydraulic conductivities are maintained, and because the limited amount of soluble (e.g. carbonate) minerals is disseminated within the clay-mineral-rich rock.
- Carbonate-rich sections in the upper confining units are prone to dissolution processes if overburden thickness is substantially reduced and the confining units are located above the groundwater discharge level. This is very unlikely for the NL and ZNO siting regions. JO is least robust in this regard, because fluvial incision of the Aare River may cause lowering of the groundwater discharge level (~ local baselevel) below the level of the Passwang Formation, enhancing the driving forces for carbonate dissolution.
- Dissolution processes below the host rock are unlikely to affect the long-term stability of the host rock because of small driving forces, slow processes and because of an appropriate position of the disposal zones with respect to larger faults.

6.6 Long-term geological evolution: Summary

This section starts with a summary of the long-term geological evolution of Northern Switzerland together with overall conclusions regarding site selection and long-term safety (Section 6.6.1). This is followed by a description of the relevant processes with respect to the anticipated evolution of the landscape around the deep geological repository with the focus on NL (Section 6.6.2).

6.6.1 General conclusions regarding the long-term geological evolution

The general conclusions follow up on the questions posed in Section 6.1.2 for the relevant climatic and erosive processes and their impact on the hydrogeology and geochemistry of the host rock and confining units.

Tectonic evolution

- Tectonic deformation rates in Northern Switzerland are small and are expected to continue to remain small over the next one million years.
- The spatial uplift pattern in Northern Switzerland over the next one million years will continue to be dominated by Alpine uplift. Uplift rates are expected to be < 0.36 mm/yr, most likely ~ 0.15 mm/yr, with relatively small differences between the NL and ZNO siting regions and slightly lower rates near JO.
- Baselevel drop due to subsidence of the Upper Rhine Graben might increase the incision potential of the Hochrhein River and the Aare River. It is expected that sediment supply and ongoing uplift of the Rhenish Massif will compensate for subsidence and work against baselevel drop.
- Inherited faults will localise strain and future deformation. Mainly the regional fault zones will be preferentially reactivated. The location of larger faults is taken into account when planning the locations of the disposal areas.
- If new faults develop in the host rock, they are expected to be segmented and small in length and offset (scaling relationships; see fault architecture in Section 5.5.4).

Climate evolution

- According to different anthropogenic CO_2 scenarios, 3 to 5 large glaciations (LGM-size or larger) are expected that might reach the external Alpine Foreland in the next one million years. The climate conditions during future glacial periods are expected to be similar to those during past cycles.
- Considering present anthropogenic climate change and the longevity of increasing CO_2 levels within the atmosphere, inception of the next glaciation is expected to be significantly delayed, and the next large glaciation may only occur in ~ 200'000 years.
- Each glacial period is expected to be associated with permafrost conditions during the phases of coldest temperatures. Permafrost is expected to reach maximum depths of 100 – 200 m.
- Ice thicknesses and the duration of the ice occupation at the sites varied during past glacial cycles because of the different distances to the Alps and different topography (ZNO > NL > JO). The same pattern will most likely be seen during future glaciations with ice thicknesses between 200 and 400 m and durations of ice occupation between 1'000 and 3'000 years.
- After a glacial state, the climate warms, and climate conditions change from a polar climate (Switzerland largely covered by ice and/or permafrost conditions) towards a continental or temperate climate. Also, a warmer-drier climate cannot be excluded, at least in the high-emission scenarios.

Erosion

- Future erosion processes (glacial and non-glacial) are expected to continue as observed in the Quaternary period, but at lower rates with no major drainage reorganisation, smaller glaciers, delay in glacial inception, and harder-to-erode rocks below the Molasse units.
- The main river system affecting erosion in the siting regions over the next one million years remains the Aare – Rhine River system. The Rhine is further growing at the expense of the Danube with a very limited impact on the incision potential.
- A residual overburden thickness of 200 m classified as reliable for maintaining self-sealing behaviour can be shown for the most likely scenarios in all the siting regions for the period under consideration. Using the 5 – 95% range as a reference, JO shows more limitation for such a 200-m criterion at the location of the provisional disposal area. This site thus depends on the preservation of the local topography (see Fig. 6-47).
- Excavation of the repository by erosion within the next one million years is extremely unlikely at all three sites. The NL site is most robust in this regard because of the greater repository depth and the expected rates of erosive processes (see Fig. 6-47).

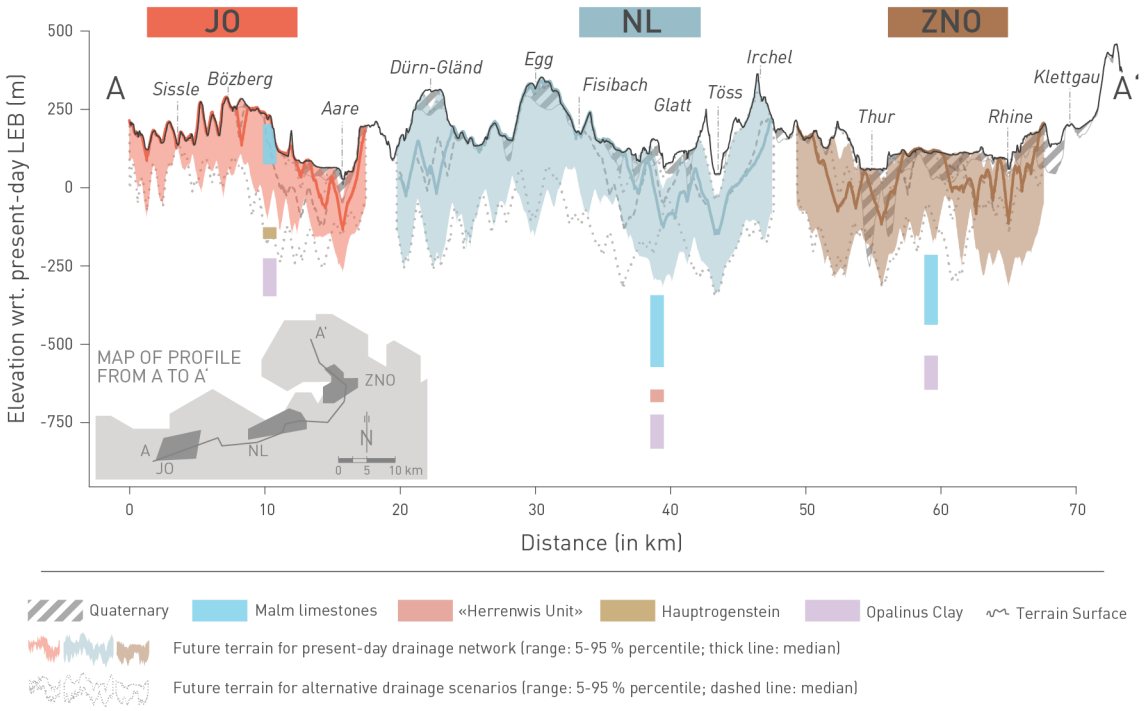


Fig. 6-47: Synthesis profiles for visualising future non-glacial erosion in the three siting regions

The profile shows ranges of future evolution of the local erosion base and local topography for selected scenarios and selected parameter combinations (see corresponding map representations in Fig. 6-35 for the present-day drainage network scenarios and Fig. 6-37 for the JO alternative drainage scenario Rinikerfeld). The profile location is the same as in Fig. 6-27. Note that the formation of glacial overdeepenings is not illustrated in this plot. Vertical exaggeration is ~ 20-fold. For the provisional disposal area at JO (lateral position corresponds to the location of lithological column in the plot), the remaining overburden thickness with respect to the coloured and dashed bands of future terrain shown here contributes to the green curve ("Local Topography"; output Model B) in Fig. 6-44.

Hydrogeology and hydrochemistry

- Deep groundwater flow systems are affected by processes of long-term geological evolution such as large changes in morphology, changing climate or by glaciations inducing high sub-glacial water pressure. This affects discharge paths, water fluxes and residence times in the aquifers. Discharge areas will be progressively located closer to the repository locations.
- Loading and unloading with a few hundred metres of ice will result in minor changes in porosity because of the pre-consolidation of the Opalinus Clay during maximum burial. At the same time, the loading and unloading induces transient over- and underpressures, respectively. The overpressures related to ice loading are of limited magnitude and duration. The overall effect on advective flux in the host rock is thus small to negligible.
- The low hydraulic conductivity of the Opalinus Clay will be maintained over the period under consideration at all sites. This is explained by the remaining overburden thickness of at least 200 m. Depending on the river network evolution, the remaining overburden thickness may be less in JO towards the end of the period under consideration (see above).
- Erosion and decreasing porewater salinity pose minor changes to diffusion properties during the next one million years.
- Dissolution processes are not expected to affect the barrier properties of the host rock and confining units in a significant way.
- Overall, the host rock and confining units provide a stable and predictable environment for hosting the repository. The deepest site, NL, is most robust in this regard.

6.6.2 Storyboard for the expected long-term geological evolution in Nördlich Lägern

In the following, we summarise the expected long-term geological evolution[21] of the NL siting region over the next one million years. This geological storyboard supports the discussion on the repository evolution in Nagra (2024p).

Long-term rock uplift, fluvial incision and remaining overburden thickness

The Rhine will grow at the expense of the Danube, by headward erosion rather than through major river capture events. The evolution of the river profile will be largely controlled by rock uplift and sediment input. The bedrock erodibility will only be of secondary importance for vertical fluvial incision but might have an influence on lateral erosion.

The spatial pattern of rock uplift in Northern Switzerland over the next million years will continue to be dominated by Alpine uplift, regardless of whether it is a matter of tectonic uplift or isostatic compensatory movements. In simplified terms, the main uplift gradient can be assumed to cause increasingly higher rates from the external foreland basin towards the Alps along a direction that is approximately perpendicular to the Alpine chain. The long-term rates are low. Total uplift of ~ 170 m (between ~ 25 m and a maximum of ~ 360 m [5 – 95%]) over a million years is assumed for the NL siting region. Short phases of significantly higher rates might be associated with glaciations of extensive foreland glaciations (Fig. 6-48). This in turn may cause temporarily enhanced fluvial incision (after backfilling of perialpine lakes).

[21] For the erosion assessment, the expected evolution presented here, includes the 5 – 95% uncertainty range.

Over long time periods, incision rates are generally expected to be in the same range as uplift rates. Significantly greater incision can only be achieved by additionally lowering the regional baselevel. As long as the Rhenish Massif continues to be uplifted, this location (approx. near Bingen; see Fig. 6-5) decouples the Upper Rhine (and thus the Hochrhein) from the sea. The sedimentary basin of the Upper Rhine south of Bingen is controlled by tectonic subsidence and sediment input at the transition to the Hochrhein near the city of Basel. Today, there is no disturbance of the river profile at this point; the subsidence is roughly compensated for by sediment accumulation. This sedimentation might be additionally linked to a buffer effect associated with the low-subsidence area of the Karlsruhe Swell. Potential elevation gain by short-term oversupply of sediment is compensated for over the long term by vertical incision into these sediments. Averaged over the next million years, however, it is considered possible that the baselevel at Basel might fluctuate by up to ± 70 m.

Under these boundary conditions, a vertical fluvial incision of ~ 160 m is most likely (between 80 and 380 m [5 – 95%]) at the confluence of the Aare and Rhine, i.e. near NL (see Fig. 6-48). This is in good agreement with Quaternary incision on a million-year timescale around the area of NL. Given these incision estimates, a remaining overburden thickness of ~ 550 m (350 – 670 m [5 – 95%]) can be expected, potentially increased by future evolution of local topography.

Given these constraints, it is therefore expected that the future groundwater discharge area will be located progressively closer to the position of the provisional disposal area. The flow path will be shortened compared to today and incipient decompaction affecting the Malm aquifer due to erosional unloading may then increase hydraulic conductivity. A more active flow system will develop, although this happens only late in the period under consideration. Importantly, the remaining overburden thickness is sufficient to avoid any decompaction effects or to affect the self-sealing capacity of the host rock and the clay-rich confining units. The upper confining units will stay well below the local erosion base, preventing dissolution of carbonate-rich sections. The host rock provides a stable and predictable system in terms of porewater chemistry, sorption, diffusion properties and hydraulic conductivity.

Because of the significant remaining overburden, the aquifers below the host rock will experience negligible changes in their properties. The Muschelkalk aquifer will not be affected by decompaction effects and will not be exposed to direct recharge of weakly mineralised waters. Therefore, deep Muschelkalk groundwaters will remain saturated with calcite and near or at saturation with respect to dolomite in the future, preventing significant dissolution of the carbonate minerals below the provisional disposal area.

Short-term modulation of fluvial incision by glacial/interglacial cycles

Long-term incision will be modulated by phases of sediment accumulation with no net vertical incision. The sediment dynamics will be largely controlled by glacial/interglacial cycles. During the interglacial warm periods, a relatively high precipitation rate is expected and consequently a relatively high water discharge. At the same time, the sediment flux may be limited by a weak coupling between the glacially conditioned sediment sources and the rivers. During a renewed Alpine glaciation, the reworking of periglacial deposits by the advancing glaciers and an increase in the area subject to subglacial erosion should lead to a peak in sediment flux. During the main glacial phase, sediment flux is assumed to be larger than the interglacial rate because of increased glacial activity, sediment generation in adjacent permafrost terrains and the effect of greater climate variability. At the termination of glacial conditions, a peak is inferred in water discharge because of the warming-induced increase in atmospheric moisture and a pulse of meltwater from the retreating ice. The greater water availability induces faster glacial sliding and hence an increase in glacial erosion. In combination with the paraglacial adjustment of the landscape, this should result in a maximum contribution of sediment to the fluvial system. However, after glacial retreat, the sediment is trapped in perialpine lakes and overdeepened basins for up to several tens of thousands of years, thus reaching into the interglacial period.

The expected glacial scenario and deep glacial erosion

According to different anthropogenic CO_2 scenarios, 3 to 5 large glaciations (LGM-size or larger) might reach the Alpine Foreland in the next one million years. The next glacial inception will be significantly delayed, and the next large glaciation will only occur after the next ~ 200'000 years (Fig. 6-48). During extensive future foreland glaciations, deep glacial erosion may take place in the eastern part of the NL siting region, where present-day relief is low. This area could be repeatedly glaciated if future glaciers are of similar or larger extent as the penultimate glaciation (Beringen). Maximum ice thickness is estimated at 400 m and a duration of the ice coverage of a few thousand years.

Total cumulative erosion depth in such a case is is most likely to reach ~ 70 m below the local erosion base (30 – 360 m [5 – 95%]). Because the baselevel has already been lowered, deep glacial erosion could reach the Malm limestone late in the period under consideration. It is expected that the Malm limestone is on average only half as erodible as the Molasse-type rocks in Northern Switzerland. It is thus highly unlikely that glacial overdeepening will reach the host rock.

During cold climate periods, the hydrogeological conditions will be affected by glaciation.

An increase in hydraulic gradient is possible during large foreland glaciations but will be limited in magnitude and with a comparably short duration. The overall effect on advective flow in the host rock during these glaciations is small to negligible. The additional ice load can result in an increase in hydraulic head in the Opalinus Clay relative to the confining units with changing direction of the hydraulic gradient between glaciation and glacial retreat. The temporary increase in advective flux because of glacial loading is considered insignificant.

Occurrence of deep-reaching permafrost

Each glacial period is expected to be associated with permafrost conditions during the phases of coldest temperatures. This timing does not necessarily correspond to the timing of the glacial maximum but might pre- or postdate this peak (Fig. 6-48). Depending on the glacial scenario, such behaviour may be expected initially after 200'000 years. During coldest temperatures, deep-reaching permafrost might affect the flow systems in deep aquifers mainly in terms of reducing water fluxes and increasing residence times. Permafrost is expected to reach maximum depths of 100 – 200 m.

Because of a lower limit of remaining overburden above Top Opalinus Clay of ~ 300 m, the expected maximum depth of 200 m permafrost does not challenge the barrier integrity of the host rock by freeze-and-thaw effects.

Earthquakes and faulting

The site is located within a low-seismicity intraplate domain. Faulting is primarily related to shortening in the Alps and in the Internal Jura, as well as transtensional deformation within the Upper Rhine Graben and the Hegau – Bodensee Graben. Current plate dynamic forces define the stress field that is predicted not to vary significantly from the present direction. Rates of strain accumulation are anticipated to be low over the next one million years.

As typical for intraplate areas, the location of faulting is expected to change over time, and areas currently seismically inactive might become the focus of future seismic activity. Earthquakes and fault ruptures are thus possible in the vicinity of the siting regions. Accordingly, changes in local stress conditions might trigger faulting. Such changes might be applied by vertical glacial loading or unloading, large erosion events, or by loading from interaction with neighbouring faults (Fig. 6-48). Importantly, irrespective of timing and trigger, significant offsets may occur along existing larger faults and not along subseismic faults or as a result of new fault creation. Such regional fault zones bound the siting region and will be considered when positioning the disposal areas. Subseismic faults and potential new faults in the Opalinus Clay are expected to be segmented and short in length and offset. Relevant changes of the barrier effect by future earthquakes and faulting are thus not expected.

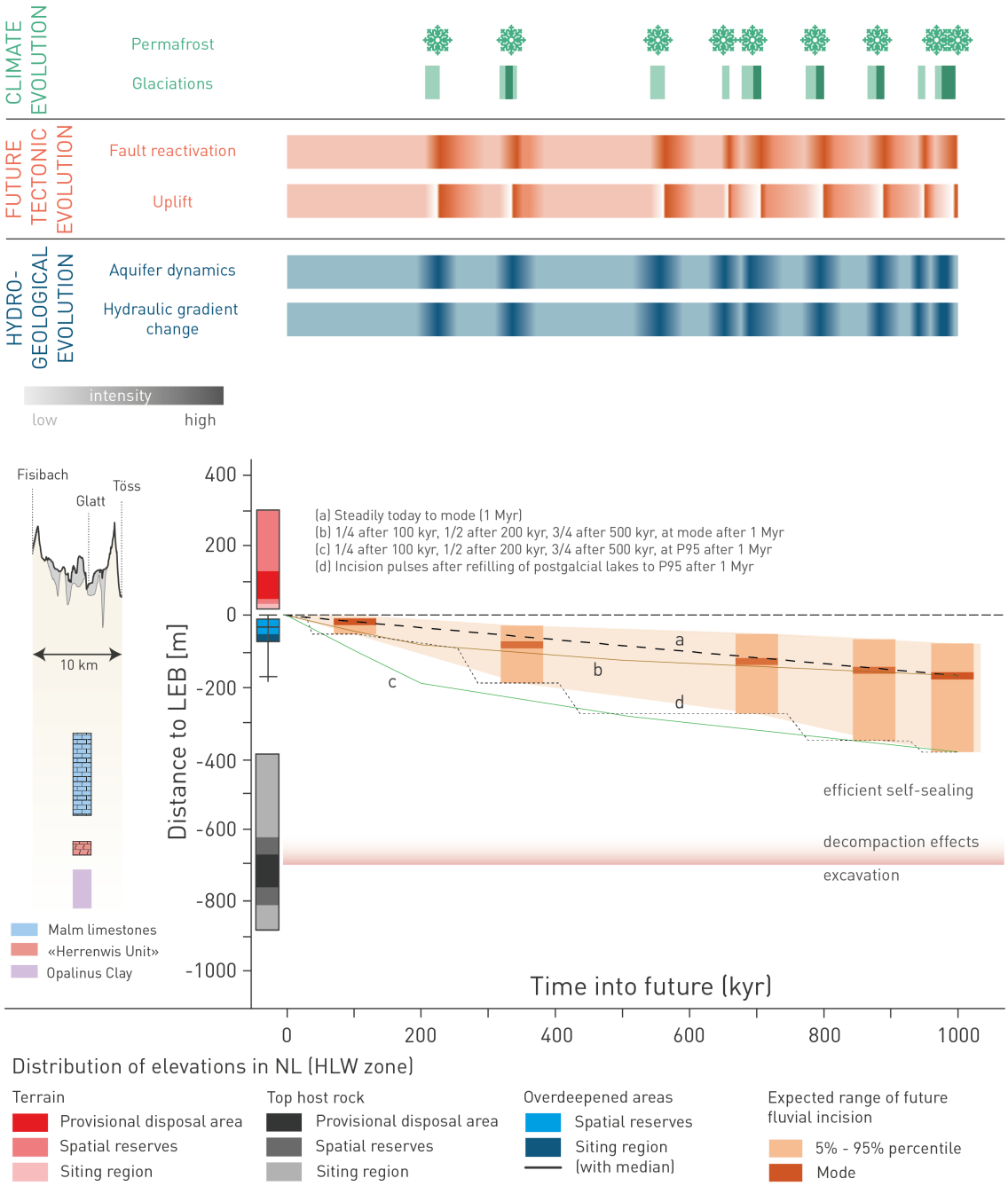

CLIMATE EVOLUTION
Permafrost
Glaciations
FUTURE TECTONIC EVOLUTION
Fault reactivation
Uplift
HYDRO-GEOLOGICAL EVOLUTION
Aquifer dynamics
Hydraulic gradient change
intensity
low
high
Fisibach
Glatt
Töss
10 km
Malm limestones
«Herrenwis Unit»
Opalinus Clay
Distance to LEB [m]
400
200
0
-200
-400
-600
-800
-1000
(a) Steadily today to mode (1 Myr)
(b) 1/4 after 100 kyr, 1/2 after 200 kyr, 3/4 after 500 kyr, at mode after 1 Myr
(c) 1/4 after 100 kyr, 1/2 after 200 kyr, 3/4 after 500 kyr, at P95 after 1 Myr
(d) Incision pulses after refilling of postgalcial lakes to P95 after 1 Myr
a
b
c
d
efficient self-sealing
decompaction effects
excavation
Time into future (kyr)
0
200
400
600
800
1000
Distribution of elevations in NL (HLW zone)
Terrain
Provisional disposal area
Spatial reserves
Siting region
Top host rock
Provisional disposal area
Spatial reserves
Siting region
Overdeepened areas
Spatial reserves
Siting region (with median)
Expected range of future fluvial incision
5% - 95% percentile
Mode

Fig. 6-48: Schematic diagram summarising the long-term geological evolution of the NL site

The diagram summarises the elements that describe the expected long-term geological evolution over the next one million years for the NL site. The panel on the left-hand side shows the present-day site-specific constraints extracted from the cross-section in Fig. 6-27 between Fisibach and Töss and a simplified depth profile with boxplots highlighting the distributions of host rock, local topography and glacial overdeepenings within the siting region, the spatial reserves and the location of the provisional disposal area. The local erosion base (LEB) constitutes the reference for the depicted present-day elevations and the future evolution. As a result of long-term rock uplift, modified by transient climate effects, the local erosion base will be lowered by fluvial incision (orange boxes in panel on right-hand side, see mode for the most likely values of fluvial incision). Potential incision pathways are possible during the one million years (e.g. a or b), others are less likely but shown nevertheless because they provide potential calculation cases to show the robustness of the site safety (e.g. c and d). Phases of glacial erosion with potential overdeepening are also highlighted in this upper right panel. Such phases of glacial erosion are coupled to large future foreland glaciations, as depicted by the dark-green bars in the panel "Climate evolution". Note that glacial overdeepening is not shown in the erosion plot below (see Fig. 6-44 for full remaining overburden, including glacial overdeepening). Glacial conditions and permafrost, however, are expected to occur in semi-regular intervals. The timings delineated here correspond to the 500 PgC scenario of future climate models. The panel "Future tectonic evolution" also highlights a certain synchronicity with future glaciations. For instance, this can be pulses of increased rock uplift after deglaciation (rebound) or phases of enhanced fault activity by reactivation from static stress changes. In general, however, fault reactivation along pre-existing structures might occur at any time within the one million years, and the increased rock uplift is expected to balance out over the long time period. The climate and tectonic triggers may alter the hydrogeological conditions (blue bottom panel). Accordingly, such changes might occur synchronously with the phases at and shortly after glaciations.

7 Conclusions

7.1 Developments of the knowledge base and key learnings compared to previous investigation phases

In the following, the development of the database and the process understanding gained since previous studies for the demonstration of disposal feasibility for high-level waste (Nagra 2002) and the more recent documentation of Stage 2 of the siting process (Nagra 2014h) are discussed with regard to specific topics relevant for post-closure safety.

The following list describes the evolution of the database and the system understanding compared to the reference studies mentioned above. Aspects that were confirmed by the new data and studies are indicated with a green checkmark (✓). Significant changes (geological situation, concepts and parameters) compared to the earlier investigation phases are indicated with a red exclamation mark (!).

- ✓ **The Opalinus Clay host rock:** Compared to the reference studies mentioned above, the database has been substantially expanded (Fig. 2-3). Key barrier properties and processes have been substantiated. The site-specific datasets also confirmed that only minor differences exist between the siting regions, as expected in SGT Stage 2.
  - ✓ Drilled host rock thicknesses are in the expected range (~ 100 – 120 m). ► *Section 4.2.6*
  - ✓ The lithological variability is small compared to other Mesozoic formations of Northern Switzerland, and the general sequence of subfacies trends can be correlated over all boreholes. A new and consistent subfacies scheme was developed, linking the observed subtle variations and trends to the depositional environment and its temporal evolution. ► *Section 4.2.6*
  - ✓ The vastly extended database confirms the mineralogical composition with consistently high clay-mineral content and a small lateral variability in all the siting regions. ► *Section 5.2.3*
  - ✓ Porosity shows only a slight depth dependency and only minor differences between the different siting regions. ► *Section 5.3.2*
  - ✓ The extended database allows for an improved understanding of the relationship between lithology, mineralogical composition, porosity and pore-space architecture. ► *Sections 5.3.3, 5.3.4*
  - ✓ The degree of tectonic deformation in the Opalinus Clay is low, with the majority of recovered drill cores free of any natural discontinuity. ► *Sections 4.3.4 and 5.5.4*
  - ! The geomechanical properties of the Opalinus Clay were constrained based on a large number of triaxial tests. Compared to previous campaigns, new testing protocols have been established and their robustness was demonstrated before the deep borehole (TBO) campaign. The intact strength of the Opalinus Clay was found to be significantly higher than estimated in SGT Stage 2, and post-peak strength (relevant for faulted Opalinus Clay) is approximately comparable with previous estimates. No relevant differences were observed with current depth or between siting regions. ► *Section 5.5.3*

- ! Many new microhydraulic fracturing tests and additional sleeve reopening tests have significantly improved the database on stress magnitudes in the Opalinus Clay. The results demonstrate a comparatively stable gradient between the minimum (S_{hmin}) and maximum (S_{Hmax}) horizontal stress with depth, irrespective of the siting region. Whereas in earlier studies, the dominant stress regime was assumed to be strike-slip faulting across all three siting regions ($S_{Hmax} > S_v$ and $S_{hmin} \approx S_v$, where S_v is the vertical stress), the dominant stress regime in the Opalinus Clay is now found to be normal faulting in NL ($S_v > S_{Hmax} > S_{hmin}$), and normal faulting to strike-slip faulting in ZNO and JO. The average of all three principal stress magnitudes (mean stress) is lower than estimated in SGT Stage 2. ► *Section 4.4.4*
- ✓ The high self-sealing potential of the Opalinus Clay was confirmed by laboratory and field tests and can be related to its consistently high clay-mineral content in combination with a minimum effective stress greater than 2 to 3 MPa. Special hydrotests in the RHE1 borehole have reaffirmed the conceptual and quantitative understanding of the role of effective stress in self-sealing and directly demonstrated a rapid reduction of transmissivity when injection was stopped. The test results also provide additional confidence that experience with self-sealing from the Mont Terri rock laboratory can be transferred to the siting regions. ► *Sections 5.7.2, 5.7.4*
- ✓ Numerous laboratory and hydraulic packer tests confirm the very low hydraulic conductivities of both undisturbed and fractured Opalinus Clay. ► *Sections 5.6.2, 5.6.3*
- ✓ Long-term monitoring systems installed in new boreholes show subhydrostatic hydraulic heads, i.e. fluid underpressures, in the Opalinus Clay, compared to the values in the over- and underlying aquifers. This observation is consistent with the long-term trend in the Benken borehole and confirms the very low hydraulic conductivities. ► *Section 5.6.5*
- ✓ A substantial number of laboratory measurements extended the database on diffusion properties and allowed an improved understanding of the influence of the clay-mineral content and ionic strength (salinity) of the porewater on diffusive transport. ► *Sections 5.4.2, 5.8.2*
- ! Porewater investigations based on dense and complementary datasets, including a substantial number of analyses based on direct sampling techniques (squeezing, advective displacement), improved the porewater model and demonstrated site-specific differences. These feed into the parametrisation for radionuclide transport (diffusion and sorption). ► *Section 5.4*

- ! **Confining units:** An important aim of the investigation campaign addressed the characterisation of the confining units across the siting regions. Key issues were resolved, and new insights were gained with the SGT Stage 3 campaign:
  - ! Lower confining units – Staffelegg Formation: In SGT Stage 2, the Beggingen Member was treated as a potential release path for radionuclides. In contrast, the intensive hydrogeological investigation programme showed only slightly elevated hydraulic conductivities, including in fractured intervals. ► *Section 4.5.3.9*
  - ✓ Lower confining units – upper Klettgau Formation: The investigations confirmed that the Gruhalde Member in the upper part of the Klettgau Formation is characterised by low hydraulic conductivities in all the siting regions. The central and lower parts of the Klettgau Formation are more variable (see next point). ► *Sections 4.5.3.9, 4.5.3.10*

- ! Lower confining units – downward delimitation: The lower confining units are bounded by the Keuper aquifer in all the siting regions. This local aquifer is internally complex and comprises three units, which may act as potential flow paths. These are (from top to bottom): Seebi Member, Gansingen Member and Ergolz Member. Facies, thickness and hydrogeological relevance of these units vary across the three siting regions. Their site-specific significance is better captured by the new boreholes. Consequently, the downward delimitation of the lower confining units is site-specifically tied to the uppermost unit with hydrogeological significance. In ZNO, the investigations confirmed the existence of a laterally continuous active Keuper aquifer in the Seebi Member, as suspected in SGT Stage 2. In Nagra (2002), the Keuper Group below the Seebi Member was treated as potentially part of the lower confining units – this is not supported by the new data. In JO, the new data point towards a laterally continuous Keuper aquifer related to the Gansingen Member. In NL, the enhanced hydraulic conductivities are limited to locally occurring sandstone channels of the Ergolz Member. ► *Sections 4.2.4, 4.5.3.10*
- ! Lower confining units – potential contribution of the units below the Keuper aquifer to the barrier function in NL: The new investigations indicated that potential flow paths in the Keuper aquifer in NL relate to locally occurring sandstone channels of the Ergolz Member. Where these sandstone channels are absent or isolated, the underlying rocks (clay-mineral- and anhydrite-rich Bänkerjoch Formation) may act as an additional transport barrier. ► *Sections 4.2.4, 4.5.3.10, 4.5.3.11*
- ! Upper confining units – clay-mineral content of units directly overlying the Opalinus Clay: The new investigations show that the Dogger Group directly above the Opalinus Clay is more clay-mineral-rich and contains fewer "hard beds" below the «Herrenwis Unit» in NL compared to JO and ZNO. The corresponding thick stack of clay-mineral-rich deposits in the eastern part of NL is interpreted to be the result of sediment accumulation by bottom currents. ► *Section 4.2.7*
- ! Upper confining units – hydraulic significance of "hard beds" in the Wedelsandstein and Passwang Formations: In SGT Stage 2, the "hard beds" were treated as potential water-conducting features (i.e. potential release paths for radionuclides). The focused investigation programme did not indicate any elevated hydraulic conductivity. ► *Sections 4.5.3.2, 4.5.3.5, 4.6*
- ! Upper confining units – «Herrenwis Unit»: The anomalous seismic facies detected on 2D seismic lines in NL in SGT Stage 2 was identified as an isolated carbonate platform, which is now designated as the «Herrenwis Unit». This platform developed on top of the positive relief formed by the directly underlying argillaceous units, which is probably the result of bottom currents (see above). On top of this swell, the conditions for coral growth were more favourable in comparison to the surrounding areas. Hydrogeological observations in the «Herrenwis Unit», and the fact that it is embedded in clay-mineral-rich units, indicate that it does not provide a relevant flow path connected to the biosphere. ► *Sections 4.2.7, 4.5.3.7, 4.6*

- ! **Independent evidence for slow transport from natural tracers in porewater and hydrogeochemistry of groundwater in deep aquifers:** The database was substantially expanded. This relates not only to the number of investigated boreholes but also to the significantly enhanced vertical resolution of data and to important analytical progress (e.g. ^{81}Kr dating of groundwater) and the improved and more integrated data analyses and interpretation:
  - ! Porewater tracers were investigated in all new boreholes and complement the hydrogeological dataset of the aquitard units. The profiles of the natural tracers indicate differences in the thickness of the zone dominated by diffusive transport. ► *Section 4.6*

- ! In combination with the hydrogeochemistry of the deep groundwaters, including the ^{81}Kr model ages (the first application of this method in Northern Switzerland), tracer profiles contain crucial information about the mechanisms and rates of transport in the aquifer – aquitard system over geological timescales. The availability of numerous tracer profiles across the siting regions allows the identification of regional trends and differences in the palaeohydrogeological evolution. In a plot of $\delta^{18}O$ vs. $\delta^{2}H$, all porewaters of the Opalinus Clay plot on the right side of the Global Meteoric Water Line. The shift away from the Global Meteoric Water Line is largest at NL, indicating a particularly large component of old porewater in this siting region and a lower influence by meteoric components. The differences in the overall shapes of the tracer profiles between the siting regions are mainly related to the presence/absence of the Keuper aquifer, the hydrogeochemical composition of the groundwater in the upper bounding aquifers (Hauptrogenstein, Malm) and the duration of the diffusive interaction, which differs for each aquifer between the siting regions. Overall, this indicates that the most stable conditions of the aquitard – aquifer system are found in NL compared to ZNO and, even more so, compared to JO. ► *Sections 4.5.6, 4.6*
- ! Groundwater from the Malm aquifer in NL is characterised by a uniform composition of stable water isotopes, showing a substantial shift to the right of the Global Meteoric Water Line. The shift is more pronounced than was previously known from boreholes in Northern Switzerland. The large dataset including ^{81}Kr model ages now makes it possible to robustly substantiate earlier hypotheses regarding a marine component in the Malm groundwater and to obtain quantitative constraints on groundwater residence times. These waters characterise a quasi-stagnant flow field. In comparison, the data from the northwestern part of ZNO evidence a more active flow system with markedly younger ^{81}Kr model ages. ► *Sections 4.5.5.2, 4.5.6*
- ✓ The hydraulic activity of the Hauptrogenstein and its classification as a deep aquifer was confirmed by the investigations in the BOZ2 borehole. The base of the Hauptrogenstein is thus regarded as the upper bound of the low-permeability confining units in JO. As expected from the Riniken borehole, the thickness of the Hauptrogenstein decreases eastwards. ► *Sections 4.2.7, 4.5.3.6, 4.5.6*
- ! Groundwater samples from the Keuper aquifer are characterised by contrasting chemical types and a large range of residence times. This reflects the variable hydraulic properties (a lithologically complex aquifer), which were expected. As a result of the new lithological and hydraulic data, the differences between the siting regions could be better captured (see point above discussing the lower confining units). Groundwater geochemistry and ^{81}Kr model ages provided further quantitative information on the activity of this flow system. The hydrogeochemical dataset supported by lithological arguments points to a quasi-stagnant flow system in NL. ► *Sections 4.5.5.4, 4.5.6*
- ✓ As expected from previous studies, the most active flow system was observed in the Muschelkalk aquifer. The cold-climate isotopic signature known from earlier boreholes was confirmed for the ZNO and NL siting regions. The trends in hydrogeochemical composition and residence times agree with the flow paths from the hydrogeological model. ► *Sections 4.5.4.5, 4.5.5.5, 4.5.6*

- ! **Tectonic setting and fault pattern**: Compared to previous phases, the structural geological knowledge base was substantially expanded, including 3D seismic reflection surveys in all the siting regions and investigations in numerous boreholes. Generally, the previously established tectonic concepts were confirmed. However, differences among the siting regions could be established:
  - ! Coherent, comparable and consistent seismic processing and interpretation allowed a detailed and robust comparison of the fault inventory in the three siting regions at the seismic scale. Differences between the siting regions were demonstrated and integrated into the larger-scale tectonic framework. In JO, an extended zone with increased faulting occurs in the Top Muschelkalk Group in the southeastern corner (the "Brugg Strukturzone"). In NL, deformation in the Mesozoic strata is focused above structures related to the Konstanz – Frick Trough, leaving a large area free of seismically mappable faults in-between. In ZNO, the nearby transtensional Hegau – Bodensee Graben predominantly controls the structural inventory, resulting in a higher number of seismically mappable faults compared to JO and NL. ► *Section 4.3.4*
  - ✓ Extensive age dating of calcite cements associated with regional fault zones supports a main orogenic phase of the eastern Jura Fold-and-Thrust Belt between 14 and ~ 8 Ma. This new quantitative dataset acquired in Northern Switzerland is consistent with earlier understanding about the timing of folding and thrusting in the Jura. ► *Section 4.3.5*
  - ✓ Seismic interpretation confirmed the influence of inherited faults (e.g. faults related to the Konstanz – Frick Trough) on subsequent strain localisation. This indicates that future deformation is likely to preferentially occur along inherited faults (i.e. zones of weakness) rather than as new faults. ► *Sections 4.3.4, 4.3.6*
  - ✓ Stress indicators in the new boreholes confirmed the dominant present-day orientation of the maximum horizontal stress from SGT Stage 2, i.e. a NNW-SSE direction, approximately perpendicular to the Jura Fold-and-Thrust Belt. ► *Section 4.4.2*
  - ! The degree of fracturing in the Opalinus Clay is lower compared to over- and underlying formations in all the siting regions. All recent boreholes show no evidence for any secondary décollement within the Opalinus Clay. ► *Sections 4.3.4, 4.3.6, 4.3.7, 5.5.4*
- ! **Long-term geological evolution:** Compared to earlier phases of investigations, the database and process understanding have been substantially expanded. Furthermore, the uncertainties related to future erosion have been addressed using a hybrid-probabilistic approach.
  - ✓ The acquired hydraulic data confirm previous understanding that a residual overburden thickness of 200 m can be considered reliable for efficient self-sealing in the Opalinus Clay (see above). Moreover, dedicated investigations in the shallow Lausen borehole demonstrated that a significant increase in hydraulic conductivity of exhumed Opalinus Clay is limited to the uppermost 20 to 30 m and showed that the increase is associated with exhumation-related fracturing and a marked increase in porosity. ► *Sections 5.6.3, 5.7.2, 5.7.4, 6.5.2 and 6.5.3*
  - ! The timing of past fluvial incision during the Early Pleistocene was refined with an extensive dating campaign using multiple geochronometers. The new data indicate a possibly younger age of the Höhere Deckenschotter and thus later fluvial incision after Deckenschotter deposition than previously assumed. ► *Section 6.4.1.2*
  - ! The timing of glacial overdeepening and the filling history was also substantially refined by dating the sediments from the drill cores. Several new ages reveal that part of the overdeepening formation is older than previously suggested, i.e. older than Marine Isotope Stage 6. ► *Section 6.4.1.4*

- ✓ The depth of glacial overdeepening in Northern Switzerland was substantiated by 2D seismic data and drilling. The maximum depth remained in the expected range. The new data from the lower Aare Valley confirm the previous assumption that bedrock type exerts a strong influence on incision depth. ► *Section 6.4.1.4*
- ! The uncertainties related to future erosion have been addressed using a hybrid-probabilistic approach allowing for a quantitative estimate of future erosion, including uncertainties. In the previous assessment deterministic cases (plausible, optimistic, pessimistic) were derived based on the evaluation of the Quaternary past. The new concept covers a broader range of evolutions and evaluates the remaining repository overburden thickness over the periods under consideration in a probabilistic way. It shows that repository excavation during the period under consideration is extremely unlikely. ► *Sections 6.4.3, 6.4.4*
- ✓ The densified seismic monitoring network seamlessly records all seismic events with a magnitude > 1 in Northern Switzerland and allows improved location of hypocentres, and in turn an improved understanding of regional seismotectonic activity. For example, it is possible to associate a sequence of micro-earthquakes occurring between 2014 and 2019 to the Neuhausen Fault, previously known from outcrop mapping and reflection seismic data. This and other micro-earthquake sequences further to the east confirm ongoing tectonic activity in the Hegau – Bodensee Graben system. ► *Section 6.2.3*
- ✓ The extended observation period of global navigation satellite system permanent stations provides an improved quantification of recent deformation and confirms that present-day horizontal motion in Northern Switzerland is small. ► *Section 6.2.3*

7.2 Overall conclusions regarding site comparison and demonstration of post-closure safety

The Opalinus Clay represents an excellent natural transport barrier and provides favourable geochemical conditions for the stability of the engineered barriers

In Northern Switzerland, the Opalinus Clay lies in a tectonically stable, large area with low uplift and deformation rates and limited structural complexity.

The thickness of the Opalinus Clay in the three siting regions is comparable, ranging between about 100 and 120 m. The variability of properties is low, and the clay-mineral content is high (usually well above 40 wt-%). This results from the specific depositional environment of the Opalinus Clay, a shallow epicontinental sea with a high influx of clay-rich sediments.

Hydraulic packer tests conducted in the deep boreholes and analyses on laboratory samples show a very low hydraulic conductivity, which can be attributed to the high clay-mineral content. There is no evidence of significant preferential flow paths in the Opalinus Clay. This is explained by the partitioning of deformation in the comparatively soft rock in combination with the high self-sealing capacity.

The high clay-mineral content of the Opalinus Clay also leads to a high sorption capacity and thus to a low mobility of most radionuclides. Regarding the stability of the engineered barriers, the geochemical conditions are reducing, the pH neutral and salinity is moderate. These conditions are very stable as a result of the efficient buffering provided by the mineralogy of the host rock.

Low-permeability confining units above and below the host rock contribute to the barrier function; the overall thickness of the aquitard sequence is greatest in NL

In all the siting regions, the Opalinus Clay is bounded above and below by low-permeability confining units. These exhibit greater variability than the Opalinus Clay and contain thin layers (< few metres) with a low clay-mineral content (hard beds). Evidence from the deep boreholes shows that the hard beds do not represent continuous flow paths. Also, a several-decametre-thick biohermal limestone («Herrenwis Unit») occurring in the eastern part of the NL siting region is part of the aquitard series around the host rock. This is evidenced by the findings in the deep boreholes (low hydraulic permeability and fluid underpressures) and is supported by the fact that the unit is embedded in clay-rich rocks.

In NL and ZNO the low-permeability confining rock units are bounded at the top by the Malm aquifer and in JO by the Hauptrogenstein aquifer. The distance between the centre of the Opalinus Clay and the overlying aquifer is greatest in NL and smallest in JO.

The next regional aquifer below the host rock is represented by the Muschelkalk aquifer, which represents the most active deep groundwater system in all the siting regions. Between the Opalinus Clay and the Muschelkalk aquifer, the local, internally complex Keuper aquifer defines the bottom of the low-permeability confining units. The distance between this and the centre of the Opalinus Clay is comparable in all three siting regions

In contrast to the other siting regions, the enhanced permeability zones in the Keuper Group in NL are limited to sandstone channels. These are found on a local scale only and their connectivity is assumed to be limited. Where sandstone channels are absent or are hydraulically isolated, the underlying units down to the Muschelkalk aquifer also contribute to the barrier function.

Independent evidence demonstrates the effective barrier function of the host rock and confining rock units over long time periods in the past; the hydrogeological situation is the most stable in NL

The slow, diffusion-dominated transport processes in the host rock and confining rock units are supported by various independent lines of evidence. The four long-term hydraulic monitoring systems installed in deep boreholes in the Opalinus Clay indicate underpressures, which are considered a transient phenomenon caused by a vertical stress decrease in response to the melting of glacial ice and/or to erosion. The long-term preservation of these underpressures can only be explained by very low hydraulic conductivities, which prevent fast pore pressure re-equilibration.

A second important independent line of evidence for the very low hydraulic permeabilities is the chemical and isotopic composition of the porewaters. The change in the composition across the host rock, low-permeability confining units and neighbouring aquifers is the result of transport processes that took place over the last $10^4 – 10^7$ years. The shape of these profiles of natural tracers in the porewater can best be explained in all the siting regions by very slow mass transport, dominated by molecular diffusion, in the host rock and in the neighbouring confining rock units.

The availability of numerous tracer profiles in all the siting regions allow the identification of regional trends and differences in palaeohydrogeological evolution. Comparing the stable water isotope composition ($\delta^{18}O$ values vs. $\delta^{2}H$ values), it can be shown that, in NL, the Opalinus Clay porewater has a comparatively large proportion of old porewater and is less affected by meteoric waters. Overall, the chemical composition of the porewaters of the host rock and the confining rock units as well as the composition and residence times of the groundwaters (^{81}Kr model age) from the neighbouring deep aquifers indicate that the aquitard – aquifer system in NL provides the most stable conditions.

With regard to the placement of a deep geological repository, all the siting regions include areas without seismically mappable faults; in NL, this area is largest

The fault pattern was mapped in detail using 3D seismic reflection data. All three siting regions show areas with no seismically mappable faults, offering flexibility in the location and design of the repository. The greatest flexibility is offered by NL, where clearly defined regional fault zones bounding the area to the north and south absorbed a large proportion of the deformation in the past. Furthermore, the influence of the Internal Jura is smaller in NL compared to the JO siting region lying further to the west, and the Hegau – Bodensee Graben has less impact on NL than on ZNO.

In the period under consideration, climatic and geodynamic processes have no relevant impact on the barrier function of the host rock and confining rock units; protection against future erosion is greatest in NL

The recent tectonic deformation rates in Northern Switzerland are low. This is expected to be the case for the next one million years. As in the past, future deformation will be preferentially located at larger-scale faults. These have been mapped using 3D seismic reflection data and will be taken into account when planning the location of the disposal areas. Subseismic faults and potential new faults in the Opalinus Clay are expected to be segmented and short in length and offset. The deformation and swelling behaviour of the Opalinus Clay also ensure reliable self-sealing of tectonic faults in the case of a rock overburden thickness > 200 m.

As in the more recent geological past, the climate is expected to go through glacial/interglacial cycles. However, because of anthropogenic CO_2 emissions, the next major glaciation of the Alpine Foreland may not be expected for at least 200'000 years. Future erosion rates are likely to be comparable to the rates observed over the last 1 – 2 million years. The erosion rates will probably be even lower, as no major regional river reorganisation or smaller glaciers are expected in the next one million years. In addition, layers of limestone with low erodibility are situated above the host rock and confining geological units.

The erosion assessment shows that, with the geological evolution expected for the period under consideration, the overburden thickness will remain large enough to ensure robust self-sealing within the Opalinus Clay. Regarding less likely erosive events, the NL siting region is the most robust, particularly because of the greater depth of the repository. JO is the least robust, especially towards possible future local river diversions.

The argumentation is robust and relevant uncertainties are captured

The improved knowledge of the geological barrier in the three siting regions is based on comprehensive field investigations and laboratory studies using data from around 200 km^2 of 3D seismic reflection surveys and nine new deep boreholes. A supplementary investigation programme served to reconstruct erosion over the past 1 – 2 million years with the objective of specifying potential future scenarios.

Uncertainties associated with the 3D seismic reflection data and its interpretation were captured by the use and comparison of different seismic processing vintages and by superimposing interpretations from different interpreters. A reference processing product with consistent workflows and processing input parameters across the siting regions and a rigorously structured interpretation approach applying established criteria ensured comparability among the siting regions.

To ensure a robust database and argumentation, key properties were measured with high frequency in multiple boreholes per siting region. Where available, multiple independent analytical and experimental approaches were applied and compared. The borehole measurements carried out at different scales and with different methods are consistent. The results of the

laboratory and downhole measurements are consistent with the tunnel-scale observations at the Mont Terri rock laboratory and in other tunnels. Conceptual models to explain the observed relationships between key parameters are in place. The observations and key processes suggested for the Opalinus Clay are consistent with international experience from research on clay-rich rocks.

Scenarios for the future long-term geological evolution are based on knowledge of past geological evolution, but, where appropriate, also consider process understanding and rates derived from other areas. The climate scenarios include both a natural evolution as well as a number of scenarios with different anthropogenic CO_2 emissions. To address the particularly large uncertainties of future erosion, a newly developed hybrid-probabilistic method was used, allowing a robust assessment.

With regard to the post-closure safety assessment, a reference long-term geological evolution is described. In addition, the erosion assessment includes the results of less likely evolutions. For numerical analyses of the post-closure safety, parameter bandwidths taking into account uncertainties are specified in a separate report (Nagra 2024m).

In summary, the significantly expanded knowledge base confirmed the safety-relevant properties of the Opalinus Clay and its long-term stability, which had already been shown in earlier stages of the siting process. Furthermore, it demonstrates key differences between the siting regions. The main conclusions are supported by multiple lines of arguments. Important results and lines of argumentation were reviewed by recognised experts from various specialist areas. Remaining uncertainties are captured and are treated further in the post-closure safety assessment.

8 References

Adams, A. & Diamond, L.W. (2017): Early diagenesis driven by widespread meteoric infiltration of a Central European carbonate ramp: A reinterpretation of the Upper Muschelkalk. Sedimentary Geology 362, 37-52. DOI: 10.1016/j.sedgeo.2017.10.002.

Adams, A. & Diamond, L.W. (2019): Facies and depositional environments of the Upper Muschelkalk (Schinznach Formation, Middle Triassic) in northern Switzerland. Swiss Journal of Geosciences 112/2, 357-381. DOI: 10.1007/s00015-019-00340-7.

Adams, A., Diamond, L.W. & Aschwanden, L. (2019): Dolomitization by hypersaline reflux into dense groundwaters as revealed by vertical trends in strontium and oxygen isotopes: Upper Muschelkalk, Switzerland. Sedimentology 66, 362-390. DOI: 10.1111/sed.12530.

Affolter, T. & Gratier, J.-P. (2004): Map view retrodeformation of an arcuate fold-and-thrust belt: The Jura case. Journal of Geophysical Research 109, B03404.

Ahn, S., Khider, D., Lisiecki, L.E. & Lawrence, C.E. (2017): A probabilistic Pliocene–Pleistocene stack of benthic $\delta^{18}O$ using a profile hidden Markov model. Dynamics and Statistics of the Climate System 2/1, dzx002. DOI: 10.1093/climsys/dzx002.

Aigner, T. & Reineck, H.-E. (1982): Proximality trends in modern storm sands from the Heligoland Bight (North Sea) and their implications for basin analysis. Senckenbergiana Maritima 14/5-6, 183-215.

Ait Addi, A. (2015): Builders and taphonomic processes of Bajocian coral patch reefs in the Moroccan Central High Atlas. Arabian Journal of Geosciences 8/10, 8583-8600. DOI: 10.1007/s12517-015-1796-5.

Akker, I.V., Schneeberger, R., Herwegh, M., Looser, N., Aschwanden, L., Mazurek, M., Decker, K., Ebert, A., Guillong, M., Bernasconi, S.M., Schrank, C., Jones, M.W.M., Langendam, A. & Madritsch, H. (2023): Microstructural characterization of natural fractures and faults in the Opalinus Clay: insights from a deep drilling campaign across central northern Switzerland. Swiss Journal of Geosciences 116/1, 1-28, 8. DOI: 10.1186/s00015-023-00438-z.

Albert, W., Bläsi, H.R., Madritsch, H., Vogt, T. & Weber, H.P. (2012): Geologie, Stratigraphie, Strukturgeologie, bohrlochgeophysikalisches Logging und Wasserproben der Geothermiebohrung Schlattingen SLA-1 (Rohdaten). Nagra Project Report NPB 12-16.

Allen, P.A., Crampton, S.L. & Sinclair, H.D. (1991): The inception and early evolution of the North Alpine Foreland Basin, Switzerland. Basin Research 3/3, 143-163. DOI: 10.1111/j.1365-2117.1991.tb00124.x.

Allenbach, R., Baumberger, R., Kurmann, E., Michael, C.S. & Reynolds, L. (2017): GeoMol: Geologisches 3D-Modell des Schweizer Molassebeckens – Schlussbericht. (Berichte der Landesgeologie, 10). Bundesamt für Landestopographie swisstopo, Wabern.

Allenbach, R.P. (2001): Synsedimentary tectonics in an epicontinental sea: A new interpretation of the Oxfordian basins of northern Switzerland. Eclogae Geologicae Helvetiae 94/3, 265-287.

Allenbach, R.P. (2002): The ups and downs of "Tectonic Quiescence" — recognizing differential subsidence in the epicontinental sea of the Oxfordian in the Swiss Jura Mountains. Sedimentary Geology 150, 323-342.

Allia, V. (1996): Sedimentologie und Ablagerungsgeschichte des Opalinustons in der Nordschweiz. (Dissertationen aus dem Geologisch-Paläontologischen Institut der Universität Basel, Nr. 10). Universität Basel.

Altmann, S., Tournassat, C., Goutelard, F., Parneix, J.-C., Gimmi, T. & Maes, N. (2012): Diffusion-driven transport in clayrock formations. Applied Geochemistry 27/2, 463-478. DOI: 10.1016/j.apgeochem.2011.09.015.

Amschwand, D., Huber, M.L., Madritsch, H., Deplazes, G. & Buechi, M.W. (2020): Quaternary Borehole QBO Hochfelden-Strassberg (QHST) Data Report. Nagra Arbeitsbericht NAB 20-02.

Amsler, A. (1915): Tektonik des Staffelegg-Gebietes und Betrachtungen über Bau und Entstehung des Jura-Ostendes. Eclogae Geologicae Helvetiae 13/4, 377-488.

Anselmetti, F.S., Drescher-Schneider, R., Furrer, H., Graf, H.R., Lowick, S.E., Preusser, F. & Riedi, M.A. (2010): A ~180,000 years sedimentation history of a perialpine overdeepened glacial trough (Wehntal, N-Switzerland). Swiss Journal of Geosciences 103/3, 345-361. DOI: 10.1007/s00015-010-0041-1.

Antoniazza, G. & Lane, S.N. (2021): Sediment yield over glacial cycles: A conceptual model. Progress in Physical Geography: Earth and Environment 45/6, 842-865. DOI: 10.1177/0309133321997292.

Appelo, C.A.J. & Van Loon, L.R. (2008): Long-term diffusion (DI-A) experiment: Modeling of Cs-data from diffusion experiments in the laboratory and in situ in DI-A experiments (phase 12) in Opalinus Clay. Part 1: Modeling laboratory data. Part 2: Modeling the DI-A1 experiment. Part 3: Modeling the DI-A2 experiment. Unpubl. Mont Terri Technical Note. Mont Terri Project, Switzerland.

Appelo, C.A.J., Van Loon, L.R. & Wersin, P. (2010): Multicomponent diffusion of a suite of tracers (HTO, Cl, Br, I, Na, Sr, Cs) in a single sample of Opalinus Clay. Geochimica et Cosmochimica Acta 74/4, 1201-1219. DOI: 10.1016/j.gca.2009.11.013.

Aschwanden, L., Diamond, L.W. & Adams, A. (2019a): Effects of progressive burial on matrix porosity and permeability of dolostones in the foreland basin of the Alpine Orogen, Switzerland. Marine and Petroleum Geology 100, 148-164. DOI: 10.1016/j.marpetgeo.2018.10.055.

Aschwanden, L., Diamond, L.W., Adams, A. & Mazurek, M. (2017): Anhydrite-dissolution Porosity in the Upper Muschelkalk Carbonate Aquifer, NE-Switzerland: Implications for Geothermal Energy and Geological Storage of Gas. Procedia Earth and Planetary Science 17, 897-900. DOI: 10.1016/j.proeps.2017.01.011.

Aschwanden, L., Diamond, L.W., Mazurek, M. & Davis, D.W. (2019b): Creation of Secondary Porosity in Dolostones by Upwelling Basement Water in the Foreland of the Alpine Orogen. Geofluids 2019, 1-23. DOI: 10.1155/2019/5210404.

Aschwanden, L., Waber, H.N., Eichinger, F. & Gimmi, T. (2024): Isotope diffusive exchange experiments for deriving porewater isotope composition in low-permeability rocks – Improvements in experimental procedure and data processing. Applied Geochemistry 160, 105844. DOI: 10.1016/j.apgeochem.2023.105844.

Baeyens, B. & Fernandes, M.M. (2022): Determination of the Cation Exchange Capacities and Exchangeable Cations of deep Drilling Core Samples from the Siting Regions Jura Ost, Nördlich Lägern and Zürich Nordost. Nagra Arbeitsbericht NAB 21-01.

Bakun, W.H. & Scotti, O. (2006): Regional intensity attenuation models for France and the estimation of magnitude and location of historical earthquakes. Geophysical Journal International 164/3, 596-610. DOI: 10.1111/j.1365-246X.2005.02808.x.

Balderer, W. (1990): Hydrogeologische Characterisierung der Grundwasservorkommen innerhalb der Molasse der Nordostschweiz aufgrund von hydrochemischen und Isotopenuntersuchungen. Steirische Beiträge zur Hydrogeologie 41, 35-104.

Ballentine, C.J., Burgess, R. & Marty, B. (2002): Tracing fluid origin, transport and interaction in the crust. Reviews in Mineralogy and Geochemistry 47/1, 539-614. DOI: 10.2138/rmg.2002.47.13.

Ballentine, C.J. & Burnard, P.G. (2002): Production, release and transport of noble gases in the continental crust. Reviews in Mineralogy and Geochemistry 47/1, 481-538. DOI: 10.2138/rmg.2002.47.12.

Baltzer, A. (1876): Der Erdschlipf von Böttstein. Vierteljahrsschrift der Naturforschenden Gesellschaft in Zürich 21/3, 285-290.

Bamber, J.L., Oppenheimer, M., Kopp, R.E., Aspinall, W.P. & Cooke, R.M. (2019): Ice sheet contributions to future sea-level rise from structured expert judgment. Proceedings of the National Academy of Sciences 116/23, 11195-11200. DOI: 10.1073/pnas.1817205116.

Bandou, D., Schlunegger, F., Kissling, E., Marti, U., Reber, R. & Pfander, J. (2023): Overdeepenings in the Swiss plateau: U-shaped geometries underlain by inner gorges. Swiss Journal of Geosciences 116/1, 19. DOI: 10.1186/s00015-023-00447-y.

Barakat, Y., Mokni, N., Cui, Y.-J. & Bernier, F. (2024): Effects of Salinity and Alkalinity on the Volumetric Deformation of the Opalinus Clay from the Lower Sandy Facies (LSF) of Mont Terri Site. Rock Mechanics and Rock Engineering. DOI: 10.1007/s00603-024-04028-9.

Barrett, E.P., Joyner, L.G. & Halenda, P.P. (1951): The determination of pore volume and area distributions in porous substances. I. Computations from nitrogen isotherms. Journal of the American Chemical Society 73/1, 373-380. DOI: 10.1021/ja01145a126.

Barron, A.J.M., Lott, G.K. & Riding, J.B. (2012): Stratigraphical framework for the Middle Jurassic strata of Great Britain and the adjoining continental shelf. British Geological Survey Research Report RR/11/06, Keyworth, Nottingham.

Beaucaire, C., Tertre, E., Ferrage, E., Grenut, B., Pronier, S. & Madé, B. (2012): A thermodynamic model for the prediction of pore water composition of clayey rock at 25 and 80 ºC – comparison with results from hydrothermal alteration experiments. Chemical Geology 334, 62-76. DOI: 10.1016/j.chemgeo.2012.09.040.

Beauheim, R.L. (2013): Hydraulic conductivity and head distributions in the host rock formations of the proposed siting regions. Nagra Arbeitsbericht NAB 13-13.

Beck, H.E., Zimmermann, N.E., McVicar, T.R., Vergopolan, N., Berg, A. & Wood, E.F. (2018): Present and future Köppen-Geiger climate classification maps at 1-km resolution. Scientific data 5, 180214. DOI: 10.1038/sdata.2018.214.

Becker, A. (2000): Der Faltenjura: geologischer Rahmen, Bau und Entwicklung seit dem Miozän. Jahresberichte und Mitteilungen des Oberrheinischen Geologischen Vereins. Neue Folge 82, 317-336. DOI: 10.1127/jmogv/82/2000/317.

Becker, A., Ammann, B., Anselmetti, F.S., Hirt, A.M., Magny, M., Millet, L., Rachoud, A.-M., Sampietro, G. & Wüthrich, C. (2006): Paleoenvironmental studies on Lake Bergsee, Black Forest, Germany. Neues Jahrbuch für Geologie und Paläontologie - Abhandlungen 240/3, 405-445. DOI: 10.1127/njgpa/240/2006/405.

Becker, J. & Marnat, S. (2024): Petrophysical Data and Core-Calibrated Multimineral Interpretation. Nagra Arbeitsbericht NAB 24-17.

Becker, J.K. & Vogt, T. (2020): WS-I Experiment: Investigation of wet spots. Mont Terri Technical Report TR 12-19. Mont Terri Project, Switzerland.

Bennett, M.R. & Glasser, N.F. (2009): Glacial Geology. Ice Sheets and Landforms. 2nd Edition. John Wiley & Sons Ltd., Chichester.

Berends, C.J., Köhler, P., Lourens, L.J. & van de Wal, R.S.W. (2021): On the cause of the mid-Pleistocene transition. Reviews of Geophysics 59/2, e2020RG000727. DOI: 10.1029/2020RG000727.

Berger, A. & Loutre, M.F. (1991): Insolation values for the climate of the last 10 million years. Quaternary Science Reviews 10/4, 297-317. DOI: 10.1016/0277-3791(91)90033-Q.

Berger, A. & Loutre, M.F. (1997): Long-term variations in insolation and their effects on climate, the LLN experiments. Surveys in Geophysics 18/2/3, 147-161. DOI: 10.1023/A:1006579708292.

Berger, A.L. (1977): Support for the astronomical theory of climatic change. Nature 269/5623, 44-45. DOI: 10.1038/269044a0.

Berger, A.L. (1978): Long-Term Variations of Daily Insolation and Quaternary Climatic Changes. Journal of the Atmospheric Sciences 35/12, 2362-2367. DOI: 10.1175/1520-0469(1978)035<2362:LTVODI>2.0.CO;2.

Berger, J.-P., Reichenbacher, B., Becker, D., Grimm, M., Grimm, K., Picot, L., Storni, A., Pirkenseer, C., Derer, C. & Schaefer, A. (2005): Paleogeography of the Upper Rhine Graben (URG) and the Swiss Molasse Basin (SMB) from Eocene to Pliocene. International Journal of Earth Sciences (Geologische Rundschau) 94/4, 697-710. DOI: 10.1007/s00531-005-0475-2.

Bernasconi, S.M., Meier, I., Wohlwend, S., Brack, P., Hochuli, P.A., Bläsi, H., Wortmann, U.G. & Ramseyer, K. (2017): An evaporite-based high-resolution sulfur isotope record of Late Permian and Triassic seawater sulfate. Geochimica et Cosmochimica Acta 204, 331-349. DOI: 10.1016/j.gca.2017.01.047.

Bertleff, B. & Watzel, R. (2002): Tiefe Aquifersysteme im südwestdeutschen Molassebecken. Eine umfassende hydrogeologische Analyse als Grundlage eines zukünftigen Quantitäts – und Qualitätsmanagements. *In:* Landesamt für Geologie, Rohstoffe und Bergbau Baden-Württemberg (ed.): Hydrogeologische Untersuchungen in Baden-Württemberg – in memoriam Jörg Werner. (Abhandlungen des Landesamt für Geologie, Rohstoffe und bergbau Baden-Württemberg, 15), 75-90.

Beutler, G. (2005): Lithostratigraphie. *In:* Deutsche Stratigraphische Kommission (ed.): Stratigraphie von Deutschland IV – Keuper. (Courier Forschungsinstitut Senckenberg, 253), 65-84.

BFE (2008): Sachplan Geologische Tiefenlager: Konzeptteil. BFE 2. April 2008 (Revision vom 30. November 2011). Departement für Umwelt, Verkehr, Energie und Kommunikation UVEK, Bern.

BGE (2020): Sub-areas Interim Report pursuant to Section 13 StandAG. As per 28/09/2020. Edited by Bundesgesellschaft für Endlagerung mbH.

Bini, A., Buonchristiani, J.F., Couterand, S., Ellwanger, D., Felber, M., Florineth, D., Graf, H.R., Keller, O., Kelly, M., Schlüchter, C. & Schoeneich, P. (2009): Switzerland during the Last Glacial Maximum (LGM). Swiss Federal Office of Topography swisstopo.

Birchall, T., Senger, K. & Swarbrick, R. (2022): Naturally occurring underpressure – a global review. Petroleum Geoscience 28/2, petgeo2021-051. DOI: 10.1144/petgeo2021-051.

Birkhäuser, P., Roth, P., Meier, B. & Naef, H. (2001): 3-D Seismik: Räumliche Erkundung des mesozoischen Sedimentschichten im Zürcher Weinland. Nagra Technischer Bericht NTB 00-03.

Bitterli-Dreher, P. (2012): Die lfenthal-Formation im nördlichen Jura. Swiss Bulletin für angewandte Geologie 17/2, 93-117.

Bitterli-Dreher, P., Graf, H.R., Naef, H., Diebold, P., Matousek, F., Burger, H. & Pauli-Gabi, T. (2007): Geologischer Atlas der Schweiz. Blatt 1070 Baden mit Erläuterungen. Bundesamt für Landestopografie swisstopo.

Bläsi, H.R. (1987): Lithostratigraphie und Korrelation der Doggersedimente in den Bohrungen Weiach, Riniken und Schafisheim. Eclogae Geologicae Helvetiae 80/2, 415-430.

Bläsi, H.R., Deplazes, G., Schnellmann, M. & Traber, D. (2013): Sedimentologie und Stratigraphie des 'Braunen Doggers' und seiner westlichen Äquivalente. Nagra Arbeitsbericht NAB 12-51.

Bloom, A.L. (2018): Gorges history: landscapes and geology of the Finger Lakes Region. (Paleontological Research Institution Special Publication, 55). Paleontological Research Institution, Ithaca, NY.

Bloos, G., Dietl, G. & Schweigert, G. (2006): Der Jura Süddeutschlands in der Stratigraphischen Tabelle von Deutschland 2002. Newsletters on Stratigraphy 41/1-3, 263-277. DOI: 10.1127/0078-0421/2005/0041-0263.

Bock, H., Dehandschutter, B., Martin, C.D., Mazurek, M., de Haller, A., Skoczylas, F. & Davy, C. (2010): Self-sealing of fractures in argillaceous formations in the context of geological disposal of radioactive waste. Review and synthesis. OECD/NEA, Paris.

Bolland, A., Kern, O.A., Koutsodendris, A., Pross, J. & Heiri, O. (2022): Chironomid-inferred summer temperature development during the late Rissian glacial, Eemian interglacial and earliest Würmian glacial at Füramoos, southern Germany. Boreas 51/2, 496-516. DOI: 10.1111/bor.12567.

Bolliger, T. (ed.) (1999): Geologie des Kantons Zürich. Ott Verlag, Thun.

Bolliger, T., Engesser, B. & Weidmann, M. (1993): Première découverte de mammifères pliocènes dans le jura neuchâtelois. Eclogae Geologicae Helvetiae 86/3, 1031-1068.

Bolliger, T., Fejfar, O., Graf, H. & Kälin, D. (1996): Vorläufige Mitteilung über Funde von pliozänen Kleinsäugern aus den Höheren Deckenschottern des Irchels (Kt. Zürich). Eclogae Geologicae Helvetiae 89/3, 1043-1048.

Bonnet, C., Malavieille, J. & Mosar, J. (2007): Interactions between tectonics, erosion, and sedimentation during the recent evolution of the Alpine orogen: Analogue modeling insights. Tectonics 26/6, 2006TC002048. DOI: 10.1029/2006TC002048.

Bons, P.D., Elburg, M.A. & Gomez-Rivas, E. (2012): A review of the formation of tectonic veins and their microstructures. Journal of Structural Geology 43, 33-62. DOI: 10.1016/j.jsg.2012.07.005.

Bosch, J.A., Ferrari, A., Leupin, O. & Laloui, L. (2023): Modelling the density homogenisation of a block and granular bentonite buffer upon non-isothermal saturation. International Journal for Numerical and Analytical Methods in Geomechanics 47/11, 1979-2002. DOI: 10.1002/nag.3547.

Bossart, P., Bernier, F., Birkholzer, J., Bruggeman, C., Connolli, P., Dewonck, S., Fukaya, M., Herfort, M., Jensen, J.-M., Matray, J.C., Mayor, A., Moeri, A., Oyama, T., Schuster, K., Shigeta, N., Vietor, T. & Wieczorek, K. (2017): Mont Terri rock laboratory, 20 years of research: introduction, site characteristics and overview of experiments. Swiss Journal of Geosciences, Special Issue: Mont Terri rock laboratory, 20 years of research 110, 3-22.

Bourg, I.C. & Ajo-Franklin, J.B. (2017): Clay, water, and salt: Controls on the permeability of fine-grained sedimentary rocks. Accounts of chemical research 50/9, 2067-2074. DOI: 10.1021/acs.accounts.7b00261.

Bourgeois, O., Ford, M., Diraison, M., Le Veslud, C.C. de, Gerbault, M., Pik, R., Ruby, N. & Bonnet, S. (2007): Separation of rifting and lithospheric folding signatures in the NW-Alpine foreland. International Journal of Earth Sciences (Geologische Rundschau) 96/6, 1003-1031. DOI: 10.1007/s00531-007-0202-2.

Braakhekke, J., Fischer, U.H. & Ivy-Ochs, S. (2017): Effects of limestone beds on glacial hydrology, erosion, sediment transport and associated landforms: a literature review. Nagra Arbeitsbericht NAB 17-26.

Bresler, E. (1973): Anion exclusion and coupling effects in nonsteady transport through unsaturated soils: I. Theory. Soil Science Society of America Journal 37/5, 663-669. DOI: 10.2136/sssaj1973.03615995003700050013x.

Brigaud, B., Vincent, B., Pessel, M., Saintenoy, A., Zeyen, H., Durlet, C., Saïag, J. & Hayet, M. (2024): Deciphering the origins of Bajocian coral ridges in the Paris Basin: Integrated 3D seismic reflection, near surface geophysics, and sedimentology. hal-04635083.

Brockamp, O., Schlegel, A. & Wemmer, K. (2015): Complex hydrothermal alteration and illite K–Ar ages in Upper Visean molasse sediments and magmatic rocks of the Variscan Badenweiler-Lenzkirch suture zone, Black Forest, Germany. International Journal of Earth Sciences (Geologische Rundschau) 104/3, 683-702. DOI: 10.1007/s00531-014-1118-2.

Brunauer, S., Emmett, P.H. & Teller, E. (1938): Adsorption of gases in multimolecular layers. Journal of the American Chemical Society 60/2, 309-319. DOI: 10.1021/ja01269a023.

Büchi, U.P., Lemcke, K., Wiener, G. & Zimdars, J. (1965): Geologische Ergebnisse der Erdölexploration auf das Mesozoikum im Untergrund des schweizerischen Molassebeckens. Bulletin der Vereinigung Schweizerischer Petroleum-Geologen und -Ingenieure 32/82, 7-38.

Budnitz, R.J., Apostolakis, G., Boore, D.M., Cluff, L.S., Coppersmith, K.J., Cornell, C.A. & Morris, P.A. (1997): Recommendations for probabilistic seismic hazard analysis : Guidance on uncertainty and use of experts : Main report. NUREG/CR-6372. U.S. Nuclear Regulatory Comission.

Buechi, M.W., Graf, H.R., Haldimann, P., Lowick, S.E. & Anselmetti, F.S. (2018): Multiple Quaternary erosion and infill cycles in overdeepened basins of the northern Alpine foreland. Swiss Journal of Geosciences 111/1-2, 133-167. DOI: 10.1007/s00015-017-0289-9.

Buechi, M.W., Kuster, A.M., Huber, M., Amschwand, D., Madritsch, H. & Deplazes, G. (2019): Quaternary Borehole QBO Neuhausen (QNEU) Data Report. Nagra Arbeitsbericht NAB 19-05.

Buechi, M.W., Landgraf, A., Madritsch, H., Mueller, D., Knipping, M., Nyffenegger, F., Preusser, F., Schaller, S., Schnellmann, M. & Deplazes, G. (2024): Terminal glacial overdeepenings: Patterns of erosion, infilling and new constraints on the glaciation history of Northern Switzerland. Quaternary Science Reviews 344, 108970. DOI: 10.1016/j.quascirev.2024.108970.

Buechi, M.W., Lowick, S.E. & Anselmetti, F.S. (2017): Luminescence dating of glaciolacustrine silt in overdeepened basin fills beyond the last interglacial. Quaternary Geochronology 37, 55-67. DOI: 10.1016/j.quageo.2016.09.009.

Buechi, M.W., Schuster, B., Reichenwallner, S., Madritsch, H. & Deplazes, G. (2022): Quaternary Borehole QBO Adlikon-Dätwil (QADA) Data Report. Nagra Arbeitsbericht NAB 22-14.

Buiter, S.J. (2012): A review of brittle compressional wedge models. Tectonophysics 530-531, 1-17. DOI: 10.1016/j.tecto.2011.12.018.

Burbank, D.W. & Anderson, R.S. (2012): Tectonic Geomorphology. 2nd edition. Wiley-Blackwell, Chichester.

Burger, H. (2011): Die Thermalwässer und Mineralwässer im Kanton Aargau und seiner näheren Umgebung. Mitteilungen der Aargauischen Naturforschenden Gesellschaft 37, 90-111.

Bürgmann, R. & Dresen, G. (2008): Rheology of the Lower Crust and Upper Mantle: Evidence from Rock Mechanics, Geodesy, and Field Observations. Annual Review of Earth and Planetary Sciences 36/1, 531-567. DOI: 10.1146/annurev.earth.36.031207.124326.

Burkhalter, R.M. (1996): Die Passwang-Alloformation (unteres Aalénien bis unteres Bajocien) im zentralen und nördlichen Schweizer Jura. Eclogae Geologicae Helvetiae 89/3, 875-934. DOI: 10.5169/seals-167927.

Burkhard, M. (1990): Aspects of the large-scale Miocene deformation in the most external part of the Swiss Alps (Subalpine Molasse to Jura fold belt). Eclogae Geologicae Helvetiae 83/3, 559-583.

Burki, V. (2009): Glaziale Erosion: Prozesse und ihre Kapazitäten. Nagra Arbeitsbericht NAB 09-06.

Butler, R.W., Bond, C. & Robledo, F. (submitted): Basement controls on structural evolution in thin-skinned thrust belts – implications for migration of deformation into orogenic forelands.

Buxtorf, A. (1916): Prognose und Befunde beim Hauensteinbasis- und Grenchenbergtunnel und die Bedeutung der letzteren für die Geologie des Juragebirges. Verhandlungen der Naturforschenden Gesellschaft in Basel 27, 184-254.

Cadisch, J. (1959): Geologische Ergebnisse der Mineralquellenbohrung Eglisau II. Bulletin der Vereinigung Schweizerischer Petroleum-Geologen und -Ingenieure 26/70, 5-8.

Caër, T., Maillot, B., Leturmy, P., Souloumiac, P. & Nussbaum, C. (2023): Parametric mechanical analysis of thin- versus thick-skinned tectonics applied to the Jura belt. BSGF - Earth Sciences Bulletin 194/5, 1-21. DOI: 10.1051/bsgf/2022022.

Caër, T., Souloumiac, P., Maillot, B., Leturmy, P. & Nussbaum, C. (2018): Propagation of a fold-and-thrust belt over a basement graben. Journal of Structural Geology 115, 121-131. DOI: 10.1016/j.jsg.2018.07.007.

Cariou, E. & Hantzpergue, P. (eds.) (1997): Biostratigraphie du Jurassique ouest-européen et méditerranéen: zonations parallèles et distribution des invertébrés et microfossiles. (Bulletin des centres de recherches exploration-production Elf-Aquitaine Mémoire, 17), Société nationale Elf-Aquitaine, Pau.

Cederbom, C.E., Sinclair, H.D., Schlunegger, F. & Rahn, M.K. (2004): Climate-induced rebound and exhumation of the European Alps. Geology 32/8, 709-712. DOI: 10.1130/G20491.1.

Cederbom, C.E., van der Beek, P., Schlunegger, F., Sinclair, H.D. & Oncken, O. (2011): Rapid extensive erosion of the North Alpine foreland basin at 5-4 Ma. Basin Research 23/5, 528-550. DOI: 10.1111/j.1365-2117.2011.00501.x.

Champagnac, J.-D., Schlunegger, F., Norton, K., Blanckenburg, F. von, Abbühl, L.M. & Schwab, M. (2009): Erosion-driven uplift of the modern Central Alps. Tectonophysics 474/1-2, 236-249. DOI: 10.1016/j.tecto.2009.02.024.

Chu, W., Creyts, T.T. & Bell, R.E. (2016): Rerouting of subglacial water flow between neighboring glaciers in West Greenland. Journal of Geophysical Research: Earth Surface 121/5, 925-938. DOI: 10.1002/2015JF003705.

Clark, I.D. & Fritz, P. (1997): Environmental isotopes in hydrogeology. CRC Press, Boca Raton.

Clark, P.U., Archer, D., Pollard, D., Blum, J.D., Rial, J.A., Brovkin, V., Mix, A.C., Pisias, N.G. & Roy, M. (2006): The middle Pleistocene transition: characteristics, mechanisms, and implications for long-term changes in atmospheric pCO_2. Quaternary Science Reviews 25/23-24, 3150-3184. DOI: 10.1016/j.quascirev.2006.07.008.

Clark, P.U., Dyke, A.S., Shakun, J.D., Carlson, A.E., Clark, J., Wohlfarth, B., Mitrovica, J.X., Hostetler, S.W. & McCabe, M. (2009): The Last Glacial Maximum. Science 325/5941, 710-714. DOI: 10.1126/science.1172873.

Clark, P.U., Hostetler, S.W., Pisias, N.G., Schmittner, A. & Meissner, K.J. (2007): Mechanisms for an ~7-kyr Climate and Sea-Level Oscillation During Marine Isotope Stage 3. *In:* Schmittner, A., Chiang, J. & Hemming, S. (eds.): Ocean Circulation: Mechanisms and Impacts: Past and Future Changes of Meridional Overturning. (Geophysical Monograph Series, 173). American Geophysical Union, Washington DC, 209-246.

Claude, A., Akçar, N., Ivy-Ochs, S., Schlunegger, F., Kubik, P.W., Christl, M., Vockenhuber, C., Kuhlemann, J., Rahn, M. & Schlüchter, C. (2019): Changes in landscape evolution patterns in the northern Swiss Alpine Foreland during the mid-Pleistocene revolution. GSA Bulletin 131/11-12, 2056-2078. DOI: 10.1130/B31880.1.

Claypool, G.E., Holser, W.T., Kaplan, I.R., Sakai, H. & Zak, I. (1980): The age curves of sulphur and oxygen isotopes in marine sulphate and their mutual interpretation. Chemical Geology 28, 199-260. DOI: 10.1016/0009-2541(80)90047-9.

Cobbold, P.R. & Rodrigues, N. (2007): Seepage forces, important factors in the formation of horizontal hydraulic fractures and bedding-parallel fibrous veins ('beef' and 'cone-in-cone'). Geofluids 7/3, 313-322. DOI: 10.1111/j.1468-8123.2007.00183.x.

Cobbold, P.R., Zanella, A., Rodrigues, N. & Løseth, H. (2013): Bedding-parallel fibrous veins (beef and cone-in-cone): Worldwide occurrence and possible significance in terms of fluid overpressure, hydrocarbon generation and mineralization. Marine and Petroleum Geology 43, 1-20. DOI: 10.1016/j.marpetgeo.2013.01.010.

Cohen, D., Jouvet, G., Zwinger, T., Landgraf, A. & Fischer, U.H. (2023): Subglacial hydrology from high-resolution ice-flow simulations of the Rhine Glacier during the Last Glacial Maximum: a proxy for glacial erosion. E&G Quaternary Science Journal 72/2, 189-201. DOI: 10.5194/egqsj-72-189-2023.

Cook, S.J. & Swift, D.A. (2012): Subglacial basins: Their origin and importance in glacial systems and landscapes. Earth-Science Reviews 115/4, 332-372. DOI: 10.1016/j.earscirev.2012.09.009.

Cooke, M.L. & Madden, E.H. (2014): Is the Earth Lazy? A review of work minimization in fault evolution. Journal of Structural Geology 66, 334-346. DOI: 10.1016/j.jsg.2014.05.004.

Cooke, M.L. & Murphy, S. (2004): Assessing the work budget and efficiency of fault systems using mechanical models. Journal of Geophysical Research: Solid Earth 109/B10, 2004JB002968. DOI: 10.1029/2004JB002968.

Cooke, R.M. (1991): Experts in uncertainty: opinion and subjective probability in science. Oxford University Press, USA.

Correia, V. (2018): Jurassic dinoflagellate cyst biostratigraphy of the Lusitanian Basin, west-central Portugal, and its relevance to the opening of the North Atlantic and petroleum geology. PhD Thesis. Univ. Algarve, Faro, Portugal.

Craig, T.J., Calais, E., Fleitout, L., Bollinger, L. & Scotti, O. (2016): Evidence for the release of long-term tectonic strain stored in continental interiors through intraplate earthquakes. Geophysical Research Letters 43/13, 6826-6836. DOI: 10.1002/2016GL069359.

Craig, T.J., Calais, E., Fleitout, L., Bollinger, L. & Scotti, O. (2023): Time-variable strain and stress rates induced by Holocene glacial isostatic adjustment in continental interiors. Tectonophysics 854, 229815. DOI: 10.1016/j.tecto.2023.229815.

Crampton, S.L. & Allen, P.A. (1995): Recognition of forebulge unconformities associated with early stage foreland basin development: Example from the North Alpine foreland basin. AAPG Bulletin 79/10, 1495-1514. DOI: 10.1306/7834DA1C-1721-11D7-8645000102C1865D.

Crisci, E. (2019): Hydro-mechanical response of Opalinus Clay shale: dependency on composition and burial depth. Thèse N° 7421. EPFL, Lausanne.

Crisci, E., Ewy, R.T., Ferrari, A., Giger, S.B., Ewy, R. & Giger, S. (2024a): Assessing swelling-induced damage in shale samples during triaxial testing. Geomechanics for Energy and the Environment 40, 100599. DOI: 10.1016/j.gete.2024.100599.

Crisci, E., Ferrari, A., Giger, S.B. & Laloui, L. (2019): Hydro-mechanical behaviour of shallow Opalinus Clay shale. Engineering Geology 251, 214-227. DOI: 10.1016/j.enggeo.2019.01.016.

Crisci, E., Ferrari, A., Giger, S.B. & Laloui, L. (2021): Effect of the mineralogical composition on the elastoplastic hydromechanical response of Opalinus Clay shale. International Journal of Rock Mechanics & Mining Sciences 143, 104747. DOI: 10.1016/j.ijrmms.2021.104747.

Crisci, E., Giger, S.B., Laloui, L., Ferrari, A., Ewy, R., Stankovic, R., Stenebråten, J., Halvorsen, K. & Soldal, M. (2024b): Insights from an extensive triaxial testing campaign on a shale for comparative site characterization of a deep geological repository. Geomechanics for Energy and the Environment 38, 100508. DOI: 10.1016/j.gete.2023.100508.

Cuss, R.J., Milodowski, A. & Harrington, J.F. (2011): Fracture transmissivity as a function of normal and shear stress: First results in Opalinus Clay. Physics and Chemistry of the Earth, Parts A/B/C 36/17-18, 1960-1971. DOI: 10.1016/j.pce.2011.07.080.

Dahlstrom, C.D.A. (1969): Balanced cross sections. Canadian Journal of Earth Sciences 6/4, 743-757. DOI: 10.1139/e69-069.

Darling, A., Whipple, K., Bierman, P., Clarke, B. & Heimsath, A. (2020): Resistant rock layers amplify cosmogenically-determined erosion rates. Earth Surface Processes and Landforms 45/2, 312-330. DOI: 10.1002/esp.4730.

Davis, B.A.S., Fasel, M., Kaplan, J.O., Russo, E. & Burke, A. (2024): The climate and vegetation of Europe, northern Africa, and the Middle East during the Last Glacial Maximum (21 000 yr BP) based on pollen data. Clim. Past 20/9, 1939-1988. DOI: 10.5194/cp-20-1939-2024.

De Craen, M., Moors, H., Honty, M. & Van Geet, M.M. (2023): The role of the HADES URL in better understanding of the Boom Clay pore water geochemistry. Geological Society, London, Special Publications 536, 11-32. DOI: 10.1144/SP536-2022-93.

de Haller, A., Tarantola, A., Mazurek, M. & Spangenberg, J. (2011): Fluid flow through the sedimentary cover in northern Switzerland recorded by calcite–celestite veins (Oftringen borehole, Olten). Swiss Journal of Geosciences 104/3, 493-506. DOI: 10.1007/s00015-011-0085-x.

de Marsily, G. (1986): Quantitative Hydrogeology. Groundwater Hydrology for Engineers. Academic Press, Inc., San Diego.

Dehnert, A., Lowick, S.E., Preusser, F., Anselmetti, F.S., Drescher-Schneider, R., Graf, H.R., Heller, F., Horstmeyer, H., Kemna, H.A., Nowaczyk, N.R., Züger, A. & Furrer, H. (2012): Evolution of an overdeepened trough in the northern Alpine Foreland at Niederweningen, Switzerland. Quaternary Science Reviews 34, 127-145. DOI: 10.1016/j.quascirev.2011.12.015.

Delage, P. & Belmokhtar, M. (2022): Drained triaxial testing of shales: insight from the Opalinus Clay. Acta Geotechnica 17/7, 2855-2874. DOI: 10.1007/s11440-021-01395-3.

Delay, J., Vinsot, A., Krieguer, J.-M., Rebours, H. & Armand, G. (2007): Making of the underground scientific experimental programme at the Meuse/Haute-Marne underground research laboratory, North Eastern France. Physics and Chemistry of the Earth, Parts A/B/C 32/1-7, 2-18. DOI: 10.1016/j.pce.2006.04.033.

Delisle, G., Caspers, G. & Freund, H. (2003): Permafrost in north-central Europe during the Weichselian: how deep? *In:* Phillips, M., Springman, S.M. & Arenson, L.U. (eds.): Permafrost. Proceedings of the 8th International Conference on Permafrost. Zürich, July 21-25, 2003. International Conference on Permafrost. Balkema, Lisse, 187-191.

Delunel, R., Schlunegger, F., Valla, P.G., Dixon, J., Glotzbach, C., Hippe, K., Kober, F., Molliex, S., Norton, K.P., Salcher, B., Wittmann, H., Akçar, N. & Christl, M. (2020): Late-Pleistocene catchment-wide denudation patterns across the European Alps. Earth-Science Reviews 211, 103407. DOI: 10.1016/j.earscirev.2020.103407.

DeMets, C., Gordon, R.G., Argus, D.F. & Stein, S. (1990): Current plate motions. Geophysical Journal International 101/2, 425-478. DOI: 10.1111/j.1365-246X.1990.tb06579.x.

Demoulin, A. & Hallot, E. (2009): Shape and amount of the Quaternary uplift of the western Rhenish shield and the Ardennes (western Europe). Tectonophysics 474/3-4, 696-708. DOI: 10.1016/j.tecto.2009.05.015.

Deplazes, G., Bläsi, H.R., Schnellmann, M. & Traber, D. (2013): Sedimentologie und Stratigraphie der Effinger Schichten. Nagra Arbeitsbericht NAB 13-16.

Dershowitz, W.S. (1985): Rock joint system. Thesis Ph.D., Massachusetts Institute of Technology.

Dershowitz, W.S. & Herda, H.H. (1992): Interpretation of fracture spacing and intensity. Paper presented at The 33rd U.S. Symposium on Rock Mechanics (USRMS), Santa Fe, New Mexico, June 1992.

Dewispelare, A.R., Herren, L. & Clemen, R.T. (1995): The use of probability elicitation in the high-level nuclear waste regulation program. International Journal of Forecasting 11/1, 5-24. DOI: 10.1016/0169-2070(94)02006-B.

Dèzes, P., Schmid, S.M. & Ziegler, P.A. (2004): Evolution of the European Cenozoic Rift System: interaction of the Alpine and Pyrenean orogens with their foreland lithosphere. Tectonophysics 389/1-2, 12055. DOI: 10.1016/j.tecto.2004.06.011.

Di Donna, A., Charrier, P., Salager, S. & Bésuelle, P. (2019): Self-sealing capacity of argillite samples. 7th International Symposium on Deformation Characteristics of Geomaterials, Jun 2019, Glasgow, United Kingdom.

Diamond, L.W. (1998): Underpressured paleofluids and future fluid flow in the host rocks of a planned radioactive waste repository. *In:* Arehart, G.B. & Hulston, J.R. (eds.): Water-Rock Interaction. Proceedings of the 9th International Symposium on Water-Rock Interaction – WRI-9/Taupo/New Zealand/30 March - 3 April 1998. A.A.Balkema, Rotterdam, 769-772.

Diebold, P. (1988): Der Nordschweizer Permokarbon-Trog und die Steinkohlenfrage der Nordschweiz. Vierteljahrsschrift der Naturforschenden Gesellschaft in Zürich 133/3, 143-174.

Diebold, P., Bitterli-Brunner, P. & Naef, H. (2006): Blatt 1069/1049 Frick-Laufenburg mit Erläuterungen. Bundesamt für Landestopografie swisstopo.

Diebold, P., Naef, H. & Amman, M. (1991): Zur Tektonik der Zentralen Nordschweiz: Interpretation aufgrund regionaler Seismik, Oberflächengeologie und Tiefbohrungen. Textband. Nagra Technischer Bericht NTB 90-04.

Diebold, P. & Noack, T. (1997): 7.3 Late Paleozoic troughs and Tertiary structures in the eastern Folded Jura. *In:* Pfiffner, O.A., Lehner, P., Heitzmann, P., Mueller, S. & Steck, A. (eds.): Deep Structure of the Swiss Alps. Results of NRP 20. Birkhäuser Verlag, Basel, 59-63.

Diedrich, C. (2011): Upper Jurassic tidal flat megatracksites of Germany—coastal dinosaur migration highways between European islands, and a review of the dinosaur footprints. Palaeobiodiversity and Palaeoenvironments 91/2, 129-155. DOI: 10.1007/s12549-010-0044-y.

Diehl, T., Kissling, E., Herwegh, M. & Schmid, S.M. (2021): Improving Absolute Hypocenter Accuracy With 3D Pg and Sg Body-Wave Inversion Procedures and Application to Earthquakes in the Central Alps Region. Journal of Geophysical Research: Solid Earth 126/12, e2021JB022155. DOI: 10.1029/2021JB022155.

Diehl, T., Madritsch, H., Schnellmann, M., Spillmann, T., Brockmann, E. & Wiemer, S. (2023): Seismotectonic evidence for present-day transtensional reactivation of the slowly deforming Hegau-Bodensee Graben in the northern foreland of the Central Alps. Tectonophysics 846, 229659. DOI: 10.1016/j.tecto.2022.229659.

Dieleman, C., Christl, M., Vockenhuber, C., Gautschi, P. & Akçar, N. (2022a): Early Pleistocene complex cut-and-fill sequences in the Alps. Swiss Journal of Geosciences 115/11, 1-25. DOI: 10.1186/s00015-022-00411-2.

Dieleman, C., Christl, M., Vockenhuber, C., Gautschi, P., Graf, H.R. & Akçar, N. (2022b): Age of the most extensive glaciation in the Alps. Geosciences 12/39, 1-20. DOI: 10.3390/geosciences12010039.

Dietl, G. (2006): Die Hamitenton-Formation (bj3) des Schwäbischen Juras – Beschreibung und Gliederung. Jahreshefte der Gesellschaft für Naturkunde in Württemberg 162, 25-45. DOI: 10.26251/jhgfn.162.2006.025-045.

Dietl, G. (2007): Die Dentalienton-Formation (bt) des Schwäbischen Juras – Beschreibung und Gliederung. Jahreshefte der Gesellschaft für Naturkunde in Württemberg 163, 5-20. DOI: 10.26251/jhgfn.163.2007.005-020.

Dietl, G. (2008): Die Variansmergel-Formation (btV) des Schwäbischen Juras – Beschreibung und Gliederung. Jahreshefte der Gesellschaft für Naturkunde in Württemberg 164, 5-19. DOI: 10.26251/jhgfn.164.2008.005-019.

Dietl, G. (2010): Die Wutach-Formation (clw) des südwestdeutschen Juras – Beschreibung und Gliederung. Jahreshefte der Gesellschaft für Naturkunde in Württemberg 166, 5-21. DOI: 10.26251/jhgfn.166.2010.005-021.

Dietze, V., Gräbenstein, S., Franz, M., Schweigert, G. & Wetzel, A. (2021): The Middle Jurassic Opalinuston Formation (Aalenian, Opalinum Zone) at its type locality near Bad Boll and adjacent outcrops (Swabian Alb, SW Germany). Palaeodiversity 14/1, 15-113. DOI: 10.18476/pale.v14.a3.

Dietze, V., Schweigert, G. & Dietl, G. (2011): Chrono-/Biostratigraphie im Mitteljura von SW-Deutschland. 1. Teil: Bajocium. Jahreshefte der Gesellschaft für Naturkunde in Württemberg 167, 49-71. DOI: 10.26251/jhgfn.167.2011.049-071.

Dietze, V., Schweigert, G. & Dietl, G. (2014): Chrono-/Biostratigraphie im Mitteljura von SW-Deutschland. 2. Teil: Bathonium. Jahreshefte der Gesellschaft für Naturkunde in Württemberg 170/1, 191-203. DOI: 10.26251/jhgfn.170.2014.191-203.

Distinguin, M. & Lavanchy, J.-M. (2007): Determination of hydraulic properties of the Callovo-Oxfordian argillite at the bure site: Synthesis of the results obtained in deep boreholes using several in situ investigation techniques. Physics and Chemistry of the Earth, Parts A/B/C 32/1-7, 379-392. DOI: 10.1016/j.pce.2006.02.056.

Doherty, J. (2004): PEST Model-Independent Parameter Estimation. User Manual. 5th ed. Watermark Numerical Computing, Brisbane, Australia.

Dold, B. & Spangenberg, J.E. (2005): Sulfur speciation and stable isotope trends of water-soluble sulfates in mine tailings profiles. Environmental science & technology 39/15, 5650-5656. DOI: 10.1021/es040093a.

Donzé, F.-V., Tsopela, A., Guglielmi, Y., Henry, P. & Gout, C. (2023): Fluid migration in faulted shale rocks: channeling below active faulting threshold. European Journal of Environmental and Civil Engineering 27/8, 2587-2601. DOI: 10.1080/19648189.2020.1765200.

Drewry, D. (1986): Glacial Geologic Processes. Edward Arnold, London.

Dronkert, H., Bläsi, H. & Matter, A. (1990): Facies and origin of Triassic evaporites from the Nagra boreholes, Northern Switzerland. Nagra Technical Report NTB 87-02.

Duprat-Oualid, F. (2019): 50 000 ans d'histoire de végétation et du climat en Europe occidentale: étude pollinique et approche multi-proxy sur la sequence sédimentaire du Bergsee (Forêt Noire, Allemagne). Archéologie et Préhistoire. Thèse de Doctorat. Université Bourgogne Franche-Comté.

Duprat-Oualid, F., Rius, D., Bégeot, C., Magny, M., Millet, L., Wulf, S. & Appelt, O. (2017): Vegetation response to abrupt climate changes in Western Europe from 45 to 14.7k cal a BP: the Bergsee lacustrine record (Black Forest, Germany). Journal of Quaternary Science 32/7, 1008-1021. DOI: 10.1002/jqs.2972.

Durlet, C. & Thierry, J. (2000): Modalites sequentielles de la transgression aaleno-bajocienne sur le sud-est du Bassin parisien. Bulletin de la Société Géologique de France 171/3, 327-339. DOI: 10.2113/171.3.327.

Ebert, A. (2014): Strukturgeologische Kernaufnahmen der Wirtgesteinsabfolgen aus Tiefbohrungen der Nordschweiz. Nagra Arbeitsbericht NAB 13-89.

Ebert, A. & Decker, K. (2019): Structural analysis manual. Nagra Arbeitsbericht NAB 19-12.

Edel, J.-B., Schulmann, K. & Rotstein, Y. (2007): The Variscan tectonic inheritance of the Upper Rhine Graben: evidence of reactivations in the Lias, Late Eocene–Oligocene up to the recent. International Journal of Earth Sciences (Geologische Rundschau) 96/2, 305-325. DOI: 10.1007/s00531-006-0092-8.

Egholm, D.L. (2022): Controls on Overdeepening Formation in a Distal Foreland Setting. Nagra Arbeitsbericht NAB 22-17.

Egli, D., Mosar, J., Ibele, T. & Madritsch, H. (2017): The role of precursory structures on Tertiary deformation in the Black Forest – Hegau region. International Journal of Earth Sciences (Geologische Rundschau) 106/7, 2297-2318. DOI: 10.1007/s00531-016-1427-8.

Ehlers, J., Gibbard, P.L. & Hughes, P.D. (eds.) (2011): Quaternary glaciations - extent and chronology. A closer look. (Developments in quaternary sciences, 15). Elsevier, Amsterdam, Boston.

Einsele, G. & Ricken, W. (1995): The Wutach gorge in SW Germany: late Würmian (periglacial) downcutting versus Holocene processes. Zeitschrift für Geomorphologie, Neue Folge Suppl. Bd. 100, 65-87.

Elkhoury, J.E., Bérard, T., Desroches, J., Peyret, E., Prioul, R., Crisci, E., Garrard, R. & Giger, S.B. (*in press*): In situ static elastic properties assessment and validation with pressuremeter testing using a formation tester tool. Geomechanics for Energy and the Environment. DOI: 10.2139/ssrn.4868572.

Elkhoury, J.E., Elias, Q.K., Prioul, R., Peyret, E., Wilcox, A., Di Giovanni, M., van der Hulst, T., Bérard, T., Desroches, J., Garrard, R. & Giger, S.B. (2022): The First Pressuremeter Testing Campaign on Wireline Formation Testers in Deep Boreholes. ARMA 22-0698. 56th US Rock Mechanics/Geomechanics Symposium, Santa Fe, NM, USA, 26-29 June 2022.

Ellwanger, D., Wielandt-Schuster, U., Franz, M. & Simon, T. (2011): The Quaternary of the southwest German Alpine Foreland (Bodensee-Oberschwaben, Baden-Württemberg, Southwest Germany). E&G Quaternary Sci. J. 60/2/3, 306-328. DOI: 10.3285/eg.60.2-3.07.

ENSI (2018): Präzisierungen der sicherheitstechnischen Vorgaben für Etappe 3 des Sachplans geologische Tiefenlager. Sachplan geologische Tiefenlager, Etappe 3. ENSI 33/649. Eidgenössisches Nuklearsicherheitsinspektorat ENSI.

ENSI (2020): Deep Geological Repositories. Explanatory Report for Guideline ENSI-G03. Swiss Federal Nuclear Safety Inspectorate ENSI, Brugg.

ENSI (2023): ENSI G03: Richtlinie für die schweizerischen Kernanlagen. Geologische Tiefenlager. Ausgabe Dezember 2020 (Änderung vom 1. November 2023). Eidgenössisches Nuklearsicherheitsinspektorat ENSI.

Escher, A., Hunziker, J., Masson, H., Sartori, M. & Steck, A. (1997): Geologic framework and structural evolution of the western Swiss-Italian Alps. In: Pfiffner, O.A., Lehner, P., Heitzman, P.Z., Mueller, S. & Steck, A. (eds.): Deep structure of the Swiss Alps: Results from NRP 20. Birkhäuser Verlag, 205-222, Basel.

Etter, W. (1990): Paläontologische Untersuchungen im unteren Opalinuston der Nordschweiz. Dissertation, Universität Zürich.

Etzold, A. & Schweizer, V. (2005): Der Keuper in Baden-Württemberg. *In:* Deutsche Stratigraphische Kommission (ed.): Stratigraphie von Deutschland IV – Keuper. (Courier Forschungsinstitut Senckenberg, 253), 214-258.

European Environment Agency (2020): EU-Hydro River Network Database 2006-2012 (vector), Europe - version 1.3, Nov. 2020. DOI: 10.2909/393359a7-7ebd-4a52-80ac-1a18d5f3db9c.

Ewy, R.T. (2015): Shale/claystone response to air and liquid exposure, and implications for handling, sampling and testing. International Journal of Rock Mechanics and Mining Sciences 80, 388-401. DOI: 10.1016/j.ijrmms.2015.10.009.

Fagereng, Å. & Biggs, J. (2019): New perspectives on 'geological strain rates' calculated from both naturally deformed and actively deforming rocks. Journal of Structural Geology 125, 100-110. DOI: 10.1016/j.jsg.2018.10.004.

Fäh, D., Giardini, D., Kästli, P., Deichmann, N., Gisler, M., Schwarz-Zanetti, G., Alvarez-Rubio, S., Sellami, S., Edwards, B., Allmann, B., Bethmann, F., Wössner, J., Gassner-Stamm, G., Fritsche, S. & Eberhard, D. (2011): ECOS-09 Earthquake Catalogue of Switzerland. Report and Database. Public catalogue. Report SED/RISK/R/001/20110417. Release 2011, 17.4.2011. Swiss Seismological Service, ETH Zürich.

Fang, Y., Elsworth, D., Wang, C., Ishibashi, T. & Fitts, J.P. (2017): Frictional stability-permeability relationships for fractures in shales. Journal of Geophysical Research: Solid Earth 122/3, 1760-1776. DOI: 10.1002/2016JB013435.

Fantasia, A., Föllmi, K.B., Adatte, T., Spangenberg, J.E. & Mattioli, E. (2019): Expression of the Toarcian Oceanic Anoxic Event: New insights from a Swiss transect. Sedimentology 66/1, 262-284. DOI: 10.1111/sed.12527.

Farinotti, D., Huss, M., Fürst, J.J., Landmann, J., Machguth, H., Maussion, F. & Pandit, A. (2019): A consensus estimate for the ice thickness distribution of all glaciers on Earth. Nature Geoscience 12/3, 168-173. DOI: 10.1038/s41561-019-0300-3.

Favero, V. (2017): Multiphysical behaviour of shales from Northern Switzerland. PhD Thesis N° 7539. École Polytechnique Fédérale de Lausanne EPFL.

Favero, V., Ferrari, A. & Laloui, L. (2016): On the hydro-mechanical behaviour of remoulded and natural Opalinus Clay shale. Engineering Geology 208, 128-135. DOI: 10.1016/j.enggeo.2016.04.030.

Favero, V., Ferrari, A. & Laloui, L. (2018): Anisotropic behaviour of Opalinus Clay through consolidated and drained triaxial testing in saturated conditions. Rock Mechanics and Rock Engineering 51/5, 1305-1319. DOI: 10.1007/s00603-017-1398-5.

Ferrari, A., Favero, V., Manca, D. & Laloui, L. (2012): Geotechnical characterization of core samples from the geothermal well Schlattingen SLA-1 by LMS/EPFL. Nagra Arbeitsbericht NAB 12-50.

Fischer, U.H., Bebiolka, A., Brandefelt, J., Cohen, D., Harper, J., Hirschorn, S., Jensen, M., Kennell, L., Liakka, J., Näslund, J.-O., Normani, S., Stück, H. & Weitkamp, A. (2021): Radioactive waste under conditions of future ice ages. *In:* Haeberli, W. & Whiteman, C. (eds.): Snow and Ice-Related Hazards, Risks, and Disasters. 2nd ed. Elsevier, Amsterdam, 323-375.

Fischer, U.H. & Haeberli, W. (2010): Glacial Erosion Modelling Results of a workshop held in Unterageri, Switzerland, 29 April-1 May 2010. Nagra Arbeitsbericht NAB 10-34.

Fisher, Q., Kaminskaite, I. & Del Pino Sanchez, A. (2023): Shale barrier performance in petroleum systems: implications for CO_2 storage and nuclear waste disposal. Geoenergy 1/1, geoenergy2023-006. DOI: 10.1144/geoenergy2023-006.

Fisher, Q., Kets, F. & Crook, A. (2013): Self-sealing of faults and fractures in argillaceous formations: Evidence from the petroleum industry. Nagra Arbeitsbericht NAB 13-06.

Fleury, M., Gimmi, T. & Mazurek, M. (2022): Porewater content, pore structure and water mobility in clays and shales from NMR methods. Clays and Clay Minerals 70/3, 417-437. DOI: 10.1007/s42860-022-00195-4.

Ford, M., Duchêne, S., Gasquet, D. & Vanderhaeghe, O. (2006): Two-phase orogenic convergence in the external and internal SW Alps. Journal of the Geological Society 163/5, 815-826. DOI: 10.1144/0016-76492005-034.

Forte, A.M., Yanites, B.J. & Whipple, K.X. (2016): Complexities of Landscape Evolution During Incision Through Layered Stratigraphy with Contrasts in Rock Strength. Earth Surface Processes and Landforms 41/12, 1736-1757. DOI: 10.1002/esp.3947.

Fossen, H. & Rotevatn, A. (2016): Fault linkage and relay structures in extensional settings - A review. Earth-Science Reviews 154, 14-28. DOI: 10.1016/j.earscirev.2015.11.014.

Fox, M., Herman, F., Willett, S.D. & Schmid, S.M. (2016): The exhumation history of the European Alps inferred from linear inversion of thermochronometric data. American Journal of Science 316/6, 505-541. DOI: 10.2475/06.2016.01.

Franz, M. (2022): Über 80 Jahre alte Bohrungen jetzt interpretierbar. LGRB-Nachrichten 2022/2.

Franz, M. & Nitsch, E. (2009): Zur lithostratigraphischen Gliederung des Aalenium in Baden-Württemberg. LGRB-Informationen 22, 123-146.

Freeze, R.A. & Cherry, J.A. (1979): Groundwater. Prentice-Hall Inc., Englewood Cliffs.

Frei, R. (1912): Monographie des Schweizerischen Deckenschotters. Beiträge zur geologischen Karte der Schweiz. Neue Folge 37 Lfg. Francke, Bern.

Frenzel, B., Pécsi, M. & Velichko, A.A. (1992): Atlas of paleoclimates and paleoenvironments of the Northern hemisphere. Late Pleistocene - Holocene. Geographical Research Institute; Hungarian Academy of Sciences; Fischer, Budapest, Stuttgart.

Fuchs, K., Gehlen, K. von, Mälzer, H., Murawski, H. & Semmel, H. (1983): Plateau Uplift. The Rhenish Shield — A Case History. Springer Verlag, Berlin/New York.

Füchtbauer, H. (1988): Sedimente und Sedimentgesteine. 4. Aufl. (Sediment-Petrologie, Teil II). Schweizerbart, Stuttgart.

Füger, A., Méheut, M., Mavromatis, V., Leis, A. & Dietzel, M. (2018): Oxygen isotope fractionation during smithsonite formation from aqueous solutions. Chem. Geol. 495, 76-89.

Fuhrmann, T., Westerhaus, M., Zippelt, K. & Heck, B. (2014): Vertical displacement rates in the Upper Rhine Graben area derived from precise leveling. Journal of Geodesy 88/8, 773-787. DOI: 10.1007/s00190-014-0721-0.

Gaar, D., Graf, H.R. & Preusser, F. (2019): New chronological constraints on the timing of Late Pleistocene glacier advances in northern Switzerland. E&G Quaternary Science Journal 68/1, 53-73. DOI: 10.5194/egqsj-68-53-2019.

Gabriel, G., Ellwanger, D., Hoselmann, C., Weidenfeller, M., Wielandt-Schuster, U. & Heidelberg Basin Project Team (2013): The Heidelberg Basin, Upper Rhine Graben (Germany): a unique archive of Quaternary sediments in Central Europe. Quaternary International 292, 43-58. DOI: 10.1016/j.quaint.2012.10.044.

Gailhanou, H., Lerouge, C., Debure, M., Gaboreau, S., Gaucher, E.C., Grangeon, S., Grenèche, J.-M., Kars, M., Madé, B. & Marty, N. (2017): Effects of a thermal perturbation on mineralogy and pore water composition in a clay-rock: An experimental and modeling study. Geochimica et Cosmochimica Acta 197, 193-214. DOI: 10.1016/j.gca.2016.10.004.

Galavotti, M.C. (2005): A Philosophical Introduction to Probability. Lecture Notes. Center for the Study of Language and Information. (CSLI Lecture notes, 167), Stanford, California.

Gale, J.F., Laubach, S.E., Olson, J.E., Eichhuble, P. & Fall, A. (2014): Natural Fractures in shale: A review and new observations. AAPG Bulletin 98/11, 2165-2216. DOI: 10.1306/08121413151.

Gander, P. (2004): Geologie und Hydrogeologie der Oberen Süsswassermolasse: Dokumentation des aktuellen Kenntnisstandes. Nagra Arbeitsbericht NAB 04-04.

Garcia-Castellanos, D., Cloetingh, S. & van Balen, R. (2000): Modelling the Middle Pleistocene uplift in the Ardennes–Rhenish Massif: Thermo-mechanical weakening under the Eifel? Global and Planetary Change 27/1-4, 39-52. DOI: 10.1016/S0921-8181(01)00058-3.

Garefalakis, P. & Schlunegger, F. (2019): Tectonic processes, variations in sediment flux, and eustatic sea level recorded by the 20 Myr old Burdigalian transgression in the Swiss Molasse basin. Solid Earth 10/6, 2045-2072. DOI: 10.5194/se-10-2045-2019.

Gautschi, A. (2001): Hydrogeology of a fractured shale (Opalinus Clay) : Implications for deep geological disposal of radioactive wastes. Hydrogeology Journal 9, 97-107. DOI: 10.1007/s100400000117.

Gautschi, A. (2017): Safety-relevant hydrogeological properties of the claystone barrier of a Swiss radioactive waste repository: An evaluation using multiple lines of evidence. Grundwasser 22/3, 221-233. DOI: 10.1007/s00767-017-0364-1.

Gbewade, C.A.F., Grgic, D., Giraud, A. & Schoumacker, L. (2024): Experimental Study of the Effect of Temperature on the Mechanical Properties of the Callovo-Oxfordian Claystone. Rock Mechanics and Rock Engineering 57/6, 4191-4212. DOI: 10.1007/s00603-023-03630-7.

Gegg, L. (2021): The Mid-Pleistocene landscape history of the Lower Aare Valley with emphasis on subglacial overdeepening. Dissertation. University of Bern.

Gegg, L., Anselmetti, F.S., Deplazes, G., Knipping, M., Madritsch, H., Mueller, D., Preusser, F., Vogel, H. & Buechi, M.W. (2023): Rinikerfeld Palaeolake (Northern Switzerland) – a sedimentary archive of landscape and climate change during the penultimate glacial cycle. Journal of Quaternary Science 38/2, 174-185. DOI: 10.1002/jqs.3471.

Gegg, L., Deplazes, G., Keller, L., Madritsch, H., Spillmann, T., Anselmetti, F.S. & Buechi, M.W. (2021): 3D morphology of a glacially overdeepened trough controlled by underlying bedrock geology. Geomorphology 394, 107950. DOI: 10.1016/j.geomorph.2021.107950.

Gegg, L., Kuster, A.M., Amschwand, D., Huber, M., Deplazes, G., Madritsch, H. & Buechi, M.W. (2019a): Quaternary Borehole QBO Gebenstorf-Vogelsang (QGVO) Data Report. Nagra Arbeitsbericht NAB 19-03.

Gegg, L., Kuster, A.M., Deplazes, G., Madritsch, H. & Buechi, M.W. (2019b): Quaternary Borehole QBO Gebenstorf-Brüel (QGBR) Data Report. Nagra Arbeitsbericht NAB 19-02.

Gegg, L., Kuster, A.M., Schmid, D. & Buechi, M.W. (2018): Quaternary Boreholes QBO Riniken -1 & -2 (QRIN1 & QRIN2) Data Report. Nagra Arbeitsbericht NAB 18-40.

Gegg, L., Kuster, A.M., Schmid, D., Lemke, K., Deplazes, G., Madritsch, H. & Buechi, M.W. (2019c): Quaternary Borehole QBO Untersiggenthal (QUST) Data Report. Nagra Arbeitsbericht NAB 19-01.

Geister, J. & Lathuilière, B. (1991): Jurassic Coral Reefs of the Northeastern Paris Basin. Fossil VI. Cnidaria, Münster 1991. VI. International Symposium on Fossil Cnidaria including Archaeocyatha and Porifera.

Gerber, C., Vaikmäe, R., Aeschbach, W., Babre, A., Jiang, W., Leuenberger, M., Lu, Z.-T., Mokrik, R., Müller, P., Raidla, V., Saks, T., Waber, H.N., Weissbach, T., Zappala, J.C. & Purtschert, R. (2017): Using ^{81}Kr and noble gases to characterize and date groundwater and brines in the Baltic Artesian Basin on the one-million-year timescale. Geochimica et Cosmochimica Acta 205, 187-210. DOI: 10.1016/j.gca.2017.01.033.

Geyer, M., Nitsch, E. & Simon, T. (2023): Geologie von Baden-Württemberg. 6., neu bearbeitete Auflage (begründet von O.F. Geyer / M.P. Gwinner). Schweizerbart, Stuttgart.

Giamboni, M., Ustaszewski, K., Schmid, S.M., Schumacher, M.E. & Wetzel, A. (2004): Plio-Pleistocene transpressional reactivation of Paleozoic and Paleogene structures in the Rhine-Bresse transform zone (northern Switzerland and eastern France). International Journal of Earth Sciences (Geologische Rundschau) 93/2, 207-223. DOI: 10.1007/s00531-003-0375-2.

Giffaut, E., Grivé, M., Blanc, P., Vieillard, P., Colàs, E., Gailhanou, H., Gaboreau, S., Marty, N., Made, B. & Duro, L. (2014): Andra thermodynamic database for performance assessment: ThermoChimie. Applied Geochemistry 49/5, 225-236. DOI: 10.1016/j.apgeochem.2014.05.007.

Giger, S. & Marschall, P. (2014): Geomechanical properties, rock models and in-situ stress conditions for Opalinus Clay in Northern Switzerland. Nagra Arbeitsbericht NAB 14-01.

Gimmi, T., Aschwanden, L., Waber, H.N., Gaucher, E.C., Ma, J. & Traber, D. (2024): Profiles of δ^{18}O and δ^{2}H in porewater of a Mesozoic rock sequence: Regional variability and relation to large-scale transport regimes. Applied Geochemistry 160, 105846. DOI: 10.1016/j.apgeochem.2023.105846.

Gimmi, T., Leupin, O.X., Eikenberg, J., Glaus, M.A., Van Loon, L.R., Waber, N., Wersin, P., Wang, H., Grolimund, D., Borca, C.N., Dewonck, S. & Wittebroodt, C. (2014): Anisotropic diffusion at the field scale in a 4-year multi-tracer diffusion and retention experiment – I: Insights from the experimental data. Geochimica et Cosmochimica Acta 125, 373-393. DOI: 10.1016/j.gca.2013.10.014.

Gimmi, T. & Waber, H.N. (2004): Modelling tracer profiles in pore water of argillaceous rocks in the Benken borehole: Stable water isotopes, chloride, and chlorine isotopes. Nagra Technical Report NTB 04-05.

Gimmi, T., Waber, H.N., Gautschi, A. & Rübel, A. (2007): Stable water isotopes in pore water of Jurassic argillaceous rocks as tracers for solute transport over large spatial and temporal scales. Water Resources Research 43/4, W04410. DOI: 10.1029/2005WR004774.

Glaus, M.A., Van Loon, L.R. & Wüst, R. (2024): Diffusion of HTO, ^{36}Cl and ^{22}Na in the Mesozoic rocks of northern Switzerland. II: Data interpretation in terms of an electrical double layer model. Applied Geochemistry 162, 105842. DOI: 10.1016/j.apgeochem.2023.105842.

Gleißner, P., Franz, G. & Frei, D. (2021): Contemporaneous opening of the Alpine Tethys in the Eastern and Western Alps: constraints from a Late Jurassic gabbro intrusion age in the Glockner Nappe, Tauern Window, Austria. International Journal of Earth Sciences (Geologische Rundschau) 110/8, 2705-2724. DOI: 10.1007/s00531-021-02075-z.

Gmünder, C., Jordan, P. & Becker, J. (2013): Documentation of the Nagra 3D geological model 2012.1. Nagra Arbeitsbericht NAB 13-28.

Gmünder, C., Malaguerra, F., Nusch, S. & Traber, D. (2014): Regional Hydrogeological Model of Northern Switzerland. Nagra Arbeitsbericht NAB 13-23.

Gómez-Hernández, J.J., Guardiolo-Albert, C. & Technical, U.o.V. (2004): Flow Mechanism (FM-) Experiment: Three dimensional model predictions of tracer evolution of HTO and iodine in the main fault. Mont Terri Technical Report TR 00-08. Mont Terri Project, Switzerland.

Gonçalvès, J., Matray, J.-M. & Yu, C.J. (2023): Assessing relevant transport processes in Opalinus Clay at the Mont Terri rock laboratory using excess-pressure, concentration and temperature profiles. Applied Clay Science 242, 107016. DOI: 10.1016/j.clay.2023.107016.

Gonzalez, R. & Wetzel, A. (1996): Stratigraphy and paleogeography of the Hauptrogenstein and Klingnau Formations (middle Bajocian to late Bathonian), northern Switzerland. Eclogae Geologicae Helvetiae 89/2, 695-720.

Gosling, J.P. (2018): SHELF: The Sheffield Elicitation Framework. *In:* Dias, L.C., Morton, A. & Quigley, J. (eds.): Elicitation, vol. 261. (International Series in Operations Research & Management Science), 61-93.

Gouffon, Y. (ed.) (2024): Tectonic Map of Switzerland 1: 500 000. Explanatory notes. Federal Office of Topography swisstopo.

Gradstein, F.M., Ogg, J.G., Schmitz, M.D. & Ogg, G. (eds.) (2020): Geologic Time Scale 2020. Elsevier, Amsterdam.

Graf, E.L.S. (2022): Controls on Sediment Flux in Active Mountain Ranges. PhD thesis. University of Edinburgh.

Graf, H.R. (1993): Die Deckenschotter der zentralen Nordschweiz. Dissertation ETH No. 10205. Eidgenössische Technische Hochschule, Zürich.

Graf, H.R. (2009a): Stratigraphie und Morphogenese von frühpleistozänen Ablagerungen zwischen Bodensee und Klettgau. Eiszeitalter und Gegenwart. Quaternary Science Journal 58/1, 12-53. DOI: 10.3285/eg.58.1.02.

Graf, H.R. (2009b): Stratigraphie von Mittel- und Spätpleistozän in der Nordschweiz. Beiträge zur Geologischen Karte der Schweiz N.F. 168. Bundesamt für Landestopografie swisstopo, Wabern.

Graf, H.R. & Burkhalter, R. (2016): Quaternary deposits: concept for a stratigraphic classification and nomenclature—an example from northern Switzerland. Swiss Journal of Geosciences 109/2, 137-147. DOI: 10.1007/s00015-016-0222-7.

Gremaud, V. & Goldscheider, N. (2010): Geometry and drainage of a retreating glacier overlying and recharging a karst aquifer, Tsanfleuron-Sanetsch, Swiss Alps. Acta Carsologica 39/2. DOI: 10.3986/ac.v39i2.100.

Grischott, R., Kober, F., Ivy-Ochs, S., Hippe, K., Lupker, M., Bros, E., Maden, C., Christl, M. & Vockenhuber, C. (2020): Dating Quaternary Terraces in Northern Switzerland with Cosmogenic Nuclides. Nagra Arbeitsbericht NAB 19-25.

Grollimund, B., Zoback, M.D. & D. Zoback, M. (2001): Did deglaciation trigger intraplate seismicity in the New Madrid seismic zone? Geology 29/2, 175-178. DOI: 10.1130/0091-7613(2001)029<0175:DDTISI>2.0.CO;2.

Grust, K. (2004): The hydrology and dynamics of a glacier overlying a linked-cavity drainage system. PhD thesis. University of Glasgow.

Guglielmi, Y., Nussbaum, C., Jeanne, P., Rutqvist, J., Cappa, F. & Birkholzer, J. (2020): Complexity of fault rupture and fluid leakage in shale: Insights from a controlled fault activation experiment. Journal of Geophysical Research: Solid Earth 125/2, e2019JB017781. DOI: 10.1029/2019JB017781.

Gygi, R.A. (1969): Zur Stratigraphie der Oxford-Stufe (oberes Jura-System) der Nordschweiz und des süddeutschen Grenzgebietes. Beiträge zur Geologischen Karte der Schweiz NF 136. Bundesamt für Landestopographie swisstopo.

Gygi, R.A. (1986): Eustatic sea level changes of the Oxfordian (Late Jurassic) and their effect documented in sediments and fossil assemblages of an epicontinental sea. Eclogae Geologicae Helvetiae 79/2, 455-491.

Gygi, R.A. (1990): Die Paläogeographie im Oxfordium und frühesten Kimmeridgium in der Nordschweiz. Jahreshefte des Geologischen Landesamtes Baden-Württemberg 32, 207-222.

Gygi, R.A. (2000a): Annotated index of lithostratigraphic units currently used in the Upper Jurassic of northern Switzerland. Eclogae Geologicae Helvetiae 93/14, 125-146.

Gygi, R.A. (2000b): Integrated stratigraphy of the Oxfordian and Kimmeridgian (Late Jurassic) in northern Switzerland and adjacent southern Germany. (Denkschriften der Schweizerischen Akademie der Naturwissenschaften, Vol. 104). Birkhäuser, Basel.

Gygi, R.A. (2012): Quantitative geology of late Jurassic epicontinental sediments in the Jura Mountains of Switzerland. Springer, Basel, Heidelberg.

Gygi, R.A., Coe, A.L. & Vail, P.R. (1998): Sequence Stratigraphy of the Oxfordian and Kimmeridgian Stages (Late Jurassic) in Northern Switzerland. *In:* de Graciansky, P.-C., Hardenbol, J., Jacquin, T. & Vail, P.R. (eds.): Mesozoic and Cenozoic sequence stratigraphy of European basins. (Special publication, 60). Society for Sedimentary Geology; SEPM, Tulsa, Oklahoma, 527-544.

Gygi, R.A. & Persoz, F. (1986): Mineralostratigraphy, litho- and biostratigraphy combined in correlation of the Oxfordian (Late Jurassic) formations of the Swiss Jura range. Eclogae Geologicae Helvetiae 79/2, 385-454.

Haeberli, W., Rellstab, W. & Harrison, W.D. (1984): Geothermal Effects of 18 ka BP Ice Conditions in the Swiss Plateau. Annals of Glaciology 5, 56-60. DOI: 10.3189/1984AoG5-1-56-60.

Haefeli, R. (1940): Zur Mechanik aussergewöhnlicher Gletscherschwankungen. Schweizerische Bauzeitung 115/16, 179-184.

Hagdorn, H. & Nitsch, E. (eds.) (2009): 6th International Triassic Field Workshop (Pan-European Correlation of the Triassic) Triassic of Southwest Germany, 175th Anniversary of the Foundation of the Triassic System by Friedrich von Alberti September 7 - 11, 2009, Tübingen and Ingelfingen. Field Guide.

Hagedorn, E.M. & Boenigk, W. (2008): The Pliocene and Quaternary sedimentary and fluvial history in the Upper Rhine Graben based on heavy mineral analyses. Netherlands Journal of Geosciences – Geologie en Mijnbouw 87/1, 21-32.

Hancock, P.L. (1985): Brittle microtectonics: principles and practice. Journal of Structural Geology 7/3-4, 437-457. DOI: 10.1016/0191-8141(85)90048-3.

Handy, M.R. & Brun, J.-P. (2004): Seismicity, structure and strength of the continental lithosphere. Earth and Planetary Science Letters 223/3-4, 427-441. DOI: 10.1016/j.epsl.2004.04.021.

Handy, M.R., Schmid, S.M., Bousquet, R., Kissling, E. & Bernoulli, D. (2010): Reconciling plate-tectonic reconstructions of Alpine Tethys with the geological–geophysical record of spreading and subduction in the Alps. Earth-Science Reviews 102/3-4, 121-158. DOI: 10.1016/j.earscirev.2010.06.002.

Hantke, R. (1967): Die neue geologische Karte des Kantons Zürich und seiner Nachbargebiete, 1:50'000. Mitteilungen aus dem Geologischen Institut der Eidgenössischen Technischen Hochschule und der Universität Zürich 88, 618-620.

Haq, B.U. (2018): Jurassic sea-level variations: A reappraisal. GSA Today 28/1, 4-10. DOI: 10.1130/GSATG359A.1.

Hardenbol, J., Thierry, J., Farley, M.B., Jacquin, T., Graciansky, P.C. de & Vail, P. (1998): Mesozoic and Cenozoic sequence chronostratigraphic framework of European basins. SEPM Society for Sedimentary Geology 60, 3-13. DOI: 10.2110/pec.98.02.0003.

Harrison, A.L., Schott, J., Oelkers, E.H., Maher, K. & Mavromatis, V. (2022): Rates of carbon and oxygen isotope exchange between calcite and fluid at chemical equilibrium. Geochimica et Cosmochimica Acta 335, 369-382. DOI: 10.1016/j.gca.2022.06.041.

Hartmann, A. (1925): Die Mineral- und Heil-Quellen des Kantons Aargau. Ihre geologischen und chemischen Verhältnisse 17, 255-319.

Hartmann, A. (1928): Der Erdrutsch von Ittenthal 1924-1926. Mitteilungen der Aargauischen Naturforschenden Gesellschaft 18, 53-70.

Hartmann, A. (1950): Der untere braune Jura des Aargaus als wichtigster zukünftiger Tonlieferant der Schweiz. Mitteilungen der Aargauischen Naturforschenden Gesellschaft 23, 3-20.

Hauber, L., Jordan, P., Madsen, F., Nüesch, R. & Vögtli, B. (2005): Tonminerale und Sulfate als Ursache für druckhaftes Verhalten von Gesteinen. Ursachen und Wirkungen des Quellvorganges. Bundesamt für Strassenbau ASTRA, Basel.

Hebestreit, C. (1995): Zur jungpleistozänen und holozänen Entwicklung der Wutach (SW-Deutschland). Dissertation. Universität Tübingen. Institut für Geologie und Paläontologie.

Heidbach, O., Rajabi, M., Cui, X., Fuchs, K., Müller, B., Reinecker, J., Reiter, K., Tingay, M., Wenzel, F., Xie, F., Ziegler, M.O., Zoback, M.-L. & Zoback, M. (2018): The World Stress Map database release 2016: Crustal stress pattern across scales. Tectonophysics 744, 484-498. DOI: 10.1016/j.tecto.2018.07.007.

Heidbach, O., Rajabi, M., Reiter, K., Ziegler, M. & WSM Team (2016): World Stress Map Database Release 2016. DOI: 10.5880/WSM.2016.001.

Heidbach, O. & Reinecker, J. (2013): Analyse des rezenten Spannungsfeldes der Nordschweiz. Nagra Arbeitsbericht NAB 12-05.

Heim, A. & Hartmann, A. (1919): Untersuchungen über die petrolführende Molasse der Schweiz. (Beiträge zur Geologie der Schweiz. Geotechnische Serie, 6). Kommission A. Francke, Bern.

Hekel, U. (1994): Hydrogeologische Erkundung toniger Festgesteine am Beispiel des Opalinustons (Unteres Aalenium). (Tübinger Geowissenschaftliche Arbeiten (TGA). Reihe C: Hydro-, Ingenieur- und Umweltgeologie, 18). Institut für Geologie und Paläontologie, Tübingen.

Henrion, E., Masson, F., Doubre, C., Ulrich, P. & Meghraoui, M. (2020): Present-day deformation in the Upper Rhine Graben from GNSS data. Geophysical Journal International 223/1, 599-611. DOI: 10.1093/gji/ggaa320.

Héran, M.A., Lécuyer, C. & Legendre, S. (2010): Cenozoic long-term terrestrial climatic evolution in Germany tracked by δ18O of rodent tooth phosphate. Palaeogeography, Palaeoclimatology, Palaeoecology 285/3-4, 331-342. DOI: 10.1016/j.palaeo.2009.11.030.

Herb, R. (1988): Eocaene Paläogegographie und Paläotektonik des Helvetikums. Eclogae Geologicae Helvetiae 81/3, 611-657. DOI: 10.5169/seals-166197.

Herold, T. (1997): Räumliche Beziehungen der Karstsysteme zu den tektonisch-geologischen Strukturen im Gebiet der Weissenstein- und Farisbergantiklinale (Solothurner Jura). Dissertation ETH Nr. 12400. ETH Zürich.

Herwegh, M., Berger, A., Baumberger, R., Wehrens, P. & Kissling, E. (2017): Large-Scale Crustal-Block-Extrusion During Late Alpine Collision. Scientific Reports 7/1, 413. DOI: 10.1038/s41598-017-00440-0.

Herwegh, M., Berger, A., Glotzbach, C., Wangenheim, C., Mock, S., Wehrens, P., Baumberger, R., Egli, D. & Kissling, E. (2020): Late stages of continent-continent collision: Timing, kinematic evolution, and exhumation of the Northern rim (Aar Massif) of the Alps. Earth-Science Reviews 200, 102959. DOI: 10.1016/j.earscirev.2019.102959.

Hesselbo, S.P., Ogg, J.G., Ruhl, M., Hinnov, L.A. & Huang, C.J. (2020): The Jurassic Period. *In:* Gradstein, F.M., Ogg, J.G., Schmitz, M.D. & Ogg, G. (eds.): Geologic Time Scale 2020. Elsevier, Amsterdam, 955-1021.

Hetzel, R. & Hampel, A. (2005): Slip rate variations on normal faults during glacial-interglacial changes in surface loads. Nature 435/7038, 81-84. DOI: 10.1038/nature03562.

Heuberger, S., Büchi, M. & Naef, H. (2014): Drainage system and landscape evolution of northern Switzerland since the Late Miocene. Nagra Arbeitsbericht NAB 12-20.

Heuberger, S. & Naef, H. (2014): Regionale GIS-Kompilation und -Analyse der Deckenschotter-Vorkommen im nördlichen Alpenvorland. Nagra Arbeitsbericht NAB 12-35.

Hillebrand, G. & Frings, R.M. (2017): Von der Quelle zur Mündung: Die Sedimentbilanz des Rheins im Zeitraum 1991-2010. (Internationale Kommission für die Hydrologie des Rheingebietes, Bericht Nr. II-22). KHR/CHR, Lelystad.

Hinderer, M. (2003): Large to Medium-Scale Sediment Budget Models - the Alpenrhein as a Case Study. In: Lang, A., Dikau, R. & Hennrich, K. (eds): Long Term Hillslope and Fluvial System Modelling Lecture Notes in Earth Sciences. 101, 137-156. Springer, Berlin, Heidelberg.

Hinderer, M. (2005): Sedimentfalle Bodensee. Veranstaltungen 4/2005: Feststoffhaushalt und Sedimentbewirtschaftung – anthropogene Steuerung natürlicher Prozesse? 7. Gewässer-morphologisches Kolloquium am 3./4. November 2004 in Koblenz, 5-17.

Hinderer, M. (2012): From gullies to mountain belts: A review of sediment budgets at various scales. Sedimentary Geology 280, 21-59. DOI: 10.1016/j.sedgeo.2012.03.009.

Hoehn, E. (1979): Hydrogeologische Untersuchungen im Gebiet westlich von Frick (Aargauer Tafeljura). (Beiträge zur Geologie der Schweiz – Hydrologie, 26), Kümmerly + Frey, Bern.

Hofmann, F. (1981): Geologischer Atlas der Schweiz. Blatt 1031 Neunkirch mit Erläuterungen. Bundesamt für Landestopografie swisstopo.

Hofmann, F., Schlatter, R. & Weh, M. (2000): Blatt 1011 Beggingen (Südhälfte) mit SW-Anteil von Blatt 1012 Singen. Bundesamt für Landestopografie swisstopo.

Hofmann, R. & Sander, P.M. (2014): The first juvenile specimens of Plateosaurus engelhardti from Frick, Switzerland: isolated neural arches and their implications for developmental plasticity in a basal sauropodomorph. PeerJ 2, e458. DOI: 10.7717/peerj.458.

Homberg, C., Bergerat, F., Philippe, Y., Lacombe, O. & Angelier, J. (2002): Structural inheritance and cenozoic stress fields in the Jura fold-and-thrust belt (France). Tectonophysics 357/1-4, 137-158. DOI: 10.1016/S0040-1951(02)00366-9.

Hooke, R.L. & Jennings, C.E. (2006): On the formation of the tunnel valleys of the southern Laurentide ice sheet. Quaternary Science Reviews 25/11-12, 1364-1372. DOI: 10.1016/j.quascirev.2006.01.018.

Horseman, S.T., Higgo, J., Alexander, J. & Harrington, J.F. (1996): Water, gas and solute movement through argillaceous media. NEA Working Group on Measurement and Physical Understanding of Groundwater Flow Through Argillaceous Media ("Clay Club"), a Sub-group of the NEA Co-ordinationg Group on Site Evaluation and Design of Experiments for Radioactive Waste Disposal (SEDE)OECD/NEA Report CC-96/1. Edited by Nuclear Enrgy Agency, Organisation for Economic Co-Operation and Development.

Hostettler, B., Reisdorf, A., Jaeggi, D., Deplazes, G., Bläsi, H.R., Morard, A., Feist-Burkhardt, S., Waltschew, A., Dietze, V. & Menkveld-Gfeller, U. (2017): Litho- and biostratigraphy of the Opalinus Clay and bounding formations in the Mont Terri rock laboratory (Switzerland). Swiss Journal of Geosciences 110/1, 23-37. DOI: 10.1007/s00015-016-0250-3.

Houlié, N., Woessner, J., Giardini, D. & Rothacher, M. (2018): Lithosphere strain rate and stress field orientations near the Alpine arc in Switzerland. Scientific Reports 8/1. DOI: 10.1038/s41598-018-20253-z.

Huber, M.L., Amschwand, D., Madritsch, H., Deplazes, G. & Buechi, M.W. (2020): Quaternary Borehole QBO Trüllikon-Rudolfingen (QTRU) Data Report. Nagra Arbeitsbericht NAB 20-01.

Hummel, W. & Thoenen, T. (2023): The PSI Chemical Thermodynamic Database 2020. Nagra Technical Report NTB 21-03.

Huysmans, M. & Dassargues, A. (2005): Review of the use of Péclet numbers to determine the relative importance of advection and diffusion in low permeability environments. Hydrogeology Journal 13/5-6, 895-904. DOI: 10.1007/s10040-004-0387-4.

Ibele, T. (2015): Tectonics of the Hegau and Lake Constance region: A synthesis based on existing literature. Nagra Arbeitsbericht NAB 12-23.

Illies, J.H. & Greiner, G. (1979): Holocene movements and state of stress in the Rhinegraben Rift System. Development in Geotectonics 13, 349-359. DOI: 10.1016/B978-0-444-41783-1.50057-X.

Illies, J.H., Prodehl, C., Schmincke, H.-U. & Semmel, A. (1979): The Quaternary uplift of the Rhenish Shield in Germany. Tectonophysics 61/1-3, 197-225. DOI: 10.1016/0040-1951(79)90298-1.

Insalaco, E. (1998): The descriptive nomenclature and classification of growth fabrics in fossil scleractinian reefs. Sedimentary Geology 118/1-4, 159-186. DOI: 10.1016/S0037-0738(98)00011-6.

IPCC (ed.) (2023): Climate Change 2023: Synthesis Report. Contribution of Working Group I, II and III to the Sixth Assessment Report of the Intergovernmental Panel on Climate Change. Intergovernmental Panel on Climate Change IPCC, Geneva.

Isler, A., Pasquier, F. & Huber, M. (1984): Geologische Karte der zentralen Nordschweiz, 1:100000 (mit angrenzenden Gebieten von Baden-Württemberg). Herausgegeben gemeinsam mit der NAGRA.

ISRM (1981): Suggested methods for the rock characterisation, testing and monitoring. ISRM Commission on Testing Methods, Pergamon Press, Oxford.

ISRM (1989): International society for rock mechanics commission on swelling rock and working group on swelling rock of the commission on testing methods. International Journal of Rock Mechanics and Mining Sciences & Geomechanics Abstracts 26/5, 415-426. DOI: 10.1016/0148-9062(89)90937-6.

Iverson, N.R. (2002): Processes of glacial erosion. *In:* Menzies, J. (ed.): Modern and Past Glacial Environments. Revised studen edition. Butterworth/Heinemann, Oxford, 131-146.

Ivy-Ochs, S., Kerschner, H., Reuther, A., Maisch, M., Sailer, R., Schaefer, J., Kubik, P.W., Synal, H.-A. & Schlüchter, C. (2006): The timing of glacier advances in the northern European Alps based on surface exposure dating with cosmogenic ^{10}Be, ^{26}Al, ^{36}Cl, and ^{21}Ne. DOI: 10.1130/2006.2415(04).

Jäckli, H. & Kempf, T. (1972): Hydrogeologische Karte der Schweiz 1:100'000. Blatt Bözberg-Beromünster mit Erläuterungen. Bundesamt für Landestopografie swisstopo.

Jacops, E., Aertsens, M., Maes, N., Bruggeman, C., Swennen, R., Krooss, B., Amann-Hildenbrand, A. & Littke, R. (2017): The Dependency of Diffusion Coefficients and Geometric Factor on the Size of the Diffusing Molecule: Observations for Different Clay-Based Materials. Geofluids 2017/1, 1-16. DOI: 10.1155/2017/8652560.

Jaeggi, D., Laurich, B., Nussbaum, C., Schuster, K. & Connolly, P. (2017): Tectonic structure of the "Main Fault" in the Opalinus Clay, Mont Terri rock laboratory (Switzerland). Swiss Journal of Geosciences 110/1, 67-84. DOI: 10.1007/s00015-016-0243-2.

Jank, M., Wetzel, A. & Meyer, C.A. (2006): Late Jurassic sea-level fluctuations in NW Switzerland (Late Oxfordian to Late Kimmeridgian): closing the gap between the Boreal and Tethyan realm in Western Europe. Facies 52/4, 487-519. DOI: 10.1007/s10347-005-0044-y.

Jeannin, P.Y., Malard, A., Eichenberger, U. & Rick, B. (2015): Grundlagen zur Beurteilung von Tiefenlagerprojekten im Hinblick auf Karstphänomene. Expertenbericht im Rahmen der Beurteilung des Vorschlags von mindestens zwei geologischen Standortgebieten pro Lagertyp, Etappe 2, Sachplan geologische Tiefenlager. ENSI 33/472. Eidgenössisches Nuklearsicherheitsinspektorat ENSI, Brugg.

Jordan, P. (1983): Zur Stratigraphie des Lias zwischen unterem Hauenstein und Schinznach (Solothurner und Aargauer Faltenjura). Eclogae Geologicae Helvetiae 76/2, 355-379.

Jordan, P. & Deplazes, G. (2019): Lithostratigraphy of consolidated rocks expected in the Jura Ost, Nördlich Lägern and Zürich Nordost Regions. Nagra Arbeitsbericht NAB 19-14.

Jordan, P., Malz, A., Heuberger, S., Pietsch, J., Kley, J. & Madritsch, H. (2015): Regionale geologische Profile durch die Nordschweiz und 2D-Bilanzierung der Fernschub-deformation im östlichen Faltenjura: Arbeitsbericht zu SGT Etappe 2. Nagra Arbeitsbericht NAB 14-105.

Jordan, P. & Nüesch, R. (1989): Deformation Structures in the Muschelkalk Anhydrites of the Schafisheim Well (Jura Overthrust, Northern Switzerland). Eclogae Geologicae Helvetiae 82/2, 429-454.

Jordan, P., Pietsch, J., Kündig, N., Bläsi, H.R. & Deplazes, G. (2016a): Grundlagen zur Definition und Unterteilung der Klettgau- und Bänkerjoch-Formation (vormals Oberer und Mittlerer Keuper) in der Nordschweiz. Nagra Arbeitsbericht NAB 16-62.

Jordan, P., Pietsch, J.S., Bläsi, H., Furrer, H., Kündig, N., Looser, N., Wetzel, A. & Deplazes, G. (2016b): The middle to late Triassic Bänkerjoch and Klettgau formations of northern Switzerland. Swiss Journal of Geosciences 109/2, 257-284. DOI: 10.1007/s00015-016-0218-3.

Jost, A., Violette, S., Gonçalvès, J., Ledoux, E., Guyomard, Y., Guillocheau, F., Kageyama, M., Ramstein, G. & Suc, J.-P. (2007): Long-term hydrodynamic response induced by past climatic and geomorphologic forcing: The case of the Paris basin, France. Physics and Chemistry of the Earth, Parts A/B/C 32/1-7, 368-378. DOI: 10.1016/j.pce.2006.02.053.

Jost, J., Kempf, O. & Kälin, D. (2016): Stratigraphy and palaeoecology of the Upper Marine Molasse (OMM) of the central Swiss Plateau. Swiss Journal of Geosciences 109/2, 149-169. DOI: 10.1007/s00015-016-0223-6.

Jouvet, G., Cohen, D., Russo, E., Buzan, J., Raible, C.C., Haeberli, W., Kamleitner, S., Ivy-Ochs, S., Imhof, M.A., Becker, J.K., Landgraf, A. & Fischer, U.H. (2023): Coupled climate-glacier modelling of the last glaciation in the Alps. Journal of Glaciology, 1-15. DOI: 10.1017/jog.2023.74.

Kahneman, D., Slovic, P. & Tversky, A. (eds.) (1982): Judgment under Uncertainty. Heuristics and Biases. Cambridge University Press.

Kamleitner, S., Ivy-Ochs, S., Manatschal, L., Akçar, N., Christl, M., Vockenhuber, C., Hajdas, I. & Synal, H.-A. (2023): Last Glacial Maximum glacier fluctuations on the northern Alpine foreland: Geomorphological and chronological reconstructions from the Rhine and Reuss glacier systems. Geomorphology 423, 108548. DOI: 10.1016/j.geomorph.2022.108548.

Kämpf, L., Rius, D., Duprat-Oualid, F., Crouzet, C. & Millet, L. (2022): Evidence for wind patterns and associated landscape response in Western Europe between 46 and 16 ka cal. BP. Quaternary Science Reviews 298, 107846. DOI: 10.1016/j.quascirev.2022.107846.

Kastrup, U., Zoback, M.L. & Deichmann (2004): Stress field variations in the Swiss Alps and the northern Alpine foreland derived from inversion of fault plane solutions. Journal of Geophysical Research: Solid Earth 109/B1, B01402. DOI: 10.1029/2003JB002550.

KEG (2003): Kernenergiegesetz (KEG) of March 21, 2003, status as of January 1, 2024. Systematische Sammlung des Bundesrechts SR 732.1, Schweiz.

Kehew, A.E., Piotrowski, J.A. & Jørgensen, F. (2012): Tunnel valleys: concepts and controversies—a review. Earth-Science Reviews 113/1-2, 33-58. DOI: 10.1016/j.earscirev.2012.02.002.

Keller, L. & Holzer, L. (2013): Spatial analysis of tomographic data and its implications on mass transport in Opalinus Clay. NEA-RWM-CLAYCLUB-2013-1. *In:* OECD/NEA (ed.): Clay characterisation from nanoscopic to microscopic resolution. NEA Clay Club Workshop Proceedings, 84-90.

Keller, L.M., Schuetz, P., Erni, R., Rossell, M.D., Lucas, F., Gasser, P. & Holzer, L. (2013): Characterization of multi-scale microstructural features in Opalinus Clay. Microporous and Mesoporous Materials 170, 83-94. DOI: 10.1016/j.micromeso.2012.11.029.

Keller, O. & Krayss, E. (2000): Die Hydrographie des Bodenseeraums in Vergangenheit und Gegenwart. (Erläuterungen zur Karte 'Vorlandvereisung des Bodensee-Rheingletschers in der Würmeiszeit'). Berichte der St. Gallischen naturwissenschaftlichen Gesellschaft 89, 39-56.

Kessler, M.A., Anderson, R.S. & Briner, J.P. (2008): Fjord insertion into continental margins driven by topographic steering of ice. Nature Geoscience 1, 365-369. DOI: 10.1038/ngeo201.

KEV (2004): Kernenergieverordnung (KEV) of December 10, 2004, status as of January 1, 2024. Systematische Sammlung des Bundesrechts SR 732.11, Schweiz.

Khaledi, S., Delbari, M., Galavi, H., Bagheri, H. & Chari, M.M. (2023): Effects of biochar particle size, biochar application rate, and moisture content on thermal properties of an unsaturated sandy loam soil. Soil and Tillage Research 226, 105579. DOI: 10.1016/j.still.2022.105579.

Kharaka, Y.K. & Hanor, J.S. (2014): Deep Fluids in Sedimentary Basins. Chapter 7.14. *In:* Holland, H.D. & Turekian, K.K. (eds.): Treatise on Geochemistry. 2nd ed. Elsevier, Amsterdam, Heidelberg, 471-515.

Kiczka, M., Wersin, P., Mazurek, M., Zwahlen, C., Jenni, A., Mäder, U. & Traber, D. (2023): Porewater composition in clay rocks explored by advective displacement and squeezing experiments. Applied Geochemistry 159, 105838. DOI: 10.1016/j.apgeochem.2023.105838.

Kiefer, L., Deplazes, G. & Bläsi, H.R. (2015): Sedimentologie und Stratigraphie des Frühen Juras in der Nordschweiz: Staffelegg-Formation und sich nach Osten anschliessende Vorkommen. Nagra Arbeitsbericht NAB 14-95.

Kipfer, R., Aeschbach-Hertig, W., Peeters, F. & Stute, M. (2002): Noble gases in lakes and ground waters. Reviews in Mineralogy and Geochemistry 47/1, 615-700. DOI: 10.2138/rmg.2002.47.14.

Kirby, S.H. (1985): Rock mechanics observations pertinent to the rheology of the continental lithosphere and the localization of strain along shear zones. Tectonophysics 119/1-4, 1-27. DOI: 10.1016/0040-1951(85)90030-7.

Klemenz, W., Blaser, P. & Küpfer, T. (2000): Hydrogeologie des Gebietes Lägern - Zürcher Weinland. Unpubl. Nagra Interner Bericht.

Knudsen, M.F., Nørgaard, J., Grischott, R., Kober, F., Egholm, D.L., Hansen, T.M. & Jansen, J.D. (2020): New cosmogenic nuclide burial-dating model indicates onset of major glaciations in the Alps during Middle Pleistocene Transition. Earth and Planetary Science Letters 549, 116491. DOI: 10.1016/j.epsl.2020.116491.

Koch, R. (2011): Dolomit und Dolomit-Zerfall im Malm Süddeutschlands – Verbreitung, Bildungsmodelle, Dolomit-Karst. Laichinger Höhlenfreund 46, 75-92.

Koch, R. (2019): Zur Fazies des Oberjura im Untergrund des Bodensees – Süddeutschland; Molasse-Becken. Wo ist das „Schwäbische Mergelbecken“? = Upper Jurassic facies development in the subsurface of Lake Constance – Southern Germany, Molasse Basin. Where did the "Swabian Marl-Basin" disappear? Jahresberichte und Mitteilungen des Oberrheinischen Geologischen Vereins 101, 359-393. DOI: 10.1127/jmogv/101/0015.

Köppen, W. (1918): Klassification der Klimate nach Temperatur, Niederschlag und Jahreslauf. Petermanns Geographische Mitteilungen 64, 193–203 & 243–248.

Koppka, J. (2015): Revision of the bivalvia from the Upper Jurassic Reuchenette Formation, Northwest Switzerland - Ostreoidea. Zootaxa 3927, 1-117. DOI: 10.11646/zootaxa.3927.1.1.

Kosakowski, G. (2004): Time-dependent flow and transport calculations for Project Opalinus Clay (Entsorgungsnachweis). Nagra Technical Report NTB 03-10.

Kozur, H.W. & Bachmann, G.H. (2008): Updated correlation of the Germanic Triassic with the Tethyan scale and assigned numeric ages. Berichte der Geologischen Bundesanstalt 76, 53-58.

Krakow, L. & Schunke, F. (2017): Aktuelles Tonpotenzial von Deutschland, Teil 6: Rohstoffe aus dem System des Jura. Ziegelindustrie International, Brick and Tile Industry International 4.

Krijgsman, W., Hilgen, F.J., Raffi, I., Sierro, F.J. & Wilson, D.S. (1999): Chronology, causes and progression of the Messinian salinity crisis. Nature 400/6745, 652-655. DOI: 10.1038/23231.

Kuhlemann, J. & Kempf, O. (2002): Post-Eocene evolution of the North Alpine Foreland Basin and its response to Alpine tectonics. Sedimentary Geology 152/1-2, 45-78. DOI: 10.1016/S0037-0738(01)00285-8.

Kuhlemann, J., Rahn, M., Kuhlemann, J. & Rahn, M. (2013): Plio-pleistocene landscape evolution in Northern Switzerland. Swiss Journal of Geosciences 106/3, 451-467. DOI: 10.1007/s00015-013-0152-6.

Kulik, D.A. & Miron, G.D. (2024): Solubility Limits for Model Opalinus Clay Porewaters as Input for Sorption (SDB) and Diffusion (DDB) Databases. Nagra Arbeitsbericht NAB 23-07.

Küpfer, T. (2005): EP-05: Hydrogeologie der Unteren Süsswassermolasse. Nagra Arbeitsbericht NAB 04-09.

Kuster, A.M., Huber, M., Amschwand, D., Deplazes, G., Madritsch, H. & Buechi, M.W. (2019): Quaternary Borehole QBO Marthalen-Oobist (QMOB) Data Report. Nagra Arbeitsbericht NAB 19-04.

Lacombe, O. & Bellahsen, N. (2016): Thick-skinned tectonics and basement-involved fold–thrust belts: insights from selected Cenozoic orogens. Geological Magazine 153/5-6, 763-810. DOI: 10.1017/S0016756816000078.

Laird, D.A. (2006): Influence of layer charge on swelling of smectites. Applied Clay Science 34/1-4, 74-87. DOI: 10.1016/j.clay.2006.01.009.

Lanyon, G.W., Martin, D., Giger, S.B. & Marschall, P. (2014): Development and evolution of the Excavation Damaged Zone (EDZ) in the Opalinus Clay – A synopsis of the state of knowledge from Mont Terri. Nagra Arbeitsbericht NAB 14-87.

Lanza, F., Diehl, T., Deichmann, N., Kraft, T., Nussbaum, C., Schefer, S. & Wiemer, S. (2022): The Saint-Ursanne earthquakes of 2000 revisited: evidence for active shallow thrust-faulting in the Jura fold-and-thrust belt. Swiss Journal of Geosciences 115/1. DOI: 10.1186/s00015-021-00400-x.

Laubscher, H.P. (1961): Die Fernschubhypothese der Jurafaltung. Eclogae Geologicae Helvetiae 54/1, 221-282.

Laubscher, H.P. (1965): Ein kinematisches Modell der Jurafaltung. Eclogae Geologicae Helvetiae 58/1, 231-318.

Laubscher, H.P. (1985): The eastern Jura: Relations between thin-skinned and basement tectonics, local and regional. Nagra Technical Report NTB 85-53.

Laubscher, H.P. (1986): The eastern Jura: Relations between thin-skinned and basement tectonics, local and regional. Int J Earth Sci (Geol Rundsch) 75/3, 535-553. DOI: 10.1007/BF01820630.

Laubscher, H.P. (1992): Jura kinematics and the Molasse Basin. Eclogae Geologicae Helvetiae 85/3, 653-675.

Lauper, B. (2021): Characterisation of lithological heterogeneity within the Opalinus Clay and at its upper lithostratigraphic boundary (N Switzerland). PhD Thesis No 2239. University of Fribourg Switzerland. Department of Geosciences.

Lauper, B., Deplazes, G., Vogel, H., Jaeggi, D., Wohlwend, S., Ariztegui, D. & Foubert, A. (2021a): Geochemical fingerprinting of key lithologies and depositional processes across the upper boundary of the Opalinus Clay (Aalenian, Middle Jurassic, northern Switzerland). The Depositional Record 7/1, 25-51. DOI: 10.1002/dep2.126.

Lauper, B., Jaeggi, D., Deplazes, G. & Foubert, A. (2018): Multi-proxy facies analysis of the Opalinus Clay and depositional implications (Mont Terri rock laboratory, Switzerland). Swiss Journal of Geosciences 111/3, 383-398. DOI: 10.1007/s00015-018-0303-x.

Lauper, B., Zimmerli, G.N., Jaeggi, D., Deplazes, G., Wohlwend, S., Rempfer, J. & Foubert, A. (2021b): Quantification of lithological heterogeneity within Opalinus Clay: Toward a uniform subfacies classification scheme using a novel automated core image recognition tool. Frontiers in Earth Sciences 9, 645596. DOI: 10.3389/feart.2021.645596.

Laurich, B., Urai, J.L., Desbois, G., Vollmer, C. & Nussbaum, C. (2014): Microstructural evolution of an incipient fault zone in Opalinus Clay: Insights from an optical and electron microscopic study of ion-beam polished samples from the Main Fault in the Mt-Terri Underground Research Laboratory. Journal of Structural Geology 67, Part A, 107-128. DOI: 10.1016/j.jsg.2014.07.014.

Laurich, B., Urai, J.L., Vollmer, C. & Nussbaum, C. (2018): Deformation mechanisms and evolution of the microstructure of gouge in the Main Fault in Opalinus Clay in the Mont Terri rock laboratory (CH). Solid Earth 9/1, 1-24. DOI: 10.5194/se-9-1-2018.

Le Quéré, C., Andrew, R.M., Friedlingstein, P., Sitch, S., Pongratz, J., Manning, A.C., Korsbakken, J.I., Peters, G.P., Canadell, J.G., Jackson, R.B., Boden, T.A., Tans, P.P., Andrews, O.D., Arora, V.K., Bakker, D.C.E., Barbero, L., Becker, M., Betts, R.A., Bopp, L., Chevallier, F., Chini, L.P., Ciais, P., Cosca, C.E., Cross, J., Currie, K., Gasser, T., Harris, I., Hauck, J., Haverd, V., Houghton, R.A., Hunt, C.W., Hurtt, G., Ilyina, T., Jain, A.K., Kato, E., Kautz, M., Keeling, R.F., Klein Goldewijk, K., Körtzinger, A., Landschützer, P., Lefèvre, N., Lenton, A., Lienert, S., Lima, I., Lombardozzi, D., Metzl, N., Millero, F., Monteiro, P.M.S., Munro, D.R., Nabel, J.E.M.S., Nakaoka, S., Nojiri, Y., Padin, X.A., Peregon, A., Pfeil, B., Pierrot, D., Poulter, B., Rehder, G., Reimer, J., Rödenbeck, C., Schwinger, J., Séférian, R., Skjelvan, I., Stocker, B.D., Tian, H., Tilbrook, B., Tubiello, F.N., van der Laan-Luijkx, I.T., van der Werf, G.R., van Heuven, S., Viovy, N., Vuichard, N., Walker, A.P., Watson, A.J., Wiltshire, A.J., Zaehle, S. & Zhu, D. (2018): Global Carbon Budget 2017. Earth System Science Data 10/1, 405-448. DOI: 10.5194/essd-10-405-2018.

Lear, C.H., Elderfield, H. & Wilson, P.A. (2000): Cenozoic deep-sea temperatures and global ice volumes from Mg/Ca in benthic foraminiferal calcite. Science 287/5451, 269-272. DOI: 10.1126/science.287.5451.269.

Lerouge, C., Grangeon, S., Claret, F., Gaucher, E., Blanc, P., Guerrot, C., Flehoc, C., Wille, G. & Mazurek, M. (2014): Mineralogical and Isotopic record of diagenesis from the Opalinus Clay formation at Benken, Switzerland: Implications for the modeling of pore-water chemistry in a clay formation. Clays and Clay Minerals 62/4, 286-312. DOI: 10.1346/CCMN.2014.0620404.

Leu, K., Zeeden, C., Mann, T., Erbacher, J., Bornemann, A. & Wonik, T. (2023): Cyclostratigraphy of the Lower Aalenian Opalinuston Formation in the Swabian Alb deduced from downhole logging data. Zeitschrift der Deutschen Gesellschaft für Geowissenschaften ZDGG 174/1, 53-67. DOI: 10.1127/zdgg/2023/0373.

Leu, W. (2008): Permokarbon-Kartenskizze (Rohstoffe) - Kompilation eines GIS-Datensatzes auf der Basis von bestehenden Unterlagen (Bereich Schweizer Mittelland). Nagra Arbeitsbericht NAB 08-49.

Leupin, O.X., Van Loon, L.R., Gimmi, T., Wersin, P. & Soler, J.M. (2017): Exploring diffusion and sorption processes at the Mont Terri Underground Rock Laboratory: lessons learned from 20 years of field research. Swiss Journal of Geosciences, Special Issue: Mont Terri rock laboratory, 20 years of research 110, 391-403.

Leverd, P.C. (2023): The French Underground Research Laboratory in Bure: An Essential Tool for the Development and Preparation of the French Deep Geological Disposal Facility Cigéo. Journal of Nuclear Fuel Cycle and Waste Technology (JNFCWT) 21/4, 489-502. DOI: 10.7733/jnfcwt.2023.035.

LGL (2010): Digitales Geländemodell DGM (Mosaic: 25m / 2m grid size). Version March 2010 / June 2010 / December 2018, Stuttgart. Landesamt für Geoinformation und Landentwicklung (LGL), Baden-Württemberg, available online at https://www.lgl-bw.de/unsere-themen/Geoinformation/Topographie/Digitale-Gelaendemodelle-DGM/index.html, Stand am 27. September 2024.

Lindgren, A., Hugelius, G., Kuhry, P., Christensen, T.R. & Vandenberghe, J. (2016): GIS-based Maps and Area Estimates of Northern Hemisphere Permafrost Extent during the Last Glacial Maximum. Permafrost and Periglacial Processes 27/1, 6-16. DOI: 10.1002/ppp.1851.

Liniger, H. (1967): Pliozän und Tektonik des Juragebirges. Eclogae Geologicae Helvetiae 60/2, 407-490.

Lisiecki, L.E. & Raymo, M.E. (2005): A Pliocene-Pleistocene stack of 57 globally distributed benthic $\delta^{18}O$ records. Paleoceanography and Paleoclimatology 20/1, PA1003, 2004PA001071. DOI: 10.1029/2004PA001071.

Liu, L., Giger, S.B., Martin, D., Chalaturnyk, R., Schuster, K., Deisman, N. & Keller, L. (2022): In-situ shear modulus determination by pressuremeter tests in Opalinus Clay and reconciliation with laboratory tests. Rock Mechanics and Rock Engineering 55/8, 4615-4635. DOI: 10.1007/s00603-022-02873-0.

Longridge, D., Vogt, T. & Pechstein, A. (2024): Datenbericht Langzeitbeobachtung Benken, Marthalen-1-1, Bözberg-1-1, Stadel-3-1: Dokumentation der Messdaten 2022. Nagra Arbeitsbericht NAB 23-35.

Looser, N. (2022): Coupling clumped isotope thermometry and U-Pb dating of carbonates for applications in stratigraphy, diagenesis, and geodyamics. Doctoral Thesis No. 28365. ETH Zürich.

Looser, N., Madritsch, H., Guillong, M., Laurent, O., Wohlwend, S. & Bernasconi, S.M. (2021): Absolute age and temperature constraints on deformation along the basal décollement of the Jura fold-and-thrust belt from carbonate U-Pb dating and clumped isotopes. Tectonics 40/3, e2020TC006439. DOI: 10.1029/2020TC006439.

Looser, N., Schneebeli-Hermann, E., Furrer, H., Blattmann, T.M. & Bernasconi, S.M. (2018): Environmental changes and carbon cycle perturbations at the Triassic–Jurassic boundary in northern Switzerland. Swiss Journal of Geosciences 111/3, 445-460. DOI: 10.1007/s00015-018-0315-6.

Lorenz, J.C. & Cooper, S.P. (2018): Atlas of Natural and Induced Fractures in Core. Wiley Blackwell, Hoboken, NJ.

Lorenz, V. & Nicholls, I.A. (1984): Plate and intraplate processes of Herzynian Europe during the late Paleozoic. Tectonophysics 107/1-2, 25-56. DOI: 10.1016/0040-1951(84)90027-1.

Lowick, S.E., Buechi, M.W., Gaar, D., Graf, H.R. & Preusser, F. (2015): Luminescence dating of Middle Pleistocene proglacial deposits from northern Switzerland: methodological aspects and stratigraphical conclusions. Boreas 44/3, 459-482. DOI: 10.1111/bor.12114.

Ludwig, A. (2018): Local topography and hillslope processes in the Jura Ost siting region (and surrounding area). Nagra Arbeitsbericht NAB 17-42.

Luetscher, M., Moseley, G.E., Festi, D., Hof, F., Edwards, R.L. & Spötl, C. (2021): A Last Interglacial speleothem record from the Sieben Hengste cave system (Switzerland): Implications for alpine paleovegetation. Quaternary Science Reviews 262, 106974. DOI: 10.1016/j.quascirev.2021.106974.

Lüthi, D., Le Floch, M., Bereiter, B., Blunier, T., Barnola, J.-M., Siegenthaler, U., Raynaud, D., Jouzel, J., Fischer, H., Kawamura, K. & Stocker, T.F. (2008): High-resolution carbon dioxide concentration record 650,000-800,000 years before present. Nature 453/7193, 379-382. DOI: 10.1038/nature06949.

Lüttge, A., Winkler, U. & Lasaga, A.C. (2003): Interferometric study of the dolomite dissolution: a new conceptual model for mineral dissolution. Geochimica et Cosmochimica Acta 67/6, 1099-1116. DOI: 10.1016/S0016-7037(02)00914-6.

Madaschi, A., Leuthold, J., Cantieni, L. & Laloui, L. (2023): Comparative numerical calculations in the context of tunnel design for nuclear waste repositories in Opalinus Clay. Proceedings 10th NUMGE 2023. DOI: 10.53243/NUMGE2023-127.

Mäder, U. (2018): Advective displacement method for the characterisation of pore water chemistry and transport properties in claystone. Geofluids 2018/1, 8198762. DOI: 10.1155/2018/8198762.

Mäder, U. & Wersin, P. (2023): Reference porewaters for SGT Stage 3 of the Opalinus Clay for the siting regions Jura Ost (JO), Nördlich Lägern (NL) and Zürich Nordost (ZNO). Nagra Arbeitsbericht NAB 22-47.

Mäder, U.K. & Mazurek, M. (1998): Oxidation Phenomena and Processes in Opalinus Clay: Evidence From the Excavation-Disturbed Zones in Hauenstein and Mt. Terri Tunnels and Siblingen Open Clay Pit. *In:* McKinley, I.G. & McCombie, C. (eds.): Scientific Basis for Nuclear Waste Management XXI. Materials Research Society Symposium 506. Davos, September 28 – October 3, 1997, 731-739.

Madritsch, H. (2015): Geology of central Northern Switzerland: Overview and some key topics regarding Nagra's seismic exploration of the region. Swiss Bulletin for Applied Geology 20/2, 3-15.

Madritsch, H., Fabbri, O., Hagedorn, E.-M., Preusser, F., Schmid, S.M. & Ziegler, P.A. (2010): Feedback between erosion and active deformation: geomorphic constraints from the frontal Jura fold-and-thrust belt (eastern France). International Journal of Earth Sciences (Geologische Rundschau) 99/Suppl. 1, S103–S122. DOI: 10.1007/s00531-009-0468-7.

Madritsch, H. & Hammer, P. (2012): Characterisation of Cenozoic brittle deformation of potential geological siting regions for radioactive waste repositories in Northern Switzerland based on structural geological analysis of field outcrops. Nagra Arbeitsbericht NAB 12-41.

Madritsch, H., Looser, N., Schneeberger, R., Wohlwend, S., Guillong, M. & Malz, A. (2024): Reconstructing the Evolution of Foreland Fold-And-Thrust Belts Using U-Pb Calcite Dating: An Integrated Case-Study From the Easternmost Jura Mountains (Switzerland). Tectonics 43/5, e2023TC008181. DOI: 10.1029/2023TC008181.

Madritsch, H., Meier, B., Kuhn, P., Roth, P., Zingg, O., Birkhäuser, P., Heuberger, S. & Naef, H. (2013): Regionale strukturgeologische Zeitinterpretation der Nagra 2D-Seismik 2011/12. Nagra Arbeitsbericht NAB 13-10.

Madritsch, H., Naef, H., Meier, B., Franzke, H.J. & Schreurs, G. (2018): Architecture and Kinematics of the Constance-Frick Trough (Northern Switzerland): Implications for the Formation of Post-Variscan Basins in the Foreland of the Alps and Scenarios of Their Neogene Reactivation. Tectonics 37/7, 2197-2220. DOI: 10.1029/2017TC004945.

Madritsch, H., Schmid, S.M. & Fabbri, O. (2008): Interactions between thin- and thick-skinned tectonics at the northwestern front of the Jura fold-and-thrust belt (eastern France). Tectonics 27, TC5005. DOI: 10.1029/2008TC002282.

Madsen, F.T. & Müller-Vonmoos, M. (1989): The swelling behaviour of clays. Applied Clay Science 4/2, 143-156. DOI: 10.1016/0169-1317(89)90005-7.

Madsen, F.T. & Nüesch, R. (1989): Quellende Gesteine, Quellmechanismen und die Bestimmung massgebender Quellparameter im Labor. Juradurchquerungen - aktuelle Tunnelprojekte im Jura. Mitteilungen der Schweizerischen Gesellschaft für Boden- und Felsmechanik 119, 31-42.

Magrani, F., Valla, P.G., Gribenski, N. & Serra, E. (2020): Glacial overdeepenings in the Swiss Alps and foreland: Spatial distribution and morphometrics. Quaternary Science Reviews 243, 106483. DOI: 10.1016/j.quascirev.2020.106483.

Malz, A., Madritsch, H., Jordan, P., Meier, B. & Kley, J. (2020): Along-strike variations in thin-skinned thrusting style controlled by pre-existing basement structure in the easternmost Jura Mountains (Northern Switzerland). Geological Society, London, Special Publications 490/1, 199-220. DOI: 10.1144/SP490-2019-090.

Malz, A., Madritsch, H., Meier, B. & Kley, J. (2016): An unusual triangle zone in the external northern Alpine foreland (Switzerland): Structural inheritance, kinematics and implications for the development of the adjacent Jura fold-and-thrust belt. Tectonophysics 670, 127-143. DOI: 10.1016/j.tecto.2015.12.025.

Marchant, R., Ringgenberg, Y., Stampfli, G., Birkhäuser, P., Roth, P. & Meier, B. (2005): Paleotectonic evolution of the Zürcher Weinland (northern Switzerland), based on 2D and 3D seismic data. Eclogae Geologicae Helvetiae 98/3, 345-362. DOI: 10.1007/s00015-005-1171-8.

Marro, A., Hauvette, L., Borderie, S. & Mosar, J. (2023): Tectonics of the Western Internal Jura fold-and-thrust belt: 2D kinematic forward modelling. Swiss Journal of Geosciences 116/1. DOI: 10.1186/s00015-023-00435-2.

Marschall, P., Croisé, J., Schlickenrieder, L., Boisson, J.-Y., Vogel, P. & Yamamato, S. (2004): Synthesis of hydrogeological investigations at the Mont Terri Site. *In:* Heitzmann, P. (ed.): Mont Terri Project - Hydrogeological Synthesis, Osmotic flow. (Berichte des BWG. Serie Geologie, 6). Bundesamt für Wasser und Geologie, BWG, Bern, 7-92.

Marschall, P., Giger, S., La Vaissière, R. de, Shao, H., Leung, H., Nussbaum, C., Trick, T., Lanyon, B., Senger, R., Lisjak, A. & Alcolea, A. (2017): Hydro-mechanical evolution of the EDZ as transport path for radionuclides and gas: insights from the Mont Terri rock laboratory (Switzerland). Swiss Journal of Geosciences 110/1, 173-194. DOI: 10.1007/s00015-016-0246-z.

Marschall, P. & Giger, S.B. (2016): Geomechanische Unterlagen: ENSI-Nachforderungen zum Indikator "Tiefenlage im Hinblick auf bautechnische Machbarkeit" in Etappe 2 SGT. Nagra Arbeitsbericht NAB 16-43.

Marty, D., Ayer, J., Becker, D., Berger, J.-P., Billon-Bruyat, J.-P., Braillard, L., Hug, W. & Meyer, C. (2007): Late Jurassic dinosaur tracksites of the Transjurane highway (Canton Jura, NW Switzerland): Overview and measures for their protection and valorisation. Bulletin für angewandte Geologie 12/1, 75-89.

Matter, A. (1980): Flysch and Molasse of Western and Central Switzerland. *In:* Homewood, P. & Trümpy, R. (eds.): Geology of Switzerland: A Guide Book. Part B: Geological Excursions. Wepf & Co. Publishers, Basel, 261-293.

Matter, A., Peters, T., Bläsi, H., Meyer, J., Ischi, H. & Meyer, C. (1988): Sondierbohrung Weiach Geologie. Nagra Technischer Bericht NTB 86-01.

Matter, A. & Peters, T. (eds.) (1987): Beiträge zur Geologie der Nordschweiz: Symposium "Geologie der Nordschweiz". (Eclogae Geologicae Helvetiae, 80/2).

Matter, A., Peters, T., Isenschmid, C., Bläsi, H. & Ziegler, H.J. (1987): Sondierbohrung Riniken, Geologie. Nagra Technischer Bericht NTB 86-02.

Mazurek, M. (2011): Aufbau und Auswertung der Gesteinsparameter-Datenbank für Opalinuston, den "Braunen Dogger", Effinger Schichten und Mergel-Formationen des Helvetikums. Nagra Arbeitsbericht NAB 11-20 mit Beilagen.

Mazurek, M. (2017): Gesteinsparameter-Datenbank Nordschweiz – Version 2. Nagra Arbeitsbericht NAB 17-56.

Mazurek, M., Alt-Epping, P., Bath, A., Gimmi, T., Niklaus Waber, H., Buschaert, S., Cannière, P. de, De Craen, M., Gautschi, A., Savoye, S., Vinsot, A., Wemaere, I. & Wouters, L. (2011): Natural tracer profiles across argillaceous formations. Applied Geochemistry 26/7, 1035-1064. DOI: 10.1016/j.apgeochem.2011.03.124.

Mazurek, M., Alt-Epping, P., Bath, A., Gimmi, T., Waber, H.N., Buschaert, S., Vinsot, A., de Craen, M., Wemaere, I., de Cannière, P., Gautschi, A., Savoye, S. & Wouters, L. (2009): Natural tracer profiles across argillaceous formations: The CLAYTRAC Project. OECD Nuclear Energy Agency, Paris.

Mazurek, M. & Aschwanden, L. (2020): Multi-scale petrographic and structural characterisation of the Opalinus Clay. Nagra Arbeitsbericht NAB 19-44.

Mazurek, M., Davis, D.W., Madritsch, H., Rufer, D., Villa, I.M., Sutcliffe, C.N., de Haller, A. & Traber, D. (2018): Veins in clay-rich aquitards as records of deformation and fluid-flow events in northern Switzerland. Applied Geochemistry 95/8, 57-70. DOI: 10.1016/j.apgeochem.2018.05.010.

Mazurek, M. & de Haller, A. (2017): Pore-water evolution and solute-transport mechanisms in Opalinus Clay at Mont Terri and Mont Russelin (Canton Jura, Switzerland). Swiss Journal of Geosciences 110/1, 129-149. DOI: 10.1007/s00015-016-0249-9.

Mazurek, M., Gimmi, T., Zwahlen, C., Aschwanden, L., Gaucher, E.C., Kiczka, M., Rufer, D., Wersin, P., Fernandes, M.M., Glaus, M.A., Van Loon, L.R., Traber, D., Schnellmann, M. & Vietor, T. (2023a): Swiss deep drilling campaign 2019–2022: Geological overview and rock properties with focus on porosity and pore-space architecture. Applied Geochemistry 159, 105839. DOI: 10.1016/j.apgeochem.2023.105839.

Mazurek, M., Hurford, A.J. & Leu, W. (2006): Unravelling the multi-stage burial history of the Swiss Molasse Basin: integration of apatite fission track, vitrinite reflectance and biomarker isomerisation analysis. Basin Research 18/1, 27-50. DOI: 10.1111/j.1365-2117.2006.00286.x.

Mazurek, M., Oyama, T., Wersin, P. & Alt-Epping, P. (2015): Porewater squeezing from indurated shales. Chemical Geology 400, 106-121. DOI: 10.1016/j.chemgeo.2015.02.008.

Mazurek, M., Pearson, F.J., Volkaert, G. & Bock, H. (2003): Features, events and processes evaluation catalogue for argillaceous media. OECD Nuclear Energy Agency, Paris.

Mazurek, M. & Peters, T. (1992): Petrographie des kristallinen Grundgebirges der Nordschweiz und Systematik der herzynischen Granite = Petrography of the crystalline basement in Northern Switzerland and systematics of Hercynian granites. Schweizerische Mineralogische und Petrographische Mitteilungen 72/1, 11-35. DOI: 10.5169/seals-54893.

Mazurek, M., Wersin, P. & Hadi, J. (2017): Opalinus Clay in the shallow decompaction zone: Geochemical investigations on drill core samples from borehole Lausen KB. Nagra Arbeitsbericht NAB 16-58.

Mazurek, M., Wersin, P., Hadi, J., Grenèche, J.-M., Prinpreecha, N. & Traber, D. (2023b): Geochemistry and palaeo-hydrogeology of the weathered zone in the Opalinus Clay. Applied Clay Science 232, 106793. DOI: 10.1016/j.clay.2022.106793.

McArthur, J.M., Howarth, R.J. & Bailey, T.R. (2001): Strontium isotope stratigraphy: LOWESS Version 3: Best fit to the marine Sr-isotope curve for 0–509 Ma and accompanying look-up table for deriving numerical age. The Journal of Geology 109/2, 155-170. DOI: 10.1086/319243.

McGlade, C. & Ekins, P. (2015): The geographical distribution of fossil fuels unused when limiting global warming to 2 °C. Nature 517/7533, 187-190. DOI: 10.1038/nature14016.

McIntosh, J.C., Schlegel, M.E. & Person, M. (2012): Glacial impacts on hydrologic processes in sedimentary basins: Evidence from natural tracer studies. Geofluids 12, 7-12. DOI: 10.1111/j.1468-8123.2011.00344.x.

Meckler, A.N., Ziegler, M., Millán, M.I., Breitenbach, S.F. & Bernasconi, S.M. (2014): Long-term performance of the Kiel carbonate device with a new correction scheme for clumped isotope measurements. Rapid Communications in Mass Spectrometry 28/15, 1705-1715. DOI: 10.1002/rcm.6949.

Meier, B. & Deplazes, G. (2014): Reflexionsseismische Analyse des 'Braunen Doggers'. Nagra Arbeitsbericht NAB 14-58.

Meier, B., Kuhn, P., Muff, S., Roth, P. & Madritsch, H. (2014): Tiefenkonvertierung der regionalen Strukturinterpretation der Nagra 2D-Seismik 2011/12. Nagra Arbeitsbericht NAB 14-34.

Merki, P. (1961): Der obere Muschelkalk im östlichen Schweizer Jura. Eclogae Geologicae Helvetiae 54/1, 137-220.

Mey, J., Scherler, D., Wickert, A.D., Egholm, D.L., Tesauro, M., Schildgen, T.F. & Strecker, M.R. (2016): Glacial isostatic uplift of the European Alps. Nature communications 7/1, 13382. DOI: 10.1038/ncomms13382.

Meyer, R.K.F. & Schmidt-Kaler, H. (1996): Jura. *In:* Freudenberger, W. & Schwerd, K. (eds.): Erläuterungen zur Geologischen Karte von Bayern, 1:500 000. Bayerisches Geologisches Ladesamt, München, 90-111.

Meyer, W. & Stets, J. (1998): Junge Tektonik im Rheinischen Schiefergebirge und ihre Quantifizierung. Zeitschrift der Deutschen Gesellschaft für Geowissenschaften ZDGG 149/3, 359-379. DOI: 10.1127/zdgg/149/1998/359.

Milankovitch, M. (1941): Kanon der Erdbestrahlungen und seine Anwendung auf das Eiszeitenproblem. Royal Serbian Academy, Section of Mathematical and Natural Sciences 33, Belgrade.

Milkert, D. (1994): Auswirkungen von Stürmen auf die Schlicksedimente der westlichen Ostsee = Influence of storms on muddy sediments in the western Baltic Sea. Berichte Geologisch-Paläontologisches Institut und Museum, Christian-Albrechts-Universität Kiel 66. Geologisch-Paläontologisches Institut und Museum, Kiel.

Minardi, A., Ferrari, A. & Laloui, L. (2019): Benchmark study of undrained triaxial testing of Opalinus Clay – analysis and comparative evaluation. Nagra Arbeitsbericht NAB 19-18.

Minardi, A., Giger, S.B., Ewy, R.T., Stankovic, R., Stenebråten, J., Soldal, M., Rosone, M., Ferrari, A. & Laloui, L. (2021): Benchmark study of undrained triaxial testing of Opalinus Clay shale: Results and implications for robust testing. Geomechanics for Energy and the Environment 25, 100210. DOI: 10.1016/j.gete.2020.100210.

Mitchell, J.K. & Soga, K. (2005): Fundamentals of Soil Behavior. 3rd ed. John & Sons Inc., Hoboken, NJ.

Monfared, M., Sulem, J., Delage, P. & Mohajerani, M. (2012): On the THM behaviour of a sheared Boom clay sample: Application to the behaviour and sealing properties of the EDZ. Engineering Geology 124, 47-58. DOI: 10.1016/j.enggeo.2011.10.002.

Moore, E.J., Karplus, V.J. & Morgan, M.G. (2024): Expert elicitation of the timing and uncertainty to establish a geologic sequestration well for CO2 in the United States. Proceedings of the National Academy of Sciences 121/1, e2307984120. DOI: 10.1073/pnas.2307984120.

Mosar, J. (1999): Present-day and future tectonic underplating in the western Swiss Alps: reconciliation of basement/wrench-faulting and décollement folding of the Jura and Molasse basin in the Alpine foreland. Earth and Planetary Science Letters 173/3, 143-155. DOI: 10.1016/S0012-821X(99)00238-1.

Mösch, C. (1867): Geologische Beschreibung des Aargauer-Jura und der nördlichen Gebiete des Kantons Zürich. Beiträge zur Geologischen Karte der Schweiz 4. Lieferung. J. Dalp, Bern.

Mudd, S.M., Jenkinson, J., Valters, D. & Clubb, F.J. (2022): MuddPILE the Parsimonious Integrated Landscape Evolution Model. LSDtopotools/MuddPILE. Version Release 0.09. Zenodo.

Mueller, D., Gegg, L., Fülling, A., Buechi, M.W., Deplazes, G. & Preusser, F. (2024): Luminescence dating of glacially sourced deposits from northern Switzerland: Comparing multigrain aliquots and single grains of quartz and feldspar. Quaternary Geochronology 82, 101551. DOI: 10.1016/j.quageo.2024.101551.

Mueller, D., Preusser, F., Buechi, M.W., Gegg, L. & Deplazes, G. (2020): Luminescence properties and dating of glacial to periglacial sediments from northern Switzerland. Geochronology 2/2, 305-323. DOI: 10.5194/gchron-2-305-2020.

Mühlberg, F. (1901): Programm der Exkursionen der Schweizerischen geologischen Gesellschaft nach der Jahresversammlung der Schweizerischen Naturforschenden und der Schweizerischen Geologischen Gesellschaft in Zofingen vom 7.-10. August 1901. Mitteilungen der Aargauischen Naturforschenden Gesellschaft 9, 80-99.

Müller, I.A., Fernandez, A., Radke, J., van Dijk, J., Bowen, D., Schwieters, J. & Bernasconi, S. (2017): Carbonate clumped isotope analyses with the long-integration dual-inlet (LIDI) workflow: Scratching at the lower sample weight boundaries. Rapid Communications in Mass Spectrometry 31/12, 1057-1066.

Müller, W.H., Naef, H. & Graf, H.R. (2002): Geologische Entwicklung der Nordschweiz, Neotektonik und Langzeitszenarien Zürcher Weinland [mit Korrigendum]. Nagra Technischer Bericht NTB 99-08.

Mullins, H.T., Hinchey, E.J., Wellner, R.W., Stephens, D.B., Anderson, W.T., Dwyer, T.R. & Hine, A.C. (1996): Seismic stratigraphy of the Finger Lakes: A continental record of Heinrich event H-1 and Laurentide ice sheet instability. *In:* Mullins, H.T. & Eyles, N. (eds.): Subsurface geologic investigations of New York Finger Lakes: implications for late Quaternary deglaciation and environmental change. (Special paper Geological Society of America, 311). Geological Society of America, Boulder, Colorado, 1-35.

Munier, T., Deconinck, J.-F., Pellenard, P., Hesselbo, S.P., Riding, J.B., Ullmann, C.V., Bougeault, C., Mercuzot, M., Santoni, A.-L., Huret, É. & Landrein, P. (2021): Million-year-scale alternation of warm–humid and semi-arid periods as a mid-latitude climate mode in the Early Jurassic (late Sinemurian, Laurasian Seaway). Climate of the Past 17/4, 1547-1566. DOI: 10.5194/cp-17-1547-2021.

Nadeau, P.H., Bjørkum, P.A. & Walderhaug, O. (2005): Petroleum system analysis: impact of shale diagenesis on reservoir fluid pressure, hydrocarbon migration, and biodegradation risks. Geological Society, London, Petroleum Geology Conference Series 6/1, 1267-1274. DOI: 10.1144/0061267.

Naef, H., Büchi, M., Bläsi, H.R., Deplazes, G. & Gysi, M. (2019): Lithology Manual : Lithological description of drill cores and cuttings in Northern Switzerland. Nagra Arbeitsbericht NAB 19-11.

Naef, H. & Madritsch, H. (2014): Tektonische Karte des Nordschweizer Permokarbontrogs: Aktualisierung basierend auf 2D-Seismik und Schwere-Daten. Nagra Arbeitsbericht NAB 14-17.

Nagra (1984): Die Kernbohrung Beznau. Nagra Technischer Bericht NTB 84-34.

Nagra (1985): Endlager für schwach- und mittelaktive Abfälle: Sicherheitsbericht. Nagra Projekt Gewähr Bericht NGB 85-08.

Nagra (1988): Sedimentstudie - Zwischenbericht 1988: Möglichkeiten zur Endlagerung langlebiger radioaktiver Abfälle in den Sedimenten der Schweiz: Textband. Nagra Technischer Bericht NTB 88-25.

Nagra (1989): Sondierbohrung Weiach Untersuchungsbericht: Textband und Beilagenband. Nagra Technischer Bericht NTB 88-08.

Nagra (1990): Sondierbohrung Riniken Untersuchungsbericht: Textband und Beilagenband. Nagra Technischer Bericht NTB 88-09.

Nagra (1992): Sondierbohrung Schafisheim Untersuchungsbericht: Textband und Beilagenband. Nagra Technischer Bericht NTB 88-11.

Nagra (2001): Sondierbohrung Benken Untersuchungsbericht: Textband und Beilagenband. Nagra Technischer Bericht NTB 00-01.

Nagra (2002): Projekt Opalinuston: Synthese der geowissenschaftlichen Untersuchungsergebnisse - Entsorgungsnachweis für abgebrannte Brennelemente, verglaste hochaktive sowie langlebige mittelaktive Abfälle. Nagra Technischer Bericht NTB 02-03.

Nagra (2008a): Vorschlag geologischer Standortgebiete für das SMA- und das HAA-Lager: Darlegung der Anforderungen, des Vorgehens und der Ergebnisse. Nagra Technischer Bericht NTB 08-03.

Nagra (2008b): Vorschlag geologischer Standortgebiete für ein SMA- und ein HAA-Lager: Geologische Grundlagen (Bericht zur Geologie). Text. Nagra Technischer Bericht NTB 08-04.

Nagra (2014a): Konzepte der Standortuntersuchungen für SGT Etappe 3. Nagra Arbeitsbericht NAB 14-83.

Nagra (2014b): SGT Etappe 2: Vorschlag weiter zu untersuchender geologischer Standortgebiete mit zugehörigen Standortarealen für die Oberflächenanlage: Geologische Grundlagen Dossier II Sedimentologische und tektonische Verhältnisse. Nagra Technischer Bericht NTB 14-02 Dossier II.

Nagra (2014c): SGT Etappe 2: Vorschlag weiter zu untersuchender geologischer Standortgebiete mit zugehörigen Standortarealen für die Oberflächenanlage: Geologische Grundlagen Dossier III Geologische Langzeitentwicklung. Nagra Technischer Bericht NTB 14-02 Dossier III.

Nagra (2014d): SGT Etappe 2: Vorschlag weiter zu untersuchender geologischer Standortgebiete mit zugehörigen Standortarealen für die Oberflächenanlage: Geologische Grundlagen. Dossier IV Geomechanische Unterlagen. Nagra Technischer Bericht NTB 14-02 Dossier IV.

Nagra (2014e): SGT Etappe 2: Vorschlag weiter zu untersuchender geologischer Standortgebiete mit zugehörigen Standortarealen für die Oberflächenanlage: Geologische Grundlagen. Dossier V Hydrogeologische Verhältnisse. Nagra Technischer Bericht NTB 14-02 Dossier V.

Nagra (2014f): SGT Etappe 2: Vorschlag weiter zu untersuchender geologischer Standortgebiete mit zugehörigen Standortarealen für die Oberflächenanlage: Geologische Grundlagen. Dossier VI Barriereneigenschaften der Wirt- und Rahmengesteine. Nagra Technischer Bericht NTB 14-02 Dossier VI.

Nagra (2014g): SGT Etappe 2: Vorschlag weiter zu untersuchender geologischer Standortgebiete mit zugehörigen Standortarealen für die Oberflächenanlage: Geologische Grundlagen Dossier VII Nutzungskonflikte. Nagra Technischer Bericht NTB 14-02 Dossier VII.

Nagra (2014h): SGT Etappe 2: Vorschlag weiter zu untersuchender geologischer Standortgebiete mit zugehörigen Standortarealen für die Oberflächenanlage: Geologische Grundlagen. Nagra Technischer Bericht NTB 14-02 Dossier I - VIII.

Nagra (2014i): Sicherheitstechnischer Bericht zu SGT-Etappe 2: Sicherheitstechnischer Vergleich und Vorschlag der in Etappe 3 weiter zu untersuchenden geologischen Standortgebiete. Nagra Technischer Bericht NTB 14-01.

Nagra (2016): Konzepte der Standortuntersuchungen für SGT Etappe 3 - Nördlich Lägern. Nagra Arbeitsbericht NAB 16-28.

Nagra (2018): 2D Reflection Seismic Exploration and Provisory Interpretation of Overdeepened Quaternary Valleys around the Nagra Siting Regions Zürich Nordost and Nördlich Lägern. Nagra Arbeitsbericht NAB 18-22.

Nagra (2019a): Arbeitsprogramm für Tiefbohrungen: Generisches Untersuchungsprogramm. Nagra Arbeitsbericht NAB 17-50 Rev.2.

Nagra (2019b): Preliminary horizon and structure mapping of the Nagra 3D seismics JO-15 (Jura Ost) in time domain. Nagra Arbeitsbericht NAB 18-34.

Nagra (2019c): Preliminary horizon and structure mapping of the Nagra 3D seismics NL-16 (Nördlich Lägern) in time domain. Nagra Arbeitsbericht NAB 18-35.

Nagra (2019d): Preliminary horizon and structure mapping of the Nagra 3D seismics ZNO-97/16 (Zürich Nordost) in time domain. Nagra Arbeitsbericht NAB 18-36.

Nagra (2021): Morphology of the Overdeepened Gebenstorf-Stilli Trough (Lower Aare Valley) from Seismic Surface Wave Investigations. Nagra Arbeitsbericht NAB 21-18.

Nagra (2022): The site for the deep geological repository – Nagra's proposal.

Nagra (2023a): Bautechnisches Dossier – Band 2: Bautechnisch relevante Auszüge geologischer Grundlagen Jura Ost. Nagra Arbeitsbericht NAB 23-01 Band 2.

Nagra (2023b): Bautechnisches Dossier – Band 3: Bautechnisch relevante Auszüge geologischer Grundlagen Nördlich Lägern. Nagra Arbeitsbericht NAB 23-01 Band 3.

Nagra (2023c): Bautechnisches Dossier – Band 4: Bautechnisch relevante Auszüge geologischer Grundlagen Zürich Nordost. Nagra Arbeitsbericht NAB 23-01 Band 4.

Nagra (2024a): 3D Seismic Interpretation of Stratigraphic Horizons and Structures in Time Domain Jura Ost. Nagra Arbeitsbericht NAB 23-17.

Nagra (2024b): 3D Seismic Interpretation of Stratigraphic Horizons and Structures in Time Domain Nördlich Lägern. Nagra Arbeitsbericht NAB 23-18.

Nagra (2024c): 3D Seismic Interpretation of Stratigraphic Horizons and Structures in Time Domain Zürich Nordost. Nagra Arbeitsbericht NAB 23-19.

Nagra (2024d): Abfallzuteilung und Betrachtungszeitraum für den Standortvergleich und Nachweiszeitraum für den Sicherheitsnachweis für das geologische Tiefenlager. Nagra Arbeitsbericht NAB 24-05.

Nagra (2024e): Definition der Bewertungsobjekte für den sicherheitstechnischen Vergleich der Standorte in Etappe 3 des Sachplans geologische Tiefenlager. Nagra Arbeitsbericht NAB 24-01.

Nagra (2024f): Depth Conversion of the 3D Seismic Interpretation for the Area of Interest in the Jura Ost, Nördlich Lägern and Zürich Nordost Siting Regions. Nagra Arbeitsbericht NAB 24-49.

Nagra (2024g): Erdbebengefährdungsanalyse für den Standort der Brennelementverpackungsanlage. Nagra Arbeitsbericht NAB 24-22.

Nagra (2024h): Erdbebengefährdungsanalyse für den Standort der Oberflächenanlage und die Betriebsphase des geologischen Tiefenlagers. Nagra Arbeitsbericht NAB 24-21.

Nagra (2024i): Geologic Scenarios for the Evaluation of Earthquake Impact on the Deep Geological Repository. Nagra Arbeitsbericht NAB 24-28.

Nagra (2024j): Geological long-term evolution: Climate and Iceflow. Nagra Arbeitsbericht NAB 24-14.

Nagra (2024k): Geological long-term evolution: Erosion. Nagra Arbeitsbericht NAB 24-15.

Nagra (2024l): Geological long-term evolution: Neotectonics. Nagra Arbeitsbericht NAB 24-13.

Nagra (2024m): Geological Properties of the Jura Ost, Nördlich Lägern and Zürich Nordost Siting Regions for Safety Assessment. Nagra Arbeitsbericht NAB 24-10.

Nagra (2024n): Hydrogeological Model of Northern Switzerland. Nagra Arbeitsbericht NAB 24-16.

Nagra (2024o): In-Situ Stress Field in the Siting Regions Jura Ost, Nördlich Lägern and Zürich Nordost. Nagra Arbeitsbericht NAB 24-19.

Nagra (2024p): Phenomenological Description of the Evolution of a Geological Repository for Radioactive Waste in Opalinus Clay. Nagra Arbeitsbericht NAB 24-20 Rev. 1.

Nagra (2024q): Post-Closure Biosphere Assessment. Nagra Arbeitsbericht NAB 24-06.

Nagra (2024r): Post-Closure Safety Report. Nagra Technical Report NTB 24-10.

Nagra (2024s): Processing 3D Seismic Surveys Jura Ost, Nördlich Lägern and Zürich Nordost. Nagra Arbeitsbericht NAB 23-16.

Nagra (2024t): Qualitative Bewertung für den sicherheitstechnischen Vergleich in Etappe 3 des Sachplans geologische Tiefenlager. Nagra Arbeitsbericht NAB 24-23.

Nagra (2024u): Radiological Consequence Analysis for a Deep Geological Repository in Northern Switzerland. Nagra Technical Report NTB 24-18.

Nagra (2024v): Synthesis of the Performance Assessment for a Deep Geological Repository for Radioactive Waste. Nagra Technical Report NTB 24-22.

Nagra (2024w): Thermo-hydraulic modelling of the temperature distribution in the siting regions JO, NL and ZNO. Nagra Arbeitsbericht NAB 24-24.

Nagra (2025a): Rahmenbewilligungsgesuch für das geologische Tiefenlager – Begründung der Standortwahl. Nagra Technischer Bericht NTB 24-03.

Nagra (2025b): Rahmenbewilligungsgesuch für das geologische Tiefenlager - Sicherheitsbericht. Nagra Technischer Bericht NTB 24-01.

Nagra (ed.) (2021a): TBO Bülach-1-1: Data Report Dossier I-XI. Nagra Arbeitsbericht NAB 20-08.

Nagra (ed.) (2021b): TBO Marthalen-1-1: Data Report Dossier I-XI. Nagra Arbeitsbericht NAB 21-20.

Nagra (ed.) (2021c): TBO Trüllikon-1-1: Data Report Dossier I-XI. Nagra Arbeitsbericht NAB 20-09.

Nagra (ed.) (2022a): TBO Bözberg-1-1: Data Report Dossier I-XI. Nagra Arbeitsbericht NAB 21-21.

Nagra (ed.) (2022b): TBO Bözberg-2-1: Data Report Dossier I-XI. Nagra Arbeitsbericht NAB 21-22.

Nagra (ed.) (2022c): TBO Stadel-2-1: Data Report Dossier I-XI. Nagra Arbeitsbericht NAB 22-02.

Nagra (ed.) (2022d): TBO Stadel-3-1: Data Report Dossier I-XI. Nagra Arbeitsbericht NAB 22-01.

Nagra (ed.) (2023a): TBO Bachs-1-1: Data Report Dossier I-XI. Nagra Arbeitsbericht NAB 22-04.

Nagra (ed.) (2023b): TBO Rheinau-1-1: Data Report Dossier I-XI. Nagra Arbeitsbericht NAB 22-03.

Näslund, J.-O., Rodhe, L., Fastook, J.L. & Holmlund, P. (2003): New ways of studying ice sheet flow directions and glacial erosion by computer modelling – examples from Fennoscandia. Quaternary Science Reviews 22/2-4, 245-258. DOI: 10.1016/S0277-3791(02)00079-3.

Neuzil, C.E. (1995): Abnormal pressures as hydrodynamic phenomena. American Journal of Science 295/June, 742-786.

Neuzil, C.E. (2015): Interpreting fluid pressure anomalies in shallow intraplate argillaceous formations. Geophysical Research Letters 42/12, 4801-4808. DOI: 10.1002/2015GL064140.

Nivière, B. & Winter, T. (2000): Pleistocene northwards fold propagation of the Jura within the southern Upper Rhine Graben: seismotectonic implications. Global and Planetary Change 27/1-4, 263-288. DOI: 10.1016/S0921-8181(01)00070-4.

Nocquet, J.-M. (2012): Present-day kinematics of the Mediterranean: A comprehensive overview of GPS results. Tectonophysics 579, 220-242. DOI: 10.1016/j.tecto.2012.03.037.

Nocquet, J.-M. & Calais, E. (2004): Geodetic Measurements of Crustal Deformation in the Western Mediterranean and Europe. Pure and Applied Geophysics 161/3, 661-681. DOI: 10.1007/s00024-003-2468-z.

Nordas, A.N., Brauchart, A., Anthi, M. & Anagnostou, G. (2024): Calibration Method and Material Constants of an Anisotropic, Linearly Elastic and Perfectly Plastic Mohr–Coulomb Constitutive Model for Opalinus Clay. Rock Mechanics and Rock Engineering 57/1, 3-25. DOI: 10.1007/s00603-023-03509-7.

Normani, S.D., Sykes, J.F., Jensen, M.R. & Sykes, E.A. (2017): Assessing alternative scenarios for the cause of underpressures in the Ordovician sediments along the eastern flank of the Michigan Basin. Geofluids 2017/1, 1-18. DOI: 10.1155/2017/8647917.

Nussbaum, C. & Bossart, P. (2004): Compilation of K-values from packer tests in the Mont Terri rock laboratory. Unpubl. Mont Terri Technical Note. Mont Terri Project, Switzerland.

NWMO (2011): OPG‘s deep geologic repository for low & intermediate level waste: Geosynthesis. NWMO-DGR-TR-2011-11. Nuclear Waste Management Organization NWMO, Toronto.

NWMO (2023): Confidence in Safety: South Bruce Site. 2023 update. NWMO-DGR-TR-2023-08. Nuclear Waste Management Organization NWMO, Toronto.

O’Hagan, A. (2019): Expert Knowledge Elicitation: Subjective but Scientific. The American Statistician 73/sup1, 69-81. DOI: 10.1080/00031305.2018.1518265.

OECD/NEA (2022): Clay Club Catalogue of Characteristics of Argillaceous Rocks - 2022 Update. Radioactive Waste Management. OECD/NEA, Paris.

Omodeo-Salé, S., Hamidi, Y., Villagomez, D. & Moscariello, A. (2021): Quantifying multiple erosion events in the distal sector of the Northern Alpine Foreland Basin (North-Eastern Switzerland), by combining basin thermal modelling with vitrinite reflectance and apatite fission track data. Geosciences 11/62, 1-29. DOI: 10.3390/geosciences11020062.

Oppenheimer, M., Little, C.M. & Cooke, R.M. (2016): Expert judgement and uncertainty quantification for climate change. Nature Climate Change 6/5, 445-451. DOI: 10.1038/NCLIMATE2959.

Orellana, L.F., Nussbaum, C., Grafulha, L., Henry, P. & Violay, M. (2022): Physical characterization of fault rocks within the Opalinus Clay formation. Scientific Reports 12/1, 4389. DOI: 10.1038/s41598-022-08236-7.

Ortner, H., von Hagke, C., Sommaruga, A., Mock, S., Mosar, J., Hinsch, R. & Beidinger, A. (2024): The northern Deformation Front of the European Alps. *In:* Rosenberg, C.L. & Bellahsen, N. (eds.): Geodynamics of the Alps 3. Collisional Processes. John Wiley & Sons Ltd., London.

Palut, J.-M., Fierz, T., Eikenberg, J., van Dorp, F., Möri, A., Bossart, P., Aubry, C., Garcia-Gutierrez, M. & Drouiller, Y. (2002): Diffusion In-situ experiment DI. Field activity and data report. Mont Terri Technical Report TR 00-03. Mont Terri Project, Switzerland.

Palut, J.-M., Montarnal, P., Gautschi, A., Tevissen, E. & Mouche, E. (2003): Characterisation of HTO diffusion properties by an in situ tracer experiment in Opalinus clay at Mont Terri. Journal of Contaminant Hydrology, 203-218. DOI: 10.1016/S0169-7722(02)00134-1.

Parisio, F. & Laloui, L. (2017): Plastic-damage modeling of saturated quasi-brittle shales. International Journal of Rock Mechanics and Mining Sciences 93, 295-306. DOI: 10.1016/j.ijrmms.2017.01.016.

Passchier, C.W. & Trouw, R. (1998): Microtectonics. Springer, Berlin, Heidelberg.

Paul, J., Wemmer, K. & Ahrendt, H. (2008): Provenance of siliciclastic sediments (Permian to Jurassic) in the Central European Basin. Zeitschrift der Deutschen Gesellschaft für Geowissenschaften ZDGG 159/4, 641-650. DOI: 10.1127/1860-1804/2008/0159-0641.

Paz, M., Buatois, L.A., Mángano, M.G., Desjardins, P.R., Notta, R., González Tomassini, F., Carmona, N.B. & Minisini, D. (2022): Organic-rich, fine-grained contourites in an epicontinental basin: The Upper Jurassic-Lower Cretaceous Vaca Muerta Formation, Argentina. Marine and Petroleum Geology 142, 105757. DOI: 10.1016/j.marpetgeo.2022.105757.

Peacock, D., Nixon, C.W., Rotevatn, A. & Sanderson, D.J. (2016): Glossary of faults and other fracture network. Journal of Structural Geology 92, 12-29. DOI: 10.1016/j.jsg.2016.09.008.

Pearson, F.J. (1999): What is the porosity of a mudrock? Geological Society, London, Special Publications 158, 9-21. DOI: 10.1144/GSL.SP.1999.158.01.02.

Pearson, F.J., Balderer, W., Loosli, H.H., Lehmann, B.E., Matter, A., Peters, T., Schmassmann, H.-J. & Gautschi, A. (1991): Applied Isotope Hydrogeology - A Case Study in Northern Switzerland. Nagra Technical Report NTB 88-01.

Penkman, K., Thew, N., Presslee, S., Taylor, S., Nelson, E., Kälin, D., Buechi, M.W. & Deplazes, G. (2024): An aminostratigraphy for the Quaternary of the Swiss Plateau. EarthArXiv. DOI: 10.31223/X57700.

Perne, M., Covington, M.D., Thaler, E.A. & Myre, J.M. (2017): Steady state, erosional continuity, and the topography of landscapes developed in layered rocks. Earth Surface Dynamics 5/1, 85-100. DOI: 10.5194/esurf-5-85-2017.

Person, M., Bense, V., Cohen, D. & Banerjee, A. (2012): Models of ice-sheet hydrogeologic interactions: A review. Geofluids 12, 58-78. DOI: 10.1111/j.1468-8123.2011.00360.x.

Peters, G. & van Balen, R.T. (2007): Tectonic geomorphology of the northern Upper Rhine graben, Germany. Global and Planetary Change 58/1-4, 310-334. DOI: 10.1016/j.gloplacha.2006.11.041.

Petit, C., Campy, M., Chaline, J. & Bonvalot, J. (1996): Major palaeohydrographic changes in Alpine foreland during the Pliocene-Pleistocene. Boreas 25, 131-143. DOI: 10.1111/j.1502-3885.1996.tb00841.x.

Pfaff, K., Romer, R.L. & Markl, G. (2009): U-Pb ages of ferberite, chalcedony, agate, 'U-mica' and pitchblende: constraints on the mineralization history of the Schwarzwald ore district. European Journal of Mineralogy 21/4, 817-836. DOI: 10.1127/0935-1221/2009/0021-1944.

Pfiffner, O.A. (1986): Evolution of the North Alpine Foreland Basin in the Central Alps. *In:* Allen, P.A. & Homewood, P. (eds.): Foreland Basins. Blackwell Publishing Ltd, Oxford, UK, 219-228.

Pfiffner, O.A. (2009): Geologie der Alpen. Haupt, Bern.

Pfiffner, O.A., Erard, P.-F. & Stäuble, M. (1997): Two cross sections through the Swiss Molasse Basin (lines E4–E6, W1, W7–W10). *In:* Pfiffner, O.A., Lehner, P., Heitzmann, P., Mueller, S. & Steck, A. (eds.): Deep Structure of the Swiss Alps. Results of NRP 20. Birkhäuser Verlag, Basel, 64-72.

Philippe, Y., Colletta, B., Deville, E. & Mascle, A. (1996): The Jura fold-and-thrust belt: a kinematic model based on map-balancing. *In:* Ziegler, P.A. & Horvath, F. (eds.): Peri-Tethys Memoir 2: Structure and Prospects of Alpine Basins and Foreland // Structure and prospects of alpine basins and forelands. (Mémoires du Muséum National d'Histoire Naturelle, 170). Éd. du Muséum, Paris, 235-261.

Pieńkowski, G., Uchman, A., Ninard, K. & Hesselbo, S.P. (2021): Ichnology, sedimentology, and orbital cycles in the hemipelagic Early Jurassic Laurasian Seaway (Pliensbachian, Cardigan Bay Basin, UK). Global and Planetary Change 207, 103648. DOI: 10.1016/j.gloplacha.2021.103648.

Pierre, C. (1989): Sedimentation and diagenesis in restricted marine basins. *In:* Fritz, P. & Fontes, J.C. (eds.): Handbook of Environmental Isotope Geochemistry 3. Elsevier, Burlington, MA, 257-315.

Pietsch, J. & Jordan, P. (2014): Digitales Höhenmodell Basis Quartär der Nordschweiz – Version 2014 und ausgewählte Auswertungen. Nagra Arbeitsbericht NAB 14-02.

Pietsch, J.S., Wetzel, A., Deplazes, G. & Filipponi, M. (2023): Lithofacies, stratigraphy and depositional history of Middle Muschelkalk evaporites (Zeglingen Formation) in northern Switzerland. Swiss Journal of Geosciences 116/16, 1-40. DOI: 10.1186/s00015-023-00441-4.

Pietsch, J.S., Wetzel, A. & Jordan, P. (2016): A new lithostratigraphic scheme for the Schinznach Formation (upper part of the Muschelkalk Group of northern Switzerland). Swiss Journal of Geosciences 109/2, 285-307. DOI: 10.1007/s00015-016-0214-7.

Piña-Valdés, J., Socquet, A., Beauval, C., Doin, M.-P., D'Agostino, N. & Shen, Z.-K. (2022): 3D GNSS Velocity Field Sheds Light on the Deformation Mechanisms in Europe: Effects of the Vertical Crustal Motion on the Distribution of Seismicity. Journal of Geophysical Research: Solid Earth 127/6, e2021JB023451. DOI: 10.1029/2021JB023451.

Pintori, F., Serpelloni, E. & Gualandi, A. (2022): Common-mode signals and vertical velocities in the greater Alpine area from GNSS data. Solid Earth 13/10, 1541-1567. DOI: 10.5194/se-13-1541-2022.

Piotrowski, J.A. (1994): Tunnel-valley formation in northwestern Germany—geology, mechanisms of formation, and subglacial bed conditions for the Bornhöved tunnel valley. Sedimentary Geology 89/1-2, 107-141. DOI: 10.1016/0037-0738(94)90086-8.

Plenkers, K. (2014): Das neue Schwachbebennetz in der Nordschweiz: Standortsuche, Standortauswahl, realisierte Stationen. Nagra Arbeitsbericht NAB 14-56.

Plum, H., Ondreka, J. & Armbruster, V. (ed.) (2008): Hydrogeologische Einheiten in Baden-Württemberg. LGRB-Informationen 20. Landesamt für Geologie, Rohstoffe und Bergbau, Freiburg i.B.

Poser, H. (1948): Boden- und Klimaverhältnisse in Mittel- und Westeuropa während der Würmeiszeit. Erdkunde 2/1-3, 53-68. DOI: 10.3112/erdkunde.1948.01.03.

Pozsgai, E., Józsa, S., Dunkl, I., Sebe, K., Thamó-Bozsó, E., Sajó, I., Dezső, J. & Eynatten, H.v. (2017): Provenance of the Upper Triassic siliciclastics of the Mecsek Mountains and Villány Hills (Pannonian Basin, Hungary): Constraints to the Early Mesozoic paleogeography of the Tisza Megaunit. International Journal of Earth Sciences (Geologische Rundschau) 106/6, 2005-2024. DOI: 10.1007/s00531-016-1406-0.

Preusser, F., Büschelberger, M., Kemna, H.A., Miocic, J., Mueller, D. & May, J.H. (2021): Exploring possible links between Quaternary aggradation in the Upper Rhine Graben and the glaciation history of northern Switzerland. International Journal of Earth Sciences (Geologische Rundschau) 110/5, 1827-1846. DOI: 10.1007/s00531-021-02043-7.

Preusser, F., Graf, H.R., Keller, O., Krayss, E. & Schlüchter, C. (2011): Quaternary glaciation history of northern Switzerland. E&G Quaternary Science Journal 60/2-3, 282-305. DOI: 10.3285/eg.60.2-3.06.

Püntener, C., Anquetin, J. & Billon-Bruyat, J.-P. (2015): Thalassemys bruntrutana n. sp., a new coastal marine turtle from the Late Jurassic of Porrentruy (Switzerland), and the paleobiogeography of the Thalassemydidae. PeerJ 3, e1282. DOI: 10.7717/peerj.1282.

Rabin, M., Sue, C., Walpersdorf, A., Sakic, P., Albaric, J. & Fores, B. (2018): Present-Day Deformations of the Jura Arc Inferred by GPS Surveying and Earthquake Focal Mechanisms. Tectonics 37/10, 3782-3804. DOI: 10.1029/2018TC005047.

Rahn, M.K. & Selbekk, R. (2007): Absolute dating of the youngest sediments of the Swiss Molasse basin by apatite fission track analysis. Swiss Journal of Geosciences 100/3, 371-381. DOI: 10.1007/s00015-007-1234-0.

Rauhut, O., Lopez-Arbarello, A., Roeper, M. & Rothgaenger, M. (2017): Vertebrate fossils from the Kimmeridgian of Brunn: The oldest fauna from the Solnhofen Archipelago (Late Jurassic, Bavaria, Germany). Zitteliana 89, 305-329.

Raumer, J.F. von, Bussy, F. & Stampfli, G.M. (2009): The Variscan evolution in the External massifs of the Alps and place in their Variscan framework. Comptes Rendus Géoscience 341/2-3, 239-252. DOI: 10.1016/j.crte.2008.11.007.

Reber, R., Akçar, N., Ivy-Ochs, S., Tikhomirov, D., Burkhalter, R., Zahno, C., Lüthold, A., Kubik, P.W., Vockenhuber, C. & Schlüchter, C. (2014): Timing of retreat of the Reuss Glacier (Switzerland) at the end of the Last Glacial Maximum. Swiss Journal of Geosciences 107/2-3, 293-307. DOI: 10.1007/s00015-014-0169-5.

Rebesco, M., Hernández-Molina, F.J., van Rooij, D. & Wåhlin, A. (2014): Contourites and associated sediments controlled by deep-water circulation processes: State-of-the-art and future considerations. Marine Geology 352, 111-154. DOI: 10.1016/j.margeo.2014.03.011.

Reichenwallner, S., Schuster, B., Deplazes, G., Madritsch, H. & Buechi, M.W. (2021): Quaternary Borehole QBO Andelfingen-Niederfeld (QANI) Data Report. Nagra Arbeitsbericht NAB 20-04.

Reinicke, A. & Frieg, B. (2021): Drilling fluid Experiment - Final Report. Nagra Arbeitsbericht NAB 20-43.

Reisdorf, A.G. & Wetzel, A. (2018): Evidence for synsedimentary differential tectonic movements in a low-subsidence setting: Early Jurassic in northwestern Switzerland. Swiss Journal of Geosciences 111/3, 417-444. DOI: 10.1007/s00015-018-0318-3.

Reisdorf, A.G., Wetzel, A., Schlatter, R. & Jordan, P. (2011): The Staffelegg Formation: a new stratigraphic scheme for the Early Jurassic of northern Switzerland. Swiss Journal of Geosciences 104/1, 97-146. DOI: 10.1007/s00015-011-0057-1.

Reiter, K., Heidbach, O. & Ziegler, M.O. (2024): Impact of faults on the remote stress state. Solid Earth 15/2, 305-327. DOI: 10.5194/se-15-305-2024.

Remane, J., Adatte, T., Berger, J.-P., Burkhalter, R., Dall'Agnolo, S., Decrouez, D., Fischer, H., Funk, H., Furrer, H., Graf, H.-R., Gouffon, Y., Heckendorn, W. & Winkler, W. (2005): Richtlinien zur stratigraphischen Nomenklatur. Eclogae geol. Helv. 98/3, 385-405. DOI: 10.1007/s00015-005-1167-4.

Renz, T., Ziegler, M. & Loew, S. (2019): Investigations in the new TBM-excavated Belchen highway tunnel. In-situ and laboratory data analyses (Part 3). *In:* ENSI (ed.): Research and Experience Report 2018. ENSI-AN-10577, Brugg, 315-325.

Revil, A. & Cathles, L.M. (1999): Permeability of shaly sands. Water Resources Research 35/3, 651-662. DOI: 10.1029/98WR02700.

Rick, B. (1990): Sulphur and oxygen isotopic composition of Swiss Gipskeuper (Upper Triassic). Chemical Geology: Isotope Geoscience section 80/3, 243-250. DOI: 10.1016/0168-9622(90)90031-7.

Riegraf, W. (1985): Mikrofauna, Biostratigraphie und Fazies im Unteren Toarcium Südwest-deutschlands und Vergleiche mit benachbarten Gebieten. (Tübinger mikropaläontologische Mitteilungen, Nr. 3). Institut und Museum für Geologie und Paläontologie der Universität Tübingen, Tübingen.

Ring, S.J., Bocherens, H., Wings, O. & Rabi, M. (2020): Divergent mammalian body size in a stable Eocene greenhouse climate. Nature Scientific Reports 10, 3987. DOI: 10.1038/s41598-020-60379-7.

Ritter, J. & Christensen, U.R. (eds.) (2007): Mantle plumes. A multidisciplinary approach. Springer, Berlin.

Roche, V., Childs, C., Madritsch, H. & Camanni, G. (2020): Layering and structural inheritance controls on fault zone structure in three dimensions: a case study from the northern Molasse Basin, Switzerland. Journal of the Geological Society 177/3, 493-508. DOI: 10.1144/jgs2019-052.

Rodriguez, J., Colàs, E., Gailhanou, H., Duro, L., Fuller, A.J. & Harvey, L. (2022): Track-changes and track-error document: From version 10d to version 11. ThermoChimie Technical Report TCIII-2022-06E-vs1, available online at https://www.thermochimie-tdb.com/, status as of October 25, 2024.

Roe, G. (2006): In defense of Milankovitch. Geophysical Research Letters 33/24, L24703. DOI: 10.1029/2006GL027817.

Röhl, H.-J. & Schmid-Röhl, A. (2005): Lower Toarcian (Upper Liassic) black shales of the Central European epicontinental basin: A sequence stratigraphic case study from the SW German Posidonia Shale. SEPM Special Publication 82, 165-189. DOI: 10.2110/pec.05.82.0165.

Rosselet, C. (1991): Die Fauna der Spaltenfüllungen von Dielsdorf (Eozän, Kanton Zürich). Documenta naturae 64, 1-177.

Rotstein, Y. & Schaming, M. (2011): The Upper Rhine Graben (URG) revisited: Miocene transtension and transpression account for the observed first-order structures. Tectonics 30/3, 2010TC002767. DOI: 10.1029/2010TC002767.

Rousseau, D.-D., Hatté, C., Duzer, D., Schevin, P., Kukla, G. & Guiot, J. (2007): 15. Estimates of temperature and precipitation variations during the Eemian interglacial: New data from the Grande Pile record (GP XXI). Developments in Quaternary Sciences 7, 231-238. DOI: 10.1016/S1571-0866(07)80040-6.

Rübel, A., Behler, M., Feinhals, J., Mönig, J., Poppei, J., Rätz, D. & Wolf, J. (2019): Projekt Konrad – Überprüfung der sicherheitstechnischen Anforderungen des Endlagers Konrad nach dem Stand von Wissenschaft und Technik (ÜsiKo). Überprüfung der sicherheits-relevanten Anforderungen zur Langzeitsicherheit, Kritikalität in der Nachbetriebsphase und thermischen Beeinflussung des Wirtsgesteins. Abschlussbericht zur Phase 1: Ermittlung des Überprüfungsbedarfs. Edited by Bundesgesellschaft für Endlagerung mbH (BGE).

Ruchat, A., Lathuilière, B., Wohlwend, S., Deplazes, G., Eberli, G.P., Feist-Burkhardt, S. & Samankassou, E. (2024): A Bajocian event of global coral reef growth: Record from northern Switzerland. Palaeogeography, Palaeoclimatology, Palaeoecology 655, 112504. DOI: 10.1016/j.palaeo.2024.112504.

Ruddiman, W.F. (2003): The anthropogenic greenhouse era began thousands of years ago. Climatic Change 61/3, 261-293. DOI: 10.1023/B:CLIM.0000004577.17928.fa.

Ruf, M., Link, E., Pross, J. & Aigner, T. (2005): A multi-proxy study of deeper-water carbonates (Upper Jurassic, southern Germany): combining sedimentology, chemostratigraphy and palynofacies. Facies 51/1-4, 327-349. DOI: 10.1007/s10347-005-0073-6.

Rufer, D. & Stockhecke, M. (2019): Field Manual : Drillcore sampling for analytical purposes. Nagra Arbeitsbericht NAB 19-13 Rev. 1.

Rufer, D. & Waber, H.N. (2015): Noble and reactive gas data of porewaters and rocks from the Schlattingen borehole SLA-1. Nagra Arbeitsbericht NAB 15-12.

Rufer, D., Waber, H.N. & Traber, D. (2024): Vertical and lateral distribution of helium in porewater of the Mesozoic sedimentary sequence of northern Switzerland – A comparative investigation across multiple boreholes. Applied Geochemistry 160, 105836. DOI: 10.1016/j.apgeochem.2023.105836.

Russo, E., Buzan, J., Lienert, S., Jouvet, G., Velasquez Alvarez, P., Davis, B., Ludwig, P., Joos, F. & Raible, C.C. (2024): High-resolution LGM climate of Europe and the Alpine region using the regional climate model WRF. Climate of the Past 20/3, 449-465. DOI: 10.5194/cp-20-449-2024.

Rybach, L. (2009): Slowly moving thermal/mineral waters in deep crystalline basement. Environmental Geology 58/8, 1645-1651. DOI: 10.1007/s00254-008-1494-7.

Sánchez, L., Völksen, C., Sokolov, A., Arenz, H. & Seitz, F. (2018): Present-day surface deformation of the Alpine region inferred from geodetic techniques. Earth System Science Data 10/3, 1503-1526. DOI: 10.5194/essd-10-1503-2018.

Sanz, E., Ayora, C. & Carrera, J. (2011): Calcite dissolution by mixing waters: geochemical modeling and flow-through experiments. Geologica Acta 9/1, 67-77.

Schärli, U. & Rybach, L. (2002): Erstellung einer aktuellen Karte der Temperaturgradienten und des Wärmeflusses der Nordschweiz. Unpubl. Nagra Interner Bericht.

Schegg, R. & Leu, W. (1998): Analysis of erosion events and palaeogeothermal gradients in the North Alpine Foreland Basin of Switzerland. Basin Modelling: Practice and Progress, Geological Society, London, Special Publications 141, 137-155. DOI: 10.1144/GSL.SP.1998.141.01.09.

Scheidt, S., Buechi, M.W., Egli, R., Biedermann, A.R. & Deplazes, G. (2023): Palaeomagnetic and mineral magnetic analyses of the Deckenschotter of northern Switzerland and southern Germany. Swiss Journal of Geosciences 116/1, 12. DOI: 10.1186/s00015-023-00439-y.

Schintgen, T.V. & Moeck, I.S. (2021): The interplay of Malm carbonate permeability, gravity-driven groundwater flow, and paleoclimate – implications for the geothermal field and potential in the Molasse Basin (southern Germany), a foreland-basin play. Geothermal Energy 9, 25. DOI: 10.1186/s40517-021-00207-x.

Schlatter, A. (2013): Rezente vertikale Oberflächenbewegungen in der Nordschweiz und in Südwestdeutschland. Kinematische Ausgleichung der Landesnivellementlinien CH/D. Nagra Arbeitsbericht NAB 12-34.

Schlatter, A. (2014): Kinematische Gesamtausgleichung der Schweizer Landesnivellementlinien 2013 und Detaildarstellung der rezenten vertikalen Oberflächenbewegungen in der Zentralschweiz. Nagra Arbeitsbericht NAB 14-38.

Schlüchter, C., Akçar, N. & Ivy-Ochs, S. (2021): The Quaternary Period in Switzerland. *In:* Reynard, E. (ed.): Landscapes and Landforms of Switzerland. (World Geomorphological Landscapes). Springer International Publishing, Cham, 47-69.

Schlunegger, F. & Kissling, E. (2015): Slab rollback orogeny in the Alps and evolution of the Swiss Molasse basin. Nature communications 6, 8605. DOI: 10.1038/ncomms9605.

Schlunegger, F. & Kissling, E. (2022): Slab Load Controls Beneath the Alps on the Source-to-Sink Sedimentary Pathways in the Molasse Basin. Geosciences 12/6, 226. DOI: 10.3390/geosciences12060226.

Schlunegger, F., Matter, A., Burbank, D.W., Leu, W., Mange, M. & Màtyàs, J. (1997): Sedimentary sequences, seismofacies and evolution of depositional systems of the Oligo/Miocene Lower Freshwater Molasse Group, Switzerland. Basin Research 9/1, 1-26. DOI: 10.1046/j.1365-2117.1997.00029.x.

Schlunegger, F. & Mosar, J. (2011): The last erosional stage of the Molasse Basin and the Alps. International Journal of Earth Sciences (Geologische Rundschau) 100/5, 1147-1162. DOI: 10.1007/s00531-010-0607-1.

Schmassmann, H. (1945): Stratigraphie des mittleren Doggers der Nordschweiz. Inaugural-dissertation. Philosophisch-naturwissenschaftliche Fakultät der Universität Basel.

Schmassmann, H.-J., Kullin, M. & Wexsteen, P. (1990): Hydrochemische Synthese Nordschweiz: Tertiär- und Malm-Aquifere. Nagra Technischer Bericht NTB 88-07.

Schmid, D.U., Leinfelder, R. & Schweigert, G. (2005): Stratigraphy and palaeoenvironments of the Upper Jurassic of Southern Germany – A review. Zitteliana B26 26, 31-41.

Schmid, S.M., Fügenschuh, B., Kissling, E. & Schuster, R. (2004): Tectonic map and overall architecture of the Alpine orogen. Eclogae Geologicae Helvetiae 97/1, 93-117.

Schmid, S.M., Pfiffner, O.A., Froitzheim, N., Schönborn, G. & Kissling, E. (1996): Geophysical-geological transect and tectonic evolution of the Swiss-Italian Alps. Tectonics 15/5, 1036-1064. DOI: 10.1029/96TC00433.

Schmincke, H.U. (2007): The Quaternary Volcanic Fields of the East and West Eifel (Germany). *In:* Ritter, J. & Christensen, U.R. (eds.): Mantle plumes. A multidisciplinary approach. Springer, Berlin, 241-322.

Schneebeli-Hermann, E., Looser, N., Hochuli, P.A., Furrer, H., Reisdorf, A.G., Wetzel, A. & Bernasconi, S.M. (2018): Palynology of Triassic–Jurassic boundary sections in northern Switzerland. Swiss Journal of Geosciences 111/1-2, 99-115. DOI: 10.1007/s00015-017-0286-z.

Schnellmann, M., Fischer, U., Heuberger, S. & Kober, F. (2014): Erosion und Landschafts-entwicklung der Nordschweiz. Zusammenfassung der Grundlagen im Hinblick auf die Beurteilung der Langzeitstabilität eines geologischen Tiefenlagers (SGT Etappe 2). Nagra Arbeitsbericht NAB 14-25.

Schöpfer, K., Decker, K., Nazari, F. & Madritsch, H. (2024): 3D-seismic evidence for thick-skinned tectonics in a 'classic' thin skinned tectonics region (external Alpine foreland, Switzerland). Terra Nova 36/3, 217-229. DOI: 10.1111/ter.12701.

Schori, M. (2021): The Development of the Jura Fold-and-Thrust Belt: pre-existing Basement Structures and the Formation of Ramps. Thèse Université de Fribourg no. 4394 (GeoFocus 50).

Schori, M., Zwaan, F., Schreurs, G. & Mosar, J. (2021): Pre-existing basement faults controlling deformation in the Jura Mountains Fold-and-Thrust Belt: Insights from analogue models. Tectonophysics 814, 228980. DOI: 10.1016/j.tecto.2021.228980.

Schreiner, A. (1992): Geologische Karte 1:50 000 Baden- Württemberg, Erläuterungen zu Blatt Hegau und westlicher Bodensee. 3. Aufl., Freiburg i.Br. Geologisches Landesamt Baden-Württemberg.

Schumacher, M.E. (2002): Upper Rhine Graben: Role of preexisting structures during rift evolution. Tectonics 21/1, 1006. DOI: 10.1029/2001TC900022.

Schuster, B., Amschwand, D., Huber, M.L., Madritsch, H., Deplazes, G. & Buechi, M.W. (2020): Quaternary Borehole QBO Kleinandelfingen-Laubhau (QKLA) Data Report. Nagra Arbeitsbericht NAB 20-03.

Sebok, E., Henriksen, H.J., Pastén-Zapata, E., Berg, P., Thirel, G., Lemoine, A., Lira-Loarca, A., Photiadou, C., Pimentel, R., Royer-Gaspard, P., Kjellström, E., Christensen, J.H., Vidal, J.P., Lucas-Picher, P., Donat, M.G., Besio, G., Polo, M.J., Stisen, S., Caballero, Y., Pechlivanidis, I.G., Troldborg, L. & Refsgaard, J.C. (2022): Use of expert elicitation to assign weights to climate and hydrological models in climate impact studies. Hydrology and Earth System sciences 26/21, 5605-5625. DOI: 10.5194/hess-26-5605-2022.

Seiphoori, A. (2019a): Self-sealing of fractures in Opalinus Clay: experiments and a conceptual framework for quantitative assessments. Nagra Arbeitsbericht NAB 19-07.

Seiphoori, A. (2019b): The effects of burial diagenesis on Opalinus clay behavior: a multiscale study of the pore structure and mechanical properties. Nagra Arbeitsbericht NAB 19-06.

Seiphoori, A., Whittle, A.J., Krakowiak, K.J. & Einstein, H.H. (2017): Insights into diagenesis and pore structure of Opalinus shale through comparative studies of natural and reconstituted materials. Clays and Clay Minerals 65/2, 135-153. DOI: 10.1346/CCMN.2017.064055.

Serpelloni, E., Cavaliere, A., Martelli, L., Pintori, F., Anderlini, L., Borghi, A., Randazzo, D., Bruni, S., Devoti, R., Perfetti, P. & Cacciaguerra, S. (2022): Surface Velocities and Strain-Rates in the Euro-Mediterranean Region From Massive GPS Data Processing. Frontiers in Earth Sciences 10, 907897. DOI: 10.3389/feart.2022.907897.

SFOE (2008): Sectoral plan for deep geological repositories. Conceptual part. Federal Department of the Environment, Transport, Energy and Communications DETEC, Bern.

Simpson, R.W. (1997): Quantifying Anderson's fault types. Journal of Geophysical Research 102/B8, 17909-17919. DOI: 10.1029/97JB01274.

Sinclair, H.D. & Allen, P.A. (1992): Vertical versus horizontal motions in the Alpine orogenic wedge: stratigraphic response in the foreland basin. Basin Research 4/3-4, 215-232. DOI: 10.1111/j.1365-2117.1992.tb00046.x.

Smeraglia, L., Looser, N., Fabbri, O., Choulet, F., Guillong, M. & Bernasconi, S.M. (2021): U–Pb dating of middle Eocene–Pliocene multiple tectonic pulses in the Alpine foreland. Solid Earth 12/11, 2539-2551. DOI: 10.5194/se-12-2539-2021.

Soler, J.M. (1999): Coupled transport phenomena in the Opalinus clay: Implications for radionuclide transport. Nagra Technical Report NTB 99-09.

Soler, J.M. (2001): The effect of coupled transport phenomena in the Opalinus Clay and implications for radionuclide transport. Journal of Contaminant Hydrology 53/1-2, 63-84. DOI: 10.1016/s0169-7722(01)00140-1.

Soler, J.M., Steefel, C.I., Gimmi, T., Leupin, O.X. & Cloet, V. (2019): Modeling the ionic strength effect on diffusion in clay. The DR-A experiment at Mont Terri. ACS Earth Space Chemistry 3/3, 442-451. DOI: 10.1021/acsearthspacechem.8b00192.

Sommaruga, A. (1997): Geology of the central Jura and the molasse basin : new insight into an evaporite-based foreland fold and thrust belt. Société Neuchâteloise des Sciences Naturelles, Neuchâtel.

Sommaruga, A., Mosar, J., Schori, M. & Gruber, M. (2017): The Role of the Triassic Evaporites Underneath the North Alpine Foreland. *In:* Soto, J.I., Flinch, J.F. & Tari, G. (eds.): Permo-Triassic Salt Provinces of Europe, North Africa and the Atlantic Margins. (Tectonics and Hydrocarbon Potential). Elsevier, 447-466.

Soom, F., Guglielmi, Y., Cook, P., Hopp, C., Rodriguez Tribaldos, V., Lanyon, G., Nussbaum, C., Schefer, S. & Birkholzer, J. (2021): Long-term evolution of fault transmissivity following a field scale controlled activation experiment in Opalinus Clay, Mt Terri, Switzerland. Abstracts. AGU Fall Meeting 2021, MR52A-06.

Spillmann, T., Schoenball, M., Tanner, R. & Diehl, T. (2022): Ergänzung Schwachbebennetz in der Nordschweiz: Installation Bohrlochseismometer Bülach-1. Nagra Arbeitsbericht NAB 22-26.

Staiger, J.K.W., Gosse, J.C., Johnson, J.V., Fastook, J., Gray, J.T., Stockli, D.F., Stockli, L. & Finkel, R. (2005): Quaternary relief generation by polythermal glacier ice. Earth Surface Processes and Landforms 30/9, 1145-1159. DOI: 10.1002/esp.1267.

Stampfli, G. & Borel, G.D. (2002): A plate tectonic model for the Paleozoic and Mesozoic constrained by dynamic plate boundaries and restored synthetic oceanic isochrons. Earth and Planetary Science Letters 196/1-2, 17-33. DOI: 10.1016/S0012-821X(01)00588-X.

Stampfli, G., Mosar, J., Marquer, D., Marchant, R., Baudin, T. & Borel, G. (1998): Subduction and obduction processes in the Swiss Alps. Tectonophysics 296/1-2, 159-204. DOI: 10.1016/S0040-1951(98)00142-5.

Staude, S., Werner, W., Mordhorst, T., Wemmer, K., Jacob, D.E. & Markl, G. (2012): Multi-stage Ag–Bi–Co–Ni–U and Cu–Bi vein mineralization at Wittichen, Schwarzwald, SW Germany: geological setting, ore mineralogy, and fluid evolution. Mineralium Deposita 47/3, 251-276. DOI: 10.1007/s00126-011-0365-4.

Steffen, H., Olesen, O. & Sutinen, R. (eds.) (2022): Glacially-triggered faulting. Cambridge University Press, Cambridge.

Steininger, F.F., Berggren, W.A., Kent, D.V., Bernor, R.L., Sen, S. & Agusti, J. (1996): Circum-Mediterranean Neogene (Miocene and Pliocene) marine-continental chronologic correlations of European mammal units. *In:* Bernor, R.L., Fahlbusch, V. & Mittmann, H.-W. (eds.): The Evolution of Western Eurasian Neogene Mammal Faunas. Columbia University Press, New York, 7-46.

Sternai, P., Sue, C., Husson, L., Serpelloni, E., Becker, T.W., Willett, S.D., Faccenna, C., Di Giulio, A., Spada, G., Jolivet, L., Valla, P., Petit, C., Nocquet, J.-M., Walpersdorf, A. & Castelltort, S. (2019): Present-day uplift of the European Alps: Evaluating mechanisms and models of their relative contributions. Earth-Science Reviews 190, 589-604. DOI: 10.1016/j.earscirev.2019.01.005.

Stober, I., Grimmer, J. & Kraml, M. (2023): The Muschelkalk aquifer of the Molasse basin in SW-Germany: implications on the origin and development of highly saline lithium-rich brines in calcareous hydrothermal reservoirs. Geothermal Energy 11, 27. DOI: 10.1186/s40517-023-00270-6.

Stober, I., Jodocy, M. & Hintersberger, B. (2013): Comparison of hydraulic conductivities determined with different methods in the Upper Jurassic of the southwest German Molasse Basin. Zeitschrift der Deutschen Gesellschaft für Geowissenschaften ZDGG 164/4, 663-679. DOI: 10.1127/1860-1804/2013/0033.

Stober, I. & Villinger, E. (1997): Hydraulisches Potential und Durchlässigkeit des höheren Oberjuras und des Oberen Muschelkalks unter dem baden-württembergischen Molassebecken. Jahreshefte des Geologischen Landesamts Baden-Württemberg 37, 77-96.

Strasser, A., Védrine, S. & Stienne, N. (2012): Rate and synchronicity of environmental changes on a shallow carbonate platform (Late Oxfordian, Swiss Jura Mountains). Sedimentology 59/1, 185-211. DOI: 10.1111/j.1365-3091.2011.01236.x.

Studer, M. & Zanini, M. (2013): Aufbau und Betrieb eines eigenständigen CORS-GNSS Netzes. Kurzbericht (für interessierte Dritte). Nagra Arbeitsbericht NAB 10-14.

Stumm, D. (2010): Deep glacial erosion. Review with focus on tunnel valleys in northern Europe. Nagra Arbeitsbericht NAB 10-33.

Swift, D.A., Cook, S., Heckmann, T., Moore, J., Gärtner-Roer, I. & Korup, O. (2015): Ice and Snow as Land-Forming Agents. *In:* Haeberli, W. & Whiteman, C. (eds.): Snow and Ice-Related Hazards, Risks, and Disasters. Elsevier, Amsterdam, 167-199.

swissnuclear (2013): PEGASOS Refinement Project Probabilistic Seismic Hazard Analysis for Swiss Nuclear Power Plant Sites. Volumes 1 Summary Report. swissnuclear, Olten.

Swisstopo (ed.) (2005): Tektonische Karte der Schweiz 1:500'000. Bundesamt für Landestopografie swisstopo, Wabern.

Talento, S. & Ganopolski, A. (2021): Reduced-complexity model for the impact of anthropogenic CO_2 emissions on future glacial cycles. Earth System Dynamics 12/4, 1275-1293. DOI: 10.5194/esd-12-1275-2021.

Tevissen, E. & Soler, J.M. (2003): In situ diffusion experiment (DI): Synthesis report. Mont Terri Technical Report TR 01-05. Mont Terri Project, Switzerland.

Thew, N., Kälin, D., Cuenca-Bescós, G., Buechi, M.W., Penkman, K., Scheidt, S., Knipping, M., Maier, F., Urresti, I. & Deplazes, G. (2024): The Hasli Formation of the Irchel Plateau – A key record for older Early Pleistocene interglacial sediments in northern Switzerland. Quaternary Science Reviews 332, 108550. DOI: 10.1016/j.quascirev.2024.108550.

Thiercelin, M.J. & Plumb, R.A. (1994): Core-Based Prediction of Lithologic Stress Contrasts in East Texas Formations. SPE Formation Evaluation 9/4, 251-258. DOI: 10.2118/21847-PA.

Thury, M., Gautschi, A., Mazurek, M., Müller, W.H., Naef, H., Pearson, F.J., Vomvoris, S. & Wilson, W. (1994): Geology and hydrogeology of the crystalline basement of Northern Switzerland. Nagra Technical Report NTB 93-01.

Timar-Geng, Z., Fügenschuh, B., Wetzel, A. & Dresmann, H. (2006): Low-temperature thermochronology of the flanks of the southern Upper Rhine Graben. International Journal of Earth Sciences (Geologische Rundschau) 95, 685-702. DOI: 10.1007/s00531-005-0059-1.

Tomonaga, Y., Buechi, M.W., Deplazes, G. & Kipfer, R. (2024): First dating of an early Chibanian (Middle Pleistocene) glacial overdeepening in the Alpine Foreland using the 4He/U-Th method. Geology. DOI: 10.1130/G52544.1.

Tournassat, C. & Steefel, C.I. (2019): Reactive transport modeling of coupled processes in nanoporous media. Reviews in Mineralogy and Geochemistry 85, 75-109.

Tournassat, C. & Steefel, C.I. (2021): Modeling diffusion processes in the presence of a diffuse layer at charged mineral surfaces: A benchmark exercise. Computational Geosciences 25, 1319-1336.

Townend, J. & Zoback, M.D. (2000): How faulting keeps the crust strong. Geology 28/5, 399-402. DOI: 10.1130/0091-7613(2000)28<399:HFKTCS>2.0.CO;2.

Trümpy, R. (1959): Hypothesen über die Ausbildung von Trias, Lias und Dogger im Untergrund des schweizerischen Molassebeckens. Eclogae Geologicae Helvetiae 52/2, 435-448.

Trümpy, R. (1980): Geology of Switzerland: A guide-book. Part A. An Outline of the Geology of Switzerland. Wepf & Co, Basel.

Tsang, C.-F., Bernier, F. & Davies, C. (2005): Geohydromechanical processes in the Excavation Damaged Zone in crystalline rock, rock salt, and indurated and plastic clays — in the context of radioactive waste disposal. International Journal of Rock Mechanics and Mining Sciences 42/1, 109-125. DOI: 10.1016/j.ijrmms.2004.08.003.

Turcotte, D.L. & Schubert, G. (2014): Geodynamics. 3rd ed. Cambridge University Press, Cambridge.

Turowski, J.M., Lague, D. & Hovius, N. (2007): Cover effect in bedrock abrasion: A new derivation and its implications for the modeling of bedrock channel morphology. Journal of Geophysical Research: Earth Surface 112/F4, 2006JF000697. DOI: 10.1029/2006JF000697.

Turowski, J.M., Pruß, G., Voigtländer, A., Ludwig, A., Landgraf, A., Kober, F. & Bonnelye, A. (2023): Geotechnical controls on erodibility in fluvial impact erosion. Earth Surface Dynamics 11/5, 979-994. DOI: 10.5194/esurf-11-979-2023.

Tütken, T. (2014): Isotope compositions (C, O, Sr, Nd) of vertebrate fossils from the Middle Eocene oil shale of Messel, Germany: Implications for their taphonomy and palaeoenvironment. Palaeogeography, Palaeoclimatology, Palaeoecology 416, 92-109. DOI: 10.1016/j.palaeo.2014.08.005.

Tütken, T. & Absolon, J. (2015): Late Oligocene ambient temperatures reconstructed by stable isotope analysis of terrestrial and aquatic vertebrate fossils of Enspel, Germany. Palaeobiodiversity and Palaeoenvironments 95, 17-31. DOI: 10.1007/s12549-014-0183-7.

Tütken, T. & Vennemann, T. (2009): Stable isotope ecology of Miocene large mammals from Sandelzhausen, southern Germany. Paläontologische Zeitschrift 83, 207-226. DOI: 10.1007/s12542-009-0011-y.

Tütken, T., Vennemann, T.W., Janz, H. & Heizmann, E. (2006): Palaeoenvironment and palaeoclimate of the Middle Miocene lake in the Steinheim basin, SW Germany: A reconstruction from C, O, and Sr isotopes of fossil remains. Palaeogeography, Palaeoclimatology, Palaeoecology 241/3-4, 457-491. DOI: 10.1016/j.palaeo.2006.04.007.

Ufrecht, W. (2006): Zusammensetzung und Herkunft der Gase in den Säuerlingen von Stuttgart-Bad Cannstatt und -Berg. Hydrogeologie des Stuttgarter Mineralwassersystems – Schriftenreihe des Amtes für Umweltschutz 3, 103-114.

Ufrecht, W. (2017): Zur Hydrogeologie veränderlich fester Gesteine mit Sulfatgestein, Beispiel Gipskeuper (Trias, Grabfeld-Formation). Grundwasser 22, 197-208. DOI: 10.1007/s00767-017-0362-3.

Ufrecht, W. (2018): Die Tiefengrundwässer im Oberen Muschelkalk zwischen Albvorland und oberschwäbischem Molassebecken – ein Hydrogeologisches Modell. Schriftenreihe des Amtes für Umweltschutz 1, 7-158.

Ustaszewski, K. & Schmid, S.M. (2007): Neotectonic activity in the Upper Rhine Graben - Jura Mountains junction (North-Western Switzerland and adjacent France). Bulletin für angewandte Geologie 12/1, 3-19.

van der Vegt, P., Janszen, A. & Moscariello, A. (2012): Tunnel valleys: current knowledge and future perspectives. Geological Society, London, Special Publications 368, 75-97. DOI: 10.1144/SP368.13.

Van Loon, L.R., Bunic, P., Frick, S., Glaus, M.A. & Wüst, R. (2023): Diffusion of HTO, ^{36}Cl and ^{22}Na in the Mesozoic rocks of northern Switzerland: I. Effective diffusion coefficients and capacity factors across the heterogeneous sediment sequences. Applied Geochemistry 159, 105843. DOI: 10.1016/j.apgeochem.2023.105843.

Van Loon, L.R., Glaus, M.A., Bunic, P., Frick, S. & Wüst, R. (2024): Diffusion Measurements of HTO, 36Cl- and 22Na+ on Rock Samples of Opalinus Clay and Confining Geological Units from Deep Boreholes of Northern Switzerland: Jura Ost, Nördlich Lägern and Zürich Nordost. Nagra Arbeitsbericht NAB 23-26.

Van Loon, L.R., Soler, J.M., Müller, W. & Bradbury, M.H. (2004a): Anisotropic diffusion in layered argillaceous rocks: a case study with Opalinus Clay. Environmental science & technology 38/21, 5721-5728. DOI: 10.1021/es049937g.

Van Loon, L.R., Wersin, P., Soler, J.M., Eikenberg, J., Gimmi, T., Hernán, P., Dewonck, S. & Savoye, S. (2004b): In-situ diffusion of HTO, $^{22}Na^{+}$, Cs^{+} and I^{-} in Opalinus Clay at the Mont Terri underground rock laboratory. Radiochimica Acta 92/9-11, 757-763. DOI: 10.1524/ract.92.9.757.54988.

Vandorpe, T.P., van Rooij, D., Stow, D.A.V. & Henriet, J.-P. (2011): Pliocene to Recent shallow-water contourite deposits on the shelf and shelf edge off south-western Mallorca, Spain. Geo-Marine Letters 31/5-6, 391-403. DOI: 10.1007/s00367-011-0248-9.

Védrine, S. & Strasser, A. (2009): High-frequency palaeoenvironmental changes on a shallow carbonate platform during a marine transgression (Late Oxfordian, Swiss Jura Mountains). Swiss Journal of Geosciences 102/2, 247-270. DOI: 10.1007/s00015-009-1326-0.

Verdicchio, G. & Trincardi, F. (2008): Mediterranean shelf-edge muddy contourites: examples from the Gela and South Adriatic basins. Geo-Marine Letters 28/3, 137-151. DOI: 10.1007/s00367-007-0096-9.

Villagómez Díaz, D., Omodeo-Salé, S., Ulyanov, A. & Moscariello, A. (2021): Insights into the thermal history of North-Eastern Switzerland - Apatite fission track dating of deep drill core samples from the Swiss Jura Mountains and the Swiss Molasse Basin. Geosciences 11/10, 1-21. DOI: 10.3390/geosciences11010010.

Villinger, E. (2003): The Palaeogeography of the rivers Alpenrhein and Upper Danube. Zeitschrift der Deutschen Geologischen Gesellschaft 154/2-3, 193-253. DOI: 10.1127/zdgg/154/2003/193.

Vinard, P. (1998): Generation and evolution of hydraulic underpressures in a marl-shale aquitard at Wellenberg, Central Switzerland. PhD Thesis, University of Neuchâtel.

Voborny, O., Resele, G., Hürlimann, W., Lanyon, G.W., Vomvoris, S. & Wilson, W. (1994): Hydrodynamic synthesis and modeling of groundwater flow in crystalline rocks of Northern Switzerland. Nagra Technical Report NTB 92-04.

Vogt, T., Ebert, A., Häring, C., Becker, J., Traber, D., Deplazes, G., Bläsi, H.R. & Rufer, D. (2016): Kernbohrung Lausen: Geologische, hydrogeologische und bohrloch-geophysikalische Untersuchungen (Rohdatenbericht). Nagra Arbeitsbericht NAB 15-10.

Vogt, T., Hekel, U., Ebert, A., Becker, J., Traber, D., Giger, S., Brod, M. & Häring, C. (2017): Hydrogeologische Untersuchungen im oberflächennahen Opalinuston (Bohrloch Lausen, Schweiz). Grundwasser 22/3, 209-220. DOI: 10.1007/s00767-017-0363-2.

Voltolini, M. & Ajo-Franklin, J.B. (2020): The sealing mechanisms of a fracture in Opalinus Clay as revealed by in situ Synchrotron X-Ray Micro-Tomography. Frontiers in Earth Sciences 8, 207. DOI: 10.3389/feart.2020.00207.

von Hagke, C., Cederbom, C.E., Oncken, O., Stöckli, D.F., Rahn, M.K. & Schlunegger, F. (2012): Linking the northern Alps with their foreland: The latest exhumation history resolved by low-temperature thermochronology. Tectonics 31/5, 2011TC003078. DOI: 10.1029/2011TC003078.

von Hagke, C., Lujiendjik, E., Ondrak, R. & Lindow, J. (2015): Quantifying erosion rates in the Molasse basin using a high resolution data set and a new thermal model. Geotectonic Research 97/1, 94-97. DOI: 10.1127/1864-5658/2015-36.

von Hagke, C., Oncken, O. & Evseev, S. (2014): Critical taper analysis reveals lithological control of variations in detachment strength: An analysis of the Alpine basal detachment (Swiss Alps). Geochemistry, Geophysics, Geosystems 15/1, 176-191. DOI: 10.1002/2013GC005018.

VSS (2019): Fels Quellversuche. VSS-70356. Schweizerischer Verband der Strassen- und Verkehrsfachleute VSS, Zürich.

Waber, H.N. (ed.) (2020): SGT-E3 deep drilling campain (TBO): Experiment Procedures and Analytical Methods at RWI, University of Bern (Version 1.0, 28.04.2020). Nagra Arbeitsbericht NAB 20-13.

Waber, H.N. & Rufer, D. (2017): Porewater geochemistry, method comparison and Opalinus Clay – Passwang Formation interface study at the Mont Terri URL. Mont Terri Technical Report TR 17-02. Mont Terri Project, Switzerland.

Waber, H.N. & Traber, D. (2022): Die Tiefengrundwässer in der Nordschweiz und im angrenzenden Süddeutschland: Beschaffenheit, Herkunft und unterirdische Verweilzeit. Nagra Technischer Bericht NTB 19-02.

Walker, M., Johnsen, S., Rasmussen, S.O., Popp, T., Steffensen, J.-P., Gibbard, P.L., Hoek, W., Andrews, J., Björck, S., Cwynar, L.C., Hughen, K., Kershaw, P., Kromer, B., Litt, T., Lowe, D.J., Nakagawa, T., Newnham, R. & Schwander, J. (2009): Formal definition and dating of the GSSP (Global Stratotype Section and Point) for the base of the Holocene using the Greenland NGRIP ice core, and selected auxiliary records. Journal of Quaternary Science 24/1, 3-17. DOI: 10.1002/jqs.1227.

Wallace, R.E. (1984): Patterns and timing of Late Quaternary faulting in the Great Basin Province and relation to some regional tectonic features. Journal of Geophysical Research 89/B7, 5763-5769. DOI: 10.1029/jb089ib07p05763.

Walsh, J.J., Watterson, J., Bailey, W.R. & Childs, C. (1999): Fault relays, bends and branch-lines. Journal of Structural Geology 21/8-9, 1019-1026. DOI: 10.1016/S0191-8141(99)00026-7.

Wang, C.-Y. & Manga, M. (2010): Earthquakes and water. (Lecture Notes in Earth Sciences, 114). Springer, Berlin.

Wang, H., La Vaissière, R. de, Vu, M.-N., La Borderie, C. & Gallipoli, D. (2022): Numerical modelling and in-situ experiment for self-sealing of the induced fracture network of drift into the Callovo-Oxfordian claystone during a hydration process. Computers and Geotechnics 141, 104487. DOI: 10.1016/j.compgeo.2021.104487.

Warnecke, M. & Aigner, T. (2019): Asymmetry of an epicontinental basin — facies, cycles, tectonics and hydrodynamics: The Triassic Upper Muschelkalk, South Germanic Basin. Depositional Rec 2019/5, 147-187. DOI: 10.1002/dep2.59.

Warnecke, M.J. (2018): Carbonate Concepts: Reservoir Patterns of the Upper Muschelkalk in the Southern Germanic Basin. Dissertation, Eberhard Karls Universität Tübingen.

Washburn, A.L. (1979): Geocryology. A survey of periglacial processes and environments. 2nd ed. Edward Arnold, London.

Wenning, Q.C., Madonna, C., Kurotori, T., Petrini, C., Hwang, J., Zappone, A., Wiemer, S., Giardini, D. & Pini, R. (2021a): Chemo-mechanical coupling in fractured shale with water and hydrocarbon flow. Geophysical Research Letters 48/5, e2020GL091357.

Wenning, Q.C., Madonna, C., Zappone, A., Grab, M., Rinaldi, A.P., Plötze, M., Nussbaum, C., Giardini, D. & Wiemer, S. (2021b): Shale fault zone structure and stress dependent anisotropic permeability and seismic velocity properties (Opalinus Clay, Switzerland). Journal of Structural Geology 144, 104273. DOI: 10.1016/j.jsg.2020.104273.

Wernicke, R.S. & Lippolt, H.J. (1997): (U+Th)–He evidence of Jurassic continuous hydrothermal activity in the Schwarzwald basement, Germany. Chemical Geology 138/3-4, 273-285. DOI: 10.1016/S0009-2541(97)00020-X.

Wersin, P., Appelo, C.A.J., Baeyens, B., Bossart, P., Dewonck, S., Eikenberg, J., Fierz, T., Fisch, H.R., Gimmi, T., Grolimund, D., Leupin, O., Möri, A., Soler, J.M., van Dorp, F. & Van Loon, L. (2010): Long-term Diffusion (DI-A) Experiment: DI-A2: Diffusion of HTO, Br-, I-, Cs+, 85Sr2+ and 60Co2+: Field activities, data and modelling. Mont Terri Technical Report TR 09-04. Mont Terri Project, Switzerland.

Wersin, P., Baeyens, B., Bossart, P., Cartalade, A., Dewonck, S., Eikenberg, J., Fierz, T., Fisch, H.R., Gimmi, T., Grolimund, D., Hernán, P., Möri, A., Savoye, S., Soler, J., van Dorp, F. & Van Loon, L. (2006): Long-term Diffusion Experiment (DI-A): Diffusion of HTO, I^-, $^{22}Na^+$ and Cs^+: Field activities, data and modelling. Mont Terri Technical Report TR 03-06. Mont Terri Project, Switzerland.

Wersin, P., Gimmi, T., Ma, J., Mazurek, M., Zwahlen, C., Aschwanden, L., Gaucher, E. & Traber, D. (2023): Porewater profiles of Cl and Br in boreholes penetrating the Mesozoic sequence in northern Switzerland. Applied Geochemistry 159, 105845. DOI: 10.1016/j.apgeochem.2023.105845.

Wersin, P., Gimmi, T., Mazurek, M., Alt-Epping, P., Pekala, M. & Traber, D. (2018): Multicomponent diffusion in a 280m thick argillaceous rock sequence. Applied Geochemistry 95, 110-123. DOI: 10.1016/j.apgeochem.2018.05.013.

Wersin, P., Mazurek, M., Mäder, U.K., Gimmi, T., Rufer, D., Lerouge, C. & Traber, D. (2016): Constraining porewater chemistry in a 250 m thick argillaceous rock sequence. Chemical Geology 434, 43-61. DOI: 10.1016/j.chemgeo.2016.04.006.

Wersin, P., Mazurek, M., Waber, H.N., Mäder, U.K., Gimmi, T., Rufer, D. & de Haller, A. (2013): Rock and porewater characterisation on drillcores from the Schlattingen borehole. Nagra Arbeitsbericht NAB 12-54.

Wersin, P., Pekala, M., Mazurek, M., Gimmi, T., Mäder, U., Jenni, A., Rufer, D. & Aschwanden, L. (2020): Porewater chemistry of Opalinus Clay: Methods, data, modelling & buffering capacity. Nagra Technical Report NTB 18-01.

Wersin, P., Soler, J.M., Van Loon, L., Eikenberg, J., Baeyens, B., Grolimund, D., Gimmi, T. & Dewonck, S. (2008): Diffusion of HTO, Br−, I−, Cs+, $^{85}Sr^{2+}$ and $^{60}Co^{2+}$ in a clay formation: Results and modelling from an in situ experiment in Opalinus Clay. Applied Geochemistry 23/4, 678-691. DOI: 10.1016/j.apgeochem.2007.11.004.

Westerhoff, W.E., Kemna, H.A. & Boenigk, W. (2008): The confluence area of Rhine, Meuse, and Belgian rivers: Late Pliocene and Early Pleistocene fluvial history of the northern Lower Rhine Embayment. Netherlands Journal of Geosciences - Geologie en Mijnbouw 87/1, 107-125. DOI: 10.1017/S0016774600024070.

Wetzel, A., Allenbach, R. & Allia, V. (2003): Reactivated basement structures affecting the sedimentary facies in a tectonically "quiescent" epicontinental basin: An example from NW Switzerland. Sedimentary Geology 157/1-2, 153-172. DOI: 10.1016/S0037-0738(02)00230-0.

Wetzel, A. & Allia, V. (1996): Der Ablagerungsraum des Opalinuston - Eine sedimentologische Analyse. LGRB-Informationen 8, 20-24.

Wetzel, A. & Allia, V. (2000): The significance of hiatus beds in shallow-water mudstones: An example from the Middle Jurassic of Switzerland. Journal of Sedimentary Research 70/1, 170-180. DOI: 10.1306/2DC40908-0E47-11D7-8643000102C1865D.

Wetzel, A. & Allia, V. (2003): Der Opalinuston in der Nordschweiz: Lithologie und Ablagerungsgeschichte. Eclogae Geologicae Helvetiae 96/3, 451-469. DOI: 10.5169/seals-169032.

Wetzel, A., Allia, V., Gonzalez, R. & Jordan, P. (1993): Sedimentation und Tektonik im Ostjura. Bericht über die Exkursion der Schweizerischen Geologischen Gesellschaft am 29. 9. 1992. Eclogae Geologicae Helvetiae 86/1, 313-332.

Wigger, C. (2017): Anion accessibility in low porosity argillaceous rocks. Inauguraldissertation, Universität Bern.

Wildi, W. (1976): Die Molluskenfauna des Gansinger Dolomites (Trias, Karnian, Mittlerer Keuper) im aargauischen Tafeljura (Nordschweiz). Eclogae Geologicae Helvetiae 69/3, 671-684.

Wildi, W., Funk, H., Loup, B., Amato, E. & Huggenberger, P. (1989): Mesozoic subsidence history of the European marginal shelves of the alpine Tethys (Helvetic realm, Swiss Plateau and Jura). Eclogae Geologicae Helvetiae 82/3, 817-840.

Willett, S.D. (1999): Orogeny and orography: The effects of erosion on the structure of mountain belts. Journal of Geophysical Research 104/B12, 28957-28981. DOI: 10.1029/1999JB900248.

Willett, S.D., McCoy, S.W., Perron, J.T., Goren, L. & Chen, C.-Y. (2014): Dynamic reorganization of river basins. Science 343/6175, 1248765. DOI: 10.1126/science.1248765.

Willett, S.D. & Schlunegger, F. (2010): The last phase of deposition in the Swiss Molasse Basin: from foredeep to negative-alpha basin. Basin Research 22/5, 623-639. DOI: 10.1111/j.1365-2117.2009.00435.x.

Winhausen, L., Khaledi, K., Jalali, M., Urai, J.L. & Amann, F. (2022): Failure mode transition in Opalinus Clay: a hydro-mechanical and microstructural perspective. Solid Earth 13/5, 901-915. DOI: 10.5194/se-13-901-2022.

Winkler, W. (2024): The North Penninic Bündnerschiefer and Flysch of the Prättigau (Swiss Alps) revisited. Swiss Journal of Geosciences 117/1, 4. DOI: 10.1186/s00015-024-00454-7.

Winterberg, S. & Willett, S.D. (2019): Greater Alpine river network evolution, interpretations based on novel drainage analysis. Swiss Journal of Geosciences 112/1, 3-22. DOI: 10.1007/s00015-018-0332-5.

Wittmann, H., Blanckenburg, F. von, Kruesmann, T., Norton, K.P. & Kubik, P.W. (2007): Relation between rock uplift and denudation from cosmogenic nuclides in river sediment in the Central Alps of Switzerland. Journal of Geophysical Research: Earth Surface 112/F4. DOI: 10.1029/2006JF000729.

Wittmann, O. (1937): Deckentuff und Molasse am Höwenegg. Ein Beitrag zur Entwicklungsgeschichte des Hegauvulkans. Jahresberichte und Mitteilungen des Oberrheinischen Geologischen Vereins 26, 1-32. DOI: 10.1127/jmogv/26/1937/1.

Wohlwend, S., Bläsi, H.R., Feist-Burkhardt, S., Hostettler, B., Menkveld-Gfeller, U., Dietze, V. & Deplazes, G. (2019): Die Passwang-Formation im östlichen Falten- und Tafeljura: Fasiswald (SO) – Unt. Hauenstein (SO) – Wasserflue (AG) – Thalheim (AG) – Frickberg (AG) – Cheisacher (AG) – Böttstein (AG) – Tegerfelden (AG) – Acheberg (AG). Nagra Arbeitsbericht NAB 18-11.

Wohlwend, S., Hostettler, B., Menkveld-Gfeller, U., Feist-Burkhardt, S., Bläsi, H., Zimmerli, G.N., Dietze, V., Bernasconi, S.M. & Deplazes, G. (2024): High-resolution bio- and chemostratigraphy of the Toarcian to Aalenian of Northern Switzerland with a focus on the Opalinus Clay. Newsletters on Stratigraphy. DOI: 10.1127/nos/2024/0823.

Woillard, G. (1979): The last interglacial-glacial cycle at Grande Pile in Northeastern France. Bulletin de la Societe Belge de Geologie 88/1-2, 51-69.

Wu, P. & Peltier, W.R. (1982): Viscous gravitational relaxation. Geophysical Journal International 70/2, 435-485. DOI: 10.1111/j.1365-246X.1982.tb04976.x.

Wullschleger, E. (1966): Bemerkungen zum fossilen Korallenriff Gisliflue-Homberg. Mitteilungen der Aargauischen Naturforschenden Gesellschaft 27, 101-152. DOI: 10.5169/seals-172523.

Wurster, P. (1968): Paläogeographie der deutschen Trias und die paläogeographische Orientierung der Lettenkohle in Südwestdeutschland. Eclogae Geologicae Helvetiae 61/1, 157-166.

Yanites, B.J., Becker, J.K., Madritsch, H., Schnellmann, M. & Ehlers, T.A. (2017): Lithologic Effects on Landscape Response to Base Level Changes: A Modeling Study in the Context of the Eastern Jura Mountains, Switzerland. Journal of Geophysical Research: Earth Surface 122/11, 2196-2222. DOI: 10.1002/2016JF004101.

Yanites, B.J. & Ehlers, T.A. (2016): Intermittent glacial sliding velocities explain variations in long-timescale denudation. Earth and Planetary Science Letters 450, 52-61. DOI: 10.1016/j.epsl.2016.06.022.

Yanites, B.J., Ehlers, T.A., Becker, J.K., Schnellmann, M. & Heuberger, S. (2013): High magnitude and rapid incision from river capture: Rhine River, Switzerland. Journal of Geophysical Research: Earth Surface 118/2, 1060-1084. DOI: 10.1002/jgrf.20056.

Yllera, A., Hernández, A. & Wersin, P. (2004): DI-B experiment: planning, design and performance of an in situ diffusion experiment in the Opalinus clay formation. Applied Clay Science Special Issue: Clays in natural and engineered barriers for radioactive waste confinement: Papers from the ANDRA meeting, Reims, 2002 26/1-4, 181-196.

Zambrano, M., Mazzoli, S. & Mosar, J. (*submitted*): Modes of deformation in sedimentary multilayers interacting with sub-décollement structures: insights from 3D seismic interpretation in the eastern Jura fold and thrust belt.

Zaugg, A., Geyer, M., Rahn, M., Wessels, M., Schlichtherle, H., Hasenfratz, A. & Burkhalter, R. (2008): Geologischer Atlas der Schweiz. Blatt 1033/1034 Steckborn-Kreuzlingen (Atlasblatt 112) mit Erläuterungen. Bundesamt für Landestopografie swisstopo.

Zaugg, A. & Vogel, G. (2014): Geologie und Hydrogeologie der Oberen Süsswassermolasse: Zusammenfassende Darstellung. Nagra Arbeitsbericht NAB 07-32 Rev. 1.

Zhang, C.-L. (2013): Sealing of fractures in claystone. Journal of Rock Mechanics and Geotechnical Engineering 5/3, 214-220. DOI: 10.1016/j.jrmge.2013.04.001.

Zhang, C.-L., Rothfuchs, T., Dittrich, J. & Müller, J. (2008): Investigations on self-sealing of indurated clay. Part of the NF-PRO Project. GRS-230. Gesellschaft für Anlagen- und Reaktorsicherheit (GRS) mbH, Braunschweig.

Zhang, C.-L. & Talandier, J. (2023): Self-sealing of fractures in indurated claystones measured by water and gas flow. Journal of Rock Mechanics and Geotechnical Engineering 15/1, 227-238. DOI: 10.1016/j.jrmge.2022.01.014.

Ziegler, M., Alimardani Lavasan, A. & Loew, S. (2022): Stress evolution around a TBM tunnel in swelling clay shale over four years after excavation. Tunelling and Underground Space Technology 128, 104649. DOI: 10.1016/j.tust.2022.104649.

Ziegler, P.A. (1990): Geological atlas of western and central Europe 1990. Shell International Petroleum Maatschappij, The Hague.

Ziegler, P.A. (1992): European Cenozoic rift system. Tectonophysics 208/1-3, 91-111. DOI: 10.1016/0040-1951(92)90338-7.

Ziegler, P.A. & Dèzes, P. (2005): Evolution of the lithosphere in the area of the Rhine Rift System. International Journal of Earth Sciences (Geologische Rundschau) 94/4, 594-614. DOI: 10.1007/s00531-005-0474-3.

Ziegler, P.A. & Dèzes, P. (2007): Cenozoic uplift of Variscan Massifs in the Alpine foreland: Timing and controlling mechanisms. Global and Planetary Change 58/1-4, 237-269. DOI: 10.1016/j.gloplacha.2006.12.004.

Ziegler, P.A. & Fraefel, M. (2009): Response of drainage systems to Neogene evolution of the Jura fold-thrust belt and Upper Rhine Graben. Swiss Journal of Geosciences 102/1, 57-75. DOI: 10.1007/s00015-009-1306-4.

Zimmerli, G.N., Wohlwend, S., Deplazes, G., Becker, J., Wetzel, A., Francescangeli, F. & Foubert, A. (2024): Facies variability and depositional cyclicity in central Northern Switzerland: insights from new Opalinus Clay drill cores. Swiss Journal of Geosciences 117/1, 18. DOI: 10.1186/s00015-024-00463-6.

Zimmermann, J., Franz, M., Schaller, A. & Wolfgramm, M. (2018): The Toarcian-Bajocian deltaic system in the North German Basin: Subsurface mapping of ancient deltas-morphology, evolution and controls. Sedimentology 65/3, 897-930. DOI: 10.1111/sed.12410.

Zoback, M.D., Townend, J. & Grollimund, B. (2002): Steady-State Failure Equilibrium and Deformation of Intraplate Lithosphere. International Geology Review 44/5, 383-401. DOI: 10.2747/0020-6814.44.5.383.

Zwaan, F., Schreurs, G., Madritsch, H. & Herwegh, M. (2022): Influence of rheologically weak layers on fault architecture: insights from analogue models in the context of the Northern Alpine Foreland Basin. Swiss Journal of Geosciences 115/1, 26. DOI: 10.1186/s00015-022-00427-8.

Zwahlen, C., Gimmi, T., Jenni, A., Kiczka, M., Mazurek, M., Van Loon, L.R., Mäder, U. & Traber, D. (2024): Chloride accessible porosity fractions across the Jurassic sedimentary rocks of northern Switzerland. Applied Geochemistry 162, 105841. DOI: 10.1016/j.apgeochem.2023.105841.